

Lecture Notes in Electrical Engineering

Volume 132

Honghua Tan (Ed.)

Informatics in Control, Automation and Robotics

Volume 1



Springer

Honghua Tan
Wuhan Institute of Technology,
China
E-mail: Honghua_tan@Yahoo.cn

ISBN 978-3-642-25898-5

e-ISBN 978-3-642-25899-2

DOI 10.1007/978-3-642-25899-2

Lecture Notes in Electrical Engineering ISSN 1876-1100

Library of Congress Control Number: 2011943103

© 2011 Springer-Verlag Berlin Heidelberg

This work is subject to copyright. All rights are reserved, whether the whole or part of the material is concerned, specifically the rights of translation, reprinting, reuse of illustrations, recitation, broadcasting, reproduction on microfilm or in any other way, and storage in data banks. Duplication of this publication or parts thereof is permitted only under the provisions of the German Copyright Law of September 9, 1965, in its current version, and permission for use must always be obtained from Springer. Violations are liable to prosecution under the German Copyright Law.

The use of general descriptive names, registered names, trademarks, etc. in this publication does not imply, even in the absence of a specific statement, that such names are exempt from the relevant protective laws and regulations and therefore free for general use.

Typeset by Scientific Publishing Services Pvt. Ltd., Chennai, India.

Printed on acid-free paper

9 8 7 6 5 4 3 2 1

springer.com

Foreword

2011 3rd International Asia Conference on Informatics in Control, Automation and Robotics (CAR 2011) is held on December 24–25, 2011, Shenzhen, China.

The purpose of the 2011 3rd International Asia Conference on Informatics in Control, Automation and Robotics (CAR 2011) is to bring together researchers, engineers and practitioners interested in the application of informatics to Control, Automation and Robotics.

The conference is organized in three simultaneous tracks: “Intelligent Control Systems and Optimization”, “Robotics and Automation” and “Systems Modeling, Signal Processing and Control”. We welcome papers from all these areas.

The book is based on the same structure, and topics of particular interest include, but not limited to: Intelligent Control Systems and Optimization, Robotics and Automation, Signal Processing, Systems Modeling and Control, Communication Theory and Technology, Sensor and sensor network, Computer Theory and Technology, Electrical and Electronic Engineering, Multimedia and Network Information, Photonic and Optoelectronic Circuits, Communication Systems and Information Technology, Electrical and Electronic Engineering, Signal Processing.

Although CAR 2011 receives 850 paper submissions, only 219 were accepted as regular papers, based on the classifications provided by the Conference Committee and the reviewers. The selected papers also reflect the interdisciplinary nature of the conference. The diversity of topics is an important feature of this conference, enabling an overall perception of several important scientific and technological trends. These high quality standards will be maintained and reinforced at CAR 2011, and in future editions of this conference.

Furthermore, CAR 2011 includes 2 plenary keynote lectures given by internationally recognized researchers. They are Prof. Patrick S.P. Wang, Ph.D., Fellow, IAPR, ISIBM and WASE Northeastern University Boston, and Prof. Jun Wang, Department of Mechanical & Automation Engineering, The Chinese University of Hong Kong, Shatin, New Territories, Hong Kong. Their presentations presented an important contribution to increasing the overall quality of the conference, and are partially included in the first section of the book. We would like to express our appreciation to all the invited keynote speakers who took the time to contribute with a paper to this book.

On behalf of the conference organizing committee, we would like to thank all participants. First of all to the authors, whose quality work is the essence of the conference and to the members of the program committee, who help us with their expertise and time.

As we all know, producing a conference requires the effort of many individuals. We wish to thank all the people from IERI, whose work and commitment are invaluable.

Committee

Honorary Chair

ChinChen Chang	National Chung Hsing University, Taiwan
Patrick S.P. Wang	Fellow, IAPR, ISIBM and WASE Northeastern University Boston, USA

Program Co-chairs

Yuntao Wu	Wuhan University of Technology, China
Weitao Zheng	Wuhan University of Technology, China

Publication Co-chairs

Honghua Tan	Wuhan Insitute of Technology, China
Dehuai Yang	Huazhong Normal Universiy, China

International Committee

Wei Li	Asia Pacific Human-Computer Interaction Research Center, Hong Kong
Xiaoming Liu	Nankai University, China
Xiaoxiao Yu	Wuhan University, China
Chi Zhang	Nanchang University, China
Bo Zhang	Beijing University, China
Lei Zhang	Tianjin Institute of Urban Construction, China
Ping He	Liaoning Police Academy, China
Alireza Yazdizadeh	International Science and Engineering Center, Hong Kong
Wenjin Hu	Jiangxi Computer Study Institute, China
Qun Zeng	Nanchang University, China

Contents

Intelligent Control Systems and Optimization

A Neural Network Based Temperature Control for Air Handling Unit	1
<i>Binhui Zheng, Jiangang Lu, Qinmin Yang, Youxian Sun</i>	
Exploration on Principles of Engineering Network Course Design	9
<i>Ying Xiao, Yan Shi, Xiaoping Li</i>	
A Combined Modular Parametric and Non-parametric Method for Planar Ship Motion's On-Line Prediction	17
<i>Jianchuan Yin, Zaojian Zou</i>	
Ultrasonic Sensor Based Material Level and Liquid Level Measurement Technology	25
<i>Gong-chang Ren, Hai-chun Guo, Yong Yang, Zhi-wei Yang</i>	
Design of a 23-DOF Small Humanoid Robot with ZMP Force Sensors	31
<i>Awais Yasin, Qian Xu, Bo Chen, Qiushi Lu, M. Waqas Khan</i>	
An Advanced Ontology Mapping Framework Based on Similarity Calculating	39
<i>Hao Tian</i>	
Analysis and Design for the Financial System in ERP Simulation Instruction Based on SOA	43
<i>Gao Chang-yuan, Chen Zhi, Yang Cai-xia, Tian Shi-hai</i>	
Variational Surface Reconstruction from Sparse and Nonparallel Contours for Freehand 3D Ultrasound	51
<i>Shuangcheng Deng, Yunhua Li, Lipei Jiang, Yingyu Cao, Junwen Zhang</i>	
STGRs over Topological Spaces for Value-Passing Processes	59
<i>Huanbao Wang</i>	

Memetic Algorithm for a University Course Timetabling Problem	67
<i>Khang Nguyen, Tien Lu, Trung Le, Nuong Tran</i>	
A Class of Autonomous Robots Prepared for Unfriendly Sunny Environment	73
<i>Lucian Grigore, Recep Ileri, Cristian Neculăescu, Anton Soloi, Ticușor Ciobotaru, Valentin Vînturiș</i>	
Step by Step Modeling and Tuning for Fuzzy Logic Controller	81
<i>Mohammed Majid Mohammed Al-Khalidy, Fatma Abdulnabi Al-attar</i>	
A Novel Method for BLDCM Control Based on Phase Back-EMF Observation	93
<i>Pan Lei, Wang Beibei, Gong Wei</i>	
Design of Wireless Monitoring System Based on CAN Bus and ZigBee Technology of Tower Crane	103
<i>Xijian Zheng, Hong Zhang, Zhengyi Xie</i>	
A Security Risk Model Using Game Theory	111
<i>Marn-Ling Shing, Chen-Chi Shing</i>	
HDR Image Synthesis Based on Multi-exposure Color Images	117
<i>Hua Wang, Jianzhong Cao, Linao Tang, Yao Tang</i>	
The Further Decomposition of Actuarial Notation's Expression on Credibility Space	125
<i>Min-ying Yuan, Da-jun Sun</i>	
Research on the Layout of Shipbuilding Steel Structure Machining Plant Based on CATIA	131
<i>Yang Liu</i>	
High-Speed Facial Recognition Using Log-Polar Transformation	139
<i>Yue Bao, Bin Qi, Fei Gu</i>	
Farmland Water Potential Soft-Sensing Network Based on WSN	147
<i>Liguo Tian, Meng Li, Zhiliang Chen, Shengli Lu, Yue Liu</i>	
A Method for Searching Image Using Characteristic Point	155
<i>Yusuke Umeda, Yue Bao, Fei Gu</i>	
One Step Method for Capturing a Multi-view 3D Image	163
<i>Tashuya Haga, Yue Bao, Fei Gu</i>	
A Method for Searching Image Using Color Sketch	171
<i>Masaya Hashimoto, Yue Bao, Fei Gu</i>	
A Touch Screen Using One Camera and Two Mirrors	179
<i>Akinobu Shimoyama, Yue Bao, Fei Gu</i>	

Hamiltonian of Line Graph under Condition of Constraint	187
<i>Yong-Zhi Kan</i>	
The Performance Persistence of Mutual Fund: The Empirical Research Based on Cross-Sectional Regression	193
<i>Cunzhi Tian, Qiuping Guo, Haijun Wang</i>	
A Driving Method of the Electro Hydraulic Proportional Valve Based on Compensation Network	199
<i>Wei Shen, Junzheng Wang</i>	
The Structure and Realization of a Compact Weeding Robot in Stamping Mode for Paddy Fields	205
<i>Qin Zhang, Huan Xia, Xiaogang Huang</i>	
Study on the Identification of Noise Sources and Reducing Noise for Diesel Engine	213
<i>Liu Shuai, Wang Zhong, Chen Lin, Xia Heng, Zhang Yifeng, Xu Guangju</i>	
The Design of UART Controller Based on FPGA	221
<i>Ying Wang, Zhan Shen</i>	
Synchronization of Fractional-Order Chaotic System with Application to Communication	227
<i>Tan Wen, Jiang Fengling, Liu Xianqun, Liu Jian Xun, Wu Feng</i>	
Infrared Smoke Online Automatic Monitoring System of Multi Components of Stationary Pollution Sources	235
<i>Dan Zhang, Chengying Li</i>	
Servo System of 6 DOF Electro-Hydraulic Shaking Table	241
<i>Liyi Yin, Zhengmao Ye, Gang Shen, Junwei Han</i>	
Study and Design of Vehicle Black Box Hardware System Based on ARM and DSP	251
<i>Xu Hui, Li Jing-zhao, Yin Zhi-xiang, Sun Xia</i>	
The Perfect on Urban Natural Function Space under Artificial Environment	257
<i>Fugang Zhang, Qiong Xue, Shanshan Jiang</i>	
Development of Real-Time Temperature Monitoring System Based on GPRS	261
<i>Jianzhong Wu, Jianping Cai, Meimei Huo, Minghui Wu</i>	
Multi-Signal Intelligence Data Fusion Algorithm Based on Pca	267
<i>Jianbin Xiong, Qinruo Wang, Haoyi Wu, Baoyu Ye, Jinghong Zhang</i>	

Research on Simulation of Motion Compensation for Omnidirectional Platform Based on Neural Network	275
<i>YuNan Zhang, ShuangShuang Wang, Peng Tian, YuHui Zhao</i>	
Study of Thrust Lever Control Loading System in Flight Simulator	283
<i>Jinsong Zhao, Zhengmao Ye, Gang Shen, Junwei Han</i>	
Survey of BMI Distribution among University Students Aged 17 - 24 in Wenzhou	293
<i>Chen Jun</i>	
Robotic Sound Source Localization with Mirror Effect of Echo from an Obstacle Board	301
<i>Juan Huo, Alan Murray</i>	
An Multi-agent Artificial Immune Network Algorithm and Its Application	305
<i>Xuhua Shi</i>	
A Novel Anti-collision Protocol Based on Binary Tree Without Prior Information about RFID Tags	313
<i>Deng Zhongting, Wu Haifeng, Wang Qian, Shi Wenyu</i>	
Application of Visual Attention in Object Search for a Mobile Robot with an Omni-directional Vision System	321
<i>Dongyi Lin, Bingwei He</i>	
Monitoring System Design of Suspension Bridge of Health Status Based on CAN-BUS	329
<i>Yang Yu, Ming-ye He, Ying-ji Hao</i>	
Research on New Neural Oscillator in CPG Model Used in Robotic Fish ...	337
<i>Wang Gang, Zhang Daibing, Shen Lincheng</i>	
Synthesis of Adaptive Control System for Formation of Program Speed of Multilink Manipulator	347
<i>Vladimir Filaretov, Anton Gubankov</i>	
Optimal Single Quantum Measurement of Multi-level Quantum Systems between Pure State and Mixed State	351
<i>Haiwei Liu, Yaoxiong Wang, Feng Shuang</i>	
Development of the Infrared Thermal Wave Detection System and Experimental Study	361
<i>Wei Zhang, Guo-wei Wang, Zheng-wei Yang, Yuan-jia Song, Guo-feng Jin</i>	
A Study on Micro Grooving Using PZT Actuator	369
<i>Pradipta Vaskar Biswas, Se-Yun Lee, Kyung-Hwan Hwang, Dong-Bae Kang, Jung-Hwan Ahn</i>	

The Test Principle and Algorithm of Laser Measuring Tree Height	381
<i>Hong-e Ren, Wei Yan</i>	
A Method of Calculation for the Shearer Drum Cutting Path	389
<i>Wei Guo, Ning Zhu, Shuanfeng Zhao</i>	
Study on Vapour Insulation Technology in MOSS-Type Tanks of LNG Carrier	397
<i>Boyang Li, Yunqiu Zhang, Diyang Li, Lixun Ding</i>	
Study of Whole Network Control Based on Ethernet for FAST Main Reflector	403
<i>Haitao Shen, Lichun Zhu, Yi Sha</i>	
Design and Implementation of the Marine Environmental Monitoring Database Construction-Cum-Visual Management System	411
<i>Xiaohui Gao, Xiangyu Zhao, Juan Wang</i>	
One Multi-ocular Image Mutual Segmentation Method	419
<i>Li Xin, Zhu Jingfu</i>	
Simulation and Analysis Groove of Wet Friction Based on Computational Fluid Dynamic	423
<i>Yu Long Lei, Jie Tao Wen, Han Yong, Zhenjie Liu, Hua Bing Zeng</i>	
Study on Dynamic Simulation Model of Telescopic Cylinder Based on Power Bond Graph and Simscape	427
<i>Yulong Lei, Huabing Zeng, Zhenjie Liu, Xingzhong Li, Jietao Wen</i>	
Progress of Coal Gangue Research	431
<i>Jianguo Feng, GuiHua Li, Liping Zhang</i>	
Verb Consciousness Passwords in the Fingers (2)	439
<i>Yunfeng Zhu</i>	
Sparse Representation-Based Face Recognition for Single Example Image per Person	447
<i>Zhen Wang, Ming Zhu</i>	
Analysis of Zero-Sequence Circulating Current in Parallel PWM Inverter System with Difference of Carrier Wave Phases	453
<i>Jianbao Liu, Xinxin Qin, Zhonglin Yang</i>	
A Novel Robust Controller for the Speed Control of Permanent Magnet Synchronous Motor	465
<i>Wei Guo, Jian-Ping Wen</i>	
Micro Machined Diaphragm Based Fiber Fabry-Perot Acoustic Sensor	473
<i>Li Zhenyu, Shao Jie, Wu Zhizong, Chen Jianyong</i>	

Catastrophe Modeling of a Nonlinear System	483
<i>Zengkun Qi</i>	
Dynamics of a Tuberculosis Model with Treatment and Self-cure	491
<i>Yayi Xu, Guorong Huang, Zhan Zhao</i>	
Headland Turning of Autonomous Robot in Corn Field	495
<i>JinLin Xue</i>	
The Study on Wide Area Antenna Array Algorithm and Its Experiments ...	507
<i>Zhu Xinying, Kong Deqing</i>	
Performance Evaluation of Listed Household Appliance Enterprises Based on Factor Analysis and Cluster Analysis	515
<i>Yiwei Guo, Wenting Liu, Jia Han</i>	
Research of the Correlation between EVA-Based Corporate Value and Stock Yield	523
<i>Yiwei Guo, Fulian Shi, Xu Zhang</i>	
Analysis of Pollution Abatement Status and Policy Recommendations of China's Agro-Food Processing Industry	529
<i>Yiwei Guo, Jing Guo, Pingdan Zhang</i>	
Rapid Prototyping for Preoperative Planning of Fibula Free Flap in Mandible Reconstruction	537
<i>Chen Yadong, Wang Hang, Qin Xingjun, Wu Wenzheng, Li Hu, Wang Wanshan</i>	
Numerical Simulation of Inner Hydro-field and Comfortable Evaluation Based on Human Thermal Comfortable Model in Cockpit	543
<i>Junwei Zhao, Xuming Mao, Ruhua Wang, Wenjiang Wang, Zhenwei Zhang, Hongjun Xue</i>	
Research on the Correlation between Extraordinary Profit and Loss and Financial Report's Quality of Chinese Listed Companies	549
<i>Fulian Shi, Jing Guo, Zhongzheng Xiang, Yan Zhang</i>	
Internal Influence Factors Study of Cash Dividend Policy of China's A and H Share Listed Companies	557
<i>Fulian Shi, Jing Guo, Yan Zhang, Ran Li</i>	
Correlation Study of EVA and Corporate Value	565
<i>Fulian Shi, Yuanbin Jiang, Xu Zhang</i>	
Study of the Impact of Legal Protection of Investors on the Cash Dividend Policy	573
<i>Fulian Shi, Jing Guo, Ran Li</i>	

Design of Greenhouse Environment Wireless Monitoring System Based on ZigBee	579
<i>Hui Wang, Xue-ren Dong, Yu-zhen Ma, Xiao-wei Yang, Feng-nan Liu</i>	
A Novel Method to Measure the Projectiles Velocity and Position of Twin-tube Volleyed Weapons with Multi-screen Target	587
<i>Yugui Song, Wenbo Wang, Guohui Wang</i>	
The Improvement on Lucene Text Analyzer	593
<i>Wu Daiwen</i>	
Satellite Pseudo-range Positioning Based on Time Series Analysis	599
<i>Guojun Zhang, Siliang Wu</i>	
H_{∞} Control for Inverted Pendulum: Input Time Delay Considered	607
<i>Keyong Shao, Miaomiao Tian, Qingyu Wu</i>	
Energy Saving of Plant Cultivation System Using LED Control System Based on Ultrasonic Sensor	615
<i>Hyung-Sun Kim, Jae-Hyun Lim</i>	
Context-Aware Architecture for Improvement of Energy Efficiency and Growth Promotion of Plants	625
<i>Hyung-Sun Kim, Heon-Taek Kong, Jae-Hyun Lim</i>	
Trajectory Estimation of Hypersonic Vehicle Based on Observations from Infrared Sensor on LEO Satellite	633
<i>Nan Wu, Lei Chen</i>	
Improvement of Energy Efficiency in Plant Factories through the Measurement of Plant Bioelectrical Potential	641
<i>Sookyoun Kwon, Jaehyun Lim</i>	
The Identification Algorithm Study of Given Area Weld Image	649
<i>Qing Jia, Ma Guo-hong, Wang Cong</i>	
Application of an Improved Performance Evaluation Model Based on Cloud Theory	655
<i>Li-jun Xie, Zhi-qiang Zhu, Zhe Chen, Yuan-ning Liang</i>	
Study on Ontology-Based Reference Model of Software Configuration Management	663
<i>Zhe Chen, Xin Li, Hong Yao, Yuan-ning Liang</i>	
The Discuss on the Machine Design Course Teaching Method	671
<i>Li Xing-hua</i>	
Automatic Recognition Algorithm of Traffic Signs in Road Tunnel	677
<i>Wang Weizhi, Liu Bingham</i>	

License Plate Localization Based on Edge Detection and Morphology	685
<i>Ying Wang, Wei Wang</i>	
Oilfield of Video Monitoring and Alarm System Based on DM642	691
<i>Ying Wang, Xiao Feng Guo</i>	
The Application of Multi-scale Modeling Technology in Artificial Bone Graft	699
<i>Hu Li, Yadong Chen, Zhiguang Zhang, Tianbiao Yu, Wanshan Wang</i>	
Observer Generalized Representation for Unstable Delayed Systems	707
<i>Omar Jiménez-Ramírez, Mario A. Quiroz-Juárez, Rubén Vázquez-Medina</i>	
Model Driven Synthesis of Behavioral Models from Textual Use Cases	713
<i>Zuohua Ding, Mingyue Jiang</i>	
A New Design of PC104 Host Controller Based on STM32F103	719
<i>Sun Shuying, Li Jun, Chen Zhijia</i>	
Design of Auxiliary Power Supply for the Solar PV Inverter	727
<i>Yunhai Hou, Shihua Sun, Ershuai Li</i>	
Modeling Method for Centralized Control of Load-Tap-Changing Transforms Based on Neural Networks	733
<i>Yu Sun</i>	
Design of System for High-Frame Frequency Image Acquisition and Remote Transmission	743
<i>Dingjin Huang, Tao Zhang, Honglu Hou, Wenfang Zhang</i>	
A New Video Feature Extraction Method Based on Local Class Information Preserving	751
<i>Yongliang Xiao, Shaoping Zhu, Weizhong Luo, Xiangbao Li, Wenbin Liu, Gelan Yang</i>	
Quadrature Kalman Probability Hypothesis Density Filter for Multi-Target Tracking	757
<i>Pu Zhang, Hongwei Li, Yuan Huang</i>	
Kaiser Window Function Non-Local Means for Image Denoising	765
<i>Hongwei Li, Pu Zhang, Yuan Huang</i>	
A Method Based on FFT and Invariable Moment Features for UTAN	771
<i>Zunyi Xu, Yi Liu, Dongwu Huang</i>	
Analysis of Singular Value under Kalman Filtering for Strapdown Inertial System Online Calibration	779
<i>Guangtao Zhou, Jian Wang, Kai Li</i>	

Design of Automatic Block Section Signalling Layout of Appling Chaos Embedded Particle Swarm Optimization Algorithm Based on Skew Tent Map	785
<i>Hua Rong</i>	
Tourism Demand Forecast and Analysis to Shanxi Based on SVM	793
<i>Jinling Guo</i>	
A Divide and Conquer Approach for Obstacles Surpassing of a Legged Robot	799
<i>Antonio Bento Filho, Paulo Faria S. Amaral, Benedito G. Miglio Pinto</i>	
Hallucinating Face by Sparse Representation	809
<i>Xue Cuihong, Yu Ming, Jia Chao, Yan Gang</i>	
Author Index	815

A Neural Network Based Temperature Control for Air Handling Unit*

Binhui Zheng, Jiangang Lu, Qinmin Yang**, and Youxian Sun

State Key Laboratory of Industrial Control Technology, Department of Control Science and Engineering, Zhejiang University, Hangzhou 310027, China
qmyang@ipc.zju.edu.cn

Abstract. In this paper, a neural network (NN) based temperature control scheme is presented for cooling coil of Air Handling Unit (AHU) to overcome the unknown system dynamics and its inherent nonlinearities. First of all, by utilizing the standard thermodynamic formulas, the cooling coil is modeled by a discrete-time uncertain nonlinear system instead of a linear one, in order to accommodate its different behaviors under various cooling loads. Thereafter, a two-layer NN is utilized to approximate the unknown dynamics within the system. The online tuning algorithm of the NN weights is also provided with no offline training needed. Consequently, the identification process of the cooling coil unit is obviated. Theoretical results show the stable tracking performance of the close-loop system, while the effectiveness of this method is demonstrated under simulation environment.

Keywords: Air handling unit, Cooling coil unit, Neural networks.

1 Introduction

In recent years, the variable air volume (VAV) air conditioning systems which can adjust the air flow of cooling coil according to the cooling load have been widely used. Compared with the traditional constant air volume air conditioning systems, they have a prominent advantage in energy cost. Meanwhile, air handling unit (AHU) within VAV systems accounts for a large part of the total building energy consumption in most large HVAC systems [1]. As a key air handling equipment connecting refrigeration unit and rooms to be conditioned, the cooling coil of AHU plays a vital important role for the energy saving purpose [2]. Therefore, the performance of the overall HVAC systems is largely affected by the control performance of the off coil temperature [3]. However, the heat exchange process between chilled water and air forced into the cooling coil is very complex and highly nonlinear [4], while an accurate dynamic model is still hard to obtain.

* This work was partially supported by the National Natural Science Foundation of China (NSFC) (No. 21076179, 60736021, 61104008), the National High-tech R&D Program of China (863 Program) (No. 2006AA04Z184), the National Basic Research Program of China (973 Program) (No. 2012CB720505), and the Natural Science Foundation of Zhejiang Province (No. Y4080339).

** Corresponding author.

In practice, due to its simplicity, traditional PID control strategy is still widely adopted. A feedforward compensation in conjunction with a conventional PI feedback loop approach was discussed in [5] to accommodate the model uncertainty. [6] presented a self-tuning PID controller for the HVAC systems. However, both of them are based on the assumption that the air flow of the cooling coils is fixed, which means their dynamics can be approximated by a linear model. That is to say, the linear control methods may fail to work when this assumption is not satisfied.

On the other hand, neural networks (NN) can approximate any nonlinear mappings and have the ability of online learning. Nowadays, rare neural networks based control strategies on the AHU system have been proposed in the literature. A cascade controller is designed in [7] by utilizing a neural network (NN) in the outer control loop for the off-coil temperature. However, the stability of the closed-loop control system is not given. In order to overcome the problem mentioned above, this paper proposes a two-layer neural network based real-time temperature control strategy. The structure of neural network is simple and its weights can be randomly initialized, which greatly reduces the online calculation cost. No *a priori* knowledge of the system dynamics is required. Simulation results verify its feasibility.

2 Preliminaries

2.1 Air Handling Unit

A typical VAV air conditioning system mainly consists of an air handling unit and control devices [8] as shown in Fig. 1.

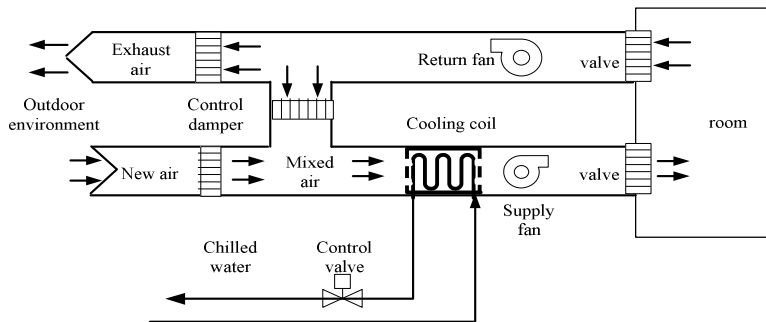


Fig. 1. Diagram of an air handling unit

The return air from the room forced by the return fan is either exhausted to the outdoor environment or mixed with the new air from the outdoor environment. Mixed air is in turn forced to the cooling coil, participating in the heat exchange process with the chilled water, which is controlled by the control valve. With the heat taken by chilled water, the off-coil air temperature is sufficient low and thus sent to the space to be conditioned. The air flow through the cooling coil is controlled by the supply fan while the chilled water flow is controlled by the control valve. When the control valve is driven wider, the water flow of the cooling coil will be increased resulting in

lower off-coil air temperature, and vice versa. Subsequently, the room temperature is regulated by the flow of the air entering the room that is controlled by the air valve. Therefore, the off-coil air temperature control plays an important role within the overall HVAC systems.

2.2 Cooling Coil Model

As a matter of fact, the off-coil air temperature can be expressed to be a nonlinear function of the on-coil air temperature T_{ai} , supply air flow m_a , the chilled water supply temperature T_{chwi} , and the supply chilled water flow m_{chw} .

$$T_{ao} = F(T_{ai}, m_a, T_{chwi}, m_{chw}). \quad (1)$$

where F is a complex unknown nonlinear function.

Essentially, T_{ai} is dependent on the outdoors environmental temperature and the return air temperature. Meanwhile, T_{chwi} is determined by evaporator control loop and the value of m_a depends on the required cooling load. Therefore, only the supply chilled water flow m_{chw} is considered to be the control variable, and its goal is to drive the off-coil air temperature T_{ao} to a desired value T_{aod} .

According to the thermodynamic formulas,

$$Q = c_{chw} m_{chw} (T_{chwi} - T_{chwo}) = c_a m_a (T_{ao} - T_{ai}). \quad (2)$$

where Q is cooling load, T_{chwo} is chilled water return temperature, and c_a , c_{chw} are air and water heat capacity respectively.

In steady state, Q can be expressed by [10]

$$Q = \frac{c_1 m_a^e}{1 + c_2 \left(\frac{m_a}{m_{chw}}\right)^e} (T_{ai} - T_{chwi}). \quad (3)$$

where c_1 , c_2 , e are unknown parameters.

By substituting (2) into (3), T_{ao} can be described by

$$T_{ao} = T_{ai} - \frac{(c_1 / c_a) m_a^{e-1} m_{chw}^e}{m_{chw} + c_2 m_a^e} (T_{ai} - T_{chwi}) \quad (4)$$

From the above steady model, it can be readily seen that with changing cooling load, which results in varying air flow, the model would be largely different over the AHU's operating range.

Next, for simplicity, define $y = T_{ao}$ as the system output and $u = m_{chw}$ as the control input. Thereafter, for control purpose, a general dynamic model of the cooling coil system can be presented in discrete-time by [11]

$$y(k+1) = f(y(k), \dots, y(k-n_a), u(k-1), \dots, u(k-n_b), d(k)) + g(d(k))u(k) \quad (5)$$

where n_a, n_b are output order and input order respectively, $d = [T_{ai} \quad m_a \quad T_{chwi}]$ denotes the measurable disturbance, and f is an unknown nonlinear function. g is an unknown by always positive nonlinear function of d .

Hence, the neural network based controller is proposed in next section.

3 Controller Design

Rewrite the system dynamics (5) as below,

$$y(k+1) = f(Y(k)) + g(d(k))u(k) \tag{6}$$

$$Y(k) = [y(k), y(k-1), \dots, y(k-n_a), u(k-1), u(k-2), \dots, u(k-n_b), d(k)]$$

By assuming the desired off-coil air temperature to be $y_d = T_{aod}$, define the tracking error as

$$e(k) = y(k) - y_d(k) \tag{7}$$

Thus, the dynamics in term of the tracking error can be written as

$$e(k+1) = f(Y(k)) - y_d(k+1) + g(d(k))u(k) \tag{8}$$

If functions $f(Y)$ and $g(d)$ are known, a desired controller can be designed as

$$u_d(k) = g(d(k))^{-1}(y_d(k+1) - f(Y(k)) + k_v e(k)) \tag{9}$$

where k_v is a constant parameter such that $|k_v| < 1$. Therefore, (9) generates

$$e(k+1) = k_v e(k) \tag{10}$$

which is asymptotic stable. However, since $f(Y)$ and $g(d)$ are unknown, the desired controller cannot be implemented directly.

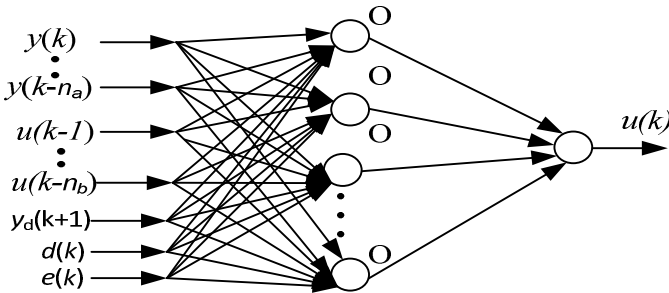


Fig. 2. Two-layer NN Structure

In the meantime, the two-layer feedforward neural networks as shown in Fig. 2 can approximate any smooth nonlinear functions [12] due to its universal approximation ability. That is to say, the desired control law can be written as

$$u_d(k) = W^T(k)\phi(V^T\bar{Y}(k)) + \varepsilon(\bar{Y}) \quad (11)$$

where W and V are NN weights in the output and hidden layers respectively. ϕ is the activation function and the NN input is $\bar{Y}(k) = [Y^T(k) \ d^T(k) \ y_d(k+1) \ e(k)]$. ε is bounded NN reconstruction error.

To estimate the desired control signal, define the actual controller $u(k)$ to be

$$u(k) = \hat{W}^T(k)\phi(V^T\bar{Y}(k)) \quad (12)$$

where \hat{W} is the estimate of W . Substitute (9) (11) (12) into (8) yields

$$e(k+1) = k_y e(k) + g(d(k))\left(\hat{W}^T(k) - W^T(k)\right)\phi(V^T\bar{Y}(k)) + \varepsilon(\bar{Y}(k)) \quad (13)$$

Furthermore, the updating law of the NN weights can be given as [13]

$$\hat{W}(k+1) = \hat{W}(k) + \alpha\phi(\bar{Y}(k))e(k+1) - \Gamma\left\|I - \alpha\phi(\bar{Y}(k))\phi^T(\bar{Y}(k))\right\|\hat{W}(k) \quad (14)$$

where α , Γ are design parameters. It has been proven that [13], when $\alpha\|\phi(\bar{Y}(k))\|^2 < 1$, $\Gamma < 1$, the tracking error of system and the NN weights estimation errors are uniformly ultimately bounded (UUB). The proof is similar to [13] and thus omitted due to page limit.

4 Simulation

A model identified in [11] is adopted here for simulation purpose.

$$y(k+1) = -a_1 y(k) + b_0 u(k) + b_1 u(k-1) \quad (15)$$

Parameters a_1 , b_0 , and b_1 are identified by the input and output data with four different cooling loads, which tabulated in Table 1.

Table 1. System Model Parameters

	Cooling Load(KW)	C_1	C_2	e	a_1	b_0	b_1
Load 1	0.40	0.7132	0.5402	0.8	-0.3292	55.48	38.43
Load 2	0.75	0.7132	0.5402	0.8	-0.4092	50.1	37.07
Load 3	1.00	0.7403	0.9183	0.8	-0.3858	49.01	35.75
Load 4	1.20	0.7403	0.9183	0.8	-0.4493	46.75	36.85

In the simulation settings, let $\Gamma = 0.00045$, $\alpha = 0.04$. The initial weights are set as $\hat{W}(0) = 0$ with 15 neurons in the hidden layer.

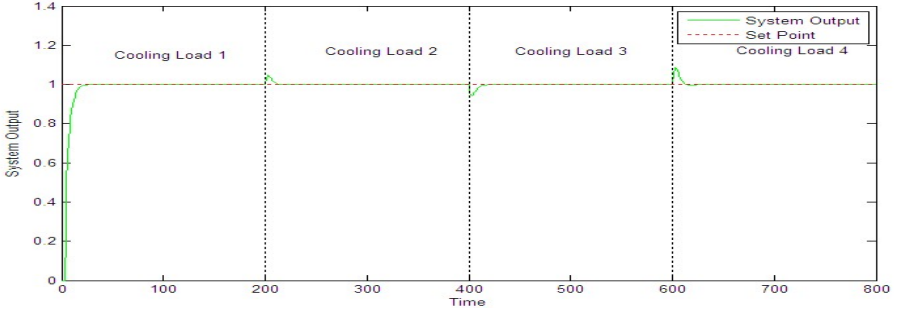


Fig. 3. System response with constant desired value

In the first simulation trial, the desired temperature is set to be 1 with four different cooling loads. The system output is shown in Fig. 3, which demonstrates that when the cooling load changes, i.e., the model parameters are varied, system output can still quickly track the desired value.

The second simulation effort is intended to show the system performance with changing desired values and cooling loads. The controller parameters are taken as the same as the above scenario.

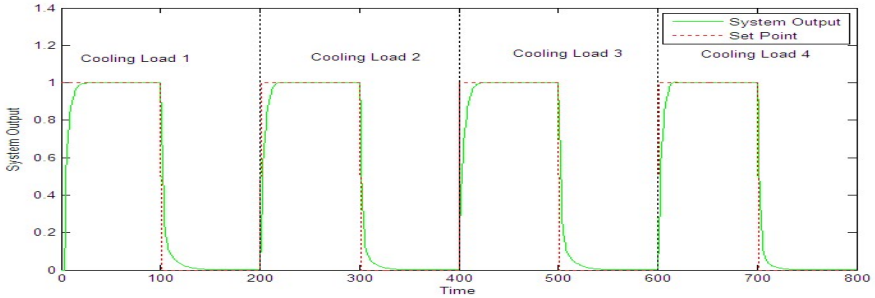


Fig. 4. System response with varying desired trajectory

Figure 4 shows that even with changing cooling loads and jumped desired temperatures, the controller can still achieve a satisfactory tracking performance.

From the simulation results shown above, it has to be noted that the neural network based temperature control strategy doesn't need to know the exact cooling coil model. Furthermore, the structure of neural network is comparatively straightforward with the initial weight simply set to be 0, i.e., no offline training phase is required.

5 Conclusions

A neural network based temperature control strategy for the cooling coil of AHU is introduced in this work. The online learning ability of the NN is able to accommodate the unknown nonlinear dynamics of the system to avoid any offline training

processes. Besides, the neural network has a two-layer structure which greatly reduces the online computing time. Meanwhile, the algorithm does not need to know the model parameters of the cooling coil so that it can be readily implemented for practical applications.

References

1. Xu, M., Li, S., Cai, W., Lu, L.: Effects of a GPC-PID Control Strategy With Hierarchical Structure for a Cooling Coil Unit. *Energy Conversion and Management* 47, 132–145 (2006)
2. Mei, K., Liang, C., Zhang, X.: Variable Flow Influence to Cooling Coil. *Chemical Industry Journal* 59, 438–1157 (2008)
3. Jin, G., Cai, W., Wang, Y., Yao, Y.: A Simple Dynamic Model of Cooling Coil Unit. *Energy Conversion and Management* 47, 2659–2672 (2006)
4. ASHRAE. ASHRAE handbook—fundamentals. American Society of Heating, Refrigerating and Air-Conditioning Engineers Inc. (1997)
5. Salsbury, T.I.: A Temperature Controller for VAV Air-handing Units based on Simplified Physical Models. *HVAC&R Res.* 3(3), 264–279 (1998)
6. Bi, Q., Cai, W., Wang, Q.G., et al.: Advanced Controller Auto-Tuning and Its Application in HVAC Systems. *Control Eng. Practice.* 8, 633–644 (2000)
7. Guo, C., Song, Q., Cai, W.: A Neural Network Assisted Cascade Control System for Air Handling Unit. *IEEE Transactions on Industrial Electronics* 54, 620–628 (2007)
8. Fu, L., Li, M.: PID Neural Net based Decouple Controller for VAV System. *Xin'an Jiaotong University Journal* 40, 13–17 (2005)
9. He, M., Cai, W.: Multiple Fuzzy Model-based Temperature Predictive Control for HVAC Systems. *Information Science* 169, 155–174 (2005)
10. Wang, Y., Cai, W., et al.: A Simplified Modeling of Cooling Coils for Control and Optimization of HVAC Systems. *Energy Convers. Mgmt.* 45, 2915–2930 (2004)
11. Xu, M., Li, S., Cai, W.: Practical Receding-Horizon Optimization Control of the Air Handling Unit in HVAC Systems. *Industrial & Engineering Chemistry Research* 44, 2848–2855 (2005)
12. Zhang, J.: Fuzzy-Neural Net. Harbin Industrial University Press, Harbin (2004)
13. Jagannathan, S., Lewis, F.L.: Discrete-Time Neural Net Controller for a Class of Nonlinear Dynamical Systems. *IEEE Transaction on Automatic Control* 41, 1693–1699 (1996)

Exploration on Principles of Engineering Network Course Design

Ying Xiao^{*}, Yan Shi, and Xiaoping Li

Dept. of Continuing Education, Beijing Institute of Technology, Haidian District, Beijing
100081, China
haha52xy@qq.com

Abstract. Network course is an important carrier of modern distance education, it has its own particularity, and the learning theory must be a design principle in the design of courses. Based on some basic views of the three modern learning theories which have great influences on the current network education, the engineering curriculum definition and characteristics were introduced; ways to realize the engineering training objectives of network course were discussed, and some principles more suitable for engineering course design were tried to put forward.

Keywords: engineering curriculum, network course, learning theory, course design principles.

1 Introduction

“China encyclopedia dictionary (second edition)” gives a clear definition to the word “engineering”, that is the various disciplines which applies natural science principle to practical production, such as engineering, mechanical engineering, chemical engineering, etc. and “technology” is a similar word of it. [1] This definition shows that the teaching objective of the engineering mainly lies in the application of natural science principles, that is to say, to master technology. As the saying goes, practice makes perfect, so engineering students need to do lots of practice and training to master the techniques.

Network course is the important carrier of modern distance education, its quality directly influences the learning effect of distance learners and the realization of the educational objectives, and as the characteristic of distributed time and location between teacher and learner, the network curriculum design model cannot be equated with the traditional curriculum design model. However, due to the Specific characteristics of engineering course, mainly for planning, technology and complexity, it need

^{*} Yan Shi is a Associate Professor of Education Technology at Beijing Institute of Technology, Beijing, China. Her research interests are in areas of Education Technology and Professional Education;

Xiaoping Li is a Professor of Education Technology at Beijing Institute of Technology, his research interests are in areas of Education Technology;

Ying Xiao is a graduate student of education technology at Beijing Institute of Technology, her study direction is Modern Distance Education Technology.

students to have a higher capacity in the meaning construction and overall knowledge using, judgment and analysis problems, collaboration and communication, etc.[1] all of capacities put forward higher requirements in the network curriculum design.

Generally, the process of technology combined with instruction involves learning theory; technique and teaching practice three aspects, [2] and this paper only chose "learning theory" this dimension to analysis. Any course design must be based on certain learning theory, which must be as a design principle throughout the whole design process. [3] The article, based on some basic views of the three modern learning theories which have great influences on the current network education, discusses how to realize the engineering training objectives of network course, and tries to put forward some principles suitable for engineering course design. The three modern learning theories include behaviorism, cognitivism and constructivism.

2 Engineering Network Course Overview and Training Objective

2.1 The Characteristics of the Network Course Design

Professor Kekang.He defined network course in 2005, he said network course is the course which based on web and with the instruction of advanced education ideology, teaching theory and studying theory. The learning process has the characteristics of interactivity, sharing, openness, coordination and autonomy, etc. [4]

E-learning is students take kinds of knowledge by some learning Styles such as autonomy, individuation and cooperativeness in the creation of network teaching environment to realize the course training target.Network course is different from traditional courses, network course design should be considered teacher-student separation form of teaching, distance learner' characteristics, technical support and other factors, So network course design can not be fully in accordance with theories of traditional course design, it should have a new set of principles of its own.

2.2 Goals of Engineering Network Courses' Design

According to the previously described definition of engineering and network course, this paper gives the definition of "Engineering online course", that is, engineering network Course is a course is developed to transmit scientific principles and applications to production practice through Internet, under the guidance of current educational theory and teaching design theory. The learning process of courses is Inter-active, independent, open, collaborative and practical.

Engineering is formed by the applying of natural science principles in production. [1] We can analyze the engineering curriculum's training objectives according to this definition: (1) master natural scientific principles; (2) learn to use natural scientific principles; (3) accurately applied them to production.

In brief, network engineering courses are Web-based engineering courses under the guidance of the educational theory and instructional design ideas. Therefore, the goal for learners is to achieve the following objectives through learning network courses: (1) to understand and master concepts and theorems in the courses; (2) to obtain the principles of use concepts and theorems; (3) to form proficient skills in the production practice.

3 Modern Learning Theory and Guidance to Engineering Network Course Design

With Anderson as a representative of the modern cognitive psychologists think knowledge can be divided into the declarative knowledge, procedural knowledge and strategic knowledge, they supply each other in the process of solving problems. Declarative knowledge plays the role of the foundation in the knowledge system, and the obtaining and using of procedural knowledge should be directed and controlled by strategic knowledge.

Three training target of engineering network course are respectively with declarative knowledge learning, procedural knowledge learning and strategic knowledge learning. Based on the training goal, this paper will analyze basic theories of three modern learning, trying to find more appropriate theoretical basis and design strategy to realize the training target.

3.1 Cognitive Learning Theory

Declarative knowledge is a knowledge to describe the definition, principle and discipline of things. Robert M Gagne pointed out that stating knowledge is not only the knowledge system based, but also the thought tool, so the training and exercise of intellectual skill cognitive strategy or motor skill all need to master stating knowledge widely and accurately. [5]

American psychologist J.S. Bruner think instruction should pay more attention to the basic structure of each subject, and the small element of these knowledge structures is what we call the declarative knowledge. To learn stating knowledge is mainly to study some definition, principle, law, etc., and it just map the training goal of engineering network course "understanding and mastery of the concepts and principles". In order to change the inner relationship of objective things into learners' cognitive structure effectively, cognitive learning theory think course design should be insisted on some basic principles, and these principles play a guiding role in learning declarative knowledge and realizing the training objective of engineering network course. (1) Gradually differentiation principle, it requires present of the course content should start with the most basic concept, then gradually differentiation according to the specific details. (2) Classification principles, it requires course designer to classify and process things according to their key features and attributes, it not only accords with human cognitive law, but also make learners form concepts easier. [4] (3) Active participation principle, that is to say, learners should not accept stimulation to react passively, but involve in learning activities actively.

Cognitive learning theory plays an important role in cognitive learning design, especially in learning concept and proposition, however, influencers of network course learning effect not only lies in the cognitive, also lies in the emotion, attitude, character, learning environment and so on, especially for the engineering network course, its key learn objective should be knowledge application and operation skills. Therefore, design engineering network course only based on cognitive learning theory principle is difficult to achieve good effect in teaching.

3.2 Constructivism Learning Theory

The strong view of constructivism is that knowledge does not exist in some objective things steadily, it is constructed by the individual through contacting with the object actually, and gaining experience eventually in particular situations. [6]According to constructivism learning theory, there are four key elements or attributes including have “environment”, “cooperation”, “conversation” and “meaning construction” generally.

Strategic knowledge refers to learners’ cognition of learning task; choice of learning method and regulation of learning process in learning situation. It mainly solve some problems about learning and application methods, application situations and so on, and to solve these problems is in keeping with engineering network course training goal, that is, using principles of obtained concepts and disciplines. Strategic knowledge should learn in the specific case or situation, in the situation, learners could share and cooperate with partners to improve their strategic knowledge. And each element involved in the process of strategic knowledge learning is just under four elements of learning environment according to constructivism learning theory.

The view of constructivism learning theory has improved the development of network course design, the development of the network course design to a certain degree, especially in study and application of strategy knowledge. Therefore, it not only denied the rationality of the traditional teaching method, but also ignored the significance of practice in the skill mastery, however, to master skills is the focus of engineering network course training goal. As a result, constructivism learning theory just applies in a certain range of engineering network curriculum design, and should be combined with other theories to direct the whole course design.

3.3 Behaviorism Learning Theory

Behaviorism theory is also known as the S-R theory. With seen “strengthening” as the core of, the theory think that only strengthening could improve learners’ learning motivation. The behaviorism theory has a great influence on network course design, and programmed instruction theory raised by American psychologist Skinner should be indisputably. The basic principles of programmed instruction theory mainly includes small steps principle; actively participation principle; instant strengthening and re-transaction principle; self-make paces principle; low error rate principle.

Procedural knowledge is operating steps to complete some concrete task, it is equivalent to skills. [7] Processing knowledge acquisition just maps the training goal of engineering network course is “to master skills, and skilled applied to practical in production”. Procedural knowledge learning is a very complicated process, according to modern cognitive psychology, this process includes three stages: stating knowledge stage; transformation stage; automation phase. With the first stage of learning process analyzed in previous paper, it won’t be involved; transformation stage is the stage to building connection, at this stage, the emphasis is to build connection between appropriate stimulus and response, and to be out of habit interference in the learning process, for example, people once danced, learn kung fu tend to showy and not substantial, so the negative transfer must be reduced; automation stage is motor skill has reached proficient operation, that is a long list of action series can be automatic without special attention and consideration, therefore, the achievement of automation need to contact

skills again and again. In the last two learning phases of procedural knowledge, the problem can be solved under the guidance of the behavioral learning theory. As a result, behavioral learning theory can be used as a guiding principles to design some procedural knowledge of engineering network course.

4 Discussion of Engineering Network Curriculum Design Principles

Based on the analysis of some basic views of behaviorism learning theory, cognitive learning theory and constructivism learning theory, It shows that these three representative learning theories are make a certain contribution on the development of the network course, and also have a far-reaching impact on engineering network course design ideas. However, due to its complexity and peculiarity, engineering network course design couldn't accord to views from a kind of learning theory completely. It needs a more suitable guiding idea and principle for engineering network course design, which should be based on the combination or the supplement of this three learning theory.

In view of the further analysis of training targets of engineering network course, based on design principles of the three learning theories, the author summed up some course design principles for engineering network course, as follows:

4.1 Learner-Centered

The network course is not tool to regulate and constrain learners, but the ladder for learners to realize themselves. Engineering network curriculum design should pay more attention to the needs and characteristics of learners, therefore, learners should play a predominant role in network learning process, according to their existing knowledge structure, to choose suitable learning content on purpose and independent to manage their learning pace and style independently.

While designing the network course, we should think about four questions. (1) Could course contents meet the needs of learners? (2) Is course design suitable for distance learners' characteristics? (3) Is there a mature evaluation and feedback mechanism for learners' autonomous learning in the course? (4) Does the course design leave space for self thinking and independent construction of learners?

4.2 Network Course Learning Environment and the Learning Process Design

4.2.1 Modular Design Course

In order to facilitate significance construction and the formation of procedural knowledge of distance learners, network course designer should design knowledge hierarchically and categorically, according to the characteristics of learners and knowledge. Suggested that , in order to meet all kinds of students' needs, designers should divide course content into small modules within several layers or categories according to the key features and attributes of knowledge, and these modules can also be on-demand

combination into different learning chain, learners can do different learning chains choices to complete learning activities gradually.

4.2.2 Content Representation Design for Variety

In the perspective of cognitive learning theory, network course should provide conditions and space for information processing activities of learners, to make them involved in the meaning construction of knowledge actively, and to acquire real knowledge eventually.

Mostly because of engineering course knowledge more abstract and drab, there are some course design proposals: (1) Present monotonous knowledge intuitively, the lively and vivid the better; (2) Consider using the introduction of problems from current hot events, video animation and so on. (3) Design interactive content in each small unit of network course, for example, show kinds of knowledge in different interactive ways such as choice question; gap-filling; writing; small games and other modes.(4) Do situational course content design, that is different intellectual content should design in different situations and different ways.

4.3 Teaching Interaction Design and Collaborative Learning Environment Design

In order to enhance distance learners' senses of belonging and responsibility, to reduce loneliness in the learning process and to train their teamwork spirit, designer should consider how to arouse the enthusiasm of learners, and make them participate in co-operation and interaction of their own accord. For example, with the support of e-learning platform, "virtual study group" Similar to learning community should be designed and organized, and team members carry on the thorough discussion and exchange through MSN, QQ, E-mail, BBS and other learning platform to get more effective problem solving strategy for the completion of common tasks.

4.4 Creation of Learning and Practice Environment

An important influencer of measuring success of engineering network course design is that learners can learn and skilled use skills effectively. And a real life similar or real situation is beneficial for the stimulation of inner motivation, to develop the learners' ability to solve problems and spirit of exploration.

In recent years, geometry and physical modeling method, high performance computing, new sensors and perception mechanism, high-speed image processing and artificial intelligence technology have been mature relatively, and the research and application of online experiment system and virtual laboratory have has achieved great development, the paper won't narrate more. And there are two problems should be taken into consideration of these technologies ' application in the course design: (1) What problem has been solved by using these technology? (2) Application of this technology for what original intention?

4.5 Creation of Learning and Practice Environment

As stated above, the default fixed line of traditional course may not necessarily be a good fit for all the students, so network course design should set several starting point

and learning path according to different levels or lights for students to choose by self-determination. Thus, the suggestion is that engineering network course design should design course content as a network structure included key concepts and small units, and set different learning path, in order to make learners random access or start from any part of the network.

By the analysis of the above, it is not hard to find the traditional curriculum design principle is not suitable for engineering network design completely. And based on introduction of engineering curriculum definition and characteristics, through anglicizing some basic views of the three modern learning theories which have great influences on the current network education, this article discusses how to realize the engineering training objectives of network course, and tries to put forward some principles more suitable for engineering course design. Hope it would be a theoretic basis and reference for the future research and curriculum design.

References

1. China encyclopedia big dictionary (The second edition). Encyclopedia of China Publishing House, Beijing (2005)
2. Chen, J., Chen, S.: Technical progress of modern distance education. Central Radio & TV University Press, Beijing (2006)
3. Wang, R.: Network curriculum teaching design system ——In"the high level language program design (based on Java)"course as an example. Master thesis, Beijing university of post and telecommunications (2010)
4. He, K., Zheng, Y., Xie, Y.: Instructional System Design. Beijing normal university publishing group, Beijing (2005)
5. Zhang, C.: Education psychology. Shandong Education Press, Jinan (2005)
6. Li, K.: Behaviorism to humanism: discussion of the influence of learning theory to CAI courseware design. E-education Research (1999)
7. Zhang, Z.: Constructivism learning theory and principle of teaching. Open Education Research (1997)
8. Chen, Q., Liu, R.: Education psychology. Higher Education Press, Beijing (2005)

A Combined Modular Parametric and Non-parametric Method for Planar Ship Motion's On-Line Prediction^{*}

Jianchuan Yin^{1,2} and Zaojian Zou^{1,3}

¹ School of Naval Architecture, Ocean and Civil Engineering, Shanghai Jiao Tong University, Shanghai 200240, China

² Navigation College, Dalian Maritime University, Dalian Liaoning 116026, China
yinjianchuan@gmail.com

³ State Key Laboratory of Ocean Engineering, Shanghai Jiao Tong University, Shanghai 200240, China
zjzou@sjtu.edu.cn

Abstract. A combined modular model is presented for planar ship motion prediction by assembling parametric and non-parametric forecasting method. This parametric module and non-parametric module represent the holistic and local time-varying dynamics of system, respectively. The nonlinear autoregressive with exogenous input model is implemented for on-line prediction, and variable-structure radial basis function network is employed to represent the time-varying dynamics of system. The experiment of planar ship motion prediction is conducted and the results demonstrate the accuracy and robustness of the presented combined model.

1 Introduction

On-line prediction of ship motion plays an important role in the navigational safety and marine economy. The common prediction models are methods based on autoregressive models of time series, such as autoregressive with exogenous input (ARX), or nonlinear autoregressive with exogenous input (NARX). Parametric methods possess merits such like simple model structure and fast computational speed, but it is difficult for them to represent the time-varying dynamics.

Ship's motion at sea is a complex nonlinear system with time-varying dynamics [1]. Their dynamics changes along with such changes like loading conditions, trim and speed; similar changes also occur resulting from environmental disturbances such as wind, waves and depth under keel, etc. Therefore, it is hard to obtain a suitable physically founded mathematical model of ship's motion merely by parametric methods due to the complexity of the time-varying dynamics and underlying processes.

The application of neural networks in the prediction of nonlinear system has been intensively researched in recent years, such as the multilayer perceptron (MLP), radial basis function (RBF) networks, and support vector machine (SVM) [2]. Neural networks are capable of taking into account more complex relations existing among

^{*} This work is supported by the National Natural Science Foundation of China (Grant Nos.: 50979060 and 51061130548).

the analyzed data, so they are able to generate more accurate prediction attributing to this feature. Sequential learning neural networks oriented for on-line applications have attracted much attention over the last decade [3]. By learning samples sequentially, the algorithms on-line construct variable-structure neural networks which are capable of representing time-varying dynamic of nonlinear systems, and their application can be found in fields of communication and control. But the network focuses only on local time-varying dynamics of system and cannot represent the holistic nature of systems [4], which limits its system identification and prediction applications.

The parametric model and non-parametric model are suitable for representing the static and time-varying dynamics, respectively. A straightforward approach is to take into account the parametric and nonlinear neural network prediction module, combine them into one ensemble system of presumably better quality and treat the combined output as the final forecast [5]. Modular neural networks can incorporate priori knowledge, thus possess merits such as robustness and parsimonious model structure. Here in the on-line planar ship motion prediction, we implement NARX model using linear method for parametric identification of the static dynamics of ship motion; and the variable-structure radial basis function (RBF) network constructed by sequential learning is employed for the identification of the time-varying dynamics. The prediction data generated by each predictor of the ensemble are combined together to form one prediction model. The two identification module is combined in series connection to form one ship motion forecast describing the current dynamics of ship motion and. The numerical results of the presented integration schemes are presented and discussed.

2 Combined Modular On-Line Prediction

2.1 Configuration of Combined Modular Prediction

The static system dynamics can be identified using parametric method, like conventional least mean squares (LMS) and partial least squares (PLS) methods. Variable-structure radial basis function neural network constructed by sequential learning algorithm is proved to be effective in represent time-varying dynamics caused by environmental disturbances, which is hard for the parametric method. In this paper, we take both advantages of the conventional parametric model and the variable-structure RBF network as the non-parametric method in series connection. The combined identification is used to give final prediction of ship motion. The learning process configuration of the proposed combined modules is illustrated in Fig.1.

The learning process is conducted in two steps. Firstly, the linear LMS algorithm is implemented to identify the linear coefficient in the NARX model, and the identified value of $y(t)$ is denoted as $\hat{y}_p(t)$. The identification residual between $y(t)$ and $\hat{y}_p(t)$, which is estimated by parametric NARX module, is used to train the RBF network which is served as the non-parametric NARX module.

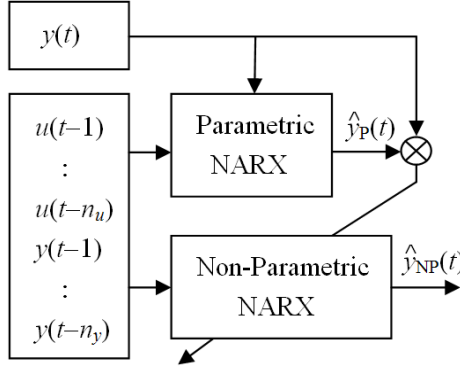


Fig. 1. Learning process of the combined modules

2.2 Parametric Identification Module

The prediction model is based on the conventional NARX model. Models with linear parameters are simpler to analyze mathematically and quicker to compute numerically, so LMS method is conducted for identifying parametric sequentially as the system samples are presented one by one or batch by batch.

At the time of t , a discrete-time nonlinear system can be described by NARX model as below:

$$y(t) = f(y(t-1), \dots, y(t-n_y), u(t-1), \dots, u(t-n_u)) + e(t) \quad (1)$$

where u , t , \dots , y , t , \dots and e , t , \dots are the system input, output and noise variables; n_u and n_y are the maximum time lags in the input and output, respectively; and f is the unknown nonlinear mapping to be identified.

All p training data are presented in the following matrix form of $Xw = d$, where

$$X = \begin{pmatrix} y(t-1) & \cdots & y(t-n_y) & u(t-1) & \cdots & u(t-n_u) \\ y(t-2) & \cdots & y(t-1-n_y) & u(t-2) & \cdots & u(t-1-n_u) \\ \vdots & \vdots & \vdots & \vdots & \vdots & \vdots \\ y(t-p-1) & \cdots & y(t-p-n_y) & u(t-p-1) & \cdots & u(t-p-n_u) \end{pmatrix},$$

$$w = \left(w_1(t) \quad \cdots \quad w_{n_y}(t) \quad w_{n_y+1}(t) \quad \cdots \quad w_{n_y+n_u}(t) \right)^T,$$

$$\text{and } d = \left(d_1(t) \quad \cdots \quad d_p(t) \right)^T.$$

The straightforward way to determine the values of the weights w is to solve the linear equation by applying pseudo inverse:

$$w = X^+ d = [X^T X]^{-1} X^T d \quad (2)$$

By solving such equations, we get all coefficients forming the weighting vectors w used for the final forecasting, by replacing the t by $t+1$ in (1).

When the volume of samples is large, the calculation based on (2) may cause problems of large computation dimension and slow proceeding speed. So, the recursive pseudo inverse algorithm [6] can be implemented to ensure the computational speed of the algorithm.

2.3 Non-parametric Identification Module

Gradient orthogonal model selection (GOMS) algorithm is a sequential learning algorithm and has been proved to be effective in time series prediction [7] and control [8] applications. Here the algorithm is employed to online construct variable-structure RBF network as the non-parametric module to express the time-varying dynamics.

The most important feature of variable-structure network is that the number and location of hidden units are adjusted at each step, thus the variable structure can capture the changes of system dynamics. The structure adjustment strategy of GOMS algorithm is that the new sample will be added as a new hidden unit, while units contributing less to the output will be excluded from the network. After the hidden units are adjusted at each step, the connecting weights of the network will be determined. The contribution of each hidden unit is evaluated by an index called normalized error reduction ratio. The detail of the algorithm can be found in [7, 8] and will not be stated here.

As the inputs of NARX model, u and y , belong to different categories, it is reasonable to employ different center width in activation functions, which is different from a common center width in conventional single scale RBF network. The resulting network is referred to as generalized multi-scale RBF network, which provides more flexible representations of system dynamics and shows better generalization properties [9]. In this application, the GOMS algorithm is improved by adopting multi-scale RBFs in the network:

$$\varphi = \exp\left\{-\frac{1}{2}\left[\left(\frac{y(t-1)-c_{i,1}}{\sigma_y}\right)^2 + \dots + \left(\frac{y(t-n_y)-c_{i,n_y}}{\sigma_y}\right)^2 + \left(\frac{u(t-1)-c_{i,n_y+1}}{\sigma_u}\right)^2 + \dots + \left(\frac{u(t-1)-c_{i,n_y+n_u}}{\sigma_u}\right)^2\right]\right\} \quad (3)$$

where φ is the response of centers corresponding to the input of sliding window, σ_y and σ_u are center widths determined for y and u , respectively.

Therefore, in GOMS algorithm, the vectors of centers and sliding window input are divided into categories of u and y , respectively.

3 Planar Ship Motion Prediction

3.1 Response Model of Ship Motion

Consider the characteristics of high frequency in ship motion, a second order response model can be expressed as :

$$T_1 T_2 \ddot{r} + (T_1 + T_2) \dot{r} + r = K(\delta + \delta_r) + K T_3 \dot{\delta} \quad (4)$$

where K and T_1, T_2, T_3 are the maneuverability indices; r is the yaw rate and δ is the rudder angle. Discretizing (4) into a difference form, yields:

$$r(t) = a_1 r(t-1) + a_2 r(t-2) + b_1 \delta(t-1) + b_2 \delta(t-2) + c \quad (5)$$

The values of parameters $\{T_1, T_2, T_3, \delta_r\}$ and the model of ship's motion can be defined once $\{a_1, a_2, b_1, b_2, c\}$ was determined [10].

3.2 Ship Motion Prediction Simulation

To validate the effectiveness of the proposed prediction method, we adopt the model-scale experiment of $10^\circ/5^\circ$ zig-zig test data of KVLCC model recommended by international towing tank conference (ITTC) as benchmark data. The changes of rudder angle and ship heading of the test are illustrated in Fig.2.

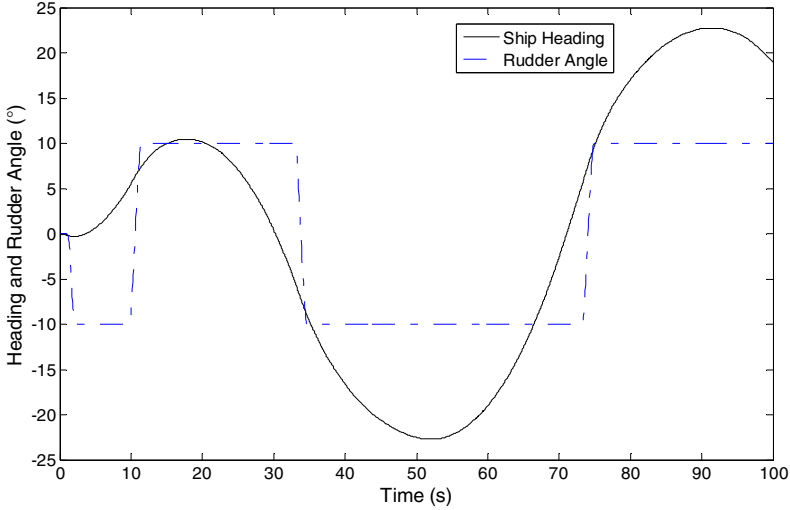


Fig. 2. Heading and rudder angle in the $10^\circ/5^\circ$ zig-zig test

In the training phase, the parametric module is used to process the received samples sequentially by identifying the parameters $\{a_1, a_2, b_1, b_2, c\}$ and form the NARX model (5). The identified value of ship's yaw rate produced by the parametric method is denoted as $r_p(t)$. The variable-structure network is then used to identify the residual unidentified part $r(t) - r_p(t)$, which can be considered as the unidentified dynamics and time-varying dynamics caused by environmental disturbances. The identification error of parametric NARX using LMS algorithm is illustrated in Fig. 3.

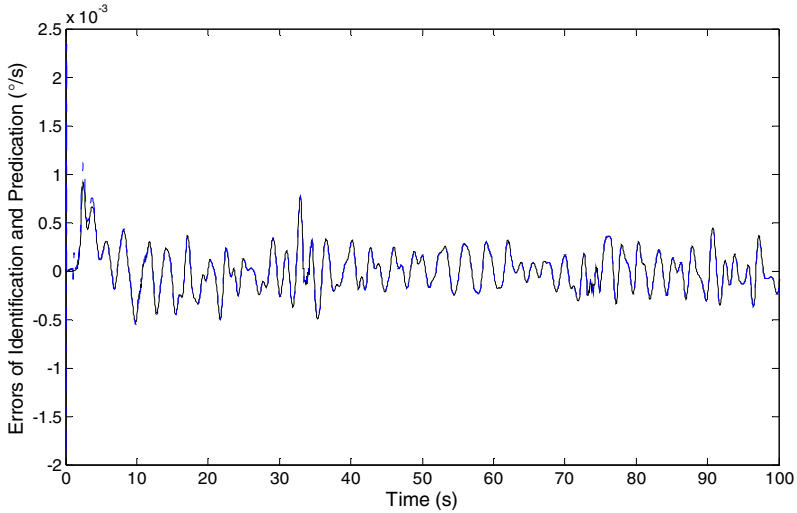


Fig. 3. Identification error and predictive error using parametric NARX model

It is shown in Fig.3 that the curve of identification and prediction error almost coincides in the latter phase of the on-line prediction, which implies that there are some feature cannot be identified by the above parametric module. So it is reasonable to represent the dynamics by some other approaches. In this paper, the variable structure on-line constructed by GOMS algorithm is used to represent the time-varying dynamics. In implementing the GOMS algorithm, the parameters are selected as follows: the width of sliding window $N=3$, accuracy tolerance $\rho = 0.2$, consecutive time span $P=3$, and the order of GOMS algorithm is set as 0. Input of NARX is set as $\{r(t-1), r(t-2), \delta(t-1), \delta(t-2)\}$ and $r(t)$ is set as the output. As the new sample is added to the RBF network structure as a hidden unit center, the identification error is rather small and remains below the order of 10^{-14} (°/s). At each step, once the neural network expression of the input-output mapping is achieved, the one-step-ahead prediction of $r(t+1)$ is made on basis of $\{r(t), r(t-1), \delta(t), \delta(t-1)\}$.

The modeling of system is a dynamic process with the number and location of hidden units in the variable structure RBF network are adjusted at each step. The average number of hidden units during the process is 6.1475. Evolution of hidden units' number is depicted in Fig.4.

The experiment result of the on-line prediction error is depicted in Fig. 5.

It can be seen from Figs. 3 and 5 that the identification error of yaw rate is significantly reduced by implementing neural network for fitting the time-varying dynamics, remains in the order of 10^{-5} (°/s) most of the time, which is lower than the order of magnitude merely by parametric prediction module. The sudden increase on the curve right corresponds to the moments of rudder changes as depicted in Fig.2, which means the dynamics of system varies rapidly at the moment. Once the ship's yaw rate is accurately predicted, the ship's motion characteristics can be estimated subsequently.

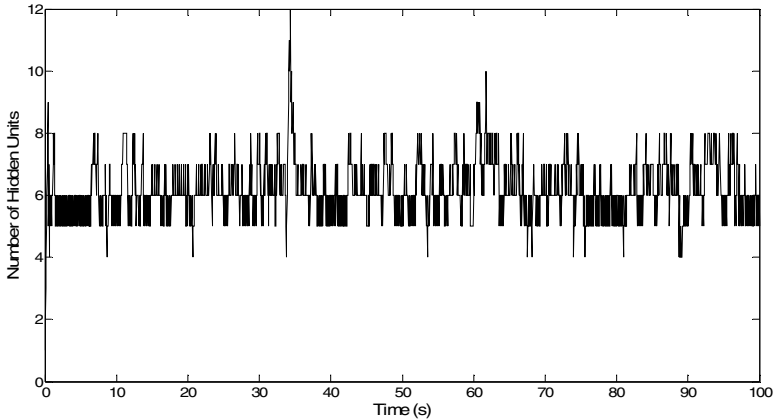


Fig. 4. Evolution of hidden units' number

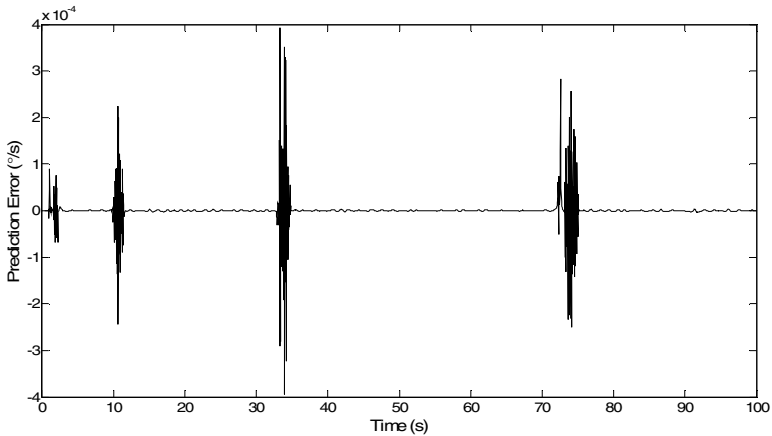


Fig. 5. Prediction error using modular model

4 Conclusion

The paper has presented an ensemble modular approach to forecast the planar ship motion. The linear parametric prediction and non-parametric variable-structure RBF network are combined to express the dynamics of ship motion and make predictions on-line. The linear module ensures the holistic expression of the nature and the nonlinear module track the time-varying dynamics of system. The sequential learning mode ensures the practical on-line application of the proposed modular prediction method. The experimental results demonstrated the effectiveness and robustness of the combined modular prediction method.

References

1. Fossen, T.I.: *A Guidance and Control of Ocean Vehicles*. John Wiley, New York (1994)
2. Haykin, S.: *Neural Networks: A Comprehensive Foundation*. Prentice Hall, New Jersey (1998)
3. Vigneshwaran, S., Sundararajan, N., Saratchandran, P.: Direction of Arrival (DoA) Estimation under Array Sensor Failures Using a Minimal Resource Allocation Neural Network. *IEEE Trans. Antennas and Propagation* 55(2), 334–343 (2007)
4. Carney, J., Cunningham, P.: Tuning Diversity in Bagged Ensembles. *Int. J. Neur. Sys.* 10, 267–280 (2000)
5. Kuntcheva, L.: *Combining Pattern Classifiers—Methods and Algorithms*. Wiley, New York (2004)
6. Ma, J., Li, G.B.: Time Series Prediction of Ship Rolling. *Beijing Inst. Mach.* 21(1), 4–7 (2006)
7. Yin, J.C., Hu, J.Q., He, Q.H.: Variable Structure Radial Basis Function Network and Its Application to On-Line Chaotic Time Series Prediction. *Pattern Recognition Artif. Intel.* 23(6), 874–879 (2010)
8. Yin, J.C., Wang, L.D., Wang, N.N.: A Variable-Structure Gradient RBF Network with its Application to Predictive Ship Motion Control. *Asian J. Control* (in Press), doi:10.1002/asjc.343
9. Billings, S.A., Wei, H.L., Balikhin, M.A.: Generalized Multiscale Radial Basis Function Networks. *Neur. Netw.* 20, 1081–1094 (2007)
10. Luo, W.L., Zou, Z.J.: Identification of Response Models of Ship Maneuvering Motion Using Support Vector Machines. *Ship Mech.* 11(6), 832–838 (2007)

Ultrasonic Sensor Based Material Level and Liquid Level Measurement Technology

Gong-chang Ren¹, Hai-chun Guo², Yong Yang³, and Zhi-wei Yang⁴

College of Mechanical & Electrical Engineering, Shannxi University of Science & Technology, Xi'an, China, 710021

¹ rengc@sust.edu.cn, ² zhangchun13891@163.com,

³ zhwyx998@163.com, ⁴ bluememorysky@163.com

Abstract. In order to accurately and efficiently apply ultrasonic measurement technology to the fields such as industry, materials and liquid levels to realize the factual measurements of measured objects, the present measuring technology based on ultrasonic waves is analyzed and researched. The measurement principles, hardware selection and calibration, and data transmission and acquisition of the ultrasonic waves are detailedly introduced. By adopting the ultrasonic measurement technology to detect and analyze the raw oil liquid level of an oilfield oil storage tank, the results show that the ultrasonic measurement technology has the characteristics of high measuring accuracy, safe and reliable operation, low cost, etc.

Keywords: RISEN-BSU ultrasonic sensor, Static calibration, Dynamic calibration, MEGA128, Data acquisition.

1 Introduction

Ultrasonic waves, the mechanical oscillation in mediums, have higher axial resolution [1]. Ultrasonic waves are insensitive to color, light intensity, outside light and electromagnetic fields, so that supersonic sounding has a certain adaptive capacity to the measured objects under the harsh environments such as darkness, dust or smog, interaction of strong electromagnet and poison, and is widely used in the measurements of liquid level and materiel level. As the ultrasonic transmission is less susceptible to be intervened, the consumption of energy is slow and the transmitting distance in mediums is further, so that the ultrasonic waves are frequently used to measure the distances of the materiel level and liquid level.

2 Principles of Ultrasonic Measurement Technology

The ultrasonic measurement technology takes the advantage of properties of ultrasonic waves, such as better directionality, less energy loss during transmitting process and reflectibility when encountering an interface when the ultrasonic waves transmit in liquid and can adopt the principles of echo location to measure the reflected time that the ultrasonic waves encounter a liquid level, so as to define the height of the liquid level [2]. Principles of the ultrasonic liquid level measurement are shown in Figure 1.

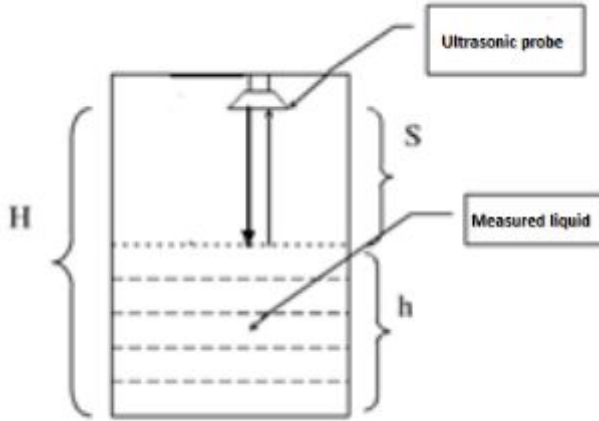


Fig. 1. Principles of the ultrasonic liquid level measurement

The figure above shows:

$$S = C * [t / 2] \tag{1}$$

$$h = H - S \tag{2}$$

The S in the equations above is the distance from an ultrasonic probe to the liquid surface and can be deduced from the equation (1); the C is the light speed, and the t is the measurement time; H is the distance from the ultrasonic probe to the bottom of the container and is needed to be measured in advance; and the h is the height of liquid level to be measured and can be deduced from the equation (2).

3 Selecting and Calibrating Process of an Ultrasonic Sensor

3.1 Selection of a Sensor

In a number of ultrasonic sensors, a RISEN-BS compact ultrasonic material level transmitter is designed for the application conditions such as low-cost, small installation space, equipment coordination, etc. It integrates an ultrasonic sensor, a temperature sensor, an ultrasonic servo circuit, a transmitter circuit as a whole and adopts an SMD component and an ASC special chip, so that the circuits of the entire device are very compact and simple; and the casing is made of NLEPF synthetic material with solid texture and good acoustic characteristics, and its shape is exquisite and beautiful. Due to the waterproof and dustproof properties, the transmitter can be suitable for most site conditions. The product drawing is shown in Figure 2, and the installation diagram is shown in Figure 3.

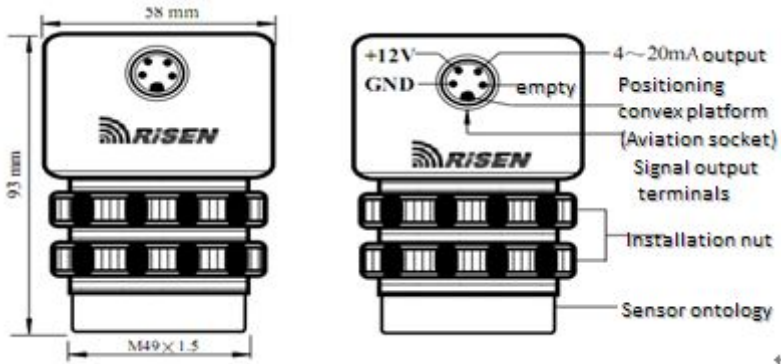


Fig. 2. RISEN-BS product drawing

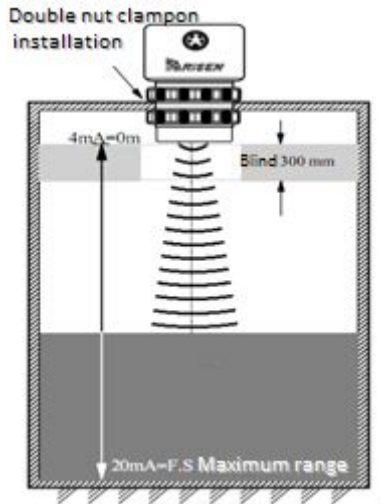


Fig. 3. RISEN-BS installation diagram

3.2 Calibrating Process

Sensor calibration is a process that a standard instrument with high-level precision is used to determine the degree of the sensor so as to establish the corresponding relationship between the output and input of the sensor and determine the errors under different using conditions. According to the purpose of the system, the input can be static or dynamic, so that the sensor calibration is divided into two kinds: static calibration and dynamic calibration.

Static Sensor Calibration

The static calibration is mainly used for testing and measuring the index of the static properties of the sensor, such as linearity, sensitivity, hysteresis, repeatability, etc.

According to the functions of the sensor, the processes of the static calibration are as follows: firstly, establishing a static calibration system, and secondly, selecting certain-degree calibrating instruments and equipment, of which the precision is corresponding to that of the calibrated sensor. Different sensors adopt different calibrating methods, such as commonly-used force calibration, pressure calibration and displacement transducer calibration.

Dynamic Calibration of the Sensor

As some sensors need to meet the requirements of not only the static properties but also its dynamic characteristics, the dynamic calibration is needed after the static calibration, so as to determine their dynamic sensitivity, natural frequency and frequency response range. When the sensor is performed the dynamic calibration, it needs to be excited by a standard signal. There are two kinds of normally used standard signals: one is the periodic function, such as a sine wave and the like; and the other are the transient function, such as a step wave and the like. The output signals of the sensor are received after the excitation of the standard signal, and after analysis and calculation, and data processing, their frequency characteristics, such as amplitude-frequency characteristic, damping, dynamic sensitivity and the like can be determined.

Actual Calibration Process of the Ultrasonic Liquid Level Measurement

An ultrasonic ranging sensor is used for measuring the changing situations of the material level and the liquid level. As the sensor has its calibration range, accurate information can be obtained in the range [3]. Provided the measuring distance of the sensor is 180 cm, the specific calibration procedures are as follows:

Firstly, the measurement range of a sensor is divided into several uniformly-spaced points, and as the uniform spaces are 10 cm, the blind spots thereamong are 0 cm ~ 30 cm.

Secondly, according to the measurement range points of the sensor, taking 30 cm as a starting point of the initial value of the sensor calibration, the input is changed gradually from 30 cm to 180 cm, so as to record the corresponding input and output values. Then the input value is further changed gradually from 180 cm to 30 cm, and then the corresponding input and output values are recorded.

Thirdly, repeating the two steps above to repeatedly measure the forward and reverse traveling distances of the sensor, and the curve drawn based on the data recorded is shown in Figure 4.

From Figure 4 can be observed that the data measured by the ultrasonic sensor approximates to linear. Through the linear equation $y = ax + b$ and the changes of y and x , the equations $a = 1$ and $b = 125$ are deduced. Therefore, the linear equation can be expressed as follows:

$$y=x+125$$

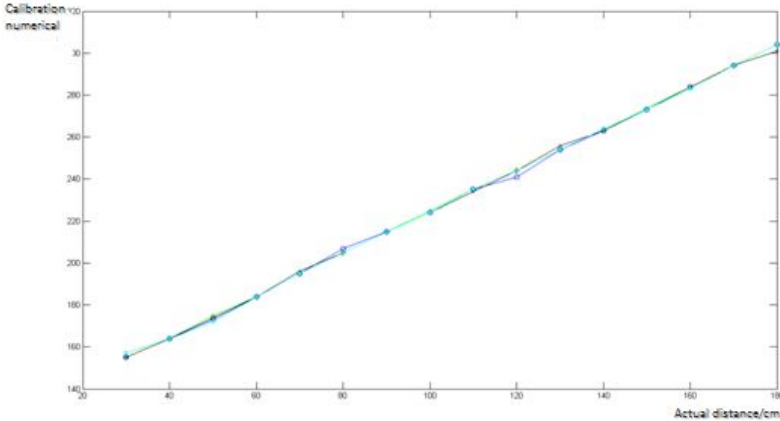


Fig. 4. Calibration displacement curve

4 Data Output and Acquisition of the Ultrasonic Liquid Level

An ultrasonic liquid level sensor can output a current signal, which has linear relationship with the range height in the material level and liquid level, according to the changes of the measured material level and liquid level in the calibration range. As MEGA128 only can convert voltage signals into digital quantity, the current output of the sensor needs to be converted into voltage signals. The data collected are finally converted to binary codes [4-6] by mode numbers through a data acquisition module. In order to eliminate the influence the outside interference exerting on the measurement accuracy, filtering processing can be adopted, so that the data obtained can more accurately reflect the height of the measured objects through the corresponding conversion.

The maximum measuring range of the RISEN-BS ultrasonic sensor is 5m, the blind spot is 30cm, and the output signals are 4 ~ 20 mA current; the current can be converted to a 0.6 ~ 3V voltage signals through the circuit shown in Figure 5. The reference voltage in the data acquisition module is 5V, and the A/D conversion resolution is 10 bits, so that the calculation formula of the converted data is:

$$\text{Data}_h = V_x / 5 * 1024$$

In the formula, the Data_h is the converted data, and the V_x is the converted voltage value of the output of the ultrasonic sensor.

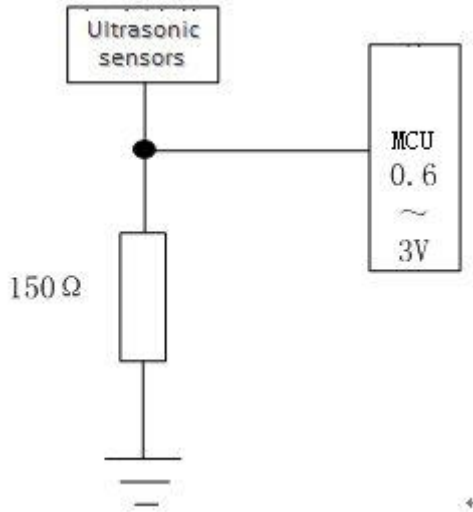


Fig. 5. Current-voltage conversion principles

5 Conclusion

In the design and realization of the ultrasonic wave based measurement technology, ultrasonic echo ranging and measurement principles of the ultrasonic waves, the selection and calibration process of the ultrasonic sensor, and the transmission, collection and analysis processing of the measured data are respectively introduced. Through the analysis of the classification of the measured data, the conclusion that the ultrasonic measurement technology can collect, process and transmit the data, and can accurately reflect the actual values of the data measurement. Therefore, the ultrasonic wave based measurement technology can be well applied to the fields of materials, liquid levels and industry.

References

1. Wang, Y.K.: The principle of ultrasonic wave and Application in Modern Milifarg. *Journal of Guizhou University(Natural Science)* 22(3), 287–290 (2005)
2. Zhu, M., Zhang, Y.: Design of Ultrasonic Ranging System for Liquid Caging. *Tractor & Farm Transporter* 34(1), 67–69 (2007)
3. Song, F., Shi, H.R., Dou, L.W.: The ultrasonic sensor material place in the measurement of the application. *Automation in Petro-Chemical Industry* (3), 67–70 (2007)
4. Zhang, Y.K., Chen, S.J., Qiu, X.H.: The single chip computer principle and application, pp. 238–330. Xian university of electronic science and technology press (2005)
5. Zhou, Z.A., Fan, L.L., Wang, X.Y.: Data collection system design and practice, pp. 207–239. Earthquake Press (2005)
6. Li, T.: Data acquisition system design based on MCU. *Information Technology* 30(4), 108–110 (2011)

Design of a 23-DOF Small Humanoid Robot with ZMP Force Sensors

Awais Yasin^{1,2}, Qian Xu^{1,2}, Bo Chen^{1,2}, Qiushi Lu^{1,2}, and M. Waqas Khan¹

¹ Key Laboratory of Biomimetic Robots and Systems, Beijing Institute of Technology, Ministry of Education, P.R. China

² Intelligent Robotics Institute, School of Mechatronics Engineering, Beijing Institute of Technology, 5 Nandajie, Zhongguancun, Haidian, Beijing, 100081, P.R. China
awaisfrombit@gmail.com, juvcry@bit.edu.cn,
{chenboiisi, qiushi.lu1986, wak.yousafzai}@gmail.com

Abstract. This paper presents a design of a 23-DOF small humanoid robot with force sensors for zero moment point (ZMP) measurement. Piezoresistive strain gauges are used under the feet of the robot to measure ground reaction force which is used to locate ZMP under the robot foot support area. The robot also uses gyroscope and acceleration sensor for motion control. The robot developed is capable of all directional walking, running and performing different kung fu like actions. Design specifications, joints distribution, walking planning of the robot, ZMP measurement scheme and vibration control using gyro sensor are discussed in this paper.

Keywords: Humanoid Robot, Biped, ZMP, Walking Planning, Force sensor.

1 Introduction

There exist a number of approaches to biped locomotion. Among the most successful ones are trajectory tracking methods that are based on pre-computed trajectories of the legs or the Zero Moment Point (ZMP). The ZMP is the point on the ground where the total moment generated due to gravity and inertia equals zero [1-4]. On flat horizontal surfaces it is equal to the center of pressure and can be imagined as the point on the ground about which the robot tilts. If the ZMP remains in the convex hull of the support polygon, the gait of the robot is considered dynamically stable, i.e. the robot does not fall. ZMP may be computed using model of the robot and information from the joint encoders or by directly using data from sensors mounted under the feet of the robot. Our robot also uses ZMP approach for stable walking and force sensors are used under feet of the robot for ZMP measurement.

The following section gives a brief description of mechanical and electronic design specifications [Table1, Fig (1-3)]. Section three discusses joint distribution and rotation range etc and section four explains gait planning. ZMP measurement and vibration control are discussed in section five and six respectively.

2 Design Specifications

Our robot is a small kid-size robot with height, width and weight as mentioned in table 1 below. A robot with these dimensions can also participate in “RoboCup” which is a worldwide soccer competition of robots. The goal of RoboCup is to

Table 1. Design Specifications

Height	55 [cm]
Width	23 [cm]
Weight	3.8 [kg]
DOF (Degree of Freedom)	23
Frame	Aluminum
Actuator	Servo Motor RX-64, RX-28
Controller	ARM9 S3C2440, 400MHz
Sensors	Piezoresistive Strain Gauge Gyro Sensor (SSSJ CRS03-04) Accelerometer (Crossbow CXL04LP3)
Battery	Li-Po 7.4 V x 2 2100Amh 20C/40C

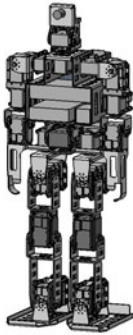


Fig. 1. 3-D View of Robot

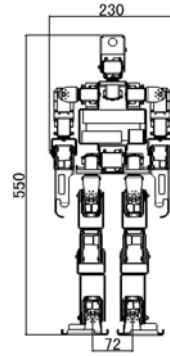


Fig. 2. Size of Robot

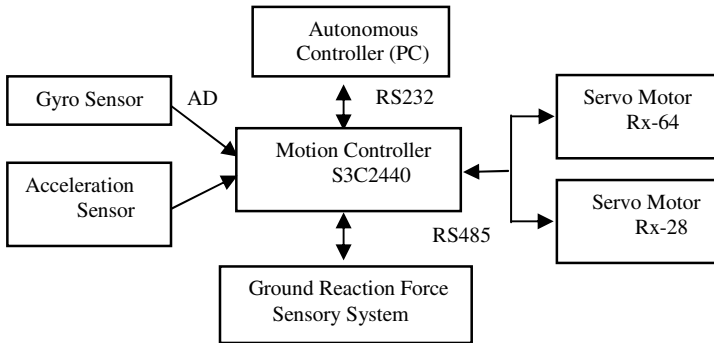


Fig. 3. System Configuration

develop humanoid robots which can win a soccer game against the world cup champion team of human until the year 2050 [7].

3 23 Joints Distribution

The robot is designed to mimic human characteristics as closely as possible especially in relation to basic physical structure through the design and configuration of joints and links. The robot has a total of 23 DOFs: six for each leg, four for each arm, one for the waist and two for the head. The high number of DOFs provides our robot with the possibility of realizing complex motions. The comparison of joint distribution in humans and this small humanoid robot is as in table 2.

Table 2. Comparison of Joint Distribution in Humans and Humanoid Robot

Joint	Number of DOFs Right / Left (Rotation Axis)	
	Human	Humanoid Robot
Neck	3 (yaw, pitch, roll)	2 (yaw, pitch)
Right/ Left Shoulder	3 (yaw, pitch, roll)	2 (pitch, roll)
Right / Left Elbow	2 (yaw, pitch)	2 (yaw, pitch)
Right / Left Wrist	3 (yaw, pitch, roll)	0
Waist	3 (yaw, pitch, roll)	1 (pitch)
Right / Left Hip	3 (yaw, pitch, roll)	3 (yaw, pitch, roll)
Right / Left Knee	1 (pitch)	1 (pitch)
Right / Left Ankle	3 (yaw, pitch, roll)	2 (pitch, roll)

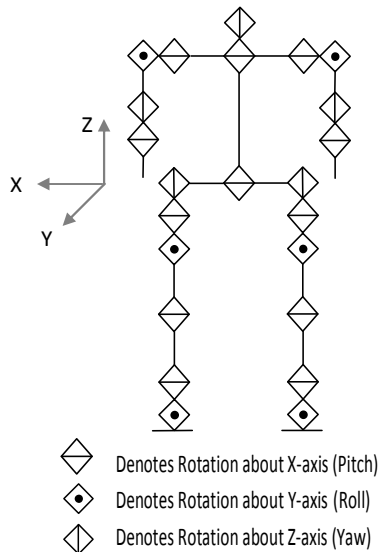


Fig. 4. Local axis Orientation

Joint rotation angles are decided from consideration of elements such as correlation with human joint rotation angles and position of body parts and body structure design. These elements lead to mobility and flexibility of humanoid manipulators to attain trajectory, as well as to avoid collision problems. Joint rotation range of our 23 DOF humanoid robot is as in table 3.

Table 3. Joint Rotation Range

Joint	Joint Rotation Range
Neck (pitch)	-45 ~ +45
Neck(yaw)	-90 ~ +90
Shoulder (pitch) right & left	0 ~ +180
Shoulder (roll) right & left	-90 ~ +90
Elbow (yaw) right & left	-90 ~ +90
Elbow (pitch) right & left	0 ~ +100
Waist (yaw)	-90 ~ 0
Hip (yaw) right & left	-45 ~ +45
Hip (pitch) right & left	-20 ~ +60
Hip (role) right & left	-40 ~ +10
Knee (pitch) right & left	-70 ~ 0
Ankle (pitch) right & left	-30 ~ +50
Ankle (Roll) right & left	-30 ~ +30

4 Gait Planning

Normalized trajectory table for each of direction X, Y, Z, and θ is used to make gait [8]. The trajectory of right and left center of gravity movement calculated by the expression (1) and (2) satisfy the reference ZMP.

$$x_{foot}(t) = C_1 \cdot \exp(K \cdot t) + C_2 \cdot \exp(-K \cdot t) + x_{ZMP}^{\max} \quad (1)$$

$$C_1 = C_2 = \frac{-x_{ZMP}^{\max}}{\exp(K \cdot K_T) + \exp(-K \cdot K_T)} \quad (2)$$

Where
$$K = \sqrt{\frac{H}{g}} \quad \text{and} \quad K_T = \frac{T}{4}$$

The trajectory table of X is a straight line and is given by expression (3) which is same as for rotation of yaw axis θ .

$$x(n) = n / SIZE \quad (3)$$

And for up and down z , we have (4) and (5) below

$$z_{up}(n) = 1 - \frac{\arcsin(1 - n/SIZE)}{\pi/2} \quad (4)$$

$$z_{dn}(n) = 1 - \frac{\arcsin(n/SIZE)}{\pi/2} \quad (5)$$

5 ZMP Measurement

Piezoresistive strain gauge is used as force sensor for ZMP measurement (Fig 6&7). Four sensors housed in a special assembly are mounted on four corners of both feet (Fig 8). A dedicated controller with data acquisition system is also mounted on each foot. The signals measured are first passed through a low pass filter and then digitized using built in A/D converter of C8051 microcontroller used (Fig 7).

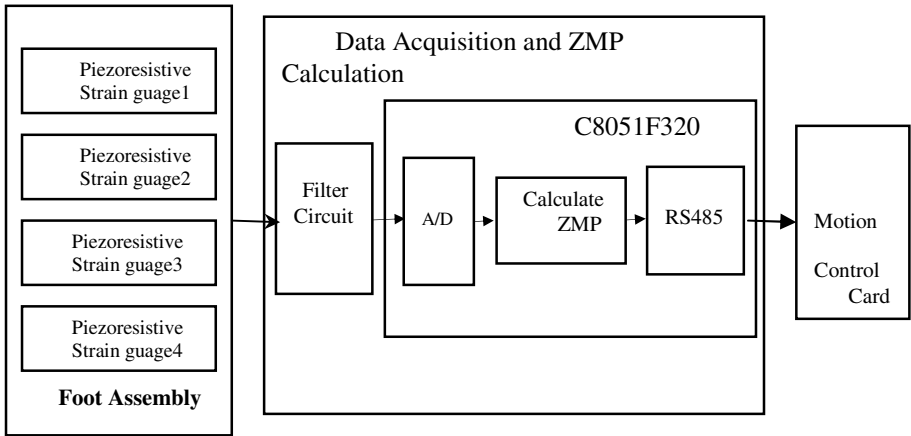


Fig. 5. Block Diagram of ZMP sensory system

The single foot support phase ZMP coordinates in the local foot coordinate frame are then computed by expression (6) and (7) below. The calculated position of ZMP is then sent to the main motion control card.

$$x_{zmp} = \frac{\sum_{i=1}^N p_{ix} f_{iz}}{\sum_{i=1}^N f_{iz}} \quad (6)$$

$$y_{zmp} = \frac{\sum_{i=1}^N p_{iy} f_{iz}}{\sum_{i=1}^N f_{iz}} \tag{7}$$

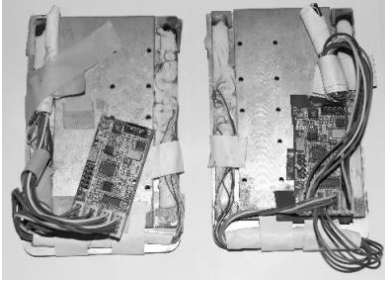


Fig. 6. Foot Assembly

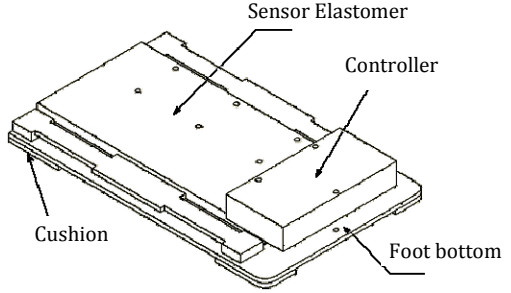


Fig. 7. Foot base with Controller

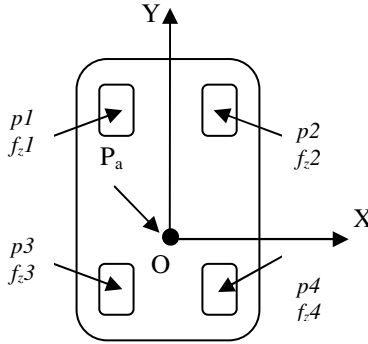


Fig. 8. Sensor's position under feet

6 Vibration Control

A gyroscope is mounted in the trunk of the robot to get the information about the angular velocity of the robot in the sagittal plane. If the angular velocity becomes too large, the robot is likely to lose balance. The idea of the gyro feedback controller is to modify the foot angle in sagittal direction in order to induce torque in the opposite direction to the possible fall.

A proportional controller (P-controller) is used to do so, according to the angular velocity ω of the rotation of pitch axis (sagittal direction). A P-controller is a control loop feedback mechanism that tries to correct the error between a measured process variable (e.g. the angular velocity of the robot's trunk) and a desired set point (e.g. zero angular velocity). To correct the error, a corrective action (e.g. foot angle

regulation) is calculated in order to minimize the error. The P-controller calculation involves only one parameter: the proportional gain that is denoted here as K_p , that determines the absolute value of the reaction to the current error (e.g. absolute change of the foot angle).

The gyroscope P-controller is then defined as (8)

$$\theta_{FootGyro} = \theta_{Foot} - K_p \omega \quad (8)$$

Where

$\theta_{FootGyro}$: Angle of joint (before control)

θ_{Foot} : Angle of joint (after control)

Experiments. Walking experiments are performed on our own developed 23 DOF small humanoid robot (Fig 9). The robot can walk in all directions and run with a maximum speed of 1km/hr. The robot is also capable of performing a number of kung fu like actions.

Fig 9 below shows images of basic stepping of the robot.

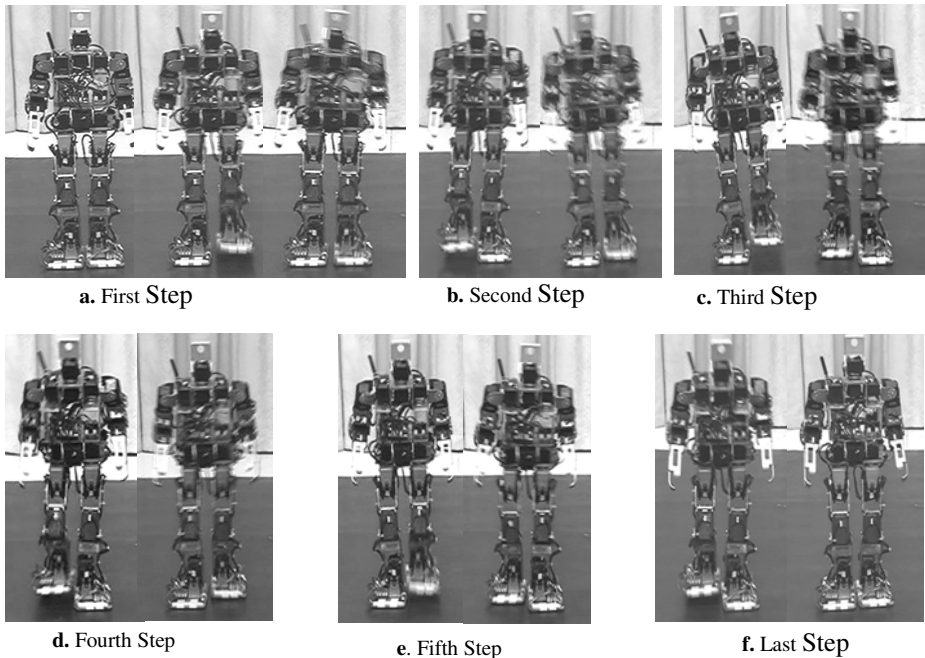


Fig. 9. Experiment results of walking

Conclusions. Complete hardware design and gait planning of a 23 DOF humanoid robot is presented in this paper. ZMP calculation using piezoresistive strain gauge is proved to be a simple and one of the direct methods of biped gait control.

Acknowledgment. This work was supported by the National Technology Research and Development, China (863 Project) under Grant 2007AA041603, National Natural Science Foundation of China under Grant 60874048, National Science Foundation for Distinguished Young Scholar under Grant 60925014, and “111 Project” under Grant B08043.

References

1. Vukobratovic, M., Juricic, D.: Contribution to the biped gate. *IEEE Trans. Bio Med. Eng.* 16(1), 1–6 (1969)
2. Goswami: Postural stability of Biped robots and the foot-rotation Indicator (FRI) point. *The Int. J. Robotics. Research* 18(6), 523–533 (1999)
3. Kajita, S.: Zero Moment Point (ZMP) and Walking Control. *JRSJ* 20(3), 229–232 (2003)
4. Hirai, K., Hirose, M., Haikawa, Y., Takenaka, T.: The Development of Honda humanoid robot. In: *Proc. IEEE Int. Conf. Robotics and Automation*, pp. 1321–1326 (1998)
5. Huang, Q., Kajita, S., Koyachi, N., Kaneko, K., Yokoi, K., Arai, H., Komoriya, K., Tanie, K.: A High Stability, Smooth Walking Pattern for a Biped Robot. In: *Proc. IEEE Int. Conf. Robotics and Automation*, pp. 65–71 (1999)
6. Li, Q., Tanishi, A., Kato, I.: Development of ZMP Measurement System for Biped Walking Robot Using Universal Force-Moment Sensors. *JRSJ* 10(6), 828–833 (1992)
7. Matsubara, H., Asada, M., Kitano, H.: History of RoboCup and Prospects for RoboCup 2002. *Journal of the Robotics Society of Japan* 20(1), 2–6 (2002), <http://www.robocup.org>
8. Sakamoto, H., Nakatsu, R.: Walking Control of Small Size humanoid robot HAMJIME ROBOT 18. In: *Proc. of SPIE*, vol. 6794, pp. 679421–679422 (2007)

An Advanced Ontology Mapping Framework Based on Similarity Calculating

Hao Tian^{1,2}

¹ State Key Laboratory of Information Engineering in Surveying, Mapping and Remote Sensing, Wuhan University, Wuhan 430205, China

² Department of Electronic Engineering, Hubei University of Economics, Wuhan 430205, China

th@hbue.edu.cn

Abstract. Ontology is a powerful tool to realize knowledge sharing and reasoning, but it is difficult to achieve ontology interoperation because of heterogeneous ontology. Ontology mapping is an effective method to solve ontology heterogeneity. This paper presents an advanced ontology mapping framework based on similarity calculating. The framework includes three main modules, and it could narrow the scope of the concept judging by setting the similarity threshold, so as to increase the mapping speed, it also has good flexibility. It provides a new method for ontology mapping.

Keywords: ontology mapping, framework, similarity calculating, module.

1 Introduction

Along with the development of information technology, ontology technology is more and more mentioned recently. Ontology can accurately describe the meaning, and can uncover the intrinsic connection between concepts, also has the very strong ability of semantic concept expression and knowledge acquisition.

Although the aim of ontology construction is to realize the knowledge sharing and reuse, but there are few successful cases in ontology applying. The main reason is the multiformity of ontology. As there is not only one criterion of ontology construction, so for the same object, different people may construct a different ontology according to their own understanding and need. And therefore, there may be several isomeric ontology models in a same domain. They could not realize interoperate and understanding each other directly. Therefore, in the same area, it must solve the heterogeneous problems between each ontology model before realizing the interoperation of them. Ontology mapping is one of the effective ways to solve the problem.

Based on the existing ontology mapping study, an advanced ontology mapping framework based on similarity calculating is putted forward in the article. It could effectively improve the mapping speed based on the premise of keeping the accuracy of the mapping.

2 Related Works

The purpose of the ontology mapping is to find the potential relationship between each ontological concept, and make corresponding mapping rules. Ontology mapping commonly includes information ontology modeling, similarity of extraction, semantic mapping, mapping execution and mapping post-treatment steps. There are several kinds of methods about ontology mapping. Ma C. *et al.* [1] presented a similarity calculation method, in accordance with the various relationships between concepts, and took into account the impact of already established mapping experience on the unsolved concept similarity. Zhou X. *et al.* [2] proposed a top-down ontology mapping method, the layer classification ontology mapping method could reduce non-related concepts among count for large scale structure ontology mapping. Pang X. *et al.* [3] proposed a domain learning-based ontology mapping method which could use domain knowledge and historical mappings to augment the training data and to find the complex mapping rules about the ontology being matched, and also used the semantic information of ontology to optimize the mapping process in order to decrease the complexity of mapping method. Pan Y. *et al.* [4] brought out a new classification-based method for ontology mapping to pursue a cost-effective approach aiming at the deficiency of current mapping methods and implemented the prototype tool (COMT) based on the method. There are also some other typical methods of ontology mapping such as DOLCE [5], QOM [6], and LSD [7] *et al.*

In general, the method based on similarity is the mainstream ontology mapping method, and the method calculate the similarity between each nodes based on grammar or semantic plan, use a similar measure to determine the mapping result. But most of these methods have unsatisfied mapping speed, so how to build an effective ontology mapping framework to improve the mapping speed and keep the accuracy of the mapping at the same time is a meaningful problem.

3 An Advanced Ontology Mapping Framework

In order to get a higher mapping speed, we present an advanced ontology mapping framework based on similarity calculating on the basis of previous research, as shown in Fig. 1. It includes three main parts such as ontology module, mapping processing module and ontology mapping list.

3.1 Ontology Module

Ontology module contains several ontology models in the same domain, these ontology models describe the parameters such as services description, registration, services input of the services within the scope of this field. They provide can all the parameters that needed in the mapping process. Due to the reason of heterogeneity these ontology models can't directly interoperate.

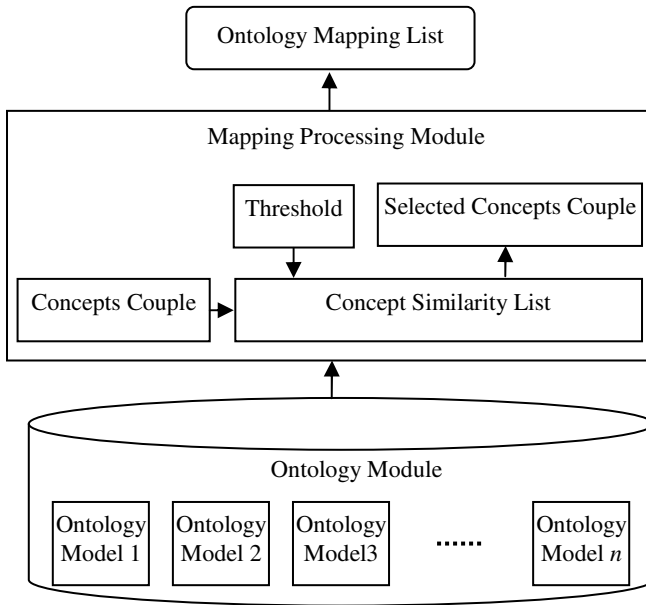


Fig. 1. Structure of the Ontology Mapping Framework

3.2 Mapping Processing Module

The module is the core part of the framework. Its purpose is to create an ontology mapping list. Firstly, it calculates the Cartesian product between each concept of every two ontology models to select the concept couples that needed to calculate its similarity, then it calculates the similarity degree of all concept couples, and it can get a concept similarity list. Need to explain, similarity calculation method basically has the following three: name similarity calculation calculates the similarity between each name of the concepts with edit distance. Example similarity calculation calculates the similarity of the concepts by using the example concept. Attribute similarity calculation through calculating the proportion of the public examples in the total number of attribute value domain. In practical applications, we can adopt one of them according to the initial conditions, and also can synthetically use these methods by a certain weight values.

Secondly, it sifts the concept couples on the list according to the threshold, and chooses the concept couples whose similarity is greater than threshold value, so it can get those couples that can be mapped.

Finally, it submits concept couples to the next module for screening and confirmation. During the process, the threshold could be given by experts or defined according to previous rules in real time.

3.3 Ontology Mapping List

According to the results of the last stage screening, the module generates a credible mapping table by some specific rules, and stores the generated mapping table in a

mapping results database. So, when the source ontology of relevant examples is inputted, the system can work by using the mapping rules which have concluded.

Based on the above description, we can see that the mapping speed can be improved because of the reduction of the mapping domain. What more, the threshold can be changed any time, so the framework could have good flexibility.

4 Conclusion

In this paper, we proposed an advanced ontology mapping framework based on similarity calculating. We can get a satisfied mapping result through three modules. It has good mapping speed and mapping accuracy, and it is also flexible in mapping process. It provides a new idea for ontology mapping, but there is not detailed research and state about specific similarity methods and concepts screening method in this paper, it is the work to be done in the next step.

Acknowledgments. This work is supported by the Science and Technology Research Funds of Educational Ministry of Hubei Province, China (Grant No. Q20112206), and the Youth Research Funds of Hubei University of Economics, China (Grant No. XJ201115).

References

1. Ma, C., Wang, N., Zhang, H.: Similarity Calculating-based Ontology Mapping Framework. *Computer Engineering* 35, 61–63 (2009)
2. Zhou, X., Liu, L., Fan, R.: A Method of Ontology Mapping Based on Classifying Schema Structure. *Acta Electronica Sinica* 39, 882–886 (2011)
3. Pang, X., Bao, S.: Domain Learning-based Ontology Mapping Method. *Computer Science* 36, 134–137, 141 (2009)
4. Pan, Y., Liang, P., He, K.: Classification-based method for ontology mapping and mapping tool implementation. *Application Research of Computers* 24, 213–215 (2007)
5. Gangemia, Guarino, N., Masolo, C., et al.: Sweetening word net with DOLCE. *AI Magazine* 24, 13–24 (2003)
6. Ehrig, M., Staab, S.: QOM – Quick Ontology Mapping. In: McIlraith, S.A., Plexousakis, D., van Harmelen, F. (eds.) *ISWC 2004. LNCS*, vol. 3298, pp. 683–697. Springer, Heidelberg (2004)
7. Doan, A.H., Domingos, P., Halevy, A.: Learning to Match the Schemas of Data Sources. A Multi-strategy Approach, *Machine Learning* 50, 279–301 (2003)

Analysis and Design for the Financial System in ERP Simulation Instruction Based on SOA^{*}

Gao Chang-yuan, Chen Zhi, Yang Cai-xia, and Tian Shi-hai

School of Management, Harbin University of Science and Technology, Harbin, 150080

Abstract. According to the ERP simulation instruction system's problems, such as the rigidified software architecture and incompleteness of comprehensive functions, the paper analyzed the functions and designed the business processes of the financial management system based on the ERP simulation instructional environment after analyzing the advantage of the SOA. SOA-based the financial system architecture was designed, which has realized the multilayer reuse of business processes layer, service layer and data layer. As the main line with business processes, the paper designed the granularity of the services. It made the system with loose coupling and flexibility, which can meet to college teaching needs better.

Keywords: SOA, ERP simulation instructional system, financial management system.

1 Introduction

With the development of enterprise's informatization, ERP software was used more widely in enterprises. It appears that lacks ERP application talents. In order to adapt to the needs of the Times and to satisfy enterprise personnel demands, ERP teaching was born in university. In the teaching process, ERP instructional simulation, which covers all the ERP management theory, had played a pivotal role in the ERP instruction. It brought great convenience for the teaching and also obtained good effect. As one core sub-system of the ERP system teaching simulation system that the financial management system existed in the current system, but still had undeniable problems as flowed: (1) the system was too complex; (2) the system function was not comprehensive. In the software architecture, most teaching simulation software lacked of flexible architecture design. In teaching requirement change, it's hard to fast configuration the system to meeting teaching needs. In view of the above problems, the paper will focus on instructional simulation degree to design the corresponding functions in the system function. In this paper, the software architecture based on SOA mind to design financial management simulation system and enabled the system with loose coupling, business agility and flexibility change characteristics. Based on SOA idea, the system function was provided as form of service. By calling service can well satisfy the college teaching needs and can integrate other system in ERP teaching simulation environment.

^{*} Educational reform engineering project of higher education in the new century for Heilongjiang province.

2 SOA Advantage Analysis

Service oriented architecture (SOA) is earliest brought out by the Gartner which is an America corporation in 1996. SOA is a kind of method of software architecture, satisfying the distributed computing loosely coupled, standardization and independent agreement demand and so on [1]. Service is the core concept in SOA, which divisions the business into a number of coarse granularity services and business processes. Service is relatively independent, self-contained and reusable. And the business process is consists of one or more of such services. In SOA architecture environment the notes of the network provides resources in the form of service, and other nodes may use standard way to visit it [2]. SOA is an open, agile, extensible, federal and can be combined framework. It contains of self-government, high quality of service, manufacturers of diversity, interoperable, found and potential reusable services, and may through Web Service technology to realize [3].

It also has the quite advantage in actual application. Its main advantage embodied in the following several aspects [4, 5, 6]: (1) Strong scalability. (2) High reusability. (3) Flexible coding.

3 SOA-Based the Financial Management Simulation System Overall Analysis and Design

3.1 Analysis Financial Management of ERP Instructional Simulation

The current design ERP sand table imitation teaching system is in order to make students to understand ERP management procedure better. It concentrates the whole enterprise management process in the system. And it involves enterprise strategic planning, product development, equipment investment and transformation, the production capacity planning and production scheduling, material requirements planning, capital demand planning, marketing and sales, financial analysis, capital operation, team communication and construction and so on [7]. Financial management plays an important role in the ERP sand table imitation teaching production enterprise operation process. ERP teaching of simulation environment of financial management's activities were mainly including daily financial accounting, paying tax, providing financial statements, the daily cash management; enterprise's financing strategy formulation, capital scheduling and risk management, financial regulations management, financial analysis and assist decision, etc.

ERP instructional simulation system is a simplified version ERP system suitable college teaching. It appears that provides support to meet the university teaching and personnel training. Financial management is the core part of the current ERP teaching simulation system, but it ignores management accounting. This paper offset defects of the existing system in this respect. It made the management accounting ideas and software good fusion and made the teaching more comprehensively.

3.2 Design Function of Financial Management Simulation System

According to above the ERP instructional simulation of financial management system analysis and existing ERP sand table in the teaching process of financial management activities designed the basic functions of financial management simulation system.

Financial management simulation system was mainly divided into financial accounting subsystem and accounting management subsystem. Financial accounting subsystem was mainly accounting functions, which includes five modules, such as general ledger, accounts receivable management, payable management, cash management and fixed assets management. Management accounting subsystem included cost management module, financial analysis module, financial budget module and financial decision-making module. Based on SOA, the functional modules were encapsulated into services. By invoking services and combination of services achieved specific functions.

3.3 Business Process Modeling

Analyzing the business processes of the financial management system on ERP instructional simulation environment provided a basis of analysis to build an operational flexible ERP simulation teaching platform. The main business processes of financial management simulation system based on SOA had general ledger, receivables/accounts payable management, cash management and fixed assets management, financial budget, cost management, etc.

The paper models the business processed based on SOA, which made the system function and business closer correspondence. Realizing the system function based on coarse granularity service was more flexible, easier to reuse and faster corresponding change. To serve as the foundation, through the explicit definition, description, implementation and management business level of coarse granularity services provided business model and related system function realizes between better 'traceability', reducing the gap between them, making the business changes more easily passed to system function. The paper was only modeling the financial budget management process by the limited length. The IBM SOMA modeling method was used of modeling, which was a method be used for the service oriented analysis and design. The operations and business function field were analyzed in this process., and then framework business model was built. Based on this, services were found and built. And the business process models were built by the combination of services. The system suitability and flexibility were becoming stronger by using this method.

3.3.1 The Business Process Analysis

Financial budget making and auditing business process were expressed by User-Case as shown in table 1.

Table 1. Budgeting and Audit Business Process Cases

Business Event	<ul style="list-style-type: none"> • all departments budget (sales department, production department and purchasing department) • the financial department aggregates the budget of each department • CEO audits the budget
Use Case Overview	The cases are used to describe budgeting and auditing business process for top header
Business Rules	<ul style="list-style-type: none"> • The financial budget is began from various department(sales department, production department, purchasing department and inventory department) • Each department budget is aggregated and balanced in financial department • CEO audits the financial budget
Event List	<ol style="list-style-type: none"> 1. Each department submit budget into the budgeting and auditing business process <ol style="list-style-type: none"> a. Call sale budget information b. Call production budget information c. Call purchasing budget information d. Call inventory budget information 2. Budgeting and auditing business process aggregates each department's budget, calculation, formulate and balance budget. This organizational method can dynamically adjust. 3. Auditing the budget 4. If the budget is passed, then enter step 7 5. If the budget is not passed, then notifying each department to adjust their budget 6. Aggregating each adjusted budget 7. The business process is over

3.3.2 Establish Service Model

The budgeting and auditing business as the top grade business activities were downward decomposed. First the process was divided into three big sub processes. They were budget preparation, budget audit and determine budget. The budget preparation still can make the following subdivision: obtaining each department's budget, budget summary, balancing the budget and making sure budget. The obtaining each department's budget process involved multiple system. The process can further subdivision the following procedures: obtaining each department's budget information, accessing to each department's last year operation history recorded.

Through the above analysis, the new candidate services can be determined. And then to know these services provide by what's function module. The result was shown in table 2.

Table 2. The Candidate Service Sets Analyzed by Top-Down Method

Numbers	Candidate Service Name	Subordinate System
0	Budgeting and audit business	financial system
1.1	Budgeting	financial system
1.1.1	Obtaining each department's budget	sales system, production system, purchasing system, inventory system
1.1.1.1	Obtain each department's budget information (sales budget, production budgets, purchasing budget, inventory budget)	sales system, production system, purchasing system, inventory system
1.1.1.2	Obtain each department's operation historical records (sales history records, production history records, purchase historical records, inventory historical records)	sales system, production system, purchasing system, inventory system
1.1.2	Budget summary	financial system
1.1.3	Balancing the budget	financial system
1.1.4	Budget	financial system
1.2	Budget audit	manager information system
1.3	Establish a budget	financial system

3.3.3 Establish Business Process

In view of the above on the financial budget process analysis, this paper had used cases to depict the general process. And then it used the SOMA method to analysis and to set up the service model for the process. It established corresponding financial budgeting and auditing business process model through the business process analysis and service model. The model was shown in figure 1.

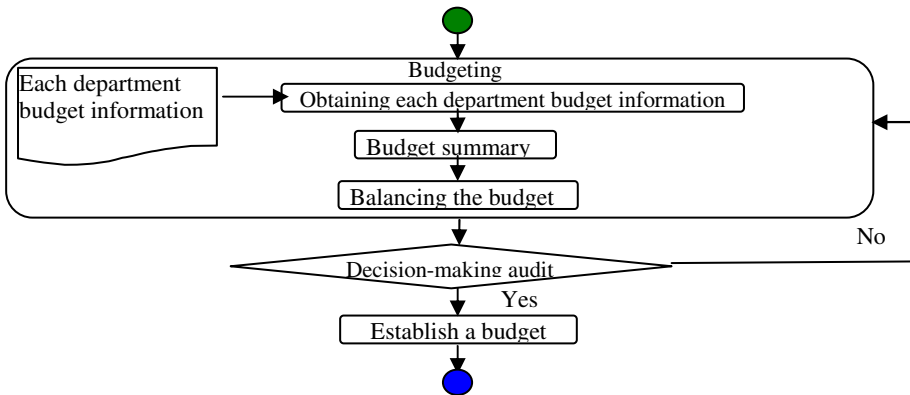


Fig. 1. Financial Budgeting and Auditing Business Process Chart

The business process was more flexibility, which was constructed based on the SOMA thoughts. The business processes of financial budget were defined as services. The services were controlled by the system self. It constructed the foundation of the coordination between the business and the system function.

3.4 Architecture Design

Using the system framework of SOA and combining the current system application combined service the agility method made ERP teaching simulated environment of financial management system more flexible. The aim of the system was that can be changed by the process of teaching in different industries of financial management in different business. As figure 2 shown, the paper adopted .NET platform construction four levels in the system logic.

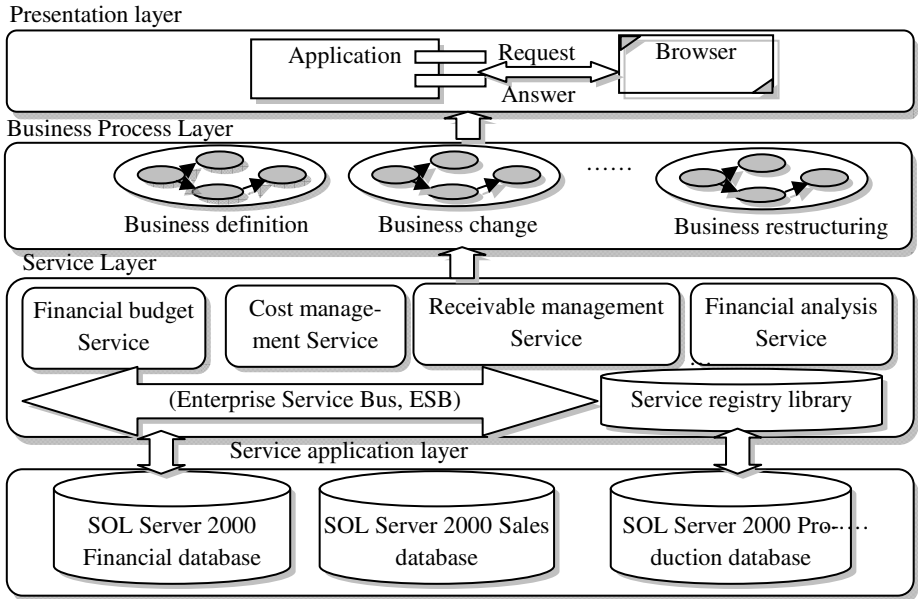


Fig. 2. Financial Management Simulation System Structure Based On SOA

3.4.1 The Presentation Layer

The layer was designed by ASP.NET, business process layer was called by SOAP. The presentation layer was exposed to users providing the interaction between user and system. It was also provided by the form of Web service, realizes the good interaction between the person and service.

3.4.2 The Business Process Layer

Through the general and standard object and service model, the corresponding Web service business process can be defined. Through BPEL engine, business process which WS-BPEL described and the corresponding functional module can be called.

3.4.3 The Service Layer

It provided an excellent service platform, for business process layer. It abstracted and encapsulated the function to which information system offered and tasks in the form of the service, and provided the service visit in the form of service description. At the

same time it also provided service registry function, which made service providers and service requestor interact better in the layer.

3.4.4 The Service Application Layer

It was called system data storage layer. It mainly consists of database and application integration layer faced to service. We utilize SOL Server 2000 database mainly of Microsoft Corporation in financial management simulation system. It included financial management database, the sales database and production database etc.

4 Financial Management Simulation System Service Design Based on SOA

Services of the financial management simulation system were analyzed and designed by using the method of IBM SOMA. When doing service design must follow the alignment of business and system functionality, reusability and non-state principles [9, 10]. Considering from the entire ERP instructional simulation system, in order to strengthen the resources sharing of information platform, and reducing repeated data entry, we put the system data into shared data and private data and put those share data called processing encapsulation into independent services. Figure 3 shows the design of services.

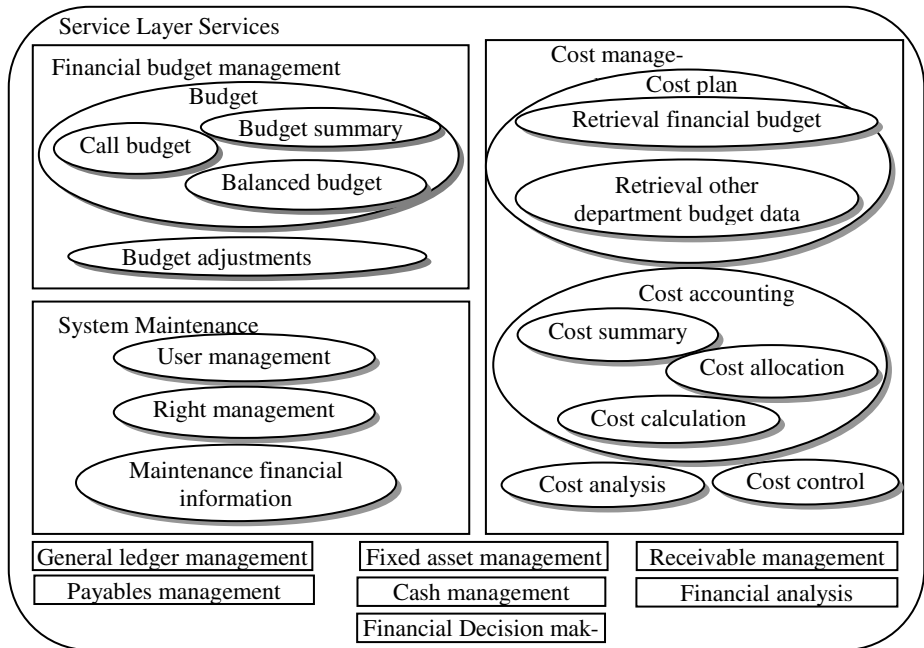


Fig. 3. Service Design Framework of Financial Management Simulation System

Using SOA architecture, which makes a service that does not depend on the status of other services. It received service requests from the client, and then found the appropriate services to achieve service interactions in the service registry. Because these services were stateless, they can be arranged into several series and sequences to perform business processes. Service orchestrated implements a business process and made the business process as a service to the customer. This made the system modules loose coupling and the system more flexible.

5 Conclusion

Through analyzing the functionality and software architecture lacks of the existing financial management system of ERP instructional simulation environment, we put the need of financial management simulation system for SOA architecture. The functions of financial management system were analyzed. The business processes were modeled by using the SOMA method. And then four-architecture was designed based on SOA. It made the system more versatile and the architecture more flexible. Finally, the services of the system design framework were constructed, which laid the foundation for the system implementation.

References

1. Papazoglou, M.P., Heuvel, W.J.: Service oriented architectures: approaches, technologies and research issues. *The VLDB Journal* 16, 389 (2007)
2. Hao, Y., Cheng, Z., Peng, D.: SOA Practice - Building Java Web Services and BPEL-based enterprise applications, pp. 16–17. Electronic Industry Press, Beijing (2009)
3. Thomas, E.R.L.: SOA concepts, technology and design, vol. 10. Machinery Industry Press, Beijing (2007)
4. Kim, J.W., Lim, K.J.: An approach to service-oriented architecture using web service and BPM in the telecom-OSS domain. *Internet Research* 17(1), 99–107 (2007)
5. Apostolos, M., Abolghasem, A., Timothy, B., et al.: A service-oriented architecture for building services integration. *Journal of Facilities Management* 6(2), 132–151 (2008)
6. Thomas, G., Greg, D.: Service-oriented concepts: bridging between managers and technologists. *Industrial Management & Data Systems* 109(1), 5–15 (2009)
7. Jie, D., Ying, S., Meiqi, F.: ERP teaching and practice of construction simulation system. *Jiaxing University* 17(S1), 34–39 (2005)
8. Arsanjani, A., Ghosh, S., Allam, A., et al.: Soma: A method for developing service-oriented solutions. *IBM Systems Journal* 47(3), 337–338 (2008)
9. Xinsheng, M.: SOA principles · Methods · Practical, pp. 44–45. Electronic Industry Press, Beijing (2007)
10. Thomas, E.: SOA service design principles, pp. 7–9. Posts & Telecom Press, Beijing (2009)

Variational Surface Reconstruction from Sparse and Nonparallel Contours for Freehand 3D Ultrasound

Shuangcheng Deng^{1,2}, Yunhua Li¹(IEEE Member), Lipei Jiang²,
Yingyu Cao², and Junwen Zhang²

¹School of Automation Science and Electrical Engineering,
Beijing University of Aeronautics and Astronautics, Beijing 100191, P.R. China
dengshuangcheng@bupt.edu.cn

²Opto-Mechatronic Equipment Technology Beijing Area Major Laboratory,
Beijing Institute of Petrochemical Technology, Beijing 102617, P.R. China

Abstract. 3D reconstruction for freehand 3D ultrasound is a challenging issue because the recorded B-scans are not only sparse, but also non-parallel. Both conventional volume and surface reconstruction methods can't reconstruct sparse data efficiently while they are arbitrarily oriented in 3D space. We developed a new surface reconstruction method for freehand 3D ultrasound based on variational implicit function. In the new method, we first constructed on- & off-surface constraints from the segmented contours of all recorded B-scans, then used a variational interpolation technique to get a single implicit function in 3D. Finally, the implicit function was evaluated to extract the zero-valued surface as reconstruction result. One phantom experiment was conducted to assess our variational surface reconstruction method, and the experiment results have shown that the new method is capable of reconstructing surface smoothly from sparse contours which can be arbitrarily oriented in 3D space.

Keywords: Surface reconstruction, freehand 3D ultrasound, variational implicit function, medical imaging.

1 Introduction

Freehand 3D ultrasound imaging uses conventional ultrasound technology to build up a 3D data set from a number of conventional 2D B-scans acquired in succession. It consists of tracking a standard 2D ultrasound probe by using a 3D localizer (magnetic, mechanical or optic). The localizer is attached to the probe, and can continuously measure the 3D position and orientation of the probe while the physician moves the probe slowly and steadily over a particular anatomical region. The measured outputs of the 3D positions and orientations are used for the localization of B-scans in the coordinate system of the localizer. In order to establish the transformation between the B-scan coordinates and the 3D position and orientation of the probe, a calibration procedure is necessary[1-3].

There are two main drawbacks of freehand imaging: The first is that the recorded B-scans are non-parallel, actually they may intersect each other, because the

movement of the ultrasound probe is unrestricted. The second is that the recorded B-scans are very sparse. This arises from the fact that it would be an advantage to reconstruct from a smaller number of ultrasound contours, since manual segmentation, which is still the only universally reliable method for ultrasound data[4], is the most time-consuming of the processes involved. So only a small number of B-scans are recorded and manually segmented in order to allow real-time response in clinic applications. These two drawbacks make the 3D reconstruction of the ultrasound data quite complex.

All the reconstruction methods for freehand 3D ultrasound fall into two categories: volume reconstruction and surface reconstruction. Volume Reconstruction methods interpolate the data to a regular 3D array (voxel array) as the first step. The most common volume reconstruction methods are Pixel Nearest-Neighbor (PNN)[5], Voxel Nearest-Neighbor (VNN)[6][7] and Distance-Weighted interpolation (DW)[8][9]. All these volume reconstruction methods can't reconstruct sparse data efficiently while not introducing geometrical artifacts, degrading or distorting the images. So they are only suitable for the reconstruction of dense data, and are not a feasible choice for our case.

Surface Reconstruction methods reconstruct the volume of interest (VOI) directly from contours (cross-sections) segmented from the original freehand 3D ultrasound B-scans in a prerequisite step. These B-scans do not contain processing artifact, hence the clinician has a better chance of outlining the contours of the organ accurately.

Nowadays methods that can handle mutually intersected contours are few and far between. Most of surface reconstruction methods mentioned in literature directly triangulate between two adjacent contours, and can't handle arbitrarily oriented contours. Usually the contours are nearly parallel and don't intersect each other[4] [10-13]. L. Liu et al. [14] proposed a method to reconstruct non-parallel contours. It is also done directly in the surface-mesh (i.e., triangle-mesh) domain and requires dense contours for input. It is also incapable of reconstructing sparse data in our case.

We develop a new surface reconstruction method for freehand ultrasound imaging. It is based on variational interpolation, which is used by Greg Turk for shape transformation[15]. It can effectively solve the surface reconstruction of the physical organ, and can handle both sparse and mutually intersected contours data.

2 Basic Description

Our new surface reconstruction method is based on variational interpolation. It casts the surface reconstruction problem to an equivalent variational problem which tries to find a function that has minimum bending energy and satisfies all constraints. The process of this method is illustrated in Fig.1.

First, we perform a spatial transformation to convert the 2D pre-segmented ultrasound contours into 3D point clouds, which casts the surface reconstruction problem as a scattered data interpolation problem in three dimensions. The spatial transformation is performed according to the 3D position and orientation information of the ultrasound probe while acquiring corresponding 2D ultrasound B-scans. Contours are manually segmented from the original B-scans in a prerequisite step.

Secondly, we define all the boundary points of the ultrasound contours as on-surface constraints for the scattered data interpolation problem in three dimensions. For unambiguously defining the solution function, we define additional constraints that indicate which points should be located inside the object. These are off-surface constraints for the scattered data interpolation.

Thirdly, variational interpolation is invoked to solve the scattered data interpolation, the solution is a single implicit function in 3D that will be at least C1-continuous, i.e., it is smooth.

Finally, an iso-surface extraction step is performed. The implicit function is evaluated to extract the zero-valued surface as the reconstruction result. The iso-surface extraction algorithm used in our paper is the Marching Cubes algorithm proposed by Lorensen and Cline[16].

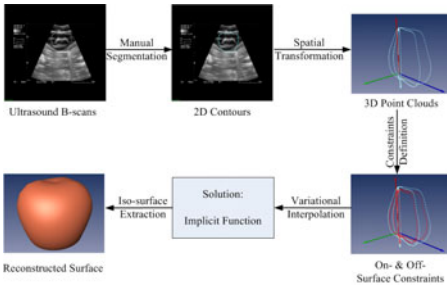


Fig. 1. Process of surface reconstruction

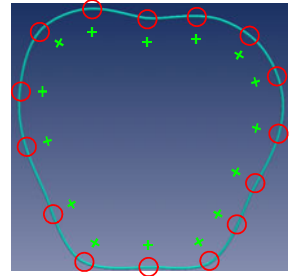


Fig. 2. Pairs of constraints

3 Variational Surface Reconstruction

3.1 Constraints Definition

On-Surface Constraints: All the contour points are considered as on-surface constraint points and will lie exactly on the surface that will be reconstructed. Hence, each on-surface is assigned a scalar value 0.

Off-Surface Constraints: In order to unambiguously define the solution function, we need some additional off-surface constraints that define which points should be located inside the object. In this paper we define some additional normal constraints which are known to be inside the reconstructed surface as off-surface constraints.

The location of a normal constraint \mathbf{c}_i^N (or off-surface constraint \mathbf{c}_i^{off}) is calculated by adding an on-surface constraint \mathbf{c}_i^{on} to the normal \mathbf{n}_i at that point, that is:

$$\mathbf{c}_i^{off} = \mathbf{c}_i^N = \mathbf{c}_i^{on} + \mathbf{n}_i \quad (1)$$

So each off-surface constraint is paired with a corresponding on-surface constraint, and the number of off-surface constraints is equal to that of on-surface constraints.

Fig. 2 shows some defined on- & off-surface constraints. The point cloud of on- & off-surface constraints is passed to the following variational interpolation routine. While contours have spatial orientation, the on- & off-surface constraint points have are not sensitive to spatial orientation. This is why our new reconstruction method can deal with arbitrarily oriented and mutually intersected contours, which is an important advantage of our approach.

3.2 Casting Surface Reconstruction to Equivalent Variational Problem

After defining the constraints, the 3D surface reconstruction problem can be cast as the following scattered data interpolation problem:

Scattered Data Interpolation Problem: Given a set of constraint points $\{\mathbf{c}_i = (c_i^x, c_i^y, c_i^z)\big|_1^n\} \subset \mathbb{R}^3$ and a set of their corresponding scalar values $\{h_i\big|_1^n\} \subset \mathbb{R}$, find a function $f : \mathbb{R}^3 \rightarrow \mathbb{R}$ as the surface reconstruction result, so that

$$f(\mathbf{c}_i) = h_i \quad (i = 1, \dots, n) \quad (2)$$

But because the contours are very sparse, a direct interpolation can't lead to an ideal reconstruction result. One solution is to introduce an extra constraint to confine the scattered data interpolation problem. We use the following energy function as the extra constraint:

$$E(f) = \int_{\Omega} [f_{xx}^2(x) + f_{yy}^2(x) + f_{zz}^2(x) + 2(f_{xy}^2(x) + f_{xz}^2(x) + f_{yz}^2(x))] d\Omega \quad (3)$$

This energy function is basically a measure of the aggregate curvature of $f(\mathbf{x})$ over the region of interest Ω , and any creases or pinches in a surface will result in a larger value of the energy measure. So it indicates the smoothness of $f(\mathbf{x})$. The more smooth is $f(\mathbf{x})$, the smaller is E . Because medical anatomic structures are usually smooth, $E(f)$ should be as small as possible.

With the energy measure, the surface reconstruction problem can be again cast to the following equivalent variational problem:

Equivalent Variational Problem: Given a set of constraint points $\{\mathbf{c}_i = (c_i^x, c_i^y, c_i^z)\big|_1^n\} \subset \mathbb{R}^3$ and a set of their corresponding scalar values $\{h_i\big|_1^n\} \subset \mathbb{R}$, find a function $f : \mathbb{R}^3 \rightarrow \mathbb{R}$ as the surface reconstruction result, so that energy measure $E(f)$ has the smallest value and

$$f(\mathbf{c}_i) = h_i \quad (i = 1, \dots, n) \quad (4)$$

The introduction of energy measure and casting of surface reconstruction problem to its equivalent variational problem makes our new reconstruction method capable of reconstructing an ideal smooth surface from very sparse contours. A small number of contours will lead to excellent reconstruction result.

3.3 Variational Interpolation: Solution to Equivalent Variational Problem

In order to solve the equivalent variational problem, we first expand $f(\mathbf{x})$ as the weighted sums of a radial basis function (RBF) $\phi(\mathbf{x})$:

$$f(\mathbf{x}) = \sum_{j=1}^n d_j \phi(\mathbf{x} - \mathbf{c}_j) + P(\mathbf{x}) \quad (5)$$

In (5), \mathbf{c}_i are the locations of the on- & off-surface constraints, d_j are the weights. $P(\mathbf{x})$ is a degree one polynomial that accounts for the linear and constant portions of $f(\mathbf{x})$. We use the triharmonic spline for $\phi(\mathbf{x})$, which is another commonly used 3D RBF, since it results in a C^2 -continuous and thus smoother interpolation[17]. It is defined by

$$\phi(\mathbf{x}) = \|\mathbf{x}^3\| \quad (6)$$

Because the variational radial basis function naturally minimizes the energy measure[15], determining the weights d_j , and the coefficients of $P(\mathbf{x})$ so that all the interpolation constraints are satisfied will yield the desired solution that minimizes the energy measure subject to the constraints.

Now substitute the constraints into equation (5), which gives:

$$h_i = \sum_{j=1}^n d_j \phi(\mathbf{c}_i - \mathbf{c}_j) + P(\mathbf{c}_i) \quad (i = 1, \dots, n) \quad (7)$$

Equation (7) can be formulated as a linear system. Let $\phi_{ij} = \phi(\mathbf{c}_i - \mathbf{c}_j)$, this linear system can be written as the following matrix form:

$$\begin{bmatrix} \phi_{11} & \phi_{12} & \dots & \phi_{1n} & 1 & c_1^x & c_1^y & c_1^z & d_1 \\ \phi_{21} & \phi_{22} & \dots & \phi_{2n} & 1 & c_2^x & c_2^y & c_2^z & d_2 \\ \dots & \dots & \dots & \dots & \dots & \dots & \dots & \dots & \dots \\ \phi_{n1} & \phi_{n2} & \dots & \phi_{nn} & 1 & c_n^x & c_n^y & c_n^z & d_n \\ 1 & 1 & \dots & 1 & 0 & 0 & 0 & 0 & p_0 \\ c_1^x & c_2^x & \dots & c_n^x & 0 & 0 & 0 & 0 & p_1 \\ c_1^y & c_2^y & \dots & c_n^y & 0 & 0 & 0 & 0 & p_2 \\ c_1^z & c_2^z & \dots & c_n^z & 0 & 0 & 0 & 0 & p_3 \end{bmatrix} = \begin{bmatrix} h_1 \\ h_2 \\ \dots \\ h_n \\ 0 \\ 0 \\ 0 \\ 0 \end{bmatrix} \quad (8)$$

According to Turk and Brien, the above system is symmetric and positive semi-definite, so there will always be a unique solution for d_j and coefficients of $P(\mathbf{x})$ [15]. Solving it will give us $f(\mathbf{x})$, and a surface-extraction from $f(\mathbf{x})$ will give us the reconstructed surface.

4 Experiments and Discussion

One phantom experiment was conducted to evaluate our new surface reconstruction method. For phantom ultrasound image acquisition, we use a ZK-3000 ultrasound machine with a 3.5 MHz ultrasound probe (Beijing Zhongke-Tianli Tech. Co., Ltd., Beijing, China). The electromagnetic tracking device is the AURORA from Northern Digital Inc. (Ontario, Canada, <http://www.ndigital.com>). The digital ultrasound image is acquired through an image-grabbing card. As mentioned above, the position and orientation of the ultrasound probe is also recorded simultaneously using the tracking device (Fig. 3). The 3D image reconstruction and visualization is performed using a personal computer with a 2.66 GHz Intel Core2™ quad CPU. We have developed an IGS (image-guided surgery) software for microwave ablation of hepatic tumor (Fig. 4), which we use as the surface reconstruction and visualization program in this paper.



Fig. 3. Phantom experiment configuration

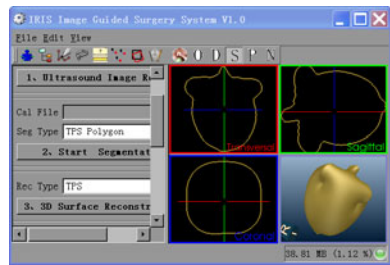


Fig. 4. Reconstruction software

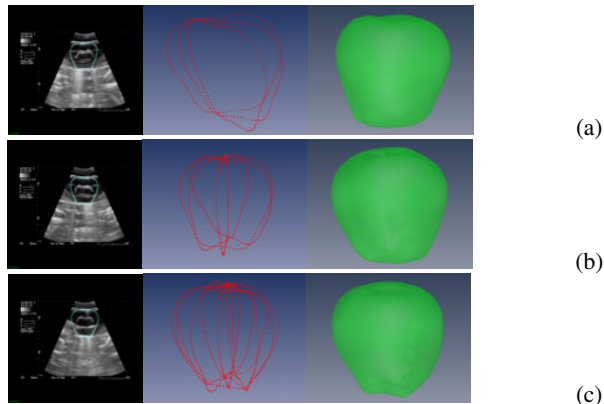


Fig. 5. Surface Reconstruction of a toy apple using phantom ultrasound data. (a) 3 slices; (b) 4 slices; (c) 7 slices.

The phantom we used is a plastic apple (Fig. 5(a)). 3, 4, or 7 mutually intersected cross-sections are used respectively to reconstruct the apple. The experiment result is

shown in Fig. 5. For each case, from left to right is: the original ultrasound data and segmented contours (light blue), the used cross-sections, and the reconstruction result. The quantitative difference between the volume of the reconstruction result and the original phantom data is illustrated in Table 1.

All the contours are non-parallel to each other; actually they are intersecting each other. This indicates that new method can handle arbitrarily oriented contours. For all the cases, the new method gets good performance: the visual difference is small and the volume difference is only 10.33% even with only three contours. Furthermore, the new method takes a small number of contours as input data, even three contours can lead to a close approximation of the original data.

Table 1. Volume difference between reconstructed surface and original data

Number of contours	Volume (mm ³)	Volume difference (mm ³)	Volume difference (%)
Original data	183300		
3	202230	18930	10.33%
4	197588	14288	7.80%
7	194807	11507	6.28%

5 Conclusion

We present a new approach for the surface reconstruction of sparse and mutually-intersected contours in freehand 3D ultrasound imaging based on variational interpolation. It is capable of creating smooth surface from both sparse and non-parallel contours.

One phantom experiment is conducted to evaluate the new surface reconstruction method. The results have shown that new method can get good performance: the visual difference and the volume difference between the reconstruction result and the original data is very small, even two contours can lead to a close approximation of the original data. This results also confirms that our reconstruction method can handle both sparse and mutually-intersected contours.

References

1. Fenster, A., Downey, D.B.: 3-D ultrasound imaging—a review. *IEEE Eng. Med. Biol. Mag.* 15, 41–51
2. Rousseau, F., Hellier, P., Barillot, C.: Confusius: a robust and fully automatic calibration method for 3D freehand ultrasound. *Medical Image Analysis* 9, 25–38 (2005)
3. Rousseau, F., Hellier, P., Barillot, C.: A novel temporal calibration method for 3-d ultrasound. *IEEE Transactions on Medical Imaging* 25(8), 1108–1112 (2006)
4. Gopal, A.S., Schnellbaecher, M.J., Shen, Z., Akinboboye, O.O., Sapin, P.M., King, D.L.: Freehand three-dimensional echocardiography for measurement of left ventricular mass: In vivo anatomic validation using explanted human hearts. *Am. Coll. Cardiol.* 30, 802–810 (1997)

5. Nelson, T.R., Pretorius, D.H.: Interactive acquisition, analysis and visualization of sonographic volume data. *International Journal of Imaging Systems and Technology* 8, 26–37 (1997)
6. Prager, R.W., Gee, A.H., Berman, L.: Stradx: real-time acquisition and visualization of freehand three-dimensional ultrasound. *Medical Image Analysis* 3(2), 129–140 (1999)
7. Sherebrin, S., Fenster, A., Rankin, R.N., Spence, D.: Freehand three-dimensional ultrasound: implementation and applications. In: Van Metter, R.L., Beutel, J. (eds.) *Proc. SPIE Medical Imaging, Physics of Medical Imaging 1996*, vol. 2708, pp. 296–303 (1996)
8. Barry, C.D., Allott, C.P., John, N.W., Mellor, P.M., Arundel, P.A., Thomson, D.S., Waterton, J.C.: Three dimensional freehand ultrasound: image reconstruction and volume analysis. *Ultrasound in Medicine and Biology* 23(8), 1209–1224 (1997)
9. Trobaugh, J.W., Trobaugh, D.J., Richard, W.D.: Three dimensional imaging with stereotactic ultrasonography. *Computerized Medical Imaging and Graphics* 18(5), 315–323 (1994)
10. Cook, L.T., Cook, P.N., Lee, K.L., et al.: An algorithm for volume estimation based on polyhedral approximation. *IEEE Trans. Biomed. Eng.* 27, 493–500 (1980)
11. King, D.L., Gopal, A.S., Keller, A.M., Sapin, P.M., Schröder, K.M.: Three-dimensional echocardiography: advances for measurement of ventricular volume and mass. *Hypertension* 23, 172–179 (1994)
12. Hodges, T.C., Detmer, P.R., Burns, D.H., Beach, K.W., Strandness Jr. D.E.: Ultrasonic three-dimensional reconstruction: in vitro and in vivo volume and area measurement. *Ultrasound Med. Biol.* 20, 719–729 (1994)
13. Altmann, K., Shen, Z., Boxt, L.M., King, D.L., Gersony, W.M., Allan, L.D., Apfel, H.D.: Comparison of threedimensional echocardiographic assessment of volume, mass, and function in children with functionally single left ventricles with two-dimensional echocardiography and magnetic resonance imaging. *Am. J. Cardiol.* 80, 1060–1065 (1997)
14. Liu, L., Bajaj, C., Deasy, J.O., Low, D.A., Ju, T.: Surface reconstruction from non-parallel curve networks, *Computer graphics forum (proceedings of eurographics)*. In: *Eurographics Association*, vol. 27, pp. 155–163 (2008)
15. Turk, G., Dinh, H.Q., O’Brien, J., Yngve, G.: Implicit surfaces that interpolate. In: *International Conference on Shape Modeling and Applications*, pp. 62–71. *IEEE Computer Society* (2001)
16. Lorensen, W., Cline, H.E.: Marching cubes: A high resolution 3-d surface construction algorithm. In: *Computer Graphics (SIGGRAPH 1987)*, vol. 21(4), pp. 163–169 (1987)
17. Rohr, K.: *Landmark-Based Image Analysis: Using Geometric and Intensity Models*. Springer, Netherlands (2001), ISBN 0792367510

STGRs over Topological Spaces for Value-Passing Processes

Huanbao Wang

Department of Maths & Physics, Anhui University of Architecture,
Hefei 230601, China
wanghuanbao@yahoo.com.cn

Abstract. In this paper we introduce a variant of symbolic transition graphs over topological spaces for value-passing processes based on CCS with infinite assignments, namely, a symbolic transition graph with a binary equivalence relation, which is abbreviated to STGR. It relies on topological spaces for value-passing processes, which is different from the original STG. These results apply to partition domains of conversations of cryptographic protocols that run in an infinite concurrent way. We work out a highly efficient solution to reduce computational complexities to prove safety properties of cryptographic protocols running in an infinite concurrent way. Our STGR can be also used to describe ordinary concurrent systems.

Keywords: topological space, concurrent computing, value-passing process, CCS, cryptographic protocol.

1 Introduction

We re-examine some complex dynamic features of cryptographic protocols that run in concurrent ways. It is very difficult to describe the complex concurrent cryptographic protocol system in formal languages and to prove its safety properties such as authentication, secrecy, and so on. Thus we introduce the notion of value-passing processes in CCS [1], i.e. calculus of communicating system, to generalize the static features of cryptographic protocols that run in concurrent ways, and provide some corresponding proofs of safety properties based on theorem proving.

CCS provides a calculus for analyzing properties of concurrent communicating processes. We shall let P, Q range over processes and A, B over alternations (sums); each alternate (or summand) of an alternation is a process guarded by an action μ of the form x or \bar{x} , where x names a channel. The syntax is $P ::= A | \nu x P | P | P$, $A ::= 0 | \mu.P | A + A$ and $\mu ::= \bar{x} | x$ [2]. The restriction $\nu x P$ defines P as the scope of the name x ; a name-occurrence in a process is *free* iff it is not scoped by ν . We say P and Q are alpha-equivalent, written $P \equiv_\alpha Q$, if they differ only in a change of their restricted names.

We introduce an automaton to express the semantics of the CCS language. An automaton A over Act , which is a given set of actions, has four ingredients such as a set $Q = \{q_0, q_1, \dots\}$ of states, a state $q_0 \in Q$ called the start ones, a subset F of Q

called the accepting states, and a subset T of $Q \times Act \times Q$ called the transition [3]. A labeled transition system (LTS) over Act is a pair (Q, T) consisting of a set Q of states and a ternary relation $T \subseteq (Q \times Act \times Q)$, known as a transition relation.

A transition $(q, \alpha, q') \in T$ is usually written $q \xrightarrow{\alpha} q'$, and we call q the source and q' the target of the transition. If $q \xrightarrow{\alpha_1} q_1 \xrightarrow{\alpha_2} \dots \xrightarrow{\alpha_n} q_n$ then we call q_n a derivative of q under $\alpha_1 \alpha_2 \dots \alpha_n$. The automaton A is said to be finite-state if Q is finite, and deterministic if for each pair $(q, \alpha) \in Q \times Act$ there is exactly one transition $q \xrightarrow{\alpha} q'$. An LTS can be thought of as an automaton without a start or accepting states. Each different selection of a start state defines a different automaton, but based upon the same LTS.

An LTS as well as its related automaton can be thought of as the semantics of the CCS language. We introduce them to express cryptographic protocols running in concurrent ways and re-examine the notion of the open bundle, which is called an event relation. An open bundle b of a strand space $(\langle s_i \rangle_{i \in I}, \#)$ is a finite, acyclic subgraph of G graph of a strand space $(\langle s_i \rangle_{i \in I}, \#)$ such that [4]:

- if $e \Rightarrow_G e'$ and $e' \in E_b$ then $e \Rightarrow_b e'$,
- if $e' \rightarrow_b e$ and $e'' \rightarrow_b e$ then $e' = e''$,
- if $e, e' \in E_b$ s. t. $act(e) = out\ new\ \bar{n}\ M$ and $n \in \bar{n} \cap names(e')$ then either $e \Rightarrow_b^* e'$ or there exists an input event $e'' \in E_b$ such that $n \in names(e'')$, $e'' \not\rightarrow_b e$ and $e'' \Rightarrow_b^* e'$,
- if $(i, h), (j, k) \in E_b$ then $\neg(i \# j)$.

We examine concurrent communicating procedures in cryptographic protocols, which are looked upon as a particularly austere representation of the abstract syntax of the value-passing process algebra in the CCS language. A symbolic transition graph (STG) [5] is obtained from the CCS language using the standard approach of its structural operational semantics. A symbolic transition graph is a directed graph in which every node n , i.e. an event of G graph of a strand space $(\langle s_i \rangle_{i \in I}, \#)$, is labeled by a set of variables $fv(n)$ and every branch is labeled by a guarded action such that

if a branch labeled by (b, α) goes from node m to n , which we write as $m \xrightarrow{b, \alpha} n$, then $fv(b) \cup fv(\alpha) \subseteq fv(m)$, denoting $m \xrightarrow{\alpha} n$ and $fv(n) \subseteq fv(m) \cup bv(\alpha)$, denoting $m \xrightarrow{true, \alpha} n$.

We use α to range over a set Act of actions. An action may be an input one, of the form $c?x$ where c is from a set of channels, $Chan$, an output one, of the form $c!e$, or a neutral one such as τ . The set of *free* and *bound* variables of these actions is defined,

for example, $fv(c!e) = fv(e)$, $bv(c?x) = \{x\}$, $fv(\alpha) = \emptyset$ and $bv(\alpha) = \emptyset$. We also presume a set of expressions, Exp , ranged over by e , which includes Var and V , and a set of Boolean expressions, $BExp$ ranged over by b , with similar properties but we use the more suggestive notation $\rho \vDash b$ to indicate that $\rho(b) = true$.

We may verify bisimulation equivalences for value-passing process languages, e. g. LTS that is an operational semantics of the CCS language, in which actions have associated with them values from a possibly infinite value set. The other operational semantics of many value-passing processes based on CCS may be expressed in terms of finite symbolic transition graph although the above-mentioned labeled transition graph, i. e. STG, is infinite. A collection of symbolic bisimulation equivalences parameterized on Boolean expressions \simeq^b are then defined over symbolic transition graphs.

Furthermore, we will introduce a quotient space theory based on topological spaces for value-passing processes to parameterize symbolic bisimulation equivalences themselves in order to verify bisimulation equivalences with values from a possibly infinite value set. We use R to range over a set \mathbb{R} of binary equivalence relations on a set Act of actions $R \in \mathbb{R}$. A collection of symbolic bisimulation equivalences parameterized on the binary equivalence relation $R \in \mathbb{R}$ is written by binary equivalence relation expressions \simeq^R .

In this paper, topological spaces for value-passing processes are defined in Section 2. In section 3, we will develop symbolic transition graphs, and introduce a variant of them, i. e. a symbolic transition graph with a binary equivalence relation R , which is abbreviated to STGR.

2 Topological Spaces

We introduce the CCS language with value-passing processes to describe concurrent communicating procedures in cryptographic protocols whereas it provides a calculus for analyzing properties of concurrent communicating processes. A STG as well as its related automaton can be thought of as the operational semantics of the CCS language. Operational behaviors are bounded by the set Act of actions, which action may be an input one, of the form $c?x$ where c is from a set of channels, $Chan$, an output one, of the form $c!e$, or a neutral one such as τ . We use α to range over a set Act of actions.

Bisimulation equivalences are verified in the STG based on the CCS language, which may be expressed in terms of finite symbolic transition graph although the above-mentioned STG is infinite. If the domain of STG is finite, there are a large number of verification tools which have at their core algorithms for checking bisimulation equivalences between processes in the CCS language. Thus it is a fundamental limitation of the existing algorithms for bisimulation equivalences.

We will introduce the binary equivalence relation $R \in \mathbb{R}$ to STG, and partition off the domain. Our work aims at verification algorithms of symbolic bisimulation equivalences using binary equivalence relation expressions. We re-examine the notion of topological spaces based on the infinite STG. Topological space, quotient space is respectively defined as follows.

Definition 1 (Topological Space)

Let X be a set and let T be a family of subsets of X . Then T is called a topology on X if both the empty set and X are elements of T , any union of elements of T is an element of T , any intersection of finitely many elements of T is an element of T . If T is a topology on X , then the pair (X, T) is called a topological space. The notation X_T may be used to denote a set X endowed with the particular topology T . \square

Definition 2 (Quotient Space)

Let (X, T_x) be a topological space, and let $R \in \mathbb{R}$ be an equivalence relation on X . The quotient space $Y = X/R$ is defined to be the set equivalence classes of elements of X , $Y = \{[x] : x \in X\} = \{\{v \in X : vRx\} : x \in X\}$, equipped with the topology where the open sets are defined to be those sets of equivalence classes those unions are open sets in X , $T_y = \{U \subseteq Y : \bigcup U \in T_x\}$. Equivalently, we can define them to be those sets with an open preimage under the quotient map $q : X \rightarrow X/R$ which sends a point in X to the equivalence class containing it. The expression is as follows:

$$\cdot \quad T_y = \{U \subseteq Y : q^{-1}(U) \in T_x\}. \quad \square$$

A collection of symbolic bisimulation equivalences parameterized on Boolean expressions \simeq^b based on STG is more abstract than one directly evaluated. But it is not more abstract than one parameterized on the binary equivalence relation $R \in \mathbb{R}$. In fact, a Boolean expression $b \in BExp$ may induce to partition off the domain. A partition of the domain obtained by a Boolean expression is of a quotient space.

A symbolic transition graph may be looked upon as a particularly austere representation of the abstract syntax of the value-passing process algebra. As an example, the abstract syntax of the value-passing process algebra is given by

$$\cdot \quad t ::= nil \mid \alpha.t \mid be \rightarrow t, t \mid t+t \mid t \mid t \setminus c \mid P(\underline{e}).$$

This contains the usual combinators in the CCS language with a Boolean choice mechanism, while there is the similarity in the strand space language.

In fact, our results at this level of abstraction are independent of any particular language. In the above-mentioned abstract syntax, it assumes a set of process names, ranged over by P . To give their semantics to the terms we presume the existence of a set of declarations of the form $P(\underline{x}) \leftarrow t$, one for each process name which occurs in the terms, where it is assumed that the free variables of t are contained in the list \underline{x} .

Symbolic bisimulation equivalences \simeq^R are, generally speaking, parameterized on the binary equivalence relation $R \in \mathbb{R}$. A process context C is, informally speaking, a process expression containing a pair of square brackets, represented by $[]$. Formally, process contexts are given by the syntax $C ::= [] \mid \alpha.C + M \mid new a C \mid C \mid P \mid P \mid C$. The notation $C[Q]$ denotes the result of filling the square brackets in the context C by the process Q . The elementary contexts are $\alpha.[] + M$, $new a []$, $[] \mid P$ and $P \mid []$.

3 A Variant of STG: STGR

We introduce a variant of symbolic transition graphs, i. e. a symbolic transition graph with a binary equivalence relation R , which is abbreviated to STGR, to define an operational semantics of topological spaces of many value-passing processes based on CCS with infinite assignments. It is differ from STG, which is an operational semantics of the value-passing process language, and is based on topological spaces of many value-passing processes with binary equivalence relation expressions, by which a collection of symbolic bisimulation equivalences parameterized on the binary equivalence relation is written.

Definition 3 (Binary Equivalence Relation)

A given binary relation \sim on a set A is said to be an equivalence relation if and only if it is reflexive, symmetric and transitive. Equivalently, for a, b and c in A :

- $a \sim a$ (reflexivity),
- if $a \sim b$ then $b \sim a$ (symmetry),
- if $a \sim b$ and $b \sim c$ then $a \sim c$ (transitivity).

A set A together with the relation \sim is called a setoid. The equivalence class of a under \sim , denoted $[a]$, is defined as $[a] = \{b \in A \mid a \sim b\}$. \square

Reflexivity follows from symmetry and transitivity if for every element $a \in A$; there exists another $b \in A$ such that $a \sim b$ holds. However, reflexivity does not follow from symmetry and transitivity alone. For example, let A be the set integers, and let two elements of A be related if they are both even numbers. This relation is clearly symmetric and transitive, but in view of the existence of odd numbers, it is not reflexive. On the other hand, let A be the set integers, and let two elements of A be related if their difference is even. This is an equivalence relation, which partitions the integers into two equivalence classes, the even and odd integers.

Definition 4 (Strong Simulation)

Let (Q, T) be an LTS, and let S be a binary relation over Q . Then S is called a strong simulation over (Q, T) if, whenever pSq , if $p \xrightarrow{\alpha} p'$, then there exists $q' \in Q$ such that $q \xrightarrow{\alpha} q'$ and $p'Sq'$ [5]. \square

Definition 5 (Strong Bisimulation)

A binary relation S over Q is said to be a strong bisimulation over the LTS (Q, T) , if both S and its converse are simulations. We say that p and q are strongly bisimilar or strongly equivalent, written $p \sim q$ if there exists a strong bisimulation S such that pSq [5]. \square

Note that a labeled transition system (LTS) over Act in Definition 4 and Definition 5 is a pair (Q, T) consisting of a set Q of states and a ternary relation $T \subseteq (Q \times Act \times Q)$, known as a transition relation. In fact, the event relation as an

example of the open bundle of strand spaces, which replaces a labeled transition system (LTS), is used to define in the above-mentioned Definition 4 and Definition 5, as a symbolic transition graph (STG) is. This paper focuses on the former.

Definition 6 (Symbolic Transition Graph, STG)

A symbolic transition graph is a directed graph in which every node n is labeled by a set of variables $fv(n)$ and every branch is labeled by a guarded action such that if a

branch labeled by (b, α) goes from node m to n , which we write as $m \xrightarrow{b, \alpha} n$, then

- $fv(b) \cup fv(\alpha) \subseteq fv(m)$, and
- $fv(n) \subseteq bv(\alpha) \cup fv(m)$.

And the transition branch $m \xrightarrow{true, \alpha} n$ is denoted by $m \xrightarrow{\alpha} n$ [5]. □

The STG is looked upon as an operational semantics of the value-passing process language based on CCS with infinite assignments. But it partitions domains of value-passing processes with Boolean expressions, which are a class of binary equivalence relation expressions. We will introduce a variant of symbolic transition graphs, which is defined with a binary equivalence relation according to Definition 3, and is denoted as STGR. It applies to an operational semantics of topological spaces of many value-passing processes based on CCS with infinite assignments. To be similar to Definition 6, STGR is defined as follows.

Definition 7 (A Variant of Symbolic Transition Graphs, i. e. a Symbolic Transition Graph with a binary equivalence relation R , STGR)

A symbolic transition graph with a binary equivalence relation R , over a (A, T_A) of topological spaces of many value-passing processes based on CCS with infinite assignments, is a directed graph in which every node n is labeled by a set of variables $fv(n)$ and every branch is labeled by a guarded action such that if a branch

labeled by (R, α) goes from node m to n , which we write as $m \xrightarrow{R, \alpha} n$, then

- $fv(R) \cup fv(\alpha) \subseteq fv(m)$, and
- $fv(n) \subseteq bv(\alpha) \cup fv(m)$.

And the transition branch $m \xrightarrow{E_A, \alpha} n$ is denoted by $m \xrightarrow{\alpha} n$, where E_A is the total relation over a (A, T_A) . □

A set A of (A, T_A) that is of topological spaces of many value-passing processes based on CCS with infinite assignments is a *closed* term, while the nodes of a symbolic transition graph with a binary equivalence relation R (STGR) play the role of *open* terms. Thus we will develop a symbolic operational semantics based on STGR of topological spaces of many value-passing processes with infinite assignments, where symbolic actions such as $c?x$, $c!e$ and their associated residuals that are associated with terms.

Note that this form of operational semantics must necessarily be given for open terms, which may contain free variables. For example, even if $c?xt$ is a closed term its residual after the symbolic action $c?x$, namely t , will in general contain free occurrences of x . We will develop a symbolic operational semantics based on STGR according to the symbolic operational semantics based on STG that is firstly presented by M. Hennessy and H. Lin [5], using the above-mentioned formal actions to define two symbolic variants of bisimulation equivalence, a late and early version.

We will apply a binary equivalence relation R to the guarded condition of formal actions. In this case, two symbolic variants of bisimulation equivalence, a late and early version, denote the form \simeq_E^R and \simeq_L^R between open terms respectively. In this section, we will apply \simeq_L^R to the symbolic operational semantics based on STGR. Therefore, we firstly re-examine concepts of open term, and closed term, in topological spaces of many value-passing processes based on CCS with infinite assignments.

In STGR, let m be a node, and let σ be a substitution, and then the set of its terms denotes $T = \{m_\sigma \mid \sigma \in \text{Sub}, \text{domain}(\sigma) \subseteq \text{fv}(m)\}$. We will usually identify the node with the term m_\emptyset , where \emptyset is the empty substitution and use t, u, \dots to range over T . To be similar of a set of variables $\text{fv}(m)$ in a node m , a set of variables of a term m_σ denotes $\text{fv}(m_\sigma) = \{\sigma(\text{fv}(m))\}$. The term m_σ is said to be closed, if its set $\text{fv}(m_\sigma)$ of free variables is empty. Also if t is a term of the term m_σ , we use $t[x \mapsto z]$ to denote the term $m_{\sigma[x \mapsto z]}$. Let $LAct$ be a set of late actions and $NAct$ is defined to be $\{c?x \mid c \in \text{Chan}, x \in \text{Var}\} \cup \{c!v \mid c \in \text{Chan}, v \in V\} \cup NAct$.

Proposition 1 (Late Operational Semantics for STGR)

Late operational semantics of topological spaces of many value-passing processes based on CCS with infinite assignments for STGR has the form as follows:

- $m \xrightarrow{R, a} n, a \in NAct$, implying $m_\sigma \xrightarrow{R\sigma, a} n_\sigma$,
- $m \xrightarrow{R, c!e} n$, implying $m_\sigma \xrightarrow{R\sigma, c!e} n_\sigma$,
- $m \xrightarrow{R, c?x} n$, implying $m_\sigma \xrightarrow{R\sigma, c?z} n_{\sigma[x \mapsto z]}$, $z = \text{new}(\text{fv}(m_\sigma))$. □

Note that there exist occurrences of some notations as follows. Let $SyAct$, ranged over by a represent the set of symbolic actions; it has the form $SyAct = \{c?x, c!e \mid c \in \text{Chan}\} \cup NAct$, where $NAct$ is some set of neutral actions. In the three above-mentioned expressions, there must exist the equation $R = R\sigma$ in topological spaces of many value-passing processes based on CCS with infinite assignments. As an example, these results apply to the event graphs [4] [6] [7] [8] of cryptographic protocols that run in an infinite and concurrent way.

4 Conclusion

In this paper, we define topological spaces for value-passing processes based on CCS with infinite assignments, and develop symbolic transition graphs. We present a variant of symbolic transition graphs. It denotes a symbolic transition graph with a binary equivalence relation $R \in \mathbb{R}$, which is abbreviated to STGR. Its results contribute to modeling for cryptographic protocols that run in an infinite and concurrent way.

To be dissimilar to the original STG, the STGR and its symbolic operational semantics rely on topological spaces, usually quotient spaces, for value-passing processes, which have a binary equivalence relation. As we know, a Boolean expression is actual an occurrence of binary equivalence relations. Thus we work out a highly efficient solution to partition domains of conversations of cryptographic protocols that run in an infinite, concurrent way in order to reduce computational complexities to prove their safety properties.

But how to deal with symbolic late or early bisimulations of STGRs remains to be resolved. Hence the further work is needed for the verification algorithm of bisimulation equivalent relation of STGRs, and the verification algorithm of safety properties of cryptographic protocols as its application.

Acknowledgments. This research is supported by the Anhui Provincial Natural Science Foundation of China under grant No. 090412057 and the Provincial Key Projects of Excellent Youth Talents Fund of the Institutions of Higher Education in Anhui Province of China under grant No. 2011SQRL113ZD.

References

1. Milner, R.: A Calculus of Communication Systems. LNCS, vol. 92. Springer, Heidelberg (1980)
2. Milner, R.: The Space and Motion of Communicating Agents. Cambridge University Press (2009)
3. Milner, R.: Communicating and Mobile Systems: the π -Calculus. Computer Laboratory, Cambridge University Press, University of Cambridge (1999)
4. Crazzolaro, F., Winskel, G.: Composing Strand Spaces. BRICS Report Series RS-02-5 (2002)
5. Hennessy, M., Lin, H.: Symbolic Bisimulations. Theoretical Computer Science 138, 353–389 (1995)
6. Wang, H., Zhang, Y., Li, Y.: A Diagram of Strand Spaces for Security Protocols. Journal of Computer Research and Development 43(12), 2062–2068 (2006)
7. Wang, H., Zhang, Y., Li, Y.: Modeling for Security Verification of a Cryptographic Protocol with MAC Payload. In: Huang, D.-S., Zhang, X.-P., Huang, G.-B. (eds.) ICIC 2005. LNCS, vol. 3645, pp. 538–547. Springer, Heidelberg (2005)
8. Crazzolaro, F., Winskel, G.: Events in Security Protocols. In: Proc. of the 8th ACM Conference on Computer and Communications Security, ACM Press, Philadelphia (2001)

Memetic Algorithm for a University Course Timetabling Problem

Khang Nguyen¹, Tien Lu², Trung Le², and Nuong Tran¹

¹ HCMC University of Science, Vietnam

² Cao Thang Technology College, Vietnam

Abstract. Evolutionary algorithm is a part of evolution computation. It often induces well approximated solutions to several kinds of hard optimization problems. This paper applies Memetic algorithms - a hybrid evolutionary method to a real-world university timetabling problem in Vietnam. Memetic algorithm and genetic algorithm are both experimentally tested on six real-world instances and obtained results show that memetic algorithm could speed up the convergence much more than genetic algorithm.

1 Introduction

It is well known that the timetabling problem is difficult to be solved, since the problem has a huge search space and is highly constrained. Therefore, this problem has attracted several researchers in the operational research community.

According to a report of ITC07 [1] - the International Timetabling Competition 2007, university timetabling problems can be classified into two groups: curriculum-based course timetabling problems and post enrolment-based course timetabling problems. In this paper, we consider a real-world curriculum-based course timetabling problem with 19 constraints; this problem is taken from the Faculty of Information Technology, HCMC University of Science in Vietnam. The approach that we use to solve our real-world problem is Memetic algorithm [2] – one of evolutionary algorithms. It has been applied to various university timetabling problems with remarkable results. Our intention is trying to adapt this algorithm to our concrete Vietnamese university timetabling problem. Furthermore, we also implement the Genetic Algorithm and compare the results of those two algorithms.

This paper is organized as follow: section 2 describes the details of the considered curriculum-based university timetabling problem, section 3 explains details of the proposed algorithm and section 4 presents the experimental results.

2 Problem Description

The general aim of the educational timetabling problem is to find an appropriate assignment of a set of courses (events) into a limited number of periods and rooms in such a way that satisfying a number of pre-defined constraints. The problem considered in this paper is a real-world curriculum – based course timetabling problem. This problem is highly constrained with 19 constraints, including 8 hard

constraints, which must be satisfied, and 12 soft constraints, which should be satisfied as much as possible. Each soft constraint is associated with a weight factor to represent its level of importance.

- Time concepts: including the concepts of period, lecture and session.
 - + Period: each period often lasts about 45 minutes.
 - + Session: is a group of consecutive periods that forms a distinct part of the day, e.g., morning session includes all the periods in the morning.
 - + Lecture: is a part that lasts one period of a course
 - + Resource concepts: including the concepts of lecturer, class, room and building
 - + Class: is a group of students that will attend the same courses.
 - + Building of the faculty: is a set of near rooms. Each building is often distanced far from the others, so there should be some constraints to eliminate the movement of lecturers and students between these buildings in the same day.
- Major concepts: including the concepts of course and curriculum
 - + Course: is a group of lectures that have the same lecturer, the same attending classes and subject. The main information of a course includes the lecturer teaching this course, one or some attending classes and the number of lectures in a week that belong to this course, i.e., the number of periods that this course must hold in a week. Note that some courses may be pre-assigned, i.e., their periods and rooms are pre-determined by the staff, these courses will not be re-scheduled again but their pre-assigned information (e.g., the assignment of their lecturer, classes) will be considered during the timetabling process of the other courses.
 - + Curriculum: is a group of courses that should not be overlapped due to the special requirements of the university. In our considered problem, a course is allowed to belong to more than one curriculum.

Next, we present the constraints of the problems. As mentioned above, each soft constraint has a relevant weight and this value is shown just right before the description of the constraint.

- Eight hard constraints (denoted by letter H and their index):
 - [H1] Lecturers, classes and rooms could not be assigned to periods at which they're not available (the availability of those resources are pre-defined)
 - [H2] All the lectures of all courses must be assigned.
 - [H3] The pre-assignment of any course must be respected.
 - [H4] The capacity of a room that is assigned to a course must be equal or greater than the planned number of students attending that course.
 - [H5] Courses that have the same lecturer or class must not overlap.
 - [H6] No room could be assigned to two simultaneous courses.
 - [H7] The lectures of each course in a day must belong to the same session
 - [H8] All lectures that belong to the same course must be assigned to the same room
- Twelve soft constraints (including one high weighted soft constraint, denoted by HS and 11 low weighted soft constraints, denoted by letter S, followed by their weight values):
 - [HS1] (60) Courses that belong to the same curriculum should not be overlapped.
 - [LS1] (10) The movement of a lecturer between two buildings in the same day should be avoided.

[LS2] (5) The movement of a class between two buildings in the same day should be avoided.

[LS3] (10) Courses should be assigned to periods that they're preferred.

[LS4] (5) The idle time between consecutive courses in the same session for a lecturer or a class should be avoided.

[LS5] (5) The number of periods that a class is assigned in a day should be equal or less than a limit named *maxStudyingPeriods*.

[LS6] (5) The idle time between consecutive courses in the same day for a lecturer or a class should be avoided.

[LS7] (10) The number of sessions that a lecturer was assigned to should be as small as possible.

[LS8] (10) The number of periods that a lecturer is assigned in a day should be equal or less than a limit named *maxTeachingPeriods*.

[LS9] (5) The number of days that a class was assigned to should be as small as possible.

[LS10] (10) In the timetable of a class in session, if there are three periods in which this class is idle, these should be consecutive periods (this is a special constraint requested by the timetabling staff because they need use these idle periods for another purpose).

[LS11] (10) All courses that belong to the same curriculum which are scheduled to the same session should be assigned to the same building at that session.

3 Memetic Algorithm for Considered Timetabling Problem

Solution Representation

Let $C = \{C_i\}_{i=1..n_C}$ be the set of courses, where n_C is the number of courses. Each solution is represented by two integer vectors with the size of n_C : period block vectors and room vectors. The i^{th} component of a period block vector expresses the period block (i.e., a group of continuous periods) and index of the room that course C_i is assigned to in the considered solution.

The Fitness of an Individual

Quality of each individual is evaluated based on the its value on objective function, which is a linear weighted sum of the soft constraints' violation. Besides that, in this approach, hard constraints H5 and H6 are also relaxed because it's really hard to find out a solution that satisfies all of the hard constraints, it means that some should be relaxed and the algorithm will try to solve all of them before it stops. Those relaxed constraints are integrated into the objective function with a very high weight (1000).

Initializing the Population

The initial population is generated as follow: one half of the population is generated randomly, and the other is created by GRASP (Greedy Random Adaptive Search Procedure) algorithm [4] whose value of the randomness-greediness balancing parameter is 0.5.

Crossover Operators

Three types of genetic algorithm's crossover operators are used in this algorithm, including one-point crossover, two-point crossover and uniform crossover [3]. These three types of operators are used alternatively. During the searching process, the number of times each operator type could induce offsprings that are better than their parents is saved. And at each crossover step, the type of operator that would be used is chosen based on that history information, i.e., the higher the number's value is, the higher probability the relevant operator's type is used.

Mutation Operators

The mutation operator would move a random course to a new random period block while choosing the best new room. The reason for choosing the best new room instead of a new random room is that in this approach, we focus more on solving the period assignment than room assignment. This reason is originated from the fact that the room assignment problem is often much easier than the period one.

Local Search

In memetic algorithm, to increase the intensification of the searching process, hill climbing local search is added to the algorithm. There are two kinds of moves used in the local search, at each iteration of the hill climbing local search, the neighbourhood generated by those two kinds of moves are exhaustively examined: the first one are single moves, in which a course is moved to another period block and the best room assignment at the new time slots would be chosen. The second one are swap moves, in which the period block assignment information of two courses would be exchanged, then, the new best rooms for those courses are decided.

Selection Method

Evolution process in nature is selection process. In this process, the better individuals will be existed and continue developing and worse individuals with less fitness would be removed.

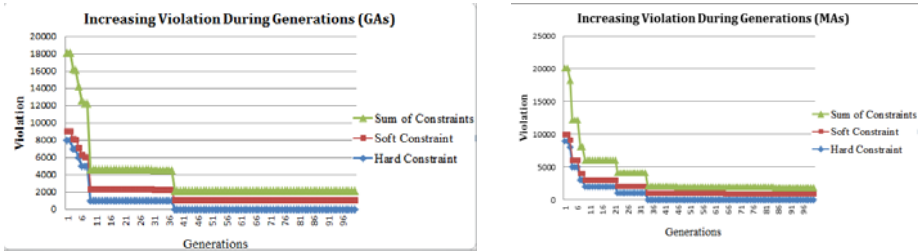
In this approach, rank-based selection is used. In this selecting method, individuals in population are descendingly sorted based on the fitness and a half of best individuals are used for generating the next generation.

4 Experimental Results

The algorithms are implemented in Visual Studio C++ 2005 under Windows XP operating system and run on a computer with the configuration of 1.6Ghz Core2 Duo CPU and 1GB RAM. The genetic algorithm (GA) and memetic algorithm (MA) are tested on 6 instances collected from real-world data in 4 studying years of the University of Science. The details of these data instances are listed in Table 1. Results of the best solution obtained in each generation during the searching process are presented in Figure 1, from which we could see that MA help to speed up the convergence when being compared with GA. Moreover, MA also induces better final solutions.

Table 1. Details of data instances

# instance	# courses	# teachers	# classes	# rooms	# curricula
Data 1	82	44	13	40	11
Data 2	80	44	10	46	10
Data 3	95	44	14	45	11
Data 4	84	45	11	40	10
Data 5	89	48	12	51	11
Data 6	51	31	19	45	0

**Fig. 1.** GA' and MA's best solution's quality in each generation

References

1. McCollum, B., McMullan, P., Paechter, B., Lewis, R., Schaerf, A., Di Gaspero, L., Parkes, A.J., Qu, R., Burke, E.: Setting the Research Agenda in Automated Timetabling: The Second International Timetabling Competition. Technical Report, International Timetabling Competition 07-08 (2007)
2. Moscato, P.: On Evolution, Search, Optimization, Genetic Algorithms and Martial Arts: Towards Memetic Algorithms. Technical Report, Caltech Concurrent Computation Program (1989)
3. Moscato, P.: Memetic algorithms: A short introduction. In: Corne, D., Glover, F., Dorigo, M. (eds.) *New Ideas in Optimization*, pp. 219–234. McGraw-Hill (1999)
4. Feo, T.A., Resende, M.G.C.: Greedy randomized adaptive search procedures. *J. of Global Optimization* 6, 109–133 (1995)

A Class of Autonomous Robots Prepared for Unfriendly Sunny Environment

Lucian Grigore¹, Recep Ileri¹, Cristian Neculăescu², Anton Soloi¹,
Ticușor Ciobotaru³, and Valentin Vinturiș³

¹ "LUMINA" University, Șos. Colentina no. 64b, sector 2, Bucharest, Romania, PC 021187

² Academy of Economic Studies, Dept. of Mathematics, Calea Dorobanți 11-13, et. 6, cam. 2625, sector 1, Bucharest, Romania., PC 010552

³ Military Technical Academy, Bd. George Coșbuc, no. 81-83, sector 5, Bucharest, Romania, PC 050141

Abstract. We present an electrical caterpillar autonomous robot demonstrator, which consists of two independent tracks with an operational platform, a system with photovoltaic panels for converting solar energy into electricity, and a system for connecting different devices to the robot chassis. One goal is to reduce operational costs in terms of fulfilling the missions and maintaining safe human operations in unfriendly environments. Other goals, imbedded in the demonstrator's design, are: mobility, lowered energy consumption, the usage of ecological energy, and an increased energetic independence. These characteristics would allow the development of a class of robots that may be used in unfriendly and isolated areas, in which solar energy is adequate. Yet another goal is to develop a database documenting how the demonstrator operates under various conditions.

Keywords: Robot, autonomous vehicle, photovoltaic cells, mobility, traction, rolling resistance.

1 Introduction

The European Union funding directions until 2020 [1] include areas such as agriculture, renewable energy, zero NO_x, CO_2 emission, as well as scientific cooperation among different countries. Based on macroeconomic data on Turkey, our research team has an increased interest on the Turkish agricultural and equipment market, with special view on tractor-type solutions, water management and green energy. Taking into account such arguments, we prepare a series of funding requests which will all include, as a component, prototypes based on our demonstrator, adapted for various needs and applications. All the requests will take advantage of the estimated characteristics of the demonstrator, which are found to be at least as good as the existing market products and, in particular areas, may reduce exploitation costs with at least 50%.

The demonstrator is obtained as a technological transfer and adaptation of preexistent military equipment for civil purposes. In Ciobotaru and Grigore [3] the initial military solution may be found; it was destined at the time for antiterrorist

activities, the robot being equipped for specific activities. We also mention some achievements of other authors, which while presenting similarities with our demonstrator, are in the same time independent. J. H. Lever and collaborators in [10] presents a simple four-wheeled, solar-powered drive named *Cool Robot* for autonomous summertime science campaigns in Antarctica and Greenland. Norman S. Nise in [12] presents the study of control systems engineering in electrical, mechanical, aerospace, biomedical, or chemical engineering for robotics. Corina Sandu and collaborators in [13] presents a multi-body model system dynamics analysis for off-road vehicles. Corina Sandu and collaborators in [14] presents an extended Kalman-Filter-type analysis, which allows, for off-road vehicle simulations, an optimal estimation of contact parameters between vehicle and terrain, and also the determination of the covariant matrix for each parameter.

In the next section we will describe the caterpillar robot with various functions that can use renewable electricity from solar energy, while mentioning from time to time aspects which we consider valuable, from the perspective of both the future prototypes, and the applications in funding-eligible areas.

2 Hardware Description

We developed a 250 kg robot with dimensions 1,4x0,8x0,65 (m x m x m) capable to transport/tractate a 250 kg payload [2] (fig. 1) on deformable and/or uneven ground and it is able to deal with 32% slopes in both movement directions. The robot is built on an aluminum frame and it is equipped with:

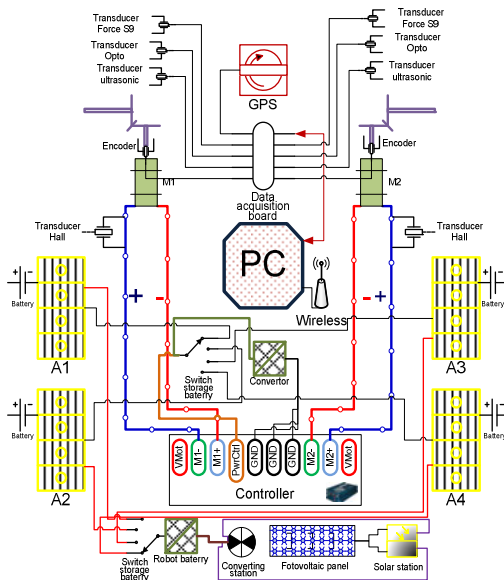


Fig. 1. Block diagram

1 navigational GPS, 2 accelerating sensors on 3 directions, 2 Hall switches for precise measurement of the input current, 2 RS38 encoders for measurement rpm of engine, 1 ROBOTEQ controller, 2 Magmotor S28-400 engines, 2 reduction gear, 4 UB300-18GM40-U-V1 ultrasonic sensors for data collection necessary for land map, 4 optoNCDT 1700-250VT intelligent laser displacement sensor with integrated controller, 1 S9 force transducer b0577 for simple, precise and economical measurement of compressive and tensile forces, and a central computer unit. The initial version was prepared for antiterrorist tasks and had an extra arm able to lift a 20 kg weight at maximum length.

3 Numerical Simulation

For numerical simulation of robot's dynamics we used Recurdyn software. The multi-body method is used to model the robot. Analysis with the software product assumes:

- Modeling with characteristic elements contained in toolboxes;
- Input of analysis constraints such as boundary conditions, characteristics of materials, and exterior forces.

The procedure followed was a trial-and-error method for adjusting parameters and characteristics, from both experimental and theoretical perspectives (fig. 2, 3 and 4):

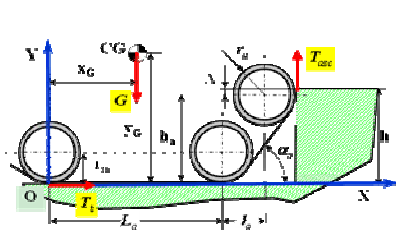


Fig. 2. The approach of the step-type obstacle

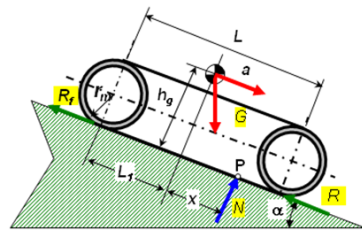


Fig. 3. Schema of mobile tracked platform descending the slope

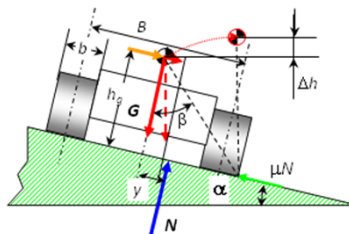


Fig. 4. Schema of transversal stability assessment

3.1 Boundary Conditions

To correctly define the boundary conditions and the forces between terrain and robot we use the following models.

The theoretical basis starts from Bekker's results [4], who quantify the vehicle mobility characteristics on deformable ground. Later Wong [5] developed these results to be able to estimate the drag amount corresponding for a vehicle equipped with wheels, respectively caterpillar tracks. The study was continued in [3] by considering the various effects of the ground on the behavior of tracks, and by adopting, as a result, a specific shape/profile of two independent caterpillar tracks.

In the following figure we present the dependence of shear unified effort and the robot's displacement for different slides or terrain types. These graphs are based on the articles of Wong [7], Laughery [8], Janosi and Hanamoto [6] (fig. 5).

❖ **Bekker's relation-based simulations:**

$$f_{terrain} = \frac{F}{G_a} = \left(\frac{c}{p_{av}} + \tan \phi \right) \cdot \left[1 - \frac{K}{\sigma \cdot L_a} \cdot \left(1 - \exp \left(-\frac{\sigma \cdot L_a}{K} \right) \right) \right]$$

$$\tau = \tau_{max} \cdot \left(1 - e^{-\frac{s}{K}} \right) = (c + p \cdot \tan \phi) \cdot \left(1 - e^{-\frac{s}{K}} \right)$$

❖ **Wong's relation-based simulations:**

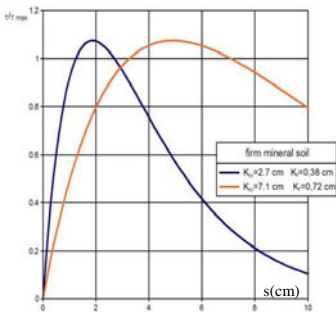
$$\tau = \tau_{max} \cdot \left[K_r + \left(\frac{1}{1 - e^{-1}} - K_r \right) \cdot e^{-\frac{s}{K_w}} \right] \cdot \left(1 - e^{-\frac{s}{K_w}} \right)$$

$$f_{terrain} = \frac{F}{G_a} = K_r \cdot \left(\frac{c + p \cdot \tan \phi}{p_{av} \cdot L_a} \right) \cdot \int_0^{L_a} \left\{ 1 + \left[\frac{1}{K_r \cdot (1 - e^{-1})} - 1 \right] \cdot e^{-\frac{\sigma}{K_w} \cdot x} \right\} \cdot \left(1 - e^{-\frac{\sigma}{K_w} \cdot x} \right) dx$$

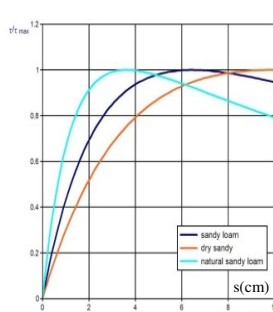
❖ **Laughery's relation-based simulations:**

$$\tau = \frac{\tau_{max}}{e^{(-K_2 + \sqrt{K_2^2 - 1})K_1 s_{max}} - e^{(-K_2 - \sqrt{K_2^2 - 1})K_1 s_{max}}} \cdot \left[e^{(-K_2 + \sqrt{K_2^2 - 1})K_1 s} - e^{(-K_2 - \sqrt{K_2^2 - 1})K_1 s} \right]$$

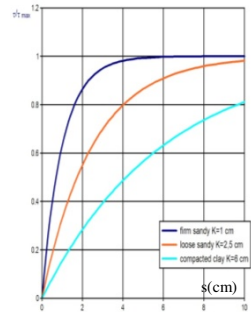
$$f_{terrain} = \frac{(c + p \cdot \tan \phi)}{K_1 \cdot \sigma \cdot y_{max} \cdot p_{av} \cdot L_a} \cdot \left(\frac{-1 + e^{(-K_2 + \sqrt{K_2^2 - 1})K_1 \sigma L_a}}{-K_2 + \sqrt{K_2^2 - 1}} + \frac{1 - e^{(-K_2 - \sqrt{K_2^2 - 1})K_1 \sigma L_a}}{-K_2 - \sqrt{K_2^2 - 1}} \right)$$



Wong [7],



Laughery[8],



Janosi and Hanamoto [6]

Fig. 5. The dependence of shear unified effort

3.2 Recurdyn Modeling

The virtual model of the independent caterpillar system has been simulated with Recurdyn [15]. Experimental and analytical data was prepared for usage with Recurdyn by filtration for various interferences and incorrect positioning of components (fig. 6). The reference ground for the simulation was chosen as horizontal hard ground (fig. 7, 8 and 9).

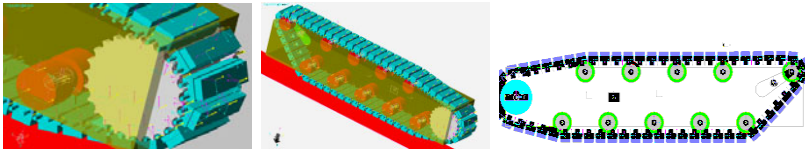


Fig. 6. The adopted track shape/profile

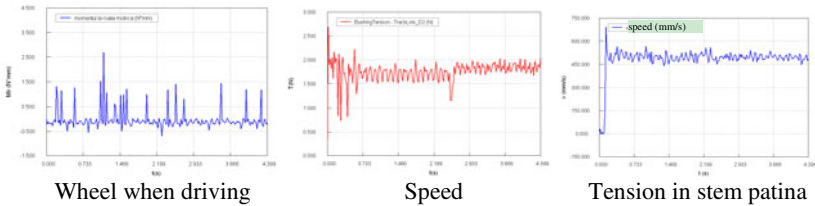


Fig. 7. Simulations of the virtual model

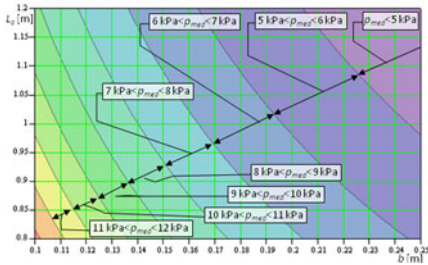


Fig. 8. Average pressure variation

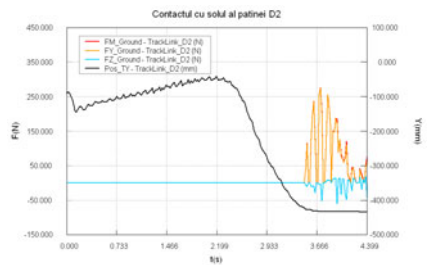


Fig. 9. Crossing the step-type obstacle

4 Experimental Results [11]

Laboratory tests have validated, until now, the basic design elements. We intent to further develop the demonstrator and to reach the prototype level, and to document the development of an autonomous hybrid robot class, with both electrical and internal H_2 combustion, to address future applications in areas such as agriculture.

Below are various results obtained for suspended platform functioning regime of the electrical engines.

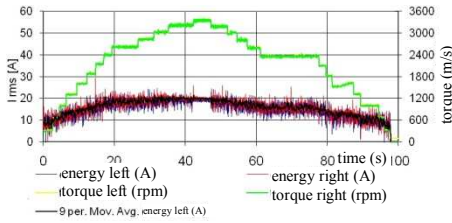


Fig. 10. Straight walking simulation

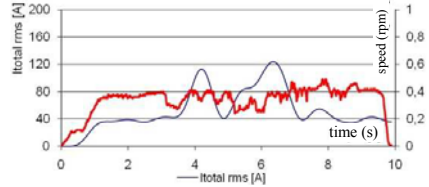


Fig. 11. Straight walking consumption

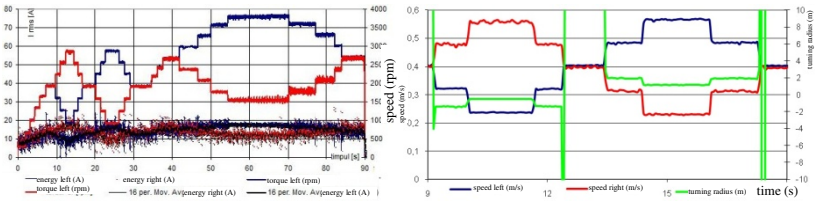


Fig. 12. Turn simulation

5 Achievements and Future Prospects on Solar Energy and Hybrid Alternatives

The robot is equipped with 4 photovoltaic panels (fig. 13) embedded in a carbon fiber frame. The capacity of the SolFocus Inc. [9] type photovoltaic cells allows for a quantity of electrical energy equivalent of $1.000 [W/m^2]$ on a total surface of $1,3156 m^2$, at $25 [^{\circ}C]$ air temperature and 60% relative humidity. The carbon fiber frame is fixed on the robot frame by means of 4 electrical actuators, which form, together with a solar radiation sensor Pyranometer SR11 and a lux meter sensor, the system for orienting the photovoltaic panels towards the sun, such that at any robot given position the panels are facing the sun as good as possible. Each panel has an independent converter; the computer manages both the system for charging the batteries and the engine fueling system. We estimate that the system will extend the active time outside the daylight period with at least 4 hours. The primary navigation strategy is GPS waypoint following along a path pre-selected for minimum terrain hazards. We will implement *smart mobility* algorithms that sense vehicle tilt and wheel speeds, torques to stop robot before immobilization. While we will avoid autonomous vision based navigation to minimize operational cost and consumed energy, we will include a camera for low-bandwidth image transmission to a base station to assist manual extraction from dangerous terrain.

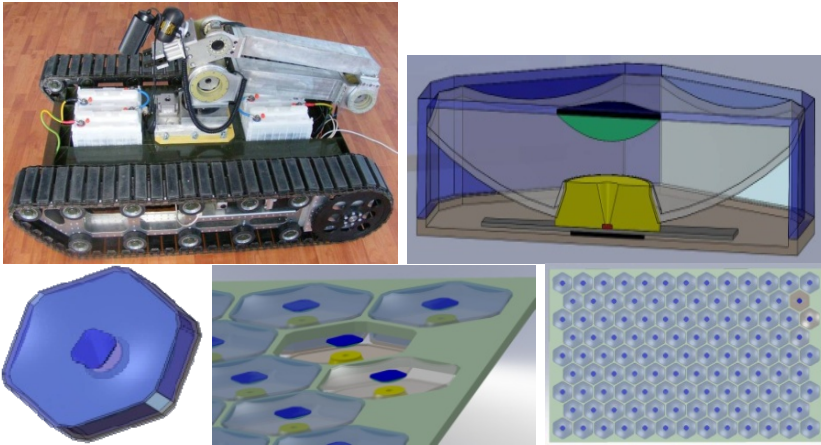


Fig. 13. Renewable energy system elements

6 Conclusions

We have designed, built and validate a simple autonomous tracked robot driven by electric solar-powered motors able to accomplish multiple missions. Tests conducted in Romania validated the basic features of the RoAgSol: mobility characteristics, power input and control and navigation. Current absorbed by the electric motors is no more than 132 A, at continuous functioning, and maximum speed is 4.5km/h. Mean working time outside the sufficient solar power need is 4h, with the possibility to cover 18 km outside the sufficient solar power at an average load cycle.

The testing and simulation of the present design of the robot enables us to be confident in preparing the next steps for the robot exploitation. This includes phases like prototype construction, funding and/or collaboration, and doesn't exclude further testing and data gathering.

References

1. ftp://ftp.cordis.europa.eu/pub/fp7/coordination/docs/ictagri_en.pdf (last accessed on July 29, 2011)
2. Ciobotaru, T., Grigore, L., Soloi, A., Vinturi, V.: Robot to combat terrorist - ROBTER (in Romanian), contract nr. 20/19.10 2006, http://www.cnmp.ro/ceex/compl_2006/oferta.php?id=1298/ (last accessed on September 15, 2011)
3. Grigore, L., Ciobotaru, T., Vinturi, V.: AMMA-2007120- Specific aspects of the stability of platforms used by medium size mobile robots, International Congress Automotive, Environment and farm machinery, AMM 2007, October 11-13, Cluj-Napoca, România (2007), http://www.atna-mam.utcluj.ro/pdf/2007no50volIV_cuprins_si_rezumate.pdf/

4. Bekker, M.G.: Theory of Land Locomotion. The University of Michigan Press, Ann Arbor (1956)
5. Wong, J.Y.: Theory of Ground Vehicle (2nd). John Willey & Sons, s.n (1993)
6. Janosi, Z., Hanamoto, B.: The analytical determination of drawbar pull as a function of slip for tracked vehicles in deformable soils. In: Proceedings of the 1st International Conference on the Mechanics of Soil-Vehicle Systems, Edizioni Minerva Tecnica, Torino, Italy (1961)
7. Wong, J.Y.: On The Role Of Mean Maximum Pressure As An Indicator Of Cross-Country Mobility For Tracked Vehicles. *Journal of Terramechanics* 31(3), 197–213 (1994)
8. Laughery, S., Gerhart, G., Goetz, R.: Bekker's Terramechanics Model for Off-road Vehicle Research. Warren: US Army TARDEC. MI 48397-5000
9. <http://www.solfocus.com/en/index.php/> (last accessed on August 22, 2011)
10. Lever, J.H., Ray, L.R., Streeter, A.: Mobility and Power Budget for a Solar-Powered Polar Rover, <http://www.ists.dartmouth.edu/library/187.pdf> (last accessed on September 23, 2011)
11. Ciobotaru, T., Vinturi, V., Gh, A., Gherman, L.: Testing vehicles (in Romanian). In: Mirton, Timioara (eds.) 204 p (2009), ISBN 978-973-52-0562-1
12. Nise, N.S.: Control Systems Engineering. In: Pomona (ed.) California State Polytechnic University, 6th edn., p. 948. John Wiley & Sons, Inc., Printed in the United States of America (2009), ISBN 13 978-0470-54756-4, ISBN 13 978-0470-91769-5
13. Sandu, C., Worley, M., Morgan, J.B.: Experimental Study on the Contact Patch Pressure and Sinkage Analysis of a Lightweight Vehicle on Sand. Paper No.JTERRA-S-09-00021, *Journal of Terramechanics* (2011), http://arc.engin.umich.edu/rsrch/rsrch1_9.html: last accessed on (September 22, 2011)
14. Sandu, C., Sandu, A., Ahmadian, M.: Modeling Multi body Dynamic Systems with Uncertainties. Part II: Numerical Applications. In: Multi body System Dynamics, vol. 15(3), pp. 241–262. Springer, Netherlands (2006), http://people.cs.vt.edu/asandu/Deposit/Blanchard_Sandu_ISTVS_07.pdf ;ISSN: 1384-5640 (paper) 1573-272X (online), DOI: 10.1007/s11044-006-9008-4 : (last accessed on September 22, 2011)
15. Recurdyn Software Product, <http://www.recurdyn.de/>

Step by Step Modeling and Tuning for Fuzzy Logic Controller

Mohammed Majid Mohammed Al-Khalidy¹ and Fatma Abdulnabi Al-attar²

¹ Dept. Electrical and Electronic Engineering, College of Engineering, Gulf University, Sanad, Bahrain

dr.mohammed.majid@gulfuniversity.net

² Dept. Electrical and Electronic Engineering, College of Engineering, Gulf University, Sanad, Bahrain

alattar_80@hotmail.com

Abstract. Fuzzy logic is a mathematical tool for dealing with uncertainty using numerical parameters. Until now many fuzzy controllers have been constructed instead of systematically designed using trail and error method guided by designers experience on fuzzy control. The contribution of this paper is to propose a systematic with step by step methodology on how to design fuzzy PID fuzzy controller and to find the effect of tuning of many parameters (e.g., membership function shapes and number , rules types and input /output scaling gain) on system output response so that the researcher can be find the most useful in learning the finer point about tuning and design of fuzzy controllers.

Keywords: Fuzzy logic system, PID controller, Tuning Fuzzy controller.

1 Introduction

Fuzzy logic controllers (FLCs) are developed to exploit human expert knowledge in designing control systems [1]. Many control applications show that a fuzzy logic controller can improve control performance especially for high order linear or non-linear system. The selected Fuzzy PID controller is designed to have the same control property with corresponding PID controller because the parameters of its control rule base are calculated according to tuned parameters of the PID controller [2],The controller consist two part one is conventional PID controller and other one is fuzzy logic control (FLC) part [3].The main features of PID controllers are the capacity to eliminate steady-state error of the response to a step reference signal [4].

An important step in designing a control strategy is proper modeling of the system to be controlled. An exact system model should produce output response similar to the actual system [5]. The success of the PID controller depends on appropriate choice of the PID gains. Tuning the PID gains to optimize performance is not trivial task [6].Based on the proposed methodology , many fuzzy controllers can be designed to enhance the output response and to overcome with the distortions in output response generated by the control process. The proposed methodology focuses on the effect of tuning many parameter (e.g. ,membership function shape and number , rules types and input /output scaling gain) on system output response. The goal is to try to provide

some basic design guidelines that are generic to all fuzzy controllers. Some basic design guidelines are listed for tuning fuzzy controllers.

2 General Design of Fuzzy Controllers

This section provides more mathematical and complete exposition on the details of the operation of fuzzy systems design often used in practical application. fuzzy PID methodology divided into seven steps.

STEP 1 : Testing the closed loop output response

It is shown that the plant model can be identified from the input and output data obtained by output over-sampling even though the conventional identifiability conditions are not satisfied [7].

The closed loop output response of the given plant should be tested firstly to take an overview about the system response so that the proper fuzzy PID parameter can be selected depending on its output response nature.

STEP2: Gains tuning and selecting PID controller In application, engineers have freedom of using the three functional elements (P, I, and D) of the PID controller in whatever combination they consider most appropriate for their problems. The combination of element(s) used is called the “action mode” of the PID controller [8]. The success of the PID controller depends on an appropriate choice of the PID gains. There are three basic controller actions, each having both good and undesirable characteristics. These are the following :

Proportional action, in which the action is Proportional to the error , the action is simple, stable and direct but causes offset .Offset can be described as steady state error associated with the response of a system disturbance.

Integral action, in which the rate of change of action is proportional to the error. Integral action eliminates offset, but is a soft action which permits oscillation of a system response.

Derivative action, in which the action is proportional to the rate of change of the error.

It gives a rapid response to counter the effect of rapidly changing errors, but is insensitive to slowly changing error and hence allows drift [9].

Three PID gains k_p , k_i and k_d were respectively calculated through fuzzy logic based on error and error rate [10]. The popularity of PID controllers can be attributed to their simplicity both from the design and the parameter tuning point of view. To implement such a controller, the proportional gains, the integral gains, and the derivative gains must be determined [11].

STEP 3: Specifying system regions

The input and output spaces are divided into fuzzy regions. This step produces initial membership functions [12]. Each input/output response should be divided into several regions that can be used by memberships and to take the input and determine the degree to which they belong to each of appropriate fuzzy set via membership function.

STEP 4: Selecting the proper memberships function

The fuzzy sets are quantitatively defined by membership functions. These functions are typically very simple functions that cover a specified domain of the value of the

system input. The functions are generally trapezoids, although simpler functions such as triangles and rectangles and even delta [13].

In this step membership function shapes and number will be tuned to achieve the desired performance.

- Tuning of membership number

Giving additional number of membership function to the system did not always improve the result but to show the effect of tuning the membership function number on the output response.

- Tuning of membership shape

Fuzzy sets can have any shape. Each shape affects how well a fuzzy system of if-then rules approximate a function. Triangles have been the most popular if-part set shape but they surely are not the best choice for approximating nonlinear systems. Overlapped symmetric triangles or trapezoids reduce fuzzy systems to piecewise linear systems[14].

STEP 5: Initializing the value of the rule table

A rule bases transforms the human decision process into fuzzy control action from the knowledge of the control rules and linguistic variable definitions [15]. Practically each point of time instants should be projected at the three graphs and find its corresponding point at the curve and decide at which membership function region this point acts. In this way the initial table can be filled with respect to the inputs/output. By using a linguistic approach, fuzzy theory can be integrated into control theory using rules of the form IF{condition} THEN{action}. Using enough of these rules, one can create a functional controller. In this same way the input variables can be partitioned into overlapping sets which have a linguistic correlation (i.e., cold, warm, hot) to form a membership function [16].

STEP 6: Applying the fuzzy inference system to the control plant.

The aim of this step is to find the output of each antecedent, consequence and the final fuzzy set of inference process. The process of drawing conclusion from available data is called inference and the computational efforts are done by inference engine [17]. At this point, the fuzzy inference system has been completely defined, in which the variables, membership functions, and the rules necessary to calculate the output are in place.

There are two types of fuzzy inference systems that can be implemented in the Fuzzy Logic Toolbox: Mamdani-type and Sugeno-type. These two types of inference systems vary somewhat in the way outputs are determined. In these cases Mamdani-type is used were it is expects the output membership functions to be fuzzy sets. After the aggregation process, there is a fuzzy set for each output variable that needs defuzzification. It enhances the efficiency of the defuzzification process [18] .At this point, the fuzzy inference system has been completely defined, in which the variables, membership functions, and the rules necessary to calculate the output are in place.

STEP 7 : parameter tuning of fuzzy PID controller

It is important to realize that there many parameters that can be tuned to improve the performance of the fuzzy control system. Indeed Sometimes it is the case that for a given rule-base a desired optimal performance cannot be achieved by tuning only the membership function often, what is needed is a more careful consideration of how to specify additional rules or shape and number of membership functions [19]. There are

however, certain methods to overcome this problem, and here four of these parameter will be examined.

- Effect of tuning rules type.
- Effect of tuning membership function shapes.
- Effect of tuning membership function numbers.
- Effect of tuning output scaling gain.

In this paper, investigation of fuzzy PID controller structures is done with Mamdani-type controller. By expressing the fuzzy rules in different forms. For purpose of analysis, a PID-like fuzzy controller is implemented under matlab for initial setting of the control system to increase the facility of system modification and control. A case study is illustrated for fuzzy control systems. Indeed, the best way to really learn fuzzy control is to design the fuzzy controller by following the previous steps and simulate the fuzzy controller to evaluate its performance.

3 Illustrative Example

This case will discuss a type of simple first order system given by:

$$G(s) = \frac{10}{s+1}$$

First of all this case will discussed from a side of its closed loop model. Secondly, the seven steps that have been discussed will be followed so that a PID like fuzzy controller can be built.

STEP 1 : Testing the closed loop output response .

Fig.1 shows the closed loop model in case of using step input. where the closed loop output response is given in Fig.2.

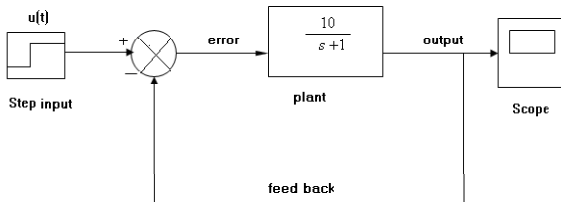


Fig. 1. Closed loop output model

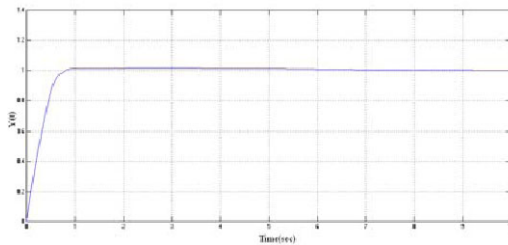


Fig. 2. Closed loop output response

STEP2: Gains tuning and selecting PID

Based on the experimental estimation PI controller is to be chosen with a set of tuning gains parameter of : $k_i=0.1$ and $k_p=2$. Fig.3 shows PI structure also Fig.4 illustrates the output response for the system equipped with conventail PI controller

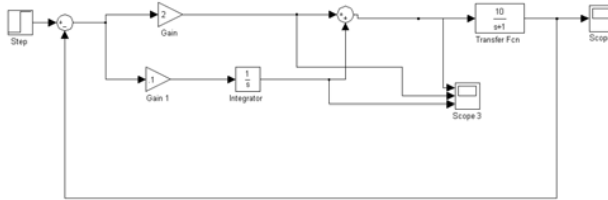


Fig. 3. PI Controller Structure

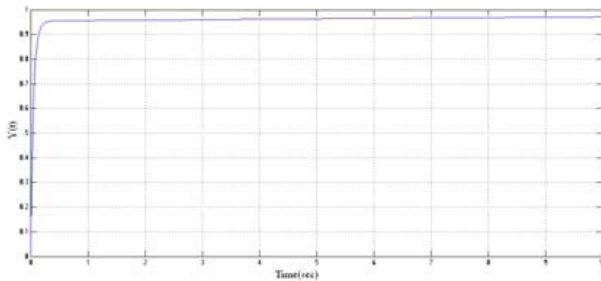


Fig. 4. Output response for system equipped with Conventail PI Controller

Fuzzy controller will be design by taken the error, integral of error and the output of the classical controller signals as its illustrated in Fig.3 .The universe of discourse in this study contains three regions for each input where illustrated in Fig.5

STEP 4: Selecting the proper memberships function

The membership functions of the fuzzy PI controller consist of three memberships functions comprising (zmf, trapmf, smf) membership function. All memberships are selected to describe all linguistic variables.

STEP 5: Initializing the value of the rule table.

For determination of the control rule, the projection of each point is given in fig.6 and Table.I shows the rule base table.

Where the circled cells are effective cell, in otherworld if the effective cells are changed the whole response will changed Also the others are assumed cells where the two inputs doesn't meet together also they are ineffective cells .Note that there is no direct relation between the cell to be ineffective and being assumption cell.

Step 6: Applying the fuzzy inference system to the control plant.

Fig.7 shows a fuzzy control system where a PI like fuzzy controller is applied to the control .The design of fuzzy PI like fuzzy controller illustrated in Fig.8.

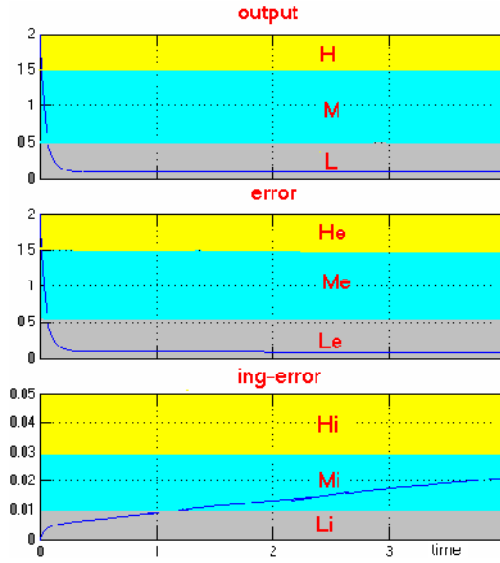


Fig. 5. Three membership distribution long (input/output)

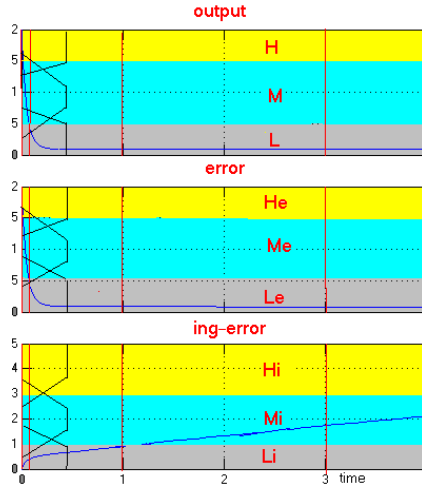


Fig. 6. Time projection for each input/output

Table 1. Rule Base Table for Three Membership Functions

e	L_e	M_e	H_e
$\int e$			
L_i	\odot	M	H
M_i	\ominus	H	H
H_i	M	\ominus	\odot

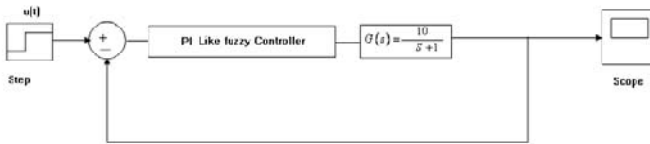


Fig. 7. Fuzzy control system

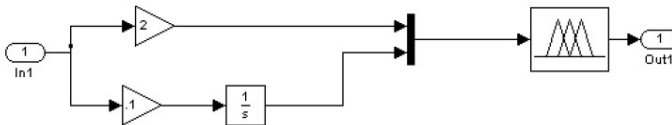


Fig. 8. PI like fuzzy controller design

The output response of the fuzzy controller is given in Fig.9

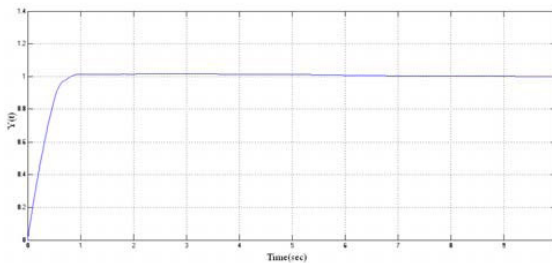


Fig. 9. Output response for three memberships (zmf,trapmf,smf)

It is obvious that this case eliminates the steady state error in the output response in comparison with the system equipped with conventional PI controller that is shown in Fig.4.

Step 7: parameter tuning of fuzzy PID controller

Effect of changing rules type

Table 2 shows the changes in the effective cells that have been discussed in the initial rule base .Also Fig.9 shows the output response due to these changes .

Table 2. Three Membership Rule Base Table with Rules Changes

		error			
		e	Le	Me	He
integral-error	$\int e$				
	Li	M	M	H	
	Mi	M	H	H	
Hi	M	M	H		

Where the circled cell and triangular cells are the changes in the effective cells and the whole cells been fixed.

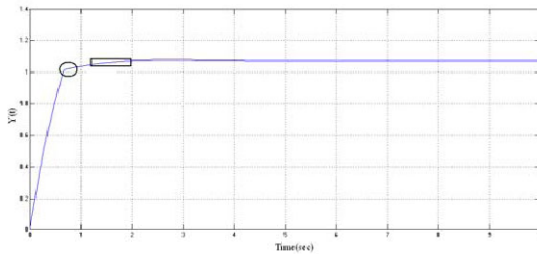


Fig. 10. Output response due to changes in the initial rules

The experimental analysis shows that the changes in the circled cell and the triangular cells have an effect on specific regions of the output response were illustrated in the previous Figure. It is useful to notice that these changes increase the steady state error in comparison with Fig.9.

- Effect of tuning the membership shapes

In this case three different shapes of membership types are used. The output response due response due to tune the membership shapes is given in Fig.11.

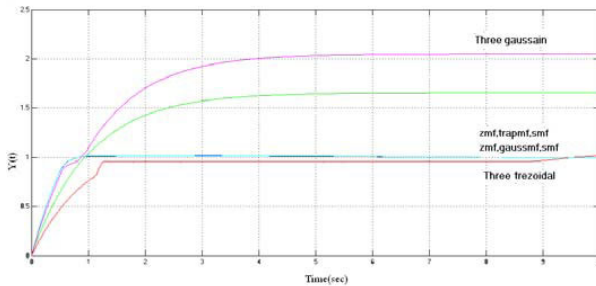


Fig. 11. Output response due to membership shapes variation

Also three memberships are used in this case ,but no simulation is occurred in compassion with other shape.

- Effect of Tuning membership functions number

Fig.12 shows different output responses behavior due to membership function number variations

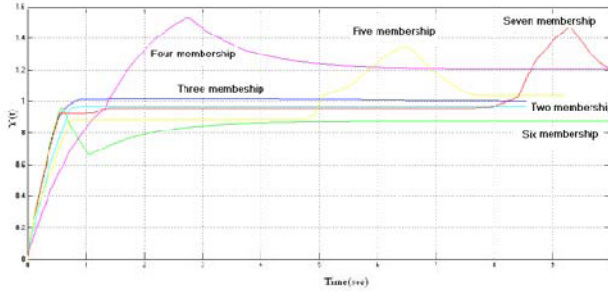


Fig. 12. Output response due to membership function number variation

For the case of six memberships were used ,the six memberships regions are used to cover a specified domain of the value of the system input and output .The membership regions distribution are given in Fig.13. Where the initial rule base table is given in Table 3 and the output response due to membership functions number tuning have been shown in Fig.12.

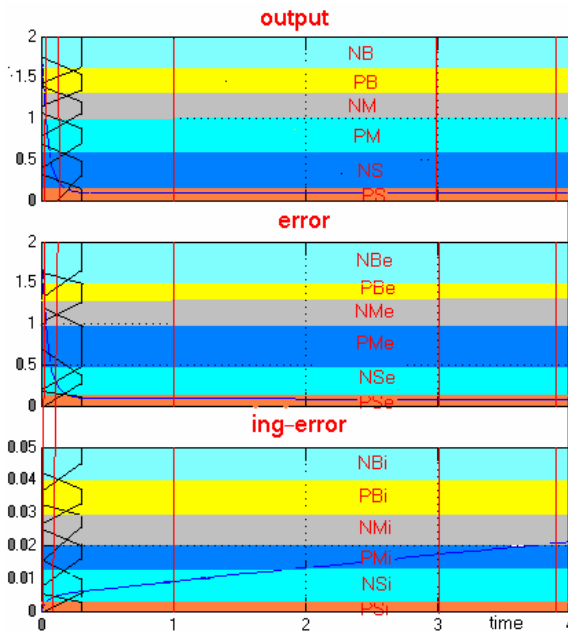


Fig. 13. Six membership distributions long input/output

Table 3. Six Membership Rule Base

		Error					
		e	NS_e	PS_e	NM_e	PM_e	NB_e
Integral -error	NS_i	NS	PS	NB	Nm	NB	PS
	PS_i	NS	NM	PB	PM	NB	NS
	NM_i	NB	PB	PB	NS	PS	NM
	PM_i	B	PM	PS	PM	NB	NB
	NB_i	PM	NS	NB	NM	PM	PS
	PB_i	PM	NB	BP	NM	PS	NS

Referring to Fig.13, the distortions increase in case of six memberships have been used in comparison with the fuzzy controller with three membership functions.

According to the previous results, its proved that it is not necessary that the increment in membership number lead to a stable and reasonable output response (for the cases of 4, 5, 6 and 7 memberships).

Effect of tuning output scaling gain.

The relationship between the scaling gains and the performance can be deduced to produce the comparative tuning algorithm [20].

Fig.14 shows the output responses due to output scaling gain variations.

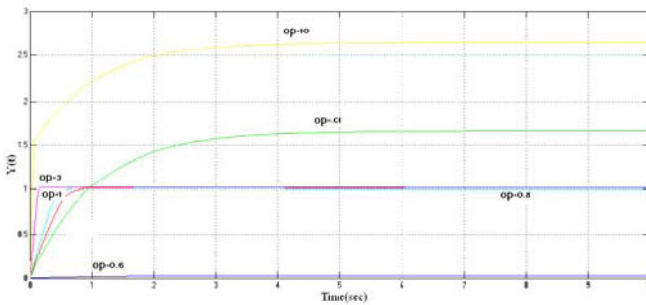


Fig. 14. Output response due to output gain variation

It's clear that the over shoot increased as the output scaling gain increased and the best choice is to select an output scaling gain of 0.8 to have a reasonable out put response.

4 Conclusion

In this paper a practical fuzzy like PI controller is designed using matlab version (7.6) under simulink. Analysis with step by step designing methodology. The

methodology is done for a study case of first order type 0 transfer function. Simulation results show the effect of tuning parameters (membership function shape and number, initial rule base, and output scaling gain) in the output response. Tuning fuzzy controller parameters will increase the facility of controlling the model output response at certain time period and enhance its performance. Also steady state error, max overshoot and settling time of the output response are affected by parameter tuning. The step by step methodology is suitable for the situation which a system model is reliable.

References

1. Fang, G., Kowk, N., Ha, Q.: Automatic Fuzzy Membership Function Tuning Using the Particle Swarm Optimization. In: IEEE Pacific-Asia Workshop on Computational Intelligence and Industrial Application (2008)
2. Y. Huang and S. Yasunobu, "A General Practical Method for Fuzzy PID Control from Conventional PID Control", Proceedings of The 6th International Conference on Fuzzy Systems and Knowledge Discovery, Vol. 4, China, 2005.
3. Therese, P., Nairm, N.: Fuzzy Self Tuning of PID Controller for Multivariable Process. *Journal of Computing* 2(8) (2010)
4. Basilio, J., Matos, S.: Design of PI and PID Controllers With Transient Performance Specification. *IEEE Transaction on Education* 45(4) (2002)
5. Zulfatman, Rahmat, M.: Application Of Self Tuning Fuzzy PID Controller On Industrial Hydraulic Actuator Using System Identification Approach. *International Journal on Smart Sensing and Intelligent Systems* 2(2) (2009)
6. Wang, L.: A course in fuzzy systems and control. Prentice-Hall (1996)
7. Sun, L., Sano, A.: "Algorithm and Implementation of Direct Closed-Loop Identification via Output Over-Sampling Scheme". In: Proceedings of the 3rd International Conference on Innovative Computing Information and Control (2008)
8. Araki, M.: PID CONTROL. In: Control Systems, Robotics, and Automation, vol. 2 (2010)
9. Reznik, L.: Fuzzy Controllers handbook. Newnes (1997)
10. Yao, L., Lin, C.: Design of Gain Scheduled Fuzzy PID Controller. *World Academy of Science, Engineering and Technology* 1 (2005)
11. Wu, C.: A Neural-Network-Based Method for Fuzzy Parameter Tuning of PID Controllers. *Journal of The Chinese Institute of Engineers* 25(3), 265–276 (2002)
12. Shafiq, M., Farooq, M., Khayam, S.: A Comparative Study of Fuzzy Inference Systems, Neural Networks and Adaptive Neuro Fuzzy Inference Systems for Portscan Detection, Next Generation Intelligent Networks Research Center (2008)
13. Murtha, J.: Applications of fuzzy logic in operational meteorology. In: Scientific Services and Professional Development Newsletter, Canadian (1995)
14. Mitaim, S., Kosko, B.: The Shape of Fuzzy Sets in Adaptive Function Approximation. *IEEE Transactions on Fuzzy Systems* 9(4) (2001)
15. Therese, P., Nair, N.: Fuzzy Self Tuning of PID Controller for Multivariable Process. *Journal of Computing* 2(8) (2010)
16. Homaifar, A., McCormick, E.: Simultaneous Design of Membership Functions and Rule Sets for Fuzzy Controllers Using Genetic Algorithms. *IEEE Transactions on Fuzzy Systems* 3(2) (1995)

17. Darestani, A., Jahromi, A.: Measuring Customer Satisfaction Using Fuzzy Inference Engine. *Journal of Applied Science* (2009)
18. Matlab User Guide Fuzzy Logic Toolbox, Version 7.6
19. Passino, K., Yurkovich, S.: *Fuzzy Control*, 1st edn. Addison Wesley Publishing Company (1997)
20. Li, H.: *A Comparative Design and Tuning for Conventional Fuzzy Control*. *Transactions on Systems, Man, and Cybernetics* (1997)

A Novel Method for BLDCM Control Based on Phase Back-EMF Observation

Pan Lei^{1,2}, Wang Beibei², and Gong Wei²

¹ School of Electrical Engineering, Hebei University of Technology, Tianjin 300310

² Department of Electronic and Information Engineering, Tianjin Institute of Urban Construction, Tianjin 300384

Abstract. This paper proposes a new zero-crossing point detection method for BLDCM without using the position sensor. Regarding phase current and phase back-EMF as state variables, the observer model of the phase back-EMF could be obtained from derivation of the mathematical model of BLDCM. This observation model could observe the value of the phase back-EMF real-timely, and the zero-crossing point could be directly detected through measuring the back-EMF at high speed. But the phase back-EMF is relatively smaller at low speed, and it is possible to cause unexpected commutation. A kind of zero-crossing point detection method is proposed based on this model for low-speed control. Combining the observation model and the zero-crossing point detection method, it could realize the zero-crossing point detection of the BLDC in full speed range. The simulation and experimental results show the feasibility of this method.

Keywords: sensorless control, phase back-emf observer, zero-crossing point, full speed range.

1 Introduction

Traditional BLDC motor requires a position sensor for acquisition of rotor position signal to control commutation of three-phase windings. However, position sensor presents several disadvantages such as big size, bad adaptability in environment of high-temperature and high-humidity, too many wire connection from sensors and so on, which reduce the reliability of the motor. Hence, the BLDCM control without using position sensor becomes an important research field[1].

Satoshi Ogasawara proposed a new method without using position sensor in [2] for detection of the conducting interval of free-wheeling diodes connected in anti-parallel with power transistors. This method has better performance at low speed, but there is large deviation for estimated position and speed signals at high speed. Many observer methods such as sliding mode observer or other state observer are adopted in [3] for real-time estimation of rotor position and speed. In those methods a mathematical model of the motor is required, and phase or line voltages could be acquired through voltage sensor or switch state of inverter. But the torque ripple, the inaccuracy of angle and speed estimation at low speed and the algorithm complexity are mainly problems. [4] proposes a method for BLDCM control without using position sensor based on the

detection of the zero-crossing of the back-EMF waveforms. The zero-crossing signal could be indirectly acquired through establishing the neutral point of the motor or using special control chips. Because commutation point lags behind zero-crossing point 30 electrical points, how to reduce the phase delay is the mainly problem for this method. [5] realizes the full range speed control of BLDCM and realizes the real-time observation of line back-EMF through using unknown input variable observer. But there are two first-order inertia links in this observer, which extends system transition process, and the torque and speed ripple are increased at low speed because the amplitude of line back-EMF is small, which leads to the inaccuracy of estimated value.

In view of the above-mentioned problems, this paper proposes a novel sensorless control method for full range speed control, which regards the phase back-EMF as the disturbance signal of the current estimation and further acquires phase back-EMF. Experimental results show that this algorithm is very effective.

2 Modeling of BLDCM

The ordinary BLDC motor applies three-phase VSI (voltage source inverter) for power supply, and its stator winding is connected in star, as shown in figure 1. Because the neutral point N of BLDC motor is not extracted, the phase voltage equation is difficult to be accurately constructed. But the line voltage expressions could be obtained through corresponding subtraction of the three-phase phase voltages:

$$\begin{cases} u_{ab} = R_s(i_a - i_b) + Lp(i_a - i_b) + (e_a - e_b) \\ u_{bc} = R_s(i_b - i_c) + Lp(i_b - i_c) + (e_b - e_c) \\ u_{ca} = R_s(i_c - i_a) + Lp(i_c - i_a) + (e_c - e_a) \end{cases} \quad (1)$$

Where, p is the differential operator d/dt ; R is the stator resistance, L_s is the self-inductance of stator winding, M is the mutual inductance of the stator winding, $L=L_s-M$.

Further consider the difference between line-voltages, and the following equation could be obtained after subtracting u_{bc} from u_{ab} :

$$u_{ab} - u_{bc} = R_s(i_a + i_c - 2i_b) + Lp(i_a + i_c - 2i_b) + (e_a + e_c - 2e_b) \quad (2)$$

Supposing that phase A and phase C are conducted and phase B is not conducted with them, then. Because the three stator windings of BLDC motor are connected in star, (2) could be simplified as:

$$\dot{i}_b = -\frac{3R_s}{3L}i_b + \frac{1}{3L}(u_{bc} - u_{ab}) - \frac{2}{3L}e_b \quad (3)$$

3 The Establishment of the Phase Back-Emf Observer

In (3), i_b , u_{bc} and u_{ab} are measurable, and e_b could not be directly measured, so regard e_b as disturbance with regular change. The estimated current of phase B \hat{i}_b

could be obtained through equation (3), and $error_{ib}$, which is the difference between i_b and \hat{i}_b , could also be acquired. Hence, the change of $error_{ib}$ could reflect the change of e_b , and (3) could be rewritten as:

$$\dot{\hat{i}}_b = -\frac{R_s}{L}\hat{i}_b + \frac{1}{3L}(u_{bc} - u_{ab}) - \frac{2}{3L}e_b + k_3 error_{ib} \quad (4)$$

$$\dot{\hat{e}}_b = k_4 error_{ib} \quad (5)$$

Where, k_3 and k_4 are proportional coefficients.

In (5), the accurate value of e_b could be acquired through reasonable selection of k_3 and k_4 . The back-EMF observer of the phase B is shown in figure 1.

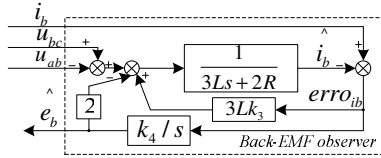


Fig. 1. The back-EMF observer of phase B

Similarly, the observer models of the other two phases could be obtained, and the system observer model could be obtained eventually:

$$\dot{\hat{x}} = A\hat{x} + Bu + K \times Error_i \quad (6)$$

Where,

$$x = \begin{bmatrix} \hat{i}_a \\ \hat{i}_b \\ \hat{i}_c \\ \hat{e}_a \\ \hat{e}_b \\ \hat{e}_c \end{bmatrix}, A = \begin{bmatrix} -\frac{3R_s}{3L} & -\frac{2}{3L} & 0 & 0 & 0 & 0 \\ 0 & 0 & 0 & 0 & 0 & 0 \\ 0 & 0 & -\frac{3R_s}{3L} & -\frac{2}{3L} & 0 & 0 \\ 0 & 0 & 0 & 0 & 0 & 0 \\ 0 & 0 & 0 & 0 & -\frac{3R_s}{3L} & -\frac{2}{3L} \\ 0 & 0 & 0 & 0 & 0 & 0 \end{bmatrix}, u = \begin{bmatrix} u_{ab} - u_{bc} \\ u_{bc} - u_{ab} \\ u_{ca} - u_{ab} \end{bmatrix},$$

$$Error_i = \begin{bmatrix} erro_{ia} \\ erro_{ib} \\ erro_{ic} \end{bmatrix} = \begin{bmatrix} \hat{i}_a - i_a \\ \hat{i}_b - i_b \\ \hat{i}_c - i_c \end{bmatrix} B = \begin{bmatrix} 1/3L & 0 & 0 \\ 0 & 0 & 0 \\ 0 & 1/3L & 0 \\ 0 & 0 & 0 \\ 0 & 0 & 1/3L \\ 0 & 0 & 0 \end{bmatrix}, K = \begin{bmatrix} k_1 & 0 & 0 \\ k_2 & 0 & 0 \\ 0 & k_3 & 0 \\ 0 & k_4 & 0 \\ 0 & 0 & k_5 \\ 0 & 0 & k_6 \end{bmatrix}$$

4 Commutation Point Detection at High Speed

The back-EMF functions of BLDC motor could be obtained according to its back-EMF’s waveform shown in figure 2, and the e_{sum} expression of a whole period could be obtained from adding all the EMF values of each phase. EMF and e_{sum} values are shown in table 1.

Table 1. The back-EMF and E_{sum} function of BLDC motor

θ_r	e_a	e_b	e_c	e_{sum}
$0-30^0$	$(6E/\pi)\theta_r$	$-E$	E	$(6E/\pi)\theta_r$
30^0-90^0	E	$-E$	$-(6E/\pi)\theta_r + 2E$	$-(6E/\pi)\theta_r + 2E$
90^0-120^0	E	$(6E/\pi)\theta_r - 4E$	$-E$	$(6E/\pi)\theta_r - 4E$
120^0-150^0	E	$(6E/\pi)\theta_r - 4E$	$-E$	
150^0-210^0	$-(6E/\pi)\theta_r + 6E$	E	$-E$	
210^0-270^0	$-E$	E	$(6E/\pi)\theta_r - 8E$	
270^0-330^0	$-E$	$-(6E/\pi)\theta_r + 10E$	E	
330^0-360^0	$(6E/\pi)\theta_r - 12E$	$-E$	E	

The waveform of e_{sum} is shown in figure 2, which shows that the period of e_{sum} is one third of that of phase back-EMF. There are six zero-crossing points in each three periods, and they are in accordance with six zero-crossing points of three-phase back-EMF in one period. In addition, the extreme point of e_{sum} is the commutation point of BLDC motor.

At high speed, the commutation point could be determined through detection of the zero-crossing point of e_{sum} , the extreme point of e_{sum} , and the periodicity of e_{sum} . The interrupt service routing used for determining commutation points is shown in figure 3. But at low speed, the amplitude of e_{sum} is small and it is easy to cause unexpected commutation, since the amplitude of back-EMF is small.

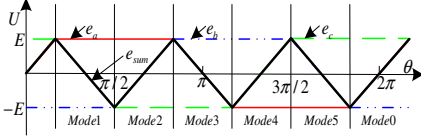


Fig. 2. Waveform of e_{sum}

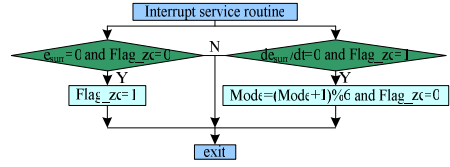


Fig. 3. Interrupt service routine of commutation detection at high speed

5 Commutation Point Detection at Low Speed

In order to solve the low-speed commutation problem of the BLDC motor, this paper proposes a kind of commutation function for determining the commutation point and realizing the low-speed control of the BLDC motor. Since the detection value of back-EMF from observer is small at low speed, the ratio between back-EMF and e_{sum} is used for determining the commutation point.

The commutation functions are:

$$ZC(\theta)_1 = \hat{e}_a / \hat{e}_{sum} \quad (7)$$

$$ZC(\theta)_2 = \hat{e}_b / \hat{e}_{sum} \quad (8)$$

The working principle of the commutation function is shown in figure 4. In figure 4(a), ZC_1 is bigger than 1 between 0 and $\pi/3$, and its absolute value increases gradually. The absolute value of ZC_1 increases rapidly towards infinity when e_{sum} approaches zero. After just entering $\pi/3 \sim 2\pi/3$, ZC_1 turns from positive infinity to negative infinity immediately, and this moment corresponds to the commutation moment of ZC_{MODE2} . The absolute value of ZC_1 decreases quickly with the increasing of the rotation angle, and its value is lower than -1 during this section. The absolute value of ZC_1 increases rapidly towards negative infinity when approaches to $2\pi/3$. Just after entering $2\pi/3 \sim 4\pi/3$ section, ZC_1 turns from negative infinity to positive infinity because \hat{e}_{sum} changes from negative to positive, and this changing moment corresponds to the commutation moment of ZC_{MODE3} . In this section, \hat{e}_a equals to \hat{e}_{sum} , and $ZC_1 \geq 1$. When the rotating angel approaches to $4\pi/3$, ZC_1 immediately increases to positive infinity. Just after entering $4\pi/3 \sim 5\pi/3$ section, ZC_1 turns from positive infinity to negative infinity because \hat{e}_{sum} changes from negative to positive, and this changing moment corresponds to the commutation moment of ZC_{MODE5} . With the increasing of rotation angle, the absolute value of ZC_1 decreases immediately, and $ZC_1 \leq -1$ during this section. When the rotating angel approaches to $5\pi/3$, the absolute value of ZC_1 increases immediately. Just after entering $5\pi/3 \sim 2\pi$ section, ZC_1 turns from negative infinity to positive infinity because \hat{e}_{sum} changes from positive to negative, and the changing moment corresponds to the commutation moment of ZC_{MODE0} . Similarly, ZC_{MODE1} and ZC_{MODE4} could be acquired from ZC_2 (as shown in figure 4(b)). Because the range of the data processed by the microprocessor is limited and it could not reach to infinity, the commutation points could be detected through setting proper threshold voltage values.

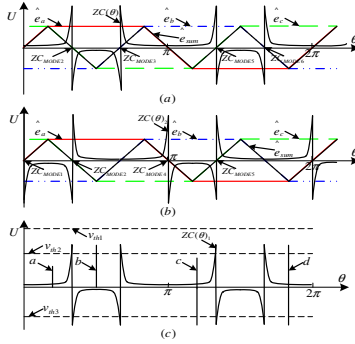


Fig. 4. Working principle of zero-crossing point function

Figure 4(c) shows the ZC_1 function curve with interference noise. Because the amplitude of the noise a is smaller than the threshold voltage v_{th2} , it could be filtered through setting the threshold voltage. The amplitude of the noise b exceeds v_{th2} , but it does not turn from negative value to positive value immediately, so it could be filtered. The negative maximum value of noise c exceeds v_{th3} , but the positive maximum value of it does not, so it could also be filtered. The negative maximum value of the noise d exceeds v_{th3} and the positive maximum it exceeds v_{th2} , so the noise d is regarded as a commutation point. This phenomenon could be filtered through adjusting the threshold voltage value according to work environment, such as increasing v_{th2} to v_{th1} , or through filtering the noise signal between two commutation points according to the rotor position.

The interrupt service routine for commutation detection at low speed is shown in figure 5. The commutation point could be determined through detection of zero-crossing point and the extreme point of e_{sum} , but not the traditional commutation method of delaying 30° .

6 The Calculation of Speed and Position

At high speed, the rotor speed and rotor position could be determined through detecting e_{sum} , as shown in table 1. At low speed, because the amplitude of e_{sum} is small, the computation deviation of this method is large. The position and speed could be calculated through detection of zero-crossing point, extreme point of e_{sum} and the angular displacement of $6/\pi$ between them (as shown in figure 6).

$$\omega_{r,k-1} = \frac{6/\pi}{t_{k-1} - t_{k-2}}; \omega_{r,k} = \frac{6/\pi}{t_k - t_{k-1}} \tag{9}$$

$$\Delta\theta = \frac{\Delta t}{t_{k-1} - t_{k-2}} \times \frac{\pi}{6} \tag{10}$$

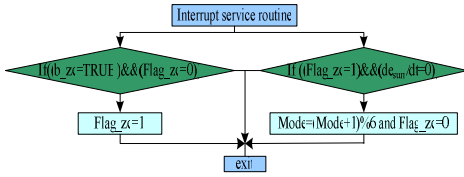


Fig. 5. Interrupt service routine for commutation

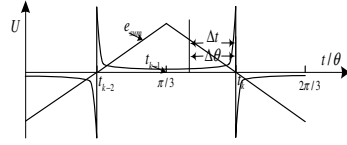


Fig. 6. Calculation method of speed and position at low speed

The calculation equations for mechanical angular velocity、 speed and torque are:

$$\hat{\Omega} = \frac{2}{P_n} \hat{\omega}_r \quad ; \quad \hat{n} = \frac{60}{2\pi} \hat{\Omega} \tag{11}$$

$$\hat{T}_e = (\hat{e}_a i_a + \hat{e}_b i_b + \hat{e}_c i_c) / \hat{\Omega} \tag{12}$$

Where, $\hat{\Omega}$ is the estimated mechanical angular velocity; \hat{n} is the estimated speed ; \hat{T}_e is the estimated electromagnetic torque ; $\hat{\omega}_r$ is the estimated electrical angular velocity ; P_n is the pole pair number.

7 Experimental Results

The system experimental platform using dsPIC6010A as CPU is established based on the above-mentioned method, and the system working principle is shown in figure 7. Motor parameters are shown in table 2, and the experimental results are shown in figure 8-11, in where the speed estimation, speed error, position estimation, output torque estimation and the estimated waveforms for \hat{e}_a and \hat{e}_{sum} under the given load torque of 5Nm and given speed of 1500rpm. The experimental results show that the speed-sensorless control method proposed in this paper is feasible.

Table 2. Parameter table of BLDC motor

rated voltage	V	310V
rated torque	T_e	15Nm
rated speed	n	1000
stator resistance	R_s	1.5Ω
stator inductance	L	5.22mH
moment of inertia	J	$0.08\text{kg}\cdot\text{m}^2$
back-EMF constant	K_e	0.175
number of pole pairs	P_n	2

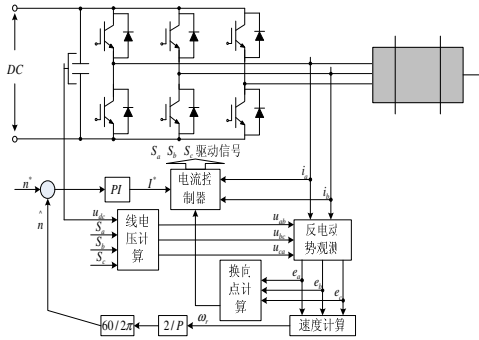


Fig. 7. The block diagram of control system

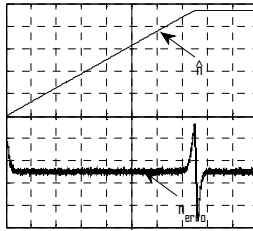


Fig. 8. Waveforms of speed estimation and speed error (n^* : 160rpm/div; n_{erro} : 2rpm/div; t : 100ms/div;)

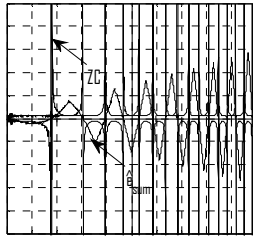


Fig. 9. Waveforms of \hat{e}_{sum} and $ZC(\hat{e}_{\text{sum}})$ (\hat{e}_{sum} : 10v/div; ZC : 20ms/div; t : 1V/div)

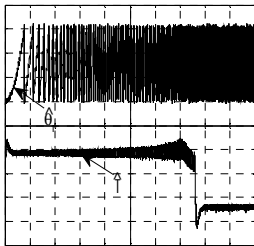


Fig. 10. Position estimation waveform and torque estimation waveform (T : 8Nm/div; θ : 2rad/div; t : 100ms/div;)

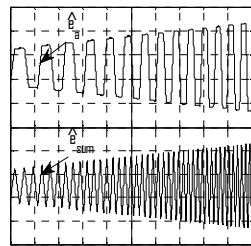


Fig. 11. Estimation waveforms of \hat{e}_a and \hat{e}_{sum} (20V/div; 60ms/div;)

8 Conclusion

This paper proposes a novel control method for BLDCM in full speed range without using position sensor, and it discusses the observation method for phase back-EMF. The experimental results show that this algorithm could effectively estimate the phase back-EMF and carries out the commutation precisely. The advantages of this algorithm are: The unnecessary external detection circuits could be omitted through using this algorithm; Precise commutation could be carried out both in steady state and transient state through using this algorithm; The motor speed could be precisely controlled and the full range precise speed control could be realized through using this algorithm; The position tracking and torque control of the BLDC motor could be carried out through using this algorithm, and the algorithm is simple.

References

1. An, Q., Sun, L., Liu, C., et al.: Flux Linkage Self-control Based Direct Torque Control of Brushless DC Motor. *Proceedings of the CSEE* 25(12), 86–92 (2010)
2. Ogasawara, S., Akagi, H.: An Approach to Position Sensorless Drive for Brushless dc Motors. *IEEE Trans. on Industry Applications* 27(5), 928–933 (1991)
3. Li, X., Zhu, Z., Zhao, H.: A position sensorless motion control system of Brushless DC Motor motor based on sliding mode observer. *Journal of Circuits and Systems* 14(2), 79–83 (2009)
4. Yang, G., Li, X.-F.: Research on the Detection of BLDCM Rotor Position by Checking Zero-crossing of Back-EMF. *Power Electronics* 4(10), 18–20 (2008)
5. Kim, T.-S., et al.: A New Approach to Sensorless Control Method for Brushless DC Motors. *International Journal of Control, Automation, and Systems* 6(4), 477–487 (2008)

Design of Wireless Monitoring System Based on CAN Bus and ZigBee Technology of Tower Crane

Xijian Zheng, Hong Zhang, and Zhengyi Xie

School of transportation & Mechanical Engineering, ShenyangJianzhu University, Shenyang,
Liaoning Province, P.R. China, 110168
xijianzheng@sina.com, yiren630@163.com,
xiezhengyi2000@163.com

Abstract. A design of wireless monitoring system based on CAN bus and ZigBee technology of tower crane has been proposed according to characteristics of the traditional safety monitoring system of tower crane and defects of cable transmission system in this paper. The application of CAN bus and ZigBee technology meets requirements of function and performance and also accomplishes the modular design of software/hardware system in wireless monitoring system of tower crane. It provides a new method to design the wireless monitoring system of tower crane.

Keywords: tower crane, CAN bus, ZigBee, wireless monitoring.

1 Introduction

With the continuous development of modern construction industry, tower cranes have obtained large-scale applications in the engineering construction. However, due to its structural defects, poor working conditions, illegal operations and other incentives, tower crane accidents occur from time to time[1]. Degree of information integration is low in traditional safety monitoring system of tower crane, where hoisting torque and weight is mainly used as monitoring parameters[2]. Because there is the state of motion for some monitoring objects in the process of tower crane operations, it increases the wiring difficulties of the cable transmission system in the construction site. What's more, electrical equipments in the actual environment can produce the electromagnetic noise, which interferes the cable transmission signal and affects the stability of data transmission system of tower crane[3]. At present, the major disadvantages of the traditional safety monitoring system of tower crane are as follows: a)poor real time of data transmission; b)poor anti-electromagnetic interference; c)non-standardized of data communication protocol; d)poor structural flexibility of the system. In order to prevent serious tower crane accidents and ensure safe and reliable operation of tower crane, and reduce accident casualties and economic losses, it becomes very imperative to research and develop a high reliability, good real time, powerful function and low cost of safety monitoring system of tower crane, which has a certain theoretical and practical value.

Controller Area Network (CAN) bus, which belongs to the scope of fieldbus, is an effective support for distributed control and real-time control of serial communication network[4]. In order to settle large amounts of data exchanges in automotive control

system, CAN bus was developed by Bosch company in the early 1980s. Then as it has the advantages of high communication rate, low error rate, good real time and high reliability, powerful error correction ability, independent design and so on, CAN bus is increasingly used in the communication and control field of engineering machinery. Setting up a wireless network of wireless monitoring system of tower crane has been currently a hot research at home and abroad. At present, commonly used wireless technology includes Bluetooth, Wi-Fi, ZigBee, GPRS, etc., but ZigBee technology applied in wireless monitoring system of the tower crane has received extensive attention for its advantages of low power consumption, easy networking, low cost, low complexity and so on[5] [6]. In this paper, it researchs application of CAN bus and ZigBee technology in wireless monitoring system of tower crane and designs a new wireless monitoring system based on CAN bus and ZigBee technology, which contributes to improve the monitoring and fault diagnosis technology of tower crane in China. It also is of great significance to improve the productivity and optimize the allocation of resources of tower cranes and other engineering machinery in China.

2 General Design of the System

Wireless monitoring system based on CAN bus and ZigBee technology of tower crane is a study of embedded system applied to tower crane. The system could complete real-time acquisition and transmission of working parameters of tower crane through the CAN bus and ZigBee technology. And it could wirelessly transmit the acquired datas to the monitoring center by Zigbee technology, which enhances real-time datas transmission. PC of monitoring center could store and analyse the received datas. Furthermore, control commands sended out by the PC could feed back to the master controller installed in the cab of tower crane, which could realize real-time LCD display, record, alarm, controlling and so on. The system adopts a hierarchical design, consisting of three parts of the hardware layer, the software layer and the application layer. Hierarchy schematic diagram of the system is shown in Fig. 1.

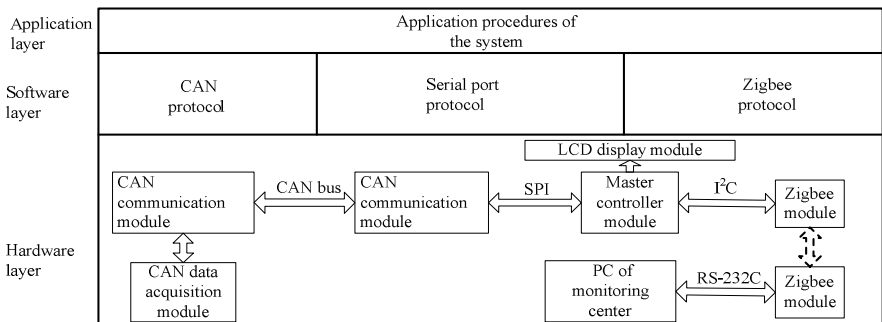


Fig. 1. Hierarchy schematic diagram of the system

Hardware layer mainly describes hardware implementation of data acquisition and wireless transmission. Software layer, including the CAN protocol, serial port protocol and Zigbee protocol, ensures the real-time data transmission among the various

protocols and provides some API functions to be transferred by application layer procedures. In addition, CAN protocol and Zigbee protocol enable data transmission of the system to tend to the standardization, which overcomes data transmission defects of non-standardization of the traditional safety monitoring system of tower crane. Application layer, running user-written application procedures, could achieve coordinated operation of the whole system.

3 Hardware Design of the System

Hardware design of the system adopts the modular design concept. The design elements mainly include master controller module, CAN data acquisition module, CAN communication module, ZigBee wireless communication module and LCD display module and so on. Hardware structure block diagram of the system is shown in Fig. 2.

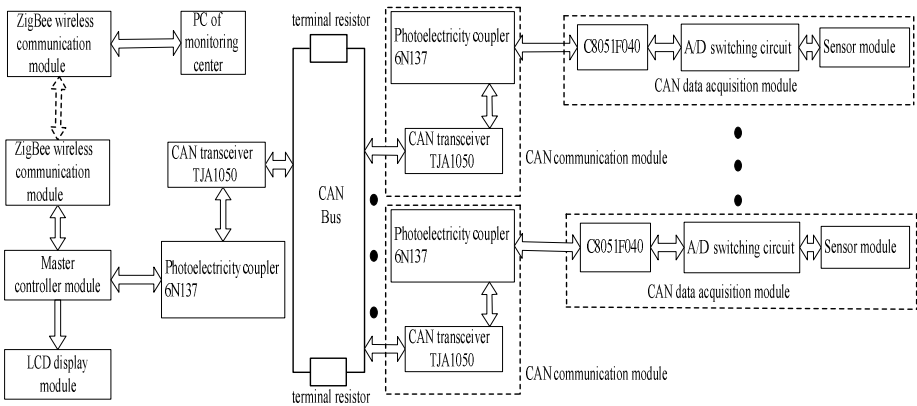


Fig. 2. Hardware structure block diagram of the system

CAN data acquisition module mainly consists of sensor module, the A/D switching circuit and the microcontroller C8051F040 which has the function of data acquisition and controlling. CAN communication module mainly is composed of photoelectricity coupler 6N137 and CAN transceiver TJA1050. Interconnection among data acquisition nodes through the STP(shielded twisted-pair) constitute the CAN bus network. 120Ω of impedance matching resistor connected at both ends of the bus is the terminal resistor, which could improve the system's stability and enhance the anti-jamming ability of the system[6]. The system could acquire operating status parameters, fault information and location parameters of the tower crane, which relies on a variety of sensor modules and the microcontroller C8051F040 installed in the tower crane. Compared with the traditional safety monitoring system of tower crane, the system could monitor a variety of parameters range from single hoisting torque and weight to hoisting height and speed, luffing position and speed, rotating angle and speed, and even wind speed and temperature of the hoisting motor. Therefore, it could improve the information integration rate of hardware system.

The modular design of hardware system could overcome the defects of poor structural flexibility of traditional safety monitoring system, and realize plug and play for system modules.

3.1 Master Controller Module

Master controller module takes MCU(Microcontroller Unit) AT90CAN128 of AVR series as a core, which could realize real-time monitoring , record and alarm for the operation statuses of tower crane. The AT90CAN128 is a low-power CMOS 8-bit microcontroller based on the AVR enhanced RISC architecture, which combines rich On-chip resources, a fast single cycle instruction system and In-System self-programmable flash. Moreover, it provides a internal integrated CAN controller which may substitute for traditional CAN controller SJA1000 and could be completely compatible with the CAN standard frame 2. 0A and expansion frame 2. 0B[7]. Therefore, it could greatly simplify the design of the hardware circuit and enhance the reliability of the system. It also could drive the high-speed CAN transceiver TJA1050 to acquire CAN bus datas. Photoelectricity coupler 6N137 used between the master controller module and CAN transceiver TJA1050 can greatly achieve electrical isolation between the bus nodes. But we must note that VCC and VI (+5 V) both sides of the 6N137 must be isolated from each other. In order to achieve electrical isolation between the CAN bus nodes and enhance the anti-electromagnetic interference of the CAN bus, DC / DC power module B0505LS-1W is used in the system.

3.2 CAN Data Acquisition Module

The analog signals gathered by the sensor module could be transformed into the digital signals through the A/D switching circuit and the digital signals would be sented to the microcontroller C8051F040. Thus it would complete data acquisition of the main operation parameters of tower crane by CAN data acquisition module. The C8051F040 provides a internal CAN controller which could be completely compatible with the CAN standard frame 2. 0A and expansion frame 2. 0B. It mainly consists of the CAN core, Message RAM which is independent of the RAM of CIP-51, the message handler unit and the registers[8]. Structure block diagram of the internal CAN controller of C8051F040 is shown in Fig. 3.

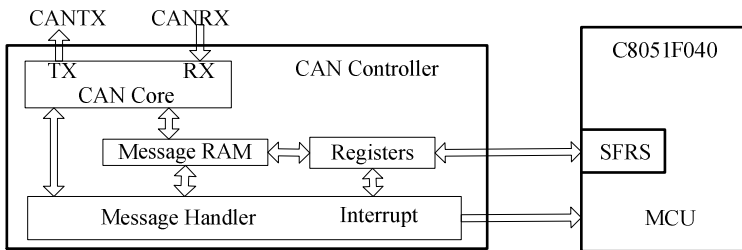


Fig. 3. Structure block diagram of the internal CAN controller of C8051F040

In Fig. 3, CAN core consists of CAN protocol controller and serial / parallel switching RX / TX shift registers which is responsible for sending and receiving messages. Message RAM could be used to store message targets and arbitration masks of each target. The kind of CAN processors have 32 message targets which can randomly be configured to send and receive and each message target has its own recognition mask. All of the data transmission and filtering receiving would be completed by the CAN controller rather than by the CIP – 51. The CAN internal registers store all of the controlling and configuration information of the CAN controller. Usually CAN core cannot directly access to Message RAM, but can access to it through interface register IF1 or IF2.

3.3 ZigBee Wireless Communication Module

ZigBee wireless communication module taking the CC2480 chip as the core connects with the master controller module through the SPI interface. It could wirelessly transmit datas of the CAN bus, which may be transmitted by the controller module, to the monitoring center by ZigBee wireless network and receive the feedback information. The CC2480 is a cost-effective, low-power Z-Accel series of ZigBee processor that provides full ZigBee functionality with a minimal development effort. Fully integrated IEEE802.15.4-compatible DSSS RF transceiver is the core of internal wireless technology of the CC2480. Moreover, the module does not need any external filter[9].

4 Software Design of the System

The software design also adopts the modular design concept. The design elements mainly include initialization procedure, data acquisition procedures, CAN bus communication procedures, ZigBee wireless communication procedures, master controller procedures, the A/D switching program, LCD display procedure, the automatic protection procedures of the system, clock procedure and so on. The following describes the initialization of the master controller and CC2480 and the software designs of CAN bus communication module and the master controller.

4.1 Master Controller Initialization

Master controller initialization includes the initialization of the watchdog circuit, the system clock, I/O interface, SPI, UART and CAN controller. The initialization of CAN controller includes resetting the CAN controller, prohibiting the CAN interrupt, the identifier initialization of the Mob, the initialization of mask registers, CAN baud rate and timer, enabling CAN and so on. Master controller initialization programm is shown as follows.

```

void    MCU_Init (void)
{
    Watchdog_Init(); // Watchdog initialization
    Clk_Init();      // clock initialization of the system
    Io_Init();       // the I/O interface initialization
    Uart_Init();     // UART initialization
    Spi_Init();      // SPI initialization
    Can_Init();      // CAN controller initialization
}

```

4.2 CC2480 Initialization

In the ZigBee wireless communication, CC2480 deals with all the ZigBee protocols, and the master controller AT90CAN128 deals with application procedures of the system. The software interface of the CC2480 consists of SYS interface, configuration interface, simple API interface, AF interface and ZDO interface. The CC2480 could not work well until the first three interfaces are correctly configured. The software configuration of the CC2480 can be divided into three steps:

- (1) CC2480 power-on → reset the CC2480 → send a SYS_RESET_IND to the master controller;
- (2) configure device type → reset the CC248 again → send the SYS_RESET_IND → configure other parameters → set ZCD_NV_STARTUP_OPTION to 0x02;
- (3) register application procedures → start to run Zigbee protocol stack.

After the ZigBee agreement stack is successfully run, the module could be integrated into the ZigBee network and work well.

4.3 The Software Designs of CAN Bus Communication Module and the Master Controller

The CAN bus communication procedures are composed of the system initialization procedure and the CAN bus sending and receiving procedures. In the beginning, C8051F040 initialize its own system and the CAN bus. Then it transmits data in the CAN inquiry way, and the master controller AT90CAN128 can send and receive the information which comes from the CAN bus by the interrupt, which may enhance real-time communication of the system. The flow charts of software design of CAN bus communication module and the master controller are respectively shown in Fig. 4 and Fig. 5.

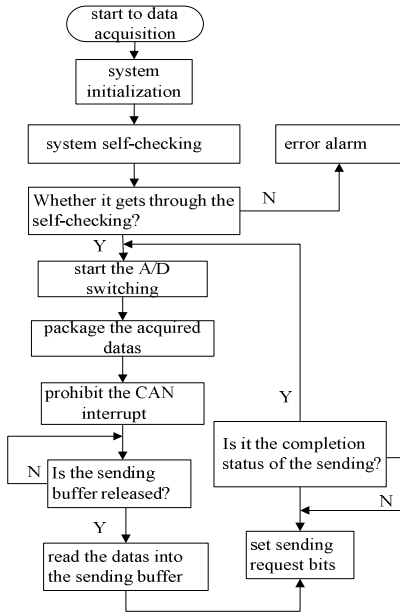


Fig. 4. The flow chart of the CAN bus

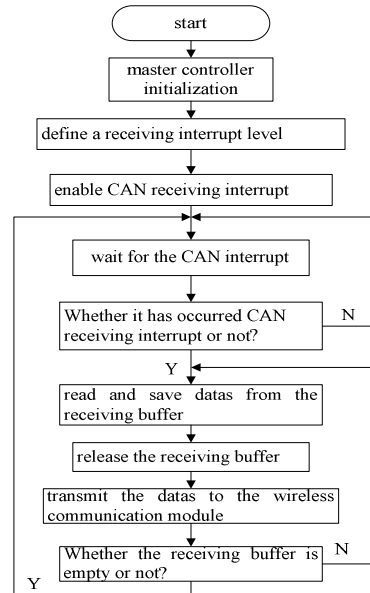


Fig. 5. The flow chart of the master controller procedures

5 Conclusions

It researchs the application of CAN Bus and ZigBee technology in wireless monitoring system of tower crane and designs a wireless monitoring system based on CAN bus and ZigBee technology in the paper. It also completes the software/hardware design of the system. Compared with the traditional safety monitoring system of tower crane, the system has standardized the data transmission system and enhanced information integration rate of the system. The innovation spot of this article lies in the modular design of the software/hardware system, which facilitates program modification and system upgrades so that the system has a high degree of flexibility and broad applicability. In the long run, this system has a certain economy and cost savings and also has a good application prospect.

Acknowledgements. Natural Science Funds of Liaoning Province, 20102184.

References

1. Yu, Q.-B., Yang, H.-L.: General Accident Analysis and Its Prevention for Tower Crane. *Construction Machinery* (02), 53–54 (2003)
2. Wu, L.-P.: Analysis of Properties of Safety Devices for Tower Crane. *Shanxi Machinery* (06), 39–40, 46 (2003)

3. Xie, Z.-J., Hu, Y.-P., Zhu, M.-X., Yao, P.: Development of Technology of DSP Based Mechanical Vibration Data Real-time Ethernet Transmission. *Journal of Chongqing University (Natural Science Edition)* (02), 6–8 (2006)
4. Wu, K.-M.: CAN bus principle and design of application system. Press of Beijing University of Aeronautics and Astronautics, Beijing (1996)
5. Gong, K.: Wireless Sensor Network and Network Information Processing Technology—2006 Communication Theory and Signal Processing Conference Proceedings. Press of Electronics Industry, Beijing (2006)
6. Chen, H.-C.: The design of telemetering and command system based on CAN bus and ZigBee technology. *Microcomputer & Its Applications* (01), 47–50 (2010)
7. AT90CAN128 Data Sheet. Atmel Corporation, (02) (2008)
8. Hu, H.-C.: The Principles and System Design of Single-chip Microcomputer. Tsinghua University Press, Beijing (2002)
9. CC2480 Data Sheet SWRS074A. Texas Instruments, (11) (2008)

A Security Risk Model Using Game Theory

Marn-Ling Shing¹ and Chen-Chi Shing²

¹Early Child Education Department and Institute of Child Development,
Taipei Municipal University of Education, 1 Ai-Kuo West Road, Taipei, Taiwan, R.O.C.
shing@tmue.edu.tw

²Information Technology Department, Radford University, Box 6933, Radford, VA 24142
cshing@radford.edu

Abstract. This paper uses game theory to model the strategies against the threats based on the cost. If the frequencies of threats occurrence are known, the optimal pure strategy can be found by expected effectiveness. However, if those frequencies are unknown, the optimal strategy is a mixed strategy provided by game theory. The problem can also be solved by linear programming method.

Keywords: game theory, risk assessment, risk management, information security model, risk model.

1 Introduction

Information security includes confidentiality, integrity and availability. There are threats designed for denial of service such as using SYN probe [3]. There also have threats such as virus or worm attacks and break-in may damage computer's data integrity. In addition, threats such as spyware can expose the privacy [2]. Traditional defense mechanism includes firewalls, intrusion detection system (IDS), and anti-virus programs. Some of these defense strategies are designed only for specific threats but not for other threats. For example, anti-virus programs are necessary for defense against virus or worm attacks. But they are not very effective when they are used to prevent break-in.

In the next section, we will describe how to use game theory to find an optimal defense strategy against those threats together. The games that discussed in the paper are restricted to the combinatorial games only. A combinatorial game is a two-player, finite, deterministic, zero-sum game with perfect information known to both players. [1]. A zero-sum game means that the total pay-off at the end of the game for both players is zero.

2 Game Theory Model

In this section we will find the optimal strategy under the cases that either prior or no prior information about how often the threats are occurred. Assume that the entries in the game matrix represent the probabilities of effectiveness of using three strategies (rows 1, 2, 3) of the player X against five threats (columns A, B, C, D, E) of the

player Y. For example, player X can be an enterprise where strategy 1, 2, and 3 can be one of the security defense mechanisms of firewalls, IDS, and anti-virus programs. Likewise, player Y can be a hacker who breaks into the enterprise computer system by SYN/ACK attacks, ICMP teardrop attacks, virus/worm attacks, password-guessing and spyware(A, B, C, D of E). The game matrix used in the section is in Table 1 below:

Table 1. Game Matrix

	A	B	C	D	E
1	.2	.5	.3	.4	0
2	0.8	0	0	0	0
3	1	.4	0	0	1

2.1 No Prior Information about Threats Occurrence

Because the maxmin of the game matrix is the maximum of those minimum in each row, it is 0 for the game in Table I. On the other hand, the minmax of the game matrix is the entry that is the minimum of those maximum in each column, it is 0.3 for the game in Table I. For any game matrix, there exists a saddle point if and only if maxmin = minmax. Since maxmin (=0) is not equal to minmax (=0.3), there is no saddle point in Table I. The equilibrium pair (row, column) of the pure strategy of the game in Table I is the saddle point which is the entry that is the minimum in its row and the maximum in the column [1]. Therefore, there is no equilibrium pair or the optimal pure strategy for the game matrix.

Even though there is no optimal pure strategy for the game matrix, according to Von Neumann’s theorem, every game matrix has at least one equilibrium pair of mixed strategies. Because each entry of the column C is less than or equal to the entry in the same row of the column B or D, that is, column C dominates column B and D. Hence both column B and D can be eliminated from the game matrix without changing the equilibrium pair for the game matrix in Table I. Similarly column E dominates column A and column A can be eliminated from the game matrix too. The resulting game matrix is

$$\begin{pmatrix} .3 & 0 \\ 0 & 0 \\ 0 & 1 \end{pmatrix}$$

On the other hand, each entry of the row1 in the matrix above is greater than or equal to the entry in the same column of the row 2, that is, row1 dominates row2. Hence row 2 can be eliminated from the above resulting game matrix without changing the equilibrium pair. And the final game matrix is in Table 2 below.

$$\begin{pmatrix} 0.3 & 0 \\ 0 & 1 \end{pmatrix}$$

Table 2. FinalGameMatrix

III	C	E
Row1	.3	0
Row3	0	1

According to Mendelson [1], if X is a mixed strategy for the row and Y is a mixed strategy for the column, there is an equilibrium pair (X*, Y*) for the game matrix

$$\begin{pmatrix} a & b \\ c & d \end{pmatrix},$$

where X*=(S,1-S) and Y*=(T, 1-T) and

$$S = (d - c) / R, T = (d - b) / R, R = a - b - c + d. \tag{1}$$

It is straightforward that a=0.4, b=c=0 and d=1. And R=1.3, S=1/1.3=10/13, T=1/1.3=10/13. And X*=Y*=(10/13, 3/13).Therefore, based on Table 2, the optimal strategy against those five threats is to use strategy 1 10/13 times and strategy 3 3/13 times.

2.2 Known Prior Threats Occurrence Frequency

Assume the frequency of occurrence of those five threats is (.1, .3, .3, .1, .2)respectively. The effectiveness for the pure strategy 1 is .3*.1+.6*.3+.4*.3+.5+.1+0*.2=0.38. Similarly, the effectiveness for the pure strategy 2 is .1 and that for the pure strategy 3 is .1+.15+.2=.45. Therefore, the optimal pure strategy for the game is strategy 3.

The pay-off function discussed in this section is the probability of the effectiveness. In practice in order to calculate the risk of the strategy used by each player, the function should include the expected gain. In the next section the payoff can be either zero-sum or non-zero-sum.

3 Security Risk

In this section, forsimplicity, a game consists of a player X having strategies 1, 2 and 3 and player Y having strategies A, B and C.The game matrix the pay-off function is assumed to be the expected gain. The expected gain can include the total investment cost, the profit gained by the player X’s strategy and the loss created by player Y’s strategy. For example, if player X uses strategy 1, one must invest \$8K cost. However, one gains profit \$40K. The player Y uses strategy A causes player X to lose \$2K. The expected gain for player X using strategy 1 and player Y using strategy A is \$40K-8K-2K=30K.The game matrix used in the section is assumed to be given in Table 3(using unit 10K) below:

Table 3. GameMatrix

	A	B	C
1	3	4	2
2	1	5	3
3	2	1	2

3.1 Zero-Sum Payoff

Assuming that the gain for payer X is the loss for player Y, there is no saddle point in Table 3. Therefore, there is no equilibrium pair or the optimal pure strategy for the game matrix. However, according to Von Neumann’s theorem, every game matrix has at least one equilibrium pair of mixed strategies. If player X uses a mixed strategy $X=(x_1,x_2,x_3)$, where $x_i \geq 0, i=1,2,3$,

$$x_1+x_2+x_3=1. \tag{2}$$

And player Y uses a mixed strategy $Y=(y_1,y_2,y_3)$, where $y_j \geq 0, j=1,2,3$,

$$y_1+y_2+y_3=1. \tag{3}$$

For the mixed strategy X. the payoff $P(X, B_j)$ and for any strategy B_j for player Y, where $y_j > 0, P(X,B_j)=v, v$ is the optimal payoff value. Therefore, $3x_1+x_2+2x_3=v, 4x_1+5x_2+x_3=v, 2x_1+3x_2+2x_3=v$. Using (2), $x_1=2/9, x_2=1/9, x_3=2/3$. Similarly, for the mixed strategy Y. the payoff $P(A_i, Y)$ and for any strategy A_i for player X, where $x_i > 0, P(A_i, Y) =v, v$ is the optimal payoff value. Therefore, $3y_1+4y_2+ 2y_3=v, y_1+ 5y_2+3y_3=v, 2y_1+ y_2+ 2y_3=v$. These give $y_1+ 3y_2 = 0$, hence $y_j=0, j=1,2,3$. This contradicts (3), which means that one of $x_i=0, i=1,2,3$.

3.1.1 Case 1. $x_1=0$

The game matrix in Table 2 reduces to

$$\begin{pmatrix} 1 & 5 & 3 \\ 2 & 1 & 2 \end{pmatrix}$$

Because column 1 dominates column 3, the matrix reduces to

$$\begin{pmatrix} 1 & 5 \\ 2 & 1 \end{pmatrix}$$

By (EQ 2.1), $X=(0, 1/5, 4/5)$ and $Y=(4/5,1/5,0)$. The $\text{minmax}=\min\{1/5+8/5, 5/5+4/5, 3/5+8/5\}=9/5$, the $\text{maxmin}=\max\{12/5+4/5, 4/5+5/5, 8/5+1/5\}=16/5$. Since $\text{minmax} \neq \text{maxmin}$, there is no equilibrium point. That is, $x_1 \neq 0$.

3.1.2 Case 2. $x_2=0$

The game matrix in Table 2 reduces to

$$\begin{pmatrix} 3 & 4 & 2 \\ 2 & 1 & 2 \end{pmatrix}$$

Because column 3 dominates column 1, the matrix reduces to

$$\begin{pmatrix} 4 & 2 \\ 1 & 2 \end{pmatrix}$$

By (1), $X=(1/3, 0, 2/3)$ and $Y=(0, 0, 1)$. The $\text{minmax}=\min\{3/3+4/3, 4/3+2/3, 2/3+4/3\}=2$, the $\text{maxmin}=\max\{2, 3, 2\}=3$. Since $\text{minmax} \neq \text{maxmin}$, there is no equilibrium point. That is, $x_2 \neq 0$.

3.1.3 Case 3. $x_3=0$

The game matrix in Table 2 reduces to

$$\begin{pmatrix} 3 & 4 & 2 \\ 1 & 5 & 3 \end{pmatrix}$$

Because column 3 dominates column 2, the matrix reduces to

$$\begin{pmatrix} 3 & 2 \\ 1 & 3 \end{pmatrix}$$

By (1), $X=(2/3, 1/3, 0)$ and $Y=(1/3, 0, 2/3)$. The $\text{minmax}=\min\{6/3+1/3, 8/3+5/3, 4/3+3/3\}=7/3$, the $\text{maxmin}=\max\{3/3+4/3, 1/3+6/3, 2/3+4/3\}=7/3$. Since $\text{minmax}=\text{maxmin}$, and hence (X,Y) is an equilibrium point. Therefore, the optimal strategy for player X against those threestrategies is to use strategy 1 $2/3$ times and strategy 2 $1/3$ times. And the optimal strategy for player Y is to use strategy A $1/3$ times and strategy C $2/3$ times.

3.2 Non-Zero-Sum Payoff

In general for a two person player game, player X (such as a business) does not have the same play off as that of player Y (such as a hacker). This is an example of a non-zero-sum game. According to Thomas [4], any two-person game with a finite number of pure strategies has at least one Nash equilibrium pair. In general, any k-person game has a mixed Nash equilibrium k-tuple. A k-tuple strategy (S_1, S_2, \dots, S_k) for player (P_1, P_2, \dots, P_k) is a Nash equilibrium if the expected payoff for player P_i ($i=1,2, \dots, k$)with respect to strategy (S_1, S_2, \dots, S_k) is at least as great as that when S_i is replaced by other pure strategy for player P_i . For example, the entry (x,y) of the game matrix used in the section, where x is the payoff for player X and y is the payoff for player Y, is assumed to be given in Table 4 (using unit 10K) below:

Table 4. GameMatrix

	A	B	C
1	(5,1)	(2,2)	(1,3)
2	(-1,2)	(3,1)	(2,1)
3	(0,3)	(1,3)	(2,2)

If player X uses a mixed strategy $X=(x_1, x_2, 1-x_1-x_2)$, where $x_i \geq 0, i=1,2$. And player Y uses a mixed strategy $Y=(y_1, y_2, 1-y_1-y_2)$, where $y_j \geq 0, j=1,2$. Let P_X and P_Y be the payoff functions for player X and Y. Then

$$P_X = x_1 (5y_1+2y_2+1-y_1-y_2) + x_2 (-y_1 + 3 y_2+2(1-y_1-y_2)) + (1-x_1-x_2) (y_2+2(1-y_1-y_2))$$

$$= x_1 (6y_1 + 2y_2 - 1) + x_2 (-y_1 + 2 y_2) + 2 - 2y_1 - y_2$$

$$P_Y = x_1 (y_1 + 2y_2 + 3(1-y_1-y_2)) + x_2 (2y_1 + y_2 + 1 - y_1 - y_2) + (1-x_1-x_2) (3y_1 + 3y_2 + 2(1-y_1-y_2))$$

$$= x_1 (-3 y_1 - 2 y_2 + 1) + x_2 (-y_2 - 1) + 2 + y_1 + y_2$$

Suppose that $X^*=(x_1^*, x_2^*, 1-x_1^*-x_2^*)$, where $x_i^* \geq 0, i=1,2$, and $Y^*=(y_1^*, y_2^*, 1-y_1^*-y_2^*)$ is a Nash equilibrium pair. $P_X(X, Y^*)$ has a maximum at $X=X^*$. The partial derivatives $\partial P_X / \partial x_1 = 0$, and $\partial P_X / \partial x_2 = 0$ at $X=X^*$ give $6y_1^* + 2y_2^* - 1 = 0$ and $-y_1^* + 2 y_2^* = 0$. Solving, this gives $y_1^* = 1/7$ and $y_2^* = 1/14$. $Y^*=(1/7, 1/14, 11/14)$. Likewise, (X^*, Y) has a maximum at $Y=Y^*$. $\partial P_Y / \partial y_1 = 0$, and $\partial P_Y / \partial y_2 = 0$. These give $-3x_1^* + 1 = 0$ and $-2x_1^* - x_2^* + 1 = 0$. Solving, this gives $x_1^* = 1/3$ and $x_2^* = 1/3$. $X^*=(1/3, 1/3, 1/3)$. The payoffs ($P_X^* = 23/14, P_Y^* = 2$).

4 Conclusion

If the frequencies of threats occurrence are known, the optimal pure strategy can be found by expected effectiveness. However, if those frequencies are unknown, the optimal strategy is a mixed strategy provided by game theory. The problem can also be solved by linear programming method.

References

1. Mendelson, E.: *Introducing Game Theory and Its Applications*. Chapman & Hall/CRC Press Co, New York (2004)
2. Bishop, M.: *Computer Security*. Addison-Wesley/Prentice-Hall, Boston (2003)
3. Whitman, M., Mattord, H.: *Management of Information Security*. Thomson Course Technology, New York (2004)
4. Thomas, L.: *Games. Theory and Applications*. John Wiley & Sons, New York (1984)

HDR Image Synthesis Based on Multi-exposure Color Images

Hua Wang, Jianzhong Cao, Linao Tang, and Yao Tang

Xi'an Institute of Optics and Precision Mechanics, Chinese Academy of Sciences,
Xi'an, 710119, China
wangh0112@126.com

Abstract. In digital camera, it's difficult to exceed the dynamic range of 60~80dB because of the saturation current and background noise of CCD/CMOS image sensor in a single exposure image. In order to obtain more information and detail of a scene, we should extend its dynamic range, which was called HDR technology. Recent years, HDR imaging techniques have become the focus of much research because of their high theoretical and practical importance. By applying HDR techniques, the performance of different image processing and computer vision algorithms, information enhancement, and object and pattern recognition can also be improved. In this paper, a new tone reproduction algorithm is introduced, based on which may help to develop the hard-to-view or nonviewable features and details of color images. This method applies on multi-exposure images synthesis technique, where the red, green, and blue (RGB) color components of the pixels are separately handled. In the output, the corresponding (modified) color components are blended. As a result, a high quality HDR image is obtained, which contains almost the whole details and color information.

Keywords: color image processing, high dynamic range (HDR) image, image enhancement, multi-exposure images synthesise.

1 Introduction

The dynamic range of an image signal generated by an image sensor in CCD or CMOS technology is limited by its noise level on the one hand, and the saturation voltage of the sensor on the other hand [1]. In our nature world, the dynamic range of a scene is always higher than that of the CCD or CMOS cameras because of different luminance values. Thus, it's difficult to capture all of the details and color information of the actual scene in one image. In order to obtain more details of a scene, researchers have tried lots of methods to improve the quality of an image. A typical example is noise elimination from the images, which yields much better results [2] but it is also impossible to exhibit all the details of that scene. A feasible way to obtain this wide dynamic range scene is that we can capture multiple images of the same scene, but each image has different exposure time and it contains the most detail of one of the regions in the scene. If the scene contains regions with high luminance values, it is necessary to take a picture with low exposure time for the visualization of

the details in this highly illuminated region. On the other hand, if the scene includes very dark regions, the exposure time should much higher so that we can capture the details in these areas. At the end, we can synthesis these different exposure time images to obtain a HDR image.

Now, there are plenty of multiple exposure fusion methods and most of them are dependent to certain image properties like the scene irradiance map [3] etc. The scene irradiance varies from region to region subject to many factors, like the local surface reflectance, occlusion and shadows etc.[4].It's not an easy thing to find a general algorithm to handle all the irradiance conditions if the irradiance across a scene varies greatly. The parameters corresponding to the image processing function in many of the case are depending on the selection of the image features, i.e these algorithms are usually in some instant sensitive image properties [5-6]. The light intensity at a point in the image is the product of the reflectance at the corresponding object point and the intensity of illumination at that point. The amount of light projected to our eyes is determined by factors such as the illumination that strikes visible surfaces, the proportion of light reflected from the surface, and the amount of light absorbed, reflected, or deflected by the prevailing atmospheric conditions, such as haze or other partially transparent media [7].

Approaching from the opposite site, if we have a set of images with different exposure times, we must decide which exposure contains the maximum detail in the case of a certain region of a actual scene.

In this paper, a novel multi-exposure based imaging technology is proposed. The basic theory is that different exposure image contains different information and each image contains a region which has the maximum level of detail. Our work is to detect these regions in these images, and then merge these regions into a new image, however, because these regions come from different image, there are sharp transitions along the borders of the region. To eliminate the transition boundaries between varies image blocks, a blending function is used as the weight for final image merging.

The paper is organized as follows: In section 2, details in a certain region is estimated. Section 3 gives a blending function for the regions merging.

2 Estimate the Level of the Color Image in an Image Region

The main task of this section is to measure the detail level in an arbitrary region of the image. For this purpose, we use the sum of the gradients of RGB intensity function corresponding to the processed image. A linear mapping function is introduced to set up the measurement of the detail level at the same time. The following is the description of the measurement method of the detail level.

Let $I^R(x, y)$, $I^G(x, y)$ and $I^B(x, y)$ be the RGB intensity components of the pixel at the location of (x, y) in the image to be processed. The gradients of the intensity function in horizontal ΔI_x and vertical ΔI_y at position (x, y) can be calculated by the differences of the RGB components between its neighboring pixels. For simplicity, we show the expression for the R component (the same has to be evaluated in case of the G and B components), i.e.,

$$\begin{aligned}\Delta I_x^R(x, y) &= |I^R(x+1, y) - I^R(x, y)| + |I^R(x-1, y) - I^R(x, y)| \\ \Delta I_x^R(x, y) &= |I^R(x, y+1) - I^R(x, y)| + |I^R(x, y) - I^R(x, y-1)|\end{aligned}\quad (1)$$

For further processing, we introduce a linear mapping function L which can be expressed as follows,

$$L(u) = u / I_{\max} \quad (2)$$

Where I_{\max} is a constant stands for the maximum intensity value. For 8-bit RGB scale, it is equal to 255.

Consider \mathbf{R} be one of the regions of width w and height h of the images, and its upper left corner at the position of (x_r, y_r) . The R component level of detail inside of region \mathbf{R} is defined as

$$M^R(\mathbf{R}) = \sum_{i=1}^{w-1} \sum_{j=1}^{h-1} L(\max(\Delta I_x^R(x+i, y+j), \Delta I_y^R(x+i, y+j))) \quad (3)$$

And the sum detail level of the RGB three components in region \mathbf{R} is

$$M(\mathbf{R}) = M^R(\mathbf{R}) + M^G(\mathbf{R}) + M^B(\mathbf{R}) \quad (4)$$

The higher $M(\mathbf{R})$ is, the more detail this region contains. In the following part, we will merge these regions together which contain the most details.

3 HDR Image Synthesization

To determine the image' sub-regions with most detail, all of the N input images are divided into $n*m$ rectangular regions (see Fig.1). These sub-regions in the image are of the same size with width w and height h . Assuming i and j denote the row and column indices of the regions, and R_{ijk} denotes the image sub-region in the i th row and the j th column of the image with index k , where $k=1, \dots, N$. Let M denote the matrix of regions with the highest level of detail, the element of the core matrix in i th row and the j th column represents the index of the input image having the largest $M(\mathbf{R})$ value, i.e.,

$$M(R_{ijl}) > M(R_{ijk}), \quad k=1, \dots, l-1, l+1, \dots, N \quad (5)$$

Because each image contains more than one region which contains the highest level of detail and these sub-regions are selected and merged together finally. There are sharp transitions along the borders of the regions (see Fig.2). The sharp transitions should be eliminated. For this purpose, some researchers use Gaussian blending function to process the image [2][8], in this paper, a blending function $\eta(x, y)$ is introduced as:

$$\eta(x, y) = \frac{1}{u + e^{-v^2((x-rx_{ij})^2 + (y-ry_{ij})^2)}} \quad 0 < u, v < 1 \quad (6)$$

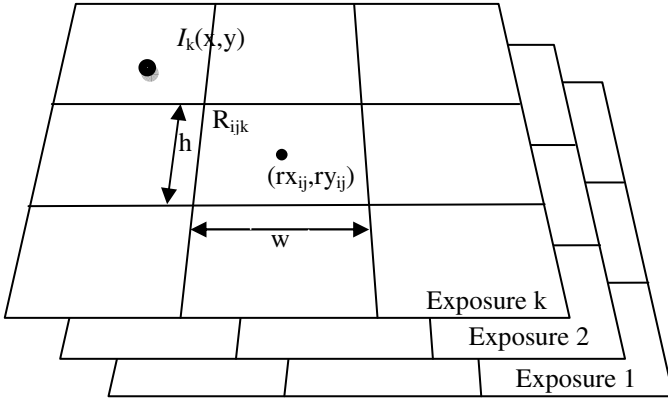


Fig. 1. Image sub-regions



Fig. 2. Sharp transitions along the borders

where u, v indicate the height of this blending function and the radius is projected in x - y plane, $(r_{x_{ij}}, r_{y_{ij}})$ is the coordinates of the center of image regions. Then the merged image can be expressed as:

$$\begin{aligned}
 I_o^R(x, y) &= \sum_{k \in o(x, y)} \eta_k(x, y) I_k^R(x, y) \\
 I_o^G(x, y) &= \sum_{k \in o(x, y)} \eta_k(x, y) I_k^G(x, y) \\
 I_o^B(x, y) &= \sum_{k \in o(x, y)} \eta_k(x, y) I_k^B(x, y) \\
 I_o(x, y) &= \langle I_o^R(x, y), I_o^G(x, y), I_o^B(x, y) \rangle
 \end{aligned} \tag{7}$$

Where $o(x, y)$ denotes a 3×3 region around (x, y) . η_k is the different weight from the image based on the element of core matrix image. $I_k^R(x, y)$, $I_k^G(x, y)$, $I_k^B(x, y)$ represent the luminance information of R, G, B at position (x, y) , respectively.

In order to illustrate the merging process more detailedly, the four original images (A,B,C,D) are showed in Fig.3, $o(x, y)$ can be represented as a matrix as:

$$M = \begin{bmatrix} 1A & 2B & 3A \\ 4C & 5B & 6A \\ 7D & 8C & 9D \end{bmatrix}$$

In this matrix, 1A denotes the first region with highest detail level is from image A. $\eta_i(x, y)$ represents the weight value of the pixel (x, y) corresponding to the same position in A. Then the final HDR image pixel $I_o(x, y)$ can be expressed by:

$$I_o^t(x, y) = \sum_{i=1}^9 \eta_i^t(x, y) I_d^t(x, y) \quad d=A,B,C,D \quad t=R,G,B \quad (8)$$

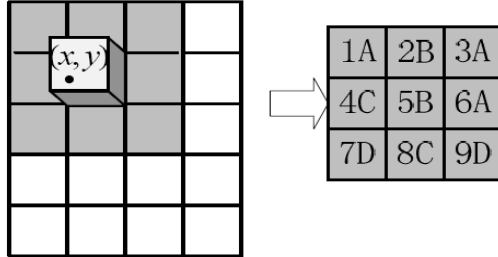


Fig. 3. Illustration of image merging at (x, y) in any sub-regions

4 Experimental Results

The effect of the proposed algorithm is illustrated by two examples. Fig.4 was taken in a park, a), b) and c) are images with different exposure of the same scene. These images are firstly divided into 19×29 sub-regions. The parameters u, v in Eqn.(6) are set to 0.05 and 0.02 respectively. And then the HDR image is showed as Fig.4d). Obviously, we get a good visual effect than the other three images. In the HDR image, the detail (sky, cloud, trees, lotus leaves, etc.) are all very clear and the color is more vivid. Fig.5 shows another experiment result. In image a), the detail of grass, house and tree are clear, but the sky and cloud are plain white due to saturation of the CCD or CMOS image sensor. In image c), although the sky and cloud have good

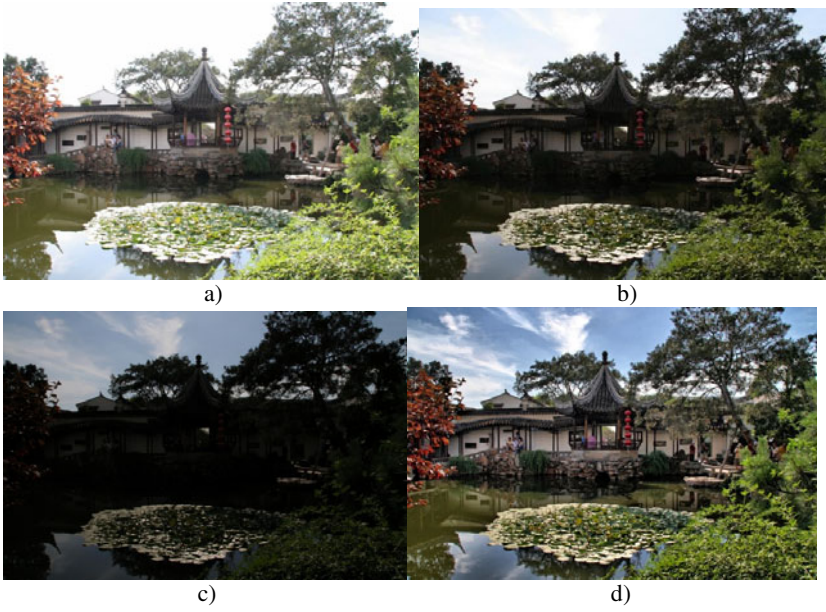


Fig. 4. a) , b) , c) are the original images with different exposure times. d) The merged HDR image

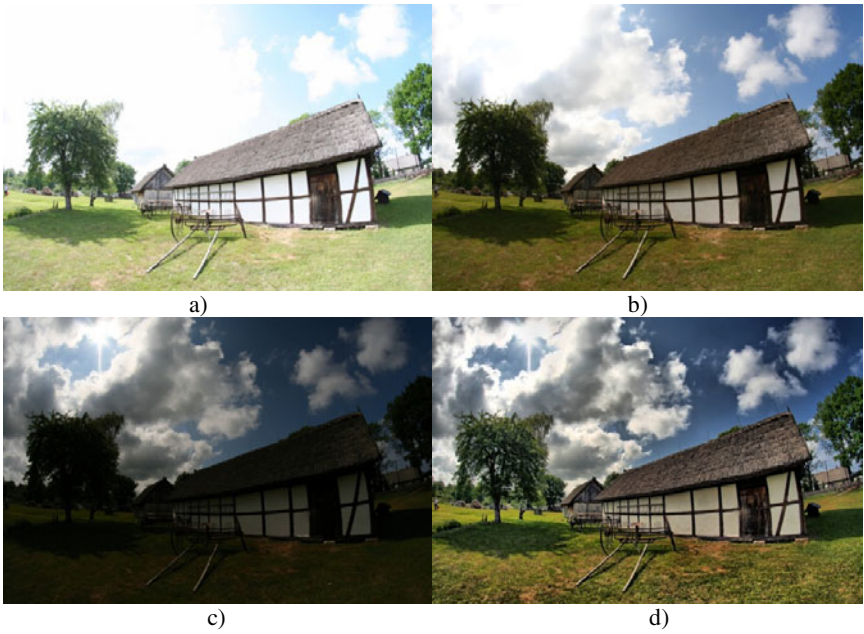


Fig. 5. a) , b) , c) are the original images with different exposure times. d) The merged HDR image

visual effect because of short exposure, the detail of the house and the lawn are lost. These images are divided into 16×29 sub-regions, and u, v are set to 0.05 and 0.04 respectively. Visual effect of the HDR image can be improved significantly as shown in Fig.5d).

5 Conclusion and Future Work

In this article, we use multiple images with different exposure times of the same scene to obtain a HDR image. Firstly, we divide the image into sub-regions, and then select these sub-regions with highest detail level. At the end, we merge these regions together and eliminate the sharp transitions along the borders of the regions. But the current implementation of this method is limited to process static scenes. As future work, this technique should be adaptive to dynamic scenes. And the complexity of this method should reduce if we want use it in real-time system. In real-time applications, like supporting vehicle systems for accident avoidance where the scene may change (possibly frequently), the exposure time and the processing time are the most important factors whose optimal determination requires further analysis.

Acknowledgment. This work is supported by the West Light Doctoral Foundation of Chinese Academy of Sciences.

References

1. Cvetković, S., Klijn, J., De With, P.H.N.: Tone-Mapping Functions and Multiple-Exposure Techniques for High Dynamic-Range Images. *IEEE Transactions on Consumer Electronics* 54(2), 904–911 (2008)
2. Várkonyi-Kóczy, A.R., Rövid, A., Hashimoto, T.: Gradient-Based Synthesized Multiple Exposure Time Color HDR Image. *IEEE Transactions on Instrumentation and Measurement* 57(8), 1779–1785 (2008)
3. Várkonyi-Kóczy, A.R.: Improved fuzzy logic supported HDR colored information enhancement. In: *I2MTC-International Instrumentation and Measurement Technology Conference*, Singapore, pp. 361–366 (2009)
4. Goshtasby, A.A.: Fusion of multi-exposure images. *Image and Vision Computing* 23(6), 611–618 (2005)
5. Russo, F.: Fuzzy filtering of noisy sensor data. In: *Proc. of the IEEE Instrumentation and Measurement Technology Conference*, Brussels, Belgium, pp. 1281–1285 (1996)
6. Russo, F.: Recent advances in fuzzy techniques for image enhancement. *IEEE Transactions on Instrumentation and Measurement* 47(6), 1428–1434 (1998)
7. Adelson, E.H., Pentland, A.P.: The Perception of Shading and Reflectance. In: Knill, D., Richards, W. (eds.) *Perception as Bayesian Inference*, pp. 409–423. Cambridge University Press, New York (1996)
8. Rovid, A., Varlaki, P.: Method for Merging Multiple Exposure Color Image Data. In: *International Conference on Intelligent Engineering Systems*, pp. 27–31 (2009)

The Further Decomposition of Actuarial Notation's Expression on Credibility Space*

Min-ying Yuan and Da-jun Sun

Department of Mathematics and Information Sciences, Langfang Teachers, College,
Langfang, China
ymy8219@sina.com

Abstract. In order to further simplify the calculation of life insurance actuarial notation on credibility space, this paper deduced the ultimate expression of life insurance actuarial notation about life distribution function and gives the value determinative conditions only by the life distribution function to determine, based on the basic properties of credibility distribution, through decomposing and discussing of every portion of the expression and seeking for the sufficient and necessary condition of judgement. Thus, the calculation of life insurance actuarial notation on credibility space is transformed from calculation of purely theoretical credibility measure to the simple arithmetic of life distribution function.

Keywords: Credibility space, Actuarial notation, Life distribution function, Credibility measure.

1 Introduction

The traditional theories of life insurance actuarial model are founded on the probability space, generally is composed of the expression of actuarial notation of future lifetime distribution function. There are three actuarial notations expressing of future lifetime distribution, ${}_tq_x$, ${}_tP_x$ and ${}_{t|u}q_x$. It is one of the basic contents to discuss the life distribution function expression of these three actuarial notations in the theoretical research and practical application of life insurance actuarial model. In the traditional theory of life insurance actuarial model, the life distribution function expression of these three actuarial notations is given out In reference [4], the traditional life insurance actuarial model on probability space is extended to credibility space, and the three actuarial notations are redefined on credibility space, that is, the new definition expressions of three actuarial notations under credibility measure. However, due to the complexity of credibility measure's calculation, it is impossible to get the value of life insurance actuarial notation from definition expression directly. Thus, reference [4] provides the life distribution function expression of the actuarial notation ${}_tq_x$ and ${}_tP_x$, and reference [5] provides the life

* Fund Project: Soft Science Research Project of Science and Technology Department of Hebei Province of China (No.10457292).

distribution function expression of actuarial notation ${}_{i|u}q_x$, yet both the expression and the value determinative conditions contain maximizing operation and minimizing operation in reference [5]. This paper accomplishes the further decomposition of life distribution function expression of life insurance actuarial notation ${}_{i|u}q_x$ to deduce the cannot be further decomposed expression. Thus, the theory of life insurance actuarial model on credibility space is improved, which facilitates the calculation of actuarial notation and consolidates the foundation for the future application of that model.

2 Preliminary

Definition 1[6] Let Θ be a nonempty set, and let $\mathcal{P}(\Theta)$ be the power set of Θ . Each element $A \in \mathcal{P}(\Theta)$ is called an event. A set function $Cr: \Theta \rightarrow [0,1]$ is called a credibility measure if (i) $Cr\{\Theta\} = 1$; (ii) $Cr\{A\} \leq Cr\{B\}$ whenever $A \subset B$; (iii) $Cr\{A\} + Cr\{A^c\} = 1$ for any event A ; (iv) $Cr\left\{\bigcup_i A_i\right\} = \sup_i Cr\{A_i\}$ for any events $\{A_i\}$ with $\sup_i Cr\{A_i\} < 0.5$.

The triplet $(\Theta, \mathcal{P}(\Theta), Cr)$ is called a credibility space [7].

Cr is a metric operator of credibility of fuzzy events.

Definition 2[8] A fuzzy variable is a function from credibility space $(\Theta, \mathcal{P}(\Theta), Cr)$ to the set of real numbers.

Definition 3[9] The credibility distribution $\Phi: \mathfrak{R} \rightarrow [0,1]$ of a fuzzy variable ξ is defined by

$$\Phi(x) = Cr\{\xi \leq x\}.$$

Definition 4[10] Let $T(0)$ be anyone's life span. The life distribution function is defined by

$$\Phi_0(x) = Cr\{T(0) \leq x\} \quad (x > 0).$$

$\Phi_0(x)$ represents the credibility that a neonatal (i.e., 0 years old) died in the next x years.

Definition 5[8] Let $(\Theta, \mathcal{P}(\Theta), Cr)$ be a credibility space, and $A, B \in \mathcal{P}(\Theta)$. Then the conditional credibility measure of A given B is defined by

$$Cr\{A|B\} = \begin{cases} \frac{Cr\{A \cap B\}}{Cr\{B\}}, & \text{if } \frac{Cr\{A \cap B\}}{Cr\{B\}} < 0.5 \\ 1 - \frac{Cr\{A^c \cap B\}}{Cr\{B\}}, & \text{if } \frac{Cr\{A^c \cap B\}}{Cr\{B\}} < 0.5 \\ 0.5, & \text{otherwise.} \end{cases}$$

When $Cr\{B\} > 0$.

In the life insurance actuarial theory on the credibility space, ${}_{t|u}q_x$ represents the credibility which a person ages x dies between $x+t$ and $x+t+u$ years old, that is ${}_{t|u}q_x = Cr\{x+t < T(0) \leq x+t+u | T(0) > x\}$.

Conclusion1[5] Let $(\Theta, \mathcal{P}(\Theta), Cr)$ be a credibility space, and $T(0)$ be anyone's life span, and $\Phi_0(x)$ be life distribution function. Then for the life insurance actuarial notation ${}_{t|u}q_x$, we have

$${}_{t|u}q_x = Cr\{x+t < T(0) \leq x+t+u | T(0) > x\}$$

$$= \begin{cases} \frac{(1-\Phi_0(x+t)) \wedge \Phi_0(x+t+u)}{1-\Phi_0(x)}, & \text{if } \frac{(1-\Phi_0(x+t)) \wedge \Phi_0(x+t+u)}{1-\Phi_0(x)} < 0.5 \\ 1 - \frac{\Phi_0(x+t) \vee (1-\Phi_0(x+t+u))}{1-\Phi_0(x)}, & \text{if } \frac{\Phi_0(x+t) \vee (1-\Phi_0(x+t+u))}{1-\Phi_0(x)} < 0.5 \\ 0.5, & \text{otherwise.} \end{cases}$$

3 Decomposition

In the following, we move on decomposing the life distribution function expression of the ${}_{t|u}q_x$ in Conclusion1 (The following discussion assumes that: $\Phi_0(x) \neq \Phi_0(x+t)$, $t > 0$). This mainly involves the conditions of decomposition establishment which must be necessary and sufficient conditions.

3.1 The decomposition of $\frac{(1-\Phi_0(x+t)) \wedge \Phi_0(x+t+u)}{1-\Phi_0(x)} (< 0.5)$

(1) If $\frac{(1-\Phi_0(x+t)) \wedge \Phi_0(x+t+u)}{1-\Phi_0(x)} = \frac{1-\Phi_0(x+t)}{1-\Phi_0(x)}$, namely $1-\Phi_0(x+t) \leq \Phi_0(x+t+u)$,

then by using $\frac{1-\Phi_0(x+t)}{1-\Phi_0(x)} < 0.5$, we obtain

$$\Phi_0(x+t) > 0.5 + 0.5\Phi_0(x).$$

Conversely, if $\Phi_0(x+t) > 0.5 + 0.5\Phi_0(x)$, then $1-\Phi_0(x+t) < 1-(0.5+0.5\Phi_0(x)) = 0.5-0.5\Phi_0(x)$. Thus $1-\Phi_0(x+t) < 0.5-0.5\Phi_0(x) < 0.5 < 0.5+0.5\Phi_0(x) < \Phi_0(x+t) < \Phi_0(x+t+u)$. Hence we obtain

$$\frac{(1-\Phi_0(x+t)) \wedge \Phi_0(x+t+u)}{1-\Phi_0(x)} = \frac{1-\Phi_0(x+t)}{1-\Phi_0(x)}.$$

The deduction above shows that $\frac{(1-\Phi_0(x+t)) \wedge \Phi_0(x+t+u)}{1-\Phi_0(x)} = \frac{1-\Phi_0(x+t)}{1-\Phi_0(x)}$ (i.e. $1-\Phi_0(x+t) \leq \Phi_0(x+t+u)$) and $\Phi_0(x+t) > 0.5+0.5\Phi_0(x)$ are equivalent under the prerequisite of $\frac{(1-\Phi_0(x+t)) \wedge \Phi_0(x+t+u)}{1-\Phi_0(x)} < 0.5$.

(2) If $\frac{(1-\Phi_0(x+t)) \wedge \Phi_0(x+t+u)}{1-\Phi_0(x)} = \frac{\Phi_0(x+t+u)}{1-\Phi_0(x)}$, namely $1-\Phi_0(x+t) \geq \Phi_0(x+t+u)$, then by using $\frac{\Phi_0(x+t+u)}{1-\Phi_0(x)} < 0.5$, we obtain

$$\Phi_0(x+t+u) < 0.5 - 0.5\Phi_0(x).$$

Conversely, if $\Phi_0(x+t+u) < 0.5 - 0.5\Phi_0(x)$, then $\Phi_0(x+t) < \Phi_0(x+t+u) < 0.5 - 0.5\Phi_0(x) < 0.5$. Thus $1-\Phi_0(x+t) > 0.5 > \Phi_0(x+t+u)$. Hence we obtain

$$\frac{(1-\Phi_0(x+t)) \wedge \Phi_0(x+t+u)}{1-\Phi_0(x)} = \frac{\Phi_0(x+t+u)}{1-\Phi_0(x)}.$$

The deduction above shows that $\frac{(1-\Phi_0(x+t)) \wedge \Phi_0(x+t+u)}{1-\Phi_0(x)} = \frac{\Phi_0(x+t+u)}{1-\Phi_0(x)}$ (i.e. $1-\Phi_0(x+t) \geq \Phi_0(x+t+u)$) and $\Phi_0(x+t+u) < 0.5 - 0.5\Phi_0(x)$ are equivalent under the prerequisite of $\frac{(1-\Phi_0(x+t)) \wedge \Phi_0(x+t+u)}{1-\Phi_0(x)} < 0.5$.

Based on the analysis above we have the decomposition expression that

$$\begin{aligned} & \frac{(1-\Phi_0(x+t)) \wedge \Phi_0(x+t+u)}{1-\Phi_0(x)} (< 0.5) \\ &= \begin{cases} \frac{1-\Phi_0(x+t)}{1-\Phi_0(x)}, & \text{if } \Phi_0(x+t) > 0.5+0.5\Phi_0(x) \\ \frac{\Phi_0(x+t+u)}{1-\Phi_0(x)}, & \text{if } \Phi_0(x+t+u) < 0.5-0.5\Phi_0(x). \end{cases} \end{aligned}$$

3.2 The Decomposition of $\frac{\Phi_0(x+t) \vee (1-\Phi_0(x+t+u))}{1-\Phi_0(x)} (< 0.5)$

Since $\Phi_0(x+t) \leq \Phi_0(x+t) \vee (1-\Phi_0(x+t+u))$, $1-\Phi_0(x+t+u) \leq \Phi_0(x+t) \vee (1-\Phi_0(x+t+u))$ and $\frac{\Phi_0(x+t) \vee (1-\Phi_0(x+t+u))}{1-\Phi_0(x)} < 0.5$, we have $\frac{\Phi_0(x+t)}{1-\Phi_0(x)} < 0.5$ and $\frac{(1-\Phi_0(x+t+u))}{1-\Phi_0(x)} < 0.5$. Further, since $\frac{\Phi_0(x+t)}{1-\Phi_0(x)} < 0.5$ is equivalent to $\Phi_0(x+t) < 0.5 - 0.5\Phi_0(x)$, and $\frac{(1-\Phi_0(x+t+u))}{1-\Phi_0(x)} < 0.5$ is equivalent to $\Phi_0(x+t+u) > 0.5+0.5\Phi_0(x)$.

Hence, we always have $\Phi_0(x+t) < 0.5 - 0.5\Phi_0(x) < 0.5 < 0.5 + 0.5\Phi_0(x) < \Phi_0(x+t+u)$, under the condition of $\frac{\Phi_0(x+t) \vee (1 - \Phi_0(x+t+u))}{1 - \Phi_0(x)} < 0.5$.

(1) If $\frac{\Phi_0(x+t) \vee (1 - \Phi_0(x+t+u))}{1 - \Phi_0(x)} = \frac{\Phi_0(x+t)}{1 - \Phi_0(x)}$, namely $\Phi_0(x+t) \geq 1 - \Phi_0(x+t+u)$, then we have $\Phi_0(x+t) + \Phi_0(x+t+u) \geq 1$ and $\Phi_0(x+t) < 0.5 - 0.5\Phi_0(x)$. Conversely, if $\Phi_0(x+t) + \Phi_0(x+t+u) \geq 1$ and $\Phi_0(x+t) < 0.5 - 0.5\Phi_0(x)$, then we have

$$\frac{\Phi_0(x+t) \vee (1 - \Phi_0(x+t+u))}{1 - \Phi_0(x)} = \frac{\Phi_0(x+t)}{1 - \Phi_0(x)}.$$

(2) If $\frac{\Phi_0(x+t) \vee (1 - \Phi_0(x+t+u))}{1 - \Phi_0(x)} = \frac{1 - \Phi_0(x+t+u)}{1 - \Phi_0(x)}$, namely $\Phi_0(x+t) \leq 1 - \Phi_0(x+t+u)$, then we have $\Phi_0(x+t) + \Phi_0(x+t+u) \leq 1$ and $0.5 + 0.5\Phi_0(x) \leq \Phi_0(x+t+u)$. Conversely, if $\Phi_0(x+t) + \Phi_0(x+t+u) \leq 1$ and $0.5 + 0.5\Phi_0(x) \leq \Phi_0(x+t+u)$, then we have

$$\frac{\Phi_0(x+t) \vee (1 - \Phi_0(x+t+u))}{1 - \Phi_0(x)} = \frac{1 - \Phi_0(x+t+u)}{1 - \Phi_0(x)}.$$

Based on the analysis above, we have the decomposition expression that

$$\begin{aligned} & \frac{\Phi_0(x+t) \vee (1 - \Phi_0(x+t+u))}{1 - \Phi_0(x)} (< 0.5) \\ = & \begin{cases} \frac{\Phi_0(x+t)}{1 - \Phi_0(x)}, & \text{if } 1 \leq \Phi_0(x+t) + \Phi_0(x+t+u), \Phi_0(x+t) < 0.5 - 0.5\Phi_0(x) \\ \frac{1 - \Phi_0(x+t+u)}{1 - \Phi_0(x)}, & \text{if } 1 \geq \Phi_0(x+t) + \Phi_0(x+t+u), \Phi_0(x+t+u) > 0.5 + 0.5\Phi_0(x). \end{cases} \end{aligned}$$

3.3 The Decomposition of ${}_{t|\mu}q_x$

Integrating 3.1 and 3.2, we obtain the further decomposition expression of actuarial notation ${}_{t|\mu}q_x$ on the credibility space. That is

$$\begin{aligned} & {}_{t|\mu}q_x = Cr\{t < T(x) \leq t+u\} \\ = & \begin{cases} \frac{(1 - \Phi_0(x+t)) \wedge \Phi_0(x+t+u)}{1 - \Phi_0(x)}, & \text{if } \frac{(1 - \Phi_0(x+t)) \wedge \Phi_0(x+t+u)}{1 - \Phi_0(x)} < 0.5 \\ 1 - \frac{\Phi_0(x+t) \vee (1 - \Phi_0(x+t+u))}{1 - \Phi_0(x)}, & \text{if } \frac{\Phi_0(x+t) \vee (1 - \Phi_0(x+t+u))}{1 - \Phi_0(x)} < 0.5 \\ 0.5, & \text{otherwise.} \end{cases} \end{aligned}$$

$$= \begin{cases} \frac{1 - \Phi_0(x+t)}{1 - \Phi_0(x)}, & \text{if } 1 \leq \Phi_0(x+t) + \Phi_0(x+t+u), \Phi_0(x+t) > 0.5 + 0.5\Phi_0(x) \\ \frac{\Phi_0(x+t+u)}{1 - \Phi_0(x)}, & \text{if } 1 \geq \Phi_0(x+t) + \Phi_0(x+t+u), \Phi_0(x+t+u) < 0.5 - 0.5\Phi_0(x) \\ 1 - \frac{\Phi_0(x+t)}{1 - \Phi_0(x)}, & \text{if } 1 \leq \Phi_0(x+t) + \Phi_0(x+t+u), \Phi_0(x+t) < 0.5 - 0.5\Phi_0(x) \\ 1 - \frac{1 - \Phi_0(x+t+u)}{1 - \Phi_0(x)}, & \text{if } 1 \geq \Phi_0(x+t) + \Phi_0(x+t+u), \Phi_0(x+t+u) > 0.5 + 0.5\Phi_0(x) \\ 0.5, & \text{otherwise.} \end{cases}$$

4 Conclusions

This paper accomplishes the further decomposition of life distribution function expression of life insurance actuarial notation ${}_{t|\mu}q_x$. We obtain the ultimate expression that cannot be decomposed any more. It transforms the numerical calculation of actuarial notation ${}_{t|\mu}q_x$ to simply arithmetic of the function value. Thus, it improves the life insurance actuarial model on credibility space, and facilitates the calculation of actuarial notation as well.

References

1. Bowers, N.L., Gerber, H.U., Hickman, J.C., Jones, D.A., Nesbitt, C.J.: Actuarial Mathematics. The Society of Actuaries, Itasca, IL (1986)
2. Lei, Y.: Life Insurance Actuarial Science. Beijing University Press, Beijing (1998)
3. Dorfman, M.Y., Adelman, S.W.: Life Insurance, 2nd edn. Dearborn Financial Publishing, Inc. (1992)
4. Yuan, M.Y.: Model of Life Actuarial on Credibility Space. College of Management, Hebei University, Master Thesis, China (2011)
5. Yuan, M.Y., Sun, D.J.: Life Distribution Function Expression of Actuarial Notation on Credibility Space. In: 2nd International Conference on Management Science and Engineering. Engineering Technology Press, Hong Kong (2011)
6. Liu, B., Liu, Y.K.: Expected value of fuzzy variable and fuzzy expected value models. IEEE Transactions on Fuzzy Systems. 10(4), 445–450 (2002)
7. Liu, B.: A survey of credibility theory. Fuzzy Optimization and Decision Making 5(4), 387–408 (2006)
8. Liu, B.: Uncertainty Theory, 2nd edn. Springer, Berlin (2007)
9. Liu, B.: Theory and Practice of Uncertain Programming. Physica, Heidelberg (2002)
10. Yuan, M.Y.: Basic formations of life function based on credibility measure (To be published soon)

Research on the Layout of Shipbuilding Steel Structure Machining Plant Based on CATIA

Yang Liu*

School of Shipbuilding Engineering, Harbin Engineering University,
Harbin 150001, China
qingtianriji@yahoo.com.cn

Abstract. The steel structure machining plant is an important process locale of modern ship manufacture. A 3-Dimensional visual layout project of this kind machining plant has been put forward based on software CATIA, seeking the optimization of plant's layout. After the initial plan was made, the Maximal Element Method were used to establish the mathematical model, and then to look for the most optimum and smallest value of plant logistics volume. Using the results, the manufacture resource library and the 3D visual model of this steel structure were constructed, and an evaluation was also made on the acquired visual parameter model. So a useful method and way is brought out for the digital manufacture plant's layout optimization.

Keywords: visual plant, optimization of layout design, CATIA, manufacturing resource library, Maximal Element Method.

1 Introduction

Since the 21st century, the technology of CAD/CAM was used a lot in the shipbuilding field. How to improve the efficiency using computer in the shipbuilding enterprise is coming into a new kind of study. Whether the layout of the steel structure machining plant is optimization can affect the plant's efficiency directly, and therefore affects the period of manufacture and quality seriously. So, it is important for studying steel structure machining plant's layout[1].

Based on the three-dimensional visualization function of the CATIA software, this paper discussed the layout design method using the example of shipbuilding steel structure machining plant. It applied the Maximal element method for the layout optimization of steel structure machining plant, established a visual workshop model, evaluated the main index of layout scheme, and then provided reference for the layout and optimization of the digital production workshop.

2 The Determination of Steel Structure Machining Plant's Layout

Good manufacturing enterprises must have a good production process, build a reasonable and "flexible" modularization process, and also must start from optimizing

* Special funds to finance operating expenses for basic scientific research of Central Colleges (HEUCF100108).

the production flow. Based on all of the above, they select the equipment according to the product production target. If to reform existing enterprises, it needs to evaluate and optimize the existing resources. According to existing resources, using the layout optimization algorithm to design and optimize the layout, get the plane layout scheme, establish the digital workshop model, mainly to set up manufacturing resource database, plant and manufacturing units classification, technics and process model, and then get a digital workshop parametric model. Using the digital software or its second time development function evaluates the parametric models. If it do not meet the requirement, it must get the optimal design scheme through the digital workshop model. Figure 1 is the levels chart of the digital workshop layout.

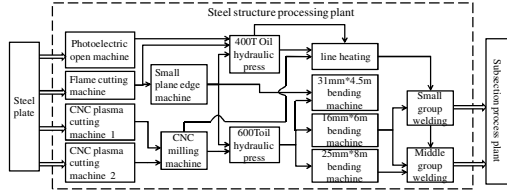
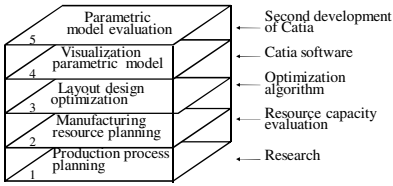


Fig. 1. Digital Workshop Layout design **Fig. 2.** Production flow chart (after optimization)

2.1 Production Process and Manufacturing Resources Planning

The processing operations of Marine products is various, and the process is complex. Generally, the plant’s logistics line appears unilateralist but also interlaced with each other. Taking the steel structure processing plant of a ship manufacturing enterprise for example, its process planning was shown in figure 2, the main technique parameters of the after optimization manufacturing resources (equipment) as is shown in table 1.

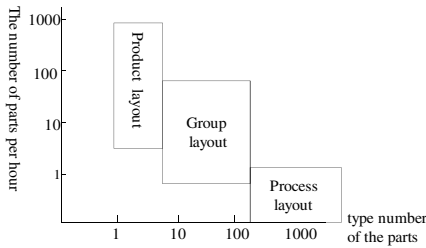


Fig. 3. Types of plant’s layout and the accessories connection chart

Table 1. Main technical parameters of equipment

Equipment name	The main technique parameters	Shape dimension(m)	Work area(m)
Plasma cutting machine	Cutting width 4.8m, cutting thickness 3-20mm, Velocity 4m/min	40*6	40*7
Photoelectric open machine	Cutting width 4m, cutting thickness 3-20mm, Velocity 4m/min	45*5	45*6
Flame cutting machine	Cutting width 6.8m, cutting thickness 3-20mm, Velocity 4m/min	50*000	50*9
CNC milling machine	The longest 15m, the shortest 1m, the thickest 80mm	15*5	15*5
Small plane edge machine	cutting thickness 5-60mm, Velocity.015-0.8m/min	0.5*0.5	1*1
400Toil hydraulic press	operating stroke Velocity 100mm/s	6.4*1.8*5.56	10*4.8*5.56
600Toil hydraulic press	operating stroke Velocity 120mm/s	8*3.5 *8.2	12*6.5 *8.2
Samsung bending machine	16mm*6m	10.52*2.580*2.12	12.52*5.58*2.12
Samsung bending machine	25mm*8m	14.2*2.8*3	16.2*5.8 *3
20T driving 2	Velocity 20m/min	13*1.5*2.5	13*1.5*18
30T driving 2	Velocity 20m/min	18*1*2.5	18*1*18
plasma cutting machine	Cutting width 4.8m, cutting thickness 3-20mm, Velocity 4m/min	40*6	40*7
Samsung bending machine	31mm*4.5m	8950*3015*2310	10.95*6.015*2.3
40T driving	Velocity 20m/min	48*2*3	48*2*18

2.2 Plant Layout Planning

Product layout, process layout, group layout and fixed layout are four basic forms of facility layout. Among them, fixed layout generally use in the processing of objects which are difficult to move, here will not be considered. The relationship between the other three types of layout forms and the processing speed and species of processing objects is shown in figure 3. Parts type of ship steel processing workshop are almost the same, and large quantity, therefore, select a product layout for layout is reasonable. The ideas of product layout are the manufacturing process into processes and procedures which are completed by special processing equipments and technical personnel.

2.3 Operation Area Planning

According to the steel and the product layout type and workshop production process, the workshop is divided into three order work area, including cutting operation,

forming and group assembly and welding. According to the table 2 representing the data of the material yard and work platform area ratio, the Table 1 representing the work area of the processing equipment, the work efficiency, and the factory ship manufacturing type sure path choice for double logistics form, that is to say to set up two parallel across each section. Every work area is divided into three parts, the two sides for equipment and working area, sharing the yard and buffer materials which are in the central, convenience for materials circulation, shorten the logistics line. As shown in figure 4. One cross is mainly for complex curvature sheet metal forming operation, the other is mainly for simple curvature plate forming operation. Each across set 2 drivings through the whole workshop. A horizontal driving which is set in the group assembly and welding area is helpful for scheduling of the facilitating materials and components.

Table 2. Area proportion of stacking yard, buffer zone and working district

Yard and buffer area/work area	Ratio
Cutting operation area	10-30%
Forming machining area	30-50%
group assembly and welding area	30-60%

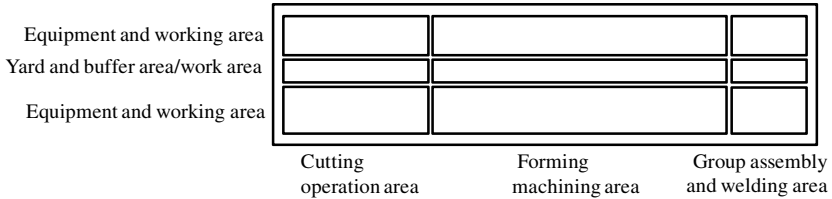


Fig. 4. Steel machining plant operation area subdivision

3 The optimization of Steel Structure Machining Plant’S Layout

The main standard of plant’s layout is to make each produce of the plant’s disposal propitious to establishment reasonable logistics, make total conveyance route the shortest, conveyance expenses minimum[2]. The main conveyance of the steel structure machining plant is driving car. We believe the transportation cost and material flow rate is proportional, and we ignore the transportation cost in the paper.

Second, the workshop layout optimization also includes the use of manufacturing resources and the minimum of the cover an area of layout. In the manufacturing resource planning, we has made detailed consideration of personnel deployment and communication convenience and flexible to add new equipment, on the premise of the configuration of the equipment meets production capacity.

3.1 The Planning of the Area of Workshop

The area of workshop layout includes equipment and working area, the necessary yard and buffer area and the size of the road. And the road includes pavements and

parts transportation roads. The total area of workshop is determined by calculation formula (1).

$$A_t = A_c + A_y + A_b + A_r + A_o \tag{1}$$

A_t —total area of workshop ;

A_c —equipment and working area;

A_y —yard;

A_b —buffer area;

A_r —the size of the road;

A_o —truss, auxiliary equipment, office area.

The calculation: $A_t \approx 12300m^2$.

3.2 Maximal Element Method for Minimum Material Flow Rate of Workshop

Assume that the equipment has set up a position in the workshop, we build coordinates plane coordinating the corner of the plant for the origin. Then we can know coordinates of each of the equipment processing knife, and according to the manufacturing process, we can get logistics track which determines the initial data (Figure 5 for mathematics abstract model). The best workshop layout is to reduce horizontally and reverse flow of logistics line[2]. According to this, we construct equipment layout target function: formula (2), which makes sure of the minimization increment of the workshop internal logistics.

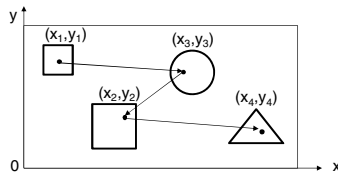


Fig. 5. Mathematical abstract model

$$\min \Delta L = \min \sum_1^i \sum_1^j \sum_1^i \sum_1^j \alpha_{xi,yi,xj,yj} \delta_{xi,yi,xj,yj} \tau_{xi,yi,xj,yj} \tag{2}$$

$$\tau_{xi,yi,xj,yj} = \begin{cases} 0, y_i < y_j \ \& \ x_i = y_j & \text{Forward direction} \\ 1, y_i = y_j & \text{Crosswise} \\ 2, y_i > y_j & \text{Reverse} \end{cases}$$

$\alpha_{xi,yi,xj,yj}$ —material flow quantity from equipment i to equipment j;

$\delta_{xi,yi,xj,yj}$ —material flow distance from equipment i to equipment j.

3.3 Plant Layout Optimization

After optimizing the layout, the designed steel long of the shipbuilding business workshops is 352 meters, the wide is 35 meters, and the total area is 12,320 square meters. With supply capacity of the engine needed for the production of water,

electricity, steam and compressed air, the condition of air, heating and ventilation, and the carrying capacity of lifting equipment installed. According to dimension processing equipment and work area, the cutting area is 4650 square meters, the forming operation area is 5560 square meters and assembly and welding area is 1800 square meters. One, an designed area is the 4576 cross- square meters, long * width dimension is 352 meters by 13 meters, equipped with 1 set of flame cutting machine, 1 set of optical opening machine, several sets of small edge planer, 1 set of hydraulic machine, 1 set of rolling machine, 1 set of fire work platform and 1 set of platform for a small group. Two, an designed area is 6336 square meters, long * width dimension is 352 meters by 18 meters, is equipped with 2 sets of CNC plasma cutting machine, 1 set of CNC milling machine, 1 set of hydraulic machine, 2 sets of coil machine and 1 set of platform for a middling group.

This program first establishes the cross-range of products, in line with cutting workshop process, with the ability to a certain line, and configure cross car in workshop, increase links of vertical and horizontal, so that the material is more convenient scheduling. Steel machining plant layout plan is shown in Figure 6.

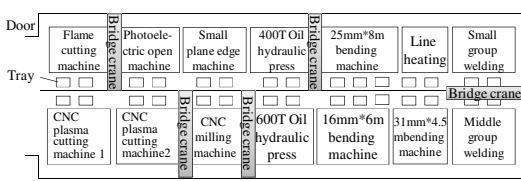


Fig. 6. Steel machining plant layout plan

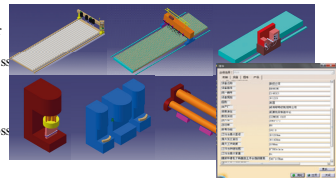


Fig. 7. Manufacturing resource library equipment model

4 Three-Dimensional Visualization Parameter Model

Plant design module of CATIA software is an object-oriented system. It allows designers to create a class factory or other type of plant design easily. It's reproduce and confirm functionality provides an efficient means of design for plant design. The entire design process can be extended and amended, so that the design can be more complete[2]. The virtual workshop environment in the open database provides a number of logical and physical design data for the user, so that we can easily and efficiently create three-dimensional digital factory model. Visual layout design includes plant design, layout of production operations area and layout of equipment in the operations area support facilities.

4.1 The Establishment of Manufacturing Resource Model Library

We establish three-dimensional model of various manufacturing resources in the same proportion. Working parts are supposed to move according to design requirements to meet the virtual operating. Save the manufacturing resources with different Classification and add their own properties, associated attributes and constraints attributes, to implement a property associated with the model. Shown in Figure 7.

4.2 The Establishment of Three-Dimensional Model of the Workshop

Import plant layout diagram as a reference; establish plant-based surface, walls, dividing the production area as shown in Figure 8. Quantitatively adjust the layout of the plant to produce a complete digital model of plant parameters. Rendering picture is shown in figure 9. The lower right corner is the micro-effects of the layout of plant.

The open database kernel of CATIA provides the development of languages. As shown in figure 10, Calls parameters of the model within the software system; assess the parametric indicators of the layout of the steel processing plant, Such as equipment utilization, space utilization, production line load, etc. And calls excel to draw graphs of assessment data.

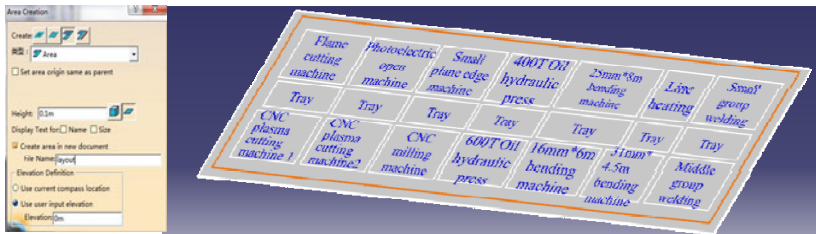


Fig. 8. Production area plan

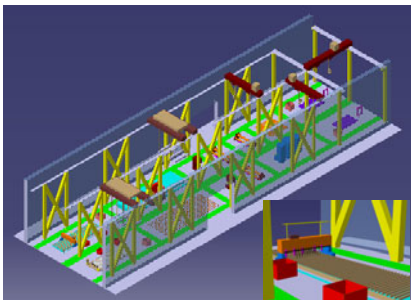


Fig. 9. Visual parameter model of steel machining plant

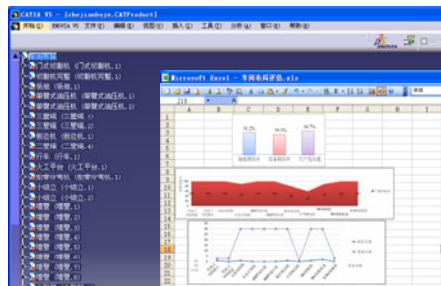


Fig. 10. Result of layout evaluation

5 Conclusion

Proposed five-step program for digital plant layout design. Shipbuilding steel plant, for example, to put forward planned production process, optimizing the manufacture resource-based plant layout mode.

Proposed that we should adopt appropriate optimization algorithm before the establishment of the digital plant model to finish plant layout design and optimization and optimal results should combine actual production. In this case the optimization algorithm we used is the largest element method and genetic algorithms. To obtain the

global optimal solution and to speed up the convergence rate, genetic algorithm needs to select the appropriate parameters.

Based on three-dimensional visualization software to create digital plant model, on the basis of the digital model to create a logical and physical contact, so that the digital model of the design upgrade to parameterized model, and attribute information of the plant model database available.

According to the calls and research of the parameters of the digital plant model information, we can evaluate the merits of plant layout. And this can provide some reference value for the research on the plant layout.

References

1. Xu, L., Li, J.-M., Wang, X.-L.: Optimal design for equipment layout of workshop based on genetic algorithms. *Modular Machine Tool & Automatic Manufacturing Technique* 12, 46–48 (2004)
2. Du, Q., Ge, S., Ge, Q.: Research of ProcessOptim iza tion in Shipbuild ing Shop Based on Method of Shipbuilding FacilitiesCollocation Optimization. *Science Technology and Engineering* 9, 3367–3370 (2009)
3. Liu, Y., Mei, M.: Hull Blocks Virtual Assembly Sequence Planning Based on Improved Genetic Algorithm. In: *The 2nd International Conference on E-Business and E-Government*, vol. 7, pp. 304–306 (2010)
4. Xiao, M.-H., Wang, M., Wang, H., et al.: Research on the Packing Problem Based on the Genetic Algorithm and Simulated Annealing Algorithm. *Computer Engineering and Applications* 36, 70–72 (2003)
5. Zheng, W., Wang, Z.-M.: *3D Plant Design*. Chemical Industry Press, Beijin (2005)

High-Speed Facial Recognition Using Log-Polar Transformation

Yue Bao¹, Bin Qi², and Fei Gu¹

¹ Tokyo City University
1-28-1 Tamazutsumi, Setagaya-ku, Tokyo, Japan
{bao, g1191801}@tcu.ac.jp

² Toshiba Corporations
1-1-1 Shibaura, Minato-ku, Tokyo, Japan
bin.qi@toshiba.co.jp

Abstract. Log-Polar transformation is an approximate model of human vision. If using it to recognize human faces, a reference point for the transformation is necessary, and the position of the reference point influences the recognition accuracy directly. However, it is difficult to extract an appropriate reference point from an image automatically. This paper proposes a face recognition method that detects the face center point as a reference point for Log-Polar transformation automatically. It is easier than before to recognize the faces by using Log-Polar transformation with the propose method.

Keywords: Log-Polar transformation, Facial recognition, High-speed, Matching.

1 Introduction

The necessity for a physical security system is increasing with the increase in incidents of theft. The place which should be protected must be clearly divided by a wall, a partition or an entrance, etc., and only the permitted persons are enabled to go in and out of the place, and it must have the capability to supervise and record the actions of the people in the surrounding area and inside the building. Facial recognition technology is extremely convenient in using security features (there is no danger of forgetting, loss, theft, or a loan) which are features of biometrics itself [1] [2].

Many researchers have proposed the methods of facial recognition, selecting the frontal face pattern from the photographed face image and performing personal identification. These methods extract the feature vectors from the input image, and identify the same person according to the smallest distance of vectors [3]. Another facial recognition method uses Log-Polar transformation that is suitable for size change or rotation of the face images [4]. However, it is difficult to take the face correctly in the middle of the frame. When the center of the face is not in the center of the image, discrimination is not possible.

In this paper, we propose the high-speed facial recognition method which using the Log-Polar transformation and the transformation center are calculated automatically. First, both eyes are detected from the captured face picture. Next, the center of a face is automatically calculated using the position of the detected eye. Log-Polar transformation is done by setting this center as a transformation center. The degree of similar is calculated by matching with the picture which had the transformed picture registered. Moreover, when checking matching of an image, high-speed matching is realized by using part matching.

This proposal method has the feature shown below.

- When doing Log-Polar transformation, a transformation center can be automatically decided from the captured image using detection of the position of an eye.
- By making the Log-Polar transformation of the image of ring form, Log-Polar transformation of the face area of only the specific range can be performed.
- Both eyes and a mouth are the parts which are the most characteristic in a face. By matching only with those parts, the high precision and high-speed of facial recognition are possible.

2 Proposal Method

In Log-Polar coordinates, ρ is the logarithm of the distance from the center in an orthogonal coordinate system and θ is the angle seen from the center. It is transformed by the following Equations.

$$(\rho, \theta) = \left(\log \left[\sqrt{(x - x_c)^2 + (y - y_c)^2} \right], \tan^{-1} \left(\frac{y - y_c}{x - x_c} \right) \right) \quad (1)$$

Where, (x_c, y_c) is the center of coordinate. In Log-Polar transformation and image recognition, it has the effective feature by Eq. (1).

For example, first rotation movement by an orthogonal coordinate system is expressed with Log-Polar system of coordinates as lateral parallel translation. Second, Change of the size in an orthogonal coordinate system is expressed with Log-Polar system of coordinates as parallel translation of a lengthwise direction. These features are very useful in order to build the image recognition algorithm which can answer to change of a size and rotation.

2.1 Automatic Extraction of Transformation Center

In order to decide the transformation center of Log-Polar transformation automatically, the iris of the eye of a face image is detected, and the center of both eyes is calculated. Here, it is defined as setting a tip of the nose as the center of a face.

As shown in Fig. 1, the height of an isosceles triangle was set to two thirds of the distance between eyes. (x_1, y_1) and (x_2, y_2) are the coordinate values of the center of both eyes.

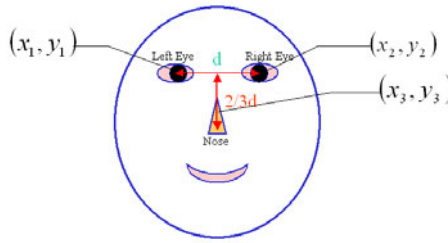


Fig. 1. Method of determining transformation center

The value of two thirds was acquired from the data of seven students face. In an isosceles triangle, a vertex (x_3, y_3) is set as a transformation center (center of a face). A vertex (x_3, y_3) is calculated using the Eq. (2).

$$\begin{cases} x_3 = \frac{1}{2}(x_2 + x_1) - \frac{2}{3}(y_2 - y_1) \\ y_3 = \frac{1}{2}(y_2 + y_1) + \frac{2}{3}(x_2 - x_1) \end{cases} \quad (x_2 > x_1) \quad (2)$$

Fig. 2 is the flow of the Log-Polar transformation which extracts a transformation center automatically. First, an input image is made into a grayscale image, and the search range is narrowed down. Next, an input image is made into a binary image and removes a noise by filter. Moreover, labeling is made and through the judgment of area detects both eyes. The coordinates centering on transformation are calculated with the coordinates of both the detected eyes by Eq. (2). Log-Polar transformation is processed using this coordinate value.

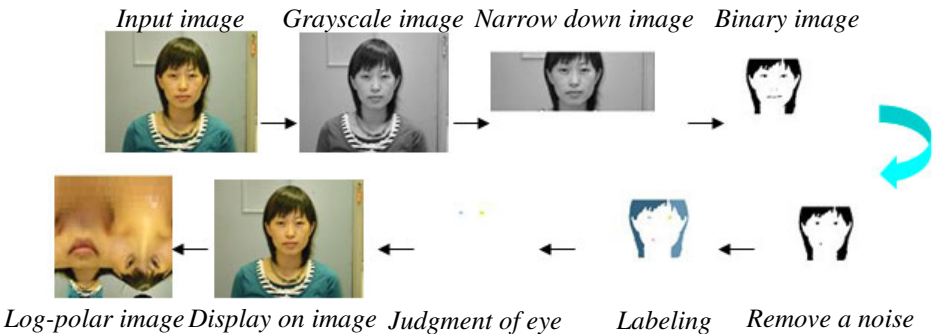


Fig. 2. The flow of the Log-Polar transformation

In the facial recognition by Log-Polar transformation, it is necessary to move a pixel to calculate the degree of similar. So, there is a problem which takes time. Then, improvement in the speed of facial recognition is proposed.

2.2 Determination of the Ring Form Area

As shown in Fig. 3, in order to include a face area correctly in a processing area, the center of the circle which passes along three points of the center of both eyes (x_1, y_1) , (x_2, y_2) and the center of a mouth (x_3, y_3) is set as a transformation center. The coordinates of the center of a circle (x_3, y_3) can be calculated by Eq. (3).

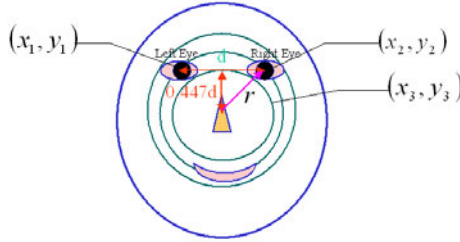


Fig. 3. Determination using a circle of the coordinates centering on transformation

$$\begin{cases} x_3 = \frac{1}{2}(x_2 + x_1) - 0.447(y_2 - y_1) \\ y_3 = \frac{1}{2}(y_2 + y_1) + 0.447(x_2 - x_1) \end{cases} \quad (x_2 > x_1) \quad (3)$$

In this case, the Log-Polar transformation explained by 2.1 only to the part enclosed with an inside circle and an outside circle is done.

2.3 Pattern Matching by the Part

The Log-Polar transformation of the face area of only the specific range in which both eyes and a mouth are settled is made. Because both eyes and a mouth are the portions which are the most characteristic in a face, it can recognize, if fixed width is given and matched with this circle. The part pattern matching which using the both eyes and a mouth is made. Therefore, high-speed processing is possible for not using a useless part.

As a concrete method, only the part of a face is matched for an input image and a template image. That is, the area of the mouth of an input image and the area of the mouth of a template image (MM: Mouth Matching), the area of the left eye of an input image and the area of the left eye of a template image (LEM: Left Eye Matching), the area of the right eye of an input image and the area of the right eye of a template image (REM: Right Eye Matching), each matching is done.

The value which integrated the value of each matching is used as an evaluation value. The value η of part pattern matching is calculated by Eq. (4).

$$\eta = MM \times LEM \times REM \quad (4)$$

It is necessary to remove the part into which individual difference does not clarify, for example the part is the cheek and the amount. If it does so, it will become easy to make facial recognition of the matching only by the part of the face of mouth and eye, and processing speed will also become quick.

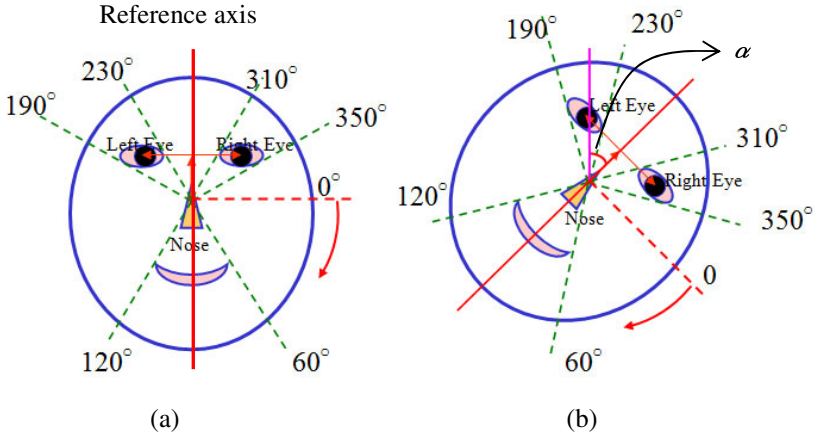


Fig. 4. Part pattern matching (a) The case of perpendicular face (b) The case of leaning face

As shown in Fig. 4. (a), the reference axis is set up after transformation center coordinates are decided. And, the area of mouth and eye can be divided by angle. Log-Polar transformation is done only to the divided area. As shown in Fig. 4. (b), when a face inclines, the angle leaned α can be calculated using the coordinates of a reference axis and an eye by Eq. (5), and it can answer also to the leaning face.

$$\alpha = \tan^{-1} \left(\frac{y_3 - y_1}{x_3 - x_1} \right) \tag{5}$$

3 Experimental Result

The verification experiment was done in order to confirm the validity of the proposal method. First, the comparative experiments of the method of proposing it as the method using the fixed conventional transformation center of extracting a transformation center automatically were done. Then, the verification experiment about the rapidity of the proposal method was done using the face image of ring form.

3.1 About the Automatic Detection of Transformation Center

In order to confirm the validity of the facial recognition by the Log-Polar transformation using transformation center detection, it has recognized by the same person using the original image and the image with which distance and the position are different. The image is shown in Fig. 5.

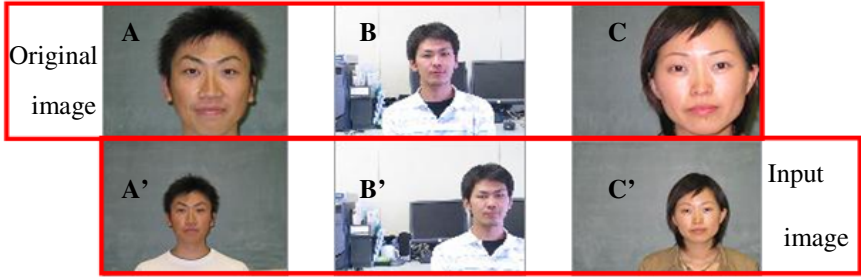


Fig. 5. The image for a verification experiment

The original image is A B C, and an input image is A' B' C'. An input image is an image captured in the place 2m away from the original image. Moreover, an input image shows that the position of a face is also different. The experimental result of matching is shown in Table 1.

Table 1. Comparison result

	A-A'	B-B'	C-C'
Fixed transformation center	0.867	0.861	0.878
Automatic extraction transformation center	0.990	0.992	0.990

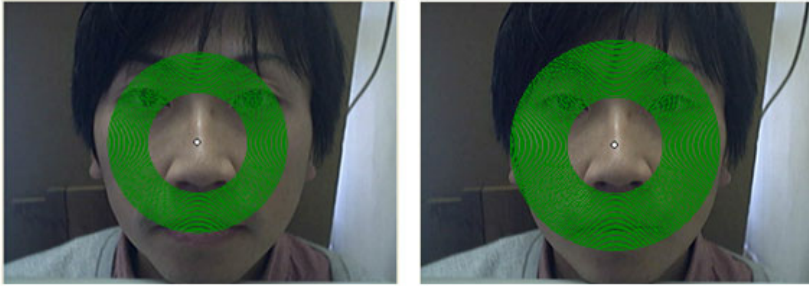
By the discernment using a fixed transformation center, the result of matching is which is 0.878 or less. However, in the discernment using an automatic extraction transformation center, the result of matching is 0.990 or more. It turned out that a maximum of 0.131 difference came out from the experimental result in spite of recognition of the same people. The validity of the facial recognition by the Log-Polar transformation using transformation center detection has been confirmed rather than the fixed transformation center.

3.2 About Improvement in the Speed of the Proposal Method

In order to realize improvement in the speed of processing, as 2.2 explained, it matches only using the part of ring form instead of the taken whole face image.

Here, two cases are considered. First, as shown in Fig. 6 (a), it is the case which uses the area only containing the minimum part of the area of both eyes and the mouth. In this case, the areas of the ring form which includes a transformation center for both eyes and the mouth as a center of a circle are 25 circles (green).

Second, as shown in Fig. 6 (b), it is the case which uses the area which can cover the area of both eyes and a mouth completely. In this case, the areas of the ring form which includes a transformation center for both eyes and the mouth as a center of a circle are 37 circles (green).



(a) The sizes of a ring area are 25 circles

(b) The sizes of a ring area are 37 circles

Fig. 6. The difference about the processing area, (a) is an area containing the minimum part of the area of both eyes and the mouth, (b) is the area which covered the area of both eyes and the mouth completely

In order to confirm the validity of the proposal method, it experimented for seven users (A~G). The captured face image is matched with the image registered. As an evaluation, we used the simple similarity to calculate. The result is shown in Table 2 and Table 3.

Table 2. The values of matching result 1

The sizes of a ring area are 25 circles							
	A	B	C	D	E	F	G
A	0.98885	0.94555	0.94372	0.91518	0.96432	0.96436	0.93536
B	0.94099	0.98248	0.88349	0.88399	0.95287	0.92182	0.94174
C	0.95647	0.9144	0.98485	0.91014	0.9375	0.95903	0.9154
D	0.91857	0.89121	0.90568	0.98991	0.89558	0.91511	0.87624
E	0.96379	0.95712	0.92036	0.89751	0.98424	0.92808	0.94736
F	0.94394	0.92932	0.95692	0.89751	0.92372	0.98762	0.91787
G	0.93968	0.95625	0.91107	0.88084	0.95898	0.93054	0.97901

The average matching value with the result of matching to others is 0.92737. It turns out that the average matching value with themselves is 0.98528. The difference of the average matching value of others' and themselves is 5.791%.

Table 3. The values of matching result 2

The sizes of a ring area are 37 circles							
	A	B	C	D	E	F	G
A	0.99109	0.91793	0.83433	0.85025	0.90683	0.8226	0.90748
B	0.89261	0.96782	0.78915	0.80803	0.83536	0.79979	0.86049
C	0.82429	0.79626	0.9714	0.88066	0.85039	0.95377	0.87496
D	0.85683	0.796	0.89137	0.96244	0.90203	0.90111	0.87192
E	0.92111	0.85571	0.87985	0.90561	0.98685	0.88721	0.94689
F	0.82094	0.79748	0.95873	0.90675	0.86781	0.98524	0.88837
G	0.91286	0.87951	0.88223	0.88983	0.95193	0.89842	0.98757

From the result of Table 3, the average matching value with the result of matching to others is 0.87323. It turns out that the average matching value with themselves is 0.97892. The difference of the average matching value of others' and themselves is 10.569%. It turned out that the difference of Table 3 is large. Because the area to cover became large, so it is thought that affect came out of the cause with hair. The run times are shown in Table 4.

Table 4. Comparison of the average of a run times

Whole image matching	Part pattern matching(25 circles)	Part pattern matching(37 circles)
(s)	(s)	(s)
61	8	10

From the result of Table 4, about 86.88% of the processing time was reduced when an area uses 25 circles, and about 83.61% of the processing time was reduced when an area uses 37 circles. From the experimental result, it can say that the proposed method is effective.

4 Conclusion

As one of the methods of facial recognition technology, there is the facial recognition method by Log-Polar transformation. However, the conventional method is the necessity of setting a transformation center manually. Moreover, it has the problem which takes the processing time.

In this paper, we proposed a method which calculated the transformation center automatically and high-speed facial recognition by Log-Polar transformation. The center of a face is automatically calculated using the position of the detected eye. Log-Polar transformation is done by setting this center as a transformation center. The degree of similar is calculated by matching with the picture which had the transformed picture registered. Moreover, when checking matching of an image, high-speed matching is realized by using part matching. The verification experiment was done in order to confirm the validity of the proposal method. The result showed that the proposal method was effective.

References

1. Hitoshi, H., Mamoru, Y., Kazuhiko, Y.: Face Recognition Using an Adaptive Discriminant Space. In: IEICE. PRMU 2001, vol. 121, pp. 59–62 (2001)
2. Maki, M., Kiyomi, N.: Real-time Iris Recognition System Using a Rotation Spreading Neural Network. In: IEICE. NC 2002, vol. 207, pp. 25–30 (2003)
3. Kazuhiro, H., Takio, K., Taketoshi, M.: Scale Invariant Recognition Method Using Spectral Features Extracted From Log-Polar Image. In: IEICE. PRMU 1999, vol. 110, pp. 69–76 (1999)
4. Takayuki, N., Yue, B., Naofumi, F.: A 3D Log-Polar transform for Pattern Recognition. Systems and Computers in Japan 38(13), 49–57 (2007)

Farmland Water Potential Soft-sensing Network Based on WSN

Liguo Tian¹, Meng Li¹, Zhiliang Chen¹, Shengli Lu¹, and Yue Liu²

¹ Key laboratory of Information Sensing & Intelligent Control, Tianjin University of Technology and Education, Tianjin 300222 China

² Tianjin Modern Vocational Technology College, Tianjin 300222 China
tlg1234@163.com, 3260711@163.com

Abstract. According to the needs of modern agriculture on the crop micro-environment information, the farmland water potential (FWP) soft-sensing network based on WSN could achieve crop micro-environment information collection, processing and transmission. The system was made up of the imbedded gateway and several WSN nodes, and configured relevant WSN nodes based on the requirements of the FWP soft-sensing, such as humiture collection node, illuminance collection node and CO₂ concentration collection node etc. The imbedded gateway received the data of all microenvironment information nodes, estimated the FWP value in real-time and communicated with the remote data center. In practical application, it works well.

Keywords: Wireless Sensor Networks (WSN), Farmland Water Potential (FWP), ZigBee, Data Acquisition.

1 Introduction

The Farmland Water Potential (FWP) that includes soil water potential, crop water potential and air water potential is important information to implement precision irrigation (PI)[1]. According to the PI requirements to the FWP information, the FWP soft-sensing network based on WSN is built. The network which is sub-net of the PI decision network is a star topology network which is made up of imbedded gateway (master node) and several collection nodes of microenvironment information (slave node). The FWP soft-sensing network adopts WSN technology [2] to collect all kinds of crop microenvironment information to the imbedded gateway through WSN's nodes distributed to different areas. The gateway transmits the preprocessed data to PI decision center through internet or Wi-Fi, thereby, to realize the long-range monitoring to the farmland environment parameters and provides data supports for the PI decision center.

2 Network Structure of FWP Soft-sensing

The FWP soft-sensing network is a subnet of the precision irrigation decision network, its over-all structure is shown in Fig.1. Many sensor network nodes and the

imbedded gateway constitute a star network; the data is transmitted to the remote data center by the common network platform (Internet or Wi-Fi). Every FWP soft-sensing network is made up of an ARM imbedded wireless gateway (master node) and several microenvironment information wireless collection nodes (slave node), and the data communication between the master and slave nodes is proceeded by ZigBee wireless communication technology [3]. ARM imbedded gateway mainly has three basic functions, namely, data receiving of microenvironment information network node, real-time evaluation of FWP, data transmission with PI center, and several sensor network nodes mainly is used to collect all kinds of microenvironment information and transmit the data to gateway.

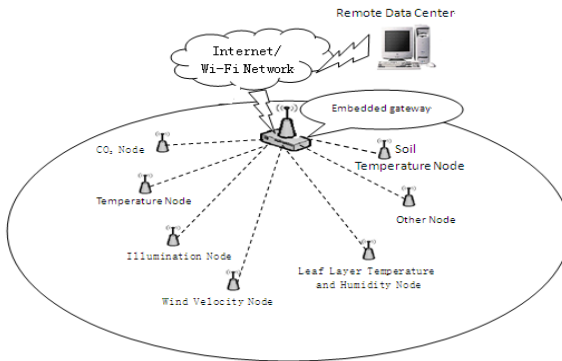


Fig. 1. The network structure of FWP soft-sensing

3 Imbedded Gateway

The imbedded gateway in the FWP soft-sensing network mainly has three basic functions, namely, data receiving of all microenvironment information network nodes, real-time evaluation of FWP value and data communication with remote data center. Under the circumstance of network, firstly, imbedded gateway takes charge of building the whole FWP soft-sensing network through ZigBee wireless route module; after the network is built successfully, the gateway could collect all microenvironment information; and then, the gateway preprocess the data which is received from all WSN nodes, and transmit the information to remote data center for next data analysis through Internet or Wi-Fi technology [4].

3.1 Hardware Design

The imbedded gateway in the FWP soft-sensing network builds a hardware platform with the core of the Samsung SoC type intelligent chip S3C6410 microprocessor, and its periphery is fitted out with ZigBee wireless route module, Wi-Fi communication module, SD card storage module and so on, so as to finish data receiving and storage of each WSN node and transparent data transformation between ZigBee and internet. The structure of gateway is shown in Fig.2.

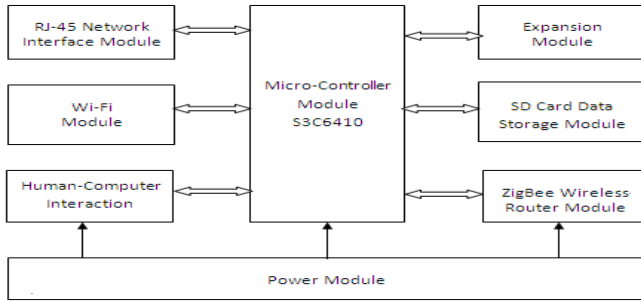


Fig. 2. The structure diagram of gateway system

The S3C6410 chip which is based on ARM1176JZF-S processor core contains 16KB instructions data Cache and 16KB TCM, and its basic frequency could reach 553MHz or 667MHz. The S3C6410 includes much peripheral hardware such as TFT 24-bit true color LCD controller, system manager (power supply management etc.), 4-channel UART, 32-channel DMA, 4-channel timer, universal I/O interface, I2C bus interface, SD primary device and high-speed multi-media interface etc.

The 54M wireless USB network card CWUSB54G used by Wi-Fi module is compatible with IEEE 802.11B/G standard, its wireless transmission rate reaches up to 54Mbps. Also, the CWUSB54G supports 64/128-bit WEP data encryption, meanwhile, supports WPA/WAP-PSK, WPA2/WPAS-PSK security regime. The CWUSB54G deployed a all-around intelligent antenna could adapt to different work circumstance, has better wireless performance and stability than any other similar products, meanwhile, supports wireless roam.

ZigBee wireless route module used the chip CC2530 which supports IEEE802.15.4, ZigBee, ZigBee PRO and ZigBeeRF-4CE standards is used for 2.4GHz free-license ISM frequency band, and establishes powerful network nodes by low cost. The ZigBee wireless route module communicated with processor by serial port is mainly used to transmit the data between the gateway and each sensor node.

3.2 Software Platform

The software system of the imbedded gateway mainly includes operation system and application system. The operation system selects imbedded Linux operation system which is an open-source, the kernel can be cut and re-configured operation system. Transplant of Linux operation system on ARM platform could be divided into the establishment of cross-compiling environment, transplant of Bootloader, Linux kernel and file system and design of system driver etc [4].

The cross-compiling environment is made up of compiler, connector and interpreter. Bootloader which is the first implemented software code after the system is electrified is used to start the operation system. This system selects YAFFS file system, which is the basis of all the data on the Linux system. The design of system driver mainly includes the driving design of Wi-Fi communication and ZigBee wireless communication etc.

The design of the application system is to compile the application program, which mainly includes the compiling of graphical interfaces, wireless data transmission and transformation of data format etc. so as to realize the necessary functions of imbedded gateway. The framework of whole software system is shown in Fig.3.

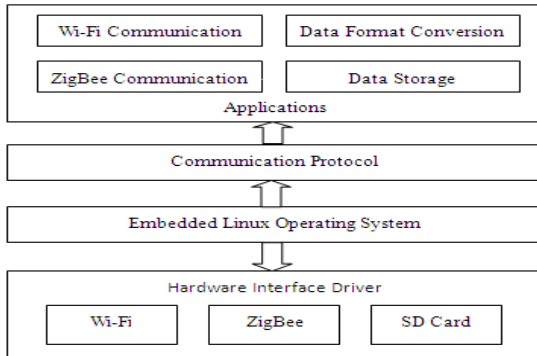


Fig. 3. The framework of software system

4 Wireless Sensor Network Node

The wireless sensor network nodes in the FWP soft-sensing network are responsible for the acquisition of all kinds of the crop microenvironment information. According to the selection of the auxiliary variables in the FWP soft-sensing technology, the microenvironment information need to be gathered mainly is illumination, humiture, air speed, CO₂ thickness, the crop canopy temperature and the soil temperature and moisture etc. so, various sensor network nodes are collocated in the FWP soft-sensing network to gather all the above microenvironment information. Configuration and arrangement of the sensor network nodes is listed in table 1.

Table 1. Software platform

Node position	Sensor configuration	Collection information
Crop Top	SHT11	Air temperature and humidity
	ZD Series Illumination Transmitter	Illumination
	M288865	Weed speed
	BM1000-CO ₂	CO ₂ concentration
Crop Root	TNR infrared temperature sensor	Canopy temperature
	PT100 thermal resistance temperature sensor	Soil temperature
	TR-5 soil moisture sensor	Soil moisture content
Crop Leaf Layer (UP、Central、Down)	SHT11	Temperature and humidity of crop leaf layer

The WSN node is mainly made up of micro-controller module, sensor module, wireless transmission module and power module. The micro-controller module is in charge of controlling the whole operation of node and completes the acquisition and processing of data; the sensor module is in charge of gathering all the microenvironment information; the wireless transmission module is in charge of the communication with

the master control node of the imbedded gateway, so as to accomplish the uploading of data; the power module is in charge of power supply to other three modules.

In view of the actual requirement of the FWP soft-sensing network, the design of the WSN nodes should be considered from the low power consumption, low cost, high reliability and expansibility. From the above, the micro-controller module in the WSN node uses AVR SCM ATmega8L; ZigBee wireless communication module uses RF chip CC2530 which is made by TI Company; the sensor module uses the relevant sensor.

4.1 The Leaf-Layer Humiture Acquisition Node

The Hardware Design. The leaf-layer humiture acquisition node is mainly made up of micro-controller module, sensor module, wireless transmission module and power module. The system chart is shown in Fig. 4.

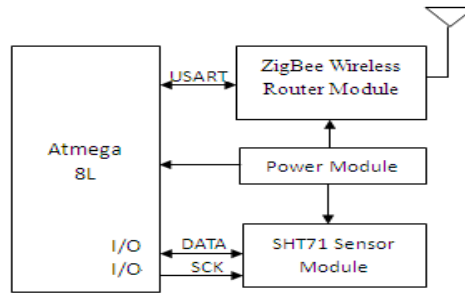


Fig. 4. The system chat of the leaf-layer humiture network node

The micro-controller module: ATmega8L made by ATMEL Company is a high-performance, low-power dissipation micro-controller; its operating frequency is 8MHz, and it has 5 kinds of sleeping modes and could be operated by the mode of low-power dissipation under the low voltage. It integrate 1K SRAM, 8K FLASH, one SPI, one USART and more common I/O ports [5].

The sensor module: SHT71 is a high-integrated chip which integrates many functions such as temperature sensing, humidity sensing and signal conversion, A/D conversion and heater, and output the digital signal. The SHT71 has high antijamming capability, higher cost performance and lower power dissipation; additional, all the technical index of the SHT71 is identical to the design requirement.

The wireless communication module: the CC2530 which is used for 2.4GHz free-license ISM frequency band is the second generation ZigBee® / IEEE 802.15.4 RF SoC of TI Company. It integrates enhancement-mode 8051 micro-controller kernel, 2.4GHz RF transceiver in accordance with IEEE802.15.4 standard, 256KB flash program memory which supports the latest ZigBee2007pro protocol stack, two powerful USART which support the multi-group serial protocol and one MAC timer which accords with IEEE802.15.4.

The power module: because the node is supplied by the battery, the integrated stabilivolt chip AMS1117 is used to stabilize the battery voltage to 3.3V which is provided to the microcontroller and CC2530 to ensure their normal operation.

The Software Design. The software design of the WSN nodes mainly includes the data gathering of the microenvironment, the data transmission of ZigBee. The output signal of the sensor module which is allocated for the microenvironment information acquisition node is divided into digital signal and analog signal. It is necessary to design different function to gather data according to the different sensors. The flow chart of node program is shown in Fig.5.

The communication between the micro-controller and CC2530 is serial operation. The serial port uses the interrupt mode to upload the data in the interrupt service routine. The initialized operation of the serial port as follows:

```
UCSRB=0x00;
UCSRA=0x00; //reset the control register
UCSRC=(1<<URSEL) | (0<<UPM0) | (3<<UCSZ0); // asynchronous
node; prohibit checkout; 1 stop bit; 8 data bit
UBRR=15; //Baud rate 57600
UCSRB=(1<<TXEN) | (1<<RXEN) | (1<<RXCIE); //receiving and
sending could be applied; receiving interruption could
be applied
```

The Flow of Network Node Program

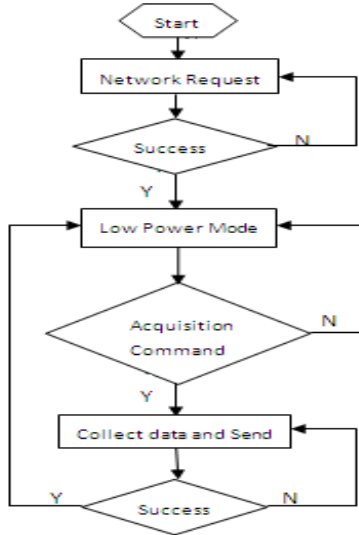


Fig. 5. The flow chat of network node program

4.2 Illumination Acquisition Node

The sensor module uses ZD series illuminance transmitter. This kind of transmitter adopts the high sensitivity silicon-blue photovoltaic detector as sensor that has the trait of wide measuring range, convenient installation and far transmission range etc. It can transfer the illumination intensity into current signal, and then after operation amplifier, the current signal can be transferred into voltage signal output, the output voltage is 0~5V, corresponding light 0~2e5Lux. The feature of ZD series transmitter is wide measurement range, convenient to use and install and far transmission distance.

4.3 The Air Speed Acquisition Node

The sensor module uses the M288865 sensor which is traditional wind-cup air velocity sensor. The wind cup adopts carbon fiber material provided with the feature of high intensity and easy to start etc.

4.4 CO₂ Acquisition Node

The sensor module uses BM1000-CO₂ sensor which is a measurement transmitter f special for measuring CO₂ in the air. It has nice cost performance. Additional, it adopts advanced infrared sensor, so, it works more steady and reliably.

4.5 The Soil Temperature Acquisition Node

The sensor module uses PT100 thermal resistance temperature sensor. The relationship between its resistance and temperature (indexing characteristics) does accord with IEC standard. PT100 can generate 0~5VDC signal, corresponding actual measuring temperature 0~80⁰C, and its precision is $\pm 0.5^0$ C.

4.6 The Canopy Temperature Acquisition Node

In order not to affect the growing of plants, the sensor module adopts non-contact lowcost TNR infrared temperature sensor (measuring range:-33~220⁰C, accuracy: $\pm 0.6^0$ C, response time: 1s, the most distance of measuring temperature: 10m). Because the infrared temperature measurement uses the radiant infrared ray of object to be tested to determine its temperature, this kind of method has superiority such as fast reflecting speed, high sensitivity, large measuring range and high precision etc.

5 Summary

Along with the WSN technology is more and more applied in the modern agriculture, the WSN technology is applied for the network of the FWP soft-sensing, which realizes the real-time monitoring and data gathering for all kinds of the crop microenvironment information, satisfies the requirements of low-power dissipation, low cost, low data transmission rate and high reliability under the farmland circumstance and provides the application of the FWP soft-sensing technology with data support.

Acknowledgements. The authors thank all the people who had given helps to them in the work.

This work is supported by the National Natural Science Foundation of China (Grant No.60772167), Tianjin University Science & Technology Fund (Grant No.20100721), and Development Foundation of Tianjin University of Technology and Education (Grant #KJ09-004).

References

1. Lu, S., Tian, L., Sun, W.: Farmland Water Potential Soft-sensing Faced to Precision Irrigation. *Tianjin University of Technology and Education Journal* 17(4), 1–4 (2007)
2. Sun, L., Li, J., Chen, Y.: *Wireless Sensor Network*. Tsinghua University Press, Beijing (2005)
3. Li, W., Duan, C.: *Introduction & Practice of ZigBee Wireless Network Technology*. Beijing Aerospace University Press, Beijing (2007)
4. Cai, H., Feng, R., Wan, J.: Wireless Sensor Networks Gateway with Multi—Communication Method. *Chinese Journal of Sensors and Actuators* 21(1), 169–172 (2008)
5. Zheng, L.: *Embedded System Design and Application Development*. Beijing Aerospace University Press, Beijing (2006)
6. Lu, S., Wang, J., Chu, J.: Selection of Auxiliary Variable & Data Processing in Farmland Water Potential Soft-sensing. *Modern Scientific Instruments* 4, 69–72 (2009)
7. Ma, C., Zhan, W., Geng, D.: *Atmega8 Principle & Application Manual*. Tsinghua University Press, Beijing (2003)

A Method for Searching Image Using Characteristic Point

Yusuke Umeda, Yue Bao, and Fei Gu

Tokyo City University, 1-28-1 Tamazutsumi, Setagaya-ku, Tokyo, Japan
bao@tcu.ac.jp

Abstract. The image processing method to discover a specific pattern out of the image is called template matching. Template matching searches the image by calculating the degree of coincidence to all pixels. However, this method has a problem which takes a long time for processing. In order to solve the problem, in this paper, we propose the image matching method using the characteristic points of the image. In the proposal method, first the original image and the template image is prepared. Next, we make the edge images which extracted from images which were prepared. And corners are extracted from edge images. In this paper, the corner is used as a characteristic point. It will use the characteristic points of those two images, when the image matching is done. As a result of the experiment, the template image was able to be searched from the original image using the proposal method.

Keywords: Template Matching, Characteristic Point, Searching Image, Edge Matching.

1 Introduction

The image which is the center of the visual means of communication of information is well used with the spread of multimedia environment. In order to utilize a lot of image information effectively, a computer needs to judge whether the object with which a user is interested and the contents are included in the picture. It is important that the domain and image situation can be extracted correctly if needed.

The technology for the image searching is called image matching or pattern matching. For example, it is used for image database search, pursuit of a move object, face detection of a digital camera[1][2]. There is template matching as a typical technique [3]. Template matching calculates the degree of coincidence based on the luminosity information on the image of two sheets. Since template matching shifts the image of two sheets for every pixel and calculates the degree of coincidence, there is a problem to which processing time becomes huge. Matching is performed using the various feature value, for example the method using a color histogram is proposed [4]. Furthermore, such as the active searching method which is searched at high speed are proposed [5].

In this paper, we propose a method to reduce the amount of calculation of matching by using image characteristic points. The place which matches a image by using a characteristic point can be looked for efficiently, and calculation of the degree of coincidence can also be reduced.

First, the template picture and the picture for search of 24-bit bitmap form are prepared. Next, image processing is carried out to the prepared image, and edge is extracted. Characteristic points are extracted after extracting edge. Then, a image is searched based on the position information on the acquired characteristic point. A characteristic point and the edge information extracted previously are used for calculation of the degree of coincidence.

2 Proposal Method

2.1 Characteristic Point Detection

A template image is discovered out of a image using the characteristic points. Unlike the conventional template matching, the proposal method matches partially. The flow of the proposal method is as follows.

First, edge is extracted from a original image and a template image. Edge and a characteristic point are extracted from the image. In order to extract edge information from the image, it is necessary to generate grayscale and binary image. Next, a characteristic point is extracted. The picture of two sheets is piled up based on the extracted characteristic point. In order to extract edge, the Canny-method is used.

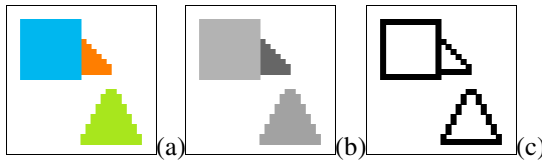


Fig. 1. (a) Color image (b) Gray scale image (c) Edge image

After extracting edge, characteristic points are extracted from the edge image. A characteristic point is taken as the corner which exists in the edge image.

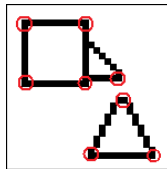


Fig. 2. The portion enclosed with a red circle is detected as a corner

This pretreatment is performed to the image which looks for a template image and template image. The degree of coincidence of a characteristic point and edge is calculated. The position of the most suitable picture is outputted with the degree of coincidence.

2.2 Image Matching by Characteristic Point

In the image matching, we use the edge and the characteristic point is extracted from the object image which looks for a template image and a template image. As shown in Fig. 3, edge and a characteristic point are extracted from an original image and a template image. A red point is a corner and let it be a characteristic point.

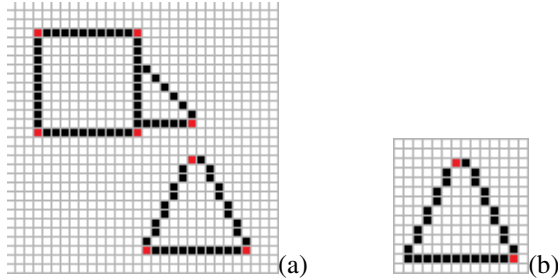


Fig. 3. (a) Original image (b) Template image, red points are characteristic point

First, the characteristic point of the original image and a template image is piled up. Next, other characteristic points of a template image check whether it overlaps with the characteristic point of the object image which looks for a template image. If it does not overlap, a template image is moved to another characteristic point.

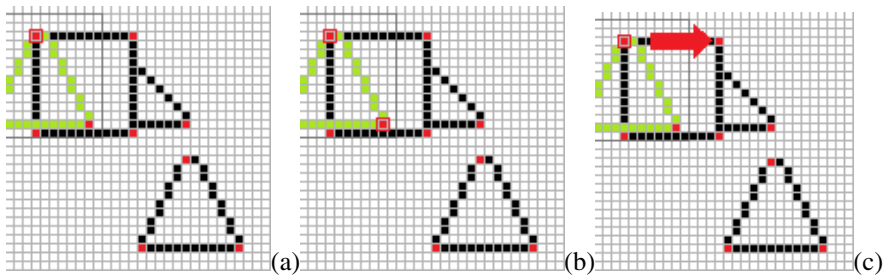


Fig. 4. (a) The characteristic point of a template image and an original image is piled up. (b) The check of other characteristic points (c) Movement of a template image.

Since a possibility that a template image is there is high when it overlaps, the degree of coincidence is calculated. The degree of coincidence counts the number of pixels of overlapping edge.

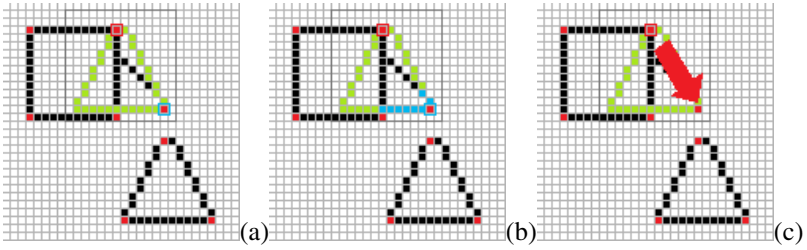


Fig. 5. (a) Other characteristic point’s overlapped (b) An overlapping edge pixel is counted (c) Movement of a template image

If the number of pixels of overlapping edge is counted and the coordinates of the piled-up characteristic point are recorded, a template image will be moved to another characteristic point. The above-mentioned processing is performed to all characteristic points. Finally the place where the degree of coincidence is the highest is outputted. As shown in Fig. 6, at (a), there are most pixels of the edge with which the template image and the original image have overlapped. As shown in Fig. 6, at (b), the place where the degree of coincidence is the highest is outputted.

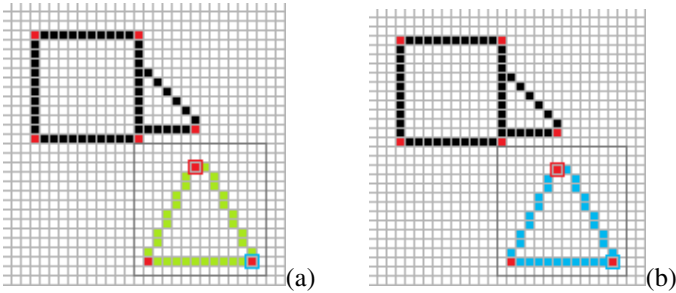


Fig. 6. (a) The place with which it overlaps best (b) A result is outputted

3 Experimental Result

The verification experiment was conducted in order to check the validity of the proposal method. The spec of the computer used for an experiment is shown Table 1.

Table 1. The spec of the computer

OS	Windows Vista Home Premium
Processor	AMD Athlon(tm)64 X2 Dual Core Processor 5000+ 2.6GHz
Memory(RAM)	2.00GB
Program environment	development Microsoft Visual Studio 2005 C++

Fig. 7 and Fig. 8 are images for the experiment. The following artificial images and natural pictures were prepared for the experiment. A template image is cut in part from a original image. And it is made smaller than the size of a original image.



Fig. 7. (a) The template image of an artificial image , the size is 60(W) \times 80(H) pixels. (b) The original image of an artificial image, the size is 240(W) \times 180(H) pixels.

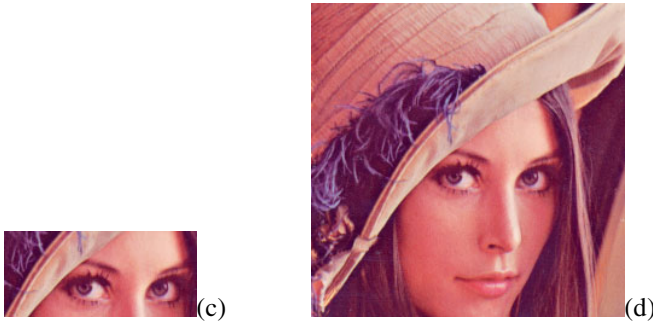


Fig. 8. (c) The template image of a natural image, the size is 160(W) \times 70(H) pixels. (d) The original image of a natural image, the size is 260(W) \times 260(H) pixels.

Image matching was performed using the method of detecting the characteristic point explained by 2. The detected characteristic point is shown in Fig. 9. First, Fig. 9 is an edge picture. Moreover, with a circle [red] shows the extracted characteristic point. It matches with the characteristic point of a former picture using these characteristic points.

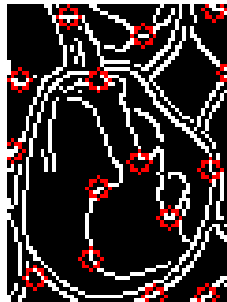


Fig. 9. Corner detection

The place enclosed with a red circle is a corner. These points were made into the characteristic point. This processing was performed to the template image and the original image.

Image search was performed using the proposal method. The place with a template image was enclosed by the red line. As a result of matching using the proposal technique, it was able to search for the template image like the following images.



Fig. 10. (a) The matching result of an artificial image (b) The matching result of a natural image

As a result of experimenting using the proposal method, the template image was able to be searched from the original image. It checked that the place searched for a template image was made to the characteristic point in a image. Unlike the conventional template matching, the proposal method has to search to not all pixels, and does not have to carry out excessive matching by matching only in the portion of a characteristic point. And it also checked that edge information could be used for calculation of the degree of coincidence.

Calculation of the degree of coincidence makes the amount of the features the number of pixels of edge, and just needs to count it. The degree of coincidence of the whole template picture is not necessarily calculated.

Since the number of times which matches fluctuates according to the extraction condition of a characteristic point, it is necessary to consider more effective pretreatment. It is required to make it correspond to the picture which rotated, and the image which changed size.

4 Conclusion

The image which is the center of the visual means of communication of information is well used with the spread of multimedia environment. In order to utilize a lot of image information effectively, a computer needs to judge whether the object with which a user is interested and the contents are included in the image.

In order to judge the contents in image, the technology of various image matching is studied. In this paper, the characteristic point in the image was used when image is matched. In the proposal method, first the original image and the template image is prepared. Next, we extract edge from the prepared images and make edge images. And corners are extracted from edge images. In this paper, the corner is used as a characteristic point. It's matched by extracting edge and a characteristic point from a template image and an original image. The place searched for a template image was used as the portion of the characteristic point in the image. And it searched by using edge information for calculation of the degree of coincidence. The template image could be searched from the original image using the proposal method as a result of the experiment, and the validity of this method was checked.

As a future subject, in the template image, rotation and a size may be changing. In such a case, it is thought that it is necessary to carry out the position information and the distance information between characteristic points.

References

1. Keiji, Y.: The Current State and Future Directions on Generic Object Recognition. IPSJ SIG-CVIM 48SIG_16(CVIM_19), 1–24 (2007)
2. Viola, P., Jones, M.: Rapid Object Detection using a Boosted Cascade of Simple Features. In: Proc. IEEE Conf. CVPR, pp. 511–518 (2001)
3. Template matching, <http://codezine.jp/article/detail/86?p=1>
4. Vinod, V.V., Murase, H., Hashizume, C.: Focussed color intersection with efficient searching for image detection and retrieval. In: IEEE International Conference on Multimedia Computing and Systems, ICMCS 1996, pp. 229–233 (1996)
5. Murase, H.: Fast Visual Search Using Focussed Color Matching: Active Search. J. IEICE J81(9), 2035–2042 (1998)

One Step Method for Capturing a Multi-view 3D Image

Tashuya Haga, Yue Bao, and Fei Gu

Tokyo City University
1-28-1 Tamazutsumi, Setagaya-ku, Tokyo, Japan
bao@tcu.ac.jp

Abstract. When creating a multi-view 3D image with one camera, the camera has to be moved from one viewpoint to another viewpoint. It would take a long time and high cost, and it can not get the image of a moving object. In this paper, we proposed the method for capturing a multi-view 3D image by one step. In order to capture a multi-view image, the lenticular lens is used in our proposed system. The captured multi-view image became reverse when we use the lenticular lens, it needs to perform reversal processing, and it also needs to calculate the best observation distance. When displaying a multi-view image, 3D image is possible to display using the same lens. As an experiment result, we got the multi-view image by our proposal system. And when we laid the multi-view image under a lenticular lens, the multi-view 3D image was confirmed.

Keywords: Multi-view Image, 3D Image, Lenticular Lens, Parallax, One Step.

1 Introduction

It is important for 3D display to get a multi-view image. As shown in Fig. 1, there were many methods for generating the multi-view image as the conventional methods. For example, there was a method to create multi-view image by moving the camera parallelly [1]. However, it takes a long time. Another method used two or more sets of cameras, one camera has one parallax [2]. However, it need many cameras, and is expensive. In this paper, we propose the method using lenticular lens and camera to generate the multi-view image.

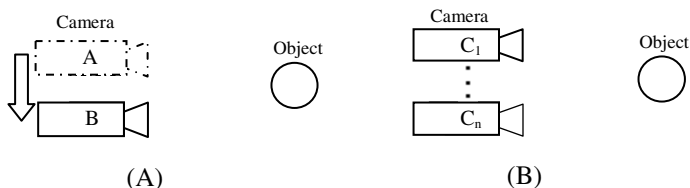


Fig. 1. (A) A photograph is moved and taken. (B) A photograph is taken by two or more sets.

As shown in Fig. 2, lenticular lens has many convex lenses. The synthetic image is placed under the lenticular lens. And when seeing through the lenticular lens, the image of B can be seen out the viewpoint position E1, and the image of A can be seen out the viewpoint position E2. It is possible to see the 3D image, If A and B are parallax pictures. When to capture the multi-view image, first, the lenticular lens is set in front of an object. Next, the camera captures an image by viewing the lenticular lens. Because this image is a mirror image, reversal processing must be carried out.

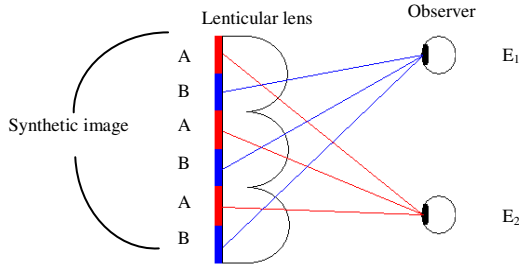


Fig. 2. Image by the lenticular lens

2 The Proposal System

As shown in Fig. 3(A), our system using a single lenticular lens and one camera, and can generate multi-view image in real time. At first, object image is captured at the underside of the lenticular lens. The image at this time is formed in right-and-left reverse by every cylindrical-surface convex lens. If displaying 3D image as shown in Fig. 2. Using this image, an observer will see a reverse stereoscopic picture in depth, so reversal processing is performed for every lens pitch as shown in Fig. 3(B).

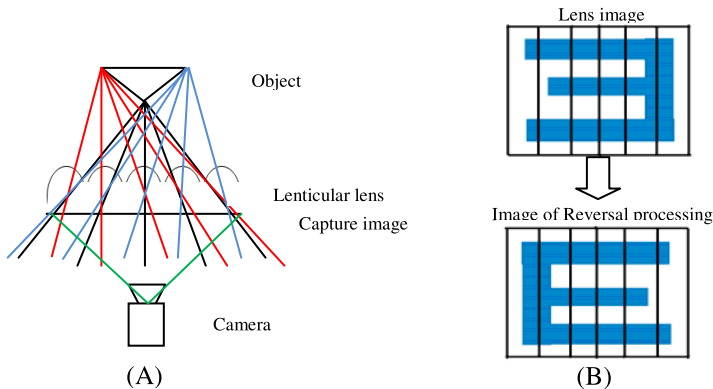


Fig. 3. (A) The situation of photography (B) Reversal processing

Furthermore, there is a point in reversal processing. Object image is captured at the underside of the lenticular lens in Fig .4 (A)-1. However, the observer sees only the center line of the image under the lens by the lens as shown in Fig. 4(A)-2.

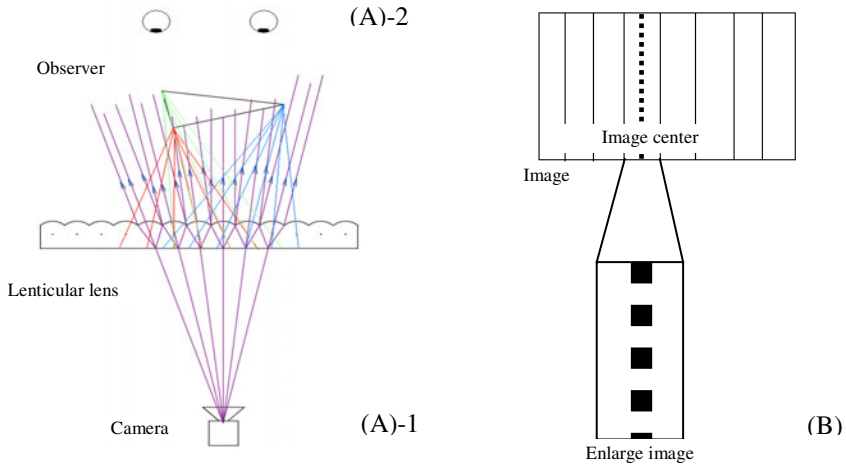


Fig. 4. (A)-1 Relation between a lens and a camera. (A)-2 Relation between a lens and an observer. (B) The situation of expansion.

And, we calculated the optimum viewing distance and view zone, by the lens formulas(Eq.(1)) in Fig. 5.As shown in Fig. 5, K is the distance between the eyes, and p is the distance between the viewing point of right eye and the viewing point of the left eye . D is the optimal viewing distance, t is the thickness of the lenticular lens, and r is the radius of curvature.

$$r = \frac{(n-1)pD}{NK} \quad K = \frac{pD}{(t-r)} \quad (1)$$

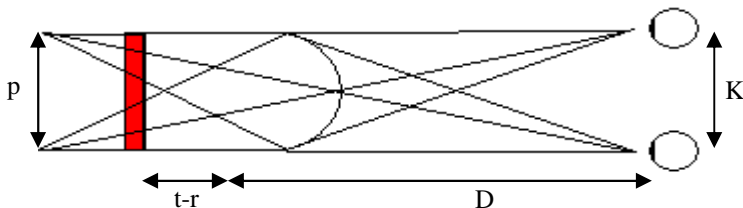


Fig. 5. Figure for calculating

3 Experimental Result

The experimental system is shown in Fig. 6, the camera is in the left side, the lenticular lens is in center, and object is in right side. If the focus of a camera is fit, there is no demand for the precision of the position of the camera. However the object should be put near the lenticular lens. If the distance between a lens and an object is optimal distance A, we can get an image-formation. However, if the distance between a lens and an object is B exceeding A, the image is not formed. (Fig.7)



Fig. 6. Experimental apparatus

If the distance between a lens and an object is optimal distance A, we can get an image-formation. His overlap area was seen from B=154mm. And, when the lens is near the object, an image formed with shallow stereoscopic effect. Image can be formed when the distance is between 48~153mm.

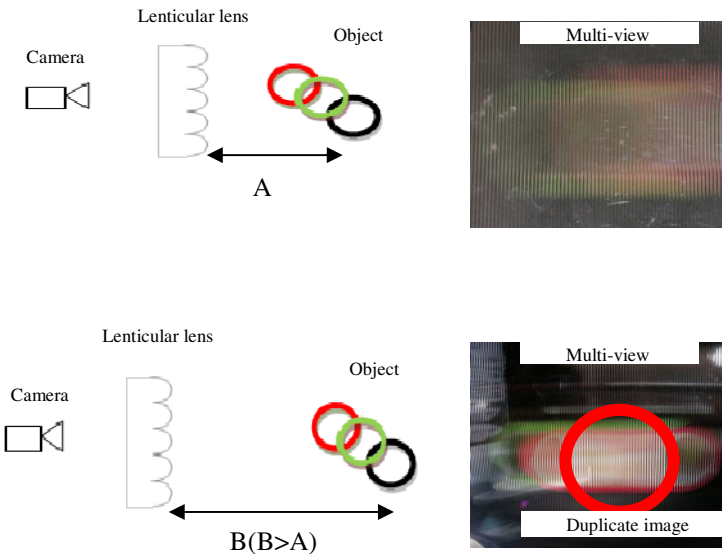


Fig. 7. Distance and image-formation

View area is much narrow, so we looked for the ideal place experimentally as shown in Fig. 8. In the end, 「 $\langle A=96\text{mm} \rangle$ 」 was found as a ideal distance of the lens and the object, but the brightness was not enough. Reversal processing is performed for every lens pitch in Fig. 9(A). The image expansion was performed based on the center position of every pitch in Fig. 9(B). Reversal processing is performed for every lens pitch as shown in Fig. 9(A).

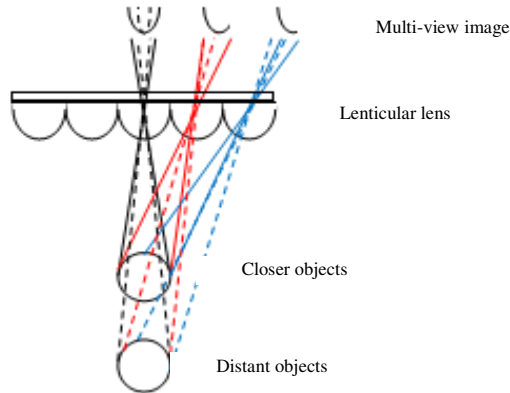


Fig. 8. Relationship between Lenticular lens and object

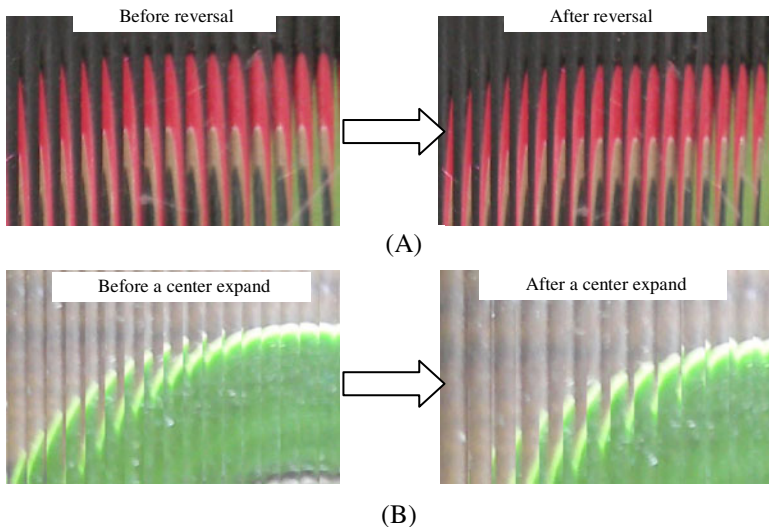


Fig. 9. This is the process of reversal processing

The displayed 3D image is shown in Fig. 10. The spec of the lenticular lens is shown in Table 1. Based on the proposal method, the observation experiment was conducted using a lenticular lens.

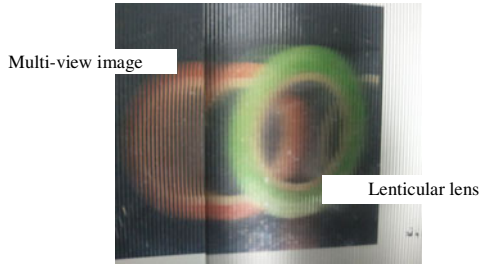


Fig. 10. Situation of display image

Table 1. The spec of the lenticular lens

Size	163mm(W)230mm(H)3.81mm(D)
Lens pitch	1.27mm(20LPI)
Radius of curvature	1.25295302mm
Material	Acrylics
Refractive index	1.49

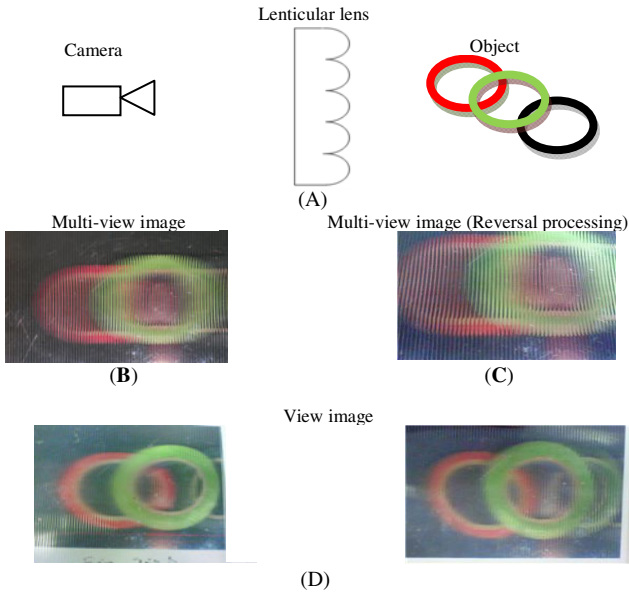


Fig. 11. (A) Capturing with camera and lenticular lens (B) Multi-view image (C) Multi-view image (Before reversal processing) (D) View images

We experimented based on the proposal method. The object first imaged on the lenticular lens as shown in Fig. 11 (A) was captured by the camera as a multi-view image of Fig. 11 (B). Because Fig. 11 (B) was reversed for every lens pitch, it is reversed by deciding center position of every lens of the lenticular lens. Then, we got

the image of Fig. 11 (C). When the observers see the image of Fig. 11 (C) by a lenticular lens for display, parallax accrues between the right eye and the left eye, and stereoscopic image is obtained. The observation experiment was conducted on ten persons. As the result, ten persons were able to see stereoscopic image. However, we found a new problem. It is that the observation region is too narrow.

4 Conclusion

The conventional methods for getting a multi-view image using one camera can not be used for moving-object. This paper proposed a method to get a multi-view image using a lenticular lens and one camera. The viewing zone and the viewing distance was calculated. The multi-view image is photographed by using the camera through the lenticular lens. However, observer looked the image reversed. However, in 3D image display using this image, an observer will see 3D image with reverse depth. Therefore, we determined the center of each pitch, and performed inversion processing. After reversal processing, the observer can see a 3D image. The observation experiment is done by ten persons, and the stereoscopic vision is appraised by all of them. However, a new problem is that the observation region is too small. Our future subject is to increase the observation region.

References

1. Stereoscopic Technology - - Forefront of Next-generation three-dimensional display technology
2. Noriji, O., Yue, B.: One-step method to take IP stereoscopic-picture by using a 2-dimensional concave lens array. ITE Technical Report 33(24), 15–18 (2009)
3. Toshiaki, F.: Multi-view Image Processing, 3-D Space Information Processing. The Journal of the Institute of Image Electronics Engineers of Japan, 891–894 (2008)

A Method for Searching Image Using Color Sketch

Masaya Hashimoto, Yue Bao, and Fei Gu

Tokyo City University, 1-28-1 Tamazutsumi, Setagaya-ku, Tokyo, Japan
bao@tcu.ac.jp

Abstract. In recent years, the number of photograph files which user holds is huge with the increase in a diffusion rate of a digital camera, and decrease in the price of storage media. For that reason, it will take a lot of times for discovering the target image from them. In this paper, searching image using a color sketch image is proposed. A color sketch image is drawn by user. The input image is changed from the value of RGB into the value of HSV for searching. It is compared with the images in the database with the value of HSV, and picture search is performed. As the result of an experiment, we confirmed validity of the proposal method.

Keywords: Searching Image, Color Sketch Image, RGB, HSV, Landscape Image.

1 Introduction

In recent years, the number of photograph files which a user holds is huge with the increase in a diffusion rate of a digital camera, and decrease in the price of storage media [1]. For this reason, it will take a lot of times for discovering the target image from them. About the conventional methods, there is a method that some keywords are given beforehand for each image, the keywords are used by searching for image. [2]. Although the method is convenient for the user who gave the keywords, it becomes difficult to search, if users don't know keywords. There is another method which uses a sketch image as a search key. Although it has high flexibility for a user, search accuracy is reduced. This method which is raising accuracy using the edge of a picture, it cannot use to a landscape image with unclear edge information [3].

In this paper, a method using a color sketch for searching landscape images is proposed. The color specification of images is changed to HSV from RGB [4][5]. Moreover, matching is performed for the images in a database. Matching is performed by comparison of pixels. The degree of coincidence is added or reduced with the relation of mutual pixels. The average of the points calculated is the degree of coincidence for the image.

2 Proposal Method

2.1 Definitions for the Image Color Information

By the proposal method, as shown in Fig.1, the colors used for matching are red, yellow, green, cyan, blue, and magenta. Moreover, as shown in Fig.2, the portion which

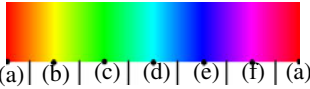


Fig.1. (a) is Red, (b) is Yellow, (c) is Green, (d) is Cyan, (e) is Blue, (f) is Magenta.



Fig. 2. The portion shown with red circles is black or white. Because it is hard to distinguish as a color, we use black and white for matching.

cannot be judged by a color is judged by black or white. For that reason, the proposal method can do intelligible searching by using only characteristic colors.

Furthermore, the color specification of HSV(Hue, Saturation, and Value) is used. For that reason, it can match without being influenced by brightness. Searching image is performed using the hue of the color sketch image.

The input image is changed from the value of RGB into the value of HSV for searching. Color specification conversion is performed by Eq. (1)~(3). R, G, and B are each value of RGB. The values of colors within a program are shown in Table 1.

$$H = \begin{cases} 30 * \frac{G - B}{\max(R, G, B) - \min(R, G, B)} + 0 & \text{if } \max(R, G, B) = R \\ 30 * \frac{G - B}{\max(R, G, B) - \min(R, G, B)} + 60 & \text{if } \max(R, G, B) = G \\ 30 * \frac{G - B}{\max(R, G, B) - \min(R, G, B)} + 120 & \text{if } \max(R, G, B) = B \end{cases} \quad (1)$$

$$S = \frac{\max(R, G, B) - \min(R, G, B)}{\max(R, G, B)} \quad (2)$$

$$V = \max(R, G, B) \quad (3)$$

Table 1. Conversion to the value of HSV from the value of RGB

Color	Hue	Saturation	Value
Red	0 and 180	255	255
Yellow	30	255	255
Green	60	255	255
Cyan	90	255	255
Blue	120	255	255
Magenta	150	255	255
White	0	0	255
Black	0	0	0

As shown in Fig.3, Sketch is divided into the image of red, yellow, green, cyan, blue, magenta, white, and black.

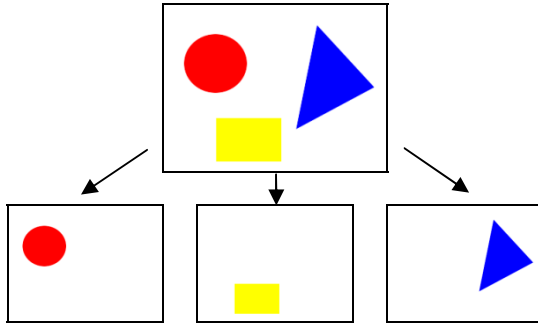


Fig. 3. Division into the picture for every color from a original picture

After the images from the database did preprocessing, the matching is performed. The flow of a preprocessing is shown below. The median of value of each pixel's hue is calculated, including the 8-neighbor pixels. As shown in Fig. 4, the 8-neighbor pixels are drawn red. These values become new value of each pixel's hue. Furthermore, the values are replaced with representative value shown in Table 2.

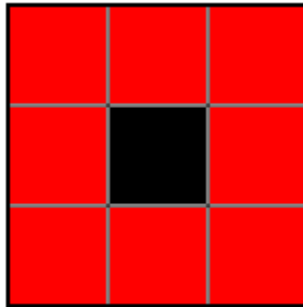


Fig. 4. The 8-neighbor pixels are red pixels. The median of the value of these nine pixels is calculated

Table 2. Replacing the calculated value with the representative value

Calculated value	Representative value
0~15 or 166~180	180(Red)
16~45	30(Yellow)
46~75	60(Green)
76~105	90(Cyan)
106~135	120(Blue)
136~165	150(Magenta)

Moreover, the new image is divided into the image of each color. At last, each the color image is performed dilation and erosion. The flow of preprocessing is shown in Fig. 5. *Img1* is original image. *Img2* is the image of median of value of hue. *Img3* is the image of Representative value. *Img4* is the image of divided image for yellow. *Img5* is the image got from *Img4* by dilation and erosion.

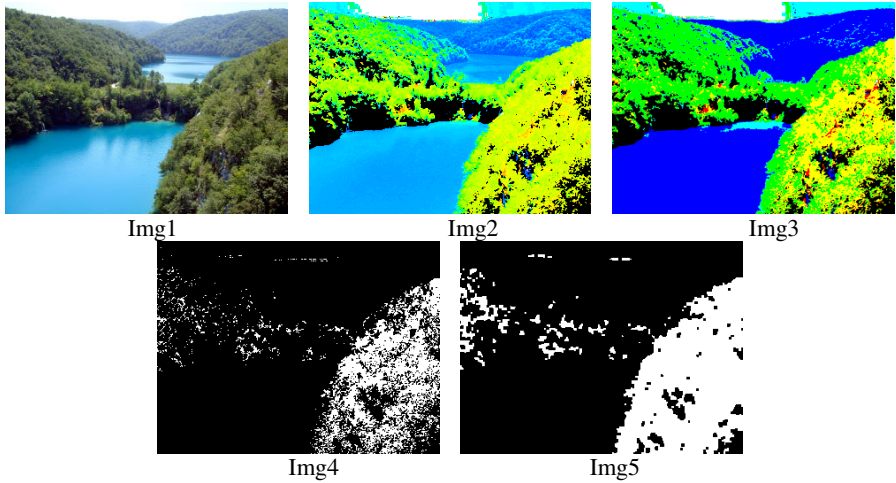


Fig. 5. Preprocessing for the image in the database

2.2 Rule of Matching

The aspect ratio of the image for matching is 4:3 because the image in the database is taken with the digital camera. The ratio is a ratio of the photograph taken with the digital camera which is sold in Japan.

Sketch image and images in the database are performed matching by using each color for calculating the degree of coincidence. Matching is performed by comparison of a pixel. The degree of coincidence is added or reduced with the relation of a mutual pixel. Score distribution is shown in Table 3 and Table 4.

For example, sketch image’s pixel is red and image in a database’s pixel is red, score is added 3 points. Furthermore from the results in Table4, sketch image’s pixel is white and value of image in a database’s pixel is 230, score is added 1 point. The average of the score calculated is the degree of coincidence for the images.

Table 3. The comparison results of color pixels

Sketch image	Image in the database	Result
Red	Red	+3
Red	Yellow	+2
Red	Green	+1
Red	Cyan	-2
Red	Blue	+1
Red	Magenta	+2

Table 4. The comparison results of black and white pixels. The images used for matching are the color sketch image and the image in the database which is changed to gray scale.

Sketch image	Gray image	Result
black	0~127	+1
white	128~255	+1

3 Experimental Results and Discussion

The landscape images of 50 sheets were used for the experiment. User decided the target image from them and experimented by drawing the sketch for search based on it. An experimental result is shown in Fig.6~ Fig.8. In case1, Res1.1 has the 1st high score (4.117473), Res1.2 has the 2nd high score(3.686013), and Res1.3 has the 3rd high score(3.216350). In case of Case1 and Case2, both of the target images of experimentation were the 3rd in scoring. Furthermore, in case of Case3, when the sketch image is drawn, the user thinks the Img3 in Fig5 as a target image. The target image of experimentation was the 2nd in scoring.

We considered the reason as following. The proposal method does not recognize the shape of the drawn sketch image correctly. The degree of coincidence is added points by the relation of the value without the matching of shapes. As a result, although the drawn shape differs from target image, the image is the 1st in scoring. Therefore, a new process should be added to the proposal method. The new process is matching on arbitrary direction based on the center of gravity of each color. By this method, Matching of shape is possible even if the position to draw is not exact.

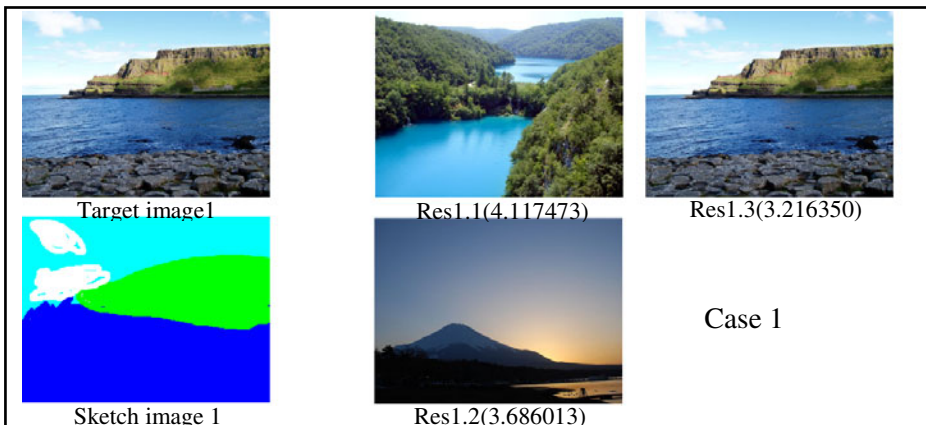


Fig. 6. Displaying the three high score images with search results of Case 1

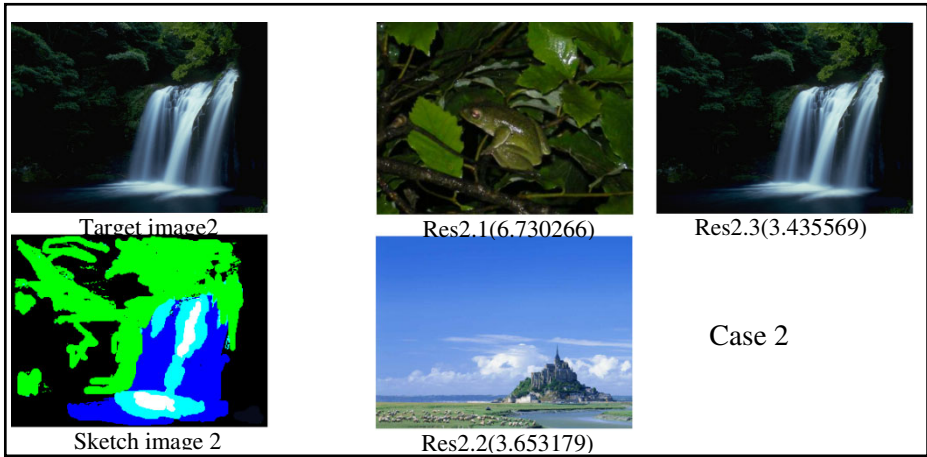


Fig. 7. Displaying to three high for search results of Case2

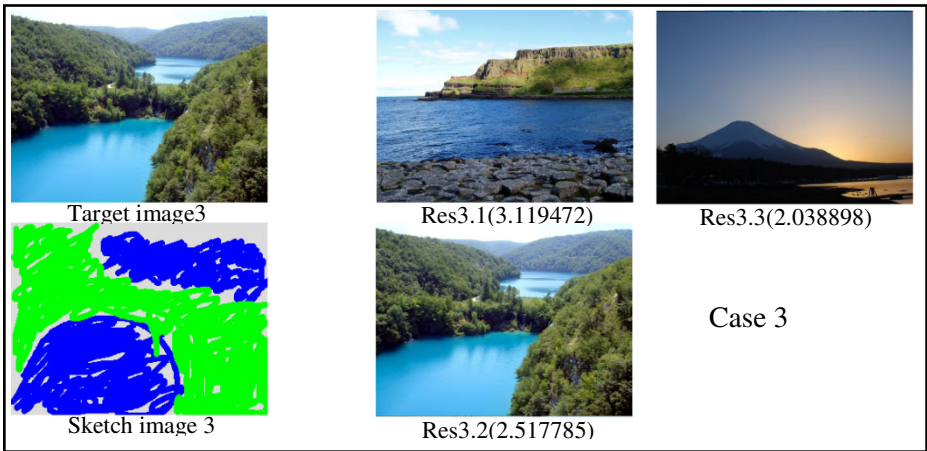


Fig. 8. Displaying the three high score images with search results of Case3

4 Conclusion

In recent years, the number of photograph files which a user holds is huge with the increase in a diffusion rate of a digital camera, and decrease in the price of storage media. For that reason, it will take a lot of times for discovering the target image from them. There were some conventional methods of searching image. The one of the conventional methods has low flexibility, because the method uses some keywords decided beforehand for searching. Another method which is raising accuracy using the edge of a picture cannot be used for a landscape image with unclear edge information. In this paper, a method for searching image using a color sketch image is proposed.

The proposal method aims at enabling correspondence to a landscape image by searching image with color information of sketch image. Color information is changed HSV from RGB for searching. The degree of coincidence for matching is decided by score from the relation nature of each color of pixels of the images which are the color sketch image and the image in the database.

The experiment was performed based on the above for confirming availability. As a result, the availability of proposal method was confirmed because the target image was displayed within the high order by the result of experiment.

References

1. Consumer's Behavior Survey by Cabinet Office in Japan
2. <http://www.esri.cao.go.jp/jp/stat/shouhi/2011/1103fukyuritsu.xls>
3. Masahiro, S., Seiki, I.: A measuring method of picture similarity by keyword sequence. *IPS, IPSJ* 39(2), 974–975 (1989)
4. Gosuke, O., Yasutake, N., Keita, M., Yoshifumi, S.: Edge-based Image Retrieval Using a Rough Sketch. *ITE, ITEJ* 56(4), 653–658 (2002)
5. Hiroyuki, S., Ichiro, F.: *Shikisai Kogaku Nyumon –Teiryoteki Na Iro No Rikai To Katsuyo-* (A Guide to Color Engineering-An Understanding and Practical Use of a Quantitative Color-). Morikita Syuppan Co., Ltd. (2007)
6. Noboru, O.: *Shikisai Kogaku (Color Engineering)*. Tokyo Denki University Publication Office (2001)

A Touch Screen Using One Camera and Two Mirrors

Akinobu Shimoyama, Yue Bao, and Fei Gu

Tokyo City University, 1-28-1 Tamazutsumi, zsetagaya-ku, Tokyo, Japan
bao@tcu.ac.jp

Abstract. We have at least one touch-screen devices. The most major touch screen is used resistive. However, resistive touch screen is not suitable for upsizing. This study proposes touch screen method with two mirrors and one camera. By using mirrors, we calculate the coordinates of the finger on one camera by triangulation. Experiments were performed to confirm the proposed method. We confirmed the effectiveness of the proposed method by the experiment results.

Keywords: Touch Screen, Optical, Camera, Mirror.

1 Introduction

Recently, the touch screen is used in various fields around the world. The touch screen is different to conventional device, we control by pressing on the screen display area. Touch screen technology changes the method by intended purpose.

Resistive touch screen uses a potential difference. Resistive film interspatially put on screen. (((When we operate the screen with your finger we current to flow through the screen contact with film.))) Resistive touch screen has many advantages, which are used in many touch screens. You can reduce costs and reduce the error due to dirt. It is unsuitable for enlargement because resistive film is need [1].

Optical touch screen technology is used as a way of upsizing [2]. The infrared emitter throws out the infrared light to be parallel to the display. There is an infrared image sensor adjacent to the emitter. Retroreflective plate is mounted in the frame of the display. Image sensor tracks the Retroreflected light of emitter. With images of the image sensor, we look for the angle of the emitter light interrupted by the finger. Optical method is comfortable to become upsizing, because it uses the normal panel in the display. However, this method requires two sets of image sensors and infrared emitters.

Our laboratory has studied on a polarization touch screen with camera [3]. The LCD panel uses straight line deflection plates. We set the straight line deflection plate on a camera. And adjust the angle of the film changed to see the display image. The camera can't take the display image through the deflection film. We calculate the coordinates of the finger with the processing camera images. This method is inexpensive touch screen with a single camera and a deflection film. However, we need to create a space between the camera and the display (Fig. 1).

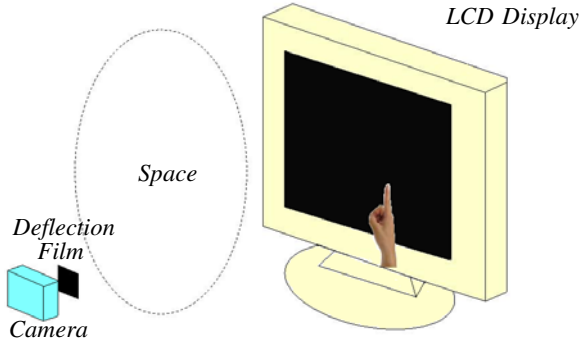


Fig. 1. Captured image with deflection film. We watch black image on the display because deflection film interrupt the display image.

In this paper, we propose the inexpensive touch screen by one camera and two mirrors. And this method doesn't take up much space.

2 System Configuration

In this study, we used two mirrors and one camera to make the touch screen system. We propose that uses triangulation to realize touch screen system. Fig. 2 is a Overview Figure of the system. Camera at K is set at right side of display. Two mirrors at A and B intersecting each other are set at left side of display. So, we can create two virtual cameras L and M. Black frames attach around the display. It will facilitate a robust processing to outside light.

ϕ is angle between the side of the display and mirrors. In this case, we can calculate the coordinates of virtual camera L(L_x, L_y), M(M_x, M_y) by Eq. (1) and Eq. (2).

$$\begin{cases} L_x = -K_y \times \tan(\phi) - (K_x + K_y \times \tan(\phi)) \times \cos(2\phi) \\ L_y = K_y + (K_x + K_y \times \tan(\phi)) \times \sin(2\phi) \end{cases} \quad (1)$$

$$\begin{cases} M_x = -K_y \times \tan(\phi) - (K_x + K_y \times \tan(\phi)) \times \cos(2\phi) \\ M_y = K_y - (K_x + K_y \times \tan(\phi)) \times \sin(2\phi) \end{cases} \quad (2)$$

2.1 Setting of Mirrors

We set up a mirror to reduce the error (Fig. 3). Camera A and Camera B take a picture of circle C. In this case, it is the smallest error with getting closer 120 degrees to the angle ACB. In this system, the angle between the mirrors A and B (2ϕ) is smaller than 120 degrees. Therefore, we adjusted so that the widest angle is between two mirrors.

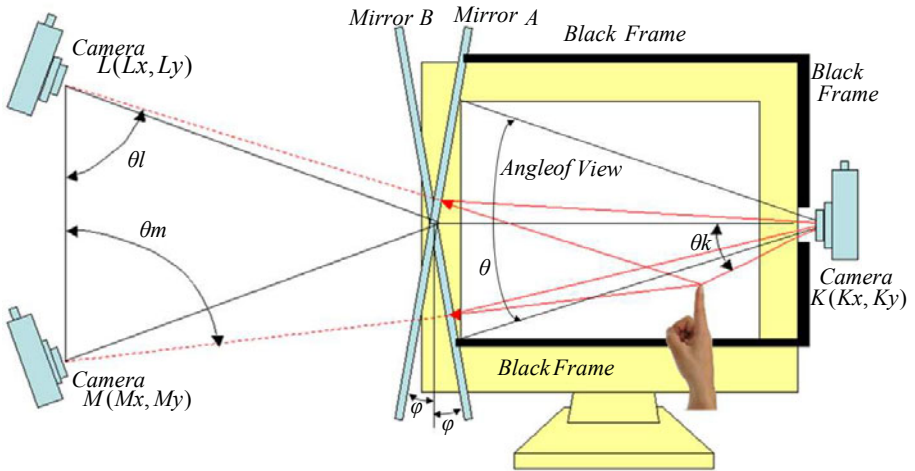


Fig. 2. Captured camera image. Three cameras take a picture of three fingers in each three areas.

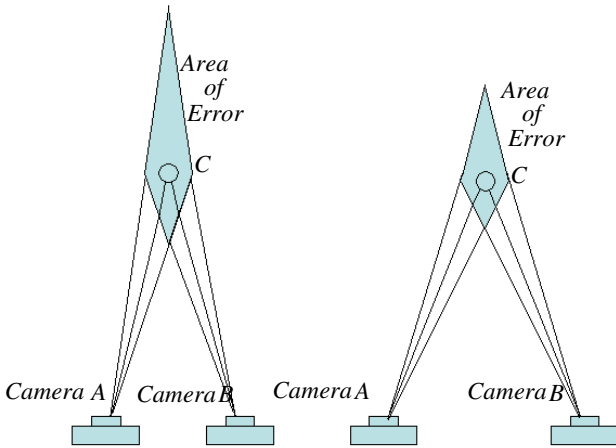


Fig. 3. Error of the camera angle. The area of error change depend on the angle ACB.

2.2 Image Processing Method

First, the input image from the camera is compensated by calibration for lens distortion. Next, we transform camera image into grayscale image and remove noise by median filtering. Then this image is binarized and by using the binarization image the fingers can be searched out at high speed. If you touch the screen, the camera will

get reflected images of the finger by the two mirrors, and the coordinate of the finger can be calculated as following. Fig. 4 shows how to detect a finger. Making area for three more fingers to measure the coordinates of the fingers. The three search area correspond to each three cameras.

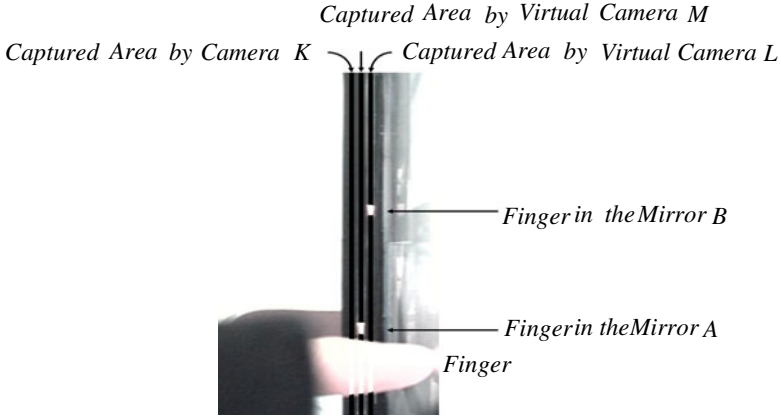


Fig. 4. Captured camera image

θ is Viewing angle of the camera K. θ_k , θ_l and θ_m are angle between line of gaze and finger in each camera image. α is The number of pixels between the finger in camera K's area and the point of gaze of the camera image. β is the total number of pixels. Therefore, θ_k is expressed by Eq. 3. Similarly θ_l and θ_m are determined. The display coordinates of finger by triangulation (x , y) is determined. Triangulation can determine the coordinates of the finger by using the two of the three cameras information. Eq. 4 was used a volume of cameras K and M. Specifically, (K_x , K_y), (M_x , M_y), θ_k , θ_m and θ .

$$\theta_k = \arctan\left(\frac{\alpha \tan(\theta)}{\beta}\right) \tag{3}$$

$$\begin{cases} x = \frac{K_y M_y + K_x \times \tan(\theta_k) + M_x \times \frac{1}{\tan(\theta_m)}}{\tan(\theta_k) + \frac{1}{\tan(\theta_m)}} \\ y = \frac{K_x M_x + K_y \times \frac{1}{\tan(\theta_k)} + M_y \times \tan(\theta_m)}{\tan(\theta_m) + \frac{1}{\tan(\theta_k)}} \end{cases} \tag{4}$$

3 Experiment

A prototype device (Fig. 5) was made for Experiment. PC, camera, and other specifications referred are shown in Tables 1.

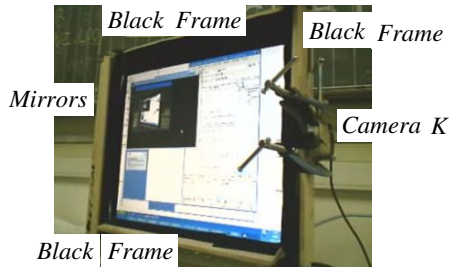


Fig. 5. Created experimental device

Table 1. Specifications

USB-cam	Model number: V-UJ15(Logitech Quickcam) Resolution: 640×480(pixel) Frame rate: 30fps Data format: RGB Angle of view: 52.5°
Mirror	(Length) 343 × (width) 5.5 × (thick) 1 (mm) Angle between two mirrors: 162.5°
Display	Model number : iiyama AS4314UT 17 inch TFT color LCD monitor Resolution: 1280×1024(pixel)
Black frame	width: 50mm

However, it was difficult to put the device on the calculated location. Therefore, we experimentally determined the position of the camera. The values of a evaluation experiment were used. Prepare a mark of the cross on the screen (Fig. 4). The location is 9 points of A(100, 100), B(100, 512), C(100, 924), D(640, 100), E(640, 512), F(640, 924), G(1180, 100), H(1180, 512), I(1180,924). The right hand point at straight the 9 points on the screen. We detected a total of five times each, and calculated the sum of squares. We evaluated error between coordinates of calculation and the coordinates of the mark. The result was shown in Fig. 6. 330mm at the side of the camera coordinates in the program, moved from 130mm to 140mm in 1mm increments ordinates, from 330mm to 370mm to move it to the abscissa. Abscissa of Fig. 6 was the result numbered.

Results, No.146 (343, 132) was most small error. From this, we set the coordinates of the camera K (343, 132).

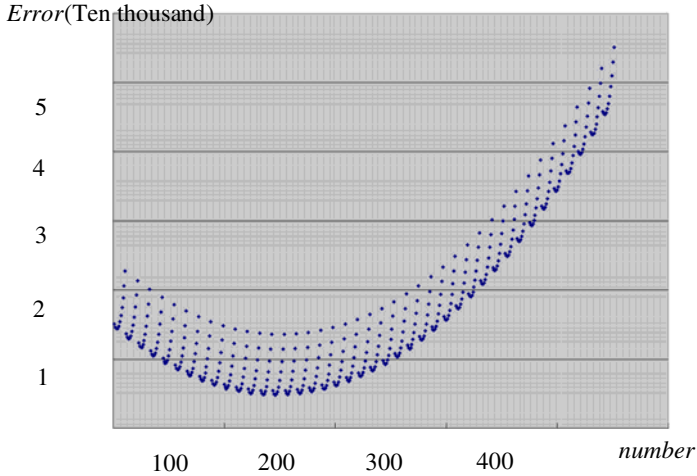


Fig. 6. Experimental result for positioning the camera

We conducted evaluation experiments using the camera coordinate (343, 132). The experiment uses same 9 points. The results is in Fig. 7.

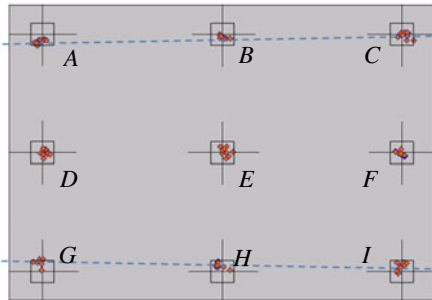


Fig. 7. Experimental result. Mark of a cross is the target and red circle was detection point.

Evaluation experiment results from all 90 trials, if you press the square button on 10 mm, there were mistakes in 44 times, and if you press the square button on 20 mm, there were mistakes in 2 times.

4 Discussion

We first think about the camera coordinate. Ordinates value (132mm) was different to expected. 135mm is the height of the center of the screen display. It had been shifted sideways 3mm. It caused by setting up a camera and mirrors. It was difficult for us to put in exact position with hand working. In this method, each error is very small, but the results lead to large errors. We need to correct an error from the program side.

We second think about evaluation experiment. The experimental results showed that the result was never significantly deviated. However, three points of A(100, 100), B(640, 100), C(1180, 100) result shifted downwards. And three points of G(100, 924), H(640, 924), I(1180, 924) result shifted upwards. This bias (Blue dotted line) is thought to have caused by the device position error. When we press the square button on 20 mm, there were mistakes in 2 times from all 90 trials.

As future work, we need to correct an error from the program side. This error will be corrected by the program side. And so, we will aim at reducing the error.

5 Conclusion

In this paper, we propose the inexpensive touch screen method performed by one camera and two mirrors. First, the input image from the camera compensate for lens distortion by calibration. Next, we transform camera image into grayscale image. And we remove noise by median filtering. Then we binarize this image. So, we are able to perform a search of the fingers. We experimentally determined the position of the camera. Then we conducted evaluation experiments using the camera coordinate.

The experimental results showed that the result was never significantly deviated. However, three points of A(100, 100), B(640, 100), C(1180, 100) result shifted downwards. And three points of G(100, 924), H(640, 924), I(1180, 924) result shifted upwards. This bias (Blue dotted line) is thought to have caused by the device position error. When we press the square button on 20 mm, there were mistakes in 2 times from all 90 trials.

As future work, we need to correct an error from the program side. This error will be corrected by the program side. And so, we will aim at reducing the error.

References

1. Masayuki, K.: Understanding touch screens. A new generation of man-machine interface. Denpa Shinbunsha Company (2005)
2. Satoshi, S., Fumihiko, N., Nobuyasu, Y., Yasuhide, I., Atsuo, I., Fumio, Y., Fumitaka, A.: Size detecting touch input panel suitable for large screens. IEICS, MVE 98(475), 55–61 (1998)
3. Takayuki, Y., Bao, Y., Yuusuke, U.: Touch screen with polarization analysis type. SSPATJ 11(1) (2008)

Hamiltonian of Line Graph under Condition of Constraint

Yong-Zhi Kan

School of Sciences, Liaoning University of Technology,
Jinzhou, Liaoning, 121001, P.R. China
kanyongzhi@yahoo.cn

Abstract. In this paper, a D -closed trail problem for a class of the graph G under condition of constraint is discussed. We prove line graph $L(G)$ of G is a Hamiltonian graph by using the method of induced sub-graph's degree analysis. The main result of this paper is that let G be a simple connected, almost bridgeless graph of order $n \geq 3$, $G \neq K_{1,n-1}$, Q_1 and Q_2 , if $d(I) \geq 2n-6$ for each induced sub-graph I isomorphic to P_4 , then, G has a D -closed trail. Accordingly, line graph $L(G)$ of G is a Hamiltonian graph.

Keywords: Hamiltonian line graph, D -closed trail, almost bridgeless graph.

1 Introduction and Main Results

This thesis discusses only simple undirected graph. Let $V(G)$ be a vertex set of G and $E(G)$ be a edge set of G . Line graph $V(G)$ of graph G satisfy: $V(L(G)) = E(G)$, $E(L(G)) = \{e_1 e_2 | e_1, e_2 \in E(G) \text{ and } |V(e_1) \cap V(e_2)| = 1\}$. Let $S \subseteq G$, $\langle S \rangle$ is the induced sub-graph that S is in the G . Let $G_1, G_2 \subseteq G$, we define the degree of G_1 : $d(G_1) = \sum_{v \in V(G_1)} d(v)$ where $d(v)$ is the degree of v which is in the G . Let $v \in V(G)$, $N_{G_1}(v)$ represents the vertex set adjacent to v in the G_1 , $N_{G_1}(G_2) = \bigcup_{v \in V(G_2)} N_{G_1}(v)$. $G_1 + G_2$ is defined the graph whose vertex set is $V(G_1 + G_2) = V(G_1) \cup V(G_2)$ and edge set is $E(G_1 + G_2) = E(G_1) + E(G_2)$. $\forall u, v \in V(G_1)$, let $d_{G_1}(u, v)$ be the distance of u to v in G . Let $V_1, V_2 \subseteq V(G)$, and $E(V_1, V_2)$ represents the number of edge for endpoints of G , which are placed in V_1 and V_2 , respectively. $\Gamma(G)$ represents the set of closed trail in G , if $T \in \Gamma(G)$, $\varepsilon_1(T)$ represents the number of edge for at least one endpoint of G is placed in the T , i.e., $\varepsilon_1(T) = |E(G)| - |E(G - V(T))|$. If $\exists T \in \Gamma(G)$, such that $\varepsilon_1(T) = |E(G)|$, then T is a D -closed trail of G . If all of bridges of G have a endpoint which degree is one, then G is almost bridgeless graph[1,2].

Harary and Nash—Williams [3] have proved that the line graph $L(G)$ of graph G is Hamiltonian graph if and only if G has a D -closed trail or $G \cong K_{1,n-1}$, and $n \geq 4$. This paper has proved the following theorem.

Theorem: Let G be a simple connected, almost bridgeless graph of order $n \geq 3$, $G \neq K_{1,n-1}$, Q_1 and Q_2 , if $d(I) \geq 2n - 6$ for each induced sub-graph I isomorphic to P_4 , then G has a D -closed trail. Accordingly, line graph $L(G)$ of G is Hamiltonian graph.

2 Preliminaries

Let $A = \{T | T \in \Gamma(G) \text{ and } |V(T)| \text{ is maximal}\}$, $A_0 = \{T | T \in A \text{ and } \varepsilon_1(T) \text{ is maximal}\}$. Hence $\forall T_0 \in A_0$, there is no $T_1 \in \Gamma(G)$ that has the property $M : |V(T_1)| > |V(T_0)|$ or $|V(T_1)| = |V(T_0)|$ and $\varepsilon_1(T_1) = \varepsilon_1(T_0)$.

Lemma 1[1,2]: Let G be a connected graph, if $T_0 \in A_0$, there is no $T_1 \in \Gamma(G)$, so that $V(T_1) \cap V(T_0) \neq \emptyset$, $V(T_1) \cap (V(G) - V(T_0)) \neq \emptyset$ and $|E(T_1) \cap E(T_0)| \leq 1$.

Lemma 2[8]: Let G be a connected graph, if $T_0 \in A_0$, K is a component of $G - V(T_0)$, and $|V(K)| \geq 2$, $\forall u_1, u_2 \in N_{T_0}(K) (u_1 \neq u_2)$ and $\forall u, v \in N_{T_0}(K) (u \neq v)$, $d = d_{G-V(K)}(u_1, u_2) \leq d_{G-V(K)}(u, v)$, $P_0 = u_1 w_1 \cdots w_{d-1} u_2$ is the shortest path of $G - V(K)$ between u_1 and u_2 , then we have the following results:

(1) if $d = 2$, namely, $P_0 = u_1 w_1 u_2$, then there is no cycle of T_0 that include $u_1 w_1$ or $u_2 w_1$, hence P_0 is included in certain cycle of T_0 .

(2) if $d = 2$, $N(w_1) \subseteq V(T_0)$, then w_1 is the cut vertex of T_0 , accordingly, $d(w_1) \geq 3$.

(3) if $d = 2$, then $\forall v \in V(K), N(v) \cap N(w_1) \cap (V(G) - \{u_1, u_2\}) = \emptyset$.

(4) if $d = 2$, then $N(u_1) \cap N(w_1) = N(u_2) \cap N(w_1) = \emptyset$.

(5) if $d = 2$, $C_0 = w_1 x_0 x_1 \cdots x_s x_{s+1} w_1 (x_0 = u_1, x_{s+1} = u_2)$ is the shortest cycle of T_0 which include $P_0 = u_1 w_1 u_2$, then

$$N(x_1) \cap N(w_1) \cap (V(G) - \{u_1, x_2\}) = N(x_s) \cap N(w_1) \cap (V(G) - \{u_2, x_{s-1}\}) = \emptyset.$$

(6) if $d = 2$, $|V(C_0)| \geq 5$, then $x_1 u_2, x_s u_1 \notin E(G)$.

(7) if $d = 2$, $C_0 = w_1 x_0 x_1 x_2 w_1 (x_0 = u_1, x_2 = u_2)$, i.e., $|V(C_0)| = 4$, P_1 is the same as one of the above, $d(x_1) = d(w_1) = 3$, and posses three different points, $v_1^0, w_1^0, x_1^0 \in V(G) - \{u_1, u_2, v_1, w_1, x_1\}$, $w_1^0, x_1^0 \notin V(K)$, such that $\{v_1 v_1^0, w_1 w_1^0, x_1 x_1^0\} \subseteq$

$E(G) - E(T_0)$, $G \neq Q_1$, then $\exists x \in \{u_1, u_2, v_1, v_1^0, w_1, w_1^0, x_1, x_1^0\}$, such that $E(\{x\}, \{u_1, v_1, v_1^0, w_1\}) \leq 1$.

(8) if $d = 2$, $C_0 = w_1 x_0 x_1 x_2 x_3 w_1 (x_0 = u_1, x_3 = u_2)$, i.e., $|V(C_0)| = 5$, P_1 is the same as one of the above, $d(w_1) = 3$ and $v_1^0, w_1^0 \in V(G) - \{u_1, u_2, v_1, w_1, x_1, x_2\}$, $v_1^0 \neq w_1^0$, $w_1^0 \notin V(K)$, such that $\{v_1 v_1^0, w_1 w_1^0\} \subseteq E(G) - E(T_0)$, $G \neq Q_2$, then

$\exists x \in V(G) - \{u_1, u_2, v_1, v_1^0, w_1, w_1^0, x_1, x_2\}$, such that $E(\{x\}, \{u_1, v_1, v_1^0, w_1\}) \leq 1$.

(9) if $d = 3$, then

$$N(u_1) \cap N(w_1) = \emptyset, N(u_2) \cap N(w_2) = \emptyset \text{ or } N(w_1) \cap N(w_2) = \emptyset.$$

(10) if $d = 3$, then

$$N(u_1) \cap N(w_2) \cap (V(G) - \{w_1\}) = \emptyset \text{ or } N(u_2) \cap N(w_1) \cap (V(G) - \{w_2\}) = \emptyset.$$

3 The Proof of Main Results

If G satisfy the conditions of the theorem, then G is not tree, and hence $\Gamma(G) \neq \emptyset$, and $A_0 \neq \emptyset$, let $T_0 \in A_0$.

We use proof by contradiction to prove the theorem. We assume $\varepsilon_1(T_0) \neq E(G)$ and G is connected so that $G - V(C_0)$ has a component $|V(K)| \geq 2$. In terms of Lemma 1 and G is almost bridgeless graph, we have $|N_{T_0}(K)| \geq 2$. Let $\forall u_1, u_2 \in N_{T_0}(K) (u_1 \neq u_2)$, and $\forall u, v \in N_{T_0}(K) (u \neq v)$, $d = d_{G-V(K)}(u_1, u_2) \leq d_{G-V(K)}(u, v)$. Let $P_0 = u_1 w_1 \dots w_{d-1} u_2$ be the shortest path of $G - V(K)$ between u_1 and u_2 , and let $P_1 = u_1 v_1 \dots v_k u_2$ be the shortest path between u_1 and u_2 , and satisfy $\emptyset \neq V(P_1) - \{u_1, u_2\} \subseteq V(K)$.

Let $V_0 = \{u_1, v_1, v_1^0, w_1\}$ and if $|V(P_1)| \geq 4$, we take $v_1^0 = v_2$, else $v_1^0 \in V(K)$, $v_1^0 \neq v_1$, $v_1^0 v_1 \in E(K)$. According to lemma 1, $\langle V_0 \rangle \cong I$.

The proof: Three points are discussed.

Point 1: $d = 2$

From lemma 2(1), let $C_0 = w_1 x_0 x_1 \dots x_s x_{s+1} w_1 (x_0 = u_1, x_{s+1} = u_2)$ be the shortest cycle of T_0 that include P_0 , from lemma 1 and lemma 2(2), $\exists w_1^0 \in V(G) - (V(K) \cup V(C_0))$, such that $w_1 w_1^0 \in E(G)$. From lemma 2(3) and (4), $E(\{w_1^0\}, V(K) \cup \{u_1, u_2\}) = 0$, we get $E(\{x_1^0\}, V_0) = 1$, and $\forall x \in V(G) - V_0$, $E(\{x\}, V_0) \leq 2$.

Point 1.1: $|V(C_0)| = 4$

Take x_i as w_1 , from lemma 2(2), we get $d(x_i) \geq 3$, and hence from lemma 1, lemma 2(2) and (5), $\exists x_i \in V(G) - (V(K) \cup V(C_0) \cup \{w_1^0\})$, such that $x_i x_1^0 \in E(G)$,

$E(\{x_1^0\}, V(K) \cup \{u_1, u_2, w_1\}) = 0$, and $E(\{x_1^0\}, V_0) = 0$. Let $V_1 = V_0 \cup \{u_2, x_1, x_1^0, w_1^0\}$.

Point 1.1.1: $d(x_1) = d(w_1) = 3$

From lemma 2(7), $\exists x \in V(G) - V_1$, such that $E(\{x\}, V_0) \leq 1$. And from lemma 1, we have $E(\{u_2, x_1\}, V_0) \leq 3$. Let $V_2 = V_1 \cup \{x\}$, then

$$\begin{aligned} d(I) &\leq 2(n - |V_2|) + 2|E(I)| + E(\{u_2, x_1, x_1^0, x, w_1^0\}, V_0) \\ &\leq 2(n - 9) + 6 + 5 = 2n - 7 < 2n - 6, \end{aligned}$$

contradiction.

Point 1.1.2: $d(x_1) > 3$ or $d(w_1) > 3$

Let $d(x_1) \geq 3$, from lemma 1, lemma 2(2) and (5), $\exists w_1^1 \in V(G) - (V(K) \cup V(C_0) \cup \{w_1^0\})$, such that $w_1 w_1^1 \in E(G)$. From lemma 2(3) and (4), we have $E(\{w_1^1\}, V(K) \cup \{u_1, u_2\}) = 0$, $E(\{w_1^1\}, V_0) = 1$. let $V_2 = V_1 \cup \{w_1^1\}$, then

$$\begin{aligned} d(I) &\leq 2(n - |V_2|) + 2|E(I)| + E(\{u_2, x_1, x_1^0, w_1^0, w_1^1\}, V_0) \\ &\leq 2(n - 9) + 6 + 5 = 2n - 7 < 2n - 6, \end{aligned}$$

contradiction.

Point 1.2: $|V(C_0)| = 5$. Let $V_1 = V_0 \cup \{u_2, x_1, x_2, w_1^0\}$.

Point 1.2.1: $d(w_1) = 3$

From lemma 2(8), $\exists x \in V(G) - V_1$, such that $E(\{x\}, V_0) \leq 1$. From lemma 1 and lemma 2(6), we have $E(\{u_2, x_1, x_2\}, V_0) = 3$. Let $V_2 = V_1 \cup \{x\}$, then

$$\begin{aligned} d(I) &\leq 2(n - |V_2|) + 2|E(I)| + E(\{u_2, x_1, x_2, x, w_1^0\}, V_0) \\ &\leq 2(n - 9) + 6 + 5 = 2n - 7 < 2n - 6, \end{aligned}$$

contradiction.

Point 1.2.2: $d(w_1) > 3$

From lemma 1, lemma 2(2) and (5), $\exists w_1^1 \in V(G) - (V(K) \cup V(C_0) \cup \{w_1^0\})$, such that $w_1 w_1^1 \in E(G)$. From lemma 2(3) and (4), we have $E(\{w_1^1\}, V(K) \cup \{u_1, u_2\}) = 0$, $E(\{w_1^1\}, V_0) = 1$. From lemma 1 and lemma 2(6), we get $E(\{u_2, x_1, x_2\}, V_0) = 3$. Let $V_2 = V_1 \cup \{w_1^1\}$, then

$$\begin{aligned} d(I) &\leq 2(n - |V_2|) + 2|E(I)| + E(\{u_2, x_1, x_2, w_1^0, w_1^1\}, V_0) \\ &\leq 2(n - 9) + 6 + 5 = 2n - 7 < 2n - 6, \end{aligned}$$

contradiction.

Point 1.3: $|V(C_0)| \geq 6$

From lemma 1, lemma 2(3) and (4), $\forall x \in V(C_0) - \{u_1, u_2, w_1\}$, we get $E(\{x\}, V_0) \leq 1$. From lemma 1, we get $E(\{u_2\}, V_0) \leq 2$. From lemma 1, lemma 2(4) and (6), we have $E(\{x_s\}, V_0) = 0$. Let $V_2 = V_0 \cup V(C_0) \cup \{w_1^0\}$, $V_1 = V_0 \cup \{u_2, w_1^0, x_1, x_2, x_s\}$, then

$$\begin{aligned}
 d(I) &\leq 2(n - |V_1| + 2|E(I)| + E(\{u_2, x_1, x_2, x_s, w_1^0\}, V_0)) \\
 &\leq 2(n - 9) + 6 + 5 = 2n - 7 < 2n - 6,
 \end{aligned}$$

contradiction.

Point 2: $d = 3$

Because $u_1, u_2 \in V(T_0)$, hence, according to choice of $P_0, \exists u_1^0, u_2^0 \in V(T_0) - V(P_0)$, such that $u_i u_i^0 \in E(T_0)$, $i = 1, 2$. From lemma 1 and choice of P_0 , we have $E(\{u_2, w_2\}, V_0) \leq 2$ and $\forall x \in V(G) - V_0, E(\{x\}, V_0) \leq 2$.

Point 2.1: $u_1^0 w_1 \notin E(G)$

If $u_2^0 w_1 \notin E(G)$, from lemma 1 and choice of P_0 , we have $E(\{u_1^0\}, V_0) = 1, E(\{u_2^0\}, V_0) = 0$. Let $V_1 = V_0 \cup \{u_2, w_2, u_1^0, u_2^0\}$, then

$$\begin{aligned}
 d(I) &\leq 2(n - |V_1| + 2|E(I)| + E(\{u_2, w_2, u_1^0, u_2^0\}, V_0)) \\
 &\leq 2(n - 8) + 6 + 3 = 2n - 7 < 2n - 6,
 \end{aligned}$$

contradiction.

If $u_2^0 w_1 \in E(G)$, from lemma 2(9), $u_2^0 w_2 \notin E(G)$, from lemma 2 (10), $u_1^0 w_2 \notin E(G)$, take u_2, w_2 as u_1, w_1 respectively; take v_k as v_1 , we can prove similarly as point 2.1.

Point 2.2: $u_1^0 w_1 \in E(G)$

From lemma 2(9), $u_2^0 w_2 \notin E(G)$, $u_1^0 w_2 \notin E(G)$, take u_2, w_2 as u_1, w_1 respectively, take v_k as v_1 , we can prove similarly as point 2.1.

Point 3: $d \geq 4$

Because $u_1, u_2 \in V(T_0)$, according to choice of $P_0, \exists u_1^0, u_2^0 \in V(T_0) - V(P_0)$, such that $u_i u_i^0 \in E(T_0)$, $i = 1, 2$. From lemma 1 and choice of P_0 , we have $E(\{u_2^0, w_3\}, V_0) = 0$, $E(\{u_2\}, V_0) \leq 1$, $E(\{u_1^0\}, V_0) \leq 2$, $E(\{w_2\}, V_0) = 1$, $E(\{w_i\}, V_0) = 0$, $i = 3, \dots, k$, and $\forall x \in V(G) - V_0, E(\{x\}, V_0) \leq 2$. Let $V_1 = V_0 \cup \{w_2, w_3, u_1^0, u_2, u_2^0\}$, hence

$$\begin{aligned}
 d(I) &\leq 2(n - |V_1| + 2|E(I)| + E(\{w_2, w_3, u_1^0, u_2, u_2^0\}, V_0)) \\
 &\leq 2(n - 9) + 6 + 4 = 2n - 8 < 2n - 6,
 \end{aligned}$$

contradiction.

4 Conclusion

This thesis discusses mainly Hamiltonian problem on line graph of simple connected, almost bridgeless graph of order $n \geq 3$, and discusses the existence of D -closed trail. We get the better results on Hamiltonian line graph under using the method of induced sub-graph's degree analysis.

References

1. Benhcine, A., Clark, L., Kohlar, N., Veldman, H.J.: On Circuits and Pancyclic line graph. *J. Graph Theory* 3(10), 411–425 (1986)
2. Zhao, L.C., Liu, C.F.: A Sufficient Condition for Hamiltonian Line Graph. *Applied Mathematics* (1), 22–26 (1990)
3. Harary, F., St. Nash-Williams, C.J.A.: On eulerian and hamiltonian graph and line graph. *Canada Math. Bull* 8, 701–710 (1965)
4. Veldman, H.J.: A Result on Hamiltonian Line Graphs Involving Restrictions on Induced Subgraphs. *J. Graph Theory* 12(3), 413–420 (1988)
5. Zhao, L.C., Liu, C.F., Wang, H.: Note on Hamiltonian Line Graph. *Journal of Applied Mathematics* 9(1), 17–20 (1986)
6. Clark, L.: On Hamiltonian line graph. *J. Graph Theory* 8(3), 303–307 (1984)
7. Zhao, L.C., Liu, C.F.: A Sufficient Condition for Hamiltonian Line Graph. *Journal of Qufu Normal University* 15(4), 15–20 (1989)
8. Liu, C.F.: On Hamiltonian Line Graph in Graph K_3 -Free. *Journal of Shenyang Golden University* 13(4), 383–386 (1994)

The Performance Persistence of Mutual Fund: The Empirical Research Based on Cross-Sectional Regression

Cunzhi Tian¹, Qiuping Guo², and Haijun Wang³

¹ Economic Research Center, Kunming University of Science and Technology, Kunming, China, 650093

² Faculty of Management and Economics, Kunming University of Science and Technology, Kunming, China, 650093

³ The Industrial Bank in Hangzhou, Hang zhou ZheJiang, China, 311500
tiancunzhi@sina.com, 154260472@163.com, whj85@126.com

Abstract. Based on cross-sectional regression, this paper investigates the performance persistence of stock fund. The empirical result shows that there is some persistence in the stock fund's short, interim or long-term performance, though it is not stable. However, there is even some reversal in several periods.

Keywords: Stock fund, Performance persistence, Jensen index, Cross-sectional regression.

1 Introduction

With the rapid development of fund and securities markets in China, how comprehensive evaluation of the Fund's performance and select the appropriate fund has been plagued by a large number of fund investors. But domestic has not yet formed some authoritative rating agencies as foreign S & P and Morningstar etc to evaluate the management efficiency and operational capacity of fund. However, in many ways of the evaluating the performance of the Fund, fund performance persistence phenomenon may provide a great help to solve the problem that how fund investors to choose fund. The performance persistence of mutual fund in essence is that mutual fund also performed at a later stage of good behavior in early can still stands in the same industry, reflected in the fund rankings for funds in the next period of the early top ranks near the top. That is, it is often said that "the strong and constant intensity, constant of the weak weaker".

If the fund's performance has a persistent, then the investor can choose the fund that the pre-fund performance is better, buy and hold and can get huge benefits. Investors can also try to avoid poor performance of the pre-fund in order to avoid risk. Therefore, fund performance persistence research has become the field of securities market theory and practice focus of attention.

In this paper, we use the 82 samples of the current domestic stock fund types and four-year data sample, using the Jensen Alpha value as the Fund's risk-adjusted returns as a performance indicator and using cross-sectional regression on fund performance

persistence of inspection and to investigate the performance persistence of stock fund continued existence or not.

Our paper proceeds as follows: Section 2 reviews the literature. Section 3 presents empirical design, and describes our data sources and sample selection. Section 4 presents the Empirical results and analysis. Section 5 concludes the paper and presents policy recommendations.

2 Literature Review

The first one to propose the fund persistence is Sharpe(1966), with the Spearman rank correlation coefficient test, who found that fund performance does not show any persistence. The other one Jensen(1968), with the Jensen index which he first proposed to assess the fund performance, found that the well-performed fund in the past doesn't perform well in the future. Hendricks, Patel and Zeckhauser (1993), Goetzmann and Ibbotson (1994), Brown and Goetzmann (1995), Wermers (1996) etc all found that mutual fund performance exactly exist certain persistence in the short period from 1 year to 3, they regarded the reason why that happened as the "hot hand" or a general investment strategy. However, Grinblatt and Titman (1992), Elton, Gruber, Das and Hlavka (1993) etc found that there are performance persistence from 5 to 10 years for the mutual fund, which can be attributed to the private information of the managers and their stock selection ability.

Nisu Yun, Xiao Hui, Wu Chongfeng (2002) studied the performance persistence of the twenty-two closed funds established before the end of 1992, which supports that, both in the single-factor model and the multi-factor model, the fund persistence exists no persistence in unilateral increasing stage, while which shows a reversal in the whole sample. Zhuang Yun zhi, Tang Xu (2004) study the performance persistence of our country's twenty-two closed-end funds from the end of 1999 to June 2003, which shows the short term performance have no persistence, but the medium-long term performance exist certain persistence. Peng Shoukang(2010) shows that the underperformance exists significant persistence, the reason is many underperformance funds assumed the high-risk do not get high-yield compensation, and the performance of those funds are still very poor.

In this paper we only select four years' data of eighty-two samples of the stock fund and use cross-sectional regression to test the performance persistence to discuss if the performance of mutual fund exist persistence or not.

3 The Empirical Design

3.1 Model Design

This article first presents the following regression equation :

$$r_{pt} - r_{ft} = \alpha_p + \beta_p (r_{mt} - r_{ft}) + \varepsilon_{pt} \quad (1)$$

We obtain the Jensen index α_p , where Jensen index α_p represents the fund's performance. In order to examine whether existence performance persistence of stock fund, we divide the sample into T group ranking and evaluation period. Specific model is as follows:

$$\alpha_{i,t+\lambda} = c_t + \varphi_{i,t} \alpha_{i,t} + \varepsilon_{i,t} \quad (2)$$

Where $t = 1, \dots, T$; $i = 1, \dots, n$. Estimated cross-sectional regression model (2), we obtained coefficient sequence φ_t .

Final we test the significance of coefficient sequence φ_t . If φ_t is significantly zero, it indicates that there is no fund performance persistence; If φ_t is significantly positive, it indicates that Existence continuity of fund performance; if φ_t is significantly negative, it indicates that Existence reversal of fund t performance.

3.2 Data and Sample

This data comes from Wind financial information terminal. To ensure that the study sample interval can better coverage to the rising and falling market index, this selection of sample spacing for 2006-6-23-- to 2010-7-2, a total of 4 years¹. This article screening duration in 2006-6-23 to 2010-7-2 total of 82 stock funds, excluding holidays, each fund has 204 week rate of return data.

3.3 Ranking and Evaluation Division of the Period

This article will examine the fund short, medium and long-term persistence of stock fund earnings². this article defines the June 23, 2006 to September 31, 2006 as the first ranking period, corresponding to October 1, 2006 to December 31, 2006 is defined as the first an evaluation period; Defines the October 1, 2006 to December 31, 2006 as the second ranking period³, from January 1, 2007 to March 31, 2007 defined as the second evaluation period⁴. From January 1, 2007 to March 31, 2007 is defined as the second evaluation period. And so on, as of July 2, 2010 we can obtain to 15 ranking period and the evaluation period. Similarly, we can obtain to the ranking period and the evaluation period of 6 months and 18 months.

4 Empirical Results and Discussion

Table 1, table 2 and table 3 respectively report the results of a cross-sectional regression model estimate of (2).

¹ During this period experienced the bull market and bear market in two waves.

² 3 months for the short-term, 6 months for the medium term, 18 months for the long-term.

³ Relative to the first ranking period pushed back three months along.

Table 1. The test results of the performance persistence of stock fund in 3 months

<i>ranking period</i>	<i>evaluation period</i>	<i>Coefficient</i>	<i>P-value</i>	<i>Adjusted R-squared</i>	<i>F value of significance</i>
The third quarter of 2006	Last quarter of 2006	0.4950	0.4623	-0.0069	0.4623
Last quarter of 2006	The first quarter of 2007	-0.0175	0.8389	-0.0147	0.8389
The first quarter of 2007	The second quarter of 2007	-0.0046	0.9435	-0.0069	0.4623
The second quarter of 2007	The third quarter of 2007	-0.0388	0.8859	-0.0151	0.8859
The third quarter of 2007	Last quarter of 2007	0.0153	0.6478	-0.0121	0.6478
Last quarter of 2007	The first quarter of 2008	0.0522	0.5571	-0.0098	0.5571
The first quarter of 2008	The second quarter of 2008	0.2491	0.3720	-0.0029	0.3720
The second quarter of 2008	The third quarter of 2008	-0.0901	0.1237	0.0209	0.1237
The third quarter of 2008	Last quarter of 2008	-0.1707	0.2010	0.0099	0.2010
Last quarter of 2008	The first quarter of 2009	-0.0763	0.5822	-0.0105	0.5822
The first quarter of 2009	The second quarter of 2009	-0.0138	0.9013	-0.0149	0.9013
The second quarter of 2009	The third quarter of 2009	0.0902	0.4041	-0.0044	0.4041
The third quarter of 2009	Last quarter of 2009	0.4940*	0.0000	0.2270	0.0000
Last quarter of 2009	The first quarter of 2010	0.5300*	0.0000	0.3043	0.0000
The first quarter of 2010	The second quarter of 2010	0.1340	0.5166	-0.0087	0.5166

Note: * indicate significance at the 5% level.

Table 2. The test results of the performance persistence of stock fund in 6 months

<i>ranking period</i>	<i>evaluation period</i>	<i>Coefficient</i>	<i>P-value</i>	<i>Adjusted R-squared</i>	<i>F value of significance</i>
The second half of 2006	The first half of 2007	0.0021	0.9862	-0.0151	0.9862
The first half of 2007	The second half of 2007	0.3004	0.0028	0.1146	0.0028
The second half of 2007	The first half of 2008	-0.0527	0.5044	-0.0083	0.5044
The first half of 2007	The second half of 2008	0.0309	0.6455	-0.0119	0.6455
The second half of 2008	The first half of 2009	0.0259	0.8720	-0.0147	0.8720
The first half of 2009	The second half of 2009	0.0679	0.5682	-0.0101	0.5682
The second half of 2009	The first half of 2009	0.3781	0.0051	0.0995	0.0051

Table 3. The test results of the performance persistence of stock fund in 18 months

<i>ranking period</i>	<i>evaluation period</i>	<i>Coefficient</i>	<i>P-value</i>	<i>Adjusted R-squared</i>	<i>F value of significance</i>
Second half of 2006 to Second half of 2007	First half of 2008 to First half of 2008	0.0675	0.1618	0.0147	0.1618
First half of 2008 to First half of 2008	Second half of 2009 to First half of 2010	0.0376	0.7708	-0.0138	0.7708

Table 1 shows the short-term gains in the fund, only two pairs of data regression coefficient is significant in the ranking period and evaluate period of 15 pairs of data. That is, the third quarter of 2009 and last quarter of 2009, last quarter of 2009 and the first quarter of 2010. Description stock fund exist performance persistence in the last quarter of 2009 and the first quarter of 2010 so that investors can use these two quarters of excess profits to prediction of excess profits in the next quarter. But overall, the remaining 13 ranking period and evaluation period's regression coefficients not pass a significant test. Therefore, this paper argues that there is exists a weak short-term performance persistence, but this persistence is not significant. That is, stock fund's returns over the past three months can not ensure the next three months can predict excess returns.

Table 2 shows the stock funds over the six-month returns have certain persistence. There is two pairs of data regression coefficient is significant in the ranking period and evaluate period of 7 pairs of data. But from the entire study period, this persistence is not significant enough.

Table 3 shows that stock funds long-term benefits (18 months) did not show significant persistence.

5 Conclusion

Using separately the cross sectional regression on short, medium and long term stock fund in China, this article has tested performance persistence of stock fund issues. Results found: there is certain continuity in 3 months, 6 months of stock fund. But this persistence is not significant, and even individual reverse phenomenon can occur in the period.

In different periods, the performance persistence phenomenon of stock fund in medium-term is more striking compared with the short-term, long-term performance persistence phenomenon. That is relatively short-term persistent medium-term persistent is more apparent. We obtain those investors to rely on reliability of medium-term performance for the medium-term performance for the past to predict the future is greater than the short, long-term performance to predict the future short-and long-term performance reliability. Alone medium-term performance of mutual fund in the past does not guarantee a great probability to predict the future medium-term

revenue, because the medium-term performance of this persistent is very weak and unstable, and even individual reverse phenomenon can occur in the period.

Investors can make the appropriate investment based on the conclusions of this study, which can purchase the funds of outstanding medium-term performance, and in the future medium-term he can ship by the probability of greater than 50% of the profit. Although this decision does not ensure that investors will profit.

References

1. Goetzmann, W.N., Ibbotson, R.G.: Do Winner Repeat? Patterns in Mutual Fund Performance. *Journal of Portfolio Management* 20, 9–18 (1994)
2. Jensen, M.C.: The Performance of Mutual Funds in the Period 1945-196. *Journal of Finance* 23, 389–416 (1968)
3. Grinblatt, M., Titman, S.: The Persistence of Mutual Fund Performance. *Journal of Finance* 42, 1984–1997 (1992)
4. Sharpe, W.F.: Asset Allocation: Management Style and Performance Measurement. *The Journal of Portfolio Management* (Winter 1992)
5. Ni, S.Y., Xiao, H., Wu, C.F.: Empirical Research on Chinese Security Funds Performance Persistence. *Forecasting* 6, 41–44 (2002)
6. Peng, S.-K.: The Risk-Return Paradox and the Source of Underperformance Persistence in Mutual Funds. *Journal of Business Economics* 11, 78–83 (2010)
7. Zhunag, Y., Zhi, T.-X.: empirical research of the persistence of the performance of China's mutual funds. *Journal of Financial Research* 5, 20–27 (2004)

A Driving Method of the Electro Hydraulic Proportional Valve Based on Compensation Network

Wei Shen and Junzheng Wang

School of Automation, Beijing Institute of Technology, Beijing 100081, China
sw_she@bit.edu.cn

Abstract. The electro hydraulic proportional valve is usually driven by the low frequency signal of PWM. However, the amplitude of chatter signal which proportional valve needs cannot be controlled independently. This is a big problem in the valve's application. In this paper, the driving theory of proportional valve is analyzed firstly. Then by deriving the driving current formula of proportional valve, the amplitude formula of chatter signal is obtained. At last, the method that compensation network is connected to the driving circuit of proportional valve is proposed. The method can bring independent control of chatter signal amplitude. The validity of the method is proved by digital simulation.

Keywords: Electro hydraulic proportional valve, PWM, chatter signal, compensation network.

1 Introduction

The electro hydraulic proportional valve (hereinafter referred to as proportional valve) is one of the important components of the Electro-Hydraulic Proportional Control System. It is widely used in the modern industry. The driving current control of proportional valve is the important problem to improve proportional valve capability. Now, the driving technology of proportional valve includes analog drive, low frequency PWM drive and high frequency PWM drive [1-5]. Among those methods, the low frequency PWM drive is very popular because it has many advantages, such as low power, strong anti-interference, simple structure and low cost. So it is widely used in proportional valve driving. However the amplitude of chatter signal which proportional valve needs cannot be controlled independently is a big problem in the low frequency PWM driving.

In this paper, the driving theory of proportional valve is analyzed firstly. Then by deriving the driving current formula of proportional valve, the amplitude formula of chatter signal is obtained. At last, the method that compensation network is connected to the driving circuit of proportional valve is proposed. The method can bring independent control of chatter signal amplitude. The validity of the method is proved by digital simulation.

2 The Driving Theory of PWM

The solenoid is the executor of proportional valve for the transformation from driving current signal to mechanical action. Then accurate control of proportional valve core is attained by exactly controlling solenoid armature. Displacement of proportional valve core is proportional to solenoid current. So the valve core displacement keeps invariant when the current keeps invariant. When current changing, the valve core will move against static friction. Then the response speed and sensitivity of proportional valve is decreased. So the valve core should vibrate so as to decrease friction and increase the response speed and sensitivity of proportional valve. This vibration is chatter. The driving signal should have characteristics of chatter signal.

The driving circuit is made up of proportional valve coil and driver in the driving technology of low frequency PWM. The work status of the driver switch tube is decided by the signal of low frequency PWM. Average output voltage of the driver will be changed with the duty cycle change of PWM. Because the proportional valve coil is inductive load, the oscillation current with nonzero mean is existed in the driving circuit. After moving to desired position, the valve core will remain vibration. The fluctuation amplitude of driving current is equal to the amplitude of chatter signal.

Based on these analyses, derivation process of proportional valve driving current is obtained. The solenoid coil of proportional valve is equivalent to a series circuit including a inductance and a resistance. So the relation between the coil voltage and coil current is shown as following:

$$L \frac{di}{dt} + i(t)R + K \frac{dx}{dt} = u(t) \quad (1)$$

In the equation (1), L is the equivalent inductance of the proportional valve coil ; R is the equivalent resistance of the proportional valve coil ; $i(t)$ is the current of the coil; $u(t)$ is the voltage of the coil ; K is the coefficient of back EMF ; x is the displacement of armature in the coil.

The response speed of the coil current is much faster than mechanical response speed of the solenoid. So the back EMF caused by the solenoid armature can be neglected in the course of current control. Then the equation (1) is rewritten as following:

$$L \frac{di}{dt} + i(t)R = u(t) \quad (2)$$

When the proportional valve driving is realized by the low frequency PWM, $u(t)$ is shown as following:

$$u(t) = \begin{cases} U & kT \leq t < kT + \alpha T \\ 0 & kT + \alpha T \leq t < (k+1)T \end{cases} \quad (3)$$

In the equation (3), T is the period of PWM, α is the duty cycle of PWM, $k=0,1,2, \dots$. The solution of equations (2) is:

$$i(t) = \begin{cases} \frac{U}{R} + (I_{MIN} - \frac{U}{R})e^{-\frac{(t-kT)R}{L}} & kT < t \leq kT + \alpha T \\ I_{MAX}e^{-\frac{(t-kT)(1-\alpha)R}{L}} & kT + \alpha T < t \leq (k+1)T \end{cases} \quad (4)$$

In the equation (4), I_{MIN} is the minimum of the steady state driving current; I_{MAX} is the maximum of the steady state driving current. When the falling edge ($t=kT+\alpha T$) of PWM appears the driving current reaches the maximum in the steady state. When the rising edge ($t=(k+1)T$) of PWM appears, the driving current reaches the minimum in the steady state. Considering the equation (4), we will get :

$$I_{MAX} = \frac{U}{R} + (I_{MIN} - \frac{U}{R})e^{-\frac{\alpha TR}{L}} \quad (5)$$

$$I_{MIN} = I_{MAX}e^{-\frac{(1-\alpha)TR}{L}} \quad (6)$$

According to the equation (5) and (6), we will get:

$$\frac{I_{MIN}}{I_{MAX}} = e^{-\frac{(1-\alpha)TR}{L}} = C \quad (7)$$

In the equation (7), C reflects the change degree of driving current in the steady state. The change degree of driving current is equivalent to the amplitude of chatter signal. Then C is inversely proportional to the amplitude of chatter signal. So Influencing factors of the chatter signal amplitude include the duty cycle of PWM, the period of PWM, the inductance of driving circuit and the resistance of driving circuit.

3 Adjustment of the Chatter Signal Amplitude

In the influencing factors of the chatter signal amplitude, the inductance and resistance of proportional valve are decided by self coil. So the inductance and resistance of proportional valve can not be adjusted. For the PWM frequency is usually invariant in control system, T can not be randomly adjusted. The driving current amplitude of proportional valve depends on duty cycle of PWM and resistance in the driving circuit. Because the resistance in the driving circuit of low frequency PWM is invariant, α is a constant. In a word, the amplitude of chatter signal can not be adjusted independently in the driving method of low frequency PWM.

In order to solve this problem, many researches have been done. The method that the chatter signal amplitude can be adjusted independently based on compensation network is proposed in this paper. The compensation network is composed of inductance and resistance which are connected in series. Then compensation network is connected to the driving circuit of proportional valve in series. The inductance and resistance of driving circuit are altered by changing inductance and resistance in the compensation

network, thus the amplitude of chatter signal can be adjusted independently in the driving circuit. The current of driving circuit is equal to the coil current of proportional valve because driving circuit is a series circuit. So the amplitude of chatter signal that proportional valve needs is adjusted independently. The theory of compensation network is shown in the Fig.1.

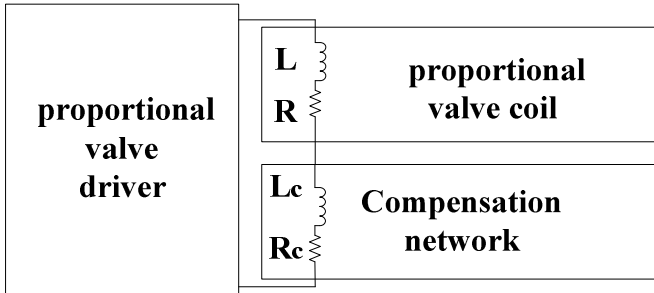


Fig. 1. The theory of compensation network

The derivation of driving method based on compensation network is obtained as follows.

When compensation network is connected to driving circuit of proportional valve, the relation between circuit voltage and circuit current is shown as following:

$$L \frac{di}{dt} + i(t)R + L_c \frac{di}{dt} + i(t)R_c = u(t) \tag{8}$$

According to equation(8), we will get:

$$(L + L_c) \frac{di}{dt} + i(t)(R + R_c) = u(t) \tag{9}$$

According to the equation (2), (7) and (9), we will get:

$$\frac{I_{MIN}}{I_{MAX}} = e^{-\frac{(1-\alpha)T(R+R_c)}{L+L_c}} = C \tag{10}$$

From equation (10), the conclusion can be obtained that the chatter signal amplitude can be adjusted with changes of R_c and L_c . The control effect in the application of proportional valve is decided by the average amplitude of driving current in steady state. So the average amplitude of driving current in steady state must be invariant when the chatter signal amplitude is independently adjusted.

Under the condition that the compensation network is connected to driving circuit, driving current in steady state can be expressed as: $I_j = \frac{\alpha U}{R + R_c}$. Because the average

amplitude of driving current keeps invariant, α can be expressed as: $\alpha = \frac{I_j(R+R_c)}{U}$.

According to equation(10), we will get:

$$C = e^{-\frac{[1-\frac{I_j(R+R_c)}{U}]T(R+R_c)}{L+L_c}} = e^{-\frac{T(R+R_c)-\frac{I_jT(R+R_c)^2}{U}}{L+L_c}} \tag{11}$$

Analyzing equation (11), we can find that C is decided by

$$-\frac{T(R+R_c)-\frac{IT(R+R_c)^2}{U}}{L+L_c} \tag{12}$$

By calculating the extremum of equation (12) numerator ($T(R+R_c)-\frac{IT(R+R_c)^2}{U}$),

we can find that $T(R+R_c)-\frac{IT(R+R_c)^2}{U}$ reaches the maximum when

$R_c = \frac{U}{2I} - R$. Because C reflects the chatter signal amplitude in the steady state, we

can find the law as following. When $R_c = \frac{U}{2I} - R$, the chatter signal amplitude can reach the maximum. And with L_c increasing, the chatter signal amplitude is monotone decreasing.

Based on the above analysis, we can find that the power of driver will be slightly increased because extra resistance is connected to driving circuit. So R_c and L_c should be reasonably chosen considering the driver capability.

4 Digital Simulation

The digital simulation of the driving method proposed in this paper is done. Supposing $U=24V$, $R=5.4\Omega$, $L=200mH$, $T=0.005s$. The parameters of compensation network are chosen as following: $R_c=14.6\Omega$, $L_c=0mH$. The average amplitude of driving current in the steady state is 0.6A. According to equation (10), we can obtain that the ratio of driving current minimum and maximum is 0.89 before compensation network is connected to driving circuit; the ratio of driving current minimum and maximum is 0.78 after compensation network is connected to driving circuit. The chatter signal amplitude of the circuit with the compensation network has been increased greatly compared to the amplitude without the compensation network. The current curve with the compensation network is shown in Fig.2. The current curve without the compensation network is shown in Fig.3.

We can find that all of average amplitude of driving current are equivalent to 0.6A in Fig.2 and Fig.3. But the chatter signal amplitude is increased and is in agreement with theoretical calculation in Fig.2.

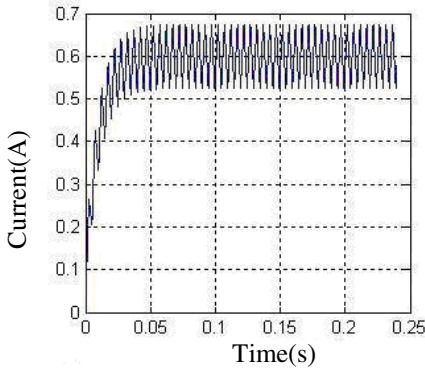


Fig. 2. The current curve with compensation network

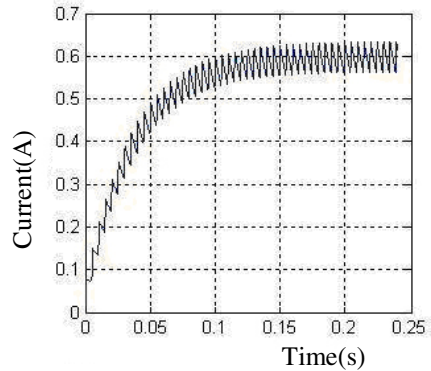


Fig. 3. The current curve without compensation network

5 Conclusion

In this paper the problem that the chatter signal amplitude of proportional valve is hard to be adjusted independently is solved. The amplitude of chatter signal will be adjusted independently by connecting the compensation network to driving circuit. Digital simulation effect proves the above theory.

References

1. Gong, W.-B., Liu, X.-H., Sun, Y.-W.: Method of electronic-hydraulic proportion control. *Journal of Jilin University (Engineering and Technology Edition)* 33(7), 104–106 (2002)
2. Zhu, Y., Tang, X.: Dither Algorithm in Pulse Width Modulation. *Journal of Mechanical Engineering* 45(4), 214–218 (2009)
3. Yee, N., Scavarda, S., Betemps, M., et al.: Models of a pneumatic PWM solenoid valve for engineering applications. *Trans. ASME* 114, 680–688 (1992)
4. Keles, O., Ercan, Y.: Theoretical and experimental Investigation of a pulse-width modulated digital hydraulic position control system. *Control Engineering Practice* 10, 645–654 (2002)
5. Vaughan, N.D., Gamble, J.B.: The modeling and simulation of a proportional solenoid valve. *Journal of Dynamic Systems, Measurement, and Control* 118(1), 120–125 (1996)

The Structure and Realization of a Compact Weeding Robot in Stamping Mode for Paddy Fields*

Qin Zhang, Huan Xia, and Xiaogang Huang

School of Mechanical & Automotive Engineering, South China University of Technology, Guangzhou, 510640, China

Abstract. A structure of a weeding robot in stamping mode for paddy fields is put forward, which includes an auxiliary supporting device, a weeding device in stamping mode and a striding device. The weeding device in stamping mode realize the evulsing and cutting of weed by walking over and stamping it flat in between the rice shoots with the crawler mobile mechanism. The stamp on weed, which also destroys its habitat, will contribute to the suppression and removal of weed. The turning radius is reduced by the striding over method with tendon-outer-tube transmission system, which greatly enlarges the planting area. The auxiliary supporting device and the striding device, which can avoid slipping and stalling caused by the paddy field pit, cooperate to make the stable movement in the bad condition possible. On the basis of this, the work process of the robot is analyzed, and the strategy of the wedding robot's movement is then proposed.

Keywords: a weeding robot in stamping mode, striding over method, tendon-outer-tube transmission, structure design.

1 Introduction

Chemical method is mainly adopted to deal with paddy field weeding at home and abroad, however, the herbicide is supposed to contaminate the environment, upset the balance among microorganism, as well as pose a threat to the safety in production and people's health. So the paddy which is free from contamination or of little contamination is becoming more and more popular all over the world, but how to do the weeding effectively still remains an issue which needs to be further studied.

A lot of methods have been proposed to deal with paddy field weeding, In Europe, fungus which is infectious to weed or insects are adopted as a biological control method, and the cultivation such as rye-grass and *Lepidium* are also planted in between the rows of paddy to suppress the growth of weed, In Japan, since organic planting and nature farming are still small-scale farming, most of the weeding is man-made by covering the weep with wrapper. In china recently, straw and plant such as green manure crops and grass are taken as wrapper for weeding, and duck and herbivorous fish are kept in the paddy field, because they can eat the worm and weed [1]. However, the methods mentioned above are still constraint due to factors such as

* This work was supported by a grant from the National High Technology Research and Development Program of China (863 Program) (No. 2008AA04Z213).

environment condition and its cost, it may not be appropriate to be promoted on a large scale.

Since mechanical weeding has virtue of high automation and efficiency commitment, it can apply to the large scale weeding. Different kinds of weeding robots have been developed in china, for example, laser weeding robot[2], which is based on the heat effect of laser to cut and burn weed. And high efficiency weeding robot[3], which can realize the weeding both in between the rows and between the paddy in the same row by its cutting mechanism in the middle and discal saw in both sideways. Although these robot can all live up to expectation of weeding, they have disadvantages such as their large turning radius, which may lead to reduction of planting area, complex structure, high cost, as well as large size. All of this constrain the application of weeding robots for paddy fields, on the other hand, young people in the countryside both at home and abroad, tend to pour into cities, leaving women and the old at home to do the farming, which makes the emergence of light and small-sized weeding robot necessary.

This paper put forward a structure of weeding robot in stamping mode for paddy fields [4] which includes an auxiliary supporting device, a weeding device in stamping mode and striding device. The robot realizes the evulsing and cutting of weed by walking over and stamping it flat in between the rice shoots. The mud generated simultaneously as robot's crawler go along the path, will also contribute to the suppression of photosynthesis of weed, as the mud deposit, which may rest on weed in between the rice shoots, will do damage to the habitat of weed and contribute to the suppression and removal of weed. The auxiliary supporting device and the mobile device cooperate to manage the striding over movement, which shorten the line-changing process and reduce turning radius, making the planting area greatly enlarged. As the weeding device in stamping mode move along its path, paddy fields pit may lead to the slipping and stalling of robot, however, the auxiliary supporting device and the striding device can cooperate to regain its desired place. Which ensure that robot has a high adaptability in the bad condition, this structure can apply to the weed of both paddy field in large scale and that in small scale on bad condition.

2 General Design of Weeding Robot Structure

The weeding robot is mainly composed of three parts, which include an auxiliary supporting device, a weeding device in stamping mode and a striding device. Just as Fig.1shows.

The auxiliary supporting device is connected with the weeding device, and the striding device is conjunct with the middle of the weeding device, The auxiliary supporting device is left up as the robot is weeding in stamping mode, the weeding device move forward in between the rice shoots with the crawler mobile mechanism, and the stamp on weed contributes to the suppression and removal of weed.

The striding device is composed of two three-layer bidirectional guide rails which are symmetrical to each other. The striding over movement can be achieved by the combination of lift up movement of auxiliary supporting device and telescopic movement of guide rails. the auxiliary supporting device and the striding device cooperate to make the stable movement in the bad condition possible.

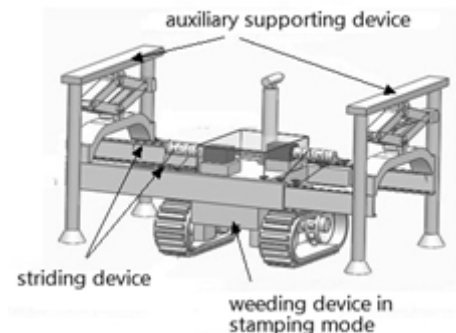


Fig. 1. Structure of weeding robot

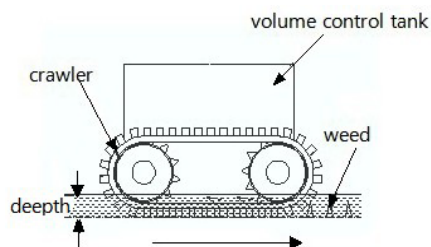


Fig. 2. Structure of weeding device

2.1 Structure of Weeding Device

The weeding device are appropriate for the removal of new weed, and the weeding begins 7 weeks after the rice shoots are transplanted, it will last about 7 weeks, and the work should be done 2 or 3 times a week.

The weeding device is shown in Fig.2.

In order to realize the portability of the weeding robot as well as the simplicity of its structure, four crawler wheels are adopted, two of which share the same crawler. Since the crawler is stinging one, and the stings on crawler are scattered irregularly, if the front stinging crawler fail to remove weed as robot go along the path, the back stinging crawler will help to do the weeding. Owing to stinging crawler, the mud in field is becoming more liable to be dragged out, which makes the weeding very effective, Driving motors and Reduction Gearbox are equipped in the volume control tank, And each of the crawler wheel is driven by one motor. The height between the bottom of the Volume Control Tank and the ground is 230 mm. which is above the rice shoots. As Fig.3 shows, the volume control tank is designed to be hermitical to prevent water.

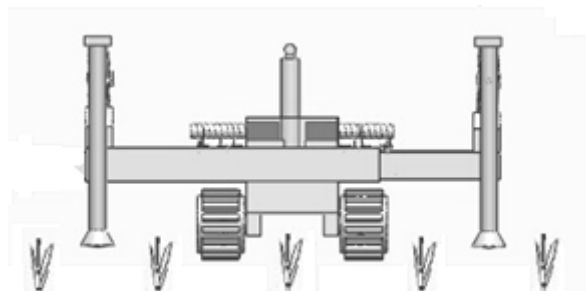


Fig. 3. Weeding state

2.2 Structure of Auxiliary Supporting Device

The auxiliary supporting device is mainly used for supporting as robot executes the striding over movement, it cooperates with the striding device to ensure stable movement. The auxiliary supporting device, which has a structure similar to jack[5], is composed of sway brace, upper junction plate, lower junction plate, screw, etc. As Fig.4 shows, the vertical motion of the device is driven by motor.

As motor rotate positively, the screw will rotate in the same direction, since the lower junction plate is connected with the weeding device in the middle of guide rails, the bottom of sway brace can be deemed as fixed as Fig.5 shows, the upper sway brace is driven by screw to lift up the upper junction plate.

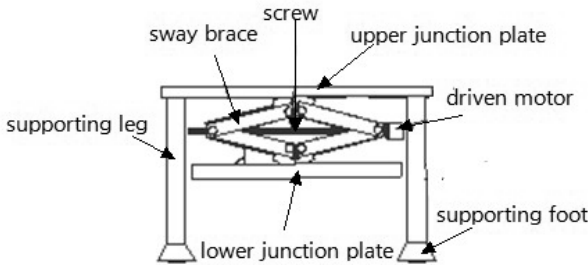


Fig. 4. Structure of auxiliary supporting device

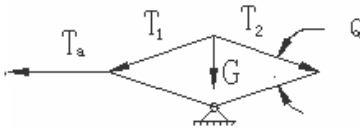


Fig. 5. Force diagram (1)

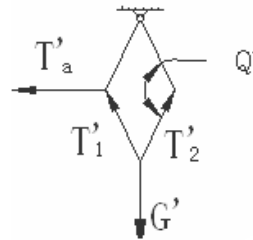


Fig. 6. Force diagram (2)

As motor rotate negatively, the screw will rotate in the same direction, the upper sway brace will lay the supporting legs and supporting foot down on both sides. The motor will keep rotating after the supporting foot touch the ground, In this situation, the upper junction plate which is connected to the supporting leg can be deemed as fixed as Fig.6 shows. Thus the weeding device can be pulled up by the lower sway brace, getting prepared for the striding over movement.

Considering the complex circumstance due to footprint and pebbles, spherical joint is adopted to connect the supporting leg with the supporting foot. It can rotate freely as the supporting foot steps on rough ground, which help to overcome the length change of supporting leg due to rough ground and realize the stable supporting. As Fig.7 shows.

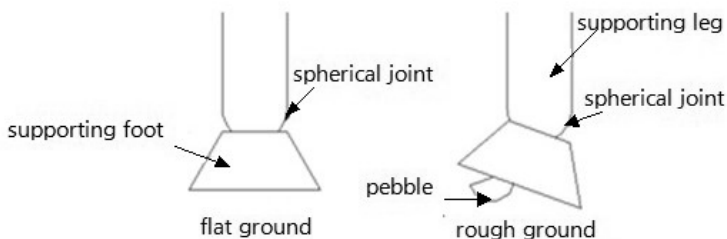


Fig. 7. Sketch map of the supporting leg and supporting foot

2.3 Structure of Striding Device

The striding device has a structure of two three-layer bidirectional guide rails which is symmetrical to each other and both driven by tendon-outer-tube transmission system. The innermost layer is connected to the weeding device as a whole, and the end of middle and outmost layers are connected with the two auxiliary supporting device respectively, all the layers are driven by tendon. The end of the middle layer and the outmost layer on both sides are connected with one end of tendon respectively, while the other end of tendon is connected with the spool with spiral cavity which is fixed to motor shaft. The telescopic motion of guide rails is driven by motor, which helps to realize controlling where the supporting foot lies and adjusting the gravity center of robot. All the motors are fixed to weeding device, which greatly improves the efficiency. The structure of the mobile device is shown as Fig.8(a) and Fig.8(b)

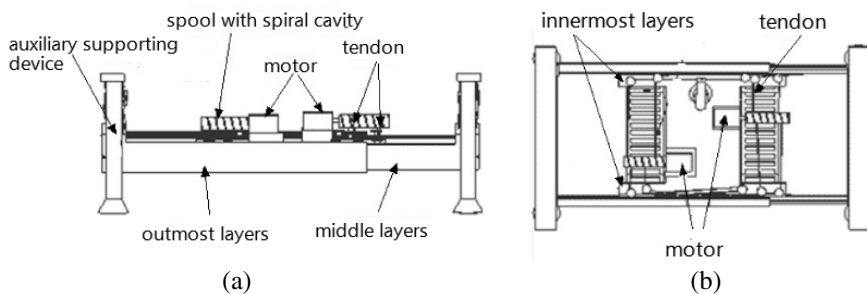


Fig. 8. Striding device

3 Motion Analysis of Weeding Robot

3.1 Weeding Motion in Stamping Mode

When weeding in stamping mode, robot will left up its supporting legs and let its crawler laid down on the ground, then rice shoots go trough the crawler as Fig.9(a) shows. The trajectory of the robot can be obtained according to the results of imagine processing, which will contribute to the controlling of the direction where the crawler is heading. Robot may slope, slip or be stalled due to the unevenness of ground as it moves along its path. In this situation, the desired place can be self maintained by

adjusting the movement of the supporting legs and foot on both two sides, making robot competent for moving in paddy field. Since gully will be generated by the rut the first time robot stamp over the ground, path can be guided according to the gully the second time, which helps to realize stable movement. The robot realizes the evulsing and cutting of weed by walking over and stamping it flat in between the rice shoots. The mud generated simultaneously as robot's crawler go along the path, will also contribute to the suppression of photosynthesis of weed, as the mud deposit, which may rest on weed in between the rice shoots, will also contribute to the suppression and removal of weed. The stamping movement should be executed 2 times each ridge every week.

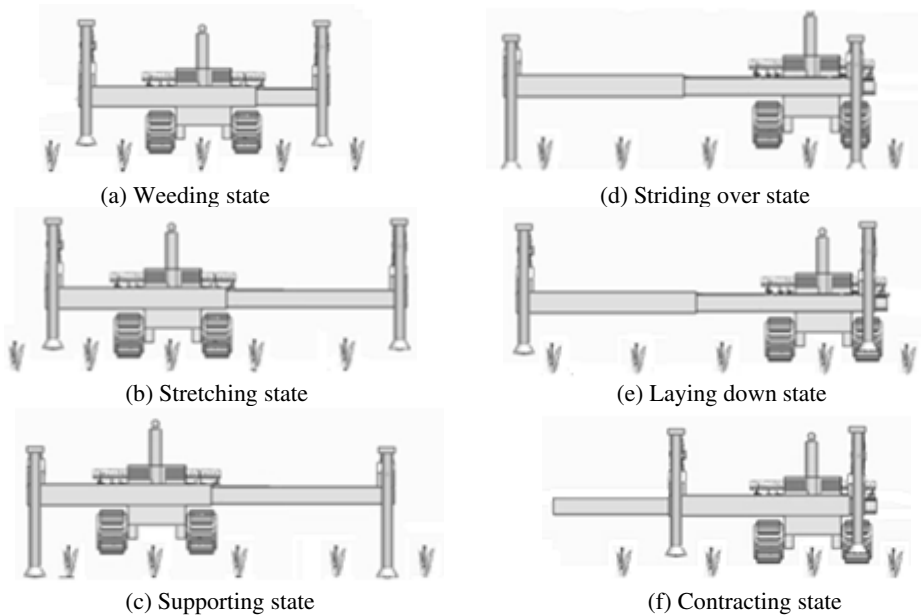


Fig. 9. Process of weeding robot motion

3.2 Line-Changing Movement

3.2.1 Strategy Analysis of Line-Changing Movement

The weeding robot is supposed to make line-changing movement when it gets to the end of paddy field, there are mainly two types of line-changing method, one is by turning around which is very common as Fig.10 shows. Since there exists turning radius, enough area should be reserved for the motion. The other one is by backing up as Fig.11 shows. The line-changing movement can be achieved successfully on the condition that the place reserved is three times the width of robot. In order to improve the efficiency of line-changing movement, the paper put forward the striding over method, which achieves line-changing by first lowering the supporting legs and lifting up the crawler above rice shoots, then moving the crawler to the adjacent row and laying it onto ground.

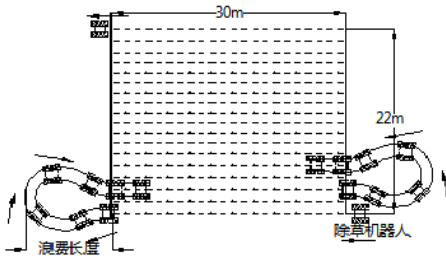


Fig. 10. Line-changing by turning around

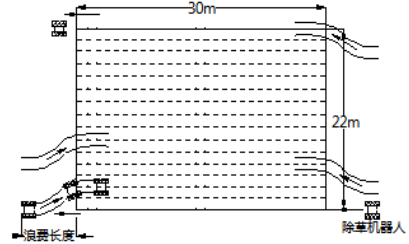


Fig. 11. Line-changing by backing up

3.2.2 Realization of Line-Changing Movement

The process of line-changing movement includes three stages which are line-changing preparation, line-changing and recovery, which needs the cooperation among the auxiliary supporting device, the weeding device and the striding device. First, the motor of striding device rotates to drag the tendon which forces the guide rail to push supporting legs for one row pitch in the line-changing direction as Fig.9 (b) shows. Then the supporting legs keep moving downward until the weeding device is lifted up over the rice shoots as Fig.9(c) shows, the innermost guide rail is driven by motor to move along the middle guide rail with the weeding device for two rows pitch which is about 600mm as Fig.9(d) shows .when the weeding device reach the desired place, the supporting legs begin to move upward, and the weeding device will be laid down on the ground, then the supporting legs will keep on moving upward until its initial position is regained as Fig.9(e) shows, the outmost guide rail is then driven by motor to move along the middle guide rail for two rows pitch which is about 600mm as Fig.9(f) shows , finally, the middle guide rail move 300mm to regain its initial place as Fig.9(a). After that the whole process of line-changing movement is completed, the distance the robot strides over can be available according to the paddy field pitch.

All of the three guide rails are driven by tendon-outer-tube transmission system, motor transfers power to guide rail through tendon, which reduces the required equipments, lighten the robot's weight, and makes the robot more compact.

4 Conclusion

The paper put forward a new structure of weeding robot for paddy fields, which can manage weeding efficiently by the cooperation among an auxiliary supporting device, a weeding device in stamping mode and a striding device. Weeding in this mode not only greatly enlarges the planting area, but also can realize stable movement in paddy field on bad condition, this structure can apply to the weed of both paddy field in large scale and that in small scale on bad condition.

References

1. Wang, Q.: Organic Weed Control. Lab of Weed Science and Herbicide, R.Taiwan (2004)
2. Liu, J., Li, P.: A laser weeding robot. P. China: 101589705 A (December 02, 2009)

3. Chen, Y., Sun, M.: High efficient weeding robot. P. China: 101707992 A (May 19, 2010)
4. Zhang, Q., Xia, H., Huang, X.: An agency of weeding robot in stamping mode for paddy fields. P. China. Utility Model Patent, ZL 201020590314.9, 9
5. Xie, H., Wang, J.: The new horizontal jack design base on SolidWorks. *J. Machinery* 5(33), 53–55 (2010)

Study on the Identification of Noise Sources and Reducing Noise for Diesel Engine

Liu Shuai¹, Wang Zhong¹, Chen Lin¹, Xia Heng²,
Zhang Yifeng², and Xu Guangju¹

¹ School of Automobile and Traffic Engineering, Jiangsu University,
Zhenjiang 212013, China

² FAW Jiefang Automotive Co., LTD Wuxi Diesel Engine Works, Wuxi 214026, China

Abstract. The noise of the main parts of high pressure common-rail diesel engine was analyzed in this article. The near-field noise of main parts of diesel engine was measured at different speed and load conditions. The major impact components on the engine noise were covered with composite materials, and the noise was measured. The noise of different fans on the diesel engine was analyzed. The results show that: Oil pump, oil pan, crankshaft pulley and air cleaner were the main noise sources of the engine. The near-field noise of Silicon-oil clutch fan was lower than crankshaft fan and the fan of the original machine. When composite material was covered, the noise of oil pan fuel pump diesel engine could reduce effectively. The near-field noise of main components reduced about 1 dB (A) ~ 2dB (A) and the engine noise reduced 1.5 dB (A).

Keywords: Diesel engine, Noise, Composite material.

1 Introduction

Vehicle noise is an important source in urban noise pollution, internal combustion engine is the ultimate source. In many cases, the noise is generated with the completion of a function. It is difficult to eliminate. If you want to eliminate, you must substantially change the combustion systems and the transmission of internal combustion engine. These changes often have a greater impact on the performance of diesel engines and they are difficult to achieve. Relatively, reduce vibration and barrier the sound source are easier to achieve. And it is more real. Around the identification of noise sources and reducing noise for diesel engine, Domestic scholars and foreign scholars have carried out the corresponding research, for example, Seyber who comes from Kentucky University of America had used the integral method of BEM and Rayleig (Monopole Point Noise Sources) to predict the noise radiation of internal combustion engine components, and he compared the differences between the two methods [1][2]. Yasuhiko Nishimura who comes from TOYOTA company of Japan had analyzed the noise radiation of internal combustion engine components, and he had used it to reduce vehicle noise [3]. Professor Shu and Professor Hao who comes from Tianjing University had done the identification of noise sources of surface radiation for vehicle engine, sound intensity measurements of internal combustion engine, the study on mechanism and control of torsional vibration[4][5]. We have measured and analysed

the noise of internal combustion engine and the surface noise of components at the different loads of the rated speed for diesel engine. We have determined the parts which largely affect the noise of diesel engine. We have measured the noise that the diesel engine used the different fan and the main components covered the different composites. We have studied the affects when the diesel engine covered the different composites. This paper have some guides to reduce the noise of the diesel engine.

2 Test

2.1 Test Conditions

The model of the diesel engine is 4110Q. It's displacement is 4.7L. It's compression ratio is 18.5. It's rated speed is 2500r/min.

We do this test in the Semi-ane choic chamber, the background noise is lower than 12dB (A). The diesel engine installed on the elastic foundation. The figure1 is diesel engine and dynamometer installation diagram. We used some test instruments, for example, Precision Sound Level Meter\ Octave filter (B&K2230), dynamometer installation, Fuel consumption meter (HZB500), Thermometer.



Fig. 1. Diesel engine and dynamometer installation diagram

2.2 Test Program

Identify the near-field noise source. There are a number of ways to identify the noise source of the diesel engine, the measurement method of the near-field sound pressure level is a good way to identify the noise source of the diesel engine. We turn arrange measuring point on the surface of the diesel engine which may be the noise source, there are 14 measuring points. We measured every near-field measurement points, then compared the measurements to find out the main noise source. The measuring points are shown in Figure2. There is 50mm between the microphone probe and the measured surface.

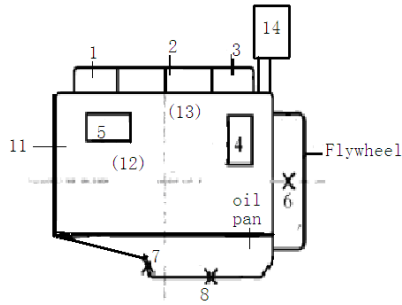


Fig. 2. Schematic diagram of near-field measurement points

Description of the measuring point,

1- Front of cylinder head 2- Middle of cylinder head 3- Back of cylinder head
 4- Pump 5- Starter motor 6- Accessories box 7- Side of oil pan 8- Bottom of oil pan
 9- Camshaft 10- Pump gear 11- Fan 12- Side of exhaust 13- Turbocharger
 14- Air Filter.

The test of noise reduction measures. According to the measurement results of the identification of noise sources, we have implemented to reduce noise test to the main noise source. We mainly through replaced of the different fans and covered the main source of radiated noise to test.

1) Replaced of the different fans. We have three kinds of fans. They are 7 leaves fan, 7 leaves fan installed silicone oil clutch, 7 leaves fan installed wind guide cover. We used these to test.

2) Covered the main source of radiated noise. We have used complex sound-absorbing material to cover the main parts of the noise source of the diesel engine. The complex sound-absorbing material is a porous foam, it has many small gap of inside and outside connected and consecutive holes. It used the principle of wave interference and diffraction to attenuate sound energy that it can absorption.

Verify the effect of noise reduction after we have implemented measures. After we selected the best plan, we measured sound pressure level of near-field and machine of the main noise source at declared working condition. We compared the difference before and after implementation.

3 Results and Analysis

3.1 Identify Noise Source

When the diesel engine at rated speed, we measured near-field noise at the different loads, for example, full load, 75% load, 50% load, 25% load. This is shown in Figure 3. As can be seen from Figure 3, higher parts of the noise are pump, accessories box, bottom of oil pan, fan, crankshaft pulley, air filter. With the diesel engine load increasing, the sound pressure level of the near-field measurement points changed slightly.

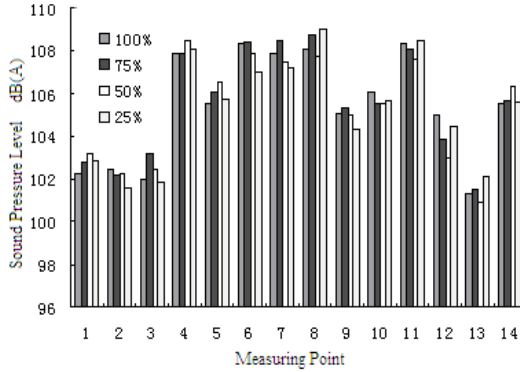


Fig. 3. Different load rated speed near-field noise

3.2 Reduced Noise Measures

3.2.1 Fan Noise Analysis

The figure4 is the noise comparison of different fans. The sound pressure level of the different fans are same from this picture. The change is obvious with the increased speed. The fan of engine prototype is highest at the 2500rpm, it is 98.9 dB (A) .The fan of the crankshaft is followed, it is 97.1 dB (A) .The fan of silicon oil clutch is lowest, it is 94.1 dB (A) .

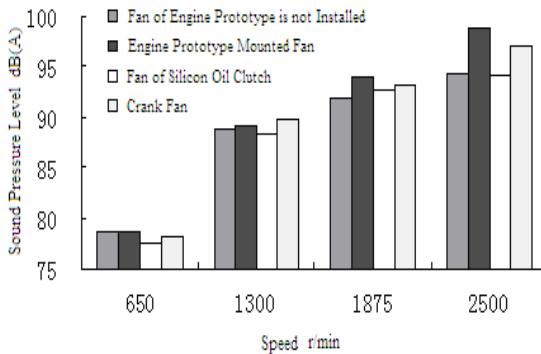


Fig. 4. Noise comparison of different fan

Because the fan of silicon oil clutch is provided torque by the silicone oil of drive power between input parts and output parts. It's thermal devices controls the liquid of the silicone oil in the working chamber. When the air temperature surrounding the radiator changes from low to high, the silicon oil clutch drives the speed of the fan from low to high, this is a flexible process of gradual increasing. This process is not only can greatly reduce the air noise because of the fan speed mutations, but also can reduce the friction noise because of rapid speed changes causes the plastic fan deformation.

3.2.2 Oil Pan Noise Analysis

The figure5 is different speed oil pan near-field noise. As can be seen from Figure5, as the speed increases, the reduction of the sound pressure level of oil pan near-field maintained at 1dB (A) around.

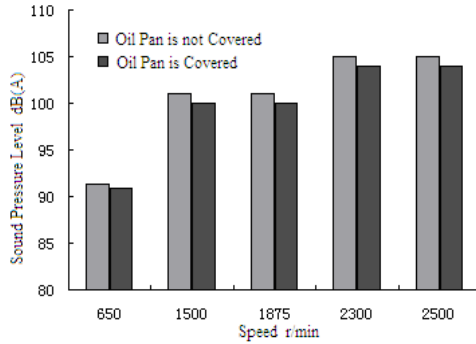


Fig. 5. Different speed oil pan near-field noise

The figure6 is oil pan at rated speed frequency spectrum map. As can be seen from Figure6, the sound pressure level reduces at almost frequency range when the oil pan is covered. The change is more obvious at the range of 500Hz ~2500Hz. The sound pressure level reduces 4.4 dB(A) at 1000Hz. The noise of the oil pan mainly concentrates in the middle and low band below 1000Hz, it's the largest peak appears at 360Hz[6]. The oil pan is stamped of thin-walled steel, it's natural frequency is lower than the average.

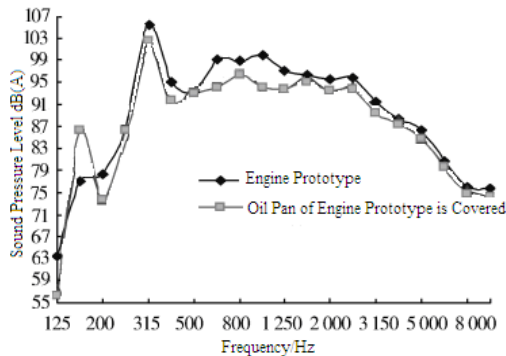


Fig. 6. Oil pan at rated speed frequency spectrum map

In addition, the radiation area of oil pan is larger than the average, it's the part of high frequency is strong vibration, so the radiated noise of oil pan is higher than the average. The test uses composite sound-absorbing material which is made of porous foam, it has many small gaps and continuous holes which are connected inside and

outside. When the sound waves from the pores to the material internal, it causes air vibration in the holes. At the same time, the friction between sound waves and the hole wall causes the difference of air velocity, it causes viscous effect which makes a considerable part of the sound energy into heat energy to dissipate. So that the sound waves are weakened, to achieve the purpose of sound absorption [7].

3.3 The Results of Noise Reduction Analysis

When the diesel engine is covered with composite materials, the noise of the main parts and the diesel engine both reduce at the declared working condition(Table 1). The noise of the front of cylinder head reduces 1.8 dB (A) ,the noise of the oil pan reduces 1.1 dB (A) ,the noise of the pump reduces 1.3 dB (A) .

Table 1. Near-Field Noise Comparison

Measuring Point	Sound Pressure Level of Engine Prototype /dB (A)	Sound Pressure Level after Engine Prototype is Covered /dB (A)
1	101	99.2
4	105.1	103.8
7	105.2	104.1

The figure7 is the noise of the diesel engine contrast. As can be seen from Figure9, after the noise reduction measures are implemented, the average sound pressure level of the diesel engine reduces 1.5dB (A).

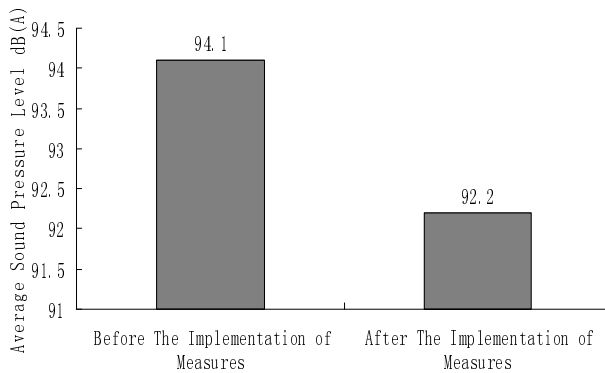


Fig. 7. Noise of Diesel Engine Contrast

4 Conclusion

1) The part which is the higher noise of the diesel engine is pump, accessories box, bottom of oil pan, fan, crankshaft pulley and air filter at the declared working condition.

2) The speed of the fan of silicon oil clutch is slower. It makes near-field noise of the fan of the diesel engine lowest at the declared working condition.

3) The effect is obvious, when the oil pan and pump are covered with composite materials. It can reduce 1 dB (A) ~ 2 dB (A) around. The noise of the diesel engine can reduce 1.5dB (A) .

References

1. Cheng, C.Y.R., Seybert, A.F.: Recent Applications of the Boundary Element method to Problems in Acoustic. SAE 870997
2. Seybert, A.F., Hamilton, D.A., Hayes, P.A.: Prediction of radiated noise from machine components using the BEM and the Raleigh integral. *Noise Control Engineering Journal* 46(3), 77–82 (1998)
3. Usuda, S., Otsuka, M., Nagata, M.: Noise and vibration reduction of newly developed 3.0L direct injection diesel engine. *JSAE Review* 23, 285–289 (2002)
4. Yue, D., Hao, Z., Liu, Y., Duan, X.: A Study on Surface Noise Sources Identification for Diesel Engine. *Automotive Engineering* 26(5), 613–615 (2004)
5. Xiong, S.: Pump Noise Generation and Control. *The Journal of Jiangnan University* 15(3), 95–97 (1998)
6. Wei, H., Shu, G., Han, R., Liang, X.: Relation Between the High-Frequency Oscillation of Combustion Pressure and Combustion Noise of DI Diesel Engine. *Combustion Science and Technology* 12(2), 131–136 (2006)
7. Li, S.: Application of Damping Materials in Automotives. *Automotive Technology and Materials* (7), 30–32 (2005)

The Design of UART Controller Based on FPGA

Ying Wang and Zhan Shen

College of Information Engineering, Shenyang University of Chemical Technology,
Shenyang, China

wyinghai@163.com, sy_shenzhan@163.com

Abstract. This paper introduces a method to implement UART based on Field Programmable Gate Array (FPGA). Its baud rate can be set and the states can be read. The structure of this system is divided in modularization so that can fit the method Top-Down. The hard core of this system is implemented with finite state machine (FSM) [1]. It makes the logic of control more intuitionistic and more briefness. The efficiency of the design is improved in a wide range. Simulating experiments, present at last to proved the validity and reliability in the whole design.

Keywords: UART, FSM, FPGA.

1 Introduction

Asynchronous serial communication that requires a few of Transmission lines, high reliability, and faraway transmission distance, is widely applied of the data exchangement of microcomputer and peripheral. Usually it is complimented by UART (Universal Asynchronous Receiver-Transmitter), For example of National INS 8250 as chip of serial interface in the IBM PC. In the practical application, some main functions of UART are required. Special interface chip may cause a waste of resources and high costs, especially the technology of SOC in the field of electronic design will implement the function of the whole system on single block or few blocks of chips. So designers should make the similar function module integrated into FPGA. This paper puts forward a way of realizing the function of UART using FPGA. The above problems can be resolved effectively.

2 Function Introduction

This UART controller transmit a frame serial data including 1 start bit, 8 bits of data and 1 bits stop bits. When ransmission, low bit is in the front, high bit is in the post. Receiver detects and confirms the start bit, 8 data bits will be received. After receiving the stop bit ,Interrupt signal will be transmitted toward CPU, in the same time Data will be transmitted to the computer 's 8 bit data bus. When sending data ,Baud rate is seted up by CPU. Then the 8 bit parallel data plus the start bit and stop bit is sent to the peripheral. After sending the stop bit, Interrupt signal will be transmitted toward CPU.In the process of sending and receiving data, CPU can load control signal to read

the working state of UART, in order to conduct real-time processing. The basic UART communication requires only two signal lines (RXD, TXD) to complete the data communication. Receiving and sending is duplex form. TXD is the UART's sending terminal, as output; RXD is UART 's receiver, as input.

3 The Realization of Function

3.1 The Overall Structure of the System

In large scale circuit designs, a hierarchical, structured design method is widely used. It will divide a complete hardware design tasks from the system level, into a number of operational module, work out corresponding model and simulation, finally make combination in the system level. This improves the design efficiency and the design quality, and is the major means of implementing complex system[2], witch is the basis of design idea in this paper. UART consists of three modules, namely the baud rate generator; the receiving module; transmitting module.

3.2 Design of Modules

3.2.1 Top Level Module

The top-level module of UART consists of a baud rate generator, a receiving module and a sending module. The UART transmitter is used to transform the parallel data for output in accordance with the basic UART frame format to TXD signal serial output. UART RXD receiver receives the serial signal, and converts it into parallel data[3]. Baud rate generator specifically produces a local clock far higher rate than the baud rate to sample the input RXD continuously to enable the receiver to maintain synchronization with the transmitter. Circuit diagram is shown in figure 1.

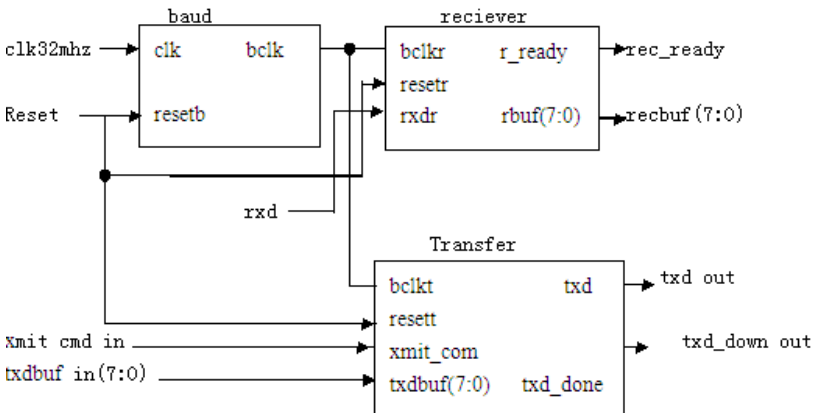


Fig. 1. Circuit diagram of top-level module

3.2.2 Baudrate Generator

Baudrate generator is a frequency divider in fact. We could calculate the baud divisor according to the given system clock and the required baud rate. Baud divisor needs to change according to different applications. The design needs to divide a frequency of 32MHz signal into that of 153600Hz signal.

3.2.3 The UART Receiver

Due to the serial data frame and a receive clock is asynchronous, by logic 1 to a logical 0 can be considered a data frame start bit. However, in order to avoid burr effect and get the correct starting bit, we must request that there is at least half of logic 0 in the received start signal in the process of sampling baudrate clock. Because internal sampling clock cycle is 16 times of transmitting or receiving baud rate clock cycle, the start bit requires that at least 8 consecutive BCLK cycle logic 0 was received. Then data bit and stop bit are sampled every 16 BCLK cycle time.

R_START STATE : After the UART receiver is resetted, the receive state machine is in this state when the state machine has been waiting for the RXD level jump, that from a logical 1 to logic 0 means the beginning of a new frame of UART data frame. Once the start bit is determined, the state machine will transfer to the R_CENTER state. RXD_SYNC signal is RXD sync signal. In the judgment of logic 1 or logic 0, we do not wish the detected signal is not stable, so we do not detect RXD signal.

R_CENTER STATE : For the asynchronous serial signal, in order to detect the correct position signal every time, detecting in each of the midpoint is advisable. In this state, we calculate mid point of each bit through the number of BCLK counts. But most probably the count value "did not actually happen to the "1000", a state should to be considered, namely after a BCLK cycle, the 1 / 2 bit in sampling is hoped.

R_WAIT STATE : When the state machine is in this state, in the sixteenth BCLK, it enter the R_SAMPLE state for data bit sampling detection, but it also determines whether the data bit length has reached a data frame length (FRAMELEM), if it come, the stop bit is coming.

R_SAMPLE STATE : After the inspection of Data bit sampling, it refers to the R_WAIT state unconditionally, waiting for the next bit of data.

R_STOP STATE : The state machine is without the specific detection of RXD in R_STOP state, just output the end signal of frame receiving (REC_DONE <= ' 1'). After this state, state machine comes back to the R_START state, waiting for the start bit of the next frame.

3.2.4 The UART Transmitter

The transmitter output one data every 16 BCLK cycle, follow that the first bit is start bit, and the eighth is stop bit in order.

X_SHIFT STATE : After the UART is resetted, the state machine is in this state when the UART transmitter has been waiting for a data frame to send commands to XMIT_CMD. Because XMIT_CMD is an external signal, it is not possible to limit the XMIT_CMD pulse width. If the XMIT_CMD is still valid after he UART has sent a data frame, then the error is considered, a new command of data transmission is coming again. The UART transmitter will start sending frame of UART again. Obviously, the frame sent is wrong. In this time, XMIT_CMD is limited on the pulse

width , use XMIT_CMD_P instead of XMIT_CMD signal, XMIT_CMD_P is a short pulse signal. When XMIT_CMD_P = ' 1 ', the state machine refer to X_START STATE, ready to send the start bit.

X_START STATE : In this state, the UART transmitter sends a logic 0 of one bit time width to TXD, i.e. the start bit. The state machine come into X_WAIT state followed.

X_WAIT STATE : In this state, the state machine waiting for the sixteenth BCLK, when it comes, it refer to the X_SHIFT state, to convert the parallel data to the serial data.

X_SHIFT STATE : State machine realizes conversion of data to send. After switching it comes back to the X_WAIT state.

X_STOP STATE : Stop bit send state namely. When the data frame is sent, the state machine comes into this state, and sends logic 1 signal of 16 BCLK cycle, i.e., 1 stop bit. After the stop bit is sent , the state machine comes back to the X_IDLE state, waiting for another command to send a data frame.

4 The Simulation Results

During the verification process, I use Modelsim in the Company of Model Technology to conduct function simulation on the UART controller.

4.1 The Simulation Waveform of UART Receiver Is Shown in Figure 2

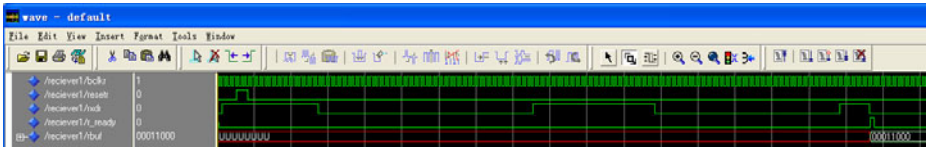


Fig. 2. The simulation waveform of UART receiver

4.2 The Simulation Waveform of Uart Transmitter Is Shown in Figure 3

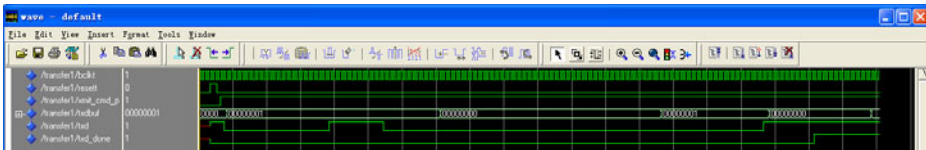


Fig. 3. The simulation waveform of UART transmitter

Through the simulation waveform , the design results correctly transmits and receives a frame data and generates a corresponding interrupt, CPU can read real-time working state. the correction and completion of this design is validated, all functions meet the expected requirements, but it also show that the design idea is completely feasible.

Using FPGA to achieve UART reduces the system area and the power consumption, improves the design of stability, but it also makes full use of the remaining resources in FPGA. The method of software realization of hardware has become the dominant trend in the field of electronic design. In many occasions, the UART controller can completely replace the dedicated IC chip. The design has already been downloaded to Xilinx 's Spartan3 series XC3S400 devices. Comprehensive report displays that the design has consumed 195 LE (Logic,Element) .in large-scale FPGA, this is only a small part of resources.

References

1. Xia, Y.: Verilog digital system design. Beihang University press, Beijing (2003)
2. Bhasker, J.: Verilog HDL Synthesis A Practical primer. Star Galaxy, London (1998)
3. Ali, L., Sidek, R., Aris, I., Ali, A.M., Suparjo, B.S.: Design of a micro-UART for SoC application. Computers and Electrical

Synchronization of Fractional-Order Chaotic System with Application to Communication

Tan Wen^{1,2}, Jiang Fengling², Liu Xianqun³, Liu Jian Xun³, and Wu Feng²

¹ Key Lab of Knowledge Processing and Networked Manufacture, Hunan University of Science and Technology, Xiangtan 411201, Hunan, China

² College of Information and Electrical Engineering, Hunan university of Science and Technology of China, Xiangtan 411201, China

³ College of Mechanical and Electrical Engineering, Hunan university of Science and Technology of China, Xiangtan 411201, China

Abstract. This paper studied the synchronization of fractional-order chaotic system based on the theory of fractional calculus, and the synchronization between the two identical fractional-order Chen systems is realized after 0.6s by using the active control, and the simulation results verify the effectiveness of the examined method. Furthermore, the control scheme can be used in secure communication via the technology of chaotic masking. Numerical simulations coincide with the theoretical analysis.

Keywords: Fractional-order system, chaos synchronization, communication.

1 Introduction

It is well known that the fractional calculus has a long mathematical history, but its applications to physics and engineering are just recent subject of interest [1]. In recent years, many researchers found that many systems have the feature of fractional-order dynamics, such as viscoelastic system [2-3], electrode-electrolyte polarization [4], and electromagnetic waves [5]. In Ref.[6], chaos and hyperchaos in the fractional-order Rossler equations were studied, in which chaos can exist in the fractional-order Rossler equation with order as low as 2.4, and hyperchaos exists in the fractional order Rossler hyperchaos equation with order as low as 3.8.

More recently, the synchronization of chaotic systems has attracted much attention since the seminal paper by Pecora and Carroll in 1990. In Ref.[7], synchronization of fractional-order chaotic systems is firstly investigated. The chaotic control and synchronization of fractional-order systems are concerned extremely [8-10]. It has recently attracted increasing attention due to its potential applications in secure communication and control processing. However, to our best knowledge, in many literatures [11-13], the authors are all concerned with the secure communication of integer order chaotic systems. In Ref.[14], A fractional-order chaotic secure communication scheme is presented using an extended fractional Kalman filter. Although the application in secure communication is achieved by the method of design filter, no matter what is used integer order or fractional order, is too complex, and the chaotic masking technology in secure communication works quite well by the

chaotic synchronization. Ref.[15], Fractional order Liu-system synchronization and its application in multimedia security is achieved by chaotic masking. In Ref.[16], the paper succeed in implementation of a secure communication by chaotic masking.

Based on the technology of chaotic masking, the approximate Gaussian white noise with statistical properties of chaotic signals are used as a carrier signal to be transmitted for hiding the information, the signal are covered up by the synchronization of chaotic signals at the receiver to restore the useful signal, and achieve the purpose of confidential communication in chaotic secure communication. Because of the chaotic dynamics, with its noise like broad band power spectra, is the best of candidate to avoid narrow-band effects, such as frequency-selective fading or narrow-band disturbances in communication systems.

In this work, the synchronization of two identical fractional-order Chen systems is achieved by using the active control technique. This method is simple and does not require computing the conditional Lyapunov exponents. Numerical simulations are given to validate the proposed synchronization approach. Moreover the information signal can be recovered undistorted when this method is applied to secure communication. The consistent of numerical simulation with the analysis results show that the scheme is effective.

2 Fractional Derivative and Its Approximation

There are several definitions of fractional derivatives [1]. In our work, we use the best known Riemann-Liouville defined by

$$\frac{d^\alpha f(t)}{dt^\alpha} = \frac{1}{\Gamma(n-\alpha)} \frac{d^n}{dt^n} \int_0^t \frac{f(\tau)}{(t-\tau)^{\alpha-n+1}} d\tau. \tag{1}$$

Where $\Gamma(\cdot)$ is the gamma function and $n-1 \leq \alpha < n$ (n is integer). This definition is significantly different from the classical definition of derivative.

Upon considering all the initial conditions to be zero, one then has the Laplace transform of (1)

$$L\left\{\frac{d^\alpha f(t)}{dt}\right\} = s^\alpha L\{f(t)\}. \tag{2}$$

Therefore, the fractional integral operator of order " α " can be represented by the transfer function $F(s) = 1/s^\alpha$. Because the standard definition of fractional derivative can not be directly computed the fractional operators in time-domain simulation. In order to effectively analyze fractional chaotic behavior of dynamical systems, a general method to solve the fractional differential is to approximate the fractional operators by using operators of the standard integer order. This approximation is fully meet to the needs of the project. Ref.[18], approximations for $F(s) = 1/s^\alpha$ ($\alpha=0.1-0.9$) in steps 0.1 are given, with errors of approximately 2dB.

3 The Fractional Order Chen System

Now, consider the fractional-order Chen system as follows:

$$\begin{cases} \frac{d^\alpha x}{dt^\alpha} = a(y - z) \\ \frac{d^\alpha y}{dt^\alpha} = (c - a)x - xz + cy \\ \frac{d^\alpha z}{dt^\alpha} = xy - bz \end{cases} \quad (3)$$

where $a=35, b=3, c=28, \alpha$ is the fractional order ($0 < \alpha < 1$).

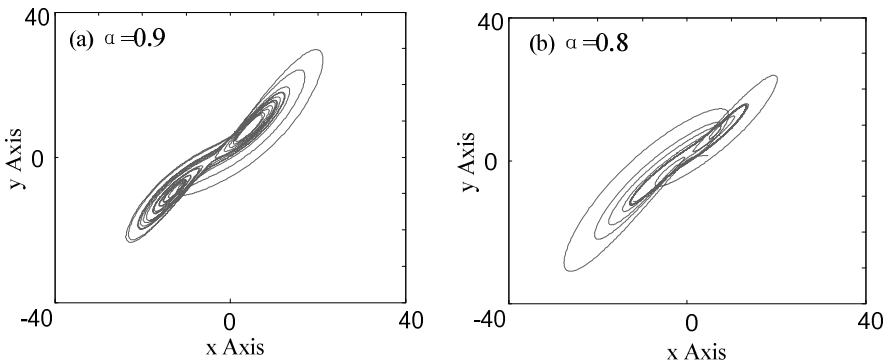


Fig. 1. Phase portraits of the fractional-order Chen system (3) when $a=35, b=3, c=28$

Simulations are performed for $\alpha=0.9, 0.8$ respectively. The simulation results demonstrate that chaos indeed exists in the fractional order Chen system with order less than 3. When $\alpha=0.9$ and 0.8 , chaotic attractors are found and the x-y phase diagrams are shown in Fig.1 (a) and (b), respectively. We can see that the chaotic attractors with $\alpha=0.9$ and 0.8 in the fractional order Chen system are similar and looks like the Lorenz system's attractor.

4 The Synchronization of the Two Identical Fractional-Order Chen System

Now, we will study synchronization between two identical fractional-order Chen systems, employing the active control technique.

The fractional-order Chen system is described by

$$\begin{cases} \frac{d^\alpha x_1}{dt^\alpha} = a(y_1 - z_1) \\ \frac{d^\alpha y_1}{dt^\alpha} = (c - a)x_1 - x_1 z_1 + cy_1 \\ \frac{d^\alpha z_1}{dt^\alpha} = x_1 y_1 - bz_1 \end{cases} \tag{4}$$

as the drive system. And response system is described by

$$\begin{cases} \frac{d^\alpha x_2}{dt^\alpha} = a(y_2 - z_2) + u_1 \\ \frac{d^\alpha y_2}{dt^\alpha} = (c - a)x_2 - x_2 z_2 + cy_2 + u_2 \\ \frac{d^\alpha z_2}{dt^\alpha} = x_2 y_2 - bz_2 + u_3 \end{cases} \tag{5}$$

Where u_1, u_2, u_3 are control function. Our aim is to design the controllers $u_i (i = 1, 2, 3)$ that will make the response system (5) achieve synchronization with the drive system (4). Then, Subtracting Eq. (4) from Eq. (5), we obtain the error dynamics system as following

$$\begin{cases} \frac{d^\alpha e_1}{dt^\alpha} = a(e_2 - e_1) + u_1 \\ \frac{d^\alpha e_2}{dt^\alpha} = (c - a)e_1 - x_2 z_2 + x_1 z_1 + ce_2 + u_2 \\ \frac{d^\alpha e_3}{dt^\alpha} = x_2 y_2 - x_1 y_1 - be_3 + u_3 \end{cases} \tag{6}$$

where $e_1 = x_2 - x_1$, $e_2 = y_2 - y_1$ and $e_3 = z_2 - z_1$.

Then consider the active control function [18] is

$$\begin{cases} u_1 = V_1(t) \\ u_2 = x_2 z_2 - x_1 z_1 + V_2(t) \\ u_3 = x_1 y_1 - x_2 y_2 + V_3(t) \end{cases} \tag{7}$$

Taking the inputs $V_1(t), V_2(t), V_3(t)$ as

$$\begin{bmatrix} V_1(t) \\ V_2(t) \\ V_3(t) \end{bmatrix} = A \begin{bmatrix} e_1 \\ e_2 \\ e_3 \end{bmatrix} \tag{8}$$

An appropriate choice of the matrix A can be

$$A = \begin{pmatrix} a-1 & -a & 0 \\ a-c & -(1+c) & 0 \\ 0 & 0 & b-1 \end{pmatrix}. \tag{9}$$

So, the error system (6) can be rewritten as

$$\begin{cases} \frac{d^\alpha e_1}{dt^\alpha} = -e_1 \\ \frac{d^\alpha e_2}{dt^\alpha} = -e_2 \\ \frac{d^\alpha e_3}{dt^\alpha} = -e_3 \end{cases}. \tag{10}$$

Obviously, as for the closed-loop system eigenvalues are -1,-1,-1,the errors e_1, e_2, e_3 will converge to zero when $t \rightarrow \infty$. Therefore, synchronization of the two identical fractional-order Chen systems (3) and (4) is achieved.

4.1 Simulation Results

In the numerical simulations, we set the parameters of (3) and (4) as $a=35, b=3, c=28$ and $\alpha=0.9$ for derive system and response system. The initial conditions of the systems are taken arbitrarily as $x_1(0) = 1, y_1(0)=2$ and $z_1(0)=-1$; $x_2(0) = 2, y_2(0) = 3$ and $z_2(0) = 3$. Numerical results show that the synchronization of two identical fractional-order Chen system is achieved using the active control as Fig.2. From Fig.2, we can see that the errors e_1, e_2, e_3 all converge to zero less than 1.5s. So, the identical fractional-order Chen chaotic systems can be synchronized.

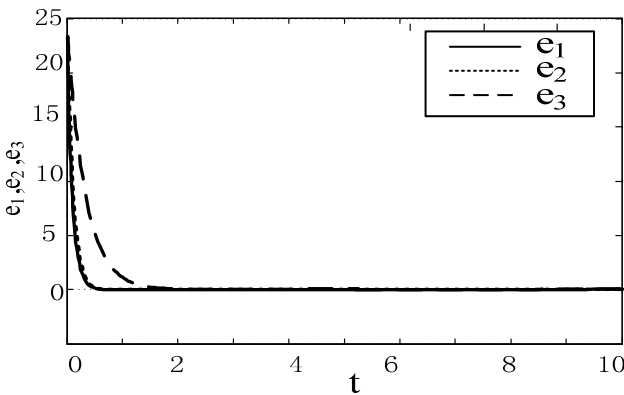


Fig. 2. (a) the errors of e_1, e_2 converge to zero about 0.6s, and the e_3 converges to zero about 1.5s.(b) the x_2 of system (4) synchronized to the x_1 of the system (3).This shows that the identical fractional-order Chen systems can be synchronized.

5 Application

In this section, to verify and demonstrate the effectiveness of the proposed method, we will display the numerical results for fractional order chaotic Chen systems in secure communication. Based on the theory of the communication, the schematic diagram of secure communication is displayed as Fig. 3 with the synchronization scheme.

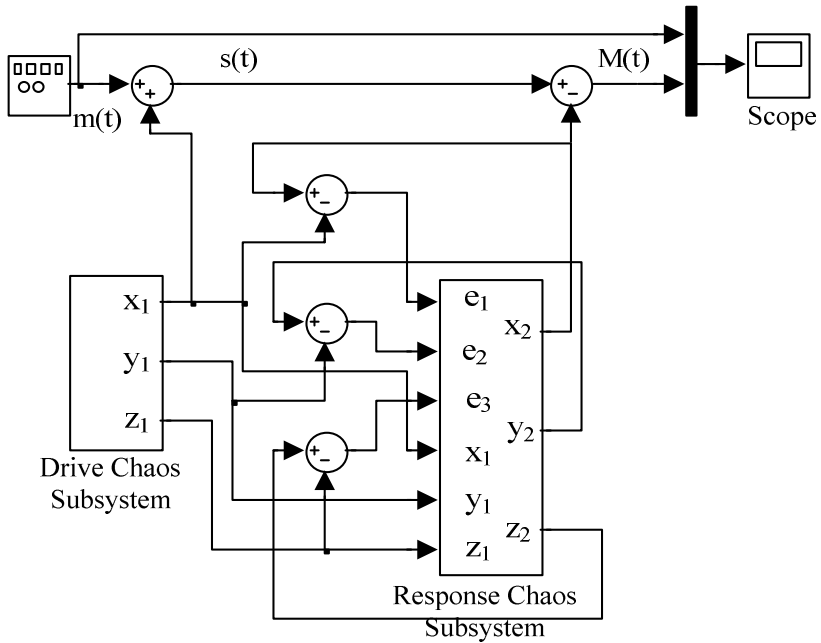


Fig. 3. Chaotic masking technology for communication system

In Fig.3, x_1 is the variable of the transmitter, $m(t)$ is the transmit information signals, $s(t)$ is added to the variable x_1 .The sum of the signal $s(t)=m(t)+x_1$ is transmitted to the receiver. $M(t)$ is the recover signal after the x_2 and x_1 synchronized at the receiver end.

Consider the transmit signal is the triangle wave with the amplitude 5 and the frequency 1 as Fig.4(a) by scope. The useful signal is added to the chaotic signal during transmission, we can find that the mixed signals is different from the original signals as Fig.4(b), so the scheme of secure communication is effective. Simulation results show that the system effectively restored the useful signals after 0.6s as Fig.4(c).

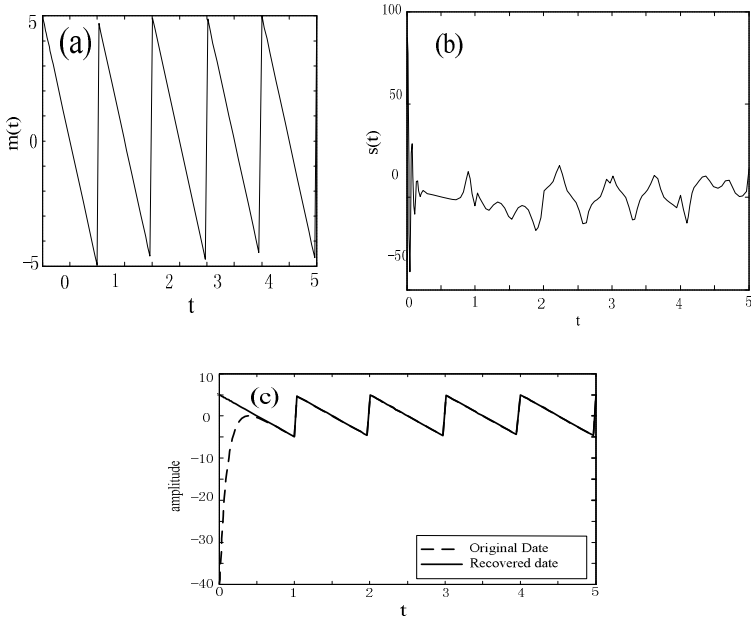


Fig. 4. (a) the useful signals for transmission.(b) the transmit information is different with the previous by masking.(c) the useful signals are recovered at the receiving end. This shows a figure application of different schemes of chaotic.

6 Conclusion

In this paper, the synchronization of fractional-order chaotic system is studied, and the synchronization between two such identical fractional order systems has been realized via active control. The simulation results show that the control method is reliable. Moreover, numerical experiments for the secure communication system indicate that the synchronization works quite well, which may has potential application in other areas.

Acknowledgments. This work was supported by the National Natural Science Foundation of China Grant 90818004 and 1101053, by the Natural Science Foundation of Hunan Province of China Grant 09JJ3117), the Natural Science Foundation of Jiangsu Province of China BK2009727, the Key Project of Chinese Ministry of Education 211118, the Excellent Youth Foundation of Educational Committee of Hunan Provincial 10B002 and the Planned Science and Technology Project of Hunan Province B11125.

References

1. Podlubny, I.: Fractional differential equations. Academic Press, New York (1999)
2. Bagley, R.L., Calico, R.A.: Fractional order state equations for the control of viscoelastically damped structures. *Journal of Guidance, Control, and Dynamics* 14, 304–311 (1991)
3. Koeller, R.C.: Application of fractional calculus to the theory of viscoelasticity. *J. Appl. Mech.* 51, 299–307 (1984)
4. Ichise, M., Nagayanagi, Y., Kojima, T.: An analog simulation of noninteger order transfer functions for analysis of electrode process. *J. Electroanal. Chem.* 33, 253–265 (1971)
5. Heaviside, O.: Electromagnetic theory, New York, Chelsea (1971)
6. Li, C., Chen, G.: Chaos and hyperchaos in the fractional order Rössler equations. *Physica A* 41, 55–61 (2004)
7. Li, C.G., Liao, X.F., Yu, J.B.: Synchronization of fractional order chaotic systems. *Phys. Rev. E* 68, 1–3 (2003)
8. Wu, X., Lu, Y.: Generalized projective synchronization of the fractional-order Chen hyperchaotic system. *Nonlinear Dyn.* 57, 25–35 (2009)
9. Yan, J.P., Li, C.P.: On chaos synchronization of fractional differential equations. *Chaos Solitons & Fractals* 32, 725–735 (2007)
10. Wang, Z., Zhang, H., Li, Y., et al.: A New Method on Synchronization of Fractional-Order Chaotic Systems. In: Proceedings of 2010 Chinese Control and Decision Conference, vol. 07, pp. 3357–3362 (2010)
11. Ruan, H., Zhai, T., Yaz, E.E.: A chaotic secure chaotic communication scheme with extended Kalman filter based parameter estimation. In: Proceeding of IEEE Conference on Control Applications, vol. 26, pp. 404–408 (2003)
12. Chen, M., Zhou, D., Shang, Y.: A sliding mode adaptive observer chaotic communication scheme. *Chaos, Solitons & Fractals* 253, 573–578 (2005)
13. Huang, C.-F., Hung, M.-L., et al.: Chaos-based Secure Communication via control. *World Academy of Science* 119, 650–653 (2010)
14. Kiani-B, A., Fallahi, K., Pariz, N., Leung, H.: A chaotic secure communication scheme using fractional chaotic systems based on an extended fractional Kalman filter. *Commun. Nonlinear Sci. Numer. Simul.* 14, 863–879 (2009)
15. Deng, Y.-S., Qin, K.-Y.: Fractional order Liu-system synchronization and its application in multimedia security. In: ICCAS, vol. 23, pp. 769–772 (2010)
16. Oppenheim, A.V., Womell, C.W., Isabelle, S.H.: Signal processing in the context of chaotic signals. In: IEEE Int. Conf. ASSP, vol. 23, pp. 117–120 (1992)
17. Hartley, T.T., Lorenzo, C.F., Qammer, H.K.: Chaos in a fractional order Chua's system. *IEEE Trans. CAS-I* 42, 485–490 (1995)
18. Agiza, H.N., Yassen, M.T.: Synchronization of Rossler and Chen chaotic dynamical systems using active control. *Phys. Lett. A* 278, 191–197 (2001)

Infrared Smoke Online Automatic Monitoring System of Multi Components of Stationary Pollution Sources

Dan Zhang and Chengying Li

School of Civil and Architectural Engineering Liaoning University of Technology Jinzhou,
Liaoning, 121001, P.R. China
zhangdan_5181910@yahoo.com.cn

Abstract. The high temperature molecular state heating tracing sampling technology was applied to eliminate the interference of steam and the loss of SO_2 . The multi-components of infrared luminosity analysis technology, which combined single beam double wavelength spectrophotometry method with gas filtering correlation method, was also used in smoke analysis. The multi-component smoke continuous monitoring with the fixed pollution source was obtained through microprocessor filtering effectively the influences of sum multiplier, auto quantitative measurement, long-range control, remote transmission, abnormality alarm, data storage and report can be met, form a set of gaseous contaminants analytical system.

Keywords: infrared luminosity, sum multiplier, heating tracing sampling.

1 Introduction

With the speed development of national economy, environmental contamination caused by emission of stationary pollution source proved to be a highlight problem. It brings great difficulties to monitoring and detection of flue gas emission as the groups of flue gas emission complex and severe environment at industry spot (such as high temperature), especially the accurate measurement of gas contaminant (sulphur dioxide, oxynitride) is highlight. Through many years of practical test, the integration electrical modulation infrared light supply and filtering sense gas analysis meter of infrared sensor can not interior calibrate and pyrometry, then develop multi components of stationary pollution source infrared gas online auto-monitor system to improve the competitiveness of native flue gas analysis meter, meet the requirement of market and promote government to accelerate monitor progress of gas emission.

2 Core Principle

The gas such as SO_2 , CO , NO , NO_2 and etc in the exhaust gas has its own characteristic absorbing wavelength in infrared band (shown in Table 1): characteristic absorbing band can be identified just like fingerprint, and it can reflect the concentration of gas through the assimilation of characteristic absorbing band to infrared energy.

According to Lambert–Beer law, the relationship of absorbance and concentration of sample gas is:

$$\ln(I/I_0) = LkC \tag{1}$$

Table 1. Characteristic absorbing wavelength of partial gases in exhaust gas

Gas	CO	CO ₂	NO	SO ₂	H ₂ O
Characteristic absorbing wave length /μm	4.65	4.3	5.3	7.3	3-6

I₀, I stand for compared light intensity and measure light intensity; L stands for the journey of infrared radiation through absorbing gas; k stands for the absorption coefficient of target gas; C stands for consistence of sample gas.

There are two light filters in single light beam double wavelength: compared light filter and measure light filter. The measured quantity groups of indigestible infrared band get through compared light filter, the changes of measured quantity groups of concentrations does not affect the light intensity through measure air chamber, I₀ acts as compared light intensity. The measured quantity groups of characteristic absorbent infrared band get through measure light filter, the light intensity through measure air chamber is corresponding with exhaust gas concentration, I acts as measure light intensity. Calculate the measured quantity groups of concentrations of exhaust gas according to Lambert–Beer law shown in Fig 1.

Gas filtering correlation method take gas filtering pond of fill high pressure measured quantity gas instead of comparison optical filter in single light beam double wavelength, the effect of filtrate characteristic absorbing infrared band is better. Fig 2 is Optics structure diagram of gas filtering correlation method.

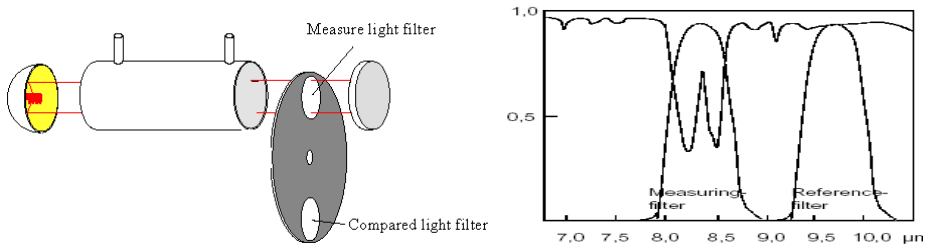


Fig. 1. Optics structure diagram of single light beam double wavelength and the assimilation, measurement and comparison infrared band of SO₂

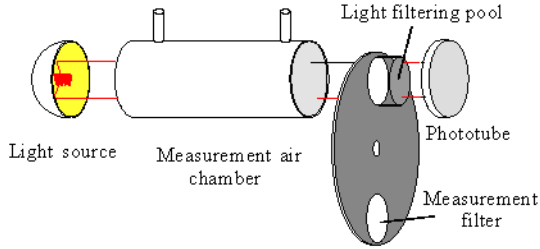


Fig. 2. Optics structure diagram of gas filtering correlation method

Multi groups of nondispersive infrared measurement system based on gas filtering correlation technique contains light source, cut light wheel, measurement air chamber, filtering wheel and phototube, and the following is optics structure diagram(Fig 3):

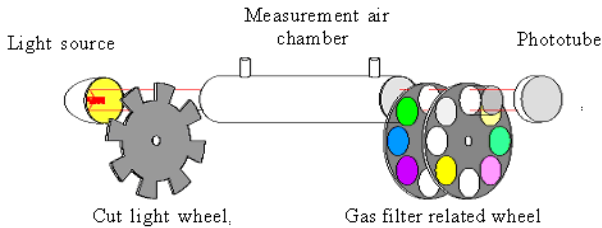


Fig. 3. Optics structure diagram of multi groups of stationary pollution source infrared gas online automatic monitoring system

Nernst lamp gives out infrared light: cut light wheel radio frequency stereotypes the signal beam; two gas filtering correlation wheels were installed on filtering pond and measurement optical filter of different measured quantity gases; the rotation of cut light wheel and gas filtering correlation wheels are driven by brushless continuous current dynamo, finish the measurement of each group according to automatic control instruction. There are filling stomata and bleeder hole in high temperature measurement air chamber to keep gas concentration gas concentration steady to prevent steam and contaminant condensing and disturbing the luminosity analysis, heat trace with high temperature heat tracing band. The signal acquired by phototube needs amplifying as it is weak.

The position of filtering pond and measurement optical filter of each group of gases are controlled by internal processor, scan each groups many times in one measuring process to improve the signal-to-noise ratio of signal. In data processing, the influence of sum disturbance and multiplier disturbance to disturbing component conducted by microprocessor: when each group of optical spectrum overlap, interferences of disturbing component to measured quantity constituent can be achieved by minus the concentration of disturbing component; interference can be

eliminated by correction factor when absorptivity of measured quantity constituent changed caused by disturbing component.

3 Key Technique

3.1 Smoke Analysis

Smoke is analysis by multi component luminosity analysis technology combine single light beam double wavelength with gas filtering correlation technique. The mutual deduct of contemporary measurement and interference parameter of gas filtering ponds on the two filtering wheels to multi component of gases improve the measurement accuracy and can high-precision continuously detect as many as 8 groups. Standard gas need not using in internally installed standard chamber. It can correct zero and range automatically according to given program and auxiliary equipment.

3.2 Signal Amplification Circuit

Signal amplification circuit is chopper stabilization combining with multistage amplification mode made by CMOS, signal amplification processing circuits constitute with multi-way switch and meter amplifier was taken into account, its advantages such as high gain, strong common mode rejection capability, fast response, small drifting, small input bias current and maladjustment, which reduce the data acquisition error brought by gain correlated error as much as possible, and it can dynamically zero makes measurement accuracy higher and performance more steady.

3.3 Continuous Monitoring System of Gas Emission

Continuous monitoring system of gas emission was set up by contamination of multidisciplinary techniques such as intelligent sampling combining with filtering algorithm, multithreading control, software automatic identification compensation slight contamination, luminous power software revise, slipping average value combining with flexible distributed process, data storage combination with long-range control, quantitative measurement of smoke, automatic zero, automatic standard, buzzer, remote transmission , data storage and report generation can be meet.

3.4 Monitor and Control Gaseous Contaminants of Pollution Source by Embedded Software

Monitor and control gaseous contaminants of pollution source by embedded software. Instantaneous value of monitoring objects, history and overweight alarm can be provided; combine with service conditions of environmental protection departments, a series of environmentally-friendly business solutions such as e-government affairs and office automation are provided. Embedded software has the following

characteristics: strong measuring signal processing flexibility, which can measure in different variables and concentration range in a device; intelligent sampling combining with filtering algorithm removes abnormal value, calculates average value, gaseous contaminant measurement on the basis of Lambert–Beer law.

3.5 Intelligent Monitoring

Single chip microcomputer is embedded in gaseous contaminants relevant parameter measuring object by Cygnol single chip core technique, intelligent monitoring can be realized. According to gaseous contaminants measuring environmental requirement, physical environment(mini-type), electric/air (reliable) , cost(cheap) were taken into account; Regarding the minimum software configuration ,hardware configuration and the corresponding interface circuit, core technology was taken, The abstract levels between bare device and application program were provided; some programs operating together can be allowed, the processor shared; all the I/O operations were abstracted, providing a simple disc I/O abstract, while every program can use it; robust network function is provided, especially the support of TCP/IP.

4 Reach Qualification

Table 2. Characteristic absorbing wavelength of partial gases in exhaust gas

Index content	SO ₂	NO ₂	NO	CO
Measure scope / mg/m ³	0-4000	0-1000	0-2500	0-2500
Detection prescribed minimum / mg/m ³	10	10	10	10

Zero drift:≤ ±2.5% F.S/3dor7d; Range drift:≤ ±2.5% F.S/3dor7d; Linearity error:≤ ±5.0% F.S; Response time:≤200s; repeatability: ≤ 0.5%; output wave:≤ 0.4% ;Alarm output: power failure, demarcate failure, analysis meter failure.

5 Conclusion

Taking multi component luminosity analysis technology of single light beam double wavelength combining with gas filtering correlation technique, high-accuracy continuous monitor many gas component simultaneously by a set of infrared luminosity analytical system, inlay normal air chamber can correct zero and range automatically; the operative modes of device such as programmed control, data processing and remote communication were conducted through PLC and compound integrated adaptive communication technology; auto quantitative measurement, long-range control, remote transmission, abnormality alarm, data storage and report can be met form a set of gaseous contaminants analytical system.

References

1. Ben-Dor, B.: Polarization properties of targets and backgrounds in the infrared. In: Proc. of SPIE, 8th Meeting on Optical Engineering in Israel: Optical Engineering and Remote Sensing, vol. 1971, pp. 68–76 (1992)
2. Michael Cathcart, J., Bock, R.D.: Analysis of Infrared Polarization Signatures for Backgrounds and Objects. In: IEEE Geoscience and Remote Sensing Symposium, IGARSS 2004. Proceedings, vol. 3(7), pp. 1593–1596 (2004)
3. Wang, Z., Hong, J., et al.: Study of thermal polarization imaging measurement in target recognition. *Optical Technique* 33(2) (March 2007) (in Chinese)
4. Aron, Y., Gronau, Y.: Polarization in the LWIR. In: Proc. of SPIE, vol. 5783, pp. 653–661 (2005)

Servo System of 6 DOF Electro-hydraulic Shaking Table

Liyi Yin^{1,*}, Zhengmao Ye¹, Gang Shen^{1,2}, and Junwei Han¹

¹ State Key Laboratory of Robotics and System, School of Mechatronics Engineering, Harbin Institute of Technology, Harbin, Heilongjiang 150001, China

² School of Mechanical and Electrical Engineering, China University of Mining and Technology, Xuzhou, Jiangsu, 221116, China
yinliyi@hitedu.cn

Abstract. Electro-hydraulic shaking table (EHST) is a useful experimental apparatus to real-time replicate the desired acceleration vibration signal for evaluating the performance of the tested specimen structural systems. A three axis six degree-of-freedom (DOF) EHST system with eight hydraulic actuators is presented in the paper. A decouple control method is employed to lower the acceleration couple among the six DOF. The procedure of the decouple controller is programmed in MATLAB/Simulink, and then compiled to a real-time PC with Microsoft Visual Studio.NET for implementation. The experimental results demonstrate that a better tracking performance with the improved servo controller is achieved in experiments by using actual EHST.

Keywords: Electro-hydraulic shaking table, decouple control, identification.

1 Introduction

Hydraulic vibration table as the pivotal basic experimental equipment is widely used in many important engineering fields to achieve environmental simulation, such as municipal and building works; high frequency fatigue test of engineering material which is used in the road simulation test of vehicles and mobile machinery; aseismic test of Large Engineering like dam and high-rise building.

The performance of multi-axis hydraulic shaking table can directly affects the technological progress of related industries. So the technical level of multi-axis hydraulic shaking table not only takes an important role in the national economic development, but also is a major sign of the development level of a country's industrial technology.

Whether in the aviation, aerospace, tanks, chariot and other military areas, or in civil engineering, water conservancy construction and other civil field, shaking test is always a kind of necessary basic experimental means.

With the rapid technological progress in these engineering above, the requirement of the environment of shaking test becomes more and more complex and strict.

* This research was supported by the 921Manned Space Project of the China Academy of Space Technology (CAST) and Self-Planned Task SKLRS200803B of the State Key Laboratory of Robotics and Systems, Harbin Institute of Technology (HIT), and also was supported by the National Natural Science Foundation of China (No. 50975055).

We would like to draw your attention to the fact that it is not possible to modify a paper in any way, once it has been published. This applies to both the printed book and the online version of the publication. Every detail, including the order of the names of the authors, should be checked before the paper is sent to the Volume Editors.

2 Paper Preparation

2.1 Composition of the Control System of EHST

The experimental carrier in this paper is an electro-hydraulic shaking table with six degree-of-freedom (DOF). The structure is shown in the Figure 1. 6 DOF contains 3 translational DOF(X, Y, Z) and 3 rotational DOF(Rx, Ry, Rz).

The motion of 8 actuators is controlled by 6 DOF. 8 actuators contains x_1 and x_2 in X axis direction, y_1 and y_2 in Y axis direction and z_1, z_2, z_3, z_4 in Z axis direction. In the mechanism theory, the mode of 8 actuators controlled by 6 DOF is named redundant driving system.

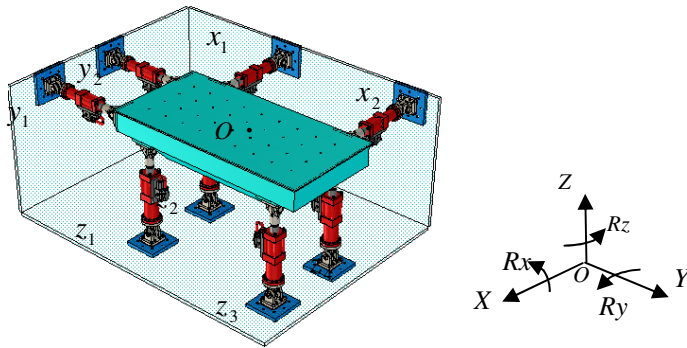


Fig. 1. The structural diagram of EHST

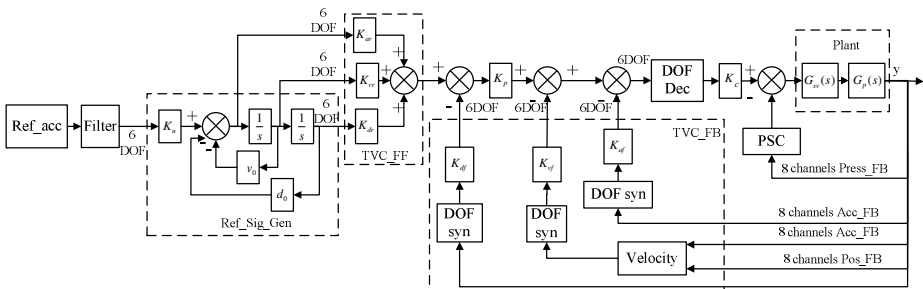


Fig. 2. Structure of EHST servo control system

2.2 Independent Control of DOF

If you have more than one surname, please make sure that the Volume Editor knows how you are to be listed in the author index.

$$\begin{cases} X = \frac{1}{2}(x_1 + x_2) ; Y = \frac{1}{2}(y_1 + y_2) ; Z = \frac{1}{4}(z_1 + z_2 + z_3 + z_4) \\ R_x = \frac{1}{4}(z_1 + z_2 - z_3 - z_4) ; R_y = \frac{1}{4}(z_1 - z_2 + z_3 - z_4) ; R_z = \frac{1}{4}(x_1 - x_2 + y_1 - y_2) \end{cases} \quad (1)$$

According to the definition of 6 DOF, the definition of DOF compounding matrix is defined as below.

$$J_h = \begin{bmatrix} 0.5 & 0.5 & 0 & 0 & 0 & 0 & 0 & 0 \\ 0 & 0 & 0.5 & 0.5 & 0 & 0 & 0 & 0 \\ 0.25 & -0.25 & 0.25 & -0.25 & 0 & 0 & 0 & 0 \\ 0 & 0 & 0 & 0 & 0.25 & 0.25 & 0.25 & 0.25 \\ 0 & 0 & 0 & 0 & 0.25 & 0.25 & -0.25 & -0.25 \\ 0 & 0 & 0 & 0 & 0.25 & -0.25 & 0.25 & -0.25 \end{bmatrix} \quad (2)$$

According to Formula 2, the decomposition matrix can be deduced by pseudo-inverse.

$$J_f = \begin{bmatrix} A & 0 \\ 0 & B \end{bmatrix} \quad (3)$$

Where $A = \begin{bmatrix} 1 & 0 & 1 \\ 1 & 0 & -1 \\ 0 & 1 & 1 \\ 0 & 1 & -1 \end{bmatrix}$; $B = \begin{bmatrix} 1 & 1 & 1 \\ 1 & 1 & -1 \\ 1 & -1 & 1 \\ 1 & -1 & -1 \end{bmatrix}$.

2.3 Pressure Stabilization Controller

The form of the electro-hydraulic shaking table is symmetrical. The system is a quadric statically indeterminate system for it uses 6 DOF to control 8 actuators. According to the reference 8, the pressure drop of 8 actuators of shaking table is zero at balanced state, when the shaking table can normally work.

We assume that the output force at one moment is $P'_{x1}, P'_{x2}, P'_{y1}, P'_{y2}, P'_{z1}, P'_{z2}, P'_{z3}, P'_{z4}$.

The internal force caused by coupling is $P_{x1}, P_{x2}, P_{y1}, P_{y2}, P_{z1}, P_{z2}, P_{z3}, P_{z4}$. Then internal force of each DOF is as below.

$$\begin{cases} \bar{P}_x = (P_{x1} + P_{x2}) / 2 ; \bar{P}_y = (P_{y1} + P_{y2}) / 2 ; \bar{P}_z = (P_{z1} + P_{z2} + P_{z3} + P_{z4}) / 2 \\ \bar{P}_{R_x} = (P_{z3} + P_{z4} - P_{z1} - P_{z2}) / 4 ; \bar{P}_{R_y} = (P_{z2} + P_{z4} - P_{z1} - P_{z3}) / 4 ; \bar{P}_{R_z} = [(P_{x1} - P_{x2}) + (P_{y1} - P_{y2})] / 4 \end{cases} \quad (4)$$

The differential value between the output force of each actuator and mean force of each DOF can be calculated by geometric relation of actuators.

$$\begin{cases} P_{x_1} = P'_{x_1} - \bar{P}_x - \bar{P}_{R_z} ; P_{x_2} = P'_{x_2} - \bar{P}_x - \bar{P}_{R_z} \\ P_{y_1} = P'_{y_1} - \bar{P}_y - \bar{P}_{R_z} ; P_{y_2} = P'_{y_2} - \bar{P}_y + \bar{P}_{R_z} \\ P_{z_1} = P'_{z_1} - \bar{P}_z + \bar{P}_{R_x} + \bar{P}_{R_y} ; P_{z_2} = P'_{z_2} - \bar{P}_z + \bar{P}_{R_x} - \bar{P}_{R_y} \\ P_{z_3} = P'_{z_3} - \bar{P}_z - \bar{P}_{R_x} + \bar{P}_{R_y} ; P_{z_4} = P'_{z_4} - \bar{P}_z - \bar{P}_{R_x} - \bar{P}_{R_y} \end{cases} \quad (5)$$

To restrain the difference, eliminate internal force, and make the output force of each actuator approach the mean force, the control variable below is introduced.

$$\begin{cases} U_{P_{x_1}} = -P_{x_1} / K_{x_1} ; U_{P_{x_2}} = -P_{x_2} / K_{x_2} \\ U_{P_{y_1}} = -P_{y_1} / K_{y_1} ; U_{P_{y_2}} = -P_{y_2} / K_{y_2} \\ U_{P_{z_1}} = -P_{z_1} / K_{z_1} ; U_{P_{z_2}} = -P_{z_2} / K_{z_2} \\ U_{P_{z_3}} = -P_{z_3} / K_{z_3} ; U_{P_{z_4}} = -P_{z_4} / K_{z_4} \end{cases} \quad (6)$$

2.4 Three-State Controller

The three-state controller is a basic controller of shaking table control system. The three-state refers to the position, speed and acceleration of the shaking table system. Figure 3 shows the principle of the three-state controller.

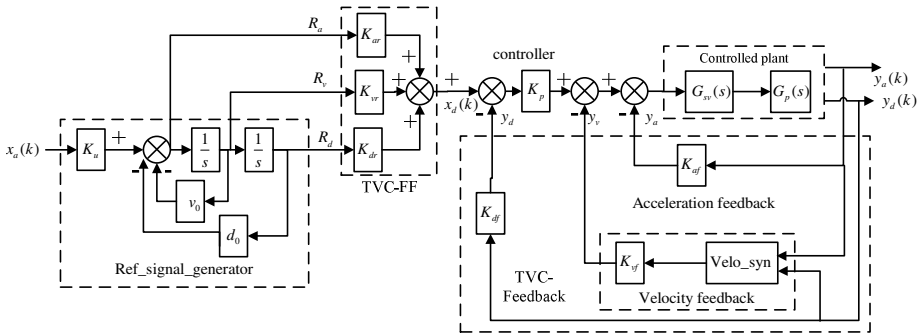


Fig. 3. Block diagram of TVC

The excitation system of shaking table can be described as a typical electro-hydraulic position servo system. Dynamic characteristics of servo valve ignored, the closed-loop frequency characteristic of the system can be approximately described as the transfer function below.

$$W(s) = 1 / [(s / \omega_r + 1)(s^2 / \omega_{nc}^2 + 2\xi_{nc}s / \omega_{nc} + 1)] \quad (7)$$

- ω_r — the corresponding frequency of acceleration response frequency bandwidth demanded by the system
- ω_{nc} — usually 1.05-1.20 times of hydraulic natural frequency
- ξ_{nc} — usually 0.7, dimensionless.

Dynamic characteristics of servo valve ignored, the open-loop characteristic of the typical electro-hydraulic position servo system controlled by proportional control can be described as below.

$$G(s) = K_v / [s(s^2 / \omega_h^2 + 2\xi_h s / \omega_h + 1)] \tag{8}$$

- ω_h ——the natural frequency of hydraulic power mechanism(rad/s)
- ξ_h ——the damping ratio of hydraulic power mechanism, no dimensionless
- K_v ——the system open-loop gain when proportional controlled

Figure 4 shows the system block diagrams added with three-state feedback controller. Then the inner open-loop transfer function of the system can be described as below.

$$G_c(s) = Y_d / R_d = K_{df} K_v / [s^3 / \omega_h^2 + (K_{df} K_v + 2\xi_h / \omega_h) s^2 + (K_{vf} K_v + 1) s + K_{df} K_v] \tag{9}$$

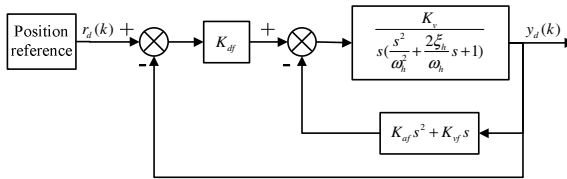


Fig. 4. The TVC feedback controller

Three coefficients(K_{df} , K_{vf} 和 K_{af}) can be obtained while designing three-state feedback controller. Make the characteristic of closed-loop system with three-state feedback controller and the expected one uniform, that is $G_c(s) = W(s)$. Make formula (9) equal with the formula (8), the expression of three coefficients is as below.

$$\begin{cases} K_{df} = \omega_r \omega_{nc}^2 / (K_v \omega_h^2) ; K_{vf} = K_{df} (2\xi_{nc} / \omega_{nc} + 1 / \omega_r) - 1 / K_v \\ K_{af} = K_{df} [2\xi_{nc} / (\omega_r \omega_{nc}) + 1 / \omega_{nc}^2] - 2\xi_h / (K_v \omega_h) \end{cases} \tag{10}$$

The effect of three-state feed-forward is adding B(s) into the system after three-state feedback has regulated well, thus the pole near to the virtual axis of position closed-loop transfer function is cancelled and frequency width of the system is expanded. The three-state feed-forward controller is described as below.

$$B(s) = K_{dr} + K_{vr} s + K_{ar} s^2$$

- K_{dr} ——the position gain of three-state feed-forward controller
- K_{vr} ——the speed gain of three-state feed-forward controller
- K_{ar} ——the acceleration gain of three-state feed-forward controller

Formula (11) can be transferred to the form below for comparing easily.

$$B(s) = K_{dr} (1 + K_{dr} s / K_{vr} + K_{ar} s^2 / K_{dr})$$

To cancel the pole at ω_{nc} in formula (8), make the $(s^2 / \omega_{nc}^2 + 2\xi_{nc}s / \omega_{nc} + 1)$ of formula (11) and formula (8) equal. Then the relation below is concluded.

$$B(s) = K_{dr}(1 + K_{dr}s / K_{dr} + K_{ar}s^2 / K_{dr}) = s^2 / \omega_{nc}^2 + 2\xi_{nc}s / \omega_{nc} + 1$$

To keep the gain of the system constant, make $K_{dr} = K_{df}$. Then three gains of the three-state feed-forward can be solved.

$$K_{vr} = K_{df}(2\xi_{nc} / \omega_{nc}) ; K_{dr} = K_{df} ; K_{ar} = K_{df} / \omega_{nc}^2$$

Therefore, all of the parameters of the three-state controller are determined.

3 Experimental System of EHST

Figure 5 shows the electro-hydraulic shaking table in this paper, which is the test carrier of all kinds of control strategy. It is mainly composed by platform, servo valves, hydraulic cylinders, hydraulic pressure source and connection hinges. The platform is used for assembling samples or apparatus, and it is connected by hinge supports and hydraulic cylinders. Servo valves and hydraulic cylinders transfer the hydraulic energy provided by hydraulic pressure source to mechanic energy, then the platform is driven by mechanic energy. The position feedback signal of the shaking table is measured by linear variable differential transformer (LVDT) fixed on each hydraulic cylinder, and the acceleration feedback signal is measured by acceleration sensor pasted at each driving orientation, and the pressure drop of each actuator is measured by pressure sensor located in upper and lower cavity. All of the feedback signal above is collected by A/D integrated circuit board PCL-816. The sampling time of the experimental system is 1 millisecond.



Fig. 5. The experimental system of EHST

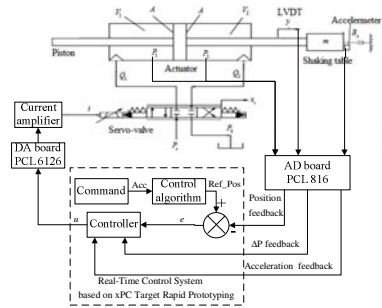


Fig. 6. Schematic of experimental system

3.1 Experiment Result of Pressure Stabilization Controller

According to Table 2, when the pressure stabilization controller does not work, the internal force of horizontal direction actuators is over 7MPa which is the pressure of hydraulic oil. So the 4 horizontal direction actuators can hardly move. After the regulation of the pressure stabilization controller, the pressure drop is below 0.3MPa.

Table 1. Main Technical Parameters

Main Technical Parameters	Value
Platform Dimension	1.5m×1.5m
Platform Mass	1500 kg
Max Sample Mass	1000 kg
Max Displacement (peak-peak)	X:75mm; Y:75mm; Z:52.5mm
Max Speed	X:0.5 m/s; Y:0.5 m/s; Z:0.5 m/s
Max Acceleration(peak-peak)	X:2g; Y:2g; Z:2g
Frequency Arrange	1-50Hz
DOF	6

There are no balance hydraulic cylinders in this shaking table, so 4 vertical direction actuators support mass of the platform. According the parameters shown in Table 1 and Table 2, the expected pressure drop in balance state under ideal condition is 1.8MPa. When the pressure stabilization controller does not work, the stress of 4 vertical direction actuators is non-uniform. After the regulation of the pressure stabilization controller, the stress of 4 vertical direction actuators is much more uniform. During to the variation of pressure drop shown in Table2, the shaking table can work well after the regulating the zero-bias of LVDT and the gain of the pressure stabilization controller.

Table 2. Pressure different with eight actuators under balance status

Cylinder No.	x_1	x_2	y_1	y_2	z_1	z_2	z_3	z_4
before Stabilization	-7.07	7.45	7.63	7.08	3.93	-0.17	-1.27	3.89
After Stabilization	0.27	-0.12	-0.11	0.28	1.75	2.11	0.845	1.651

3.2 Experiment Result of Pressure Stabilization Controller

The frequency width of acceleration response is a key index of the shaking table. The shaking table applies the technique of three-state input and three-state feedback based on pole assignment to enhance stability and frequency width of the system.

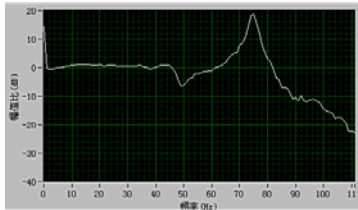
First of all, we use square wave signal to regulate three-state feedback controller based on position closed-loop circuit(mainly regulating acceleration gain K_{af}) to make response speed fastest and overshoot smallest. Then we use random signal to regulate three-state feed-forward controller(mainly regulating acceleration feed-forward gain K_{ar} and speed feed-forward gain K_{vr}) to make the frequency of the system best.

Table 3 shows parameters of all the three-state controllers of the shaking table in 6 DOF. The frequency response curve of Z-direction and Rx-direction shown in Figure 7 is measured by real-time online measuring by Labview. After the regulation of three-state controller, the frequency width of the system is over 45Hz(maximum is 2dB, minimum value is -3dB).

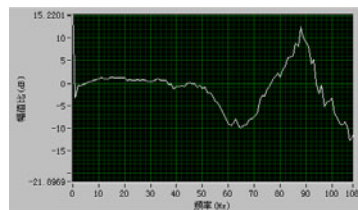
There is a wave trough in Z-direction at 50Hz, and there is a large resonant peak at 75Hz, for the foundation is weak. The same problem appears in X-direction at 65Hz and 88Hz. Therefore, the response frequency width can not larger even three-state controller is applied.

Table 3. Adjusted parameters of servo control system

	TVC K _{ar}	TVC K _{vr}	TVC K _{dr}	df	vf	af	kv	ka	零偏补偿值	单缸增益	压差增益	位移零偏	
X自由度	0.0016	1.65	0.85	1	0	0.02	1	1.6500	x1	0.1700	10	-0.12	0.68
Y自由度	0.0035	1.75	1	1	0	0.028	1	1.7	x2	-0.205	10	-0.05	0
Rx自由度	0.012	2.1	1	1	0	0.02	1	1.5	y1	0.075	7	-0.05	0
Tx自由度	0	0	1	1	0	0	1	1	y2	0.12	7	-0.05	0.43
Z自由度	0	2.9	1	1	0	0.016	1	1.7	z1	0.06	6	-0.05	0.2
Rz自由度	0	2.8	1	1	0	0.015	1	1.7	z2	0.15	6	-0.05	0.01
Ry自由度	0	4.5	1	1	0	0.008	1	1	z3	0.08	6	-0.05	0.01
Ty自由度	0	0	1	1	0	0	1	1	z4	2.05	6	0	0.2



a) Magnitude characteristic of Z DOF



b) Magnitude characteristic of Rx DOF

Fig. 7. Acceleration experimental results with TVC

References

1. Li, H., Jia, Y., Wang, S.: Theoretical and experimental studies on reduction for multi-model seismic response of high-rise structures by tuned liquid dampers. *Journal of Vibration and Control* 10(7), 1041–1056 (2004)
2. Ji, X., Kajiwara, K., Nagae, T., et al.: A substructure shaking table test for reproduction of earthquake response of high-rise buildings. *Earthquake Engineering & Structural Dynamics* 38(12), 1381–1399 (2009)
3. Kim, J.W., Xuan, D.J., Kim, Y.-B.: Design of a forced control system for a dynamic road simulator using QFT. *International Journal of Automotive Technology* 9(1), 37–43 (2008)
4. Plummer, A.R.: Control techniques for structural testing: a review. *Proc. Instn. Mech. Engrs. Part I: Systems and Control Engineering* 221(3), 139–169 (2007)
5. Severn, R.T.: The development of shaking tables—a historical note. *Earthquake Engineering & Structural Dynamics* 41(2), 195–213 (2011)

6. Houman, G., Gouri, S.B., Carlos, V.: Seismic behavior of flexible conductors connecting substation equipment-Part II: shake table tests. *IEEE Trans. Power Deliv.* 19(4), 1680–1687 (2004); Appendix: Springer-Author Discount
7. Feng, G.G.: Six degrees of freedom hydraulic vibration test system control strategy. Harbin Institute of Technology doctoral dissertation (2007)
8. Han, J.: Large-scale shaking table of the development of. Harbin Institute of Technology postdoctoral report (1996)
9. Li, H.: Hydraulic control system. National Defence Industry Press, Beijing (1990)
10. Shen, G., Zheng, S.T., Ye, Z.M., et al.: Tracking control of an electro-hydraulic shaking table system using a combined controller for real-time testing. *Proceedings of the Institution of Mechanical Engineers, Part I: Journal of Systems and Control Engineering* 225(5), 647–666 (2011)

Study and Design of Vehicle Black Box Hardware System Based on ARM and DSP*

Xu Hui¹, Li Jing-zhao¹, Yin Zhi-xiang², and Sun Xia²

¹ School of Computer Science and Engineering Anhui University of Science and Technology
Huainan, P.R. China
austxuhui@163.com

² School of Science Anhui University of Science and Technology
Huainan, P.R. China
austsunxia@163.com

Abstract. A design of vehicle traveling data recorder is presented, in which the microcontroller S3C2410 and TMS320DM642 are adopted. Assembly language is used to develop programs. The experiment show the system is effective and safe.

Keywords: vehicle traveling data recorder, DSP, hardware system.

1 Introduction

The vehicle traveling data recorder, named vehicle “black box” alternately, is a digital electronic recording equipment to record running speed, time, mileage and some other state information, through interface(s) which can record, save and output these information[1-4]. It can record states about vehicle fully, and reappear these states by software, so it facilitates traffic police to manage vehicles. Besides accident-analysis functions, it can control the runtime, speed, route, etc., and then reduce the number of traffic actions such as speeding, fatigue driving and so forth.

2 Overall Design of the System

The system consists of master controller module and audio/video acquisition module. The system schematic diagram is shown in Fig.1. The master controller module is in charge of LCD-controlling, USB interface, network interface and other information saving except for audio/video information.

* This work is supported in part by the National Natural Science Foundation of China (No. 60873144,61170172,61073102,60973050), the Excellent Young Staff Foundation of High School of Anhui Province of China (No.2009SQRZ059, 2011SQRL035), the Natural Science Foundation of Department of Education of Anhui Province of China(No.KJ2009B174Z, KJ2009B071Z), the Young Staff Science Foundation of Anhui University of Science and Technology of China(No.QN200836).

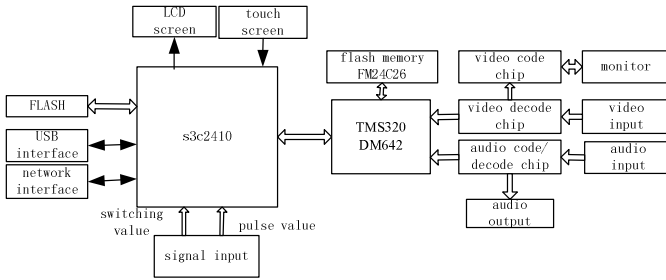


Fig. 1. System schematic diagram

3 Design of System Hardware

S3C2410 , which is a 32-bit microcontroller based on ARM920T core in 90nm CMOS technology, as the master controller of the system, it is produced by Samsung corporation. In it ,there are separate 16KB instruction cache and 16KB data cache, MMU, LCD controller supporting TFT, NAND flash memory, 3-route UART, 4-route DMA, 4-route Timer with PWM, I/O interface, RTC, 8-route 10-bit ADC, Touch screen interface, IIC-BUS interface, IIS-BUS interface, two USB hosts, one USB Device, 2-route SPI. S3C2410 CPU can work on 203MHz at most.

The main module is the core of vehicle “black box”, which deals with data by main controller. It displays, sends and saves all kinds of data promptly.

In the hole procedure, the system may deal with 3-rout video data at most, the data flow is so much that S3C2410 works difficultly. Therefore, the DSP chip produced by TI corp., TMS320DM642, is adopted to do this.

In order to save the cost, we use LCD as the display equipment connected to main controller, and use analog monitor to display video information.

3.1 Connection between Main Controller and DSP

The interface circuit between S3C2410 and TMS320DM642 is shown in Fig.2 . Two address line ADDR[3:2] connect to HCNLT[1:0] of the HPI interface, so ARM can visit three registers of HPI. Because the WAIT signal of S3C2410 is opposite to HRDY of DM642’s interface, we reverse HRDY signal and then connect with WAIT signal. In S3C2410, there is no HR/W signal, so we use ADDR4 instead of read/write chip-selecting signal to connect with HR/W of HPI interface. The chip-selecting signal nGCS1 of S3C2410 connect to chip-selecting signal HCS of HPI, mapping HPI interface of DSP as external physical address to kernel space of S3C2410, they are located in BANK1 of I/O interface[5-6].

Hardware Platform Interface (HPI) of DSP is an effective parallel interface, which main used for two parallel interfaces connect to each other. To the main CPU ARM, HPI interface of DSP correspond with I/O equipment of asynchronous memory interface. ARM visits DSP hole memory space through address three registers (register (HPIA), data register (HPID), control register (HPIC)) of HPI.

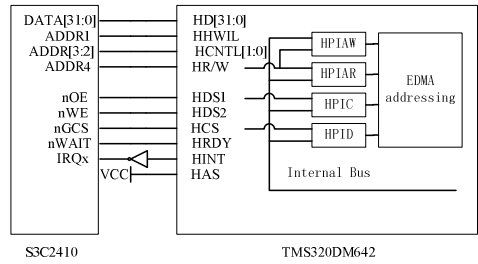


Fig. 2. Connection between S3C2410 and TM320DM642

3.2 Audio/Video Data Acquisition

TMS320DM642 handle works about audio/video data, its work frequency can reach 203MHz at most, it has 8 parallel processing units; it is applicable to design an audio/video coder unit for its second generation Very Long Instruction Word (VLIW); DM642 integrates a variety of peripherals on chip that make audio/video development easier; there are three configurable audio/video ports, supply seamless interface of audio/video input/out and bit stream inputting, if you develop an audio/video coder, its audio/video coder part need only an audio/video data acquisition chip. In the system , SAA7115 is adopted as audio/video encoder unit without control circuits, the hardware is simpler[7].

The work procedure is as follows: three CCD cameras bring three route video signal and audio signal to audio/video encoder chip, SAA7115. The signal convert to audio/video data stream and inputted to the compression unit, DM642, through circuits of clamping, filtering, analog-to-digital (A/D) conversion and YUV separation. Among them, one route converted data convert to analog signal through digital-to-analog (D/A) conversion circuit is inputted to a monitor, so the driver can view real-time picture.

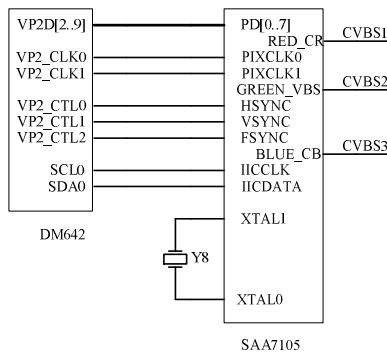


Fig. 3. Connection between SAA7105 and TM320DM642

The video input module works through TVP5150 connected to DM642. TVP5150 is a ultra-low power video encoder chip supporting automatic distinguish

NTSC/PAL/SECAM format. It transforms analogs signal into digital signal according to format of YcbCr4:2:2, the connection is shown in Fig.4. YOUT[0..7] are data output pins connected to VP0D[12..19] in DM642 video interface, the clock synchronizing signal(PCLK) connect to VP0CLK0.

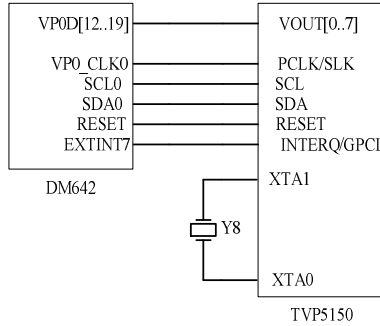


Fig. 4. Connection between DM642 and TVP5150

3.3 Display Module

The vehicle traveling data recorder will display its states and refresh per 0.5 second in the national standard. We use LCD to display information in the master controller module of the system.

There is a LCD controller in S3C2410. It can display information at different frequencies and support STN-LCD and TFT-LCD.

As an active matrix LCD equipment, TFT is used widely. The lattice pixel is divided into red, green and blue sub-pixel; there are three micro color filters on the equipment surface. By controlling each sub-pixel light valve, we can decide light pass through color filters or not. By controlling the gray scale of color filters, we can decide how much light would pass through color filters, and then get more colors[8]. LQ080V3DG01, produced by Sharp Corp., is used in the system, of witch the resolution of LQ080V3DG01 is 640×480. There is a touch screen and used easily. The interface circuit of S3C2410 and LCD is shown in Fig.5.

The LCD controller consists of REGBANK, LCDCDMA, VIDPRCS, TIMEGEN and LPC3600. There are 17 configurable registers to set up parameter s of LCD; LCDCDMA bring video data to LCD driver from frame memory automatically.

3.4 Switching Values Acquisition

In accordance with the national standard, switching values include signal of braking, horn, left lights, right lights, master lights, pressure and doors and so on[9-10]. The switching value is simple, namely open and close, we mark them as 1 and 0. There to much switching values, for example, four doors need four switching values. If so many switching values input to the processor directly, it will waste I/O ports, so we select CD4021 to extend I/O ports.

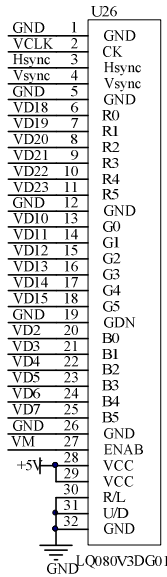


Fig. 5. Connection between LCD and S3C2410

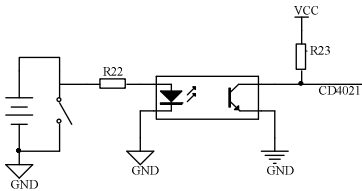


Fig. 6. Circuit of switching values sampling

3.5 Vehicle Speed Acquisition

When vehicle is running, hall sensor output pulse signal whose frequency is in direct proportion to speed in response to alternating magnetic field[11]. In order to get regular Rectangle wave and get accurate speed, we shape the wave firstly. Then signal is brought to the configurable equipment and handled further. At last, the signal is brought to CPU S3C2410 after get rid of spurious signal trying its best. The interface circuit of vehicle speed-sampling is shown in Fig.7.

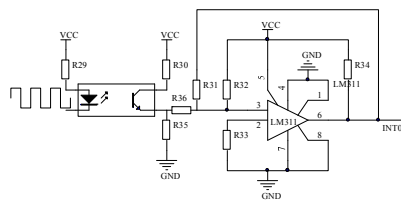


Fig. 7. Circuit of vehicle speed-sampling

4 Conclusion

The hardware system is made up to PCB with some peripheral equipment such as power supply, etc. And then assembly language is used to develop programs. The experiment show the system is effective and safe.

References

1. Yu, H., Xu, C., Lou, S.: Research on A Novel Automobile Black Box. *Journal of Highway and Transportation Research and Development* 21(9), 124–126 (2004)
2. Cao, L., Yin, Y., Liu, H., Li, Y.: Design and Implementation of Video Surveillance System Based on ARM and DSP. *Chinese Journal of Electron Devices* 32(1), 213–217 (2009)
3. Fu, R., Wu, T.: A software platform based on $\mu C/OS-II$ for vehicle data recorder. *Journal of Guangxi University of Technology* 19(3), 10–13, 26 (2008)
4. Gao, B., Tao, D., Wang, J., Bei, S., Bi, M.: Design of an Intelligent Monitoring System Based on S3C2410 and DM642. *Journal of Heilongjiang August First Land Reclamation University* 21(1), 59–62 (2009)
5. Liao, W.: Vehicle Traveling Data Recorder Based on ARM (7), 72–74 (2008)
6. Shen, M., Cong, J., Zhang, X., Sun, Y., Xiong, Y., Zhou, L.: Design and Implementation of Terminal for Agricultural Data Real-time Acquisition Based on ARM and DSP 41(6), 147–152 (2010)
7. Sun, B., Su, L.: Vehicle Recording System Based on MCU of Model AT89C51ED2 (9), 322–324 (2010)
8. Yu, S., Deng, Z., Cai, H.-B., Cui, J.-Z., Chen, L.-T.: Design of black box of vehicle system based on ARM+DSP. *Application Research of Computers* 25(2), 629–631 (2008)
9. Zhan, H., Ye, X.: ARM-based LCD design of vehicle running experiment data recorder. *Journal of Nanjing University of Information Science & Technology* (4), 314–318 (2009)
10. Zhang, W., Jing, S.: The Design of Data Acquisition System for Vehicle Traveling Data Recorder. *Instrumentation Technology* (3), 27–28,31 (2009)
11. Gong, Z., Zhang, W., Yu, B.: Host USB Interface Design for Vehicle Travelling Data Recorder. *Measurement & Control Technology* 28(2), 90–92 (2009)

The Perfect on Urban Natural Function Space under Artificial Environment

Fugang Zhang¹, Qiong Xue², and Shanshan Jiang³

¹ Henan Polytechnic University, School of Architectural & Artistic Design,
454000, Jiaozuo, China

² Shandong Water Polytechnic, Student Work Department, 272826, Rizhao, China

³ Lanzhou University, School of Management, 730000, Lanzhou, China
fugangzhang@163.com

Abstract. The continue loss of urban natural function space produces a fact that urban residents can not really enjoy nature, result in many problems about urban residents, so we should improve the urban natural environment features, the perfect on urban natural function space mainly focuses four aspects: to take full advantage of natural space, to layout natural function space contiguously, to establish the corresponding management departments and to develop valuable benefits. The article make urban function space more reasonable by perfecting natural function.

Keywords: urban, natural function, perfect.

1 Preface

The so-called urban natural function is defined as a function provide the natural living environment for urban residents. Urban development often leads to urban natural environment decline and artificial environment dominated[1], urban artificial environment often leads to many urban problems[2], such as pollution problems, Heat island effect and so on, in addition the lack of natural environment has important effects on the health of the residents in body and spirit[3], especially children growing up in an artificial environment is also extremely detrimental to their mental development, so the perfect on urban natural function space is critical.

2 The Need for Perfect

Firstly, the Urban Natural Environment Severely Damaged. The current urban environment is man-made environment of reinforced concrete, a large number of production and living activities led to the city's natural environment less and less, but more and more man-made environment is not conducive to human health, while not conducive to human growth.

Secondly, the Human Development Needs the Natural Environment. Human beings are a product of natural development, natural environment, human growth and development of the soil, although the natural environment through the transformation of mankind to improve people's living environment, but excessive man-made

environment is not conducive to human survival and development, while people in the artificial environment reduced ability to adapt to the natural environment; the same time the formation of people's thinking has often been designed thinking of the binding, is not conducive to integrated development of thinking, a great need for human survival and development of the natural environment. Despite the increasing emphasis on urban ecological environment, leaving a large number of urban green space, green environment but also have human-designed green space is not conducive to people's feelings of pure natural atmosphere.

Thirdly, Children Need for Healthy Growth. From Figure 1 and Figure 2 is easy to see, this piece of urban space is temporarily "artificial soil space", despite health problems, but the children is fun and excitement ,not difficult to see children like this space and natural ingredients to actively participate in the experience of this space, the children have the courage to overcome the difficulties of the character in the figure at a glance.



Fig. 1. The map about the soil functions fun of children(1)



Fig. 2. The map about the soil functions fun of children(2)

Fourthly, Helping to Release Urban Residents Heart Pressure. Natural space is not only conducive to people's health, but also help people relax and release stress. Table 1 is a pressure on the city caused by the questionnaire, the survey group is sophomore and junior students of the rural students, rural students was chosen because of their two living environments in urban and rural areas under their own for two kind of environment contrast, data from the table because the city is easy to see the lack of pressure on the natural environment is one important reason, we can see that the city release the pressure on the natural environment has a role in mood mediation. While urban residents use to travel to feel the natural space, but long working life in the city, you need close to normal in the natural space.

Table 1. Urban stress questionnaire

The reason on psychological stress caused by the city	Lack of urban natural environment	Fast-paced city life	Environment unsuited	Other
Number of students	97	92	26	35

3 The Strategy about the Perfect on Urban Natural Function

The main perfect on urban natural functions is the following:

(1) Urban natural function space fully make use of existing natural space and artificial natural space. Urban function space is made up of some natural space and the artificial nature space, natural space includes rivers, lakes, wetlands, mountains and others , semi-natural space includes parks, green spaces and other types, these natural space and the artificial nature space are essential to maintain urban environment.The perfect on urban natural function space should take advantage of these types, the development of natural space try to maintain the natural properties and then carry out appropriate planning, planning and construction should make full use of natural materials, reduce artificial materials, the space development try to reflect the natural properties of space.

(2) Urban natural function space is developed into lines and slices. To make people really feel the natural function space, a certain size natural space has natural space functions[4], so when you create a natural space in addition to making full use of urban space has natural and artificial natural space, but also to moderate the natural space set aside a certain amount of natural space the whole city to form an overall scale. Modern agriculture can be part of garden need to join within the city proper, you can also set the number of participating venues and strong nature, which requires the city to focus on functional areas and the dispersed phase with the layout of the living area is about the layout of industrial areas and natural area layout mixed together.

(3) Urban natural function space should establish appropriate management and services departments. Urban residents need related activities in some natural function space, such as relax, take a nature experience, the natural recreational activities,

increased knowledge of nature and so on, so cities should establish the corresponding natural functional space management services for management services. Management services is mainly reflected in two aspects: one is to protect the natural functions of the natural properties of space, so that the natural function space to sustainable development and utilization; the other is the experience of those who protect the health and safety, such as danger zones, where mosquitoes are more established the appropriate place to establish a rational guide management, not only to protect the safety of experience, but also a corresponding increase in the ability of nature to survive, another example for the "earth space" to establish the appropriate entertainment for children's health infrastructure, so that after the end of a child entertainment health treatment.

(4) The development on the urban natural function space combines with efficiency and value. Driven by economic interests, the urban natural function space is often invaded. the best way to protect the natural functions space is to combine urban space and urban development with value of benefits[5]. In addition the natural function space not only provide urban natural environment, but also produce reasonable value benefits combined with other urban functions, such as appropriate use of natural space to create a certain "soil entertainment", "soil culture" to produce the entertainment value, the appropriate use of natural function space for the development of modern agriculture have some economic benefits, the use of natural function space as the city's open space, farm use of the natural function space for fun activities and so on. Urban natural function space is fully protected by value effect produced by urban natural function, in addition the natural function space for urban development can take full advantage of the value of the developer community on the rational and effective development.

4 Summary

Through perfecting urban natural function space, the article makes urban function space more reasonable and conducive to urban residents healthy development , the city truly make life better.

References

1. Xu, X., et al.: Urban Geography. Higher Education Press, Beijing (1997)
2. Li, D.: Principles of Urban Planning. China Building Industry Press, Beijing (2001)
3. Wu, L.: Mumford academic thinking and living environment study for the construction of the Enlightenment. Urban Planning
4. McDonnell, M.S., Pickett: Ecosystem structure and function along urban-rural gradients: an unexploited opportunity for ecology. *Ecology* 71(4), 32–37 (1990)
5. Alain Bourdin with QHA translation. Urban Functions and Management Modes of the Multimodality Places. *Abroad Urban Planning* (3), 35–37 (2005)

Authors

Zhang Fu-gang (1978 -), male, Ph.D., Henan Polytechnic University lecturer, research direction for urban regional planning.

Xue Joan (1980 -), female, teachers in Shandong Water Conservancy College., research direction for urban management.

Development of Real-Time Temperature Monitoring System Based on GPRS

Jianzhong Wu, Jianping Cai^{*}, Meimei Huo, and Minghui Wu

School of Computer Science, Zhejiang University City College, Hangzhou, China
wujianzhong@zucc.edu.cn, caijp@zucc.edu.cn

Abstract. Temperature data collection and manage system plays an increasingly important role in modern agriculture and industrial fields and even daily works. The design and development of a slow changed real-time temperature detecting and monitoring system is presented in this paper. It is composed with two parts: the computer side and the sensor side. An 8 bit MCU board with its peripheral devices and temperature sensor is used to collect data continually and transmit the processed true time data to monitor program in GPRS way. A Delphi program is designed to collect temperature and monitor the fields on the spot, while the main features including dynamic temperature displaying, top limit and bottom limit threshold setting their exceeding alarming, data analyzing and storing. This study could be implemented in real-time remote temperature monitoring situations.

Keywords: Monitor, temperature sensor, GPRS stacks.

1 Introduction

Temperature is a very important physical quantity and the temperature measuring and controlling are both very important in real life. It is also an urgent need to detect and control temperature in the human living environment. The temperature detection and related technologies is keeping on focused in certain industrial fields: metallurgy, steel, petrochemicals, cement, glass, and pharmaceutical industry, etc.. There are almost 80% of the industrial sector had to take into account the temperature factor. Meanwhile, a temperature detection system equipped with 8 bits Micro controller chip has the advantages of lower cost, reliable and easy to use[1].

Slowly varying temperature detection system has been widely used in much agriculture, industrial and other situations because of its distinct advantages: long time automatic monitoring, data log keeping, temperature differential monitoring and even early fire alarming which decided by a sudden overheat, while the other alarming way like general heat sensors or smoke sensors are hard to accomplish with[4, 5].

^{*} Corresponding author.

2 System Hardware Design

2.1 MCU Board Block Diagram

System hardware design includes the following sections, the block diagram shown in Fig. 1:

MCU system, single-wire digital temperature sensor DS18B20, GPRS Interface, I2C memory, λ LED digital tube, Key, Power.

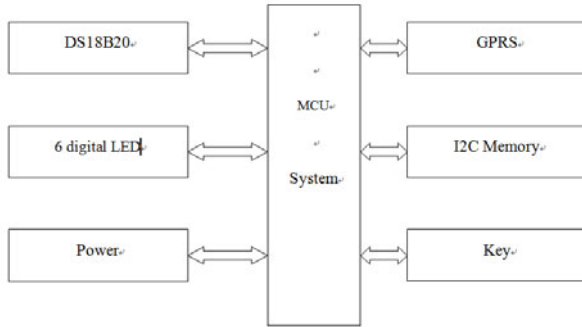


Fig. 1. System hardware design block diagram

2.2 GPRS Module

The GPS module connects to MCU through serial port, it receives instructions from remote pc service program and sends temperature data to the server. The GPS module communicates to MCU with AT communication instructions.

The M580 GPRS module is adapted in the project, which is made by Neoway technology. This module is a dual band GSM/GPRS industry wireless communication module and provides a high-quality voice, messaging, data services and other features.

2.3 Temperature Sensor

DS18B20 is an improved smart temperature sensor which is made by Dallas semi Conduct Company of USA, following the model of DS1820. Other than the traditional thermistor, the temperature data could be directly achieved from the sensor. Meanwhile, the data format could be programmed in a 9 to 12 bits mode quickly according to actual requirements. The transform time costs are 93.75ms and 750ms corresponding to 9 and 12 bits separately. Moreover, only one wire connection is needed to read data from or write date to the sensor chip while the power supply comes from the data wire and need no extra power. The other advantages that the DS18B20 has are the temperature measurement accuracy, conversion time, distance, resolution, etc. There could be a simple structure and high reliability when constructing the temperature system with DS18B20. Lots of modifications have been made from the DS1820 and which could bring much convenient and satisfactions to the developers

and final users. This sensor could be used for temperature measurement in harsh environments or other environmental control, equipment or process control, and temperature measurement in consumer electronic products[3].

2.4 Other System Modules

As shown in Fig.1, the control board includes the following parts[6]:

1) 6 digital LED and its driver circuit: The LED Used for on board temperature displaying, and with connections to the realization of dynamic scanning. ZLG7298B is used as the display driver and keyboard scan management chip[2]. It accepts instructions and data from the MCU and directly drives the 6 digital LED on the board.

2) Memory circuit: Used to store programs and real time temperature data.

3) Buzzer circuit: Used for temperature exceeding and other abnormal status alarming.

4) Communication part: MAX232 receiver/transmitter is adapted in this system using for connecting and communicating between the GPRS module and MCU.

5) Power supplying circuit: Both the 3.3V power and 5v power are demanded to supply the chip and different modules.

7) Clocking circuit: Providing a 12M HZ clock for the MCU.

8) Peripheral devices: Including buttons, rocker switch, reset key and status LEDs.

2.5 Operations

1) Pressing the S2 key to display the current temperature value;

2) Pressing S3 button to enter the alarm temperature setting, the alarm temperature could be stored in nonvolatile memory when S6 key being pressed finally while the LED displaying the current temperature. If only the current temperature exceeding the alarm temperature value, the buzzer makes a voice beep prompts immediately. As shown in Fig.2.

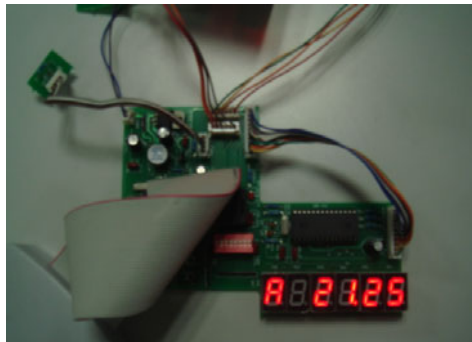


Fig. 2. Temperature data collecting board

3 MCU Control Software Design

The MCU code is program using C51, the program structure including system initialization, the temperature reading, displaying and alarming module. Fig. 3 shows the software working flow which has the following features:

- 1) Reading the current temperature data from the temperature sensors through the single-wire bus, then displaying it in the digital LEDs;
- 2) Setting the upper and lower limitation of temperature alarm threshold to the memory;
- 3) Communicating data and instructions between the GPRS module the MCU through the serial port.

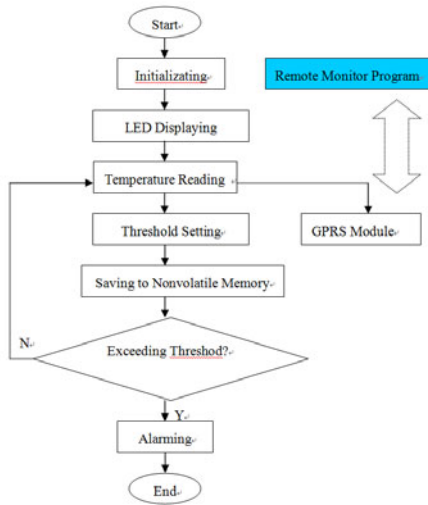


Fig. 3. Computer software process

4 Remote Monitoring Software Design



Fig. 4. Remote monitoring software interface

As showing in Fig. 4, the remote monitoring software is developed with Delphi which provides the following features:

- 1) Displaying the collected real time temperature dynamically, including the Celsius and Fahrenheit temperature value;
- 2) Setting the upper and lower limit temperature threshold.
Flashing the indicator to alarm in the interface when the display temperature is higher than the upper limit or below the lower limit threshold and beeping as well.
- 3) Recording temperature data and their time intervals to a spreadsheet.

5 Conclusion

A slowly varying real-time temperature monitoring system based on GPRS is introduced in this paper. The system is used to collect real time temperature values from the excellent temperature sensor DS18B20. It provides a long period real time monitor in all kinds of different environments. Threshold could be set to make alarm for the temperature abnormal. A main feature is GPRS wireless module is adapted in the system.

The MCU and GPRS based temperature acquisition system has not only low cost, reliable and easy to use features, but also a significantly improving to the technical specifications of the measured temperature. The temperature acquisition management systems presented in this paper combines with existing modern electronic technologies together, and greatly reduces the hardware design complexity to have a fully functional, accurate temperature control and friendly user interface in all.

Acknowledgment. This work is partly supported by the National Natural Science Foundation of China under Grant No. 61070001, the Special Funds for Key Program of the China No. 2011ZX0302-004-02, the Key Science Foundation of Zhejiang Province under Grand No. 2010C11048.

References

1. Dequan, S.: MCS-51 MCU interface and application. Press of Beijing University of Aeronautics and Astronautics (1990)
2. Qiushi Technology, MCU peripheral devices and applications. The People's Posts and Telecommunications Press (2006)
3. Yang, R.: Smart temperature sensor based on the granary of the temperature detection system design, Instruction user (2007)
4. Sun, N., Chen, X.: Multi-channel wireless temperature measurement system design. *Micro-Computer Information* 25(4-2) (2009)
5. Guan, S., Zhang, J., Ding, Y.: Computer master-slave communication system to connect more than 232 circuit design. *Micro-Computer Information* 21(4) (2005)
6. Dong, L., Wang, F., Wang, H.: AT89S52 based on the temperature alarm system. *Micro-Computer Information* 25(4-2) (2009)

Multi-Signal Intelligence Data Fusion Algorithm Based on Pca

Jianbin Xiong, Qinruo Wang, Haoyi Wu, Baoyu Ye, and Jinghong Zhang

Guangdong University of Technology, Guangzhou, Guangdong 510006, P.R. China
xiongjianbin@21cn.com

Abstract. By combining Neural Networks with Principal Component Analysis, an algorithm about multi-signal intelligence data fusion is proposed, which is an effective feature selection method. The experiments in sampling real time ship's sensor data show that its performance is better. The proposed method can prove the fusion rate effectively and reduce the PCA computation time. The discussed algorithm has strong practicability.

Keywords: Neural network, Principal Component analysis, Data fusion algorithm.

1 Introduction

The aim of this paper is to present preliminary results of a feasibility study about the use of the Principal Components Analysis and Neural Network (PCANN) for the multi-signal intelligence data fusion (MSIDF) of ships. MSIDF is defined as a process of intelligence information fusion from multiple sources so as to produce the most specific and comprehensive unified data about an entity, event or activity, which can be obtained by multi-sensor [1]. Multi-sensor intelligence systems (MSIS) are becoming increasingly important in a variety of military and civilian applications. Because a single sensor generally can only generate small perceive information about the environment; multiple similar and /or dissimilar sensors are required to provide sufficient local information with different environments [2]. We can achieve the improved accuracy and the specific inferences by properly administrating multiple sensor and their measurements.

To assess the reliability and quality of multi-sensor fusion system, most algorithms assume that these sensors are reliable and do not deal with sensor selection. In fact, due to the affection by sensor's accuracy, environment noise, transmit error and other disturbances, the sensor's observed data are uncertain. So it is important to know the causal relationship between the sensors' information and detect noisy of sensors or the number of sensors and the resulting fused output in a clear way.

2 Ship'S Three Layer Fusion Structure

Ships are exposed to wind, waves, and current forces. The requirements of the various operations performed by the vessel, together with the characteristics of the

environmental forces, define the modes of operation and the objectives of the motion-control system [3]. The control system processes motion-related multi-signal to filter disturbances, to data fusion, to infer the state of the ship, and to generate an appropriate command for the actuators so as to reduce the difference between the actual and desired ship trajectories. The ship’s navigation systems, which provided multi-signal from the multi-sensors, such as Global Position System(GPS), speed log, compass, gyros, motion reference system(MRU), wind direction and wind speed sensor, radar, and accelerometers. The navigation system performs signal quality checking and transforms the measurements to a common reference frame used by information fusion. The navigation system is multi-sensor management system. Sensor management merits incorporation in information fusion processes. The multi-sensor management architectures are shown in Fig.1.

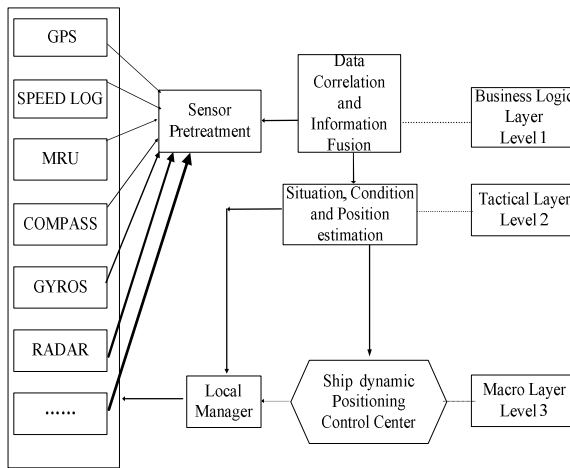


Fig. 1. Ship’s Dynamic Positioning three-layer fusion structure

3 Neural Networks (NN)

Ship’s Wireless sensor networks (SWSNs) are typical made up of small, unreliable nodes, and inexpensive. The most common type of ship’s wireless sensor neural network architecture (SWSNNA) is called feed-forward network shown in Fig.2.

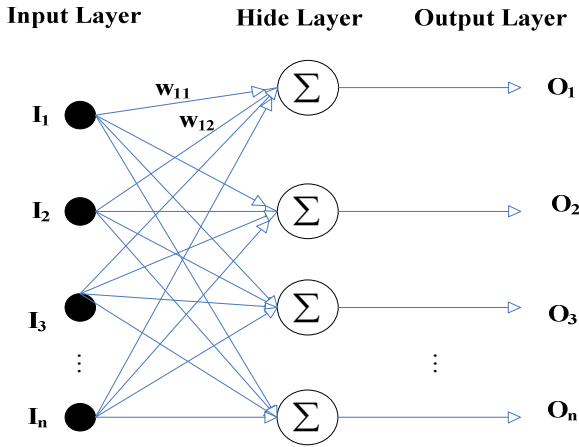


Fig. 2. SWSNNA model

The above figure clearly shows the characteristics of a neural network. It is an attempt to simulate the brain because biological neurons are extracted and applied to simulations. The input nodes [5] take in the information, which is supplied by activation values. The activation of the information from the input nodes is passed through the hidden layers to the output nodes. Thus, the output could, to a certain degree, reflect the input if a network is trained properly. The SWSNNA model can be written as

$$\begin{bmatrix} O_1 \\ O_2 \\ O_3 \\ \vdots \\ O_n \end{bmatrix} = \begin{bmatrix} w_{11} & w_{12} & w_{13} & \dots & w_{1n} \\ w_{21} & w_{22} & w_{23} & \dots & w_{2n} \\ w_{31} & w_{32} & w_{33} & \dots & w_{3n} \\ \dots & \dots & \dots & \dots & \dots \\ w_{n1} & w_{n2} & w_{n3} & \dots & w_{nn} \end{bmatrix} \begin{bmatrix} I_1 \\ I_2 \\ I_3 \\ \vdots \\ I_n \end{bmatrix} \quad (1)$$

Where $I_i (i=1,2,\dots,n)$ is the measured signal of ship sensor and $w_{ij} (i=1,2,\dots,n; j=1,2,\dots,n)$ is the output "weight" from hidden layer node j to output layer node i , and $O_i (i=1,2,\dots,n)$ is the output signal node, as shown in Fig.2.

The SWSNNA model used learning rules for training base on Hebb symmetric subspace [6].

$$W(k+1) = W(k) + \mu(k)W(k)I(k)I^T(k)[E - W^T(k)W(k)] \quad (2)$$

We show the evaluation of function performance (EFP) of the SWSNNA, the EFP is taken as the evaluating neural network performance standard. EFP is defined as [7]:

$$J(k) = \| I(k) - W^T(k)O(k) \| \quad (3)$$

Where k is the network training series, $0 \leq \mu \leq 1$ is the learning rate and E is unit matrix.

Here n_h is the hider layer node, $n_h = \sqrt{n_i + n_o + \alpha}$, where n_i is input node, n_o is output node, and $1 \leq \alpha \leq 10$ is experiential value.

In addition, in our view, identifying significant multi-sensor signal as inputs before SWSNNA modeling could be advantageous in filtering out irrelevant features, decreasing eigenvectors dimensions, alleviating computational demands and reducing the risk of over fitting in data-based training. This motivation includes the dashed block feature selection in Fig.3 as a potentially desirable component [2].

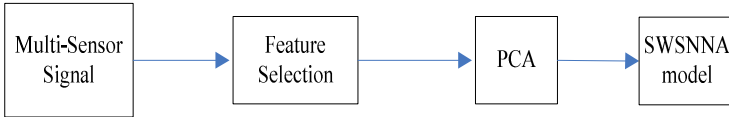


Fig. 3. SWSNNA for priority assignment

4 Principal Components Analysis(PCA)

PCA involves an eigenanalysis of covariance matrix or the correlation of the given multi-signal feature vector. It reduces the data dimensionality by performing an analysis of covariance [4]. PCA is a useful statistical technique that has been found application in various fields such as image compression [6] and face recognition [7, 8], image recognition [8]. Furthermore, it is also a common technique for finding patterns in data of high dimension. The main advantage of PCA is that you can find these signals in the data, and you compress the data, i.e. by reducing the number of dimensions, without much loss of energy and without much loss of information . The PCA technique used in processing signals, as we will see in the coming section.

An important theory field of the successful application of PCA in SWSNN is: solving the vector of covariance matrix for solving special problems, removing noise, and reducing the dimension of the feature vector. However, the reservation is the distribution characteristic that describes the sample best, due to dimension reduction in the process of introduction of classified information. But it is not the most beneficial features of the classification. Transformation will suffer difficulty in the case of high dimension. Hence, it exits theoretical defects of this method.

5 Experimental

In this section we illustrate the characteristics of the algorithms PCANN through simulation. There are 7 sensors to measure wind direction around the ship. Fig.4 shows the collection and handling a mass of real time data in matlab7.1. The actual value is 270, the sampling time is 1s, and the sampling 300 times.

PCA Simulation: we assume $X = [x_1, x_2, x_3, x_4, \dots, x_7]^T$, $x_i (i = 1, 2, \dots, 7) \in R^{300 \times 1}$ which is i th wind direction sensor collection real time data for 300 times. *In following,*

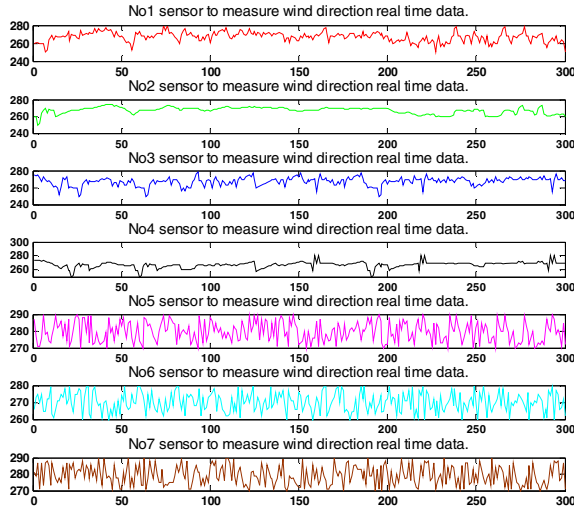


Fig. 4. 7 sensors to measure wind direction real time data

we calculate the mean $\bar{X}_i = \frac{1}{300} \sum_{j=1}^{300} x_{ij}$, $a_{ij} = x_{ij} - \bar{X}_i$, standard process

$$x_{ij} = \frac{a_{ij}}{\sqrt{a_{i1}^2 + a_{i2}^2 + \dots + a_{i300}^2}} \quad (i = 1, 2, 3, \dots, 7)$$

is shown in Fig.5. We calculate the covariance matrix $\text{COV}(X)$, the eigenvectors $V = [V_1, V_2, \dots, V_7]$, eigenvalues λ_i , and Y .

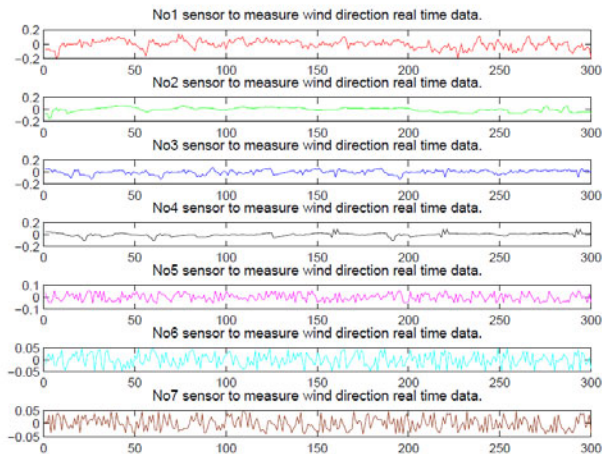


Fig. 5. 7 sensors to measure wind direction real time data standard processing

Since all the vector are dimensional, according to *PCA Simulation*, we will get eigenvector $Y = I$. In practice, we are able to leave out some of the less significant eigenvectors, and the recognition still performs well. We use neural network toolbox of matlab7.1. For example the newff function creates a feed-forward back propagation network. Where $\mu = 0.5$, $n_i = 20$, $n_o = 10$, $\alpha = 5$. According to *equation (3)*, hider nodes $n_h = 10$, and weight coefficient w_{ij} are calculated. The first layer has weights coming from the input. Each subsequent layer has a weight coming from the previous layer. All layers have biases. The last layer is the network output. Here the network is trained for 1000 epochs, the network is trained goal for 0.001, and the learning rate is 0.01.

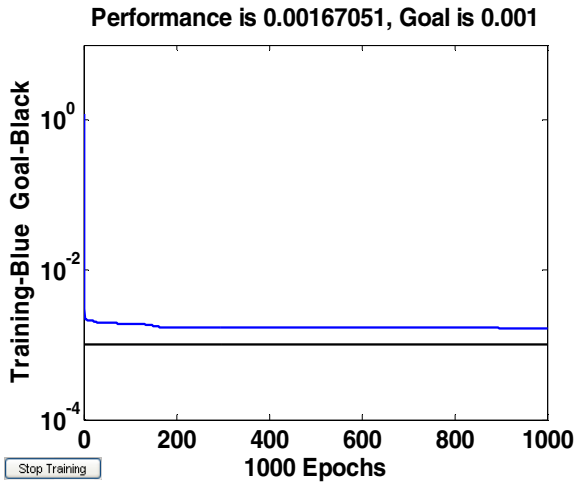


Fig. 6. SWSNNA is trained for 1000 epochs and goal is 0.001

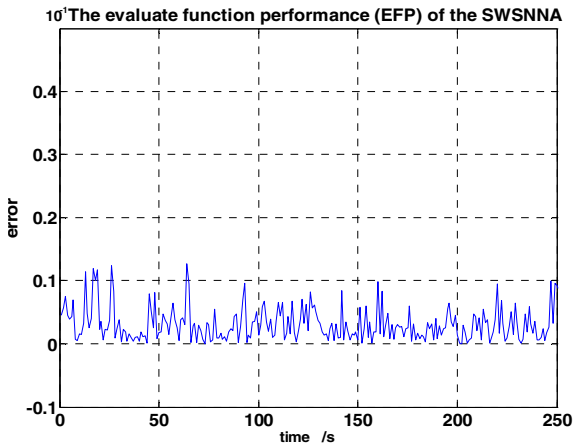


Fig. 7. Evaluated function performance (EFP) of the SWSNNA

From the above deduction, the SWSNNA is simulated and its output plotted against the targets as is shown in Fig.6. According to *equation (3)*, the performance of the SWSNNA is shown in Figs.6

Fig.7 shows the evaluated performance of the SWSNNA. EFP has the lowest error ratio around 0.012. In order to verify the effectiveness that we proposed SWSNNA algorithm, we use the newly generated random sample of 4000 times into the SWSNNA algorithm, then EFP has the lowest error ratio around 1.5%.

6 Conclusions

A MSIDF which improves the speed performance of the data transfers and effectiveness in reducing the number of dimensions on sensor's data is proposed. By using the proposed approach on sampling real time data from ship, the EFP has the lowest error ratio around 1.5%. Hence, the fusion algorithm is computationally efficient and can accurately fusion data. It can also handle an arbitrary number of ships from an arbitrary number of sensors of arbitrary type as long as they can provide some of the features used for fusion.

Acknowledgment. This work is supported by the Key Item in the Guang Dong Province Science & Technology Special Program under Grant NO:2009A080202006; the Natural Science Foundation of Guangdong Provincial of China under Grant No. 9151009001000021; the Ministry of Education of Guangdong Province Special Fund funded projects through Cooperative under Grant No. 2009B090300341.

References

1. Gao, H.: A Simple: Multi-sensor Data Fusion algorithm based on principal component analysis. In: 2009 ISECS International Colloquium on Computing, Communication, Control and Management, pp. 423–427 (2009)
2. Xiong, N., Svensson, P.: Multi-sensor management for informaton fusion: issues and approaches. *Information fusion* 3, 163–186 (2002)
3. Fossen, T.I., Kalman, T.P.: Filtering for Positioning and heading control of ships and offshore rigs. *IEEE Control Systems Magazine* 29(6), 32–46 (2009)
4. Raai, J.R.: Multi-sensor data fusion with matlab, pp. 505–510. CRC Press Taylor & Francis Group (2010)
5. Wu, Y., Wu, Y., Yan, Z., Qu, L., Xiang, B., Zhang, Y., et al.: An optimal tumor marker group-coupled artificial neural network for diagnosis of lung cancer. *Expert Systems with Applications* 38, 11329–11334 (2011)
6. Chen, M., O'Sullivan, J.A., et al.: Laser Doppler Vibrometry Measures of Physiological Function: Evaluation of Biometric Capabilities. *IEEE Transactions on Information Forensics and Security* 5(3), 449–460 (2010)
7. Han, W., Fang, X., Berger, A.L., Yin, Q., et al.: Face recognition based on Bhattacharyya Distance and PCA method. *Computer Engineering and Applications in China* 23 (2011)
8. Jillela, R., Ross, A., Flynn, P.J.: Information fusion in low-resolution Iris Videos using Principal Components Transform. In: 2011 IEEE Workshop on Applications of Computer Vision, pp. 262–269 (2011)

Research on Simulation of Motion Compensation for Omnidirectional Platform Based on Neural Network

YuNan Zhang, ShuangShuang Wang, Peng Tian, and YuHui Zhao

Department of control engineering, Academy of Armored Force Engineering,
FengTai District, DuJiaKan No.21, 100072, Beijing, China
wss2312@163.com

Abstract. In order to improve the accuracy of omnidirectional platform, this paper makes an analysis of kinematics and builds the dynamic virtual prototyping. The anisotropy of slippage and its influence on translation is simulated by virtual experiment. A method of neural network is proposed for nonlinear motion compensation. Simulation results show that motion error can be reduced and the performance is greatly improved, which indicates that the method is effective and feasible.

Keywords: omnidirectional platform, neural network, motion compensation, simulation.

1 Introduction

Omnidirectional locomotion of wheeled decive is usually implemented by so-called omnidirectional wheels based on their orientation and direction functions. The omnidirectional platform has three degree of freedom (DOF) on two-dimensional plane, i.e. translation along X or Y axis and revolution around Z axis, so that it can translate towards arbitrary direction on the plane without changing its posture and make a center revolution as well. Compared with traditional wheeled decive, it is more agile and more suitable for confined space and can meet the demand of accurate positioning[1].

Owing to the special mechanism of omnidirectional wheel, there is inevitable slip phenomenon in the process of motion, which results in errors of direction and velocity and makes significant influence on the accuracy of omnidirectional translation. We build a nonlinear model for motion compensation by neural network and carry out virtual experiment by coordinated simulation model. Finally, experimental results prove the validity of this method.

2 Kinematic Analysis

2.1 Kinematic Equation

Mechanism characteristics of omnidirectional wheel are as follows: It consists of the hub and a serial of free rolling rollers, as shown in Figure 1. Seen from the axes of the

hub, outline of the rollers is overlapped with the theoretical circle of the whole wheel, each roller can rotate around its axes, all of the rollers have the same tilted angles which is usually 45 degree [2].



Fig. 1. Omnidirectional platform

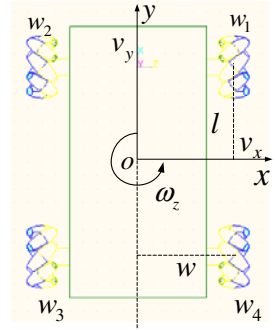


Fig. 2. Frame coordinate

As shown in Figure 2, four-wheeled longitudinal symmetric layout is similar with the arrangement of a car, two wheels of both sides are mirrored. We define Y and X axis as the direction of longitudinal and transverse translation respectively, counter-clockwise is the positive revolution. Inverse and forward kinematic equation are as follows[3]:

$$\begin{bmatrix} \omega_1 \\ \omega_2 \\ \omega_3 \\ \omega_4 \end{bmatrix} = J \begin{bmatrix} v_x \\ v_y \\ \omega_z \end{bmatrix} = \frac{1}{R} \begin{bmatrix} -1 & 1 & (l+w) \\ 1 & 1 & -(l+w) \\ -1 & 1 & -(l+w) \\ 1 & 1 & (l+w) \end{bmatrix} \begin{bmatrix} v_x \\ v_y \\ \omega_z \end{bmatrix} \quad (1)$$

$$\begin{bmatrix} v_x \\ v_y \\ \omega_z \end{bmatrix} = J^+ \begin{bmatrix} \omega_1 \\ \omega_2 \\ \omega_3 \\ \omega_4 \end{bmatrix} = \frac{R}{4} \begin{bmatrix} -1 & 1 & -1 & 1 \\ 1 & 1 & 1 & 1 \\ \frac{1}{(l+w)} & -\frac{1}{(l+w)} & -\frac{1}{(l+w)} & \frac{1}{(l+w)} \end{bmatrix} \begin{bmatrix} \omega_1 \\ \omega_2 \\ \omega_3 \\ \omega_4 \end{bmatrix} \quad (2)$$

Where, w_i is angular velocity of No.i wheel; J is Jacobian matrix of inverse kinematic equation; v_x , v_y and w_z are generalized velocity of the platform; R is radius of the wheel; l is a half length between centers of forward and backward wheels; w is a half width between centers of left and right wheels; J^+ is the pseudo inverse matrix of J .

2.2 Analysis of Anisotropy

Due to the feature of omnidirectional wheel, maximum velocity and acceleration that can be achieved are variable respectively in different direction, which is called

kinematic anisotropy[4]. It is assumed that maximum velocity of each wheel is 1m/s, then maximum velocity for specific direction can be calculated by inverse kinematic equation. As shown in figure 3, it is fastest in the direction of portrait and transverse, while velocity in the direction of diagonal 45 degree is minimal.

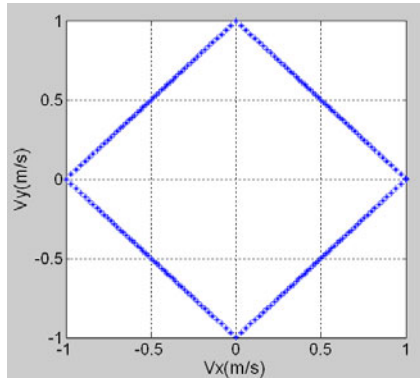


Fig. 3. Kinematic anisotropy of velocity

2.3 Slippage of Motion

There is inevitable slippage between the wheel and the ground due to free rolling of the roller, especially during the process of acceleration and brake, which will result in errors of direction and velocity and make significant influence on the accuracy. The definition of slippage is expressed below:

$$s = \frac{\omega_i R - V}{\max\{\omega_i R, V\}} \in [-1, 1] . \tag{3}$$

Where, V is translational velocity of the wheel.

3 Modeling and Simulation of Prototyping

In this paper, the dynamic virtual Prototyping model is made by multi-body dynamic software RecurDyn, as shown in Figure 4. Radius of the wheel is 0.23m and the total mass of the platform is about one ton. Nonlinear factors are taken into consideration during the process of physical modeling, mathematic analysis model can be derived by generalized recursive algorithm, so as to validate the control strategy latter.

The open-looped control model of the platform is built in this paper. Maximum velocity for specific direction can be calculated by disired direction and the maximum angular speed of the wheel, therefore angular speed of each wheel can be dirived by equation(1). Coordinated Simulation by Matlab/Simulink and RecurDyn is carried out and slippage of each wheel is derived by equation (3). Angular velocity of two wheels in line of diagonal is the same on condition of translation. We can get the actual direction by calculating the displacement components of X and Y axis.

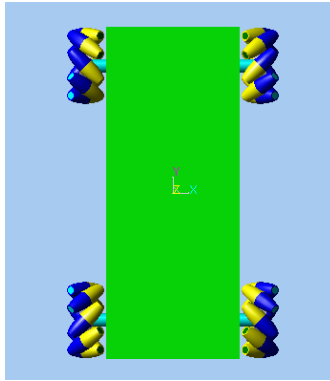


Fig. 4. Planform of virtual prototyping

Due to the symmetric layout of omnidirectional platform, the results of each quadrant are the same, we can take the first quadrant for instance. Maximum desired angular velocity of each wheel is 3rad/s and desired directions are taken from 0 degree to 90 degree every other 10 degree. Virtual experiment is carried out and simulation results are listed in Table1.

Table 1. Simulation results of translation before motion compensation

Desired direction (degree)	Errors of direction (degree)	Simulation velocity (m/s)	Errors of Velocity (m/s)	Slippage of No.1,3 wheel	Slippage of No.2,4 wheel
0	-0.08	0.569	0.121	0.174	0.174
10	2.427	0.472	0.1236	0.022	0.315
20	5.077	0.42	0.1185	-0.235	0.389
30	7.977	0.402	0.1031	-0.54	0.416
40	9.565	0.401	0.0888	-0.849	0.416
50	9.872	0.416	0.0738	-0.855	0.395
60	9.376	0.445	0.0601	-0.585	0.354
70	9.306	0.516	0.0223	-0.376	0.252
80	6.671	0.533	0.0626	-0.093	0.227
90	0.831	0.604	0.086	0.122	0.122

We can get conclusions from simulation results as follows: (1) Actual direction of the platform deviates from desired direction to different extent except translating along X or Y axis absolutely. Compared with desired direction, actual direction is closer to Y axis, and directional error is maximal in direction of diagonal 45 degree; (2) Comparing two desired direction with the same desired velocity, simulation velocity of the direction closer to Y axis is faster than that of the direction closer to X axis. Furthermore, directional error of the direction closer to Y axis is bigger than that of the direction closer to X axis; (3) The slippage of each wheel has anisotropy in different direction, it increases with the direction degree augment and get to the peak

value in direction of diagonal 45 degree, then decreases when the direction converges to Y axis. There is minimal slippage in direction of moving forward, so that its simulation velocity is maximal.

4 Method of Motion Compensation and Simulation

Seen from the analysis above, in order to improve the accuracy of omnidirectional motion, it is necessary to compensate the direction and velocity respectively. According to the anisotropy of velocity and slippage, the compensation should be nonlinear in different direction. It is difficult in building mathematic analysis model for motion compensation, therefore we adopt the method of neural network.

Back Propagation (BP) network is the most widely used neural network, it is a kind of self-learning, self-organizing and adaptive nonlinear system, which can simulate human brain for heavily parallel processing.

Owing to two components of direction and velocity to be compensated, there are two input and output for our BP network. The input data is simulation result of translation and the output data is given command to the prototyping, there is single hidden layer as well. We still take the first quadrant for instance, maximum angular velocity of the wheel is limited to 12rad/s for our omnidirectional platform, the bound of given angular velocity for simulation is taken from 3rad/s to 11rad/s and the step is 2rad/s, so that 50 groups of experiment are carried out for the sample data. In this paper, we set 10 hide nodes and 0.01 as error goal. Module of BP network is derived by training the sample data and the coordinated simulation model for translation is built as shown in Figure5.

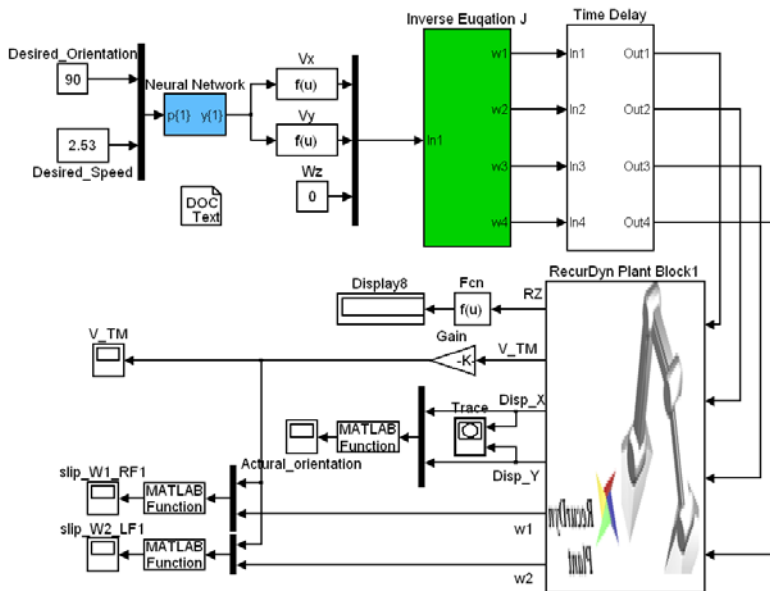


Fig. 5. Coordinated simulation model of Matlab/Simulink and RecurDyn

Two groups of virtual experiment are carried out with desired maximum angular velocity of 3rad/s and 11rad/s respectively, simulation results with compensation are shown in Figure 6. Comparing simulation results before and after motion compensation, it is obvious that motion compensation method based on BP network can reduce errors of direction and velocity effectively, which improves the accuracy of omnidirectional platform greatly.

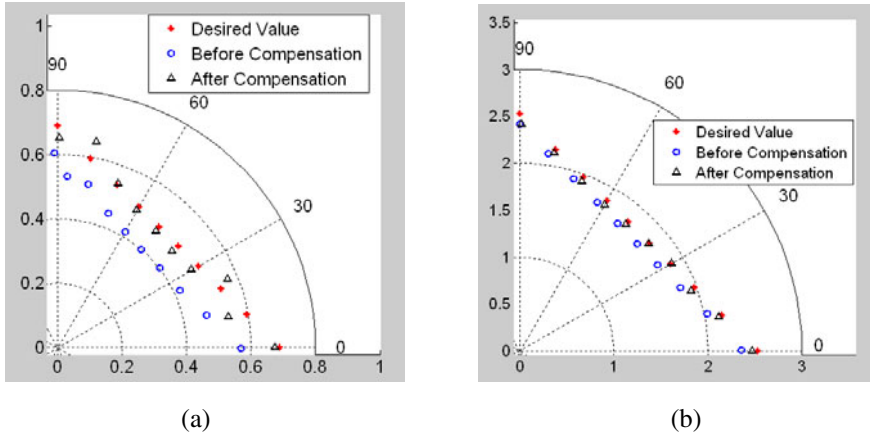


Fig. 6. Simulation results with maximum angular velocity of 3rad/s (a) and 11rad/s (b) in polar coordinate

5 Conclusion and Future Work

In this paper, we make an analysis on kinematic characteristic of omnidirectional platform and build the model of virtual prototyping. The anisotropy of slippage and influence on translation are derived. A method based on BP network is proposed for nonlinear motion compensation, and simulation results prove the validity of this method.

Next step, we will implement experiment on real platform to make a further validation of this method. An improved control strategy should be proposed to adapt for different ground.

References

1. Zhao, D.B., Yi, J.Q., Deng, X.: Structure and Kinematic Analysis of Omni-directional Mobile Robots. *Robot* 25(5), 394–398 (2003) (in Chinese)
2. Stephen, L.D., Brett, D.L.: Control of an omni-directional robotic vehicle with Mecanum wheels. In: *IEEE National Telesystems Conference*, pp. 323–328. IEEE Press, Atlanta (1991)
3. Wang, Y.Z., Chang, D.G.: Motion Performance Analysis and Layout Selection for Motion System with Four Mecanum Wheels. *Journal of Mechanical Engineering* 45(5), 307–310 (2009) (in Chinese)

4. Leng, C.T., Cao, Q.X.: Anisotropy of 4-wheeled omnidirectionally mobile robots. *Transactions on Intelligent Systems* 2(3), 45–51 (2007) (in Chinese)
5. Zhang, Y.N., Wang, S.S.: Research on Motion Characteristic of Omnidirectional Robot Based on Mecanum Wheel. In: *Digital Manufacturing & Automation*, pp. 237–241. IEEE Press, Chang Sha (2010)
6. Shi, L., Chen, T.J.: *The Grid: Theory and Application of Intelligent Control*. TsingHua University Press, Beijing (2009) (in Chinese)

Study of Thrust Lever Control Loading System in Flight Simulator

Jinsong Zhao^{1,*}, Zhengmao Ye¹, Gang Shen^{1,2}, and Junwei Han¹

¹ State Key Laboratory of Robotics and System, School of Mechatronics Engineering, Harbin Institute of Technology, Harbin, Heilongjiang 150001, China
jinsongzhao@163.com

² School of Mechanical and Electrical Engineering, China University of Mining and Technology, Xuzhou, Jiangsu, 221116, China

Abstract. Aiming at computing the force feel to be simulated at real time, thrust lever control loading system's simulation model is set by software called SimMechanics after its control mechanism being analyzed. The dynamic characteristics of control systems and model torque are studied based on the simulation model. Then the counter potential, primary element to cause the surplus torque, is pointed out according to the dynamic characteristics of control. To make the loading system not only flow the model torque precisely but also retrain surplus torque effectively, the low frequency of the current loop is designed due to frequency spectrum of counter potential and follow-up component in model torque, while the medium frequency is on basis of the step component in model torque. Finally, the reasonableness of the designed current loop is verified by computer simulation of the torque output by motor and loading torque.

Keywords: Flight simulator Control Loading System thrust lever current loop simulation model.

1 Introduction

Thrust lever control loading system belongs to secondary control loading system. Its function and principle is similar to the primary control loading system. The characteristics of secondary control loading system are reflected on the bellowing items:

First, the control force feel at the control handle is counter friction torque which is nearly invariable during control process, but the torque output by the motor will not be equal to that at the handle because of the connecting rod mechanism of the control system and which leads to the motion and torque transfer is nonlinear. Moreover, inertia and gravity of each rod also cause the torque at the loading end to follow the position of the handle in certain rules which can't be simplified a second-order

* This research was supported by the 921Manned Space Project of the China Academy of Space Technology (CAST) and Self-Planned Task SKLRS200803B of the State Key Laboratory of Robotics and Systems, Harbin Institute of Technology (HIT), and also was supported by the National Natural Science Foundation of China (No. 50975055).

system[1,2] as primary control loading system. Second, the loading system must follow the model torque precisely. Last, the thrust lever control is seemed very slowly so that the primary element to cause surplus torque is the compelled velocity. The method to reduce surplus torque on primary control loading system is the principle of structure invariable [3,4]which is used to offset the interference of position. If retraining surplus torque according this way on secondary control loading system, not only make the loading system complicated but also introduce noise to effect the force feel simulation[5].

To resolve above problems, the simulation model is set by software SimMechanics so that the mass and size of every part of the control system is equal to the real system to make sure that the computed model torque is more precise than other method. Then use the Permanent Magnet Synchronous Motor as the execute component and design the control loop in the view of torque servo system. On behalf of retraining surplus torque, analysis the primary competent by computer simulation and put forward a new and simple method to reduce it effectively.

2 Principle of Thrust Lever Control Loading System

The construction of thrust control loading system is showed as figure 1. It is composed of control mechanism and loading system. When push the handle, the simulation model in the secondary control loading system computer compute the model torque according to the angle or velocity signal at real time. Then the model torque as instruction signal will be sent to the control loop driving the motor to output the counter torque so that the pilot can feel the invariable friction control force.

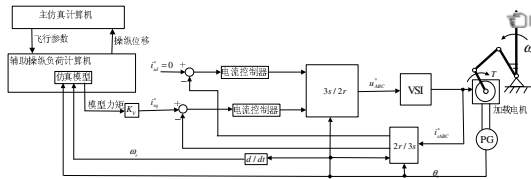


Fig. 1. Composition of control thrust lever control loading system

3 Simulation Model of Thrust Lever Control Loading System

3.1 Control Mechanism

The mechanism of thrust lever control loading system is listed in figure 2(a), including control handle, rocker-arm, connecting rod crank and motor. Figure 2(b) is the simplified mechanism, in which l_0, l_1, l_2, l_3 represents control handle, rocker-arm, connecting rod crank respectively. The whole mechanism is a four-bar mechanism.

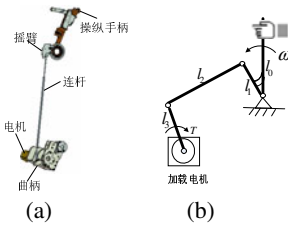


Fig. 2. Mechanism of thrust lever

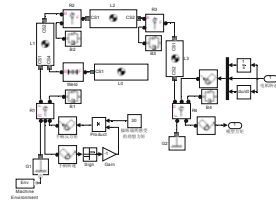


Fig. 3. Model of engine control thrust lever

3.2 Simulation Model

Each rod in Figure 2(b) is considered as well-proportioned and their parameters is given in the table 1. Moreover, the damp of every joint is supposed 0.01(Nms/rad).

Table 1. Parameters of mechanism

serial number	mass		length	
	value	unit	value	unit
l_0	1.24	Kg	299.0	mm
l_1	1.00	Kg	76.2	mm
l_2	1.00	Kg	700.3	mm
l_3	0.606	Kg	92.7	mm

The simulation model from the handle to the motor shaft is set by the software SimMechanics is showed as figure 3 in which joint R_4 represents the motor shaft. This model not only can compute model torque at real time but also can be used to analysis the dynamic characteristics of the control mechanism.

4 Analysis of the Loading System

4.1 The Mathematic Model of Permanent Magnet Synchronous Motor

The mathematic model of Permanent Magnet Synchronous Motor is set according to figure 1 as the bellowing equations.

$$u_{sq} = R_s i_{sq} + L d i_{sq} / dt + \omega_r \psi_r \tag{1}$$

$$T_e = n_p \psi_r i_{sq} \tag{2}$$

$$T_e - T_f = J d^2 \theta / dt^2 + B d \theta / dt \tag{3}$$

$$T_f = G(\theta - \theta_f) \tag{4}$$

Where u_{sq} and i_{sq} are Voltage and current at q axis of stator respectively; R_s and L are Resistance and inductance at q axis of stator; Ψ_r is Flux at q axis of rotator; ω is Synchro-speed of rotating magnetic field; n_p is Number of pole-pairs; T_e and T_f are output torque of motor and loading torque; J and B are Rotary inertia and damp of motor; θ and θ_f Shaft angle of motor and crank angle of I_3 ; G is Stiffness of mechanics converted into motor's shaft.

If cutting off the output model torque of simulation model connecting to the loading system, the loading system can be viewed as a torque servo system with position disturbance. The block diagram of torque loading system can be drawn as figure 4 associated with figure 1 and equation (1),(2)and (3). In figure 4, the part in dotted line frame is current loop. Element $K_m=n_p\Psi_r$ is coefficient of torque and $K_e=\Psi_r$ is coefficient of counter potential. K_S and T_S is the gain and time const of dc-to-ac converter respectively. $W(s)$ is correction link.

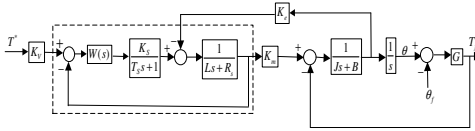


Fig. 4. Block diagram

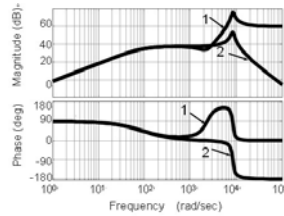


Fig. 5. Surplus torque frequency response

To analysis the components of the loading torque substantially, take out the current loop and correction link even omit the time const of dc-to-ac converter for the moment in figure 4. Then the expression of the loading torque can be deduced as below

$$T_f = N_1(s)T^*(s) / D(s) - N_2(s)\theta_f(s) / D(s) \tag{5}$$

Where $D(s) = J L s^3 + (J R + B L) s^2 + (K_m K_e + L G + B R) s + G R$, $N_1(s) = K_v K_s K_m G$, and $N_2(s) = G [J L s^3 + (J R + B L) s^2 + (K_m K_e + B R)]$.The first item of equation(5) is the component of loading torque caused by model torque and the other part is the surplus torque raised by the compelled position.

4.2 Analysis of Surplus Torque

Due to the definition of surplus torque, if Make $T^*=0$ in equation(5), we can get the expression of surplus torque

$$T_f = - \frac{J L s^3 + (J R + B L) s^2 + (K_m K_e + B R) s}{J L s^3 / G + (J R + B L) s^2 / G + (K_m K_e + L G + B R) s / G + R} \theta_f \tag{6}$$

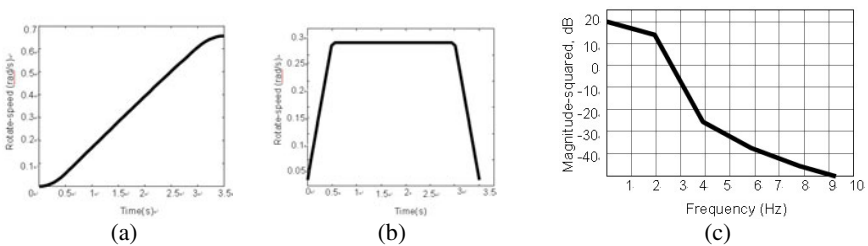
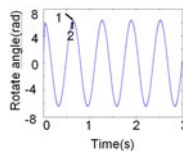
Table 2. Parameters of loading system

parameter	value	unit	parameter	value	unit
J	1.5×10^{-5}	Kgm ²	K _V	1	Nm/A
B	0.02	Nms/rad	K _e	1.2	Vs/rad
G	750	Nm/rad	K _m	1	Nm/A
L	0.015	H	K _S	40	V/A
R _s	0.5	Ω	T	1.7×10^{-7}	s

From equation (6) we can see that surplus torque is related with the parameters of the loading system and dynamic characteristics of the compelled position. The parameters of the loading system are listed in the table 2. We can know from the parameters in table2 that surplus torque is mainly caused by the compelled velocity when the dynamic is low. We can make the bode diagram of surplus torque in software Matlab shown as figure 5. Curve 1 represents the whole surplus torque and Curve 2 is the counter potential surplus torque. We can see that the two curves nearly coincide with each other in the low frequency field.

When controlling the thrust lever normally, dynamic of rotator compelled by external position can be anglicized by the simulation model in figure 3. When controlling normally, the approximate velocity curve of handle and position curve of motor shaft is shown in figure 6(a), 6(b). Figure 6(c) is the frequency spectrum of the motor's shaft angle. We can see from figure 6(c) that the range of shaft angle's frequency is below 3HZ, so that surplus torque is mainly caused by counter potential.

If the motor shaft is given a compelled position such as $\theta_f = 0.4\sin(10t)$, the response curve of surplus torque is shown in figure 7 Curve 1 represents the whole surplus torque and Curve 2 is the counter potential surplus torque. The counter potential is nearly 99% percents of the whole surplus torque.

**Fig. 6.** Curves of control Mechanism's motion**Fig. 7.** Curves of surplus torque

As is anglicized above, if the counter potential can be retrained, the other surplus torque will not effect on the loading system obviously. The method to reduce surplus torque is that deem the counter potential as the disturbance of the current loop and designing the current loop properly. The current loop can be simplified as figure 8 in which the element $G_1(s)$ is the production of correction link and dc-to-ac converter, $G_2(s)=1/(Ls+ R_s)$, $E(s)$ is counter potential. Then we can get the bellowing expression

$$I(s) / E(s) = G_2(s) / [1 + G_1(s)G_2(s)] \tag{6}$$

When $G_1(s)G_2(s) \gg 1$, equation(6)can be simplified as

$$I(s) / E(s) \approx 1 / G_1(s) \tag{7}$$

If the system is corrected to make $G_1(s)$ become type I link, its expression of low frequency model

$$G_1(s) = K(Ts + 1) / [s(aTs + 1)] \tag{8}$$

Associate equation (8) with (7)

$$I(s) / [sE(s)] = (aTs + 1) / [K(Ts + 1)] \tag{9}$$

The bode diagram of equation(9) is shown in figure 9.

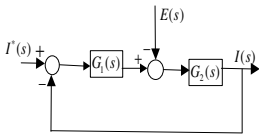


Fig. 8. Model of current loop

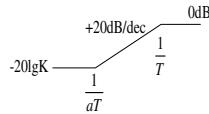


Fig. 9. Low frequency model

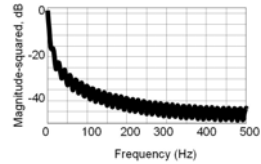


Fig. 10. Model torque

If make sure that the frequency spectrum of $sE(s)=K_c s^2 \theta_f(s)$ is located below the first turning point of the figure 9, the equation (9) can be expressed by equation (10).

$$I(s) = sE(s) / K \tag{10}$$

In the view of retraining the counter potential, if K is large enough, the output current $I(s)$ raised by counter potential can be reduced effectively. $s^2 \theta_f(s)$ is the angle acceleration of the joint R4 in figure 3. We can get the angle acceleration by simulation model in accordance with the control curve shown in figure 6. Then the result of the angle acceleration producing with K_c is the counter potential whose frequency spectrum is shown in figure 10. the frequency of the counter potential can be seemed locating in the range of 20HZ, so we can design the system according to 150rad.

4.3 Designing of Current Loop

The function of the current loop need to considering two aspects: First, it can follow the model torque precisely. Second, reduction of surplus torque whose method is mentioned above. Next, we mainly talk about how to design current loop to make it follow the model torque precisely.

The equation (11) can be deduced by figure 8.

$$\varepsilon(s) = 1/[1+G(s)] \quad (11)$$

$G(s)=G_1(s)G_2(s)$, $\varepsilon(s)=I(s)-T^*(s)$ is the flowing error of current loop. To analysis the flowing characteristic of current, the instruction signal must be anglicized firstly. The model torque curve which is got by the simulation model is shown as figure 11(a). we can see that model torque is composed of a step signal and a follow-up signal. Figure 11(b) is the frequency spectrum of the follow-up competent. From the analysis of the model torque, we know that current need not only to following the step signal but also to satisfying the performance index of low frequency follow-up signal. The performance indexes for step signal are steady state error, response time and overshoot. So the current loop is designed type system with enough bandwidth and phase margin. While dynamic error is the measure for following follow-up signal.

At low-frequency stage, if $G(s) \gg 1$, approximate calculation of equation (11) is

$$\varepsilon(s)/T^*(s) = 1/G(s) \quad (12)$$

Be related with the method to retrain surplus forenamed, we can make low-frequency stage of $G(s)$ and $G_1(s)$ same by correction link. So equation (12) at low-frequency stage is expressed as

$$\varepsilon(s)/[sT^*(s)] = (aTs+1)/[K_0(Ts+1)] \quad (13)$$

If $T^*(s)$ is located below the first turning point of the figure 9, equation (13) can be simplified as

$$\varepsilon(s)/[sT^*(s)] = 1/K_0 \quad (14)$$

Where $\varepsilon(t) = C_1 \dot{T}^*(t) + C_2 \ddot{T}^*(t)/2! + \dots C_k T^{*(k)}(t)/k! + \dots$ (15)

In equation (15), $C_1, C_2/2, \dots$ are dynamic error coefficients. Comparing equation (14) to (15), in the condition of the model torque below the first turning point of the figure 9

$$\varepsilon(t) \approx C_1 \dot{T}^*(t) = \dot{T}^*(t)/K_0 \quad (16)$$

So make the frequency of the follow-up signal and the counter potential both locate below the first turning point of the figure 9. Then increase the value of K_0 according to the reduction of surplus and the precise of model torque following. While the medium frequency stage of current loop can be designed according to the index of step response. With reference to the method above and the parameters in table 2, we can make the correction link contains a PI adjustor and a hysteresis link in series.

$$W(s) = K_p (Ts + 1)(aT_0s + 1) / [Ts(T_0s + 1)] \tag{17}$$

In equation (17), $T=L/R$. The hysteresis link can make the cut-off frequency not be affected by the gain of the open loop and increase the phase margin to heighten the stability of the current loop. The bode is shown in figure 12, in which frequency of the first turning point is less-than 200rad, gain of the open loop 2500, gain of the point head of the counter potential 5000 and cut-off frequency 1890rad, and phase margin 69° .

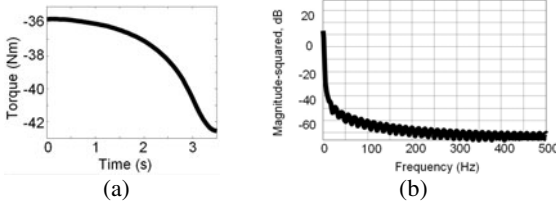


Fig. 11. Curves of model torque

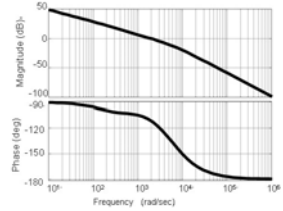


Fig. 12. Bode diagram of open loop

5 Simulation of the Control Loading System

When control the handle as the motion curves in figure 6, the torque output by the motor and caused by the counter potential is listed in figure 13, in which the solid curve represents model torque and the dotted is the torque output by the motor.

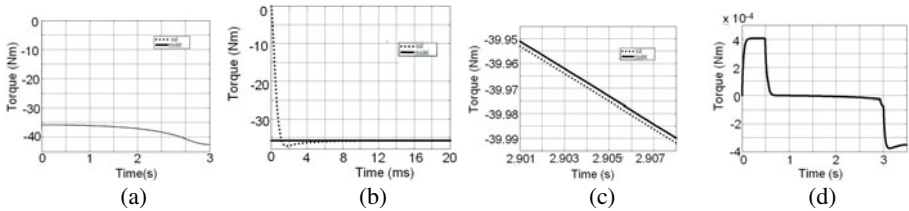


Fig. 13. Simulation curves of torque output by the motor

Figure 13(a) shows the whole curves and Figure 13(b) and 13(c) is an amplified part of the curves which are at initial time and in process respectively. From figure 13(b), we can see that the response time is 0.002s and the overshoot is less-than 5%. Figure 13(c) gives the information that the dynamic error is about 0.002Nm. Figure 13(d) point out the maximum of torque caused by the counter potential is about 4.1×10^{-4} Nm after cutting off the model torque.

Figure 14shows us the simulation curves of model torque and loading torque. Figure 14(a) represents the whole process of the simulation, which error is less-than 0.1Nm. Figure 14(b) is an amplified part of the curves which are at initial time which is similar to Figure 13(b). Figure 14(c) is a part of the curves in simulation process,

which make us know that the loading torque waves tiny because of the surplus torque caused by items of s^3 and s^2 in equation (6). Figure 14(d) is surplus torque, in which curve 1 represents surplus torque before being retrained while curve 2 after being reduced. Figure 14(d) can verify that the method in my research is effective to retrain surplus torque.

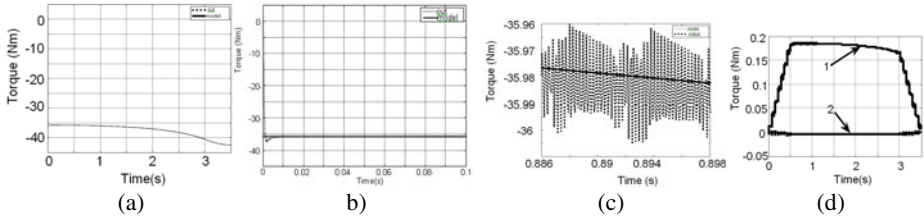


Fig. 15. Simulation Curves of loading torque

6 Conclusion

(1)Set simulation by software SimMechanics;(2)Point out the surplus torque is mainly caused by counter potential;(3)Put forward a new and simple method to retrain the surplus torque. Meanwhile, make the current loop can follow the torque precisely;(4)Verify the validity of the loading system by computer simulation.

References

1. Takats, J.R., Van Duivenbode, E.: Advances in Electric Control Loading & Electric Motion Technology. In: Flight Simulation Engineering and Maintenance Conference (2002)
2. Wang, H.: Research on Essential Technology and Principle Prototype Development of Control loading System in the Simulator. School of Mechanical Engineering, Tianjin University, Tianjin (2006)
3. Gerretsen, A., Mulder, M., van Paassen, M.M.: Comparison of Position-loop, Velocity-loop and Force-loop based Control Loading Architectures. In: AIAA Modeling and Simulation Technologies Conference and Exhibit, San Francisco, CA, pp. 1–18 (2005)
4. Mikael Eklund, J.: Aircraft Flight Control Simulation Using Parallel Cascade System Identification, p. 32. Queen's University, Canada (1998)
5. Fokker, B.V.: Realistic feel in Flight Simulators is Based on Precise Control Loading. Aircraft Engineering 55, 10–12 (1983)

Survey of BMI Distribution among University Students Aged 17 - 24 in Wenzhou

Chen Jun

College of Oujiang, Wenzhou University, Wenzhou 325035, China

Abstract. To study the body mass index of university students of different ages in Wenzhou, a screening of underweight, overweight and obesity is carried out according to the “Body Mass Index Reference Norm for Screening Overweight and Obesity in Chinese Children and Adolescents” issued by WGOC. The result shows that the BMI percentile fluctuates little among students aged 17 - 24. BMI P85, P95 are both lower than the norm issued by WGOC, particularly among female students. About 79% students have a normal BMI and 21% students are in exception. While the screening of obesity rate is comparatively low in both genders, the overweight rate and underweight rate exhibit a gender difference with the former favors male groups aged 21-23 and the latter favors female group. In terms of the normal BMI distribution, the two genders show little difference at each age except 18. But for underweight rate and overweight rate, there is a significant difference between two genders at the age of 19 – 23. Obesity rate only shows a gender difference in the age group of 18. It is concluded that the BMI classification norm for Chinese adults should be adopted in evaluating overweight and obesity situation in university students. With the increasing of age, male students have the tendency of overweight and obesity and female students have the tendency of underweight. At each age, the underweight rate in female students is higher than that of male students and the overweight and obesity rate in male students are higher than those of female students.

Keywords: university students, BMI, screening standard, overweight, obesity.

1 Introduction

In 2000, WHO defined obesity as an epidemic worldwide, regarding it as one of the ten factors leading to serious diseases. This suggests the urgency in preventing and controlling obesity. In recent years, obesity in universities has increasingly caught public attention. BMI (body mass index) recommended by WHO is a simple and convenient way to judge overweight and obesity of adults and has been proved to be more reliable than weight index. This article conducts a survey of the BMI of university students in Wenzhou to study the distribution of underweight, overweight and obesity so as to put forth some valuable suggestions for public physical education and some countermeasures for potential health problems.

2 Research Object and Methodology

2.1 Research Object

The research takes the physical fitness test data of non-P.E students in universities in Wenzhou between 2008 and 2009 as its study object and works out BMI based on the ratio of height and weight. Altogether 10413 students yield valid data among whom 4719 are male and 5712 are female. Table 1 presents the general situation of the participants.

Table 1. The General Situation of participants (M±SD)

Gender	Number of people	age (y)	height (cm)	weight(kg)	BMI
Male students	4719	20.1±1.42	170.8±5.74	61.7±7.66	21.2±2.25
Female students	5712	19.9±1.38	158.9±5.23	51.8±5.96	20.5±2.02

2.2 Research Methodology

2.2.1 Literature Review

Literature review is adopted in this research. The formulae of BMI is: $BMI = \text{weight(kg)}/\text{height (m)}^2$. According to the “Body Mass Index Reference Norm for Screening Overweight and Obesity in Chinese Children and Adolescents” issued by WGOC, a BMI lower than 18.5 indicates that the person is underweight; a BMI between 18.5 and 23.9 indicates a normal weight and a BMI between 24 and 27.9 indicates overweight and a BMI above 28 suggests obesity.

2.2.2 Statistic Method

Statistic method is adopted with Excel, SPSS17.0 for data processing and χ^2 test for comparison of data.

3 Results Analysis

3.1 The Distribution of BMI Percentile in Students in Different Age Group

BMI is an index for human body fat based on an individual’s height and weight. When measuring the degree of obesity, BMI could reduce the influence of different heights on the weight index so that a better comparison between groups or individuals could be made. The weight index of most individuals are obviously related to the percentage of their body fat and could reflect the degree of obesity. The internationally adopted BMI reference issued by WHO set the value as follows: an index between 25.0~29.9 indicates overweight and an index above 30 suggests obesity. WGOC surveyed 240,000 students between the ages of 7 to 18 to study the distribution of BMI percentile

Table 2. BMI Percentile of Male University Students Aged 17–24 in Wenzhou (kg/m²)

Age (y)	n	percentile												
		5	10	20	30	40	50	60	70	80	85	90	95	97.5
17	102	18.0	18.6	19.3	19.9	20.4	20.9	21.5	22.1	22.8	23.3	24.0	24.9	25.4
18	518	17.9	18.5	19.3	19.9	20.4	20.9	21.5	22.1	22.9	23.4	24.1	25.1	25.8
19	1050	17.9	18.5	19.3	19.9	20.4	20.9	21.5	22.1	22.9	23.4	24.1	25.1	25.8
20	1128	17.9	18.5	19.3	19.9	20.4	20.9	21.5	22.1	22.9	23.4	24.1	25.1	25.8
21	1131	17.9	18.5	19.3	19.9	20.4	20.9	21.5	22.1	22.9	23.4	24.1	25.1	25.8
22	630	17.9	18.5	19.3	19.9	20.4	20.9	21.5	22.1	22.9	23.4	24.0	25.1	25.8
23	112	18.1	18.7	19.4	19.9	20.5	21.0	21.5	22.1	22.9	23.4	24.0	25.1	25.7
24	48	18.0	18.6	19.3	19.9	20.4	20.9	21.5	22.0	22.8	23.2	23.8	24.6	25.2

Table 3. BMI Percentile of Female University Students Aged 17- 24 in Wenzhou (kg/m²)

Age (y)	n	Percentile												
		5	10	20	30	40	50	60	70	80	85	90	95	97.5
17	143	17.6	18.2	18.8	19.4	19.8	20.3	20.8	21.4	22.1	22.6	23.2	24.1	24.7
18	824	17.6	18.2	18.8	19.4	19.8	20.3	20.8	21.4	22.1	22.6	23.2	24.1	24.7
19	1400	17.6	18.2	18.8	19.4	19.8	20.3	20.8	21.4	22.1	22.6	23.2	24.1	24.7
20	1328	17.6	18.2	18.8	19.4	19.8	20.3	20.8	21.4	22.1	22.6	23.2	24.1	24.7
21	1284	17.6	18.2	18.8	19.4	19.8	20.3	20.8	21.4	22.1	22.6	23.2	24.0	24.7
22	613	17.6	18.2	18.8	19.4	19.8	20.3	20.8	21.4	22.1	22.6	23.1	24.0	24.7
23	105	17.9	18.4	18.9	19.4	19.9	20.4	20.8	21.4	22.1	22.6	23.2	24.0	24.6
24	15	18.0	18.3	18.9	19.3	19.8	20.2	20.6	21.0	21.6	21.9	22.2	22.6	22.8

at different ages and found out the difference between BMI of Chinese children and adolescents and the international standards. It set up three experimental standards composed by P85、P90 and P95 , suggesting that P85 and P95 could be set as the standards for the measurement of overweight and obesity due to their sensitivity and peculiarity. It introduced the index of 24 as the threshold of overweight and 28 for obesity for Chinese adults. This standard corresponds to the already issued standards for overweight and obesity for Chinese adults.

The research finds that the P85 (on average 23.4) and P95 (25) of male university students in Wenzhou are both lower than the standards for Chinese children and adolescents issued by WGOC. The P85 (on average 22.5) and P95 (23.9) of female university students in Wenzhou are even lower.(see table 3 and 4) This indicates that P85 and P95 might not be the appropriate index for measuring overweight and obesity for university students. It is more advisable to adopt the standard for Chinese adults issued by WGOC, that is, at 18, the thresholds for overweight and obesity should respectively be 24 and 28. The research also finds that the BMI percentile changes little for the university students during their four-year university life. So when measuring overweight and obesity among university students, age factor is not very significant.

3.2 Screening of Underweight, Overweight and Obesity in Male University Students Aged 17- 24 in Wenzhou

From table 4 we can find that the percentage of underweight, overweight and obesity for male students from the age of 17 to 24 are respectively 9.9%、 10.2% and 0.7%. 79.2% of students enjoy a normal BMI. Underweight students are mainly in the age groups of 17 to 19. With the increasing of age, underweight is declining. Overweight students mainly appear in the age groups of 21 to 23, occupying an percentage of 38.1% and overweight tends to climb with the increasing of age. Overweight in the age groups of 19 to 20 takes the lowest percentage of 16.6%. The percentage of obese students is quite low. Even in the age group of 18, there are only 1.2% students suffering from it.

Table 4. Percentage of Underweight, Overweight and Obesity Among Male University Students Aged 17-24 in Wenzhou[n (%)]

Age (y)	Male				
	Number of people	Underweight	Normal	Overweight	Obesity
17	102	17 (16.7)	77 (75.5)	8 (7.8)	0 (0)
18	518	64 (12.4)	394 (76.1)	54 (10.4)	6 (1.2)
19	1050	120 (11.43)	840 (80)	88 (8.4)	2 (0.2)
20	1128	111 (9.8)	914 (81)	92 (8.2)	11 (1)
21	1131	92 (8.1)	888 (78.5)	141 (12.5)	10 (0.9)
22	630	53 (8.4)	495 (75.6)	77 (12.2)	5 (0.8)
23	112	6 (5.4)	90 (80.4)	15 (13.4)	1 (0.9)
24	48	3 (6.3)	40 (83.3)	5 (10.4)	0 (0)
Total	4719	466 (9.9)	3738(79.2)	480 (10.2)	35 (0.7)

Table 5. Percentage of Underweight, Overweight and Obesity Among Female University Students Aged 17-24 in Wenzhou[n (%)]

Age (y)	Female				
	Number of people	Underweight	Normal	Overweight	Obesity
17	143	17 (11.9)	108 (75.5)	16 (11.2)	2 (1.4)
18	824	110 (13.3)	664 (80.6)	49 (5.9)	1 (0.1)
19	1400	202 (14.4)	1126(80.4)	69 (4.9)	3 (0.2)
20	1328	190 (14.3)	1075 (80.9)	57 (4.3)	6 (0.5)
21	1284	205 (15.9)	1017 (79.2)	58 (4.5)	4 (0.3)
22	613	99 (16.2)	472 (76.9)	40 (6.5)	2 (0.3)
23	105	15 (14.3)	86 (81.9)	3 (2.9)	1 (0.95)
24	15	1 (6.7)	14 (93.3)	0 (0)	0 (0)
Total	5712	839 (14.7)	4562 (79.9)	292 (5.1)	19 (0.3)

From Table 5 we can find that the percentage of underweight, overweight and obesity among female students from the age of 17 to 24 are respectively 14.7%、5.1% and 0.3%. 79.9% female students enjoy a normal weight. The distribution of BMI of female students shows similar features to those of male students. The screening finds that underweight female students at each age enjoy a comparatively high percentage which reaches its highest point of 16.2% . Overweight students take a comparatively low percentage. Its highest point 11.2% comes at the age of 17. The number of overweight students tend to decrease with the increasing of age. The percentage of obesity in female students is rather low. It reaches its highest point 1.4% at the age of 17 while in other age groups obesity students only take up a percentage of 1%.

Obesity is a medical condition in which excess body fat has accumulated to the extent that it may have an adverse effect on health. Modern medicine defines obesity as a kind of obvious metabolic disorder which will influence the normal functioning of body. Obesity has swept through European countries since 60s in 20th century and caused great concern. In China, better living conditions, the change of diet and less exercise contribute to the problem of obesity. The percentage of overweight and obesity is on a sharp rise. In 2003, the Department of Disease Control in the Ministry of Health published “Preventing and Managing Obesity Among Adults in China (for Trial Implementatioon)” pointing out that 22.4% adults were overweight and 3.01% were obese. “Report on Chinese Cardiovascular Disease 2005” published by NCCD points out that over 200 million Chinese are overweight and 60 million are obese. Obesity has become a serious and urgent social problem. It’s found that if an individual’s BMI exceeds the normal range at youth, the risk of getting disease is higher than those people who have become obese at old age. Obesity at juvenile stage will develop into obesity at adulthood which will lead to serious diseases such as heart disease, hypertension and diabetes etc.

This research finds that the BMI of most of the university students are in the normal range and the percentage of overweight, especially of obesity are quite low. According to the standard of overweight and obesity issued by WHO, the ratio of overweight to obesity among adults is 8:1. This research shows that the ratio of overweight to obesity among male university students is 14:1 and the ratio among the female students is 15:1. Both are lower than the ratio of adults. This indicates that university students are at a lower risk of getting obesity than adults.

Obesity is detrimental to health, so is underweight. Extreme low fat mass caused by chronic dieting, malnutrition, anorexia nervosa and other diseases will lead to metabolic disorder, physical dysfunction and even death. The research finds that the number of underweight female students exceeds that of the overweight and obese female students which calls for our attention.

3.3 Comparison of BMI Distribution among Male and Female University Students in the Same Age Group

The comparison indicates that the percentage of underweight female students is higher than that of the male and the percentage of overweight is lower than that of the male. A notable difference shows between them ($P < 0.01$) . (see table 6) But for the percentage

of obesity, there is not much difference between the two groups($P>0.05$) . The research also finds that with the increasing of age, the percentage of overweight and obesity among male students tend to rise while those of the female students tend to decline.

Table 6. BMI Distribution Comparison Between Male and Female University Students Aged 17-24 in the Same Age Group

Age (y)	Male vs female							
	χ^2 under-weight	P	χ^2 normal weight	P	χ^2 over-weight	P	χ^2 obesity	P
17	1.138	0.286	0.000	0.995	0.754	0.385	1.438	0.230
18	0.279	0.597	3.896	0.048*	9.159	0.002**	6.591	0.010**
19	4.730	0.029*	0.069	0.792	11.924	0.000**	0.0167	0.897
20	11.317	0.000**	0.003	0.960	15.979	0.000**	2.431	0.119
21	34.193	0.000**	0.172	0.678	50.260	0.000**	3.421	0.064
22	17.329	0.000**	0.445	0.505	11.826	0.000**	1.212	0.271
23	4.943	0.026*	0.085	0.771	7.908	0.005**	0.002	0.963
24	0.003	0.954	0.933	0.334	1.697	0.193	—	—
合计	54.699	0.000**	0.683	0.409	96.527	0.000**	8.322	0.004**

Note: Comparison between male and female university students in the same age group: * < 0.05 , ** < 0.01 .

In terms of underweight percentage, male and female students show little difference at the age of 17-18 ($P>0.05$) ,but there is a notable difference between male and female at the age of 19 and 23 ($P<0.05$) and an even bigger difference in the age group of 20 to 22 ($P<0.01$) . In terms of the normal BMI, except at the age of 18 when male and female students show a notable difference($P<0.05$) , there is not much difference at the other ages ($P>0.05$) . In terms of percentage of overweight, male and female students show a notable difference from the age of 19 to 23 ($P<0.01$) while at the age of 17 and 24 there is not much difference between them ($P>0.05$) . In terms of obesity, a saliant difference only comes to the age group of 18 ($P<0.01$) .

This research indicates that generally the average BMI of male students (21.2) is higher than that of female students(20.5). The underweight percentage among female students is far higher than that among male while the overweight percentage is far lower than that among the male students although there is not much difference between them in terms of normal weight percentage and obesity percentage. This might be related to their eating habits, aesthetic values and life styles. Male students prefer a muscular body to a lean figure and they would like to take in more food with high calory. Female students pay more attention to their figure and would like to take dieting to maintain a desirable figure ignoring their health which often leads to underweight. On the other hand, male students have a different physical composition from female students. They have more muscles which also contributes to a higher BMI than that of

female. At the age of 19 to 22, most university students are at their best physical state. So the potential danger of an abnormal BMI could be easily ignored. This calls for our great attention.

4 Conclusion and Suggestions

4.1 Conclusion

4.1.1 The BMI percentile of university students in Wenzhou fluctuates little. BMI P_{85} , P_{95} are both lower than the standards issued by WGOC, especially among female students. The standards of overweight and obesity for Chinese adults should be adopted in terms of evaluation.

4.1.2 The general distribution of BMI of university students in Wenzhou is fine with 79% normal BMI and 21% exception. The percentage of obesity is low both among male students and female students. The percentage of normal weight and exceptional weight among female students is in accordance with that of male students. Male students have a comparatively higher overweight percentage in the age group of 21-23 while female students have a comparatively lower percentage of overweight and obesity and a higher percentage of underweight. With the increasing of age, overweight and obesity tend to develop in male and underweight tend to develop in female.

4.1.3 The average BMI of female university students in Wenzhou is lower than that of the male students. There is a notable difference between the two groups in normal BMI and obesity percentage at the age of 18, in underweight and overweight percentage at the age of 19~23. The underweight percentage among female students is notably higher than that of the male students while the overweight and obesity percentage of male students are notably higher than female students.

4.2 Suggestions

4.2.1 In light of the exceptional weight phenomenon among university students, a correct attitude toward weight should always be emphasized and advocated in physical education in universities. Students should strike a balance between health and aesthetic tendency so as not to go to extreme in terms of weight.

4.2.2 Guide students to change their bad living habits and keep a healthy diet with appropriate amount of physical exercises. A warning mechanism should be set up for university students' physical health so that they could be prepared for future work physically.

4.2.3 Enhance the guidance of students both within P.E.lessons and after class and introduce some specific physical fitness exercises to students to improve the present situation of exceptional body weight.

4.2.4 It is also advisable to group those students with exceptional BMI into same class so that P.E.lesson could be more target-oriented and effective.

References

1. World Health Organization. Obesity: Preventing and managing the global epidemic. Report of a WHO consultation. WHO Technical Report Series, No. 894, WHO, Geneva (2000)
2. Chinese Obesity Working Group. "Body Mass Index Reference Norm for Screening Overweight and Obesity in Chinese Children and Adolescents. Chinese Journal of Epidemiology 25(2), 97–102 (2004)
3. Obesity Working Group, International Life Science Association of China. A Brief Introduction to BMI Classification Among Chinese Adults. Chinese Journal of Preventive Medicine 35(5), 349–350 (2001)
4. National Institutes of Health, National Heart Lung and Blood Institute in Cooperation with the National Institute of Diabetes and Digestive and Kidney Diseases: Clinical Guidelines on the Identification Evaluation and Treatment of Overweight and Obesity in Adults. The Evidence Report. NIH Publication no. 98-4083 (September 1998)
5. National Health and Medical Research Council: Acting on Australia's Weight: a Strategic Plan for the Prevention of Overweight and Obesity (1998)
6. Disease Control Division in the Ministry of Health of the People's Republic of China. In: Preventing and Managing Overweight and Obesity Among Chinese Adults, People's Medical Publishing House, Beijing (2003)
7. Deng, S., Wang, J.: Advanced Exercise Physiology-Theory and Practice, pp. 241–243. Higher Education Press, Beijing (2003)
8. Deng, S., Chen, P., Qiao, D.: An Introduction to Exercise Physiology, p. 236. Beijing Sport University Press, Beijing (2003)
9. Bo, Y., Gu, X., Ni, W.: Influence of exceptional BMI on the Physical Health Index of University Students. China Sport Science and Technology 41(2), 138–139 (2005)
10. Cai, H.: Characteristics of the BMI of University Students in Shanghai and New Trends in its Change. Journal of Shanghai Normal University (Natural Sciences) 36(6), 103–107 (2007)
11. Zheng, Z., Ma, R., Chen, H.: Study of the Distribution of BMI in China. Mathematical Theory and Applications 20(3), 121–128 (2000)
12. Zhao, J.: Report on the Research Result of Physical Health of Chinese Students in 2000. China School Sport (6), 4–5 (2001)

Robotic Sound Source Localization with Mirror Effect of Echo from an Obstacle Board

Juan Huo and Alan Murray

Shanghai Jiao Tong University, China & The University of Edinburgh
J.Huo@sjtu.edu.cn, Alan.Murray@ed.ac.uk

Abstract. This paper studied a special echo scenario. Three micro-phones are used for 360° in an azimuth plane. Results of real-time robotic experiments are compared and analyzed, which has shown an mirror effect for sound direction path.

1 Introduction

Some night predators such as barn owl have advanced sound localization system which assists them to localize target when visual signal is absent or weak. For barn owl and most mammals, this advanced ability is based on the calculation of Interaural Time Difference (ITD) between two ears. [1-3] have used ITD for robotic tracking due to the advantage of binaural sound localization over vision, sonar in environment estimation. The sound reection and reverberation off walls and surrounding objects can help us to perceive the surrounding objects. In this paper, besides the 3 microphone localization technology, we study the echo effect with an obstacle board placed near the sound source and compare the results with the sound direction test in anechoic chamber.

2 Method

The robot we used has 3 microphones, whose positions can be seen in Fig. 1. The positions of them are shown as black circles(B,C,D). B and C are in the diametrical line of the robot, another one D is located at the back semicircle with equal distance to the other two microphones. Every pair of microphones can locate target in 180° field. With all three microphones, we can locate target in 360° azimuth.

Fig. 1(a) shows the geometry used for calculating sound direction based on Interaural delay between microphones A and B. Since the sound direction is from the sound source to the robot center, the target direction is defined as θ , the azimuth angle between 0° line and the sound source line. Compared to the robot size, the target is always in a long distance. Therefore, the sound source A point is far away compared to the robot diameter. The left target distance $|AB|$ is approximate to $|AE|+|BE|$. In geometry, EC is orthoganal to the sound direction line AO, so $|AE| = |AC|$. BE is a line parallel to AO, as E is a point on the circle $\angle AOC = \angle AOE = \alpha$. Since $\theta = \angle ECB$, $\sin \theta = \frac{|BE|}{|BC|} = \frac{\Delta t V}{L}$, the calculation of θ is thus in equation 2.

The sound input signal is processed by a Fast Fourier Transform (FFT) in a time window. When the average amplitude of the input signal is above a chosen threshold, the characteristic frequency \bar{f} and phase difference $\Delta\phi$ between the left and right ear are calculated. Equations 2 then yield the ITD Δt and the target azimuth direction θ . V is the speed of sound and L the diameter of the robot. The distance between the two microphones of this robot is 62mm which is similar to the owl head.

$$\Delta t = \frac{\Delta\phi}{2\pi\bar{f}} = ITD \tag{1}$$

$$\theta = \arcsin\left(\frac{\Delta t V}{L}\right) \tag{2}$$

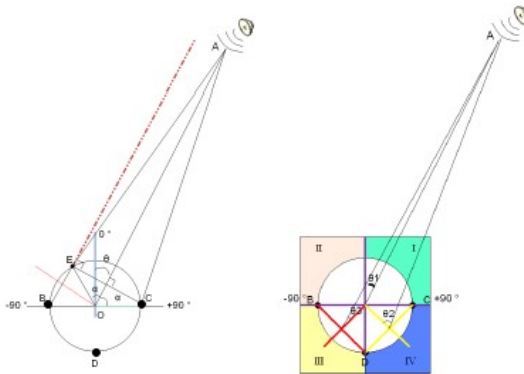


Fig. 1. The geometry of sound localization (a) Sound localization with two microphones. $|AB| \approx |AE| + |BE|$. (b) Each pair of the microphones has one direction. $B,C - \theta_1, B,D -\theta_2, C,D -\theta_3$. θ_1 is defined as the direction of the robot.

As shown in Fig. 1(b), for three microphones, we can get $\sin\theta_1, \sin\theta_2$ and $\sin\theta_3$. $\sin\theta$ is not an identify function of variance θ , but in each quadrant of the Cartesian system, θ and $\sin\theta$ is one to one projection. With the value of $\sin\theta_2$ and $\sin\theta_3$, the quadrant of θ_1 can be accurately located by finding the corresponding field in table. 1. The unique θ_1 thus can be acquired through inverse trigonometric function.

Table 1. Quadrant and corresponding trigonometric value

quadrant	$\sin\theta_1$	$\sin\theta_2$	$\sin\theta_3$	quadrant	$\sin\theta_1(0)$	$ \sin\theta_2 (\frac{\sqrt{2}}{2})$	$ \sin\theta_3 (\frac{\sqrt{2}}{2})$
I	[0,1]	$[\frac{\sqrt{2}}{2}, 1]$	$[-\frac{\sqrt{2}}{2}, \frac{\sqrt{2}}{2}]$	I	\geq	\geq	\leq
II	[-1,0]	$[-\frac{\sqrt{2}}{2}, \frac{\sqrt{2}}{2}]$	$[-1, -\frac{\sqrt{2}}{2}]$	II	\leq	\leq	\geq
III	[-1,0]	$[-1, -\frac{\sqrt{2}}{2}]$	$[-\frac{\sqrt{2}}{2}, \frac{\sqrt{2}}{2}]$	III	\leq	\geq	\leq
IV	[0,1]	$[-\frac{\sqrt{2}}{2}, \frac{\sqrt{2}}{2}]$	$[\frac{\sqrt{2}}{2}, 1]$	IV	\geq	\leq	\geq

3 Results

In the anechoic chamber, the error for the sound localization is very small. We use standard deviation to measure the errors of the direction after data processing. Results are shown in table 2, each actual direction has more than 20 sound sample group. The averaged test results are approaching the actual target direction and the error expressed as standard deviation is small. The standard deviation of the error in the anechoic chamber is within 1°.

Table 2. Localization in anechoic chamber

actual direction °	average robot angle °	error(STD) °
6	5.9950	0.1962
-10	-9.3286	0.1208
0	-0.5310	0.2233
-24	-23.9937	0.2594
..

In an open environment, the error is increased due to echoes and the presence of ambient noise. The accuracy of sound localization is obviously degraded in the normal environment compared to anechoic room. But robot still can locate the object in the general right direction if walls or the other obstacles on the sound propagation path is far away.

To test the effect of sound reection, a board is put on the right hand side of the robot 0.5m away. This disturbance of sound wave is so near to the robot, the robot can not locate the object in the right place any more. 25 group of test results are averaged and shown in Fig. 2(b) in time sequence. Although these groups of data are sampled from one sound burst within 1 second, obviously the early data and the late data are showing two different directions. Fig. 2(a) shows a hypothesis for the cause of localization disparity. The function of the board is quite like a mirror to the sound wave. It changed the path of part of the sound from the sound source and shifted its phase. We assume the later wrong target position comes from a virtual target on the other side of the board.

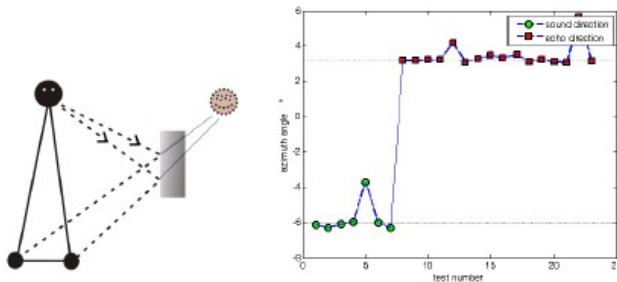


Fig. 2. (a) The echo scenario with reection from a nearby object. The reection of the soundwave shifted the phase. The position of the object is "mirrored" to the other side. (b Sound direction. 25 groups of sound wave amplitude are acquired before FFT process during a sound buzz in 1 second.

Another part of the sound went to the microphone directly, it can be seen from experimental in Fig. 2(b) that sound which travels directly from the source arrives at the microphones before its corresponding echoes. The sound source direction is -6° while a board is put in the right side. Echo sound arrived at the sensor later than the direct sound and showed a "mirrored" direction which is approximately where the board is located.

4 Conclusion

In this paper, we demonstrate real-time sound localization experiments with 3 microphones in a robot. The algorithm for sound localization is based on bioinspired binaural ITD identification and calculation. With an extra microphone, the robot is equipped with the ability to detect the sound source in 360° . The test results in anechoic chamber environment is high accurate. By analyzing an echo scenario, a mirror effect is found when an obstacle board is near the sound source. The mirror effect can also provide information for obstacle direction calculation in future research.

References

1. Murray, J., Wermeter, S., Erwin, H.: Auditory robotic tracking of sound sources using hybrid cross-correlation and recurrent networks. In: 2005 IEEE International Conference on Intelligent Robots and Systems, pp. 3554–3559 (2005)
2. Shimoyama, R., Yamazaki, K.: Acoustic source localization using phase difference spectrum images. *Acoust. Sci. & Tech.* 24(4), 161–171 (2003)
3. Huang, J., Ohnishi, N., Sugie, N.: Building ears for robots: sound localization and separation. *Artif. Life Robotics* 1, 157–163 (1997)

An Multi-agent Artificial Immune Network Algorithm and Its Application*

Xuhua Shi

Institute of Information Science and Engineering, NingBo University,
NingBo 315211, China
xuhuaashi@hotmail.com

Abstract. An multi-agent artificial immune network algorithm (Maopt-aiNet) is introduced in this paper. Unlike other intelligent algorithms, Maopt-aiNet combines the idea of immune mechanics and multi-agent technology to overcome premature problem and fully make use of the agent ability of sensing and acting on the environment. The operators of Maopt-aiNet include neighborhood clonal selection, neighborhood competition, self-confidence motivation, and neighborhood collaboration. The performance of the proposed method is studied with the use of six benchmark problems and compared with other well-known intelligent algorithms. The experiments conducted show that Maopt-aiNet outperforms the other algorithms. Furthermore, it is applied to determine the murphree efficiency of the distillation column, and satisfactory results are obtained.

Keywords: Optimization, immune network, multi-modal optimization.

1 Introduction

Recently, bio-inspired optimization has become increasingly popular in the areas of engineering and science. Generally, for multimodal optimization problems, several global and local solutions exist in the search space. Immune system with advantages as diversity, learning and memory can produce a variety of antibodies and solve the population diversity issues. Therefore, relative immune mechanism is used to design the appropriate strategy to solve multimodal optimization problems. Based on the mechanism of clonal selection, De Castro[1] proposed immune clonal selection algorithm (Clonal), which has high parallel and global convergence. However, it only clones and mutates those antibody groups with high affinity, and has limited capability of dealing with complex multimodal function optimization problems. Then, De Castro and Timmis developed opt-aiNet[2] (Artificial Immune Network for Optimization) for multimodal optimization problems. Because of the complexity of the immune mechanism, only small part of it has been used by the authors in all studies above. For Opt-aiNet algorithm, which is considered to be an effective multimodal function optimization, still has a series of limitations [3]. To overcome

* Foundation item: Zhejiang Technology Programme (2011C21077), Zhejiang Natural science Fund (Y1090548), Ningbo Natural science Fund(2011A610173), Ningbo key construction service-oriented professionals(Sfwxzdzy200903).

the disadvantages of Opt-aiNet algorithm, an multi-agent artificial immune network algorithm (Maopt-aiNet), combining the ideas of multi-agent and immune network is introduced in this paper. With the current studies, the combination of multi-agent and immune technology can provide us useful clues for complex optimization problems.

2 Maopt-AiNet Algorithm

2.1 Definitions for Maopt-aiNet

The mathematic model for optimization problem can be expressed as:

$$\min_{\mathbf{x} \in \mathbf{S} \subset R^q} f(\mathbf{x}) \tag{1}$$

Where $\mathbf{S} = \prod_{i=1}^q \langle \alpha_{i-}, \alpha_i^- \rangle$ is the domain, $\mathbf{x} = (x_1, x_2, \dots, x_q) \in \mathbf{S}$, q is the dimension of the system. $f(\mathbf{x})$ is the objective function. For any $\mathbf{x} \in \mathbf{S}$, if $f(\mathbf{x}^*) \leq f(\mathbf{x})$, then $\mathbf{x}^* \in \mathbf{S}$ is the global optimum solution.

The main operators of Maopt-aiNet include neighborhood clonal selection, neighborhood competition, self-confidence motivation, and neighborhood collaboration operator. According to the description for agent system [4] by Russel, we define matrix L as multi-agent grid[5]. One agent represents a possible solution to the objective function. Agent can be placed on the grid L ; $size(L) = L_{s1} \times L_{s2}$, where size means the dimension of L and each agent in a grid can sense the local environment.

Definition 1. The local environment of agent A_{mn} is

Loc. $A_{mn} = \{A_{m-,n}, A_{m,n-}, A_{m+,n}, A_{m,n+}\}$, of which

$$\begin{aligned} m_- &= \begin{cases} m-1, & m \neq 1 \\ L_{s1}, & m = 1 \end{cases}, n_- = \begin{cases} n-1, & n \neq 1 \\ L_{s2}, & n = 1 \end{cases}, \\ m_+ &= \begin{cases} m+1, & m \neq L_{s1} \\ 1, & m = L_{s1} \end{cases}, n_+ = \begin{cases} n+1, & n \neq L_{s2} \\ 1, & n = L_{s2} \end{cases} \end{aligned} \tag{2}$$

Each agent occupies one grid-point and interacts with its four adjacent agents in its local environment.

Definition 2. An agent $A_{mn} = (a_1, a_2, \dots, a_q) \in \mathbf{S}$ is an element in the search space \mathbf{S} .

The competitive edge of agent $C(A_{mn})$:

$$C(A_{mn}) = -f(A_{mn}) \tag{3}$$

Where f is the objective function to be optimized. In multi-agent grid, each agent exits with certain probability and competitiveness.

Definition 3. The matrix $\mathbf{B}_{L_{s1} \times L_{s2}}$ describes the status or confidence degree of multi-agent grid. Its element corresponds to the individual self-confidence in the grid. The

self-confidence for A_{mn} is $B(A_{mn})$, with a value $[0,1]$, of which “1” is corresponding to the maximum and “0” to the minimum.

2.2 The Steps of Maopt-AiNet

Suppose $A_{\max, mn}^c$ and $A_{\max, mn}^B$ are individuals with the most competitive edge and the largest self-confidence in neighborhood. Maopt-aiNet algorithm is described as follows:

(1) Initialization operation

The initialized immune agent grid system is $L(0)$. $size(L) = L_{s1} \times L_{s2}$. Initial antibody group A_0 generated randomly from S domain is placed in $L(0)$ by real number coding. l is the code length. The initial confidence degree with the threshold ζ is set randomly within $[0, 1]$. Open up the memory with a size of N_M , calculate the individual competitiveness $C(A_{mn})$, and select $A_{\max, mn}^c$ and $A_{\max, mn}^B$ in neighborhood, and set the current iteration number $T = 0$.

(2) Determine the search agent and development agent

According to the self-confidence $B(A_{mn})$ and the threshold ζ , picked out the search agents satisfying the condition $B(A_{mn}, T) > \zeta$ and development ones satisfying the condition $B(A_{mn}, T) \leq \zeta$.

(3) Perform neighborhood clonal selection operation

The neighborhood clonal selection of Maopt-aiNet is described as

$$A_{mn} \leftarrow T_s \circ T_m \circ T_c (A_{mn} \cup A_{\max, mn}^B) \quad (4)$$

Where T_c is clone operation: $A_{mn}' = I_{Kc} \cdot (A_{mn} \cup A_{\max, mn}^B)$, Kc is the cloning multiple. T_m is aberrance operation: $A_{mn}'' = m_{\Theta m} (A_{mn}')$, and $m_{\Theta m}$ is mutation operator. To balance the global and local search, Q-variation [6] and μ -variation [7] are used for search agent and the development agent at aberration rate P_m . T_s is selection operation: $A_{mn} = \max(A_{mn}'', A_{mn})$.

(4) Perform neighborhood competition

If $A_{mn} = (a_1, a_2, \dots, a_q)$ has more competitive edge than $A_{\max, mn}^c$ or more confidence degree than $A_{\max, mn}^B$, it can survive in the grid, or it will die and leave space for new individuals $\beta_{mn} = (b_1, b_2, \dots, b_q)$.

(5) Perform self-confidence motivation

Here we define the manipulations of the positive and negative feedbacks for self-confidence regulation. If A_{mn} has more competitive edge or confidence degree than A_{mn} , then the self-confidence of A_{mn} needs the positive feedback adjustment. While, if A_{mn} has less competitive edge or self-confidence than A_{mn} , then the self-confidence of A_{mn} needs the negative feedback adjustment.

(6) Perform neighborhood collaboration

The collaboration operator is:

a) Choose $A_{\max, mn}^B$, $A_{\min, mn}^B$ and $A_{\max, mn}^C$ to operate:

$$\hat{A}_{mn}^T = A_{\max, mn}^C + 0.5(A_{\max, mn}^B - A_{\min, mn}^B) \tag{5}$$

b) Cross distribution will be implicated into \hat{A}_{mn}^T and A_{mn}^T to

$$\text{get } \bar{A}_{mn}^T : \bar{A}_{mn}^T = \begin{cases} A_{mn}^T, & \text{if } r(0,1) > c_r, k=1,2,\dots,q \\ \hat{A}_{mn}^T, & \text{else} \end{cases}$$

Where $c_r \in [0, 1]$ is the crossover constant $\in [0,1]$.

c) \bar{A}_{mn}^T competes with A_{mn}^T , the winner will stay into the next generation.

(7) Take the most competitive individuals into memory, and let its self-confidence $B(A_{mn}) = \zeta$. If the results meet the termination conditions, then stop, or set $T = T + 1$ and go to step (2).

If searching algorithm reaches to the terminate conditions, stop the iteration and choose the best individual from the memory preserved during iterative process as the result of algorithm.

3 Benchmark Studies

3.1 Experimental Results

Six benchmark functions[8] were used in our experimental studies. They are given in Table 1. The initialization range and the dimensions of these 6 benchmarks are also listed in the table.

Table 1. Parameters setting for the benchmark functions

Test functions	x domain	dimension	optimum
<i>Schwefelha function</i> : $f_1(x) = \sum_{i=1}^n (-x_i \sin \sqrt{ x_i })$	[-500,500]	30	-12569.5
<i>Rastrigin function</i> : $f_2(x) = \sum_{i=1}^n (x_i^2 - 10 \cos(2\pi x_i) + 10)$	[-5.12, 5.12]	30	0
<i>Ackley function</i> : $f_3(x) = -20 \exp(-0.2 \sqrt{\frac{1}{n} \sum_{i=1}^n x_i^2}) - \exp(\frac{1}{n} \sum_{i=1}^n \cos(2\pi x_i)) + 20 + e$	[-32, 32]	30	0
<i>Schwefell function 1</i> : $f_4(x) = \sum_{i=1}^n x_i + \prod_{i=1}^n x_i $	[-10,10]	30	0
<i>Schwefell function 2</i> : $f_5(x) = \sum_{i=1}^n \left(\sum_{j=1}^i x_j \right)^2$	[-100,100]	30	0
<i>Schwefell function 3</i> : $f_6(x) = \max_i \{ x_i , 1 \leq i \leq n\}$	[-100,100]	30	0

In this section, the performance of Maopt-aiNet is studied with the use of the 6 benchmark problems, and the obtained results are compared with those of OGA/Q proposed by Leung [8], MAGA proposed by Zhong and Xue[5]. The stopping criterion of OGA/Q is that no elite solution is found in the latest 50 generations after the implementation of 1000 generations in reference [8]. And MAGA stops after running 150 generations in reference [5]. In order to maintain the consistency of parameters and make the comparison meaningful, the stopping criterion of Maopt-aiNet is running 150 generations. The parameters of Maopt-aiNet are $L_{s1} \times L_{s2} = 5 \times 5$, cloning coefficient $k_c = 5$, threshold $\zeta = 0.5$.

Table 2 lists the statistical results of 50 repeated experiments for these benchmark functions with OGA/Q [8], MAGA [5] and Maopt-aiNet. The results of OGA/Q and MAGA are picked from reference [8] and [5] respectively. In 6 benchmark functions, OGA/Q and MAGA can get the optimal solution 0 in 4 benchmark functions, while Maopt-aiNet in 5 functions. For f_1 and f_3 , Maopt-aiNet obtains better solutions than OGA/Q and MAGA do. And the average number of evaluations used in Maopt-aiNet is about 10 000, which is similar to that used in MAGA, meanwhile, about 18 000 for OGA/Q. Furthermore, the optimum deviation of Maopt-aiNet is lower than OGA/Q, while close to MAGA. This result suggests that Maopt-aiNet works better in high dimensional function optimization than OGA/Q and MAGA do.

Table 2. Performance comparison of four algorithms

Test function	Mean function value (standard deviation)			Mean number of function evaluations		
	OGA/Q	MAGA	Maopt - aiNet	OGA/Q	MAGA	Maopt - aiNet
f_1	-12569.4537 (6.447×10^{-4})	-12569.4866 (7.121×10^{-12})	-12569.4902 (4.019×10^{-12})	302 166	10 866	10 884
f_2	0 (0)	0 (0)	0 (0)	224 710	11 427	11 229
f_3	4.440×10^{-16} (3.989×10^{-17})	4.440×10^{-16} (0)	0 (0)	112 421	9 656	9 766
f_4	0 (0)	0 (0)	0 (0)	112 612	9 591	9 598
f_5	0 (0)	0 (0)	0 (0)	112 576	9 479	9 506
f_6	0 (0)	0 (0)	0 (0)	112 893	9 603	9 671

4 Application

In petrochemical field, the process simulation for distillation is an important task. The key parameter in the distillation process simulation is the tray efficiency, which can not be obtained easily. The tray efficiency can be defined as:

$$Eff_{i,j}^M = \frac{Y_{i,j} - Y_{i,j+1}}{K_{x,y} X_{i,j} - Y_{i,j+1}} \quad (6)$$

where Eff^M is murphree efficiency; K is equilibrium constant; X is the liquid phase mole fraction; Y is the vapor phase mole fraction; i is the component i ; j is the tray j .

Actually, the temperature distribution of the trays can characterize the separation efficiency of the distillation columns indirectly. Hence a model where the objective function [9] is the minimum of F is proposed.

$$F = \min \sum_i \left(\frac{T_i - \hat{T}_i}{T_i} \right)^2 \tag{7}$$

Where i is the tray number with a temperature measuring point; T is the tray temperature measured($^{\circ}C$); \hat{T} is the tray temperature calculated($^{\circ}C$).

Collect 100 groups of typical steady-state operation data as sample data. Then correct the distillation unit with 60 trays, and tray temperature test points are 10. Additionally, we also use (8) as the objective function, and determine the murphree efficiency using Maopt-aiNet. Figure 1. shows the fitting results of two options for the tray temperature distribution. Based on the determination of the tray murphree efficiency, the calculated temperatures are consistent with the measured, which suggests that the model describes the separation efficiency of the column very well. In Maopt-aiNet, the average absolute deviation between the calculated value and measured temperature is $0.6^{\circ}C$, the relative average deviation is 0.27, and the search time is about 3.55h. As the tray murphree efficiency has been determined, we establish the distillation unit model and predict the productions from the tower top and bottom. Table 3. displays the calculated values and measured values of main products under the steady-state operation. The average absolute error in evaluating the main products from tower top and bottom is 1.22kmol/hr and 1.318kmol/hr for Maopt-aiNet, while the relative average error is about 0.36% for Maopt-aiNet.

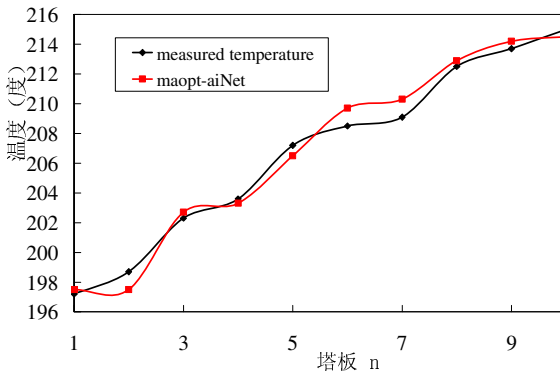


Fig. 1. Tray temperature comparison

Table 3. Tower products comparison

Distillation unit	Measured value	Maopt-aiNet	
	(kmol/hr)	(kmol/hr)	
	TOL	25.7	25.4
	PX	611.1	611.7
Product from tower top	MX	1393.8	1394.3
	OX	527.9	529.4
	EB	237.5	235.2
	NA	190.4	189.8
	PMET	48.6	47.1
Product from tower bottom	1,2,4-BZ	56.3	58.2
	1,3,5-BZ	21.2	20.9
	OET	15.1	13.7
	C9A	3.2	3.0

5 Conclusions

An multi-agent artificial immune network (Maopt-aiNet) algorithm is proposed in our study. Unlike other intelligent algorithms, Maopt-aiNet combines the idea of artificial immunization and multi-agent technology ingeniously. The operators of Maopt-aiNet include the neighborhood clonal selection, neighborhood competition, self-confidence motivation, and neighborhood collaboration operator. In benchmark function experiments, compared with OGA/Q and MAGA, Maopt-aiNet has stronger search capability for high-dimensional function optimization. In the application of distillation unit modeling, Maopt-aiNet can determine the murphree efficiency fairly well.

References

1. De Castro, L.N., Von Zuben, F.J.: Learning and optimization using the clonal selection principle. *IEEE Trans. on Evolutionary Computation* 6(3), 239–251 (2002)
2. De Castro, L.N., Timmis, J.: An artificial immune network for multimodal function optimization. In: *Proc. of IEEE Congress on Evolutionary Computation, Hawaii*, pp. 699–704 (2002)
3. Timmis, J., Edmonds, C.: A Comment on Opt-AiNET: An Immune Network Algorithm for Optimisation. In: Deb, K., et al. (eds.) *GECCO 2004*. LNCS, vol. 3102, pp. 308–317. Springer, Heidelberg (2004)
4. Russell, S., et al.: *Artificial Intelligence: A modern Approach*. Prentice-Hall, New York (1995)
5. Zhong, W., Xue, M., Liu, J.: Multi-agent genetic algorithm for high dimensional function optimization. *Progress in Natural Science* 15(10), 1078–1083 (2005)
6. Li, Z.-H., Zhang, Y.-N.: An enhanced artificial immune network with elitist-learning capability for optimization problems. *Control Theory & Application* 26(3), 283–290 (2009)

7. Trojanowski, K., Wierzchon, S.T.: Immune-based algorithms for dynamic optimization. *Information Sciences* 179, 1495–1515 (2009)
8. Leung, Y.W., et al.: An orthogonal genetic algorithm with quantization for global numerical optimization. *IEEE Transactions on Evolutionary Computation* 5(1), 41 (2001)
9. Yan, X., Yu, J., Li, F.: Simulation of atmospheric-vacuum distillation unit based on evolution algorithm. *Acta Petrolei Sinica* 22(1), 41–48 (2006)

A Novel Anti-collision Protocol Based on Binary Tree without Prior Information about RFID Tags*

Deng Zhongting, Wu Haifeng*, Wang Qian, and Shi Wenyu

School of Electrical and Information Technology, Yunnan University of Nationalities,
650500 Kunming, People's Republic of China
{seamild, wangqian19861124, kammy87920}@163.com,
whf5469@gmail.com

Abstract. In order to enhance radio frequency identification (RFID) tag identification efficiency, people proposes a anti-collision protocol in tree slot ALOHA. The new protocol adopts FKSS (Fast k-Slot Selection) algorithm and BFKSS (Binary Tree Fast k-Slot Selection) algorithm, the former which adjust the value of the slot's number, or the frame size in dynamic, through judging whether the first k-slots are all idle or all collision in each frame; and the later decompose the collision slot in binary basing on the former. The most advantage of the proposed protocol is no prior information about RFID tags. No matter how abrupt the tag number increase or reduce, the system can always keep the frame length and the number of tags at a reasonable level, thus can let the system efficiency not be affected by the changes tag number; and the advantages of binary decomposition is that it won't produce estimation error and reduces the computational complexity, meanwhile once again improve the system throughput. In our simulations, the proposed protocol's system efficiency reached at 0.43, BFKSS in the most optimal value is little higher than FKSS when to 0.432, and above the conventional dynamic frame slotted ALOHA and Q algorithm protocol, furthermore, compared with TSA, the system efficiency curve is above during the tag number is not close to the initial frame size.

Keywords: anti-collision, Tree Slotted Aloha, FKSS algorithm, system efficiency, Binary Tree, BFKSS algorithm.

1 Introduction

At present, RFID is a key technology for IoT(internet of things). Usually, RFID tag anti-collision protocol have combined the traditional multiple access anti-collision algorithm, and the most important things for EPC Gen2 RFID system is the anti-collision algorithm[1]. Presently, there are mainly two directions which based on the Slotted Aloha[3] and the Binary Tree[4] anti-collision algorithm respectively to solve

* This work is supported by Innovative Research Team in Yunan University of Nationalities, and the Scientific Research Foundation of Yunnan Provincial Department of Education (2010Y423).

* Corresponding author.

the tag collision problems. The type of Tree protocol divided the collision tags into two subsets, one for sending, the other for waiting, then decomposed repetitively until one tag were identified. The basic idea of the type of Aloha protocol is divided the tag recognition process into many information frames, and the frame is divided into many slots, in each information frame the unidentified tags randomly selected one slot and send information to the reader for identification. According to receiving tag information by the reader in one slot, it can be divided into the idle slot, the collision slot and the success slot, which respectively represent no tag information received, two above tag information received and only one tag information received. Among them, the dynamic frame slot Aloha (DFSA) protocol is being studied more. It is according to estimating the number of tags to dynamic adjustment the frame slot number. However, both of the pure tree type protocol and DFSA protocol, their max throughput were lower, and it cannot exceed 4.0. In order to enhance the system efficiency, someone combined the tree type protocol into the Aloha protocol, and proposed several higher throughput mixed protocol, Tree Slotted Aloha (TSA), Dynamic Tree Slotted Aloha (DyTSA), compared to the type of pure tree protocol, these mixed types of TSA protocol can let the system efficiency get the sharp rise, the highest can reach about 0.43. FKSS (Fast k-Slot Selection) protocol[7] which we proposed before shows that, no matter how abrupt the tag number increase or reduce, the system can always keep the frame length and the number of tags at a reasonable level, thus can let the system efficiency not be affected by the changes tag number.

However, one weakness of FKSS protocol is when tags are decomposed in a collision slot and based on the Q system, We need to know the number of success slot and the number of collision slot so that we can confirm the next length of frame, so we need to estimate the tag number before. But the disadvantages of estimating is increasing the computational complexity.

This work proposes a BFKSS (Binary Tree Fast k-Slot Selection) protocol based on FKSS protocol, if there is a collision slot, then decompose this slot on binary which instead of Q system. Although this protocol system efficiency is not much better than the FKSS algorithm, it can reduce the computational complexity obviously.

The paper is organized as follows. In Section 2, introduces the basic principle of FKSS protocol and point out the existing problems, In Section 3, proposes BFKSS algorithm, basic processes and pseudo-code. In Section 4, presents the simulation results, and finally Section 5 draws conclusions.

2 BFKSS Algorithm and Protocol

2.1 BFKSS Algorithm

The performance of any algorithm is optimized, when the probability of only one tag response in a slot (P_s) is maximized. Assuming that the number of tags is N and the frame size is L , the probability of multiple tag responses in a slot is P_c , the probability of no tag response in a slot is P_i , and P_s is the probability of one tag response in a slot, where

The probabilities of encountering a burst collision and a burst idle can be derived using a Markov chain model, which can be derived as in [5]. The probabilities in the Markov chain can be calculated using $A^{(j+1)}=TA^{(j)}$. Consequently, let k be the threshold of burst collision and burst idle in the first k slots respectively.

In Aloha protocol, the probability of a conflict slot is P_c , the probability of a idle slot is P_i , and the probability of a success slot is P_s . If we know the tag number N and the frame length L , then the probabilities can expressed as:

$$\begin{cases} P_i = \left(1 - \frac{1}{L}\right)^N \\ P_c = 1 - P_i - P_s \\ P_s = \frac{N}{L} \left(1 - \frac{1}{L}\right)^{N-1} \end{cases} \tag{1}$$

From (1) we know if the tag number N is far big than frame length L , then P_c will be big, by contrast, if frame length L is far big than tag number N , then P_i will be big. If we just think about first few slots in front of the frame, we can import Markov algorithm.

$$B^{(j+1)} = TB^{(j)} \tag{2}$$

Among them, $B^{(j)}$ is j slot probability vector, determined by

$$B^{(j)} = [B_{c1}^{(j)} \dots B_{ck}^{(j)} B_s^{(j)} B_{i1}^{(j)} \dots B_{ik}^{(j)}] \tag{3}$$

Then the first slot probability vector can be determined by

$$B^{(1)} = [P_c \ 0 \ \dots \ 0 \ P_s \ P_i \ 0 \ \dots \ 0] \tag{4}$$

The transfer matrix $T=(t_{ij})$ can be determined by

$$T = \begin{pmatrix} 0 & P_c & 0 & \dots & 0 & P_s & P_i & 0 & \dots & 0 \\ 0 & 0 & P_c & \dots & \vdots & & & & & \\ \vdots & & & \ddots & & \vdots & \vdots & & & \vdots \\ 0 & & & & P_c & & & & & \\ 0 & 0 & \dots & 0 & 0 & P_s & P_i & 0 & \dots & 0 \\ P_c & 0 & \dots & 0 & P_s & P_i & & & & \\ \vdots & & & & \vdots & & & \ddots & \vdots & \\ P_c & & & & & & & & & P_i \\ P_c & 0 & \dots & 0 & P_s & 0 & \dots & 0 & & 0 \end{pmatrix} \tag{5}$$

If $i=1, k+1 \leq j \leq 2k+1$ and $2 \leq i \leq k$ and $j=i-1$, then $t_{ij}=p_c$; if $i=k+1, 1 \leq j \leq 2k+1$ and $t_{ij}=p_s$; else $i=k+2, 1 \leq j \leq k+1$ and $k+3 \leq i \leq 2k+1, j=i-1, t_{ij}=p_i$

From (5), we can get the first k slot state probability. Table.1 shows when $L_0=128, N$ from 100 to 500, P_{c1}, P_{c2}, P_{c3} and P_{i1}, P_{i2}, P_{i3} . And we can find that if $L_0=128$, when tag number increasing, P_{c_j} growth, P_{ij} drop; when tag number decreasing, P_{c_j} drop, P_{ij} growth; and $i=1, 2, 3$.

Table 1. The status probability of first K-slot

Tag Number	P_{c1}	P_{c2}	P_{c3}	P_{i1}	P_{i2}	P_{i3}
100	0.18	0.03	0.01	0.46	0.21	0.10
200	0.46	0.21	0.10	0.21	0.04	0.01
300	0.68	0.46	0.31	0.10	0.01	0
400	0.82	0.67	0.55	0.04	0	0
500	0.90	0.81	0.73	0.02	0	0

then we set k as the continuous time buttress threshold, C_c express the number of first few slots are all collision slots, when $C_i=k$, the next frame length is half of the initial value; C_i means the number of first few slots are all idle slots, when $C_s=k$, the next frame length has doubled the initial one.

$$\begin{cases} L_0 = 2L_0, C_c = k \\ L_0 = L_0/2, C_i = k \end{cases} \tag{6}$$

2.2 BFKSS Protocol

This section will give the BFKSS protocol which realized by BFKSS algorithm, Fig.1 and Fig. 2 are given out the reader operation pseudo-code and the tag operation pseudo-code of BFKSS protocol respectively. When reader start reading tags, the value of initial frame length is L_0 , and then reader send a query command with frame length L called AdjQuery. After each tag received orders, the counter S will choose a random number from 0 to $L-1$, this tag will send its ID at the S slot. Reader detects the tag response at the first k -slots in the frame. If the first k -slot are all collision, then $L=\max(2L, 2^{15})$, reader ends this frame in advance, send an AdjQuery with a new L , and detects the next frame tags response. And if the first slot is success, then L changeless, at this time, the algorithm will turn into FKSS protocol. The frame length of i layer is 2.

BFKSS protocol: reader operation

```

1   $L = L_0$ 
2  BFKSS( $L, k$ )

function BFKSS( $L$ )
3  Broadcast AdjQuery with  $L$ 
4  Receive tag responses in the first  $k$  slots and detect collision
5  if  $k$  slots are all collision
6     $L = \min(2L, 2^{15})$ 
7    FFKSS( $L$ )
8  elseif  $k$  slots are all idle
9     $Q = \text{round}(L/2)$ 
10   FFKSS( $L$ )
11  elseif only a tag response
12     $level = 0$ 
13     $s = -1$ 
14    TSA( $L, level, s$ )
15  end

function TSA( $L_i, level, s$ )
16  broadcast Query with ( $L_i, level, s$ )
17  for  $s = 1$  to  $L_i$  do receiveIDs
18     $L_{i+1} = 2$ 
19  for  $s = 1$  to  $L_i$  do
20    if (collision[ $s$ ] = 1)
21      identify tag and sendAck;
22    elseif (collision[ $s$ ] > 1)
23       $level++$ ;
24      TSA( $L_{i+1}, level, s$ )
25    end
26  end

```

Fig. 1. Pseudocode of BFKSS protocol: reader procedure**BFKSS protocol: tag operation**

```

1  while receive Reader's AdjQuery with  $L$ 
2    do {  $s$  = random number form 0 to  $L - 1$ 
3      send myID in slot  $s$ 
4    } end
5  }
6
7  if receive Reader's Query with  $L$ 
8     $identified = \text{false}$ 
9     $myLevel = 0$ 
10    $previousValue = -1$ 
11   while (not  $identified$ )
12     do {
13       Receive Query with ( $L_i, level, slot$ )
14       if (( $level = myLevel$ ) & ( $previousValue = slot$ ))
15          $s = \text{random number form 0 to } L_i - 1$ 
16          $myLevel++$ ;
17          $previousValue = s$ 
18         send myID in slot  $s$ 
19         if (receivedAck)  $identified = \text{true}$  end
20       } end
21   }

```

Fig. 2. Pseudocode of BFKSS protocol: tag procedure

3 Simulation Results

The following is simulation results, and computational processes are all adopt the monte carlo method, we obtained the average results after completing 500 experiments.

Fig.3 illustrates system efficiency of the different algorithms. We set the initial frame length $L_0=128$, N from 10 to 500. As we can see, Q algorithm throughput is lowest, the highest just reached 0.34 around, relatively DFSA protocol efficiency is also lower, the biggest throughput cannot be exceed 0.40. Compared with Q algorithm and DFSA protocol, the system efficiency of mixed type of protocol such as Tree Slotted Aloha(TSA), dynamic Tree Slotted Aloha(DyTSA) have got vastly improved and the highest can reach about 0.43. But, in TSA protocol, the system efficiency achieve maximum only when the initial frame length equals to the tags number, and when the initial frame length more or less than the tag number, the system efficiency have dropped seriously from peak 0.43 to 0.38. And the maximum of FKSS protocol which we proposed is 0.43, the same as DyTSA protocol, but no matter tag number increases or decreases, the system efficiency will not get significant reduction, and will remain above 0.40, higher than TSA protocol, at the same time, the throughput curve also higher than Q algorithm and DFSA protocol. BFKSS experiences little better than FKSS when it at the optimal value. But others are little worse. Totally, the value is alike between them.

So we can use BFKSS instead of FKSS, because it dose not make the calculation that complicated. Due to using 2 instead of Q when the next frame decomposing, it has dramatically decreased the computational complexity.

Fig.4 illustrates the system efficiency of BFKSS in different initial frame length, $L_0=2^Q$, $Q=2, 3, \dots, 8$, N from 1 to 500. We can see according to the different initial frame length, BFKSS algorithm can still make the system efficiency stay above 0.40 after it reached the peak.

Fig.5 illustrates the system efficiency of BFKSS in different threshold, $L_0=128$, N from 50 to 500. We can see when threshold $b_s=2$, the system efficiency achieve the optimal value, that is to say, we can use the 2 slot's status as the standard to measure that whether the tag number is more or less to the frame.

4 Analysis of the Simulation Results

In this paper, we investigated the tag identification problem in RFID systems. The slot-count algorithm as a framed slotted ALOHA algorithm satisfies the complexity constraint of Gen2 passive tags. It has been proved as a simple and efficient anti-collision method for the low cost power-constricted tags. However, the value of the initial L is important to the performance of an inventory process. The BFKSS algorithm illustrates a novel L selection method, which requires lower computational complexity than the FKSS algorithm.

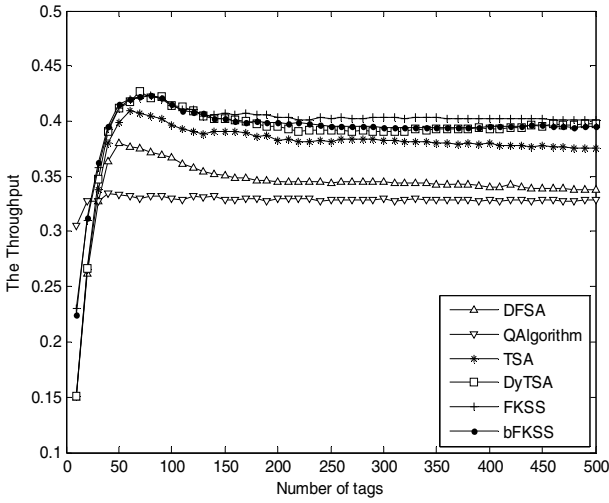


Fig. 3. The system efficiency of various algorithm

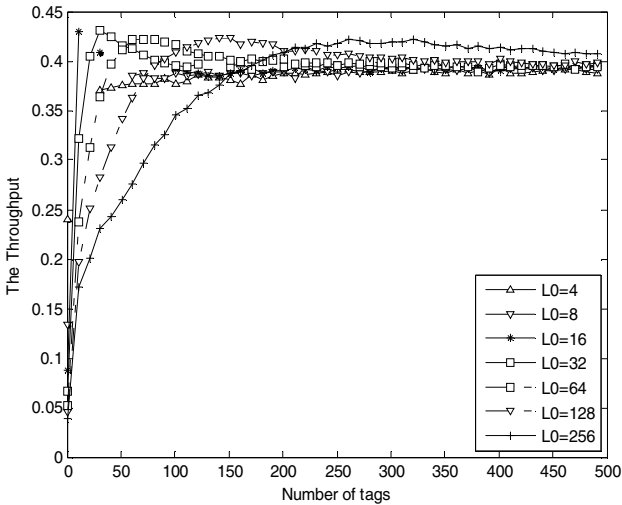


Fig. 4. The system efficiency of BFKSS in different initial frame length

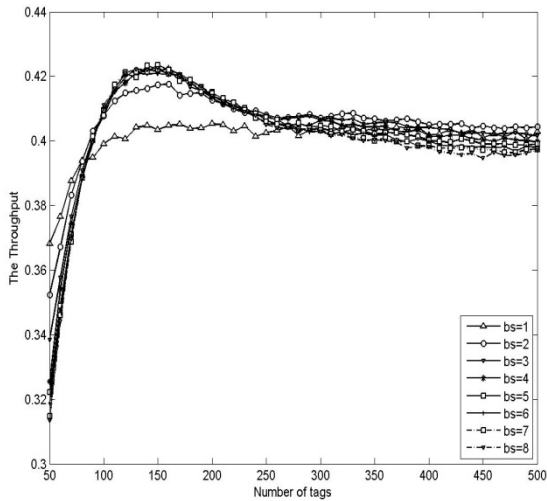


Fig. 5. The system efficiency of BFKSS in different threshold

References

1. Cha, J.R., Kim, J.H.: Novel anti-collision algorithms for fast object identification in RFID system. In: Proceedings of the 11th International Conference on Parallel and Distributed System, pp. 63–67. IEEE, Washington D.C (2005)
2. Vgot, H.: Mutiple object identification with passive RFID tags. In: Proceeds of IEEE International Conference on System, Man and Cybernetics, pp. 1–6. IEEE, Hammamet (2002)
3. EPC Radio-Frequency Identity Protocols Class-I Generation-2 UHF RFID Protocol for Communications at 860Mhz-960Mhz version 1.0.9 (2004)
4. Hush, D.R., Wood, C.: Analysis of tree algorithm for RFID abitration. In: Proceeds of IEEE International Symposium on Information Theory, vol. 107, IEEE, Cambridge (1998)
5. Wang, L.-C., Liu, H.-C.: A Novel Anti-Collision Algorithm for EPC Gen2 RFID Systems. In: Proceeds of IEEE International Conference on System, Man and Cybernetics, pp. 6–7. IEEE, Hammamet (2006)
6. Wu, H., Zeng, Y.: Bayesian Tag Estimate and Optimal Frame Length for Anti-Collision Aloha RFID System. IEEE Transactions on Automation Science and Engineering, (99): 1 (2010)
7. Deng, Z., Wu, H., Tan, Y., Liu, J.: Novel Anti-collision Protocol in Tree Slot Aloha without Prior Information about RFID Tags. In: Proceeds of IEEE International Conference on System, Industrial Engineering and Application, vol. 7, IEEE, ShenZhen (2010)

Application of Visual Attention in Object Search for a Mobile Robot with an Omni-directional Vision System

Dongyi Lin and Bingwei He

School of Mechanical Engineering, Fuzhou University,
Fuzhou 350108, P.R. China
mebwhe@fzu.edu.cn

Abstract. A visual attention method for object search for a mobile robot with an Omni-directional vision system is presented. Firstly, the explored scene is separated into salient and non-salient regions in the image and some salient objects in above salient regions are detected with a kind of saliency detection method. And then, SIFT feature points of the salient objects are extracted. The 3D coordinates of the object feature points, which are used to represent the spatial positions of the objects, are computed from the Omni-directional 3D reconstruction method. At last, the first searching region is determined by synthetically considering some factors, such as the number of detected objects in each region and the distance between the objects and the mobile robot. To validate the effectiveness of the proposed method, the experiment is performed in a realistic indoor scenario.

Keywords: Object Search, Visual Attention, Omni-directional Vision System, Mobile Robot.

1 Introduction

The aging of population and the improvement of living level in modern society have brought wide application prospects for indoor service robotics. The future applications have more requirements for such autonomous agents: they not only need to be able to navigate in the environment and communicate with humans, but also need to have the ability of performing some challenging tasks, such as scene recognition, object finding and fetching et al. As object search is a common behavior we often perform in our daily life, it is now an important research area in the robot vision field as well. For example, the well-known “semantic robot vision challenge” [1] and the “robocup@home” [2] competition are two famous competition that refer to robot object search problem.

In recent literatures, many search methods include two processes: the attention process (i.e. object detection process) and the observation planning process. For example, Saidi et al. [3] presented a visual attention framework for the search behavior of a 3D object by a humanoid robot. They utilized a binocular vision system with pan-tilt capability to explore the environment. A visibility map was constructed to guide the attention of the robot to candidate stacks, and the next best view position was determined by a rating function, which considered target detection probability, new information gain, and motion cost. While their method had shown an efficient search

result, the attention process by constructing visibility map is still computationally expensive. Masuzawa et al. [4] developed an observation planning method for environment semantic map construction. The process included two stages: Firstly, the robot explored unknown regions with a laser range finder; then it used a stereo camera to detect object candidates with color information, and planned an optimum observation path to validate them. The detection approach they used was based on color histogram intersection, which is a kind of top-down (or mode-driven) attention process and the detection result may be affected by changes in lighting condition. Foreseen et al. [5] designed a mobile platform called Curious George, which is equipped with a peripheral-foveal vision system. When the robot navigated through the room, it used its peripheral cameras to get low-resolution images and utilized an attention method combining bottom-up saliency information and top-down stereo disparity information to detect interesting image regions, which may correspond to potential objects. These regions were later focused on by the foveal camera to obtain images, which were sharp enough to perform a reliable recognition. Their detection method is computation-ally efficient, and has lower requirement for lighting condition.

Most mobile agents proposed in previous literatures utilize conventional vision sensors (such as monocular vision, binocular vision et al.) to explore the environment and detect/recognize objects. However, such sensors usually have a limited field of view. To acquire entire environment information, a pan-tilt unit is used to change the vision system's viewing direction, which brings about extensive image processing and high computing cost. In contrast, the Omni-directional vision system has a horizontal 360° field of view, and is capable of gaining abundant and complete information rapidly in indoor environments. And because of the unique advantages, Omni-directional vision systems have now been widely used in many mobile robot tasks, such as the soccer robots [6], navigation [7], environment reconstruction [8] and object tracking [9] et al.

In this paper, we attempt to introduce visual attention to object search problem in indoor environments for a mobile robot equipped with Omni-directional vision system. As the imagery of objects in the Omni-directional image is distorted and small, and the lighting condition is uncertain, the visual attention mechanism used is a bottom-up fashion, which mainly detects sharp change of color or intensity information in the image without any prior information of target objects as proposed in [10].

We divide the search process into the attention stage and the observation stage as previous literatures done. And the main idea of this article include (i) separating the scenario into different search regions and detecting potential objects in the image with visual attention mechanism, (ii) estimating the spatial positions of the potential objects based on an Omni-directional localization method, (iii) choosing a first search region for the robot to observe in the next stage by synthetically considering two factors—the number of potential objects in a search region and the region distance (i.e. the distance from the region to the mobile robot).

2 The Object Detection Method Based on Visual Attention

The visual attention mechanism we used is based on a spectrum residual model proposed by Hou et al. [10], the method is computational efficient, and we introduce the principle briefly as follows. Given a natural image as illustrated in Fig. 1-(a), we

can obtain its amplitude spectrum $A(f)$ and phase spectrum $P(f)$ by Fourier transformation, then the log spectrum (see Fig. 1-(b)) can be computed by $L(f) = \log(A(f))$. Fig. 1-(c) illustrates the frequency-orientation averaged log spectrum curve, which shows a local linearity.

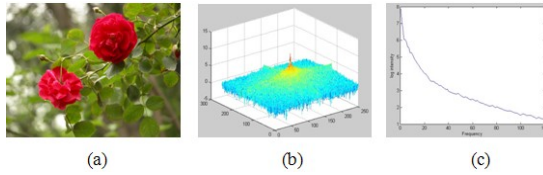


Fig. 1. An example of image and its log spectrum: (a) Input image; (b) Log spectrum; (c) The orientation averaged curve of log spectra

It was analyzed that the local sharp changes in the log spectra curve correspond to anomalous regions in the image, which may be interesting objects.

After the log spectrum $L(f)$ is computed, the averaged spectrum $S(f)$ can be obtained by smoothing $L(f)$ with a local average filter. $L(f)$ and $S(f)$ are subtracted to get the spectral residual $R(f)$, which is used in conjunction with phase to compute inverse Fourier transform and get the saliency map. To improve the detection accuracy, we extend this approach to intensity channel, red-green channel, and yellow-blue channel, as done in [11].

Saliency maps of the three channels are finally combined linearly to obtain the final saliency map at last, as shown in Fig. 2-(a) and Fig. 2-(b).

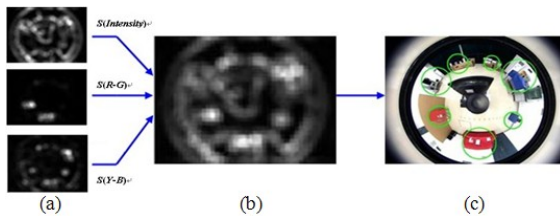


Fig. 2. Detection results of large objects: (a) Saliency maps of three color channels; (b) Final saliency map; (c) Region extraction result

2.1 Two-Stage Saliency Detection

A vision system works under certain scales as Hou et al. [10] said, and they had shown different saliency detection results under different image scales in their experiment. The results demonstrate that when the visual attention mechanism is performed under a large scale (i.e. the image is small), detailed features are omitted. In contrast, under a small scale, many small sharp change regions will be detected in the image instead. As the imagery of an object in the Omni-directional image is small and the image information is abundant, and it has shown bad results to perform visual attention directly under a small scale in our experiment, we present a two-stage saliency detection here: First, detect large salient objects in the image under a large scale as

shown in Fig. 2-(c); Second, set windows upon previous detected regions, and detect small potential objects under a fine scale as shown in Fig. 3.

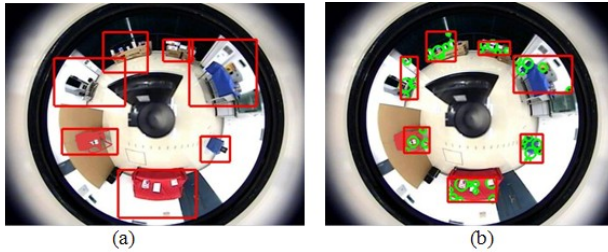


Fig. 3. An example of image and its log spectrum: (a) Input image; (b) Log spectrum; (c) The orientation averaged curve of log spectra

The detection of large objects can help separate the whole image search region into several regions that containing different number of potential objects and eliminate the invalid image part that belongs to the background. A window that is set upon previous detected large objects has a size decided by the corresponding area magnitude in the saliency map. The final detection results of small objects are shown in Fig. 3-(b), and we can see that most potential objects are detected in spite of some error detections.

2.2 Eliminating Parts of the Error Detection Results

As it is said in previous contents, the visual attention mechanism we used mainly detects regions that have sharp changes of color or intensity in the image, and many details will be detected when it is used under a small scale. As a result, we can see in Fig. 3-(b) that there are some error detection results, which are actually borders between the objects and the background (e.g. the border between the red sofa and the white wall et al.). Here we propose a method based on region growing segment to eliminate parts of the error detection results. The method mainly considers the color similarity between the seed region. And the main steps are as follows:

- For a saliency detection result, set a window (the size is 50×50 pixels here) whose centre is in accordance with the centroid of the salient region in the Omni-directional image as shown in Fig. 4-(a), and then get the sub-image out as shown in Fig. 4-(b).
- Choose the most salient point as the seed point as the red asterisk shows.
- Translate the color space into HSV space and implement region grow algorithm by computing the similarity between the current pixel and the seed point. Two examples of the segment results are shown in Fig. 4-(c).
- Compute the ratio of the area of the segmented region (red region in Fig. 4-(c)) and the area of the salient region (region inside the red circle in Fig. 4-(b)), if the value is above the threshold, the error detection will be find and eliminated.

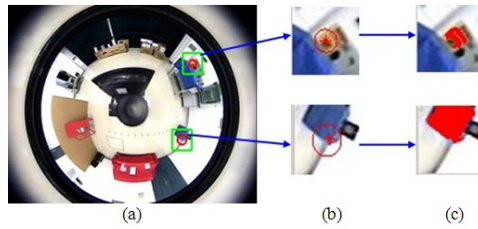


Fig. 4. Examples of error detection elimination: (a) Windows set upon saliency detection results; (b) Seed points chosen in the salient regions; (c) Segment result



Fig. 5. Final detection result

The final processing result is demonstrated in Fig. 5, which shows that the proposed method can eliminate most of the error detections.

3 Spatial Localization of the Potential Objects

The use of attention mechanism enables the robot to judge that if there are objects in the environment and in which direction are them. However, it still doesn't have knowledge of the distance between a detected object and it. Generally it is better for the robot to move close to an object to recognize it more reliably. As the scene is separated into several search regions, it is necessary to estimate the distance from each search region to the robot so that it can learn which region is closer and determine where to move.

In this section, an approach for localization of potential objects is presented. We use the 3D coordinates of SIFT feature points extracted the potential objects in the image to re-present their spatial positions. The construction of the coordinates is based on the Omni-directional 3D reconstruction method presented in [12]. The main steps are:

- The robot gets two Omni-directional images at two different positions at the beginning and then uses visual attention algorithm to detect the salient potential objects in both images. The detected results represented with green circles can be seen in Fig. 6.
- Extract SIFT feature points in both images and only match the part that belong to potential objects.
- Calculate the essential matrix use a method of RANSAC and estimate camera motion parameters, compute 3D coordinate by geometrical triangulation.
- Use the average coordinate of features that belong to the same object to represent its spatial position

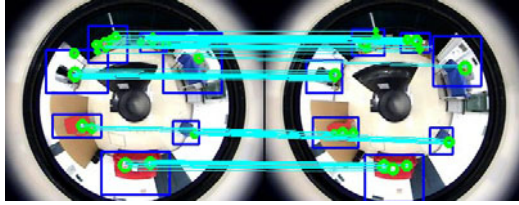


Fig. 6. SIFT matching result in salient regions (green circles) of two images

The localization result can be seen intuitively in Fig. 7 with specific explain in the experiment section. The visual attention is implemented in both images for the reason that if a potential object is not detected in one image, it can be detected complementally in another image (e.g. the book on the sofa in Fig. 6).

4 Search Rule for Choosing a First Search Region

In this section, we introduce a search rule for the robot to choose the first search region due to the different probability of target presence in different search regions. As no prior knowledge (such as color, shape et al.) of the target is given in the detection stage, regions that have more potential objects generally have higher possibility of target presence. Another factor that should be considered is the motion cost for the reason of saving motion energy. From the above, the search rule proposed mainly give search priority to regions which have more potential objects or are closer to the mobile robot. The mathematical description is as follows.

In the absence of prior knowledge, all detected potential objects have the same probability to be the target wanted. The probability value is $1/N$, where N is the total number of detected objects. Then the probability of target presence of a search region depends on the number of potential objects in it, the value is the sum of each object's probability

$$P_i = \sum_{j=1}^k P_j, \quad (1)$$

where P_i represents the probability of the each region, and K is the number of potential objects in that region.

Considering the distance from a search region to the robot, a utility function is given to obtain the utility value of that search region:

$$U_i = P_i / dist_i, \quad (2)$$

where U_i is the utility value of each region, and $dist_i$ is the distance between the region and the robot, which is obtained by computing the average distance from each potential object to the robot in that region. The region with highest utility value should be observed firstly.

5 Experimental Results

The platform we used in the experiment is the Grandar AS-R mobile robot, which is equipped with an Omni-directional vision system on top of it. The Omni-directional vision system consists of a CCD camera and a hyperboloid mirror, which can acquire an image sequence with an image size of 640×480 pixels.

The localization result of the potential objects is shown in Fig. 7. The pink cubes represent the potential objects, while the transparent cubes with labels are the search regions of the scene. The pink cubes approximately demonstrate the spatial positions of the potential objects.

To test the effectiveness of the search rule presented in last section, a table is presented here giving related data of each region. For example, the number of potential objects, distance, and the utility value. Then we analyze as follows:

- Comparing to region 1, 3, 4, 7, region 2, 5, 6 have more detected potential objects, so they have higher possibility of target presence and should be considered firstly;
- Region 2 has fewer objects than region 5, 6, but it is far more near the mobile robot, so the motion cost is smaller.

Table 1. Related data of each region

Region	Number of objects	The distance(m)	The utility value
1	2	1.7373	0.059241
2	3	1.5027	0.092496
3	1	2.2511	0.026639
4	1	2.2969	0.022896
5	4	3.6948	0.065123
6	6	4.4222	0.080392
7	1	4.4087	0.012936

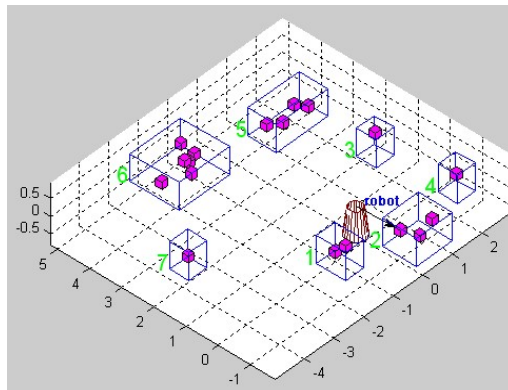


Fig. 7. The localization result and planning result

As a result, region 2 has the highest utility value and should be chosen first to search. The arrow in Fig. 7 show the choose result which comply with the search rule well.

6 Conclusions

This article presents a solution for object search problem in a realistic environment for a mobile robot equipped with an Omni-directional camera. In the perception stage, a spectrum residual based visual attention mechanism is used to separate the scene into different regions and detect potential objects. Then SIFT features of potential objects are extracted and the Omni-directional 3D reconstruction method is employed to estimate the spatial positions of them. The experimental results indicate that the proposed method is efficient and reliable.

References

1. The semantic robot vision challenge, <http://www.semantic-robot-vision-challenge.org/>
2. Website, <http://www.robocupathome.org/>
3. Saidi, F., Stasse, O., Yokoi, K., Kanehiro, F.: Online Object Search with a Humanoid Robot. In: The 2007 IEEE/RSJ International Conference on Intelligent Robots and Systems, pp. 1677–1682. IEEE Press, New York (2007)
4. Masuzawa, H., Miura, J.: Observation Planning for Efficient Environment Information Summarization. In: The 2009 IEEE/RSJ International Conference on Intelligent Robots and Systems, pp. 5794–5800. IEEE Computer Society Press, St. Louis (2009)
5. Forssen, P., Meger, D., Lai, K., Helmer, S., Little, J., Lowe, D.: Informed Visual Search: Combining Attention and Object Recognition. In: 2008 IEEE International Conference on Robotics and Automation, pp. 935–942. IEEE Press, New York (2008)
6. Lima, P., Bonarini, A., et al.: Omni-directional Catadioptric Vision for Soccer Robots. *Robotics and Autonomous Systems*. *J. Robot. Autonomous Syst.* 36, 87–102 (2001)
7. Koyasu, H., Miura, J., Shirai, Y.: Mobile Robot Navigation in Dynamic Environments Using Omnidirectional Stereo. In: 2003 IEEE International Conference on Robotics and Automation, pp. 893–898. IEEE Press, New York (2008)
8. Ranschotem, R., Krose, B.: Robust Scene Reconstruction From an Omnidirectional Vision System. *IEEE Trans. Rob. Autom.* 19, 351–357 (2003)
9. Ortegon-Aguilar, J., Bayro-Corrochano, E.: Omnidirectional Vision Tracking with Particle Filter. In: 18th International Conference on Pattern Recognition, pp. 1115–1118. IEEE Press, Piscataway (2006)
10. Hou, X., Zhang, L.: Saliency detection: A Spectral Residual Approach. In: The IEEE Conference on Computer Vision and Pattern Recognition, pp. 1–8. Inst. of Elec. and Elec. Eng. Computer Society Press, Piscataway (2007)
11. Choi, C., Christensen, H.I.: Cognitive Vision for Efficient Scene Processing and Object Categorization in Highly Cluttered Environments. In: 2009 IEEE/RSJ International Conference on Intelligent Robots and Systems, pp. 4267–4274. IEEE Computer Society Press, Piscataway (2009)
12. Svoboda, T., Pajdla, T.: Epipolar Geometry for Central Catadioptric Cameras. *International Journal of Computer Vision* 49, 23–37 (2002)

Monitoring System Design of Suspension Bridge of Health Status Based on CAN-BUS

Yang Yu, Ming-ye He, and Ying-ji Hao

School of Mechanical Engineering, Xi'an University of Science and Technology,
Xi'an, Shannxi, China, 710054

yuy@xust.edu.cn, myhe922@hotmail.com

Abstract. The article introduces a data acquisition system of multi-channel suspension bridge vibration acceleration with the core of STC12C5606AD single chip. The system used CAN Bus to accomplish the communication between the front extension and IPC. The IPC could quickly get up to 42 channels acceleration value of mean-square deviation in a second and the real time oscillogram from the partial channels after the front machine had the statistical process. The article also analyses problems in the process of system design such as A/D data acquisition rate, transport protocol, and establishing database more than 10 G bytes storage.

Keywords: Suspension Bridge, STC12C5616AD, Acceleration, CAN Bus.

1 Introduction

After bridge is built and put into use, the strength and stiffness of the bridge structure will decrease with the growing use, due to the impacts of various factors like climate, corrosion and under the long-term effect of the static load and live load. This will not only affect traffic safety, but will also shorten the life of the bridge, especially a bridge as a vital line [1]. Meanwhile many bridges gradually enter the maintenance stage. Through testing stress the key section of the bridge, analyzing and evaluating the safety and reliability of the structure, timely discovering problems, it can not only extend the use of the bridge life span, but also provide a reasonable decision for the safe operation of maintenance and reinforcement of the bridge structure.

2 System Solution Design

The system task is to monitor the bridge's health status of the dam Guantou in Gansu Province. The bridge is 213 meters long, and the main span is 180 meters. The whole system mainly monitored the shift, strain, temperature, fiber grating, acceleration, wind speed & direction and other multi-target factors in a distribution placement. The paper's design of the monitoring system was mainly for acceleration factors, wind speed & direction factors. Sensors distribution is shown in Figure 1.

As we can see in Figure 1, the full-bridge totally used fourteen sensors of three-axis piezoelectric accelerometers, seven acceleration signal conditioners, one wind

speed sensor and one wind direction sensor which installed in 140 meters of the bridge, seven acceleration acquisition cards with the frequency range from dozens of Hz to hundreds of MHz.

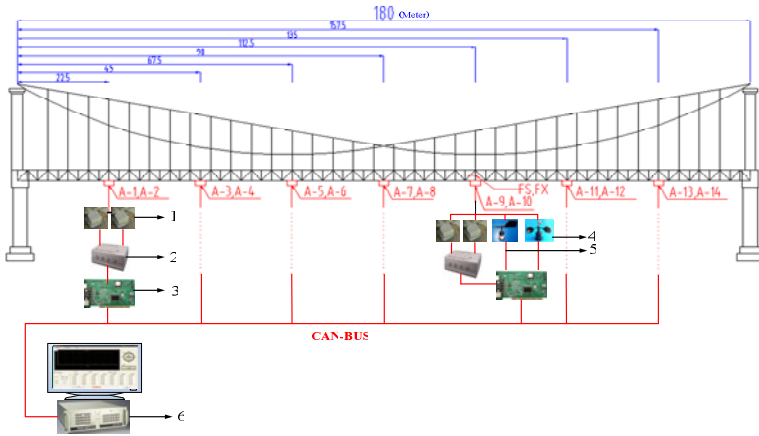


Fig. 1. Schematic diagram of monitoring system, 1- accelerometers, 2- Signal Conditioner, 3- Data Acquisition Card, 4- wind speed sensor, 5- wind direction sensor, 6- IPC.

3 System Principles and Design

3.1 Monitoring System Components and Hardware Description

In figure 2, it shows the constitution of this system and the consequence of signals transmission. Each sensor will be introduced separately as follows:

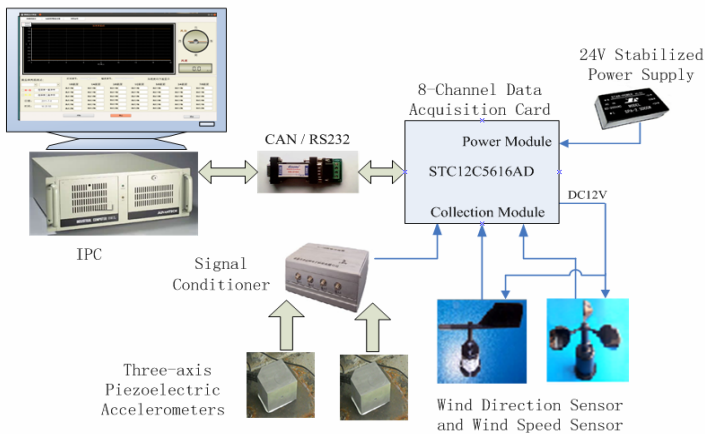


Fig. 2. Signal transmit sequences

3.1.1 Acceleration Sensor and Wind Speed and Direction Sensor

The three-axis sensors for collecting acceleration data mainly used low-frequency small-g measurement [2]. The sensitivity could be up to 1800 mv/g, and ranges from -2g to +2g corresponding to ±5V voltage. Besides, the frequency scope ranges from 0.2 to 600Hz. All parameters had fully met requirements of the design measurement. Meanwhile the sensor linearity is less than 1%, the transverse sensitivity is less than 5%, properly working in the certain temperature ranges from -40°C to +120°C. The wind speed and direction sensors, in this design system, we used 12 DC to supply the voltage. The measurement of speed sensor is from 0~45 m/s, and it could recognize a signal minimum 0.1m/s. The measurement of direction sensor range is 0~360°, and it could recognize a signal minimum 1°[3].

3.1.2 Signal Acquisition Circuit

The input signal range is ±5V, corresponding to the ±2g acceleration signals, so we used military-grade operational amplifier OP-07 formed this acquisition circuit and the chip has some advantages such as a wide voltage input, low offset voltage, high stability and so on.

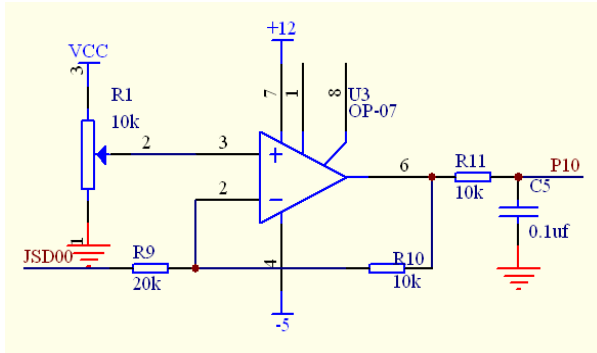


Fig. 3. Schematic capture signal

In figure 3, the acquisition circuit is as the subtraction circuit, U3 for a raising voltage. JSD00 (from 00 ~ 05 6 channels) is one of the 6 channels input signal, which ranges from -5V to +5V. So the raise voltage here is up to 2.5V. At this time if the input signal is -5V, the corresponding signal collected from Pin1.0 is 5V. If input signal is 5V, the corresponding signal from Pin1.0 is 0V. We can clearly see these linear relationships between the input signal and the acquired signal in Pin1.0 shown in figure 5. The voltage of Pin1.0 is calculated with equation (1) and it as follows:

$$U_{P1.0} = U_3 - U_2 * R10/R9 \quad (R10 = 9.1K\Omega, R9 = 20K\Omega) \quad (1)$$

3.1.3 CAN Communication Schematic

CAN is an abbreviation of Controller Area Network (hereinafter referred to as CAN), and the serial communication protocols have met ISO international standard. In this design, we used the software function to replace CAN controllers like SJA1000CAN

and resolved self-transmitting and self-receiving, multi-machine communication and other issues. By means of removing received bits which produced by the receiver sending bits and reasonable delay time to resolve the multi-machine communication. In this field, CAN-Bus consisted of two strands of twisted-pair cables which reduce electromagnetic interference and improve communication stability [4].

3.2 CAN-Communication Design

The instruction format of CAN communication protocol is shown as follows:

Table 1. IPC send the command

	First Bite	Second Bite	Third Bite	Remarks
Send	0xFE	0xFA	Board Number (0x05-0x65)	Called in a certain order

Table 2. Single-chip returns data

	Bites	Content	Remarks
Back	211bites	6-channel A/D values(198 bytes), standard deviation (7 bytes) , wind speed and direction values (6 bytes) totally equal 211 bytes (including the parity bit)	The high byte in front of the low byte

3.3 Data Storage and Data Replay

The software system was developed by C++ builder 6, and it can be divided into five parts, including the waveform selection interface, the waveform display interface, the wind speed & direction display interface, and the waveform playback interface. The waveform interface could display any two of 42 channels real-time waveforms at the same time. And the system used ADO databases to realize the function of saving 42 channels data and querying the saved data [5] by connecting Microsoft's ACCESS databases. In order to store massive data, the software used year and month as the file name, saved the 42 channel data per month, each profile include 14 separate databases, which could form up to 10G-byte database. The capacity of database only depended on the capacity of hard drive. The measured amount of data size after the optimized in one week was about 56MB.

4 Software Flowchart

Working process of control system in Single-chip is shown in figure 4. The main task was to cycling compute the eight channels A/D values and the six channels of variance values. Before each convert processing, the process would check the flag of serial port to determine whether it received the IPC commend. When the process

detected the serial port had received any command, it would produce one breaking point. If the command was called for exactly the right acquisition card, this card would return 211 bytes data to IPC, and if it was not called for the right card, then the process would back to the breaking point.

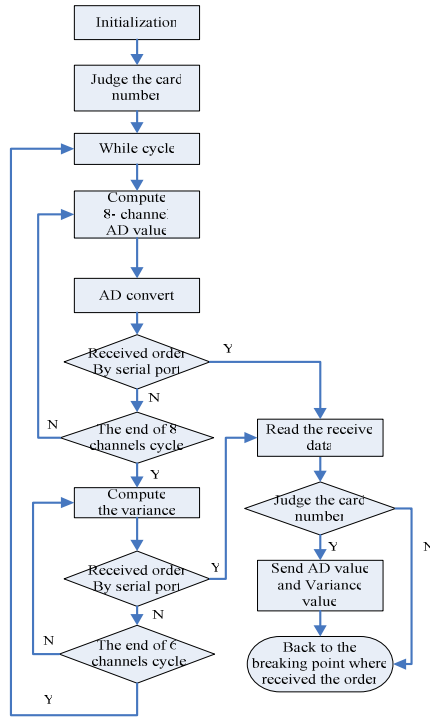


Fig. 4. System’s Software flow chart

5 Experiment

5.1 Calibration Experiments

As for the data from table 3, we drew the Scatter diagram in figure 5, which we used for the selecting the sensor voltage as horizontal axis, A/D value as vertical axis; the result shows like a liner relationship between the voltage and A/D value through two point form of linear equation. The slope of this line equation could be calculated in equation (2).After calculated, the slope K equaled -93 and intercept B equaled 512.

$$K = \frac{y_2 - y_1}{x_2 - x_1} \tag{2}$$

Table 3. Calibration data

Sensor voltage(V)	Collecting voltage(V)	A/D value
5	0.23	47
3	1.14	233
1	2.05	420
0	2.5	512
-1	2.96	606
-3	3.87	792
-5	4.77	977

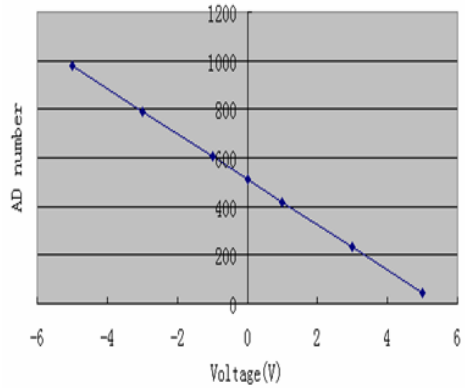


Fig. 5. Scatter diagram of Voltage and A/D

5.2 The Field Test

In the scene field, there are two different situations in this monitoring system. One is that no vehicle pass by the bridge, as we can see from figure 6, no fluctuation is shown in the waveform display interface and the value of standard deviation is equals zero. By contrast to another one (shown in figure 7), it has fluctuating wave in two channels (the red one and the yellow one), and the value of standard deviation of display interface varied from 0 to 2, which reflects the real-time fluctuations of the acceleration of measuring points.

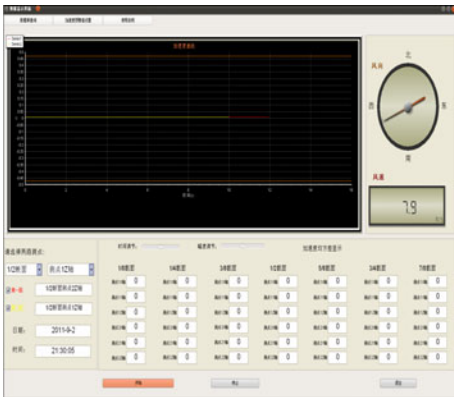


Fig. 6. No vehicle pass

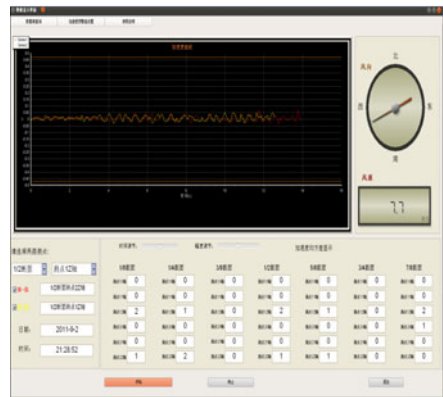


Fig. 7. Vehicle was passing

6 Conclusions

Suspension Bridge is very special due to its complex engineering structures and materials. The research on the bridge health real-time monitoring System, has been a

key work of focus on the bridge health monitoring, including the efficient parameters' acquisition and transmission. As it has no mature product widely used in the domestic market, so the research of bridge health evaluation system has shown to be important theoretical and practical value. This paper presents a bridge of acceleration vibration real-time monitoring system with CAN-bus. CAN-bus achieves on-site data efficient and reliable transmission as a form of data transmission protocol. STC12C5616AD microcontroller can realize on-site data acquisition and process as the core of control unit. IPC ultimately shows and saves data. Our designed communication methods are based on CAN-bus by using STC12C5616AD, they can further improve anti-jamming capability to bridge inspection under a complex circumstances, due to multi-master approaches. The field practice has shown the feasibility and rationality of this design by means of the hardware acquisition board, CAN bus and the joint IPC debugging.

References

1. Huang, P., Liu, X.: Suspension Bridge of Large-span Structure Assessment Based on Health Observation. Jiangnan University Journal 4, 211–214 (2008)
2. Acceleration sensor Datasheet, <http://www.myutech.cn/>
3. Wind speed & direction sensor Datasheet, <http://www.whxph.com/>
4. Xue, M.: Distributed Control System Design and Research Based on CAN Bus. D. Wu Han University of Technology (2005)
5. Li, Y., Zheng, H.: The Structure Analyze and Application about TeeChart Component. Product Applied 4, 57–59 (2004)

Research on New Neural Oscillator in CPG Model Used in Robotic Fish

Wang Gang¹, Zhang Daibing², and Shen Lincheng²

¹ China Satellite Maritime Tracking and Control Department, No.850, Mailbox103, Jiangyin, China, 214400

² National University of Defense Technology, Changsha, China, 410073
wanggang.seu@gmail.com

Abstract. CPG control method is a modern control way in robotic control area. The problem is how to design a CPG model which can control the robot well. Neural oscillator is an important part in CPG model, in this paper, a new kind neural oscillator has been designed for CPG model. With this new neural oscillator, detailed analysis work has been done. The most achievement thing is the meanings of the parameters in CPG model are clear. With these parameters, the amplitude and the period of the CPG model's output can be set to fit the robotic control. In this paper, we make a three-joint robotic fish as prototype, the simulation results show the new neural oscillator in CPG model can well used in robotic fish control.

Keywords: Neural Oscillator, CPG Model, Robotic fish.

1 Introduction

Rhythmic movement, such as swimming, walking, running and flying are produced by central pattern generators (CPGs) [1,2], which are neural circuits that produce coordinated oscillatory signals in the absence of sensory input or descending inputs from higher cognitive elements [3,4].

CPGs control method is considered as a biomimetic control way which has been used in robotic control area. The neural oscillators are the basement of CPGs network, so the research on CPGs network is to study the characteristics of the neural oscillators.

In this paper, we analyzed the new oscillator used in CPG model, which has been pilot studied in our forward paper [5,6,7]. Using this new kind oscillator, we make detailed analysis in this paper. The organization of this paper is as follows. Section 2 presents the design of the new oscillator. The new oscillator's characteristics are detailed presented in Section 3. Section 4 shows the application of the CPG model, and conclusions are given in Section 5.

2 Design of CPG Model

The most fundamental CPG model using the neural oscillator was proposed by Brown [8]. It consists of two neurons, which contact each other by reciprocal inhibition. After

that, a number of neural oscillators have been proposed. Wilson and Cowan [9] proposed a famous oscillator in 1972, which has been widely adopted in bionic robot control [10]. Matsuoka [11] also proposed a particular artificial neural oscillator composed of four neurons to imitate the symmetry inhibitory properties.

Our group has also proposed an artificial neural oscillator based on sine-cosine model [12], which is shown in Fig.1.

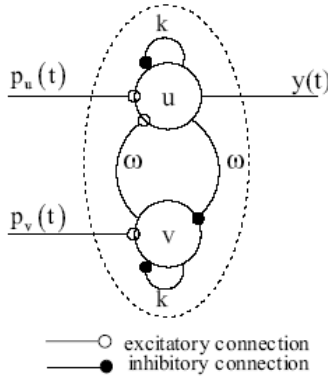


Fig. 1. The neural oscillator based on sine-cosine model

The new neural oscillator’s dynamic model can be described by the following differential equations:

$$\begin{cases} \dot{u} = \omega v + f(u) + p_u(t) \\ \dot{v} = -\omega u + f(v) + p_v(t) \end{cases} \quad (1)$$

Where u denotes the activity of excitatory neuron, v denotes the activity of inhibitory neuron, ω is the strength of mutual connections, P_u and P_v denote the external inputs composed of descending commands and sensor feedback, these are also the start signals, and $f(x)$ is a nonlinear self feedback function. In this new neural oscillator’s dynamic model, $f(x)$ is described as follows:

$$f(x) = kx(1 - rx^2) \quad (2)$$

Where k denotes the convergence speed to limit cycles, and r denotes the oscillatory amplitude control parameter. The material meanings of these parameters will be detailed analyzed in latter paper. So the dynamic model of this new neural oscillator can be described by the following differential equations:

$$\begin{cases} \dot{u} = \omega v + ku(1 - ru^2) + p_u(t) \\ \dot{v} = -\omega u + kv(1 - rv^2) + p_v(t) \\ y = u \end{cases} \quad (3)$$

y is the output of this model, which can be seen in Fig.3, we can use the output to do the control system, because the output has the rhythmic characteristic, it is useful in robotic fish control, the single control system can be seen in Fig.2.

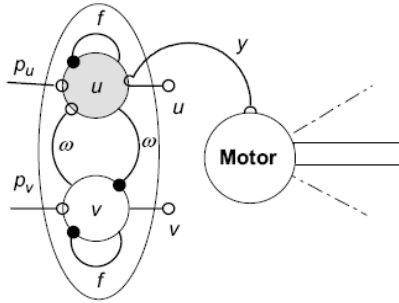


Fig. 2. The single joint neural oscillator control system

The startup signals, p_u and p_v is given as:

$$\begin{cases} p_u(t) = \text{step}(t - t_s) - \text{step}(t - t_s - t_d) \\ p_v = 0 \end{cases}$$

$$\begin{cases} \text{step}(t) = 0, t \leq 0 \\ \text{step}(t) = 1, t > 0 \end{cases} \quad (4)$$

Where t_s is onset time and t_d is the time width of the pulse. The output of the oscillator can be seen in Fig.3.

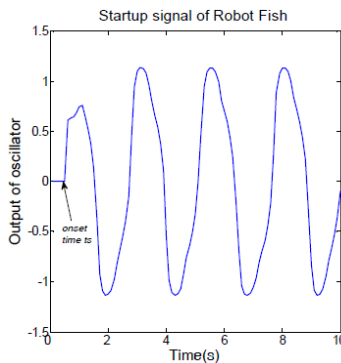


Fig. 3. The output of the oscillator

From Fig.3, we can see that, given stimulation to the oscillator, the output can persist a sine wave for a long time, which is one of the CPG’s characteristics.

3 Characteristics of CPG Model

The output of the neural oscillator y is determined by parameters k , r and ω . There are two parts factors which can determine the characteristics of the output y , one is the amplitude, the other is the period. To analyze this parameters how to affect the characteristic of the output, we use Matlab/Simulink to simulate the neural oscillator model.

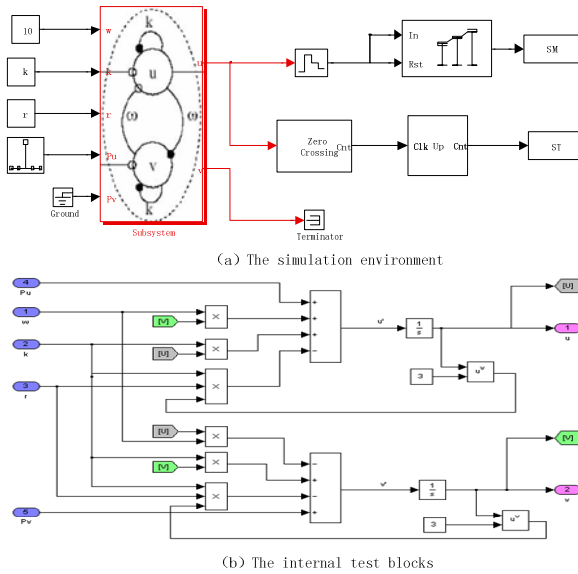


Fig. 4. The simulation environment of the neural oscillator in CPG model

3.1 The Effects of Parameters k and r

To analyze the effect of parameters k and r to the output of this model, we let the parameter ω equals 10, the parameter k ranges from 1 to 20, the parameter r ranges from 1 to 15, the effect can be shown in Fig.5.

Form Fig.5, we can see that the parameter r is minus correlative with the amplitude of the output but irrelative with the period of the output. And the parameter k is irrelative with the amplitude of the output, but determines the period of the output. In Fig.5(d), when k ranges from 0 to 10, when $k < 6$, the parameter k is correlative with the period, but when k ranges from 0 to 20, k is correlative periodically, when k in a special location, the period of the output will change very hugely.

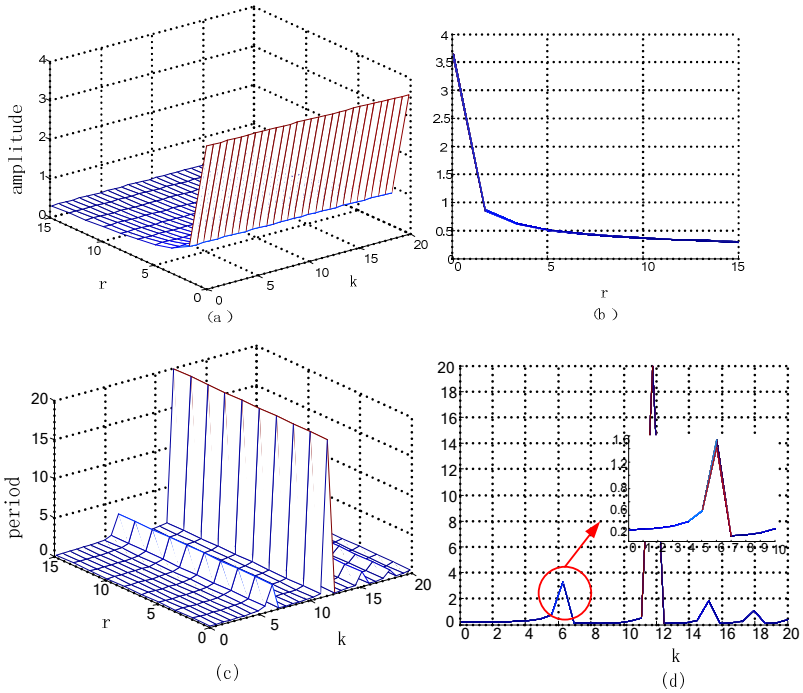


Fig. 5. The amplitude and the period of the output of the oscillator on the effects of the parameters k and r

3.2 The Effects of Parameters k and ω

To take the same steps as above, the effects of parameters k and w to the output will be shown in Fig.6 , in this part, parameter r equals 3.

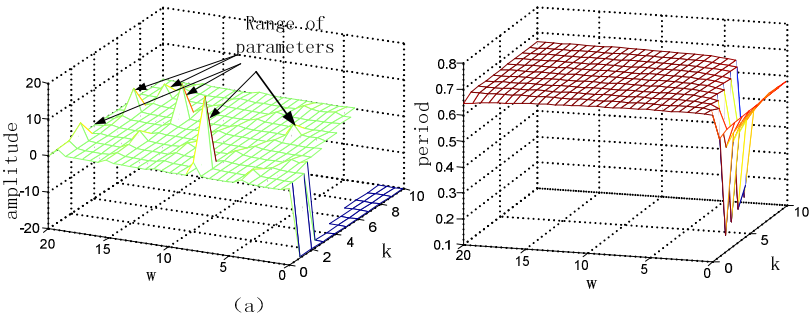


Fig. 6. The amplitude and the period of the output of the oscillator on the effects of the parameters k and ω

From Fig.6, parameter ω exists a lower limit, and is very sensitivity to the output amplitude of the neural oscillator. The range of parameter ω is showed in Fig.6 (a), also to the output period, the parameter ω exists a higher limit.

3.3 The Effects of Parameters r and ω

To take the same steps as above, the effects of parameters r and ω to the output will be shown in Fig.7 , in this part, parameter k equals 3.

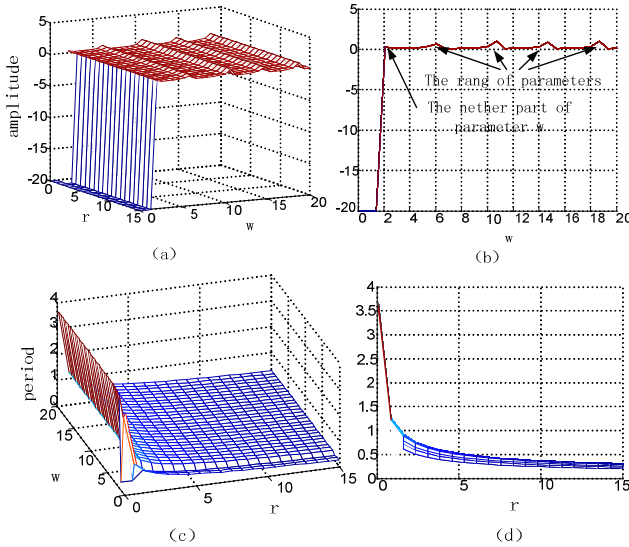


Fig. 7. The amplitude and the period of the output of the oscillator on the effects of the parameters r and ω .

From Fig.7, for the amplitude of the output, the parameter ω exists a lower limit, and the ω ranges periodically, and the parameter ω can be ranges form $[\pi, 2\pi, \dots, n\pi]$.

4 The Application of CPG Model

From the former analysis, we know how to control the amplitude and period of the neural oscillator output with the parameters k , r and ω . In our former research, a typical and simple CPG control system has been built, seen in Fig.8.

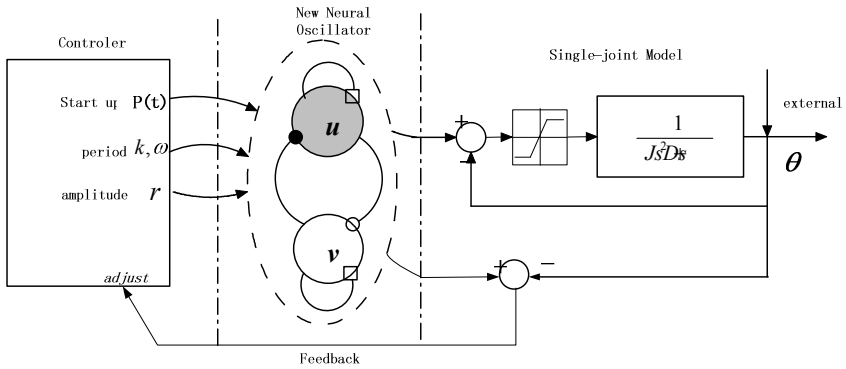


Fig. 8. The CPG control system for the single-joint based on new neural oscillator

In this paper we will use our CPG model to design a whole control system, which can be used in robotic fish control.

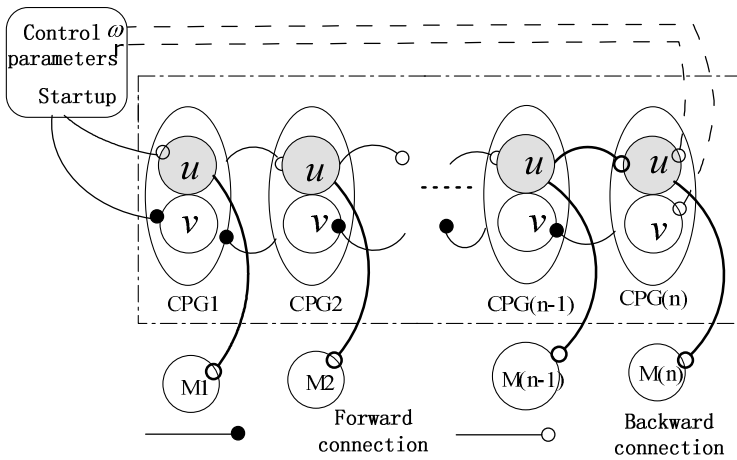


Fig. 9. The Robotic control system based on the CPG control system

The connection of forward and backward joints is determined by a pair of parameters, the model of whole CPG control system can be described as follows:

$$\begin{cases} \dot{u}_i = \omega v_i + k u_i (1 - r u_i^2) + \sum_j (a_{ij} u_j + b_{ij} v_j) \\ \dot{v}_i = -\omega u_i + k v_i (1 - r v_i^2) \\ y_i = u_i \end{cases} \quad (5)$$

Where a_{ij} , b_{ij} are the connection rights of the i th joint and the j th joint, so the connection rights matrixes can be shown as:

$$\begin{aligned}
 W_A &= \begin{bmatrix} a_{11} & a_{12} & a_{13} & \cdots & a_{1,n-1} & a_{1,n} \\ a_{21} & a_{22} & a_{23} & \cdots & a_{2,n-1} & a_{2,n} \\ \cdots & \cdots & \cdots & a_{ij} & \cdots & \cdots \\ a_{n-1,1} & a_{n-1,2} & a_{n-1,3} & \cdots & a_{n-1,n-1} & a_{n-1,n} \\ a_{n,1} & a_{n,2} & a_{n,3} & \cdots & a_{n,n-1} & a_{n,n} \end{bmatrix} \\
 W_B &= \begin{bmatrix} b_{11} & b_{12} & b_{13} & \cdots & b_{1,n-1} & b_{1,n} \\ b_{21} & b_{22} & b_{23} & \cdots & b_{2,n-1} & b_{2,n} \\ \cdots & \cdots & \cdots & b_{ij} & \cdots & \cdots \\ b_{n-1,1} & b_{n-1,2} & b_{n-1,3} & \cdots & b_{n-1,n-1} & b_{n-1,n} \\ b_{n,1} & b_{n,2} & b_{n,3} & \cdots & b_{n,n-1} & b_{n,n} \end{bmatrix}
 \end{aligned} \tag{6}$$

To make the system simpler, we consider that in the CPG control model, the connection matrix can be simple formed as:

$$\begin{aligned}
 W_A &= \begin{bmatrix} 0 & a_{12} & 0 & \cdots & 0 & 0 \\ a_{21} & 0 & a_{23} & \cdots & 0 & 0 \\ \cdots & a_{32} & \cdots & \cdots & a_{n-2,n-1} & \cdots \\ 0 & 0 & a_{43} & \cdots & 0 & a_{n-1,n} \\ 0 & 0 & 0 & \cdots & a_{n,n-1} & 0 \end{bmatrix} \\
 W_B &= \begin{bmatrix} 0 & b_{12} & 0 & \cdots & 0 & 0 \\ b_{21} & 0 & b_{23} & \cdots & 0 & 0 \\ \cdots & b_{32} & 0 & \cdots & b_{n-2,n-1} & \cdots \\ 0 & 0 & b_{43} & \cdots & 0 & b_{n-1,n} \\ 0 & 0 & 0 & \cdots & b_{n,n-1} & 0 \end{bmatrix}
 \end{aligned} \tag{7}$$

So the connection matrix can be described as:

$$(W_A, W_B) = (a_{i,i-1}, b_{i,i-1}, a_{i,i+1}, b_{i,i+1}) \tag{8}$$

5 Conclusion

Detailed analysis is taken in this paper for new neural oscillator in CPG model, the new CPG model is improved from our newly work. The amplitude and the period, which are two important factors of the CPG model’s output, are determined by the parameters in the model. Detailed work makes how the parameters affect the output.

Use the new neural oscillator, a CPG model for multi-joint control system was built, where the connection matrixes play an important role. The connection matrixes can be in two simple forms, different connection matrixes show different characteristics.

The CPG model is simulated for a three-joint robotic fish, our later work will do the simulation to validate that the CPG control system fit the three-joint robotic fish, to validate whether it can control well or not. Further work will be an advantage in robotic control.

References

1. Yu, J., Tan, M., Wang, S., Chen, E.: Development of a biomimetic robotic fish and its control algorithm. *IEEE Trans. Syst, Man, Cybern. B, Cybern.* 34(4), 1798–1810 (2004)
2. Rybak, I.A., Paton, J.F.R., Schwaber, J.S.: Modeling neural mechanisms for genesis of respiratory rhythm and pattern: II. Network Models of the Central Respiratory Pattern Generator. *J. Neurophysiol.* 77, 2007–2026 (1997)
3. Marder, E., Bucher, D.: Central pattern generators and the control of rhythmic movements. *Current Biology* 11, 986–996 (2001)
4. Wang, G.: CPGs Control Method Using a New Oscillator in Robotic Fish. *Science China Technological Sciences* 53(11), 2914–2919 (2010)
5. Zhang, D., Hu, D., Shen, L., Xie, H.: Design of an artificial bionic neural network to control fish-robot's locomotion. *Neurocomputing* 71, 648–654 (2008)
6. Zhang, D.: A novel bionic neural network control method for vivid animation of virtual animal's locomotion. In: *Proceeding of the 26th Chinese Control Conference*, Hunan, China (July 2007)
7. Marder, E., Bucher, D.: Central pattern generators and the control of rhythmic movements. *Current Biology* 11, 986–996 (2001)
8. Brown, G.: On the nature of the fundanmental activity of the nervous centers; together with an analysis of the conditioning of the rhythmic activity in progression, and a theory of the evolution of function in the nervous system. *J. Physiol.* 48, 18–46 (1914)
9. Wilson, H.R., Cowan, J.D.: Excitatory and inhibitory interactions in localized populations of model neurons. *Biophysical Journal* 12, 1–24 (1972)
10. Kazuki, N., Tetsuya, A., Yoshihito, A.: Design of an artificial central pattern generator with feedback controller. *Interligent Automation and Soft Computing* 10, 185–192 (2004)
11. Matsuoka, K.: Mechanisms of frequency and pattern control in the neural rhythm generators. *Biological Cybernetics* 56, 245–353 (1987)
12. Zhang, D.: Design of a Central Pattern Generator for Bionic-robot Joint with Angular Frequency Modulation. In: *Proceeding of the 2006 IEEE International Conference on Robotics and Biomimetics*, Kunming, China (December 2006)

Synthesis of Adaptive Control System for Formation of Program Speed of Multilink Manipulator

Vladimir Filaretov¹ and Anton Gubankov²

¹ Robotics Laboratory, Institute of automation and control processes, Radio 5,
Vladivostok, Russia

² Department of automation and control, Far Eastern federal university, Sukhanova 8,
Vladivostok, Russia

{filaret, gubankov}@iacp.dvo.ru

Abstract. The paper deals with adaptive control system of multilink manipulator. This system taking into account power restriction of executive elements is capable to set to the gripper the greatest possible speed at spatial trajectory. For providing necessary dynamic accuracy at high speeds of work, the self-turning correcting device has been entered into control chain of each drive. Results of simulating have completely confirmed high quality of the synthesized control system.

Keywords: multilink manipulator, control system, maximum speed, high accuracy.

1 Introduction

At present growing manufactures require more and more wide involving automation means which integral part is automatic robots-manipulators. They allow to carry out a wide range of production operations at high speed and accuracy, to raise essentially an operational efficiency and completely to expel the human factor from a flow process [1-3].

However, exact movement of the working tool of the manipulator on any spatial trajectory with a high speed is possible only then it's executive elements possess a sufficient resource of control on all sections of this path. In other words all actuators of multilink manipulator without entry in saturation should be capable complete precisely a signal of any program movement of the manipulator and simultaneously to compensate negative effects of dynamic interactions between all its degrees of mobility which lead to essential changes of loading parameters in these actuators [3].

In connection with noted in the report the problem of synthesis of adaptive control system for formation of program speed of working tool of multilink manipulator is defined and solved. This system taking into account restriction of power of all executive elements is capable to set the specified speed so that it will be greatest possible on corresponding section of this trajectory, and dynamic accuracy of control remained in the set limits.

2 Description of Kinematics and Dynamics of the Manipulator

Consider the manipulator, containing two degrees of freedom, each of which is moved by the DC motor independent excitation or with constant magnets. Each of specified actuators contains a control system (CS)

$$u_i(t) = f_{ii}(\varepsilon_i(t), Q^*(t)), \tag{1}$$

Where $\varepsilon(t) = Q^*(t) - Q(t) \in R^n$ - vector of dynamic error of actuators, $Q(t) = (q_1, q_2)^T$ and $Q^*(t) = (q_1^*, q_2^*)^T$ - accordingly vectors of the generalized coordinates setting real and desired positions of manipulator's working tool. Specified CS (1) provides to each actuator given quality of control and allows to reduce dynamics of these electric motors to the desired.

Let the desirable trajectory of gripper movement is set in the form of function $s^*(t)$ - which should pass manipulator's gripper with desirable speed $\dot{s}^*(t) = v^*(t)$. That the CS (1) provided movement of working tool on given spatial trajectory $s^*(t)$, it is necessary to define the law of change $Q^*(t)$. Specified vector $Q^*(t)$ is connected with a vector of desirable position of manipulator's gripper in absolute system of coordinates $r^*(t) = (x^*(t), y^*(t))^T$ by means of expression:

$$Q^*(t) = F_I(r^*(t)), \tag{2}$$

where $F_I(r^*(t)) = (f_I^1(r^*(t)), f_I^2(r^*(t)))^T$ - vector which contains the functions describing solution of inverse kinematic problem of manipulator. The law of change $r^*(t)$ is formed by means of the expression defining desirable speed $v^*(t)$ of gripper movement in absolute system of coordinates:

$$\dot{r}^*(t) = \begin{pmatrix} \dot{x}^*(t) \\ \dot{y}^*(t) \end{pmatrix} = A(s)v^*(t) = \begin{pmatrix} \cos(\varphi(s)) \\ \sin(\varphi(s)) \end{pmatrix} v^*(t), \tag{3}$$

where $\varphi(s)$ - angle between vector of desirable speed $v^*(t)$ and axis x of absolute system of coordinate, which in case of linear path will be constant.

Taking into account (2) and (3), expression for the desirable generalized speed in i degree of mobility will look like:

$$\dot{q}_i^* = \frac{\partial f_i^i}{\partial x^*} \dot{x}^* + \frac{\partial f_i^i}{\partial y^*} \dot{y}^* = \left(\frac{\partial f_i^i}{\partial x^*} \quad \frac{\partial f_i^i}{\partial y^*} \right) (\dot{x}^* \quad \dot{y}^*)^T = J_i \dot{r}^* = J_i A(s) v^*(t), \tag{4}$$

and expression for desired generalized acceleration:

$$\begin{aligned} \ddot{q}_i^* &= \dot{J}_i \dot{r}^* + J_i \ddot{r}^* = (\Gamma_i \dot{r}^*)^T \dot{r}^* + J_i \left(\frac{\partial A(s)}{\partial s} v^*(t) + A(s) \dot{v}^*(t) \right) = A(s)^T v^*(t) \Gamma_i^T A(s) v^*(t) + \\ &+ J_i \frac{\partial A(s)}{\partial s} v^*(t)^2 + J_i A(s) \dot{v}^*(t) = (A(s)^T \Gamma_i^T A(s) + J_i \frac{\partial A(s)}{\partial s}) v^*(t)^2 + J_i A(s) \dot{v}^*(t) \end{aligned} \tag{5}$$

$$\text{where } \frac{\partial A(s)}{\partial s} = \begin{pmatrix} -\sin(\varphi(s)) \\ \cos(\varphi(s)) \end{pmatrix}, \quad \Gamma_i^T = \begin{pmatrix} \partial^2 f_i^i / \partial x^2 & \partial^2 f_i^i / \partial y \partial x \\ \partial^2 f_i^i / \partial x \partial y & \partial^2 f_i^i / \partial y^2 \end{pmatrix}, \quad i = 1, 2.$$

At accelerating and moving at high speed there are strong interactions between all degrees of mobility in manipulator [3] which in a general view look like:

$$P_i = H_{ii}(q)\ddot{q}_i + h_i(q, \dot{q})\dot{q}_i + M_i(q, \dot{q}, \ddot{q}), \quad (6)$$

where $H_{ii}(q)$ - a component characterizing inertial properties of corresponding degree of mobility of the manipulator; $h_i(q, \dot{q})$ - a component of Coriolis and high-speed forces; $M_i(q, \dot{q}, \ddot{q})$ - component considering gravitational forces and effects of interaction between degrees of mobility of the manipulator; $i = 1, 2$. Taking into account (6) differential equation describing dynamics of the actuator of the manipulator, at small inductance and absence of a dry and viscous friction, in a general view:

$$R_i(H_{ii}(q) + I_i i_{ri}^2)\ddot{q}_i + (R_i h_i(q, \dot{q}) + K_{\omega_i} K_{M_i} i_{ri}^2)\dot{q}_i + R_i M_i(q, \dot{q}, \ddot{q}) = K_{y_i} K_{M_i} U_i i_{ri}, \quad (7)$$

where K_{y_i} - gain factor; K_{M_i} - torque factor; U_i - input voltage of power amplifier; K_{ω_i} - counter emf factor; R_i - active resistance of an anchor chain of the electric motor; i_{ri} - reduction ratio; I_i - moment of inertia of a rotor of the electric motor and rotating parts of a reducer.

3 Synthesis of Adaptive Control System for Formation of Program Speed of 2 Degrees of Freedom Manipulator

That the gripper of manipulator moved on trajectory with the given dynamic accuracy on high speed executive elements should possess a certain power reserve. If reserve is not enough the gripper will lose trajectory and all requirements to quality of control will be broken. Since as executive elements DC motors of independent excitation or with constant magnets are chosen, and control of them occurs by means of input voltage then on level of control signal voltage on each actuator it is possible to make decision about degree of affinity of the actuator to saturation. Thus, for the set of the greatest possible speed of gripper movement on spatial trajectory it is necessary that at the law of its formation in an explicit form there was a voltage of an input signal. Further, having substituted in the specified law of formation of speed the maximum value of voltage, it is possible to calculate the maximum speeds, taking into account saturation of each electric motor. Minimum from them will be in the required speed. Physically it means that the given speed is calculated for the most loaded actuator the input signal of which is already close to restriction.

To receive dependence of speed of gripper movement from values of control voltages of actuators, it is necessary to substitute (4) and (5) in (7), to substitute instead of U_i is maximum value U_{\max_i} and express in explicit form $\dot{v}_i^*(t)$. For example, for the actuator of the first degree of freedom one can calculate the maximum speed as follows

$$\begin{aligned} \dot{v}_1^*(t) = & K_{y1} K_{m1} U_{\max} i_{r1} - R_1 (I_1 i_{r1}^2 + H_{11}(\dot{q}^*)) A(s)^T \Gamma_1^T A(s) v_1^*(t)^2 - R_1 M_1(q^*, \dot{q}^*, \ddot{q}^*) - \\ & - (R_1 h_1(q^*, \dot{q}^*) + K_{\omega 1} K_{m1} i_{r1}^2) J_1 A(s) v^*(t) / [R_1 (I_1 i_{r1}^2 + H_{11}(\dot{q}^*)) (\frac{\partial f_1}{\partial x} \cos(\varphi(s)) + \\ & + \frac{\partial f_1}{\partial y} \sin(\varphi(s)))] . \end{aligned} \quad (8)$$

From all $\dot{v}_i^*(t)$ taking into account power restriction will be that speed which is calculated for the most loaded actuator at which the control signal has accepted the maximum value. Thus, gripper's movement without an exit on restriction on power of executive elements will be provided with the minimum speed on the absolute value, calculated by means of (8).

Thus, in given paper the adaptive control system of multilink manipulator is designed. This system taking into account power restriction of executive elements is capable to set the gripper the greatest possible speed at spatial trajectory. For providing necessary dynamic accuracy at high speeds of work, the self-turning correcting device has been entered into control chain of each drive [3]. Results of simulating have completely confirmed high quality of the synthesized control system.

Acknowledgments. This work is supported by Russian Fund of Basic Research (Grants № 09-08-00080, 11-08-98505) and Federal target program "Scientific and educational personnel of innovative Russia " 2009-2013.

References

1. Fu, K.S., Gonzalez, R.C., Lee, C.S.G.: Robotics: Control, Sensing, Vision and Intelligence (1987)
2. Zenkevich, S.L., Yushenko, A.S.: The basis of manipulator robots control. BMSTU Press, Moscow (2004) (in Russian)
3. Filaretov, V.F.: Self turning control systems of manipulators actuators. FENTU Press, Vladivostok (2000) (in Russian)

Optimal Single Quantum Measurement of Multi-level Quantum Systems between Pure State and Mixed State

Haiwei Liu, Yaoxiong Wang, and Feng Shuang*

¹ Department of Automation, University of Science and Technology of China, Hefei, 230026, China

² Robot Sensors and Human-Machine Interaction Laboratory, Institute of Intelligent Machines, Hefei, 230031, China

Abstract. We derive analytic solution of the particular case of the optimal quantum measurement between pure state and mixed state of the multi-level system. In order to figure out the physical essence rather than the facial complex mathematical expression, we restrict the system to be 3-level and the mixed state to be a diagonal matrix to get a obvious result. Generally the optimal solution is determined by the 9 free elements of the transformation unitary matrix. To our surprise, the results actually are so simple that we just have to search 3-dimensional Hilbert space for the optimal solutions. However, the optimal solutions depend on the relative scale among the diagonal elements. Some guessing analytical solution of the optimal target function is given, but the general cases of transformation between mixed state and pure state without imposing these restrictions is still unavailable.

Keywords: Quantum control, Unitary transformation, Multi-level quantum system, State transformation.

1 Introduction

One of the general goal of quantum control is to maximize the expectation of the desired target operator usually by suitable external interactions on the system. The external interactions often includes 3 methods. The first one is the tailored coherent control field [1] and the second is the tailored environment variables [2]. Non-unitary controlled quantum dynamics can also be realized by external interaction named as quantum measurement [3], which can drive the system to evolve to the desired state. At times the methods will be combined together to realize the goal [4,5,6].

In theoretical research, the general physically allowable state transformation of open quantum system can be definitely described by Kraus maps [7] which is robust to variations in the initial state. The evolution of the closed system in some particular cases can described by unitary matrices owing to the quantum

* Corresponding author.

assumption [8]. The unitary operators have been realized in the experiment [9]. The research of unitary dynamics has found some interesting phenomena [10,11,12] and also leads to the fundamental physical meaning [13,14,15,16].

In this paper, we focus on the the optimal solutions to the projective operator by measurement to get the maximum possibility that the system transforms to the desired state. Some special cases have been solved [17] previously. This paper mainly discusses the transformation between the pure state and the mixed state of multi-level systems and is organized as follows. In Sect. 2, we introduce some basic concepts and notations about non-selective measurements with the aid of the unitary matrix. Sect. 3 analyzes the case with the projective operators between pure state and diagonal mixed state. Analytical solution to the transformation between pure state to the special state with equal possibilities besides the desired state is in Sect. 4 Discussion and conclusion are presented in sect. 5.

2 Notation About Non-selective Measurements

The fundamental hypothesis about measurement based on experimental observation in quantum mechanics [8]. Every quantum state can be described by density matrix[18]. The state becomes $\rho = \sum_i p_i \rho_i$ if the system state ρ has the the possibility of p_i to be the state ρ_i , where ρ_i is determined by the eigenstates $\{p_{ij}, |\psi_{ij}\rangle\}$, namely $\rho_i = \sum_j p_{ij} |\psi_{ij}\rangle$. As a whole, ρ is the mixture of ψ_i with the possibility of p_i compacting the unnecessary induces, so we lose the exact components of the measurement result i . The state turns $\rho = \sum_i p(i) \rho_i = \sum_i M_i \rho_0 M_i^+$ with the possibility of $p(m) = \sum_i p_i p(m|i) = \sum_i p_i Tr(M_m^+ M_m |\psi_i\rangle \langle \psi_i|) = Tr(M_m^+ M_m \rho)$, namely the non-selective measurement formulation.

Unitary matrices can be used to parameterize the projective measurement [17], and each projector P_i can be represented as

$$P_i = UI_iU^+, i = 1, 2, \dots, n \tag{1}$$

here I_1, I_2, \dots, I_n are diagonal matrix with elements 0 or 1 and satisfy the condition $\sum_{i=1}^n I_i = U^+(\sum_{i=1}^n P_i)U = I$. The single measurement can be characterized finally as

$$\rho = M(U)\rho_0 = \sum_{i=1}^{i=n} UI_iU^+ \rho_0 UI_iU^+. \tag{2}$$

And it is easy to confirm the possibility of ρ projecting to the desired state Θ i.e. target function, is

$$J = Tr[\rho\Theta] \tag{3}$$

3 Transformation between Pure State and Mixed State with the Multi Projector Operators

We consider the transformation between pure state and diagonal mixed state and this leads to two benefits that we readily work out the target function as a

parametric expression and the physical meaning of the diagonal matrix is explicit at the same time. Since this general case is still quite complicated to figure out a direct analytical expression.

3.1 Description about the General Formulation of the Target Function

Assuming the target state is

$$|\Theta\rangle \sim |1\rangle\langle 1| \tag{4}$$

The projective operators and the initial diagonal state are

$$P_i = U|i\rangle\langle i|U^\dagger \tag{5}$$

$$\rho_0 = \sum_i \lambda_i |i\rangle\langle i| \tag{6}$$

respectively. Here λ_i is the eigenvalue of ρ projective to the eigenstate $|i\rangle$. Obviously the projectors must satisfy the completeness condition.

Without loss of generality, we might as well restrict that

$$0 \leq \lambda_2 \leq \lambda_3 \leq \dots \leq \lambda_N \tag{7}$$

which satisfied the completeness condition

$$\sum_{i=1}^N \lambda_i = 1 \tag{8}$$

The target function becomes

$$J = Tr[\sum_{i,j} \langle 1|u|j\rangle\langle j|u^\dagger \lambda_i |i\rangle\langle i|u|j\rangle\langle j|u^\dagger |1\rangle] = \sum_{i,j} |u_{1j}|^2 |u_{ij}|^2 \lambda_i \tag{9}$$

here u_{ij} denotes the elements of the unitary matrix U .

What we will do next is to search for the global maximum in the unitary space and the only available approach currently is numerical searching in high-dimensional space. From the equation above, we focus on a 3-level system to (for 2-level system has been solved already) to get a direct understanding about the solution structure of the transformation.

3.2 Derivation about the Parametric Form of the Function

Any unitary matrix in the Hilbert space can be divided into the product of 2-level unitary matrices[18]. Every rotation in a 3-dimensional real space can be replaced by 3 axis-rotations in turn. Here, we consider the 3-level case and define $U = U_{23}U_{13}U_{12}$. Then substituting $N = 3$ into the Eq. [3] and get the target function

$$J = Tr[\sum_i U_{23}U_{13}U_{12}|i\rangle\langle i|U_{12}^\dagger U_{13}^\dagger U_{23}^\dagger \rho_0 U_{23}U_{13}U_{12}|i\rangle\langle i|U_{12}^\dagger U_{13}^\dagger U_{23}^\dagger \Theta] \tag{10}$$

We can parameterize the target function as below since that any 2-level unitary matrix can be decomposed as triangle function,

$$e^{i\theta_0} \begin{pmatrix} e^{i\theta_1} \cos \phi & e^{i\theta_2} \sin \phi \\ -e^{-i\theta_2} \sin \phi & e^{-i\theta_1} \cos \phi \end{pmatrix} \tag{11}$$

then we can define the three 2-level unitary matrices as

$$U_{12} = e^{i\theta_{03}} \begin{pmatrix} e^{i\theta_{13}} \cos \phi_3 & e^{i\theta_{23}} \sin \phi_3 & 0 \\ -e^{-i\theta_{23}} \sin \phi_3 & e^{-i\theta_{13}} \cos \phi_3 & 0 \\ 0 & 0 & e^{-i\theta_{03}} \end{pmatrix} \tag{12}$$

$$U_{13} = e^{i\theta_{02}} \begin{pmatrix} e^{i\theta_{12}} \cos \phi_2 & 0 & e^{i\theta_{22}} \sin \phi_2 \\ 0 & e^{-i\theta_{02}} & 0 \\ -e^{-i\theta_{22}} \sin \phi_2 & 0 & e^{-i\theta_{12}} \cos \phi_2 \end{pmatrix} \tag{13}$$

$$U_{23} = e^{i\theta_{01}} \begin{pmatrix} e^{-i\theta_{01}} & 0 & 0 \\ 0 & e^{i\theta_{11}} \cos \phi_1 & e^{i\theta_{21}} \sin \phi_1 \\ 0 & -e^{-i\theta_{21}} \sin \phi_1 & e^{-i\theta_{11}} \cos \phi_1 \end{pmatrix} \tag{14}$$

So, the general 3-level unitary is

$$U_{3D} = \begin{pmatrix} e^{-i\theta_{01}+i\theta_{12}+i\theta_{13}} \cos \phi_2 \cos \phi_3 & -e^{i\theta_{13}+i\theta_{21}-i\theta_{22}} \cos \phi_3 \sin \phi_1 \sin \phi_2 - e^{-i\theta_{02}+i\theta_{11}-i\theta_{23}} \cos \phi_1 \sin \phi_3 \\ e^{-i\theta_{01}+i\theta_{12}+i\theta_{23}} \cos \phi_2 \sin \phi_3 & e^{-i\theta_{02}+i\theta_{11}-i\theta_{13}} \cos \phi_1 \cos \phi_3 - e^{i\theta_{21}-i\theta_{22}+i\theta_{23}} \sin \phi_1 \sin \phi_2 \sin \phi_3 \\ e^{-i\theta_{01}-i\theta_{03}+i\theta_{22}} \sin \phi_2 & e^{-i\theta_{03}-i\theta_{12}+i\theta_{21}} \cos \phi_2 \sin \phi_1 \\ -e^{-i\theta_{11}+i\theta_{13}-i\theta_{22}} \cos \phi_1 \cos \phi_3 \sin \phi_2 + e^{-i\theta_{02}-i\theta_{21}-i\theta_{23}} \sin \phi_1 \sin \phi_3 \\ -e^{-i\theta_{02}-i\theta_{13}-i\theta_{21}} \cos \phi_3 \sin \phi_1 - e^{-i\theta_{11}-i\theta_{22}+i\theta_{23}} \cos \phi_1 \sin \phi_2 \sin \phi_3 \\ e^{-i\theta_{03}-i\theta_{11}-i\theta_{12}} \cos \phi_1 \cos \phi_2 \end{pmatrix} \tag{15}$$

Obviously, the 3 module variables ϕ_1, ϕ_2, ϕ_3 are independent. Actually, only 6 of 13 phase variables are independent (see Appendix A). So, we have verified that the 9 freedom degree of arbitrary parametric 3-level unitary matrix.

In general, we should simplify the 13 linear combinations with 6 independent variables for further simplification of the target function. However, the target function already has a simple form if we substitute the "unsimplified" unitary matrix form into Eq 10. Defining that

$$f(x, y) = (x \sin^2 \phi_2 (7 + \cos 4\phi_3) + 2y \sin^2 2\phi_3) \tag{16}$$

then the target function becomes

$$J = \frac{1}{4} (\lambda_1 \cos^4 \phi_2 (3 + \cos 4\phi_3) + 4\lambda_1 \sin^4 \phi_2 + \cos^2 \phi_2 (\cos^2 \phi_1 f(\lambda_3, \lambda_2) + \sin^2 \phi_1 f(\lambda_2, \lambda_3) + (\lambda_2 - \lambda_3) \cos \theta \sin 2\phi_1 \sin \phi_2 \sin 4\phi_3)) \tag{17}$$

here $\theta \equiv (\theta_{11} + \theta_{22}) - (\theta_{02} + \theta_{13} + \theta_{21} + \theta_{23})$. The last 3 phase variables $\theta_{03}, \theta_{12}, \theta_{01}$ disappear magically.

3.3 Analysis of the Definition Region and Its Periodical Conditions

Now we analyze the periodicity of the 4 variables $\theta, \phi_1, \phi_2, \phi_3$ to reduce the searching space for the numerical solution. The expression containing θ is $\cos \theta$ which can traverse all possible value within half a period for that $\cos \theta = \cos(2\pi - \theta)$, we locate the region is $0 \leq \phi_1 < \pi$. The expressions containing ϕ_1 are $\cos^2 \phi_1, \sin^2 \phi_1, \sin 2\phi_1$ with period of π , so the region is set to $0 \leq \phi_1 < \pi$. And the expressions containing ϕ_2 are $\cos^4 \phi_2, \sin^4 \phi_2, \cos^2 \phi_2 \sin^2 \phi_2, \cos^2 \phi_2, \sin \phi_2$, the rigid restriction is $\sin \phi_2$ which period is 2π . However the former 3 terms all satisfy $f(\phi_2 + \pi) = f(\phi_2)$, and $\sin \phi_2$ has the coefficient $\cos \theta$. Owing to $\sin(\phi + \pi) \cos \theta = \sin \phi \cos \theta'$ when $\theta' = \pi - \theta$. So we restrict the region in ϕ_2 is $0 \leq \phi_2 < \pi$ since the region of θ' and θ can be set the same. At last, it is easy to set the region in $0 \leq \phi_3 < \pi/2$ for the expressions containing ϕ_3 are $\cos 4\phi_3, \sin^2 2\phi_3, \sin 4\phi_3$.

The maximum is at the edge of the region or just one of the extreme points. For the only phase parameter θ the partial differential is

$$J'(\theta) = -\frac{1}{4}(\lambda_2 - \lambda_3) \sin \theta \sin 2\phi_1 \sin \phi_2 \cos^2 \phi_2 \sin 4\phi_3 \tag{18}$$

The properties depend on whether λ_2 equals to λ_3 . The equal case is discussed in Sect. 4. Now we assume that $\lambda_2 \neq \lambda_3$ indicating 6 kind of cases to make the constant coefficient 0 besides which θ has to be at the edge of the region to achieve the maximum.

$$\phi_1 = 0, \frac{\pi}{2} \quad \phi_2 = 0, \frac{\pi}{2} \quad \phi_3 = 0, \frac{\pi}{4} \tag{19}$$

Next, the partial differential operation with respect to ϕ_1 is such complex as below.

$$J'(\phi_1) = \frac{1}{2}(\lambda_2 - \lambda_3) \cos^2 \phi_2 (\cos \theta \cos 2\phi_1 \sin \phi_2 \cdot \sin 4\phi_3 + f(1, -1) \sin \phi_1 \cos \phi_1) \tag{20}$$

So we resort to search for the optimal numerical computation with these necessary conditions to confirm the validity.

3.4 Concise Numerical Solution to the Optimal Target Function

The numerical method to search for the maximum is Table. [1] as below. The results show that it fits close the former analytical results of equation 19 taking account of the numerical accuracy.

In fact, to restrict U in the real space i.e. $\theta \equiv 0$ can easier get the max J . The numerical results Table. [2] below turns out to reach the same results as searching in the complex space. Actually, it is not difficult to make such restriction from the Eq. [9] that indicates target function just depends on the nonlinear combination of the elements' module of the unitary matrix.

Table 1. The parameters' value reaching the maximum J corresponding to the random λ_s

Jmax	θ	ϕ_1	ϕ_2	ϕ_3	λ_1	λ_2	λ_3
0.52178	1.76228	0.56006	0.00028	1.57057	0.521783	0.178407	0.299811
0.49960	0.64785	0.00059	2.35619	1.57022	0.253632	0.000789	0.745579
0.37948	0.37921	0.00129	0.78539	1.56905	0.064834	0.241033	0.694132
0.60565	0.32847	0.32406	0.00036	1.57039	0.605651	0.348158	0.046190
0.47644	1.75684	0.55913	0.00005	1.57075	0.476448	0.170326	0.353226
0.39405	1.16282	0.79012	1.57080	1.10099	0.394055	0.185168	0.420777
0.45260	0.69719	0.00095	2.35619	1.56991	0.190474	0.094798	0.714728
0.39131	0.73764	0.00193	2.35619	1.56994	0.386383	0.217379	0.396237
0.75954	1.73610	0.45766	0.00015	1.57067	0.759541	0.042061	0.198398
0.92599	0.34036	0.34007	0.00033	1.57050	0.925993	0.062606	0.011400
0.48864	1.56839	0.00122	0.00121	0.78539	0.071673	0.905611	0.022715
...

Table 2. The parameters' value reaching the maximum corresponding to the λ_s with the real U

Jmax	ϕ_1	ϕ_2	ϕ_3
0.52178	0.36800	0.00014	1.57058
0.49960	0.00186	0.78539	1.56949
0.37948	0.00118	0.78539	1.56928
0.60565	0.38880	0.00027	1.57047
0.47644	0.65794	0.00034	1.57057
0.40741	0.00229	0.78539	1.56914
0.45260	0.00205	0.78539	1.56923
0.39130	0.00362	0.78539	1.56842
0.75953	0.32313	0.00068	1.57010
0.92599	1.73669	0.00001	1.57077
0.48864	0.00088	0.00100	0.78539
...

3.5 Analytical Guess of Maximum of the Target Function

From the numerical results, we guess cautiously J reaches a maximum when $\phi_3 \equiv \frac{\pi}{2}$ for nearly most cases, then the target function turns to be

$$J1 = \lambda_1(\cos^4 \phi_2 + \sin^4 \phi_2) + \lambda_T 2 \cos^2 \phi_2 \sin^2 \phi_2 \tag{21}$$

with $\lambda_T \equiv (\lambda_2 \sin^2 \phi_1 + \lambda_3 \cos^2 \phi_1)$, the weighted average of λ_2 and λ_3 . J is the weighted average of λ_1 and λ_T with the max weight of λ_T is $\frac{1}{2}$.

$$J1_{max} = \frac{1}{2} (\lambda_1 + Max\{\lambda_1, \lambda_T\}) = \frac{1}{2} (\lambda_1 + Max\{\lambda_s\}) \tag{22}$$

Another occasional case is $\phi_3 \equiv \frac{\pi}{4}$. then

$$J2 = \lambda_1 \left(\frac{1}{2} \cos^4 \phi_2 + \sin^4 \phi_2 \right) + \frac{1}{2} \cos^2 \phi_2 (\sin^2 \phi_1 (\lambda_3 + 3\lambda_2 \sin^2 \phi_2) + \cos^2 \phi_1 (\lambda_2 + 3\lambda_3 \sin^2 \phi_2)) \quad (23)$$

Define that $x \equiv \sin^2 \phi_2$, the same λ_T and $\lambda_R \equiv \lambda_3 \sin^2 \phi_1 + \lambda_2 \cos^2 \phi_1 = (\lambda_2 + \lambda_3) - \lambda_T$ which gets its extremes corresponding to λ_T . Reformulating the target function given the completeness condition 8, we have

$$J2(x) = \frac{1}{2} (x^2(\lambda_1 - \lambda_T) + x(3\lambda_T - 1) - (\lambda_T - 1)) \quad (24)$$

Obviously, it is a quadratic polynomial with the symmetric axis is $S = \frac{1-3\lambda_T}{\lambda_1-\lambda_T}$ with the maximum in 5 cases as below.

Case 1: $\lambda_1 - \lambda_T > 0, S > \frac{1}{2}$ i.e. $\lambda_T < \lambda_1, \lambda_T < \frac{\lambda_2+\lambda_3}{2}$ It is easily to satisfy this condition with a suitable ϕ_1 and $\lambda_2 < \lambda_1$. So

$$J2(x)_{max} = J2(0) = \frac{1 - \lambda_T}{2} = \frac{\lambda_1 + Max\{\lambda_2, \lambda_3\}}{2} \quad (25)$$

Case2: $\lambda_1 - \lambda_T > 0, S < \frac{1}{2}$ i.e. $\lambda_T < \lambda_1, \lambda_T > \frac{\lambda_2+\lambda_3}{2}$ It is easily to satisfy this condition with a suitable ϕ_1 and $\lambda_2 < \lambda_1$ with that restrictions 7. So

$$J2(x)_{max} = J2(1) = \frac{\lambda_1 + \lambda_T}{2} = \frac{\lambda_1 + Max\{\lambda_2, \lambda_3\}}{2} \quad (26)$$

For the other 3 cases that $\lambda_1 - \lambda_T < 0$, such as $S < 0, S > 1$ and $0 < S < 1$ respectively, we know that $J2(x)_{max} = J2(0), J2(x)_{max} = J2(1)$, and $J2(x)_{max} = J2(S)$. All get the maximum $\frac{\lambda_1 + Max\{\lambda_2, \lambda_3\}}{2}$.

Comparing the results up, we can always set $\phi_3 = \frac{\pi}{2}$ to get the maximum target function since Eq. [22] is never smaller than Eq. [25].

4 Transformation with Equal Possibilities Besides the Desired State

Now we consider the first case left in the previous section, i.e the state space possibilities are equal besides the desired projective dimension of the initial state. Here it is an particular physics that the indirect eigen states have equal right. Then Eq. [16] satisfies $f(\lambda_2, \lambda_3) = f(\lambda_3, \lambda_2)$. and the target function is fairly simple with only 2 independent variables.

$$J1 = \frac{1}{4} (\lambda_1 \cos^4 \phi_2 (3 + \cos 4\phi_3) + 4\lambda_1 \sin^4 \phi_2 + \lambda_3 \cos^2 \phi_2 (\sin^2 \phi_2 (7 + \cos 4\phi_3) + 2 \sin^2 2\phi_3)) \quad (27)$$

The landscapes of the function are quit different corresponding to different arrangements of the λ_s shown in the typical illustrations as below.

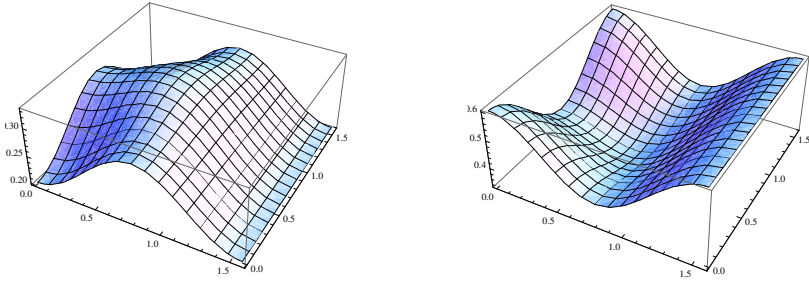


Fig. 1. Global landscapes of $J = J(\phi_2, \phi_3)$ when $\lambda_s = 0.2, 0.4, 0.4$ (left) and $\lambda_s = 0.6, 0.2, 0.2$ (right)

Actually, we can analyze the more general equal possibilities case in a N-level system. The density operator is

$$\rho_0 = \begin{pmatrix} 1 - (n - 1)\lambda & & & \\ & \lambda & & \\ & & \ddots & \\ & & & \lambda \end{pmatrix} \tag{28}$$

The desired final state is still the Eq. [4]. Obviously, we can simplify like that

$$\rho_0 = \lambda I + (1 - n\lambda)\Theta \tag{29}$$

So the target function turns out

$$J = \sum_{i=1}^n \lambda \langle i|U^+\Theta U|i\rangle + (1 - n\lambda)(\langle i|U^+\Theta U|i\rangle)^2 \tag{30}$$

It seems to be a quadratic form, so its extremal value depends on that the sign of $1 - n\lambda$. The first section is actually a constant because that the trace of density matrix is 1.

$$\sum_{i=1}^n \lambda \langle i|U^+\Theta U|i\rangle = \lambda Tr[U^+\Theta U] = \lambda Tr[UU^+\Theta] = \lambda \tag{31}$$

The second section can be discussed in 2 cases as follows: Case 1 is $0 \leq \lambda \leq \frac{1}{n}$. The sum-of-squares of n numbers which sum to 1 achieves the maximum only if one of the numbers is 1 and the others are all 0. Considering the symmetry of the 2, 3, ..., n degree, there are two possible conditions, i.e. $\langle i|U^+\Theta U|i\rangle = \delta_{i1}$ or $\langle i|U^+\Theta U|i\rangle = \delta_{in}$. $U = I$ just satisfies the former condition to our surprise and $J_{max} = 1 + (1 - n)\lambda$. Case 2 is $\frac{1}{n} \leq \lambda \leq \frac{1}{n-1}$. Similar as the former high-school mathematic conclusion, that the sum-of-squares achieves the minimum only when the N numbers are equal, i.e. $\langle i|U^+\Theta U|i\rangle = 1/n, \forall 1 \leq i \leq n$. The solution

of U with the restriction of the N equations above is not impossible to achieve since the general unitary matrix U has N^2 degrees of freedom. As a consequence, we get $J_{max} = 1/n$. Now we will prove the existence of the solution of U . On one hand, denoting the second section as $\alpha = U^+\Theta U$, i.e. $\alpha_{ij} = U_{ik}^+\Theta_{km}U_{mj}$. The elements of the target pure state satisfy $\Theta_{km} = \delta_{k1}\delta_{m1}$ and $U_{ik}^+ = U_{ki}^*$. So,

$$\alpha_{ii} = |U_{1i}|^2 = \frac{1}{n}, \quad \forall i = 1, 2, \dots, n \quad (32)$$

On the other hand, for a general unitary without any restriction,

$$\sum_j |U_{ij}|^2 = 1 = \sum_i |U_{ij}|^2, \quad \forall i, j \quad (33)$$

$$\sum_j U_{ij}U_{kj}^* = 0 = \sum_j U_{ji}U_{jk}^*, \quad \forall i \neq k \quad (34)$$

Obviously, Eq. [32] satisfies the condition that the sum of modular squaring of any row vector is 1 and does not introduce any more restrictions. So, such solutions to the U to get the maximum target function must exist. The 3-level case is just examination in previous discussion.

5 Conclusion and Summary

From the discussion above including the numerical results and the analysis based on the reasonable guessing, we have some rudimental understanding about the optimal quantum measurement between the mixed state and the pure state. In this particular case that the 3-level mixed state is not tangled, the optimal target function only depends on the the relative scale of the eigenvalue projecting to the desire pure state and the maximal eigenvalue of the ones projecting to the other eigenstates. And the searching space reduces in a much smaller dimension which may benefit the multi-measurement cases. Finally, we derive the special case with equal eigenvalues projecting the eigenstates except the desired state from the beginning which verifys the validation of the numerical results and the guessing that may be right probably. However, future works have to be done in such aspects, as the conditions that ϕ_3 is at the edge of its definition region for maximal target function, that the multi-level cases also can ignore the small eigenvalues projecting to the non-desired eigenstates, and the more general cases with multi-measurements.

Acknowledgments. This work is supported by Major Program of National Natural Science Foundation of China (60635040).

A Verification of the Freedom of the 3-Level Unitary Matrix

There are 13 phase items in Eq. [15] and it actually has only 6 free variables rather than 9 apparently. The proof is as below. Rewrite all the linear combining phase expressions in the matrix form following the order as $\theta_{03}, \theta_{13}, \theta_{23}, \theta_{02}, \theta_{12}, \theta_{22}, \theta_{01}, \theta_{11}, \theta_{21}$. With simple computation, the rank of the coefficient matrix is exactly 6, i.e the 13 phase expressions only have 6 independent free variables.

References

1. Shapiro, M., Brumer, P.: Coherent Control of Atomic, Molecular, and Electronic Processes. *Journal Advances in Atomic, Molecular, and Optical Physics* 42, 287–345 (2000)
2. Jalabert, R.A., Pastawski, H.M.: Environment-Independent Decoherence Rate in Classically Chaotic Systems. *Journal Phys. Rev. Lett.* 86, 24–90 (2001)
3. Roa, L., Delgado, A.: Measurement-driven quantum evolution. *Physical Review A* 73, 012322 (2006)
4. Sugawara, M.: Measurement-assisted quantum dynamics control of 5-level system using intense CW-laser fields. *Chemical Physics Letters* 428, 457 (2006)
5. Sugawara, M.: Quantum dynamics driven by continuous laser fields under measurements: Towards measurement-assisted quantum dynamics control. *Journal of Chemical Physics* 123 (2005)
6. Sugny, D., Kontz, C.: Optimal control of a three-level quantum system by laser fields plus von Neumann measurements. *Physical Review A* 77, 063420 (2008)
7. Vilela Mendes, R., Man'ko, V.I.: Quantum control and the Strocchi map. *Journal Physical Review A* 67, 053404 (2003)
8. Zeng, J.Y.: *Quantum Mechanics*, vol. 1. The Science Press (2007)
9. Reck, M., Zeilinger, A.: Experimental realization of any discrete unitary operator. *Journal Physical Review Letters* 73, 58 (1994)
10. Shuang, F., Rabitz, H.: Cooperating or fighting with decoherence in the optimal control of quantum dynamics. *Journal of Chemical Physics* 124 (2006)
11. Shuang Feng, R.H., Dykman, M.: Foundations for cooperating with control noise in the manipulation of quantum dynamics. *Physical Review E* 75, 021103 (2007)
12. Shuang, F., Rabitz, H.: Cooperating or fighting with control noise in the optimal manipulation of quantum dynamics. *Journal of Chemical Physics* 121, 9270 (2004)
13. Gong, J.B., Rice, S.A.: Measurement-assisted coherent control. *Journal of Chemical Physics* 120, 9984 (2004)
14. Alexander, P., Il'in, N., Shuang, F., Rabitz, H.: Quantum control by von Neumann measurements. *Physical Review A* 74, 052102 (2006)
15. Shuang, F., Zhou, M., Pechan, A., Wu, R., Shir, O.M., Rabitz, H.: Control of quantum dynamics by optimized measurements. *Physical Review A* 78 (2008)
16. Shuang, F., Pechen, A., Ho, T.S., Rabitz, H.: Observation-assisted optimal control of quantum dynamics. *Journal of Chemical Physics* 126 (2007)
17. Wang, Y., Wu, R., Chen, X., Ge, Y., Shi, J., Rabitz, H., Shuang, F.: Quantum state transformation by optimal projective measurements. *Journal of Mathematical Chemistry* 49, 507 (2011)
18. Nielsen, M.A., Chuang, I.L.: *Quantum Computation and Quantum Information*, pp. 80–98. Cambridge University Press (2004)

Development of the Infrared Thermal Wave Detection System and Experimental Study

Wei Zhang, Guo-wei Wang, Zheng-wei Yang, Yuan-jia Song, and Guo-feng Jin

203 office Xi'an Research Inst of Hi-Tech Hongqing town, Xi'an P.R. China, 710025

Abstract. As a new non-destructive testing technology, Infrared wave testing technology has lots of virtues, as testing fast, large detection area, non-contact, and etc. Based on studying Systematic on infrared heat wave theories and key technologies, we developed a set of thermal wave detection system, which was suitable for detecting defects in the composite materials and steel shell. We designed several types of specimen which simulated common defects in the solid rocket motor case, and we did experimental study too. The experimental results show that: the infrared thermal wave method for testing the corrosion and the tack defects of the composite materials and steel shell, and detected fast.

Keywords: Thermal Excitation, Infrared Thermal Wave, Composite Materials.

1 Introduction

The Infrared thermal wave detection techniques was a new non-destructive testing technology ,which was rose in the U.S. aerospace and defense area, because of its advantages for fast speed, high efficiency, large observation area and easy online, in-service inspection, so it was attracted widespread attention at home and abroad [1]. Against the structure, materials and process characteristics of the solid rocket motor and the other key equipments, we in-depth studied the thermal wave theory and technology, and we developed a set of thermal wave detection system based on addressing these key technologies, which can do fast and efficient non-destructive testing, so it will have wide applications in aviation, aerospace and defense.

2 The Infrared Thermal Wave Detection Techniques

The theoretical basis of the Infrared thermal wave detection is the thermal radiation heat and the Planck's law. Heat wave theory describes the interaction between the changing temperature field and the material, the infrared thermal wave detection is through the imposition of different forms of heat waves, making the internal structure of the object to be shown by surface temperature differences through the imposition of different forms of heat waves [2]. The surface temperature and the internal structure of materials were closely related to the conduction law of the heat waves within the material. Only after had designed the effective thermal excitation, and we can obtain the heat wave image that was similar with the truth, and determine the exact internal defect information, according to the change of the Surface temperature [3].

The infrared thermal wave method is an active non-destructive testing technology, It's basic principles was that it applied the active control of the thermal excitation on

the detected objects, and we recorded the surface temperature changes by the infrared; achieved the rapid detection and quantitative identification to the defects within the objects, through the collection, analysis and processing of the infrared heat map sequence, the Infrared thermal wave detection principle was shown in the Figure 1[4]. For the common cracks, holes, tacks, Layering, inclusions and other defects, the thermal conductivity of it is less than it of the material itself, so the surface temperature corresponding to the defects was higher than it to the normal area, and it was easy to found the defects by the surface temperature anomalies. For the thermal conductivity defects, the low surface temperature region appears, however, this defect is relatively rare, such as water defects in the cellular composite.

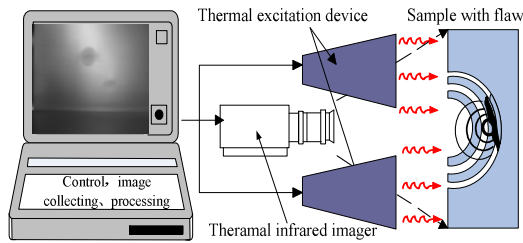


Fig. 1. The block diagram of the infrared thermal wave detection principle

According to the figure 1, a complete infrared heat wave detection system included three parts: the thermal excitation source, infrared imaging equipment, computer control and processing system. Among them, the heat source is the linchpin, the thermal wave was produced and it was transmitted to the surface of the detected object and was used to stimulate material internal defect information; Infrared was the core equipment, it was used to monitor the sample surface temperature distribution and record the data; the function of computer was to control the thermal excitation source and thermal, adjusted the thermal excitation parameters and the collection frequency, At the same time, processed and analyzed the temperature data t collected by the thermal, improved image quality, enhanced the defect contrast, achieved the quantitative identification of defects, and etc[5].

3 Design of the Infrared Thermal Wave Detection System

3.1 System Functional Design

As shown, the falling were specific functions that need to achieve of the infrared thermal wave detection system hardware for solid rocket motors components:

- (1) The flash should trigger timely upon request, heat the measured surface uniformly and can replenish their energy in time quickly;
- (2) The infrared can collect and transport the real-time image information of the measured object surface;
- (3) D/A converter cards can precisely control the flash to trigger and output a variety of DC levels that required.

3.2 Design Requirements

Based on a variety of function for the system to achieve and a good overall performance for the whole system to pursuit, we raised the following specific design requirements in the design of the hardware system;

- (1) The infrared we selected must be accuracy, especially the sensitivity, spatial resolution and image acquisition rate (frame rate), while it was easy extension;
- (2) The thermal excitation can heat the measured surface effective, the energy can be adjustable and replenish; the flash should have long life and can charge and discharge quickly;
- (3) We should ensure to heat the measured objects uniform, which requires a suitable number of flash, reasonable lay-out, uniform heating.

3.3 Performance Analysis and Appraisal

According to design, combined with the testing requirements, we selected the appropriate frame rate, heat sensitivity, working band and lens of the infrared, and we studied on the pulse width of the flash and the heating energy, at last, we got the following conclusions:

- Frame rate: greater than 50Hz;
- Working band: 7.98--9.75 μm ;
- Thermal Sensitivity: better than 0.05 $^{\circ}\text{C}$;
- Lens: 70mm standard lens;
- Pulse width: 0.5ms--15ms;
- Heating energy: 4000J--6000J.

3.4 The Implementation of the Infrared Thermal Wave Detection System

According to the practical needs for defecting rocket engine, and based on studying the infrared thermal wave detection techniques theory in-depth, then determined the functional requirements, the performance indicators and the structural design, at last we completed the formation of the whole system.

4 Experimental Study

The solid rocket motor case generally used the metal steel or the composite materials. In order to test the effectiveness of the system for defecting detection inside the metal and the composite steel shell, We designed several types specimen that simulated different defects in the shell structures, did the preliminary experimental study by using the infrared thermal wave detection system that We had developed, and we made the preliminary processing and analysis of the experimental results preliminary.

4.1 Detection of the Steel Shell Corrosion Defect That Simulated by Flat Hole

1) The Description of the Specimen

The steel corrosion defects general simulated by a flat-bottomed cave or a wedge-shaped groove.

This specimen made of metal steel, 280mm Length, 200mm width, 6mm thick, eight flat-bottomed Caves processed on the back, the diameter of the top four was identical

20mm and the depth of them were respectively 2mm, 3mm, 4mm, 5mm; The depth of the bottom four was 1mm and the diameter of them were respectively 5mm, 10mm, 16mm, 20mm(As shown in the Figure 2). Choosing of the experimental parameters: the frequency of the Image acquisition was 50Hz, the acquisition time was 20s and the ambient temperature is 22°C.

2) The Experimental Results and Analysis

The original thermal wave image of the experiment was shown in the Figure 3, the figure shown that the defects which were larger and shallow appeared firstly, as the time went on, diameter, the flaws which were smaller and deeper began to emerge, then became more and more clear, approximately in the 0.64 sec, the contrast between the hot spots and the surrounding environment got maximize, Then began to fall down, approximately in the 1.96 sec, the hot spot of the flaw whose diameter was smallest disappeared firstly, then approximately in the 3 sec, the hot spots of the flaw whose depth was deepest disappeared, while the other hot spots gradually became blurred and the surface temperature field tended to be uniform

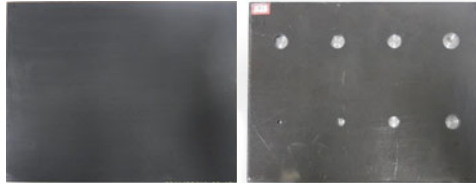


Fig. 2. The specimen physical map, (left) specimen positive; (right) specimen back

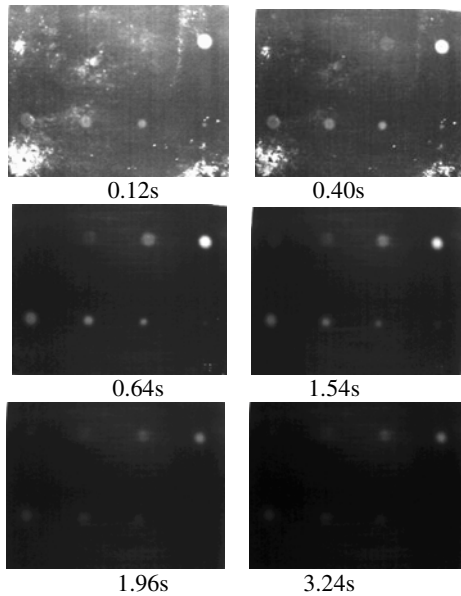


Fig. 3. The original infrared wave images of the specimen detection

As shown in the Figure 4: L1 was the line which was on the center of the top four flat-bottomed Caves, L2 was the line which was on the center of the bottom four flat-bottomed Caves, the line temperature distribution was shown in the Figure 4, the figure shown that: the temperature of the defects location was significantly higher than the ambient temperature, and we can extract the exact position and the diameter information according to line temperature distribution.

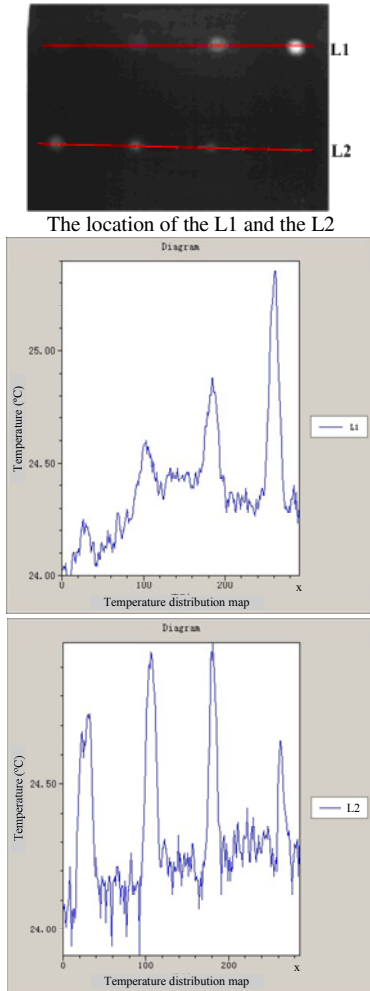
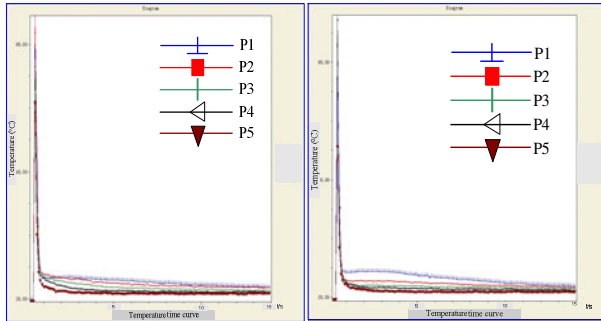


Fig. 4. The line temperature distribution L1 (top) and L2 (lower)

For the more study in-depth of the surface temperature change process, we extracted the temperature of the surface defects and the normal region respectively, as shown in the Figure 5. The points P1, P2, P3, P4 were the center of the defect region, and the point 5 was the center of the normal region, we can found that the surface temperature rose sharply at the heating Instantaneous, at the moment it reached about 65°C, then it

decreased rapidly, at first decline fast, then it gradually slow down. Finally, the surface temperature tended to the ambient temperature.



(a) The defects with the same diameter (b) The defects with the same depth

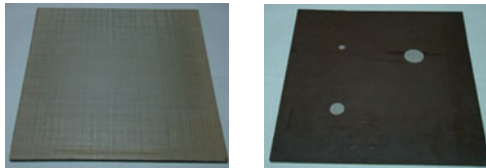
Fig. 5. The surface temperature curve corresponded to the center of the defects

Experimental results show that: the effect of detection for the solid rocket motor internal defects by infrared thermal wave detection system was very significant.

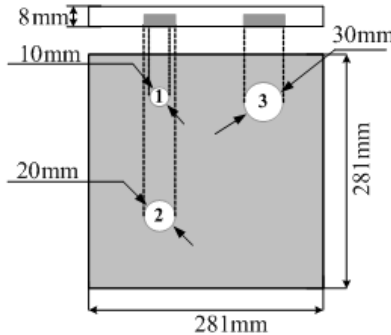
4.2 The Detection of the Glass Fiber Composite Materials Tack Defect

1) The Description of the Specimen

The specimen made by the fiberglass material, 281mm length, 281mm width, 8mm thickness, there were 3 flat-bottom hole tack-defects, whose depth was 5mm, and the diameters were respectively 30mm, 20mm and 10mm(As shown in the Figure 6).



The Specimen physical map (left) specimen positive; (right) specimen back



(C) The design of the specimen defects

Fig. 6. The composite / insulation off specimen

2) Experimental Results and Analysis

The original thermal wave image of the experiment was shown in the Figure 7, the figure showed that the larger two defects began to be felt through the hot spots on the surface approximately in the 5 sec, as the time went on, then it became more and more clear; approximately in the 15 sec, the contrast between the hot spots and the surrounding environment got maximize, then it began to fall down, however, the smallest defect did not apparent; and after the 27 sec, the hot spots of the other two larger defects were slowly became blurred. According to the analysis, during the experiment, the serious surface reflective of composite specimen affected the quality of image acquisition.

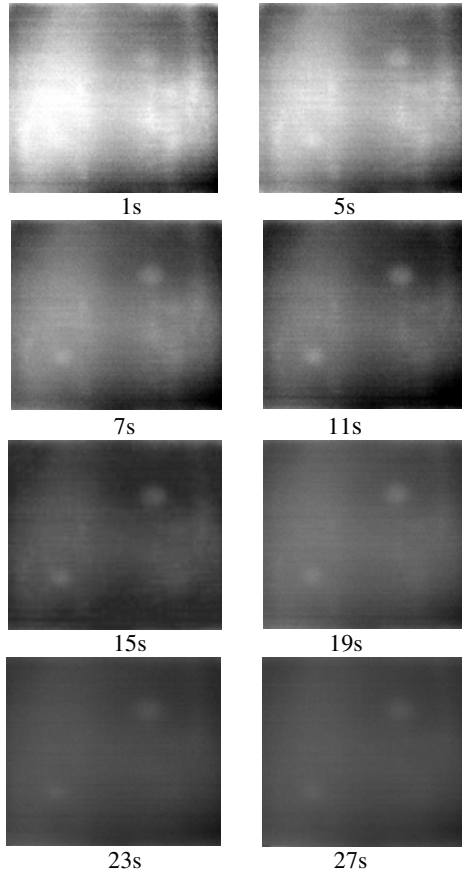


Fig. 7. The original infrared wave images of the specimen detection

And the Figure 7 showed that: the infrared image obtained from the infrared thermal wave detection was rich in lot of defect information, the surface temperature anomaly area corresponded to the location of defects inside the material, and the different sizes defects can be performance of different sizes surface hot spots. The brightness of the hot spots were corresponding to the surface temperature of the defect region, and the

higher the temperature, the greater the brightness, the best time to identify defects was in the 7s - 19s, while the display of defects were the best.

5 Conclusion

Through studied the infrared thermal wave theory, and carry out system design and development, we had completed the infrared thermal wave detection system. Through the experiment, we got the following conclusions:

1) The effect of detection for the solid rocket motor internal defects by infrared thermal wave detection system was very significant;

2) The speed of the infrared thermal wave detection was very fast, and the better the thermal conductivity of the material, the faster the detection (such as the deflection for the steel shell corrosion defects);

3) The infrared thermal wave detection system used the pulse excitation method, but the test result of the detection for composite defect was poor, and that mainly due to the higher reflectivity of the composite materials surface, so the quality of the image is not well.

4) The infrared thermal wave test results were visually, we can determine the size and location of the defects by observing the infrared images.

References

1. Berger, J.T.: Thermo Graphic Detection of Impact Damage in Graphite Epoxy Composites. *Material Evaluation* 50(12), 1446–1453 (1992)
2. Lv, Z.-C., Tian, Y.-P., Zhou, K.-Y.: Study on the Thermal Excitation in the Infrared Thermal Wave Nondestructive Testing. *Nondestructive Testing* 29(6) (2005)
3. Yang, X.-L., Lv, B.-P., Xian, M.-L.: Heat Stimulating Methods in the Infrared Thermal Image Testing of Airplane composite. *Nondestructive Testing*
4. Yang, Z.-W., Zhang, W., Tian, G.: The Thermal Wave Quantitative Detection of the Small Curvature Shell Bonding Structure Tack Defects. *Materials Engineering* (12), 39–43 (2010)
5. Zhang, W., Wang, Y., Yang, Z.-W.: Powder, The Infrared Heat Waves Detection of the Glass fiber composites layer defect. *Nondestructive Testing* (11), 37–41 (2010)

A Study on Micro Grooving Using PZT Actuator

Pradipta Vaskar Biswas¹, Se-Yun Lee¹, Kyung-Hwan Hwang^{1,*},
Dong-Bae Kang², and Jung-Hwan Ahn²

¹ Mechanical and Intelligent Engr., Pusan National University, Republic of Korea
hkhnow@pusan.ac.kr, seyun2@pusan.ac.kr, pvbiswas@yahoo.com,

² Mechanical Engr., PNU and ERC/NSDM, Korea
dbkang@pusan.ac.kr, jhwahn@pusan.ac.kr

Abstract. Flat display panels are becoming more popular, day-by-day. Therefore, optical quality has been a major concern in recent years. In flat display panels, micro-features with such optical features as grooves and lens should be manufactured within tight form accuracy because it is directly related to their optical performance. This study presents a PZT based vibration cutting method to ensure a smoother and more uniform cutting surface in machining of micro grooves using a single crystal diamond tool. Experiments prove that the proposed method is an efficient way to produce high quality micro grooves on a flat plate die surface.

Keywords: PZT actuator, Vibration Cutting, Micro Grooving.

1 Introduction

In recent years, flat display panels have increased in popularity. Use of flat displays is increasing due to this high demand as well as to the technological development of the optical performance of the display. In manufacturing, it is technically challenging to maintain a certain level of form accuracy and surface roughness for micro-features.

In the Liquid Crystal Display (LCD), the Light Guide Plate (LPG) and Black Light Unit (BLU) play an important role in scattering the incident light over the entire display area. The basic idea is to scatter the light uniformly. To do so, many long prismatic-shaped, parallel micro-grooves are created uniformly by injection molding or micro-grooving. Among these options, injection molding is the most popular method for mass production. Many micro-grooves are manufactured with the help of micro precessing machines, and a comparison between injection molding and micro-grooving methods shows that more uniform characteristics can be achieved by micro-grooving. This is because the micro-grooving process produces much less heat, resulting in no chance of thermal deformation.

Therefore, even if a die is machined using a very precise and stiff tool, the tool deflection caused by the cutting force can create inaccurate grooving. This results in the non-uniform prismatic shape. As such, tool deflection minimization is critical to uniformity.

* Building #3216 MI Laboratory, School of Mechanical Engineering, Pusan National University
Jangjeong 2-dong, Gumjeong-gu, Pusan, Korea ZIP 609-735.

In this study, The PZT based vibration cutting method and tool holder design was developed to compensate for the cutting vibration. Tool vibration, along the cutting direction and in the transverse direction, was studied to maximize the performance. An AE sensor was used to monitor the vibration while cutting the workpiece to determine the real time vibration on the surface. Its feasibility is examined through application to alumina plates.

2 Design of Vibration Cutting Tool

2.1 Vibration Cutting Process

Fig. 1 shows a schematic of a vibration cutting overcoming the limitations of the conventional process. Through a micro actuator, like PZT, the cutting tool vibrates at a frequency that avoids the natural frequencies of the machine structure. When the cutting tool vibrates, the workpiece is fed in the forward direction and the material is removed repeatedly through sequential cutting. Thus, a relative motion exists between the workpiece and the cutting tool. With the help of PZT the tool vibrates along the cutting direction as if it creates a sweeping motion according to the vibration rate. Thus the applied frequency of the cutting tool is very important in regard to the vibration cutting as it defines the maximum cutting speed that can be applied.

During the cutting process, a workpiece sheet is vacuum chucked and then fed in the X direction at a very high speed using a linear motor that is adequate for high velocity and acceleration. With a servo motor a linear feed is given along the Y direction after every stroke along the X direction.

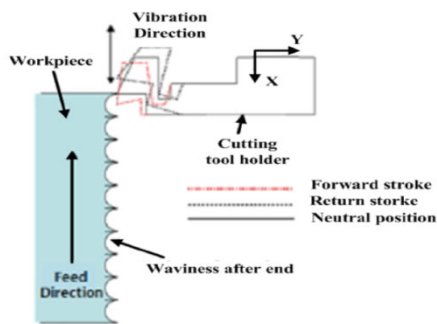


Fig. 1. Schematic of vibration cutting

2.2 Design and Dynamic Analysis of Tool Holder

In order to realize better surface quality and better cutting performance, the vibration tool holder technique, based on PZT actuator, is chosen. Fig. 2(a) shows the design of the cutting tool holder.

When the PZT actuator is inserted in the extracted empty space of the cutting tool holder, it repeatedly expands and shrinks according to the control signal. Deflections occur in the vertical direction of the tool tip because the notch in front of the cutting

tool holder acts as a hinge point that is identical to the mechanism of a cantilever beam. Two steel balls are also inserted at opposite ends to ensure the point contacts between the PZT actuator and the cutting tool holder, because the eccentricity of the center-line along the direction of vibration causes significant and unexpected deflections of the tool tip. The preload bolt, located in front of the tool tip, makes it possible to adjust the resonant frequency, slightly, for any mismatch in the resonant frequencies that arises from errors in the machining of cutting tool holder or the notch.

The cutting parameters, with related in vibration cutting, are shown in Fig. 2(b). Their relations are described, as follows:

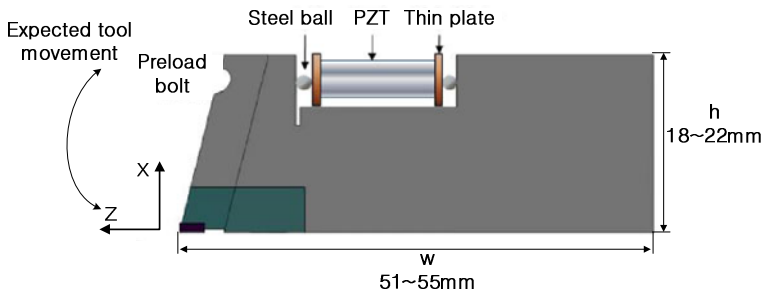
$$x = a \sin wt = a \sin 2\pi ft \tag{1}$$

$$V_t = 2\pi fa \cos(2\pi ft) \tag{2}$$

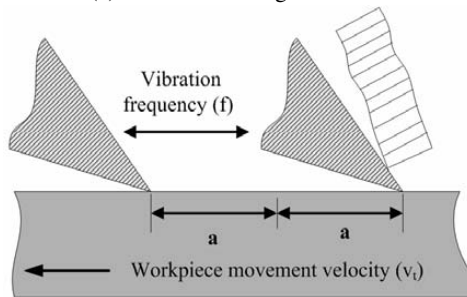
$$(V_t)_{\min} = 0 \tag{3}$$

$$(V_t)_{\max} = 2\pi fa \tag{4}$$

In the above equations, V_t is the cutting speed, a is the amplitude of the vibration cutting tool, and f is the oscillating frequency. As noted in the equations above, it is clear that the cutting speed, the amplitude, and the applied frequency are organically related. If the applied cutting speed exceeds V_t , the cutting will transform from conventional cutting to vibration-assisted cutting.



(a) Vibration cutting tool holder



(b) Principle of vibration cutting

Fig. 2. Proposed mechanisms of vibration cutting tool holder

2.3 Dynamic Analysis of Cutting Tool Holder through Simulation

Zhang et al. [1] experimentally investigated the possibility that an increase of the vibrational amplitude of the tool in the UVC system improves the cutting quality. Their findings were theoretically implemented by others [5-7]. However, the larger the expansion distance of the PZT actuator, the smaller the expansion force. This means that, even under a notch mechanism, a large displacement cannot be achieved at high frequency due to the weak expansive force. Thus, the most effective approach is to vibrate the cutting tool in the range of the resonant frequency.

Fig. 5 shows the mode shapes of the cutting tool at its natural frequencies for the first and second modes obtained from ANSYS Workbench. During the second mode, at a frequency of approximately 7 to 11 kHz, the cutting tool vibrates in the previously explained X direction, which represents the desired direction of cutting.

Resonance will be present if the same frequency is applied in the cutting tool using the PZT actuator as the natural frequency of the vibration cutting tool. In this case, the tool tip deflection will be the same as found in the deflections caused by the PZT expansion force and the deflection caused by resonance, as the two deflections are at the same phase of the frequency.

Fig. 3 shows the variable notch size tool holder. Research has shown that if the height (a) of the notch increases, then the tool holder stiffness decreases and, in case of width (b), if the notch increases then the transverse vibration along the X

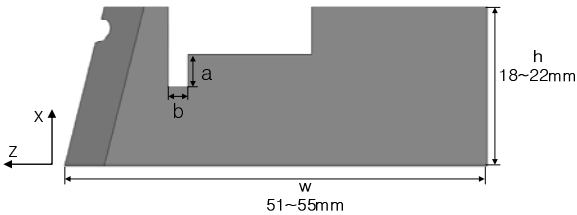


Fig. 3. Variable notch size for tool holder

Table 1. Simulation results with a forced vibration tool holder

Model (h × w)mm	Vibration Mode(Hz)		
	1st	2nd	3rd
18×51	6967.1	9346.9	19559
18×53	5781	7821.7	16989
18×55	8387.3	7095.8	15813
20×51	7008.5	10693	19700
20×53	5814.5	8959.2	17058
20×55	5435.7	8176.4	15865
22×51	7009.3	11906	19601
22×53	6159.1	10398	17362
22×55	5466.7	9185.8	15730

direction increases, as well. This eventually causes the In Fig. 3 variable notch size tool holder. From the research it has been seen that if the height (a) of the notch increases then the tool holder stiffness decreases and in case of width (b) if it increases then the transverse vibration along the X direction increases. Which eventually causes the natural frequency of the tool holder to decrease. Therefore, to minimize these effects, the best notch dimension is $2\text{mm} \times 0.5\text{mm}$ (a**x**b).

Table 1 lists the simulation results of the modal analysis for the vibration cutting tool and forced vibration of the tool holder for different dimension (h**x**w) with PZT excitation. Fig. 4 shows the curve for the second vibration mode from the Table 1 for different tool holders.

3 Displacement Measurement of Vibration Tool

3.1 Configuration of Displacement Measurement System

The cutting speed is related to both the tool tip deflection and the applied frequency. A basic investigation of tool tip deflections is necessary to determine the critical cutting speed or the feedrate of the workpiece sheet at various applied frequencies. Fig. 6 shows a schematic diagram for investigation of the displacement of the designed vibration cutting tool. The PZT actuator, P-885.30, (Physik Instrumente, Germany) is used for actuating the cutting tool with a high speed bipolar amplifier.

The tool tip deflections are measured using two laser displacement sensors with a resolution of 50 nm and sampling rates of up to 50 kHz in a direction perpendicular to each other along the X and Y directions. This was done to measure the vibrational displacement of the cutting tool along the X direction and Y direction.

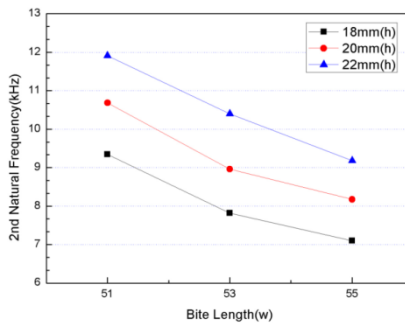


Fig. 4. Second resonant frequency of the tool holder in PZT excitation

PZT was actuated by using the signal from a function generator through the PZT amplifier. Both of the laser sensor signals were amplified with a sensor amplifier. The signal was then analyzed using the DAQ board attached to a PC. An oscilloscope was connected to the sensor amplifier to investigate the real signal.

Previous research [1-3, 8-9] has shown that tool tip deflections are maximized at the natural frequency of the cutting tool. Thus, the applied voltages are fixed at 10, 20, and 30V and are varied from 7 kHz to 12 kHz in order to identify the optimized oscillating frequency with a maximum displacement.

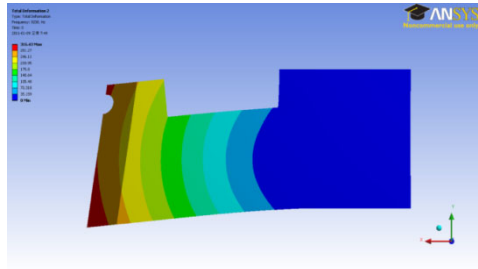


Fig. 5. Vibration of tool holder in the second vibration mode

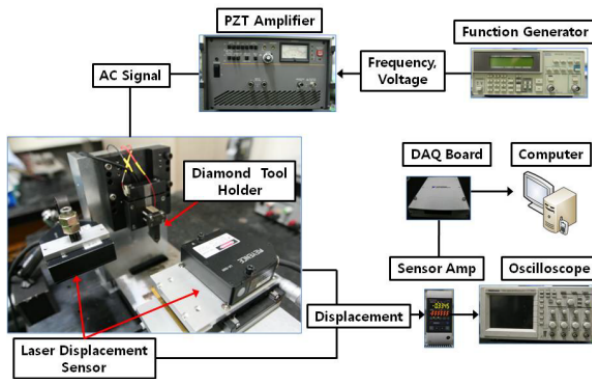


Fig. 6. Schematic diagram of the vibration cutting system

Table 2. Specification of the PZT vibrator

Model	P-885.31
Travel range for 0 to 100V	11 [μm] $\pm 20\%$
Max displacement	13 [μm] $\pm 20\%$
Blocking force at 120V	870 [N]
Push / Pull force capacity	1000/5 [N]
Stiffness	67 [N/ μm]
Resonant frequency	90[kHz] $\pm 20\%$

3.2 Measurement of Displacements

The experimental results for the second model frequency of the specified PZT vibrator, shown in Table 2, were almost the same as the theoretical results. In Fig 8(a), displacement of the vibration tool holder along X-axis was shown for the different bit lengths (w) for the three distinct voltages, i.e., 10V, 20V, and 30V. In Fig. 8(b), the displacement of the vibration tool holder was shown along the Y direction for the same conditions noted in Fig. 8.(a)

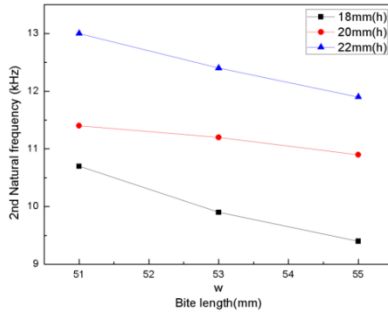


Fig. 7. The second resonant frequency of vibration tool holder

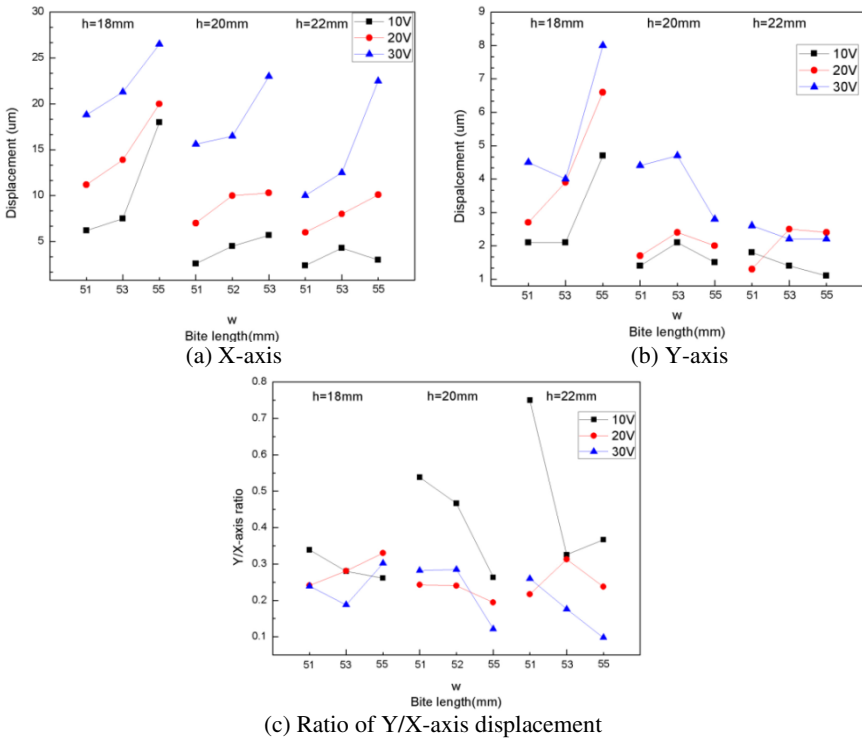


Fig. 8. Displacements of the vibration tool

According to the simulation results, the vibration of the tool holder should occur only along the X direction. However, from a practical standpoint, it also vibrates along the Y direction. Investigation shows that this Y-directional vibration arises from the preload bolt of the PZT, the eccentricity of the PZT load, and inevitable manufacturing and assembly errors. Therefore, it is necessary to find the optimized value for the Y-directional vibration. To do so, Y to X-axis vibrational ratios were plotted, in Fig. 8(c), to determine the minimum value for the different bite lengths (w) of the three distinct voltages, as previously mentioned. For the 30V, the minimum Y/X-ratio was found to be $22 \times 55(h \times w)$. We used 30V, because would provide the maximum power for the vibration of the PZT and thus for the cutting.

4 Experiments of Micro-grooving with Vibrational Tool

4.1 Machine Tool for MICRO GROOVING

Fig. 9 shows a schematic diagram of the micro-grooving machine tool. The machine tool is comprised of three axes, X, Y, and Z. The X-axis is guided by an air bearing, with negligible friction, and driven by a coreless linear motor. The Y and Z axes are actuated by core-typed linear motors, with a resolution of $0.1 \mu\text{m}$. The effect of the motion error on the micro-groove form error is negligible because the straightness of the air bearing is below $0.1 \mu\text{m}$. is executed by a motion controller, PMAC.[10].

4.2 Experimental Setup

In our system, a micro precision machine was used. The machine has three degrees of freedom, mounted with a flat groove diamond tool. The tool holder is mounted with a PZT, actuated with a signal from the function generator with the help of a function generator and an amplifier. The workpiece is mounted with an AE sensor to detect the vibration while cutting the workpiece. The AE sensor is connected with a DSP, which transmits the data through Bluetooth to the remote PC.

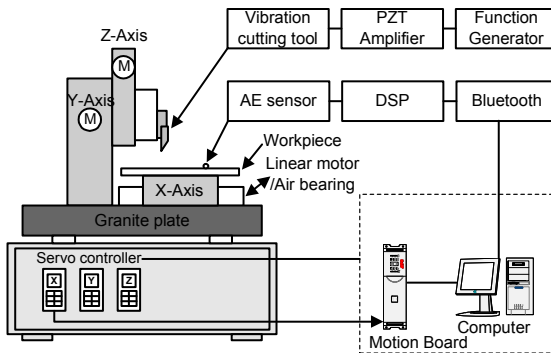


Fig. 9. Micro-grooving machine tool system

Table 3. Specifications of AE sensor

Model No.	Nano30
AE Amp	Charge amp + main Amp
Gain	x1, x10, x100, Dip switch
Filter	5kHz ~500kHz
A/D Resolution	12Bit, 200KSps
Transmission	11520 bps

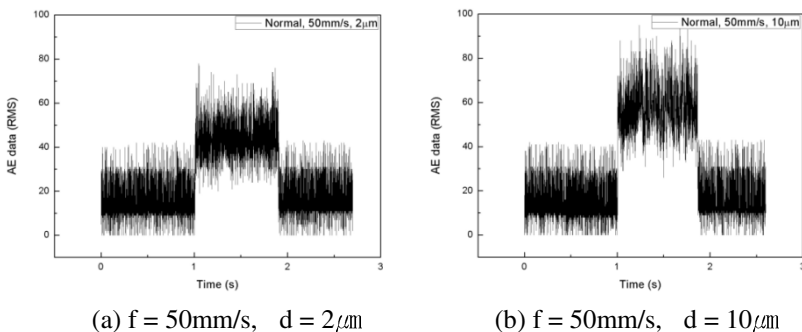
The tool holder has a built-in PZT actuator that compensates for the vibration of the cutting force. Table 3 shows the specifications of AE sensor developed in this study.

4.3 Experimental Result

Fig. 10 and Fig. 11 show the AE sensor signal while cutting is conducted in both the normal mode and in the vibration mode, respectively. In cases of normal cutting mode, the signal is smooth for a low depth of cut. This is because when the cut has less depth, the cutting force is also less and the vibration is lower. In case of higher depth of cut the cutting back force is larger which causes larger amplitude for the RMS signal.

For vibration cutting mode, in case of lower depth of cut the RMS signal is small in amplitude compared with the higher depth of cut. This is due to small amount of cutting back force in case of less depth of cut. For higher depth of cut, tool cannot vibrate well for the higher force and larger depth, rather the cutting force vibrates the tool so high amplitude and rough RMS signal is observed.

So from the AE signal it is possible to notice and monitor how bigger or smaller depth of cut we are using for micro grooving by observing the signal amplitude.

**Fig. 10.** AE signal for normal cutting

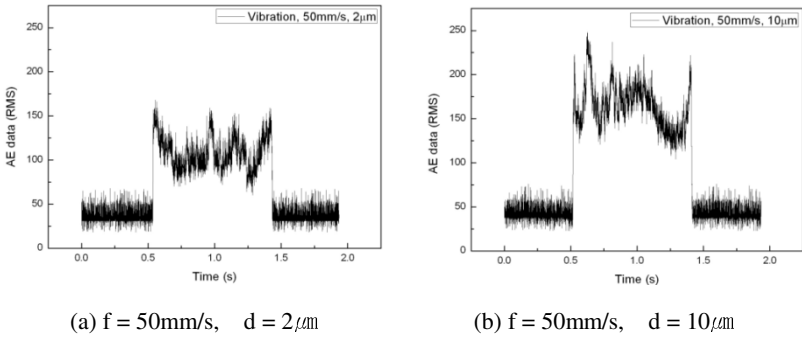


Fig. 11. AE signal for vibrationl cutting

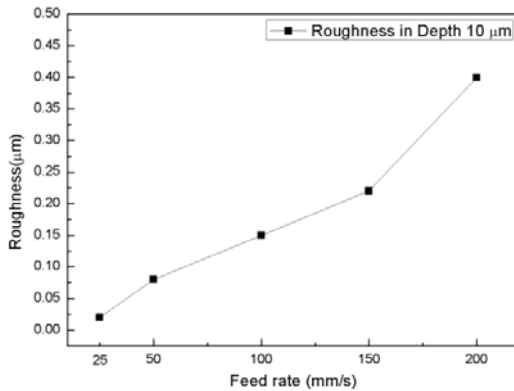


Fig. 12. Surface roughness versus feed rate

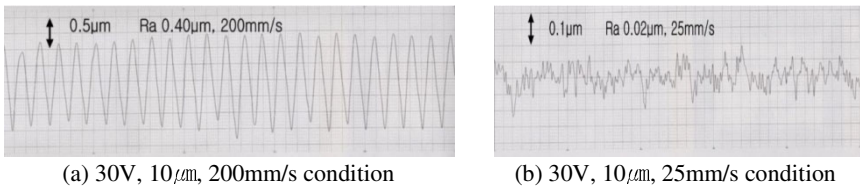


Fig. 13. Surface roughness profile

As shown in Fig. 12, if the feed rate is low then the vibration cutting method can efficiently cut the surface, resulting in decreased roughness. Fig. 13(a) and 13(b) also verify these situations.

5 Conclusions

In this paper, the vibration cutting process was introduced as a way to improve surface roughness. Furthermore, this paper compared this approach with the

conventional machining process. piezoelectric devices were mounted to the diamond tool holder to create vibration with micro-grooving system, as follows:

- 1) Compared to non-vibration cutting mechanisms, the vibration cutting mechanism decreases the cutting force by approximately 30~50%. It also decreases the surface roughness by approximately 30~70%. Therefore, vibration cutting applied to optical components can improve the machining accuracy of these components as well as the longevity of the tool life.
- 2) Higher feed rate and depth of cut can be used with a low surface roughness, as compared to conventional non-vibration machining mechanisms, with vibration cutting.
- 3) Using piezoelectric actuators, combined with the dual-servo system, it is possible to decrease the errors along the Z-axis to 1 μ m, even with a high feed rate.

Therefore, vibration cutting can increase the efficiency and accuracy of the micro-grooving process and extend the life of the tool. As a result, the vibration cutting mechanism can be effectively applied to a large surface area if piezoelectric actuators, is used.

References

1. Zhang, Y.-L., Zhou, Z.-M., Xia, Z.-H.: Diamond turning of titanium alloy by applying ultrasonic vibration. Transactions of the Nonferrous Metals Society of China 15(Special 3), 279–282 (2005)
2. Nath, C., Rahman, M.: Evaluation of Ultrasonic Vibration Cutting while machining Inconel 718. International Journal of Precision Engineering and Manufacturing 9(2), 63–68 (2008)
3. Morihiko, S., Heiji, Y., Kondo, S., Kawada, M., Akira, H.: Experimental Investigation of Surface Roughness in Ultra-Precision Cutting of Plastics. Journal of the Japan Society for Precision Engineering 67(2), 311–315 (2001)
4. Brehl, D.E., Dow, T.A.: Review of vibration-assisted machining: Precision Engineering, vol. 32, pp. 153–172 (2008)
5. Kim, J.D., Choi, I.H.: Characteristics of chip generation by ultrasonic vibration cutting with extremely low cutting velocity. The International Journal of Advanced Manufacturing Technology 14, 2–6 (1998)
6. Babitsky, V.I., Kalashnikov, A.N., Meadows, A., Wijesundara, A.A.H.P.: Ultrasonically assisted turning of aviation materials. Journal of Material Processing Technology 132, 157–167 (2003)
7. Jin, M., Murakawa, M.: Development of a particle ultra-sonic vibration cutting tool system. Journal of Material Processing Technology 68, 342–347 (2001)
8. Zhang, G.P., Huang, Y.M., Shi, W.H., Fu, W.P.: Predicting dynamic behaviors of a whole machining tool structure based on computer-aided engineering. International Journal of Machine Tools & Manufacturing 42, 699–706 (2003)
9. Jang, S.H., Kim, S.M., Kim, S.G., Choi, Y.H., Park, J.K.: Structure design optimization of a micro milling machine for minimum weight and compliances using Genetic algorithm. In: Proceedings of the 3rd IWMT, pp. 23–24 (2007)
10. Kang, D.B., Son, S.M., Ahn, J.H.: Real-time geometric error compensaton in micro grooving the workpiece with large surface area. Key Engineering Materials 339, 314–320

The Test Principle and Algorithm of Laser Measuring Tree Height

Hong-e Ren* and Wei Yan

Forest Woodworking Machinery Research and Development Center, Northeast Forestry University, Harbin Heilongjiang 150040, China
renhonge163@163.com

Abstract. Survey of tree height always plays an important role in forest production, investigation, scientific research and education. This paper presents works, measurement process of measuring tree height in laser and the precision compute. This paper presents two measurement methods, to elucidate the conceptual and practical feasibility of the measurement provided in this paper, respectively by comparing the two typical measurement methods which significantly reduce the measurement error. The result reveals that its better performance, much more efficient and convenient to deploy and work than previous altimeter instruments.

Keywords: laser, tree height measurement, precision analysis, principle.

Foreword

Commonly, it is much more difficult to measure standing tree than the felled tree, due to the unfavourable standing position. In the survey and production of the tree, it is often measuring tree height before cutting down the tree, even unnecessarily. This is a difficult and crucial problem in the forest and production survey [1]. Till now, scientists have already launched several types of measurement instrument to solved this problem, but suffered the low precision relatively. Subsequently, it can not meet the accuracy requirements of tree measurement in forestry. Nevertheless, neither does these conventional forest measuring tools (such as tape measure, optical compass, altimeter device and around the foot, etc.) reach the standard^[2]. Some of these devices require to measuring the horizontal distance by tape, others need to measuring the angle by the related equipment, so it brings a lot of inconvenience.

With the development of science and technology, Laser, ultrasonic range finder and other advanced measuring instruments has come out. The method in this paper combined the technology of laser with the tree measuring instrument in order to make the operation more convenient and simple. It manages to eliminate many tedious measurements and calculations, thus it would greatly improve the efficiency of forest inventories.

* Corresponding author. Hong-e Ren, Ph.D., professor, Ph.D. supervisor. Field of research: Image processing and pattern recognition, optimized design and computer-aided modeling etc. Tel.: 0451-82192077.

1 Laser Measuring Instrument Works and Its Tree-Precision Computation

1.1 Principle of Laser Ranging

Usually, There are two ways to measure distance with laser rangefinder: Pulse and the phase. Phase-shift laser rangefinder modulate amplitude of the laser beam with frequency of radio band and measure the phase delay of modulated light during the time for a single round-trip, then conversion from phase delay into distance which is according to the wavelength of modulated light. That is how the time delay measured indirectly by comparing the signal from the laser with the delayed signal returning from the target. Phase-shift laser rangefinder is generally used in precise measurement. In order to effectively reflected signal, this kinds of range finder is configured to be known as cooperation objective mirror. Nowadays, it recommend handhold laser rangefinder in the market. It is a new pulsed kind of laser rangefinder, it is not only have a small size and light weight, but also adopt the technology of measuring phase with digital and pulse broadening, it can achieved the millimeter accuracy level without cooperation object. Measurement range over 100m and it can quickly, accurately and directly display the distance[6].

As is shown in Figure 1, this paper adopt the principle of pulsed laser ranging, transmitter of scanner emit laser beam of near-infrared wavelength to the target through the laser diode. Laser diffuse reflection occurs after through the target, part of the reflected signal received by the receiver. The distance between transmitter to target is measured through calculating the round-trip time of the signal in the surface of instrument and the target, then, we got the distance between them by several computing steps[4].

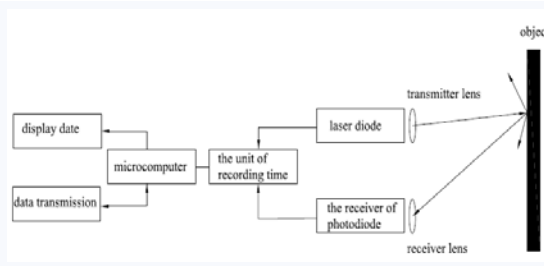


Fig. 1. Schematic diagram of pulsed laser ranging

1.2 The Principle of Laser Measuring Tree Height

Figure 2(a) shows the instrument in a certain distance away from the tree which would be measured, there should be easy to observe top of tree and tree feet. Next, we aligned the laser beam with the foot tree by the telescope. Then, the instrument is ready for measurement.

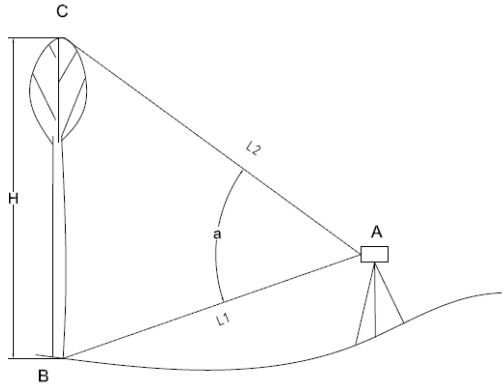


Fig. 2. (a). Schematic diagram of laser measuring tree height

Firstly, observe the distance (L_1) with the telescope when the laser beam is aligned with the foot tree, it is the first data we need; rotate up the instrument until the laser beam is aligned with the top of the tree and then observe the angle (a), it is the second data we need; Keep the angle constant, measuring the distance (L_2) between A and C and it is the third data we need.

Whether the terrain is flat or not, the result of this measurement method would not be affected. And it can simply and fast obtain the calculated parameters. The formula of tree height calculation:

$$H = \sqrt{L_1^2 + L_2^2 - 2L_1L_2 \cos a} \tag{1}$$

In the formula: H represents the tree height; L_1 represents the distance between the measuring point(A) and the tree foot(B); L_2 represents the distance between measuring point and the top of the tree; a represents the angle which the measurement instrument rotated from tree foot to the top of the tree.

The dense foliage of trees will block the laser beam when measuring the distance L_2 (the distance between the measuring point and the top of the tree), and then the measured value are not the true value of L_2 , that is that measurement errors exist. We will modify the above method to get the following measurements.

Figure 2(b) shows, placed the instrument in a certain distance (A) away from the tree which would be measured. We need to measure four parameter : the distance L_1 between A and B; the horizontal distance L_0 between the measurement point and the trunk; the angle a_1 between AB and AD , the angle a_2 between AC and AD. The formula of tree height calculation:

$$H = H_1 + H_2 = L_1 \sin a_1 + L_0 \tan a_2 \tag{2}$$

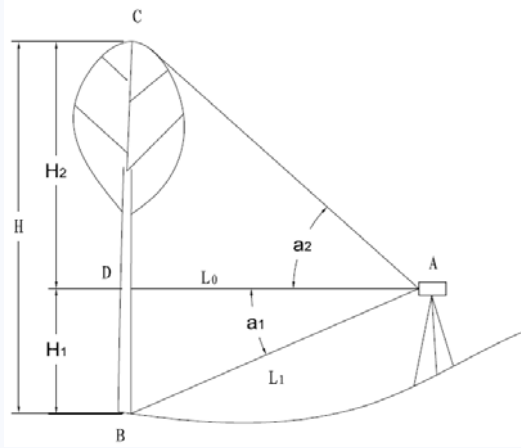


Fig. 2. (b). Schematic diagram of laser measuring tree height

1.3 Accuracy Calculation

(1) Compute the internal accuracy and external accuracy for the formula (1) of tree height calculation and finally determine the overall accuracy[1].

① Compute the internal accuracy

compute the total differential for the formula (1) of tree height calculation:

$$HdH = (L_1 - L_2 \cos a)dL_1 + (L_2 - L_1 \cos a)dL_2 + L_1L_2 \sin a d\left(\frac{a}{\rho}\right) \tag{3}$$

According to the law of erroneous propagation:

$$(Hm_H)^2 = (L_1^2 - L_2^2 \cos^2 a)m_{L_1}^2 + (L_2^2 - L_1^2 \cos^2 a)m_{L_2}^2 + (L_1L_2 \sin a)^2 \left(\frac{m_a}{\rho}\right)^2 \tag{4}$$

In the formula: m_H represents middle errors of H ; m_{L_1} represents middle error of L_1 ; m_{L_2} represents middle error of L_2 ; m_a represents middle errors of a . Then

$$\sigma_{x内} = \sqrt{\frac{\sum(Hm_H)^2}{n}} \tag{5}$$

② compute the external accuracy

$$\sigma_{x\text{外}} = \sqrt{\frac{\sum(x_i - x_0)^2}{n}} \tag{6}$$

In the formula: x_i represents true value; x_0 represents value from doing experiment. According to the formula (5) and (6): the total accuracy

$$\sigma_x = \sqrt{(\sigma_{x\text{内}})^2 + (\sigma_{x\text{外}})^2} \tag{7}$$

Its errors of measurement: σ_x / x_0 , it is required the error of tree measurement should be less than 5% in forestry.

(1) Compute the internal accuracy and external accuracy for the formula (2) of tree height calculation.

① Compute the internal accuracy

compute the total differential for the formula (2) of tree height calculation:

$$dH = L_1 \cos a_1 d\left(\frac{a_1}{\rho}\right) + \sin a_1 dL_1 + L_0 \sec^2 a_2 d\left(\frac{a_2}{\rho}\right) + \tan a_2 dL_0 \tag{8}$$

According to the law of erroneous propagation:

$$m_H^2 = L_1^2 \cos^2 a_1 \frac{m_{a_1}^2}{\rho^2} + \sin^2 a_1 m_{L_1}^2 + L_0^2 \sec^4 a_2 \left(\frac{m_{a_2}}{\rho^2}\right) + \tan^2 a_2 m_{L_0}^2 \tag{9}$$

In the formula: m_H 、 m_{L_0} 、 m_{L_1} 、 m_{a_1} 、 m_{a_2} Separately represent middle errors of H 、 L_0 、 L_1 、 a_1 、 a_2 . Than

$$\sigma_{x\text{内}} = \sqrt{\frac{\sum m_H^2}{n}} \tag{10}$$

② Compute the external accuracy

$$\sigma_{x\text{外}} = \sqrt{\frac{\sum(x_i - x_0)^2}{n}} \tag{11}$$

In the formula: x_i represents true value; x_0 represents value from doing experiment. According to the formula (10) and (11): the total accuracy

$$\sigma_x = \sqrt{(\sigma_{x\text{内}})^2 + (\sigma_{x\text{外}})^2} \tag{12}$$

Its errors of measurement: σ_x / x_0 , it is required the error of tree measurement should be less than 5% in forestry.

2 The Implementation Process of Laser Measuring Tree Height

This paper introducing tree height measurement by the instrument of laser measuring tree height, the tree height can be directly measured without any other aid (such as tape). Measurement process shown in Figure 2 (b):

(1) Choose a location which should be able to see both the top of trees and the tree feet. The site can be on the slope surface or a flat surface; the horizontal light of laser beam should pass through the trunk.

(2) Measure the distance (AB) between the instrument and tree foot. Make sure the laser beam is aligned with the tree foot and then measured the distance (AB) L_1 .

(3) Rotate the instrument until it cover the horizon, then measure the angle α_1 ; Hold on this position and measure the horizontal distance (L_0) between the instrument and the trunk.

(4) Continue to rotate the instrument to the location of the top of the tree and measure the angle (α_2), which is the inclination of the instrument relative horizontal position, instead of measuring the distance between the instrument and the top of the tree.

The value of the tree height can be obtained through calculation after the above steps and this value will be displayed directly on the instrument display.

3 Conclusion

Since the birth of the world's first laser in 1960, and then the laser technology was used in the measurement of the distance in 1961, thus the world's first laser rangefinder was come out. Laser measuring distance has a long history, however, it has only just begun which the laser is used to measure the tree. Traditional instruments of measuring tree highlight shortcomings in the measurement process and it is inevitable that these instrument would be gradually withdraw from the forest survey of the stage of history. Laser measuring tree height is a new measurement method after the traditional measurement method, this method expand the space of measuring tree and opened up a new path for the development of future instruments of measuring tree.

The instrument of laser measuring tree height referred in this paper set the features of measuring distance and angle in a single instrument, thus, it is significant savings in measurement time. The instrument is small size, light weight and easy to carry and the measurement results can be directly displayed in the instrument display. These advantages will provide great convenience for forest workers.

Acknowledgements. This study is supported by national projects of "948" (2010-4-05).

References

1. Feng, Z., Sui, H., Deng, X., Zang, S.: Survey and Precision Analysis of Tree Height by Trigonometric Leveling. *Journal of Beijing Forestry University* 29(supp. 2), 31–35 (2007)
2. Liu, F., Luyong, Zeng, S.: Status and Prospects of Forest Measurement Instruments. *Forest Resource Management* 2(1), 96–99 (2011)

3. Feng, Z., Zhao, Y., Deng, X., Zang, S.: Measurement and Precision Analysis of Tree Height by 3D Forward Intersection. *Journal of Beijing Forestry University* 29(supp. 2), 36–39 (2007)
4. Han, G., Feng, Z., Liu, Y., Wang, X.: Forest Measurement Principles and Precision Analysis of Three 2Dimensional Laser Scanning System. *Journal of Beijing Forestry University* 27, 187–190 (2005)
5. Chen, Y., Sui, H., Feng, Z., Sun, Y.: Comparative Analysis on the Precisions between Two Methods for Tree Height Measurement. *Forest Inventory and Planning* 34(6), 1–4 (2009)
6. Optical School,
<http://www.coema.org.cn/study/li/20070916/211728.html>

A Method of Calculation for the Shearer Drum Cutting Path

Wei Guo, Ning Zhu, and Shuanfeng Zhao

School of Mechanical Engineering, Xi'an University of Science and Technology,
Xi'an, China
81293567@qq.com

Abstract. The paper studies an automatically heightened technology in the shearer drum. It establishes a mathematical model of spacial status in coal minning mechine, Structures of the coal mining machine test-bed and determines the space coordinates of the shearer drum and its body, in addition it derives the relevant formulas. The cutting path of shearer drum is computed based on the cubic spline fitting. The correctness and feasibility of the proposed method is verified by the computation algorithm with VB6.0 program.

Keywords: Shearer, automatically heightened technology, curve-fitting.

1 Introduction

The drum shearer is the most widely used machine in coal exploiting and mining equipments. The automatically adjustable height of drum is one of key technologies to realize the automation of coal mining[1]. The shearer adjusts the height of the roller automatically based on the ups and downs change of the face roof and floor the coal mining equipments, in order to avoid the roller of coal minning machine cutting rocks. In coal mining machines, the determination of the spacial location of body and roller is a significant technology in order to realize the automatically adjustable height of the drum.

The shaft encoder algorithm is proposed by many researchers and literatures for determining the spacial location by computing the traveling distance of shearers[2]. However, the travelled distance is computed in a direction of the journey. Some scholars established the shearer drum mathematical model based on the plane rectangular coordinate system, but considering the actual conditions it cannot be used in actual production[3]. In this paper, an novel computation method is proposed to determine the spacial coordinates location of coal minning machine. according to the complex work environment of coal minning machine and the characteristics of automatically adjustable height, the cubic spline fitting is applied to compute the cutting path of shearer drum. In the experiments, it is shown that the proposed method is correct and feasible.

2 Paper Preparation

2.1 The Coordinate System Determination

Absolute coordinate system: it is shown in figure 1. In the initial situation, the origin of coordinate is the body of equipment. the positive direction of Y axis is the development

direction along the working surface. the X axis is the movement direction for coal winning machine body , the Z axis is the vertical direction.

The relative coordinates: when coal mining machine is moved to i point, the central of body is the origin of coordinate O' . The direction of relative coordinate is the same as the absolute coordinate system, namely the coordinate system. (i = 1, 2, 3.....) where i is the sample point for coal mining machine , 0 is the initial state of coal mining machine

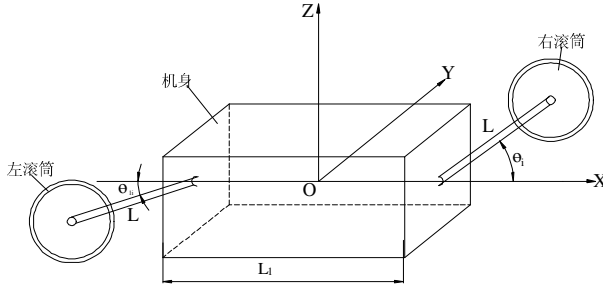


Fig. 1. Coal winning machine space situation schemes

2.2 The Movement Analysis for Coal Mining Machine Situation

In the coal mining process, the working coal mining machine changes operation attitude according to the movement of the working surface. The 3-axis acceleration sensor, rotary encoder and Angle sensor is used as the testing device for the spatial location system of the coal mining machine body and roller according to the actual operation.

In the actual cutting process, there are four situations for the Coal winning machine:

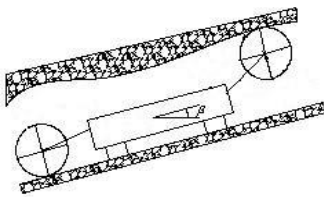


Fig. 2. The front view for upward movement of coal mining machine along the working surface

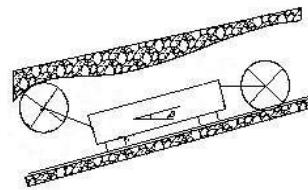


Fig. 3. The front view for downward movement of coal mining machine along the working surface

From the figure 3 and figure 2, when the coal winning machine is moving downward and upward directions. the Y axis is the rotated axis for the body. β is rotation Angle.

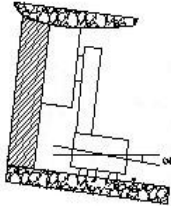


Fig. 4. The upward view for the coal winning machine along the development direction of the working surface

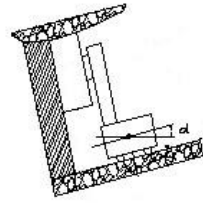


Fig. 5. The downward view for the coal winning machine along the development direction of the working surface

From the figure 4 and figure 5, when the coal winning machine is mining upward and downward along the development direction of the working surface. the X axis is the rotated axis for the body. α is rotation Angle.

In addition, the coal mining machine is at work, for the rotated Angle is γ with the Z axis.

3 The Calculation of Space Coordinates for the Coal Winning Machine

3.1 The Calculation of Space Coordinates for the Body of the Coal Winning Machine

The following is used to explain the parameters:

$\alpha_i, \beta_i, \gamma_i$ --the body of coal winning machine is rotated Angle around X axis, Y and Z axis Angle in the space of the right Angle coordinate system, respectively. and $\alpha_i, \beta_i, \gamma_i \in [0^\circ 90^\circ)$;

X'_i, Y'_i, Z'_i are the absolutely coordinate for the coal winning machine;

$\Delta X_i, \Delta Y_i, \Delta Z_i$ are the absolutely coordinate for roller compared with the body;

X_i, Y_i, Z_i are the absolute coordinates-for the roller;

θ_{li}, θ_i -are the rotated angles for left and right arms compared with the body, and $\theta_{li}, \theta_i \in (0^\circ 90^\circ]$;

L--the arm length; L1--the length of the body;

S--the length of coal minning machine along the working surface.

From Figure 1, in the initial state of coal winning machine, the relative coordinates $O'X'Y'Z'$ and absolutely coordinate system is OXYZ are coincided, namely the coordinate of body is (0,0,0), the coordinate of right roller is $(\frac{L_1}{2} + L \cos \theta_i, 0, L \sin \theta_i)$, the coordinate of left roller is

$(-\frac{L_1}{2} + L \cos \theta_i), 0, -L \sin \theta_i)$, and the rotated angle of drum is 0 compared to 3 axis. namely the inclination of coal minning machine is 0 in every direction.

The movement of The coal mining machine keeps stable between two sampling points, i.e. between i-1 and i, namely, the coal mining machine is run dissectedly in the angle of α_i 、 β_i 、 γ_i , the distance from the i-1 point to the point i is

$$S = S_i - S_{i-1}$$

Compared with i-1, the calculation of i point coordinate for the body of coal minning machine is,

$$X' = (S_i - S_{i-1}) \cos \beta_i \cos \gamma_i ; Y' = (S_i - S_{i-1}) \cos \beta_i \sin \gamma_i ; Z' = (S_i - S_{i-1}) \sin \beta_i$$

For every point, The value of coordinate can be obtained by

$$X'_i = \sum (S_i - S_{i-1}) \cos \beta_i \cos \gamma_i \tag{1}$$

$$Y'_i = \sum (S_i - S_{i-1}) \sin \gamma_i \cos \beta_i \tag{2}$$

$$Z'_i = \sum (S_i - S_{i-1}) \sin \beta_i \tag{3}$$

3.2 The Calculation of Space Coordinate in the Roller of Coal Mining Machine

The right roller is for example:

- (1) the calculation of ΔX_i , ΔZ_i value, as shown in figure 6

$$\overline{O'A} = \frac{L_1}{2} + L \cos \theta_i ; \overline{AB} = L \sin \theta_i \sin \alpha_i ; \overline{O'N} = \frac{L_1}{2}$$

Then, $\angle 1 = \arctan(\frac{\overline{AB}}{\overline{O'A}}) = \arctan(\frac{L \sin \theta_i \sin \alpha_i}{\frac{L_1}{2} + L \cos \theta_i})$, and $\angle 1 + \gamma_i \in [0^\circ \ 90^\circ]$

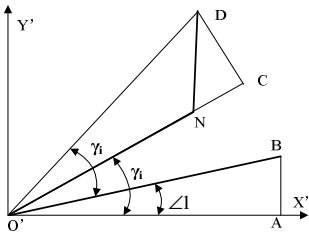


Fig. 6. The projection in the $O' X' Y'$ plane after the coal minning machine rotating by X' axis and Z' axis

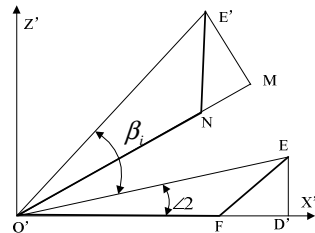


Fig. 7. The projection in the $O' X' Y'$ plane after the coal minning machine rotating by X' axis, Z' axis and then Y' axis

Coal winning machine bobbin, in the projection on the map

A, B-the projection in X' axis and the $O' X' Y'$ plane after the body of coal minning machine rotating by X' axis respectively.

D--the projection in the $O' X' Y'$ plane after the roller of coal minning machine rotating by X' axis and then Z' axis

N--the projection of the body and hinge joint coal minning machine in the $O' X' Y'$ plane after the body of coal minning machine rotating by X' axis and then Z' axis

E--the projection in the $O' X' Y'$ plane after the roller of coal minning machine rotating by X' axis and Z' axis

E' --the projection in the $O' X' Y'$ plane after the roller of coal minning machine rotating by X' axis and Z' axis and Y' axis.

F--the projection of the body and hinge joint coal minning machine in the X' axis after the body of coal minning machine rotating by X' axis and then Z' axis

D' --the projection in the X' axis after the coal minning machine rotating by X' axis, Z' axis and then Y' axis.

When $\angle 1 = 0$ (namely the body is free for rotation, $= 0$),

$$\overline{ED'} = L \sin \theta_i, \overline{O'D'} = \left(\frac{L}{2} + L \cos \theta_i\right) \cos \gamma_i \text{ is:}$$

$$\angle 2 = \arctan\left(\frac{\overline{ED'}}{\overline{O'D'}}\right), \text{ and } \angle 2 + \beta_i \in (0^\circ 90^\circ)$$

According to the actual conditions, indicates that $\angle 2 \neq 0$

$$\Delta X_i = \overline{O'E'} \cos(\angle 2 + \beta_i) = \frac{L \sin \theta_i}{\sin \angle 2} \cos(\angle 2 + \beta_i) \tag{4}$$

$$\Delta Z_i = \overline{O'E'} \sin(\angle 2 + \beta_i) = \frac{L \sin \theta_i}{\sin \angle 2} \sin(\angle 2 + \beta_i) \tag{5}$$

When $\angle 1 \neq 0$:

$$\overline{ED'} = L \sin \theta_i \cos \alpha_i, \overline{O'D'} = \frac{L \sin \theta_i \sin \alpha_i}{\sin \angle 1} \cos(\angle 1 + \gamma_i) \text{ is: } \angle 2 = \arctan\left(\frac{\overline{ED'}}{\overline{O'D'}}\right)$$

According to the actual conditions, indicates that $\angle 2 \neq 0$

$$\Delta X_i = \frac{L \sin \theta_i \cos \alpha_i}{\sin \angle 2} \cos(\angle 2 + \beta_i) \tag{6}$$

$$\Delta Z_i = \frac{L \sin \theta_i \cos \alpha_i}{\sin \angle 2} \sin(\angle 2 + \beta_i) \tag{7}$$

(2) The value of ΔY_i calculation

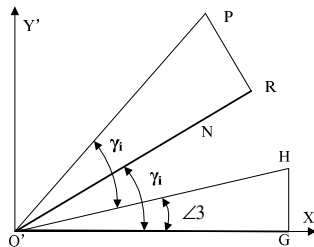


Fig. 8. Coal minning machine around the first axis, axis rotation, pivoting again after the projection map in

G, H--the projection in X' axis and the $O' X' Y'$ plane after the roller of coal minning machine rotating by X' axis respectively.

P--the projection in the $O' X' Y'$ plane after the roller of coal minning machine rotating by X' axis and then Z' axis;

$$\overline{HG} = L \sin \theta_i \sin \alpha_i; \overline{O'G} = (\frac{L_1}{2} + L \cos \theta_i) \cos \beta_i, \text{Is: } \angle 3 = \arctan \left(\frac{\overline{HG}}{\overline{O'G}} \right)$$

When $\angle 3=0 (\alpha_i=0)$: $\Delta Y_i = [\frac{L_1}{2} \cos \beta_i + L \cos(\theta_i + \beta_i)] \sin \gamma_i$

When $\angle 3 \neq 0$: $\Delta Y_i = [\frac{L_1}{2} \cos \beta_i + L \cos(\theta_i + \beta_i)] \sin \gamma_i$

(3) the absolute right roller center coordinate calculation:

When $\alpha_i=0$:

$$X_i = X'_i + \Delta X_i = \sum (S_i - S_{i-1}) \cos \beta_i \cos \gamma_i + \frac{L \sin \theta_i}{\sin \angle 2} \cos(\angle 2 + \beta_i) \tag{8}$$

$$Y_i = Y'_i + \Delta Y_i = \sum (S_i - S_{i-1}) \sin \gamma_i \cos \beta_i + [\frac{L_1}{2} \cos \beta_i + L \cos(\theta_i + \beta_i)] \sin \gamma_i \tag{9}$$

$$Z_i = Z'_i + \Delta Z_i = \sum (S_i - S_{i-1}) \sin \beta_i + \frac{L \sin \theta_i}{\sin \angle 2} \sin(\angle 2 + \beta_i) \tag{10}$$

When indicates $\alpha_i \neq 0$:

$$X_i = \sum (S_i - S_{i-1}) \cos \beta_i \cos \gamma_i + \frac{L \sin \theta_i \cos \alpha_i}{\sin \angle 2} \cos(\angle 2 + \beta_i) \tag{11}$$

$$Y_i = \sum (S_i - S_{i-1}) \sin \gamma_i \cos \beta_i + \frac{L \sin \theta_i \sin \alpha_i}{\sin \angle 3} \sin(\angle 3 + \gamma_i) \tag{12}$$

$$Z_i = \sum (S_i - S_{i-1}) \sin \beta_i + \frac{L \sin \theta_i \cos \alpha_i}{\sin \angle 2} \sin(\angle 2 + \beta_i) \tag{13}$$

Because the two rocker arms of the coal mining machine are always in the same plane , coordinate's analysis and solution are similar as the right roller. Namely, θ_{li} is replaced by θ_i in ΔX_i 、 ΔY_i 、 ΔZ_i . Left roller of absolutely obtained by the relative coordinates of Left roller and the coordinates of body.

4 Curve Fitting for the Coal Mining Machine Roller Path

In the section 3, The roller coordinates are discrete points. to realize the drum automatic adjustment, the cutting track of roller should be calculate. The curve fitting is applied to approximate the actual track according to these discrete points in order to control exactly repeated cutting. In this paper, the target curve for roller track is calculated based on three spline curve fitting method in the N dim vector space[4][5].

Supposed a curve T in the 3th dim space, a arbitrary point $P_0 (x_0, y_0, z_0)$ is the origin of coordinate on the curve T . Another arbitrary point $P(x, y, z)$ is unique in the term of the length and position on the curve T .The function of arc length is shown as

$$T: \begin{cases} x = X(S) \\ y = Y(S) \\ z = Z(S) \end{cases} \quad T: \begin{cases} x = x \\ y = f(x) \\ z = g(y) = g(f(x)) \end{cases}$$

Supposed that there are m points P_0, P_2, \dots, P_m on the curve. the curve is can be determined uniquely by the calculation of $f(x), g(y)$.

First of all, according to theory of three mement:

$$y = f(x) = M_{i-1} \frac{(x_i - x)^3}{6h_i} + M_i \frac{(x - x_{i-1})^3}{6h_i} + \left(y_i - \frac{M_i h_i^2}{6} \right) \frac{x - x_{i-1}}{h_i} + \left(y_{i-1} - \frac{M_{i-1} h_i^2}{6} \right) \frac{x_i - x}{h_i}$$

And then, according to equations set of three mement: Make,

$$h_i = s_i - s_{i-1}, \quad S''(s_i) = M_i \quad (i=1,2,\dots,m), \quad \mu_i M_{i-1} + 2M_i + \lambda_i M_i = d_i$$

$$\text{Where } \lambda_i = \frac{h_i}{h_i + h_{i+1}}; \quad \mu_i = 1 - \lambda_i; \quad d_i = \frac{6}{h_i + h_{i+1}} \left(\frac{x_{i+1} - x_i}{h_{i+1}} - \frac{x_i - x_{i-1}}{h_i} \right)$$

Because the coefficient matrix of equations set is strictly diagonally dominant, the Chase-after method is applied to calculate M_0, M_1, \dots, M_m , the cubic spline interpolation function $f(x)$ can be obtained. And then, $z = g(y) = g(f(x))$ is calculated. The function of curve T is obtained.

5 The Results Analysis and Conclusions

The results of the calculation of space coordinates for the coal mining machine and curve fitting for the coal mining machine roller path are considered. Visual Basic6.0 is used to programming and software designing. the correctness of the proposed algorithm is verified. In fig 9 and 10, it is shown that the calculation of roller coordinate is obtained correctly after 10 input points of the coal mining machine are rotated by 3 angles compared with absolute coordinate axis.

The results of fitting curve are shown in Figure 9, figure 10, where the blue line is the given sin and the red line is the fitting curve.

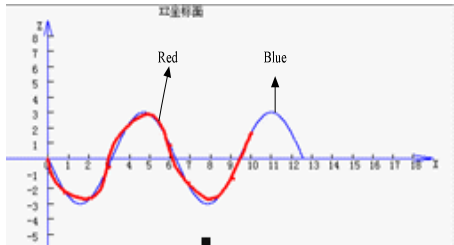
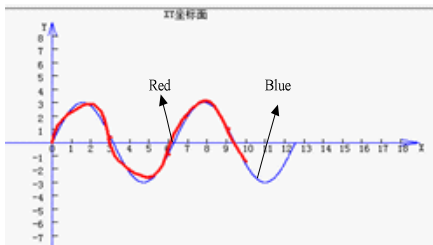


Fig. 9. The projection in XOY plane fitting curve **Fig. 10.** The projection in XOZ plane fitting curve

Based on this algorithm to build a coal mining machine space positioning test bench, Test bench as shown in Figure 11. After the initial experiment, the algorithm can achieve the expected purpose.

In the future, a lot of experiments will test the proposed algorithm for practical applications. In the next step, we will cooperate with Xi'an coal mine machinery Co., LTD for the further experiments. The development and improvement of the proposed algorithm will be studied according to updated experiment results.

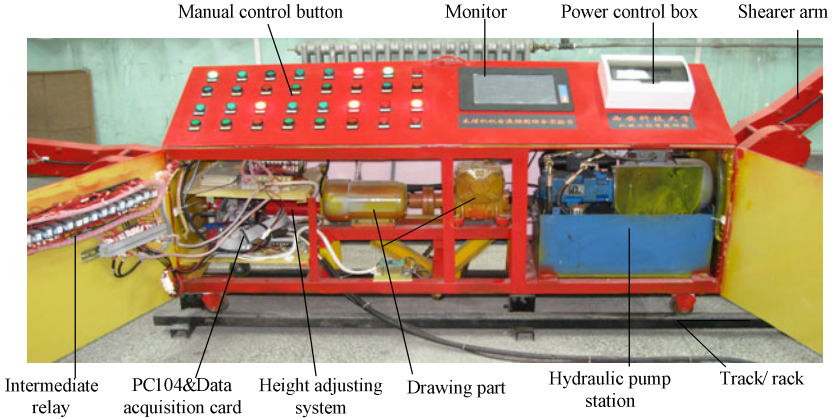


Fig. 11. Coal mining machine memory cutting experiment bench

Acknowledgment. The paper is supported by scientific research plan projects of Shaanxi Province Education Department (09JK604). The Project Supported by Natural Science Basic Research Plan in Shaanxi Province of China (Program No. 2011JM7018).

References

1. Liu, C.S., Jing, K., Yang, Q.: Control strategy of sample intervals of cutting memory program controlling for shearer drum. *Journal of Liaoning Technical University* 26(5), 751–753 (2007)
2. Xia, H.G.: Shearer position monitoring device principle and Application. *Mining Machinery* 11, 43–45 (2007)
3. Wang, D.: Research of Mnemonic Lifting Control System Based on Coal shearer Test Model. Xi'an University of Science and Technology, Xi'an (2010)
4. Liu, F.X.: Based on three spline curve fitting method in the N dim vector space. *HongDu Science and technology* (01) (1982)
5. Long, X.H.: Numerical Analysis, pp. 82–86. Shaanxi Press of Science and Technology, Xian (2005)

Study on Vapour Insulation Technology in MOSS-Type Tanks of LNG Carrier

Boyang Li, Yunqiu Zhang, Diyang Li, and Lixun Ding

Department of Marine Engineer, Qingdao Ocean Shipping Mariners College,
Qingdao 266071, China
libocean@126.com

Abstract. The paper introduces the importance of LNG carrier cargo tank insulation, the principle of vapour insulation technology and practical applications. Then, gives the vapour insulation mathematical model and the boil off rate calculation methods and through simulation of 125000 m³ example of the mother-ship and the results comparison with the actual ship, reaches a conclusion that vapour insulation technology can reduce the boil off rate of tanks cargo greatly. Finally, provides vapour insulation system optimization design of the cargo tank.

Keywords: Vapour insulation, Liquefied natural gas carrier, Moss type tank, Cargo tank insulation.

1 Introduction

As crude price rising quickly, annual global trade in LNG transportation increased dramatically, therefore, LNG carriers study are concerned more and more by the shipping industry. As one specific ship, the LNG carrier loads -163 °C liquefied natural gas, so higher request to its tank insulation is brought up. Otherwise, the poor heat insulation will cause the boil off rate (BOR) approaching or exceeding the standard value (the IMO required standard value of BOR for LNG carrier is 0.12%) [1], lead to loss of tanks cargo and reduce transport capacity of LNG carriers.

Therefore, the study of the tank insulation technology is very necessary and can provide more technical support for LNG carrier insulation design and manufacturing. In order to research purposefully, the study selects MOSS type 125000 m³ LNG carrier as the mother ship.

2 Vapour Insulation Technology of Liquid Cargo Tank

The vapour from liquid cargo hold absorbs heat from the outside, which is still around -150 °C and has large cooling energy, needs to be warmed in heater (usually above 0 °C) before burning in ship boiler, which wastes a lot of cooling energy. Therefore, a new technology which improves the performance of tank insulation by using the cooling energy is proposed, called cargo tank vapour insulation. The so-called cargo tank vapour insulation is that firstly the nitrogen temperature is reduced by heat

exchange between the vapor of LNG cargo and nitrogen and then the cooled nitrogen is fed into the annular passage around the MOSS cargo tanks. The nitrogen flow upward along the surface of the tank and carry the absorbed energy from liquid cabin insulation out of the system, so as to reduce further infiltrated heat from the surrounding environment to the tank through the insulation layer and reduce the boil off rate of the tank cargo. In the vapour insulation system, cold nitrogen is made as the tank insulation medium instead of cargo vapour, mainly taking into account the safety of the insulation system and eliminating fire, explosion safety hazard when leakage occurred.

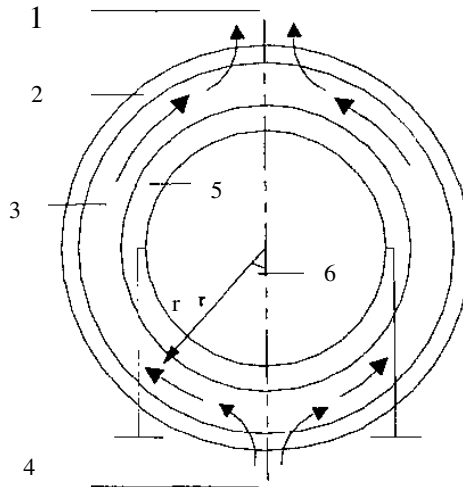


Fig. 1. Steam insulation of cargo tank, 1-Nitrogen export, 2-Outer insulation, 3-Nitrogen channel, 4-Nitrogen inlet, 5-Inner insulation, 6- ϕ

In order to optimize the vapour insulation system, careful analysis of some important system parameters such as gas flow, vapour temperature, gas-channel position and other parameters is very important for the improvement of the system's economy, reliability, and security.

3 Mathematical Model of Vapour Insulation

In order to properly evaluate the system, the flow and thermal analysis should be carried out. The MAC charts application of k-equation and finite difference method is used for numerical calculation during the analysis of compressible fluid turbulence which temperature changed greatly in spherical coordinates. Following a complex system of numerical calculation of the material, the calculated value is very close to the actual value. In order to achieve maximum endothermic effect, the cold gas passage insulation design should be based on the determination of total heat flow into the tank.

3.1 Analysis on Heat Flow in Vapour Channel

Analysis of gas flow and temperature changes in the spherical coordinate system. According to the material, momentum and energy conservation, the cold gas flow equation is written in vector expression, as below:

$$\frac{\partial Q}{\partial \tau} + \frac{\partial E}{r^2 \partial r} + \frac{\partial F}{r \sin \phi \partial \phi} + \frac{\partial P_1}{\partial r} + \frac{\partial P_2}{r \partial \phi} = G, \quad Q = \begin{bmatrix} \rho \\ \rho u \\ \rho v \\ \rho c_p t \end{bmatrix}, \quad E = \begin{bmatrix} \rho r^2 u \\ \rho r^2 u^2 \\ \rho r^2 uv \\ \rho r^2 uc_p t \end{bmatrix} \quad (1)$$

Where ρ is the density, u and v are the viscosities, c_p is the specific heat, p is the pressure, R is the gas constant, t is the temperature, G is the condition of speed diffusion, Coriolis force and thermal diffusion ($p = \rho RT$).

Through the FDM of MAC chart, with discrete calculation area method carried out isometric numerical calculation. Along the latitude the calculate area is divided into four parts, each of which will be divided into five equidistant units in the radial direction and 70 to 90 units in the latitude direction.

3.2 Vapour Approximate One-Dimensional Flow Analysis

It is believed generally that the smaller the gap of the vapor flow passage, the smaller the flow rate fluctuation and the less the radial temperature distribution.

The one-dimensional flow energy equation along the spherical surface can be obtained from the following formula:

$$c_p S_s \frac{\partial \rho t}{\partial \tau} + c_p w \frac{\partial t}{\partial x} = \frac{\partial}{\partial x} \left(k S_s \frac{\partial t}{\partial x} \right) + k_a S (t_a - t) + k_L S (t_L - t) \quad (2)$$

Where S_s is the flow area, w is the flow rate, k is the vapour thermal conductivity, k_a and k_L are the heat transfer coefficient of insulated layer, S is the sectional area.

In these calculations, in comparison with air forced convection, the impact of thermal conductivity of nitrogen is considered negligible. In this way, the equation becomes more stable and simple, as follows:

$$c_p w \frac{dt}{dx} - k_a S (t_L - t) = 0 \quad (3)$$

Where $x = r\phi$, $dx = r d\phi$, $S = 2\pi r \sin \phi$, when $\phi = \phi_0$, $t = t_0$.

The analysis equation is obtained in the appropriate latitude of the vapour passage that the gas flow average temperature changes with the depth, as below:

$$t = t_m - (t_m - t_0) e^{-\frac{2\pi^2 (k_a + k_L) \cos \phi_0 - \cos \phi}{c_p w}} \quad (4)$$

3.3 The Heat Transferred into Cargo Tank

The Heat can be calculated by the product of temperature difference between cold nitrogen gas and cargo tank and the insulation coefficient of inner insulation layer in the following equation. So the equation between the $\Delta\phi$ and Δq in the appropriate position is obtained:

$$\Delta q = 2k_L(t - t_L)\pi r^2 \sin\phi \Delta\phi \quad (5)$$

The heat transferred into cargo tank :

$$Q = \int dq = \sum_{i=1}^n \Delta q_i \quad (6)$$

For the cargo tank, the heat transferred into the tank is as small as possible, so the loss of cargo is the smallest because of evaporation. Therefore, the minimum can be calculated under certain conditions.

3.4 The Calculation of Boil off Rate

Based on the equation (6) and (7) ,BOR (boil off rate) is the following equation:

$$\text{BOR} = \frac{Q}{\gamma m} \quad (7)$$

Where Q is the heat transferred into cargo tank, γ is the Latent heat of vaporization of LNG, m is the quantity of the cargo in the tanks.

4 Calculation and Analysis of Actual Ship and System Optimization

Calculation conditions: the main membrane intact, air temperature 28 °C, sea water temperature 20 °C, wind speed 20 knots, sea water flow speed 0 knot; the conditions according to " International Code for the Construction and Equipment of Ships Carrying Liquefied Gases in Bulk ".

In addition, other common known parameters (tank size, tank capacity, insulation thickness, thermal conductivity; natural gas heat, nitrogen heat, etc.) can be found in reference [2-4].

In order to reduce variable, we added on the outside of every tank 50mm thick insulation materials the same as the original and leave a 10mm space between the inner and outer layers to allow the cryogenic nitrogen to pass so as to achieve the vapour insulation. Then insert the parameters in the above formula and solve the problems of 5 cargo tanks one by one as shown in figure 2, starting from NO.5 cargo tank, we will find the outlet nitrogen temperature of NO.3 cargo tank above 0°C and very close to the ambient temperature. Therefore, NO.2 and NO.1 cargo tanks no need to be insulated by nitrogen. Assume the appearance temperature of two tanks is ambient temperature, the results shown in Table 1.

Table 1. BOR of tanks and comparison

Cargo tank	BOR %	mean %	referenced data %	Reduction %
NO.5	0.01			
	94			
NO.4	0.04	0.0597	0.11	45.8
	38			
NO.3	0.07			
	21			
NO.2	0.09			
	13			
NO.1	0.09			
	13			

As can be seen by Table 1, the mean BOR of the entire ship is 0.0597 (assuming the same capacity of every tanks) after the NO.3, NO.4, NO.5 tank using vapour insulation, and is down by 45.8% over the referenced data (no vapour insulation), thus cargo loss reduce greatly and transport capacity increase. Therefore, the application of vapour insulation has a huge potential for development.

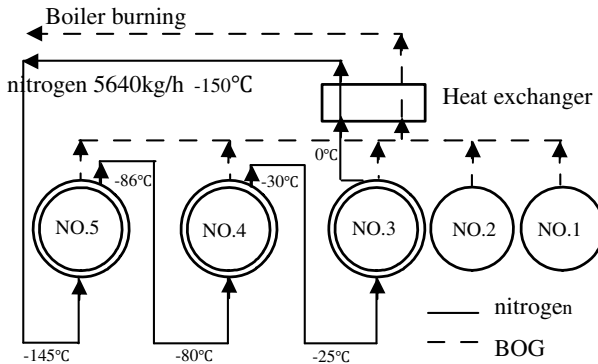


Fig. 2. Steam insulation system of cargo

According to calculation and analysis of the example in this condition, the vapour insulation system optimization design can be carried out and the necessary parameters can be marked, shown in Figure 2.

5 Conclusion

Through the introduction of vapour insulation technology and simulation calculation in actual application, the vapour insulation technology can improve the LNG carrier cargo

tank insulation performance greatly and reduce the BOR of the cargo of tanks greatly. Meanwhile, boil off gas which temperature can increase in the heat exchange process needs not be warmed up and can be sent to boiler burning directly. Therefore, the vapour insulation technology can reduce the loss of tanks cargo, simplify the treatment process of boil off gas, and improve the economic of LNG carrier.

References

1. Li, P.-Y.: Shipping technology of liquefied gas, Dalian Maritime University, Dalian (2003)
2. Huimiyangyan, H.-S. (Translate): Liquefied gas ship book, pp. 126–152, 272–284. Haerbin shipping engineering University publish society, Haerbin (1992)
3. Li, Y.-K.: An overview of cold-retaining technology for tank on LNG ship. Shanghai Shipbuilding 2, 45–48 (2002)
4. Daewoo Heavy Industries Ship Design Laboratory. Analysis of Temperature Distribution in the LNG Carrier Hull, Daewoo Heavy Industries study, Korea (1999)
5. Zhang, X.-B., Lin, Y., Ji, Z.-S., et al.: Finite Element Analysis for Pontoon Structural Strength during Ship Launching. Journal of Ship Mechanics 18(6), 113–122 (2004)

Study of Whole Network Control Based on Ethernet for FAST Main Reflector

Haitao Shen¹, Lichun Zhu¹, and Yi Sha²

¹National Astronomical Observatories, Chinese Academy of Sciences
20 Datun Road, Chaoyang District, Beijing, China. 100012

²Northeastern University, Shenyang, China, 110819
maomao5945@126.com

Abstract. The control of Main Reflector is one important part of FAST. This article introduces the control of the Main Reflector with Ethernet network technology, using TCP/IP protocol, cross-platform programming tool—Qt to accomplish the interface and network communication program running in upper computer. After testing and debugging the design on site for the 30 meters Model of FAST, the result illustrates that controlling the FAST Main Reflector based on Ethernet is feasible.

Keywords: FAST, Main Reflector, Ethernet, Control.

1 Introduction

Five-hundred-meter Aperture Spherical radio Telescope (FAST) is one of the China's major scientific research projects, it is currently under construction and will be completed in 2016 according to the plan of the project and will be the largest single dish radio telescope in the world beyond Arecibo Telescope (305 meters)[2]. After accomplished, it is predicted that FAST will be at the lead position for about 30 years at its high sensitivity and other aspects [5].

While celestial source is observed with FAST, by changing the spatial position of the main reflector and the receiver accurately, astronomer can collect the radio signal from the universe. The FAST project is a gigantic complex system composed with astronomy, surveying, architecture, mechanics, electronics, automation technology and other disciplines [1]. In order to receive the extremely weak radio signal from the universe, the Active Main Reflector is one of the major outstanding features and the principal part of FAST.

2 Control of the Main Reflector

The Main Reflector of FAST is divided into 4600 triangular panels installed on the Cable Structure, which consists of almost 10 thousand steel cable and have 2300 joining points[5]. The 11 meters length triangular panel is installed by the joining point and used for receive the radio signal from the universe. Each joining point has the under cable and actuator fixed on the anchor on the ground.

While observing a celestial source, the illuminated part of the spherical reflector is deformed into a 300 meters instantaneous paraboloid, meanwhile the receiver is moved at the focus location of the paraboloid to receive the radio signal. Only if all the joining points are controlled accurately and synchronously, the paraboloid could be deformed. Therefore, whether 2300 joining points could be controlled accurately to an instantaneous paraboloid directly concerns the observing efficiency and results of the telescope. This article mainly introduces the study and experiment about controlling the main reflector based on Ethernet and the program in the upper computer.

3 Characteristics of Controlling Main Reflector Based on Ethernet

In the multi-node control system, Fieldbus are mostly applied traditionally, but the protocol of some Fieldbus is not free completely, so we need special expert to design and develop the control system leading to the development difficulty and cost. In the past, Lonworks and Can Fieldbus have been used in the experiment to control a few joining points of the Main Reflector [2], both Fieldbus are have their own protocol standard and very mature in the field of industry. While there are 2300 joining points located about 300 meters away, and multiple nodes, long Data transmission distance, vast amount of data so that the traditional Fieldbus technology could not meet the requirement of FAST actually in transfer distance and transmission rate.

Industrial Ethernet is the Ethernet technology used in the field of industrial control. It focuses on the use of switched Ethernet technology and provides an interactive mechanism for the cooperation and coordination among controllers, operator stations and other workstations to make them can build seamless integration with upper network. With the development of the Internet and message switching technology, the 100Mb/s transfer rate has been very stable which is much faster than the transmission rate of traditional Fieldbus. As we know, normal Ethernet could transfer more than 100 meters away. In addition, compared with Fieldbus, industrial Ethernet could provide an open standard, and make the company achieve a comprehensive and seamless integration from field control to enterprise management as it solves incompatibility of protocol among the traditional fieldbus. Owing to the Ethernet protocol standard is open completely and its unity with the interface of computer and server, the difficulty and cost of the development based on Ethernet could be reduced significantly. It's worth noting that Ethernet technology has the sustainable development potential, which has wide development space after apply the control system based on Ethernet without other research investment for upgrading the system.

This article main studies the Ethernet-based FAST Main Reflector control program, designs the interface of upper computer and the control procedure with cross-platform programming tool—Qt. using Arm7 chip as the controller chip and TCP/IP communication protocol to achieve the accurate control of joining points. Apart from that, this article also introduces the overall design architecture, the programming in the upper computer and the test on the FAST 30 meters model.

4 The Control Design Scheme Based on Ethernet

4.1 Overall Frame Structure

FAST Main Reflector Control System is made up of master control PC, communication network and controllers, while the communication network is in accordance with the form and structure of Ethernet.

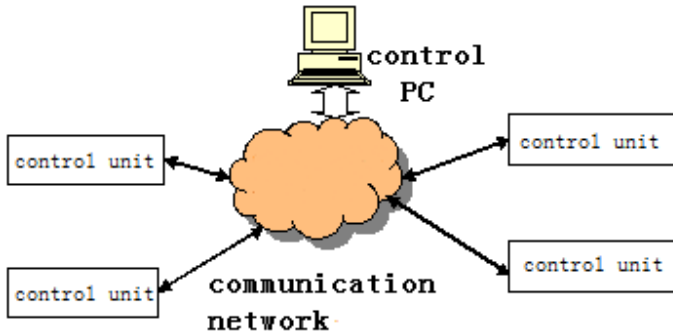


Fig. 1. Ethernet control frame for FAST

4.2 Composition of the Communication Network

The network architecture of FAST 30 meters Model is shown in the fig 2, the overall network consists of upper computer, 24-channel switch with optical transmitter and receiver, 6-channel router and node controller unit(C U). They are formed four levels on the communication functions to achieve the control and monitoring all the joining points in real time. While, the bandwidth of the switch is 1000MHz and the bandwidth of the Ethernet network is 10MHz.

Controller unit controls the actuator to move the joining points to the target location, monitor the status of the joining points, and send data including alarm message back to the upper computer. The upper computer could show the current position and status information of all the joining points and store all the data with database, operator may look up all the information stored in the database conveniently.

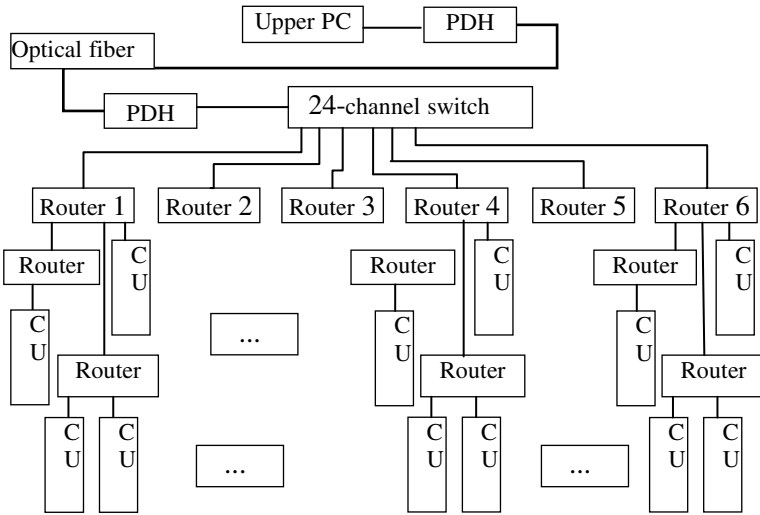


Fig. 2. Ethernet Control Structure for FAST Main Reflector

4.3 The Control System of FAST 30 Meters Model

Topology of the network is shown in fig 3, and there are 131 joining points in the FAST 30meters Model. The nodes in the figure show the actual physical location, and they are divided into 6 zones for balancing to the network load, and each of zones has about 23. every router has no more than 4 next node including next joining point and routers. .In this case, the switches and routes are all working at light loads by which the transfer rate and reliability can be improved considerably.

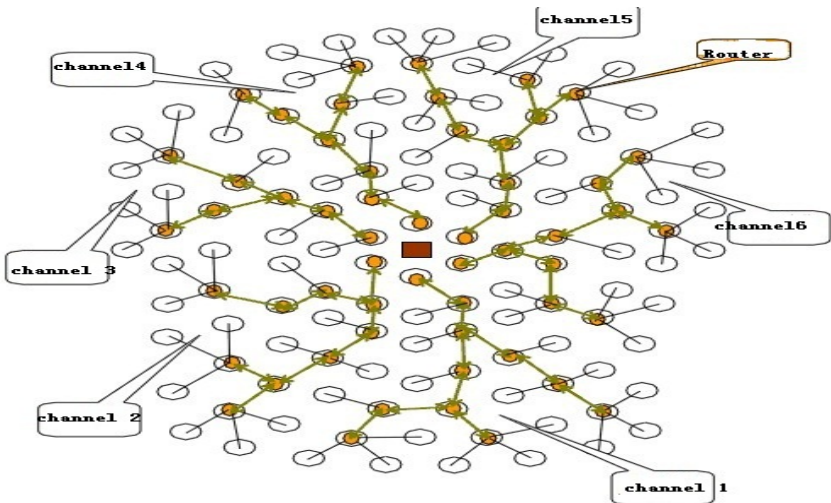


Fig. 3. Ethernet topology structure for FAST 30meters Model

5 Control and Manage Interface of the Upper Computer

The control system based on Ethernet uses cross-platform programming tool--Qt to design the control interface running Windows platform. We use TCP/IP protocol and socket to implement the communication. The control system is consisted of GUI module, Communication Module and Database Module.

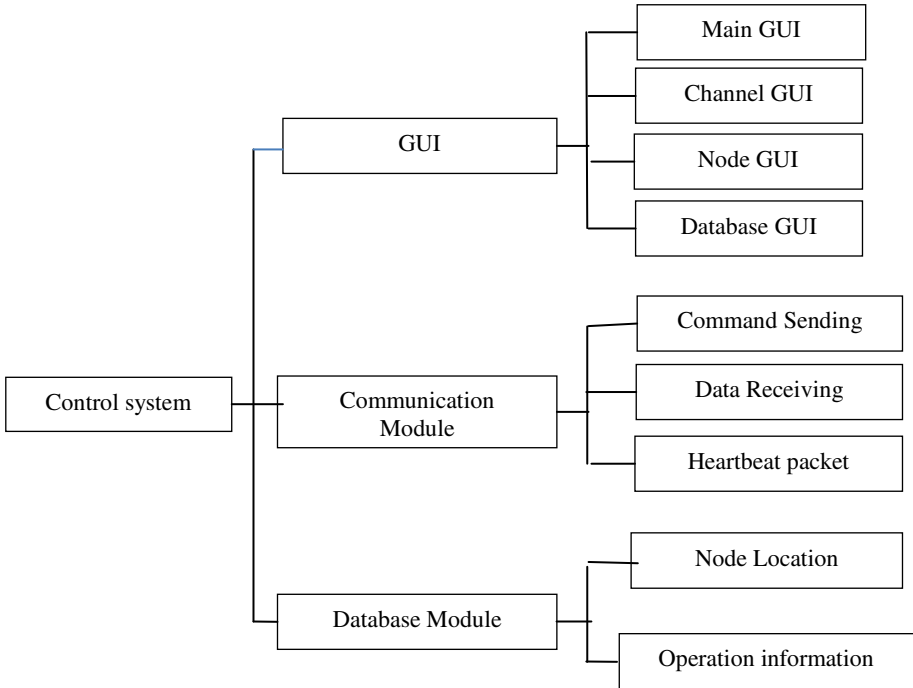


Fig. 4. Ethernet Control Structure for FAST Main Reflector

5.1 GUI Module

The entire control interface in this system is designed by Qt designer. The Main Interface is used to show the location information and status of all the joining points; Node interface and Channel interface have the control details of one or some joining points; Database Module is made for looking up the data stored in the database. all the interface are integrated together finally.

5.2 Communication Module

The core of the whole control system is the communication module, which takes charge of maintaining the communication between the upper computer and the actuator controller, using TCP/IP protocol and applying socket to guarantee each command could be send. At the same time, operator could monitor all the information about the

joining points in real time. In the system, upper computer is the socket client and sends connecting application to the socket server--actuator controller, while the actuator controller is initialized once supplied with power to monitor the connecting application from the client. There are 131 socket objects will be created in the meantime, that is, each joining point has its own communication channel respectively. In addition, In order to reduce the information congestion and collision, after the client sends the application to a socket server, there is 6s time delay before the next application. The actuator controllers send the data information every other 500ms being in motion. The data send from the controller is 12 bytes including 2 bytes for location information, 3 bytes for time, 1 byte for current status and other reserves for extensions in the future.

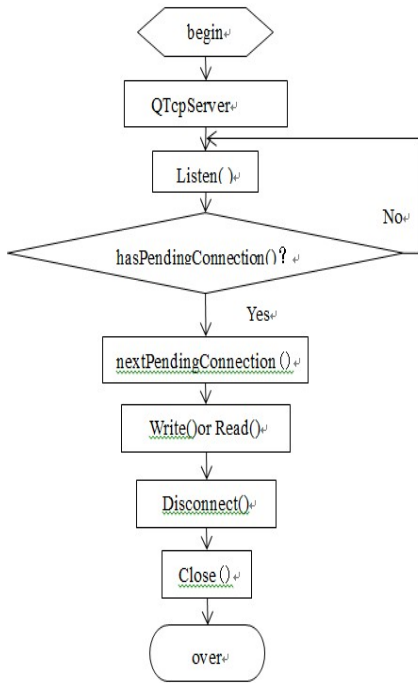


Fig. 5. initialization procedure flow chart of socket-server

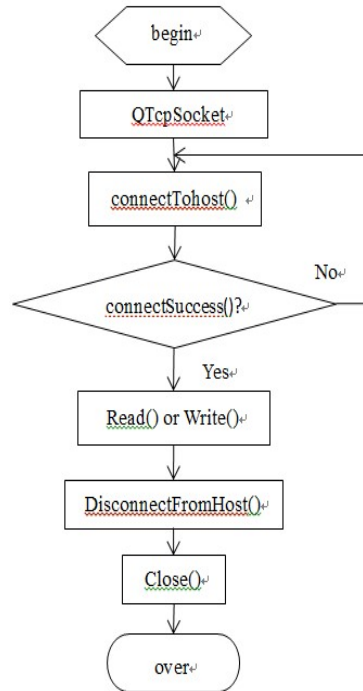


Fig. 6. initialization procedure flow chart of socket-client

To insure that the connection between upper computer controller and lower computer controller is still fine when no command is given or no data is transferred, the system has designed heartbeat packet heartbeat packet mechanism in which heartbeat packet is sent every 6 seconds by the upper computer to improve the reliability.

5.3 Database Module

Using Access database developed by Microsoft, upper computer control system operates dates on the basis of ODBC driving. In this database, tables for recording

observed data, parameters related to sidereal time, and the position of every joining point are designed; also, query operation of database can be implemented.

6 Summary

The design of the control system based on Ethernet for FAST 30meters Model has been implemented, and achieved the target for control and monitor location of the joining points accurately in real time. The experiment proved that applying Ethernet to control the FAST Main Reflector is feasible. According to the control mode of astronomic observation, the system still needs further extension in the future.

References

1. Zhu, L.: Automatic control system for FAST Main Reflector. *Science Technology Engineering* 6, 1671–1815 (2006)
2. Huang, H., Wang, Q., Zhang, H., Zhu, L.: Development of the control system based on Ethernet for FAST Main Reflector. *Computer Engineering and Applications* 42, 97–100 (2006)
3. Peng, B., Nan, R.: Modeling FAST—the world’s largest single dish. *The Radio Science Bulletin* 300, 12–20 (2002)
4. Liu, X.: Complete Collection of Ethernet networking technology. Tsinghua University Press (2001)
5. Preliminary design of FAST (2010)

Design and Implementation of the Marine Environmental Monitoring Database Construction-Cum-Visual Management System

Xiaohui Gao^{1,2,*}, Xiangyu Zhao³, and Juan Wang^{1,2}

¹ North China Sea Environment Monitoring Center, SOA, 266033, Qingdao, China

² Key Laboratory of Marine Spill Oil Identification and Damage Assessment Technology, SOA, 266033, Qingdao, China

³ North Sea Marine Forecast Center of SOA, 266033, Qingdao, China
gXH777@sina.com

Abstract. According to the investigation, monitoring of hard-won Marine environmental data, design the Marine environmental monitoring database construction-cum-visual management system. In this paper, the function of the system and the module design are discussed, realized the monitoring database import, export, monitoring data query, the analysis and evaluation of monitoring data and other functions, to meet the ocean environment monitoring data management.

Keywords: Marine monitoring, Database, Analysis and evaluation.

1 Introduction

Marine informatization is an important part of national information, also is our country marine career development important constituent, in the development of marine enterprises plays a basic, public welfare and strategic role. In recent years, with new and intelligent sea environmental monitoring information service technology development, the north sea monitoring center urgently need a stable, sharing, user-friendly and exchange data platform. The north sea monitoring center as the north sea area the Marine environment monitoring department, long-term since, accumulated a lot of investigation, monitoring, surveillance and scientific research material, to a large number of the monitoring data, how to quickly and effectively for marine environmental data storage, management, analysis, processing and sharing is Marine monitoring data management is a vital task. To establish a set of data to the ocean for object, set Marine data management, data processing and data issued share as one of the marine environmental monitoring database construction-cum-visual management system, is the Marine environmental protection, ocean engineering development, Marine disaster prevention and mitigation, Marine defense security related business development the important basis of the one [1].

* Sponsored by Marine national commonweal research project(200905030).

2 System Development Environment

(1) Operating system

The operating system using Windows XP or Windows Server2003, assure the operating system, the system is fully compatible with the installation and use of the machine, and the original operating system does not conflict.

(2) Software development environment

This system chooses Microsoft's Visual Studio 2008 Suite to sound as a software development environment, and choose for.net new development with C#. C# is a modern fully object-oriented programming language, it makes the programmer to in the new Microsoft.net platform in the rapid development of the rich variety of application. The.net platform provides a lot of tools and services, and to maximize the discover and use calculation and communication ability [2].

Data storage means uses Oracle10g database as data storage solution. Oracle database including Oracle database server and client. Oracle server is an object-relational database management system. It provides open, comprehensive and integrated information management method, has the autonomy and provide data storage mechanism, can be realized by transparent data storage transparency. Oracle client for database user operation, the application, the tool, the SQL * asp.net composition, user operations, must be connected to the database server, this database called the local database. In the network environment on the server DB called other remote database. If the user access the data on the remote DB, must establish database chain.

GIS development platform for ArcEngine 9.3, contains a complete class library embedded GIS software, it supports multifold language (com, JAVA, the.net and c++) and multifold system (Windows and Unix). Developers through the ArcEngine processing can be customized to complete GIS software, also can make the function of GIS embedded into other software already in existence[3].

3 The System Function Module Composition and Design

3.1 System Function Constitute

The marine environmental monitoring database construction-cum-visual management system will be completed by multiple sources, multiple phase, a variety of precision based distributed data integration and storage, a construct containing the basic data, historical data, real-time observation and quasi real time monitoring data dynamic ocean surveillance information integrated database. On the basis of the Marine environment monitoring data query module, and integrated Marine environment evaluation module, to obtain intuitive visual products for ocean management, provide decision-making results, improve the comprehensive Marine analysis ability. The system function structure see the map 1.

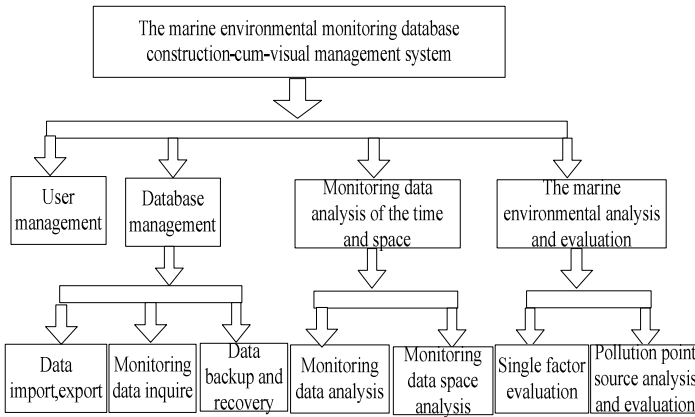


Fig. 1. Function Structure

3.2 The System Function Module Design

3.2.1 User Management Module

The whole system according to user role is different from the information management system of different jurisdiction. Character is divided into administrators, advanced users and ordinary users. In login, according to senior administrator permissions, can add, delete, modify user access to users, distribution, management database; Advanced users can access database; Ordinary users can only access to parts of the database, unable to export data.



Fig. 2. User management interface

3.2.2 Monitoring Data Import and Export Modules

The system realizes the Marine environment monitoring data in the batch, solve the introduction into manual low speed, low efficiency, easy to go wrong. The first standard sea environmental monitoring data report form a unified format, and then through the import module, its all monitoring data of automatic import batch to comprehensive database. In the introduction, the monitoring data are data selection, data cleaning, quality control, to ensure the accurate data into the database.

Data output function, according to the user to the monitoring data of report form demand, can export different formats of data report.

Figure 3 for the Marine environment monitoring data import, export interface.

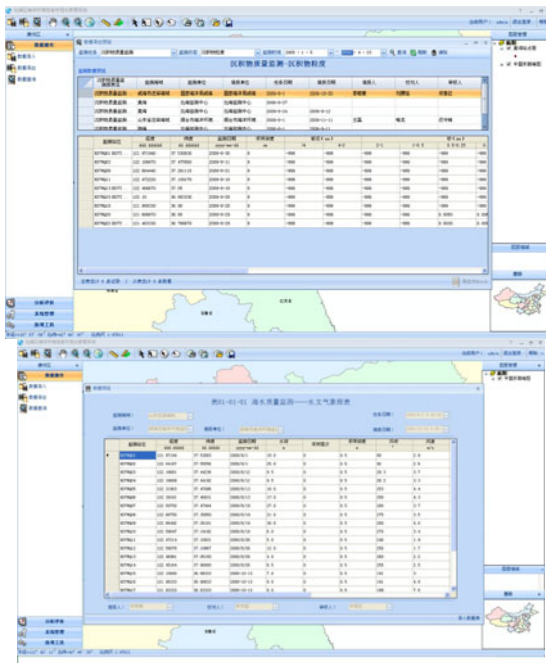


Fig. 3. Data import, export interface

3.2.3 Monitoring Data Query Model

This module can be by time, in a space, according to category combined conditions querying data. Results in the list, query, sort and can be combined, can be paged display, also can save another for documents, Figure 4 for the Marine environment monitoring data query interface.

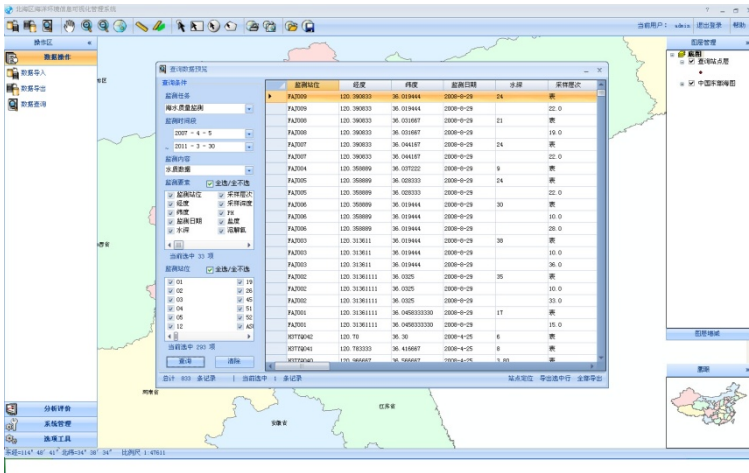


Fig. 4. Data query interface

3.2.4 Monitoring Data Analysis Module

Monitoring data analysis module is implemented a certain time in a different site monitoring elements of the change trend monitoring values, and with line charts, bar chart and based on the map in the form of the bar chart to display intuitive. Figure 5 is the chemical oxygen demand (cod) at the same time different stance change trend of the figure.

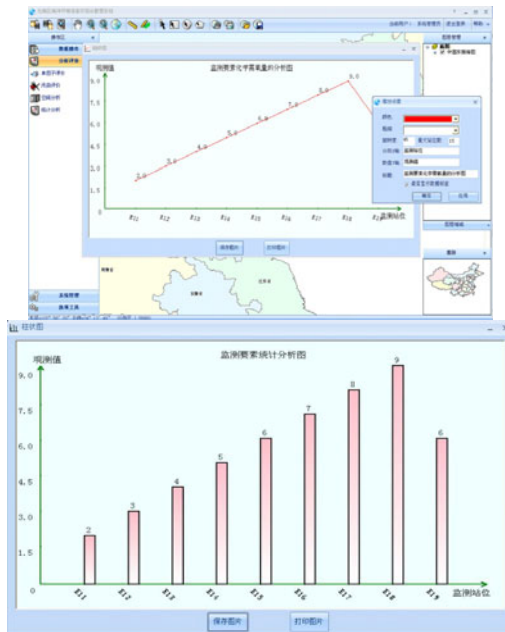


Fig. 5. Statistical analysis interface

3.2.5 Monitoring Data Space Analysis

The purpose of isoline space analysis is based on geographic information in space to specified waters of the monitoring data, the strength of the distribution according to them or density, monitoring values of the same points corresponding links up, then the isoline formation analysis with the change rule of the space.

Figure 6 is chemical oxygen demand (cod) at a certain time in the bohai sea area contour trend chart.

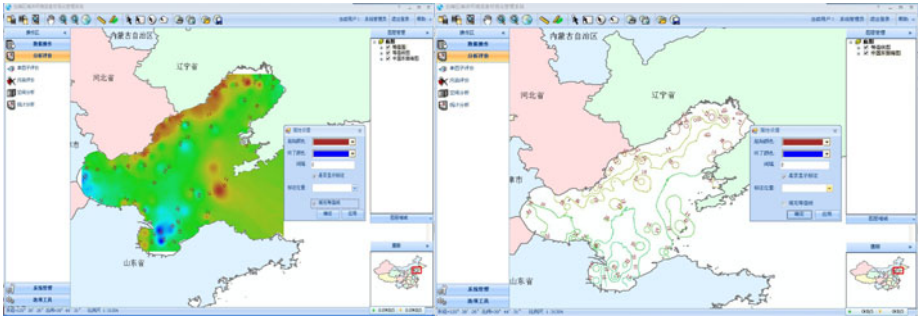


Fig. 6. Space analysis interface

3.2.6 Single Factor Analysis and Evaluation Module

The Marine environment quality assessment mainly adopts the single factor evaluation[4]. Use conditions in mapping out the map query satisfy certain conditions, according to standard site index calculation formula to calculate the monitoring of the elements of the standard index, will be monitoring values of each factor and evaluation standard index differences, the bar chart way to visual said, so as to determine the sediments and biology, the main pollution factor and the impact factor. Figure 7 is different the site's chemical oxygen demand (cod) are compared with the values of the bar chart.

Single factor evaluation formula:

$$P_i = C_{i.} / C_{si}$$

3.2.7 Pollution Point Source Analysis and Evaluation Module

The "emission standard" model, according to emissions of pollutants, and each of the pollution sources such as emissions and the corresponding standard size the cumulative percentage, determine the main pollutant and the main pollution source.. Use conditions in mapping out the map query satisfy certain conditions, according to the user's selection, site selection contaminated area is according to each point source and evaluation standard and the emissions pollutants standard and computing results to emissions to pie charts and three-dimensional pie charts form and direct-viewing showing, but clearly identify some of the key sources of pollution within the region and other information. Figure 8 is a site evaluation and analysis of different monitoring elements of the map.

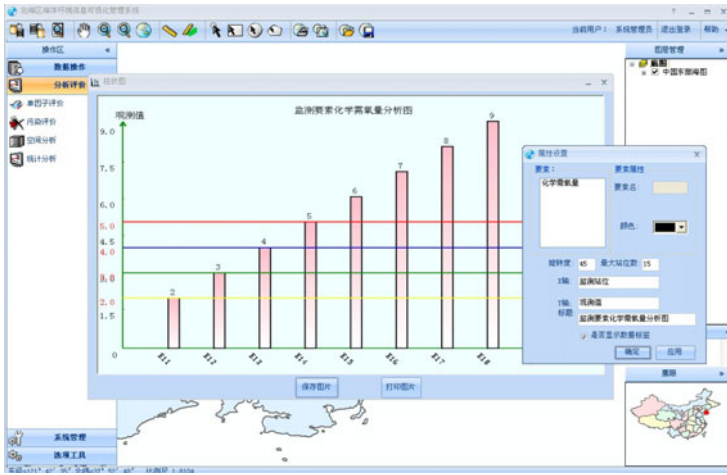


Fig. 7. Single factor analysis and evaluation interface

Standard method such as emissions oncalcati formula:

$$P = \frac{M}{S}$$

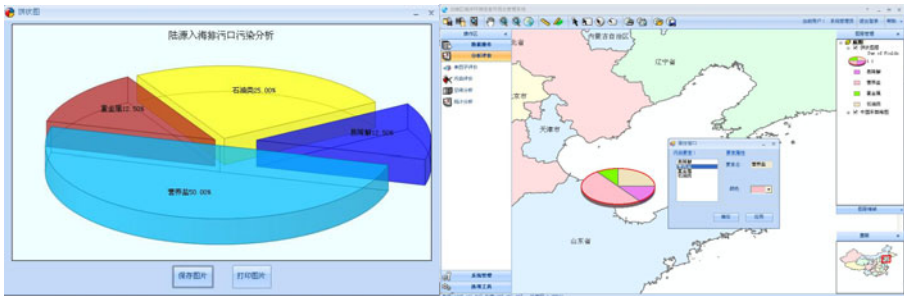


Fig. 8. Pollution point source analysis and evaluation interface

4 Last Word

The marine environmental monitoring database construction-cum-visual management system through the ocean foundation information integration technology, sea heterogeneous data integration quickly access extraction and intelligence analysis technology, the Marine evaluation model of the integrated technology research, to realize the integration of the Marine environmental information with dynamic management to provide technical support. The system through the ocean foundation database, the evaluation model of construction, realize the Marine environment professional

information of integrated, business application of dynamic and management decision-making scientific, in order to further improve the Marine economic development to the planning and management of the support ability, further strengthen the comprehensive management ability ocean lay the foundation.

References

1. Li, L., Zhao, C.: Design and implementation of the data management system for marine environment monitoring. *Marine Forecasts* 27, 53–57 (2010)
2. Zhao, X., Wang, C.: Discussion of Technology on Seafloor Gravity Sampling. *Hydrographic Surveying and Charting* 29, 59–69 (2009)
3. Zhu, S., Nan, Z.: Building GIS Framework with ArcEngine. *Remote Sensing Technology and Application* 21, 385–390 (2006)
4. Yuan, Z.: Time and space analysis of nearshore water environment based GIS., Master's degree paper of Wuhan university (2004)

One Multi-ocular Image Mutual Segmentation Method

Li Xin¹ and Zhu Jingfu²

¹ College of Art and Science, HeiLongJiang BaYi Agricultural University, DaQing, China

² College of Information Technology, HeiLongJiang BaYi Agricultural University, DaQing, China

Abstract. A segmentation method of parallel multi-ocular image is introduced. The camera is rectangle arranged four channel multi-spectral camera, the four channels is R, G, B and NIR respectively. The corn canopy images are captured in field by the camera. The main corn leaves in NIR are segmented based on CV model. One matching method of the multi-ocular image is applied to all images of one group, the main corn leaves in R, G and B images can be matched with the corn leaves in NIR image based on matching transforms. So the main corn leaves in R, G and B images are segmented.

Keywords: Image Segmentation, Multi-Ocular Image, Matching Transform.

1 Introduction

The segmentation is the process of partitioning an image into a set of nonoverlapping and homogeneous regions. Segmentation is completed by some method according to homogeneity of regions. There are some criteria for such homogeneity, such as texture coherence, color homogeneity, grayscale level, etc.

Farrokhnia et al. [1] presented a texture segmentation algorithm inspired by the multichannel filtering theory. M. Unser [2] presented a new approach to the characterization of texture properties at multiple scales by the wavelet transform. Soo et al. [3] proposed a scheme for texture classification and segmentation. The methodology involved an extraction of texture features using the wavelet packet frame decomposition. Mausumi et al. [4] proposed an adaptive approach to unsupervised texture segmentation by M-Band wavelet transform.

Mumford-Shah [5] propose a model, in which an optimal image partition is defined as a solution of a variational problem that tended to simplify the original image, while preserving the borders of original regions. Chan and Vese [6] proposed a new active contours model to detect objects in a given image, based on curve evolution techniques with Mumford–Shah functional for segmentation and level sets.

For getting the growth information of crop, the remote methods [7-8] are applied in recent years, including space remote, aviation remote and near earth remote. The survey of crop growth was done about 1m from crop canopy to camera in near earth remote, the visible spectrum and NIR (near infrared) were used. Changes in different bandwidth reflected different growth state. For analyzing each point of crop canopy, the images were captured at the same time for different bandwidth. There was one multi-ocular cameras, each lens was one wave band. The image captured by the multi-ocular cameras

at different lens had different scene. The images must be matched, and the main region of images must be segmented before they can be processed, so that the different spectrum of each point can be received.

The cameras are mounted at different location as nonparallel methods in general multiple camera system. Zheng [9] introduce the general binocular vision system and propose an image matching method. In some application, parallel multiple ocular cameras are applied, and to match these images is more difficult. One parallel binocular image matching method is proposed in ref [10]. In the method, SIFT (Scale Invariant Feature Transform) algorithm is used to extract feature vector of image. One matching method of parallel multi-ocular image is proposed in ref [11]. One channel image act as source, others as destination, and the edge points of the corn leaf in source image are source feature points. The feature point pair sets are constructed. The affine transform from destination image to source image is constructed, and the match of images is implemented.

The outline of the paper is as follows, Section 2 one multi-ocular images mutual segmentation method is proposed. In the last section, the conclusion is drawn.

2 Multi-ocular Images Mutual Segmentation

There are many segmentation techniques to single gray image introduced in section 1. These segmentation methods are applied to single image, not available to all gray images of one group multi-ocular images. So it is needed to find one effective method for the multi-ocular images. A new method is proposed next.

2.1 Segmentation to Single Multi-ocular Image

The camera adopted in my research is the TetraCam MCA made in USA. There are 4 channels in the camera, Red(R), Green(G), Blue(B) and Near infrared(NIR). The four channels are rectangle arranged, and there is one lens which diameter is 2.5mm and one 1.3M CMOS sensor which resolution is 1280*1024 in each channel.

The Fig.1 shows one group image captured by the camera. (a) –(d) is image of NIR, R, B and G channel respectively. The images are captured in field. It is about 0.5m from lens to corn canopy. The leaves flash in the sunlight, and they are sheltered each other. There are shadows of leaves on ground. It is very difficult to segment the main leaves for it is complexity in these images.

The Fig.2 shows the segment results of images in Fig.1. Fig.2 (a) is result of Fig.1 (a) based on watershed methods, the red lines are edge of segmented region. Fig.2 (b) is result of Fig.1 (c) based on CV model [6], the green lines are edge of segmented region. The leaves are not segmented in Fig.2 (a), there are many mosaics in main leaves, and the shadows are not the whole connected region too. In Fig.2 (b), the main leaves are segmented, but not very complete, there are some irregular edges in dark region of leaves are not segmented, and some useless shadows still do not be wiped off completely.

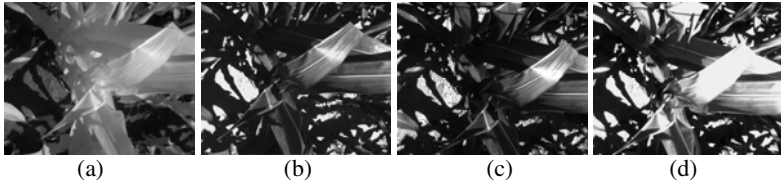


Fig. 1. One group image of corn canopy

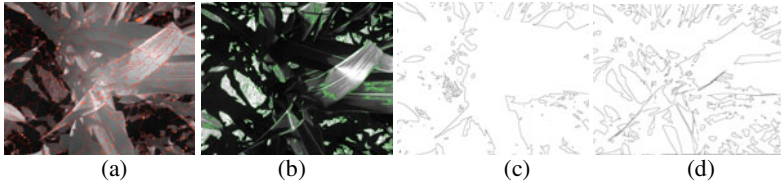


Fig. 2. Segmental results of Fig.1 based on watershed methods and CV model

2.2 Multi-ocular Images Mutual Segmentation

For to segment the main leaves from images, one new method is proposed as:

Step 1. The images are enhanced by log transform.

Step 2. The affine transforms between NIR image and others are built based on the method in ref. 11.

Step 3. The images are segmented based on CV model, and different connected components are labeled.

Step 4. The main leaves region in NIR image is extracted.

Step 5. Based on the transforms in step 1, the intersect regions between NIR image and others are extracted. So the main leaves in R, G and B images are segmented too.

$$T_{10} = \begin{bmatrix} 0.9967 & 0 & 0 \\ -0.0013 & 1.0029 & 0 \\ 7.5216 & -133.0673 & 1 \end{bmatrix}. \quad (1)$$

To images in Fig.1, based on the method in ref 11, the affine transforms between NIR image and others are built. Equation 1 is affine transform from R image to NIR image.

In Fig.2, (c)-(d) is segmented results that just remain the edge of region based on method in step 3. In Fig.2 (c), the main leaves region are selected, so the image of Figure 1 (a) is segmented, showed in Fig.4 (a). In Fig.2 (d), the leaves region in them are partitioned into many small connected region, these small region maybe be not closed region, and can not be merged into one whole leaf.

In Fig.3 (a), the segmented main leaves region in NIR image is showed. For the intensity of leaves in NIR wave band are bigger than other region in image, the region is segmented relatively completed. According to the equation in step 2, the regions in Fig.2 (d) that are matched with the main leaves region in Fig.3 (a) can be found. These regions are merged into one whole leaf region though may be not connected.

The segmented results of R, B, G image are showed in Fig.3 (c)-(d), the main leaves are segmented not very completed, and there are some small background region beside main leaves still included, but it is enough to meet our practice needs.

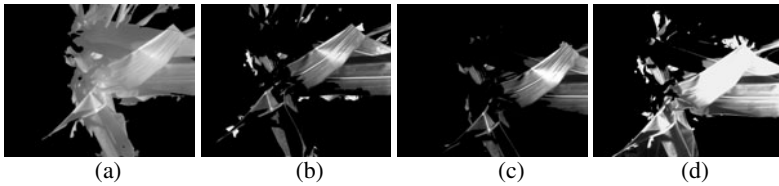


Fig. 3. Segmented results of Figure 1 based on new method

3 Conclusion

The Multi-ocular images mutual segmentation method proposed above is a new method applied in multi-ocular images. The method built on the preview segmentation and the mutual affine transform between NIR image and others. It can be applied to some complicated background multi-ocular images. The improvement will be done to find a method wipe off the small useless region in future.

References

1. Jain, A.K., Farrokhnia, F.: Unsupervised texture segmentation using Gabor filters. *Pattern Recognition* 12, 1167–1186 (1991)
2. Unser, M.: Texture classification and segmentation using wavelet frames. *IEEE Trans. Image Processing* 11, 1549–1560 (1995)
3. Kim, S.C., Kang, T.J.: Texture classification and segmentation using wavelet packet frame and Gaussian mixture model. *Pattern Recognition* 40(4), 1207–1221 (2007)
4. Acharyya, M., Kundu, M.K.: An adaptive approach to unsupervised texture segmentation using M-Band wavelet transform. *Signal Processing* 81(7), 1337–1356 (2001)
5. Mumford, D., Shah, J.: Optimal approximations by piecewise smooth functions and associated variational problems. *Commun. Pure Appl. Math.* 42, 577–684 (1989)
6. Chan, T.F., Vese, L.A.: Vese: Active Contours Without Edges. *IEEE Transactions on Image Processing* 10(2), 266–277 (2001)
7. Yang, B., Pei, Z.: Definition of Crop Condition and Crop Monitoring Using Remote Sensing. *Transactions of the Chinese Society of Agricultural Engineering* 15(3), 214–218 (1999)
8. Wu, S., Mao, R., Li, H., et al.: Review of Corn Condition Monitoring Using Remote Sensing in China. *Chinese Agricultural Science Bulletin* 21(3), 319–322 (2005)
9. Zheng, B., Duan, J., Tian, B.: On-line Calibration Technique of Vision Sensor in Moving Vehicles. *Modern Electronics Technique* 31(22), 187–191 (2008)
10. Liu, T., Yu, Z., Ma, Q.: Target Distance Computing Based on Parallel Binocular Stereo Vision. *Journal of QingDao University (Natural Science Edition)* 22(1), 59–62 (2009)
11. Zhu, J., Li, M., Zhang, Y., et al.: Matching method of parallel multi-cular image for corn canopy. *Transactions of Chinese Society of Agricultural Engineering* 26(11), 189–193 (2010)

Simulation and Analysis Groove of Wet Friction Based on Computational Fluid Dynamic

Yu Long Lei, Jie Tao Wen, Han Yong, Zhenjie Liu, and Hua Bing Zeng

State Key Laboratory of automotive simulation and Control, Jilin University
Changchun 130022, China
wenjietao@126.com

Abstract. Applying 3D graphics software UG to create three kinds of typical oil groove structure for wet friction plate model, using T / Grid hybrid mesh for the model grid and finally using Fluent RNG $k - \epsilon$ turbulence model and the moving reference frame for simulation, one can get to know the different flow field of cooling oil in three kinds of typical oil grooves. Comparatively analyze the inner flow fields of three kinds of oil grooves, so as to understand cooling characteristics of the different oil grooves and provide certain reference for the design of oil groove.

Keywords: Wet dual clutch, CFD, Internal flow fields.

1 Introduction

With the continuous development of automatic transmissions, the use of wet clutches has more and more proportion. A prominent feature of wet clutch is that the friction disc has some grooves of certain depth and shapes on its surfaces. The grooves contribute to heat dissipation of wet friction disc, the improvement of friction coefficient (The oil film can be damaged by the grooves, so friction coefficient is improved), and washing away clastic produced by slipping.

This paper analyses the three-dimensional flow field of three typical oil grooves of friction disc (radial, square and parallel), as reference 1 and 2 research results for reference, based on CFD technology. So one can get to know flow fields of cooling oil in different grooves.

2 Model Building

Apply 3D graphics software UG to create respectively three kinds of wet friction plates, which have radial, square and parallel grooves on it. The inner and outer diameters are respectively 139.7mm and 168.4mm. The width of radial and parallel grooves is 2.0mm, square 1.5mm. See fig.1 (a), (b) and (c).

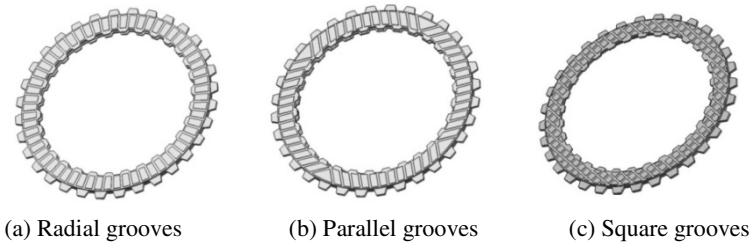


Fig. 1. Models of three kinds of oil grooves

In order to improve the accuracy of simulation, the whole plate is taken for numerical simulation. Because the requirement for accuracy in practical engineering is different, the computational domain where the variables change strongly will have more grids; In contrast, the computational domain will have fewer grids. So, this not only ensures the simulation precision, but also reduces the computing time. The 3-D mesh model was constructed by GAMBIT. With various input parameters such as mesh type, size, inner radius, GAMBIT automatically generates various mesh files for CFD. See fig.2.

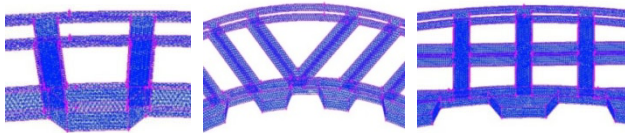


Fig. 2. Meshing the computational domain

The grid type, size and quantity of wet friction disc, see Table 1:

Table 1. Meshing oil groove

Oil groove	Radial	Square	Parallel
Size	0.5	0.3	0.5
Quantity	259126	1127834	268199
Type	T/Grid	T/Grid	T/Grid

3 CFD Simulation

The simulated situation is that cooling oil flows in the grooves when the clutch is closed. Cooling oil in grooves is high speed rotation mode, and because of the wall influence, its interior is a complex three-dimensional turbulent flow field. In this paper, we use the RNG $k - \epsilon$ model for the numerical simulation. RNG $k - \epsilon$ model has considered the swirling and rotating flow in the average flow. This algorithm effectively enhances accuracy for flows.

The setup of boundary conditions is illustrated in Figure 3. The inlet boundary was specified as a mass inlet 20L/min with the direction normal to the boundary. The outlet boundary was specified as a pressure outlet with atmospheric pressure. The walls were specified as moving walls 1500r/min.

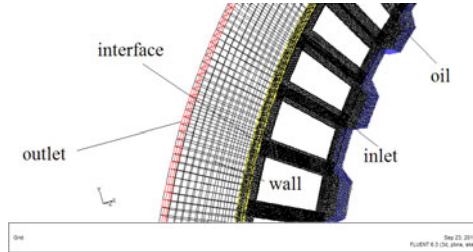


Fig. 3. Computing domain and boundary conditions

4 Results and Discussion

During clutch engagement process, temperature would be raised, because of the heat produced by the sliding between the friction discs and separators. When slip time lasts from 0.2 to 2.0s, heat is absorbed by the steel plates and friction discs. A negligible amount of heat is transferred to cooling oil. The effect of oil cooling heat dissipation is mainly reflected after the clutch engagement. On the city traffic, the clutch engagement is ordinary. The temperature of friction discs was easily raised, so the efficiency of oil heat dissipation was very important. The heat transfer between friction discs and flow belongs to convection heat transfer. The efficiency is mainly affected by velocity and turbulence.

Fig.4 shows the velocity of radial grooves. As we can see, with the increase of the radius, the velocity of flow also increases gradually. The velocity distribution between oil grooves is consistent. So the coefficient of heat transfer between grooves would not the velocity. This was good for the uniform heat dissipation of frictions. Fig.4 shows the turbulent of radial grooves. Serious turbulence appears at the entrance of flow. This is caused by the shock between flow and the walls. Turbulence is not good for heat dissipation. So the entrance is needed to improve. Moreover, the turbulence also appears at the export of grooves. This is because that the outlet is so small and the velocity is too high. So the shape is needed to optimize.

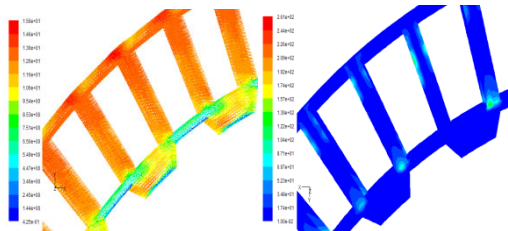


Fig. 4. Velocity and turbulence of radial grooves

Fig.5 shows the velocity of parallel grooves. It can be seen from the figure, the fluid velocity distribution of left and right sides vary strongly, the maximum speed of the left 17.8m/s, the maximum speed of the right 10.9m/s. This was bad for uniform cooling and easily caused internal stress of friction disc. Fig.6 shows the velocity of square grooves. It can be seen from the figure, the left and right cross on the friction plate, the distribution of the fluid velocity is more evenly. This is advantageous for uniform cooling.

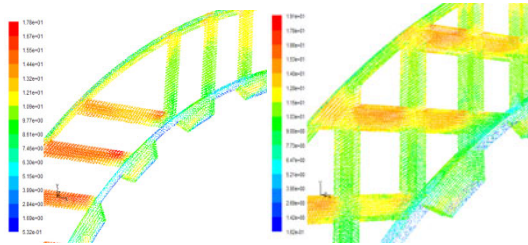


Fig. 5. Parallel velocity and square velocity

5 Conclusion

In this paper, one uses UG, mesh software Gambit and Fluent to simulate the flow field in the wet friction discs, and analyzes the flow of cooling oil to understand the effect of different grooves on the cooling oil flow and cooling effect.

Because the radial groove is short and simple structure, it is advantageous for cooling oil flow in the wet clutch, but has lower efficiency. This kind of groove is suitable for small and medium sized cars. The square groove has complex structure, the flow rate of cooling oil is low. Cooling oil has a long residence time in the clutch and higher efficiency. But it affects the oil quality because of the high temperature. So the square groove is suitable for heavy vehicles or construction machinery vehicles.

Acknowledgments. The authors would like to thank Technology development project of Jilin Province of China (No.20096008) & Program for Chang jiang Scholars and Innovative Research Team in University(No. IRT1017) for their support & Chinese National Natural Science Foundation (No. 51075182).

References

1. Zagrodzki, P., Samuel, A.T.: Generation of Hot Spot sin a Wet Multidisk Clutch during Short - Term Engagement. *Wear* 254(5/6), 474–491 (2003)
2. Zhao, S., Hilmas, G.E., Dharani, L.R.: Behavior of a Composite Multidisk Clutch Subjected to Mechanical and Frictionally Excited Thermal Load. *Wear* 264(11/12), 1059–1068 (2008)

Study on Dynamic Simulation Model of Telescopic Cylinder Based on Power Bond Graph and Simscape

Yulong Lei, Huabing Zeng, Zhenjie Liu, Xingzhong Li, and Jietao Wen

State Key Laboratory of automotive simulation and Control, Jilin University
Changchun 130022, China
zenghb11@mails.jlu.edu.cn

Abstract. The power bond graph is used to establish the dynamic model of telescopic cylinder. Simscape platform enables modeling and simulation of the hydraulic system. Analysis of the telescopic cylinder position characteristic curve and speed characteristics curve demonstrates the accuracy and reasonableness of the simulation model. All of this provides theoretical basis for the analysis and design of multistage hydraulic cylinder.

Keywords: Power Bond Graph, Simscape, Telescopic Cylinder.

1 Introduction

Telescopic cylinder is a non-standard hydraulic component of hydraulic cylinder. There is no recognized effective analysis method. Fewer research papers refer to the study on dynamic simulation model of telescopic cylinder. Establishment of mathematical model and solution of cylinder system in Simulink is a common research method. Reasonable simulation results can be obtained with the foundation of multi target theory of rigid body dynamics and through software collaboration methods. But there are some bottlenecks problems to solve, such as process complex, compute heavy and dynamic equation parameters is difficult to determine. This article will establish a power bond graph model of telescopic cylinder. The information of power flows in hydraulic system will be reflected by diagram method from the point of power. Simscape is used to build the model of telescopic cylinder and simulation. Simulation result provides theoretical basis for the analysis and design of multistage hydraulic cylinder.

2 Power Bond Graph Modeling

General method and steps modeling hydraulic system by power bond graph can be expressed as following. The first step is establishing a potential 0 node on each different pressures in the system. Measurement of pressure in the hydraulic system pressure is atmospheric pressure. So there is no need to establish a 0 node for atmospheric pressure. The second step is joining the capacitive components which simulate the liquid volume effect with 0 nodes. Then, resistive components join the 1 node between 0 nodes which

simulate the liquid resistance effects. Next step is joining the resistive components to 1 node between 0 nodes which simulate the leakage outside capacity.

Then, resistive components join the 1 node between 0 nodes which simulate the leakage inside capacity. Next step is joining inertial components to 1 node which simulate the pipeline fluid effect. The next is marking the correct direction of power flow. The last step is simplifying the power bond graph and marking a causal.

Based on the above assumptions and power bond graph modeling method, the model of telescopic cylinder in bond graph was shown in Figure 1.

In the figure, S_e refers to constant flow source. P and Q are input potential source and flow source, respectively. 0 node is collection of flow variable. 1 node is collection of potential variables. R_1 refers to internal resistance. C_1 represents internal capacity of hydraulic pipe. TF_1 is the No.3 cylinder energy converter. TF_2 is the No.2 cylinder energy converter. TF_3 is the No.1 cylinder energy converter. I_1 and R_2 are inertial components and resistive components of internal leakage in No.3 cylinder. C_2 and R_3 are capacitive components and resistive components of external leakage in No.3 cylinder. I_2 and R_4 are inertial components and resistive components of internal leakage in No.2 cylinder. C_3 and R_5 are capacitive components and resistive components of external leakage in No.2 cylinder. I_3 and R_6 are inertial components and resistive components of internal leakage in No.1 cylinder. C_4 and R_7 are capacitive components and resistive components of external leakage in No.1 cylinder. S_f refers to external constant potential source. F and V are external force source and flow source.

3 Simscape Model of Telescopic Cylinder

Simscape is a high performance simulation platform, including mechanical, electrical and hydraulic. Five main library files are Foundation library, SimDriveline, SimHydraulics, SimMechanics and Utilities, which provides full range construction capabilities of modeling mechanical, hydraulic, and electronic system. Three component libraries of SimDriveline, SimHydraulics, SimMechanics and Utilities will be used in this article. Simscape modeling of telescopic cylinder is shown in Fig 1.

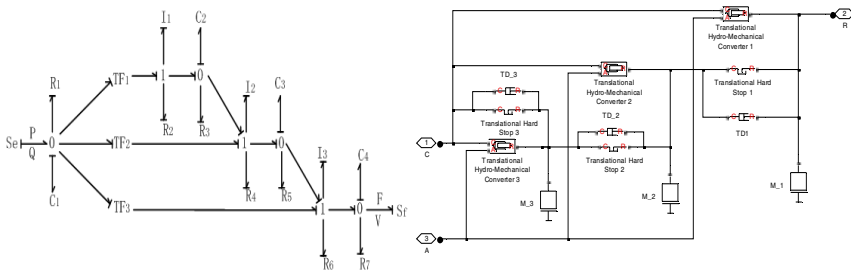


Fig. 1. Power bond graph modeling and Simscape modeling of telescopic cylinder

In the modeling, M_1, M_2 and M_3 are for simulation quality of each cylinder, which is the manifestation of inertia components in power bond graph. TD_1, TD_2 and TD_3, corresponding three cylinder vibration reduction mechanism, are the reaction of capacitive element in the power bond graph. Translational Hard Stop 1, Translational Hard Stop 2 and Translational Hard Stop 3 are for simulation of resistance elements in power bond graph, which refer to three cylinder moving emergency stop device. Translational Hydro-Mechanical Converter 1, Translational Hydro-Mechanical Converter 2 and Translational Hydro-Mechanical Converter 3 are the rod of telescopic cylinder. In the process of hydraulic cylinder movement, the No.3 rod move first.

4 Simulation Analysis of Hydraulic Cylinder System

For the dynamic performance analysis of hydraulic cylinder, sensor should be added to the modeling. Addition of sensor provides a convenient of observation and analysis of hydraulic cylinder rod position characteristic. At the same time for simple simulation system, Simscape modeling will be encapsulated.

Next, a hydraulic cylinder circuit should be designed to verification and analysis the subsystem of telescopic cylinder. The power source of this circuit is a constant angular velocity of oil pump. The back pressure of the relief valve is 50 bar. Load force is 2100N, which can be adjusted. Reversing valve is 2 position 3 way slide valve. The initial opening of P-A and A-T are -1.5 mm and 1.5 mm, respectively. Maximum flow area is 1 cm². The rod qualities are 6.4 kg with initial velocity zero. No.1 rod piston area is 12 cm². No.2 and No.3 rod piston area are 16 cm² and 22 cm², respectively. The slide valve will be controlled by signal, which is shown in Fig 2.

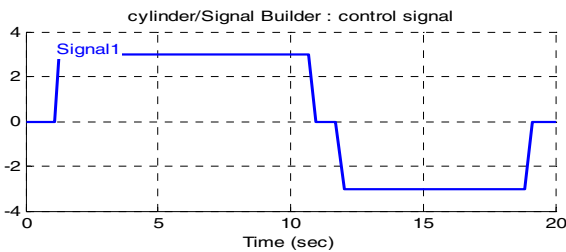


Fig. 2. Control signal

Run the system model, character diagram of rod position and speed come out, respectively. As shown in Fig 3.

Under the effect of control signal, No.3 rod act first, uniform at a 0.18m/s rate and move 0.8m to top. Then No.2 rod act, uniform at a 0.18m/s rate and move 0.8m to top. The last is No.1 at a 0.74m/s rate and reached out to the end of cylinder, under pressure to maintain 1.2 s. slide valve moves to the right side under the effect of control signal. The back pressure of relief valve is 50 bar. No.1 began to fall, last No.3, dropped to initial position, the speed to zero.

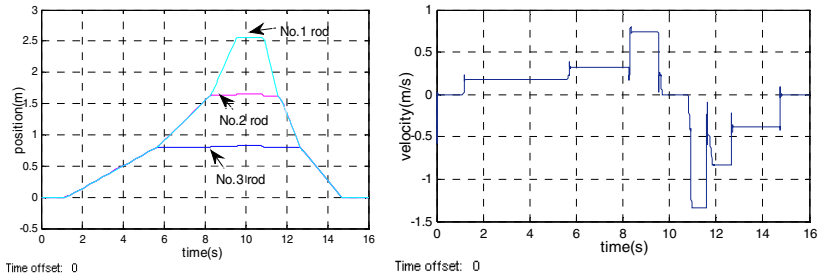


Fig. 3. Character diagram of rod position and speed

5 Conclusion

Hydraulic cylinders dynamic model establish based on power bond graph and Simscape. For modeling of multistage hydraulic cylinder, Simscape modeling methods can not only intuitive manifestation of its physical structure, simulation results consistent with the actual situation, but also easier to modify the model. This method can be used as a fixed mode of analysis and design of multistage hydraulic cylinder. Application of power bond graph and Simscape unites simulation provides theoretical basis for the analysis and design of multistage hydraulic cylinder.

Acknowledgments. The authors would like to thank Technology development project of Jilin Province of China (No.20096008) & Program for Chang jiang Scholars and Innovative Research Team in University (No. IRT1017) for their support & Chinese National Natural Science Foundation (No. 51075182) & National high technology research and development project (No. 2008AA11A127).

References

1. Yuan, S., Wang, D., Liu, D.: Application of Power Bond Graph and Matlab/Simulink in Dynamic Simulation and Analysis of Hydraulic System. *Coal Mine Machinery* 31(03), 76–78 (2010)
2. Yang, Y., Chen, L., Dong, C., Gao, Q.: ADAMS Based Modeling and Simulation for Multistage Hydraulic Cylinder. *Machine and Hydraulic*, 216–217 (2006)
3. Li, Z., Li, X., Gan, H.: Study on Dynamic Simulation Model of Peltry Energy Accumulator Based on Simulink and Power-bond Graph. *Mining and Metallurgical Engineering* 29(3), 19–22 (2009)

Progress of Coal Gangue Research

Jianguo Feng^{1,2}, GuiHua Li^{1,2}, and Liping Zhang^{1,2}

¹ Shandong Provincial Key Laboratory of Depositional Mineralization & Sedimentary Minerals, College of Geological Sciences & Engineering, Shandong University of Science and Technology, Qingdao, Shandong, China

² 579 Qianwangang Road Economic & Technical Development Zone, Qingdao Shandong Province, P.R. China

fengjianguo20316@sohu.com

Abstract. China is carrying out a large-scale energy bases in the early stages. Historical experience shows that a large number of coal gangue will be produce in the development of coal process. The coal gangue will occur environmental pollution when the improper disposal. This paper summarized the domestic and international coal gangue researching issues, such as basic characteristics, pollution mechanism, model research, and utilization and pollution control. Furthermore, the research directions in future were prospected.

Keywords: Coal gangue, Pollution control, China.

1 Introduction

Coal is the remains of plants through biochemical and physical chemistry and organic minerals into the sediment, is a mixture of polymer and mineral composition. Coal formation generally requires tens to hundreds of millions of years. China is a country rich in coal resources, is one of a coal as the main energy sources in developing countries. In primary energy consumption of China, the proportion of coal (about 75%) is higher than the world average of 1 time. The development of coal resources has formed nearly 3×10^9 t of coal gangue, and still more than 1×10^8 t per year to increase [1]. Therefore, a comprehensive grasp of gangue status and problems of research is particularly important.

Coal gangue is the solid waste generated in the coal mining, washing and processing. In narrow sense, coal gangue is the carbonaceous mudstone, carbonaceous sandstone when the coal mining to bring out. In general, coal gangue is a mixed rock when coal mine construction and production process exhaust out [2].

2 Gangue Research

Domestic and international research focus on coal gangue is summarized below.

2.1 Basic Characteristics of the Gangue

Deng Shao-xia, Xue Qun-hu analyzed the coal gangue to the appearance of the classification, chemical composition, mineral composition analysis and X-ray

diffraction of Whitewater Lane 5 # coal seam in Pucheng, Shaanxi, and divided into five different appearance of the gangue [3].

The X-ray fluorescence and diffraction analyzer were applied to qualitatively and quantitatively study on the chemical and mineral compositions of coal gangue from different places. The results showed that the chemical composition of the coal gangue had a close relation with the rock type of the coal gangue and the mineral composition of the coal gangue would be locally different with the location distribution [1].

Xu Zong-Xian, Zhao Hong-zhen collected 4 composite samples for laboratory analysis, results showed that the coal gangue in Hung Ling showed different layers of different mineral, rock chemistry and geochemistry, and different characteristics indicated differences of the gangue depositional environments and source [4].

Cui long-peng, Bai Jian-feng, Huang Wen-hui collected 44 samples of raw coal gangue in the Huainan coal mine, coal gangue was determined that 46 kinds of trace elements, and then filter out 11 kinds of harmful elements has environmental significance: Cd, Cu, Ni, Sn, Hg, Mn, As, Cr, Pb, Zn, F [5].

The geochemical characteristics of mine-affected areas on the south west of England were studied, results showed that Sn, As, Cu, Pb, Zn enriched [6].

B.R.Stewart, W.L.Daniels determined the physical and chemical properties and the reclamation potential of samples from 27 coal refuse piles of varying age. The results indicated that some refuse piles may be suitable for direct seeding, but many will require heavy lime and/or organic treatment for successful reclamation [7].

2.2 Mechanism of Environmental Pollution

Coal gangue pollution mechanism can be divided into the following areas.

2.2.1 Law of the Dissolution of Contaminants

Through the analyses of harmful trace elements existed in surface water and shallow groundwater in long duration gangue filled subsidence areas in Yanjiteng mining area, Worked out the mechanism of those trace elements precipitate from gangue through both eluviation and immersion[8].

Based on the immersing experiments of coal gangue from the Pansan Mine and the Xieqiao Mine, WU Dai-she, ZHENG Bao-shan studied deal with the leaching behavior of trace elements. According to the calculation of maximal trace element emission and comparison of clean soil with contaminated soil, the environmental impacts of coal gangue from the Panxie mining district on water and soil were evaluated [9].

Xiao Li-ping carried out soaking experiments of contamination dissolution releasing regularity of coal gangue with different efflorescence degree of Xinqu strip mine. The result showed that the higher efflorescence degree of coal gangue, the more mass of dissolution releasing inorganic salt contamination [10].

Liu Gui-jian , Yang Ping-yue based on the leaching experiments , hazardous trace elements from coal gangue are studied in relation to their forms of occurrences and contents, leaching times , leaching temperatures , and the pH values of the media[11].

Taken the coal gangue from Shandong Jining NO.3 coal mine as research object, a researching about the differences of the leaching characteristics of heavy metal between dynamic leaching and static immersion was carried out. The result showed

that the concentration of heavy metals which were leached is affected by the background value of the heavy metals in the coal gangue [12].

2.2.2 Adsorption and Desorption

A series of leaching experiments are conducted to research the leaching mechanism of pollutants from coal gangue in Jiaozuo mine field and their adsorption- desorption behaviors in soil. The concentrations of SO_4^{2-} , Cl⁻, Ca, Mg, Cr, Pb, Zn, Mn, Cu, Cd, pH and electrical conductivity in Leaching solution are measured [13].

Natural organic matter absorb organic pollutants has effect on microbial degradation rate in Soil and sediment, and experiment and simulation studies were carried out using Philippines as target pollutants [14].

2.2.3 Distribution Characteristics in Water or Soil Environment

Distribution of Zn, Cd, Cr, Cu and Mn in soil around Yanma mine of Jiaozuo coal mining area was studied, and pollution status of heavy metals on the soil environment was evaluated. Topography, climatic characteristics and soil property in the research area were used to study the distribution and source of heavy metals [15].

Heavy metals including Cr, Pb, Cu and Zn of soil nearby coal gangue dump in a coal mining area were tested. The results showed that the contents of four heavy metals in coal gangue of two mines are higher than the local background concentration; the gangue pile has polluted surrounding soil in a varying degree by the heavy metals [16].

J.Szczepanska, L.Twardowska studied on coal gangue distribution and impact on the environment in Silesia, Poland. The results showed that coal mining waste dumps is a long-term pollution source of groundwater, will continue for many decades [17].

Clark MW, Walsh SR, Smith JV analyzed the distribution of heavy metals of an abandoned mine in Australia; provide the basis for the environmental management of the mining area [18].

Gnandi K., Tobschall H.J. sampled soil near the Kpogame and Hahotoe mining area in south of Togo, analyzed the distribution of heavy metals [19].

Lin Z., Roger B., and Herbert Jr investigated the retention of heavy metals in secondary precipitates from a sulfidic mine rock dump and underlying podzolic soils by means of mineralogical and chemical extraction methods. Optical microscopy and electron microprobe analyses confirmed that pyrrhotite weathering has proceeded much further in the leached horizon relative to the accumulation horizon. The weathering of sulfides in the leached zone has resulted in the migration of most heavy metals to the accumulation zone or underlying soils [20].

The geochemical distributions of Co, Cr, Cu, Fe, Mn, Ni, Pb, and Zn were investigated to provide information about the mobility and availability of these elements in polluted sediments from the BaiXo Jacui region, southern Brazil. Higher percentages of the available fraction were verified in the Conde stream for the elements Cu, Fe, Ni, Pb, and Zn, indicating the sediment contamination by Coal-related activities [21].

2.2.4 Migration Laws

Coal gangue releasing a large quantity of Inorganic salts category polluting substances into the environment by precipitation leaching, causing surrounding areas of extensive

salinization with the soil and groundwater salinity far to exceed its normal, by laboratory simulated dynamic column experiment, the multi-component transport mechanism and pollution laws of the main pollution components of total hardness, sulfate radical and sodium ion in groundwater system are studied [22].

Kwong Y.T.J., Roots C.F., Roach P., and Kettley W. studied on post-mine metal transport and attenuation in the Keno Hill Mining district, central Yukon, Canada [23].

2.2.5 Environmental Impact

There are many kinds of polycyclic aromatic hydrocarbon (PAH) in gangue, and they can be liberated and enter into water body, which bring about an organic contamination [24].

WANG Xin-yi, YANG Jian studied the pollution caused by coal gangue dump, fresh and weathered coal gangue were collected from Yanma coal gangue dump, and groundwater was gathered near the dump. 22 contaminations were examined, and exceeding standard multiple and practice concentration were used to assess the level of groundwater pollution [25].

Gutta D. C. Paid attention to environmental aspects of selected trace elements associated with coal and natural waters of Pench Vally coalfield of India and their impact on human health [26].

2.3 Numerical Simulation of Contaminant Transport

Based on the porous media fluid mechanics and solute transport theory, the mathematical models are developed for describing the transportation and transformation of the trace elements in groundwater aquifer. Solutions to the coupled model are accomplished by finite-element method. The effects of pH value on coal mine spoil trace elements were analyzed on the basis of column leaching experiments [27].

The gangue mountain in Xinqiu Strip mine of Fuxin city was studied for the pollution of groundwater. The mechanism of gangue mountain leaching transport in the aquifer was analyzed. On the basis of considering flow, diffusion, absorption and fountain, a dynamic model was developed for simulating coal gangue leaching transport in groundwater system. Solutions to the model were accomplished by finite difference, which predicted the temporal and spatial distribution features of contaminant concentration. The supervised data of water quality was used to provide a quantitative verification of the model. The model simulations were compared to the measured data, which are reasonably agreed with model simulation. The simulation model provides scientific evidence for pollutions control of groundwater [28].

Transport of organic chemicals in vadose zone was simulated by using a coupling model of solute transport and water flow. In the solute transport equation, convective-dispersive transfer in liquid phase and diffusion in gas phase were considered. Furthermore, the effects of climatic conditions on transport were included in the boundary conditions of the governing equations [29].

Stromberg, B. Banwart, and S.Kinetieal established model of geochemical processes at Altik mining waste site in north Sweden [30].

JamesJ.Deitsch simulated desorption of organic contaminants form long term contaminated soil using distributed mass transfer rates [31].

2.4 Coal Gangue Utilization and Pollution Control

Ye Ji-wen, Shen Guo-dong, Lu Lu discussed the coal gangue comprehensive application for power, manufacture of building materials, agricultural application, engineering, chemical industry [2].

Based on the samples from the Xinjiang main coal mine regions, the coal gangues were classified by different criterions. Furthermore, the discussions and suggestions of the coal gangue practical utilization were made [32].

3 Gangue Research Prospects

It can be found through the summary on coal gangue that the future of Coal Gangue's research mainly concentrates in the following aspects:

- (1) Analysis method of harmful trace elements in coal gangue. Currently, some harmful trace element analysis methods require higher software and hardware equipment for laboratory, and complicated operation, there is further improvement.
- (2) Mechanism studies of coal gangue pollution have more achievements and indoor simulation development is rapider nearly ten or twenty years. Control on the condition of indoor simulation is strict, cannot reflect complex process of the natural conditions. So, research in the field or in situ conditions is important in further.
- (3) Controlling water, soil, ecological environment has polluted. It still has long distance from the achievements to practical application.

References

1. Gu, B.-W., Wang, P.-M.: Study on Different Coal Rejects Features and Volcanic Ash Activity from Different Areas. *Coal Science and Technology* 37(12), 113–116 (2009)
2. Ye, J.-W., Shen, G.-D., Lu, L.: Hazards and Comprehensive Utilization of CoalGangue. *China Resources Comprehensive Utilization* 28(5), 32–34 (2010)
3. Deng, S.-X., Xue, Q.-H.: Research and Analysis on the Essential Performance of Gangue from Baishui Coal. *Mineral Petrol* 30(3), 34–37 (2010)
4. Xu, Z.-X., Zhao, H.-Z.: Coal Gangue Geochemistry and Ancient Environmental Restoration on Hongling Coalmine of Hongyang Coalfield. *Resource Development & Market* 26(4), 349–353 (2010)
5. Cui, L.-P., Bai, J.-F., Huang, W.-H., et al.: Environmental trace elements in coal mining wastes in Huainan coal field. *Geochimica* 33(5), 535–540 (2004)
6. Pirrie, D., Gajnm, G.S., Sear, L.G., Hughes, S.H.: Mineralogical and geochemical signature of mine waste contamination. *Environmental Geology* 29(1/2), 58–65 (1997)
7. Stewart, B.R., Daniels, W.L.: Physical and chemical properties of coal refuse from southwest Virginia. *Environ. Qual.* 21, 635–642 (1992)
8. Wang, H., Hao, Q., Yin, E.: A Study on Water Pollution from Eluviating and Immersing Gangue. *Coal Geology of China* 18(2), 43–45 (2006)
9. Wu, D.-S., Zheng, B.-S., Kang, W.-D., et al.: Leaching Behavior of Coal Spoils and Environmental Impacts. *Earth and Environment* 32(1), 55–59 (2004)

10. Xiao, L.-P., Liang, B., Lu, H.-J., et al.: Releasement of Contaminants within Coal Gangue Based on Soaking Experiment. *The Chinese Journal of Geological Hazard and Control* 17(2), 151–155, 163 (2006)
11. Liu, G.-J., Yang, P.-Y., Peng, Z.-C., et al.: Study on Leaching of Potentially Hazardous Trace Elements from Coal-Waste Rocks. *Geological Journal of China Universities* 7(4), 449–457 (2001)
12. Cao, Y.-Q., Zhang, S.-S., Liu, H.-H., et al.: Leaching Characteristics of Heavy Metals in Coal Gangue in Both Dynamic Leaching and Static Immersion. *Journal of Hebei University of Engineering (Natural Science Edition)* 27(1), 76–80 (2010)
13. Guo, H.-X., Yang, J., Wang, X.-Y., et al.: Adsorption-desorption Behaviors of Pollutants from Coal Waste Rock on Soil in Jiaozuo Mine Field. *Journal of Agro-Environment Science* 27(1), 194–199 (2008)
14. Grosser, R.J., Friedrich, M., Ward, D.M., Inskeep, W.P.: Effect of model sorptive phases on phenanthrene biodegradation: different enrichment conditions influence bioavailability and selection of phenanthrene-degrading isolates. *Appl. Environ. Microbiol.* 66, 2695–2702 (2000)
15. Yang, J., Chen, J.-J., Wang, X.-Y.: Spatial Distribution of Heavy Metals in Soils around the Coal Waste Rock Pile and Their Environmental Pollution Assessment. *Journal of Agro-Environment Science* 27(3), 873–878 (2008)
16. Ji, L.-Y., Zhou, L., Feng, Q.-Y., et al.: Study on Heavy Metal Pollution of Soil nearby CoalGangue Dump in a Coal Mining Area. *Mining Safety & Environmental Protection* 34(1), 14–16 (2007)
17. Szczepanska, J., Twardowska, L.: Distribution and environmental impact of coal-mining wastes in Upper Silesia, Poland. *Environmental Geology* 38(3), 249–258 (1999)
18. Clark, M.W., Walsh, S.R., Smith, J.V.: The distribution of heavy metals in an abandoned mining area: a case study of Strauss pit, the Drake mining area, Australia: Implications for the environmental management of mine sites. *Environmental Geology* 40(6), 655–663 (2001)
19. Gnandi, K., Tobschall, H.J.: Heavy metals distribution of soils around mining sites of cadimium-rich marine sedimentary phosphorites of Kpogame and Hahotoe (southern Togo). *Environmental Geology* 41, 593–600 (2002)
20. Lin, Z., Herbert Jr., R.B.: Heavy metal retention in secondary precipitates from a mine rock dump and underlying soil. *Environmental Geology* 33(1), 1–12 (1997)
21. Teixeira, E.C., Ortiz, L.S., Alves, M.F.C.C., et al.: Distribution of selected heavy metals in fluvial sediments of the coal mining region of Baixo Jacui, RS, Brazil. *Environmental Geology* 41, 145–154 (2001)
22. Xiao, L.-P., Liang, B., Jin, X.-T.: Multi-component Transport Laws of Coal Gangue Leaching Solution in Groundwater System: an Experimental Study. *Journal of Natural Disasters* 17(3), 90–95 (2008)
23. Kwong, Y.T.J., Roots, C.F., Roach, P., Kettley, W.: Post-mine metal transport and attenuation in the Keno Hill Mining district, central Yukon, Canada. *Environmental Geology* 30(1/2), 98–106 (1997)
24. Yu, Y.-B., Tang, M.-G., Zhong, Z.-S., et al.: The Influence of Coal-Mining waste Piles on Hydro-Environment in Shandong Province. *Earth Science Frontiers* 18(11), 163–168 (2001)
25. Wang, X.-Y., Yang, J., Guo, H.-X.: Groundwater Pollution near Coal Waste Rock Dump. *Journal of Jilin University (Earth Science Edition)* 37(2), 326–330 (2007)

26. Gutta, D.C.: Environmental aspects of selected trace elements associated with coal and natural waters of Pench Vally coalfield of India and their impact on human health. *International Journal of Coal Geology* 40, 133–149 (1999)
27. Wang, X.-F.: Study on Trace Elements Transport from Coal Mine Spoil under the Condition of Rainfall. *Journal of Wuhan Polytechnic University* 26(1), 73–75 (2007)
28. Liang, B., Lu, H.-J., Xiao, L.-P., et al.: Numerical Imitation for Coal Gangue Leachate Transport in Groundwater System. *Journal of System Simulation* 19(7), 1439–1441, 1616 (2007)
29. Li, H., Li, X.-G., Huang, G.-Q., et al.: Numerical Simulation of Contaminant Transport in Vadose Zone during Rainfall and Evaporation. *Chemical Engineering (China)* 35(9), 51–54 (2007)
30. Stromberg, B., Banwart, S.: Kinetieal modeling of geochemical processes at Altik mining waste site in north Sweden. *Applied Geochemistry* 9, 583–595 (1994)
31. Deitsch, J.J.: Modeling the Desorption of Organic Contaminants form Long Term contaminated Soil Using Distributed Mass Transfer Rates. *Environ. Sci. Technol.* 31(6), 1581–1588 (1997)
32. Qi, X.-X., Wang, X.-J., Li, Y., et al.: Study on Properties of the coal Gangue from Xinjiang Main Coal Mine Regions and Their Utilization Suggestions. *Journal of China Coal Society* 35(7), 1197–1201 (2010)

Verb Consciousness Passwords in the Fingers (2)

Yunfeng Zhu

Department of Physics and Electronics Information Science, Baise University, Baise, China
yunfengzhu12345@126.com

Abstract. The process from the body motion studied by Aristotle before the 4th century BC to the Newton's Law of Motion and the Law of Universal Gravitation Established by Newton 1687 AD, took Human 2000 years, the Nature Science obeys the Western Logic; The process from the Feminine and Masculine, the Eight Diagrams found by Fuxi 7000 years ago to the breakthrough point of Consciousness Passwords, took Human 7000 years, the Humanities obey the Eastern logic. The basis of Intelligent Science is the Consciousness Passwords. When Human and Robots own the same set of Consciousness Passwords, we can achieve the Human-Robot interaction.

Keywords: Feminine and Masculine, Eight Diagrams, Zhouyi, Consciousness Password, Heaven.

1 Introduction

The Universe, Life and Brain are three Riddles of Modern Science, but the Nature Science obeys the Western Logic, the Humanities obey the Eastern logic.

7000 years ago Fuxi found the Feminine and Masculine, the Eight Diagrams, 5000 years ago Cangjie invented the Chinese characters, 3000 years ago Jichang wrote out the Zhouyi, these are the source of Chinese Civilization. Leibnitz saw the Binary of 0 or 1 in a computer from the Feminine and Masculine, he gave us a lessons: Studying the Humanities must start from the Zhouyi, including the Intelligent Science as well.

Before the Intelligent Science was born, the Artificial Intelligence and Computer Technology became two legs to push the Smart Robots. With the help of the combination of Intelligent Science and Computer Technology, Mankind will be able to achieve the precise control on Robot and overcome the infinite diversity of reality. The virtues of Intelligent Science is just the shortcoming of Artificial Intelligence, the Intelligent Science will replace the Artificial Intelligence. The steps to look for the Chinese Alphabetic Passwords and the Consciousness Passwords are that adjusting the hand forms through the Chinese Alphabet and looking for the Consciousness Passwords through the hand forms. The step adjusting the hand forms through the Chinese Alphabet has been solved [1, 2, 3, 4, 5], the step looking for the Consciousness Passwords through the hand forms has been solved partly [6]. I have finished 3456 Verb Consciousness Passwords, and what to follow is looking for 3456 Noun Consciousness Passwords. I will publish one-fourth of 6912 Consciousness Passwords, and apply for a patent.

2 Distribution of Verb Consciousness Passwords in the Fingers

The running rules of Verb Consciousness Passwords in the fingers have been shown [6]. We put the Consciousness Password distribution in the fingers out: the anterior dactylopod of thumb wipes the forefinger and little finger, the 4 groups contain 48 verb Consciousness Passwords.

2.1 The First Group: 12 Chinese Words Relating to Getting One's Clothes Dirty

The gestures that the outside of thumb's anterior dactylopod wipes the outside of forefinger and little finger's anterior dactylopod indicate a group of objective verbs relating to taking clothes off, then the gestures that the outside of thumb's anterior dactylopod wipes the outside of forefinger and little finger's middle dactylopod indicate a group of objective verbs relating to washing clothes because of having someone's clothes dirtied.

- miè (nothing; Small ; besmirch; disdain)
- lā ta (dirty; sloppy)
- rǎ n (dye; catch; be contaminated by)
- hùn (muddy; turbid; confused)
- wū (smear; soil; dirty)
- huì (dirty; filthy)
- mě i (contaminate; request)
- wò (get dirty; dye) [wòchuò (dirty;filthy)]
- ā za (filthy ; dirty)
- zhǎ n (make dirty)
- zā η (dirty; filthy; smear; stain) [ā ηzā η (dirty; filthy; foul)]
- rá η (get one's clothes dirty)

These 12 Chinese words are the objective verbs, the anterior dactylopod's outside of thumb wipes the outside of forefinger and little finger's middle dactylopod, their distribution in the fingers is showed as follows (Figure 1, Figure 2):

miè—the anterior dactylopod's outside of forefinger→the middle dactylopod's outside of little finger {out } (Fig 1), wū miè= defame.

lā ta—the middle dactylopod's outside of little finger→the anterior dactylopod's outside of forefinger {in}(Fig 2)

rǎ n—the anterior knuckle's outside of forefinger→the middle dactylopod's outside of little finger {out } (Fig 1),

hùn—the middle dactylopod's outside of little finger→the anterior knuckle's outside of forefinger {in}(Fig 2)

wū —the middle dactylopod's outside of forefinger→the middle dactylopod's outside of little finger {out } (Fig 1), wū rǎ n= pollute.

huì—the middle dactylopod's outside of little finger→the middle dactylopod's outside of forefinger {in}(Fig 2), wū huì= filthy.

mě i——the middle knuckle's outside of forefinger→the middle dactylopod's outside of little finger {out } (Fig 1)

wò[wòchuò] ——the middle dactylopod's outside of little finger→the middle knuckle's outside of forefinger {in}(Fig 2)

ā za ——the rear dactylopod's outside of forefinger→the middle dactylopod's outside of little finger{in}(Fig 2)

zhǎ n——the middle dactylopod's outside of little finger →the rear dactylopod's outside of forefinger {out } (Fig 1),

zā η [ā ηzā η] ——the rear knuckle's outside of forefinger→the middle dactylopod's outside of little finger{in}(Fig 2)

ránη——the middle dactylopod's outside of little finger→the rear knuckle's outside of forefinger {out } (Fig 1)

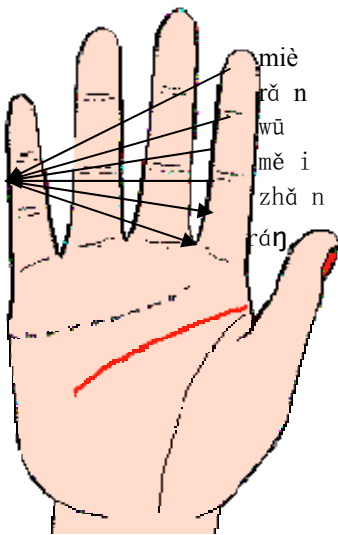


Fig. 1.

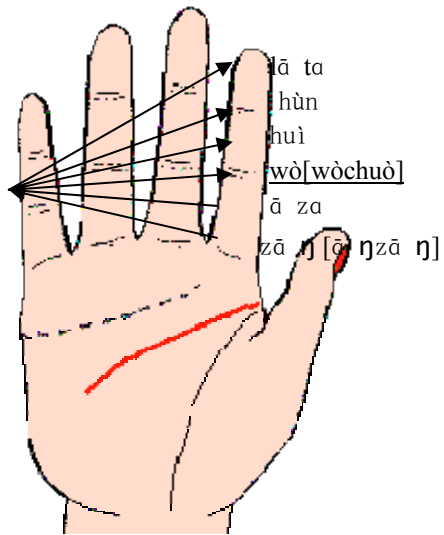


Fig. 2.

2.2 The Second Group: 12 Chinese Words Relating to Red, Request and Integrity

The gesture that the anterior dactylopod's inside of thumb wipes the inside of forefinger and little finger's anterior dactylopod stands for a group of subjective verbs relating to infra red and loyalty, however the subjective verbs relating to dirty are dyeing, měi means both the pollution and the request, therefore the gestures that the anterior dactylopod's inside of thumb wipes the inside of forefinger and little finger's middle dactylopod indicate a group of subjective verbs relating to red, request and integrity.

- dā n(red; a small pill; a powder)
- gàn(dark purple)
- hóng(red; vermilion; very popular)
- chēng(red; redden)
- tóng(red)
- qiàn(deep red; Indianmadder)
- fēi(bright red)
- chén(sincere; honest; candid)
- xún(trust; be in confidence; indeed; true; real; truly)
- dǎ n(kind and sincere)
- xìn(honest; trust; believe; believe in)
- fú(believe in ; inspire confidence in somebody)

These 12 Chinese words are a group of subjective verbs, the anterior dactylopod's inside of thumb wipes the inside of forefinger and little finger's middle dactylopod, their distribution in the fingers is showed as follows (Figure 3, Figure 4):

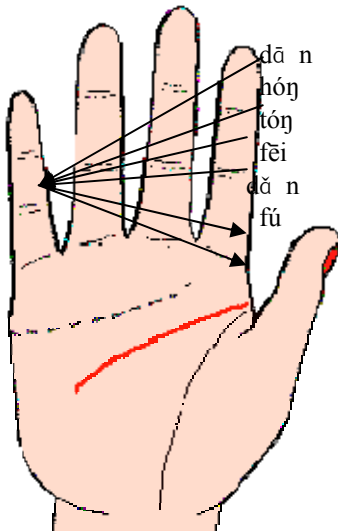


Fig. 3.

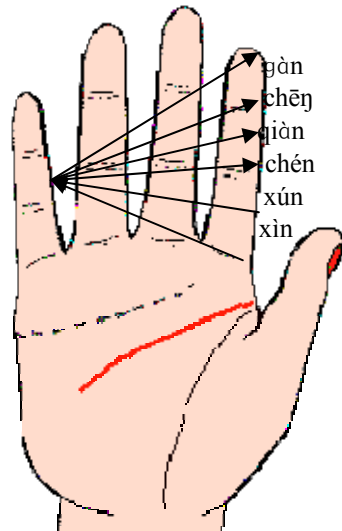


Fig. 4.

dā n—the anterior dactylopod's inside of forefinger→the middle dactylopod's inside of little finger {out } (Fig 3)

gàn—the middle dactylopod's inside of little finger→the anterior dactylopod's inside of forefinger {in } (Fig 4)

hóng—the anterior knuckle's inside of forefinger→the middle dactylopod's inside of little finger {out } (Fig 3) , hóngxīn=red heart.

chēng—the middle dactylopod's inside of little finger→the anterior knuckle's inside of forefinger {in } (Fig 4)

tóng——the middle dactylopod's inside of forefinger→the middle dactylopod's inside of little finger {out } (Fig 3) , hóng tóng tóng= strawberry pie.

qiàn——the middle dactylopod's inside of little finger→the middle dactylopod's inside of forefinger {in } (Fig 4) , qiàn hóng =alizarin red.

fēi——the middle knuckle's inside of forefinger→the middle dactylopod's inside of little finger {out } (Fig 3) , fēi hóng =bright red.

chén——the middle dactylopod's inside of little finger→the middle knuckle's inside of forefinger {in } (Fig 4)

xún——the rear dactylopod's inside of forefinger→the middle dactylopod's inside of little finger {in } (Fig 4)

dǎn——the middle dactylopod's inside of little finger→the rear dactylopod's inside of forefinger {out } (Fig 3)

xìn——the rear knuckle's inside of forefinger→the middle dactylopod's inside of little finger {in } (Fig 4) , xìn yòη= credit.

fú——the middle dactylopod's inside of little finger→the rear knuckle's inside of forefinger {out } (Fig 3) , fúxìn = solutia – saflex.

2.3 The Third Group: 12 Chinese Words Relating to Washing Clothes

The first group indicates a group of objective verbs relating to getting one's clothes dirty, the third group indicates a group of objective verbs relating to washing clothes, the third group is the antonyms of the first group.

\
 v (bathe)
 mù (wash one's hair)
 jiā n (wash)
 g uàn (wash one's hands; wash)
 zǎ u (wash hand; bathe)
 xǐ (wash; bathe)
 \
 hū v (have a bath)
dí (wash; cleanse)
 huàn (wash; launder)
 jié (clean)
 zhuó (wash; rinse)
 jìη (clean; unadulterated; net)

These 12 Chinese words are a group of objective verbs, the anterior dactylopod's outside of thumb wipes the outside of forefinger and little finger's middle dactylopod, their distribution in the fingers is showed as follows (Figure 5, Figure 6):

\
 v ——the anterior dactylopod's outside of forefinger→the middle knuckle's outside of little finger{out} (Fig 5) , xǐ v = bath.
 mù——the middle knuckle's outside of little finger→the anterior dactylopod's

outside of forefinger {in} (Fig 6) , mù ν = have a bath.

jiā n——the anterior knuckle's outside of forefinger→the middle knuckle's outside of little finger {out} (Fig 5) .

g uàn——the middle knuckle's outside of little finger→the anterior knuckle's outside of forefinger {in} (Fig 6) , guàn xī = wash one's hands and face.

zǎ u——the middle dactylopod's outside of forefinger→the middle knuckle's outside of little finger {out} (Fig 5) , xī zǎ u = have a bath.

xī——the middle knuckle's outside of little finger→the middle dactylopod's outside of forefinger {in} (Fig 6) , xī zǎ u = have a bath.

hū ν ——the middle knuckle's outside of forefinger→the middle knuckle's outside of little finger {out} (Fig 5)

dí——the middle knuckle's outside of little finger→the middle knuckle's outside of forefinger {in} (Fig 6) , xī dí = scrubbing.

huàn——the rear dactylopod's outside of forefinger→the middle knuckle's outside of little finger {in} (Fig 6)

jié——the middle knuckle's outside of little finger→the rear dactylopod's outside of forefinger {out} (Fig 5) , jiéjìη = clean.

zhuó——the rear knuckle's outside of forefinger→the middle knuckle's outside of little finger {in} (Fig 6)

jì η——the middle knuckle's outside of little finger→the rear knuckle's outside of forefinger {out} (Fig 5) , jiéjìη = clean.

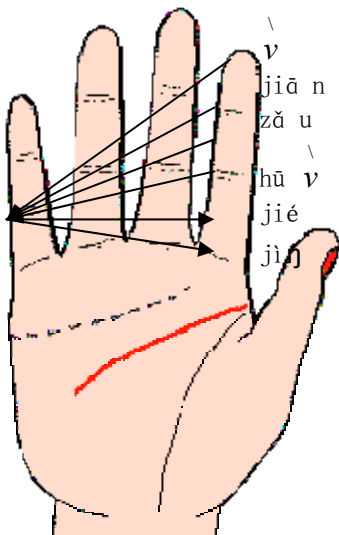


Fig. 5.

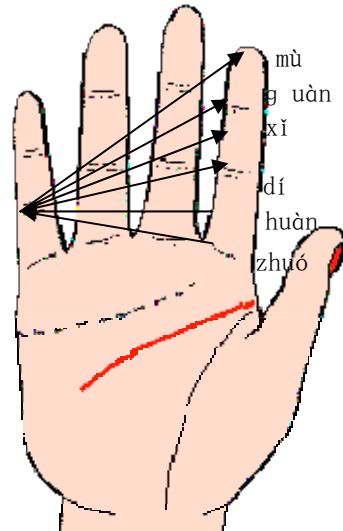


Fig. 6.

2.4 The Fourth Group: 12 Chinese Words Relating to Green, Insincere and Ablution

The second group indicates a group of subjective verbs relating to red, request and integrity, the fourth group indicates a group of subjective verbs relating to green, insincere and ablution, the fourth group is the antonyms of the second group.

qí (dark grey)

cā η (dark blue; cold)

lǜ (green)

lù (green)

zǒu (black red)

cùi (green)

xì (semiannual exorcism performed at the water's edge in ancient times)

bì (bluish green)

sài (unkind)

fú (ceremony of offering sacrifice to gods to wash away evil influence)

hòu (bright ; luminous)

jiǎ u (clear and bright; white; clean)

These 12 Chinese words are a group of subjective verbs, the anterior dactylopod's inside of thumb wipes the inside of forefinger and little finger's middle dactylopod, their distribution in the fingers is showed as follows (Figure 7, Figure 8):

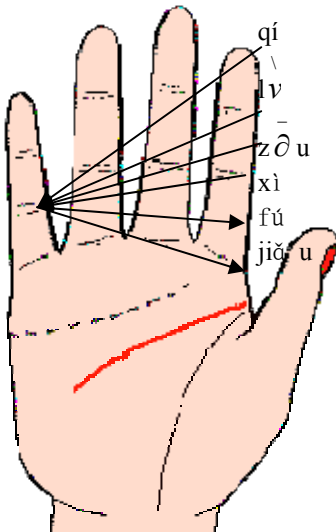


Fig. 7.

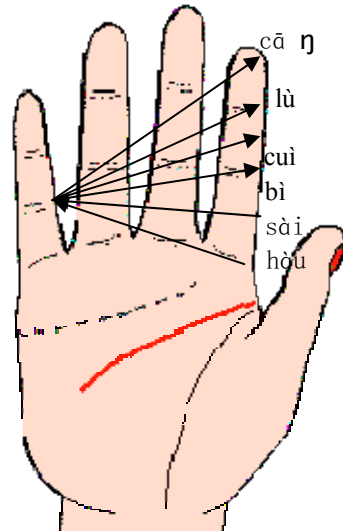


Fig. 8.

3 Conclusion

The process from the body motion studied by Aristotle before the 4th century BC to the Newton's Law of Motion and the Law of Universal Gravitation Established by Newton 1687 AD, took Human 2000 years, the Nature Science obeys the Western Logic; The process from the Feminine and Masculine, the Eight Diagrams found by Fuxi 7000 years ago to the breakthrough point of Consciousness Passwords, took Human 7000 years, the Humanities obey the Eastern logic. When Human and Robots own the same set of Consciousness Passwords, we can achieve the Human-Robot interaction.

Nobody believes in my success in looking for the Consciousness Passwords, the process looking for the breakthrough point has taken me 17 years.

Heaven be praised!

References

1. Zhu, Y., Qin, H., Pan, C.: The Chinese Alphabetic Passwords in the Fingers. In: 2010 2nd Asia-Pacific Conference on Information Processing (APCIP 2010), ushan (Nanchang), China, September 17-18, pp. 53–56 (2010)
2. Zhu, Y., Qin, H., Wang, Z., Wei, W., Zhu, M.: Vowel Passwords and Vowels Group in the Fingers. In: 2010 International Conference on Computer and Computational Intelligence (ICCCI 2010), Nanning, China, December 25-26, pp. V3-118–V3-124 (2010)
3. Zhu, Y., Qin, H., Pan, C.: Consonant Passwords in the Fingers (1). In: 2011 International Conference on Fuzzy Systems and Neural Computing (FSNC 2011), Hong Kong, China, February 20-21, pp. 214–217 (2011)
4. Zhu, Y., Qin, H., Pan, C.: Consonant Passwords in the Fingers (2). In: 2011 International Conference On Fuzzy Systems and Neural Computing (FSNC 2011), Hong Kong, China, February 20-21, pp. 218–222 (2011)
5. Zhu, Y., Qin, H.: Adjusting the Hand Forms through the Chinese Alphabet. It is Being Contributed to a Foreign Journal
6. Zhu, Y.: Verb Consciousness Passwords in the Fingers (1). In: 2011 3rd International Conference on Computer Technology and Development (ICCTD 2011), Chengdu, China, November 25-27 (2011)

Sparse Representation-Based Face Recognition for Single Example Image per Person

Zhen Wang and Ming Zhu

Department of Automation, University of Science and Technology of China
wzno@mail.ustc.edu.cn, mzhu@ustc.edu.cn

Abstract. A new algorithm is proposed to deal with single training sample face recognition. After geometric normalization of human faces, we generate 13 virtual samples for each face by using geometric transformation and svd decomposition. The distribution of gray value of each image is processed to be normal standard distribution. Finally sparse representation is used to recognize faces. The result of experiments on ORL database shows that our algorithm is better than classical algorithms and new algorithms proposed recently.

Keywords: Face recognition, single sample, sparse representation.

1 Introduction

Face recognition has been an active research area in computer vision and pattern recognition for many years and significant achievements have been made by researchers. The potential application of face recognition is very broad, such as identification and verification, human-computer interaction, virtual reality, database retrieval, multimedia, and computer entertainment[1]. But due to the effect of different illumination, facial expressions, head pose and age variations, face recognition is still an unsolved problem[2]. Chellappa etc. summarized the future research trends of face recognition which include remote face recognition, video-based face recognition, face recognition in a camera network, face recognition in web 2.0 and face recognition across aging. This paper is focusing on face recognition with single example image per person. To be precise, only one image per person can be used as the training image. A real world task is to search all clips where a special person appears in surveillance video. For a variety of reasons, such as the low resolution, varying illumination, different head poses and occlusion, it is pretty challenging to settle this problem. Chen etc.[3] proposed a novel method to use integral projection to generate virtual images, and then apply PCA(principle component analysis) to the new images and the initial images to perform recognition. Zhang etc.[4] used singular value perturbation method to generate new images and PCA was still utilized. Gao etc. firstly decomposed the only image into a smooth general appearance image and a difference image. Then the later image was used to estimate the within-class scatter matrix. Finally FLDA(fisher linear discriminate analysis) was used to extract face features. Koc etc. thought out a new way using QR decomposition to construct within-class scatter matrix, and then FLDA was also

utilized to computer face features. Ebrahimpour etc. [7] proposed a new method to generate new faces using gabor filters with different angles, then 2DPCA was used to extract face features and finally nearest neighbor classifier and enhanced majority voting classifier were applied to do recognition. Chang etc. generated virtual faces using Shift and PCA reconstruction method, and then sparse representation was used. Sparse representation was firstly applied to face recognition by Wright etc.[8][9] in 2008 and this work was judged breakthrough in face recognition.[10]. In this paper, we firstly generate thirteen virtual samples by geometric transformation and SVD, then we integrate sparse representation to solve single sample per person face recognition problem with difference facial expressions and slightly head pose variations. Experiments on ORL face database show that our method is much better than the above methods proposed in [3][4][5][6][7][8].

2 The Algorithm

2.1 Virtual Face Image Generation

One of the difficulties of single sample problem is the limit of the number of training face images. Due to varying head poses, facial expressions and illumination in real circumstances, the recognition rate would be very low if we only make use of single image per person. In this paper, we focus on slightly head pose and expression variations and we don't care about the different illumination. We generate virtual images using mirroring, scaling, head pose approximation [11], which can be called geometric transformation methods, and SVD method. After virtual image generation, we integrate sparse representation here to perform face recognition. The generation process is summarized as follows:

1. For every person, we have a frontal face image, denoted by A1;
2. We mirror A1 to eliminate part effects of head rotation, denoted by A2;
3. Due to inaccuracy of geometric normalization of face images, the size of faces of the same person can also be different. We enlarge A1 by 1.1 times, and then crop the size to be similar with A1 and we get A3. Also we shrink A1 by 0.9 times and the blank part is filled by zero, then A4 is generated. By mirroring A3 and A4, we obtain A5 and A6 respectively;
4. Recently a simple method to simulate head pose variations is proposed[11], the main idea of this method is to divide the face by central vertical line, and then enlarge one side of the face image while shrink the other side. The experiment shows that the result is acceptable in 15°. We denote a $m \times n$ image by $I(x, y)$, where $x \in [1, m]$, $y \in [1, n]$, $I(x, y) \in [0, 1]$. We compute the generated image by the following formula:

$$y' = (1 + \text{sign}(y - n/2)) \sin(\partial)(y - n/2) + n/2 \quad (1)$$

$$x' = x \quad (2)$$

5. We set ∂ to be 5°, 10° and 15° then we get A7, A8 and A9, after mirroring the three images we get A10, A11, A12 respectively;

6. We first apply SVD on A_1 , then we have $A_1=U*\Sigma*V'$. The size of face image we are handling is 32×32 , so Σ is a diagonal matrix with 32 non-zeros parameters at most. When we only consider the first 8 numbers on the diagonal line of Σ while other positions are filled with 0, we can reconstruct a new image, denoted by A_{13} . If we only consider the second 8 numbers on the diagonal line of Σ , we can reconstruct A_{14} .

2.2 Sparse Representation

Sparse representation is a signal acquisition and codec theory[12], considering sparsity of signals, introduced by David Donoho, Emmanuel Candes and Terence Tao. The distinctive feature of sparse representation is that it breaks through the restrictions of sampling theorem. John Wright[13] firstly applied sparsity to face recognition in 2008 and made great progress in this field. The main idea of sparsity representation based face recognition is to construct an over-complete dictionary, the recognition is done by calculating the sparsity representation of the test sample over the dictionary.

We consider single face per person face recognition in this paper. For training sample P_i , we first generate $w-1$ virtual image using the methods stated in section 2.1, so we have w images for P_i . The images are denoted by $P_{i,1}, P_{i,2}, \dots, P_{i,w}$ and it should be noticed that the images are all processed to be a vector by head-tail connecting column vectors. When we finish virtual images generation for all k samples, we get the so called dictionary:

$$P = [P_{1,1}, P_{1,2}, \dots, P_{k,w}] \tag{3}$$

According to sparsity representation theory, for the test sample y , we can approximate the test sample by linear combination of column vectors of the dictionary:

$$y = Ix \tag{4}$$

The process of calculating x can be regarded as an optimization problem:

$$\hat{x} = \min \{ \|y - Px\|_2 + \lambda \|x\|_1 \} \tag{5}$$

We solve equation(5) by iteration of Newton interior-point method[13]. Ideally, we can have

$$x = [0, \dots, 0, x_{i,1}, \dots, x_{i,w}, 0, \dots, 0]^T \tag{6}$$

If we have the solution of (5) like (6), we are convinced that the test sample is the i th person. But due to different illumination and expression etc., this rarely happens. Normally, we identify which person the test image belongs to by comparing the 2 norm of the difference between the test sample and the estimated image of one person:

$$identity(y) = \arg \min_i \|y - P\delta_i(\hat{x})\|_2 \tag{7}$$

Here, $\delta_i(\hat{x}) = diag[0, 0, \dots, \underbrace{1, \dots, 1}_{(i-1) \times w + 1, \dots, i \times w}, \dots, 0, 0]x$ (8)

When we consider occlusion problem, (4) should be rewritten as:

$$y = Px + e \tag{9}$$

Also, (9) can be written as: $y = [P, I] \begin{bmatrix} x \\ e \end{bmatrix}$ (10)

Our identification function is modified to be the following accordingly:

$$identity(y) = \arg \min \|y - I\delta_i(\hat{x}) - \hat{e}\|_2 \tag{11}$$

The resolution of (11) is the same as (5), we don't repeat here.

3 Experiments

We conduct experiments on ORL[14] human face database to verify our algorithm. ORL is composed of 400 face image from 40 people, each has 10 images, with different shooting time, facial expression, facial details(glasses or no glasses) and slight rotation of faces. The faces are normalized to be 32x32 in this paper. The face images of the first person is shown in Fig.1:



Fig. 1. Example faces of the first person in ORL face database

We should tell that we do a simple histogram normalization besides geometric normalization. We assume the histogram follows Gaussian distribution, so we can normalize the distribution to be a standard Gaussian distribution, then the gray scale are mapped to [0,1].

For each person, we use the first picture as the training image, the rest nine images are used as test images. The new generated virtual faces after the above histogram processing are shown in Fig.2 and the corresponding serial-number according to section 2.1 is shown in Table 1.



Fig. 2. Virtual faces of the 1st person in ORL

Table 1. Serial number of the virtual images

A1	A2	A13	A14	A4	A6	A3
A5	A7	A10	A8	A11	A9	A12

Comparing with [3][4][5][6][7][8], our recognition rate on ORL database is higher. The result is shown in Table 2 :

Table 2. Comparison of recognition rate

ORL database	Method in [3]	Method in [4]	Method in [5]	Method in [6]	Method in [7]	Method in [8]	Our Method
Recognition rate(%)	44.17	42.39	75.56	76	74.44	71.39	77.50

The experiment results show that our method is highest in these algorithms and our method is more robust to expression and head rotation.

4 Conclusion

In this paper, we propose a novel solution to single face per person recognition, when only considering facial detail, expression and slight head rotation. We first generate virtual images through geometric transformation and SVD related method. Then we organize the virtual faces into an over-complete dictionary. Finally sparse representation is utilized to recognize the test image. The experiment shows that our method has higher recognition rate comparing with other methods. But this recognition still can't meet the requirement of the real world. We will concern 3D face reconstruction from a single image and hope that the problem of head poses can be solved in the future.

Acknowledgment. The authors would like to thank the support received from National Research Program of China under contract No.2011BAH11B01 and National Natural Science Foundation of China under contract No.60975045.

References

1. Chellappa, R., Sinha, P., Phillips, P.J.: Face Recognition by Computers and Humans. Computer 43, 46–55 (2010)
2. Ross, A.A., Jain, A.K., Nandakumar, K.: Handbook of Multibiometrics. Springer, Heidelberg (2006)
3. Chen, S., Zhang, D., Zhou, Z.-H.: Enhanced (PC)2A for face recognition with one training image per person. Pattern Recognition Letters 25, 1173–1181 (2004)
4. Zhang, D., Chen, S., Zhou, Z.: A new face recognition method based on SVD perturbation for single example image per person. Applied Mathematics and Computation 163, 13 (2005)
5. Gao, Q.-X., Zhang, L., Zhang, D.: Face recognition using FLDA with single training image per person. Applied Mathematics and Computation 205, 726–734 (2008)

6. Koç, M., Barkana, A.: A new solution to one sample problem in face recognition using FLDA. *Applied Mathematics and Computation* 217, 10368–10376 (2011)
7. Ebrahimpour, R., Nazari, M., Azizi, M., Amiri, A.: Single Training Sample Face Recognition Using Fusion of Classifiers. *International Journal of Hybrid Information Technology* 4 (2011)
8. Chang, X., Zheng, Z., Xie, C.: Sparse Representation-based Face Recognition for Single Sample. *Computer Engineering(Chinese)* 36 (2010)
9. Wright, J., Ganesh, A., Zihan, Z., Wagner, A., Yi, M.: Demo: Robust face recognition via sparse representation. In: 8th IEEE International Conference on Automatic Face & Gesture Recognition, FG 2008, pp. 1–2 (2008)
10. Kroeker, K.L.: Face Recognition Breakthrough. *Commun. ACM* 52, 18–19 (2009)
11. Zhang, S.: Various pose face recognition with one front training sample. *Journal of Computer Applications(Chinese)* 26 (2006)
12. Candes, E.J., Romberg, J., Tao, T.: Robust uncertainty principles: exact signal reconstruction from highly incomplete frequency information. *IEEE Transactions on Information Theory* 52, 489–509 (2006)
13. Seung-Jean, K., Koh, K., Lustig, M., Boyd, S., Gorinevsky, D.: An Interior-Point Method for Large-Scale L1-Regularized Least Squares. *IEEE Journal of Selected Topics in Signal Processing* 1, 606–617 (2007)
14. Samaria, F.S., Harter, A.C.: Parameterization of a stochastic model for human face identification. In: *Proceedings of the Second IEEE Workshop on Applications of Computer Vision*, pp. 138–142 (1994)

Analysis of Zero-Sequence Circulating Current in Parallel PWM Inverter System with Difference of Carrier Wave Phases

Jianbao Liu, Xinxin Qin, and Zhonglin Yang

Navy Engineering University/School of Electrical and Information Engineering
Wu Han, China

ljbtt@hotmail.com, xjtu@xinhuanet.com, bluduny@sina.com

Abstract. Disaccord of inverter instantaneous output voltages is the ultimate factor that causes circulating current between inverters in parallel inverter system. As a familiar control method of inverter, sinusoidal Pulse Width Modulation is widely used to control output voltage of inverter to realize energy transformation. In this paper, the circulating current characteristics in parallel PWM inverter system with same sinusoidal modulating waves and different phase triangular carrier waves are analyzed. By using Fourier Transform of circulating current, the principle of zero-sequence circulating current changing with carrier wave phase difference is obtained. Simulation results are presented to verify the proposed analytical method.

Keywords: Circulating Current, Parallel Inverter, Phase-shifted, Pulse Width Modulation, Harmonic Analysis, Zero-sequence Circulating Current, Basic-frequency Circulating Current.

1 Introduction

The parallel inverter system has various advantages in the cost and maintenance effectiveness compared with the single unite structure and may meet the desirable properties such as higher output power, lower harmonic currents and higher reliability[1]-[7]. And the control of circulating current between inverters is a key issue in parallel inverter system. Circulating current does not exist in the ideal operation status of parallel inverters among parallel inverters when the inverters' output voltages have the same frequency, phase, and amplitude[8]-[15], in other words, there is no circulating current in the parallel inverter system when inverters have the same instantaneous output voltages[1].

However, in some cases, keeping the output voltage of each inverter accordant strictly at all time is a difficult work. Furthermore, in order to achieve output voltage of lower harmonic distortion, synchronized phase shifted technology has been applied widely in the system of parallel inverter[4,5], and death time infection can be considered a causation which results phase shift of triangular carrier wave[2,14,15]. So the condition that triangular carrier waves have different phases exists practically in parallel PWM inverter system. And some literatures have discussed and analyzed

the influences of triangular carrier waves phases on the output voltages' harmonic characteristics [4, 5], by means of various carriers with appropriate phase differences, such as multilevel carriers, undesirable harmonics are eliminated and the waveforms of the output currents become acceptably sinusoidal. But the influences on the circulating current which have been resulted from asymmetrical modulation with different triangular carrier phases have not been treated.

In this paper, the model of parallel PWM inverter system is structured and the equivalent equations of circulating current and output current are obtained in part II. Adopting this model, the instantaneous circulating current control and the instantaneous current control can be completely separated. To analyze the characteristics of circulating current in the condition of the different carrier phases, the relationship between the circulating current and the inverter output voltage difference is discussed when two inverters have the same sinusoidal modulating waves, the different phase triangular carrier waves and the symmetrical circuit parameters in part III. Then harmonic wave analysis of circulating current is carried out by using Fourier Transform, the principle of zero-sequence circulating current changing with carrier wave phase difference is obtained. Finally, the propriety of the above analysis is conformed by simulations with a typical example in part IV.

2 Model of Parallel Inverter System

Fig.1 shows a parallel inverter system composed of two inverters units through the current sharing reactor L_0 . V_1 , V_2 and V represent the output voltage vectors of inverter 1, inverter 2 and the load respectively, and in the same way, i_1 , i_2 and i represent the output current vectors of inverter 1 and inverter 2 and the load.

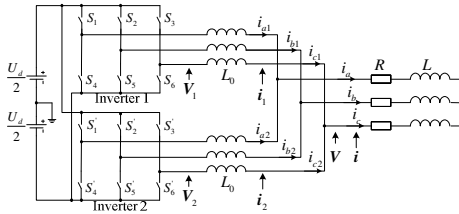


Fig. 1. Main circuit of parallel inverter system

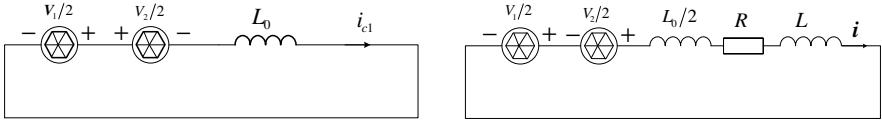
$$V_1 - V = L_0 di_1 / dt \tag{1}$$

$$V_2 - V = L_0 di_2 / dt \tag{2}$$

So, it can be concluded that the half difference of the output voltage vectors is differential coefficient of the half difference of the output current vectors.

$$V_1/2 - V_2/2 = d[(i_1 - i_2)/2] / dt \tag{3}$$

Based on the definition of circulating current with equal load sharing [6, 7], circulating current of the first converter $i_{c1} = (i_1 - i_2)/2$, Fig.2 (a) shows the equivalent circuit of circulating current for parallel inverter system.



(a) circulating current equivalent circuit

(b) output current equivalent circuit

Fig. 2. Equivalent circuit of parallel inverter system

It shows that the circulating current in the parallel inverter system results from the difference of the output voltage vectors of parallel inverters. The current sharing reactor L_0 is used to restrict the circulating current.

In the same way, the circuit equation of output current can be concluded as follows:

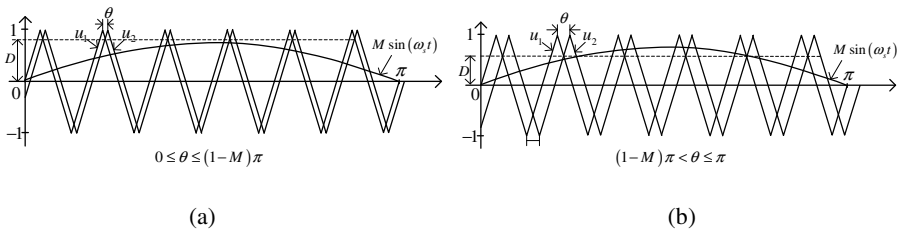
$$V_1/2 + V_2/2 = L_0/2 \cdot di/dt + Ri + L di/dt \tag{4}$$

From equation (4), the equivalent circuit of output current for parallel inverter system is shown in Fig.2 (b). Fig.2 (b) shows the relationships between the half summations of inverter output voltages and the output current for inverter system. It can be concluded that the current sharing reactor L_0 reacts on the output voltage and depressing output voltage is its shortcoming.

3 Analysis of Circulating Current

3.1 Parallel Inverter System with Different Carrier Phases

Fig.3 shows conditions of modulation according to phase difference θ of triangular carrier waves. When $0 \leq \theta \leq (1-M)\pi$, the absolute value D of point of intersection for two triangular carrier waves is always bigger than the sinusoidal modulating wave, which is called condition A. Where, M is coefficient of modulation. When $(1-M)\pi < \theta \leq \pi$, D is smaller than M which is called condition B.



(a)

(b)

Fig. 3. Sketch map of modulation waves

Fig.4 explains the relationship of absolute value D and phase difference θ . For the sake of analyzing simply, two triangular carrier waves are symmetrical by the y-axis potentially. So the coordinate for the intersectant point of two carrier waves is $[0, D]$. The relationship of D and θ can be expressed by (5).

$$D=1-\theta/\pi \tag{5}$$

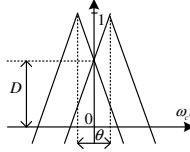


Fig. 4. Relationship of D and θ

On the condition A, $D \geq M$, so $0 \leq \theta \leq (1-M)\pi$. Similarly, it satisfies $(1-M)\pi < \theta < \pi$ on the condition B. Which can be concluded from above that the difference of voltage between V_1 and V_2 is the cause of formation of circulating current. In order to analyses simply, single-phase inverter is used in the model instead of three-phase inverter. Fig.5 shows the principle of $(V_1 - V_2)/2$ in a parallel inverter system of two single-phase inverters. Fig.5 (a), (b), (c) and (d) shows modulating wave and carrier waves with different phase, and then the process of sinusoidal PWM waves of V_1 and V_2 , finally the wave of $(V_1 - V_2)/2$ by calculating on the condition A. Fig.5 (e), (f), (g) and (h) shows the same contents on the condition B.

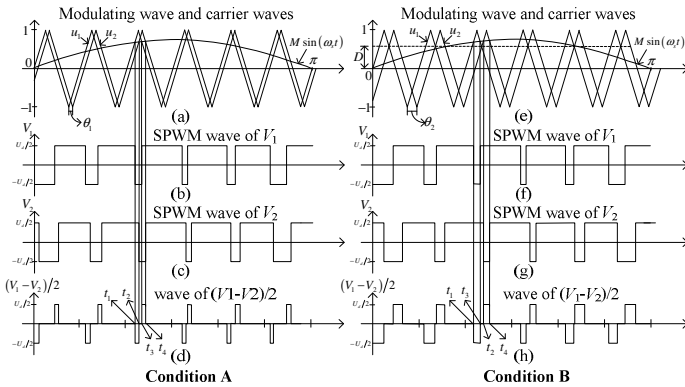


Fig. 5. Principle of $(V_1 - V_2)/2$

On the condition A and B, there is a negative pulse and a positive pulse in each and every triangular carrier wave period which can be concluded from the figure in Fig.5 (d) and (h). And the characteristics of pulses are corresponding to the time when the triangular carrier waves intersect sinusoidal modulating wave.

3.2 Analysis of Pulse Width for $(V_1-V_2)/2$ in Condition A

The two triangular carrier waves with different phase are expressed as the following equations:

$$u_1=2\omega_c t/\pi+(1+\theta/\pi-4k) \quad t \in [(4k\pi-2\pi-\theta)/(2\omega_c), 4k\pi-\theta/(2\omega_c)] \tag{6}$$

$$u_1=-2\omega_c t/\pi+(1-\theta/\pi+4k) \quad t \in [(4k\pi-\theta)/(2\omega_c), (4k\pi+2\pi-\theta)/(2\omega_c)]$$

$$u_2=2\omega_c t_1/\pi+(1-\theta/\pi-4k) \quad t \in [(4k\pi-2\pi+\theta)/(2\omega_c), (4k\pi+\theta)/(2\omega_c)] \tag{7}$$

$$u_2=-2\omega_c t_1/\pi+(1+\theta/\pi+4k) \quad t \in [(4k\pi+\theta)/(2\omega_c), (4k\pi+2\pi+\theta)/(2\omega_c)]$$

Where, $\theta \in [0, \pi]$, $k \in \mathbb{Z}$. When $k=0$, the basal period of carrier waves is denoted as described in Fig.4.

Assuming the expression of sinusoidal modulating wave is $M\sin(\omega_s t - \varphi)$, the modulation equations are expressed as follows:

$$2\omega_c/\pi \cdot t_1+(1+\theta/\pi-4k)=M\sin(\omega_s t_1-\varphi) \tag{8}$$

$$2\omega_c/\pi \cdot t_2+(1-\theta/\pi-4k)=M\sin(\omega_s t_2-\varphi) \tag{9}$$

$$-2\omega_c/\pi \cdot t_3+(1-\theta/\pi+4k)=M\sin(\omega_s t_3-\varphi) \tag{10}$$

$$-2\omega_c/\pi \cdot t_4+(1+\theta/\pi+4k)=M\sin(\omega_s t_4-\varphi) \tag{11}$$

Where, ω_c denotes angle-frequency of triangular carrier wave and ω_s denotes angle-frequency of sinusoidal modulating wave. Width of negative pulse can be calculated through (9)-(8) in condition A:

$$t_2-t_1=\theta/\omega_c+(\pi M/\omega_c) \cdot \cos[\omega_s \cdot (t_2-t_1)/2-\varphi] \cdot \sin[\omega_s \cdot (t_2-t_1)/2]$$

Because $\omega_s(t_2-t_1)/2 \ll 1$, so $\sin[\omega_s(t_2-t_1)/2] \approx \omega_s(t_2-t_1)/2$. Above equation can be predigested as follows:

$$t_2-t_1 \approx \theta / \{ \omega_c - \pi/2 \cdot M \omega_s \cos[\omega_s \cdot (t_2+t_1)/2-\varphi] \} \tag{12}$$

Similarly, width of positive pulse (t_4-t_3) can be conducted based on (11) and (10):

$$t_4-t_3 \approx \theta / \{ \omega_c + \pi/2 \cdot M \omega_s \cos[\omega_s \cdot (t_3+t_4)/2-\varphi] \} \tag{13}$$

Width of zero voltage (t_3-t_2) between negative pulse and positive pulse can be expressed as follows:

$$t_2-t_1 \approx (\pi-\theta)/\omega_c - (M\pi/\omega_c) \cdot \sin[\omega_s \cdot (t_2+t_3)/2-\varphi]$$

3.3 Analysis of Circulating Current

Replacing $(i_1-i_2)/2$ by i_{c1} in equation (3), we obtain

$$(V_1-V_2)/2=L_0 di_{c1}/dt$$

Thus, the effect of $(V_1-V_2)/2$ on the circulating current i_{c1} is to drive fluctuating. That is, if there is a negative pulse in $(V_1-V_2)/2$, i_{c1} will descend at slope of $-U_d/(2L_0)$ and if

there is a positive pulse in $(V_1-V_2)/2$, i_{c1} will ascend at slope of $U_d/(2L_0)$, and if $(V_1-V_2)/2=0$, i_{c1} does not change.

Fig.6 shows the characteristic of circulating current i_{c1} . From Fig.6, it can be concluded that the circulating current is in a rage between two sine waves in condition A. And the properties of marginal sine waves are related to pulse width of $(V_1-V_2)/2$. The relationship of the upper sine wave current i_{u1} and the charge of pulse width of $(V_1-V_2)/2$ can be expressed as follows:

$$i_{u1}(t_4)-i_{u1}(t_1)=U_d/(2L_0)\cdot[(t_4-t_3)-(t_2-t_1)]$$

Based on formulas (12) and (13), i_{u1} can be expressed as follows:

$$i_{u1} = -U_d M \theta / (4L_0 \omega_c) \cdot \sin(\omega_s t - \varphi) \tag{14}$$

Similarly, the nether sine wave i_{l2} is expressed as follows:

$$i_{l2} = -U_d M \theta / (4L_0 \omega_c) \cdot \sin(\omega_s t - \varphi) + U_d \theta / (2L_0 \omega_c) \tag{15}$$

So the circulating current i_{c1} can be decomposed to a sinusoidal current i_{u1} and a trapeziform current i_{cp} as follows:

$$i_{c1} = i_{u1} + i_{cp} \tag{16}$$

Fig.7 shows the characteristic of the trapeziform current i_{cp} and its micrograph. By above treating, the high of every trapeziform is equal approximately about $(U_d \theta) / (2L_0 \omega_c)$. Take the main period of i_{cp} out for analyzing in Fig.7, Where, i_{cp} is figured by real line. In order to analysis simply by using Fourier Transform, i_{cp} is taken for rectangular current i_p approximately which is figured by broken line in Fig.8.

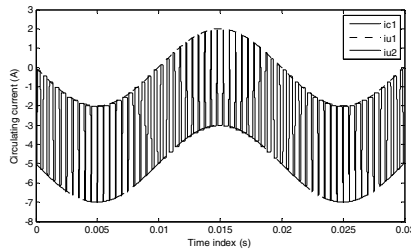


Fig. 6. Characteristic of circulating current

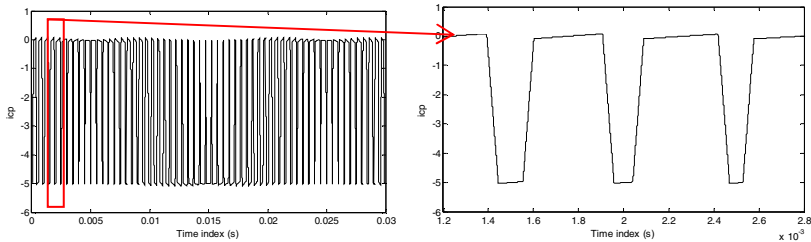


Fig. 7. Characteristic of trapeziform current i_{cp}

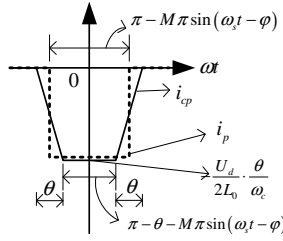


Fig. 8. Circulating current in a carrier period

The Fourier Transform for $i_p/[(U_d\theta)/(2L_0\omega_c)]$ is

$$i_{cp} / \left(\frac{U_d\theta}{2L_0\omega_c} \right) = \frac{1}{2}a_0 + \sum_{n=1}^{\infty} (a_n \cos n\omega_c t + b_n \sin n\omega_c t) \tag{17}$$

Where

$$\begin{cases} a_n = \frac{1}{\pi} \int_{-\pi}^{\pi} \left[i_{cp} / \left(\frac{U_d\theta}{2L_0\omega_c} \right) \right] \cos(n\omega_c t) d(\omega_c t) & (n = 0, 1, 2, \dots) \\ b_n = \frac{1}{\pi} \int_{-\pi}^{\pi} \left[i_{cp} / \left(\frac{U_d\theta}{2L_0\omega_c} \right) \right] \sin(n\omega_c t) d(\omega_c t) & (n = 1, 2, \dots) \end{cases}$$

That is

$$\begin{cases} a_0 = M \sin(\omega_s t - \varphi) - 1 \\ a_n = -\frac{2}{n\pi} \sin \left\{ \frac{n}{2} \pi [1 - M \sin(\omega_s t - \varphi)] \right\} & (n = 1, 2, \dots) \\ b_n = 0 \end{cases}$$

So

$$i_p = -\frac{1}{2} \left(\frac{U_d\theta}{2L_0\omega_c} \right) + \frac{1}{2} \left(\frac{U_d\theta}{2L_0\omega_c} \right) M \sin(\omega_s t - \varphi) - \left(\frac{U_d\theta}{2L_0\omega_c} \right) \cdot \sum_{n=1}^{\infty} \left\{ \frac{2}{n\pi} \sin \left[\frac{n}{2} \pi [1 - M \sin(\omega_s t - \varphi)] \right] \right\} \cos n\omega_c t \tag{18}$$

In equation (18), the first item is DC component, the second item is basic-frequency component and the last item is harmonic component.

In conclusion, the circulating current existing in the parallel PWM inverter system has characteristics as follows on the condition of the same sinusoidal modulating waves and the different triangular carrier waves with small phase difference θ :

1. The absolute value of DC circulating current is $(U_d\theta)/(4L_0\omega_c)$, which is direct proportion with carrier phase difference θ , and is inverse proportion with current sharing reactor L_0 ;
2. The basic-frequency circulating current is the sum of the upper sine wave current i_{u1} shown in (14) and the basic-frequency component of the rectangular circulating current i_p shown in (18).

$$i_{u1} + \frac{M}{2} \cdot \frac{U_d\theta}{2L_0\omega_c} \sin(\omega_s t - \varphi) = 0$$

So, the basic-frequency circulating current is inexistent, which is compatible with the theory of PWM. According to the theory of PWM, the basic-frequency output voltage is interrelated only with the sinusoidal modulating wave and the coefficient of modulation; it is disrelated with the phase of triangular carrier wave. There is no circulating current existing in the parallel inverter system when the inverters have the same basic-frequency output voltages.

4 Simulation Results

Simulations have been carried out on the parallel PWM inverter system with parameters shown in Table 1 by Matlab/Simulink.

Table 1. Parameters of parallel SPWM inverter system

Frequency of sinusoidal modulating wave f_s	50Hz
Initialization of modulating wave phase φ	0rad
Frequency of triangular carrier wave f_c	2000Hz
Coefficient of modulation M	0.8
Volts d.c. of inverter U_d	200V
Current sharing reactor L_0	1mH
Resistance of load R	3Ω
Reactor of load L	2mH

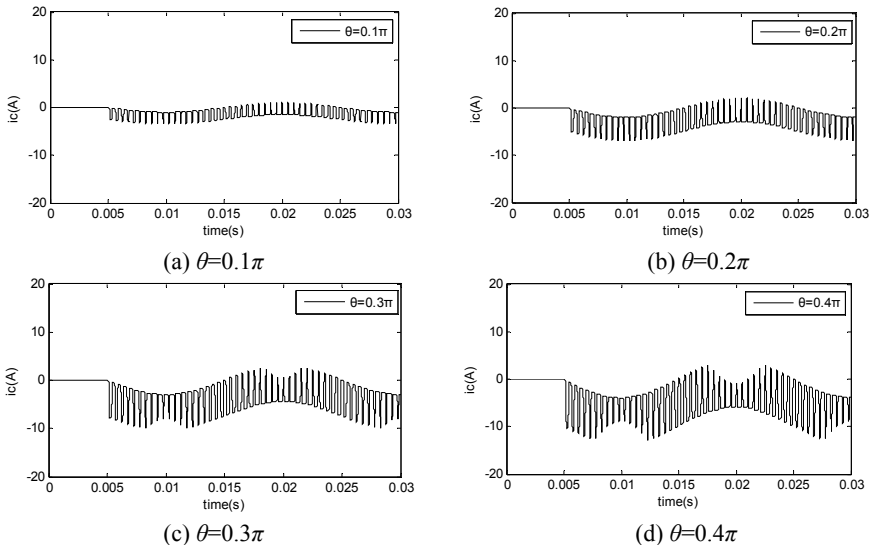


Fig. 9. Waveforms of circulating currents

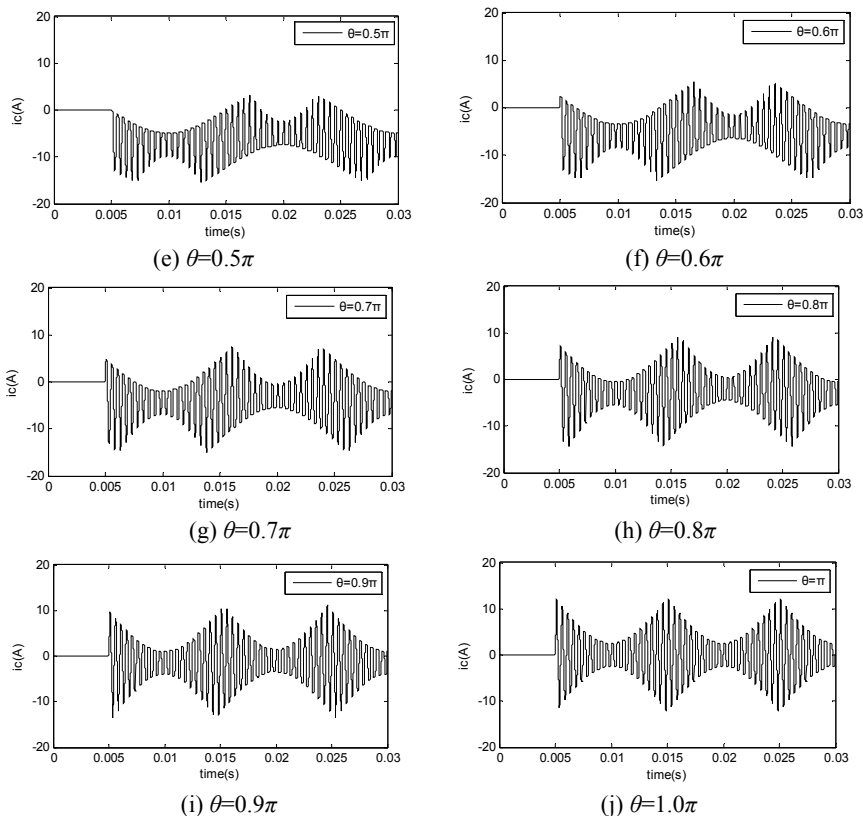


Fig. 9. (continued)

Fig.9 shows the various conditions of circulating currents when triangular carrier phase difference θ charges from 0.1π to π at the same interval 0.1π . From Fig.9, it can be concluded that the ripple value of circulating current increases with the carrier wave phase difference θ increasing from 0.1π to π . In order to analyse the

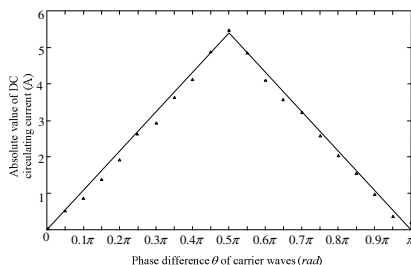


Fig. 10. Principle of relationship between zero-sequence circulating current and phase difference θ of carrier waves

characteristic of circulating current, the harmonic analysis tool “Powergui FFT Analysis Tool” have been used to calculate the absolute value of DC circulating current. And Fig.10 shows the principle of relationship of between DC circulating current and phase difference θ of carrier waves based on the data which have been obtained by calculating. The simulation results verify the proposed analytical method.

5 Conclusions

In this paper, the model of parallel inverter system is structured and the equivalent equations of circulating current and output current are obtained. Based on this model, the equivalent control equations of instantaneous circulating current and instantaneous output current can be expressed separated. Furthermore, the principle of half output voltage difference is discussed when there is phase difference between triangular carrier waves in parallel SPWM inverter system. Then the relationship between the circulating current and the inverter output voltage difference is shown up when two SPWM inverters have the same sinusoidal modulating waves, the different phase triangular carrier waves and the symmetrical circuit parameters. To analyze the characteristics of circulating current in the condition of the different carrier phases, harmonic wave analysis of circulating current is carried out by using Fourier Transform; the principle of circulating zero-sequence current changing with carrier wave phase difference is obtained.

References

1. Cai, H., Zhao, R., Yang, H.: Study on Ideal Operation Status of Parallel Inverters. *IEEE Trans. Power Electron* 23(6), 2964–2969 (2008)
2. Zhang, Y., Chen, X., Kang, Y., et al.: The Restrain of the Dead Time Effects in Parallel Inverters. In: *IEEE International Electric Machines and Drives Conference, Texas, USA*, vol. 1, pp. 797–802 (May 2005)
3. Matsui, K., Murai, Y., Watanabe, M., Kaneko, M., Ueda, F.: A Pulsewidth-modulated Inverter with Parallel Connected Transistors Using Current-sharing Reactors. *IEEE Trans. Power Electron* 8(2), 186–191 (1993)
4. Matsui, K., Kawata, Y., Ueda, F.: Application of Parallel Connected NPC-PWM Inverters with Multilevel Modulation for AC Motor Drive. *IEEE Trans. Power Electron* 15(5), 901–907 (2000)
5. Mori, H., Matsui, K., Kondo, K., Yamamoto, I., Hasegawa, M.: Parallel-connected Five-level PWM Inverters. *IEEE Trans. Power Electron* 18(1), 173–179 (2003)
6. Pan, C.-T., Liao, Y.-H.: Modeling and Coordinate Control of Circulating Currents in Parallel Three-Phase Boost Rectifiers. *IEEE Trans. Ind. Electron* 54(2), 825–838 (2007)
7. Pan, C.-T., Liao, Y.-H.: Modeling and Control of Circulating Currents for Parallel Three-Phase Boost Rectifiers with Different Load Sharing. *IEEE Trans. Ind. Electron* 55(7), 2776–2785 (2008)
8. Wu, T.F., Hsieh, H.M., Wu, Y.E.: Parallel-inverter system with failure isolation and hot-swap feature. *IEEE Trans. Ind. Appl.* 43(5), 1329–1340 (2007)
9. Chen, T.P.: Circulating zero-sequence current control of parallel three-phase inverters. In: *Proc. Inst. Electr. eng. Electr. Power Appl.*, vol. 153, pp. 282–288 (2006)

10. Yeong, J.C., Sng, E.K.K.: A novel communication strategy for decentralized control of paralleled multi-inverter systems. *IEEE Trans. Power Electron* 21(1), 148–156 (2006)
11. Sun, X., Lee, Y.S., Xu, D.H.: Modeling, analysis, and implementation of parallel multi-inverter systems with instantaneous average-current-sharing scheme. *IEEE Trans. Power Electron* 18(3), 844–856 (2003)
12. Chen, T.-P.: Common-Mode Ripple Current Estimator for Parallel Three-Phase Inverters. *IEEE Trans. Power Electron* 24(5), 1330–1339 (2009)
13. Chen, T.-P.: Dual-Modulator Compensation Technique for Parallel Inverters Using space-Vector Modulation. *IEEE Trans. Ind. Electron* 56(8), 3004–3012 (2009)
14. Gu, L., Wen, X., Hua, Y.: Analysis of Dead-Time Effect and Suppression on High Power Induction Machines with Voltage Source Inverter Drive. In: *IEEE Vehicle Power and Propulsion Conference (VPPC)*, pp. 145–149 (2008)
15. Holmes, D.G.: A general analytical method for determining the theoretical harmonic components of carrier based PWM strategies. In: *IEEE Ind. Appl. Society Annual Meeting*, pp. 1207–1214 (1998)

A Novel Robust Controller for the Speed Control of Permanent Magnet Synchronous Motor

Wei Guo and Jian-Ping Wen

School of Mechanical Engineering, Xi'an University of Science and Technology,
Xi'an, P.R. China
guow@xust.edu.cn, wenegle@gmail.com

Abstract. A robust speed controller which is designed by employing fuzzy logic control and particle swarm optimization (PSO) is presented for a permanent magnet synchronous motor (PMSM) drive system. The prime problem of fuzzy PI controller is the design of fuzzy rules with expert experience. The performances of fuzzy PI controller are degraded because of expert experience. In order to solve default of conventional fuzzy PI controller, the PSO is used to optimize the parameters of membership functions of fuzzy logic controller to automatically acquire the fuzzy space structure of system. Simulation results show that the proposed approach gives a better dynamic speed response and is robust to external load disturbance.

Keywords: permanent magnet synchronous motor, fuzzy logic controller, particle swarm optimization, speed control.

1 Introduction

Permanent magnet synchronous motor (PMSM) possesses many fine characteristics such as high efficiency, high power density and small inertia moment. PMSM are widely used in motion control applications where very high efficiencies are desirable in addition to high speed or torque response [1-4], the control of which is most important to realize the high performances of motor system. As we all know, vector control has found widespread using in fields. Conventional PID approach in vector control is to use PID control schemes to operate the static and dynamic performance of control system [5]. However, the nonlinear effects of motor system and model uncertainty such as external disturbances, unpredictable parameter perturbations and unmodeled plant nonlinear dynamics, the common PID control is not able to get good transient response and small overshoot. Furthermore, due to the derivatives of the signals are difficult to pick up, the PI control becomes the most widespread control combination. In recent years, extensive research has been developed in order to overcome the deficiency of conventional PI controller and improve its performance [6]. In many applications, the fuzzy PI control that is designed through combining the fuzzy technique with the conventional PI control is used widely [7-8]. The fuzzy control is proved to an efficient way to implement engineering heuristics into control solution [9]. The key of fuzzy PI control design is the design of fuzzy rules with

expert experience [10]. Fuzzy control is effective to the humanistic system and usually built on expert knowledge [11]. These cause the fuzzy control various with different experts.

In view of the problem, optimization scheme is introduced in this paper. The parameters of the membership functions of the fuzzy control are optimized by using the PSO algorithm, which ensure the fuzzy control optimal. Simulation results indicate that the proposed scheme can effectively improve the global convergence ability of fuzzy logic control and enhance dynamic performance of the PMSM drive system.

2 Machine Model

The governing equation of a PMSM motor consists of two parts, electrical and mechanical. On the basis of assumptions that the stator windings generates sinusoidal magnetic field, air gap is uniform and saturation is negligible. Taking d-q axes rotor coordinates of the motor as reference coordinates, the dynamic equations of PMSM can be described as [12].

$$\frac{di_d}{dt} = -\frac{R_s}{L_d}i_d + \frac{L_q}{L_d}\omega i_q + \frac{1}{L_d}u_d \quad (1)$$

$$\frac{di_q}{dt} = -\frac{R_s}{L_q}i_q - \frac{L_d}{L_q}\omega i_d + \frac{1}{L_q}u_q - \frac{1}{L_q}\omega\psi_f \quad (2)$$

$$\frac{d\omega}{dt} = \frac{1}{J}(T_e - T_m - B\omega) \quad (3)$$

$$T_e = \frac{3}{2}p_n[\psi_f i_q + (L_d - L_q)i_d i_q] \quad (4)$$

Where i_d and i_q are the currents on the d-q reference frame, respectively. R_s is resistance of the stator windings. L_d and L_q are the inductances on the d-q reference frame, respectively. u_d and u_q are the voltages on the d-q reference frame, respectively. ω is motor electrical angular velocity. J is moment of inertia of the motor. T_m is load torque. T_e is electromagnetic torque. B is viscous damping coefficient. ψ_f is amplitude of the flux induced by the permanent magnets of the rotor in the stator phases. p_n is number of pole pairs.

3 The Robust Controller Design

3.1 The PSO

Suppose that the search space is D -dimensional. A swarm consists of N particles moving around in the D -dimensional search space [13]. The i th particle has an

associated current position, $X_i = (x_{i1}, x_{i2}, \dots, x_{iD})$, a current velocity, $V_i = (v_{i1}, v_{i2}, \dots, v_{iD})$, a personal best position achieved so far, $pbest_i$, which is represented by $P_i = (p_{i1}, p_{i2}, \dots, p_{iN})$. The best position achieved so far by the whole swarm, $gbest$, which is represented by $G = (g_1, g_2, \dots, g_N)$. At each step, the velocity of particle and its new position will be updated according to the following two equations:

$$v_{id}(t+1) = wv_{id}(t) + c_1r_{1i}(t)(p_{id}(t) - x_{id}(t)) + c_2r_{2i}(t)(g_d(t) - x_{id}(t)) \quad (5)$$

$$x_{id}(t+1) = x_{id}(t) + v_{id}(t) \quad (6)$$

Where w is called inertia weight; c_1 and c_2 are constants, called cognitive learning coefficient and social learning coefficient, respectively. $r_{1i}(t)$ and $r_{2i}(t)$ are two separately generated uniformly distributed random number in the range $[0,1]$ and the values of $r_{1i}(t)$ and $r_{2i}(t)$ are not same for every iteration. The position of each particle is updated every iteration by adding the velocity vector to the position vector, as given in (6).

3.2 The Robust Controller

The conventional fuzzy PI controller for PMSM speed control chooses velocity error, e , and velocity error change, ec , as input variables, which can reflect the dynamic characteristics of increments of output variables, ΔK_p , ΔK_i . Three primary parts of fuzzy controller are interface of acutance data fuzzed, fuzzy control rules and arithmetic and interface of fuzzy data. The structure of fuzzy controller and fuzzy PI controller are presented in fig. 1 and fig. 2.

The fuzzy controller design exist two main problems which are determine and select parameters of fuzzy control rules and membership functions. The main factors of affecting the veracity of the fuzzy Inference are that the membership functions select and certain the fuzzy matrix makes. The conventional fuzzy controller is effective to the humanistic system and the PMSM is a nonlinear system with significant coupling, which degrade the performance of fuzzy control system. In this paper, the PSO is used to optimize the parameters of fuzzy controller to obtain minimizing objective function. In order to overcome the problem of huge calculation, the parameters of membership functions are optimized but the fuzzy rules remain constant. The dimensions of PSO are established by the parameters of membership functions. The higher the dimensions of PSO, the larger the size of particle swarm and the more the number of iterations in order to obtain the global optimal solution. The running time of the methods will increase rapidly as the number of the dimensions increases. Then, a minimal number of variables is expected to define membership functions.

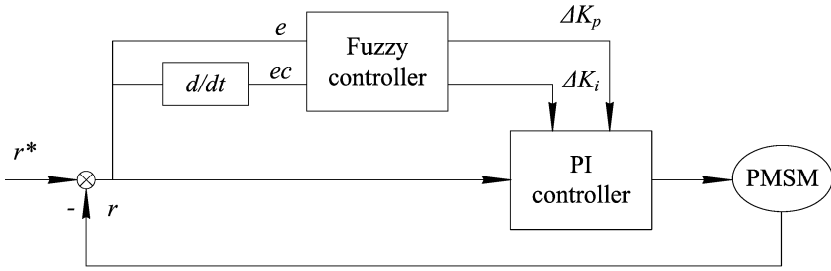


Fig. 1. The frame of fuzzy PI controller

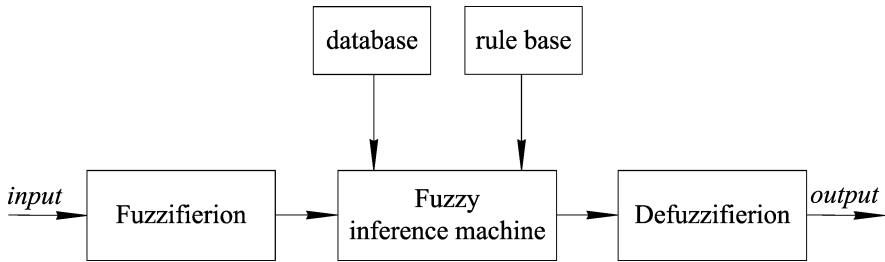


Fig. 2. The fuzzy controller

The range of velocity error and velocity error change rate are [-3 3], respectively. Fuzzy set of the variables, e and ec , is defined as negative big (NB), negative median (NM), negative small (NS), zero (ZE), positive small (PS), positive median (PM), positive big (PB). The centre point of each membership function subset is defined as $Ec1, Ec2, Ec3, Ec4$ and $Ec5$. the half membership function width is defined as $Ew1, Ew2, Ew3, Ew4, Ew5, Ew6$ and $Ew7$. The particle can be defined as:

$$P = (Ec1, Ec2, Ec3, Ec4, Ec5, Ew1, Ew2, Ew3, Ew4, Ew5, Ew6, Ew7) \quad (7)$$

The optimization process consists of five step.

Step1 defining optimization variable, P , as the particle and encoding the particles of each dimension by using real number, initializing position and velocity of each particle randomly in the allowable range.

Step2 decoding the each particle as the parameter of membership function and feeding into fuzzy controller,

Step3 calculating the average fitness, f_{ave} , and the best fitness, f_{opt} , operating mutation.

Step4 updating individual best value, $pbest$, and global optimization, $gbest$.

Step5 goto step2, ending iteration when the maximum number of iterations has been reached, decoding $gbest$ as output parameter of membership function and obtaining the optimized fuzzy controller.

Table 1. The range of optimization variables

Optimization variable	Range
Ec1	(-3, -1.5)
Ec2	(-1.5, -0.5)
Ec3	(-0.5, 0.5)
Ec4	(0.5, 1.5)
Ec5	(1.5, 3)
Ew1	(0, 1)
Ew2	(0, 1)
Ew3	(0, 1)
Ew4	(0, 1)
Ew5	(0, 1)
Ew6	(0, 1)
Ew7	(0, 1)

4 Simulation Results

To verify the performance of proposed control scheme in PMSM speed regulation system, this system is tested in several operating conditions. The specifications of the PMSM are: rated power, 1.5kW; rated voltage, 72V; rated current, 25A; rated speed, 2800r/min; number of poles $p_n = 4$; winding resistance $R_s = 0.1\Omega$; direct axis inductance $L_d = 0.4\text{mH}$; quadrature axis inductance $L_q = 0.5\text{mH}$; $B = 8.5 \times 10^{-3} \text{ N}\cdot\text{m}\cdot\text{s}/\text{rad}$; $J = 0.2 \times 10^{-4} \text{ kg}\cdot\text{m}^2$. The performances of the optimizing fuzzy PI controller and the fuzzy PI controller are compared in order to observe the influence of the proposed control method.

Fig. 3 shows dynamic step response curves of PMSM using the optimized fuzzy PI controller and the fuzzy PI controller respectively while the rotor speed is changed from 0rpm to 1500rpm. It is demonstrated that the optimized fuzzy PI controller can maintain good dynamic response in wide operation range.

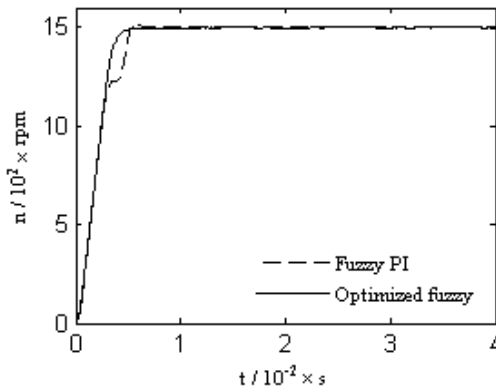


Fig. 3. The comparison of speed step response with optimized fuzzy PI controller and fuzzy PI controller

Load torque $T_L=5N\cdot m$ is applied to the PMSM at the time 0.02s. Fig. 4 shows the speed response curves of PMSM with load torque step disturbance while the rotor speed is 1500rpm. It is shown that the optimized fuzzy PI controller can provide fast response ability to changing load torque.

In order to demonstrate the robust, the load torque is changed from 5Nm to 2Nm at the time 0.03s. The result is as shown in Fig. 5. The optimized fuzzy PI controller can make fast response to the random load disturbance.

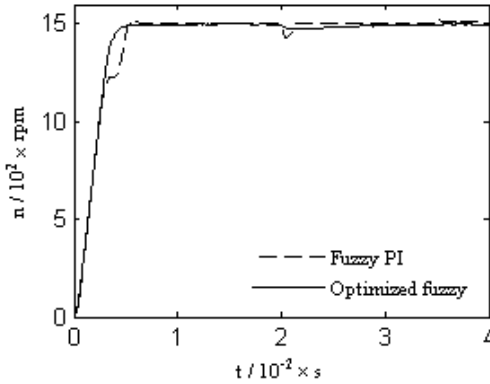


Fig. 4. The comparison of speed response with external torque disturbance

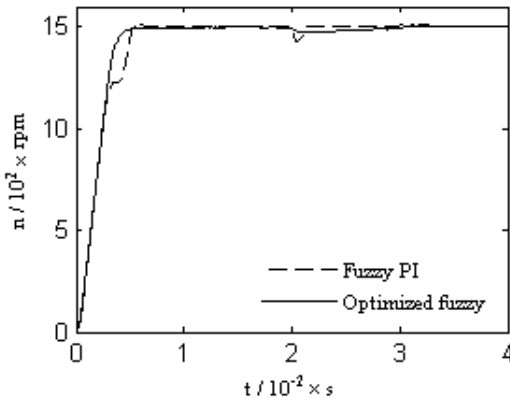


Fig. 5. The comparison of speed response with random torque disturbance

5 Conclusions

In this paper, an adaptive fuzzy PI speed controller design is proposed for the PMSM drive. The parameters of membership functions are determined by using the PSO algorithm in order to eliminate the effect of the humanistic system on the performance

of fuzzy logic control system. Finally some simulation results are demonstrated to confirm the performance of the optimized fuzzy PI speed controller for PSM drive system.

References

1. Ojo, O., Osaloni, F., Wu, Z.Q., et al.: A Control Strategy for Optimum Efficiency Operation of High Performance Interior Permanent Magnet Motor Drives. In: Proc. 38th Annu. Conf. Industry Applications, pp. 604–610 (2003)
2. Caponio, A., Cascella, G.L., Neri, F., Salvatore, N., Summer, M.: A Fast Adaptive Memetic Algorithm for Online and Offline Control Design of PMSM Drives. *IEEE Trans. on Systems, Man, and Cybernetics—Part B: Cybernetics* 37(1), 28–41 (2007)
3. Shyu, K.K., Lai, C.K., Tsai, Y.W., Yang, D.: A Newly Robust Controller Design for the Position Control of Permanent-Magnet Synchronous Motor. *IEEE Trans. on Industrial Electronics* 49(3), 558–565 (2002)
4. Kung, Y.S., Tsai, M.H.: FPGA-Based Speed Control IC for PMSM Drive With Adaptive Fuzzy Control. *IEEE Trans. on Power Electronics* 22(6), 2476–2486 (2007)
5. Su, Y.X., Zheng, C.H., Duan, B.Y.: Automatic disturbances rejection controller for precise motion control of permanent magnet synchronous motors. *IEEE Trans. on Industrial Electronics* 52, 814–823 (2005)
6. Jan, R.M., Tseng, C.S., Liu, R.J.: Robust PID control design for permanent magnet synchronous motor: A genetic approach. *Electric Power Systems Research* 78, 1161–1168 (2008)
7. Wei, J., Fan, Y.: A fuzzy PID controller for ship course based on engineering tuning methods. In: *International Conferences on Info-Tech and Info-Net*, pp. 376–381 (2001)
8. Zhang, J., Zhang, Y., Chen, L., et al.: A Fuzzy Control Strategy and Optimization for Four Wheel Steering System. In: *IEEE Conf. on Vehicular Electronics and Safety*, pp. 1–6 (2007)
9. Tao, C.W., Taur, J.S.: Robust fuzzy control for a plant with fuzzy linear model. *IEEE Trans. on Fuzzy Systems* 13(1), 30–41 (2005)
10. Chen, J., Zhu, W.: Ant colony algorithms for Fuzzy rules optimization. *Computer Engineering and Applications* 5, 113–115 (2007)
11. Iijima, N., Koizumi, K., Mitsui, H., et al.: Fuzzy control design system based on DSP. In: *The Third IEEE Conf. on Computational Intelligence*, vol. 3, pp. 1786–1790 (1994)
12. Tang, R.Y.: *Modern permanent magnet machines-theory and design*, pp. 244–252. China Machine Press, Beijing (1997)
13. Kennedy, J., Mendes, R.: Population structure and particle swarm performance. In: *Proc. IEEE Cong. Evolutionary Computation*, pp. 1671–1676 (2002)

Micro Machined Diaphragm Based Fiber Fabry-Perot Acoustic Sensor

Li Zhenyu*, Shao Jie, Wu Zhizong, and Chen Jianyong

Laser and Optoelectronics Lab,
The Third Research Institute of the Ministry of Public Security, Shanghai, P.R. China
Lizhenyu1959@yeah.net

Abstract. This paper presents the design and characterization of the micro machined Diaphragm and the Fabry-Perot interferometer of the fiber Fabry-Perot acoustic sensor. The design for micro diaphragm-type acoustic sensors have been established by characterization of the relationships among diaphragm thickness, side length, sensitivity, and resonant frequency. According to the study, the thickness need to be thin and the side length need to be small in order to get the sensitive diaphragm with high resonant frequency. Theoretical equations for the sensitivity, visibility are proposed. The relations between the reflectivities of the F-P surfaces and the visibility are discussed. Design of different cavity lengths and reflectivities are proposed for the diaphragm-based micro machined optical F-P sensors which have the visibility up to 100%.

Keywords: Fabry-Perot, visibility, MEMS diaphragm, optical acoustic sensor.

1 Introduction

Early fiber optical sensors for pressure or strain detection were mostly based on fiber optic intrinsic interferometers such as all-fiber Michelson interferometers and Mach-Zehnder interferometers 1,2. High sensitivity could be present in the intrinsic fiber interferometric sensors when a long fiber was used in the sensing arm. However, those kinds of sensors suffer from the fringe fading problems resulting from random polarization rotation. Also they are unstable because of drift in the wavelength of light source and temperature-induced optical path-length changes.

By employing the MEMS technology, a variety of optical MEMS acoustic sensors based on Fabry-Perot interferometry have recently been proposed and fabricated 3,4,5. The major advantages of the optical sensors over the conventional electrical sensors are simple and compact, insensitive to environmental fluctuations and polarization-induced signal fading, being capable of point measurements with minimal cross sensitivity, offering high resolution and sensitivity, and capable for multiplexing. A Fabry-Perot interferometer consists of two partially reflecting mirrors composing a cavity. With this robust structure, one can easily measure a loaded pressure by detecting the changes of the reflected or transmitted optical signals

* Corresponding author.

due to the shift of this cavity. MEMS technology is used to manufacture the sensing elements with a small and definite size.

A fiber F-P acoustic sensor is a transducer that converts acoustic energy into electrical energy, which can be partitioned into three stages where transductions between energy domains occur: acousto-mechanical stage, the mechano-optical stage, and the opto-electrical stage. The FFPI transduce acoustic energy into optical intensity changes. A fiber F-P acoustic sensor may use intensity modulation, phase modulation, or polarization modulation as the optical domain transduction mechanism. Changing optical power from the optical path varies the light intensity in an intensity-modulated acoustic sensor. In a phase modulation sensor, optical interference is used to modulate the optical intensity in the optical path. Polarization modulation sensors vary the polarization selective optics to vary the optical intensity incident on a photodiode. Since all photodiodes respond to optical intensity, any optical modulation strategy will require a variation in optical intensity received at a photo detector to properly convert the signal into the electrical domain.

Different configurations of optical MEMS Fabry-Perot acoustic sensors have been proposed, those kinds of sensors usually suffer from the complicity of demodulations, which whether use the fringe counting or the spectroscopy assisted adjusted methods, in our previous work a feedback control method was used to confine the operating point to the system Q point, so a linear demodulating method is used, which shows merits in convenient use and simple configuration.

In this work a sound F-P structure concomitant is introduced which shows prominent quality and easy to produce. A fiber Fabry-Perot interferometer (FFPI) is fabricated, a low-finesse F-P cavity is used to simplify the sensor fabrication and take advantage of the two beam interference approximation in signal demodulation. Demonstration of fabrication method and theoretical simulation are given to guiding the fiber F-P cavity execution.

2 Fiber Fabry-Perot Interferometer Structure

The fiber F-P Interferometric acoustic sensor head contains a small sensing element known as a Fabry-Perot cavity formed by two parallel reflecting surfaces, one of them

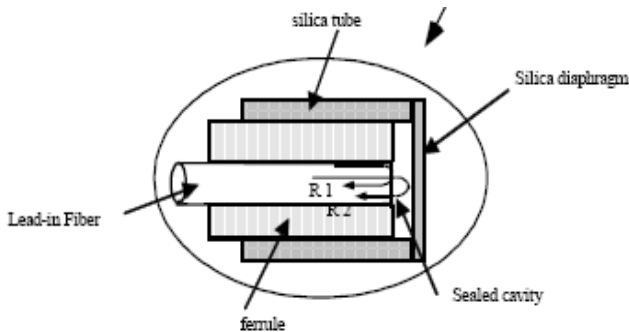


Fig. 1. Diaphragm based Low finesse F-P sensor head

is just the tip of the fiber and the other is usually a silicon diaphragm made by micro-electric machine system (MEMS) technology, as shown in Fig.1. Two optical beams reflected from the diaphragm and the fiber tip interface interfere with each other at the fiber tip, generating signals as function of optical path difference(OPD) changes.

2.1 Diaphragm Design

The load-deflection method is a well-known method for the measurement of elastic properties of thin films. In this technique, the deflection of a suspended film is measured as a function of applied pressure. The motion equation of load-deflection relationship for a flat square diaphragm is given by 6:

$$\frac{EK^2}{\rho(1-\sigma^2)} \nabla^4 \eta + \frac{\partial^2 \eta}{\partial t^2} = 0 \tag{1}$$

Here E is young’s modulus, ρ is the density, σ is Poisson ratio of diaphragm material, K is slew radius: $K = h/\sqrt{12}$, define:

$$k^4 = \frac{\omega^2 \rho (1-\sigma^2)}{K^2 E} \tag{2}$$

For a diaphragm clamped on its edges, from a mathematical point of view, the diaphragm can be viewed as a thin plate and the exact solution for the differential equation that describes its oscillation is given in 7. Assuming that the deflection of the diaphragm is small compared to its thickness, the Reyleigh–Ritz method 8 can be used to find the frequency of the lowest mode of vibration. Separate the variables, consider the boundary conditions:

$$\eta^1(x)_{x=0} = \eta^1(x)_{x=2a} = \eta^1(y)_{y=0} = \eta^1(y)_{y=2b} = 0$$

The space result part becomes:

$$\eta^1(x, y) = A \sin \frac{n\pi}{2a} x \sin \frac{m\pi}{2b} y \tag{3}$$

In condition:

$$\left(\frac{n\pi}{2a}\right)^2 + \left(\frac{m\pi}{2b}\right)^2 = k^2 \tag{4}$$

a, b , are the side length of the flat square, When $a=b$, the frequency response of the diaphragm can thus be calculated by combining Eq. (2) and (4) into the following:

$$\omega_{mn} = \frac{\pi^2 h(m^2 + n^2)}{8a^2} \sqrt{\frac{E}{3\rho(1-\sigma^2)}} \tag{5}$$

Considering a plate is under a load varying harmonically with time, the equation of motion is:

$$u'' + 2nu' + d \frac{\nabla^4 \eta_o}{\eta_o} u = p e^{j\omega t} \tag{6}$$

The plate with clamped edges is under uniformly static pressure, the maximum displacement (u_{\max}) is expressed as following:

$$u_{\max} = \frac{Pa^4(1-\sigma^2)}{4.2Eh^3} \tag{7}$$

Considering the maximum displacement of the diaphragm occurs when frequency is 0 (static case), the solution of Eq. (6) represent the vibration response of the diaphragm, at its central point is:

$$\eta_n = \frac{Pa^4(1-\sigma^2)}{4.2Eh^3} \cdot \frac{\omega_n^2 e^{j\omega t + \phi}}{\sqrt{(\omega_n^2 - \omega^2)^2 + (2n\omega)^2}} \tag{8}$$

Here n is the damping factor; Fig.2 shows the relationships among half of side length, thickness, and resonant frequency. With a given side length, resonant frequency increases with thickness. With a given thickness of diaphragm, frequency decreases with side length. The figure also shows that diaphragm thickness has more effect on resonant frequency than side length. In order to get large natural frequency and large deflection, the thickness should be thin, and large deflection and large resonant frequency of the diaphragm could be acquired when the side length and thickness of the diaphragm are small.

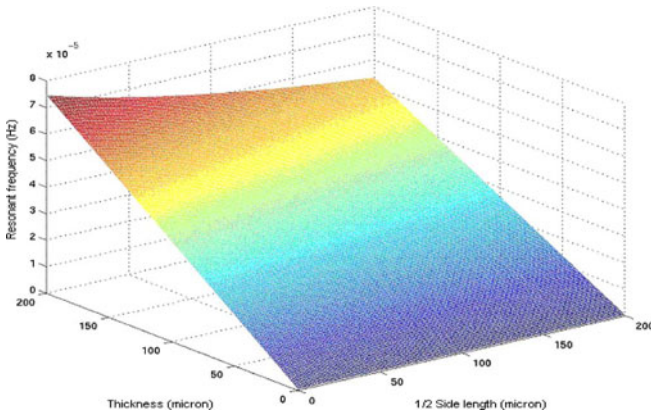


Fig. 2. The relationships among the side length, thickness, and resonant frequency at a given pressure

In the proposed pressure sensor, the diaphragm works as the key sensing element. In the low-finesness interferometer case, a blank thin fused silica plate is simply utilized. This kind of sensor is limited in the sensitivity due to the low reflectivity of the diaphragm interface (~4%). In order to achieve higher sensitivity, the diaphragm can be coated with dielectric or metal layers for a higher reflectivity (Fig.3).

Benefiting from the Micro Electro Mechanical System (MEMS) technology, we applied standard IC processing technologies for manufacturing our sensor diaphragms, including photolithography, dry/wet etching, and metal evaporates deposition.

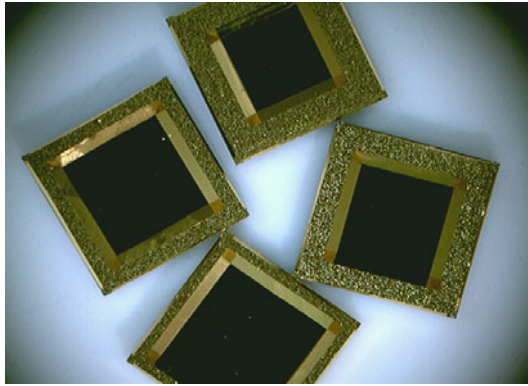


Fig. 3. Micro machined based diaphragm with gold coated layers

2.2 Fiber F-P Interferometric Theory

An F-P interferometer, rigorously speaking, is a multibeam interference device. As a low-finesse FFPI consists of two interfaces with a reflectivity less than 4%, its higher order interferences in the cavity are weak and often negligible, and therefore can be approximately treated as a two-beam interference.

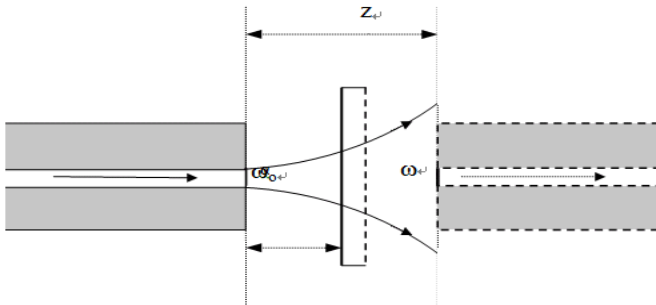


Fig. 4. A symmetrical graph showing the two-beam interference of the sensor head

For simplicity and applicability we discuss the sensor with a simplified model, shown in Fig.4, which means a normally incident Gaussian beam is considered. The beam amplitude ejecting from the fiber tip can be expressed as9:

$$u(r, z) = \frac{u_0 w_0}{w(z)} \exp\left\{-\frac{r^2}{w^2(z)} \exp\left[-i\left[kz - \tan^{-1} \frac{z}{z_0} + \frac{kr^2}{2\Re(z)}\right]\right]\right\} \tag{9}$$

Where u_0 is the output amplitude at the axis; z is axial distance from the fiber tip; λ is the wavelength; $k = 2\pi / \lambda$ is the wave vector; w_0 is the waist of Gaussian beam at $z = 0$; $w(z)$ is the beam spot size, $w(z) = w_0 \sqrt{1 + z^2 / z_0^2}$ $z_0 = \pi w_0^2 / \lambda$ and $\Re(z) = z + z_0^2 / z$.

The Gaussian beam partially transmits from the fiber tip and propagates to the diaphragm, and then reflected to the fiber tip. Taking the beam divergence into consideration, the returned beam will be broadened according to Eq.(9) with $z = 2l$, as shown in Fig.4 in symmetrical view, where l is the Fabry-Perot cavity length. The beam injects into the fiber partially with the coupling coefficient determined by interchange integration expressed as follows:

$$\eta = \frac{\iint u(r, 0) |u(r, 2l)| ds}{[\iint u^2(r, 0) ds \cdot \iint |u(r, 2l)|^2 ds]^{1/2}} = \frac{2w_0 w(2l)}{w_0^2 + w^2(2l)} \tag{10}$$

Interference will occur inside the fiber tip. The F-P cavity used in this type of sensor is usually with low reflective mirrors, in terms of low finesse F-P interferometer. Thus the multiple reflections between the mirrors can be neglected, only the first two beams need to be accounted: one is the beam reflected from the tip inside the fiber and the other is the beam emitted from the fiber, propagating through the cavity, returned and coupled into the fiber. The interference intensity can be written as:

$$I = \iint |u_T|^2 ds \approx I_0 \{R_1 + \eta^2 R_2 (1 - R_1)^2 + 2\eta \sqrt{R_1 R_2} (1 - R_1) \cos[2kl + \tan^{-1}(2l / z_0)]\} \tag{11}$$

Where I_0 is the optical input intensity, R_1 is the intensity reflectivity of the fiber tip and R_2 is the intensity reflectivity of the diaphragm. The visibility of the interference fringe can be expressed as:

$$V = \frac{4\eta \sqrt{R_1 R_2} (1 - R_1)}{R_1 + \eta^2 R_2 (1 - R_1)^2} \tag{12}$$

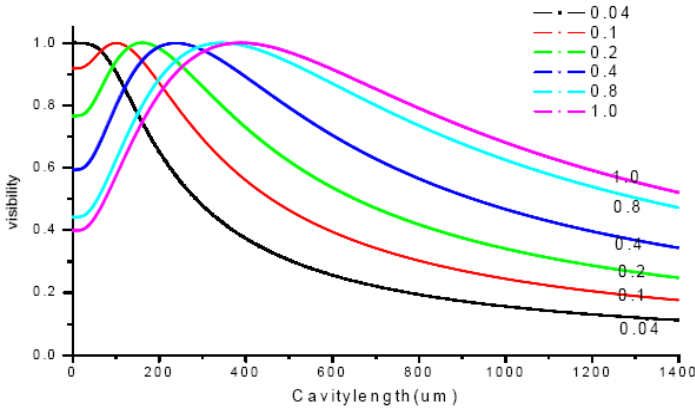


Fig. 5. Fringe visibility for different R_2 with the same uncoated fiber tip reflectivity $R_1=4\%$

Fig.5 shows the Visibility changes for different reflectivity of R_2 , here reflectivity of R_1 is fixed to 4%. Visibility of the interference fringe is an important factor for high sensitivity. The visibility relies on the surface reflectivity R_1 , R_2 , and the cavity length l , which are the three parameters to be adjusted for highest visibility. From Eq.(12), the maximum of $V = 100\%$ can be obtained if proper parameters reached.

3 Experiment

A function generator which is connected to a computer speaker was used to produce acoustic waves. The sensor detects signals from the function generator. Then the detected signals were sent to the digital oscilloscope for demonstration.

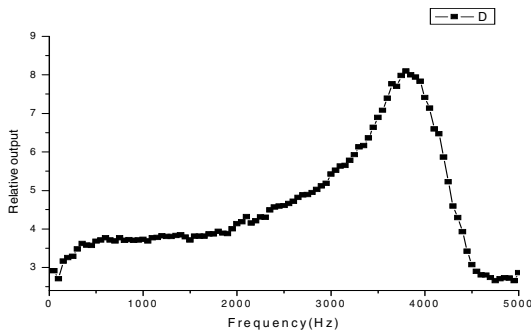


Fig. 6. Frequency response of the fiber optical sensor

Fig.6 shows the sensor response to acoustic signals with same amplitude and increasing frequencies. For this measurement, the diaphragm has an expected resonant frequency of about 4 kHz. The sensor is seen to have a fairly broad

resonance centered on about 3.85 KHz, with small structure peaks below this frequency. It shows that the sensor has a dynamic response that is close to the expected value.

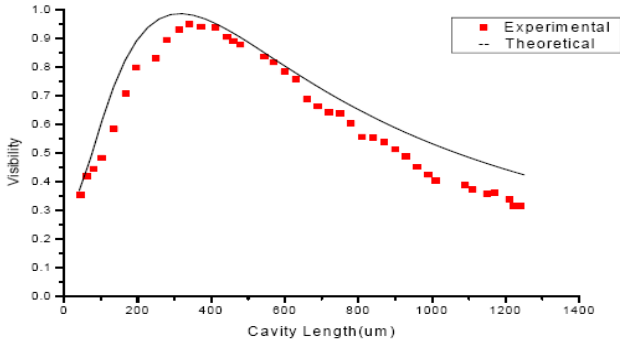


Fig. 7. Interference visibility versus cavity length experimental and theoretical results

Fig.7 is a calculated interference fringe visibility vs. cavity length with $R_1 = 4.0\%$, $R_2 = 95\%$, $\lambda = 1550\text{nm}$ and $w_0 = 4.5\mu\text{m}$, showing the highest visibility is obtained near $l = 380\mu\text{m}$. In the experiment a broadband light source is used, in the rear end connect a spectral analyzer, change the length of the F-P cavity length, and measure the fringe visibility for different F-P cavity length. There are some different from previous published work 9,10, in which a symmetric cavity of $R_1 = R_2$ was considered, so in their works the dependence of visibility on cavity length showed a monotonic declined curve.

4 Conclusion

The design guidelines for micro diaphragm-type acoustic sensors have been established by characterization of the relationships among diaphragm thickness, side length, sensitivity, and resonant frequency. According to the investigations, the thickness need to be thin and the side length need to be small in order to get the sensitive diaphragm with high resonant frequency. A Fabry–Perot based acoustic sensor has been designed based on the guidelines, fabricated and characterized. An optical fiber sensor with ultra-sensitivity is designed, fabricated, and tested. Improvements have been made in the fringe visibility and sensitivity of the sensor, the visibility of near 100% has been achieved so as to get a very high sensitivity. A simple micromachining process compatible with MEMS has been developed for fabricating the optical fiber sensor. The use of MEMS technology is advantageous because of the potential for enormous economical manufacturing.

References

1. Jackson, D.A.: Recent progress in mono-mode fiber optic sensors. *Measurement Sci. Technol.* 5, 621–638 (1994)
2. Dandridge, Kersey, A.D.: Overview of mach-Zehnder sensor technology and applications. In: *Proceedings of SPIE 985, Fiber Optic and Laser Sensors VI*, Boston (September 1988)

3. Chau, H.L., Wise, K.D.: Scaling limits in batch-fabricated silicon pressure sensors. *IEEE Trans. Electron Devices* ED-34, 850–858 (1987)
4. Kung, J.T., Lee, H.-S.: An integrated air-gap-capacitor pressure sensor and digital readout with sub-100 attofarad resolution. *IEEE J. Microelectromech. Syst.*, 1121–1129 (1992)
5. Mastrangelo, C.H., Zhang, X., Tang, W.C.: Surface-micromachined capacitive differential pressure sensor with lithographically defined silicon diaphragm. *IEEE J. Microelectromech. Syst.* 5, 89–105 (1996)
6. Du, G., Zhu, Z., Gong, X.: *Acoustics*. University Nanjing, Nanjing (2001)
7. Morse, P.M., Ingard, K.U.: *Theoretical Acoustic*. McGraw-Hill, New York (1968)
8. Harrays, C.M.: *Shock and Vibration Handbook*. McGraw-Hill, New York (1966)
9. Chin, K.K., Sun, Y., Feng, G., Georgiou, G.E., Guo, K., Niver, E., Roman, H., Noe, K.: Fabry-Perot diaphragm fiber-optic sensor. *Appl. Opt.* 46, 7614–7619 (2007)
10. Yu, B., Kim, D.W., Deng, J., Xiao, H., Wang, A.: Fiber Fabry-Perot sensors for detection of partial discharges in power transformers. *Appl. Opt.* 42, 3241–3250 (2003)

Catastrophe Modeling of a Nonlinear System

Zengkun Qi

College of Engineering, Heilongjiang Bayi Agricultural University, Xinyang Rd.2,
163319 Daqing, China
zengkun-qi@163.com

Abstract. Catastrophe theory is widely used in almost every aspect since it was founded, and usually the research target is the nonlinear system. However, how to build the catastrophe models of a nonlinear system is a hard problem. Catastrophe models are the key points to analyze the catastrophe characteristics of a system. This paper discussed the universal transformation methods of four elementary catastrophe modeling, which are fold catastrophe modeling, cusp catastrophe modeling, swallowtail catastrophe modeling and butterfly catastrophe modeling. Once the catastrophe model of the system is deduced, the catastrophe analysis of the system then can be applied.

Keywords: Catastrophe, modeling, nonlinear system.

1 Introduction

Catastrophe theory originated from Whitney's singularity theory and Poincare-Andronov's bifurcation theory [1]. The core content of it is the jumping output caused by smooth input of a system. Though the theory involves so many abstruse mathematics, its application is so widely that many hard problems are successfully solved by this theory in almost every subject.

According to Thom's theory, catastrophe models are the key points to analyze the catastrophe characteristics of system. However, how to transform the mathematical models into catastrophe models of a system is a worth studying problem. Generally, trial and error method is adopted, but there are not any universal mathematical methods to achieve the transformation goals in the existing literatures. For this purpose, this paper discuss the transformation methods to change the mathematical models into catastrophe models of a nonlinear system. These catastrophe models are fold catastrophe model, cusp catastrophe model, swallowtail catastrophe model and butterfly catastrophe model. The common feature of these models is the potential function of catastrophe model has the single output form. Once the catastrophe model is deduced, the catastrophe characteristic of the system is obviously obtained [2].

2 Catastrophe Modeling

In scientific research and engineering, the common method we take is to build the mathematical model of research object, which is the foundation to conduct theoretical analysis. For an ordinary nonlinear system, its differential equations can be described as:

$$\dot{X} = F(X). \tag{1}$$

Where $X = (x_1, x_2, \dots, x_n)^T \in R^n$ are state variables, $F = (f_1, f_2, \dots, f_n) : R^n \times R^m \rightarrow R^n$ are functions of X .

For a nonlinear system that has catastrophe characteristics, after non-essential variables are removed according to splitting lemma, the system's differential equation can be transformed to potential function or its approximate form by diffeomorphism [3]. Then analyze the singularity of the system, the equilibrium surface M and singularity set S can be obtained:

$$M : D_x F(X) = 0. \tag{2}$$

$$S : \det D_x F(X) = 0 \tag{3}$$

The bifurcation set of the system can be deduced from (2) and (3), that is, the critical points of the system can be obtained. When control variables cross bifurcation set, the phase point locates in the unstable equilibrium state area, catastrophe occurs.

By observing the catastrophe potential function with the multi-output and single-input form, it can be seen that the potential function model is a high order polynomial which has no second higher order item. Because the nonlinear system can be approximated by Taylor expansion, as long as remove the second higher order item in Taylor expansion by mathematical transformation, catastrophe model is then achieved. If Taylor expansion is approximated to first power, the nonlinear system is transformed to a linear system. As we know, catastrophe characteristics are unique properties of some nonlinear system, so the first power expansion is neglected in this paper.

2.1 Fold Catastrophe Modeling

If Taylor expansion of the nonlinear system (equation (1)) is approximated to second power, as equation (4) shows:

$$F(t) = a_0 + a_1 t + a_2 t^2. \tag{4}$$

Through elementary transformation, let $t = x - \frac{a_1}{2a_2}$, we get:

$$F(x) = a_2 x^2 + a_0 - \frac{a_1^2}{4a_2}. \tag{5}$$

The corresponding potential function of expression (5) is:

$$Y(x) = \frac{1}{3} a_2 x^3 + (a_0 - \frac{a_1^2}{4a_2}) x. \tag{6}$$

Change the coefficient of the highest order item to be 1:

$$V(x) = x^3 + (\frac{3a_0}{a_2} - \frac{3a_1^2}{4a_2^2}) x. \tag{7}$$

Let $u = \frac{3a_0}{a_2} - \frac{3a_1^2}{4a_2^2}$, then we get:

$$V(x) = x^3 + ux . \tag{8}$$

Expression (8) is the catastrophe manifold potential function form of fold catastrophe model [4], which has two dimensions. The corresponding catastrophe manifold is:

$$3x^2 + u = 0 . \tag{9}$$

And the singularity set is:

$$x = 0 . \tag{10}$$

Bifurcation set is the projection of singularity set on control space (the line $x = 0$), so the point ($u = 0$) is the bifurcation set (see Fig .1).

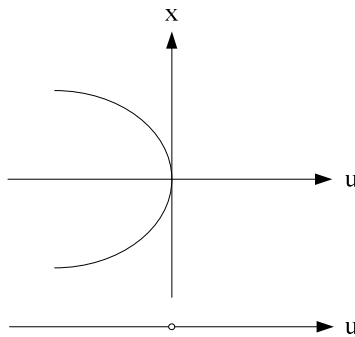


Fig. 1. Catastrophe manifold and bifurcation set of fold catastrophe

Bifurcation set splits the control space into two areas, $u > 0$ and $u < 0$.when control variable u crosses the point ($u = 0$), catastrophe occurs.

2.2 Cusp Catastrophe Modeling

If Taylor expansion of the nonlinear system is approximated to third power, as expansion (11) shows:

$$F(t) = a_0 + a_1t + a_2t^2 + a_3t^3 . \tag{11}$$

Through elementary transformation, let $t = x - \frac{a_2}{3a_3}$, we get:

$$F(x) = a_3x^3 + (a_1 - \frac{a_2^2}{3a_3})x + (\frac{2a_2^3}{27a_3^2} - \frac{a_1a_2}{3a_3} + a_0) . \tag{12}$$

The corresponding potential function of expression (12) is:

$$Y(x) = \frac{1}{4}a_3x^4 + (\frac{1}{2}a_1 - \frac{a_2^2}{6a_3})x^2 + (\frac{2a_2^3}{27a_3^2} - \frac{a_1a_2}{3a_3} + a_0)x . \tag{13}$$

Change the coefficient of the highest order item to be 1:

$$V(x) = x^4 + \left(\frac{2a_1}{a_3} - \frac{2a_2^2}{3a_3^2}\right)x^2 + \left(\frac{8a_2^3}{27a_3^3} - \frac{4a_1a_2}{3a_3^2} + \frac{4a_0}{a_3}\right)x. \tag{14}$$

Let

$$\begin{cases} u = \frac{2a_1}{a_3} - \frac{2a_2^2}{3a_3^2} \\ v = \frac{8a_2^3}{27a_3^3} - \frac{4a_1a_2}{3a_3^2} + \frac{4a_0}{a_3} \end{cases},$$

we get:

$$V(x) = x^4 + ux^2 + vx. \tag{15}$$

Expression (15) is the normal potential function form of cusp catastrophe model [5], and the corresponding catastrophe manifold is:

$$4x^3 + 2ux + v = 0. \tag{16}$$

The bifurcation set is:

$$8u^3 + 27v^2 = 0. \tag{17}$$

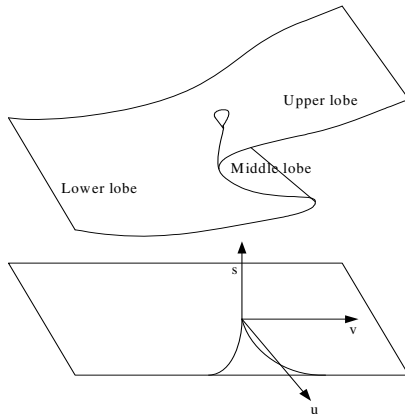


Fig. 2. Catastrophe manifold and bifurcation set of cusp catastrophe

By looking at expression (17), it can be found that the system state can be expressed by the phase point of (s, u, v) on the catastrophe manifold [6]. Suppose q is a point on the $u-v$ control plane. When q crosses the bifurcation set, if phase point is right on the edge of middle lobe, then it must skip on the other lobe (upper or lower), i.e. catastrophe occurs (see Fig .2).

2.3 Swallowtail Catastrophe Modeling

If Taylor expansion of the nonlinear system is approximated to fourth power, as expansion (18) shows:

$$F(t) = a_0 + a_1t + a_2t^2 + a_3t^3 + a_4t^4. \tag{18}$$

Through Tschirnhaus transformation [7], let $t = x - \frac{a_3}{4a_4}$, we get:

$$F(x) = a_4x^4 + (a_2 - \frac{3 a_3^2}{8 a_4})x^2 + (-\frac{1}{2} \frac{a_2 a_3}{a_4} + \frac{1}{8} \frac{a_3^2}{a_4^2} + a_1)x + a_0 - \frac{1}{4} \frac{a_1 a_3}{a_4} - \frac{3}{256} \frac{a_3^4}{a_4^3} + \frac{1}{16} \frac{a_2 a_3^2}{a_4^2}. \tag{19}$$

The corresponding potential function of expression (19) is:

$$Y(x) = \frac{1}{5} a_4 x^5 + (\frac{1}{3} a_2 - \frac{1}{8} \frac{a_3^2}{a_4}) x^3 + (-\frac{1}{4} \frac{a_2 a_3}{a_4} + \frac{1}{16} \frac{a_3^2}{a_4^2} + a_1) x^2 + (a_0 - \frac{1}{4} \frac{a_1 a_3}{a_4} - \frac{3}{256} \frac{a_3^4}{a_4^3} + \frac{1}{16} \frac{a_2 a_3^2}{a_4^2}) x. \tag{20}$$

Change the coefficient of the highest order item to be 1:

$$V(x) = x^5 + (\frac{5}{3a_4} a_2 - \frac{5}{8} \frac{a_3^2}{a_4^2}) x^3 + (-\frac{5}{4} \frac{a_2 a_3}{a_4^2} + \frac{5}{16} \frac{a_3^2}{a_4^3} + a_1) x^2 + (\frac{5a_0}{a_4} - \frac{5}{4} \frac{a_1 a_3}{a_4^2} - \frac{15}{256} \frac{a_3^4}{a_4^4} + \frac{5}{16} \frac{a_2 a_3^2}{a_4^3}) x. \tag{21}$$

Let
$$\begin{cases} u = \frac{5}{3a_4} a_2 - \frac{5}{8} \frac{a_3^2}{a_4^2} \\ v = -\frac{5}{4} \frac{a_2 a_3}{a_4^2} + \frac{5}{16} \frac{a_3^2}{a_4^3} + a_1 \\ w = \frac{5a_0}{a_4} - \frac{5}{4} \frac{a_1 a_3}{a_4^2} - \frac{15}{256} \frac{a_3^4}{a_4^4} + \frac{5}{16} \frac{a_2 a_3^2}{a_4^3} \end{cases},$$

we get:

$$V(x) = x^5 + ux^3 + vx^2 + wx. \tag{22}$$

Expression (22) is the normal potential function form of swallowtail catastrophe model [8], and the corresponding catastrophe manifold is:

$$M : 5x^4 + 3ux^2 + 2vx + w = 0. \tag{23}$$

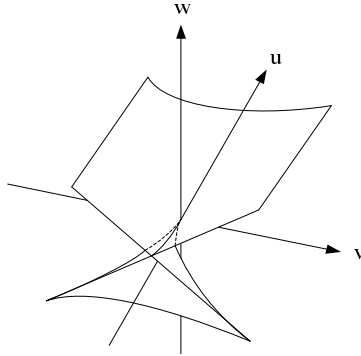


Fig. 3. Bifurcation set of swallowtail catastrophe

The singularity set is:

$$20x^3 + 6ux + 2v = 0 . \tag{24}$$

Eliminate x from expression (23) and (24), and then bifurcation set can be obtained (see Fig. 3). Because the bifurcation set looks like a swallowtail, we call it swallowtail catastrophe.

2.4 Butterfly Catastrophe Modeling

If Taylor expansion of the nonlinear system is approximated to fifth power, as expansion (25) shows:

$$F(t') = a_0 + a_1t' + a_2t'^2 + a_3t'^3 + a_4t'^4 + a_5t'^5 \tag{25}$$

Through elementary transformation, let $t' = x - \frac{a_4}{5a_5}$, we get:

$$F(x) = a_5x^5 + (a_3 - \frac{2 a_4^2}{5 a_5})x^3 + (a_2 + \frac{4 a_4^3}{25 a_5^2} - \frac{3 a_3 a_4}{5 a_5})x^2 + (-\frac{2 a_2 a_4}{5 a_5} + \frac{3 a_3 a_4^2}{25 a_5^2} - \frac{3 a_4^4}{125 a_5^3} + a_1)x + a_0 - \frac{1 a_1 a_4}{5 a_5} + \frac{4 a_4^5}{3125 a_5^4} + \frac{1 a_2 a_4^2}{25 a_5^2} - \frac{1 a_3 a_4^3}{125 a_5^3} . \tag{26}$$

The corresponding potential function of expression (26) is:

$$Y(x) = \frac{1}{6}a_5x^6 + (\frac{1}{4}a_3 - \frac{1}{10}\frac{a_4^2}{a_5})x^4 + (\frac{1}{3}a_2 + \frac{4}{75}\frac{a_4^3}{a_5^2} - \frac{1}{5}\frac{a_3 a_4}{a_5})x^3 + (-\frac{1}{5}\frac{a_2 a_4}{a_5} + \frac{3}{50}\frac{a_3 a_4^2}{a_5^2} - \frac{3}{250}\frac{a_4^4}{a_5^3} + \frac{1}{2}a_1)x^2 + (a_0 - \frac{1}{5}\frac{a_1 a_4}{a_5} + \frac{4}{3125}\frac{a_4^5}{a_5^4} + \frac{1}{25}\frac{a_2 a_4^2}{a_5^2} - \frac{1}{125}\frac{a_3 a_4^3}{a_5^3})x . \tag{27}$$

Change the coefficient of the highest order item to be 1:

$$\begin{aligned}
 V(x) = & x^6 + \left(\frac{3 a_3}{2 a_5} - \frac{3 a_4^2}{5 a_5^2}\right)x^4 + \left(-\frac{6 a_2 a_4}{5 a_5^2} + \frac{9 a_3 a_4^2}{25 a_5^3} - \frac{9 a_4^4}{125 a_5^4} + 3 \frac{a_1}{a_5}\right)x^2 \\
 & + \left(2 \frac{a_2}{a_5} + \frac{8 a_4^3}{25 a_5^3} - \frac{6 a_2 a_4}{5 a_5^2}\right)x^3 + \left(6 \frac{a_0}{a_5} - \frac{6 a_1 a_4}{5 a_5^2} + \frac{24 a_4^5}{3125 a_5^5} + \frac{6 a_2 a_4^2}{25 a_5^3} - \frac{6 a_3 a_4^3}{125 a_5^4}\right)x. \quad (28)
 \end{aligned}$$

Let

$$\begin{cases}
 t = \frac{3 a_3}{2 a_5} - \frac{3 a_4^2}{5 a_5^2} \\
 u = 2 \frac{a_2}{a_5} + \frac{8 a_4^3}{25 a_5^3} - \frac{6 a_2 a_4}{5 a_5^2} \\
 v = -\frac{6 a_2 a_4}{5 a_5^2} + \frac{9 a_3 a_4^2}{25 a_5^3} - \frac{9 a_4^4}{125 a_5^4} + 3 \frac{a_1}{a_5} \\
 w = 6 \frac{a_0}{a_5} - \frac{6 a_1 a_4}{5 a_5^2} + \frac{24 a_4^5}{3125 a_5^5} + \frac{6 a_2 a_4^2}{25 a_5^3} - \frac{6 a_3 a_4^3}{125 a_5^4}
 \end{cases},$$

we get:

$$V(x) = x^6 + tx^4 + ux^3 + vx^2 + wx. \quad (29)$$

Expression (29) is the normal potential function form of butterfly catastrophe model [9], and the corresponding catastrophe manifold is:

$$6x^5 + 4tx^3 + 3ux^2 + 2vx + w = 0. \quad (30)$$

The singularity set is:

$$30x^4 + 12tx^2 + 6ux + 2v = 0. \quad (31)$$

Eliminate x from (30) and (31), and then bifurcation set can be obtained. The bifurcation set equation is a four dimension function, and the corresponding figure looks like a butterfly, we call it butterfly catastrophe.

3 Conclusions

This paper discussed the universal transformation methods of four elementary catastrophe modeling, which are fold catastrophe modeling, cusp catastrophe modeling, swallowtail catastrophe modeling and butterfly catastrophe modeling. The common feature of these models is the potential function of catastrophe model has the single output form. Once the catastrophe model of the system is deduced, the catastrophe analysis of the system then can be applied, which has significant meaning in many domains, such as aviation, navigation, coal mining and danger forecast.

References

1. Arnold, V.I.: *Catastrophe Theory*. Springer, Heidelberg (1986)
2. Zengkun, Q.: *Research on Catastrophe Control Mechanism and Its Application on Nonlinear Ship Roll Motion*. Doctoral thesis of Harbin Engineering University, Harbin (2010)
3. Qinghua, D.: *Nonlinear Ship Rolling Analysis Based on Catastrophe Theory*. Master's thesis of Harbin Engineering University, Harbin (2009)
4. Fuhua, L.: *Catastrophe Theory and its Application*. Shanghai Jiao Tong University, Shanghai (1987)
5. Saunders, P.T.: *An introduction to catastrophe theory*. Cambridge University Press, Cambridge (1980)
6. Zengkun, Q., Yao, S., Hongwei, M.: *Catastrophe Analysis on Ship Single-degree-of-freedom Nonlinear Rolling*. In: *International Symposium on Knowledge Acquisition and Modeling Workshop Proceedings*, pp. 518–521. IEEE Press, New York (2008)
7. Zhengwen, L., Jianming, T.: *Converted S P Wave Prestack Depth Migration of Common Shot Records With Hybrid Extrapolation Formula*. *Journal of Mineralogy and Petrology*, 87–93 (1998)
8. Ping, H., Zidu, Z.: *Catastrophe Theory and its Application*. Dalian University of Technology, Dalian (1989)
9. Rene, T.: *Mathematical Models of Morphogenesis*. Ellis Horwood Limited, Chichester (1983)

Dynamics of a Tuberculosis Model with Treatment and Self-cure

Yayi Xu¹, Guorong Huang², and Zhan Zhao³

¹ Department of Applied Mathematics and Physics, Air Force Engineering University,
Xi'an 710051, China

² Department of Aviation Automatic Control Engineering, Air Force Engineering University,
Xi'an, 710038, China

³ Unit 94170 of the PLA, Xi'an, 710082, China
hgr126@126.com

Abstract. A tuberculosis (TB) model with treatment and self-cure is investigated. The basic reproduction number is found and its epidemiological interpretation is given. It has been shown that the dynamics of the model is determined by its basic reproductive number. If the basic reproduction number is less than or equal to one, there exists only the disease-free equilibrium which is globally asymptotically stable, and the disease dies out eventually. When the basic reproduction number exceeds one, there exists a unique endemic equilibrium which is uniformly persistent. At last, some measures to control the spread of TB are discussed.

Keywords: Tuberculosis, Treatment, Self-cure, The basic reproduction number, Stability.

1 Introduction

Tuberculosis (TB) is a bacterial disease caused by *Mycobacterium tuberculosis* (Mtb), which is usually acquired through airborne infection from active TB cases[1,2]. There are nine million new cases per year, of which about three million population die[3,4]. A person with active TB disease has a large amount of TB bacteria in the body. TB disease can be treated by taking several drugs for six to twelve months. If they stop taking the drugs too soon, they can become sick again; if they do not take the drugs correctly, the germs that are still alive may become resistant to those drugs. TB that is resistant to drugs is harder and more expensive to treat[5,6].

The average length of latent period ranges from months to decades[1]. In the paper, we assume that the treated individuals are in isolated environment, and they can not infect others. After a period of treatment, the treated one leaves the isolated environment. It assumes that a susceptible individual, after being infected, may enter latent compartment. After being treated the TB symptoms of a patient may disappear, and there may still be a few of tubercle bacillus in the body of the patient, the individual may still be TB carriers and become latent; or may be enter the infectious compartment for failure treatment[7,8].

This paper is organized as follows. In Section 2, an *SLIT* TB model with treatment and self-cure is formulated. In Section 3, the basic reproduction number is determined, and the existence of equilibrium is analyzed. Furthermore, the global asymptotical stability of the disease-free equilibrium and the endemic equilibrium uniformly persistent are discussed in Section 4. In Section 5, we discussed control measures for TB.

2 Formulate the Model

The total population is divided into four epidemiological compartments: the susceptible compartment S , the latent compartment L , the infectious compartment I , the treating compartment T . an *SLIT* epidemic model with incomplete treatment is given by the following system of differential equations:

$$\begin{cases} \dot{S}(t) = \mu(A - S) - \beta SI + p_1 \delta T, \\ \dot{L}(t) = \beta SI + p_2 \delta T - b_1 L + q \gamma I, \\ \dot{I}(t) = \varepsilon L + p_3 \delta T - b_2 I, \\ \dot{T}(t) = (1 - q) \gamma I - b_3 T. \end{cases} \tag{1}$$

where $b_1 = \mu + \varepsilon, b_2 = \mu + \alpha_1 + \gamma, b_3 = \mu + \delta + \alpha_2$. The parameters $\mu, \beta, \varepsilon, \gamma, \delta$ are all positive constants. The constant μ is the natural death rate coefficient. β is the probability per unit time of transmitting the infections between two individuals taking part in a contact. ε is the transfer rate coefficient of the latent individuals becoming infective. γ is the treated rate coefficient of the infectious individuals. $q (0 \leq q < 1)$ is the fraction of infectious individuals reentered the latent compartment through self-cure. δ is the transfer rate coefficient of the treatment individuals. $p_i \geq 0 (i = 1, 2, 3), \sum_{i=1}^3 p_i = 1$ and p_1, p_2, p_3 are the fraction of the treated individuals reentered S, L, I compartments, respectively. α_1, α_2 are non-negative constants and represent the death rate coefficient due to disease (the disease-related death rate). μA is the recruitment rate into the population.

From system (1), let $N(t) = S(t) + L(t) + I(t) + T(t)$, then it follows from (1) that $\dot{N}(t) = \mu A - \mu N(t) - \alpha_1 I(t) - \alpha_2 T(t) \leq \mu A - \mu N(t)$. It implies that $\limsup_{t \rightarrow \infty} N(t) \leq A$. So $N(t)$ is uniformly ultimately bounded. Therefore, in the rest of the paper we will study the system (1) in the feasible region $\Omega = \{(S, L, I, T) \in \mathbf{R}_+^4 : 0 < S + L + I + T \leq A\}$.

3 The Basic Reproduction Number and Equilibria

For the system (1), it is obvious that it always exists disease-free equilibrium $E_0(A, 0, 0, 0)$ on the region Ω . By using the method of next generation matrix[9], we can obtain the basic reproduction number

$$R_0 = \frac{\beta A b_3 \epsilon}{b_1 b_2 b_3 - \delta \gamma (p_3 b_1 + p_2 \epsilon)(1 - q) - q \epsilon \gamma b_3} \tag{2}$$

Furthermore, by straightforward calculation, it can be given the following results on the existence of endemic equilibrium of system (1) in the region Ω .

Theorem 1. When $R_0 > 1$, besides the disease-free equilibrium E_0 , system (1) also has a unique endemic equilibrium $E^*(S^*, L^*, I^*, T^*)$, where

$$S^* = \frac{\mu A + p_1 \delta T^*}{\mu + \beta I^*} = \frac{A}{R_0}, L^* = \frac{b_2 b_3 - p_3 \delta \gamma (1 - q)}{b_3 \epsilon} I^*, T^* = \frac{(1 - q) \gamma}{b_3} I^*,$$

$$I^* = \frac{\mu \{b_1 [b_2 b_3 - p_3 \delta \gamma (1 - q)] - p_2 \delta \gamma \epsilon (1 - q) - q \gamma b_3 \epsilon\}}{\beta \{b_1 [b_2 b_3 - p_3 \delta \gamma (1 - q)] - (p_1 + p_2) \delta \gamma \epsilon (1 - q) - q \gamma b_3 \epsilon\}} (R_0 - 1).$$

4 Conclusion and Simulation

By construct Liapunov function, LaSalle Invariance Principle[10] and the persistence in terms of repeller[11], we have the following theorem 2.

Theorem 2. When $R_0 \leq 1$, the disease-free equilibrium E_0 of system (1) is globally asymptotically stable on the region Ω ; when $R_0 > 1$, the disease-free equilibrium E_0 of system (1) is unstable on the region Ω and the disease persists if it is initially present.

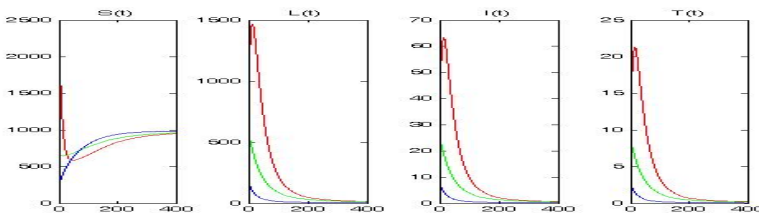


Fig. 1. Globally asymptotically stable of the disease free equilibrium E_0 for system (1)

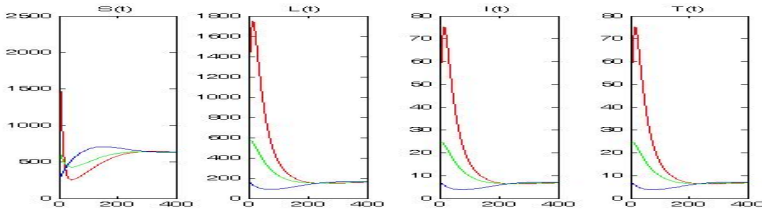


Fig. 2. Globally asymptotically stable of the disease free equilibrium E^* for system (1)

When $R_0 \leq 1$, the simulation shows that the endemic equilibrium E_0 of system (1) is globally asymptotically stable in the interior of Ω (see Fig.1). In Fig.1, $A=1000, \mu=1/70.0, \beta=0.0014, p_1=0.94, p_2=0.05, \epsilon=0.05, p_3=0.01, \alpha_1=0.4, \alpha_2=0.1, \gamma=0.75, \delta=2$ and $q=0.05$, then $R_0=0.9880 < 1$. When $R_0 > 1$, the simulation shows that the endemic equilibrium E^* of system (1) is globally asymptotically stable in the interior of Ω (see Fig.2). In Fig.2, $q=0.8$, and other parameters are the same as those of the Fig.2, then $R_0=1.2731 > 1$.

References

1. Kochi, A.: The global tuberculosis situation and the new control strategy of the world health organization. *Tubercle* 72, 1–6 (1991)
2. Russell, D.G., Barry 3rd, C.E., Flynn, J.L.: Tuberculosis: What we don't know can, and does, hurt us. *Science* 328, 852–856 (2010)
3. Bjune, G.: Tuberculosis in the 21st century: an emerging pandemic? *Norsk Epidemiology* 15, 133–139 (2005)
4. Dye, C., Floyd, K., Uplekar, M.: World health report 2008: Global tuberculosis control: surveillance, planning, financing. World Health Organization, WHO/HTM/TB/2008. 393 (2008)
5. Blower, S.M., Tom, C.: Modeling the emergence of the 'hot zones' tuberculosis and the amplification dynamics of drug resistance. *Nature Medicine* 10, 1111–1116 (2004)
6. Ganeux, S., Long, D.C., Small, P., et al.: The competitive cost of antibiotic resistance in *Mycobacterium tuberculosis*. *Science* 312, 1944–1946 (2006)
7. Neyrolles, O., Hernandez-Pando, R., Pietri-Rouxel, F., et al.: Is Adipose Tissue a Place for *Mycobacterium tuberculosis* Persistence? *PLoS One* 1(1), e43, doi:10.1371/journal.pone.0000043
8. Science Daily. Tuberculosis Bacillus Hides from Immune System in Host's Fat Cells, <http://www.sciencedaily.com/releases/2006/12/061221074735.htm>
9. Van Den Driessche, P., Watmough, J.: Reproduction numbers and sub-threshold endemic equilibria for compartmental models of disease transmission. *Math. Biosci.* 180, 29–48 (2002)
10. LaSalle, J.P.: The stability of dynamical systems. Regional Conference Series in Applied Mathematics. SIAM, Philadelphia (1976)
11. Fonda, A.: Uniformly persistent semi-dynamical systems. *Proceedings of American Mathematical Society* 104, 111–1161 (1988)

Headland Turning of Autonomous Robot in Corn Field

JinLin Xue

College of Engineering, Nanjing Agricultural University, Nanjing, 210031, China
xuejinlin@njau.edu.cn

Abstract. Headland turning operation has been difficulties in field application for autonomous agricultural vehicles based on machine vision. A method using variable field of view of camera to solve deficiencies in blind spots or limited image information with a settled field of view, which is controlled by two DC motors to rotate in vertical and horizontal planes, is proposed to detect crops near the end of crop rows, guide an agricultural robot and implement headland turning operation in corn field. The lateral field of view of camera was chosen firstly to detect crops near the end of corn row and guide the robot according to guidance information from crop images by using the image processing technology based on mathematically morphological operations. Headland turning was mainly composed of two 90° turning and one backing control. Three repetition tests were conducted to perform the headland turning operation in corn field. A maximum error of 17.4mm when using the lateral view and good headland turning operation were observed. It was successful for variable field of view to implement headland turning operation in corn field.

Keywords: Headland turning, machine vision, robot, row guidance, end of row.

1 Introduction

Autonomous agricultural vehicles have potential benefits in increasing productivity, improving application accuracy and promoting safety. But autonomous navigation functionality of such vehicles, as a key and basis to perform selective operations in field, has been a focus and hotspot of study. The methods based on machine vision with performances in low cost, flexibility, real time and high precision navigation, have been studied and applied in agricultural vehicles due to main characteristics of crop planted in rows or agricultural production operated in lines.

Since the potential of agricultural vehicle navigation based on machine vision was first proposed, it has led to the development of visual navigation systems to guide tractors along crop rows [1-5]. Such systems were also adopted to guide vehicles for spraying, weeding, cultivating and for harvesting [6-10]. In addition, many autonomous agricultural robots with machine vision performed well in fields [11-14]. These studies and applications have proven applicability of machine vision of agricultural vehicles in straight or curve line guidance. However, no author has implemented headland turning operation in the end of crop rows by merely using machine vision so far, except that Åstrand and Baerveldt [9] concerning end-of-row detection and Subramanian and Burks [15] making efforts in headland turning by using a combination of machine vision and laser radar. The end-of-row guidance and

turning operation, which usually were evaded in researches, have been considered as difficulties for autonomous agricultural vehicles with a settled field of view (FOV) of machine vision due to a fixed direction (angle) of view of machine vision. Although the settled FOV of machine vision has performed good to navigate vehicles with long distance in straight or curve crop rows, it has difficulty in detecting the end of rows with a settled FOV due to limited image information and blind spots, especially for headland turning operation at the end of crop rows.

The objective of this work is to implement headland turning operation of an autonomous agricultural robot, with variable FOV of machine vision, which is achieved by changing the direction of view of machine vision. In order to detect crops near the end of crop rows, a variable FOV camera, controlled by two DC motors, was developed to obtain a changeable FOV of camera in the horizontal plane paralleling to the ground and the vertical planes along the forward direction of a robot. The lateral FOV of camera, which means that the direction of view of machine vision points at left or right side of a robot relative to the forward direction of the robot, was chosen to detect row crops near the end of crop rows, which cannot be observed with a settled FOV of camera due to blind spots or limited image information. During headland turning operation, the camera's direction of view was changed to determine position of the robot in order to complete headland turning operation of the robot into the next rows.

2 Materials and Methods

2.1 Experimental Equipments

AgTracker, which was developed by Department of Agricultural and Biological Engineering at University of Illinois to demonstrate crop guidance functionality with ruggedness, simplicity and low cost in mind, about 920mm×500mm×480mm (length×width×height), was selected as robot platform for this study. The basic crop guidance functionality was implemented by using a single microcontroller. This involved controlling speeds of two motors and receiving steering information from a main laptop computer, which is relayed to drive the motors in Pulse Width Modulation (PWM) form with simple skid steering. AgTracker's drive motors are DC brushless High Torque types. The output of the motors was geared down significantly using chains and gearboxes. To interface the microcontroller with the motors, motor controller boards OSMC Power Unit were used. The robot platform is shown in Fig. 1.



Fig. 1. The robot platform

For the purpose of low cost, a family webcam (Logitech QuichCam) was chosen as visual device with 640×480 pixels and 30 fps frame rate, and was connected to a main computer with AMD Turion 64 X2 TL-50 dual-core processors through High-Speed USB 2.0 cable. This camera characterized by variable FOV will be introduced in the next section. Matlab image acquisition and processing software were mainly applied to acquire and process images from the camera in the main computer. After completing image processing, the computer sent commands to the microcontroller in the robot through serial communication. Then the motor controller boards received PWM signals to drive the motors. The control scheme of the visual system is shown in Fig. 2.



Fig. 2. Control scheme of visual system

RTK GPS (Trimble 5800 GPS) receiver was equipped to determine the running trajectory of this robot and evaluate control performances in headland turning operation of the robot with variable FOV machine vision. GPS data was stored in the main computer via serial communication.

2.2 Headland Turning

Machine vision with a settled FOV has difficulty in supplying sufficient information for guidance and other field operations. In this work, a variable FOV of camera was developed to detect corps near the end of rows and implement headland turning control in corn field. There are two DC motors (motor 1 and motor 2, shown in Fig. 3 to implement the variable FOV of camera, where motor 1 controls camera rotation in the vertical plane along the forward direction of vehicle, motor 2 controls camera rotation in the horizontal plane paralleling to the ground.

Given that all angle of camera are calculated on the basis of camera position where camera is looking straight ahead. In the vertical plane (Fig. 3(a)), elevation angle of camera is defined as α_{up} when camera is looking up; depression angle is defined as α_{down} when camera is looking down. In the horizontal plane (Fig. 3(b)), rotation angles of camera to the left and the right are defined as β_{left} and β_{right} , respectively.

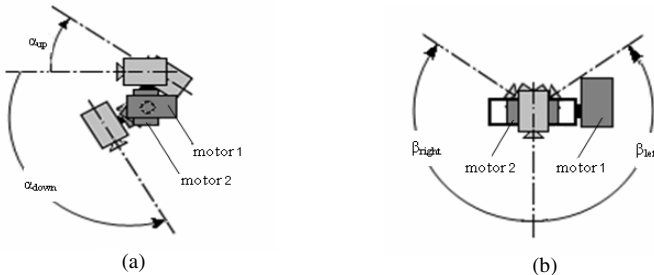


Fig. 3. Control scheme of variable FOV

The machine vision developed was mounted in the front of the robot with the height of 535 mm from central line of camera to the ground when the camera looks straight forward. This camera not only has continuously changeable angle in the vertical plane, which can change FOV of camera in front of robot, but also can observe crops according to a lateral FOV through control of the two DC motors. In this work, a lateral FOV of camera was chosen firstly to detect crops near the end of corn rows and guide the robot forward, because there was a blind spot with about 1.5m in front of the robot, when image from the camera can be segmented to find guidance line with a minimum forward FOV. Then a far FOV of camera, which means a smaller α_{down} in Fig. 3(a), was performed to determine the robot position and its backing distance during headland turning operation, by rotating the camera to the horizontal direction perpendicular to longitudinal direction of the robot.

Fig. 4 shows the process of headland turning operation of the autonomous robot in corn field, when the robot turn left into the next rows. This process can be divided to the following steps:

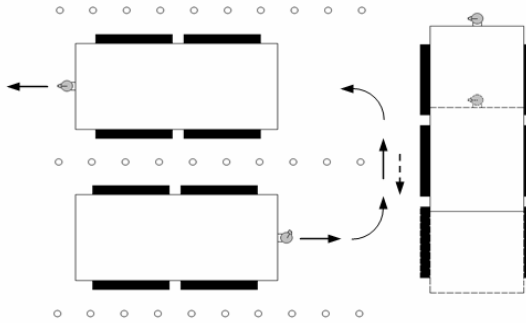


Fig. 4. Process of headland turning operation

(1) End of row detection and guidance. The robot must be able to detect and identify crops near the end of corn row and guide the robot before turning operation. During the end-of-row detection, a lateral FOV of machine vision was used to observe crop rows and guidance information was calculated by image processing to guide the robot forward. When there is no crop in image, it indicates that the robot reaches the end of crop rows and will prepare for turning operation.

(2) Go blind for a distance. The robot continues moving forward with current heading for a distance without image acquisition and processing. This is mainly to ensure the robot completely off the crop rows before headland turning operation. In this work, the robot moved forward 1m after it reached the end of rows.

(3) Turn 90° to left. In this work, no direction sensor such as compass was equipped in the tested robot. In order to achieve 90° turn to left, speeds of left and right wheels and steering time were determined through indoor tests and field trials in sequence. In addition, the wheels speeds were fixed to simplify the control program during this turning stage. In this work, the left wheel speed was set to 0.01 m/s, the right wheel speed 0.2 m/s and the turning time 7 s.

(4) Stop the robot, and then rotate the camera into the direction perpendicular to longitudinal direction of the robot in the horizontal plane to observe the left crop rows. The position and direction of the robot relating to the next crop rows will be determined by processing the image.

(5) Back the robot a distance. In this work, this backing operation must be performed after the first 90° turn, which depends on the inter-rows distance in corn field and the size of the tested robot. Based on the step (3), the backing distance and the speeds of the left and right wheels will be calculated. If the robot is perpendicular to the crop rows, it will move backward a distance with the same speed of the left and right wheels. Otherwise, it is necessary to adjust the speeds of the left and right wheels to make the robot perpendicular to the crop rows as far as possible when the robot backs a distance.

(6) Turn 90° to left again with a turning time of 5s. The similar operation was realized between this step and the step (3) except the different turning time. The reason for choosing the turning time of 7 s in the step (3) is to ensure that the robot direction is not deviated from corn rows after the first 90° turn in the case of the resistance of soil. Otherwise, it is difficult for the robot to acquire crops image when the robot stopped with a bigger direction angle to the right due to the bigger resistance of soil when turning.

(7) Stop the robot. It indicates that headland turning operation is completed and the robot locates before the next corn rows. In order to move the robot forward in the next rows, another far FOV of camera, with which the robot can look forward along the longitudinal direction, will be chosen to acquire corn rows image. However, this part does not discussed in this work.

2.3 Image Segmentation

There always exists blind spot in front of robot with a certain distance when using a minimum forward FOV, with which the smallest row crop navigation information can be obtained. In this work, there was a blind spot with 1.5m distance in front of robot. Therefore, lateral FOV of machine vision, as shown in Fig. 5(a), was chosen to detect crops near the end of crop rows and navigate the robot, although only several corn stems were contained in crop image (Fig. 5(b)). In this case, crops objects in image were mainly corn stems, and an algorithm mainly based on mathematically morphological operations with specific structure element was adopted to identify and segment corn stems, as shown in Fig. 5(c). The crop row line, also as the guidance line, was shown in Fig. 5(d).

As mentioned above, a far FOV of machine vision was chosen to determine the position and direction of the robot during turning operation, which further determines how to make the robot back. In order to determine the position of robot relative to the crop rows, the simulated experiments were implemented in advance, as shown in Fig. 6(a). There were three black tapes, which have a contrast with the ground, to represent three actual corn rows. After the robot firstly turned 90° to left, the camera angle was changed to observe corn rows, especially to observe the third corn row, whose position in image determines the relative position of the robot. The different position of the robot relative to the simulated rows were acquired to find out

correspondence relationship between the actual position information (distance and heading) of the robot relative to the crop rows and the crop rows position in images. Therefore, in the upcoming applications, the robot position information will be obtained only by the crop rows position information in image, thus the information about backing distance of the robot and how to make the robot backward will be determined to ensure the robot perpendicular to crop rows as far as possible after the robot completes the backing operation. Of course, after the simulated test, the correspondence relationship was verified in corn field, as shown in Fig. 6(b).

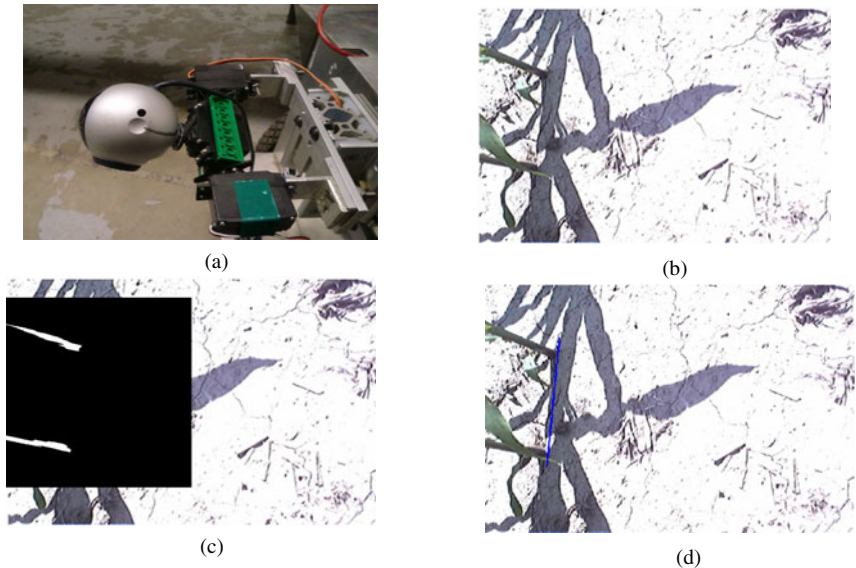


Fig. 5. Lateral FOV and its image processing

2.4 Control of Headland Turning

According to Fig. 4, the control of headland turning operation can be divided into the following 5 stages: end-of-row guidance control, going-blind control, first 90° turning control, backing control and second 90° turning control. During the end-of-row guidance control, the robot moved forward by adjusting the wheels speeds in the light of guidance information. After that, the robot was controlled to go blind a distance with its previous direction to ensure that the robot turned after it was out of the end of corn rows. But for the two 90° turning control, it was implemented by controlling wheel speeds and the turning time mentioned above. As for the backing control, position information of the robot, which includes distance of the robot from the referred crops row and direction of the robot relative to the referred crops row, were determined. Then, the backing distance and two wheel speeds of left and right wheels were calculated to ensure that the robot was controlled to appropriate position and perpendicular to the crops row as far as possible.



Fig. 6. Indoor simulation and field verification of far FOV

Wheel speeds are achieved by control PWM signals. Therefore, the speed difference of the left and right wheels was controlled according to the difference of PWM signals, thus the robot performed straight driving during the end-of-row guidance control and backing control. Fuzzy control with two inputs and one output was adopted to realize the control of row guidance. The two input signals were offset and heading angle of the robot platform respectively, which is in accordance with the control strategy of human drivers. The PWM values were obtained from a look-up table to achieve skid steering according to output signal of the fuzzy control. Triangular membership function using uniform distribution, Max-Min fuzzy inference algorithm and decoupling sentencing law with the method of center of gravity were applied in the fuzzy guidance control. The discourse domain of the fuzzy subset of input and output all were of 5 levels as {NG, NS, ZE, PS, PG}. As for the discourse domain of the fuzzy subset of output, ZE indicates that the robot maintains the last state; PS, PG, NS and NG represents small shift to the left, large shift to the left, small shift to the right and large shift to the right, respectively. In order to establish control rule base, the indoor simulation approach was chosen to find out the correspondence relationship between the actual position of the robot and the position information of the robot from images. For the backing control, the approach in Fig.8 was used to acquire image and calculate. For lateral FOV in the end-of-row guidance, the simulation approach similar to the far FOV was adopted to acquire image and calculate, except that the camera angle and the robot position are different. The robot was put at different positions to obtain the correspondence relationship according to the acquired images for the different camera FOV. Then, the control rule base was formed according to driving experience of human drivers.

3 Experimental Procedures

In order to verify performances of the designed visual guidance system in headland turning control, tests were conducted in corn field of experimental farm in the University of Illinois. Corn crops were planted in rows with about 750mm inter-row distance and about 150mm intra-row distance, the height of corn was about 700mm during the tests. And the robot ran between two corn rows. In addition, the initial

speed of robot was set to 0.2m/s, backing speed 0.1m/s. Left and right wheels speeds were fixed to 0.01m/s and 0.2m/s during two 90° turn. And the starting point of the tests was 2m away from the end of corn rows.

At the beginning of tests, a lateral FOV of camera was chosen to acquire image of crops for detecting crops near the end of corn row and guiding the robot along the corn row. Once no crop appears in image, the headland turning operation at the end of corn rows was performed.

The tests were repeated for 3 times with the same starting position which ensures the same reference point of the robot trajectory. And a RTK GPS (Trimble 5800 GPS) receiver was equipped to form the running trajectory of the robot and evaluate performances of detection and guidance in the end of rows and headland turning control based on the variable FOV of machine vision. Once positioned, the robot was started under autonomous control and stopped automatically.

GPS data stored were analyzed to evaluate performance of the headland turning operation. The maximum error, average error, RMS (root mean square) error and standard deviation were calculated to evaluate the guidance accuracy during the end-of-row guidance. And some position points, such as the point after the first 90° turning, the points after second 90 turn, the farthest point in the robot trajectory and the back distance during turning operation, were recorded to reflect the turning performances. The effect of going blind stage on headland turning was analyzed by comparing the positions of the end point and the farthest point during the first 90° turning and observing the turning trajectory of the robot. In addition, the performance of the backing control was evaluated by measuring the backing distance and observing the backing trajectory. And the performance of the second 90° turning was judged by measuring the position of the end point and observing its trajectory.

4 Results and Discussion

Experiments were conducted to observe the behavior of the robot during headland turning operation in corn field. During each trial run, the data from RTK GPS, which would be used to represent trajectory of the robot and evaluate accuracy of guidance and turning operation, were recorded automatically at regular intervals of 1s in the laptop computer via serial data communication cable. The maximum error, average error, RMS error and standard deviation were calculated to evaluate the lateral FOV guidance performance for each experiment. Some points including the end points after the first 90° turn and the second 90° turn, the farthest point and the back distance, which all were calculated relative to the starting point, were listed for each experiment. Then the results were compared for the three repetitions. The trajectory of robot running was plotted over the length of the test path by processing GPS data, that is, the latitude and longitude vectors from GPS data were converted into UTM (Universal Transverse Mercator) coordinates, and the data, which were used to form trajectory of the robot, were further calculated from UTM coordinates relative to the coordinate of the original point. The performance measures in the lateral FOV guidance stage and the whole turning process are shown in Table 1 and Table 2, respectively. It should be noted that, the “-” sign in Table 1 indicates that the error is biased in favor of the right, and X and Y in Table 2 represent positions coordinates in the directions parallel and perpendicular to crop rows, respectively.

Table 1. Performance measures of the lateral FOV guidance and going blind stages

	Maximum error (mm)	Average error (mm)	RMS error (mm)	Standard deviation (mm)
I	15.4	-12.7	49.3	8.1
II	16.1	-12.4	36.7	12.3
III	17.4	3.0	28.4	8.0

The sign “-” indicates that the error is biased in favor of the right.

Table 2. Performance of the whole turning process

	Position after first 90° turn		Position after second 90° turn		Position at farthest point		Back distance (mm)
	X (mm)	Y (mm)	X (mm)	Y (mm)	X (mm)	Y (mm)	
I	3183.6	693.2	2611.1	740.4	3282.5	427.8	303.4
II	3182.3	698.1	2675.0	738.2	3281.4	408.8	287.9
III	3182.9	716.8	2643.0	757.0	3302.0	407.6	286.7

According to the data of position after 90° turn and at farthest point in Table 2, the main difference appeared in Y direction. The offsets in Y direction were 23.6mm and 20.2mm at the positions after first 90° turn and at farthest point, respectively. It shows that the stage of going blind has effect on the first 90° turn, but this effect, due to good backing control mentioned below, cannot deteriorate the performance of turning. The offset of backing distance was no more than 16.7mm, and the backing control algorithm strived to make the robot perpendicular to the corn rows parallel to the crop rows when the backing control was end, as shown in Fig. 7, if the robot is not perpendicular to the corn rows at the starting position of backing stage. These show good performance of back control based on the far FOV machine vision. According to the data in Table 2, where the maximum deviation from the center line was 14.8mm after the turning operation in the second test, and the trajectory in Fig. 7, they indicate that the control algorithm can make the robot locate near the central line of the next corn rows with high accuracy.

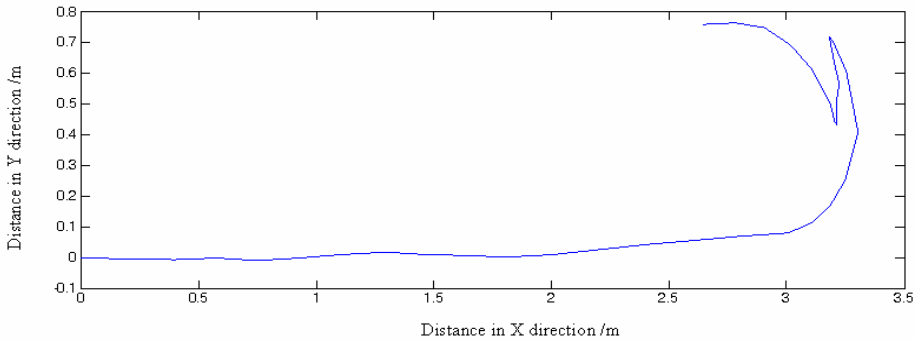


Fig. 7. Lateral FOV and its image processing

The headland turning operation based on variable FOV of camera have feasibility by calculating error values or observing the robot running. Therefore, it is worthwhile to look forward to field operation of autonomous vehicles with variable FOV of machine vision.

5 Conclusions

Variable FOV of machine vision was developed to implement headland turning operation for an agricultural robot in corn field. The robot was controlled by control algorithm of headland turning operation developed and tested in the light of the information from variable FOV camera. Three repetition tests were conducted at the same starting point with the same starting speed. The running trajectory of the robot was available by the RTK-GPS data stored automatically in the main computer during tests.

Lateral FOV machine vision showed acceptable performance in the end-of-row detection and guidance. The average errors were no more than 12.7 mm in most cases. The maximum error was not more than 17.4mm in any test run. The turning process performed well, especially the far FOV of camera, which was applied before backing control, ensured the completion of headland turning. These experiments demonstrated the accuracy of the guidance system and headland turning control system and successful operation of the robot in corn field. However, the farther tests will be performed to verify the application of variable FOV of machine vision.

Acknowledgment. Research was supported by “the Fundamental Research Funds for the Central University (KYZ201127) and AMAB of Jiangsu Province and College of Engineering of Nanjing Agricultural University (gxz09006).

References

1. Fehr, B.W., Gerrish, J.B.: Vision-guided row crop follower. *Appl. Eng. Agric.* 11, 613–620 (1995)
2. Gerrish, J.B., Fehr, B.W., Van Ee, G.R., Welch, D.P.: Self-steering tractor guided by computer-vision. *Appl. Eng. Agric.* 13, 559–563 (1997)
3. Brandon, J.R., Searcy, S.W.: Vision assisted tractor guidance for agricultural vehicles. SAE Technical Paper No. 921650 (1992)
4. Han, S., Zhang, Q., Ni, B., Reid, J.F.: A guidance directrix approach to vision-based vehicle guidance systems. *Comp. Electron. Agr.* 43, 179–195 (2004)
5. Subramanian, V., Burks, T.F., Arroyo, A.A.: Development of machine vision and laser radar based autonomous vehicle guidance systems for citrus grove navigation. *Comp. Electron. Agr.* 53, 130–143 (2006)
6. Torii, T., Teshima, T., Okamoto, T., Imou, K., Kaizu, Y., Taniwaki, K., Nagasaka, Y.: Vision based navigation of a boom sprayer. *JSAM* 65, 70–75 (2003)
7. Okamoto, H., Hamada, K., Kataoka, T., Terawaki, M., Hata, S.: Automatic guidance system with crop row sensor. In: *Proceedings of the Automation Technology for Off-road Equipment. ASABE 2002, Chicago, Illinois*, pp. 307–316 (2002)

8. Tillett, N.D., Hague, T., Miles, S.J.: Inter-row vision guidance for mechanical weed control in sugar beet. *Comp. Electron. Agr.* 33, 163–177 (2002)
9. Åstrand, B., Baerveldt, A.-J.: A vision based row-following system for agricultural field machinery. *Mechatronics* 15, 151–269 (2005)
10. Benson, E.R., Reid, J.F., Zhang, Q.: Machine vision-based guidance system for agricultural grain harvesters using cut-edge detection. *Biosyst. Eng.* 86, 389–398 (2003)
11. Søggaard, H.T., Olsen, H.J.: Determination of crop rows by image analysis without segmentation. *Comp. Electron. Agr.* 38, 141–158 (2003)
12. Chen, B., Tojo, S., Watanabe, K.: Machine vision for a micro weeding robot in a paddy field. *Biosyst. Eng.* 85, 393–404 (2003)
13. Bak, T., Jakobsen, H.: Agricultural robotic platform with four wheel steering for weed detection. *Biosyst. Eng.* 87, 125–136 (2004)
14. Xue, J.L., Xu, L.M.: Autonomous agricultural robot and its row guidance. In: 2010 International Conference on Measuring Technology and Mechatronics Automation, pp. 725–729. IEEE, Changsha (2010)
15. Subramanian, V., Burks, T.F.: Autonomous vehicle turning in the headlands of citrus groves. In: ASAE Annual Meeting (2007)

The Study on Wide Area Antenna Array Algorithm and Its Experiments*

Zhu Xinying and Kong Deqing

National Astronomical Observatories, Chinese Academy of Sciences,
20#, Datun Road, Chaoyang District, Beijing 100012, China
zhuxy@bao.ac.cn

Abstract. In wide area antenna array, it is difficult to combine the signal of each element because of the big delay and phase offset. Prior values of delay and delay rate, calculated according to the position and velocity of space probe and ground antennas, are used for correlation of antenna signal. The signals from each array element could be combined using residual delay, delay rate and phase offset obtained by correlation. Observation data received by Shanghai Sheshan 25-meter-diameter antenna and Beijing Miyun 50-meter-diameter antenna during Chang'E-2 lunar satellite mission are processed to verify the above algorithm. The experiment result indicates that the signals from each antenna could be combined successfully.

Keywords: Deep Space Exploration, Antenna Array, Delay model, Correlation, Full-Spectrum Combining.

1 Introduction

Recently, deep space exploration have received remarkable attentions in the world. As the space probe gets into the space further and further, the signal arriving from space probe becomes weaker and weaker. Because of the technical limits of single parabolic antenna and receiver, the need arises for devising antenna array to compensate for the reduction in signal-to-noise ratio (SNR).

In recent years, antenna array technology becomes an active research topic in deep space exploration field. NASA's worldwide deep space network successfully completed a serious of remarkable deep space missions such as pioneer 10, Voyager II, Megallans and Galileo by using antenna array Technology [1].

Wide area antenna array consist of existing Large-diameter antennas Located in different regions. Signals from each element of antenna array are combined In order to improve the signal-to-noise ratio. The great advantage of this array is you can use the existing antenna and receiver, without the construction of new ones, short development cycle, low cost, low risk, only some additional back-end data processing equipment are needed to combine the signals.

In wide area antenna array, it is difficult to combine the signals of each element because of the big delay and phase offset. Prior values of delay and delay rate, calculated according to the position and velocity of space probe and ground antennas,

* Supported by the Natural Science Foundation of China(10903016).

are used for correlation of antenna signals. Signals from each array element could be combined using residual delay, delay rate and phase offset obtained by correlation. Observation data received by Shanghai Sheshan 25-meter-diameter antenna and Beijing Miyun 50-meter-diameter antenna during CE-2 lunar satellite mission are processed to verify the above algorithm. The experiment result indicates that the signals from each antenna could be combined successfully.

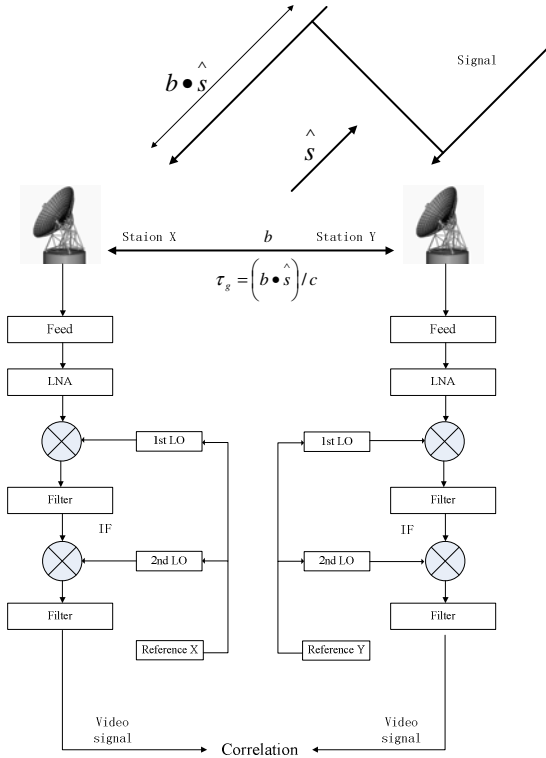


Fig. 1. The procedure of deep space probe signal reception

2 Algorithm

2.1 Signal Model

The procedure of Deep space probe signal reception is shown in Figure 1. The signals emitted by the Deep space probe are propagated as a series of electromagnetic waves, and one wave-front will reach two widely spaced antennas on the earth at different times. This delay τ in the time of arrival of the signal consists of two parts:

Propagation Delay: The delay caused by thick layer consisting of the atmosphere and the overlaying ionosphere.

Geometric Delay: The delay caused by the geometric location of antenna.

As view from the earth, the direction of travel of a radio signal emitted by space probe appears to change depending on the time and observer location. This is due to changes occurring in the earth's orbital path, resulting in delay changing accordingly. It is difficult to combine the signals of each element because of existing of this delay.

The signal arriving at the antenna has been focused, feed selected and amplified. After mixing with the first-order local oscillator, the amplified radio signal is converted into intermediate frequency signal. The video signal obtained by mixing the intermediate frequency signal with the second -order local oscillator is sampled, quantified and filtered for correlation[2].

According to the above description, the video signal received by station X, expressed in frequency domain notation as:

$$X_v(f) = X(f + f_x)e^{-i\phi_x} = S(f + f_x)e^{-i\phi_x} + N_x(f + f_x)e^{-i\phi_x} \tag{1}$$

The video signal received by station Y:

$$Y_v(f) = Y(f + f_y)e^{-i\phi_y} = S'(f + f_y)e^{-i\phi_y} + N_y(f + f_y)e^{-i\phi_y} \tag{2}$$

Where: $X_v(f)$ 、 $Y_v(f)$ are received video signal at station X and station Y respectively, $S(f)$ 、 $S'(f)$ are received signal without frequency conversion, f_x 、

f_y are LO signal、 ϕ_x 、 ϕ_y are initial phase of LO, N_x 、 N_y are the Gaussian noise components added to the signals at respective receiving station. Since S' is the S signal delayed by τ , we have $S'(f) = S(f)e^{-i2\pi f\tau}$.

We have the cross spectrum of received video signals at station x and station Y as:

$$\begin{aligned} C_{xy}^v(f) &= X_v(f)Y_v^*(f) \\ &= S(f + f_x)e^{-i\phi_x}S'^*(f + f_y)e^{i\phi_y} \\ &\quad + S(f + f_x)e^{-i\phi_x}N_y^*(f + f_y)e^{i\phi_y} \\ &\quad + N_x(f + f_x)e^{-i\phi_x}S'^*(f + f_y)e^{i\phi_y} \\ &\quad + N_x(f + f_x)e^{-i\phi_x}N_y^*(f + f_y)e^{i\phi_y} \end{aligned} \tag{3}$$

The second and subsequent terms on the right-hand side of the above equation are products of statistically independent Gaussian noise components, and applying an appropriate time interval zeroes their means, which leaves only the first term. The equation (3) thus becomes:

$$C_{xy}^v(f) = S(f + f_x)e^{-i\phi_x}S'^*(f + f_y)e^{i\phi_y} \tag{4}$$

From the relationship $S'(f) = S(f)e^{-i2\pi f\tau}$ and $f_y = f_x - \Delta f$, the equation (4) becomes

$$C_{xy}^v(f) = |S(f + f_x)|^2 e^{i\{2\pi(f + f_x)\tau + 2\pi(\Delta f)t + \phi_y - \phi_x\}} \tag{5}$$

Where: $\theta = 2\pi(\Delta f)t + \phi_y - \phi_x$, represents the phase difference, he $\phi_y - \phi_x$ part of θ represents the local oscillator phase difference, the $2\pi(\Delta f)t$ part of θ represents the phase difference set up by the slightly shift in local oscillator frequency. The $2\pi(f + f_x)\tau$ represent the phase component caused by delay τ . The signals $X_v(f)$ and $Y_v(f)$ can't be added coherently due to the factor $2\pi(f + f_x)\tau$ and θ , even though the data symbols are aligned. Therefore, cross-correlation is carried out to get the additional phase adjustment parameters for signal combining.

2.2 Prediction Geometry Model

According to above section ,in order to combine the signals coherently, cross-correlation processing is needed to get the phase adjustment parameters θ and τ . In local area antenna array, delay τ and delay rate $\dot{\tau}$ caused by continue changes occurring in position between the space probe and antenna are small because of the relative close distance between antenna array elements. Therefore cross-correlation could take place properly without pre-treatment of signals .In contract, delay τ and delay rate $\dot{\tau}$ in wide area antenna array are much bigger compared with its equivalence in local area antenna array due to the large distance between antenna array elements, which sometimes can reaches thousands of kilometers. For this reason, prior values of delay and delay rate with a certain degree of precision are required for proper cross-correlation.

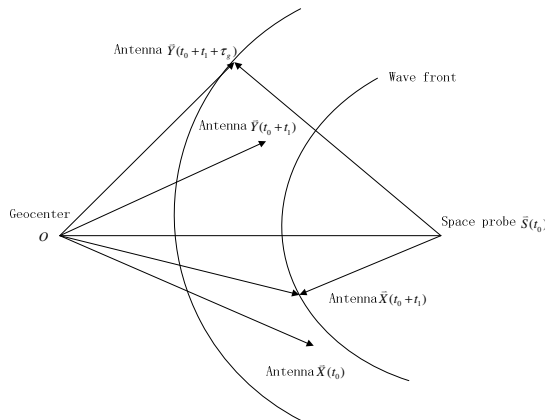


Fig. 2. Dynamic geometric position of space probe \bar{S} 、 antenna state vector \bar{X} 、 and antenna state vector \bar{Y}

In order to calculate the prior values of correction parameters, both space probe state vector and antenna state vector are required. In the inertial reference frame, the state vector of space probe can be forecast by orbital; the antenna state vector is considered to be known parameters, from which inertial reference frame coordinates are deduced according to ITRF2000 with the correction of the tide, pole tide, ocean loading, atmospheric loading, tectonic and other geophysical effects[4-7]. The distance between space probe and receiving antenna is not so far that signal wave front emitted by probe can't be approximated as plane waves, bending effect of wave front should be considered. Dynamic geometric position of space probe \vec{S} , antenna state vector \vec{X} , and antenna state vector \vec{Y} are shown in Fig. 2.

2.3 Signal Combining Scheme

There are five basic signal-processing schemes that can be employed to combine the output of separate antennas that are observing a spacecraft-type signal. These schemes have come to be known as: (1) full-spectrum combining (FSC), (2) complex-symbol combining, (3) symbol-stream combining, (4) baseband combining, and (5) carrier arraying [1]. FSC scheme does not crucially depend on spectral characteristics of the signal source and the combining operation is transparent to demodulation back-end. These advantages make the FSC become the most commonly scheme for signal combination.

The block diagram of FSC is shown in Figure 3. The signals from each antenna are decode for combination. To ensure coherence, the signals must be delayed and phase adjusted by using the prior calculated by geometry model before combining. Then the residuals of the delay and phase are determined by cross-correlation of the signals from each antenna. These residuals plus priori are used to correct the antenna signals, and then they are combined by using SUMPLE Algorithm [8].

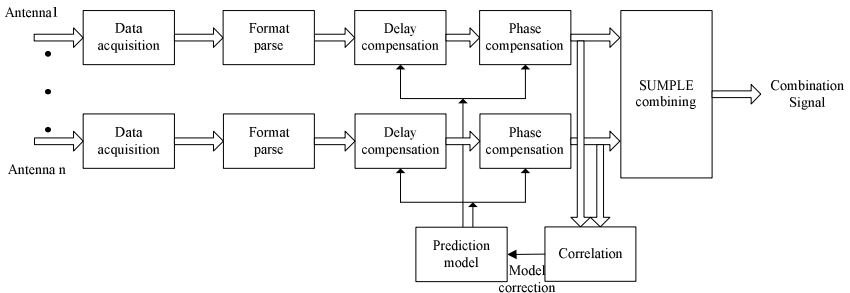


Fig. 3. The block diagram of full-spectrum combining

3 Experiments and Result

3.1 Data Acquisition

A 2 minutes VLBI observation data recorded from November 3, 2010 03 09 minutes and 31 seconds during the Chang'E-2 mission are used for the experimental study of

signal combination. The signals were received by the 25-meter-diameter antenna located at Shanghai Sheshan station and the 50-meter-diameter antenna located at Beijing Miyun station respectively. The characteristics of the observation data are shown in Table 1.

Table 1. The characteristics of the observation data

Parameter	Sheshan Station	Miyun Station
File name	sh2010307030931+2m.dat	bj2010307030931+2m.dat
File length	480,768,000 bytes	480,768,000 bytes
Start time	2010-11-03 03: 09: 31	2010-11-03 03: 09: 31
Duration	120s	120s
Target	Chang'E 2	Chang'E 2
Clock offset	6.43e-5	6.96e-5
Clock rate	7.77e-13	-1.7649e-12
Bandwidth	2MHz	2MHz
Quantization	1bit	1bit

3.2 Experimental Result and Analysis

The prior delay model for the observation data is shown in following equation:

$$\tau(t) = 1.30028857e-3 - 1.38990730e-07 \times t - 6.885028389981e-12 \times t^2 - 1.282957655627e-15 \times t^3$$

Before correlation, the observation data are delayed and phase adjusted by using the priori calculated by above equation. The Phase-frequency characteristic curve of the cross-correlation spectrum for observation data is shown in Fig. 4.

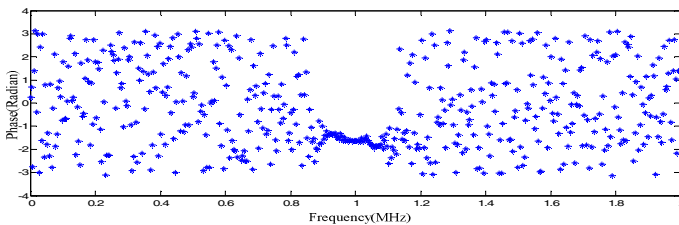


Fig. 4. The phase-frequency characteristic curve of the cross-correlation spectrum for observation data

The residual delay, delay rate and phase obtained by fringe search and Parameter fitting[3] of the Phase-frequency characteristic curve are shown in table 2.

Table 2. The correction parameters from correlation

Parameter	Priors	Residuals	Errors	Correction
Delay(s)	1.30028857e-3	-6.98878e-07	3.90114e-10	1.2995897e-03
Delay rate(s)	-1.3899073e-07	3.12137e-11	3.53076e-13	-1.3895952e-07
Phase(radian)	0	-1.6738	-0.01571	-1.6738

The Phase-frequency characteristic curve of the observation data corrected by above values is shown in figure 5. As can be seen in Figure 5, residual delay and residual phase are close to zero which proves that residuals obtained by cross correlation correct the delay and phase of observation data successfully.

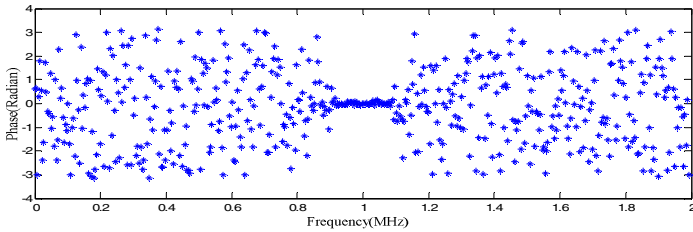


Fig. 5. The phase-frequency characteristic curve of the observation data after correction

The Sumple method which can be described as the cross-correlation of each antenna with a reference antenna composed of the weighted sum of all the other antennas is used to combine the signals. The weight of signals from 25m antenna is set as 1 and the weight of signals from 50m is set as 1.8 according to the signal –noise rate of each signal. The amplitude-frequency characteristic curves of the auto correlation spectrum for signal from 25m antenna, 50m antenna and combination are shown in figure 6.

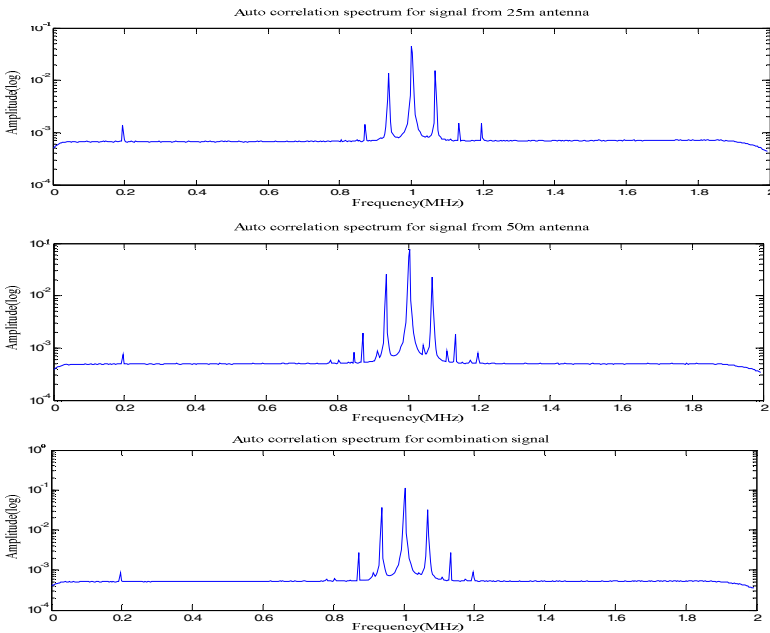


Fig. 6. The amplitude-frequency characteristic curves of the auto correlation spectrum for signal from 25m antenna, 50m antenna and combination

The effect of antenna array is evaluated by array gain and combining efficiency. Array gain is defined as the ratio of the SNR of combining signal to that of the reference antenna signal. The combining efficiency is defined as the ratio of real array gain to the theoretical array gain. The more the combining efficiency close to 1, the more the combining signal close to ideal situation. In above experiments, SNR of Chang'E 2 telemetry main carrier for 25m antenna, 50m antenna and combining signal is 19.55dB, 21.86dB and 23.46dB respectively. The theoretical array gain is 2dB (50-meter antenna as the reference antenna), the real array gain reaches 1.6db, thus the combining efficiency is 91.2%.

4 Conclusions

By the study of the wide area antenna array algorithm, signals from each antenna could be combined by using the residuals obtained by correlation which is guided by priori calculated by Prediction geometry model. The experiment result indicates that the signals from each antenna could be combined successfully, and the combining efficiency can be up to 91.2%.

References

1. Rogstad, D.H., Mileant, A., Pham, T.T.: *Antenna Arraying Techniques in the Deep Space Network*. JPI Publication 03-001 (2003)
2. Thompson, A.R., Moran, J.M., Swenson, G.W.: *Interferometry and Synthesis in Radio Astronomy*, 2nd edn. Wiley-VCH, New Jersey (2001)
3. Takahashi, F., Kondo, T., Takahashi, Y., Koyama, Y.: *Very Long Baseline Interferometer*, pp. 45–107. Ohmsha Ltd., Tokyo (2000)
4. Ping, J., Yang, Z., Qian, Z.: The VLBI Time Delay Model Applied to the Observation of the Objects in the Solar System. *Chinese Journal of Space Science* 17(4), 317–320 (1997)
5. Ulvestad, J.S.: Use of the VLBI Delay Observable for orbit Determination of Earth-Orbiting VLBI Satellites, TDA Progress Report, Jet Propulsion Laboratory, Pasadena, pp. 42–110 (1992)
6. Eubanks, T.M.: A Consensus Model for Relativistic Effects in Geodetic VLBI. In: *Proceedings of the USNO workshop on Relativistic Models for Use in Space Geodesy*, Washington, pp. 60–82 (1991)
7. Sekido, M., Fukushima, T.: Relativistic VLBI delay model for finite distance radio source. In: *Proceedings of the International Association of Geodesy IAG General Assembly Sapporo, Japan*, vol. 128, pp. 141–145 (2003)
8. Rogstad, D.H.: The SUMPLE Algorithm for Aligning Arrays of Receiving Radio Antennas: Coherence Achieved with Less Hardware and Lower Combining Loss. In: *Inter Planetary Network (IPN) Progress Report*, Jet Propulsion Laboratory, Pasadena, pp. 42–162 (2005)

Performance Evaluation of Listed Household Appliance Enterprises Based on Factor Analysis and Cluster Analysis

Yiwei Guo, Wenting Liu, and Jia Han

School of Economics and Management, North China Electric Power University,
Beijing, China
guoyiwei5000@sina.com

Abstract. This paper chooses 28 listed household appliance companies in China's stock market as examples, extracts four factors: ability to pay debt, profitability, operation capability and development capability and then evaluate the performance of listed household appliance enterprises by factor analysis and cluster analysis.

Keywords: household appliance industry, performance evaluation, factor analysis, cluster analysis.

1 Introduction

After two decades of development of household appliance industry, China has become the third largest household appliance manufacturer chasing closely after the United States and Japan in 21st century. By December 31, 2010, there are 34 household appliance enterprises in Shanghai and Shenzhen Securities Markets. Since 2009, due to the good effect of China's effective policies of Home Appliance Subsidy Program for Rural Areas, trade-in and save-energy product and benefiting civilian project, the household appliance industry has shaken off the influence of severe setback of export caused by the financial crisis, began to aggressively expand in the domestic market and its management performance has began to increase gradually. The household appliance enterprises urgently need to optimize their business performance and raises their competitive capacity. Good performance evaluation system contributes to the overall analysis and the evaluation of the performance of household appliances enterprises can help business managers and investors to develop appropriate business and investment strategies.

2 Samples and Variable Selection

This paper selects 28 (A total of 34, except for five ST companies and one with incomplete financial statements) companies that listed in A share market on March 31, 2011 as samples, All data are from the company's 2010 Annual Report, Information from the China Securities, Sina.com, and Xin Netcom Marsh Financial

Software. EXCEL and the statistical software PASW Statistics 18 is used in the analysis process of the paper.

The variables are shown in Table 1.

Table 1. Indexes

Number	Index	Date source
X1	Current Ratio	Current assets / current liabilities
X2	Quick Ratio	(Current Assets - Inventories) / Current liabilities
X3	Asset-liability Ratio	Total liabilities / total assets
X4	gross profit margin	(Sales revenue - cost of sales) / sales
X5	Inventory Turnover	Cost of sales / average inventory
X6	Net Profit Growth	(Ending net profit - beginning net profit) / beginning net profit
X7	Main Business Revenue Growth	(Ending main business revenue - beginning main business revenue) / beginning main business revenue
X8	Annual Rate of Return on Total Assets	Total profit / average total assets
X9	Rate of Return on Net Asset	Net profit / average net assets
X10	Total Asset Turnover	Sales / average total assets
X11	Account Receivable Turnover	Sales / average accounts receivable

In this paper, the original indexes will be standardized.

3 Factor Analysis Process

This process uses PASW software.

3.1 Feasibility and Common Degrees Inspection of Factor Analysis

KMO and Bartlett inspection results are shown in Table 2.

Table 2. KMO and Bartlett inspection

Sampling sufficient degree of Kaiser-Meyer-Olkin measure		.578
Bartlett's sphericity inspection	Approximation Chi-square	98.125
	df	55
	Sig.	.000

We can see that KMO= 0.578, so factor analysis is acceptable. Besides, the sig value of Bartlett inspection is less than 0.01, thus deny the null hypothesis that correlation matrix is unit matrix. The result shows that there is significant correlation between the variables.

Table 3. Common factor variance

	Initialization	Extraction
X1	1.000	.788
X2	1.000	.889
X3	1.000	.715
X4	1.000	.705
X5	1.000	.883
X6	1.000	.849
X7	1.000	.651
X8	1.000	.898
X9	1.000	.905
X10	1.000	.476
X11	1.000	.653

Extraction method: Principal component analysis.

Table 3 shows that interpretation degree of most variables is above 70%, which illustrates that the common factors explain the original variable well.

3.2 Common Factor Extraction

After inputting the data which has been standardized to PASW software, the total variance explanation table is available. Table shows that first four cumulative variance explained by common factors reach 76.482%, which means that each variable of the four main factors rarely lose information, and the four main factors keep a more complete information amount. Therefore, four common factors extraction is appropriate.

3.3 Common Factors Explanation

Table 4. Rotation component matrix

	components			
	1	2	3	4
X1	-.019	.882	-.026	.091
X2	-.050	.940	.031	-.045
X3	-.046	-.767	-.010	.353
X4	.574	.142	-.271	-.531
X5	-.240	-.097	.899	-.086
X6	.406	.148	.814	.016
X7	-.029	-.056	-.133	.793
X8	.921	.189	.078	-.091
X9	.934	-.130	.106	.069
X10	.525	-.299	-.186	.275
X11	.516	-.070	.060	.615

Extraction method: Principal component analysis.

Rotation method: Orthogonal rotation with standardized Kaiser.

As we can see from Table 4, F1 corresponding to the X4 (gross profit margin), X8 (return on total assets) and X9 (return on net assets) have larger load coefficient, reflecting the company's profitability, may be designated as profit factor. F2 corresponding to the X1 (current ratio), X2 (quick ratio) and X3 (asset-liability ratio) have larger load coefficient, reflecting the company's solvency, may be designated as debt factors. F3 corresponding to the X5 (inventory turnover rate) have larger load coefficient, reflecting the company's operations capacity, may be designated as operating factors. F4 corresponding X7 (main business revenue growth) have larger load coefficient, reflecting the company's development capacity, the growth factor can be named.

We makes Covariance matrix of component scores to prove that each factor is independent of each other, as shown in Table 5.

Table 5. Covariance matrix of component scores

Component	1	2	3	4
1	1.000	.000	.000	.000
2	.000	1.000	.000	.000
3	.000	.000	1.000	.000
4	.000	.000	.000	1.000

Extraction method: Principal component analysis.

Rotation method: Orthogonal rotation with standardized Kaiser.

As we can see from Table 5, factor variables is orthogonal and unrelated, which meets the goal of 'less relevant to different groups.

3.4 Factor Scores Computation

When calculating factor scores, we use regression method. Factor scores coefficient matrix is given in Table 6.

Table 6. Component score coefficient matrix

	Component			
	1	2	3	4
X1	-.014	.399	-.027	.190
X2	-.022	.404	.006	.104
X3	-.023	-.284	.011	.142
X4	.225	-.013	-.187	-.378
X5	-.096	-.066	.561	-.052
X6	.131	.053	.496	.033
X7	-.033	.090	-.069	.551
X8	.329	.063	.030	-.066
X9	.330	-.054	.054	.002
X10	.183	-.092	-.115	.132
X11	.164	.053	.040	.409

Extraction method: Principal component analysis.

Rotation method: Orthogonal rotation with standardized Kaiser.

According to Table 8, you can get the formula of the factor scores.

$$F1=-0.014X1-0.022X2-0.023X3+\dots+0.164X11$$

$$F2=0.399X1+0.404X2-0.284X3+\dots+0.053X11$$

$$F3=-0.027X1+0.006X2+0.011X3+\dots+0.4X11$$

$$F4=0.19X1+0.104X2+0.142X3+\dots+0.409X11$$

The following formula is used to calculate the scores of each factor.

$$F_{pi}=\sum_{j=1}^k W_{pj}X_{ji} \quad (1)$$

W_{pj} is on behalf of the coefficient between the p th and j th variable factor, X_{ji} is on behalf of the value of the j th variable in i th sample.

In addition, we also need to calculate each sample's comprehensive factor score, the formula is as follows:

$$F=\frac{\sum_{i=1}^4 F_i N_i}{\sum_{i=1}^4 N_i} \quad (2)$$

F is the score of the each sample company's comprehensive performance. The score of factor i is F_i , variance contribution rate of factor is N . Using the above formula, we can obtain each sample's four factor scores.

4 Cluster Analysis

We take the four factor scores of the 28 companies and a comprehensive score as original data of cluster analysis, and apply PASW software to carry out cluster analysis. The cluster analysis results are given in Table 7.

Table 7. The interpretation of cluster analysis

Type		Profit factor	Debt factor	Operating factor	Growth factor	Comprehensive score	Sample company
1	Total	107.1953	7.8267	1.1174	36.1868	33.3723	TCL, ASD,
	N	13	13	13	13	13	AUCMA, ETI,
	Mean	-8.2458	0.6021	0.0860	2.7836	-2.5671	SVA-I, MIDEA,
	Standard deviation	3.0604	1.3474	1.2649	2.5356	1.3605	KONKA GROUP, SOYEA,
	Total N,%	0.4643	0.4643	0.4643	0.4643	0.4643	SICHUAN JIUZHOU, HANGHONG, LITTLESWAN, CNLIGHT, ELECPRO

Table 7. (continued)

2	Total	18.8399	4.0870	2.1533	5.3438	7.2538	SUNLIGHT, SUPOR, FSL, HSSM, HAIER, HXDQ, HFML, YANKON, GREE
	N	9	9	9	9	9	
	Mean	2.0933	0.4541	0.2393	0.5938	0.8060	
	Standard deviation	2.1267	2.4313	0.6494	2.1848	0.9423	
	Total N,%	0.3214	0.3214	0.3214	0.3214	0.3214	
3	Total	74.4449	2.3830	4.1286	16.2048	24.229	HF-SANYO, VATTI, JOYOUNG, VANWARD ELECTRIC, MTC
	N	5	5	5	5	5	
	Mean	14.8890	0.4766	0.8257	-3.2410	5	
	Standard deviation	4.4792	2.1367	0.6805	1.4821	4.8459	
	Total N,%	0.1786	0.1786	0.1786	0.1786	0.1786	
4	Total	13.7956	1.3430	5.1813	14.6351	1.8435	MACRO
	N	1	1	1	1	1	
	Mean	13.7956	1.3430	5.1813	14.6351	1.8435	
	Standard deviation	
	Total N,%	0.0357	0.0357	0.0357	0.0357	0.0357	

We can see the general performance of four types of companies From Table 7.

- The growth ability of the first type of enterprises is best, but profit ability is not good, comprehensive performance is the worst. According to the scores of this type of enterprises, except for the growth factors, are negative, we can classify this type of enterprises as low growth type. This type contains the largest number of sample enterprises, which means that the overall profitability of current China's household appliance industry is lower, solvency and operation ability also is not very ideal.

- The indexes of the second type are relatively mediocre .Except for growth factor is negative, the rest factor scores are positive, but the score is not prominent. Because such companies have cultivated a more mature market, their financial indexes show a mediocre state. Such enterprises should also focus on new products, new technology research and development to improve their growth ability.

- Comprehensive performance of the third type of enterprises is best, which thanks to its strong profitability, in addition, solvency and operational capacity is the key advantage of such enterprises. According their standard deviation data, development of such enterprises is uneven. In contrast with the first class enterprise, they can be classified as higher efficiency and lower growth ability companies. The main product kind of such enterprises is more single, which results in its lower capacity of subsequent development.

- The fourth type has only one company, Macro, the company has the best profitability and good solvency, so the comprehensive performance is the best , but the company's operational capacity and ability to grow is the worst of the four types.

Although the comprehensive performance of the company is better, it is lack of capacity of sustainable development.

5 Conclusions

This paper uses the factor analysis and cluster analysis method to divide the 28 listed companies of household appliance industry into four types. The first kind of enterprises includes most of the companies, their comprehensive performance is poor, they are lack of profitability, but good at growth. The second type enterprises have good market share in their respective fields, have poor ability to grow, and the performance of the remaining factors is fairly good. Operating range of the third type companies is relatively more single, but they have stronger profitability and solvency, so their comprehensive performance is best. The fourth type has only one company, the main advantages of the company's are profitability and solvency, but its operational capability and growth ability are all poor, so its comprehensive performance is mediocre.

This paper is open to questions as follows. First, the raw data selection of listed companies can not ensure to accurately and completely reflect the performance of the companies. Secondly, the paper chooses the straightforward statistical methods, such as selecting principal component analysis method in factor analysis, using hierarchical clustering method in cluster analysis. We are not sure whether these methods are entirely suitable for the sample variables. Finally, the paper ignores evaluation role of non-financial information, which may lead to incomplete evaluation results.

References

1. Liu, W.: Comprehensive Evaluation of GEM Listed Companies Based on Factor Analysis and Cluster Analysis. *Accounting and Finance* 3 (2010)
2. Zhu, L., Zhang, C.: Operating Performance Evaluation of Listed Companies Based on Factor Analysis – Taking the Household Appliance Industry as the Example. *Technology and Industry* 10(4), 4 (2010)
3. Huo, Y., Wang, H.: The Cluster Analysis of the Financial Situation of Listed Companies. *Statistics and Decision* 9 (2007)
4. Pornprasitpol, P., Ye, D., Sun, M.-B.: An Approach to Risk Events Analysis for ERM—Using AHP and Cluster Analysis. In: 2010 IEEE 17th International Conference on Industrial Engineering and Engineering Management, IE&EM (2010)
5. Zheng, J., Xu, J.: Study of Ningbo – Zhoushan Port Logistics Competitiveness Based on Factor Analysis and Cluster Analysis. In: 2010 Third International Conference on Information and Computing (2010)
6. Sun, M.: Comparative Study of Comprehensive Performance Evaluation Methods of Listed Companies. *Hainan Finance* (4) (2009)

Research of the Correlation between EVA-Based Corporate Value and Stock Yield

Yiwei Guo, Fulian Shi, and Xu Zhang

School of Economics and Management, North China Electric Power University,
Beijing, China
guoyiwei5000@sina.com

Abstract. This paper selected 261 listed manufacturing companies in China's stock market as samples, made an analysis of the correlation between the EVA-based corporate value and stock yield. The study result had shown that there is significant linear relationship between the EVA-based index system of corporate value and stock yield. The paper established a linear model to reflect the linear relationship between the stock yield variable and the comprehensive corporate value variables.

Keywords: EVA, corporate value, stock yield, correlation.

1 Introduction

The correlation study of corporate value and stock yields has become an important research field in recent years. How to understand the corporate value and how to analyze the relationship between stock yield and corporate value scientifically and objectively has been growing concerned by business operators and stakeholders. The correlation study of corporate value and stock yield contributes to investors rationally understand the true corporate value of invested enterprise and promote investors to make reasonable investment decisions. In terms of the enterprise itself, recognizing fundamental driving force of stock yield growth can improve their ability to survival and development. Therefore, studying the correlation between EVA-based index system of corporate value and stock yield has certain positive significance to investors and business operators.

2 Index Design

This paper selected the stock yield as the dependent variable, independent variable indexes are shown in Table 1.

Table 1. Indexes description

Index	Symbol	Description
Stock yields	R	Dependent variable
Corporate value	MVAPC	Market Value Added/total capital, ie. MVA created by \$1 capital.
EVA per share	EVAPS	EVA per share
Cost of capital	COC	Weighted-average cost of equity capital and liability capital
The difference of return on capital and cost of capital,	SPREAD	The difference of return on capital and cost of capital,
Capital size	LNC	Natural logarithm of total capital
Earnings per share	EPS	Net income/total outstanding shares
Return on assets	ROA	Net income/total assets

3 Research Hypotheses and Sample Selection

The basic hypotheses in this paper are as follows:

Hypothesis 1: A corporate value model of the comprehensive index system can be established, which has explanatory and analysis power to corporate value.

Hypothesis 2: There is a significant linear relationship between EVA-based corporate value and stock yield.

This paper selected some A-share listed manufacturing companies in Shanghai Stock Exchange and Shenzhen Stock Exchange as samples. The main data are from professional database CCER. During the process of sample selection, we excluded those companies which issued both stock A and other kind stocks, which have severe losses of successive years, which don't have complete data available and ST or PT companies. Ultimately, there are 261 companies selected.

4 Explanatory Power of the EVA-Based Comprehensive Index System to Corporate Value

Both EVA-based index system and traditional financial index system have some explanatory power to corporate value. From a business point of view, even though taking the EVA evaluation system, we must also continue to monitor the accounting profit indexes. From an investor's perspective, not only EVA-based index system but also traditional profit indexes should be used to evaluate corporate value.

So this paper established the following model to study explanatory power of EVA-based index system to corporate value, multiple regression results of the comprehensive index system are given in Table 2.

$$MVAPC = \beta_0 + \beta_1 EVAPS + \beta_2 COC + \beta_3 SPREAD + \beta_4 LNC + \beta_5 ROA + \beta_6 EPS + \varepsilon \quad (1)$$

In the process of model building, the paper adopts the LNC rather than LNA (After verification, the result is Basically same when using LNA instead of LNC in the regression mode, and the regression model containing both LNC and LNA exactly exists serious multicollinearity), and eliminates ROA which did not pass the verification in the Single-element Regression analysis.

Table 2. Multiple regression analysis results (1) of the comprehensive index system

	Coefficients	standard error	t Stat	P-value	VIF
Intercept	46.6877	22.0404	2.1183	0.0351	
EVAPS	-0.4043	0.7910	-0.5112	0.6097	2.144
COC	16.3729	4.6167	3.5465	0.0005	7.2809
SPREAD	18.6179	2.2989	8.0987	0.0000	2.839
LNC	-2.0676	1.0615	-1.9478	0.0525	1.704
ROA	14.8253	28.8987	0.5130	0.0608	1.183
EPS	-2.4751	1.9040	-1.2999	0.1948	2.004

$R^2=0.4563$ Adjusted $R^2=0.4324$ $F=19.5069$ $P=0.0000$

As we can see from Table 2, according to F values and p-value, the regression equation was highly significant. According to the regression analysis result, some multicollinearity exists among the variables, which results in the coefficient of EVAPS and EPS is negative, and regression coefficients of several independent variables are not significant. In order to further test the model’s collinearity, the paper makes the collinearity diagnostics analysis to the model. The analysis result is shown in Table 3.

Table 3. Collinearity diagnostics analysis result

CollinearityDiagnostics

Model	Dimension	Eigenvalue	Condition Index	VarianceProportions						
				(Constant)	eva	ROA	EPS	LNC	SPREAD	COC
1	1	4.326	1.000	.00	.01	.01	.01	.00	.01	.00
	2	1.387	1.766	.00	.05	.01	.01	.00	.01	.13
	3	.629	2.622	.00	.06	.00	.11	.00	.16	.00
	4	.317	3.696	.00	.13	.79	.08	.00	.00	.04
	5	.205	4.596	.00	.74	.18	.01	.00	.02	.44
	6	.136	5.640	.00	.01	.01	.77	.00	.80	.37
	7	.001	72.541	1.00	.00	.00	.01	1.0 0	.01	.01

a. Dependent Variable: MVA

As we can see from Table 3, the variance proportions of the fifth dimension to EVAPS and COC is 74% and 44% respectively, the variance proportions of the sixth dimension to EVAPS and COC is 77% and 38% respectively, and the Condition Index are all significant, especially the last condition index, which is 72.541, higher than 10, that shows that has some collinearity. The significance test results to the model are given in Table 4.

Table 4. Multiple Regression analysis results (2) of the comprehensive index system

	Df	SS	MS	F	P
Regression analysis	6.0000	24305.627	4050.937	19.506	0.000
Residual error	253.000	52539.651			
	0	8	207.6666		
Total	259.000	76845.279			
	0	5			

As we can see from Table 4, F=19.5069, P=0.000, when the level of significance is 0.01, P<0.01, linear relationship between independent variables and dependant variable is significant, a linear model can be established to express the linear relationship between MVAPC and above six index.

According to the interpretation coefficients of the regression equation, the author believes that the comprehensive index system which includes EVA-based and traditional financial index has higher explanatory power to corporate value.

‘Three wastes’ is major environmental pollution sources of China’s agro-food processing industry.

5 Correlation between EVA-Based Corporate Value and Stock Yield

Combining the above research results, based on EVA indexes, this paper established the following model (see Model 2) to study the Correlation between EVA-based corporate value and stock yield.

$$R = \beta_0 + \beta_1 EVAPS + \beta_2 COC + \beta_3 SPREAD + \beta_4 LNC + \beta_5 ROA + \beta_6 EPS + \varepsilon \quad (2)$$

Table 5. Model Summary

Model Summary

Model	R	R Square	Adjusted R Square	Std. Error of the Estimate
1	.802 ^a	.642	.634	**** **

a. Predictors: (Constant), LNC, SPREAD, ROA, COC, EPS, eva

The analysis result of the 261 listed companies is shown in Table 5.

We can see from Table 5, the model’s adjusted R2 is 0.634, which indicates that in this model, the corporate value and stock yield has a high correlation, which verified the hypothesis 2. Comprehensive index system has perfect explanatory power to corporate value. The model significance test is carried out and the results are shown in Table 6.

Table 6. ANOVA^b

ANOVA ^a						
Model		Sum of Squares	df	Mean Square	F	Sig.
1	Regression	16520.936	6	2753.489	75.768	.000 ^a
	Residual	9194.330	253	36.341		
	Total	25715.266	259			

a. Predictors: (Constant), LNC, SPREAD, ROA, COC, EPS, eva

b. Dependent Variable: RETURN

From Table 6 we can see that this model passed the F value and P value test, P value is 0.000, which is below the 0.01 significance level, P value is less than 0.01, the model is to explain all the variables and explanatory variables of the Linear relationship between dependent variables and independent variables is significant, a linear model can be established to reflect linear relationship between the stock yields variable and comprehensive corporate value variables. Significant test result shows it is appropriate that the linear model describes the stock yields variable and the comprehensive corporate value variables.

The paper made the collinearity diagnostics analysis to the model, the analysis result is shown in Table 7.

Table 7. Collinearity Dianostics

Model	Dimension	Eigenvalue	Condition Index	Variance Proportions						
				(Constant)	COC	EPS	ROA	eva	SPREAD	LNC
1	1	4.385	1.000	.00	.00	.01	.01	.01	.01	.00
	2	1.389	1.777	.00	.09	.01	.01	.03	.01	.00
	3	.580	2.749	.00	.04	.09	.01	.00	.15	.00
	4	.327	3.661	.00	.01	.04	.63	.14	.04	.00
	5	.228	4.385	.00	.04	.03	.30	.31	.37	.00
	6	.090	6.964	.00	.82	.74	.00	.50	.42	.00
	7	.001	76.736	1.00	.00	.08	.05	.01	.01	1.00

a. Dependent Variable: RETURN

As we can see from Table 7, the last condition index is above 10. The variance proportion of the sixth dimension to EPS, EVA and SPREAD is 77%, 50% and 42% respectively, which shows that the equation has some collinearity. It should be noted that multicollinearity here doesn't matter, because we are not concerned about the regression coefficient of single variable, but the overall value of the explanatory power of these variables to corporate value.

6 Conclusions

Based on the above analysis, this paper argues that there is significant linear relationship between corporate value and stock yield, a linear model can be established to reflect the linear relationship between the stock yield variable and the comprehensive corporate value variables. Our studies has shown that EVA-based

index system of corporate value has some explanatory power to Shanghai and Shenzhen stock yield, which indicates that it is general in our country to use a EVA-based index system of corporate value to explain stock yield.

Although the explanatory power of EVA-based indexes of corporate value to stock yields is above 50%, still nearly half of the changes of stock yield can not be explained, which shows that the information of corporate value can only explain a part of changes of stock yield. Another part of the changes of stock yield derives from non-corporate value information. Therefore, during the analysis of stock yield of listed companies, investors not only need to take into account corporate value information, but also need to note the impact of non-corporate value information.

References

1. Farslo, F., Degel, J., Dinger, J.: Economic Value Added and Stock Yields. *The Financier* 7(1-4), 115–118 (2000)
2. Biddle, G., Bowen, R.M., Wallace, J.S.: Does It Beat Earnings Evidence on Associations with Stock Yields and Firm Values. *Journal of Accounting and Economics* 24, 301–336 (1997)
3. Griffith, J.M.: The Search for the Best Financial Performance Measure. *Financial Analyst Journal* 53, 11–20 (2004)

Analysis of Pollution Abatement Status and Policy Recommendations of China's Agro-Food Processing Industry

Yiwei Guo¹, Jing Guo², and Pingdan Zhang³

¹ School of Economics and Management, North China Electric Power University, Beijing, China

guoyiwei5000@sina.com

² School of Economics and Business Administration, Zhejiang Sci-tech University, Hangzhou, Zhejiang Province, China

³ School of Economics and Business Administration, Beijing Normal University, Beijing, China

Abstract. This paper is to expound the development of agro-food processing industry from three aspects: the scale of the industry, the production and marketing situation and the output of major products. In an effort to analyze the current situation in light of the pollution abatement of the agro-food processing industry in China, emphasis with elaborate details and graphs, is then to be turned onto the consumption of energy, emission and control of "three wastes" and output value of comprehensive utilization. In the end, feasible suggestions concerning pollution abatement are proposed.

Keywords: Agro-food processing industry, pollution abatement, industrial "three waste".

1 Introduction

Entering into the 21 century, China's resource and environment face austere challenge, and have become the important factor of restricting sustainable development of economy. The discharge of waste gas, waste water and industrial residue severely harms people's health and growth of production, also breaks natural ecosystems. According to the Plan Outline for National Economic and Social Development, during the eleventh Five-Year, Unit GDP Value should drop by 20%, and the total discharge of major pollutants will drop by 10%.

Since 2003, the amount of china's agro-food processing enterprises has increased rapidly, and the size of a single enterprise also has enlarged considerably, which led to the rise in energy consumption and discharge amount of 'three wastes'. The paper will analyze the status of energy consumption and the discharge amount of "three wastes" of China's agro-food processing industry, and propose feasible suggestions concerning pollution abatement. In this paper, the research is sponsored by the Fundamental Research Funds for the Central Universities (11MR25) and the environmental research and special funding public service sectors (201009066).

2 Development of China's Agro-Food Processing Industry

2.1 Industry Scale

Industrial enterprises of china's agro-food processing industry above designated size makes up 5.0%~5.7% of China's industrial enterprises above designated size. Total assets of agro-food processing enterprises makes up 2.5%~2.7% of china's industrial enterprises above designated size. The amount, total assets and the annual average of employees of industrial enterprises of china's agro-food processing industry above designated size from 2003 to 2009 are shown in table 1.

Table 1. Industry scale of agro-food processing enterprises above designated size

Year	Quantity of enterprises	Increase rate	Total assets (Million Yuan)	Increase rate	Annual average of all employees	Increase rate
2003	11192		414180		1817000	
2004	12244	9.4	484320	16.9	1909000	5.1
2005	14575	19.0	575070	18.7	2226000	16.6
2006	16356	12.2	692430	20.4	2386000	7.2
2007	18140	10.9	879810	27.1	2648000	11.0
2008	22800	25.7	1097720	24.8	3151000	19.0
2009	24550	7.7	1334490	21.6	3377000	7.7

2.2 Production and Marketing

From 2005 to 2009, the scale of China's agro-food processing industry has been continuously enlarged, and Total industrial output value has been increasing, see Table 2. Due to the influence of international financial crisis, in 2009, the year-on-year increase of the indexes decreased.

Table 2. Production and marketing of agro-food processing enterprises above designated size

Year	Total industrial output value (Million Yuan)	Increase rate	Total profit (Million Yuan)	Increase rate
2005	1061495		39871	
2006	1297349	22.22%	56514	41.74%
2007	1749608	34.86%	89358	58.12%
2008	2391737	36.70%	121388	35.84%
2009	2796103	16.91%	150116	23.67%

3 Energy Consumption of China's Agro-Food Processing Industry

3.1 Total Amount of Energy Consumption and Main Energy Consumption Amount

Statistic data shows that from 2001 to 2008, the total amount of energy consumption of China's agro-food processing industry is 0.88%~1.43% of total amount of industry energy consumption. Since 2003, the total amount of energy consumption of China's agro-food processing industry has been increasing gradually each year in 5 years, and reached max in 2008.

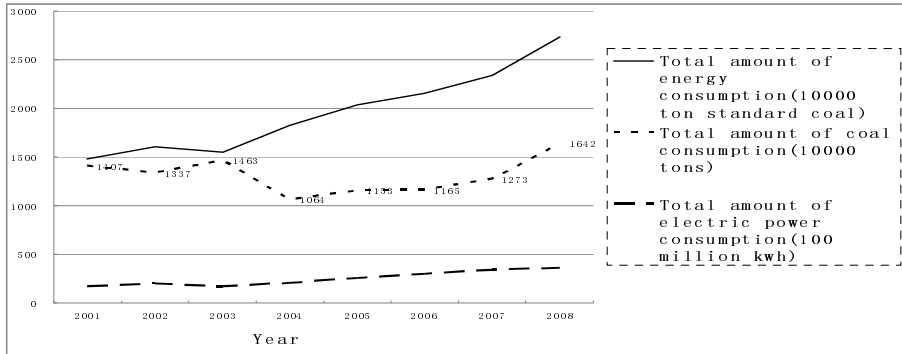


Fig. 1. Total amount of energy consumption of China's agro-food processing industry

Coal and electric power are main energy of China's agro-food processing industry. From 2000 to 2003, the amount of coal consumption of the industry has a gentle downward trend, but has a upward trend from 2004 to 2008. From 2001 to 2002, the amount of electric power consumption of the industry was relatively stable, slightly dropped in 2003, but from 2004 to 2007 grew steadily.

3.2 Energy Consumption Amount Per Unit Output Value

We can see from Table 3, from 2005 to 2008, Energy consumption amount per unit output value of China's agro-food processing industry went down gradually, which indicates China's agro-food processing industry has been making progress in energy saving.

Table 3. Energy consumption amount per unit output value of China's agro-food processing industry

Year	Total amount of energy consumption (10000 ton standard coal)	Total industrial output value (Million Yuan)	Energy consumption amount per unit output value (10000 ton standard coal/100 Million Yuan)
2005	2034	1061495	0.192
2006	2156	1297349	0.166
2007	2336	1749608	0.134
2008	2731	2391737	0.114

4 'Three Wastes' Discharge of China's Agro-Food Processing Industry

'Three wastes' is major environmental pollution sources of China's agro-food processing industry.

4.1 Solid Waste Discharge of China's Agro-Food Processing Industry

From 2004 to 2009, the Solid waste discharge of China's agro-food processing industry grew rapidly, as well as the solid waste utilization, which was always lower than the solid waste discharge (See Fig. 2).

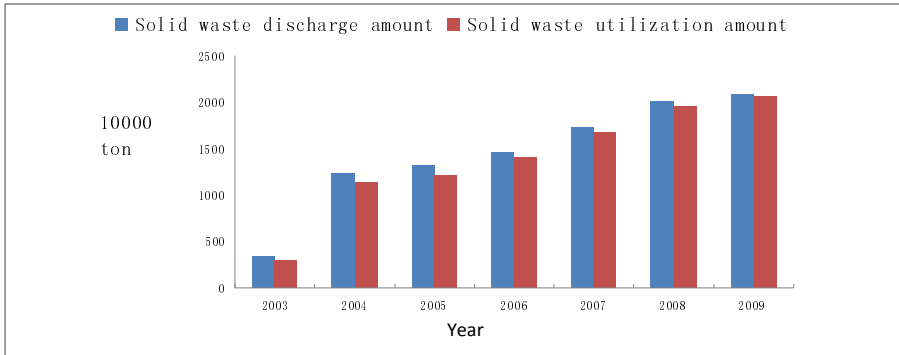


Fig. 2. Solid waste discharge/ utilization amount of China’s agro-food processing industry

From 2003 to 2009, Solid waste comprehensive utilization rate of China’s single agro-food processing enterprise was very stable, varying from 86.76% to 98.33%, much higher than 57.42%~67.45% of that of all industries, and taking on ascend trend, which indicates that China’s agro-food processing industry has been making progress in comprehensive utilization of solid waste.

4.2 Waste Water Discharge of China’s Agro-Food Processing Industry

The pollution contribution rate of waste water discharge of China’s agro-food processing industry is very high, which has great progressive space.

Waste Water Discharge Amount. The discharge amount and attainment amount of the industrial waste water of China’s agro-food processing industry from 2003 to 2008 are given in Fig. 3.

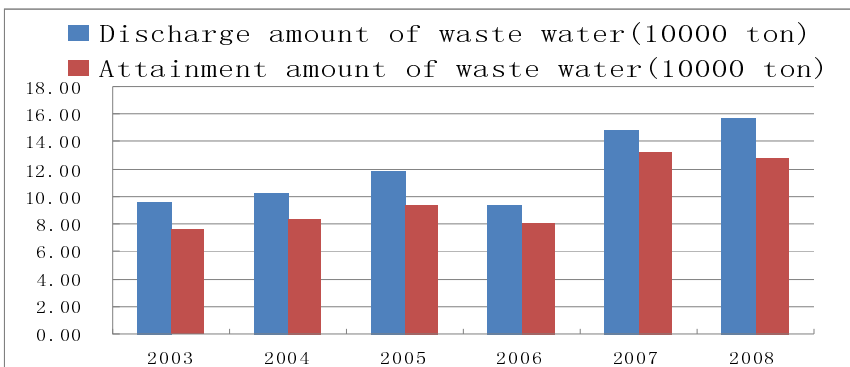


Fig. 3. Discharge amount and attainment amount of waste water of China’s agro-food processing industry

Chemical Oxygen Demand (COD). In 2005, the COD amount of agro-food processing industry was 677200 tons, which was in the second place in all investigated industries. In 2008, the COD removal amount of agro-food processing industry was 91000 tons, which was in the third place in all industries with greatest removal amount. The COD removal amount of agro-food processing industry displayed the increasing trend from 2004 to 2008.

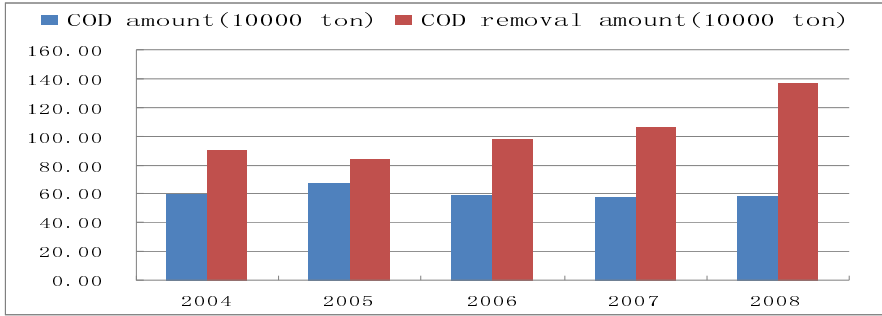


Fig. 4. COD amount and COD removal amount of China's agro-food processing industry

4.3 Waste Gas Discharge of China's Agro-Food Processing Industry

Discharge Amount of Sulfur Dioxide, Industrial Smoke Dust and Industrial Dust. From 2003 to 2009, the discharge amount of Sulfur dioxide and industrial smoke dust was much more than that of industrial dust, the discharge amount of industrial smoke dust and industrial dust presented downward trend in a fairly extent, but the discharge amount of Sulfur dioxide did not change much, see Fig. 5.

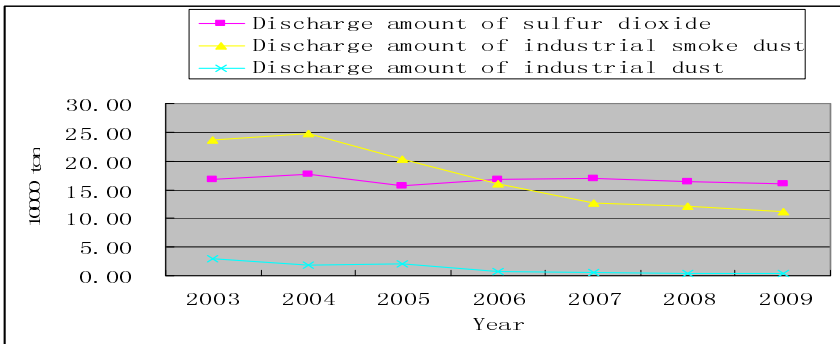


Fig. 5. Waste gas discharge amount of China's agro-food processing industry

Removal Amount of Sulfur Dioxide, Industrial Smoke Dust and Industrial Dust. From 2003 to 2009, the removal of sulfur dioxide, industrial smoke dust and industrial dust of China's agro-food processing industry was good, see Fig. 6, which shows that the discharge of industrial smoke dust of China's agro-food processing industry was improved most effectively.

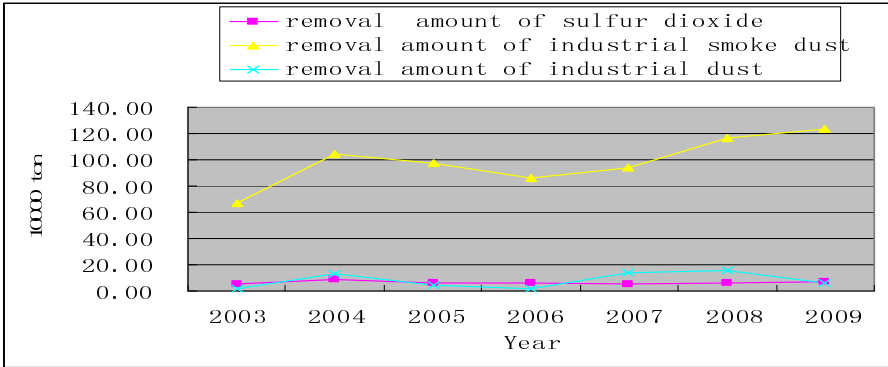


Fig. 6. Waste gas removal amount of China’s agro-food processing industry

4.4 Output Value of the Comprehensive Utilization of ‘Three Wastes’

From 2003 to 2007, the output value of comprehensive utilization of ‘three wastes’ of China’s agro-food processing industry grew gradually, but from 2008 to 2009, the index presented stable, see Fig. 7.

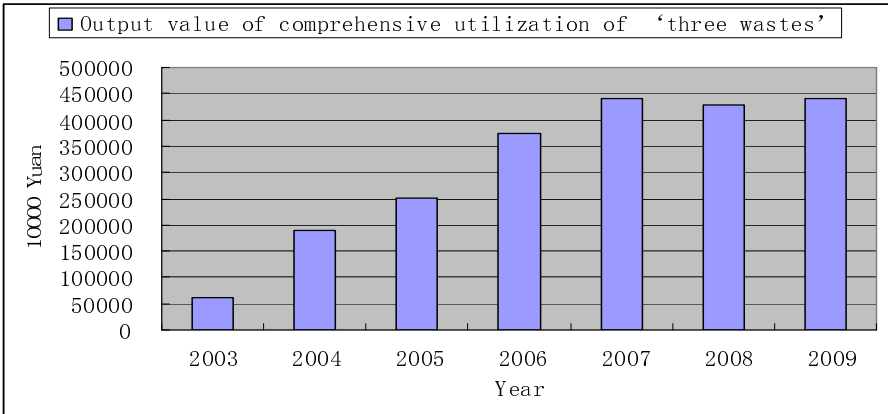


Fig. 7. Output value of comprehensive utilization of ‘three wastes’ of China’s agro-food processing industry

5 Pollution Abatement Policy Recommendations of China's Agro-Food Processing Industry

According to above statistic data and analysis, the discharge of waste water of China’s agro-food industry presents an upward trend, which needs to be improved. The discharge of COD has been controlled effectively, that needs to be kept.

5.1 Strengthen Supervision and Establish Uniform Standards

Governments and environmental protection department at all levels should strictly employ the national unified standards, even higher standard for discharge of pollutants in some developed areas, include discharge of 'three wastes' into the assessment of local government at all levels.

5.2 Set Up Green Production Strategy, Pursue Cleaner Production

The relevant departments in the government should establish an evaluation standard system of clearer production of China's agro-food industry in conformity with cleaner Production Promotion Law, encourage and support enterprises to introduce and develop advanced technology to conduct clearer production, and raise utilization rate of waste resource, strictly control water consumption in production, advance the saving water, recovery processing and utilization of waste water of Enterprises, adjust product structure appropriately to produce healthy, green environmental-protective agro-food, and increase the added value of agro-food processing industry.

5.3 Encourage Process and Equipment Reforms, Strengthen Production Management

More technical support should be given to pollution abatement and comprehensive utilization of resources of agro-food processing industry. More policy and funds support should be given to research, development and process and equipment reforms which should be popularized to speed up the industrialization of agro-food processing industry.

5.4 Promote Informationization Construction of Agro-Food Processing Industry

The government should strongly support informationization of agro-food processing industry, provide talented personnel of information construction to the enterprises and incorporate pollution abatement into the informationization course.

5.5 Develop Biomass Industry

Biomass can partly replace fossil power, reduce emission of greenhouse gas and else air pollution of fossil power. China should strengthen science research of the field, and combine the research results with practical application.

References

1. National Bureau of Statistics. 1997-2009 China Statistical Yearbook. China Statistics Press, Beijing (1997-2009)
2. Economic forecast Ministry of National Information Center. China's Agro-food Manufacturing Industries Running Report. Money China 04, 52-54 (2010)

3. Oikonomou, V., Becchis, F., Steg, L., Russolillo, D.: Energy Saving and Energy Efficiency Concepts for Policy Making. *Energy Policy* 37, 4787–4796 (2008)
4. Wang, G., Wang, Y., Zhao, T.: Analysis of Interactions among the Barriers to Energy Saving in China. *Energy Policy* 36, 1879–1889 (2008)
5. Yuan, C., Liu, S., Fang, Z., Wu, J.: Research on the Energy-saving Effect of Energy Policies in China: 1982–2006. *Energy Policy* 37, 2475–2480 (2009)

Rapid Prototyping for Preoperative Planning of Fibula Free Flap in Mandible Reconstruction

Chen Yadong¹, Wang Hang¹, Qin Xingjun², Wu Wenzheng¹,
Li Hu¹, and Wang Wanshan¹

¹ School of Mechanical Engineering and Automation, Northeastern University,
Shenyang, P.R. China
neucyd@163.com

² Department of Oral and Maxillofacial Surgery, School of Stomatology,
China Medical University, Shenyang, Liaoning 110002, China

Abstract. The most frequent cause of defect in the mandible is tumor-related surgery. Larger defects cause severe morbidity due to disturbances in function and esthetics. A fibular free flap is one way of filling a bony hole in either the upper or lower jaw. In this study, a new method combining preoperative planning and rapid prototyping for mandible fibula free flap reconstruction after preoperative planning was made based on Mimics software simulating surgery on a workstation. The preparatory work of surgery is divided into two parts: software simulation and model building. During software simulation the authors were able to choose the best site for the osteotomy regarding circulation and the model building can increase the precision and speed of treatment. A description of our surgical approach is presented and is supplemented by an illustrative case.

Keywords: Mandible Reconstruction, Rapid Prototyping, Computer Applications.

1 Introduction

The mandible plays a major role in airway protection and support of the tongue, lower dentition, and the muscles of the floor of the mouth permitting mastication, articulation, deglutition, and respiration. It also defines the contour of the lower third of the face. So when undertaking mandible reconstruction, the restoration of bony continuity alone should not be considered the measure of success. The functions of chewing, swallowing, articulation, and oral competence must also be addressed [1, 2]. The development of endosseous implants and free flap grafting has permitted increased possibilities of mandible reconstruction in patients with oral cancer.

Since Hildalgo [3, 4] introduced the free fibular flap it has become the standard for reconstructions of broad osseous defects in mandibular reconstruction.

This technique allows for larger resections and reconstruction, which allows patients to return to normal function in a much shorter period of time when compared with multistage local, regional flaps and free bone grafts. The traditional surgical process of the free fibula flap in mandible reconstruction is as follows:

The doctors remove one of the bones from the lower part of the patient's leg. The fibular bone runs on the outside of the leg from the knee joint to the ankle joint. It is a small thin bone that can be entirely removed without affecting ability to bear weight [5]. Once the bone is raised the doctors must cut this bone so that it can fit for the

shape of mandible. At last it is transferred to the head and neck and secured in position with small plates and screws. The blood vessels supplying and draining the flap are then joined to blood vessels in patient's neck under a microscope. These blood vessels then keep the flap alive while it heals into its new place.

However, this process is very time-consuming and inconvenient, in which doctors can only rely on their experience to cut and abrade the fibular time and time again because the graft has to be contoured to fit the mandible defect of patient [6].

In recent years, many researches have developed some new methods of surgical plan for mandible reconstruction. [7] designed an osteotomy system, and it has been applied successfully in patients, especially for anterior mandibular reconstructions, but in more complex reconstructions the intra-operative situation is difficult to handle accurately.[8] and[9]preoperatively simulated the reconstruction and manufactured a surgical template using Computer Aided Design and Manufacturing technique.A Belgian company called Materialise developed a new system—CMF. It has a powerful function for complex reconstructions[10]. Nevertheless, the process of re-establish bony of fibular free flap, which is the most troublesome and time-consuming part of surgery, was not be properly handled.

2 Case Report

A 53-year-old woman was referred to the Hospital of stomatology, China Medical University for surgery of right lower gingival carcinoma. We then focus on the free fibula flap which is most versatile in reconstruction of the mandible defect according to her condition.

Preoperative Preparation. The aim of virtual surgery simulation of mandible reconstruction is to reshape the fibula and find the position and angle which doctors really need in actual operation.

The first step of surgery planning is to acquire the patient's CT data sets from the mandibulofacial region and from the fibula; both stored using DICOM as a medical image file format. The data were then imported to the image processing software –Mimics, which is used as an interactive tool for 3D visualization and segmentation of CT images. After that, the virtual surgery could be performed by using the functions of the software.

We separated the mandibula from other tissue by threshold segmentation, and then, we could make sure the department which would be cutout according to the location and size of the local disease focus without any disturbance (Fig. 1).

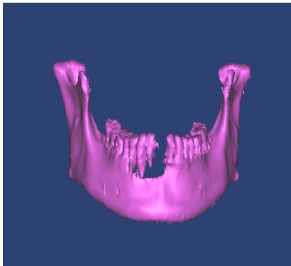


Fig. 1. The three-dimensional visualization

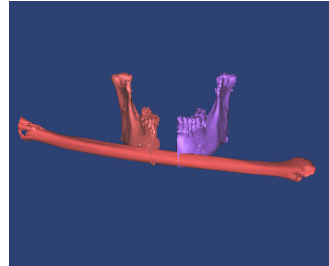


Fig. 2. Fibular fitted to the mandible

The fibula of the patient's left leg was also be extracted by dynamic increase in the same workspace, the 3D object of the fibular was then imported into the head scan and fitted to the mandible.(Fig. 2).

The length of the bone segments as well as the position and angle of the osteotomies has to be determined with respect to the blood supply. As thus, we got the intercept position, length, and curving angle of the fibula.

Traditional surgery simulation just got the data information to doctor, which can hardly give powerful support to operation in most cases. In this paper, we developed a patient-specific transfer system of the virtual plan to be used during the operation, based on software and hardware. We exported STL model of the result of surgery simulation which was the mandibula that be repaired (Fig. 3);

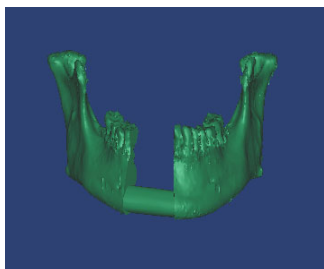


Fig. 3. The repaired mandible in simulate surgery

Assembly of Model and Customize Titanium. We Measurement parameters of fibular free flap, and model customize titanium. To Ensure that the model made by Pro/e with other models of data of RP consistency, we must set Modeling template of Default template model at time in the establishment of the screw in Pro/e. By measuring the fibular we determine the screw length is 8 mm, and assemble Customize Titanium. (fig. 4)

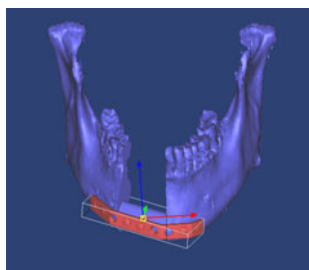


Fig. 4. Assembly of model and Customize Titanium

The data of STL models were then imported into rapid prototyping machine for actual production. Doctors used these models for confirming the shape of titanium plate (Fig. 5) and cutting the fibula in real surgery , which could improve the surgical precision and reduce operating time to a large extent.



Fig. 5. The actual model of repaired mandible and cutting

The Surgical Procedures. The doctors were divided into two groups and undergo surgery simultaneously while the patient under general anesthesia. One group performed conventional mandible surgical incision, which came into the exposed layer by layer under the mandible and the tumor, according to solid model design osteotomy line and fixed hole position in the virtual planning; the other group was in charge of free flap fibula and vascularized bone graft by making use of the data which be got from virtual surgery.

When make sure the shape of the fibula, they made the lower edge flush with the inferior margin of mandible by molding titanium plate with titanium screw fixation in the bone graft.

Then check the occlusion and mandibular movements in normal relations with drainage. The surgery would complete if the free fibula flap and vascularized graft anastomosed in the establishment of blood supply.

3 Discussion

Reconstruction of the mandible is a difficult task to perform consistently with good results. Multiple procedures are often required to achieve a result that is almost always less than ideal. Numerous reconstructive options are available; however, no single option has yet emerged as the staple for management of this defect.

Software of visualization and rapid prototyping are important techniques and instruments in complex mandible reconstruction. This report illustrates the authors' method of performing reconstructions virtually and transforming the design to real time surgery by manufacturing a rapid prototyping, which can be fitted at any site of the microvascular flap, taking into account the vascular anatomy. The authors' experience shows that the surgery time can be reduced with more accurate surgical procedures, which relied on the accuracy of the virtual planning and rapid prototyping machine. This leads to higher precision because measurements on the virtual model of distances, angles and volumes can be performed with an accuracy.

The paper compares traditional osteotomy planning procedures using only radiographs and 2D CT images to planning with full-scale physical bio-models. The bio-models had a clearly beneficial impact on the accuracy of surgery and positively influenced the clinical outcome. however, rapid prototyping models also increase the cost of surgery. We will continue work on this direction and try to find a costless method for mandibular reconstruction.

References

1. Cordeiro, P.G., Disa, J.J., Hidalgo, D.A., Hu, Q.Y.: *Plast. Reconstr. Surg.* 104, 1314–1321 (1999)
2. Wolff, K.D., Ervens, J., Herzog, K., Hoffmeister, B.: *J. Craniomaxillofac Surg.* 24, 330–338 (1996)
3. Hidalgo, D.A.: *Plast Reconstr. Surg.* 84, 71–79 (1989)
4. Hidalgo, D.A., Pusic, A.L.: *Plast. Reconstr. Surg.* 110, 438–449 (2002)
5. Do, R.M.G., Volker, K.H., Sonntag, M.D.: *Bone Graft Harvest Barrow Quarterly* 19, 17–20 (2003)
6. Bahr, W., Stoll, P.: *Journal of Oral and Maxillofacial Surgery* 56, 33–44 (1998)
7. Strackee, S., Kroon, F., Spierings, P.: *Plast Reconstr. Surg.* 114, 851–1858 (2004)
8. Xu, X., Ping, F.Y., Chen, J., Yan, F.G., Mao, H.Q., Shi, Y.H., Zhao, Z.Y.: *Zhejiang University Transaction* 36, 498–502 (2007)
9. Zhang, T., Zhang, Y., Li, Y.S., Gui, L., Mao, C., Chen, Y.N., Zhao, J.Z.: *Chinese Journal of Plastic Surgery* 22, 325–327 (2006)
10. Leiggener, C., Messo, E., Thor, A., Zeilhofer, H.-F., Hirsch, J.-M.: *International Association of Oral and Maxillofacial Surgeons* 38, 187–192 (2009)

Numerical Simulation of Inner Hydro-field and Comfortable Evaluation Based on Human Thermal Comfortable Model in Cockpit*

Junwei Zhao¹, Xuming Mao¹, Ruhua Wang¹, Wenjiang Wang¹,
Zhenwei Zhang¹, and Hongjun Xue²

¹ General Configuration and Aerodynamic Design Division, Shanghai Aircraft Design and Research Institute, 200235

² School of Aeronautics, Northwestern Polytechnical University, Xi'an 710072
zhaojunwei@comac.cc

Abstract. Traditional research on inner hydro-field of cockpit only paid attention on the airflow itself except human thermal comfort, which is not really consistent with the rule “human center”. This paper builds Human Thermal Comfortable Model based on Radtherm platform. The model, combined with CFD results, focuses on human comfort and can output the human thermal sensation. Utilizing this model, virtual cockpit has been evaluated and the conclusions have been obtained. The evaluation method for hydro-field of cockpit is effective. And it can be used in engineering applications.

Keywords: Thermal comfort, inner hydro-field, numerical calculation, cockpit.

1 Introduction

Cockpit air flow and heat transfer research, which involved aircraft cabin ventilation and air conditioning, thermal comfort, etc., are important aspects of aircraft design and the use of department. They are also important research questions in the field of man-machine-environment system engineering [1] [2]. Research on inner hydro-field included temperature, pressure and speed, is the core elements of micro-environment in cockpit. A lot of international and domestic works about distribution form of air flow have been done, and a lot of mature evaluation models have been built. A standard k- ϵ model was adopted on numerical simulation of air conditioning in passengers' compartment by AWDeJager in Boeing Company in 1992 [3]. Mathematical model on heat transfer of pilot and cockpit systems was established by Professor Yuan Xiugan in 1980s [4] [5] [6]. The computational model on heat transfer characteristics of two-dimensional of the cockpit was built in 1991. These studies mainly aimed at the distribution form of air flow inside the cockpit, included the distribution of temperature and velocity field. They only study the effect about the distribution form of air flow, but do not establish models based on the characteristics of the human body itself to study human subjective feelings of thermal comfort. The study on the distribution of air flow and comfort in training aircraft cabin was

* Project by the National Key Basic Research Program of China(973 Program, Grant No. 2010CB734101).

done by Xiong Xianpeng in 2007 [7]. But only a series of analysis about comfort was put up, and a complete assessment of the flow field model for comfort was not established. This paper builds Human Thermal Comfortable Model based on Radtherm platform. The model, combined with CFD results, focuses on human comfort and can output the human thermal sensation. Utilizing this model, virtual cockpit has been evaluated and the conclusions have been obtained.

2 Assessment Model

2.1 Assessment Index

PMV (Predicted Mean Vote) index is a statistical result based on body temperature environment subjective comfort score. The index represents the majority of the average hot and cold sensation at the same environment. The value is smaller, the comfort is higher. In the early 1980s, the index has been recognized by ISO, and it is a comprehensive evaluation index on environment comfort. According P.O.Fanger's assumption, PMV relationship can be given from the above equations and other relevant equations.

$$PMV = f(\Delta q, \frac{H}{A_{Du}})$$

The thermal comfort equation can be calculated in comfort of a variety of clothing and activity state of the thermal environment. The feeling is usually divided into seven degrees, with the PMV index. The relationship between PMV values and the thermal sensation is shown as follow[8]:

Table 1. The relationship between PMV values and the thermal sensation

Description of subjective thermal sensation	PMV values
Hot	3
Warm	2
Slightly warm	1
Comfort	0
Slightly cool	-1
Cool	-2
Cold	-3

This paper builds Human Thermal Comfortable Model based on Radtherm platform. The conduction, convection, radiation and evaporative heat exchange between human body and environment, and metabolic heat and blood flow of energy levels, skin and respiratory evaporative heat loss and heat including body temperature regulation and other mechanisms are considered in the human thermal comfort model. Environmental conditions around the human body are provided by the CFD calculations.

2.2 Assessment Method

This paper builds Human Thermal Comfortable Model based on Radtherm platform. Fluent software is used for CFD numerical calculation. Holistic assessment for inner hydro-field distribution is given, included the analysis of temperature and velocity field. The calculation results of CFD are inputted into human thermal comfortable model. And change state of thermal feeling and integrated field distribution are finally outputted, which are the assessment results of inner hydro-field distribution in cockpit.

3 Calculation Examples

3.1 Foundation of Cockpit Model

Before numerical calculation, the hypothesis is made as following:

1. The wall of cockpit is considered as rigid, incompressible and isotropy.
2. Because the velocity of air flow is not too fast in the cockpit, the inner hydro-field is laminar flow.
3. The air in the cockpit is considered as Newton fluid, and the viscosity coefficient is constant.

Selected dummy cockpit model is show in Figure 1. There are 9 inlets, included 3 inlets at the top, 4 inlets at sides and 2 inlets beside the feet. At the precondition that it do not affect the precision of calculation, a lot of predigestions are made as following:

1. The frame of cockpit is symmetrical in geometric space, and physical boundary is also symmetrical. So one side of cockpit can be selected for numerical analysis. It can not bring any disadvantage to the precision of calculation. The calculation time is greatly reduced, and work efficiency is increased.

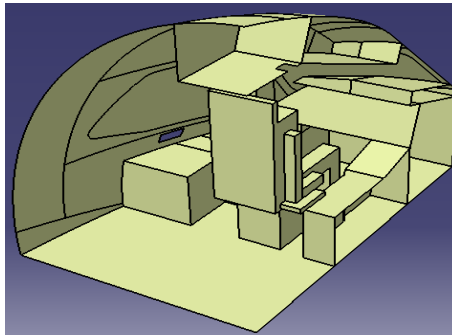


Fig. 1. Cockpit model (left side)

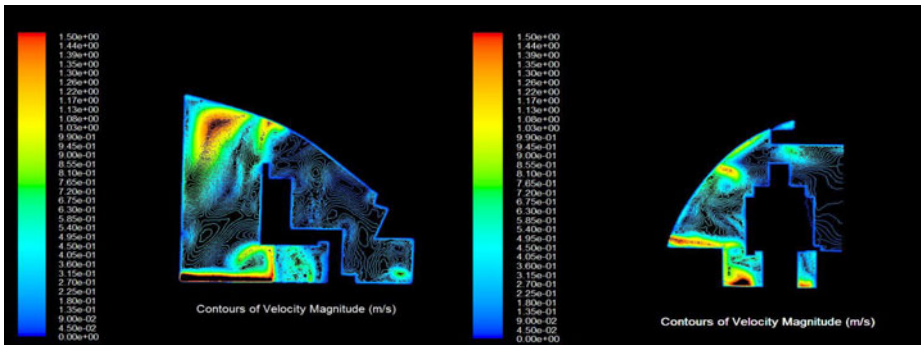
2. The factors that can not affect the distribution in cockpit are predigested. For example, the buttons on instrument panel should be moved out. And some tines should be smoothed.

3.2 Numerical Calculation Results and Assessment

The assessment of the flow field model for comfort in cockpit include the CFD calculation results, such as temperature and velocity field and change state of thermal feeling.

3.2.1 Analysis of Temperature and Velocity Field

The average velocity in the front cockpit is lower, the variety of which is calm. It is shown in Figure 2. The variety of airflow is complex be behind the cockpit panel and on the floor, and the velocity is higher, which is vortex about 1.5m/s. The velocity is higher near floor, and there is a “vacuum” area with the velocity exceeding 1.5m/s. There is a vortex with the center velocity near 1.3m/s.near the windshield. The vortex obviously affects the distribution of airflow, and it accelerates the heat exchange from environment. There is airflow with the velocity of 0.88m/s behind the pilot head. And it blows and affects comfort of the head. The variety of velocity is calm at the right side of pilot, and the distribution of airflow is oppositely complex at the left side. The Airflow with the center velocity near 1.2m/s blow towards the left hand of pilot, and it becomes faint when the airflow reaches the hand. So it does not affect the comfort of pilot.

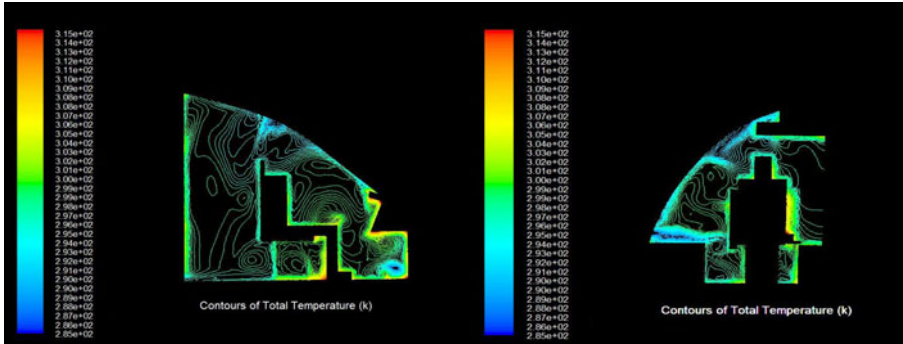


(a) Distribution of side velocity field (b) Distribution of frontal velocity field

Fig. 2. Velocity field distribution of cockpit

The average temperature in the front of the cockpit is different from the rear of the cockpit, which is shown in Figure 3. The average temperature in the front of the cockpit is 25°C, and the rear is 22°C. The difference in temperature is 3°C. There is a vortex; and the variety of velocity is calm at the bottom with temperature of 23°C. Because the airflow is under the seat of pilot, it does not affect the comfort. The temperature near cockpit panel is about 32°C. The average temperature at left side of pilot is 3-4°C higher than that at right side. The temperature at left side is 25°C, and that at right side is 29°C.

There is a vortex with lower grads behind the pilot head, and it made the variety of temperature more smoothly in the rear of the cockpit.



(a) Distribution of side temperature field (b) Distribution of frontal temperature field

Fig. 3. Temperature distribution of cockpit

3.2.2 Assessment on Human Thermal Comfortable Model

Temperature, velocity, humidity and parameters of human body such as heart rate, skin temperature change rate are synthetically considered in human thermal comfortable model. And human thermal comfortable index is built on the integrated factors.

After 30 minutes entering the cockpit, we analyze heat feeling value.

Between 30 minutes and 90 minutes, the thermal feeling value increases linearly from -0.4 to 0.5. The growth rate is great, and the thermal feeling of pilot is in the scope of comfortable. After 90 minutes the growth rate is slower, the thermal feeling value increases linearly to 0.56. the feeling is a little warm. During the whole process, the thermal feeling value gradually increased, and the thermal feeling of pilot is in the scope of comfortable.

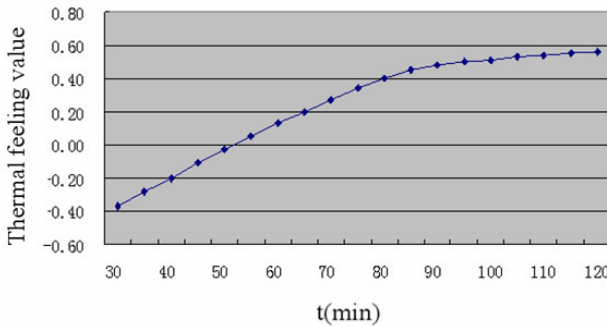


Fig. 4. Thermal feeling values vs. t curve after 30 minutes

4 Conclusion

This article shows the distribution of temperature and velocity field in the cockpit, which is carried out by CFD software through inner fluid field numerical simulation. Though vortex with high velocity in the center appeared in the local area, the velocity field is

uniformity and does not affect the feeling of pilot obviously. Through analyzing with the temperature field, the temperature between the front and rear of the cockpit is 3°C, and the same as both sides of the cockpit. It is basically satisfied the comfortable requirement of cockpit. And according to the analysis of output data from the human comfortable model, it can be concluded that the thermal feeling value of the pilot ranges from -0.4 to 0.56 between 30 minutes and 120 minutes in the cockpit. In the whole flight phase, the feeling of pilot is comfort.

Previously it cannot combine the fluid field state computed by numerical method with human comfortable through the weakly accurate quantification evaluation of human comfortable in the previous computation. This article shall construct evaluation method of cockpit inner fluid field comfortable which is based on the human temper comfortable. The method combines numerical computation and human comfortable evaluation, and forms integrated method system to evaluate the inner fluid field comfortable. And it can be better used in the engineering area to evaluate the relative comfortable of the project in the cockpit design during primitive stage.

References

1. Yuan, X.: Thermodynamics mathematics model and application of airplane cockpit. HJB30088 (1983) (in Chinese)
2. Shou, R., He, H.: Aircraft's environment control. Beijing University of Aeronautics and Astronautics Press, Beijing (2004) (in Chinese)
3. Dejager, A.W., Lytle, D.B.: Commercial airplane air distribution system development through the use of computational fluid dynamics. AIAA-1992-0987 (1992)
4. Yuan, X.: Study on mathematic model of human-cockpit's environment temperature. Selected Papers of The Key Research Topic of Human-Machine-Environment Engineering, 17–23 (1987) (in Chinese)
5. Yang, C.: The numerical simulation on airflow and heat transfer in finite room. Beijing University of Aeronautics and Astronautics, Beijing (1991) (in Chinese)
6. Shen, H., Yuan, X.: Numerical Simulation and Experiment on Airflow and Heat Transfer in Fighter Plane Cockpit. *Acta Aeronautica et Astronautica Sinica* 30(1), 30–39 (2009) (in Chinese)
7. Xiong, X., Liu, W., Ang, H., et al.: Flow fields and thermal comfort in training-plane's air-conditioned cockpit. *J. Applied Sciences* 25(6), 639–644 (2007) (in Chinese)
8. Li, R., Tang, S.: Thermal comfort prediction model for cloth wearing condition and its application. *Space Medicine & Medical Engineering* 7(4), 258–265 (1994) (in Chinese)

Research on the Correlation between Extraordinary Profit and Loss and Financial Report's Quality of Chinese Listed Companies

Fulian Shi¹, Jing Guo², Zhongzheng Xiang¹, and Yan Zhang¹

¹ School of Economics and Management, North China Electric Power University,
Beijing, China

sf18290@sina.com

² School of Economics and Business Administration, Zhejiang Sci-tech University,
Hangzhou, Zhejiang Province, China

Abstract. This paper is an empirical research which regarded audit report opinion given by Certified Public Accountants as dependent variable, treated main business revenue change ratio, Insolvency Index and the natural log of total assets as control variable, which regarded 146 listed companies listed in Shanghai or Shenzhen stock market as the main research samples. The research shows that there is significant linear relationship between extraordinary profit and loss and financial report's quality and listed company's management layer can manipulate its financial reports through handling extraordinary profit and loss, especially the companies whose main business are in the crisis. This article assumes and provides the evidence to show there is negative correlation between extraordinary profit and loss and financial report's quality of listed company. Besides, there also has significant correlation between company growth and company size.

Keywords: extraordinary profit and loss, financial report's quality, correlation.

1 Introduction

CSRC Announcement [2008] No.43 -- Explanatory Announcement No.1 on Information Disclosure for Companies Offering Their Securities to the Public which was revised by China Securities Regulatory Commission (CSRC) in 2008 defines that extraordinary profit and loss arises in various trading and issues that have no direct relation with the normal operations of a company, or that are related with normal operations but affect the users of the statement to make reasonable judgment of the company's operation performance and profitability due to the special and occasional nature of such trading and issues. We can see from the definition that extraordinary profit and loss essentially relates to those no repetitive, non-predictability, non-sustainable income or expenditure. Financial report's quality relates to the sum of Characteristics that reflect the capability of financial reports (or accounting information) satisfying actual and implied needs of financial reports user.

Concerning for extraordinary profit and loss can reflect the Information on profitability of listed companies in the income and its components. However, income structure information is good for stakeholders to concern about the income quality when they are making decision. According to that point, concerning and improving the quality of listed company's financial reports has important theoretical and practical significance.

2 The Correlation Analysis of Extraordinary Profit and Loss and Financial Report's Quality

2.1 Research Hypothesis

Hypothesis 1(H1): negative correlation between extraordinary profit and loss and financial report's quality;

Hypothesis 2(H2): positive correlation between listed company financial position and financial reports quality;

Hypothesis 3(H3): positive correlation between company growth and financial reports quality of listed company;

Hypothesis 4(H4): positive correlation between the size of listed companies and financial reports quality of listed company;

Hypothesis 5(H5): U-shaped relationship between proportion of the largest shareholder and financial reports quality.

2.2 Sample Selection and Data Sources

Sample selection is based on the financial statements data of 1421 listed companies in 2006 which gets 149 samples through selecting companies whose operating profit is less than zero while the net profit is greater than zero. Because of the missing Data, three companies are deleted and one primary sample has been selected and data during 2006-2007 is treated as research sample. The main reason of selecting by this way is these companies' main businesses have some problems in 2006, but net profit is positive number, this shows to us that non-operating profit is large, Non-recurring gains and losses must play a larger role in it. This sign tells us that management layer manipulate the financial reports quality.

Annual financial statement data and audit opinion of this article are from the CSMAR database, the CCER database, the CSRC website and the SSE website and the SZSE website.

2.3 Variable Selection and Definition

Dependent Variable—— Financial Report's Quality(QFR). This article is regarded audit report opinion given by Certified Public Accountants as the judgment standard of financial reports quality and rejects part of the abnormal audit report, which regards audit report opinion as dependent variable.

Control Variables

(1) Extraordinary profit and loss

Nonrecurring item (IGL) = net profit- net Profit after deducting Extraordinary profit and loss

The extraordinary profit and loss definition of this article is mainly in accordance with the CSRC Announcement [2008] No.43 -- Explanatory Announcement No.1 on Information Disclosure for Companies Offering Their Securities to the Public. And the data selection is mainly on the basis of extraordinary profit and loss which is after the annual financial statements of companies disclosed in the notes, and the data of part of the companies have some adjustment according to the new rules answers.

(2) Financial position – bankrupt index (Z)

$$Z = \frac{6.56 \times \text{net working capital}}{\text{Total assets}} + \frac{3.26 \times \text{Retained earnings}}{\text{Total assets}} + \frac{1.05 \times \text{EBIT}}{\text{Total assets}} + \frac{6.72 \times \text{Book value of the stock}}{\text{Total liabilities}}$$

Net working capital = current assets – current liabilities

Retained earnings = surplus reserves + undistributed profits

EBIT= Earnings before Interest and Tax

(Indexes including the book value of the stock take the end of the value obtained index)

(3) Company growth—the increasing rate of main business revenue (GROWTH)

$$GROWTH = \frac{\text{The main business revenue}_i - \text{the main business revenue}_{i-1}}{\text{The main business revenue}_{i-1}}$$

The Main business revenue shows the i (such as third) year main business revenue. The Main business revenue_{i-1} shows the main business revenue during i-1 year.

(4) Company size – total assets (SIZE)

With larger companies, their internal governance structures are often relatively norm, therefore, Information Disclosure has a strong tendency (Chow & Wong-Boren, 1987; Cui Xuegang, 2004) . This article use total assets of the company at the end of year as Substitution variable to evaluate company size.

(5) The shareholding ratio of the first majority shareholder (FIRST)

FIRST = the shareholding numbers of the first majority shareholder / Number of total capital

(6)The shareholding ratio of the first 10 majority shareholders squares sum (FIRST10)

$$FIRST10 = \sum_{i=1}^{10} \text{first}_i^2$$

First_i shows the shareholding ratio of the i majority shareholder. Selected variables are showed in table 1.

Table 1. Variables and significances

Variables property	Variables name	Abbreviation	Significance of Variables
Dependent variable	Audit reports opinion	QFR	As the criterion of financial reports quality. When there is no retained opinion , getting 0, otherwise 1
Control variables	Extraordinary profit and loss	IGL	Net profit- net Profit after deducting Extraordinary profit and loss
	Bankrupt index	Z	When $Z < 1.23$, bankrupt; when $1.23 < Z < 2.9$ company stays in the grey area; when $Z > 2.9$, company stays in the safe area
	Increasing rate of main business revenue	GROWTH	Listed company growth
	Total capital	SIZE	Size of a listed company
	The shareholding ratio of the first majority shareholder	FIRST	The shareholding numbers of the first majority shareholder / Number of total capital
	The shareholding ratio of the first 10 majority shareholders squares sum	FIRST10	The shareholding ratio of the first 10 majority shareholders squares sum of listed company

2.4 Data Processing and Model

As there is a large difference among selection data, this article takes standardizing ways for data processing in order to carry out empirical research when conducts regression analysis. Processing formula as follows:

$$a' = \frac{a - u_i}{S_i} \tag{1}$$

u_i means single indicator sample mean, s_i means single indicator sample standard difference, a means original data, a' means data which has been disposed.

According to the previous discussion, this article designs Multivariate regression model as follows to analysis the relevance between extraordinary profit and loss and listed company financial reports quality.

$$QFR_{it} = \frac{e^{\beta_1 IGL_{it} + \beta_2 Z_{it} + \beta_3 GROWTH_{it} + \beta_4 SIZE_{it} + \beta_5 FIRST_{it} + \beta_6 FIRST10_{it} + \epsilon}}{1 + e^{\beta_1 IGL_{it} + \beta_2 Z_{it} + \beta_3 GROWTH_{it} + \beta_4 SIZE_{it} + \beta_5 FIRST_{it} + \beta_6 FIRST10_{it} + \epsilon}} \tag{2}$$

QRE represents financial reports quality, QRE=1 when register accountants have no retained opinion on listed company annual financial reports, others occasions, QRE =0. IGL_{it} means the t year extraordinary profit and loss of company. Subscript it means the t year target of company. β means regression coefficient, ϵ means residual. This article uses logistic regression and SPSS17.0 analysis software.

2.5 Descriptive Statistic Analysis

According to the descriptive statistics of the study variables and comparison of the average index from 2006 to 2008 made by Model (2), we may know that in 2006 the

non-recurring gains and losses had staged high to 54.6 million on average, which means that the problems had appeared in the primary business of the majority of the companies. While in 2007, the average level of non-recurring gains and losses increased by 5.77 percentage, indicating that the company's core business is deteriorating, of course the implementation of the New Edition of Accounting Standard had affected it in some degree, but the main reason for that lies in the motivation of earnings management for delist as is shown in the sample of 50 ST companies in 2006. In 2008, the non-recurring gains and losses of the sample companies decreased dramatically by 38.73 percentage, the main cause for this is that the non-recurring gains and losses is a temporary and accidental event which won't maintain at a high level forever; the average bankruptcy index of the sample companies in the three years is within the limits considered safe, however, in the year 2006, the bankruptcy index of 69 companies is below 2.9, that is right below the gray area, and so is the 61 companies in 2007, and the 57 in 2008. It implies that the crisis in the primary business will highly probably push the company on the verge of bankruptcy, and make a risk to manipulate the financial statement. Due to the preferable domestic economic condition in 2007 and 2008, through the three years the average total assets of the enterprises are stably increasing, and a majority of them even made an added investment. As for the ratio quadratic sum, Neither the first majority shareholder nor that of the top 10 have changed a lot, this has something to do with the domestic market, and also the calculating stock concerns. We can see out of the interaction between the non-recurring gains and losses of this passage and the quality of the financial report that the decrease in Recurring is helpful in enhancing the quality of financial report, the conclusion needs to be confirmed in additional studies.

2.6 The Result and Analysis of the Empirical Test

The Separate Regression of Three-Year Data. According to the regression result of the last three years data, we can know that the model does not fit the fact very well. During the three years, the Nagelkerke R-square is 0.31, 0.26 and 0.35 respectively, and all of which haven't passed the test of Hosmer and Lemeshow, declaring that the model fails to explain the independent data of each year, and then there followed the Misjudge matrix by the classification table caused by the weak model. The discriminant rate of the model is 85.6%, 87.7% and 88.4% each year, implying that the model is predictable in some degree. In the predetermination of the Standard financial report, the model did relatively good job as the accuracy rate is as high as 99.2%, 100% and 99.2% each year, however when did with the non-standard financial report it got wrong often, which part of the model needs improving.

But we still can find the common point of the regression from Equation parameters coefficient of this three-year, that the coefficient of both non-recurring and the shareholder ratio of the first majority shareholder are negative, while that of the bankruptcy index, company growth and scale, and also the shareholder ratio of the top ten shareholders are positive, this conforms to our assumption, although not completely right.

The Summary Regression of Three-Year Data. This article will carry on regression analysis of three year sum data which is based on three years data regression respectively. Results of the process of the regression are shown in table 2 to table 5.

Table 2. Models summary

Step	-2 Log Likelihood	Cox & Snell R Square	Nagelkerke R Square
1	307.981a	.184	.253

According to table2, generally, equation goodness of fit is low, statistic of Cox & Snell R² and Nagelkerke R² are 0.184 and 0.253. The model just explains the 25% fluctuation of explained variable. The main reason is the contribution level of the dependent variables are forced returning for the sake of finding out every control variable. We can see from the results that bankrupt index and stock rights ratio have a weak relevant with financial reports quality.

Table 3. Hosmer–Lemeshow test

Step	Chi-square	df	Sig.
1	25.007	8	.002

According to table 3, the result is that the model is significant overall. Table 4 shows the misjudge matrix according to the model.

Table 4. Classification table

	Observed	Predicted			Percentage correction
		Audit opinion			
		.00	1.00		
Step 1	Audit opinion	.00	2	57	3.4
		1.00	1	378	99.7
	Total Percentage				

According to table 4, the Overall classification rate is 86.8%, which shows the model has a certain degree of predictability. Specifically the model has a high right rate when it predicts standard financial reports, almost comes to 99.7%, only one wrong sample. However, when it predicts off-standard financial reports, it only has 3.4% right rate. The model should be improved in the aspect. Variable coefficients and their test results are showed in table 5.

Table 5. Variable coefficients and test

Step		β	S.E	Wald	df	Sig.	Exp
	IGL	-.464	.177	6.860	1	.009	.629
	Z	.535	.359	2.222	1	.136	1.707
	GROWTH	1.900	.977	3.777	1	.050	6.684
	SIZE	2.549	.857	8.845	1	.003	12.795
	FIRST	-.522	.596	.767	1	.381	.593
	FIRST10	.783	.643	1.483	1	.223	2.189
	ε	2.630	.272	93.200	1	.000	13.867

According to table 5, regression analysis results are basic same with the hypothesis of the article, Negative correlation exists between extraordinary profit and loss and financial report's quality of Chinese Listed Companies. Through significant test ($p=0.009<0.05$), the increasing of extraordinary profit and loss will cause the reduction of financial report's quality of Chinese Listed Companies, which confirms the hypothesis 1 of the article research.

As to the bankruptcy index Z, the smaller the indicator is, the more likely for the clients to confront business failure. When $Z < 1.23$, the company goes bankrupt; when $1.23 < Z < 2.9$, the company is within the grey area; when $Z > 2.9$, the company is within the security zone. Among the 438 samples, the bankruptcy indexes of 38 samples are lower than 1.23, and 149 are within the grey area. The bankruptcy index of the samples, on average, is 20.819, and the regression coefficient of Z, in this test, is 0.535, which is in accordance with Hypothesis 2, yet it did not pass the significance test ($P \text{ value}=0.136 > 0.05$), the reason of which may be related to the choice of sample, and from another side it shows a loose connection between the CPA's audition opinion and the company's financial position.

With regards to the Growth, the regression coefficient of GROWTH in this test is 1.9, and it has passed the significance test ($p=0.05$), in accordance with the research hypothesis, indicating that the Growth is in positive correlation with the financial reports quality, and it is easier for the company in the low-growth period to control the financial reports than the high growth companies. Besides, it has testified Hypothesis 3 in this research.

As to the scale of the company, the regression coefficient of SIZE in this test is 2.549, and it has passed the significance test ($p=0.003 < 0.05$), in accordance with Hypothesis 4, indicating the positive correlation between the scale of company and the financial reports quality. Just as the previous hypothesis goes, big companies enjoy higher honorary cost, and receive more attention from supervisory organs, and they reveal more items, to some extent, can raise the companies' financial reports quality.

As to the concentricity of the stock, negative correlation exists between the first majority shareholder's shareholding ratio and the financial reports quality, positive correlation exists between the top 10 shareholders' shareholding ratio quadratic sum and the financial reports quality. In this model, the sign of the two control variables'

regression coefficient is in accordance with the hypothesis 5, showing that an over-high rate of the first majority shareholder's share ratio or an over-scattered share rights are not beneficial for the exercise of the company's governance mechanism, proving that companies owning the holding big shareholders have a relatively objective surplus management system, and a higher financial reports quality. But in the model the p values of either the two control variable have not passed the significance test, and it is greatly influenced by the fact that the current stock market of China is in weak strong type of efficiency, indicating that the concentricity of the stock has a weak correlation with the financial reports quality.

3 Conclusions

Firstly, negative correlation exists between extraordinary profit and loss and financial report's quality of Chinese Listed Companies, which shows the increasing of extraordinary profit and loss will cause the reduction of financial report's quality of Chinese Listed Companies. Secondly, positive correlation exists between listed company growth and financial reports quality. Company experiencing low growth is easier than high growth company to manipulate financial reports. Once more, positive correlation exists between financial position of listed companies and financial report's quality of Chinese Listed Companies, Which shows company financial position has some relevant with financial reports-quality of company. However it hasn't passed on significant test, which CPA reflects the link between the company's financial position and the audit opinion of CPA is not close enough on the side aspect. Finally, negative correlation exists between proportion of the largest shareholder and financial reports quality and positive correlation exists the shareholding ratio of the first 10 majority shareholders squares sum and financial reports quality, which explains the shareholding high ratio of the first majority shareholder or options are too scattered is bad for the function effect of Corporate Governance and also confirms that corporate earnings management is relatively more objective and company financial quality is higher when company exists relative controlling shareholders. However, the two indexes haven't gone through the significant test.

References

1. Xu, X., Li, L., An, Y.: Earnings Management Research of Listed Companies Based on Extraordinary Profit and Loss—Empirical Analysis of Extraordinary Profit and Loss Disclosure of listed companies. *Journal of Huazhong University of Science and Technology (Social Science Edition)* 1, 68–71 (2003)
2. Liang, J., Zhao, M.: Research on Extraordinary Profit and Loss Disclosure of Listed Companies. *Finance and Accounting Monthly* 10, 22–23 (2004)
3. Zhou, Q., Zhou, C.: Research on the Effect of Extraordinary Profit and Loss on Financial Performance of Listed Companies in Shanghai Stock Market. *Journal of Shanghai Lixin University of Commerce* 1, 1–8 (2005)
4. Zhou, X., Li, X.: Research on the Extraordinary Profit and Loss Information of Listed Companies and its Validity of the Disclosure Regulation. *Accountant* 11, 14–18 (2007)

Internal Influence Factors Study of Cash Dividend Policy of China's A and H Share Listed Companies

Fulian Shi¹, Jing Guo², Yan Zhang¹, and Ran Li¹

¹ School of Economics and Management, North China Electric Power University,
Beijing, China
sf18290@sina.com

² School of Economics and Business Administration, Zhejiang Sci-tech University,
Hangzhou, Zhejiang Province, China

Abstract. Dividend policy is one of core content and sensitive issues of modern corporate financial decision-making, playing an extremely important role in the management and development of listed companies. For the same listed companies, different listing destination caused the difference cash dividend policy research has important theoretical and practical significance. This paper Selects both listing in the mainland A share market and Hong Kong H share market in 2007, 44, 2008, 50, 2009, 53 companies as samples, during the period 2007-2009, studies cash dividend policy of A and H share listed companies' internal influence factors by SPSS17.0 software, Logarithm of total assets, current ratio and net capital gains rate is different on the A share and H share companies, the main affect factors is different between the two places, the levels of internal affect factors is different between the two places.

Keywords: A and H share listed companies, cash dividend policy, internal influence factors.

1 Introduction

In context of China's capital market opening and the factor that the linkage between A share and H share market will Strengthen, we research the cash dividend policy differences of the same company due to different locations listed, explore a variety of factors affecting the dividend policy of A shares and H shares, which will provide a theoretical reference and practice evidence for the improvement of China's securities market, and has important theoretical and realistic significance. This paper will research the internal influence factors, which affecting cash dividend policy of A and H share listed companies (hereinafter referred to as 'dual listed company').

2 Samples Selection and Variables Setting

In this paper, the samples include 40 companies of 2007, 50 companies of 2008, 53 companies of 2009, a total of 147. When selecting samples, we excluded the companies that: (1) dual listed company which did not distribute cash dividend during

the last three years.(2) the dual listed company with special nature ,including the company of ST and incomplete data of companies as well as qualified opinion having been issued. Data of Samples comes from Xenophon database, cninfo, RESSET databases, and China Securities Regulatory Commission Web site and finance website.

The paper selected 7 variables.

Profitability. In this paper, earnings per share and return on net assets are used to measure the profitability.

Liquidity. In this paper, current ratio is used to measure the liquidity of corporate.

Growth Ability. In this paper, the growth in operating profit and total assets growth rate are used to measure business ability to grow.

Ability to Pay Debt. In this paper, debt ratio is used to measure ability to pay debt of corporations.

Operational Ability. In this paper, the total asset turnover ratio is used to measures the operating skills of corporation.

Company Size. In this paper, the natural logarithm of total assets is used to measure the size of the business assets.

Equity Structure. In this paper, the proportion of the outstanding shares in A share market and H share market is used to measure ownership structure of corporate.

The variables are shown in Table 1.

Table 1. List of variables and their significance

Variable name	Representative symbol	Variable significance	Category
Return on equity	ROE	Profitability	Explanatory variables
Earnings per share	EPS	Profitability	Explanatory variables
Current Ratio	FLOW	Liquidity	Explanatory variables
Operating profit growth rate	PROFITR	Growth Ability	Explanatory variables
Total assets growth	ASSERTR	Growth Ability	Explanatory variables
Debt ratio	DEBT	Ability to pay debt	Explanatory variables
Total asset turnover	ASSERTS TURNOVER	Operational ability	Explanatory variables
Logarithm of total assets	SIZE	assets scale	Explanatory variables
A / H ratio of outstanding shares	CURRENCY	equity structure	Explanatory variables
Cash dividend per share	SCASH	Ability to pay dividend	Dependent variable

3 Research Assumptions

Assumption 1: there is positive correlation between dual-listed company's profitability and cash dividend

Assumption 2: there is positive correlation between dual-listed company's liquidity and cash dividend

Assumption 3: there is negative correlation between dual-listed company's ability to grow and cash dividend.

Assumption 4: there is negative correlation between dual-listed company's ability to pay debt and cash dividend

Assumption 5: there is positive correlation between dual-listed company's operating capacity and cash dividend

Assumption 6: there is positive correlation between dual-listed company's assets and cash dividend.

4 Model Building

This paper selects A and H share listed companies from 2007 to 2009 as a research sample, the internal influence factors are mainly asset-liability ratio, company size (natural logarithm of total assets), cash dividend per share, return on equity, total assets growth, total asset turnover and so on. We take Cash dividend per share as the dependent variable, and take other variables as independent variables, establishing multiple linear regression Model 1.

$$SCASH = \alpha + \beta_0 ROE + \beta_1 EPS + \beta_2 FLOW + \beta_3 PROFITR + \beta_4 ASSERTR + \beta_5 DEBT + \beta_6 ASSERTS\ TURNOVER + \beta_7 SIZE + \beta_8 CURRENCY + \varepsilon \quad (1)$$

α is constant, and $\beta_0 \sim \beta_8$ are the regression coefficient, indicating the influence extent various factors on the variable extent, ε is a random error term representing the impact on cash dividend per share of other factors that the model does not include.

5 Regression Results of A Share

Variance analysis and regression results of A share, as shown in table 2.

Table 2. Variance analysis and regression results of A share

	Sum of squares	df	Mean square	F	Sig.
Regression	1.417	9	0.046	2.848	0.004
Residual value	3.012	137	0.016	--	--
Total	4.429	146	--	--	--
R2 =0.320 after adjustment R2=0.267 the value of D.W. =1.945					

We can see from Table 2 the analysis of variance and regression result of A share, the value of R2 is 0.320, adjusted value of R2 is 0.267, indicating that the equation’s overall goodness of fit is not too high, but the Value of Sig is 0.004, so the equation pass the test of significance, it is significant in the 0.05 significance level. The value of DW is 1.945, the model variables is not autocorrelation (when the value of DW is about 2 or so, it passes the autocorrelation test).

According to the residuals statistical table of Model regression, mean of residual is 0, in line with the requirements of linear regression.

Multicollinearity diagnostics of Linear regression results are shown in Table 3.

Table 3. Multicollinearity diagnostics table

Dimension	Eigen value	Conditions Index	Proportion of variance									
			(Constant)	EPS	ROE	FLOW	DEBT	ASSETS TURNOVER	SIZE	A CURRENCY	ASSET RTR	PROFIT
1	6.418	1.000	0.00	0.00	0.00	0.01	0.00	0.00	0.00	0.00	0.01	0.00
2	1.119	2.395	0.00	0.02	0.02	0.00	0.00	0.00	0.00	0.02	0.03	0.47
3	0.783	2.863	0.00	0.07	0.03	0.03	0.00	0.01	0.00	0.02	0.13	0.39
4	0.483	3.643	0.00	0.02	0.06	0.03	0.00	0.33	0.00	0.11	0.06	0.01
5	0.395	4.033	0.00	0.14	0.04	0.04	0.01	0.10	0.00	0.02	0.52	0.04
6	0.343	4.328	0.00	0.00	0.07	0.76	0.01	0.00	0.00	0.01	0.14	0.01
7	0.265	4.925	0.00	0.15	0.20	0.07	0.02	0.04	0.00	0.50	0.03	0.01
8	0.142	6.732	0.00	0.58	0.58	0.01	0.05	0.16	0.00	0.28	0.05	0.07
9	0.051	11.201	0.03	0.01	0.00	0.04	0.61	0.31	0.01	0.02	0.04	0.00
10	0.002	55.355	0.97	0.01	0.00	0.01	0.28	0.06	0.99	0.03	0.01	0.00

As we can see from Table 3, the regression model is not multiple collinear.

Regression coefficient and significance test results of A share are shown in Table 4.

Table 4. Regression coefficient and significance test results of A share

Internal influence factors	Non-standardized coefficient		Standard coefficient	t	Sig.	Collinearity Statistics	
	B	Standard error	Trial			Tolerance	VIF
(constant)	-0.030	0.155	--	-0.195	0.846	--	--
EPS	0.068	0.021	0.366	3.256	0.001	0.484	2.065
ROE	0.733	0.344	0.672	2.129	0.040	0.140	7.161
FLOW	0.033	0.016	0.250	2.014	0.049	0.899	1.112
DEBT	-0.271	0.105	-0.506	-2.584	0.013	0.433	2.309

Table 4. (continued)

ASSETS TURNOVER	-0.017	0.024	-0.065	-0.708	0.480	0.732	1.367
SIZE	0.007	0.007	0.107	1.017	0.311	0.547	1.829
A CURRENCY	-0.013	0.045	-0.024	-0.285	0.776	0.849	1.178
ASSERTR	-0.029	0.037	-0.072	-0.772	0.441	0.704	1.420
PROFITR	-0.110	0.037	-0.809	-2.994	0.005	0.191	5.245

As we can see from Table 4, in the linear regression equation, Nine explanatory variables Participate in the regression calculation, five variables pass the significant test ,namely earnings per share, Return on net assets, current ratio, assets and liabilities rates, operating profit growth, there are four variable do not pass the significant test (If Sig. value <0.05 significant test pass),we need to remove variables from the Model, the all value of VIF are less than 10, so multicollinearity is not serious, result is meaningful.

6 Regression Results of H Share

Variance analysis and regression results of A share are shown in table 5.

Table 5. Variance analysis and regression results of H shares

	Sum of squares	df	Mean square	F	Sig.
Regression	1.534	9	0.170	7.530	0.000
Residual value	3.102	137	0.023	--	--
Total	4.636	146	--	--	--
R2 =0.331 after adjustment R2=0.282 the value of D.W. =1.999					

From Table 5, we can see the analysis of variance and regression result of A share, the value of R2 is 0.331, adjusted value of R2 is 0.282, indicating that the equation's overall goodness of fit is ordinary, but the Value of Sig is 0, so the equation pass the test of significance, it is significant in the 0.05 significance level. The value of DW is 1.999, the model variables is not autocorrelation (when the value of DW is about 2 or so, it passes the autocorrelation test).

According the residuals statistical table, mean of residual is 0, in line with the requirements of linear regression.

Multicollinearity diagnostics of linear regression results are shown in Table 6.

Table 6. Multicollinearity diagnostics

Dimension	Eigenvalue	Conditions Index	Proportion of variance										
			(Constant)	EPS	ROE	FLOW	DEBT	ASSERTS TURNOVER	SIZE	H CURRENCY	ASSERTR	PROFITR	
1	6.244	1.000	0.00	0.00	0.00	0.00	0.00	0.00	0.00	0.00	0.00	0.01	0.00
2	1.417	2.099	0.00	0.02	0.03	0.00	0.00	0.12	0.00	0.00	0.00	0.01	0.25
3	0.708	2.970	0.00	0.01	0.00	0.00	0.00	0.45	0.00	0.00	0.00	0.02	0.48
4	0.548	3.374	0.00	0.23	0.08	0.00	0.00	0.12	0.00	0.00	0.14	0.10	
5	0.449	3.727	0.00	0.01	0.00	0.08	0.00	0.17	0.00	0.01	0.64	0.01	
6	0.360	4.164	0.00	0.01	0.01	0.29	0.03	0.00	0.00	0.00	0.13	0.03	
7	0.164	6.172	0.00	0.70	0.83	0.01	0.00	0.03	0.00	0.01	0.02	0.12	
8	0.083	8.650	0.00	0.02	0.04	0.16	0.10	0.01	0.00	0.68	0.01	0.00	
9	0.025	15.916	0.04	0.00	0.00	0.36	0.77	0.09	0.04	0.17	0.01	0.00	
10	0.002	58.415	0.96	0.00	0.00	0.09	0.09	0.00	0.96	0.13	0.02	0.00	

As we can see from table6, the regression model isn't multiple collinear. Regression coefficient and significance test results of H share are shown in Table 7.

Table 7. Regression coefficient and significance test results of H share

Internal influence factors	Non-standardized coefficient		Standard coefficient	t	Sig.	Collinearity Statistics	
	B	Standard error	Trial				B
(constant)	-0.410	0.210	--	-1.948	0.053	--	--
EPS	0.107	0.025	0.417	4.353	0.000	0.531	1.882
ROE	0.145	0.134	0.112	1.081	0.282	0.451	2.216
FLOW	-0.012	0.022	-0.051	-0.557	0.578	0.574	1.742
DEBT	-0.249	0.087	-0.306	-2.844	0.005	0.421	2.373
ASSERTS TURNOVER	-0.007	0.021	-0.027	-0.352	0.726	0.823	1.216
SIZE	0.027	0.008	0.314	3.229	0.002	0.515	1.942
H CURRENCY	-0.025	0.153	-0.012	-0.160	0.873	0.890	1.123
ASSERTR	0.042	0.059	0.054	0.713	0.477	0.858	1.166
PROFITR	-0.107	0.054	-0.310	-1.980	0.049	0.761	1.313

As we can see from Table 7, in the linear regression equation, Nine explanatory variables Participate in the regression calculation, four variables pass the significant test, namely earnings per share, debt ratio, Logarithm of total assets, operating profit growth rate, there are five variable do not pass the significant test (If Sig. value <0.05 significant test pass), we need to remove variables from the Model, the all value of VIF are less than 10, so multicollinearity is not serious, the result is meaningful.

7 The Difference of Cash Dividend Policy between the Two Places

Above regression results show that dividend distribution policy of dual-listed company's A share and H share companies exists the following differences:

Firstly, the logarithm of total assets, current ratio and return on equity affect the policy differently. Logarithm of total assets affected the H share companies significantly, and its effect on A share companies are not significant, indicating that the company to distribute cash dividend in Hong Kong, even more attention to the company's size. Company scale has greater impact on dividend policy. The company with larger scale and abundant funds will be more tend to distribute cash dividend. Current ratio influences A share companies significantly, but its effect on H share was not significant, indicating the corporation more attention to the liquidity in the mainland, the company with strong liquidity will be more tend to distribute cash dividend. ROE influences significantly the A share listed companies, its effect on the H share was not significant. For the H share, the company's profitability affecting its cash dividend policy is mainly achieved by the earnings per share. For A share companies, earnings per share and ROE as indicators of the profitability affect its cash dividend policy.

Secondly, the main factors affecting two places are different. In Mainland, the most important factor that influences the cash dividend policy of dual listed companies is profitability. In Hong Kong, the most important factor is the ability to pay debt. This paper argues that in the Mainland, cash dividend policy pays more attention to enterprise profit ability, corporation profitability is stronger, the possibility of cash dividend is greater, and shareholders will also receive a guarantee. In Hong Kong, companies' dividend distribution policy pays more attention to the ability to pay debt. The timely repayment of maturing debt is an important indicator reflecting the financial status is good or bad. Through the analysis of ability to pay debt, we can examine the ability and risky of business continuity management and contribute to predict future earnings. Companies with high debt are less likely to distribute cash dividend, or they will face greater financial pressure. The stronger the ability to pay debt of enterprises, the greater the possibility of distribution of cash dividend.

Finally, A share is susceptible to internal influence factors, the influence of internal factors on H share is relatively small. Cash dividend policy of A share is affected significantly by five internal influence factors, H share companies are affected by the four factors significantly. This shows that H shares may be more subject to be influenced by its external and other factors such as market conditions, laws and policies, shareholders.

8 Conclusions

In this paper, through the study of internal factors which influence dual-listed company's cash dividend policy, we find that Logarithm of total assets current ratio and ROE influence the A and H share listed company differently. Total assets affect the H shares significantly and is positively correlated with cash dividend per share, not significant for A share. Current ratio affects the A share significantly and is positive correlated with cash dividend, is not significant for H share. ROE affects the A share significantly and is positive correlated with cash dividend, not significant for H share. Next, the main factors affecting the two places are different. In mainland, Profitability is the most important factor that affects A and H share listed companies' cash dividend policy. In Hong Kong, the most important factor is ability to pay debt. In addition, A share is susceptible to internal influence factors, the influence of internal factors on H share is relatively smaller.

References

1. Fama, E., French, K.: Disappearing dividends: Changing firm characteristics or lower propensity to pay? *Journal of Financial Economics* 60, 3–43 (2001)
2. Smith Jr., C.W., Watts, R.L.: The Investment Opportunity Set and Corporate Financing, Dividend and Compensation Policies. *Journal of Financial Economics* (32), 263–292 (1992)
3. Kallapur, S.: The Investment Opportunity Set: Determinants, Consequences and Measurement. *Managerial Finance* (27), 3–15 (2001)
4. Wang, Y.: Dividend Policy Study of China's Listed Companies. Xiamen University Ph.D. thesis, Xiamen (2009)

Correlation Study of EVA and Corporate Value

Fulian Shi, Yuanbin Jiang, and Xu Zhang

School of Economics and Management, North China Electric Power University,
Beijing, China
sf18290@sina.com

Abstract. This paper selects 2006~2008 data of 261 listed manufacturing companies in Shanghai Stock Exchange and Shenzhen Stock Exchange as investigative samples, corporate value as dependent variable, EVA-based index system and traditional financial index system as independent variable. By single-element and multiple regression analysis, the paper verifies the correlation of EVA-based indexes and traditional financial indexes, and constructs a corporate value model of comprehensive index system. The research results show that the comprehensive index system which includes EVA-based indexes and traditional financial indexes has higher explanatory power to corporate value.

Keywords: EVA, financial indexes, corporate value.

1 Introduction

Economic Value Added (EVA) is the difference of income after tax and capital cost. Market Value Added (MVA) is modified EVA, indicating the difference of enterprise market value and total capital input, and showing the expectation of capital market to enterprise future earning ability. The evaluation effect of MVA to enterprise performance depends on the market efficiency. Under the environment of China's capital market, the paper tries to verify the correlation of EVA-based indexes and traditional financial indexes, and construct a corporate value model of comprehensive index system, which has higher explanatory power to corporate value.

2 Indexes Selection

In the paper, dependent variable is corporate value. Independent variable indexes fall into EVA-based indexes and traditional financial indexes. EVA per share, cost of capital, return on capital, the difference of return on capital and cost of capital, and natural logarithm of total capital are selected in the EVA-based index system. In the traditional financial index system, EPS, P/E ratio, return on assets and return on equity are selected which are key indexes of evaluating corporate liquidity, profitability and Development Capability, widely used in the studies of financial performance evaluation on companies.

Indexes descriptions are given in Table 1.

Table 1. Indexes description

Index	Symbol	Description
Corporate value	MVAPC	Market Value Added/total capital, ie. MVA created by \$1 capital.
EVA per share	EVAPS	EVA per share
Cost of capital	COC	Weighted-average cost of equity capital and liability capital
The difference of return on capital and cost of capital	SPREAD	The difference of return on capital and cost of capital,
Capital size	LNC	Natural logarithm of total capital
P/E ratio	PE	Price per share/ earnings per share
Earnings per share	EPS	Net income/total outstanding shares
Return on equity	ROE	Net income/equity
Return on assets	ROA	Net income/total assets
Assets size	LNA	Natural logarithm of total assets

3 Research Hypothesis, Sample Selection and Data Sources

The paper will compare and analyze the explanatory Power of the EVA-based indexes to corporate value and the explanatory power of the traditional financial indexes to corporate value. The basic hypotheses are following.

Hypothesis 1: The traditional financial index system has some explanatory power to corporate value, the financial index system should not be completely give up in evaluating corporate value.

Hypothesis 2: The EVA-based index system has higher explanatory power than traditional financial indexes to corporate value.

Hypothesis 3: A corporate value model of the comprehensive index system can be established, the model has explanatory and analysis power to corporate value.

The paper selects 2006~2008 data of 261 listed manufacturing companies in which do not include those publishing both stock A and other kind stocks, with successive years of severe losses, without complete data available or ST, PT companies in Shanghai Stock Exchange and Shenzhen Stock Exchange as investigative samples which are from professional database CCER.

4 Single-Element Regression Analysis of Explanatory Power to Corporate Value by the EVA-Based and Traditional Financial Indexes

In order to test EVA-based index' influence direction and power to corporate value, the paper will do Single-element Regression analysis to MVAPC and selected EVA-based index. The analysis results are shown in Table 2.

$$Y = \beta_0 + \beta_1 X + \varepsilon \quad (1)$$

Y is MVAPC, X is EVA-based index. β_0 and β_1 are regression coefficients, ε is regression residual.

Table 2. Single-element regression analysis results of explanatory power to corporate value by the EVA-based and traditional financial indexes

		Regression coefficient	t value	p value	F value	R^2	Adjusted R^2
EVA index	COC	-6.8910	-2.0995	0.0367	4.4080	0.0168	0.0130
	LNC	-4.7473	-3.9875	0.0001	15.9005	0.0581	0.0544
	EVAPS	1.6083	6.4152	0.0000	40.3320	0.0940	0.0902
	SPREAD	14.6866	10.3649	0.0000	107.4312	0.2940	0.2912
Financial index	ROE	0.6938	1.1285	0.2602	1.2735	0.0049	0.0011
	ROA	105.7571	3.3972	0.0008	11.5411	0.0428	0.0391
	PEc	-187.2615	-1.1563	0.2486	1.3371	0.0051	0.0013
	EPS	8.3142	5.4509	0.0000	29.7125	0.1033	0.0998
	LNA	-3.2698	-3.7420	0.0002	14.0025	0.0515	0.0478

As we can see from Table 2, with confidence of 5%, EVA-based variables all can pass the T test and F test, which shows that all Regression Models are effective, and linear relationship is significant.

With confidence of 5%, except for ROE and PE, all financial indexes can pass T test and F test, which shows that all Regression Models are effective, and linear relationship is significant.

According to Single-element Regression results, in Single-element Regression analysis model, Explanatory power of each EVA-based index is not very high to the dependent variable. On the one hand, it is related to the analysis ability of the models. On the other hand, it is related to China's stock market. That is to say, single financial index has lower Explanatory power to corporate value, which has same reason with lower Explanatory power of EVA-based index system in Single-element Regression analysis.

5 Multiple Regression Analysis of Explanatory Power to Corporate Value by the EVA-Based and Traditional Financial Indexes

After finished single-element regression analysis, in order to further study Explanatory power of EVA-based index system to corporate value, the paper established a multiple

regression analysis model, see model 2, to analyze the Explanatory power of EVA-based index system to corporate value. The analysis results are shown in Table 3.

$$MVAPC = \beta_0 + \beta_1 EVAPS + \beta_2 SPREAD + \beta_3 COC + \beta_4 LNC + \varepsilon \quad (2)$$

Table 3. Multiple regression analysis results (1)

Index	R Square		Adjusted R Square		F		Significance F	
	EVA index	Financial index	EVA index	Financial index	EVA index	Financial index	EVA index	Financial index
Value	0.3912	0.2100	0.3817	0.2008	40.9655	22.6965	0.0000	0.0000

The results show, in adjusted R2, explanatory power of EVA-based index variables to corporate value has increased to nearly 40%, but adjusted R2 of financial index is 0.2008, on account of the 2007 and 2008 off-normal fluctuation of stock market, financial indexes still has some explanatory power to corporate value. But Compared with EVA-based index system, the explanatory power of traditional financial index system has decreased, that verified the hypothesis 2.

The significance test results to the model are given in Table 4.

Table 4. Multiple regression analysis results (2)

	df		SS		MS		F		P	
	EVA Index	Financial Index	EVA Index	Financial Index	EVA Index	Financial Index	EVA Index	Financial Index	EVA Index	Financial Index
Regression analysis	4.0000	3.0000	30062.4428	16144.7825	7515.6107	5381.5942	40.9655	22.6965	.000 (a)	0.000
Residual error	255.0000	256.0000	46782.8367	60700.4970	183.4621	237.1113				
Total	259.0000	259.0000	76845.2795	76845.2795						

A explanatory variables: constant, EVAPS, SPREAD, COC, LNC

As we can see from Table 4, when using EVA-based index, F=40.9655, P=0.000. When using financial index, F=22.6965, P=0.000. When the level of significance is 0.01, P<0.01, regression coefficients of the model are not zero significantly, the linear relationship of dependent variables and all independent variables is significant, A linear model can be constructed to express the linear relationship between MVAPC and EVA-based index variables and financial index variables. The significance test result shows that it is appropriate to use linear model to describe MVAPC and EVA-based index, MVAPC and financial index.

The multicollinearity test results of the model are shown in Table 5.

Table 5. Multiple regression analysis results (3)

		Regression coefficient	Standard error	T	P	VIF
EVA-based index	Intercept	109.3923	20.5698	5.3181	0.0000	-
	COC	8.1808	3.8944	2.1007	0.0000	2.4830
	LNC	-5.1039	0.9899	-5.1559	0.0000	1.0550
	EVAPS	-1.4913	0.7852	-1.8992	0.0000	2.1380
	SPREAD	18.5316	1.6096	11.5131	0.0000	1.4030
Financial index	Intercept	106.5528	19.3368	5.5104	0.0000	
	EPS	10.7011	1.6172	6.6169	0.0000	1.271
	ROA	0.4229	31.8259	0.0133	0.0000	1.286
	LNA	-4.8911	0.8938	-5.4720	0.0000	1.253

When using EVA-based index, the highest VIF value of all variables is 2.4830, which shows the regression equation has some multicollinearity, but the collinearity degree are not very high. When the level of significance is 0.01, the partial regression coefficients' P value of EVAPS, COC, LNC and SPREAD are all 0.0000, which is less than 0.01, therefore, the partial regression coefficients of EVAPS, COC, LNC and SPREAD are significantly not zero. Consequently, EVA-based index can effectively explain Linear Variation of MVAPC.

When using financial index, the highest VIF value of all variables is 1.286, which shows the regression equation has some multicollinearity, but the collinearity degree are not very high. When the level of significance is 0.01, the partial regression coefficients' P value of ROA, EPS and LNA are all 0.0000, which is less than 0.01, therefore, the partial regression coefficients of ROA, EPS and LNA are significantly not zero. Consequently, financial index can effectively explain Linear Variation of MVAPC.

Combining the above research results, based on EVA indexes, this paper established.

6 Analysis of Explanatory Power to Corporate Value by the Comprehensive Index System

The previous analysis results show that the financial index system and EVA-based index system both has some Explanatory power to corporate value. EVA-based index system has higher explanatory power in explaining corporate value change than financial index system, but financial index system still has some Explanatory power

to corporate value. We should not completely give up financial index system in evaluating corporate value. Therefore, the paper set model 3 to comprehensively explain and analyze corporate value, the results are given in Table 6.

$$MVAPC = \beta_0 + \beta_1 EVAPS + \beta_2 COC + \beta_3 SPREAD + \beta_4 LNC + \beta_5 ROA + \beta_6 EPS + \varepsilon \quad (3)$$

The model adopts the LNC rather than LNA, and eliminates ROA which did not pass the verification in the previous Single-element Regression analysis.

Table 6. Multiple regression analysis results (1) of the comprehensive index system

	Coefficients	standard error	t Stat	P-value	VIF
Intercept	46.6877	22.0404	2.1183	0.0351	
EVAPS	-0.4043	0.7910	-0.5112	0.6097	2.144
COC	16.3729	4.6167	3.5465	0.0005	7.2809
SPREAD	18.6179	2.2989	8.0987	0.0000	2.839
LNC	-2.0676	1.0615	-1.9478	0.0525	1.704
ROA	14.8253	28.8987	0.5130	0.0608	1.183
EPS	-2.4751	1.9040	-1.2999	0.1948	2.004

$$R^2=0.4563 \quad \text{Adjusted } R^2=0.4324 \quad F=19.5069 \quad P=0.0000$$

As we can see from Table 6, the regression equation was highly significant. According to regression analysis results, some multicollinearity is existed among the variables. Several independent variables' regression coefficients are not significant. In order to further test the model's collinearity, the paper makes the collinearity diagnostics analysis to the model. The analysis results are shown in Table 7.

Table 7. Collinearity diagnostics analysis results

Collinearity Diagnostics										
Model	Dimension	Eigen value	Condition Index	Variance Proportions						
				(Constant)	eva	ROA	EPS	LNC	SPREAD	COC
1	1	4.326	1.000	.00	.01	.01	.01	.00	.01	.00
	2	1.387	1.766	.00	.05	.01	.01	.00	.01	.13
	3	.629	2.622	.00	.06	.00	.11	.00	.16	.00
	4	.317	3.696	.00	.13	.79	.08	.00	.00	.04
	5	.205	4.596	.00	.74	.18	.01	.00	.02	.44
	6	.136	5.640	.00	.01	.01	.77	.00	.80	.37
	7	.001	72.541	1.00	.00	.00	.01	1.00	.01	.01

A. Dependent Variable: MVA

As we can see from Table 7, the variance proportions of the fifth dimension to EVAPS and COC is 74% and 44% respectively, the variance proportions of the sixth dimension to EVAPS and COC is 77% and 38% respectively, and the Condition Index are all significant, especially the last condition index, which is 72.541, higher than 10, that shows that has some collinearity. The significance test results to the model are given in Table 8.

Table 8. Multiple regression analysis results (2) of the comprehensive index system

	df	SS	MS	F	P
Regression analysis	6.0000	24305.6277	4050.9379	19.5069	0.0000
Residual error	253.0000	52539.6518	207.6666		
Total	259.0000	76845.2795			

As we can see from Table 8, $F=19.5069$, $P=0.000$, when the level of significance is 0.01, $P<0.01$, linear relationship between independent variables and dependant variable is significant, a linear model can be established to express the linear relationship between MVAPC and above six index.

According to adjusted R^2 , the Regression Model which includes EVA-based index variables and financial index variables has higher explanatory power than the Regression Model which only includes financial index variables. The explanatory power of regression model 3 is respectively higher than model 1 and model 2 (0.4324-0.3817) 0.0507 and (0.4324-0.2008) 0.2316. Therefore, the author believes that the comprehensive index system which includes EVA-based and traditional financial index has higher explanatory power to corporate value.

7 Conclusions

From the analytical result on the 2006-2008 data of the listed companies we can find that both EVA-based index system and traditional financial index system have some explanatory power to corporate value. Although EVA-based index system has higher Explanatory power to corporate value than traditional financial index system, EVA-based indexes cannot totally replace financial indexes. Therefore, the comprehensive index system including EVA-based indexes and traditional financial indexes has higher explanatory power to corporate value.

References

1. Wang, X., Cong, H., Ouyang, L.: What Explains Corporate Value: EVA or Financial Index. *Economic Science* (2), 98–106 (2003)
2. Zhang, L., Deng, X.: The Empirical Study of Explanatory Power to Stock Return by EVA and MVA. *Inquiry into Economic Issues* (6), 44–47 (2004)
3. Xiong, S.: The Empirical Study of the Factors Effecting the Relation between Stock Return and Accounting Earnings. [Master Degree Paper]. Zhejiang University college of Economics (2008)
4. Zhuo, J.: The Correlation Studies of EVA and Corporate Value. [Master Degree Paper]. Yangzhou University (2008)

Study of the Impact of Legal Protection of Investors on the Cash Dividend Policy

Fulian Shi¹, Jing Guo², and Ran Li¹

¹ School of Economics and Management, North China Electric Power University,
Beijing, China
sf18290@sina.com

² School of Economics and Business Administration, Zhejiang Sci-tech University,
Hangzhou, Zhejiang Province, China

Abstract. This paper select both listing in the mainland A-share market and Hong Kong H-share market in 2007, 44, 2008, 50, 2009, 53 companies as samples to study the impact of legal protection of investors on cash dividend policy of A and H share double listed companies. The result shows that the impact of legal protection of investors on cash dividend policy of A and H share double listed companies is significant, which verified the result model of legal protection and dividend policy, and different degrees of legal protection lead to different cash dividends policy between two places.

Keywords: A and H share double listed companies, cash dividend policy, legal protection of investors.

1 Introduction

Although different accounting standards, accounting policies and methods, accounting recognition and measurement, accounting disclosure requirements of the mainland and HK produce different calculation results, which leads to different conclusions of cash dividend policy of A and H share double listed companies (Hereinafter referred to as "dual listed company"), what really impact cash dividend distribution of the same company listed in two places is just the external environment of the two places, different legal systems, different investment opportunities, different culture and other factors. This paper will mainly research the impact of legal protection of investors to cash dividend policy of A and H share double listed companies (hereinafter referred to as 'dual listed company').

2 Research Design and Assumptions

This paper chose financial data of the dual listed companies from 2007 to 2009 as samples, use logistic regression and multiple regression method to study the relationship between legal protection of investors, legal enforcement efficiency and cash dividend policy.

The impact of legal protection of investors on cash dividend policy is based primarily on agency theory, which is divided into two models: substitute model and outcome model. The substitute model argues that cash dividend is a substitute of legal protection. When legal protection of minority shareholders is inefficient, the companies more likely to pay higher cash dividends. Otherwise, the less cash dividends will be paid. Outcome Model argues that cash dividend is the outcome of effective legal protection of minority shareholders. Under an effective system of legal protection, minority shareholders can make use of their powers under the law to obtain more cash dividends.

According to the outcome model of legal protection of investors and dividend policy, this paper proposed hypothesis 1.

Hypothesis 1: In case that other conditions are equal, if the outcome model hypothesis of legal protection of investors and dividend policy comes into existence, the higher the level of legal protection of investors, the higher the possibility and level of cash dividends payment.

According to the substitute model of legal protection of investors and dividend policy, this paper proposed hypothesis 2.

Hypothesis 2: In case that other conditions are equal, if the substitute model hypothesis of dividend policy and legal protection of investors comes into existence, the higher the level of legal protection of investors, the lower the possibility and level of cash dividends payment.

According to the outcome model of law enforcement efficiency and dividend policy model, this paper proposed hypothesis 3.

Hypothesis 3: In case that other conditions are equal, if the outcome model hypothesis of dividend policy and law enforcement efficiency comes into existence, the higher the level of law enforcement efficiency of the legal protection of investors, the higher the possibility and level of cash dividends payment.

According to the substitute model of law enforcement efficiency and dividend policy model, this paper proposed hypothesis 4.

Hypothesis 4: In case that other conditions are equal, if the substitute model hypothesis of dividend policy and law enforcement efficiency comes into existence, the higher the level of law enforcement efficiency of the legal protection of investors, the lower the possibility and level of cash dividends payment.

3 Variables Design and Model Building

3.1 Substitution Variable of Legal Protection of Investors

Legal Protection Index of Investors. This paper adopts protection index of property rights in the international equity index reports of Reputex (a rating and research firm) as the substitution variable of legal protection of investors. As the calculation of protection index of property rights is based on the data obtained from previous year, the study data of 2007-2009 in this paper come from the data of 2008-2010. The relevant data are shown in Table 1.

Table 1. 2008-2010 protection index of property rights

	2008	2009	2010
Mainland China	5.0	4.7	5.1
Hong Kong	7.7	7.3	7.5

Law Enforcement Efficiency Index. The efficiency substitution variable of legal protection of investors is the law enforcement efficiency index. The relevant data are shown in Table 2.

Table 2. 2007-2009 law enforcement efficiency index

	2007	2008	2009
Mainland China	-0.45	-0.33	-0.35
Hong Kong	1.552	1.521	1.491

3.2 Variable Selection

This paper adopts the cash dividend per share to present level of cash dividend payments, and whether to pay cash dividends to present probability of cash dividends payment. For example, payment of cash dividends will be recorded as 1, otherwise 0. The variables, significance and data sources are shown in Table 3.

Table 3. The list of name, significance and data source of research variables

Name	Symbol	Significance	Data source	Literature
Legal protection index of investors	IPRI	The higher the value of index, the higher the lever of legal protection of investor	RepuTex (a rating and research firm) International Property Rights Index – IPRI	LaPorta etal. (2000)
Law enforcement efficiency index	LAW EFF	The higher the value of index, the higher the law enforcement efficiency	World Bank website http://info.worldbank.org/governance/wgi/index.asp	FidnucJanaP, Mareus Jacob (2008)

3.3 Research Model

The purpose that this paper establishes the multiple regression model is to study the impact of legal protection of investors on the cash dividend policy of A and H share Double listed companies. See model 1 and model 2.

$$\Pr(cddum=1) = \text{logistic}(\alpha_0 + \alpha_1 IPRI + \alpha_2 LAWEFF + \mu) \quad (1)$$

$$Y = \beta_0 + \beta_1 IPRI + \beta_2 LAWEFF + \varepsilon \quad (2)$$

IPRI represents legal protection index of investors, LAWEFF represents law enforcement efficiency index, cddum represents whether a company paid cash dividends, for example, if the company paid cash dividends, we recorded it as 1, otherwise 0. Y stands for the level of cash dividends per share of A and H share double listed companies.

4 Empirical Research Results

4.1 The Impact of Legal Protection of Investors on Whether a Dual listed Company to Pay Cash Dividends

The result of Logistic model classification is shown in table 4.

Table 4. Logistic model classification table

Observed		Predicted		
		Whether to pay cash dividend		Percentage correction
		0.00	1.00	
Whether to pay cash dividend	0.00	62	26	70.5
	1.00	0	253	100.0
Total percentage		--	--	92.4
The cut value is 0.500				

As can be seen from table 4, Model is more significant under 5% of significance lever. From classification table, in case of classifying the companies of non-payment of dividends, the correct classification is 62, error classification is 26. In case of classifying the companies that cash dividends have paid, the correct classification is 253, the errors classification is 0. Overall discrimination rate of Logistic model is 92.4%, so this model is proved to be highly reliable.

The result of Logistic model regression coefficient analysis is shown in table 5.

Table 5. Logistic model regression coefficient analysis

	B	S.E	Sig.	Exp(B)
IPRI	0.138	0.135	0.007	1.148
LAWEFF	0.256	0.149	0.005	1.292
constant	0.981	0.142	0.000	2.667

As we can see from table 5, the impact of legal protection of investors on cash dividend is more prominent. The coefficient of IPRI is 0.138, the value of sig is 0.007 <0.05. The coefficient of LAWEFF is 0.256, the value of sig is 0.005 <0.05.

The result of Logistic model regression coefficient analysis indicates that the impact of legal protection of investors on whether dual listed company to pay cash dividends is more prominent, and is positively correlated, which is consistent with the hypothesis 1 of outcome model. That is, the higher the level of legal protection of investors, the higher the possibility of the payment of cash dividends. As all Hong Kong’s three consecutive years result of Legal protection index of investors and law enforcement efficiency index are larger than that of the mainland, it reflects the system of legal protection of investors in Hong Kong is sounder than the system of the mainland, and that management of security company are more restrictive and burdensome. Therefore, it results in that the probability of cash dividends payment in Hong Kong is larger than the probability in mainland, thus causing different cash dividend policy in the two places.

4.2 The Impact of Legal Protection of Investors on Cash Dividend Per Share

The result of variance analysis of the multiple regression model is shown in Table 6.

Table 6. Variance analysis table

R square	Adjusted square	R	Standard error of estimate	F statistic	SIG	Durbin-Watson
0.706	0.703		0.15633	25.06	0.00	2.066

In table 6, R square is 70.6%, showing that the regression model has a certain goodness of fit. DW statistic is 2.066, indicating that there is no first-order residual autocorrelation. F statistic is 25.06 and exact p-value is less than 5%, reflecting that the model has a good predicting ability.

The result of regression model coefficient analysis is shown in Table 7.

Table 7. Regression model coefficient analysis

	B	Standard error	t	Sig.
(Constant)	0.128	0.010	--	--
IPRI	0.131	0.009	10.418	0.007
LAWEFF	0.235	0.007	9.512	0.002

As we can see from table 7, coefficient of IPRI is 0.131, the value of sig is 0.007 <0.05, coefficient of LAWEFF is 0.256, the value of sig is 0.005 <0.05. Therefore, the policy of cash dividends is positive correlated with legal protection of investors. The result of Logistic model regression coefficient analysis indicates that the impact of legal protection of investors on whether a dual listed company to pay the cash dividend is more prominent, and is positively correlated, which is consistent with the hypothesis 1of outcome model. That is, the higher the level of legal protection of investors, the higher the possibility of cash dividends payment. As the Hong Kong

legal system is greatly influenced by the West, the Western countries pay more attention to protect interests of investors, protection system is more perfect. Thus, the cash dividends payment level and intensity of dual listed companies in Hong Kong is higher than that in the mainland, resulting in different cash dividend policy between the two places.

5 Conclusion

Through the study of this paper, we found that legal protection of investors affects the cash dividends policy of dual listed company significantly and verify the outcome model of legal protection of investors and dividend policy. The cash dividend payment ratio and the cash dividend payment level of Dual listed companies are significantly higher than the mainland A-share listed companies. Moreover, the cash dividend payment level of H-share is higher than that of A-share. Therefore, the distribution tendency and distribution intensity of the dual listed companies are all stronger than mainland A-share listed companies.

References

1. Fama, E., French, K.: Disappearing Dividends: Changing Firm Characteristics or Lower Propensity to Pay? *Journal of Financial Economics* 60, 3–43 (2001)
2. Smith Jr., C.W., Watts, R.L.: The Investment Opportunity Set and Corporate Financing, Dividend and Compensation Policies. *Journal of Financial Economics* (32), 263–292 (1992)
3. Kallapur, S.: The Investment Opportunity Set: Determinants, Consequences and Measurement. *Managerial Finance* (27), 3–15 (2001)

Design of Greenhouse Environment Wireless Monitoring System Based on ZigBee

Hui Wang¹, Xue-ren Dong^{*}, Yu-zhen Ma², Xiao-wei Yang², and Feng-nan Liu²

School of Mechanical Engineering, University of Jinan, Jinan 250022, China
kjcdxr@ujn.edu.cn

Abstract. In the greenhouse environmental monitoring, the wired sensor networks have some problems, for example, complex wiring, inflexible sensor location, cable aging and corrosion and so on. To solve the above problems, we use ZigBee technology to build a wireless sensor network for monitoring temperature, humidity, light intensity, carbon dioxide concentration. And each node is low-power design. Based on the Modbus protocol, we built RS-485 bus to achieve the communication between a number of greenhouse sensor networks and upper computer (PC). The system has advantages such as flexible sensors placement, low power consumption, easy installation maintenance and expansion, low cost, strong practicability.

Keywords: ZigBee, wireless sensor networks, RS485 bus, Visual Basic 6.0.

1 Introduction

Greenhouse cultivation techniques let agriculture break down geographical, natural environment and other factors' constraints; it has great significance for agricultural production. Greenhouse cultivation environment such as temperature, humidity, carbon dioxide concentration, light intensity is an important factor influencing crop, so a good environmental monitoring and control of greenhouse is an important measure to ensure that greenhouse production[1]. The wired sensor networks have some problems, for example, complex wiring, inflexible sensor location, cable aging and corrosion and so on. And maintenance is difficult[2-3]. The greenhouse environment wireless monitoring network was designed based on ZigBee technology. Sensor nodes and the network coordinator node are low-power design. The network coordinators communicate with the host computer in the monitoring center via RS485 bus.

2 Overall System Design

Wireless monitoring system of the greenhouse environment consists of wireless sensor nodes and the network coordinator nodes located in the greenhouse.

* Corresponding author. Tel.: +86 13869182197.

The network coordinator nodes of greenhouses connect to the host computer in the control room by the RS-485 bus. Managers can view real-time environmental parameters of greenhouses by the PC. Taking into account the size of the greenhouse within the communication range of wireless sensor nodes, this wireless network system only sets up a network coordinator node (FFD) and several sensor nodes (RFD), no router nodes. Considering the wireless network coverage, power and reliability, choose a star topology[4].

According to the characteristics and requests of the greenhouse environmental monitoring, we build a wireless sensor network includes a coordinator node and six wireless sensor nodes. The network coordinator nodes and wireless sensor nodes are built based on the CC2430, and the network coordinator placed among the top of greenhouse. Coordinator node is responsible for establishing and managing the network, and communicating with the host computer through RS485 bus. Sensor node is responsible for data acquisition and data transmission to the coordinator node, and receiving command of the host computer coming through the coordinator node.

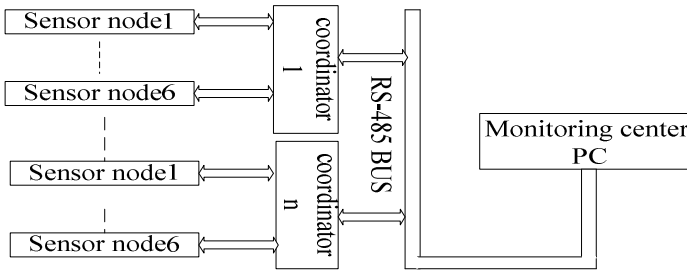


Fig. 1. Overall system plan

3 System Hardware Design

3.1 Sensor Node Hardware Design

Sensor nodes of wireless sensor networks typically contain the sensor unit, processor unit, the wireless communication unit and power unit[5]. CC2430 ,the chip Chipcon Introduces, is used to implement the embedded ZigBee applications, uses an enhanced 8051 MCU, 32/64/128 KB flash memory, 8KB SRAM and other high-performance modules, and contains the ZigBee protocol stack, integrated RF transceiver which support 2.4GHz IEEE 802.15.4/ZigBee protocol. The chip also includes analog-digital converter, 3 timers, AES128 coprocessor, watchdog timer, the sleep mode timer of 32 kHz crystal oscillator, power-on reset circuit, power failure detection circuit, and 21 programmable I/O pins.

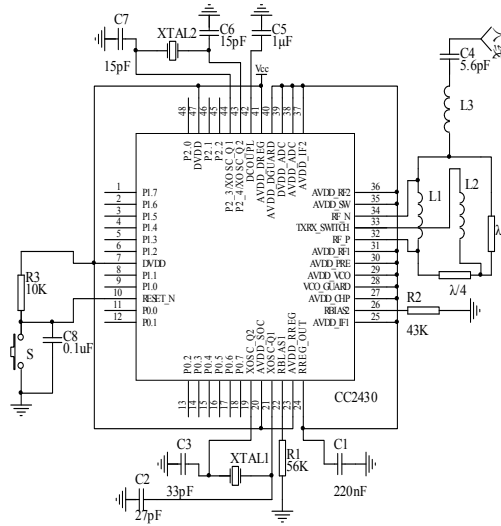


Fig. 2. Basic transceiver circuit of CC2430

Using CC2430 the basic transceiver circuit was set up (including the reset circuit, crystal oscillator clock circuit, the RF input/output matching circuit and microcontroller interface circuit). Shown in Fig.2.

3.1.1 Temperature and Humidity Sensors and Interface Circuits

Temperature and humidity sensor uses SHT10. SHT10 is the new temperature and humidity sensor based on CMOSens™ technology. The sensor combine CMOS chip technology with sensor technology, and temperature and humidity sensors, signal amplifiers, A/D conversion are integrated in a chip. The working voltage is 2.4-5.5V. Measuring humidity accuracy is ±4.5%RH, measuring temperature accuracy is ±0.5°C when it's 25°C. SHT10 adopt two serial lines for data communication with the processor. It has characters like good stability, high accuracy and low energy consumption. Interface circuit shown in Fig.3.

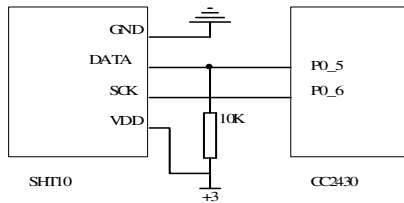


Fig. 3. Interface circuit of SHT10 and the CC2430

3.1.2 Light Intensity Sensor and Interface Circuit

Light intensity sensor uses TSL2561. TSL2561 chip is a light intensity digital conversion chip which has characters like high-speed, low power, wide range, programmable and flexible configuration. The chip offers 16-bit linear output, interrupt capability, high/low interrupt thresholds adjustable, and it integrates integrating A/D converter. Using the digital signal output, it has a strong anti-interference capability than comparable chips. Interface circuit shown in Fig.4.

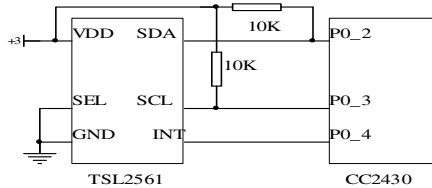


Fig. 4. Interface circuit of TSL2561 and the CC2430

3.1.3 Carbon Dioxide Sensor and Interface Circuit

Carbon dioxide sensor uses MH-410D. MH-410D is an infrared gas sensor with 5 pins, 2 pins for the UART pins can communicate directly with the meter circuit. It uses non-dispersive infrared (NDIR) principle to detect CO₂ present in the air, with good selectivity, non-oxygen-dependent, stable performance, long life, and has EEPROM memory. While providing high accuracy, it has smaller size and lower power consumption. It is widely used in the CO₂ detection needed in all areas. Circuit connection is that the TXD interface of MH-410D is connected to the P1_7 of CC2430, the RXD interface is connected to P1_6.

3.2 Network Coordinator Node Hardware Design

The sensor unit of coordinator node adopts the same design to sensor node. Based on the sensor node hardware, the RS-485 interface is built by using MAX485 chip. MAX485 obtained power by the RS485 bus. The P1_5, P1_3 and P1_4 interfaces of CC2430 are connect to the RO, RE, DI interfaces of MAX485 respectively. The RE and DE interface of MAX485 are also connected together.

3.3 PC RS-485/232 Converter Design

The 9-pin serial interface of PC is RS-232 interface. In order to achieve communications between host and network coordinators of greenhouses through RS-485 bus, using MAX232 and MAX485 chip, RS-485 and RS-232 conversion circuit is designed as follows.

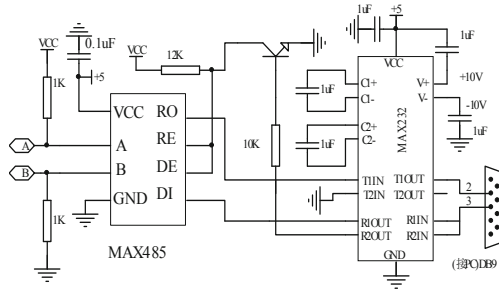


Fig. 5. RS-485/232 converter circuit

3.4 Power Module Design

The system uses two 1.5V rechargeable batteries to power the CC2430, SHT10 and TSL2561. Using the TPS60130 DC-DC regulator to convert the 3V battery voltage to 5V voltage, it supplies power to the MH-410D. Rechargeable battery, compared to solar-powered, is conducive to maintaining a small node size, protected from the weather and lighting effects. When the battery comes into the low power state, the low battery alarm signal can be issued to remind staff to recharge batteries. It's environmentally friendly and easy maintenance[6].

4 Software Design

4.1 Sensor Node Programming

Sensor nodes need to complete the work: the sensor data acquisition and data transmission to the network coordinator node; received command from the network coordinator node and execute the operation corresponding command. Because it is battery powered, it needs to ensure low power consumption.

After sensor node power up, it initializes the module within the sensor node first, and configures the module. Then the sensor node sends a network request to the coordinator. After receiving the request response, the sensor node sends a connection request to the coordinator node. If the connection request response is correct, the network is built successfully, and then the coordinator assigns a unique ID to every sensor node. The sensor node ID is associated with the MAC address and gets registration. Otherwise fail. Sensor node collects data when it receives the acquisition command. When sensor node doesn't collect data, it enter sleep mode, leaving only the MCU timer, interrupt and wireless modules, and others power down. When wireless module receives data, sensor nodes wake up. After node receives a data packet, it compares the packet header ID with their ID are the same or not, the same is received, otherwise discarded. Sensor node sends its own MAC address to the coordinator node. After receiving confirmation of the coordinator, the sensor node collects data and sends it to the coordinator. When it's complete, the sensor node enter sleep mode.

In the IAR Embedded Workbench for MCS-51 Evaluation environment, we use C-language to develop the software of sensor node and coordinator node. The main program flow chart of sensor node is shown in Fig.6.

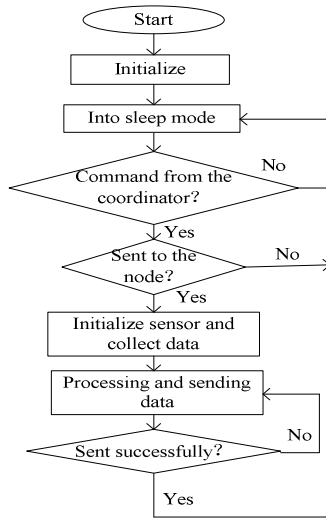


Fig. 6. Main program flow chart of sensor node

4.2 Network Coordinator Node Programming

Coordinator node is the center of the greenhouse wireless network. Its main function contains organizing wireless networks, communicating with sensor nodes, communicating with the host computer and checking the sensor nodes are normal or not.

Coordinator initializes the hardware configuration, network configuration and protocol stack, and then it enters into network monitoring state. After the coordinator receives a network request from the sensor node, it assigns addresses to each node and stored in the node list, and then sent to each network node to confirm the information, establish a connection. Coordinator receives the MAC address of the sensor nodes, compared with the stored address, and checks sensor nodes joined the network or not. Coordinator receives data from sensor nodes through the stack, and parse data packet, extracts the obtained data information. The information is sent to the host via RS-485 bus. The coordinator receive commands from the host computer through the MAX485 RS-485 bus interface, and send commands to each node in the wireless network. RS-485 in the protocol stack is modified to interrupt.

By the way to design and change the application of ZigBee protocol stack, the coordinator node and sensor node can achieve functions, such as sending and receiving data, organizing network. Software flow chart of coordinator is shown in Figure 7.

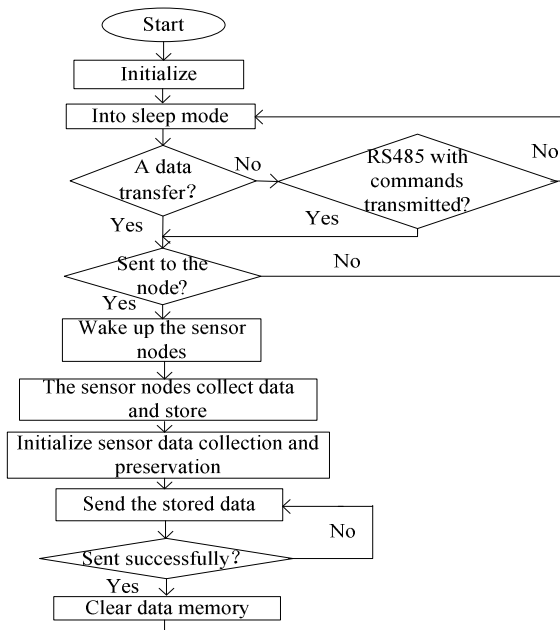


Fig. 7. Main program flow chart of coordinator node

4.3 PC Software Design

PC software includes man-machine interface, communications module, the data reception and transmission, data processing and display, Access database operation.

PC sends commands to the network coordinators of the greenhouses via RS-485 bus. Coordinator uniformly wakes up wireless sensors by wireless network, so you can ensure that the entire system time synchronization. If the host computer command is absent, the wireless sensor networks go to sleep, minimizing power consumption. Host computer can periodically check the parameters of greenhouses environment, and the staff can also always check the parameters of the greenhouse environment.

A serial communication control MSComm is provided in Visual Basic 6.0 controls toolbox. It provides all the details to be used in the top development of serial communication. By using MSComm control, it's easy to achieve that the serial port initialization, data transceiver. The communication program of RS-485 bus based on Modbus RTU protocol is written in VB. First create an Access database and then connect to the database using VB. The data of environmental parameters received from the greenhouse is stored in the Access database to facilitate management.

5 Experiment and Analysis

Six sensor nodes are uniformly distributed in the laboratory that 70m long 10m wide uniform to experiment. And the network coordinator node is placed in the middle of

the laboratory top to form a star network. Network coordinator nodes of two laboratories are attached to the RS-485 bus, and system testing.

After testing, data transmission is accurate, and there is no loss phenomenon. The measured data of each node is very close to the actual value. Errors are within the allowable range. Moreover, the installation and maintenance is convenient.

6 Conclusions

The system which combines ZigBee wireless sensor networks with RS-485 bus is used in greenhouses environmental monitoring system in greenhouse cultivation base. By using wireless sensor networks, the factors of greenhouse, such as temperature and humidity, light intensity, carbon dioxide, are collected. The hardware and software of the coordinator node and sensor node both are designed completely, and the software of PC is also prepared. The RS-485 bus based on Modbus protocol is constructed, and the RS-485/232 converter interface is also designed. The system has sensor arrangement of flexible, simple structure, low power consumption, low cost, easy installation and maintenance, easy expansion characteristics. The system can be expanded based on the actual situation, to meet needs of the greenhouse environment control center.

References

1. Li, Y.-H., Ji, G.-F., Han, J.-Y.: Application of the Wireless Sensor Network in Environment Monitoring System of Greenhouse. *Process Automation Instrumentation* 31(10), 61–62 (2010)
2. Jiang, R.-X., Lin, K.-Y., Wu, J.-H., Yang, X.-J.: Study & Design on Monitoring and Controlling System for Greenhouse Group Based on ZigBee. *Journal of Shanghai Jiaotong University(Agricultural Science)* 26(5), 440–444 (2008)
3. Qiao, X., Zhang, X., Wang, C., Ren, D., He, X.: Application of the wireless sensor networks in agriculture. *Transactions of The Chinese Society of Agricultural Engineering* 21(2), 232–234 (2005)
4. Zhou D.-H., He C.-A.: Introduction to Fieldbus control technology development and application examples. China Electric Power Press. 245-257,(2010)
5. Yu, H.-Y.: Wireless sensor network theory, technology and implementation, pp. 1–18. National Defence Industry Press (2008)
6. Cai, B., Bi, Q.-S., Li, F.-C., Wang, D., Yang, Y., Yuan, C.: Research and Design of Agricultural Environment Monitoring System Based on ZigBee Wireless Sensor Network. *Acta Agriculturae Jiangxi* 22(11), 153–156 (2010)

A Novel Method to Measure the Projectiles Velocity and Position of Twin-Tube Volleyed Weapons with Multi-screen Target

Yugui Song, Wenbo Wang, and Guohui Wang

School of Optoelectronic Engineering, Xi'an Technological University
Xi'an 710032, China

petersong96@yahoo.com.cn, ww050111@126.com, booler@126.com

Abstract. The velocity and position measurement of projectile is two important parameters in ballistic research. The multi-screen target is one approach to obtain the two items. In this paper, we present a novel method to measure the projectile velocity and position of twin-tube volleyed weapons with the multi-screen target and use Matlab software to take a simulation test. The designed system has a new structure and shows the capability of precisely detecting the velocity and position of two projectiles at the same time.

Keywords: multi-screen, projectiles velocity, simulation testing, target coordinates.

1 Introduction

The projectile speed and density are one mainly technical specification when the gun, artillery, bomb manufacturers are in their product inspection, but the basis of shooting density of projectile is the projectile target coordinate measurement[1-2].

Domestic target range and abroad has a high enthusiasm to realize the automatic measurement of the target coordinates, which could be applied in place of the board target and net target, those are in backward technology, poor efficiency and low precision.

There are many non-contact test methods to measure the velocity and position, such as the acoustic target, CCD target, four or six screens target and the net target. The acoustic target exists partial shaft error and edge error, it is only applied to the small supersonic projectile of close distance; CCD intersection target technology is a non-contact measurement method which is developing rapidly in recent years. It has characteristics of simple structure, powerful performance and a higher automation degree, but it has a lower capture rate and accuracy problems; Four sky screen target not only can measure the velocity [3], but also obtain the coordinates. However, with the development of science and weapon, sometimes it needs to accurately measure the azimuth and elevation angle of projectiles. Then the six sky-screen target solves the problem perfectly, but it can't realize the measurement of twin-tube volleyed weapons.

This paper based on the vertical target, increased two screens in the original of six sky-screen, and designed a kind of structure to realize the projectile velocity and

position of twin-tube volleyed weapons. It takes two similar structures to constitute multi-screens array, each screen of the angle and distance has different parameters. When they are flying via the screen, data receiver instrument records the moment information and it will count up the coordinates and other parameters according to the identification method. Finally, the results output and display to the computer terminal.

2 The System Structure and Operating Principles

2.1 System Structure

The detection device system has two parts (T_I and T_{II}) which are made up of two four-screens array. The eight screens are arranged in the trajectory direction[4-5]. Four screens detection components are formed by slit diaphragms, optical lenses and a phototube. The detection component of screen will fix in the same cabinet, the lens axis lay in the same plane, but it tilts at a relative angle. The reference of the system is defined by each of the two screen's adjacent angles. The symmetric center of screens S_1 and S_2 is at the YOZ plane with the angle θ , and the intersection is lying at the coordinate origin O , S_1 rotates the clockwise angle γ by itself. S_3 is perpendicular to the XOZ plane which rotates the clockwise angle ϕ and with the distance d to the origin O , the distance between two target is l . The relation is shown in Figure 1.

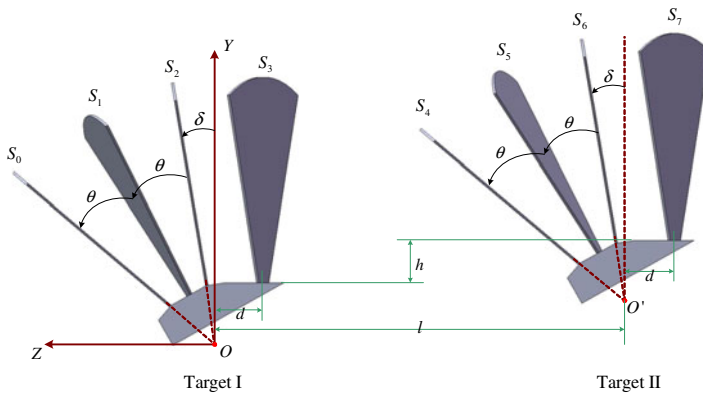


Fig. 1. Geometry relation between target I and II

2.2 Operating Principle

The sky-screen is an instrument to measure the parameter of flying projectile in the range[6-7]. It has a certain thickness screen. It supposes that the general space equation of the screen in conditions of the screen's thickness is neglected. Their relation can be expressed by formula (1).

$$\vec{n}_i \cdot [X, Y, Z]^T + D_i = 0, (i = 0, 1, \dots, 7) \tag{1}$$

The screens $S_0 \sim S_7$ correspond normal vector which is begin from \bar{n}_0 to \bar{n}_7 , after the corresponding mathematical deduction, we can express the normal vector of each screen as formula (2).

$$\begin{cases} \bar{n}_0 = [0, -\sin(\delta + 2\theta), \cos(\delta + 2\theta)]^T \\ \bar{n}_1 = [\sin(\gamma), -\sin(\delta + \theta)\cos(\gamma), \cos(\delta + \theta)\cos(\gamma)]^T \\ \bar{n}_2 = [0, -\sin(\delta), \cos(\delta)]^T \\ \bar{n}_3 = [-\sin(\phi), 0, \cos(\phi)]^T \\ \bar{n}_4 = [0, -\sin(\delta + 2\theta), \cos(\delta + 2\theta)]^T \\ \bar{n}_5 = [-\sin(\gamma), -\sin(\delta + \theta)\cos(\gamma), \cos(\delta + \theta)\cos(\gamma)]^T \\ \bar{n}_6 = [0, -\sin(\delta), \cos(\delta)]^T \\ \bar{n}_7 = [-\sin(\phi), 0, \cos(\phi)]^T \end{cases} \quad (2)$$

Then we take the geometry relation between target I and II into the above conditions to get the parameter $D(i = 1 \sim 7)$.

If the velocity of the projectile is $\bar{V} = [V_x, V_y, V_z]^T$, the coordinates of the screen is $P = [x, y, z]$, and the moment is t_0 , supposing that t_0 is time reference point of "0". When the projectile is reaching the screen S_i , it brings in the moments t_i ($i = 1, 2, \dots, 7$). Then taking the screen expression into the linear equation $AX = B$, and their relation can be expressed by formula (3-5).

$$\begin{bmatrix} 0 & -\sin(\delta + 2\theta) & \cos(\delta + 2\theta) & 0 & 0 & 0 \\ \sin(\gamma) & -\sin(\delta + \theta)\cos(\gamma) & \cos(\delta + \theta)\cos(\gamma) & \sin(\gamma)t_1 & -\sin(\delta + \theta)\cos(\gamma)t_1 & \cos(\delta + \theta)\cos(\gamma)t_1 \\ 0 & -\sin(\delta) & \cos(\delta) & 0 & -\sin(\delta)t_2 & \cos(\delta)t_2 \\ -\sin(\phi) & 0 & \cos(\phi) & -\sin(\phi)t_3 & 0 & \cos(\phi)t_3 \\ 0 & -\sin(\delta + 2\theta) & \cos(\delta + 2\theta) & 0 & -\sin(\delta + 2\theta)t_4 & \cos(\delta + 2\theta)t_4 \\ -\sin(\gamma) & -\sin(\delta + \theta)\cos(\gamma) & \cos(\delta + \theta)\cos(\gamma) & -\sin(\gamma)t_5 & -\sin(\delta + \theta)\cos(\gamma)t_5 & \cos(\delta + \theta)\cos(\gamma)t_5 \\ 0 & -\sin(\delta) & \cos(\delta) & 0 & -\sin(\delta)t_6 & \cos(\delta)t_6 \\ -\sin(\phi) & 0 & \cos(\phi) & -\sin(\phi)t_7 & 0 & \cos(\phi)t_7 \end{bmatrix} \quad (3)$$

$$X = [x, y, z, V_x, V_y, V_z]^T \quad (4)$$

$$B = \begin{bmatrix} 0 \\ 0 \\ 0 \\ -\cos(\phi)d \\ -\sin(\delta + 2\theta)h - \cos(\delta + 2\theta)l \\ -\sin(\delta + \theta)\cos(\gamma)h - \cos(\delta + \theta)\cos(\gamma)l \\ -\sin(\delta)h - \cos(\delta)l \\ -\cos(\phi)(d + l) \end{bmatrix} \quad (5)$$

According to the linear algebra equation $AX = B$, we take the parameter into to it and solving the proposed parameter $X = A^{-1}B$.

2.2.1 Single Objective Measurement

When the single projectile is crossing eight screens, it will generate eight trigger moments, and it can be worked out by using the normal vector and the unknown parameter[8]. Then we just need to build six screen equations to get the parameter. Because sky screen is made up of target I and II, it has 16 combinations through choosing six screens from eight. These 16 combinations by the results of the calculation should be exactly the same in theory.

2.2.2 Double Objective Measurement

As to the twin-tube volleyed weapons, we take the first screen as time zero. When the flying objects are passing through the screen, the moment of the screen S_i has an output t_{1i} and t_{2i} respectively($i = 1, 2, \dots, 7$). Then it arranges the moment with $2^7 = 128$ combinations. It includes the true moment $t_1 = \{0, t_{11}, t_{12}, t_{13}, t_{14}, t_{15}, t_{16}, t_{17}\}$
 $t_{128} = \{0, t_{21}, t_{22}, t_{23}, t_{24}, t_{25}, t_{26}, t_{27}\}$.

Every moment group has 16 combinations, the true moment corresponds 16 kinds of test result which should be the same in theory. However, other moments combinations, such as $t_2, t_3 \dots t_{126}, t_{127}$, can get different results with each single objective test which has 16 combinations. According to this rule, it is easy to realize the measurement of the twin-tube volleyed weapons.

3 Simulation and Analysis

3.1 Single Objective Simulation

To meet the practical engineering conditions, many time test results at t_i time obey the gaussian distribution $N(0, 0.000005^2)$ in the simulation[9]. It will comply the requirement of the actual instrument in the process of simulation with 1000 projectiles, while adding the mean of t_i with 0, and the RMS is $5\mu s$.

Projectiles reach the screen through a simulated test, and the following formula is $t_i (i = 1, 2, \dots, 7)$:

$$t_1 = \frac{\sin(\gamma)x - \sin(\delta + \theta)\cos(\gamma)y + \cos(\delta + \theta)\cos(\gamma)z}{-\sin(\gamma)V_x + \sin(\delta + \theta)\cos(\gamma)V_y - \cos(\delta + \theta)\cos(\gamma)V_z}$$

$$t_2 = \frac{-\sin(\delta)y + \cos(\delta)z}{\sin(\delta)V_y - \cos(\delta)V_z}$$

$$t_3 = \frac{-\sin(\phi)x + \cos(\phi)z + \cos(\phi)d}{\sin(\phi)V_x - \cos(\phi)V_z}$$

$$t_4 = \frac{-\sin(\delta + 2\theta)y + \cos(\delta + 2\theta)z + \sin(\delta + 2\theta)h + \cos(\delta + 2\theta)l}{\sin(\delta + 2\theta)V_y - \cos(\delta + 2\theta)V_z}$$

$$t_5 = \frac{-\sin(\gamma)x - \sin(\delta + \theta)\cos(\gamma)y + \cos(\delta + \theta)\cos(\gamma)z + \sin(\delta + \theta)\cos(\gamma)h + \cos(\delta + \theta)\cos(\gamma)l}{\sin(\gamma)V_x + \sin(\delta + \theta)\cos(\gamma)V_y - \cos(\delta + \theta)\cos(\gamma)V_z}$$

$$t_6 = \frac{-\sin(\delta)y + \cos(\delta)z + \sin(\delta)h + \cos(\delta)l}{\sin(\delta)V_y - \cos(\delta)V_z}$$

$$t_7 = \frac{-\sin(\phi)x + \cos(\phi)z + \cos(\phi)(d + l)}{\sin(\phi)V_x - \cos(\phi)V_z}$$

It also gives screen parameters $d = 0.1m$, $l = 5.0m$, $h = 0.1m$, $\delta = 1.0^\circ$, $\theta = 13.0^\circ$, $\gamma = 7.5^\circ$, $\phi = 20.0^\circ$. On the assumption that the projectile velocity is $X = -900m/s]^T$,the target position is $P_1 = [-1m, 4m, 2.0381m]$,simulation is measured by the time t_i of projectile S_i reaches the screen to calculate \vec{V} , X is in the linear equation $AX = B$.

3.2 Double Objective Simulation

It gives screen parameters $d = 0.1m$, $h = 0.1m$, $l = 5.0m$, $\delta = 1.0^\circ$, $\theta = 13.0^\circ$, $\gamma = 7.5^\circ$, $\phi = 20.0^\circ$.Supposing that the speed of the projectile 1 and 2 respectively is $\vec{V}_1 = [10m/s, 10m/s, -900m/s]^T$, $\vec{V}_2 = [15m/s, 25m/s, -950m/s]^T$, the target coordinates are $P_1 = [-1m, 4m, 2.0381m]$, $P_2 = [-2m, 9m, 4.5857m]$.We have to do a simulation testing to take the moments t_{1i} 、 t_{2i} to get V and P .

By using the calculation method, we can get the moment t_{1i} 、 t_{2i} ,and obtain the results of the twin-tube volleyed weapons with 16 combinations.

According to the corresponding decision rules, the combination of the $t = 1$ and $t = 128$ are the parameters we want. The flight vector and the position coordinates of the target are obtained respectively at the same time, it also can obtain the flying azimuth and elevation.

4 Conclusion

The measurement based on the sky screen has been successfully used impact coordinate between different calibres and a large spread range. The result demonstrates that it is not only accurately test single projectile or double barrels weapons, but also has the advantage of a simple principle and structure, low cost and even better optimization performance. With the development of modern weapon technology, varieties of new weapons emerge in endlessly. It has great impact on the existing measurement of projectile, and it shows a positive significance for the range test system.

Acknowledgments. This work is supported by the program of the Project Supported by National Natural Science Foundation of China (Program No. 61102144) and Natural Science Basic Research Plan in Shaanxi Province of China (Program No. 2011JQ8004). At the same time, this work is supported by Scientific Research

Program Funded by Shaanxi Provincial Education Department (Program No. 11JK0996) and the Program for Innovative Science and Research Team of Xi'an Technological University. We would like to thank the anonymous reviewers for their valuable and constructive comments that helped us improve this presentation.

References

1. Ni, J., Yang, L.: Measurement Principle for Two Kinds of Six-light-screen Array Composed by a Large Area Light Screen. *Opto-Electronic Engineering* 35(2), 7–11 (2008)
2. Gauthier, L.R., Drewry, D.G., Brunner, L.: Optical sensor and method for detecting projectile impact location and velocity vector (2005)
3. Lu, S.T., Yu, A.T., Chou, C.: Electro-optics target for position and speed measurement. *IEE Proceedings-A* 140(4) (July 1993)
4. Di, C., Wang, C.H.M., Kong, D.R.: Analysis of velocity measurement with single coil target based on wavelet transform. *Chinese Journal of Scientific Instrument* 24(5), 442–448 (2003)
5. Li, H.S., Lei, Z.Y.: Principle and analysis of high altitude projectile location measurement using multi-screen target method. *Chinese Journal of Scientific Instrument* 30(3), 621–625 (2009)
6. Gao, H., Jiang, M.: Across screen fire Precision measuring Principal and Application. *Journal of Xi'an Institute of Technology* 15(3), 242–245 (1995)
7. Wu, R., Hou, J., Lu, G.: Problems in the Development of SPTMB-1 Horizontal Sky Screen Target. *Opto-Electronic Technology* 14(3), 34–39 (1996)
8. Wang, T., Ni, J.: Working Principle and Application of Photoelectric Target. *Journal of Xi'an Institute of Technology* 17(1), 31–36 (1997)
9. Li, H.S., Lei, Z.Y., Wang, Z.M., et al.: A new type of firing accuracy measurement system for cross sky screen. *Electronics Optics & Control* 14(5), 153–154 (2007)

The Improvement on Lucene Text Analyzer

Wu Daiwen

Digital Media Art Lab, College of Media Engineering, Weinan Normal University,
Weinan Shanxi, 714000, China
wudaiwen@foxmail.com

Abstract. This paper extract the text from non-text documents. Then it indexes them by lucene. The experimental results show that it can greatly enhance retrieval adaptability by improving Lucene text parser.

Keywords: Full-Text Retrieval, Text Analyzing, Extract, Encapsulation.

1 Introduction

Lucene is an information retrieval API, users can develop a variety of full-text retrieval applications based on It. It is a full text retrieval engine architecture, providing a complete query engine, retrieval engine and text analysis engine. As an open source project, From its inception, the open source community caused great repercussions in Lucene, it not only can be used to construct specific full-text retrieval application, and can be integrated into a variety of system software for various full-text retrieval applications based on Web[1].

At the same time, Lucene is an open platform, allowing the user to extend its functions and API. The Lucene default only analysis and index HTML and TXT documents[2]. In this paper, through the introduction of other open-source tool for DOC, XLS, PPT and PDF document text extraction, so that Lucene can index DOC, XLS, PPT and PDF format of the documentation.

2 Overall Solve Train of Thought

According to the Lucene default only analysis and index HTML and TXT document shortcomings, firstly the paper used POI and PDFBox and other open source tools to extract the DOC, XLS, PPT and PDF document text. Then by using the Lucene index these extracted from the text, and encapsulated the extracted text to the Lucene Document object in a field. Of course, you can also extract other document information, such as file path, file name and the last modified time, then these information as an auxiliary field is added to the Lucene Document object. Eventually different format documents are encapsulated as Document object, the Document object can be written to the index file for later retrieval using.

3 Programming Implementation

The experimental code prepared by Java, the procedure used for other open source function package file as follows [3].

Lucene-core-3.0.2.jar, Lucene 's core API.

PDFBox-0.7.3.jar, used to operate the PDF document API.

Poi3.0.2.jar and tm-extractors.jar, Excel, Word and PPT for API document. Each function module detailed implementation code is as follows.

3.1 Word Text Extraction and Lucene Encapsulation

Word text extraction and Lucene package code as follows [4].

```
public static Document getWordDOC(File f){
    // extract the text of the DOC document
    String bodyText = null;
    try {
        FileInputStream is=new FileInputStream(f);
        WordExtractor extractor = null;
        extractor = new WordExtractor();
        bodyText = extractor.extractText(is);
    }
    catch (Exception e) {
        e.printStackTrace();
    }
    // Create a Lucene Document object, the field is added to the Document object.
    Document DOC = new Document();
    if ((bodyText != null) && (bodyText.trim().length() > 0)) {
        DOC.add(new Field("contents", bodyText,Field.Store.YES,
Field.Index.ANALYZED));
    }
    .....// Add additional fields to the Document object.
    return DOC;
}
```

3.2 Excel Text Extraction and Lucene Encapsulation

Excel text extraction and Lucene package code as follows [5].

```
public static Document getExcelDOC(File f){
    //extract the text of the Excel document
    String filepath = f.getPath();
    String bodyText = getExcelText(filepath);
    // Create a Lucene Document object, the field is added to the Document object.
    Document DOC = new Document();
    if ((bodyText != null) && (bodyText.trim().length() > 0)) {
        DOC.add(new Field("contents", bodyText,Field.Store.YES,
Field.Index.ANALYZED));
    }
}
```

```

.....// Add additional fields to the DOCument object.
return DOC;
}
private static String getExcelText(String filepath){
    String bodyText=null;
    try{
        ExcelReader er=new ExcelReader(filepath);
        String line=er.readLine();
        while(line!=null){
            bodyText+=line+"\r\n";
            line=er.readLine();
        }
        er.close();
    }catch(Exception e){
        e.printStackTrace();
    }
    return bodyText;
}

```

3.3 PowerPoint Text Extraction and Lucene Encapsulation

PowerPoint text extraction and Lucene package code as follows [6].

```

public static DOCument getPPTDOC(File f){
// extract the text of the PPT document
String filepath = f.getPath();
String bodyText=getPPTText(filepath);
// Create a Lucene DOCument object, the field is added to the DOCument object.
DOCument DOC = new DOCument();
if ((bodyText != null) && (bodyText.trim().length() > 0)) {
    DOC.add(new Field("contents", bodyText,Field.Store.YES,
Field.Index.ANALYZED));
}
.....// Add additional fields to the DOCument object.
return DOC;
}
private static String getPPTText(String PPTpath){
    StringBulder sb=new StringBulder();
    try {
        SlideShow PPT = new SlideShow(new HSLFSlideShow(PPTpath));
        Slide[] slides = PPT.getSlides();
        for (Slide each : slides) {
            TextRun[] textRuns = each.getTextRuns();
            for (int i=0 ;i< textRuns.length; i++ ) {
                sb.append(textRuns[i].getText());
                RichTextRun[] richTextRuns = textRuns[i].getRichTextRuns();
            }
        }
    }
}

```

```

    } catch (IOException e) {
        e.printStackTrace();
    }
    return sb.toString();
}

```

3.4 PDF Text Extraction and Lucene Package

PDF text extraction and Lucene package code as follows [7].

```

public static DOCUMENT getPDFDOC(File f){
// Read the text of the PDF document
PDFParser parser = new PDFParser(new FileInputStream(f));
parser.parse();
COSDOCUMENT cosDOC = parser.getDocument();
PDFTextStripper stripper = new PDFTextStripper();
String DOCText = stripper.getText(new PDDOCUMENT(cosDOC));
// Create a Lucene DOCUMENT object, the field is added to the DOCUMENT object.
DOCUMENT DOC = new DOCUMENT();
if((DOCText!=null)&&(!("").equals(DOCText)))
    DOC.add(new Field("contents", DOCText,Field.Store.YES,
Field.Index.ANALYZED));
.....// Add additional fields to the DOCUMENT object.
return DOC;
}

```

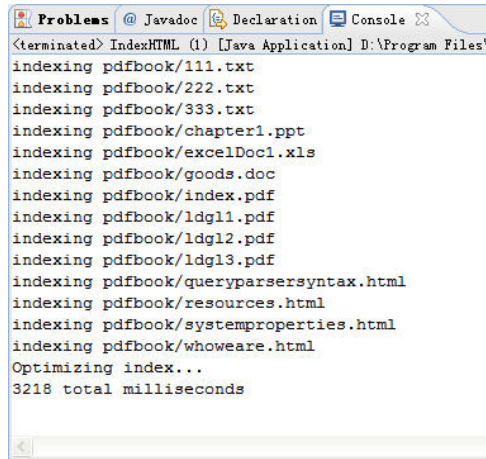
4 Experimental Analysis

4.1 Experiment Environment

The experiment is done by HP 520 notebook, Whose processor is Core Duo T2600 and memory is 2G. The running software is Eclipse.

4.2 Experiment Result

The program running results as shown in Figure 1, you can see from Figure 1, with the introduction of other open-source tool for DOC, XLS, PPT and PDF document text extraction, thus realizing the Lucene on multiple format document indexing. This improves the versatility of Lucene indexing and retrieval[8].



```
<terminated> IndexHTML (1) [Java Application] D:\Program Files\  
indexing pdfbook/111.txt  
indexing pdfbook/222.txt  
indexing pdfbook/333.txt  
indexing pdfbook/chapter1.ppt  
indexing pdfbook/excelDoc1.xls  
indexing pdfbook/goods.doc  
indexing pdfbook/index.pdf  
indexing pdfbook/ldgl1.pdf  
indexing pdfbook/ldgl2.pdf  
indexing pdfbook/ldgl3.pdf  
indexing pdfbook/queryparsersyntax.html  
indexing pdfbook/resources.html  
indexing pdfbook/systemproperties.html  
indexing pdfbook/whoware.html  
Optimizing index...  
3218 total milliseconds
```

Fig. 1. Running results of the Program

References

1. He, W., Xue, S., Kong, M., Yang, Z.: The design and Implementation of full-text retrieval engine based on Lucene. *Journal of Information* 09, 88–90 (2006)
2. Wang, X.: The development of search engine based on Lucene and nutch, vol. 08. People's Posts and Telecommunications Press, Beijing (2008)
3. Qiu, Z., Fu, T.: To develop its own search engine—Lucene 2.0+Heriterx, vol. 06. People's Posts and Telecommunications Press, Beijing (2007)
4. Wu, D., Guo, J.: The design and implementation of Full-Text Retrieval system in website based on Lucene. *Modern Electronic Technology* 03, 42–44 (2011)
5. He, L., Zhang, Z., Huang, S.: The design and implementation of OA full-text retrieval system based on Lucene. *New Technology about Library and Information Service* 11, 44–46 (2009)
6. Zhu, A., Huang, J.: The research and development of Full-text retrieval system model based on Lucene. *Journal of Jinan University(NATURAL SCIENCE EDITION)* 10, 504–506 (2009)
7. Wen, Y., Hu, G., Peng, S.: The full-text retrieval application research of books Based on Lucene. *Journal of Mianyang Normal University* 11, 88–90 (2010)
8. Li, Z., Yun, Q., Chen, S.: The application study of information retrieval technology Based on full-text retrieval engine. *Computer & Digital Engineering* 9, 81–85 (2008)

Satellite Pseudo-range Positioning Based on Time Series Analysis

Guojun Zhang and Siliang Wu

School of Information Science and Technology, Beijing Institute of Technology,
Beijing, China
zhangguojun539@sohu.com, siliangfortoday@gmail.com

Abstract. A novel real-time positioning model for single frequency receiver is proposed. The position parameters are expressed in the form of linear time series combination, and the positioning problem is converted into estimation problem of time series coefficients. Space mapping method is presented to process the measurement information of single-frequency pseudo-range. It is used to deduct clock bias, ionosphere refraction, amend residual error and other system errors. Error transfer function is improved for high precision.

Keywords: Satellite navigation positioning, time series analysis, cubic B-spline, space mapping.

1 Introduction

Accuracy of satellite navigation positioning is the core and foundation in application of satellite navigation. To improve the accuracy of satellite navigation positioning, researchers proposed many methods, such as differential positioning, combination of dual frequency, carrier phase smoothing and so on [1-3], which effectively improved the accuracy of satellite navigation positioning. But for a large number of users who use the single frequency receiver, there are no conditions for combination of dual frequency, it is difficult to establish a differential reference station, and solving integer ambiguity resolution in carrier phase smoothing is necessary, the actual positioning calculation mainly takes the form of single point positioning calculation. For the results of point positioning, Chinese scholars use Kalman filter method to carry out secondary filtering [4], which filters out most of the random errors, but they can not do anything to the effects of system error.

The traditional least squares estimation method used in satellite navigation positioning, which only uses observed data of pseudo-range of many navigation satellites collected by the receiver at the same time, can not effectively estimate residual errors and remove them. Considering the observation sequence has strong correlation in time, this paper analyzes various factors which affect the navigation positioning accuracy, and proposes a new real-time positioning model for single frequency receivers. The proposed model can show the position parameters to be estimated in the form of linear combination of a set of time series basis, and convert the positioning problem into estimation problem of coefficient of the time series fit basis. By using the space mapping method to process the measurement information of

single-frequency pseudo-range, not only can it deduct clock bias, ionosphere refraction, amend residual error and other system errors, but also it can improve error transfer function.

2 General Positioning Principles

The equations of pseudo-range of receiver observation satellite are

$$\begin{cases} \rho_1 = \sqrt{(x_1 - x_u)^2 + (y_1 - y_u)^2 + (z_1 - z_u)^2} + ct_u \\ \rho_2 = \sqrt{(x_2 - x_u)^2 + (y_2 - y_u)^2 + (z_2 - z_u)^2} + ct_u \\ \dots \\ \rho_n = \sqrt{(x_n - x_u)^2 + (y_n - y_u)^2 + (z_n - z_u)^2} + ct_u \end{cases} \quad (1)$$

where x_u, y_u, z_u are the components of the receiver position, x_j, y_j, z_j are the position components of the satellite s_j ($j=1,2,\dots,n, n \geq 4$), t_u is the bias between satellite and ground station clocks.

Conduct linearized processing for (1), that is unfolding (1) in x_u, y_u, z_u, t_u in the form of first-order Taylor series, we can get

$$\begin{cases} \hat{\rho}_1 - \rho_1 = \frac{x_1 - \hat{x}_u}{\hat{r}_1} \Delta x_u + \frac{y_1 - \hat{y}_u}{\hat{r}_1} \Delta y_u + \frac{z_1 - \hat{z}_u}{\hat{r}_1} \Delta z_u + ct_u \\ \hat{\rho}_2 - \rho_2 = \frac{x_2 - \hat{x}_u}{\hat{r}_2} \Delta x_u + \frac{y_2 - \hat{y}_u}{\hat{r}_2} \Delta y_u + \frac{z_2 - \hat{z}_u}{\hat{r}_2} \Delta z_u + ct_u \\ \dots \\ \hat{\rho}_n - \rho_n = \frac{x_n - \hat{x}_u}{\hat{r}_n} \Delta x_u + \frac{y_n - \hat{y}_u}{\hat{r}_n} \Delta y_u + \frac{z_n - \hat{z}_u}{\hat{r}_n} \Delta z_u + ct_u \end{cases} \quad (2)$$

where

$$\hat{\rho}_j = \sqrt{(x_j - \hat{x}_u)^2 + (y_j - \hat{y}_u)^2 + (z_j - \hat{z}_u)^2} + c\hat{t}_u$$

$$\hat{r}_j = \sqrt{(x_j - \hat{x}_u)^2 + (y_j - \hat{y}_u)^2 + (z_j - \hat{z}_u)^2} \quad (j=1,2,\dots,n)$$

Introduce the following variables

$$\begin{aligned} \Delta\rho_j &= \hat{\rho}_j - \rho_j \\ a_{xj} &= \frac{x_j - \hat{x}_u}{\hat{r}_j}, a_{yj} = \frac{y_j - \hat{y}_u}{\hat{r}_j}, a_{zj} = \frac{z_j - \hat{z}_u}{\hat{r}_j} \quad (j=1,2,\dots,n) \end{aligned} \quad (3)$$

Change (2) to matrix form, we can get

$$\Delta\rho = H\Delta x \quad (4)$$

$$\text{where } \Delta\rho = \begin{bmatrix} \Delta\rho_1 \\ \Delta\rho_2 \\ \dots \\ \Delta\rho_n \end{bmatrix}, H = \begin{bmatrix} a_{x1} & a_{y1} & a_{z1} & 1 \\ a_{x2} & a_{y2} & a_{z2} & 1 \\ \dots & & & \\ a_{xn} & a_{yn} & a_{zn} & 1 \end{bmatrix}, \Delta x = \begin{bmatrix} \Delta x_u \\ \Delta y_u \\ \Delta z_u \\ c\Delta t_u \end{bmatrix} = \begin{bmatrix} x_u - \hat{x}_u \\ y_u - \hat{y}_u \\ z_u - \hat{z}_u \\ ct_u - \hat{ct}_u \end{bmatrix}.$$

Solution of (4) is

$$\Delta x = (H^T H)^{-1} H^T \Delta\rho \quad (5)$$

$$\begin{bmatrix} x_u \\ y_u \\ z_u \\ ct_u \end{bmatrix} = (H^T H)^{-1} H^T \Delta\rho + \begin{bmatrix} \hat{x}_u \\ \hat{y}_u \\ \hat{z}_u \\ \hat{ct}_u \end{bmatrix} \quad (6)$$

3 Algorithm of Satellite Navigation Positioning Based on Time Series Analysis

3.1 Basic Principles

The traditional least squares algorithm used for satellite navigation positioning utilizes only observed quantities of pseudo-range of many navigation satellites collected by the receiver at the same time, it does not make use of temporal correlation of observation sequences at different times. In fact, there exists a strong correlation in the observation sequences in time. Based on this feature, we can indicate the unknown parameters with linear combination of a set of time series basis, and convert the positioning problem into the estimation problem of coefficient of the time series fit basis. In addition, the clock bias, ionospheric error and other large residual errors in model processing can be estimated as coefficients to be estimated. With this treatment, we can make full use of the spatial correlation and temporal correlation of measurement information, ensure effective deduction of systematic error while completing the trajectory calculation, and can obviously improve accuracy of the navigation positioning. Algorithm flow of satellite navigation positioning based on time series analysis is shown in Fig. 1.

Fig. 1 shows that, the main difference between algorithm of satellite navigation positioning based on time series analysis and the traditional least squares algorithm for satellite navigation is: (a) Reduce the dimensions of the total parameters to be estimated through space mapping; (b) Achieve synchronization of positioning and estimation of system error; (c) Increase the space of parameters to be estimated in single estimation.

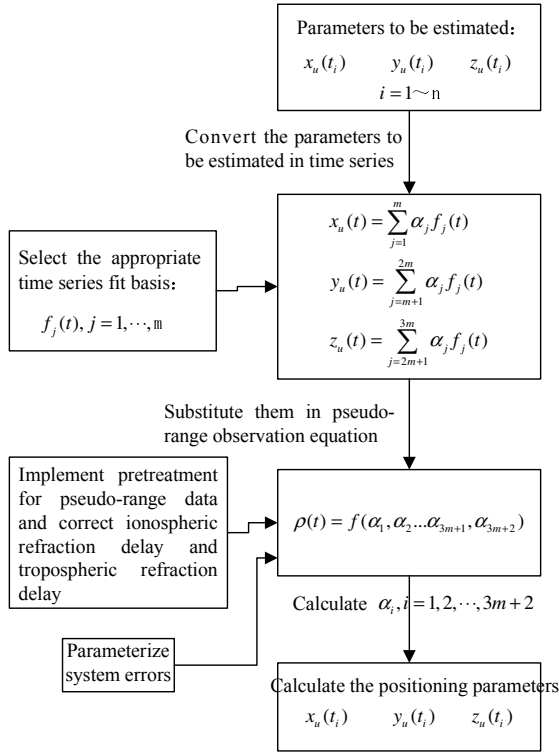


Fig. 1. Diagram of the basic ideas of algorithm of satellite navigation positioning based on time series analysis

3.2 Algorithmic Model

As shown in Fig. 1, specific calculation of satellite navigation positioning based on time series analysis mainly solve the three key problems, which include the selection of time series fit basis, expression of parameterization of systematic error and calculation of fit coefficients. Therefore, the algorithm of satellite navigation positioning based on time series analysis is shown as follows:

- a. Use cubic B-spline as ballistic parameters $x_u(t), y_u(t), z_u(t)$, $t \in [a, b]$, that is

$$\begin{aligned}
 x_u(t) &= \sum_{j=1}^{N+1} \alpha_{x,j} B\left(\frac{t-\tau_j}{h}\right) = B\alpha_x^T \\
 y_u(t) &= \sum_{j=1}^{N+1} \alpha_{y,j} B\left(\frac{t-\tau_j}{h}\right) = B\alpha_y^T \\
 z_u(t) &= \sum_{j=1}^{N+1} \alpha_{z,j} B\left(\frac{t-\tau_j}{h}\right) = B\alpha_z^T
 \end{aligned}
 \tag{7}$$

where :

$$B(t) = \begin{cases} 0 & |t| \geq 2 \\ |t|^3 / 2 - t^2 + 2 / 3 & |t| < 1 \\ -|t|^3 / 6 - t^2 - 2|t| + 4 / 3 & 1 \leq |t| < 2 \end{cases}$$

$\tau_j = \tau_{j-1} + h$, $\tau_{-1} = -h + a$, $\tau_N = b$, $\tau_{N+1} = b + h$, h is the interval between the neighboring nodes.

$$\alpha_x = [\alpha_{x,-1} \quad \alpha_{x,0} \quad \dots \quad \alpha_{x,N+1}] \quad \alpha_y = [\alpha_{y,-1} \quad \alpha_{y,0} \quad \dots \quad \alpha_{y,N+1}]$$

$$\alpha_z = [\alpha_{z,-1} \quad \alpha_{z,0} \quad \dots \quad \alpha_{z,N+1}]$$

$$B = [B(\frac{t-\tau_{-1}}{h}) \quad B(\frac{t-\tau_0}{h}) \quad \dots \quad B(\frac{t-\tau_{N+1}}{h})].$$

b. Carry out pretreatment for pseudo-range measurement data gained by the receiver, pick out outliers and correct ionospheric delay and troposphere refraction delay.

c. Substitute (7) into the pseudo-range observation equation, and use $\alpha_0, \alpha_e / f_{L_i}^2 \sin \theta_E$ to represent clock error and residual error of ionospheric refraction correction, that is

$$\rho_k(t_i) = \sqrt{(x_k(t_i) - \sum_{j=-1}^{N+1} \alpha_{x,j} B(\frac{t_i - \tau_j}{h}))^2 + (y_k(t_i) - \sum_{j=-1}^{N+1} \alpha_{y,j} B(\frac{t_i - \tau_j}{h}))^2} + (z_k(t_i) - \sum_{j=-1}^{N+1} \alpha_{z,j} B(\frac{t_i - \tau_j}{h}))^2 + \alpha_0 + \frac{\alpha_e}{f_{L_i}^2 \sin \theta_k} \quad (k = 1, 2, \dots, m, i = 1, 2, \dots, n) \tag{8}$$

d. Adopt least squares estimation to solve (8) and get $\alpha_{x,j}, \alpha_{y,j}, \alpha_{z,j}, \alpha_0$ and α_e . If the approximate values of $\alpha_{x,j}, \alpha_{y,j}, \alpha_{z,j}, \alpha_0$ and α_e are known, least square can be adopted by using linearized form for (9); if there is no prior knowledge concerning $\alpha_{x,j}, \alpha_{y,j}, \alpha_{z,j}, \alpha_0$ and α_e , nonlinear optimization method is adopted to conduct iterative computation for $\alpha_{x,j}, \alpha_{y,j}, \alpha_{z,j}, \alpha_0$ and α_e .

e. Calculate $x_u(t)$, $y_u(t)$ and $z_u(t)$ according to (7). In practical calculation, in order to ensure real time property and simplification of determination of the specific parameters of the fit basis, the data can be segmented, in order to conduct piecewise completion of ballistic solution.

3.3 Precision Analysis

According to theory of random error, $cov(x) = E[xx^T]$, and it can be inferred from (7) that $x = B\alpha_x^T$, therefore:

$$cov(x) = E[B\alpha_x^T \alpha_x B^T] = B cov(\alpha_x) B^T \tag{9}$$

$$cov(\alpha_x) = (H_\alpha^T H_\alpha)^{-1} \tag{10}$$

The definition of H_α is shown in (11)

$$H_\alpha = \begin{bmatrix} \frac{(x_1(t_1) - \hat{x}_1(t_1))}{\hat{r}_1(t_1)} B(\frac{t_1 - \tau_{s1}}{h}) & \dots & \frac{(y_1(t_1) - \hat{y}_1(t_1))}{\hat{r}_1(t_1)} B(\frac{t_1 - \tau_{s1}}{h}) & \dots & \frac{(z_1(t_1) - \hat{z}_1(t_1))}{\hat{r}_1(t_1)} B(\frac{t_1 - \tau_{s1}}{h}) & \dots & \frac{(z_1(t_1) - \hat{z}_1(t_1))}{\hat{r}_1(t_1)} B(\frac{t_1 - \tau_{sN+1}}{h}) & 1 & \frac{1}{f_1^2 \sin \theta_1(t_1)} \\ \dots & & & & & & & & \\ \frac{(x_1(t_2) - \hat{x}_1(t_2))}{\hat{r}_1(t_2)} B(\frac{t_2 - \tau_{s1}}{h}) & \dots & \frac{(y_1(t_2) - \hat{y}_1(t_2))}{\hat{r}_1(t_2)} B(\frac{t_2 - \tau_{s1}}{h}) & \dots & \frac{(z_1(t_2) - \hat{z}_1(t_2))}{\hat{r}_1(t_2)} B(\frac{t_2 - \tau_{s1}}{h}) & \dots & \frac{(z_1(t_2) - \hat{z}_1(t_2))}{\hat{r}_1(t_2)} B(\frac{t_2 - \tau_{sN+1}}{h}) & 1 & \frac{1}{f_1^2 \sin \theta_1(t_2)} \\ \dots & & & & & & & & \\ \frac{(x_2(t_1) - \hat{x}_2(t_1))}{\hat{r}_2(t_1)} B(\frac{t_1 - \tau_{s1}}{h}) & \dots & \frac{(y_2(t_1) - \hat{y}_2(t_1))}{\hat{r}_2(t_1)} B(\frac{t_1 - \tau_{s1}}{h}) & \dots & \frac{(z_2(t_1) - \hat{z}_2(t_1))}{\hat{r}_2(t_1)} B(\frac{t_1 - \tau_{s1}}{h}) & \dots & \frac{(z_2(t_1) - \hat{z}_2(t_1))}{\hat{r}_2(t_1)} B(\frac{t_1 - \tau_{sN+1}}{h}) & 1 & \frac{1}{f_2^2 \sin \theta_2(t_1)} \\ \dots & & & & & & & & \\ \frac{(x_n(t_n) - \hat{x}_n(t_n))}{\hat{r}_n(t_n)} B(\frac{t_n - \tau_{s1}}{h}) & \dots & \frac{(y_n(t_n) - \hat{y}_n(t_n))}{\hat{r}_n(t_n)} B(\frac{t_n - \tau_{s1}}{h}) & \dots & \frac{(z_n(t_n) - \hat{z}_n(t_n))}{\hat{r}_n(t_n)} B(\frac{t_n - \tau_{s1}}{h}) & \dots & \frac{(z_n(t_n) - \hat{z}_n(t_n))}{\hat{r}_n(t_n)} B(\frac{t_n - \tau_{sN+1}}{h}) & 1 & \frac{1}{f_n^2 \sin \theta_n(t_n)} \end{bmatrix} \quad (11)$$

Make the comparison between (11) and (4), we can regard H_α as the extension of H without considering the modified differences of the ionospheric delay models. In the row direction, the three direction cosines are extended into $N + 3$, each of which has increment in weight concerning the coefficient of cubic B-spline. It is equivalent to changing the observational geometry of parameter estimation. In the column direction, the observation matrix is extended in accordance with the observation time, which is equivalent to averaging measurement date at the time period, which can reduce the random errors in data. Therefore, compared with the traditional least squares algorithm, the algorithm of satellite navigation positioning based on time series analysis can improve the accuracy in the following three aspects: (a) Adopting the algorithm of satellite navigation positioning based on time series analysis can change the computational geometry of parameters to be estimated; (b) Through combined treatment of multi-point observation data over a period of time, you can filter out the random errors in measurement data to improve measurement accuracy; (c) Adopting the proposed algorithm enables the system error deduction and ballistic parameter estimation to be calculated uniformly in accordance with least mean square criterion, to ensure the accuracy of estimates.

4 Simulation Analyses

Adopt the proposed algorithm and the traditional positioning algorithm individually to conduct positioning for flight path whose time period is 300s from certain spatial object, the results can be used to check validity of algorithm of this paper. The data sampling rate is 1Hz, pseudo-range measurement error is set at 5m, α_0 is taken as 2m, α_e / f_{L1}^2 is taken as 3m.

In Fig. 2, a comparison is made between the two geometric transfer factors of the two algorithms, and 100 simulation calculations are conducted individually by adopting the two algorithms, the resultant error curves are shown in Fig. 3. Table 1 shows the estimation results of systematic error by using the proposed algorithm.

Table 1. Estimation Results of System Errors

Clock bias		Residual error of ionospheric delay	
Setting values	Estimated values	Setting values	Estimated values
2m	1.966m	3m	2.977m

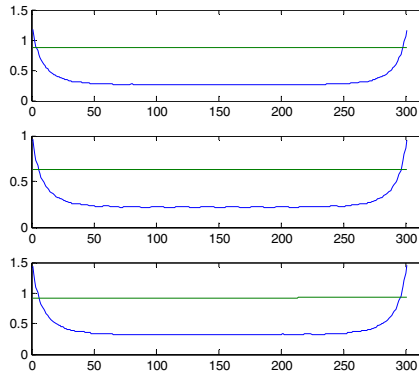


Fig. 2. Comparison of the geometric transfer factors

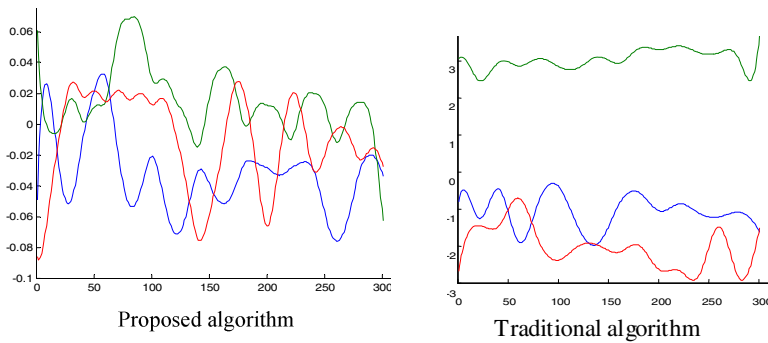


Fig. 3. Error curves for algorithm based on time series analysis

Table 1 shows that the algorithm of satellite navigation positioning based on time series analysis deducts 98% of system errors, which certifies that this algorithm can effectively deduct the system error.

Fig. 2 shows that, the geometric transfer factors of algorithm of satellite navigation positioning based on time series analysis are significantly less than traditional navigation positioning algorithm and the proposed algorithm can significantly improve the positioning accuracy. The proposed algorithm presents the feature of "twin tips", which is mainly caused by the compactness property of fit basis.

From Fig. 3 we can conclude that for observed data that contains systematic errors, the algorithm based on time series analysis can realize unbiased estimation, and effectively filter out the influence of random errors in the data.

5 Conclusions

By using the feature that strong correlation exists among observation sequences in time, this paper puts forward an algorithm of satellite navigation positioning based on time series analysis. Compared with the traditional algorithm, the proposed algorithm

not only can deduct clock error, residual error of ionospheric refraction correction and other system errors, but also can improve the error transfer factors. Simulation results show that the method can deduct over 90% of the system errors, improve 30% to 50% of the error transfer factors, and significantly improve positioning accuracy. If the sampling rate of measurement data is raised, the proposed algorithm can also be used for real-time data processing.

References

1. Liu, Y., Xu, X., Wei, J.: Application of BP Neural Network to GPS Differentiation Positioning (in Chinese). *Journal of Northeastern University* 29, 1537–1539 (2008)
2. Xue, G., Duan, Z., Wang, M.: Complement of Detecting and Repairing Cycle Slip by Combination of Dual Frequency (in Chinese). *Geomatics and Spatial Information Technology* 29, 77–79 (2006)
3. Yang, C., Wu, D., Lu, Y.: A Phase-smoothed Pseudo-range Algorithm Based on Complementary Kalman Filtering (in Chinese). *Journal of Air Force Engineering University* 9, 53–56 (2008)
4. Jia, P., Xiong, Y.: An Orbit Determination Algorithm with Onboard GPS using Kalman Filter (in Chinese). *Acta Astronomica Sinica* 46, 442–451 (2003)
5. ARINC Research Coporation, NAVATAR GPS Space Segment/Navigation User Interface, Interface Specification, IS_GPS_200D(Public Release Version), ARINC Research Coporation, Fountain Valley, CA (2004)
6. Kaplan, E., Hegarty, C.: *Understanding GPS principles and applications*. Electronics Industry Press, Beijing (2007)
7. Taylor, J., Barnes, E.: GPS Current Signal_in_space Navigation Performance. In: Proc. of The Institute of Navigation National Technical Meeting, San Diego, CA (January 2005)

H_∞ Control for Inverted Pendulum: Input Time Delay Considered

Keyong Shao^{1,*}, Miaomiao Tian¹, and Qingyu Wu²

¹ School of Electric and Information Engineering, Northeast Petroleum Institute,
Gaoxin Zone, 163318 Daqing, China

² Well-logging Company, Zhongyuan Oilfield,
Hualong Zone, 457001 Puyang, China

Shaokeyong@tom.com, pigeon01@126.com, beautylife0712@163.com

Abstract. In this paper, H_∞ control for single linear inverted pendulum with input time delay is studied, which is an unavoidable factor influencing the stability of inverted pendulum system. An H_∞ feedback controller of the system has been obtained by using Lyapunov function combined with linear matrix inequality method, and the criterion can be readily tested by using standard numerical software. And the uncertainties are also considered. The simulation results show the availability of the proposed method.

Keywords: H_∞ control, Lyapunov function, linear matrix inequality, inverted pendulum system, input time delay.

1 Introduction

Inverted pendulum is a multivariable, nonlinear, strong coupling and unstable system. The inverted pendulum balance control process effectively reflects many key issues of control theory. And the control method is widely used in military, aerospace, robotics and general industrial process areas. Therefore, the research on inverted pendulum system is of great theoretical meaning and practical value. [1]

In the process of motion, time-delay of system control happens inevitably as the controller needs a certain response time, and friction and other nonlinear factors exist between the inverted pendulum system components. The presence of delay degrades the system performance, even leads to system instability. [1] And it is an important factor influencing the system performance and stability. References [1] and [2] discussed the related problems of time delay in inverted pendulum system. Reference [1] designed the controller using the linear quadratic optimal control strategy, and critical stable time delay is obtained through the Routh-Hurwitz stability criterion. Reference [2] proposed a time delay compensation strategy, and the LQR method is adopted to design the controller. In this paper, pure input delay is used to represent the time-delay phenomenon of inverted pendulum systems, and the inverted pendulum model with time-delay is established. An H_∞ state feedback controller is designed

* This work was supported by Postdoctoral Science Research Foundation, Heilongjiang Province.

based on Lyapunov theory, and numerical examples have been provided which can be solved with LMI method expediently and directly.

2 Problem Description

The state-place model to represent the inverted pendulum system can be given by

$$\begin{cases} \dot{x}(t) = A(t)x(t) + B_1\omega + B_2(t)u(t-d) \\ z(t) = Cx(t) \\ x(t) = \phi(t), \forall t \in [-d, 0] \end{cases}, \tag{1}$$

where $\begin{cases} A(t) = A + \Delta A(t) \\ B_2(t) = B_2 + \Delta B_2(t) \end{cases}$,

$x(t) \in R^n$ is the state vector, d represent input time-delay, and A, B_1, B_2, C are constant matrices of appropriate dimensions. $u(t) = Kx(t)$ is the feedback controller. $\phi(t)$ is a given initial condition on $[-d, 0]$.

$\Delta A(t), \Delta B_2(t)$ are unknown matrices of appropriate dimensions, which represent the time varying structured uncertainties of the system. And they are assumed to be norm-bounded:

$$[\Delta A(t) \quad \Delta B_2(t)] = DF(t)[E_a \quad E_b], \tag{2}$$

where D, E_a, E_b are constant matrices of appropriate dimensions. $F(t) \in R^{n \times n}$ is an unknown time-varying uncertain matrix, which satisfies

$$F^T(t)F(t) \leq I, \tag{3}$$

where I is an identity matrix of appropriate dimensions.

The following lemmas are needed in the proof of main results in this note:

Lemma 1: (Schur complement) [3] For given symmetric matrix $S = \begin{bmatrix} S_{11} & S_{12} \\ S_{21} & S_{22} \end{bmatrix}$,

where $S_{11} \in R^{r \times r}$, the following 3 conditions are equivalent:

$$\textcircled{1} S < 0; \textcircled{2} S_{11} < 0, \quad S_{22} - S_{12}^T S_{11}^{-1} S_{12} < 0; \textcircled{3} S_{22} < 0, \quad S_{22} - S_{12} S_{22}^{-1} S_{12}^T < 0.$$

Lemma 2: [4] A, L, E and F are assumed to be real matrices satisfying $F^T(t)F(t) \leq I$, for any positive symmetric matrix P and positive number ε such that $P - \varepsilon LL^T > 0$, then

$$(A + LFE)^T P^{-1} (A + LFE) \leq A^T (P - \varepsilon LL^T)^{-1} A + \varepsilon^{-1} E^T E. \tag{4}$$

3 Main Results

Theorem 1: For given constant $\gamma > 0$, the nominal system of system (1) under the control $u(t) = YX^{-1}x(t)$ is robustly stable, and the H_∞ performance index is less than the given bound γ , if there exist symmetric matrices $X > 0$, $R > 0$, $S > 0$ and any matrix Y , satisfying

$$\Xi^0 = \begin{bmatrix} \Xi_{11}^0 & 0 & B_1 & dXA^T & dB_2Y & XC^T \\ * & -R & 0 & dY^T B_2^T & 0 & 0 \\ * & * & -\gamma^2 I & dB_1^T & 0 & 0 \\ * & * & * & -dS & 0 & 0 \\ * & * & * & * & -dX & 0 \\ * & * & * & * & * & -I \end{bmatrix} < 0, \tag{5}$$

where $\Xi_{11}^0 = AX + B_2Y + XA^T + Y^T B_2^T + R$.

Proof: Define the following Lyapunov functional

$$V(t) = V_1 + V_2,$$

$$V_1 = x^T(t)Px(t),$$

(6)

$$V_2 = \int_{t-d}^t x^T(s)Qx(s)ds + \int_{-d}^0 ds \int_{t+s}^t \xi^T(\theta)S^{-1}\xi(\theta)d\theta,$$

where $\xi(\theta) = Ax(\theta) + B_2Kx(\theta - d) + B_1\omega$.

Note that $x(t - d) = x(t) - \int_{t-d}^t \xi(\theta)d\theta$, by substituting it into (1), we obtain

$$\begin{cases} \dot{x}(t) = (A + B_2K)x(t) + B_1\omega - B_2K \int_{t-d}^t \xi(\theta)d\theta \\ z = Cx(t) \\ x(t) = \phi(t), \forall t \in [-d, 0] \end{cases} \tag{7}$$

Taking the time-derivative of $V(t)$ leads to

$$\dot{V}(t) \leq \eta^T(t)\psi\eta(t), \tag{8}$$

where $\eta(t) = [x^T(t) \quad x^T(t-d) \quad \omega^T(t)]$,

$$\psi = \begin{bmatrix} \psi_{11} & dA^T B_2K & \psi_{13} \\ * & \psi_{22} & d(B_2K)^T S^{-1}B_1 \\ * & * & dB_1S^{-1}B_1 \end{bmatrix},$$

$$\psi_{11} = P(A + B_2K) + (A + B_2K)^T P + Q + dPB_2KS(B_2K)^T P + dA^T S^{-1}A,$$

$$\psi_{13} = PB_1 + dA^T S^{-1}B_1, \quad \psi_{22} = d(B_2K)^T S^{-1}B_2K - Q.$$

$$\forall T > 0,$$

$$J_T = \int_0^T (z^T z - \gamma^2 \omega^T \omega) dt \leq \int_0^T (z^T z - \gamma^2 \omega^T \omega + \dot{V}(x)) dt \leq \int_0^T \eta^T \tilde{\psi} \eta(t) dt \quad , \quad (9)$$

where $\tilde{\psi} = \psi + \text{diag}\{C^T C, 0, -\gamma^2 I\}$.

Then define $X = P^{-1}$, $Y = KX$, $R = P^{-1}QP^{-1}$. By pre-and post-multiplying inequality $\tilde{\psi} < 0$ by $\text{diag}\{P^{-1}, P^{-1}, 1, 1, P^{-1}, 1\}$, and using lemma 1, the proof is completed.

Theorem 2: For given constant $\gamma > 0$, system (1) under the control $u(t) = YX^{-1}x(t)$ is robustly stable, and the H_∞ performance index is less than the given bound γ , if there exist symmetric matrices $X > 0$, $R > 0$, $S > 0$ and any matrix Y , satisfying

$$\Xi = \begin{bmatrix} \Xi_{11} & 0 & B_1 & \Xi_{14} & dB_2 Y & 0 & 0 & XC^T & XE_a^T & Y^T E_b^T \\ * & -R & 0 & dY^T B_2^T & 0 & 0 & 0 & Y^T E_b^T & 0 & 0 & 0 \\ * & * & -\gamma^2 I & dB_1^T & 0 & 0 & 0 & 0 & 0 & 0 & 0 \\ * & * & * & \Xi_{44} & 0 & 0 & 0 & 0 & 0 & 0 & 0 \\ * & * & * & * & -dX & dY^T E_b^T & 0 & 0 & 0 & 0 & 0 \\ * & * & * & * & * & -\lambda I & 0 & 0 & 0 & 0 & 0 \\ * & * & * & * & * & * & -\lambda I & 0 & 0 & 0 & 0 \\ * & * & * & * & * & * & * & -I & 0 & 0 & 0 \\ * & * & * & * & * & * & * & * & -\lambda I & 0 & 0 \\ * & * & * & * & * & * & * & * & * & -\lambda I & 0 \end{bmatrix} < 0 \quad (10)$$

where $\Xi_{11} = AX + B_2 Y + (AX + B_2 Y)^T + R + 3\lambda DD^T$, $\Xi_{14} = dXA^T + d^2 \lambda DD^T$, $\Xi_{44} = -dS + 2d^2 \lambda DD^T$.

Proof: Inequality $\tilde{\psi} < 0$ can be converted to

$$\Omega = \begin{bmatrix} \Omega_{11} & 0 & PB_1 & dA^T & dPB_2 K \\ * & -Q & 0 & d(B_2 K)^T & 0 \\ * & * & -\gamma^2 I & dB_1^T & 0 \\ * & * & * & -dS & 0 \\ * & * & * & * & -dP \end{bmatrix} < 0 \quad , \quad (11)$$

where $\Omega_{11} = P(A + B_2 K) + (A + B_2 K)^T P + Q + C^T C$.

Then substitute A , B_2 for $A + DFE_a$ and $B_2 + DFE_b$, we have

$$\Omega + HFE + (HFE)^T < 0 \quad , \quad (12)$$

where
$$H = \begin{bmatrix} PD & PD & 0 & PD \\ 0 & 0 & 0 & 0 \\ 0 & 0 & 0 & 0 \\ dD & 0 & dD & 0 \\ 0 & 0 & 0 & 0 \end{bmatrix}, \quad E = \begin{bmatrix} E_a & 0 & 0 & 0 & 0 \\ E_b K & 0 & 0 & 0 & 0 \\ 0 & E_b K & 0 & 0 & 0 \\ 0 & 0 & 0 & 0 & dE_b K \end{bmatrix}.$$

By pre-and post-multiplying the inequality by $diag\{P^{-1}, P^{-1}, I, I, P^{-1}, I, I, I, I, I\}$, and using lemma 1 and lemma 2, the proof is completed.

4 Illustrative Example

In this section, we will use numerical examples to illustrate the usefulness of above theorems. Consult the inverted pendulum model in reference [5], which considers the acceleration of robot cart as input. Then consider the following state-place model of inverted pendulum with input time-delay

$$\begin{bmatrix} \dot{x}(t) \\ \ddot{x}(t) \\ \dot{\varphi}(t) \\ \ddot{\varphi}(t) \end{bmatrix} = \begin{bmatrix} 0 & 1 & 0 & 0 \\ 0 & 0 & 0 & 0 \\ 0 & 0 & 0 & 1 \\ 0 & 0 & \frac{3g}{4l} & 0 \end{bmatrix} \begin{bmatrix} x(t) \\ \dot{x}(t) \\ \varphi(t) \\ \dot{\varphi}(t) \end{bmatrix} + \begin{bmatrix} 0 \\ 1 \\ 0 \\ \frac{3}{4l} \end{bmatrix} u(t-d) + B_1 \omega, \tag{13}$$

$$z(t) = \begin{bmatrix} x(t) \\ \varphi(t) \end{bmatrix} = \begin{bmatrix} 1 & 0 & 0 & 0 \\ 0 & 0 & 1 & 0 \end{bmatrix} \begin{bmatrix} x(t) \\ \dot{x}(t) \\ \varphi(t) \\ \dot{\varphi}(t) \end{bmatrix},$$

where x is the position of the cart, φ denotes the angle of the pendulum with respect to vertical line, denotes inertia of the pendulum, $l = 0.25$ denotes distance between center of mass of pendulum and tip attached to the cart., $g = 0.98$ denotes the acceleration due to gravity, u denotes the external force applied to the cart.

4.1 The Nominal System

Consider the nominal system with the following parameters:

$$A = \begin{bmatrix} 0 & 1 & 0 & 0 \\ 0 & 0 & 0 & 0 \\ 0 & 0 & 0 & 1 \\ 0 & 0 & 29.4 & 0 \end{bmatrix}, \quad B_1 = \begin{bmatrix} 0.01 \\ 0 \\ 0.02 \\ 0 \end{bmatrix} \quad B_2 = \begin{bmatrix} 0 \\ 1 \\ 0 \\ 3 \end{bmatrix}, \quad C = \begin{bmatrix} 1 & 0 & 0 & 0 \\ 0 & 0 & 1 & 0 \end{bmatrix}.$$

where $d = 0.001$.

The controller gain matrix obtained by Theorem 1 is $K = YX^{-1} = [14.6107 \ 10.2794 \ -49.5857 \ -6.9046]$, and the inverted pendulum system is stable. The position x and angle φ are shown in Fig.1.

4.2 The Uncertain System

Consider the system (1) with the following parameters:

$$D = \begin{bmatrix} 0.01 & 0 & 0 & 0 \\ 0 & 0.01 & 0 & 0 \\ 0 & 0 & 0.01 & 0.02 \\ 0 & 0 & 0 & 0.01 \end{bmatrix}, \quad E_a = \begin{bmatrix} 0 & 0.1 & 0 & -0.05 \\ -0.3 & 0.01 & -0.34 & 0 \\ 0 & -0.03 & 0.03 & -0.1 \\ -0.05 & 0.04 & 0.02 & 0.04 \end{bmatrix}, \quad E_b = \begin{bmatrix} 0 \\ -0.01 \\ 0 \\ -0.03 \end{bmatrix}.$$

The controller gain matrix obtained by Theorem 2 is $K = YX^{-1} = [35.0129 \ 27.0705 \ -99.9935 \ -16.6364]$. The control results are shown in Fig.2.

The simulation results show that the method proposed in this paper can obtain the control matrix conveniently and control the stability of the inverted pendulum system effectively. In actual control processes, estimating system input delays according to the circumstances and fully considering them as control factors will get more satisfactory control effect.

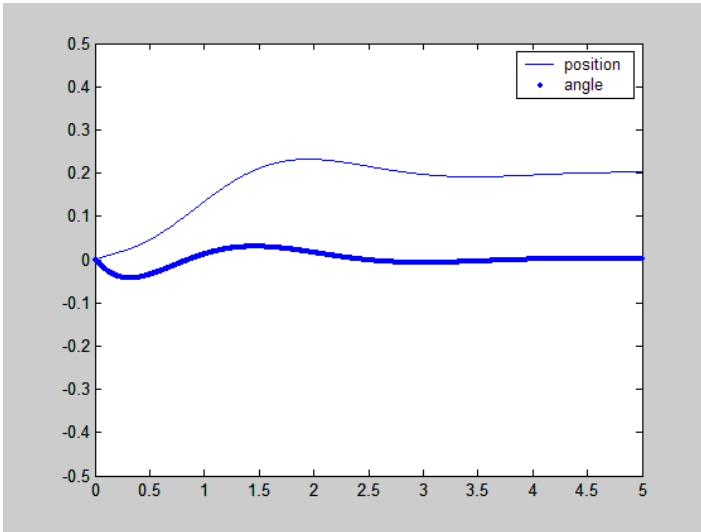


Fig. 1. Position and angle in robust stabilization (the nominal system)

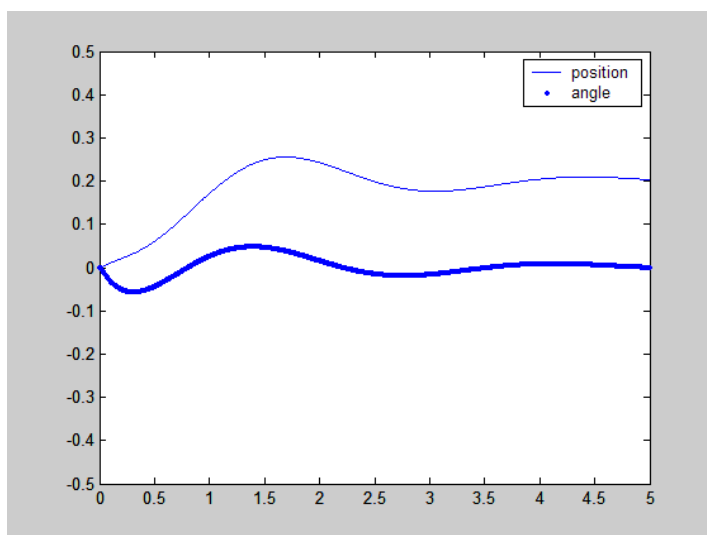


Fig. 2. Position and angle in robust stabilization (the uncertain system)

5 Conclusions

A new stability condition for inverted pendulum system has been proposed. And the influence of input time-delay and uncertainties to the stability of the system are considered. A H_{∞} feedback controller for the inverted pendulum system with time-delay is derived by exploiting a Lyapunov functional and making use of integral inequality approach. The conclusion is given in the form of linear matrix inequalities and the solutions can be obtained directly and easily. The idea in this paper can be used to analyze the stability of inverted pendulum system in a more general and practical view.

References

1. Cao, Q., Zhang, M., Zhou, J., Li, L.: Optimal Control for Inverted Pendulum System with Time Delay. *Information and Control* 39(4), 397–401 (2010)
2. Yang, Y., Wang, Y., Xu, J.: Output Feedback Control for Networked Control System with Stochastic Time Delay Compensation. *Huazhong Univ. of Sci. & Tech. (Nature Science Edition)* 34(5), 95–98 (2006)
3. Yu, L.: *Robust Control: Linear Matrix Inequalities Method*. Tsinghua University Press, Beijing (2002)
4. Wang, Y., Xie, L., de Souza, E.: Robust Control of Uncertain Nonlinear Systems. *Systems and Control Letters* 19(2), 139–149 (1992)
5. Experiment of Inverted Pendulum and Automatic Control. Googol Technology (Shenzhen) LTD, Shenzhen (2005)

Energy Saving of Plant Cultivation System Using LED Control System Based on Ultrasonic Sensor

Hyung-Sun Kim and Jae-Hyun Lim

Computer Science Department, Kongju National University
Budeadong 275, Cheonan, Chungnam - Korea
{ddaker98, defacto}@kongju.ac.kr

Abstract. For great economics and capable commercialization of fully controlled plant factory, various researches are required such as energy-efficient design of artificial light which is major of energy consumption and the best environmental controlling technology for plant photosynthesis and so on. To reduce energy consumption and promote the plant growth, appropriate combination of wave length and PPF(D(Photosynthetic Photon Flux density)) must be supplied according to the stages of plant growth and the sort of plants. Therefore, this paper suggests the architecture of LED control system based on ultrasonic sensor to promote plant growth by supplying appropriate PPF(D. Using ultrasonic sensor, the distance between the light and plant according to the stages of plant is measured to supply proper PPF(D and light equipment is moved directly. Using proposed system, it is verified that PPF(D heavily influences the growth of plant and supplying of suitable PPF(D according to the stages of growth promotes the plant growth. Promotion of plant growth reduces the periods of plant cultivation and leads to reduce energy consumption in plant factory.

Keywords: LED lighting control, plant factory, energy saving, PPF(D.

1 Introduction

Recently the Farm production has been sharply decreased because of impact of anomaly climate. In addition, Korea faces to a serious shortages of agricultural products since the outdoor product is reduced by the unexpected changes of climate such as high-temperature, heavy rain. To overcome such problems of climate and protect natural ecosystem, plant factory could be a very useful part of industries [1].

Plant factory is a kind of system where crops can be produced deliberately. The productions from the plant factory are very similar to the natural productions and also the climates affection could be not regarded by controlling the environmental conditions such as light, temperature, humidity and nutrient in limited space. Plant factory is categorized into hybrid controlled type and fully controlled type according to structure of facilities and system of cultivating plant. Hybrid controlled type is difficult to manage growth of plant and control environment in this facilities, because it is difficult to predict about changes of outdoors environment. Therefore a study on fully controlled type is in progress more actively in these days.

LED is the suitable light as spotlight for the fully controlled type of plant factory which has the advantage of contact radiation. LED is not involved ingredient of heat that released from light. In addition, it can make a better space for cultivation and as its function of thermal radiation cause to minimize the damage of plant. However, fully controlled type of plant factory needs various researches such as reduction of initial installation, costs of light, operating expenses and light control technology which cause to reduce energy consumption power using contact radiation and so on[2].

In general, the difference of wavelength, intensity of light and the duration of light emitting are strongly affected to the growth of plant and morphogenesis. Especially, the revelation rate of red and blue in plant leaves changes according to the intensity of light [2]. In addition, the response of plant depending on light environment is very different according to the sort of plant and the speed of plant growth. Therefore, if light environment such as the wavelength and intensity of light (PPFD) were operated exquisitely according to the sort of plant and the speed of plant growth, the growth velocity could be controlled and the plant growth could be promoted.

Therefore, this paper suggests LED control system based on ultrasonic sensor to supply appropriate PPFD according to the sort and growth velocity of target plant. First of all, LED light equipment which is manufactured considering appropriate wave length and PPFD for target plant is installed in top of plate in mini plant factory. Secondly, Ultrasonic sensor is attached to the LED equipment. Then, the distance between the light and plants is measured in every duty-cycle by sensor. By the measured information, the growth stage can be figured out. Finally, by moving the light device directly and controlling the light intensity, appropriate PPFD could be supplied according to the growth stage and the growth of plant could be promoted.

2 Related Work

2.1 The Change of Growth Rate According to the Growth Stage of Plant

In general, the growth of plants means quantitative change of plants and is often defined as "phenomenon increasing tissue, organ, size and weight of plant irreversibly as time goes by [3]. The growth stages of the sort of salad in fully controlled type of plant factory were assorted into a germinating period, a vegetative period, a promoting period and growth variation rate according to the best environment condition of each growth stage is identical to Fig. 1[4].

2.2 The Growth of Plant and PPFD

An appropriate daily PPFD (Photosynthetic Photon Flux) should be supplied uniformly to keep the stable growth of plant and to produce a steady and high-quality production. PPFD means the light intensity of plant photosynthesis and the amount of PPFD can be different according to the sort of plant and the stage of growth. Table 1 shows required PPFD according to the sort of plant [5]. The speed of plant photosynthesis is increased with light intensity during the process of plant growth. However, the speed of plant photosynthesis does not increase further after a particular

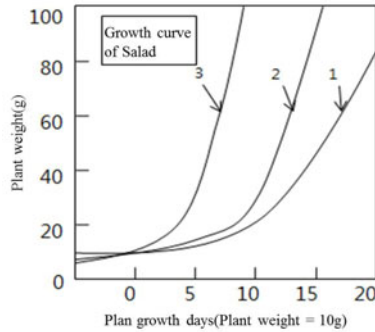


Fig. 1. Cultivation phase by growth curve of Salad

point, and the light intensity at this moment is called the light saturation point. The light compensation point means the point that the amount of carbon dioxide used for photosynthesis and the amount of carbon dioxide the used for respiration of plants is same.

Table 1. Light Saturation Point and Light Compensation Point

Cultivation crops	Light saturation point lx(PPFD)	Light compensation point lx(PPFD)
Tomato, watermelon	70,000(847)	3,000(36)
cucumber	55,000(665)	2,000(24)
pea	40,000(484)	2,000(24)
Lettuce and pimienta	40,000(484)	1,500(18)
grapes	40,000(484)	400(5)
orange	40,000(484)	200(2.5)
pear	40,000(484)	300(3.6)
peach	40,000(484)	400(5)
ginseng	12,000(145)	500(6)

3 Experimental Environment

3.1 Mini-plant Installation for Plant Cultivation

For the experiment, the two of growing plates are installed in mini-plant (140×150×80cm)[Fig. 2]. LED light device with red light (wavelength-660nm) and

light device with blue lights (wavelength-450nm) is manufactured at the rate of 11 to 7 and controller based on ZigBee is attached at the top of each growing plate. Each plate consists 32 pots(4 rows×8columns).

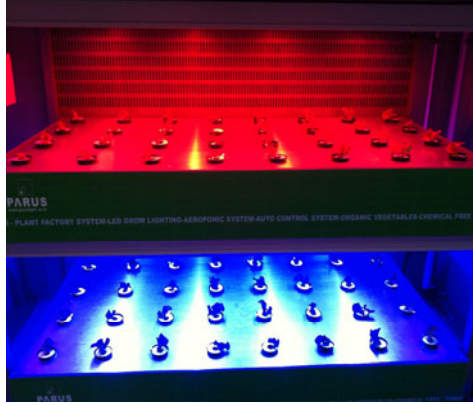


Fig. 2. Mini-Plant for plant cultivation

3.2 LED Control System Based on Ultrasonic Sensor

Measurement principle of ultrasonic sensors is as follows. First of all, ultrasonic pulse that launched from the sensor is reflected from the surface of measure object and the time-delay is measured. Then, the method of calculating the distance is calculated by using the velocity of sound according to the temperature of ultrasonic in the air.

Proposed system uses such ultrasonic sensor that depending on the stage of target plant, to measure the distance between the light device and the plant to supply appropriate amount of PPFD. The light device is moved directly according to the measured distance to promote plant growth and to reduce energy consumption from the light device. Fig. 3 shows the simulation system configuration installed for this experiment.

The components of this system are as follows. A plate in acrylic consist 3-rows and 4-columns of pots and nutrient buckets. To measure the distance between the light device and the plant, ultrasonic sensor of Lego mindstorms is used and by communication of brick server, light device is moved directly according to the stages of plant growth. In addition, ACD (Appliance Control Device) based on ZigBee communication is used to measure the energy consumption of the light device.

Two such systems are installed to compare the plant growth rate and the energy consumption. One of them contains fixed light device and the other one contains moving light device. Fig. 4 shows the configuration of moving LED control system for the future.

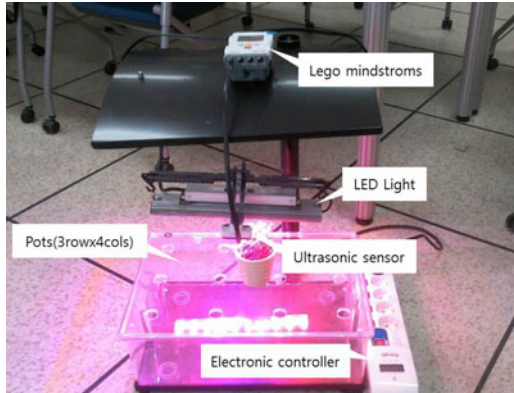


Fig. 3. Simulation of Plant Cultivation System using Lego Mindstorms

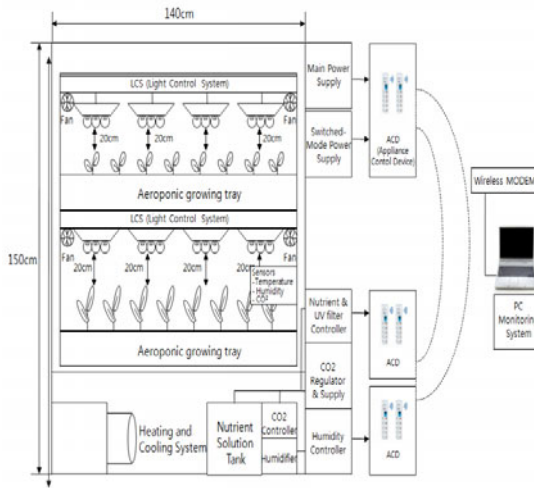


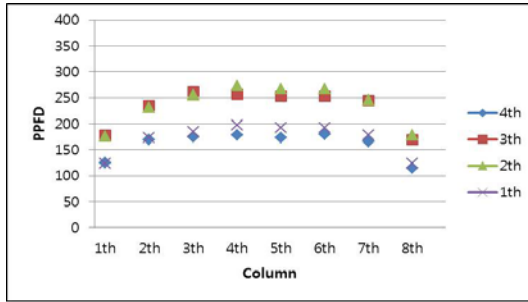
Fig. 4. System Configuration

Integrated sensor is attached to each plate to gather changing environment factors such as temperature, humidity, CO₂ and energy consumption and so on. The measured distance between the light device and plant is stored into database and other collected data of environment is also stored in it. Most of data is gathered in real time and is showed in the environment control monitoring screen. According to the sort of plant and the stages of growth, stored information of distance, the amount of PPFD and so on are retrieved from the database and they are applied to move the light device.

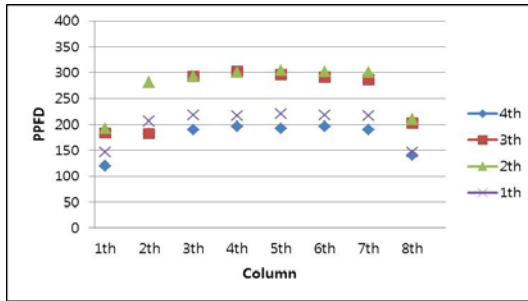
4 Experimental Result

4.1 Distribution of PPFD According to the Height of LED Device

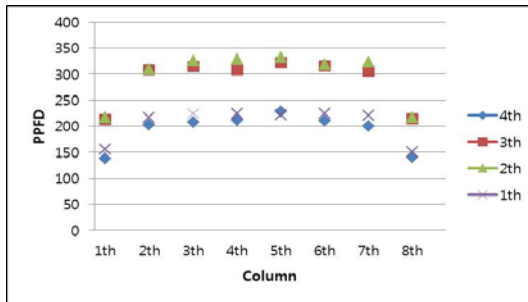
Fig. 5 shows the average of PPFD measured by quantum meter according to the four different distances (28cm, 25cm, 22cm, 19cm) between the light device and the plate.



Distance : 28cm

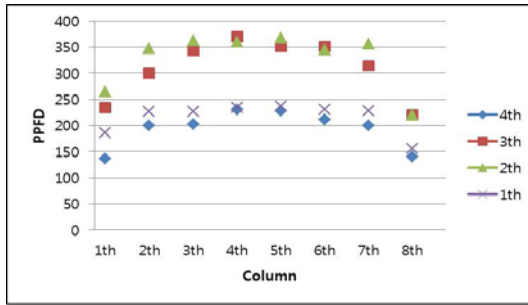


Distance : 25cm



Distance : 22cm

Fig. 5. PPFD average distribution according to height



Distance : 19cm

Fig. 5. (continued)

Fig. 6 shows the average of PPFD based on each row according to the distance from the light device. According to the result of Fig. 6, PPFD average of the 2nd row and 3rd row is higher than other rows. In addition, when the distance between the light and the plant is decreased, average of PPFD based on row is increased up. Therefore, it is thought that appropriate information of distance between the light is needed according to the sort of plant and the stage of growth to promote the plant growth.

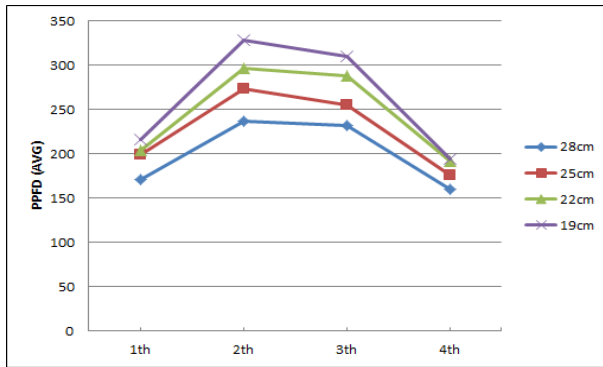


Fig. 6. PPFD average distribution based on the distances

The amount of PPFD is strongly affected to the plant growth. Fig. 7 and Fig. 8 show the experimental result about the relationship between PPFD and plant growth.

Fig.7 depicted the measured PPFD value by Quantum meter from the height of 28cm. The measurement interval is 10cm.

According to the Fig 5 and Fig 7, PPFD average of the center region of the plate is higher than the other region of the plate. In other words, we could predict while the plant growth rate of the center region is high, and the other region is low. In addition, each plate is considered when the distance is decided depending on the sort of plant and plant growth stage since the amount of PPFD that absorbed by plants is different according to the distance, uniformity of supplied PPFD.

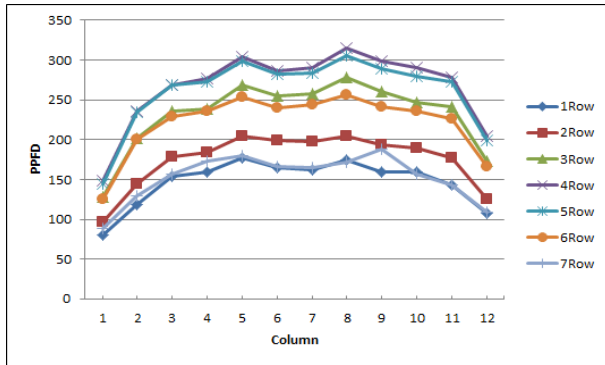


Fig. 7. PPFD distribution(28cm)

Fig. 8 shows the fresh weight of lettuce. To verify the relationship between PPFD and plant growth, the target plant is a lettuce and the plant has been cultivated for 30 days.

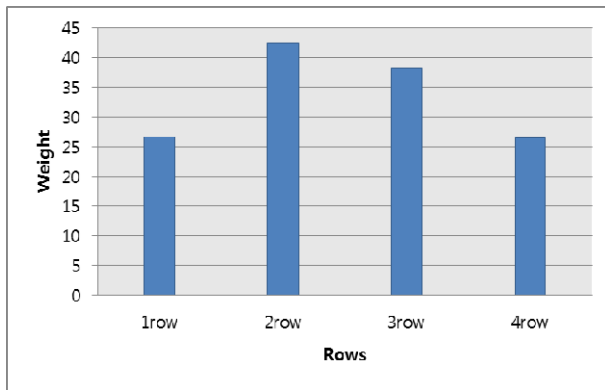


Fig. 8. The fresh weight of lettuce based on row

As shown in Fig 8, the fresh weight of plant which is located in the center region of plate is high and also the quality is excellent.

It is verified through this experiment that the amount of PPFD is strongly affected to the plant growth. The growth of plant would be promoted and energy consumption would be reduced if the appropriate amount of PPFD supplied according to the stage of plant, growth of plant and the sort of plant through controlling the distance between the light device and plant,. Eventually, these results would be lead to reduce energy consumption effect.

5 Conclusions

This paper suggests the architecture of LED control system based on ultrasonic sensor for energy efficiency in fully controlled type of plant factory. It is verified that the relationship between the plant growth and PPFD is very close and the method of measuring distance using ultrasonic sensor is useful for promotion of growth of plant in controlled environment. Such LED control system based on ultrasonic sensor could promote the plant growth and at the same time reduce the energy consumption in plant factory. In the future, various distance-measurement sensors must be tested to measure the plant growth stage in real time besides the ultrasonic sensor.

Acknowledgments. “This work was supported by the IT R&D program of KEIT, [10040037, An intelligent IT lighting system development using interactive information exchange in complex space]”. This work was supported by Priority Research Centers Program through the National Research Foundation of Korea (NRF) funded by the Ministry of Education, Science and Technology (2011-0022977).

References

1. Despomimer, D., Ellingsen, E.: The vertical farm: The sky-scraper as vehicle for a sustainable urban agriculture. In: CTBUH 8th World Congress, pp. 2–8 (2008)
2. Kim, J.H.: Trend and Implications of plant factory in Japan. *Monthly World Agricultural News* 118, 3–17 (2010) (in Korean)
3. Suk, J., Kim, S., Ryoo, I.: Non-Contact Plant Growth Measurement Method and System Based on Ubiquitous Sensor Network Technologies. *Open Access Journal* 6(1), 4312–4334 (2011) (in Korean)
4. Takatsuji, M.: *Kanzen Seigyō Gata Shokubutsu Koujyō*. World Science Co. (2008)
5. Lee, H.: Control of Daily Integral PPFD by the Artificial Lighting and Shading Screen in Greenhouse. *Journal of Bio Environment Control* 12(1), 45–53 (2002) (in Korean)

Context-Aware Architecture for Improvement of Energy Efficiency and Growth Promotion of Plants

Hyung-Sun Kim, Heon-Taek Kong, and Jae-Hyun Lim

Computer Science Department, Kongju National University
Budeadong 275, Cheonan, Chungnam - Korea
{ddaker98, htkong, defacto}@kongju.ac.kr

Abstract. To product steadily high-quality plants in a plant factory, proper PPFD should be supplied according to the sort of plants. In order to produce the plant, the artificial lighting system should be installed in the greenhouse. This system is controlled itself according to the quantity of sunrays (dynamic changes of sunray). This phenomenon cause to supply the required quantity of rays without any interpretation process and also the PPFD of the artificial-rays equal to the PPFD of sunrays. This paper suggests context-aware architecture to improve energy efficiency by controlling artificial-rays.

Keywords: Plant factory, LED control, Energy efficiency, Energy saving.

1 Introduction

Recently the climate changes terribly affect to the agricultural production such as the flood in Australia exposure of nuclear and earthquake in Japan. These disasters cause to create a food problem such as unstable supply and sudden rise. Also there are many requirements that a plant require to be grown up [1-3]. A good artificial-environment could be created for the plants by controlling systems. Therefore plants will not be interrupted by natural-environment.

To produce high-quality plants continuously in a plant factory, PPF (Photosynthetic Photon Flux) which is depending on quantity of plant should be supplied. It is important to know that quantity of PPF is directly affected to design a proper greenhouse. Because it directly affect to growth of plants [4][5].

When we build up a greenhouse, transmittances of sunray can be different according to the direction and structural materials. In order to supply the required amount of supplemental light we must develop a technology about controlling light [6].

Thus, in this paper we measure change of PPF (which depend on sunray) in greenhouse. After interpreting of the required amount of supplemental light, to supply the proper PPF according to the plant species, Context-Aware structure is suggested.

This paper comprised of 5 chapters. We explain related work in chapter 2. Chapter 3 illustrates effect of PPF on growth of plants by comparing with PPF and fresh-weight of plants. We design the Context-Aware structure to interpret the amount of supplemental light in real-time in chapter 4. We present future works in chapter 5.

2 Related Work

2.1 Photosynthetic Photon Flux(PPFD)

The light is a factor that affect to growth of plant. PPFD(Photosynthetic Photon Flux Density) is the density of light that needed as plant photosynthesize. The definition of PPFD is "Quantity of photons that survey on a unit area per a second". The unit of PPFD is $\mu\text{mol}\cdot\text{s}^{-1}$ (micromole per square meters per second). This is the amount of photons emitted for 1 second in an area of one square meter.

2.2 Light-Saturation-Point According to Crops

If density of light is increased while plant is growing, also speed of photosynthesize is increased. But from a particular point, density of light saturation and speed of photosynthesize don't increase anymore. The density of light at this point is called the Light Saturation Point at the moment[7].

Table 1. Illustrates the Light Saturation Point based on tube lights

Cultivation Crops	Light saturation point(PPFD)
tomato and watermelon	70,000(847)
cucumber	55,000(665)
pea	40,000(484)
Lettuce and flagellum	25,000(302)
grapes	40,000(484)
orchid	10,000(121)
ginseng	55,000(665)

3 Structure of Experimental Environment

3.1 Experimental Environment

In this chapter, we design a type of showcase to place our Mini-Plant and research the effects of PPFD where the object is Red-lettuce.

There are two plates, and each plate contains 32 pots where plants can be placed in the Mini-Plant. In order to supply PPF, Four bars of LEDs are located at above 27cm from plate. The details of experimental environment show in Table 2.

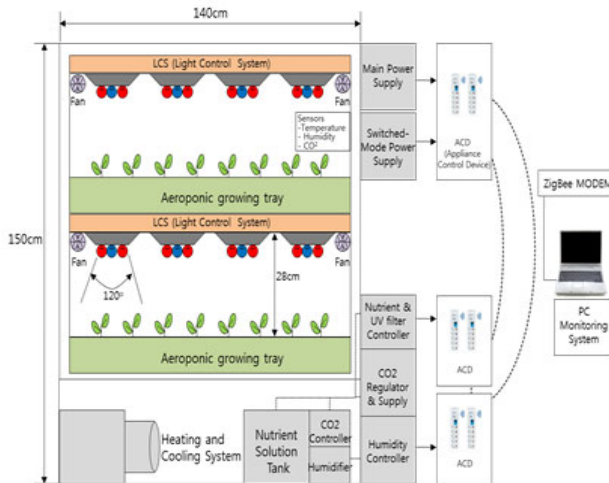
Also blueprint of Mini-Plant illustrates in Fig.1 and picture of Mini-Plant shows in Fig. 2.

3.2 Growth of Plant by Amount of Light

To analyze the relationship between the amount of PPFD and fresh weight of plant, we must measure the average of PPFD and fresh weight of plants in each row (each row consist 8 pots) by Quantum Meter (MQ-200) and the scale.

Table 2. Specification of experimental environment

Section	Standard
Mini-Plant	140 * 150 * 80(cm) (width * height * depth)
Growth floor	120 * 60 * 30(cm) (width * height * depth)
Pots	4rows * 8columns(32pots)
LED Bar	The mixed wavelength -blue : 450(nm) -red : 630-660(nm) (Rate of the number of blue leds and red leds, 11:7)

**Fig. 1.** Blueprint of Mini-Plant

Referring to Fig. 3, average PPFD of the (center regions) 2nd and 3rd rows are higher than the other rows of the plate. In other words, we could predict that the rate of plants growing speed in the center region is high and the other region is low. Fig. 4 is the expected result of the prediction. The fresh average-weight of plants located in the center regions in the plate is heavy, and the others are light. As the experimental results, the amount of PPFD is closely related to plant growth. In addition, the amount of PPFD should be supplied according to the sort of plants and the growth stages of plants as well. Therefore, artificial light control system provides the appropriate amount of PPFD according to the dynamic change of sunray for the growth promotion of plants.

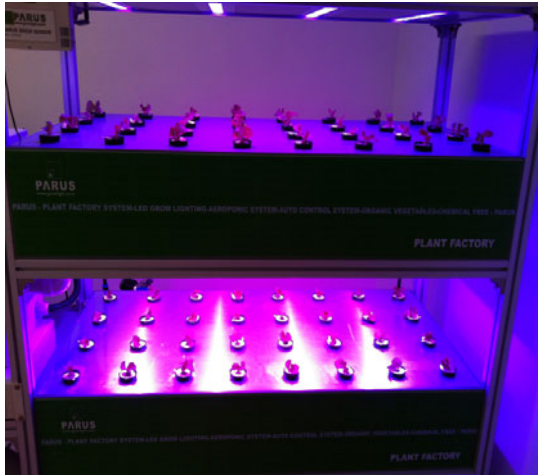


Fig. 2. Growth floor of Mini-Plant

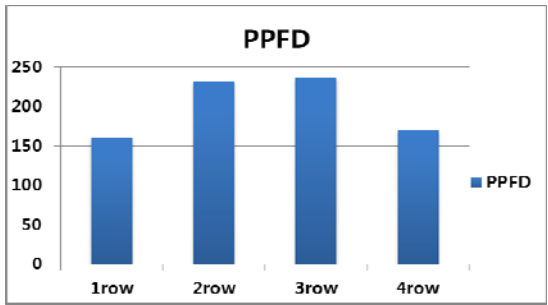


Fig. 3. PPFD in Each rows Shelf



Fig. 4. Shoot Fresh Weight of Red Leaf Lettuces

4 Context-Awareness Architecture

In this paper, we suggest the artificial lighting control system based on context-awareness to promote plant growth and to reduce energy consumption by supplying interpreted supplemental lighting in real-time according to the dynamic changes of sunray. Proposed system consists five models as in Fig. 5 and the process of each model is as follows.

Firstly, Context Collector collects external environmental information such as intensity of sunray, temperature, humidity, CO₂ and nutrient related to the growth of plant by the integrated sensors which is installed at several points in plant factory. Collected data is converted into appropriate data type and then it is stored into database of external context information. Internal context information means a kind of intelligence such as proper PPFD according to the sort of plant and the stages of growth, environmental factors such as temperature, humidity, the amount of plant photosynthesis, weight of plant and weather information. Those are collected in real-time by the RSS reader from the meteorological administration.

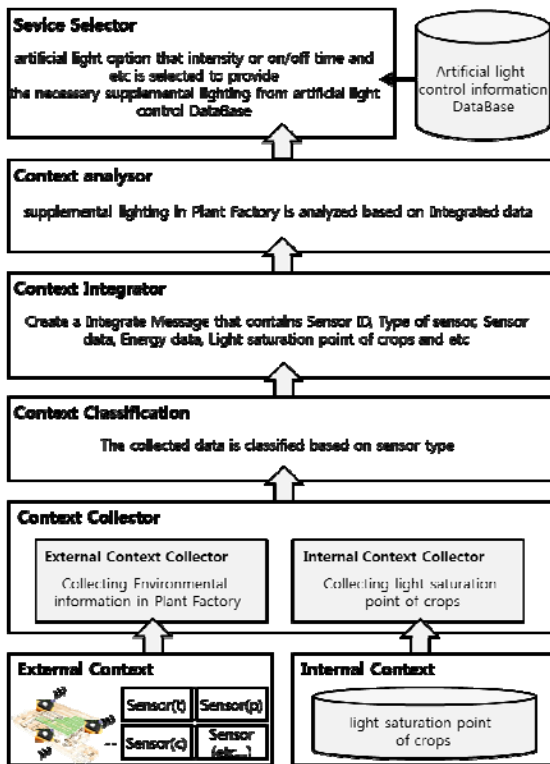


Fig. 5. Context-Awareness Architecture

The process of interpretation according to the variation of each environmental factor is needed on a cycle since a correlation between environmental factors such as light intensity, temperature, humidity, CO₂ and the required amount of supplemental lighting,....ect are depending on the other environmental factors and weather changings[8].

Collected internal and external context information by context collector are classified as three periods as like as the germinating period, the vegetative period and the promotive period. In general, the growth stages of leaf vegetables are classified by weight of plant. (a germinating period(2g~3g), a vegetative period(3g~10g), a promotive period(10g~100g)).

Context information interpreter analyzes needed the amount of supplemental lighting according to dynamic changings of weather using light compensation level and light saturation point which are depending on the sort of plant that are stored in the internal context information database .

Service selector executes the artificial lighting control service based on context-awareness possibly for dramatic environmental changes by controlling the system according to the informations of the light device such as intensity, duty rate, stages of on/off.

5 Conclusions

This paper suggests the architecture of artificial lighting control system based on context-awareness to provide and interpreted the appropriate amount of supplemental lighting according to the sort of plant and the stages of growth for the improvement of energy consumption in the hybrid type of plant factory.

Through the proposed system, we can produce high-quality crops by providing needed amount of supplemental according to the variation of sunrays and reduce energy consumption in plant factory. We expect that such development of business model could make economization and commercialization of plant factory.

In the future, the architecture of wireless network environment based on sensors must be installed in hybrid plant factory to verify the proposed system. After that, we could verify the effect of energy consumption reduction through the artificial lighting control system based on context-awareness by supplying the required amount of supplemental lighting according to the collection of information of each environment factor according to the weather changes.

Acknowledgments. This research was supported by the MKE(The Ministry of Knowledge Economy), Korea, under IT/SW Creative research program supervised by the NIPA(National IT Industry Promotion Agency)" (NIP A-2011-(C1820-1101-0010)). “ This work was supported by the IT R&D program of KEIT, [10040037, An intelligent IT lighting system development using interactive information exchange in complex space]”.

References

1. Um, Y.-C., Oh, S.-S., Lee, J.-G., Kim, S.-Y., Jang, Y.-A.: The Development of Container-type Plant Factory and Growth of Leafy Vegetables as Affected by Different Light Sources. *Journal of Bio-Environment Control* 19(4), 333–342 (2010) (in Korean)
2. Trussell, H., Nilsson, A., Patel, P., Wang, Y.: Estimation and detection of network traffic. In: *Proc. of 11th Digital Signal Processing Workshop*, pp. 246–248 (2004)
3. McGregor, A., Hall, M., Lorier, P., Brunskill, J.: Flow Clustering Using Machine Learning Techniques. In: Barakat, C., Pratt, I. (eds.) *PAM 2004*. LNCS, vol. 3015, pp. 205–214. Springer, Heidelberg (2004)
4. Sebastian, Z., Thuy, N., Grenville, A.: Self-learning IP traffic classification based on statistical flow characteristics. In: *Proc. of 6th Int. Workshop on Passive and Active Measurement*, pp. 325–328(2005)
5. Hyun-Woo, L., Suk-Gun, L., Sang-Ho, L.: Relationship between Total Solar Radiation and PPF, and Transmittance in Greenhouse at Different Weather Conditions. *Journal of Bio-Environment Control* 11(2), 56–60 (2002) (in Korean)
6. Young Hah, C., Kyoung Sub, P., Nam Jun, K., Hong Lim, K., Yong Bum, K., Heung Deug, K., Dae Hoe, G., Myoung Hwan, C.: Effects of Greenhouse Orientation on the Greenhouse Environment and the Growth of Tomato in Forcing Culture. *Journal of Bio-Environment Control* 19(1), 6–11 (2010)
7. Sook-Youn, K., Jae-Hyun, L.: Improvement of Energy Efficiency in Plant Factory using Optimum light Intensity Control According to Growth Stages of Plant (2011) (in Korean)
8. Young-Hae, B., Young-Soo, K.: Development of a photosynthetic Numerical Model Explaining the Relationships between Light Intensity, CO₂, CO₂ Concentration, Temperature and Photosynthetic Rate. *Journal of Korean Society of Biology Education* 31(1), 87–93 (2003) (in Korean)

Trajectory Estimation of Hypersonic Vehicle Based on Observations from Infrared Sensor on LEO Satellite

Nan Wu and Lei Chen

College of Aerospace and Material Engineering, National University of Defense Technology,
Changsha, China
wunanfortoday@gmail.com, clwhl@263.net

Abstract. Strong nonlinear observation model of satellite infrared sensor is established and transformed into linear pseudo-measurement equation by unscented transform method. A kind of noise adaptive three-dimensional constant acceleration model is constructed for non-cooperative and strong maneuvering target. Real-time estimation on process noise is carried out to reduce dependence of the model on prior information. The trajectory of hypersonic vehicle is estimated using Kalman filter based on the proposed model and linear pseudo-measurement equation. Simulation results show that the proposed algorithm has high filtering precision, strong robustness and adaptability. It is applicable to the state estimation of strong maneuvering target with fuzzy or unknown dynamic characteristics and nonlinear measurement equation.

Keywords: hypersonic vehicle, infrared sensor, trajectory estimation, adaptive filter, constant acceleration model.

1 Introduction

Hypersonic vehicle is characterized by high flight speed, low flight trajectory, far operating distance and strong maneuver ability [1]. It has brought challenges to tracking system. Longer tracking arch can be obtained by using low-orbit satellite constellation to observe hypersonic vehicle [2], but trajectory estimation of hypersonic vehicle by using Kalman filter have two problems: (a) the observation model is strongly nonlinear; (b) hypersonic vehicle is non-cooperative and strong maneuvering target, the dynamic model is difficult to construct.

Yang and Li carry out Taylor series expansion on nonlinear equation and ignore higher order derivatives to transform nonlinear equation into linear one [3,4], the disadvantages are that linearization error increases rapidly with the enhancement of the system's nonlinearity and the nonlinear equation must be derivable. Compared with approximation of nonlinear function, the approximation of error distribution characteristics is much simpler. Based on this thought, Unscented Kalman Filter (UKF) were presented successively [5]. Unscented Transform (UT) method in UKF is the suitable method for solving linearization problem of nonlinear equation.

Constant Acceleration Model (CAM) and Current Statistical Model (CSM) are widely used in the filed of maneuvering target motion modeling [6]. CAM has simple

form but it requires the use of adaptive detection technology to adjust process noise covariance matrix in real time. If better process noise covariance matrix adaptation method is found, CAM can get better precision than CSM and the dependence on prior information can be reduced at the same time [7].

Double-satellite observation model is established and transformed into linear pseudo-measurement equation using UT method, a kind of process noise adaptive three-dimensional CAM is constructed, carried out real-time estimation on process noise through innovation to reduce dependence on prior information. At last, based on the proposed model and linear pseudo-measurement equation, the trajectory of hypersonic vehicle is estimated using Kalman filter.

2 Derivation of Pseudo-measurements

Coordinate systems used include Earth-Centered Inertial coordinate system $O_e - X_I Y_I Z_I$ (ECI), Earth-Centered Fixed coordinate system $O_e - XYZ$ (ECF) and Satellite Orbital coordinate system $o_s - x_s y_s z_s$ (SO), among which, SO coordinates is defined as follows: coordinate origin locates at the centroid of satellite; the fundamental plane is motion plane of satellite; z-axis points toward the geocenter; y-axis points toward the cross product of z-axis and satellite velocity and x-axis is toward the direction of the velocity and completes the right-handed system.

The position vector and state vector of target in ECF coordinates are denoted by $\mathbf{P} = [X \ Y \ Z]^T$ and $\mathbf{X} = [X \ \dot{X} \ \ddot{X} \ Y \ \dot{Y} \ \ddot{Y} \ Z \ \dot{Z} \ \ddot{Z}]^T$, respectively. Azimuth A and Elevation E are the satellite measurements defined in SO-CS. Double-satellite measurement equation is

$$\begin{aligned} \mathbf{r} &= h(\mathbf{X}) + \mathbf{v} \\ \mathbf{C}_r &= E\{\mathbf{v}\mathbf{v}^T\} = \text{diag}[\sigma_{A1}^2, \sigma_{E1}^2, \sigma_{A2}^2, \sigma_{E2}^2] \end{aligned} \tag{1}$$

where $\mathbf{r} = [A_1 \ E_1 \ A_2 \ E_2]^T$, \mathbf{v} and \mathbf{C}_r are the measurement noise vector and its covariance matrix respectively, σ^2 denotes the variance of corresponding measurement.

The measurement equation in (1) is nonlinear. \mathbf{P}_r is the position vector of the target in ECF calculated by using \mathbf{r}

$$\mathbf{P}_r = f(\mathbf{r}). \tag{2}$$

\mathbf{P}_r is taken as the pseudo-measurement, the pseudo-measurement equation is simple and linear as below:

$$\begin{aligned} \mathbf{y} &= \mathbf{P}_r = \mathbf{H}\mathbf{X} + \mathbf{V} \\ \mathbf{R} &= E\{\mathbf{V}\mathbf{V}^T\} \end{aligned} \tag{3}$$

where $\mathbf{H} = \begin{bmatrix} 1 & 0 & 0 & 0 & 0 & 0 & 0 & 0 & 0 \\ 0 & 0 & 0 & 1 & 0 & 0 & 0 & 0 & 0 \\ 0 & 0 & 0 & 0 & 0 & 0 & 1 & 0 & 0 \end{bmatrix}$, \mathbf{V} and \mathbf{R} is the pseudo-measurement

noise vector and corresponding covariance matrix respectively, which can be calculated by \mathbf{C}_r .

Firstly, the expression of $f(\bullet)$ in (2) is derivated, then UT method is used to transform \mathbf{r} and \mathbf{C}_r into \mathbf{y} (or \mathbf{P}_r) and corresponding covariance matrix \mathbf{R} .

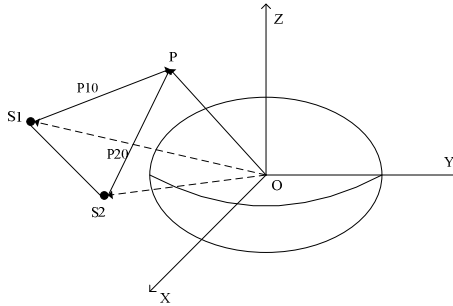


Fig. 1. Gometric relationship between satellites and target

As shown in Fig. 1, without measurement errors, line of sight vectors of satellites S1 and S2 to target P intersect at P, so P is accurate position of the target. The pseudo-measurement \mathbf{y} can be calculated by using \mathbf{r} according to triangulation relationship of $\Delta S_1 S_2 P$.

In $\Delta S_1 S_2 P$, three angles are defined as S_1 , S_2 and P , so the opposite sides are s_1 , s_2 and p respectively. Position vectors of the two satellites in ECI coordinates are given as:

$$\begin{aligned} \overline{OS_1} \Big|_{ECI} &= [X_{IS1} \quad Y_{IS1} \quad Z_{IS1}]^T \\ \overline{OS_2} \Big|_{ECI} &= [X_{IS2} \quad Y_{IS2} \quad Z_{IS2}]^T \end{aligned} \tag{4}$$

The length of p is:

$$p = \sqrt{(X_{IS2} - X_{IS1})^2 + (Y_{IS2} - Y_{IS1})^2 + (Z_{IS2} - Z_{IS1})^2} \tag{5}$$

In orbital coordinate system of satellite 1, the vector $\overline{S_1 S_2}$ is described as follows:

$$\overline{S_1 S_2} \Big|_{S_1 O} = \mathbf{T}_{ECI}^{S_1 O} \begin{bmatrix} X_{IS2} - X_{IS1} \\ Y_{IS2} - Y_{IS1} \\ Z_{IS2} - Z_{IS1} \end{bmatrix} \tag{6}$$

\mathbf{T}_{ECI}^{SO} represents transformation matrix from ECI to SO, and symbols below have the similar meaning. Take any point P_0 on the line of sight $\overline{S_1P}$ (it is assumed that $\rho_{10} = 1000000\text{m}$), then the vector $\overline{S_1P_0}$ in orbital coordinate system of satellite 1 is described as follows:

$$\overline{S_1P_0}\Big|_{S_1O} = \begin{bmatrix} \rho_{10} \cos E_1 \sin A_1 \\ \rho_{10} \cos E_1 \cos A_1 \\ \rho_{10} \sin E_1 \end{bmatrix} \tag{7}$$

Angle S_1 can be calculated by $\overline{S_1P_0}$ and $\overline{S_1S_2}$:

$$S_1 = \arccos \left(\frac{\left(\overline{S_1P_0}\Big|_{S_1O} \right) \cdot \left(\overline{S_1S_2}\Big|_{S_1O} \right)}{\left| \overline{S_1P_0}\Big|_{S_1O} \right| \left| \overline{S_1S_2}\Big|_{S_1O} \right|} \right) \tag{8}$$

Similarly, S_2 can be calculated by $\overline{S_2P_0}$ and $\overline{S_1S_2}$. In ΔS_1S_2P , sine theorem is used to obtain module of the line of sight vector $\overline{S_1P}$:

$$\rho_p = s_2 = \frac{p \sin S_2}{\sin(\pi - S_1 - S_2)} \tag{9}$$

Therefore, in orbital coordinate system of satellite 1, the line of sight vector $\overline{S_1P}$ is described as follows:

$$\overline{S_1P}\Big|_{S_1O} = \begin{bmatrix} \rho_p \cos E_1 \sin A_1 \\ \rho_p \cos E_1 \cos A_1 \\ \rho_p \sin E_1 \end{bmatrix} \tag{10}$$

Finally the pseudo-measurement \mathbf{y} is:

$$\mathbf{y} = \overline{OP}\Big|_{ECF} = \mathbf{T}_{S_1O}^{ECF} \begin{bmatrix} \rho_p \cos E_1 \sin A_1 \\ \rho_p \cos E_1 \cos A_1 \\ \rho_p \sin E_1 \end{bmatrix} + \mathbf{T}_{ECI}^{ECF} \begin{bmatrix} X_{IS_1} \\ Y_{IS_1} \\ Z_{IS_1} \end{bmatrix} \tag{11}$$

The expression of $f(\bullet)$ has to be derived from (4) to (11). Satellite measurement vector $\mathbf{r}(k)$ and covariance matrix $\mathbf{C}_r(k)$ at the time of t_k can be transformed into pseudo-measurement vector $\mathbf{y}(k)$ and corresponding covariance matrix $\mathbf{R}(k)$ using function $f(\bullet)$ through UT method.

Symmetric sampling theory is used to calculate $(2n + 1)$ σ sampling points χ_i and corresponding weight W_i (n is dimension of random vector):

$$\begin{cases} \boldsymbol{\chi}_0 = \mathbf{r}(k), W_0 = \frac{\kappa}{n + \kappa}, i = 0 \\ \boldsymbol{\chi}_i = \mathbf{r}(k) + \left(\sqrt{(n + \kappa) \mathbf{C}_r(k)} \right)_i, W_i = \frac{1}{2(n + \kappa)}, i = 1, 2, \dots, n \\ \boldsymbol{\chi}_{n+i} = \mathbf{r}(k) - \left(\sqrt{(n + \kappa) \mathbf{C}_r(k)} \right)_i, W_{n+i} = \frac{1}{2(n + \kappa)}, i = 1, 2, \dots, n \end{cases} \quad (12)$$

The following expression of each σ sampling point is obtained through the propagation of nonlinear function $f(\bullet)$:

$$\mathbf{y}_i = f(\boldsymbol{\chi}_i), i = 0, 1, \dots, 2n \quad (13)$$

After nonlinear transformation, pseudo-measurement vector and covariance matrix are:

$$\begin{cases} \mathbf{y}(k) = \sum_{i=0}^{2n} W_i \mathbf{y}_i \\ \mathbf{R}(k) = \sum_{i=0}^{2n} W_i [\mathbf{y}_i - \mathbf{y}(k)][\mathbf{y}_i - \mathbf{y}(k)]^T \end{cases} \quad (14)$$

Equations (3) and (14) show that pseudo-measurement equation after transformation using UT method is linear, but covariance matrix of pseudo-measurement vector is always changing and correlative.

3 Trajectory Estimation Algorithm

3.1 Target Dynamic Model

The three-dimensional constant acceleration model is used as state equation of hypersonic vehicle, define T as sampling period, then discrete time state equation is as follows:

$$\mathbf{X}_{k+1} = \mathbf{F}_{k+1,k} \mathbf{X}_k + \mathbf{W}_k \quad (15)$$

$$\text{where, } \mathbf{F}_{k+1,k} = \begin{bmatrix} \mathbf{F} & \mathbf{O}_{3 \times 3} & \mathbf{O}_{3 \times 3} \\ \mathbf{O}_{3 \times 3} & \mathbf{F} & \mathbf{O}_{3 \times 3} \\ \mathbf{O}_{3 \times 3} & \mathbf{O}_{3 \times 3} & \mathbf{F} \end{bmatrix}_{9 \times 9}, \mathbf{F} = \begin{bmatrix} 1 & T & T^2/2 \\ 0 & 1 & T \\ 0 & 0 & 1 \end{bmatrix}, \mathbf{O}_{m \times n} \text{ is zero matrix of } m$$

rows and n columns, \mathbf{W}_k is the discrete process noise vector.

3.2 Kalman Filter

The state equation and measurement equation are given by (15) and (3) respectively. The following steps are executed at each time step for Kalman filter:

$$\begin{cases} \hat{\mathbf{X}}_{k+11k} = \mathbf{F}_{k+1,k} \hat{\mathbf{X}}_{k1k} \\ \hat{\mathbf{P}}_{k+11k} = \mathbf{F}_{k+1,k} \hat{\mathbf{P}}_{k1k} \mathbf{F}_{k+1,k}^T + \mathbf{Q}_k \\ \mathbf{K}_{k+1} = \hat{\mathbf{P}}_{k+11k} \mathbf{H}_{k+1}^T \left[\mathbf{H}_{k+1} \hat{\mathbf{P}}_{k+11k} \mathbf{H}_{k+1}^T + \mathbf{R}_{k+1} \right]^{-1} \\ \hat{\mathbf{X}}_{k+11k+1} = \hat{\mathbf{X}}_{k+11k} + \mathbf{K}_{k+1} \left[\mathbf{y}_{k+1} - \hat{\mathbf{y}}_{k+11k} \right] \\ \hat{\mathbf{P}}_{k+11k+1} = \left[\mathbf{I} - \mathbf{K}_{k+1} \mathbf{H}_{k+1} \right] \hat{\mathbf{P}}_{k+11k} \end{cases} \quad (16)$$

3.3 Process Noise Covariance Matrix Adaptation

To non-cooperative maneuvering target, when CAM is used to describe its motion, time-varying process noise will be inevitably introduced. According to above analysis, it can be seen that real-time estimation of matching process noise covariance matrix decides whether CAM can show excellent performance.

According to (15), suppose that the process noise vector is constant in time interval $[t_k, t_{k+1}]$, then the process noise covariance matrix \mathbf{Q}_{k+1} is described as follows:

$$\mathbf{Q}_{k+1} = \begin{bmatrix} \mathbf{Q}_I \sigma_X^2(t_{k+1}) & \mathbf{O}_{3 \times 3} & \mathbf{O}_{3 \times 3} \\ \mathbf{O}_{3 \times 3} & \mathbf{Q}_I \sigma_Y^2(t_{k+1}) & \mathbf{O}_{3 \times 3} \\ \mathbf{O}_{3 \times 3} & \mathbf{O}_{3 \times 3} & \mathbf{Q}_I \sigma_Z^2(t_{k+1}) \end{bmatrix}_{9 \times 9}, \quad \mathbf{Q}_I = \begin{bmatrix} T^6/36 & T^5/12 & T^4/6 \\ T^5/12 & T^4/4 & T^3/2 \\ T^4/6 & T^3/2 & T^2 \end{bmatrix} \quad (17)$$

Where $\sigma^2(t_{k+1})$ is the variance of the process noise.

$$\begin{cases} \sigma_X^2(t_{k+1}) \approx E \left\{ \left[\frac{\hat{\mathbf{x}}_{k+11k+1} - \hat{\mathbf{x}}_{k+11k}}{T} \right] \left[\frac{\hat{\mathbf{x}}_{k+11k+1} - \hat{\mathbf{x}}_{k+11k}}{T} \right]^T \right\} = \frac{1}{T^2} \left[\mathbf{K}_{k+1} \left[\mathbf{H}_{k+1} \hat{\mathbf{P}}_{k+11k} \mathbf{H}_{k+1}^T + \mathbf{R}_{k+1} \right] \mathbf{K}_{k+1}^T \right]_{33} \\ \sigma_Y^2(t_{k+1}) = \frac{1}{T^2} \left[\mathbf{K}_{k+1} \left[\mathbf{H}_{k+1} \hat{\mathbf{P}}_{k+11k} \mathbf{H}_{k+1}^T + \mathbf{R}_{k+1} \right] \mathbf{K}_{k+1}^T \right]_{66} \\ \sigma_Z^2(t_{k+1}) = \frac{1}{T^2} \left[\mathbf{K}_{k+1} \left[\mathbf{H}_{k+1} \hat{\mathbf{P}}_{k+11k} \mathbf{H}_{k+1}^T + \mathbf{R}_{k+1} \right] \mathbf{K}_{k+1}^T \right]_{99} \end{cases} \quad (18)$$

Suffix mn represents element in the m th row and the n th column. Equation (18) shows that the nature of adaptive estimation of process noise is to constitute certain corresponding relationship with innovation. When the innovation increases, the current model matches worse with the target actual motion, and the process noise of state equation increases correspondingly.

4 Simulation

In this section the performance of the algorithm proposed in this paper is evaluated and compared with Extended Kalman Filter (EKF) based on a CS model. The standard trajectory of hypersonic vehicle is obtained according to the dynamic model presented in [8].

The measurement standard deviation of the sensor on satellite is 0.01 deg, the sampling rate is 0.05 s. The CS model design parameters are $\alpha = 0.01$ and $a_{\max} = 70 \text{ m/s}^2$. The results of simulation are shown in Fig. 2 and Fig. 3.

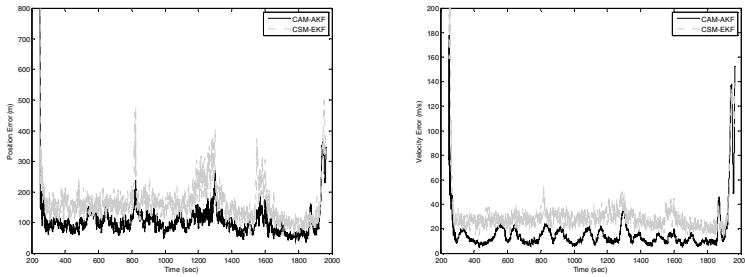


Fig. 2. The Root Mean Square Error (RMSE) of the target position and velocity

Fig. 2 shows the Root Mean Square Error (RMSE) of the target position and velocity respectively, solid lines show our algorithm behavior and dots show CS model behavior. Fig.3 shows the true acceleration of the target and the filtered one using our algorithm. Solid lines show the true value of the target acceleration and dots show the filtered one using our algorithm.

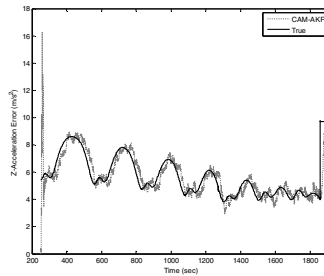


Fig. 3. The acceleration of the target

The results show that: (a) the steady-state precision of the algorithm proposed is higher than that of CSM-EKF algorithm. There are two reasons: firstly, the algorithm in this paper has more accurate approximation of nonlinear measurement equation than EKF; secondly, it is very difficult to accurately give prior information of CS model; (b) when target acceleration changes violently, error increases to a certain degree but the filter is still steady. This shows that the algorithm in this paper has strong adaptability.

5 Conclusion

This paper conducts adaptive estimation on process noise using innovation based on CA model to reduce the dependence on the prior information, and the UT method is used to transform nonlinear measurement equation into linear pseudo-measurement equation. Therefore, the nature of the algorithm in this paper is adaptive-UKF algorithm based on CA model. Compared with EKF, the algorithm in this paper has higher precision in solving linearization problem of nonlinear measurement equation. Compared with UKF, computational complexity of the algorithm in this paper is smaller and only one UT transformation is required. Moreover, C_r is diagonal matrix, according to (12), it is very easy to find the solution of root mean square. Simulation results show that the algorithm proposed has high filtering precision, strong robustness and adaptability. It is applicable to the state estimation of strong maneuvering target with fuzzy or unknown dynamic characteristics and nonlinear measurement equation.

References

1. George, R.: The Common Aero Vehicle-Space delivery system of the future. In: AIAA Space Technology Conference & Exposition, pp. 1–11 (1999)
2. Pu, J., Cui, N., Guo, J.: Space-Based Infrared System and the Analysis of its Detecting Capability (in Chinese). *Modern Defence Technology* 36, 69–72 (2008)
3. Yang, A., Zhang, T., An, W.: Trajectory Estimation in Free Coast Phase Using Pseudolinear Estimator for SBIRS-Low (in Chinese). *Journal of Ballistics* 18, 4–7 (2006)
4. Li, D., Zhou, Y., Miao, Y.: Ballistic Trajectory Estimation with LOS Measurement (in Chinese). *Acta Electronica Sinica* 31, 248–251 (2003)
5. Julier, S., Uhlmann, J.: Unscented filtering and nonlinear estimation. *Proc. IEEE* 92, 401–422 (2004)
6. Li, X.R., Jilkov, V.P.: A Survey of Maneuvering Target Tracking: Dynamic Model. In: *Proceeding of SPIE*, pp. 212–235 (2000)
7. Pan, Q., Liang, Y., Yang, F.: *Modern Target Tracking and Information Fusion* (in Chinese). National Defense Industry Press, Beijing (2009)
8. Yong, E., Chen, L., Tang, G.: Trajectory Optimization of Hypersonic Gliding Reentry Vehicle Based on the Physical Programming (in Chinese). *Acta Aeronautica Et Astronautica Sinica* 29, 1092–1097 (2008)

Improvement of Energy Efficiency in Plant Factories through the Measurement of Plant Bioelectrical Potential

Sookyoun Kwon and Jaehyun Lim

Computer Science Department, Kongju National University
Budeadong 275, Cheonan, Chungnam - Korea
{sookyoun, defacto}@kongju.ac.kr

Abstract. To create the best environment for plant growth, research is needed to resolve the economic challenges faced by plant factories using methods such as energy-efficient artificial lighting and light control technology. Plants react sensitively to environmental changes in temperature, humidity, and carbon dioxide, and to changes in the wavelength and intensity of light. Among these environmental factors, light is essential for photosynthesis. Therefore, to promote plant growth and improve energy savings in plant factories, we need a better understanding of the appropriate light wavelength and the PPFD (Photosynthetic Photon Flux Density) required by each type of plant. In this paper, a system has been designed to measure and analyze the plant bioelectrical potential which differs depending on the type of plant and the lighting conditions. This experiment identifies the optimal lighting environment for different types of plants through a comparative analysis process of growth rate and energy consumption.

Keywords: Plant Bioelectrical Potential, Plant Factory, LED, Photosynthetic Photon Flux Density, PPFD, Energy Saving, Energy Efficiency.

1 Introduction

Recently, the depletion of energy resources, soil degradation, and abnormal weather phenomena has lead to a serious threat to global food security. Interest in plant factories has increased along with the need for safer farming that can reliably supply food; free from the uncertainty caused by rapid climate change [1].

A plant factory is a type of factory that is capable of planned plant production which does not rely upon the weather or the season. A plant factory artificially controls various environmental factors for plant growth such as light, temperature, and humidity [2]. This system has the benefit of producing plants regardless of natural climate change, the geographical position of production facilities, and the regional environment since the plants are grown in environmentally controlled facilities. In addition, it is possible to produce normalized product of uniform size and shape through a controlled process by supplying the optimum growing conditions in its facilities. It also has the advantage of making product pricing easier by way of production forecasts. Despite the advantages, the plant factory business has had difficulty breaking into new markets because of the initial investment costs for

facilities and equipment, the lack of cultivation techniques for growing different plant varieties, and operating expenses [1].

Among the various types of artificial lighting used for growing plants, LED is in the spotlight since it can emit an effective wavelength for plant photosynthesis. In addition, it can operate at lower voltages and lasts longer than other artificial lighting. It is also available for contact radiation because it does not include heating elements. Therefore, it has a high investment value as an artificial light source for plant factories. In particular, red light with a wavelength of about 640 and 660 nanometers contributes largely to plant photosynthesis and blue light with a wavelength of about 430 and 450 nanometers aids plant morphogenesis. Depending on the type of plant, mixed wavelength in light with the appropriate intensity is very useful in improving growth, quality, and functionality of plants. Moreover, red and blue light use very little energy [5]. However, despite the advantages LED lights have on the issues of cost-effectiveness and practicality, their initial cost of installation is higher than other artificial lights [4].

To reduce the energy consumption of LED lights in plant factories, it is necessary to determine the appropriate wavelength for plant photosynthesis and minimize the loss of light by emitting the appropriate amount of light to target plants. Determining the proper PPF (Photosynthetic Photon Flux Density) and identifying characteristics according to plant type and their growth rates are required for precise control. Relationship analysis between such lighting factors and other environmental factors like temperature and humidity is also needed. Such a process is an effective way to reduce the total energy consumption of a plant factory by decreasing the entire growing season of plants and by promoting plant growth. To precisely control the light environment, the growth characteristics of plants must be determined by type. Plants react sensitively to various environmental changes such as changes in light, temperature, humidity, carbon dioxide, and nutrients. Among these factors, light is essential for plant photosynthesis [3]. The wavelength of light and PPF can be optimized for each plant type and their growing period.

In this paper, after selecting the target plants for the experiment, a Plant Bioelectric Potential Response Analysis Method is applied to measure the direct response of plant changes depending on PPF and each wavelength of LED (red and blue light), the continuous emission of mixed wavelengths, and the blinking emission of mixed wavelengths. Plant Bioelectric Potential is generated by the difference of the ion concentration between the interior and the exterior of plant cell tissue. Such a method is one of the best measurement techniques to detect the biological activity of the plant without damaging it [3][6][7][8]. In previous studies, relationship analysis between each wavelength and intensity of LED or surrounding environmental factors and plant bioelectrical potential response had been actively discussed but energy consumption measurements and analysis were not considered.

Unlike these studies, in this thesis, a system is designed to analyze the relationship between Plant Bioelectrical Potential and PPF and the relationship between the growth of plants and the energy consumption according to each light wavelength. The system is constructed in the form of a mini-factory based on a sensor network. Through this experiment, the best lighting environmental condition for the target plant is derived. The structure of this paper is as follows: on page 2, related research on the light saturation point and bioelectrical potential according to plant type are discussed,

and on page 3 experiments and results are explained. Page 4 contains the conclusion and the future project is described.

2 Related Work

2.1 Light Saturation Point According to Plant Type

The speed of plant photosynthesis is increased with light intensity during the process of plant growth. However, the speed of plant photosynthesis does not increase further after a certain point, and the light intensity at this moment is called the light saturation point. In general, the light intensity that is felt by humans is expressed in Lux units but the light intensity that is available for photosynthesis in plants is shown in PPFD. PPFD is the light intensity for plant photosynthesis and its unit is the $\mu\text{mol}^{-2}\text{s}^{-1}$. $\mu\text{mol}^{-2}\text{s}^{-1}$ (micromole per square meters per second). This is the amount of photons emitted for 1 second in the area of one square meter and PPFD can be converted into LUX through the measurement of environmental conditions [1]. Light saturation points according to plant types are shown in Table 1 [9].

Table 1. Light saturation point (Fluorescent Lamp)

Crops	LSP LUX(PPFD)
Tomatoes, Watermelon	70,000 lux(847)
Cucumber	55,000 lux(665)
Peas	40,000 lux(484)
Lettuce, Pimento	25,000 lux(302)
Grapes	40,000 lux(484)
Tangerine	40,000 lux(484)
Pear	40,000 lux(484)
Peach	40,000 lux(484)
Ginseng	55,000 lux(665)

2.2 Plant Bioelectrical Potential

According to related research, plant bioelectrical potential changes along with changes in environmental factors such as light, temperature, and carbon dioxide. Plant bioelectrical potential response changed momentarily at the start as the emitting light increased with the rate of photosynthesis in plants. Such a micro-electrode measurement method has been used mainly for the electrophysiological studies of animals and plants [6].

Ki ANDO et al (2008) analyzed that plant potential response behaviors is changed by the period and the duty rate of blinking light irradiation. Shin-ichi Shibata et al (2009) showed experimental results using blue, green, red and white LED and concluded that the maximum correlation coefficient increased as the light wavelength is increased and V_{h1} (summation of plant bioelectrical potential for one hour) decreased. In addition, various studies related to relationship analysis between plant bioelectrical potential response and various environmental factors are in progress [8].

3 Experimental Results and Analysis

To measure the plant bioelectrical potential response under four different kind of light environments (red, blue, continuous emission under mixed wavelength, and blinking emission under mixed wavelength), a plant cultivation system of two sets which consists of two plates for plant cultivation are constructed as in Fig 1.

An LED controller is located at each plate and consists of two types of wavelength at a rate of 11:7 which is effective for plant photosynthesis; specifically, red light with a wavelength of about 640 and 660 nanometers and blue light with a wavelength of about 430 and 450 nanometers. Each LED controller is designed to control each wavelength and the ratio of mixed wavelength. Using an Aeroponic nutrient supply system, needed nutrients for plant photosynthesis is supplied periodically and this system is energy efficient because it is not pump operated.

To collect and analyze subtle environmental changes inside the lab, two integrated sensors which consist of temperature, humidity and carbon dioxide sensors are installed. The collected data is stored in a database server and is displayed through a monitoring program in real time. Energy consumption depending on each light environment is measured using an ACD (Appliance Control Device) and an all system environment is constructed based on wireless communication.

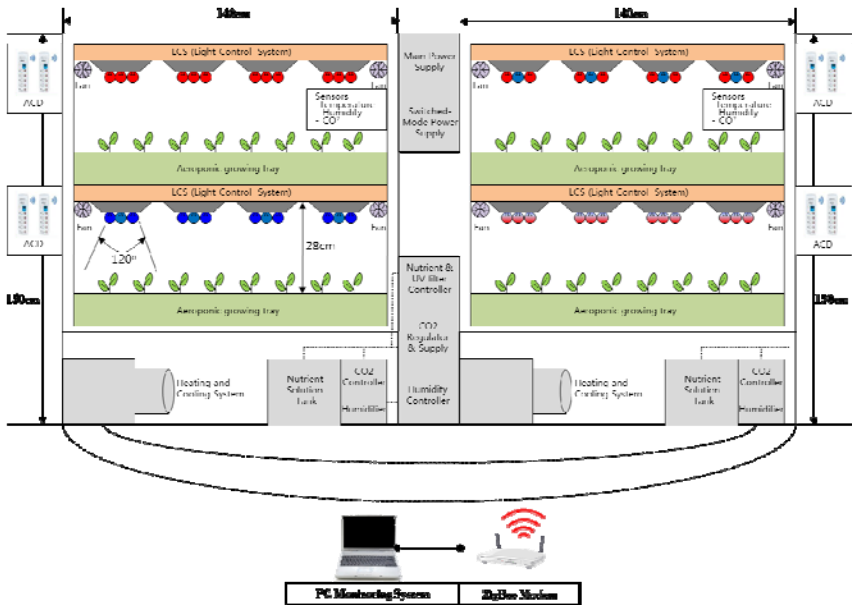


Fig. 1. Plant Cultivation System Building

Fig 2 shows the wavelength result measured under blue and red light using a Spectrometer (JAZ-ADP_GPIO).

To measure the bioelectrical potential response of plants according to different light environments, the light environment on each plate is set up differently as show

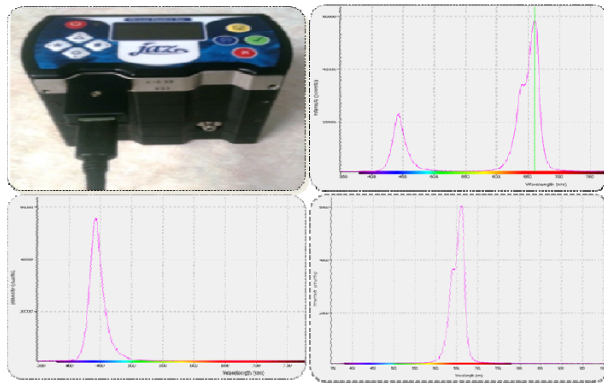


Fig. 2. Spectrometer(JAZ-top left), mixed wave length (top right), Blue(bottom left), Red(bottom right)

in Table 2. Here, the light intensity can be set from 1(minimum value) to 10(maximum value).

In the case of the first and second plate, red and blue light are continuously emitted with maximum light intensity. In the case of the third plate, mixed light with red and blue are continuously emitted with median light intensity. The last light emits intermittently with maximum light intensity.

Table 2. Light environment of each plate

ID	Wave Length	Frequency	Duty Rate	Intensity
1	Red	2500Hz	100%	10(Max)
2	Blue	2500Hz	100%	10(Max)
3	Mixed Light(Cont)	2500Hz	100%	5(Median)
4	Mixed Light(Blink)	2500Hz	50%	10(Max)

The resulting measured average of PPFD according to each row in four different kinds of light environment is shown in Fig. 3.

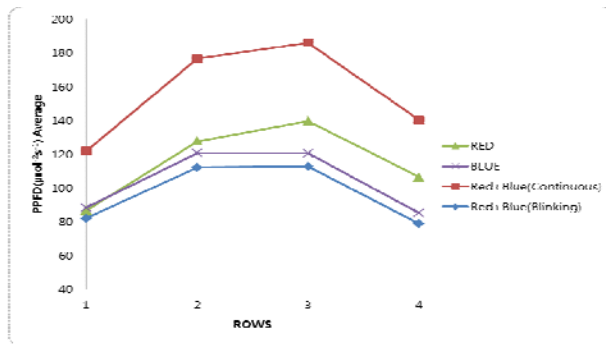


Fig. 3. PPFD Average of each light environment

While the PPFD average of the third plate is the highest value, the fourth plate showed the lowest value. In addition, the PPFD average in the central region of the plate is higher than the outermost region.

The target plant for the experiment is lettuce and it has been grown for 30 days with a temperature of about 22°C, humidity of about 80%, and CO2 of about 400PPM. After 20 days, the plant bioelectrical potential according to wavelength and intensity of light is measured using the measurement system shown in Fig 4. To measure the changes in plant bioelectrical potential according to the wavelength and intensity of light, data is sampled every 0.1sec during a 14 hour period, and for data analysis data is accumulated each hour.

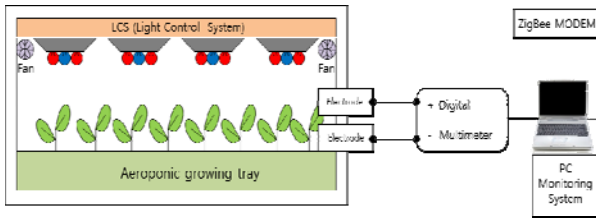


Fig. 4. Plant Bioelectrical Potential Measurement System

Fig 5 shows accumulated data depending on each light environment and on a dark environment.

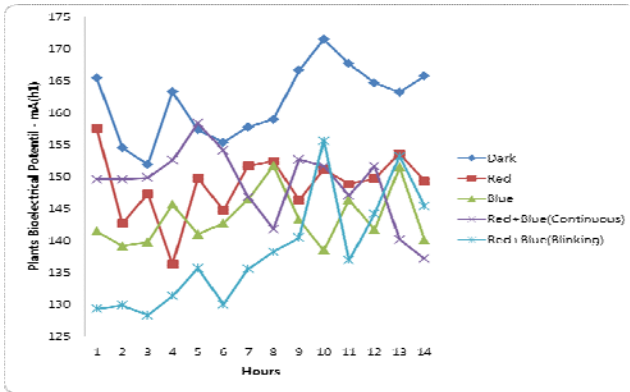


Fig. 5. Plant Bioelectrical Potential Response

Referring to Fig. 5, the summation value (V1) of plant bioelectrical potential in darkness is higher than the others and all data except the last light showed similar patterns. Related research suggests that the plant is stressed in darkness and the same feature is obtained at temperatures under 10 degree C [7].

Table 3 shows the accumulated value of plant bioelectrical potential for 14 hours, the average PPFD measured at each plate, energy consumption measured at each plate for 14 hours, and the fresh weight of plants grown for 30 days.

Table 3. Plant Bioelectrical Potential, PPFD, Fresh Weight, Energy Consumption

	PBP(avg)	$\mu \text{ mol}^{-2}\text{s}^{-1}$ (avg)	g(avg)	W(14h)
Red	0.004129	115.063	46.75	1615.3
Blue	0.003985	103.719	29.75	1680.9
Mixed Light (Continuous)	0.004132	156.125	48.75	2087.2
Mixed Light (Blinking)	0.003836	96.438	37.03	1621.0

The average plant bioelectrical potential and the average PPFD are proportionate. For example, while plants under the third light with the highest PPFD value has the highest plant bioelectrical potential value, plants under the fourth light with the lowest PPFD value has the lowest plant bioelectrical potential value. However, the fresh weight of plants does not perfectly match with the PPFD average.

Even if the average of the PPFD under blue light is about 60% higher than in the PPFD under mixed light (blinking), the fresh weight average of the plant is 70% lower. It is thought that intermittent light emitting with a mixed wavelength promotes the growth of plants. By comparison, the energy consumption, measured from all light equipment for 14 hours, shows that while red light produces excellent energy efficiency, energy consumption of blue light is very high. However, plants grown under red light have a pigment expression problem.

Even if the sort of plant is a red-leaf lettuce, the red color does not appear. In addition, the leaves of the plant are very thin. The plants grown under blue light show a similar form as those grown under the red light but the red pigment does appear. On the other hand, the plants grown under mixed light show the appropriate amount of red color on the leaves and its leaves are appropriately thick.

As a result, it is thought that, depending on the type of plant, proper control of the wavelength and the intensity of light promotes plant growth and reduces energy consumption. In addition, measurement of plant bioelectrical potential according to environmental changes enables the detection of the characteristics of the plant.

In conclusion, appropriate wave length and intensity of light differs according to plant type and intermittent emission of light promotes growth in plants. In addition, among each wavelength of LED, red light is the most energy efficient.

4 Conclusions

This paper shows, through experimentation, that the appropriate wavelength and intensity of light has an impact on the growth of plants and on energy consumption. Using plant bioelectrical potential response analysis methods, it could be verified that

plant bioelectrical potential response is proportional to the intensity of light. In addition, red lighting is an energy-efficient light and mixed light with red and blue promotes the growth of plants when it is emitted intermittently. In the future, the relationship between other environmental factors such as temperature, humidity, and CO₂ and plant bioelectrical potential response can be analyzed and result in the development of a photosynthetic efficiency model.

Acknowledgments. "This research was supported by the MKE (The Ministry of Knowledge Economy), Korea, under IT/SW Creative research program supervised by the NIPA (National IT Industry Promotion Agency)" (NIP A-2011-(C1820-1101-0010)). This work was supported by Priority Research Centers Program through the National Research Foundation of Korea(NRF) funded by the Ministry of Education, Science and Technology(2011-0022977).

References

1. Jae Whune, K.: Trend and direction for plant factory system. *Journal of Plant Biotechnology* 37(4), 442–455 (2010) (in Korean)
2. Sook Youn, K., Jae Hyun, L.: Improvement of Energy Efficiency in Plant Factory using Optimal Light Intensity Control According to Growth Stages of Plant. In: *Proceedings of the Korean Society for Internet Information Conference*, vol. 12(1), pp. 85–86 (2011) (in Korean)
3. Shibata, S., Oyabu, T., Kimura, H.: Bioelectric potential characteristic of pothos under light emitting diode. In: *ICROS-SICE International Joint Conference* (2009)
4. Jae Whune, K.: Trend and implication of Japan's plant factory. *Report of Korea Rural Economic Institute*, vol. 118 (2010) (in Korean)
5. Sun Won, P.: Plant Factory, Vertical Farm. *Agriculture and Horticulture* 3, 148–151 (2010) (in Korean)
6. Ando, K., Hasegawa, Y., Maekawa, H., Katsube, T.: Bioelectric Potential Response Analysis of Plant under Blinking Light Irradiation for Evaluation of Photosynthetic Activity. In: *The International Conference on Electrical Engineering*, vol. (97), pp. 1–5 (2008)
7. Tatsuya, S., Takashi, O., Yuki, H., Shigeki, H., Kosaburo, T.: Bioelectric Potential characteristic of potted plant for temperature change in a residential space. *Transactions of the Institute of Electrical Engineering of Japan* 125(6), 253–258 (2005)
8. Kozue, Y., Kunihiro, H., Yoshiyuki, S.: Relationship between Plant Bioelectrical Potential and Water Consumption Environment. *Journal of the Faculty of Agriculture, Kyushu University* 55(2), 365–370 (2010)
9. (Co.,Ltd.)Parus: System installation status of plant factory using LED in domestic and overseas. *Seminar for plant factory using LED*, no. 7 (2011) (in Korean)

The Identification Algorithm Study of Given Area Weld Image

Qing Jia^{1,2}, Ma Guo-hong^{1,*}, and Wang Cong¹

¹ School of Mechanical & Electrical Engineering, Nanchang University,
Nanchang 330031, China
mgh2002@126.com

² Huanggang Polytechnic College, Huanggang 438002, China

Abstract. In this paper, a idea based on given area weld image is proposed, based on the idea, this thesis designs a vision sensor, and discusses the way the device work, designs a new seam tracking algorithm based on a circular and given point of view. Through simulate experiments conducted on MATLAB, it can receive desirable result, and prove that the algorithm is effective.

Keywords: image processing, weld recognition, given area.

1 Introduction

With the development of Computer Vision Technology and Welding robot technology, Vision sensing technology has been widely used in seam tracking. In the aspect of acquire seam feature, the Vision sensing technology possesses several advantages, more information, no contact with workpiece, strong capacity in anti-electromagnetic interference, and so on. Image Processing Technology[1] is the core link Weld recognition system, it can handle the image captured by CCD, draw information of seam feature, and receive seam deviation signal. Then, output Robot real-time tracking welding seam based on the controller. This article, discusses a new identification algorithm based on a given area angle of view. And seam tracking simulation experiments prove that the algorithm can reliably recognize seam.

1.1 Visual Sensor Designment

1.1.1 Basic Structure of Sensor

In order to realize fixed size angle, a metal gasket which was used to shade light must be installed on the CCD, it is shown in figure 1. So the sensor this paper discusses should improve on the basis of original sensor, a detailed plan as follows. install a spacer on the support frame of sensor, which can make spacer under control by stepping motor, keep angle-limit spacer ahead of CCD so as to achieve purpose that control photography angle . If with no need for spacer, stepping motor can revolve the spacer, drive angle-limit spacer and withdraw CCD, it can recover to an intact and original visual sensor.

* Corresponding author.

The size of spacer is related with welding torch length, spacer installation location and CCD installation site. Besides, it can also can resize spacer according to weld size and perspective area. The size of spacer is preliminarily set to a thickness of 8 mm and diameter of 0.5 mm, and external diameter is the same as diameter of CCD scene.

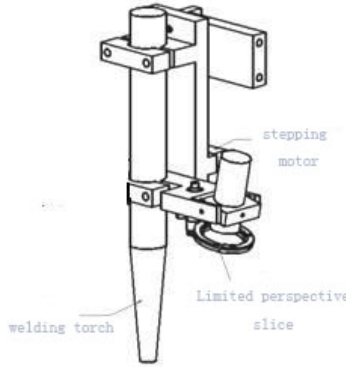


Fig. 1. Vision sensor

1.2 Sensor Characteristics

The characteristics of sensor this paper discuss are:

- 1) Photography Angle is fixed relative to torch. In the process of welding, CCD follow s the trail of torch, so the image collected is real-time.
- 2) Size of perspective area is fixed, that only can require information in small sector. So the visual angle is related with size of seam, weld shape. And select a proper datum mark is very important.
- 3) Hardware is simple and cheap.

But demand a high requirement to install, as is shown in figure 1). According to algorithm this paper design, the lateral point of circular perspective need to coincide with welding spot. As is shown in figure 2, so require to adjust established angle. After experiments and calibration, the established angle is about 20°.

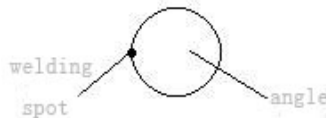


Fig. 2. Visual orientation

1.3 Working Mode

According to position of planar weld, the algorithm is: as is shown in figure 3, points of intersection between circular perspective and weld edge are dot A and B, their segment

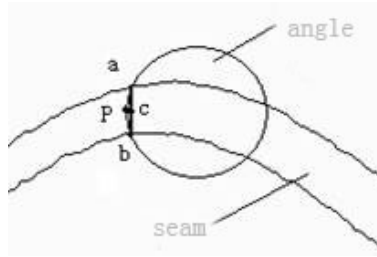


Fig. 3. Algorithm schematic diagram

is regarded as chord length of perspective round. The midpoint of chord length C is next destination location of torch. Segment between dot P and C is torch trajectory.

2 Implementation Algorithm and Experimental Result

2.1 Edge Extraction

2.1.1 Seam Image Denoising

Homomorphic filtering[2] is a image processing methods which combine frequency filtered with gray level transformation . It is based on Image Intensity and reflectance model, utilize Compress brightness range and intensify contrast to improve quality of image. Its theory is: regard gray value as product of illumination and reflectivity. For change of illumination is smaller, it can be seen as a low-frequency aspect of image. And the high-frequency part is reflectivity. Through separately deal with the impact of gray value that illumination and reflectivity create, it can reveal detailed features of shadow region. For Intensity of illumination component is slowly change in area, reflection components in different object boundary sharply change, so low-frequency part which through Fourier change is mainly corresponding to Intensity of illumination component. And high-frequency is mainly corresponding to reflection components.

2.1.2 Threshold Segmentation of Seam Image

Image threshold segmentation mainly include two steps, first should ascertain threshold value which will be cut apart. Then draw an analogy between threshold value and pixel value, so as to divide pixel into area belongs. And the key step is to ascertain the threshold value. In the experiment this paper conduct, because grayscale values of different image is so different, if use fixed threshold segmentation method will not receive satisfactory results.

In order to make segmentation more robust , adopt a method which based on the distance between the kind of adaptive threshold, the method is used to conduct a binary processing toward image, the most kinds of variance method[3] is proposed by Japanese scholars Taking in 1979, which called method Taking, for short OTSU. Its fundamental ideology is to make a partition toward pixels, the distant among every kind to be maximized, So as to determine the right threshold.

Assume that the given the images have L a gray level , threshold value T indicate gray value in image gradation histogram , and divide parts which above T and below T

into two types , type 1 and type 2 . And according to the mean and variance of two types and the ratio of all variance, ascertain the threshold value T.

Assume that the number of pixels in type 1 is $n_1(T)$, mean value of grey value is $v_1(T)$, variance is $\sigma_1^2(T)$; the number of pixels in type 2 is $n_2(T)$, mean value of grey value is $v_2(T)$, variance is $\sigma_2^2(T)$. Average of all pixels is V_T , and inter-class variance can be acquired from the follow formula.

$$\sigma_w^2 = n_1(T)\sigma_1^2(T) + n_2(T)\sigma_2^2(T)V_T \tag{2.1}$$

inter-class variance can be acquired from the follow formula.

$$\sigma_b^2 = n_1(T)n_2(T)(v_1(T) - v_2(T))^2 \tag{2.2}$$

If make σ_b^2 / σ_w^2 value to be maximum, it might as well to make σ_b^2 value to be maximum, and evaluate gray value which the maximal σ_b^2 value is corresponding. Segmentation results as is shown in figure 4 b).

2.1.3 Weld Image Refined

Through cutting, filtering, enhance, and binary threshold segmentation, seam and test plate edge information can be extracted from the mage. According to high numbers of edge point data, Weld marginal form is rough, edge thinning should be taken. Make seam and test plate edge can be indicated through single pixel. This paper uses a traditional edge extraction algorithm which can make a edge extraction and edge thinning toward image. Utilize Canny edge detector[4] In figure 4 b) and make a edge extraction and edge thinning on image , acquire results as follows .

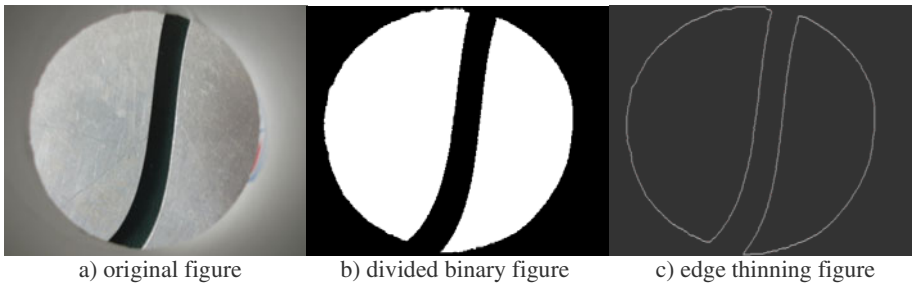


Fig. 4. Pretreatment results

2.2 Target Location Selection

Intersection algorithm: this paper acquires points of intersection between circular perspective and weld edge through neighborhood algorithm. Its fundamental is: picking up some pixels which in the range of 3x3 neighbourhood, then to detect data in figure 5. If the number of '1' surpasses a certain number, imply that the intersection is found.

Among four intersection which be found out, the two intersection which nearer dot P are the needed dot.

Then figure out coordinate value of midpoint C through the two acquired spots. And dot C is the next torch destination point, can get relative displacement after combine with circular angle template. The displacement can convert to torch actual offset.

Through simulation experiments in MATLAB, results as follows.

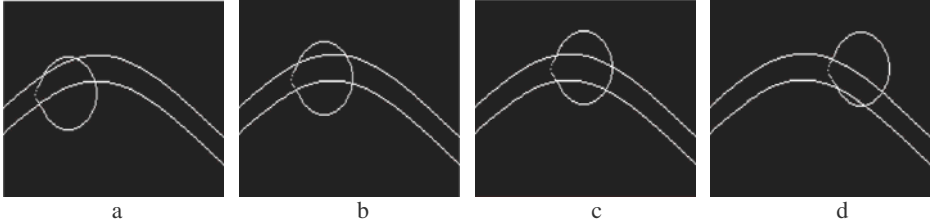


Fig. 5. Seam trajectory tracking

Figure 5 indicate that seam can be distinguished and followed, so the algorithm is demonstrated theoretically.

3 Conclusion

This paper propose a idea based on recognize seam in given regional perspective, and design a vision sensor on these grounds; make a pretreatment on image with homomorphic filtering , the maximum between-class variance method (OTSU) , and edge detection. This paper designs a new algorithm that based on seam tracking in circular given angle. And then proves it through experiments implemented on MATLAB, the result shows that the algorithm is effective.

Acknowledgments. This research is supported by NSFC (N0.50705041 and No.61165008). The authors thank to anonymous reviewers and editors.

References

1. Jia, Y.: Digital image processing, pp. 169–172. Publishing, Wuhan (2003) (in Chinese)
2. Luo, H., Liu, B., Long, Y., Tan, X.: Application of homomorphic filtering in illumination compensation. *Journal of Hunan University of Technology* 9 (2008) (in Chinese)
3. Zhang, D.: *Automated Biometrics Technologies and Systems*, vol. 5, pp. 44–47. Kluwer Academic Publishers, USA (2000)
4. Zhu, G., Huang, Y., Yu, S.: Application of edge detection operators in region detection of automobile license plate. *Computer Technology and Development* 3 (2006) (in Chinese)

Application of an Improved Performance Evaluation Model Based on Cloud Theory

Li-jun Xie, Zhi-qiang Zhu, Zhe Chen, and Yuan-ning Liang

Zhengzhou Information Science and Technology Institute, Zhengzhou, China
xie20060220130@sina.com, 471242775@qq.com,
Chenzhe197012@yahoo.com.cn, lyn577@163.com

Abstract. Scientific research performance evaluation is to make qualitative and quantitative evaluation to the achievements of projects. It is critical for its sustainable development to reduce the fuzziness and randomness in the academic scientific research performance evaluation by scientific and objective methods. Based on the Cloud Theory, this paper proposes an improved scientific research evaluation model. The model transforms qualitative indexes to countable quantitative descriptions with Cloud Theory, and then makes an integrated evaluation by Cloud Center of Gravity Evaluation method (CCGE). Finally, the experimental result shows that, this model increases scientificity and objectivity of scientific research evaluation.

Keywords: scientific research evaluation model, cloud theory, CCGE.

1 Introduction

Scientific research performance evaluation (SRPE) is an important part of academic scientific research management and the foundation of academic scientific research developing healthily. It can achieve that optimization and advantage of resource in academic scientific research by SRPE. However, as results of traditional qualitative evaluation with too simple measurements, fuzzy standards, subjectivity and randomness, there are many problems in academic scientific research performance evaluation: lack of generally recognized scientific research performance classified system for chaos classification of scientific research performance; quantitative standard of scientific research performance has not been uniformed; the results of the quantitative evaluation lack credibility and effectiveness [1].

Many researchers have carried on research and practice in academic scientific research performance evaluation. First is the study of evaluation index. Second is the research of evaluation system. Third is the study of the performance evaluation method. There exist some scientific research performance evaluation methods: (1) Exports weighting method, which is the integration of exports method and weighting method. Exports method is a kind of exports intuition thinking method, and weighting method is a direct comparison method. The combination of the two methods makes

evaluation be built on the expert's opinions, it is a method that mostly qualitative and partly quantitative. (2) Exchange metrological method, which is based on scientific metrology, literature metrology, intelligence metrology and technology metrology, is a qualitative method with the basis of quantitative method. (3) Literature measurement, which is based on the cited, indexed and abstracted forms, is a peer-reviewed form with strongest correlation.

Cloud theory is based on Fuzzy Set Theory and Probability and Statistics [2], it can achieve uncertainty transformation between quality and quantity and reduce the fuzziness and randomness of qualitative indexes. CCGE is proposed on the foundation of cloud theory, and it measures the change of whole system status information by the change of cloud center. This paper integers fuzziness and randomness by Cloud theory, making the mutual mapping between quality and quantity, and transforms some qualitative concepts described by natural language to quantitative value, then establishes the cloud model of every index and center of gravity of comprehensive cloud. Finally, it makes comprehensive evaluation for scientific research performance with CCGE. This model comprehensively takes all factors into account in SRPE so that the result of evaluation is more objective and scientific.

2 Academic Scientific Research Performance Evaluation Indexes System

There are three kinds of traditional academic scientific research performance evaluation indexes [3]:

(1) Source indexes. For example, papers, monographs, invention patents, productions, technology privacy, technology transfer and technology income. Papers and monographs are the important source quality indexes.

(2) Additional indexes. They are produced from the source indexes with high quality, such as technical prize, cited paper, etc. As they are based on source indexes, they belong to the additional indexes.

(3) Derived indexes. Derived Indexes refer to the social rewards to outstanding contribution groups and individuals in scientific research, including academician, Governmental Special Allowance of the State Council and Distinguished Professor, etc.

As the traditional scientific research performance only pays attention to results and despises the process, in this paper, the indexes related to process of research are added to evaluation index system and make it more perfect, e.g. innovation ability, project management level, team composition, team cooperation and sustainable development ability. Academic scientific research performance evaluation index system is shown in Fig.1.

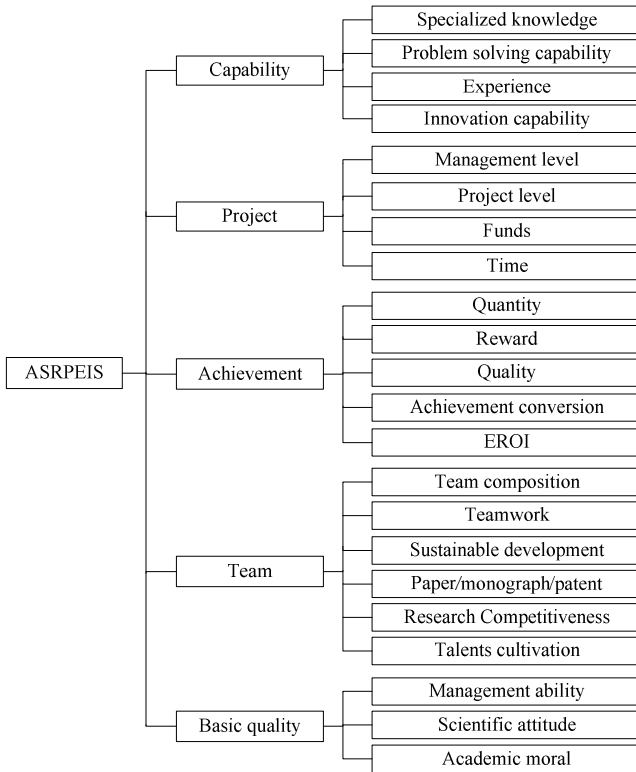


Fig. 1. ASRPEIS

3 Cloud Theory and Performance Evaluation Model

Let U be the set $U = \{u\}$, as the universe of discourse [4], and A a qualitative concept associated with U . The membership degree of quantitative numerical representation u in U to the concept A , $\mu_A(u) \in [0,1]$ is a random number with a stable tendency, which is $\mu_A(u) : U \rightarrow [0,1], \forall u \in U, \mu \rightarrow \mu_A(u)$. The distribution of u in the universe of discourse U is called cloud, and u is called a drop. A piece of cloud is made up of lots of cloud drops, visible shape in a whole, but fuzzy in detail, which is similar to the natural cloud in the sky. Any one of the cloud drops is a mapping in the discourse universe from qualitative concept.

The overall characteristics of cloud model may be reflected by its three digital characteristics: Expected value (Ex), Entropy (En) and Hyper-Entropy (He) [5]. Ex is the position corresponding to the center of the cloud gravity (CCG); En is a measure of the concept coverage, i.e. a measure of the fuzziness, which indicates how many elements could be accepted to the qualitative linguistic concept; and He is a measure of the dispersion on the cloud drops, which can also be considered as the entropy of En . The CCG is expressed as $G = L \times H$, and L is the position of CCG; as En, H is the

height of CCG. L refers to the center of qualitative concept in universe of discourse, reflects the weight of cloud in the system. The higher CCG refers to the bigger weight. So, the expected curve equation of membership cloud can be built with Ex and En . The membership cloud of linguistic value of about 175 centimeters is shown in Fig. 2. The uncertainty of qualitative and quantitative conversion can be known from the shape of cloud.

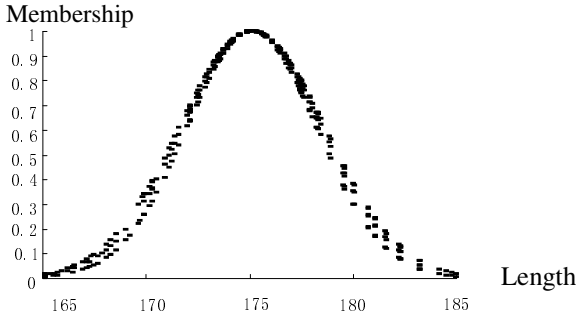


Fig. 2. Membership cloud

3.1 Cloud Model

The cloud model in this paper is normal cloud model, and the expected curve is [6]:

$$MEC(\lambda) = \exp[-(x - Ex)^2 / (2En^2)] \tag{1}$$

Let $R_i(Ex, En)$ be the random normal distribution function, and

$$x_i = R_i(Ex, En) \tag{2}$$

$$P_i = R_i(En, He) \tag{3}$$

$$\mu_i = \exp[-(x_i - Ex)^2 / (2P_i^2)] \tag{4}$$

The normal cloud model is constructed by the couple of data (x_i, μ_i) that meet the conditions of equations (2), (3), (4), and it is presented with (Ex, En, He) . (x_i, μ_i) is a drop. The forward cloud generator means to produce a drop by the digital characteristics of cloud, as well the transformation from qualitative to quantitative. On the contrary, it is the converse cloud generator.

3.2 CCGE

1) Build the Evaluation Index System. $R = \{R_1, R_2, \dots, R_n\}$, and $R_i (i \in [1, n])$ is the i th index of the system. $R_i = \{R_{i1}, R_{i2}, \dots, R_{im}\}$, and $R_{ij} (j \in [1, m])$ is j th index of R_i . Then, we can get the multi-level evaluation index system.

2) Cloud Model of Each Kind of Index. The scientific research performance evaluation system includes precise value indexes, qualitative comment value indexes and linguistic value indexes.

a) Cloud model of precise value index. In the cloud model with t precise value indexes,

$$Ex = \frac{Ex_1 + Ex_2 + \dots + Ex_t}{t} \tag{5}$$

$$En = \frac{\max(Ex_1, Ex_2, \dots, Ex_t) - \min(Ex_1, Ex_2, \dots, Ex_t)}{6} \tag{6}$$

b) Cloud model of qualitative comment value index. The comment set is worked out by some experts, and the corresponding coverage is $[0, 1]$. Each comment in the set is corresponding to a range of $[D_{inf}, D_{sup}]$. The cloud model of qualitative comment value is presented by symmetrical cloud model, and cloud model of the comments of two sides is

$$\begin{cases} Ex_i = \frac{D_{inf} + D_{sup}}{2} \\ En_i = \frac{D_{inf} - D_{sup}}{2} \end{cases} \tag{7}$$

c) Cloud model of linguistic value index. In the cloud model with l linguistic value indexes

$$Ex = \frac{Ex_1En_1 + Ex_2En_2 + \dots + Ex_lEn_l}{En_1 + En_2 + \dots + En_l} \tag{8}$$

$$En = En_1 + En_2 + \dots + En_l \tag{9}$$

3) Comprehensive cloud model with p dimensions. The system status can be represented as a comprehensive cloud model with p dimensions, and each dimension can be worked out by l comment values. The CG of comprehensive cloud model can be represented as G

$$\begin{cases} G = (G_1, G_2, \dots, G_p) = L \times H \\ G_i = L_i \times H_i, i = 1, 2, \dots, p \end{cases} \tag{10}$$

4.2 Transformation between Qualitative and Quantitative with Cloud Model

According to the cloud model of qualitative comments set in CCGE, set the eight comment values on the range of [0, 1], the range of each comment value is shown in table 2.

Table 2. Range of Each Comment Value

Comment	Worst	Worse	Bad	Normal
Range	(0,0.1)	(0.1,0.2)	(0.2,0.3)	(0.3,0.5)

Comment	Good	Better	Best	Perfect
Range	(0.5,0.7)	(0.7,0.8)	(0.8,0.9)	(0.9,1.0)

With the characteristic of normal distribution of cloud and data in table 3, work out q of each cloud model and construct a cloud generator.

Table 3. Ex and En of each Comment Value

Comment	Worst	Worse	Bad	Normal
Ex	0.0	0.15	0.25	0.4
En	0.0139	0.0278	0.0278	0.0278

Comment	Good	Better	Best	Perfect
Ex	0.6	0.75	0.85	1.0
En	0.0278	0.0278	0.0278	0.0139

According to the qualitative evaluation curve in cloud model and Ex of each linguistic evaluation, combined with the state value of each index from experts, evaluate the index of scientific research team by G_4 and get the matrix $G_4 = (G_{41}, G_{42}, G_{43}, G_{44}, G_{45}, G_{46})$, which refer to the indexes in the sub-layer of scientific research team. With G_4 and the cloud models of each index, get Ex and En of each index based on the equation (8) and (9). The Ex and En of team composition is

$$Ex_4 = \frac{Ex_{41}En_{41} + Ex_{42}En_{42} + \dots + Ex_{46}En_{46}}{En_{41} + En_{42} + \dots + En_{46}} = 0.4$$

$$En_4 = En_{41} + En_{42} + \dots + En_{46} = 0.0278 \times 5 + 0.0139 = 0.1529$$

Get Ex and En of other five indexes based on this method, as shown in table 4.

Table 4. *Ex* and *En* of each Index

Index	1	2	3	4	5	6
<i>Ex</i>	0.4	0.4	0.6114	0.5558	0.4421	0.4833
<i>En</i>	0.1529	0.1668	0.1529	0.1529	0.1529	0.1668

In ideal state, CCG vector of team composition is $G_4^0 = (0.18, 0.18, 0.15, 0.14, 0.18, 0.17)$. In fact, the CCG vector of team composition is $G_4 = \{w_{41}Ex_1, w_{42}Ex_2, w_{43}Ex_3, w_{44}Ex_4, w_{45}Ex_5, w_{46}Ex_6\}$, normalize G and get $G^T = (0.6, 0.6, 0.389, 0.444, 0.558, 0.517)$. Finally, $\theta = 0.524$.

5 Conclusions

Based on cloud theory and cloud center of gravity evaluation, this paper solves the fuzziness and randomness of academic scientific research performance evaluation with the improved performance evaluation model and make an integrated evaluation. Firstly, improves the performance evaluation index system of scientific research and deal with the problem that only paying attention to results and ignoring the process in traditional index systems. Secondly, based on the cloud theory, evaluates from bottom to top with CCGE and makes linguistic value index of every level reasonable quantitative and scientific computing. Finally, gets the integrated evaluation value of the whole scientific research performance. Analysis of example proves the method is scientific and reasonable, and it can effectively promote the systematization and objectivity of academic scientific research performance evaluation.

Acknowledgments. We are grateful to the anonymous referees for their valuable comments and suggestions that have led to the better presentation of this paper.

References

1. Feng, L.: Research on academic scientific research performance evaluation model. *Science and Technology Management Research* 7, 271–272 (2009)
2. Yide, L., Haijun, M., Xuemei, S.: Membership Cloud and Membership Cloud Generator. *Computer Research and Develop.*, 15–20 (1995)
3. Fuhu, D.: Scientific Research Performance Evaluation Theory and Method. *Science and Technology Management Research* 3, 45–48 (2000)
4. Lin, P.G., et al.: A New Knowledge Representation Method Based on Ontology and Cloud Theory. In: 2008 International Seminar on Future Information Technology and Management Engineering, pp. 49–52 (2008)
5. Jin-chun, Z., Guyu, H.: Application of Uncertainty Reasoning Based on Cloud Model in Time Series Prediction. *Journal of Zhejiang University Science* 4, 578–583 (2003)
6. Yudong, Z., Lenan, W., Geng, W.: Improved ant colony algorithm based on membership cloud models. *Computer Engineering and Applications* (2009)
7. Dandan, C., Jiping, Y.: Realization of Evaluation System for Scientific Research Project Based on AHP. *Development Research and Design Technology*, 739–740 (2007)

Study on Ontology-Based Reference Model of Software Configuration Management

Zhe Chen, Xin Li, Hong Yao, and Yuan-ning Liang

Zhengzhou Information Science and Technology Institute, Zhengzhou, China
Chenzhe197012@yahoo.com.cn, 361603720@qq.com,
491265305@qq.com, lyn577@163.com

Abstract. When dealing with hundreds of components, keeping track of version changes and various dependency constraints imposed on the system, Software configuration management (SCM) can be defined as the control of the evolution of complex software systems. In recent years, researchers have argued that using ontology to represent and drive knowledge infrastructure of software projects provides procedural knowledge. The advantages of using ontology for SCM are immense and cover various aspects of software development and evolution. In this paper, key challenges must be face for designing and implementing SCM is summarized. One of them is the limited capability on interoperating in different SCM tools. An ontology-based reference knowledge model base for SCM is presented. The reference model allows depicting complex relations between concepts and services operating in configuration management.

Keywords: Software configuration management, Ontolog-Driveny, Reference model, Interoperability.

1 Introduction

Whether in teams or working individually, developers usually rely on a version control system or software configuration management solution to store and manage their source code. Operations like check-in/check-out, versioning, branching/merging, code repository sharing, and remote & distributed access are part of the overall application lifecycle management process. Modern integrated development environments (IDE), such as Microsoft Visual Studio, allow the use of various SCM systems to cope with heterogeneous environments.

For enterprises and developers, there are many possible choices for their IDE and SCM systems, which often results in having to deal with multiple IDE and SCM systems both within and across project teams. According to the Guide to Software Engineering Body of Knowledge (SWEBOK) [1], SCM aims to control the evolution and integrity of a product by identifying its elements, managing and controlling changes, and verifying, recording, and reporting on configuration information.

It is a supporting software life cycle process, which benefits project management, development and maintenance activities, quality assurance activities, and the customers and users of the final product. Without some sort of automated support, it is very difficult (if not impossible) to successfully implement a SCM process.

Different types of tool capabilities are necessary to support SCM activities; this scenario leads to an important requirement for SCM tools: interoperability. Obstacles to interoperability arise from the fact that the tools are generally created independently, and do not share the same semantics for the terminology used to describe its domain of interest. Some sort of interoperability can be achieved by translation programs that enable communication from one specific tool to another. But this approach presents problems. As the number of tools increases and the information becomes more complex, it is more difficult for software developers to provide translators between every pair of software tools that need to exchange information [2].

Using ontology to establish a formal specification of the semantics of the software configuration management domain is the way to deal with this problem. Ontology-based method can provide a standard and powerful way of representing knowledge about a software engineering project. There are a number of systems that use ontology-driven method to represent some of their metadata. These include Cupboard [3], the alignment server [4], and Oyster [5], the ontology-based representation of metadata focuses on describing intrinsic properties of ontology and other objects that are shared across applications. An ontology is a formal description of the entities within a given domain: the properties they possess, the relationships they participate in, the constraints they are subject to, and the patterns of behavior they exhibit.

Thus, ontology can be used to establish a common conceptualization about the SCM domain in order to support SCM tools integration. Using SCM ontology as an interlingua, we aim to facilitate tools interoperability by means of the development of translators between native formats of those tools and the SCM ontology. This approach has potential to ease the process of integrating tools that focus on different activities of the SCM process and therefore it can be used for creating a proper SCM environment.

This paper is organized as follows. Section 2 talks about the evolving of the context in software configuration management. Section 3 specifically describes the ontology on interoperability approach. In section 4, the ontology-based reference model on SCM is presented, and finally, section 5 describes conclusions of this paper.

2 Evolving of Software Configuration Management

While there is no single definition of software configuration Management, there are three widely disseminated views from three different sources: the Institute of Electrical and Electronics Engineers (IEEE), The International Organization for Standardization (ISO), and the Software Engineering Institute (SEI) at Carnegie Mellon University.

IEEE Standard 828-1990 goes on to list specific activities associated with each of the four functions: Identification, Control, Status accounting, audits and reviews [6]. While the SEI advocates a broader definition of CM in SEI-92-TR-84 [7]. Guidelines for the application of ISO 9001 to the development, supply and maintenance of software, the International Organization for Standardization identifies a similar set of practices as SCM is describe: Configuration management provides a mechanism for identifying, controlling and tracking the versions of each software item. In many

cases earlier versions still in use must also be maintained and controlled [8]. Looking at ISO/IEC 12207, CMMI, SWEBOK [1], and books such as Software Engineering: A Practitioner's Approach [9], the activities of a SCM process can be summarized as:

a) SCM Process Implementation: a plan should be developed describing: the configuration management activities; procedures and schedule for performing these activities; the organization responsible for performing these activities; and their relationship with other organizations, such as software development or maintenance. The plan shall be documented and implemented.

b) Software Configuration Identification: identifies items to be controlled (called Software Configuration Items, SCIs), establishes identification schemes for the items and their versions, and establishes the tools and techniques to be used in acquiring and managing controlled items.

c) Version Control: combines procedures and tools in order to manage different versions of SCIs that are created during the software process.

d) Change Control: is concerned with managing changes during the software life cycle. A change management process should be established including activities for: (i) requesting changes; (ii) evaluating change requests; (iii) checkout; (iv) change execution; (v) change review, (v) check in of modified items.

e) Configuration Audit: checks, among other things: if the change specified in the request has been made, and if any additional modifications have been incorporated; if a technical review was conducted to assess correctness; if organizational standards have been properly applied; if related SCIs have been properly updated.

f) Configuration Status Report: is the recording and reporting of information needed for effective management of the software configuration.

Software items evolve as a software project proceeds. On this ongoing process, versions of the SCI are stored in order to keep track of the differences between the starting point and the current state of a given SCI. A version of a software item is a particular identified and specified item. It can be thought of as a state of an evolving item for each version a unique identifier is given.

SCM emerged as a separate discipline in the late 1970s, with the advent of tools. Each system targeted a specific functionality and focused either on what is now known as "version control" or on supporting an efficient builds process for generating an executable program out of source files. In a relatively short time thereafter, these functionalities were integrated in single SCM systems with the following main functionalities: (i) to manage the files involved in the creation of a software product, (ii) to track changes to these files in terms of their resulting versions, and (iii) to support the building of an executable system out of the files. Fundamentally, this focus has not changed to date.

As illustrated in Fig.1, the context in which SCM systems operate has changed significantly. First, they were used for managing critical software by a single person on a mainframe. This resulted in a need for versioning and building support, which was typically provided by some homegrown system. Use of SCM systems then changed to primarily supporting large-scale development and maintenance by groups of users on a Unix system. This resulted in a need for workspace management, which was quickly provided by newer, more ad-hoc SCM systems. Now, SCM systems manage the evolution of any kind of software by many different people in many,

perhaps distributed locations utilizing many kinds of machines. This often requires explicit process support, which today’s advanced, off-the-shelf SCM systems integrally provide. Indeed, SCM is one of the few successful applications of automated process support.

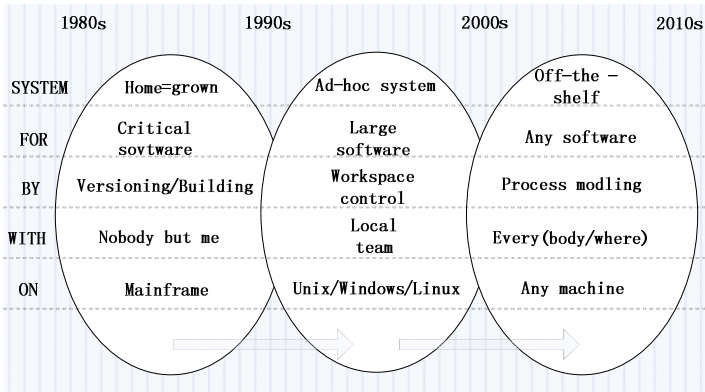


Fig. 1. Evolution of the context of SCM systems

Traditional SCM focused on controlled creation of relatively simple products. Nowadays, implementers of SCM face the Issues of dealing with relatively minor increments under their own control in the context of the complex system being developed. Today’s software organizations need to manage complex technologies across multiple domains. The majority of SCM-related tools normally focus on a particular set of activities of the software engineer process. Thus, a proper SCM environment cannot be achieved with a single tool. A solution for this problem lies on integrating different tools.

3 Ontology: Approach of Interoperability

Ontology has received increasing interest in computer science and information systems. They explicitly encode a shared understanding of a domain that can be communicated between people and application programs. Computer scientists use the term ontology to specify a conceptualization [8] in the context of knowledge sharing. By conceptualization we understand an abstract, simplified view of the environment we want to represent. Every knowledge base explicitly or implicitly uses some sort of conceptualization. An ontology can be used to set a vocabulary of a certain domain, describe its main concepts and relations between them. Various logical operations can be carried out on the item of the ontology. A correctly formulated ontology allows us to check and guarantee consistency, but not completeness of the stored information with respect to queries and assertions formulated using the vocabulary defined in the ontology.

In our perspective, ontology as a conceptualization of a domain explicitly captures the semantics of the entities in that domain. It comprises the definition of concepts,

their properties, attributes, relations, as well as constraints and axioms that constrain the meaning of the concepts. It formally specifies the meaning of the concepts in order to make domain assumptions explicit and prevent errors in data interpretation.

Some critical issues to be considered regarding ontology is the cost of developing and maintaining ontology, and the fact that ontology should be extensible and evolve over time. In reaching for systems interoperability, two solutions are possible at the semantics level:

1) A single shared common set of semantic elements is defined, so that disparate systems that are built upon it achieve semantics interoperability at once.

2) A translation mechanism between two (or more) ontology is defined so that minimal semantics interoperability is achieved.

It is argued that interoperability at the semantics level is not always possible. Fig. 2 shows an illustration of this as two systems can only interoperate if they share some of the semantic elements their distinct ontology capture. The shared elements may be expressed differently but they nonetheless have to exist in both ontology.

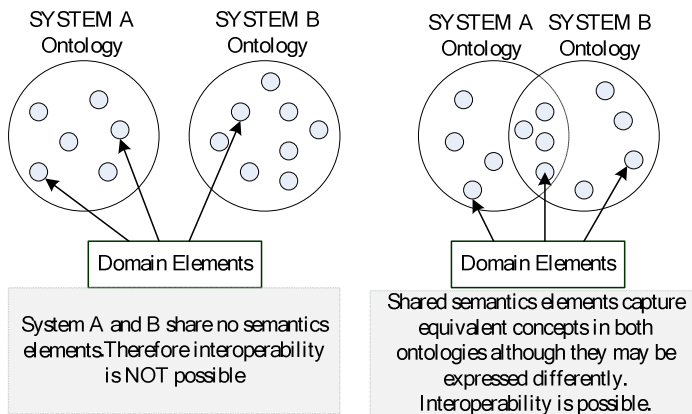


Fig. 2. Ontology-based Interoperability

Due to formal, expressive and shared properties, ontology constitute domain can be reused across applications, facilitating knowledge sharing and reuse. Moreover, ontology facilitates semantics information integration and interoperability between heterogeneous sources at a high level of abstraction. ontology can also be exploited to index and access semi-structured information sources. Thus, ontology can be used to establish a common conceptualization about the SCM domain in order to support SCM tools integration. Using SCM ontology as an interlingua, we aim to facilitate tools interoperability by means of the development of translators between native formats of those tools and the SCM ontology. This approach has potential to easy the process of integrating tools that focus on different activities of the SCM process and therefore it can be used for creating a proper SCM environment.

4 The Ontology-Based Reference Model on SCM

Different types of tool capabilities are necessary to support the SCM process. Therefore, to provide a widely automated support for this process, it is necessary to use different tools, which should be integrated in order to interoperate. As we can see, SCM is essential to every software organization. Thus, the concepts that surround it should be well defined and people and tools should share a common conceptualization about this domain. In this context, ontology can be used to avoid misunderstanding and for establishing a common conceptualization.

Arantes [10] have already proposed SCM ontology. It covers well some activities of the SCM process, such as configuration items identification and change request control, but it lacks some important concepts mainly related to change and version control. Concepts such as repository, branch and copy are presented in most all SCM tools, but are not addressed by the ontology.

Most SCM tools focus on a subset of the activities of the SCM process. For example, CVS and Subversion focus only on version control. Thus, to adequately support the SCM process, organizations need to use several tools, which in turn should be integrated. The integrated tools must be able to understand the data produced by each other, and should be able to communicate. Therefore, they need to share a common conceptualization about the SCM domain. This is the main motivation for building an ontology-based reference Model of SCM (Fig.3). With SCM ontology technology applying, an integration middleware could be built, composed by adaptors for different tools transform their data according to an ontology-based reference model which conceptual based on XML schema excavation, respectively.

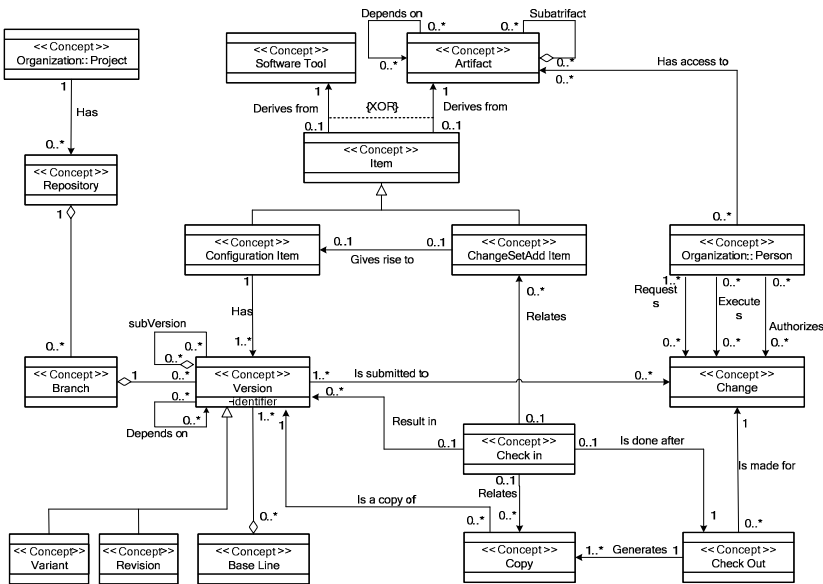


Fig. 3. Ontology-based reference Model of SCM

As we can see, SCM is essential to every software organization. Thus, the concepts that surround it should be well defined and people and tools should share a common conceptualization about this domain. In this context, ontology can be used to avoid misunderstanding and for establishing a common conceptualization.

An artifact can depend on another one (for example, a requirement specification can depend on a use case diagram) and thus the same applies for the corresponding SCIs. Thus, when a change on a version of a given CI is requested, an analysis has to be done in order to look for possible impacts on versions of other SCIs. A configuration manager shall analyze if a change should be done, and which are the versions involved that should be checked out. In a checkout action, copies of each requested version are generated. Once the copies are changed, they should be checked in. The configuration manager should evaluate the changes and according to his/her decision, new versions can be created. When a change request is approved, the versions involved can be checked out. In a checkout, copies of each requested version are generated to the person that requested them.

According to the ontology-based reference model, artifacts and software tools can be placed under configuration management and therefore be treated as SCIs. During its lifecycle, a SCI can have many variations. Tracing the SCI's evolution, a variation of a SCI can be decomposed or it can depend on another variation. A baseline is a set of variations grouped for some purpose. Variations can be versions, which are variations that are intended to replace an old one, or variants, which are not intended to replace an old one. SCI's variations are submitted to changes, and the dates of checkout and check in actions are treated as properties of a change. Responsibilities for requesting, authorizing and performing a change are also taken into account. Finally, kinds of access to SCIs were assigned to organization project. Due to space limitations, axioms and dictionary of terms are not presented.

5 Conclusions

SCM will fall into the public domain, as basic services anyone can expect from a platform, for instance versioning, rebuilding, basic work space support and so on. In the near future, provided the number of core topic issues to be solved and the efficiency, scalability and usability issues will be seriously addressed by SCM research. Achieving systems interoperability requires that there is sufficient semantic overlap between systems' respective ontology. Different types of tool capabilities are necessary to support the SCM process. Therefore, to provide a widely automated support for this process, it is necessary to use different tools, which should be integrated in order to interoperate. In this context, domain ontology can be used to establish a common conceptualization about the SCM universe of discourse, serving as a reference model to map the conceptual models underling SCM tools.

Acknowledgments. We are grateful to the anonymous referees for their valuable comments and suggestions that have led to the better presentation of this paper.

References

1. SWEBOK: Guide to the Software Engineering Body of Knowledge. IEEE Computer Society (2004)
2. Schlenoff, C., Gruninger, M., Tissot, F., et al.: The Process Specification Language (PSL) Overview and Version 1.0 Specification. NISTIR 6459, National Institute of Standards and Technology, Gaithersburg, MD (2000)
3. d'Aquin, M., Lewen, H.: Cupboard – A Place to Expose Your Ontologies to Applications and the Community. In: Aroyo, L., Traverso, P., Ciravegna, F., Cimiano, P., Heath, T., Hyvönen, E., Mizoguchi, R., Oren, E., Sabou, M., Simperl, E. (eds.) ESWC 2009. LNCS, vol. 5554, pp. 913–918. Springer, Heidelberg (2009)
4. Euzenat, J.: Alignment infrastructure for ontology mediation and other applications. In: Workshop on Mediation in Semantic Web Services (2005)
5. Palma, R., Haase, P., Gomez-Perez, A.: Oyster: sharing and re-using ontologies in a peertopeer community. In: 15th International Conference on World Wide Web (WWW 2006), pp. 1009–1010. ACM, Edinburgh (2006)
6. IEEE Std 828–1990, IEEE Standard for Software Configuration Management Plans, IEEE, 345E, 47th St, New York, NY (1991)
7. Susan, A.D.: The Past, Present, and Future of Configuration Management. CMU/SEI-92-TR-84, Software Engineering Institute, Carnegie Mellon University, Pittsburgh PA (1992)
8. ISO 9001:1987 Model for design, development, production, installation and servicing. International Organization for Standardization, Geneva, Switzerland (1987)
9. Pressman, R.: Software Engineering: A Practitioner's Approach, 6th edn. McGraw-Hill (2005)
10. Arantes, L., Falbo, R., Guizzardi, G.: Evolving a Software Configuration Management Ontology. In: Proceedings of the Second Workshop on Ontologies and Metamodeling in Software and Data Engineering, João Pessoa, Brazil, pp. 123–134 (2007)

The Discuss on the Machine Design Course Teaching Method

Li Xing-hua

School of Mechanical Engineering, Tongji University, Shanghai, China
lixinghua@tongji.edu.cn

Abstract. This paper in view of the Machine Design course characteristics and research problem rules summarizes the systemic and the regularity of the Machine Design course content, to improve the students' learning effect. In the process of teaching, some common knowledge is completed and summed up in order to train students' ability to analyze and solve problems. In the classroom teaching, the contents are set mainly in accordance with design, and through the great homework of the corresponding design type to consolidate the training, strengthen practice links, the students' learning interest and design ability will be raised.

Keywords: machine design, machine element, teaching method, education, design ability.

1 Introduction

The Machine Design course is a technical foundation course for the general theory of machine design and the common machine elements working abilities design. That is one of the important technical foundation courses for mechanical engineering in engineering colleges. To meet the training needs of wide caliber of mechanical engineering, college graduates are required to have more solid foundation, wider expertise and stronger adaptability. Therefore, improving the quality of teaching the Machine Design course has become more important [1]. This paper discusses the teaching methods of this course in the following aspects, with many years practice of Machine Design course teaching.

2 Introducing This Course Characteristics and Research Problems Rules to Improve Students' Learning Effects

Machine Design textbook [2] contains more content and involves a wide range, but the number of teaching hours is less, and teaching contents must be selection [3] during teaching. Based on training objectives for mechanical engineering and the analysis of general machinery drives, we can learn that, the contents of the threaded joints, key joints on the mechanical connection part and the gear drive, belt drive on the mechanical transmission part and the bearings, shaft on the shaft system etc. need to be focused during teaching. In addition, the standard spur gear transmission in the

mechanical transmission should be explained in detail, while compared with the spur gear transmission, and based on a little more explanation, the contents of helical gear design, bevel gear design and worm drive design can be understood.

The feature of Machine Design course is using theory in the foundation courses, discussing working abilities design issues for various common machine elements. The design issues in machine elements, involves a wide range of knowledge and a number of factors. Design methods and theories of various machine elements are very different from each other, and there is no obvious relationship between each other. Moreover, there are more design parameters, information and data. Exercise answers and design results are not as unique as those in the foundation course. Evaluation criteria are no longer simply divided into right or wrong, but how to be more reasonable. As beginners are often not adapted, they will find this course sporadic and clutter [4]. In essence, Machine Design course content are also systematic and regular. In order to be easily memorized, the block diagram can be used to represent, shown in Figure 1. Each chapter of Machine Design course introduces the contents of the basic knowledge, the basic theory and the basic skills in three areas about the common machine elements.

Therefore, we should emphasize that this is the important idea to learn the contents of later chapters, which can reduce the difficulty of learning this course. So that students can avoid the blindness in the learning process and improve learning effects. In the teaching contents of the later chapters, not simply copy the order of the contents of the teaching material, but also try to organize contents in accordance with the above ideas to teach. At the end of teaching the contents of each chapter, doing some chapter summaries or stage class discussions help to deepen understanding.

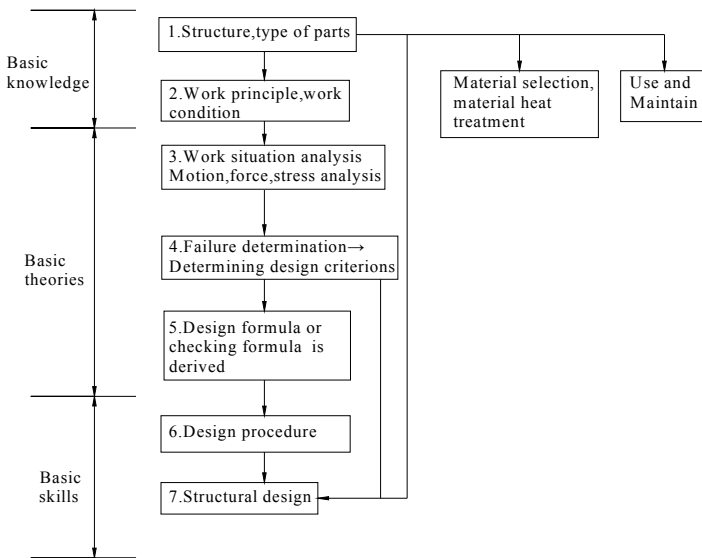


Fig. 1. The systemic of the Machine Design course content

3 Provide Additional Information on Some Common Knowledge to Train Students' Abilities to Analyze and Solve Problems

Machine design task is to ensure the life of machine elements within the specified period and any possible failure modes not happen which lead to the loss of function of the machine elements. Therefore, determining the failure modes of machine elements, and providing the design criteria for corresponding to various failure modes, has become a very important issue in the machine elements design.

Figure 1 show that, the structures and the functions of various machine elements are different, but, determining the failure modes of machine elements during the work and establishing the appropriate design criteria is a necessary part for machine elements design.

For students have no practical experience, they don't understand the structure and the function of machine elements well, and often cannot determine the failure modes of machine elements during the work, so that it's difficult to understand the design process of machine elements, which affects the teaching effectiveness.

In fact, machine elements will appear a variety of the failure modes during the work, for different working conditions, they will be transformed into another failure modes, therefore, summarized by the working conditions and the macro performance of failure in machine elements, which is shown in Figure 2. Accordingly, machine elements can be analyzed, in which failure modes they may occur in some working conditions, and can also according to the specific working conditions and the failure modes of machine elements analyze the causes. Through such summary, when taught the work situation analysis of the specific machine elements, most students are able to analyze possible failure modes of the machine elements, in order to better understand the specific design procedure of the machine elements.

Therefore, supplying and summarizing some common knowledge in the teaching process can train students' abilities to analyze and solve problems.

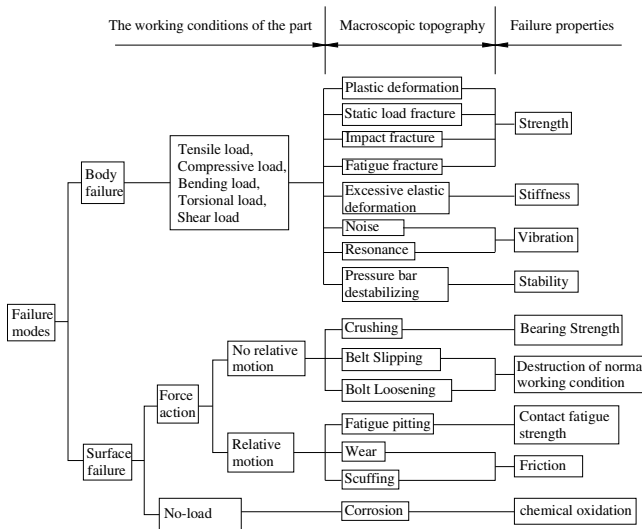


Fig. 2. Failure modes of machine elements

4 Strengthening Practice and Improving Students' Learning Interest and Design Abilities

The purpose of the teaching is to let students to grasp the design of common machine elements and have the design capability of simple mechanical transmission device. Therefore, the core of the practical teaching in this course is how to strengthen students' design abilities, especially the design ability of structure, in order to simulate the interests of students' learning and cultivate their abilities of creation.

The specific practice in the classroom teaching is listed as followed: The contents are set mainly in accordance with design, and every time at the end of teaching the design theory of major machine elements, the great homework of the corresponding design type is arranged or students are allowed to select topics of some interesting design types, to consolidate the training [5]. For example:

Great homework topics of the threaded joint and the screw transmission parts are (1) Structural design of the threaded joint, (2) bolt design on the sliding bearing, (3) Screw jack design.

Great homework topic of the mechanical transmission parts is (1) Design V-belt drive for blower by the motor-driven.

Great homework topics of the shaft system are (1) Structure correction of the shaft system, (2) design of the shaft components for cylindrical gear drive.

For each great homework topic, the content of the job is determined, the homework guide is written, students are required to complete specific design in accordance with homework guide, and finally finish assembly drawings and write the manual of design calculations, so that they have the chance to independently make plans and carry them out, but it must be completed within a certain time to think, look up data and do some researches to complete. Thus letting students to overcome and deal with the difficulties and problems by themselves during the design. In the process of the design practice, understanding and grasping the required knowledge and skills of the course, experiencing the hardship and fun of creation, training the ability to analyze and solve problems, which is a challenging work for the students, and can contribute to make the creative talents stand out.

In addition, after the course, the course design has three weeks time to further strengthen the student's design ability. Through course design, students are let to better understand a complete design process, expand their thinking in the field, train their computing power and drawing skills, improve the comprehensive analytical ability, and know the use of standards, manuals and data, so that students have a more comprehensive design training. After the course design, most of the students reflect that, the harvest of the course design is very large, even better than a few courses, and they get the basic training as engineering and technical personnel in mechanical design.

The above are my explorations in the teaching process, through the application, students' enthusiasm for learning are increased, the learning initiative has also been improved significantly, and the knowledge of Machine Design is mastered more strongly.

It should be noted that the level of improving students' design ability depends not only on factors of teachers or the objective conditions provided by the courses, the

enthusiasm and initiative of learning is also a very important factor. In addition, students' level of understanding and master the knowledge of the foundation courses (Such as the Interchangeability and Measurement Technology, Engineering Materials, Theoretical Mechanics, Material Mechanics, Engineering Drawings, etc.) is also one of the important factors [6].

References

1. Tong, M.-J., Tong, Z.-X., Guo, R.-F.: How to Improve Engineering Quality and Comprehensive Abilities of Students—"Mechanical Design" Teaching Methods Discussion. *Modern Manufacturing Technology and Equipment* (5), 62–63 (2010)
2. Pu, L.-G., Ji, M.-G.: *Design of Machinery*. Higher Education Press, Beijing (2006)
3. Zhao, H.-Y., Zhao, H.-P.: Some Advices of Teaching Reform on Mechanical Design Courses. *Theory Research* (14), 196–197 (2009)
4. Lu, W.-B.: Teaching the Mechanical Design. *Journal of Lujiang University* 11(1), 89–91 (2003)
5. Li, X.-H.: The exploration of the mechanical transmission teaching in the machine design course. In: 2010 Third International Conference on Education Technology and Training (ETT 2010), Wuhan, China, November 27-28, vol. 7, pp. 467–469 (2010)
6. Xi, Y., Zhu, M.-H., Li, X.-J., Li, X.-H., Xu, Z.-M.: The exploration of the mechanical foundation course teaching reform. In: 12th National Conference on Mechanical Design Teaching, Hangzhou, China, August 7-10, pp. 137–138 (2010)

Automatic Recognition Algorithm of Traffic Signs in Road Tunnel

Wang Weizhi and Liu Binghan

Fuzhou University, Fuzhou 350108
lbh@fzu.edu.cn

Abstract. We conduct feature extraction and feature selection of the pattern of traffic signs based on environmental characteristics of the road tunnel, and the color and shape information of traffic signs, then further accomplish multi-level classification of traffic signs using decision tree method. The method proposed in this paper based on decision tree classification algorithm can convert a complex multi-class problem into several simple classifications. Experimental results show that the algorithm has good recognition results.

Keywords: Traffic signs, pattern recognition, multilevel classifier.

1 Introduction

With the rapid development of highways, the number and length of the road tunnel rise dramatically. The road tunnel was hidden due to its structural characteristics of ribbon, bringing a series of changes to the road traffic environment. Tunnel security situation is very grim, especially those of several kilometers, as a result, a major highway tunnel traffic accident have occurred. In most cases, enclosed in a small space inside the tunnel, the monotonous visual environment, the blocked driver's sight, and a sense of isolation from the outside world caused by emotional stress, many vehicle drivers often ignore the road sign information, and further leading to road traffic violations events, and even causing a traffic accident. How to guarantee the safety of highway tunnels and avoid tragedy has attracted wide attention in all aspects.

The real-time detection of traffic signs information within the highway tunnel by the use of computer image processing technology, and giving directions or making timely warnings to drivers to prevent traffic accidents is one of important tasks in safe driving support system of intelligent transportation system. Highway tunnel traffic sign detection is an example of image recognition technology, which can be applied to other aspects of the automotive industry. Automatic detection of traffic signs within the tunnel is based on image processing and pattern recognition algorithm, and the demand for camera-based driver assistance systems in automotive industry is also growing [1].

The difficulties of highway tunnel traffic signs detection lie in image segmentation, feature extraction and classifier design. This paper presents a color and shape-based multilevel classification of traffic sign recognition algorithm as for environmental characteristics of the tunnel and the morphological characteristics of road traffic signs

in China. This algorithm can realize feature extraction and feature selection according to image color and shape information on traffic signs, and then, multi-level classification of traffic sign recognition using the decision tree method, converting a complex multi-class problem into several simple classification problems, basically guaranteeing of the effectiveness of real-time traffic sign recognition algorithm in tunnel.

2 Characteristics Analysis on Color and Shape of Traffic Signs

Traffic signs has been designed considering the driver's visual ability, hearing ability, the ability to understand information as well as motor ability, hence, being brightly colored, simple images and eye-catching. Existing automatic traffic sign recognition algorithms are mostly based on the color, shape and location information of traffic signs.

Traffic signs in China are divided into ban signs, direction signs and warning signs. The characteristics of other categories are as followed (shown in fig.1).

- ban signs: ① red border, white background, black design, round and the angle of the triangle down; ② black frame, round shape.
- direction signs: Blue and white pattern, round and rectangular shapes.
- warning signs: Black frame, yellow, black design, equilateral triangle upward.

In short, the colors of traffic signs border are blue, black, red etc., the shapes include round, triangle and rectangle, the area of traffic signs can be detected according to the color and shape of the traffic signs border (seen in Table 1).



Fig. 1. Representative traffic sign pictures



Fig. 1. (continued)

Table 1. Shape and color of traffic signs

class	factors			
	Frame color	Pattern color	Background color	shape
ban signs	red	Black, white	Black, blue	Round ,triangle
direction signs	blue	white	blue	Round ,rectangle
warning signs	black	black	yellow	triangle

3 Automatic Recognition Algorithm of Traffic Sign

The focus on tunnel traffic safety receives continuous improvement, traffic sign recognition methods are constantly emerging, some of the old method has been improved.

G. Piccioli [2] proposed a traffic sign recognition method based on template matching, developed template matching target identification system, extracted internal pattern in traffic signs using the edge detector, matching the internal design and database template to achieve the recognition of traffic signs classification. However, this method is limited to the traffic sign recognition in experimental condition, if there is distortion and noise images in the traffic signs to be identified, this identification method might be ineffective.

Zheng Fangping, etc. [3] proposed a neural network structure based on two layers traffic sign recognition methods. Due to many types of traffic signs, two layer neural network structure are used for identification, image features are sent to first-class classifiers to obtain the rough classification of image type, and then into the second

layer for appropriate classification. This traffic signs recognition method has good results on standard images.

Xu Huaqing [4] proposed a traffic sign detection method searching and determining the position based on color and shape. First, set the HSB color space threshold to segment color region, search the segmented color image make the initial position of the region of interest, to narrow the color search area, to improve detection efficiency; Then, according to characteristics of the consistent pixel color of traffic signs border, traffic signs detection has been done to the color region of interest. This approach focuses on the selection of features and training and updates of characteristics library.

There are other methods of classification of traffic signs [5], such as genetic algorithms, simulated annealing, the identification based on moment invariants and based on statistical and classifier and other.

The process of Image identification from real traffic signs is shown in Figure 2.

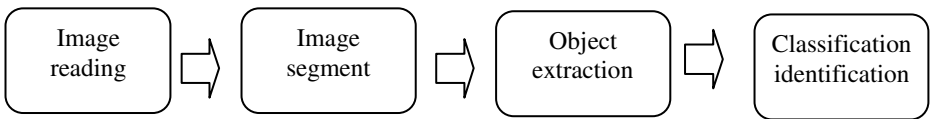


Fig. 2. Recognition algorithm flowchart of traffic sign

Through the analysis of characteristics of color and shape of traffic signs, border color is the best classification characteristics, the values of which are blue, black, red. In addition, traffic signs have a regular geometric shape (circle, triangle, rectangle). Therefore, the shape of traffic signs are also essential characteristics of the classification.

Decision tree method [6] is one of effective methods in the pattern recognition to classify, for multi-peak distribution for multi-class problem, this method is particularly simple and convenient. A complex multi-class problem can be converted into several simple classification problems to solve using the decision tree. It is not an attempt to use an algorithm or a decision rule to separate a number of categories, using hierarchical form, so that classification problems are gradually solved.

A decision tree is formed by a root node n_1 , some terminate nodes n_i and a group of non-terminated nodes t_j and a few components (shown in Figure 3), can be marked with various types of t_j label, and sometimes different termination can occur on the same node category label. If T is the decision tree, then a decision tree T corresponds to a feature space division, it divided the feature space into several zones in each area, and the category dominated by the sample can be marked with the types of class labels.

The decision tree classifier can be expressed mathematically as follows:

Given sample set A , where the samples are c categories, with A_i that A belongs to class i in the sample set, define a target set $I = \{1, 2, \dots, c\}$ and a non-empty sets I set $T = \{I_1, I_2, \dots, I_p\}$.

Design a decision tree, we should primarily address the following questions:

- to select a suitable tree structure, that is a reasonable arrangement of nodes and branches of trees;

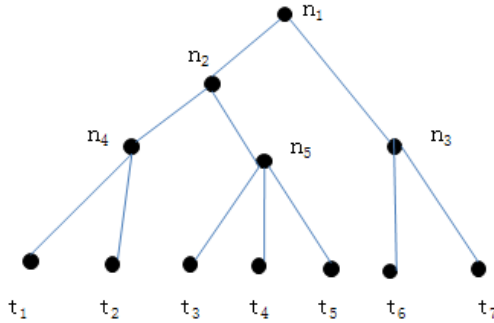


Fig. 3. Decision tree diagram

- identify each non-terminal node on the characteristics to be used;
- select the appropriate decision-making rules in each non-terminal node.

According to the characteristics and classification rules of traffic signs and decision-making, decision tree to identify the traffic signs can be constructed.

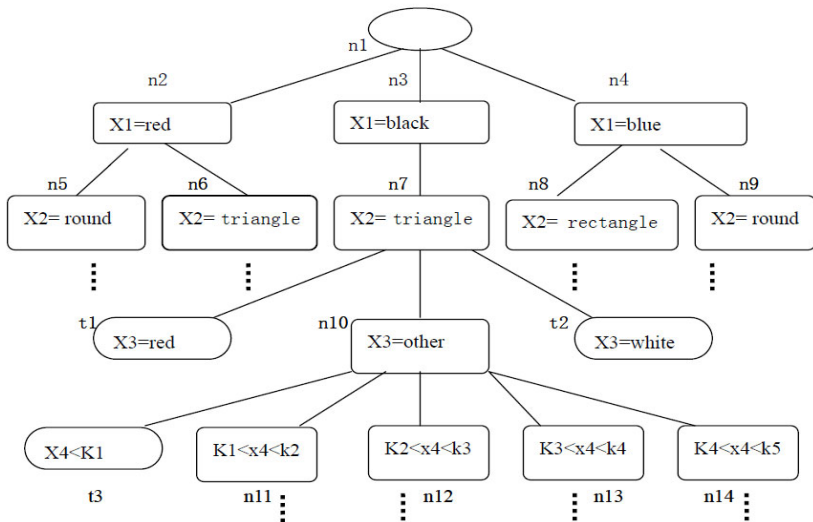


Fig. 4. Decision tree of traffic signs

In Figure 4, n_1 is the root node, select the border color as a feature x_1 , by the value of x_1 the signs are divided into three categories, n_2 , n_3 , n_4 are non-terminal nodes, then select the frame geometry as a feature are, non- end nodes n_2 , n_3 , n_4 further subdivided, the triangle symbol on the black borders of non-terminal node n_7 , select a special color pattern as classification features x_3 , t_1 and t_1 have been two end nodes, which have identified the category of signs. Select the percentage of the width pattern as

classification features of non-terminating node n_{11} , terminated node t_3 and non-terminal node n_{11} - n_{14} have been obtained. To select category features and classify at the same time back and forth, until there is no non-terminating node. In figure 4, k_1 - k_5 is the classification threshold characteristics, and its value has been obtained from the training samples, which can be changed as the change of training of the system.

4 Experimental Results and Analysis

To test this traffic sign recognition algorithm performance, we conducted 100 real images and 200 test standard map, the results are shown in Table 2. Through experiments, the method can obtain good experimental results.

Table 2. Identification rate in the algorithm of traffic signs

image types	test number	image	pass number	image	identification rate(%)
real images	100		86		86%
standard images	200		192		96%

In this paper, the more successful model of HSV visual image segmentation technique has been used to segment the traffic images. Through the method, the connectivity of traffic images is quite good, which directly affects the further object extraction and recognition. The decision tree is used in multi-level classifier. The traffic sign recognition and classification have been conducted on hundreds of pieces of the real images and the standard images. Amongst, the classification feature selection of the decision tree algorithm is very important, this paper adopts the form of a percentage value to indicate the classification feature, which can improve the classification characteristics of robustness, thereby increasing the recognition rate of the algorithm. In contrast, the real images have a higher identification error rate, mainly due to poor quality of the pictures when the image segmentation stage too much information has been lost, but also the extraction process led to some noise disturbance resulting in false identification, additionally, lack of classification features is also a major factor.

5 Conclusion

The real-time recognition algorithm in highway tunnel traffic sign is a typical application of complicated scenarios automatic target extraction and recognition. The process of completion of the human detection, identification and other visual tasks is quite complex, involving not only the visual system, and has a close relationship with the human brain intelligent system, many of the mechanisms are not clear. To conduct automatic extraction and target recognition deeply in the field of computer vision research, there is a lot of work to do. As an important part of artificial intelligence, computer vision research and development are at an early stage, but it also means that this area has broad prospects and development.

This traffic sign recognition involves image processing and pattern recognition fields, due to traffic signs in the actual situation are more complex and diverse, so in practical applications there is need for further testing and research. This traffic sign recognition method is simple, there are some reliability and validity. But there is still some areas needed for attention and improvement:

The contents of this paper does not conduct the actual verification in the actual vehicle, but only images from the visual sensor have been studied, the practical application need to be researched in the future.

Although this algorithm has some robustness, but also is lack of adaptability, algorithm has been improved to achieve better results in more practical environment,.

The characteristics of the extraction of traffic signs is affected by the image quality and light factors greatly, how to reduce image interference and greatly the retaining factor characteristics is to be further studied. In addition, how to define and extract the characteristics of complex graphics, so to ensure the accuracy of the case to maintain a reasonable amount of computation, the algorithm needs further exploration.

References

1. Paclík, P., Novovičová, J., Pudil, P., Somol, P.: Road sign classification using Laplace kernel classifier. *Pattern Recognition Letters* 21, 1165–1173 (2000)
2. Piccoli, G., Demicheli, E., Parodi, P., Campani, M.: Robust Method for Road Sign Detection and Recognition. *Elsevier Science Image and Vision Computing* (14), 209–223 (1996)
3. Zheng, F., Wang, W.: An approach to recognize road signs based on RBF NN using wavelet theories. *Journal of Fuzhou University* 35(3), 397–401 (2007)
4. Xu, H., Chen, R., Lin, J., Liu, B.: Study on the method of road traffic sign detection. *Journal of Fuzhou University* 38(3), 387–392 (2010)
5. Zhu, S., Lu, X.: A survey of the research of traffic sign recognition. *Computer Engineering and Science* 28(12), 50–52 (2006)
6. Zhu, J., Luo, X.: Recognition of traffic sign images based on decision-tree-based support vector machine. *Journal of Changsha University of Science and Technology* 1(2), 13–17 (2004)

License Plate Localization Based on Edge Detection and Morphology

Ying Wang and Wei Wang

College of Information Engineering, Shenyang University of
Chemical Technology, Shenyang, China
wyinghai@163.com, wangw960@163.com

Abstract. This paper presents a new method based on edge detection and morphology for the license plate localization, in this method ,first pre-processing of license plate image, then using Sobel operator for edge detection, and then using mathematical morphology processing image, then according to the priori knowledge and license plate aspect ratio to get the exact location of the license plate, and finally use horizontal projection and vertical projection to accurate positioning of the license plate. Simulation results show that the algorithm speed, high accuracy, to achieve the desired effect.

Keywords: Edge detection, license plate localization, morphology.

1 Introduction

With the development of social economy, the car has increased dramatically, the number of traffic control, safety management, charge management requirements also is increasing day by day, using electronic information technology to realize safe and high intelligent transportation become the main development direction of traffic management . Car license plate number is the only vehicle "status" logo, license plate recognition technology can not make any alterations in car to realize "identity" registration and verification, the technology have been used in road charges, parking management, traffic induction, traffic law enforcement, a road check, vehicle scheduling, vehicle testing and other various occasions. Position the image and character segmentation is the key to license plate recognition.

2 License Plate Location Method

According to the different characteristics of the license plate,we can use different positioning methods. The most common positioning technologies are mainly based on edge detection [1,2],based on color segmentation [3,4,5], based on genetic algorithm approach[6],basedonneural network[7,8],based on mathematical morphology[9],based on gray degree of image texture feature analysis[10] etc. But the method based on mathematical morphology, plate area location can not accurately determine the location of the border around the plate, it must be combined with other positioning methods for accurate positioning. Analyze the advantages and disadvantages of

various positioning methods, this approach based on edge detection and mathematical morphology for the license plate localization.

3 License Plate Localization Process

3.1 Gray Image

Color images contained a large color information, not only in the storage, and dealing with them will reduce the execution speed of the system, so in the image recognition color image often change to gray image, so as to speed up the processing speed. The color conversion for gray process called gray processing. the standard of the choice is after gray transform, the dynamic range of pixels increases, the image contrast expansion , make the image become clearer, exquisite, easy to recognize. In the color image, the color of each pixel decisions by the R, G, B components, each byte for 8 bit, says different brightness values between 0 to 255 , the three bytes combination can produce 16.7 million different colors.. In the gray image, pixel gray level with 8 bit said, so each pixel is one of the 256 kinds of gray between black and white . The description of the gray image reflect the same with color images , still reflects the local color and brightness level of the distribution and characteristics in the entire image.Gray image, the processing methods are the following three:

Maximum method: $R = G = B = \text{Max}(R, G, B)$,

Average method: $R = G = B = (R + G + B) / 3$,

Weighted average method: $R = G = B = (0.299R + 0.588 G + 0.113 B) / 3$.

This paper used the weighted average method for gray-scale image processing, gray-processed image shown in Figure 1.



Fig. 1. Gray image

3.2 Binary Image

Graying later, there are 256 separate colors in image, to reduce pixels interference, further enhance the processing speed, should be converted grayscale to binary image,

binary image is only have black and white two color pixels, the license plate area character can be a clear distinction to background . This paper uses a global threshold binarization method. Set the original gray image is $f(x, y)$, after binarization the images is $g(x, y)$, binarization processing as follows:

$$g(x, y) = \begin{cases} 0 & f(x, y) \leq T \\ 1 & f(x, y) > T \end{cases}$$

Here, T is called the binarization threshold (Threshold), in gray-scale image ,pure black is 0, pure white is 1. After binarization processing, the foreground and background colors separated by the black and white, choose a different threshold may be different separation. Image binarization show in Figure 2:



Fig. 2. Binary image

3.3 Edge Detection

There are many edge feature extraction method, commonly used edge detection algorithms can be divided into the first derivative and second derivative algorithm categories. First order differential algorithm main have gradient operator、Roberts operator、Sobel operator、prewitt operator、Krisch operator, etc, the second order differential algorithm is Laplacian operator and Wallis operator for representative. in several classic operators of edge detection , Sobel operator is simple, fast processing speed, and the edge after process is smooth and continuous. This article chooses the Sobel operator on edge detection, Sobel operator is the form of filter operator, used for edge extraction, can use the fast convolution function, simple and effective, so widely used. Usually use the following two convolution nuclear (h_1 and h_2) respectively on the horizontal and vertical image edge detection.

$$h1 = \begin{bmatrix} 1 & 2 & 1 \\ 0 & 0 & 0 \\ -1 & -2 & -1 \end{bmatrix} \quad h2 = \begin{bmatrix} -1 & 0 & 1 \\ -2 & 0 & 2 \\ -1 & 0 & 1 \end{bmatrix}$$

The results shown in figure 3:



Fig. 3. Sobel operator edge detection

3.4 Morphological Processing

Mathematical morphology, there are four basic operations: dilation, erosion, opening operation and closing operation. Dilation and erosion is the most basic morphological transformations, they are each dual relationship. Morphology of erosion is the basic arithmetic. Its implementation is based on the filling structure element concept. one of the most simple use is eliminate irrelevant details according to size of the binary image. The erosion of A by B can be expressed as:

$$A \ominus B = \{Z | (B)_Z \subseteq A\}$$

Dilation is the dual operation to erosion , dilation has expanded the role of the image, The dilation of A by B can be expressed as:

$$A \oplus B = \{Z | (\hat{B}) \cap A \neq \emptyset\}$$

The morphological opening of the image A by element B, denoted $A \circ B$, is simply erosion of A by B, followed by dilation of the result by B:

$$A \circ B = (A \ominus B) \oplus B$$

Opening operation generally make contours becomes smooth of the object, disconnect the narrow piece, eliminate fine protrusions.

The morphological closing of A by element B , denoted $A \bullet B$, is dilation followed by erosion:

$$A \bullet B = (A \oplus B) \ominus B$$

Closing operation is similar to make contour more smooth, but in contrast with the open operation, it is usually to eliminate a narrow discontinuous and long thin gap, eliminate small holes and fill the fracture of the contours.

Selection structure elements to operator is the key of morphological operations, the different size and shape of structural elements produce different results in the image morphological operations. Common structural elements generally shows the square, quasi-circular and rectangular. This algorithm selected 2×1 rectangle structure element, first, make erosion operations with binary image, de-noising processing. After denoising the binary image also contains many other areas outside the region in addition to containing the license plate, then use 25×25 structuring element to make closing operation and opening operations with image. See fig 4 and 5:

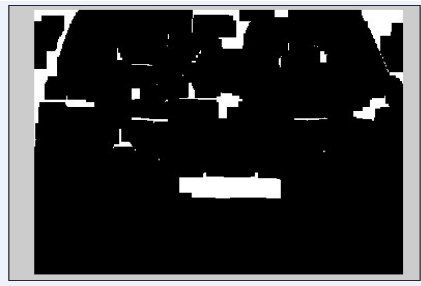


Fig. 4. Image closing operation



Fig. 5. Image opening operation

3.5 License Plate Tilt Correction and Accurate Positioning

According to the prior knowledge, analysis the image after morphological processing, to compare whose aspect ratio is closer to the actual license plate aspect ratio, then extraction and display it. After treatment the location of the license plate can be initially determined, as shown in Figure 6, then make local analysis with the basic orientation of the license plate images to further define the range of characters, this paper use the Hough transform to get the license plate tilt correction, and then use the level projection and vertical projection to process the image, to reduce the license plate of the left, right and bottom margins to determine the specific location of a car license. The end result shown in Figure 7.



Fig. 6. Initial positioning plate



Fig. 7. Precise positioning plate

4 Experiment Results

This paper presents a new method based on edge detection and morphology for the license plate localization, make simulation with 200 vehicles images of different background and light conditions on MATLAB, the experimental results shows that the method speed and recognition rate are ideal.

References

1. Yu, M., Kim, Y.D.: An Approach to Korean License Plate Recognition Based on Vertical Edge Matching. In: Proceedings of IEEE International Conference on Systems, Man, and Cybernetics, vol. 4, pp. 2975–2980 (2000)
2. Bai, H.L., Zhu, J., Liu, C.: A fast license plate extraction method on complex background. In: Proceedings of Intelligent Transportation Systems, October 12–15, vol. 2, pp. 985–987. IEEE (2003)
3. Xu, J., Li, S., Chen, Z.: Robotics: Color analysis for Chinese car plate recognition. Intelligent Systems and Signal Processing (2003)
4. Finlayson, G., Hordley, S., Hubel, P.: Color by correlation: A simple, unifying framework for color constancy. IEEE Transactions on Pattern Analysis and Machine Intelligence 23(11), 1209–1221 (2001)
5. Lee, E.R., Kim, P.K., Kim, H.J.: Automatic recognition of a Car License Plate Using Color Image Processing. In: Proceeding of International Conference on Image Processing, pp. 301–305 (1994)
6. Kim, S.K., Kim, D.W., Kim, H.J.: A Recognition of Vehicle License Plate Using a Genetic Algorithm Based Segmentation. In: Proceedings of International Conference on Image Processing, vol. 2, pp. 661–664 (1996)
7. Nijhuis, J., Brugge, M., Helmholt, K., Pluim, J., Spaanenburg, L., Venema, R., Westenberg, M.: Car license plate recognition with neural networks and fuzzy logic. In: Proceedings of IEEE International Conference on Neural Networks, vol. 5, pp. 2232–2236 (1995)
8. Park, H., Kim, I., Jung, K., Kim, J.: Locating car license plates using neural networks. Electronics Letters 35(17), 1475–1477 (1999)
9. Hsieh, J.-W., Yu, S.-H., Chen, Y.-S.: Morphology-based License Plate De-tECTION from Complex Scenes. In: 16th International Conference on Pattern Recognition, pp. 176–179 (2002)
10. Ching-Tang, H., Yu-Shan, Kuo-Ming: Multiple license plate detection for complex background. In: Proceedings of 19th International Conference on Advanced Information Networking and Applications, vol. 2, pp. 389–392 (2005)

Oilfield of Video Monitoring and Alarm System Based on DM642

Ying Wang and Xiao Feng Guo

College of Information Engineering, Shenyang University of Chemical Technology,
Shenyang, China
wyinghai@163.com, guoxiaofeng272@sohu.com

Abstract. In order to enhance the oil production safety management and to detect the abnormal state production and curb illegal phenomenon in time, design video alarming system of petroleum. The central chip of system is TMS320DM642, and system is divided into three parts, video acquisition module for real-time monitoring of oil field, the function of video processing module is image processing and analysis, when the abnormalities occurred, alarm wireless alarm module, achieve remote monitoring of oil fields.

Keywords: Video surveillance, TMS320DM642, Wireless alarm system.

1 Introduction

In recent years, with the rapid development of digital video technology, digital monitoring system becomes more and more robust. Because special environment of Oil field, for example Oil wells are scattered in a large area in oil field, where the terrain is complex, and extractive process of petroleum is continuous and with poisonous gas,. If professional staffs manage and service productive process of the oil Wells, it requires a lot of time and money, and the processing of abnormal state often is not solved timely. Therefore the oil exploitation require video monitoring and alarm system to achieve production monitoring, then it realize safe and efficient production process.

This paper design video monitoring and alarm system based on DM642. This system accomplish the remote monitoring of oil Wells, In the abnormal state cases, it starts alarm system and transmit video, This allows us to analyze the situation and prepare for analysis. The Video transmission reduce the occurrence of false alarms.

2 The Design of System Hardware

2.1 The Hardware Structure of the Whole System

Video monitoring alarm system consists of Video capture module, the video processing module and the Wireless Alarm Module. the diagram for system architecture as follows:

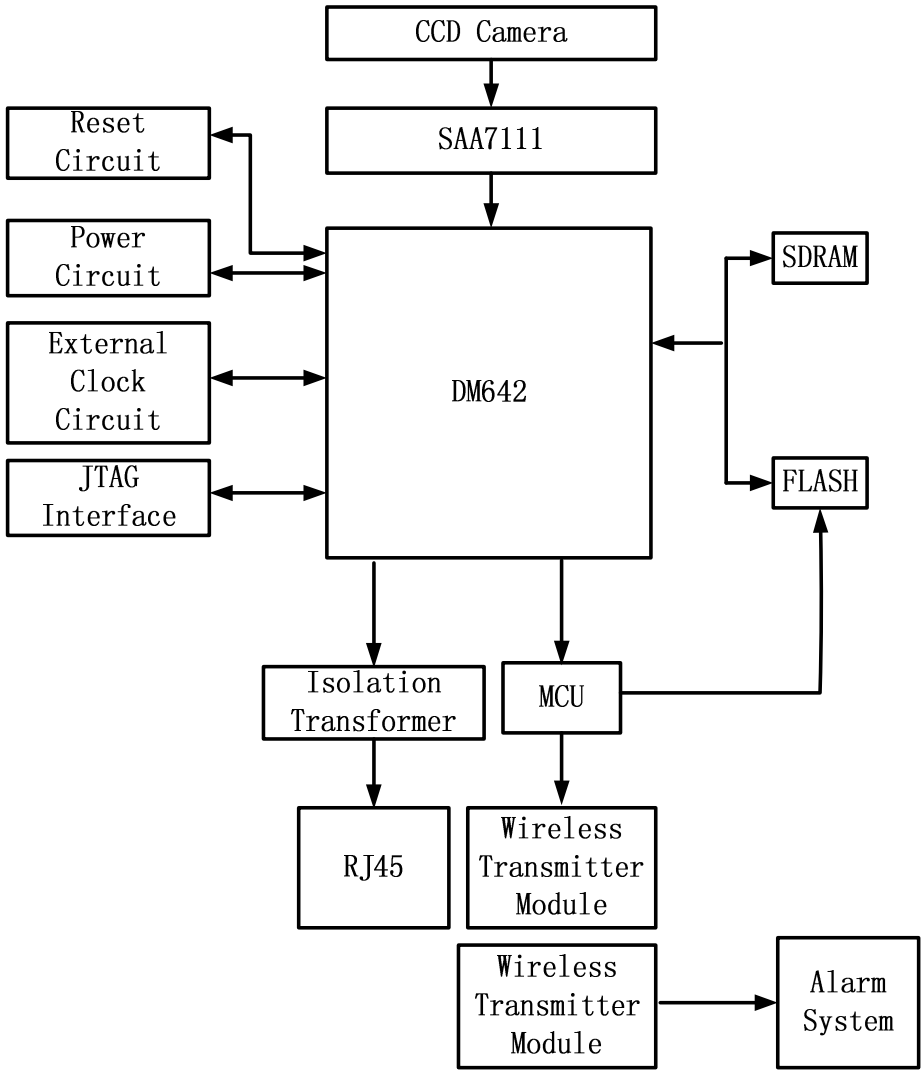


Fig. 1. The whole system

Through the CCD camera collects the video signal, then send the signal to the video decoder, after decoder decode the signal, the DSP processing complete video compression and transmission it to the network, then store processed video signal, while the MCU to determine the alarm. If there is an abnormal situation, the MCU transmit a signal to the wireless transmitter, After wireless receiver receives the alarm signal, the alarm system alarm.

2.2 The Video Processing Module

Because the system needs 24 hours of video capture, Using the built-in auto-focus zoom color CCD camera, the camera can work normally in the night. Using a programmable video Input processing chip SAA7111 to act as a decoder chip [1]. SAA7111 has four analog video inputs, two analog preprocessing channels, and it can implement anti-aliasing filtering, analog to digital conversion, automatic gain control, Multi-standard decoder and so on. The connection between SAA7111 and video camera, the output of camera Link to SAA7111 input terminal directly. The SAA7111 connection with the DM642 as shown in Figure :

SAA 7111 converted video which is from the camera into digital format, The I2C of DM642 configured the format of the output signal to the CCIR-656 model, system outputs 8BIT signal of YUV format and transferred it to SDRAM memory by DMA. As the CCIR-656 format, Output data is in accordance with the form of UYVY, clock signal which is locked by the horizontal synchronization signal link to VCLK0. the input of horizontal synchronization and vertical synchronous VREF, HREF link to VCL0, VCL1 pins.

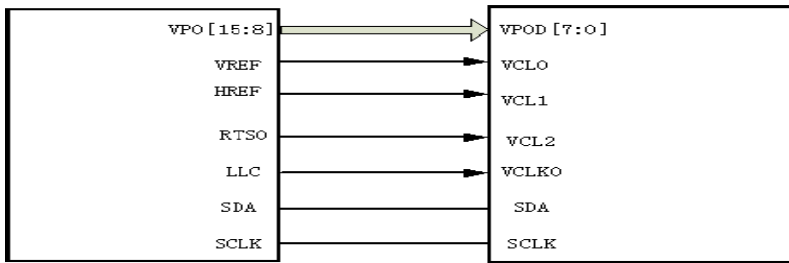


Fig. 2. The video processing module

2.3 The Video Processing Module

The core chip of the video processing module is DM642 DSP. DM642 DSP is Chips developed by Texas Instruments for multimedia applications, based on C64x core, With 64 32-bit general purpose registers, eight independent calculation function units, using the high performance long instruction word structure. In an instruction cycle, TMS320DM642 DSP can handle 8 instructions of 32-bit. DM642 has a level 2 cache, with the rich peripheral configuration, so DM642 can accomplish video processing's Requirements. In order to achieve system requirements, DM642 should work with some basic circuit.

2.3.1 Power Circuit

In system configuration circuit, power circuit module plays an important role, it is the basis for the design. In the power supply circuit, DM642 need CPU Vcore (+1.4V) and peripheral I / O voltage (+3.3V). When we design the circuit, we need to

consider a system-level sorting of power supply voltage, the purpose is to prevent power disturbances which may damage the circuit. TPS54310 power chip[2], To complete the requirement of the power circuit design, hardware circuit shown in figure, The design allows the normal and orderly supply order and ensure the effective operation of the whole system.

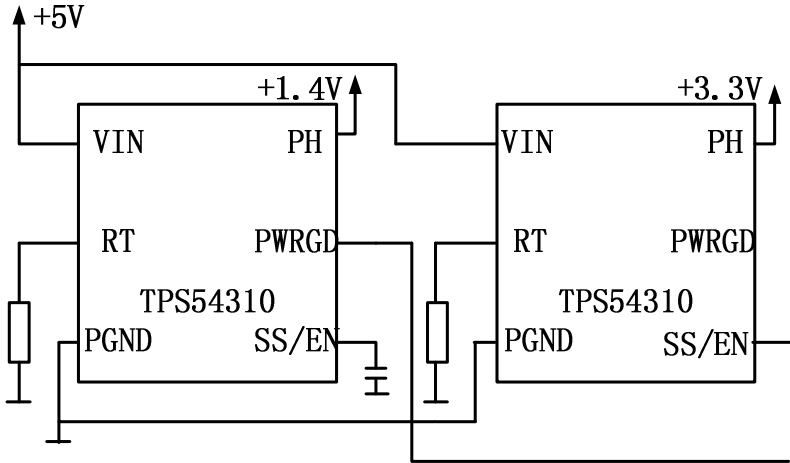


Fig. 3. Power circuit

In the design, there are 5 volts of power on the TPS54310 chip, after the corresponding chip setting, The output voltage of tpps54310 are 1.4 volts and 3.3 volts, design make the first TPS54310 's pin PWRGD connect with the second TOS54310's pin SS/EN. When the first chip output reaches + 1.4V stably. The first chip send a high level to the second one. When the value is higher than 1.2 V, the second chip start. This ensures that CPU Vcore's supply is earlier than peripheral voltage.

2.3.2 Reset Circuit

The role of reset monitoring circuit is to ensure that the system can be adjusted by the reset state at any time. To prevent the system in the state of uncontrolled. In the design we use TPS3823-33 chip to monitoring power system, WATCHDOG circuit receive DM642 timing signal from the CPU through WDI pin[3] That avoid the system program failure problems. Circuit diagram is as follows:

2.3.3 External Clock Circuit

In the system, DSP's operating frequency is 600MHZ. The EMFI pin of DM642 need frequency of 133MHz ;25MHz for EMAC control chip ,and UATR driver chips

required 30.72MHz,so the system needs to adopt a number of different clock signals.High-speed programmable chips ISC8430 which is produced by ICSI is used to produce the clock signal.

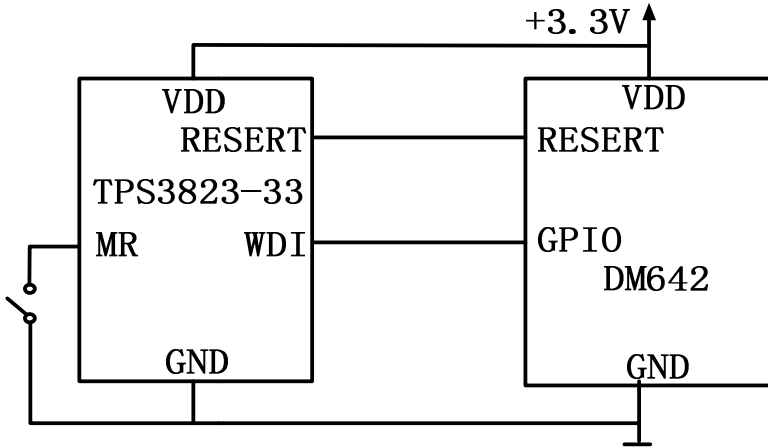


Fig. 4. Reset circuit

2.3.4 Network Interface Circuit

LXT971 is used as fast ethernet physical layer adaptive transceiver[4]. LXT971 supports the IEEE 802.3 standard, provides MII (media independent interface) interfaces, supports MAC. And DM642 integrates Ethernet media access controller, so LXT971 can seamlessly connect DM642. The circuit shown in Figure :

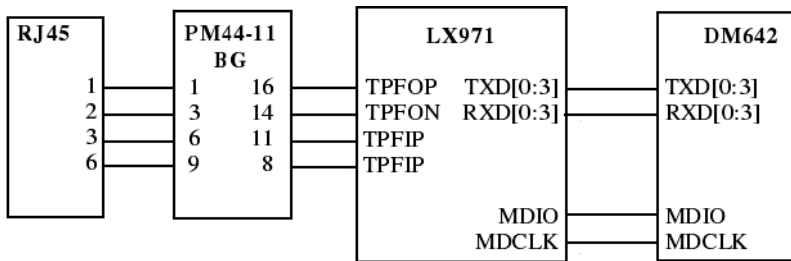


Fig. 5. Network interface circuit

PM44-11BG network isolation transformer. The data that transfer from DM642 is Converted by LXT971 to the data which can be receive by Ethernet physical layer,then transmitted to the Internet thoughRJ-45.

2.3.5 Wireless Alarm Module

Wireless alarm module is divided into two parts. One part is communication with the DM642, when abnormal phenomenon occurred, it sends alarm signals, Another part of the design is in the control room, to receive an alarm signal and achieve alarm function. Alarm module to predict consist of DM642, MCU and wireless transmitter chip. DM642 chip communicate with MCU. MCU processes the data from DSP and decides whether start the alarm or not. Figure for wireless alarm circuit :

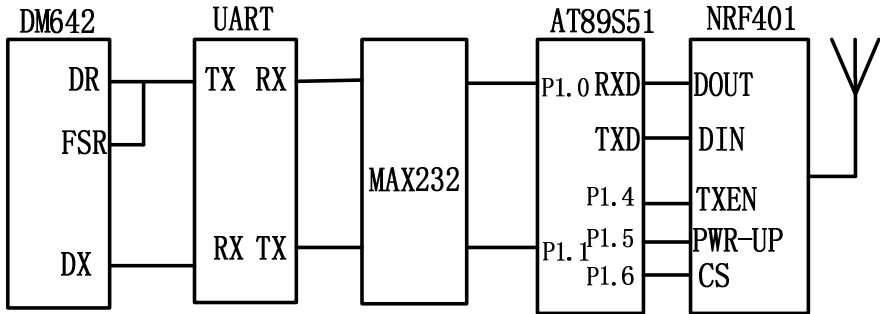
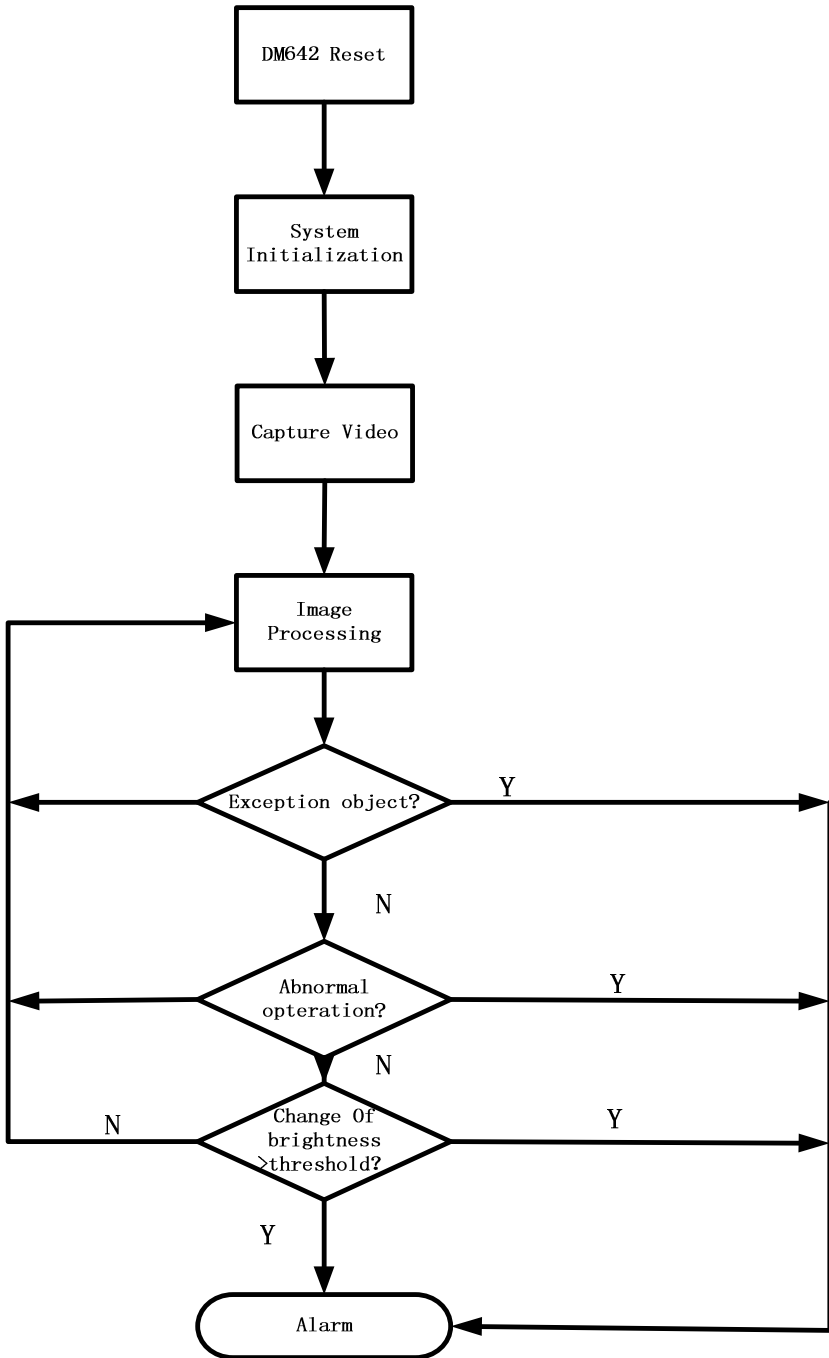


Fig. 6. Wireless alarm module

System selected NRF401 wireless transmitter and T89S51 chip. Video data transmit through the DSP UART interface, be switched the level by MAX232, and then AT89S51 make the decide to send the alarm. If it is needed to alarm, the NRF401 start to work.

3 Software Design

System is alarm Real-time image processing and alarm system. Software process describes the video image processing functions and alarm functions, As shown in Figure 8, after DM642 reset, the system make initialization. Including the EMIF, memory, SAA7111 and the microcontroller and other parts are initialized, and the CCD camera and capture video of Wells. After the video signals are processed, Video information are transmitted through the UART to the microcontroller, The data is compared with threshold in the MCU. If it is greater, Alarming.

**Fig. 7.** Software Design

4 Conclusion

This paper studies and analysis of intelligent video systems based on TMS320DM642, design the hardware to complete the most basic minimum intelligent video alarm system, Such oil monitoring system can detect the status of oil well and the unusual circumstances surrounding. Sensors are traditional on-site collection equipments, it make errors frequently because of complex environment surrounding the well. The system replace the sensor with camera. It determine whether treatment is right through the screen, accurate and reliable. System can be monitored for oilfield, it can also be adapted to other monitoring and alarm applications. With the improvement of device functions, DSP-based monitoring and warning system will have great prospects.

References

1. SAAA7111A Enhanced Video Input Processor Date Sheet. Philips Semiconductors (May 15, 1998)
2. TexasInstruments.3-V TO 6-V INPUT, 3-A OUTPUT SYNCHRONOUS-BUCK PWM SWICHER WITH INTEGRATED FETs.pdf.SLVS412B (December 2001) (revised April 2005)
3. TexasInstruments.processor Supervisory Circuits(Rev.E).Pdf (revised December 2002)
4. Intel.LXT971A datasheet (2001)

The Application of Multi-scale Modeling Technology in Artificial Bone Graft

Hu Li, Yadong Chen, Zhiguang Zhang, Tianbiao Yu, and Wanshan Wang

School of Manufacture Engineering & Automation, Northeastern University,
Shenyang 110004, China
hhuli@mail.neu.edu.cn

Abstract. In view of the preparation of the individual implants for artificial bone grafting procedures, this paper puts forward a new kind multi-scale modeling idea for artificial bone. First, build up the corresponding macro-level CAD model of the patients based on CT data; Secondly, realize the bone's internal property by analyzing the gray-scale of the patients' CT image and build up the micro-scale model in Pro/E; Finally, obtain the multi-scale CAD model of the artificial bone that match with the remaining parts by combing the macro-scale and micro-scale model and convert it into STL files to complete the preparation of implants. The further mechanical analysis was finished for the structure selection of multi-scale implantation.

Keywords: CT data, bone tissue engineering, multi-scaled modeling, Rapid Prototyping (RP).

1 Introduction

At present, the therapy methods for bone deflection sufferer contain self bone graft, variant bone graft and artificial bone graft. [1-2] There's more benefits of artificial bone graft than other surgery schemes such as little wound, none exclusion action, easy done and etc. But, the artificial bone used in surgery is of serial standard parts which match the stump with low decision, bring about the self-adaptive reshape of bone tissue and deduce the stability of implants in body. How to solve these problems brings out the work of individual customization artificial.

Including bone tissue engineering technology, multi-scale modeling methods was applied based on CT/RE/RP technology which can be used for CAD modeling of suited implants.

2 Macro Implantation Modeling with CT Datum

To get the CAD model of implantation, there're several kinds of data procession and rehabilitation methods. One is the STL data processing method which describes the true surface and its easy operated for no-complex structure deflection. The second method is of NURB, which can create sleek surface for the more complex restructure. There are numerous steps with the second method where the Boolean operation

between STL and solid model is needed firstly, and then the outer side with contour design can be repaired to thin, last the thickness of thin layer should be increased to the size needed. The third is of datum which can restructure the model automatically compared with the model in data base to find the best resolution. [7, 8, 9]

The patient in this case is of male with age of 40 years and the original datum was supplied by Chinese Medical University which was gathered by transect scanning the thighbone with multi-detector-row computed tomography. 375 layers picture was gathered and saved with the criterion of DICOM 3.0. The scanning parameters selected listed in table 1.

Table 1. The scanning parameter of row CT

voltage(V)	current (mA)	thickness(mm)	interval (mm)	pitch(mm)	velocity (mm/s)
120	300	1.25	0.625	12.5	9.4

The areas with different gray scale containing background, parenchyma and bone tissue scanning datum of thighbone was created and was put into the software by setting right gray scale value and drawing out the information from different area to restructure inter and outer surface of bone tissue. [3, 4] The dot cloud datum of 3D model can be created by reverse engineering interface from which the triangular patch model was gotten by simplifying and filtering. Lastly the CAD model can be gotten by NURBS surface fitting, see figure 1.

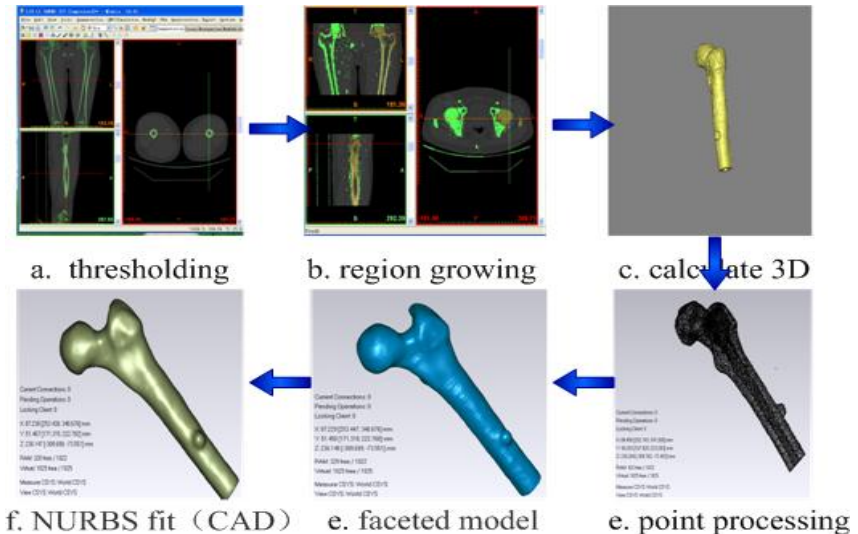


Fig. 1. The flow chart of 3D modeling of bone tissue

The removal area should be defined by the doctor who works out the surgery scheme and the serial operation can be done with the 3D CAD model of bone tissue such as the mirror and Boolean operation. Eventually, the macro-scale CAD model of implant was built up.

When the big surface patches were built up, the smaller grid should be used to dissection them. The grid numbers can be controlled by defining its precision. The higher precision of grid, the more detail of model be contained, see figure 2 and 3.

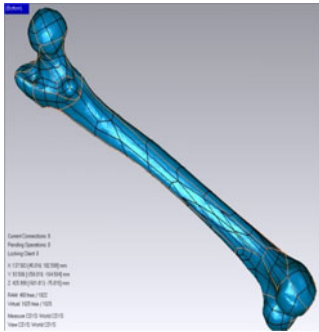


Fig. 2. The construct patches of femur

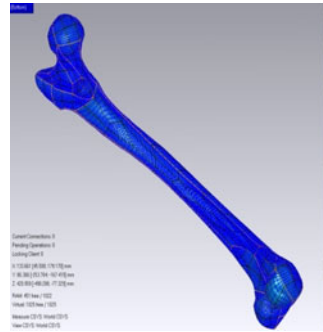


Fig. 3. The femur grid model

In the processing of thigh bone restructuring, there's some deviation between model and the real for the datum simplification and smooth operation, so the deviation detecting should be done to compare the restructuring datum with original dot cloud, see fig. 4. The deviation in the middle of thigh bone is smaller than in the both ends which is less then 0.4 mm. Compared to the discrete original datum, the deviation was permitted for the further prosthesis design and biomechanics computer.

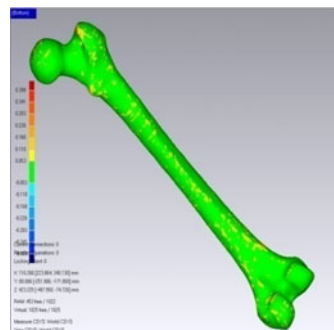
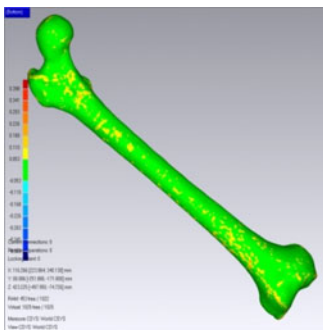


Fig. 4. Deviation of NURBS surface reconstruction

3 Micro-scale Modeling of Thigh Bone Tissue

Ideal artificial implantation contents both sides of precision outer shape and inter micro-scale structure match with human self bone tissue to ensure the long term stability when it was implanted in human’s body. Bone tissue is a kind of heterogeneity material which exhibits different structure and mechanical character in different dissection part, where the linear relation between surface density ρ and the HU value N_t can be approximate represented as formula 1. [5]

$$\rho = 2.0 \text{ g / cm}^3 \times N_t / 1600 \tag{1}$$

The material character can be represented as formula 2.[4]

$$E = 2605[\rho / (\text{g / cm}^3)]^{3.09}$$

$$E = 1904[\rho / (\text{g / cm}^3)]^{1.64} \tag{2}$$

$$\lambda = 0.3$$

Where, $E(MPa)$ is of modulus of elasticity, λ is of Poisson ratio.

Utilizing the value of HU computed by draw profile line, see figure 5, the distributed function of surface density ρ of artificial implantation and equivalent modulus of elasticity E can be computed.

Where, x is of the distance between dot on implantation and the centre of circle.

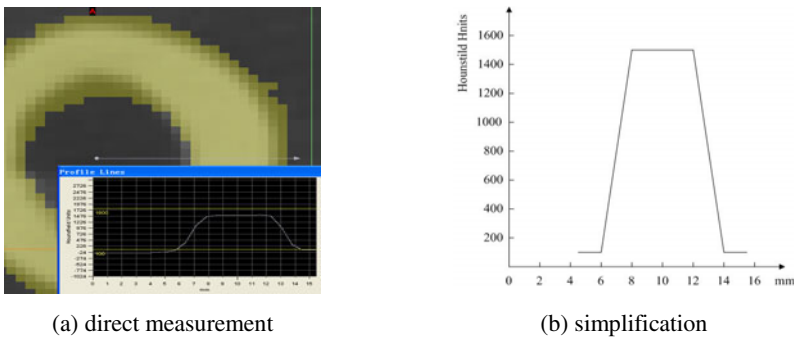


Fig. 5. The distribution of HU value of bone tissue

4 Micro-scale Structural Analysis of Implantation

The implantation plays the role of ground substance outside of cell in tissue engineer, which is to simulate the structure and function of ground substance in bionics. So the listed unit cell structure was applied.

A new type of cell unit structure was put forward by comparing other kind of cell structure, where several pore plates were put together to build the frame construction, see fig. 6. The original shape of cell unit can be controlled by plate thickness t , side length l and circular orifice r . For the every layer in the case was one third of cylinder all with 1 mm thickness and 30 mm highness, the cell unit was modified, see fig.6 (b). As the basic unit of micro-scale model, the material for this structure was proposed as tension dominant and the structure contains high strength-apparent density ratio which the ideal cell unit used in bone tissue engineer.

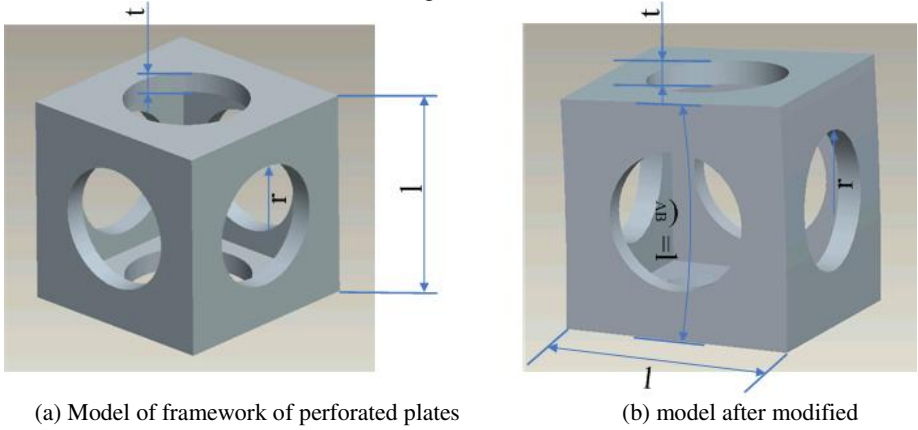


Fig. 6. The illustration of the unit-cell applied in this paper

When the Boolean operation was done between built macro-scale model and micro-scale unit cell, the prosthesis multi-scale model was built for the further surgery and mechanics analysis, see fig. 7.

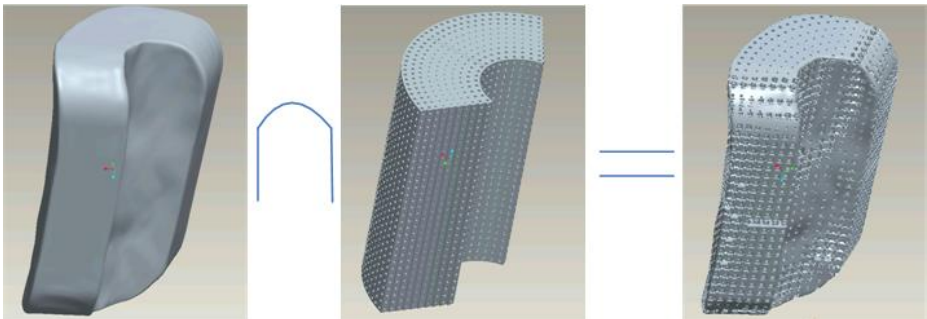


Fig. 7. The generation of the multi-scale model of femoral prosthesis

5 The Mechanics Analysis of Multi-scale Model

Through the analysis of the built multi-scale model, the micro cell units were arrayed in the way of seriation and piled up to be a kind of macro-shape cellular structure which

includes more details and is not suitable for finite element analysis. The model can be equivalent as a kind of layer model with function grads material based on uniformity theory, see fig. 8. The parameters used in formula 1 were listed in table 2.

Table 2. The material parameter of the multi-scale model of prosthesis

layer	1	2	3	4	5	6	7	8	9	10
<i>E</i>	6.6	7.8	11.5	14.2	15.0	15.0	14.3	10.5	7.1	6.8

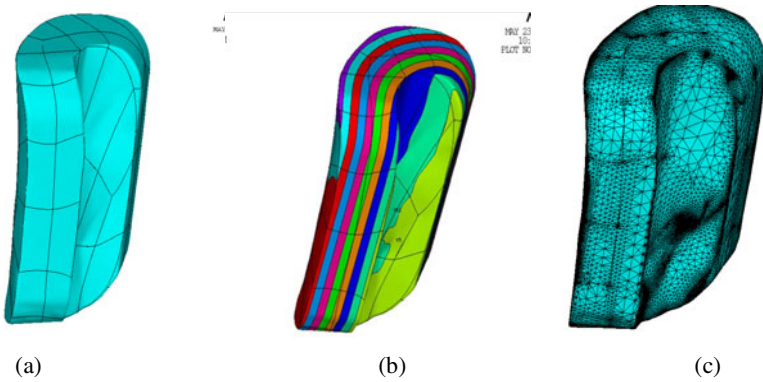


Fig. 8. The finite element modeling process of prosthesis

Von Mises equivalent stress was selected as the main guide line of the model, which contains many kind of stress components. The stress distribution was described in positive correlation with mechanical property of prosthesis material showed as figure 9 and figure 10 and the stress value is bigger in the middle than in ends. The biggest stress value appeared in the one third of parts and the stress distribution of multi-scale model consisted with it of the original bone.

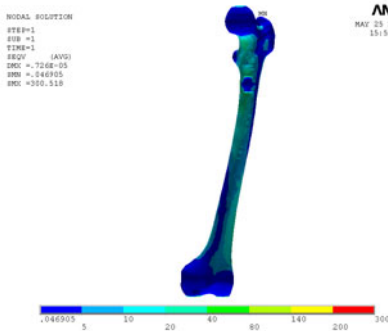


Fig. 9. The contour plot of Von Mises stress in complete femur model

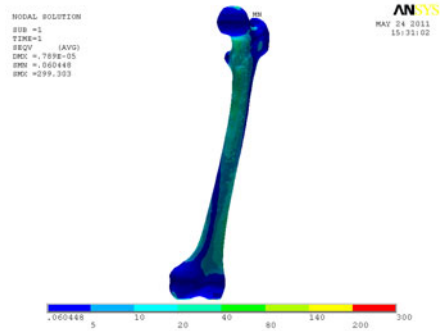


Fig. 10. The contour plot of Von Mises stress in femur with tumor excision

6 Conclusions

The multi-scale implantation modeling method was applied to simulate the self bone structure in biology, which is good at the match ability and the permeability to fulfill the needs of bone tissue engineer. It both realizes mechanism and biology fixation which can deduce the movable probability of prosthesis and ensures the stability.

References

1. Jin, L.-M.: The investigation status of bone defect therapy. *Chinese Clinic Healing* 10(1), 144–146 (2006)
2. Mittrmayer, F., Krepler, P., Dominkus, M., et al.: Long-term follow-up of uncommented tumor endoprosthesis ES for the lower extremity. *Clin. Orthop.* 388, 167–177 (2001)
3. Peng, L.: The infinite modeling method of thigh bone based on CT datum. *Journal of Qinghua University: Natural Science* 47(3), 416–419 (2007)
4. Wirtz, D.C., Schiffers, N., Pandorf, T., Radermacher, K., et al.: Critical evaluation of known bone material properties to realize anisotropic FE-simulation of the proximal femur. *J. Biomechanics* 33(10), 1325–1330 (2000)
5. Remin, E., Harris, R.A.: Advanced computer-aided design for bone tissue engineering scaffolds. *Engineering in Medicine* (223), 289–301 (2009)
6. Wang, H.: A unit cell approach for lightweight structure and compliant mechanism. School of Mechanical Engineering, Ph.D. Georgia Institute of Technology, Atlanta (2005)
7. Bergmann, G., Deuretzbacher, G., Heller, M., et al.: Hip contact force and gait patterns from routine activities. *Journal of Biomechanics* 34, 859–871 (2001)
8. Sun, W., Starly, B., Nam, J., Darling, A.: Bio-CAD modeling and its applications in computer-aided tissue engineering. *Computer-Aided Design* 37, 1097–1114 (2005)
9. Wei, J., Li, Y.: Tissue engineering scaffold material of nano-apatite crystals and polyamide composite. *Eur. Polymer J.* 40, 509–515 (2004)

Observer Generalized Representation for Unstable Delayed Systems

Omar Jiménez-Ramírez¹, Mario A. Quiroz-Juárez¹, and Rubén Vázquez-Medina^{1,2}

¹ Instituto Politécnico Nacional, ESIME-Culhuacan, Santa Ana 1000,
04430, D.F., México

² Centro de Física Aplicada y Tecnología Avanzada, UNAM, Boulevard Juriquilla 3001,
76230, Juriquilla, Querétaro, México

{ojimenezr@, mquirozj0700@alumno., ruvazquez@}ipn.mx

Abstract. This paper proposes a method for representing a delayed input system through state variables. The main idea is to use a finite-dimensional approximation for the delay operator in order to find a state-space representation of an input-delay system. This representation is based on the canonical observer form, and a Luenberger-type observer has been proposed. The delay has a rational representation and it is obtained by means of a classical Pade approximation. A linear observer is used to estimate the delay-free output, which is used within a compensation scheme to stabilize the real process by means of a suitable controller.

Keywords: State-space representation, PID controller, observer canonical form.

1 Introduction

Time delays commonly appear in process control problems, because of the distance velocity lags, recycle loops, loops composition analysis, or when approximating higher-order systems with a lower-order system with a time delay. Many controllers have been developed for stable processes. When the time delay is small, a Proportional-Integral-Derivative (PID) controller commonly suffices to give acceptable performance. For large time delays, the Smith predictor [1] provides an open-loop estimate of the delay-free output, leading to an effective compensation scheme. Watanabe and Ito [2] presented a modification of the Smith predictor to reject a load disturbance. The main drawback of these control schemes is that the time delay of the process should be exactly known, otherwise there will be a small steady-state error. Along the same idea, Åström et al. [3] proposed a new Smith predictor structure that provides superior performance. Its advantage is that the disturbance response is decoupled from the set-point response and hence can be independently optimized. The Smith predictor schemes, for stable processes, give improved performance for dominant delays, whereas the original Smith predictor cannot be applied to unstable processes because it cannot cancel unstable poles. This has motivated the design of modified forms of the Smith predictor [4-7]. It is clear that the performance of the proposed modified Smith predictor strongly depends on the stabilization of the unstable processes. This work focuses in proposing a stabilization

scheme for unstable processes with time delay. A Luenberger-type observer is constructed. The reconstructed (i.e. observed) output of the delay-free process is fed back to stabilize the real process by means of a suitable controller

2 State Space Representation of Time Delay

The real process is assumed to be linear time invariant, and is denoted as $P(s)$. The model is denoted as $P(s) = G(s)e^{-\tau s}$, where $G(s)$ is delay-free process. A state space representation for $G(s)$ can be easily obtained for the process $P(s)$ using $\tau = 0$ (system without time delay) as,

$$\begin{aligned} \dot{x}_l &= A_l x_l(t) + B_l u(t). \\ w(t) &= C_l x_l(t) + D_l u(t). \end{aligned} \tag{1}$$

In general, a realization in state space in the canonical observer form of delay can be represented of as follows.

$$\begin{aligned} \dot{x}_{rn} &= A_{rn} x_{rn}(t) + B_{rn} w(t) \quad . \\ y(t) &= C_{rn} x_{rn}(t) + D_{rn} w(t) \quad . \end{aligned} \tag{2}$$

Where the coefficient of the previous equations is defined in general form by

$$A_{rn} = \begin{bmatrix} -a_1 & 1 & 0 & 0 & \cdots & 0 & 0 \\ -a_2 & 0 & 1 & 0 & \cdots & 0 & 0 \\ -a_3 & 0 & 0 & 1 & \cdots & 0 & 0 \\ \vdots & \vdots & \vdots & \vdots & \vdots & \vdots & \vdots \\ -a_{n-1} & 0 & 0 & 0 & \cdots & 0 & 1 \\ -a_n & 0 & 0 & 0 & \cdots & 0 & 0 \end{bmatrix}, \quad B_{rn} = \begin{bmatrix} 2a_1 \\ 0 \\ 2a_3 \\ 0 \\ \vdots \\ 0 \\ 2a_n \end{bmatrix}. \tag{3}$$

$$C_{rn} = [1 \ 0 \ 0 \ 0 \ 0 \ \cdots \ 0], \quad D_{rn} = [(-1)^n].$$

with

$$a_{n-k} = \frac{(2n-k)}{k!(n-k)!} \frac{1}{\tau^{n-k}} \quad . \tag{4}$$

The state space representation of the delay term, for a Pade approximation of order n (2), and the process delay-free (1) can be integrated to a state variable representation of the system denoted as $P(s)$, as follows.

$$\begin{aligned} \dot{x} &= Ax(t) + Bu(t) \quad . \\ y(t) &= Cx(t) + Du(t) \quad . \end{aligned} \tag{5}$$

The coefficients of the representation in previous state variables can be determined by applying the following equations (6), and then the state vector is defined by $x(t) = [x_r(t) \ x_l(t)]^T$.

$$A = \begin{bmatrix} A_l & 0 \\ B_{rn}C_l & A_{rn} \end{bmatrix}, B = \begin{bmatrix} B_l \\ B_{rn}D_l \end{bmatrix}, C = [D_{rn}C_l \quad C_{rn}], D = [D_{rn}D_l] \quad (6)$$

3 Design of Continuous Estimator and Controller PID

Consider a first order unstable system with delay, e^{-s} , and the transfer function

$$\frac{Y(s)}{U(s)} = \frac{1}{s-1} e^{-s} \quad (7)$$

The estimator design is based on a Pade approximation of order $n = 4$ to estimate the state variable $W(s)$ of the system without time delay, this signal cannot be measured. A control scheme with the feedback of the estimated state is shown in the Fig. 1. The observer of states estimates the state variables based on the measurement of the output variables and control. The gain vector $G = [G_1 \ G_2]^T$ of the state estimator is determined by a continuous mathematical model constituted by two parts. The first is obtained from delay-free lineal component and the other is obtained from the delayed component. Then, it is possible to build a asymptotical estimator for function $w(t)$ (see Fig. 1a). The complete estimator is designed; the estimated state function $w(t)$ can be obtained using the vector of the estimated state $\hat{x}(t)$. A PID controller was designed to have a damping factor of 0.7 and an undamped natural frequency of 4 rad/sec. In close loop, using a scheme as shown in Fig. 1a, the resulting gains of the design of the controller are the following: $\{K_p = 11.09, K_i = 20.19, K_d = 1.5\}$. Fig. 1b is shows a control structure with two freedom degrees, using this criterion the gains are $\{k_1 = 4, k_2 = 5\}$. The calculation of the gains for the reconstructor can be done by calculating the vector G such that the roots of the characteristic equation $\det(sI - (A_{lr} - GC_{lr})) = 0$ are located in $\{-6, -4, -4, -4, -4\}$. The resulting vector for previous location in closed loop poles are $G = [4.4 \ -1.4 \ 118 \ 496.7 \ 4126.7]^T$ for both schemes.

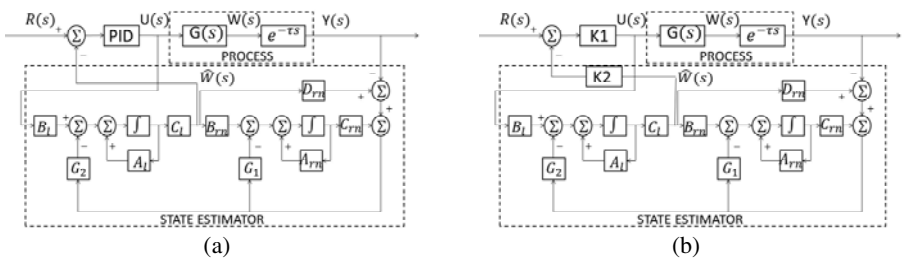


Fig. 1. a) Control scheme with a continuous asymptotic estimator, b) Scheme proportional control with two freedom degrees from a continuous asymptotic estimator

Fig. 2a shows the response of the two schemes proposed in Figs. 1a and 1b. In a comparative way, the response y_2 has a maximum overshoot of 30%, while y_1 at the

same time has not exceeded reference. Otherwise, the time establishment for y_1 and y_2 are 2.5 seconds and 3 seconds respectively. Fig. 2b shows the responses of the two proposed options, with a variation of 20% of the nominal value of time delay. It can be seen that the response for y_2 corresponding to PID structure is slightly better than y_1 obtained of proportional controller with two freedom degrees, to variations in the value of delay.

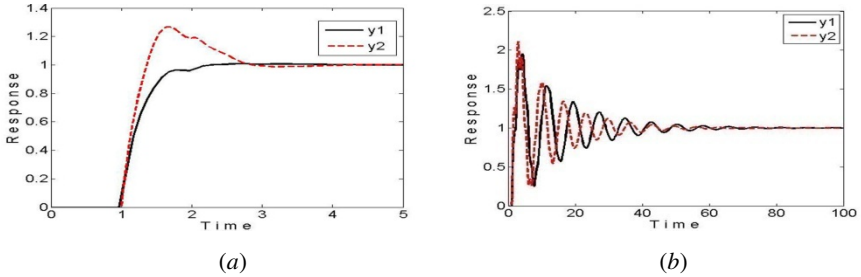


Fig. 2. *a)* Response of the proposed control schemes with analog estimator, *b)* Response of the proposed control schemes with $\tau = 1.2$ seconds

4 Conclusions

In this paper a method to obtain an approximate state variable representation of a system with delay is presented. A controller Proportional-Integral-Derivative (PID) with a control structure using a continuous estimator asymptotic was designed. Digital simulation shows how to evaluate the performance of the proposed strategy. The results that this structure presents satisfy the design specifications, the response of the system presents one overshoot that corresponds to the established one.

Acknowledgements. The authors acknowledge to the COFAA-IPN and M. A. Quiroz-Juarez acknowledges the scholarship given by Telmex. This work was partially supported by ICYTDF 270/2010 and SIP-IPN 20110670 projects and it is fully acknowledged.

References

1. Smith, O.J.M.: Close Control of Loops with Dead Time. Chem. Eng. Prog. 53(5), 217–219 (1957)
2. Watanabe, K., Lto, M.A.: Process Model Control for Linear Systems with Delay. IEEE Trans. Autom. Control 26, 1261–1264 (1981)
3. Åström, K.J., Hang, C.C., Lim, B.C.: A New Smith Predictor for Controlling a Process with an Integrator and Long Dead Time. IEEE Trans. Autom. Control 39, 343–345 (1993)
4. Kaya, I.: Obtaining controller parameters for a new PI-PD Smith predictor using autotuning. J. Process Control 13, 465–472 (2003)

5. Zhang, W., Gu, D., Wang, W., Xu, X.: Quantitative Performance Design of a Modified Smith Predictor for Unstable Processes with Time Delay. *Ind. Eng. Chem. Res.* 43, 56–62 (2005)
6. Rao, A.S., Chidambaram, M.: Enhanced Smith Predictor for Unstable Processes with Time Delay. *Ind. Eng. Chem. Res.* 44(22), 8291–8299 (2005)
7. Del Muro-Cuellar, B., Velasco-Villa, M., Jiménez-Ramírez, O., Fernandez-Anaya, G., Álvarez-Ramírez, J.: Observer-based Smith Prediction Scheme for Unstable Plus Time Delay Processes. *Ind. Eng. Chem. Res.* 14(46), 4906–4913 (2007)

Model Driven Synthesis of Behavioral Models from Textual Use Cases

Zuohua Ding and Mingyue Jiang

Lab of Scientific Computing and Software Engineering,
Zhejiang Sci-Tech University, Hangzhou, Zhejiang, 310018, China
zouhuading@hotmail.com, jiang_my@126.com

Abstract. Software system's requirements are often specified by textual use cases due to their concrete and narrative style of expression. However, textual use cases have limitation in the synthesis of behavior since they have a poor basis for the formal interpretation. Existing synthesis techniques are either largely manual or focused on the use case interactions. In this paper, we present a framework from a model-based point of view to automatically synthesize system behavior from textual use cases to Petri net model. The generated Petri net model can describe component module interactions, and can be checked with the model checking tools. We have implemented our framework and demonstrated the synthesis process via an example.

Keywords: System requirement, use case metamodel, behavior metamodel, Petri net, model transformation.

1 Introduction

Software requirements can be described by use cases in natural language [2] since their concrete, narrative style of expression makes them very effective for eliciting software requirements. However, the textual use case approach raises the problem in the synthesis of behavior. The reason is that use cases are stated in natural languages lacking in formal syntax and semantics thus have a poor basis for formal interpretation of the behavior. Besides, there rarely exist systematic approaches to analyze dependencies among use cases. All these disadvantages make it hard to synthesize behavioral models from textual use cases.

Recently, numerous efforts have been made to synthesize behavioral models from textual use cases. However, these synthesis processes are largely manual such as [9] that builds Action-Condition table by domain expert, which can introduce errors in the behavior models and thus increase the system testing effort; or the obtained models focus on describing interactions between use cases [9], global state changes [14] and the event traces [3][12][13], but miss the behaviors of subsystems and interaction behaviors between subsystems, which makes formal reasoning about those aspects impossible.

To address the above issues, this paper presents a framework from a model-based point of view to automatically synthesize Petri net based behavior models from textual use cases. We put a few constraints on the use case writing to reduce the vagueness of

use cases written in natural language. Our restricted language style is falling to the language categories used by Breaux et al.[1], Gervasi and Zowghi [6], and Kof [8]. Our Petri net model is a subclass of regular Petri net. In the model, each subsystem is described by a Petri-net-state-machine, called Process Cycle, and the interactions between the subsystems are through a rendezvous mechanism. Such description language can be mapped to the extensively used high level languages such as CCS of Milner [10], CSP of Hoare [7] and Ada, which are also rendezvous-based. Besides, our Petri net model can be further used for the performance analysis [5] and static analysis [4].

The following is the sketch of our method. We first construct Source Metamodel from use cases, and Behavior Target Metamodel from Petri net, and then define rules to transform source model to the target model. The model transformation relies on the model transformation platform ADT (ATL Develop Tools).

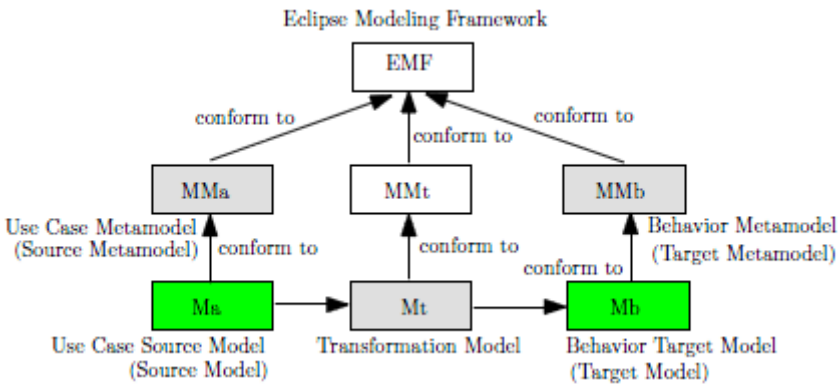


Fig. 1. Model transformation structure

Fig.[1] illustrates part of our novel model generation process. We first map a collection of use cases to a use case source model M_a . We then use the transformation model M_t to map the use case source model M_a to the behavior target model M_b . We build MM_a and MM_b in UML. We write M_t in ATL (Atlas Transformation Language), and we write M_a and M_b in ecore. M_t conforms to the transformation metamodel MM_t , M_a conforms to the source metamodel MM_a , and M_b conforms to the target metamodel MM_b . The transformation model is built on top of the model transformation platform ADT (ATL Development Tools) provided by Eclipse. In particular, ADT constructed the transformation metamodel MM_t .

2 An Example

In this paper, we choose the format specified by Cockburn [2] to write the use cases. Cockburn's use case format is an example of a *structured* use case format. A use case contains the following elements:

**Use Case | System under Discussion | Primary actor | Scope |
Main scenario: 1. step 1, 2. step 2, ..., n. step n | Variation | Extension**

In the main scenario, extension and variation, the sentence in every step describes only one activity of the actor (primary actor, SuD, and supporting actor). The sentence can be specified in the following structures.

- subject+verb+[object]
- subject+verb1+object1+to+verb2+[object2]
- subject+verb+object1+to/from+object2
- subject+verb+object+adjective
- subject+verb+object+present participle
- subject+verb+object+past participle

We will use three use cases of Market Information System (MIS) by Plasil and Mencil [11] to illustrate our model transformation. The follows are the use cases (Fig.2).

<p>Use Case 1: Seller submits an offer. Scope: Marketplace. SuD: MIS. Primary Actor: Seller. Main scenario. 1 Seller sends item description. 2 System gives acknowledgement to Seller. 3 System validates the description. 4 .System asks Seller to provide price information 5 Seller submits price and enters contact and billing information. 6 System validates Seller's contact information. 7 System verifies the Seller's history to permit the seller to operate. 8 System validates the whole offer with the Trade Commission. 9 Trade Commission gives response to system. 10 System lists the offer in published offers. 11 System responds Seller with a uniquely identified authorization number. Extensions. 3a Item not valid. 3a1 Use case aborted. 7a Seller's history inappropriate. 7a1 Use case aborted. 9a Trade commission rejects the offer. 9a1 Use case aborted. Variations. 3b Price assessment available. 3b1 System provides a price assessment.</p>	<p>Use Case 2: Clerk submits an offer. Scope: MIS SuD: CS. Primary Actor: CL. Main scenario. 1 Clerk submits information describing an item. 2 System validates the description. 3 System asks CL to input price information. 4 Clerk enters price and billing information. 5 System validates Seller's contact information. 6 System asks the Supervisor to validate the seller. 7 Supervisor permits the seller to operate. 8 System validates the whole offer with the Trade Commission. 9 Trade Commission gives response to system. 10 System lists the offer in published offers. 11 System responds an uniquely identified acknowledgment to CL. Extensions. 3a Item not valid. 3a1 Use case aborted. 9a Trade commission rejects the offer. 9a1 Use case aborted. Variations. 3b Price assessment available. 3b1 System provides a price assessment.</p>	<p>Use Case 3: Seller to Clerk. Scope: MIS SuD: CL. Primary Actor: Seller. Main scenario. 1 Seller sends item description to the Clerk. 2 System submits information describing an item. 3 CS asks CL to input price information. 4 System asks Seller to provide price information. 5 Seller submits the price, billing and contact information to the Clerk. 6 System enters the price, billing and contact information to the CS. 7 CS responds with an uniquely identified acknowledgment. 8 System responds Seller with an uniquely identified authorization number. Extensions. 3a Item not valid. 3a1 Use case aborted.</p>
--	--	---

Fig. 2. Three use cases of MIS

After transformation, we get a Petri net model for these use cases as shown in Fig.3.

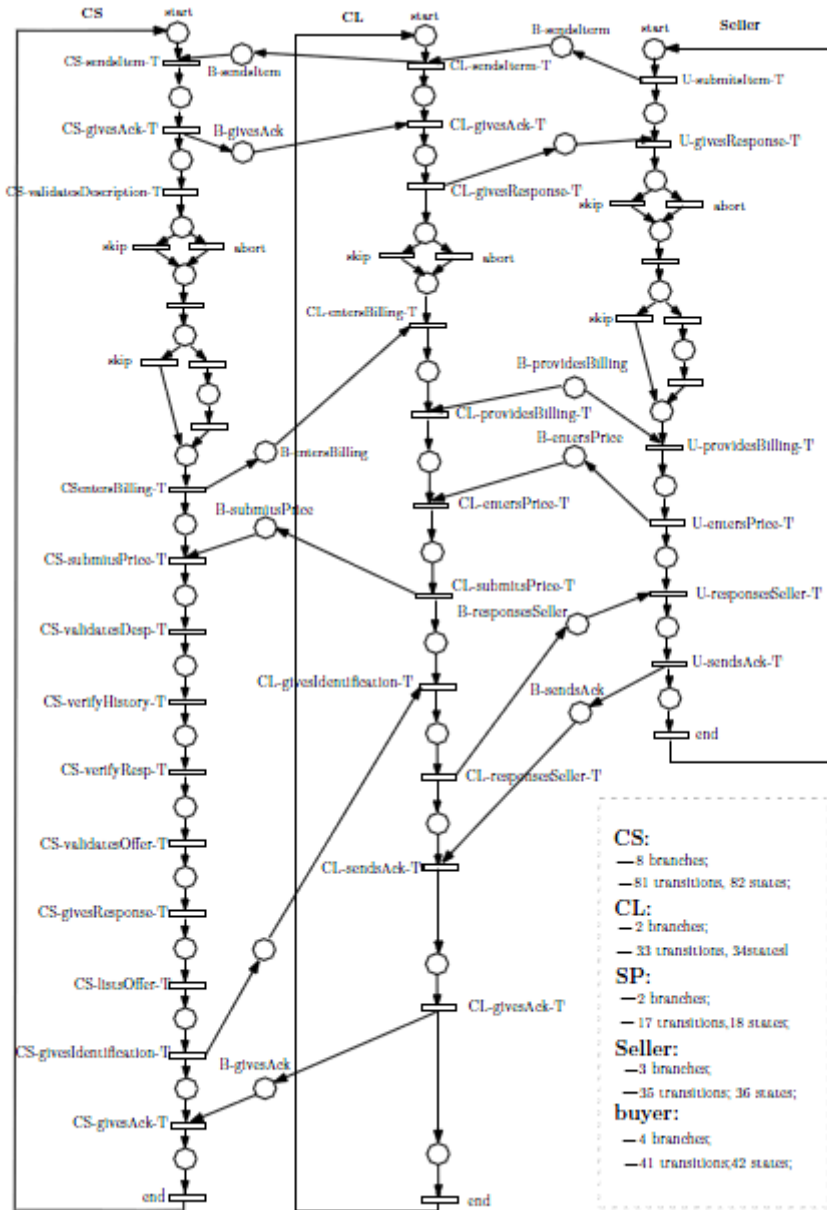


Fig. 3. Part of Petri net model of MIS

3 Conclusion

We have presented a method to automatically map textual use cases to Petri net based behavior models. We have implemented our approach in a model-generation tool that

is integrated with the ADT platform provided by Eclipse. In the future work, we continue to work on language processing techniques so that the prototype can reach a higher level of automation, and consider the timed requirements as well.

Acknowledgments. This work is supported by the NSF under Grant No. 90818013 and Zhejiang NSF under Grant No.Z1090357.

References

1. Breaux, T.D., Anton, A.I., Doyle, J.: Semantic Parameterization: A Process for Modeling Domain Descriptions. *ACM Transactions on Software Engineering and Methodology* 18(2), Article 5 (2008)
2. Cockburn, A.: *Writing Effective Use Cases*. Addison-Wesley (2001)
3. Damas, C., Lambeau, B., Dupont, P., van Lamsweerde, A.: Generating annotated behavior models from end-user scenarios. *IEEE Transactions on Software Engineering* 31(12), 1056–1073 (2005)
4. Ding, Z.: Static Analysis of Concurrent Programs Using Ordinary Differential Equations. In: Leucker, M., Morgan, C. (eds.) *ICTAC 2009*. LNCS, vol. 5684, pp. 1–35. Springer, Heidelberg (2009)
5. Ding, Z., Shen, H., Kandel, A.: Performance Analysis of Service Composition Based on Fuzzy Differential Equations. *IEEE Transactions on Fuzzy Systems* 19(1), 164–178 (2011)
6. Gervasi, V., Zowghi, D.: Reasoning About Inconsistencies in Natural Language Requirements. *ACM Transactions on Software Engineering and Methodology* 14(3), 277–330 (2005)
7. Hoare, C.A.R.: Communicating sequential processes. *Communication of ACM* 21(8), 666–677 (1978)
8. Kof, L.: Scenarios: Identifying Missing Objects and Actions by Means of Computational Linguistics. In: *Proceedings of RE 2007*, pp. 121–130 (2007)
9. Lee, W.J., Cha, S.D., Kwon, Y.R.: Integration and Analysis of Use Cases Using Modular Petri Nets in Requirements Engineering. *IEEE Transactions on Software Engineering* 24(12), 1115–1130 (1998)
10. Milner, R.: *Communication and Concurrency*. Prentice-Hall (1989)
11. Plasil, F., Mencl, V.: Getting 'Whole Picture' Behavior in a Use Case Model. *Transactions of the SDPS: Journal of Integrated Design and Process Science* 7(4), 63–79 (2003)
12. Uchitel, S., Kramer, J., Magee, J.: Synthesis of behavioral models from scenarios. *IEEE Transactions on Software Engineering* 29(2), 99–115 (2003)
13. Uchitel, S., Kramer, J., Magee, J.: Incremental elaboration of scenario-based specifications and behavior models using implied scenarios. *ACM Transactions on Software Engineering and Methodology* 13(1) (2004)
14. Whittle, J., Schumann, J.: Generating statechart designs from scenarios. In: *Proceedings of ICSE (2000)*

A New Design of PC104 Host Controller Based on STM32F103

Sun Shuying, Li Jun, and Chen Zhijia

Ordinance Engineering College, Shijiazhuang, 050003

Abstract. In order to deal with some small scale or low power dissipation applications, this paper presents the STM32F103 as the core to construct PC104 host controller. This design can efficiently save costs, reduce power dissipation and enhance reliability. For hardware design, uses the rich General Purpose Input/output (GPIO) resources provided by STM32F103 to map address bus, data bus and control bus of PC104 bus. For software design, simulate PC104 bus by configure and operate the GPIO, and package the operation as library function for easy use. Use STM32F103 to simulate PC104 bus is proved to have high performance for its 72 MHz clock rate. The design has been tested on 8 bit and 16 bit PC104 bus functional card.

Keywords: STM32F103, PC104 bus, host controller.

1 Introduction

The PC104 bus is a widely used industrial control embedded bus standard [1]. It adopts 16-bit data bus and 20-bit address bus which is completely compatible with standard PC architecture [2]. It is a multi-host bus which can be controlled by CPU and DMA controller.

The PC104 bus standard has many advantages than other standards, such as high reliability, low-power dissipation, high mechanical intensity and cards inter-connection by way of stack [3]. But most PC104 host controller use CPU based on X86 architecture, makes the system scale too large to use in small applications. On the other hand, use X86 CPU has many shortages, such as high power dissipation, high system cost and low reliability. This paper come up with STM32F103 as the PC104 host controller to solve these problems.

2 STM32F103 Profile

The STM32F103xx enhanced series has a 32-bit high performance RISC core which is based on ARM Cortex-M3 architecture. Its operating frequency is 72MHz and builds-in high-speed memory (up to 128K bytes of flash memory 20K bytes of SRAM). Two APB bus connect the core to the rich I/O port and peripherals. The work temperature ranges from -40°C to 105°C , power supply voltage ranges from 2.0V to 3.6V, a series of energy conservation modes to ensure it meets requirements of low power dissipation and industrial applications [4].

The 100 pin packaging STM32F103 MCU contains 80 fast General Purpose Input/output (GPIO) port, these 80 pins are divided into 5 group of 16-bit I/O port and each group can be mapped to 16 external interrupt, the maximum input voltage is 5V. The I/O ports have many kinds of input/output modes, most of them are alternate ports. By setting I/O port as alternate open drain output or alternate push-pull output the I/O port can be alternated used as input/output pin of peripheral or communication interface.

3 Hardware Design

STM32F103 didn't provide any standard address, data and control bus, but it provides very rich GPIO resources. The essence of hardware design is mapping these GPIO ports to data, address and control bus of PC104. On the other hand, the power supply voltage of STM32F103 is 3.3V, although most GPIO pin tolerate 5V input signal, its output high voltage is less than 3.3V, which is hard to drive 5V TTL device. So voltage converter is necessary. The following sections take IO operations as example to explain how to design hardware.

3.1 Address, Data and Control Bus

The design uses two groups of GPIO port PD and PE to build PC104 bus, use PD as control bus and PE as address/data alternate bus. Address, data separation is achieved by using ALE (PD4) and two 8-bit latches (74HCT573). When ALE is high, PE output address. While ALE is low, PE output data. Shown in Figure 1.

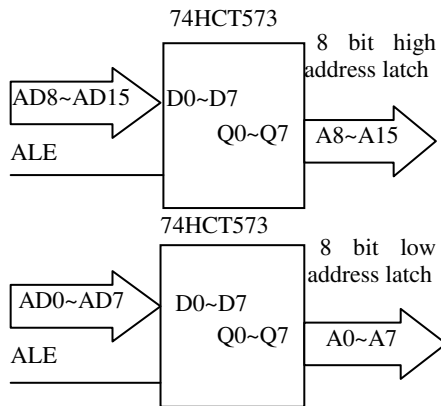


Fig. 1. Address, data bus and address latch

There are more than 30 control signals of PC104 bus, but the design just select some widely used signal of them. If the actual needs for more, the GPIO port can be easily increased into this application. The following paragraph takes some widely used signal as example to explain how control signal work.

AEN is the bus enable signal, when low, the CPU controls the bus, otherwise, DMA controller controls the bus. ALE is the address latch signal, active high, the address is

latched to the device address buffer when the ALE active. IOW# is the port write signal, active low, the rising edge latches data to the device data buffer. IOR# is the port read signal, active low, the rising edge latches data to the CPU data buffer. IOCS16#, active low, controlled by device, inform the CPU that the device will receive a 16-bit bus operation.

3.2 Voltage Conversion

74HCT series is 5V TTL-compatible CMOS integrated circuits, while most of STM32F103 GPIO port is 5V TTL-compatible ports. Therefore, use 74HCT573 latches can easily realize voltage conversion. The voltage conversion of control bus can use buffer such as 74HCT541 or 74HCT244, see Figure 2. The voltage conversion of data bus is achieved by use 8-bit bus transceiver 74HCT245, the direction is controlled by IOR#, the chip enable pin is connected to ground (always valid), as shown in Figure 3. IOCS16# is generated by the device, and the GPIO port is 5V compatible, so voltage conversion is not necessary.

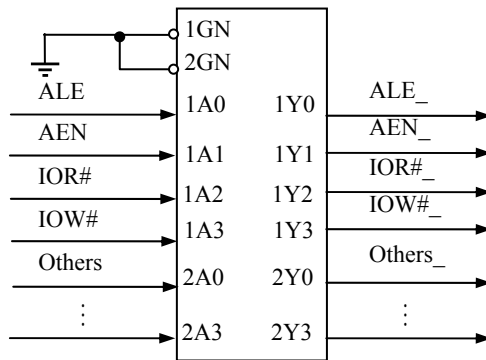


Fig. 2. Voltage conversion of control bus

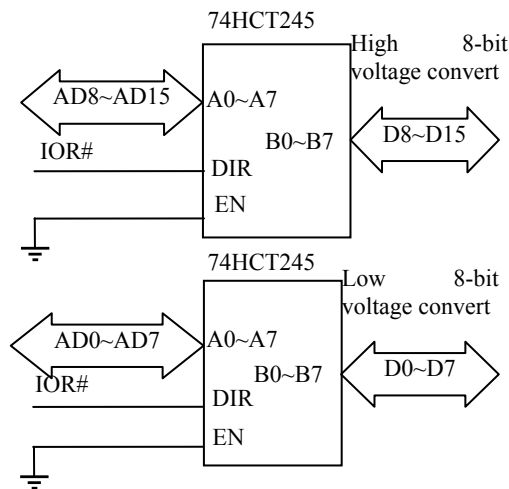


Fig. 3. Voltage conversion of data bus

4 Bus Timing and Software Design

There are 7 kinds of basic operations of PC104 bus, corresponding to seven different bus timing. Among them, 5 are controlled by CPU, 2 by DMA controller:

- memory read bus timing;
- memory write bus timing;
- I/O port reading bus timing;
- I/O port writing bus timing;
- interrupt response timing;
- memory to I/O's DMA bus timing;
- I/O to memory's DMA bus timing.

The key to compose PC104 bus is software design, the software controls GPIO to emulate the bus signal to operating as the PC104 does. The basic idea is to determine the mapping relationships between GPIO port and PC104 bus and use macros to define it. Then operate the GPIO port as the mapping relationships shows.

4.1 Port Initialization

Because most of GPIO port is alternated port, it's necessary to initialize before using it. The initialization including the pin selection, pin clock rate and input/output mode choice:

Define port PE as address/data alternate bus, the input/output mode of the 16 pin corresponding to port PE is defined as floating input, clock rate is 50MHz.

Port PD is defined as control bus, the input/output mode of the following pins PD4 (ALE), PD11 (IOR#), PD13 (IOW#) and PD15 (AEN) are defined as push-pull output, clock rate is 50MHz. The input/output mode of PD2 (IOCS16#) is floating input, clock rate is 50MHz.

The following sections take I/O read and write as example to introduce bus timing.

4.2 I/O Read Timing and Software

As shown in Figure 4, first, CPU sets AEN low, indicating the bus is controlled by the CPU. Then send the address and set ALE high. Pull ALE low while the address is effective to latch the address, and then remove it. After the address' cancellation, pull IOR# low. The device-side data signal should appear on the data bus, the data will be read to the CPU during IOR# is low. Then set IOR# high, inform the device set data buffer (or latch) high impedance state. Set AEN high, indicating that the CPU release the bus. When read, CPU determines the device accepts 8-bit or 16-bit operation according to IOCS16#. When IOCS16# is low, CPU reads 16-bit data, otherwise, read 8-bit data.

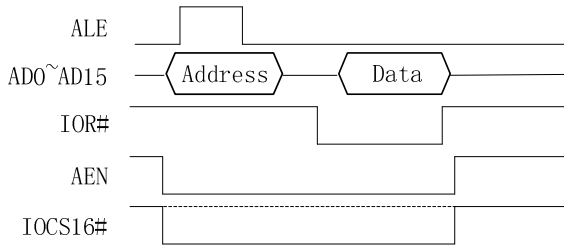


Fig. 4. PC104 bus I/O read timing

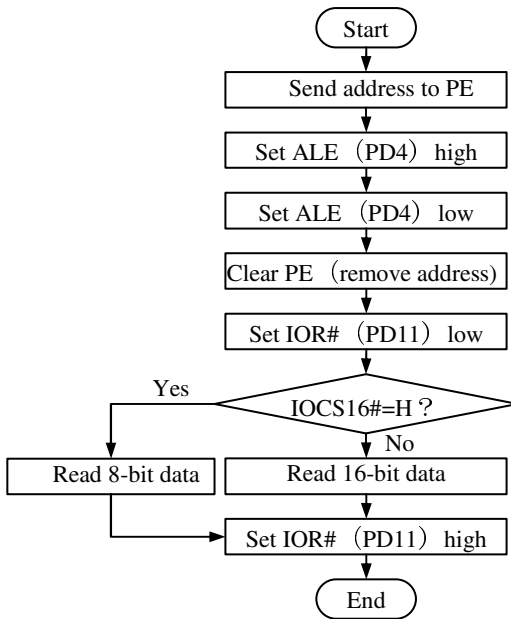


Fig. 5. PC104 bus IO read flow path

4.3 I/O Write Timing and Software

Similar to the I/O read, when the I/O write starts, CPU first sets AEN low, indicating the bus is controlled by the CPU. Then send the address signal, while ALE is set high. CPU sets ALE low while the address is effective to latch address and removes it later. Then set IOW# low and send the data signal. CPU sets IOW# high after the data appears on the bus. The data is latched to the device data buffer at the rising edge of IOW#. Last, CPU sets AEN high, indicating that the I/O write timing is over and release the bus. When writing, CPU determines the device accepts 8-bit or 16-bit operation according to IOCS16#. When IOCS16# is low, CPU writes 16-bit data, otherwise, writes 8-bit data.

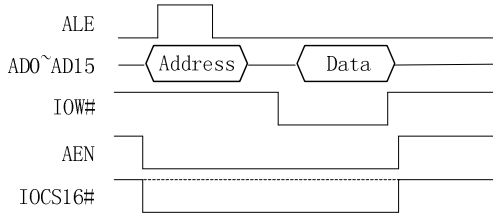


Fig. 6. PC104 bus I/O write timing

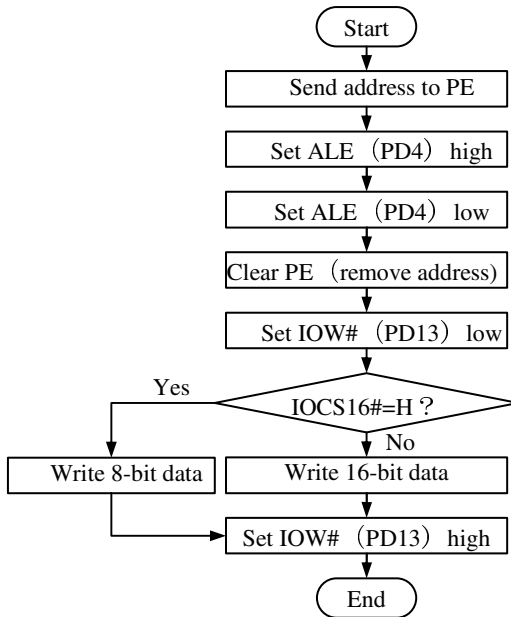
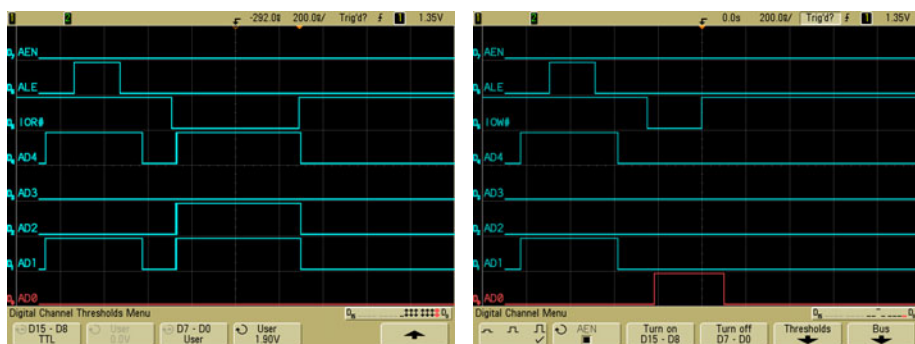


Fig. 7. PC104 bus IO write flow path

In fact, PC104 bus signal is synchronized with the clock, this design doesn't use clock because the PC104 bus timing is implemented by software design. The actual application simulates PC104 bus timing by improving the GPIO rate or using software delay.

5 Result

Figure 8 shows the actual waveforms of PC104 bus reading and writing operating of this design. This figure only shows 5 LSB of address/data alternated bus. These figure shows that the waveform corresponds to that of PC104 bus standard.



a) I/O write timing

b) I/O read timing

Fig. 8.

6 Conclusion

Using STM32F103 MCU to compose PC104 bus host controller, has been tested on 8-bit PC104 digital axial angle convert board and 16-bit multi-functional ADC-board. This design has advantages such as low-cost, easy to develop, small scale system, less power dissipation and so on. This design can be used as a solution of cheap, lightweight and low-power applications.

References

1. Li, D., Liu, Y.: PC104 bus used in the brake control unit. CSR Zhuzhou Electric Locomotive Co. Ltd., Zhuzhou (2011)
2. PC/104 Embedded Consortium: PC/104 Specification V2.5 (2003), <http://www.pc104.org>
3. Zhang, R., Deng, H.: PC104-based timing control system design. China Academy of Engineering Physics, Institute of Applied Electronics, Mianyang (2011)
4. STMicroelectronics (2008), <http://www.st.com>

Design of Auxiliary Power Supply for the Solar PV Inverter

Yunhai Hou, Shihua Sun, and Ershuai Li

School of Electric & Electric Engineering, Changchun University of Technology,
130012 Changchun, China
houyunhai@mail.ccut.edu.cn, {sunshihua100, liershuai}@126.com

Abstract. In order to design PV inverter auxiliary power supply, circuit with isolated single-ended anti-flyback current-control mode, is obtained by experimental design of the circuit for the conclusions of PV Inverter. This experiment involves some of the basic switching power supply design specifications, the transformer core and winding design, feedback and regulation circuit. The auxiliary switching power supply is already used in the inverter, which is high stability, output ripple is small and the phenomenon of transformer no fever, meets the design objectives.

Keywords: Switching power supply, transformer, pulse width control chip, UC3842.

1 Introduction

As China's power electronic technology innovation and photovoltaic energy technology extensive application, the internal power supply part of pv inverter power supply has great practical value. This paper the characteristics of the auxiliary power of photovoltaic inverter power supply, design a kind of isolated single-ended anti-flyback multiplex output switching power supply, it has the advantages of small volume, high performance and is easy to realize the multiple output, etc.

2 Principles and Design

2.1 Auxiliary Power Supply Working Principle

Isolated single-ended flyback power supply circuit diagram shown in Figure 1.

Isolated single-ended power supply is to make the high-frequency transformer as the main isolation device, and the transformer core work only on one side of its hysteresis loop[1]. The so-called anti-flyback is as switching power transistor VT_1 turns on, it stores energy in the primary induction coil, and when VT_1 is turned off, the energy stored in the primary coil and then released to the load through the secondary induction.

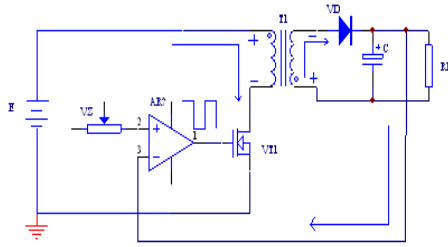


Fig. 1. Isolated single-ended anti-flyback power supply circuit diagram

The circuit works as follows:

When MOS tube VT_1 turn-on, current from the pulse transformer battery positive top to bottom of the pulse transformer, and again from power tube VT_1 D pole to S pole, and finally returned to the battery negative[2]. The current flows through its pulse transformer and in transformers inductance coils do work and stored energy. Through transformer-coupled, the transformer secondary produces a positive voltage in the bottom and the negative voltage in the above, while the transformer secondary is connected to the anti-bias diode VD state, so the diode VD deadline. In the transformer secondary circuit side, no current flows through, neither energy transfer to the load. When the MOS tube VT_1 is closed, self-induction electromotive force due to the role of the coil inductance and current, under the direction of the negative into a positive on, the coupling transformer secondary inductance coil voltage reversed, that is next on the negative so that the diode pass, the primary voltage by the diode rectifier on the way into DC pulsating voltage, the charging voltage to the output capacitor C , while the load RL also has current I_L flow[3].

2.2 Switching Power Supply Design

2.2.1 Technical Index

Specific technical requirements:

- (1) Input power supply voltage
DC24V.48V.110V.220V.330V $\pm 30\%$
- (2) Output voltage current
 $VCC1 = 15V \pm 1\%$ 0.7A ; $VDD1 = 5V \pm 1\%$ 0.3A ;
 $VCC2 = 12V \pm 1\%$ 0.1A ; $VCC3 = 15V \pm 1\%$ 0.2A ;
 $VCC4 = 24V \pm 1\%$ 0.1A ; $VCC5 = 24V \pm 1\%$ 0.3A ;
- (3) Rated output power: 30 W, maximum output power 40 W.
- (4) Voltage adjustment rate: 1 I (I refer to the rated output current).
- (5) Load regulation rate: 0.2 ~ 1 I.
- (6) Ripple coefficient: $VPP \leq 200MV$.

- (7) Efficiency: multi-channel power above 80%.
- (8) Work environment temperature: $-10 \sim 45^{\circ}\text{C}$.
- (9) Temperature rise: below 35%.
- (10) Overload capacity: 1.1I(10 minutes).

2.2.2 Main Circuit Switching Power Supply

The main circuit switch voltage-driven power tubes used IRF530, compared with the traditional self-oscillating flyback transistor switching power supply, has the advantages of a frequency of large, simple drive control, drive power is small[4]. In order to reduce the switch stress of the switch, designed with the primary side inductance parallel RC snubber circuit, over-voltage turn-off to absorb the energy. In order to meet the requirements of low ripple output, the output consisting of the TL431 precision optocoupler feedback circuit and multi-capacitor filter [5].

2.2.3 Transformer Design

First, high frequency transformer design should start from the core selection, then the winding turns. The design process need to understand associated with a variety of core characteristics and parameters, and need to calculate and verify various parameters[6].

This design of the transformer compared with the conventional linear transformers, has the advantages of a small size, light weight, high energy transfer efficiency, easy modification, etc.

Transformer magnetic core computing:

Flyback switching power supply high-frequency transformer magnetic core can be calculated by area product calculation method (AP).

$$AP = A_e A_w = \frac{2P_0 \sqrt{D}}{\eta K_w J \Delta B f} \times 10^4 \quad (1)$$

Where: AP is the unit of cm^4 ; p_0 is the output area in W; A_e is the cross-sectional area for the magnetic core; A_w is the window area; D is the duty ratio of 0.4; η is the efficiency elected 0.8; K_w is the Window area utilization factor of 0.4; $J = 400 \text{ A} / \text{cm}^2$; $\Delta B = B_m - B_r$.

AP calculations can be simplified as:

$$AP = A_e A_w = \frac{99P_0}{(B_m - B_r)f} = \frac{99 \times 40}{0.15 \times 150000} = 0.2 \text{ cm}^2 \quad (2)$$

Where: $B_m - B_r$ is the value of 0.15T.

Look-up table can be directly choose EE25 type, in order to set aside enough magnetic core power surplus, the actual choose EE28 type magnetic cores[7].

2.2.4 Each Output Winding

Transformer primary winding turns formula :

$$N1 = \frac{V_{i\max} \times 10^8}{4BfS} \times 1.2 \quad (3)$$

Where : s is the core cross-sectional area, unit of cm^2 ; f is the operating frequency of 150K; B is the Core magnetic induction intensity 1000; S is the Capacity of $(s/0.11) \cdot 2 \cdot 0.8$; V_i is the input voltage; V_0 is the output voltage.

Secondary coil turns formula:

$$N2 = \frac{N1(V_0 + \Delta V)}{0.85^2 V_{i\max}} \times 1.1 \quad (4)$$

Where: ΔV is the Value of 1.5.

Considering the skin effect, too thick wound is not easy, try to cover the core area, and can be used with multi- roots winding way. In addition, the winding of the three windings in high side, as far as possible around the core in the middle position, that is, away from the core on the bottom of the department to have a certain distance, and in the core on the bottom are a few millimeters of tape wraps, ensures that there is enough distance with the low pressure side of the winding inside the transformer in the switching power supply[8].

3 Experiment

3.1 Experimental Main Circuit

The main circuit shown in Fig.2:

This circuit uses the transformer primary side with RCD clamp flyback converter, the six outputs; control circuit to the core for the UC3842, which together with a small amount of external components. In the entire power operation system, power system implementation process is a negative feedback. If some reason the output voltage rises, the sampling circuit to increase the signal acquisition to the system amplifier that UC3842 reverse side, the internal comparison to the output of a process reducing narrow pulse, through the pulse transformer to the secondary transmission, the secondary area corresponding reduced conduction, etc. So that the output voltage drops. Similarly, when the output voltage drops, also be interpreted as a reverse process of the output voltage rises.

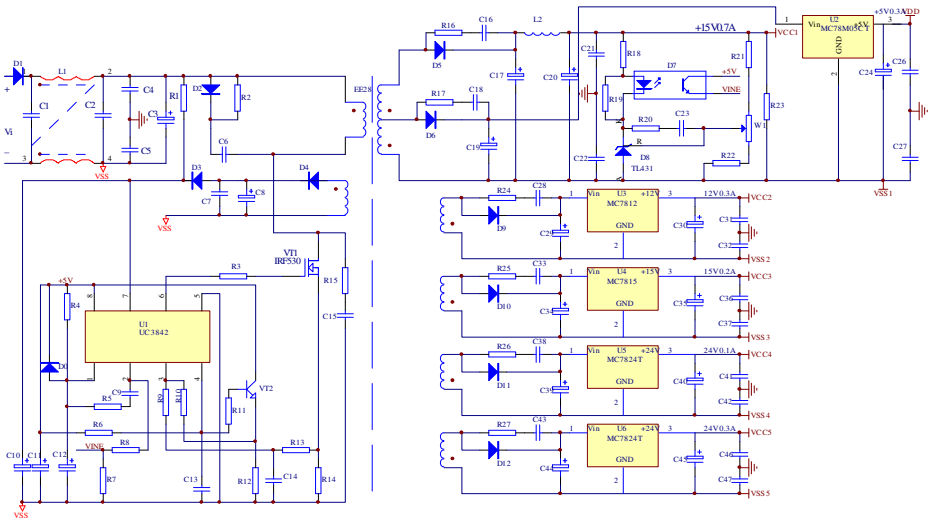


Fig. 2. Main circuit

3.2 Experimental Result Analysis

DC voltage supplied from R_1 to the UC3842⑦ feet, As voltage greater than 17V when the circuit starts, After the start, feedback winding through D_3 , D_4 , C_7 , C_8 to UC3842 power supply, R_7 , R_8 form the emitter of the optocoupler output signal to the introduction of high-speed amplifier② feet within the inverting input, and ultimately the formation of a negative feedback system, leaving the output power voltage stability. AS power output at rated power, the main circuit output voltage 15V, relatively smooth. Peak to peak ripple is about 140mv, machine efficiency of 90% ,short circuit over-current conditions can also give good protection chip,and achieve the design goals. Experimental output voltage waveform shown in Fig.3.

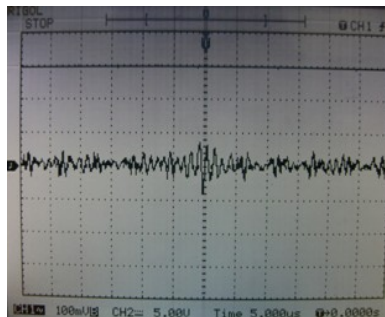


Fig. 3. Output voltage waveform

4 Conclusion

This paper introduces the design of auxiliary switch power supply stable work, output ripple small, transformer no fever phenomenon. The investment to the PV inverter power supply system, has the good work performance, and prove the correctness of design.

References

1. Zhang, Z., Cai, X.: Switching power supply schematic and design. Electronic Industry Press, Beijing (2004)
2. Zhou, Z., Zhou, J., Ji, A.: Switching power supply practical technology. Beijing: China Electric Power Press (January 2006)
3. Zhang, L.: Based on current control anti-flyback DC/DC converter. Nanjing University of Aeronautics and Astronautics (2001)
4. Ma, H., Sha, Z.: The switching power production and debugging. China Electric Power Press, Beijing (2010)
5. Yu, A.: On the harmonic suppression of switching power supply. Electrical Technology Magazine (7), 15–17 (2001)
6. Liu, S.: Practical high-frequency switching power supply technology. Mechanical Industry Press, Beijing (2006)
7. Ni, H., Yu, P.: Switching power supply circuit design and application-specific. China Electric Power Press, Beijing (2008)
8. Wang, Z., Huang, J.: Power Electronics Technology, 4th edn. Mechanical Industry Press, Beijing (2003)

Design of System for High-Frame Frequency Image Acquisition and Remote Transmission

Dingjin Huang, Tao Zhang, Honglu Hou, and Wenfang Zhang

Department of Photoelectric, Xi'an Technological University, Xi'an, 710032, China
zhys008@126.com

Abstract. The high-frame rate camera can capture, store and display the high-speed moving subject in real time, it can analyze the mechanism and the motion law of the high speed transient event by video playback. Therefore it has been widely used in the field of measurement of the high-speed moving subject. This article has proposed a parallel data bus FPGA image acquisition and transmission system which successfully solves the problem of a large amount of data quantity, fail to store and transport in real-time during the image acquisition process with high frame. The system's hardware composition and the working principle have been described; meanwhile, the image output structure and algorithm have been introduced in detail. Experimental results show that the system is reliable and absolutely fulfill the requirements of real-time performance.

Keywords: FPGA, SOPC, Image Acquisition, Long-distance Transmission, Image Storage.

1 Introduction

The appearance of the high-frame rate and large arrays image sensor has made it possible that researchers could detect the attitude and the trajectory of the fast moving subject especially the transient change of the specific progress. Meanwhile, it has provided a precondition of the more image information acquisition more deeply and refined analysis on it.

With the constant perfection and development of the CMOS image device, the digital camera has a large improvement both in the aspect of not only the frame frequency, frame rate and the resolution but the performance index of dynamic range and sensibility. However, the high frame rate and the high resolution require a high demand in the data bandwidth in image transport, data rate in image storage, disk space and the real-time performance in data transport. This essay is in the background of the high-speed industry on-line detection and proposes a high frame rate image processing system. The image processing system is an important part of the high frame rate camera and performs the pretreatment of the images collected by the COMS image sensor. The system will filter and decrease noise which will improve the quality of the video image. In addition, the system is able to realize storage and long-distance transport by compressing and coding the video information and reducing data quantity.

2 System General Design

Generally speaking, a complete image acquisition system consists of image acquisition, image pretreatment, image storage and image transport. It has not only to collect images but also display, store and transport in real-time which needs to format conversion and algorithm processing (such as image compressing) about the image signal, usually these need a large amount of operation. Secondly, for the high frame rate image acquisition system, the higher data huff and puff ability is needed which can satisfy the requirement of real-time performance. Hence, this essay utilized the EF2C8Q208 type FPGA of Altera company as the core processor unit. The block diagram of image acquisition and transport system based on FPGA is showed in Fig.1.

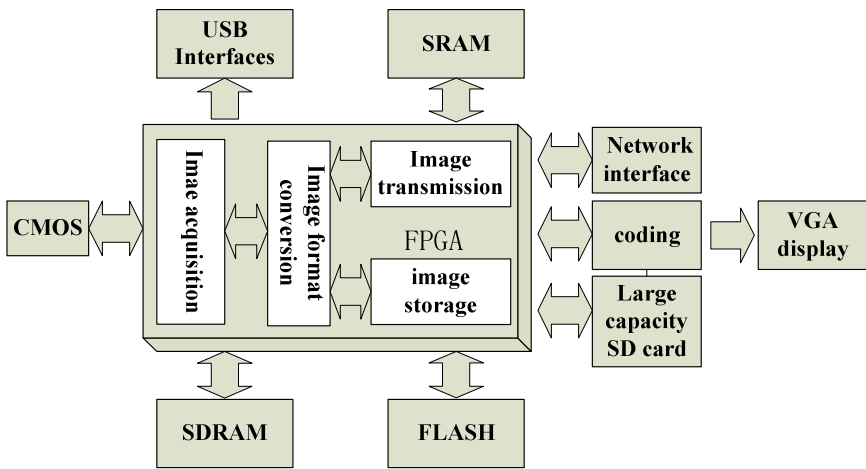


Fig. 1. Block diagram of image acquisition and transport system based on FPGA

The core processor unit FPGA adopted the IIC bus. With the configuration of the registers the unit could control the output of the image data in the mode of 10bit data bus. The M4K memory cell in the FPGA has constructed a FIFO buffer. The data is sent to SDRAM that of the external memory unit of the FPGA. Then smoke and code frame from the image data of SDRAM and sent the output data to VGA controller . In another way the data can be stored into the large capacity SD card by means of general serial bus or the RJ45 network interface through which the data can transport to the PC.

3 Hardware System Design

3.1 Design of Image Acquisition Model

The front end of CMOS image sensor adopted the MT9T031 from Micron, the maximum resolution is 2048*1536 with the maximum frame frequency of 93fps.

The advantage of the CMOS image sensor compared with the CCD image sensor is that the output is the digital signal which need not the analog-digital conversion step and can export the signal to the subsequent core processor unit directly. By the IIC bus, the FPGA can transfer the parameters to the registers in the CMOS image sensor and realize the driving function of the CMOS image sensor; on the basis of mentioned above, the parameter of the resolution of the CMOS sensor, the frequency of the output frame, the exposure time and the readout method of the image data can be obtained. It will gain a higher frame frequency output if the effective pixels or the sampling precision is reduced. The output image information can export to the FPGA image acquisition module. The block diagram of the MT9T031 image sensor is showed in Fig.2.

The inner FPGA image acquisition module introduced an asynchronous FIFO, the image data can be integrated to continuous video stream mode by the timing control. After putting the image data of each row into the buffer, it is convenient for the pipeline operation in the subsequent image pretreatment module and will accelerate the processing speed of the image data.

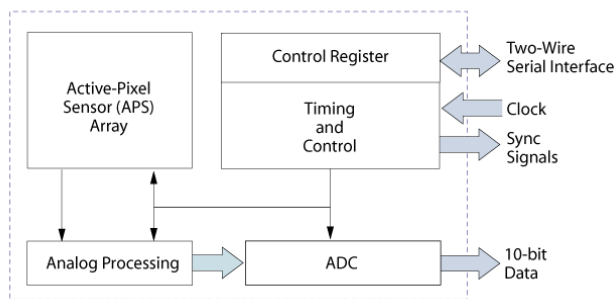


Fig. 2. Block diagram of the image sensor

3.2 Image Pretreatment System

Firstly, we perform the pretreatment process about the data collected by the data acquisition system. The median filtering algorithm in this paper will reduce the image noise. The parallel algorithm can improve the operating speed and realize the real-time treatment of the high frame image; the image after the pretreatment is sent to the latter image main processor module through the data transport system.

Under the control of the main-control module, the digital video signal with 8-bit will be converted to 16-bit counterpart by the serial-parallel module and store in the subsequent FIFO buffer module. Then, with the effect of the SDRAM control module, the data is stored into the two external SDRAM using the ping-pong memory mode. When one SDRAM is in the write operation the other one will readout the data to the main process module. Then the progress is repeated. The image data after treatment will be transmitted remote by the transport module and display on the VGA.

3.3 Image Storage and Display Module

The device that use for image storage is the exterior large capacity SD card which has a small volume and is easy to carry and change. The other advantage of the SD card is that it is convenient to operate and unease to lose data. The SD card supports three transmission modes: SPI mode(independent sequence input and output); one-bit SD mode(independent structure and data channel and unique transmission format); four-bit SD mode(use extra pins and pins reset; support four-bit wide parallel output). Low speed SD card support SPI and one-bit transmission mode with 400kb/s of the transfer rate of the SD card. High speed SD card supports four-bit wide mode and the transfer rate is 100Mb/s. Aiming at the limitation of the transfer rate that from the high frame rate image sensor, this essay adopted the four-bit SD transfer mode.

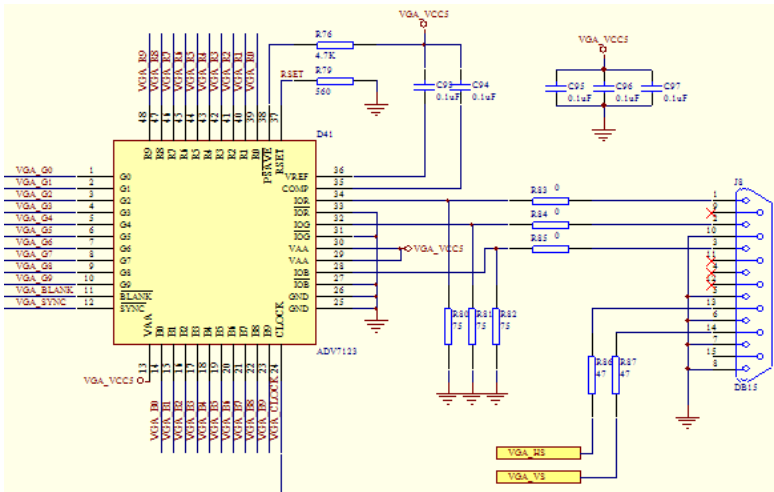


Fig. 3. Connection mode of the VGA controller

The image display module adopted the ADV7123 video D/A converter. ADV7123 is the video signal conversion chip of the ADI Company and supports the maximum 1600*1200 pixel resolution at the refresh frequency of 100MHZ. ADV7123 contains three 10-bit video D/A converters with the maximum rate 240MS/s and the clock frequency of 50MHZ while the minimum power of 30 mW.

ADV7123 consists of three complete 10-bit high-speed D/A converters. Fig.3. shows the VGA controller connection mode. The RGB video data is divided into R0-R9, G0-G9, B0-B9 and the data is latched to the data register at the rising edge of the CLOCK, then converted into the analog signal employing the high-speed D/A converter. The three independent video D/A converters are current-type output with the 75Ω grounding resistance at output terminal. Active low BLANK signal is the compound blanking signal. As BLANK is at low level, the analog video outputs the blanking signal and all the data are neglected at this time; likewise, as the compound synchronous signal is low, the current source is closed and the output signal is low. Fig.4. shows the timing analysis diagram of the VGA with the help of the SignalTapII logic analyzer.

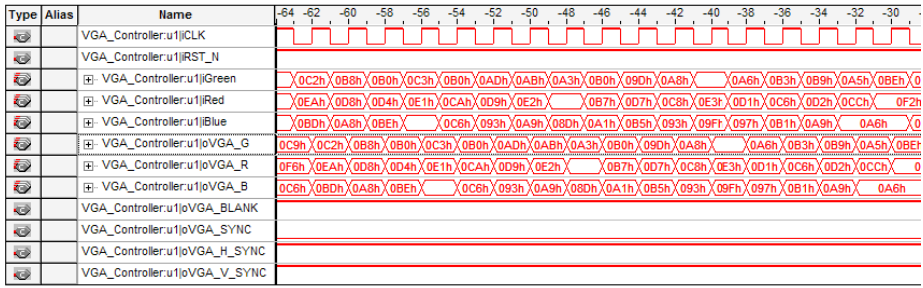
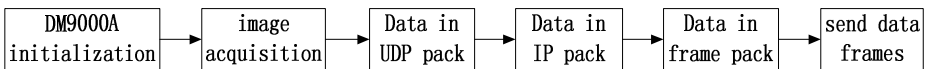


Fig. 4. Timing analysis char of the VGA display

3.4 Image Transmission Module

The pretreatment of images will be packed and then transported to the distal end by the network interface. This will realize the communication between the PC and the camera which is so called the “nervous system” of the camera. The network transmission system consists of ethernet media access layer(MAC) and physical layer(PHY), including package/resolution and transceiver of the MAC data frames, address recognition, CRC coding checkout, MLT-3 encoder, restrain the received noise, output pulse forming, retransmit-overtime, link integrity testing, signal polarity detection and correction etc. The image transport module carries out the function by the configuration of the DM9000A network controller. Firstly, when the system power is on, FPGA will allocate the network control register(NCR) and the interrupt register(ISR) in the DM9000A, then the initialization is finished. Secondly, the data transceiver is at waiting state. NIOS II will convert the image data into MAC frame format by the MAC module when the image transport module begins to receive the image data, the data will be packaged in UDP, IP and frames and then sent into the data buffer in the DM9000A by the 16-bit bus. The information such as the data length will fill the corresponding registers to ensure it is enable to be sent and transported through the RJ45 interface. At the receiving terminal, in order to distinguish the beginning of each image correctly, the 4-byte packet first is sent before 1-frame data is sent by the main program. The software diagram is showed in Table.1.

Table 1. Software diagram of image transport



The system components are shown in Fig.5. The configuration includes Nios II soft core, system timer, Avalon bus, DDM9000A interface and SDRAM controller, etc. Since the tools model do not include DM9000A interface, it requires compiling independently. The external extension SDRAM which connects to the SDRAM controller is used to store the program and data; FPGA connects to Ethernet by the Ethernet controller DM9000A and RJ45 connector; FPGA connects to the computer

by the JTAG which is an downloading debug interface used for download the hardware configuration, software program, and the display of the debug information, etc.

Use	Connect...	Module Name	Description	Clock	Base	End	Tags	IRQ
<input checked="" type="checkbox"/>		cpu_0	Nios II Processor	clk				
		instruction_master	Avalon Memory Mapped Master					
		data_master	Avalon Memory Mapped Master					
		jtag_debug_module	Avalon Memory Mapped Slave					
<input checked="" type="checkbox"/>		jtag_uart_0	JTAG UART					
		avaion_jtag_slave	Avalon Memory Mapped Slave	clk	0x01004000	0x01004007		
<input checked="" type="checkbox"/>		sdram_0	SDRAM Controller					
		s1	Avalon Memory Mapped Slave	clk	0x00000000	0x007fffff		
<input checked="" type="checkbox"/>		tri_state_bridge_0	Avalon-MM Tristate Bridge					
		avalon_slave	Avalon Memory Mapped Slave	clk				
		tristate_master	Avalon Memory Mapped Tristate Master					
<input checked="" type="checkbox"/>		cfi_flash_0	Flash Memory Interface (CFI)					
		s1	Avalon Memory Mapped Tristate Slave	clk	0x00800000	0x008fffff		
<input checked="" type="checkbox"/>		timer_0	Interval Timer					
		s1	Avalon Memory Mapped Slave	clk	0x00900000	0x0090001f		
<input checked="" type="checkbox"/>		sysid	System ID Peripheral					
		control_slave	Avalon Memory Mapped Slave	clk	0x00900020	0x00900027		
<input checked="" type="checkbox"/>		uart_0	UART (RS-232 Serial Port)					
		s1	Avalon Memory Mapped Slave	clk	0x00900040	0x0090005f		
<input checked="" type="checkbox"/>		timer_1	Interval Timer					
		s1	Avalon Memory Mapped Slave	clk	0x00900060	0x0090007f		
<input checked="" type="checkbox"/>		DM9000A	DM9000A					
		avalonS	Avalon Memory Mapped Slave	clk	0x00900090	0x00900097		

Fig. 5. Component information of image transport system

4 System Software Design

4.1 The Communication Protocol

The maximum length of Ethernet frame is 1518 bytes and the minimum is 64 bytes. The maximum length of data is 1500 bytes and the minimum is 46 bytes. Before every transmission of UDP data, an 8-byte-header of UDP must be added in order to constitute a UDP packet; then, a 20-byte-header of IP is added to constitute an IP packet; finally, a 14-byte-header of MAC is added to constitute an Ethernet frame. This is the so-called “encapsulation of packet”. In order to avoid the trouble of segment, the maximum length of UDP data is 1500-28=1472 bytes. In the practical application, we transmit data by encapsulating each line of image data into a packet. The communication protocol is as shown in Table.2.

Table 2. Image communication protocol

MAC address 6bytes	The type of MAC 6bytes	Type or length 2bytes	IP message head	UDP message head	UDP data	verify
Ethernet frame data (46-1500bytes)						4bytes

5 System Test and Analysis

According to CMOS image sensor settings of the different parameters, this system can be divided into several different modes in order to satisfy the detection

requirements on the online industry in the condition of high speed motion detection or to tiny objects. In the full resolution conditions as shown in Fig.6, the maximum output frame frequency is 15 FPS. This picture shows the detection of the solar panels surface texture defects on-line. Table.3 shows the measuring parameters of this detection. In full frame frequency for measuring whereabouts table tennis in Fig.7 show.

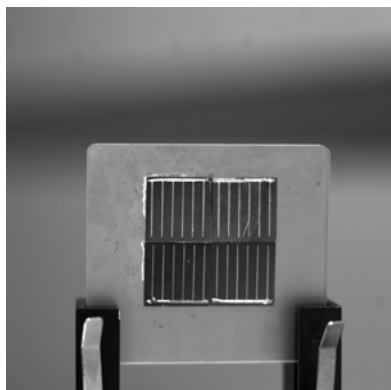


Fig. 6. Solar panels surface texture defects detection

Table 3. Measuring parameters of solar panels surface texture defects detection

Image capture average value	14.93fps
Display frame average value	14.80fps
resolution	2048*1536
Image depth	8bit
Exposure time	66830us

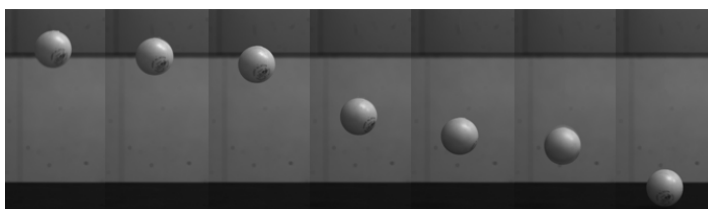


Fig. 7. High frame frequency mode whereabouts of the table tennis measurement

6 Conclusions

The proposed system is a combination of software technology, communication technology, embeded auto control technology and image acquisition technology. This system can meet the industry high speed online testing requirments through the online image acquisition and transmission technology. Currently, the proposed system works in good condition, and can meet the common manufacture requirements.

References

1. Thanassis, M., Peter, M.: High Frame Rate Imaging Using Parallel Transmission of Focused Coded Fields. In: IEEE Ultrasonics Symposium, vol.2, pp. 1417–1420 (2004)

2. Masanori, H., Kensaku, Y., Michitaka, K.: FPGA Implementation of A Vehicle Detection Algorithm Using Three-dimensional Information. In: IPDPS 2008 - 22nd IEEE International Parallel and Distributed Processing Symposium, April 14-18 (2008)
3. Cambier, J.L., Nelson, M.R., Brown, S.I., Goldbaum, M.H., Rehkopf, P.G., Warnicki, J.L.: Image Acquisition and Storage for Ophthalmic Fluorescein Angiography. In: IEEE Computer Society International Symposium on Medical Images and Icons, ISMII 1984, pp. 224–231. IEEE (1984)
4. Oike, Y., Ikeda, M., Asada, K.: A CMOS Image Sensor for High-Speed Active Range Finding Using Column-Parallel Time-Domain ADC and Position Encoder. *IEEE Transactions on Electron Device* 50(1), 152–157 (2003)
5. Tripti, J., Prashant, B., Singh Kushwah, C.B., Mayenk, M.: Reconfigurable hardware for median filtering for image processing applications. In: 3rd International Conference on Emerging Trends in Engineering and Technology, ICETET 2010, pp. 172–175 (2010)
6. Cui, Z., Wang, H., Chen, Z., Xu, Y., Yang, W.: A high-performance digital system for electrical capacitance tomography. *Measurement Science and Technology* 22(5) (May 2011)
7. Yogindra, A., Sajish, C., Subrahmanya, C.R.: Design of a FPGA based data acquisition system for radio astronomy applications. In: The International Conference on Microelectronics, ICM, pp. 555–557 (2004)
8. Fan, H., Yang, F., Liao, Q.: Frame frequency multiplier system for stereo video on programmable hardware. In: 1st International Symposium on Computer Network and Multimedia Technology, CNMT 2009 (2009)
9. Qiu, W., Yu, Y., Sun, L.: A programmable, cost-effective, real-time high frequency ultrasound imaging board based on high-speed FPGA. In: 2010 IEEE International Ultrasonics Symposium, IUS 2010, pp. 1976–1979 (2010)
10. Si, X.: The design of FPGA real-time image acquisition system based on SDRAM. *Journal of Southwest University (Natural Science Edition)* 33(01), 128–132 (2011)
11. Yiming, S., Juan, L., Chunmao, L.: Design of SDRAM Controller Based on FPGA. *Electronic Engineer.* 29(09), 10–13 (2003)

Modeling Method for Centralized Control of Load-Tap-Changing Transforms Based on Neural Networks

Yu Sun

College of Information, Guangdong Ocean University

Abstract. The paper presents a modeling method of neural network based centralized control scheme for load tap-changing transformers. To implement the coordinated tap adjustment, the developed scheme employs successive linearization techniques to evaluate the interactions among different transformers represented by a sensitivity matrix. Through updating the matrix using neural network methods, only the local information associated with the participating transformers is desired to perform the centralized tap control. The developed scheme has been verified to be superior to conventional decentralized methods in terms of avoiding unnecessary dynamics and enhancing voltage stability of power systems.

Keywords: Modeling Method, Load-Tap-Changing, Neural Networks.

1 Introduction

Electrical utilities have been compelled in recent years to provide maximum possible power through expanding interconnection of bulk systems. Secure operation of power systems, therefore, has been becoming a much more important subject than ever before. Among these, the control of loadtap-changing (LTC) transformers was given particular attention due to their extensive applications in improving local or global voltage profiles of power utilities. It is known that tap changes, under certain abnormal operating conditions, may speed up "draining" of system reactive power, cause reverse actions, and result in voltage collapse [1-4].

Tap changing control is usually performed in a decentralized manner, i.e. independently, and only at the locations where voltage violations are present. The methodology neglects the system-wide effect of individual tap changing. It may yield oscillations and/or non-convergence problems due to lack of coordination. The potential of systemwide coordinated LTC control has been investigated in recent years. References [5,6] proposed the concept of centralized tap-changing. As a more sophisticated method, during the voltage regulation, the centralized tap control coordinates all participating LTC transformers. Under the control, certain linear combination of the participating LTC node voltages is used to determine the desired action for each tap changer. It was believed that such a sophisticated voltage control can improve dynamic voltage profiles and moderate undesirable reactive power fluctuations. Although a system-wide centralized LTC control can achieve better performance in voltage regulation, it may be infeasible to implement on existing power systems. The applied control relies on the performance of SCADA

(supervisory control and data acquisition) systems with respect to sufficient speed and reliability of system-wide communications. While a global centralized LTC control for a large-scale power system may be impractical or very costly, the coordinated tap changing in a tightly coupled subsystem is feasible and desirable.

2 Dynamics due to Tap Changing

The necessity of centralized tap control has been highlighted. To perform such control, the sensitivity matrix relating the controlled voltages to the tap positions is a prerequisite. For an N-bus power system, it is assumed that the n participating LTC transformers ($a_1 \sim a_n$) connected to Buses 1~n' ($n' > n$) are used to control the load voltages of Buses 1~n. For the N-bus power system, the reactive power flow equations are expressed as:

$$Q_i(V, a) = 0, \quad i = 1, 2, \dots, N \tag{1a}$$

or in vector form

$$Q(V, a) = 0 \tag{1b}$$

Where $Q = [Q_1, Q_2, \dots, Q_N]^T$ represents the reactive power mismatch equations, $V = [V_1, V_2, \dots, V_N]^T$ is the vector of the load voltages, and

$a = [a_1, a_2, \dots, a_N]^T$ is the vector of the tap positions. Linearizing (1b) around a static equilibrium we have:

$$\frac{\partial Q}{\partial V} \Delta V + \frac{\partial Q}{\partial a} \Delta a = 0 \tag{2a}$$

Separating the n' tap change connected buses from the others (2a) becomes:

$$\begin{bmatrix} \frac{\partial Q_{n'}}{\partial V_{n'}} & \frac{\partial Q_{n'}}{\partial V_{N-n'}} \\ \frac{\partial Q_{N-n'}}{\partial V_{n'}} & \frac{\partial Q_{N-n'}}{\partial V_{N-n'}} \end{bmatrix} \begin{bmatrix} \Delta V_{n'} \\ \Delta V_{N-n'} \end{bmatrix} + \begin{bmatrix} \frac{\partial Q_{n'}}{\partial a} \\ \frac{\partial Q_{N-n'}}{\partial a} \end{bmatrix} \Delta a = 0 \tag{2b}$$

Where

$Q_{n'} = [Q_1, Q_2, \dots, Q_{n'}]^T$, $Q_{N-n'} = [Q_{n'+1}, Q_{n'+2}, \dots, Q_N]^T$, $V_{n'} = [V_1, V_2, \dots, V_{n'}]^T$, $V_{N-n'} = [V_{n'+1}, V_{n'+2}, \dots, V_N]^T$, ($\Delta V_{n'}$ and $\Delta V_{N-n'}$ have the similar definitions). From (2b) we have

$$\frac{\partial Q_{n'}}{\partial V_{n'}} \Delta V_{n'} + \frac{\partial Q_{n'}}{\partial V_{N-n'}} \Delta V_{N-n'} + \frac{\partial Q_{n'}}{\partial a} \Delta a = 0 \tag{3a}$$

$$\frac{\partial Q_{N-n'}}{\partial V_{n'}} \Delta V_{n'} + \frac{\partial Q_{N-n'}}{\partial V_{N-n'}} \Delta V_{N-n'} = 0 \tag{3b}$$

Equation (3b) is obtained by noting $\partial \mathbf{Q}_{N-n'} / \partial \mathbf{a} = \mathbf{0}$ (with $\mathbf{0}$ as a zero vector, since all these nodes are not connected to the LTC transformers). It follows, under the assumption that $\partial \mathbf{Q}_{N-n'} / \partial \mathbf{V}_{N-n'}$ is non-singular that

$$\Delta \mathbf{V}_{N-n'} = -(\frac{\partial \mathbf{Q}_{N-n'}}{\partial \mathbf{V}_{N-n'}})^{-1} \frac{\partial \mathbf{Q}_{N-n'}}{\partial \mathbf{V}_{n'}} \Delta \mathbf{V}_{n'} \tag{4}$$

By substituting $\Delta \mathbf{V}_{N-n'}$ with (4), (3a) becomes:

$$[\frac{\partial \mathbf{Q}_{n'}}{\partial \mathbf{V}_{N-n'}} (\frac{\partial \mathbf{Q}_{N-n'}}{\partial \mathbf{V}_{N-n'}})^{-1} \frac{\partial \mathbf{Q}_{N-n'}}{\partial \mathbf{V}_{n'}} - \frac{\partial \mathbf{Q}_{n'}}{\partial \mathbf{V}_{n'}}] \Delta \mathbf{V}_{n'} = \frac{\partial \mathbf{Q}_{n'}}{\partial \mathbf{a}} \Delta \mathbf{a} \tag{5}$$

Thus we have

$$\Delta \mathbf{V}_{n'} = [\frac{\partial \mathbf{Q}_{n'}}{\partial \mathbf{V}_{N-n'}} (\frac{\partial \mathbf{Q}_{N-n'}}{\partial \mathbf{V}_{N-n'}})^{-1} \frac{\partial \mathbf{Q}_{N-n'}}{\partial \mathbf{V}_{n'}} - \frac{\partial \mathbf{Q}_{n'}}{\partial \mathbf{V}_{n'}}]^{-1} \frac{\partial \mathbf{Q}_{n'}}{\partial \mathbf{a}} \Delta \mathbf{a} \tag{6}$$

provided that $[\frac{\partial \mathbf{Q}_{n'}}{\partial \mathbf{V}_{N-n'}} (\frac{\partial \mathbf{Q}_{N-n'}}{\partial \mathbf{V}_{N-n'}})^{-1} \frac{\partial \mathbf{Q}_{N-n'}}{\partial \mathbf{V}_{n'}} - \frac{\partial \mathbf{Q}_{n'}}{\partial \mathbf{V}_{n'}}]^{-1}$

is also non-singular. Let

$$\mathbf{S}' = [\frac{\partial \mathbf{Q}_{n'}}{\partial \mathbf{V}_{N-n'}} (\frac{\partial \mathbf{Q}_{N-n'}}{\partial \mathbf{V}_{N-n'}})^{-1} \frac{\partial \mathbf{Q}_{N-n'}}{\partial \mathbf{V}_{n'}} - \frac{\partial \mathbf{Q}_{n'}}{\partial \mathbf{V}_{n'}}]^{-1} \frac{\partial \mathbf{Q}_{n'}}{\partial \mathbf{a}} \tag{7}$$

we obtain

$$\Delta \mathbf{V}_{n'} = \mathbf{S}' \Delta \mathbf{a} \tag{8}$$

Where \mathbf{S}' is an $n' \times n'$ matrix. Because only the voltages at the controlled busbars (buses 1~n)

$\mathbf{V}_n = [V_1, V_2, \dots, V_n]^T$ are concerned, the first n rows of (8) are thus extracted to describe the system dynamics after tap changing:

$$\Delta \mathbf{V}_n = \mathbf{S} \Delta \mathbf{a} \tag{9}$$

where \mathbf{S} , consisting of the first n rows of \mathbf{S}' , is an $n \times n'$ square matrix. Equation (9) evaluates the steady-state voltages at the n LTC nodes after each tap changing. Before subsequent tap changes, the bus voltages have been assumed to settle in a static equilibrium. After the k^{th} tap changing, the controlled voltages are described by the difference equation obtained from (9):

$$\mathbf{V}_n(k+1) = \mathbf{V}_n(k) + \mathbf{S}(k)[\mathbf{a}(k+1) - \mathbf{a}(k)] \tag{10}$$

Where $[\mathbf{V}_n(k), \mathbf{a}(k)]$ and $[\mathbf{V}_n(k+1), \mathbf{a}(k+1)]$ represent, respectively, the initial and the final operating point (steady state) at the k^{th} cycle of the tap changes, and $\mathbf{S}(k)$ is the current sensitivity matrix.

3 Tap Changing Control Algorithms

In this section, control algorithms of the centralized and decentralized control schemes are formulated.

3.1 Decentralized Control

Under the decentralized control law, the voltage control for each LTC node is performed independently. Whenever the voltage of the controlled bus swings out of the specified range, the tap position adjustment is initiated automatically to correct the deviation. The control law can be expressed by the following discrete logic [2,5,6]:

$$a_i(k+1) = a_i(k) + \lambda_i f_D(V_i(k) - V_i^{fin}) \quad i = 1, 2, \dots, n \tag{11a}$$

$$f_D(V(k)_i - V_i^{fin}) = \begin{cases} -1, & V(k)_i - V_i^{fin} > \delta V_i \\ 0, & |V(k)_i - V_i^{fin}| \leq \delta V_i \\ 1, & V(k)_i - V_i^{fin} < -\delta V_i \end{cases} \tag{11b}$$

Where $a_i(k)$ is the tap position of the LTC transformer controlling the i^{th} bus (at the k^{th} cycle), λ_i is the step size of the tap-change, δV_i is the threshold effecting the control action, and V_i^{fin} is the specified voltage. Each tap change is performed independently, by assuming that the control to V_i from a_i is dominant, whilst the influences from all other tap changers ($\{a_j\}_{j \neq i}$) are trivial.

Since the above control law does not consider the interaction among different LTC transformers, a rigorous condition is desired to ensure the convergence of the load voltages. It is seen from (9) that the S is actually a sensitivity matrix. The entries of S can be viewed as $S_{ij} = (\frac{\partial V_i}{\partial a_j})$, $i, j = 1, 2, \dots, n$, reflecting the sensitivity of the i^{th} bus voltage to the tap ratio of the j^{th} LTC transformer. After tap changes, improvement of each controlled voltage is given by:

$$\Delta V_i = \sum_{j=1}^n S_{ij} \Delta a_j \tag{12}$$

For bus- i , the voltage variation, due to the tap change of the correspondent LTC transformer (a_i), is $S_{ii} \Delta a_i$, while the variation due to the interaction from all other transformers is $\sum_{j=1, j \neq i}^n S_{ij} \Delta a_j$. The element S_{ij} determines the effect of each control or interaction. It can be easily proved that the sensitivity matrix S , for stable operation, should be diagonally dominant with all diagonal entries positive [5]. If the condition is not satisfied, it could be impossible to maintain the controlled voltages within the limits. Such nonconvergence of the LTC control has been recognised as one of the main causes leading to voltage collapse.

3.2 Coordination of Tap Changes

The potential voltage problems due to the lack of coordination of the decentralized control can be improved by taking into account interaction among different tap changes during

voltage regulation. In (10), let $\mathbf{V}_n(k+1) = \mathbf{V}_n^{fin}$, ($\mathbf{V}_n^{fin} = [V_1^{fin}, V_2^{fin}, \dots, V_n^{fin}]^T$), the correspondingly desired tap changes can be estimated by

$$\Delta \mathbf{a}(k+1) = \mathbf{a}(k+1) - \mathbf{a}(k) = \mathbf{S}^{-1}(k)(\mathbf{V}_n^{fin} - \mathbf{V}_n(k)) \tag{13}$$

where \mathbf{S} is assumed non-singular. Instead of being driven by single voltage error $V_i^{fin} - V_i(k)$, the performed tap change for each LTC is now determined by a linear combination of the voltage errors involved with all regulated buses:

$$a_i(k) = \sum_{j=1}^n S_{ij}^{-1}(k)[V_n^{fin} - V_n(k)] \tag{14}$$

Where $S_{ij}^{-1}(k)$ is the $(i,j)^{th}$ entry of $\mathbf{S}^{-1}(k)$, determining the weight of each bus in the combination. The control governed by (14) is based on the linearization around the current operating point of the power system. Thus the accuracy of the control can only be ensured in a small range around the equilibrium. Besides, the tap change is usually performed in a fixed small step. Consequently, the actual control is further modified into the following set of equations:

$$\Delta a_i(k+1) = f_c[U_i(k)] \quad i = 1, 2, \dots, n \tag{15a}$$

Where: $U_i(k) = \sum_{j=1}^n S_{ij}^{-1}(k)[V_n^{fin} - V_n(k)]$ and the function $f_c(\cdot)$ is

Defined as:

$$f_c(U_i) = \begin{cases} \lambda_i U_i, & |U_i| > \lambda_i \\ 0, & |U_i| \leq \lambda_i \end{cases} \tag{15b}$$

The control embodied in (15a) and (15b) represents a series of discrete tap changes. Whenever the desired tap change for any node is larger than the step size λ_i , one step adjustment is performed. Otherwise the tap will remain unchanged.

By de-coupling the voltage errors involved all participating LTC transformers, the control to each individual tap changer is totally determined by each U_i , $i = 1, 2, \dots, n$, as shown in (15a) and (15b). The control keeps aiming at the target voltages by letting

$\mathbf{V}_n(k+1) = \mathbf{V}_n^{fin}$ at each operating cycle and takes into account the interaction

among different LTC transformers, reflected by the entries of \mathbf{S}^{-1} . Obviously, the centralized control can prevent voltage instabilities caused by lack of coordination of tap changes.

3.3 Successive Linearization Using Neural Network

One key link of the proposed centralized control is the transform $\mathbf{S}^{-1}(k)$. Should the matrix $\mathbf{S}(k)$ (\mathbf{S}^{-1}) be assumed constant, the control would be implemented easily. Under this assumption, only the voltages of the participating LTC nodes are needed in performing such control. However it is questionable to treat \mathbf{S} as a constant matrix in a

wide range of (V, a). To avoid the inaccuracy brought about by the linearization, therefore, the sensitivity matrix should be updated to modify the control issued by (14) at every step throughout the discrete evolution of the voltages and the tap changes. However, in doing this, the system communication facilities may arise to be a problem as aforementioned. For trade-off between the control quality and the cost, the neural network based centralized LTC control scheme is proposed. After each cycle of tap controls, the sensitivity matrix (the weight matrix of the neural network) is updated with the prediction errors.

As shown in (9), the improvement of the controlled voltages due to the tap changes is $\Delta V_n = S\Delta a$. At the beginning of voltage regulation, the sensitivity matrix can be initialized with the nominal operating point of the power system. To update the S at each subsequent tap changing cycle, a neural network is constructed to predict the voltage improvements as illustrated by Fig 1. After each tap-changing cycle, the prediction is compared with the actual voltage variations and the errors are then employed to modify the neural weights using the back propagation method. The learning is governed by the delta rule modified by introducing a momentum term:

$$\Delta S_{ij}(k+1) = \alpha \Delta S_{ij}(k) + \eta e_j \Delta a_j \tag{16}$$

Where $\Delta S_{ij}(k)$ is the change of the weight S_{ij} representing the connection strength between a_j and V_i , α is the momentum constant, η is the learning rate, and e_j is the prediction error of ΔV_i . The modified S (S^{-1}) will then be used in the next step of tap control. In this way, only the local information involved with the controlled voltages is desired to perform the tap adjustment. It is known from (16) that linear neurons are adopted in the networks. The momentum term $\alpha \Delta S_{ij}(k)$ is included to increase the learning rate and yet to avoid the danger of instability and prevent being stuck at shallow local minima.

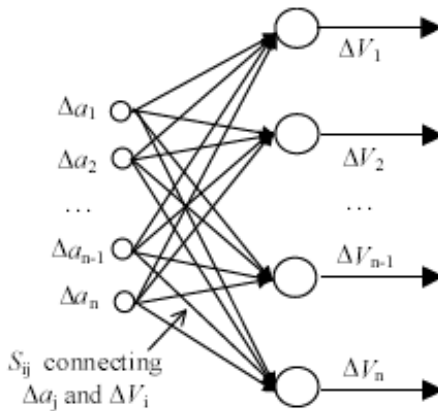


Fig. 1. The neural network used for sensitivity evaluation

3.4 Implementation of Tap Controls

Under the decentralized control law, the tap changing is carried out independently governed by 11(a) and 11(b). By comparing the measured voltage with the target value at each LTC node, the tap change will be activated automatically should a voltage error exceeding the dead-band be detected. The control does not take into account inter-LTC transformer dynamics and thus no system-wide communication is required. On the contrary, the centralized control scheme performs tap changing for all participating transformers simultaneously. As governed by 15(a) and 15(b), the control to each tap changer is now determined by all the participating LTC nodes through their voltage errors and relative sensitivities. The centralized control scheme is illustrated in Fig. 2, where the delay unit is introduced to let the power system settle down before each subsequent tap changing. It is seen that the prediction using the sensitivity matrix is compared with the actual controlled voltages and the errors are then utilized to modify the neural weights, i.e. the sensitivity matrix.

4 Stability Analysis of Centralized Control

The sufficient condition for convergence of decentralized tap changing is very strict due to the lack of coordination of the control method (Section 3.A). On the contrary, the condition for a stable centralized control is much more relaxed as shown by the following analysis. Subtracting \mathbf{V}^{fin} from both sides of (10) and substituting $\Delta a_i = a_i(k+1) - a_i(k)$ with (15a)

we have:

$$V_i(k+1) - V_i^{fin} = V_i(k) - V_i^{fin} + \sum_{j=1}^n S_{ij} f_C(U_j), \quad i=1,2,\dots,n \tag{17}$$

According to the definitions of $f_C(\cdot)$ and U_i , (17) can be rewritten as

$$V_i(k+1) - V_i^{fin} = (1 - \alpha_i)(V_i(k) - V_i^{fin}) \tag{18}$$

Equation (18) shows that the proposed LTC control results in a decreasing sequence $|V_i(k) - V_i^{fin}|$, $i = 1,2,\dots,n$, ensuring the convergence of the controlled voltages, and preventing the reverse action. Due to the dead band of the LTC control, the voltages could not converge exactly at the target. The errors at the end of the tap changing indicated by $|U_i| \leq \lambda_i$, $i = 1,2,\dots,n$ [Equation (15b)] can be estimated with (14):

$$|V_j(k) - V_j^{fin}| \leq |\mathbf{V}(k) - \mathbf{V}^{fin}| = |\mathbf{S}||\mathbf{U}| \leq |\mathbf{S}| \sqrt{\sum_{i=1}^n \lambda_i^2} \tag{19}$$

which could be of arbitrary accuracy if the step size of each LTC transformer is sufficiently small

In the deduction of the control law we have assumed nonsingular of $\frac{\partial \mathbf{Q}_{N-n'}}{\partial \mathbf{V}_{N-n'}}$ and $[\frac{\partial \mathbf{Q}_{n'}}{\partial \mathbf{V}_{N-n'}} (\frac{\partial \mathbf{Q}_{N-n'}}{\partial \mathbf{V}_{N-n'}})^{-1} \frac{\partial \mathbf{Q}_{N-n'}}{\partial \mathbf{V}_{n'}} - \frac{\partial \mathbf{Q}_{n'}}{\partial \mathbf{V}_{n'}}]^{-1}$. Since the S is directly calculated from these matrixes these two requirements are finally reflected by the non-singular of the matrix S. As aforementioned, the entries of the S represent the sensitivity of the control voltages to the tap positions. With a nonsingular S ($|\mathbf{S}| \neq 0$), the transform $\mathbf{U}(k) = \mathbf{S}^{-1}(k)(\mathbf{V}_n^{log} - \mathbf{V}_n(k))$ can be performed, and the load voltages are controllable by the proposed centralized control. It is known that $|\mathbf{S}| \neq 0$ is a much more relaxed condition compared with that of the decentralized control. When the operating point is close to the limit of the power system, the effect of the tap change in controlling the load voltages will degrade notably. With the draining out of the reactive reserve, the determinant of the S will drop to zero. Then an arbitrary small voltage improvement may require infinite tap changes, and the load voltages are uncontrollable by means of tap changing. For the sake of the operation security, certain reactive reverse is always desired. In the proposed LTC control system, the determinant of the S can be used as the voltage stability index during the tap changing. Whenever $|\mathbf{S}|$ is detected smaller than a preset value, the tap change should be prohibited to avoid untangle tap changes. Since the matrix S is available in the deduction of the centralized LTC control the estimation of the voltage stability does not increase the cost of the control scheme.

5 Conclusion

By using the neural network based successive linearizations techniques, a centralized LTC control scheme is developed. Working towards pre-specified target voltages, the desired control to all the tie and load transformers are derived with linearized loadflow equations by using the local information involved with the participating LTC nodes only. To show performance enhancements over conventional methods, in terms of suppression of unnecessary dynamics, algorithm flexibility and prevention of voltage collapse, the designed control scheme has been simulated.

References

1. Hong, Y.Y., Wang, H.Y.: Investigation of the Voltage Stability Region Involving on-Load Tap Changers. *Electric Power system Research* 32, 45–54 (2005)
2. Liu, C.C., Vu, K.: Analysis of Tap-Changer Dynamics and Construction of Voltage Stability Regions. *IEEE Trans. CAS* 36(4), 575–590 (2007)
3. Ohtsuki, H., Yokoyama, A., Sekine, Y.: Reverse Action of On-load Tap Changer in Association with Voltage Collapse. *IEEE Trans. Power System* 6(1), 300–306 (2003)
4. Lee, B.H., Lee, K.Y.: A study on Voltage Collapse Mechanism in Electric Power System. *IEEE Trans. Power System* 6(3), 966–974 (2008)

5. Medanic, J., Ilic-Spong, M., Christensen, J.: Discrete Models of Slow Voltage Dynamics for Under Load Tap- Changing Transformer Coordination. *IEEE Trans. Power System*, PWRS- 2(4), 873–882 (1997)
6. Lim, K.K.: Decentralized Control of Under Load-Tap Changer in Power Systems. In: *International Power Engineering Conference*, Singapore, pp. 31–36 (2003)
7. Llic, M.: New Approaches to Voltage Monitoring and Control. *IEEE Control System Magazine*, 5–11 (2007)
8. Pai, M.A.: *Computer Techniques in Power System Analysis*. Tata McGraw-Hill Publishing Company Limited (2007)
9. Yorino, N., Danyoshi, M., Kitagnwa, M.: Interaction among Multiple Controls in Tap Changing Load Transformers. *IEEE Trans. Power Systems* 12(1) (2008)
10. Chang, C.S., Huang, J.S.: Centralized Control of Transformer Tap Changing for Voltage Stability Enhancement. *Electric Machines and Power Systems* 27(10)

A New Video Feature Extraction Method Based on Local Class Information Preserving

Yongliang Xiao¹, Shaoping Zhu¹, Weizhong Luo¹, Xiangbao Li¹, Wenbin Liu¹,
and Gelan Yang²

¹ Hunan University of Finance and Economic, Changsha, Hunan, China

² Hunan City University, Changsha, Hunan, China
xylroc@gmail.com

Abstract. Video feature extraction is the first step of video shot boundary detection. In this paper, a more useful and discriminating video feature extraction method based on local class information preserving is proposed. Maximum margin criterion is a very famous feature extraction method, which seeks to preserve global structure of samples, and can resolve small sample size problem. But this method ignores the local structure information of samples. To address the issue, we develop a new method namely local class information preserving (LCIP). We redefine the local between-class scatter matrix and within-class scatter matrix with the local structure information of each sample. Experimental results show the effectiveness of the proposed method.

Keywords: Shot boundary detection, local structure information, class information preserving.

1 Introduction

Extracting more useful and discriminating video feature from the original video feature is very important to improve the precision of shot boundary detection. People often extract color, motion, edge or texture feature of video to detect video shot boundary [1-3]. However, only using single feature may make the detection accuracy decreasing. Such as flash make brightness changed, which results to shot boundary misjudgment. Thus, we often combine different and more complex visual feature to avoid such problems [4]. But these methods will make high dimension data, which make “cures of dimensionality”.

To obtain more useful and discriminating video feature, people have proposed many methods to reduce the dimensionality of high dimensional data. Linear discriminant analysis (LDA) [5] is one of the most famous linear dimensionality reduction methods. A major drawback of LDA is small sample size problem. In order to resolve this problem, maximum margin criterion (MMC) [6] is proposed. But this method ignores the local structure information of samples, which is very important for new samples.

In this paper, we propose local class information preserving (LCIP) method to extract more useful and discriminating video feature from the original video feature. In this method, we redefine the between-class scatter and within-class scatter with

neighborhood relationship and class label information of each sample. The experimental results show that the proposed method is effective.

2 Related Works

In this section, we will briefly introduce LDA method and MMC method. LDA is a very efficient feature extraction method. The purpose of LDA is to maximize the between-class scatter matrix while simultaneously minimizing the within-class scatter matrix, i.e.

$$J(W) = \text{tr} \left((W^T S_w W)^{-1} (W^T S_b W) \right) \quad (1)$$

where $S_b = \sum_{i=1}^c l_i (m_i - m)(m_i - m)^T$ is named between-class scatter matrix, m_i and

l_i are mean vector and size of class i respectively, $m = \sum_{i=1}^{l_i} n_i m_i$. $S_w = \sum_{i=1}^c S_i$ is the within-class scatter matrix, and S_i is the covariance matrix of class i . The mapping matrix W must be constituted calculating the matrix inversion S_w^{-1} . So, LDA cannot be applied when S_w is singular due to the small sample size (SSS) problem.

In order to solve the above problem, Maximum Margin Criterion (MMC) is proposed. MMC seeks to find a subspace, in which the sample is close to those in the same class while far from those in the different classes. The objective function of MMC is as follows:

$$J(W) = \text{tr} \left(W^T (S_b - S_w) W \right) \quad (2)$$

We can see that there is no need to calculating any matrix inversion. So this method do not suffer from the SSS problem, and has been shown to more effective than LDA.

MMC seeks to preserve global structure of samples, and has solved SSS problem. But this method ignores the local structure information of samples, which is very important for new samples.

3 Local Class Information Preserving

MMC uses the difference of both between-class scatter and within-class scatter as discriminant criterion, so the SSS problem of LAD is avoided. MMC seeks to preserve global structure of all samples, but this method ignores the local structure information of samples, which is very important for new samples. For this purpose, we propose local class information preserving (LCIP) method to extract more useful and discriminating video feature from the original video feature. In this method, we redefine the between-class scatter and within-class scatter with neighborhood relationship and class label information of each sample, which can make nearby samples with the same class label and separated samples with different class label.

Consider a linear mapping $W^{D \times d}$ that map $X = [x_1, x_2, \dots, x_n]$ ($x_i \in R^D$) in the original space to a lower dimensional space $Y = [y_1, y_2, \dots, y_n]$ ($y_i \in R^d$) by

$$Y = W^T X \tag{3}$$

where D and d are the dimension of the data before and after the transformation, respectively, $D \gg d$.

Suppose there are c known pattern classes w_1, w_2, \dots, w_c . x_j^i ($i = 1, 2, \dots, l_c, j = 1, 2, \dots, c$) denotes the i th sample in the j th class, l_j is the number of training samples of class j and satisfies $l_1 + l_2 + \dots + l_c = N$. Suppose set $N(x_i) = \{x_i^1, x_i^2, \dots, x_i^k\}$ includes k neighborhoods of sample x_i , $l(x_i)$ denotes the class label of x_i , set $N_w(x_i)$ includes the samples in $N(x_i)$ which have the same class label of x_i , then set $N_b(x_i)$ includes the samples in $N(x_i)$ which have the different class label of x_i , and the k neighborhoods of samples which have the different class label of x_i in $N_w(x_i)$. So, we have

$$N_w(x_i) = \left\{ x_i^s \mid l(x_i^s) = l(x_i), 1 \leq s \leq k \right\} \tag{4}$$

$$N_b(x_i) = \left\{ \left(x_i^s \mid l(x_i^s) \neq l(x_i), 1 \leq s \leq k \right) \text{ and } \left(N_w(x_i^s) \mid x_i^s \in N(x_i) \wedge l(x_i^s) \neq l(x_i) \right) \right\} \tag{5}$$

For each sample x_i , we calculate the corresponding local same class mean

$$\text{vector } u_{x_j} = \frac{1}{k} \sum_{x_j^i \in N_w(x_i)} x_j^i, \text{ and local different class mean vector } m_{x_j} = \frac{1}{k} \sum_{x_j^i \in N_b(x_i)} x_j^i.$$

The local within-class scatter of sample x_i can defined

$$S_{x_i}^w = \frac{1}{k} \sum_{j=1}^k (x_i^j - u_{x_j})(x_i^j - u_{x_j})^T \tag{6}$$

Thus the all within-class scatter can defined

$$S_w' = \frac{1}{N} \sum_{i=1}^N S_{x_i}^w \tag{7}$$

The local between -class scatter of sample x_i can defined

$$S_{x_i}^b = (u_{x_j} - m_{x_j})(u_{x_j} - m_{x_j})^T \tag{8}$$

Thus the all between -class scatter can defined

$$S_w^b = \frac{1}{N} \sum_{i=1}^N S_{x_i}^b \tag{9}$$

So, the objective function of LCIP is as follows:

$$J(W) = tr(\alpha S_b^W - (1-\alpha) S_w^W) \tag{10}$$

where S_b^W and S_w^W are the between-class scatter matrix and within-class scatter matrix in the lower dimensional feature space.

Since W is a linear mapping, we can get that $S_b^W = W^T S_b' W$ and $S_w^W = W^T S_w' W$. We submit $S_b^W = W^T S_b' W$ and $S_w^W = W^T S_w' W$ into Eq.(10), and obtain

$$J(W) = tr(W^T (\alpha S_b' - (1-\alpha) S_w') W) \tag{11}$$

We can get $W = [w_1, w_2, \dots, w_d]$ to solve the following constrained optimization problem

$$\begin{cases} \max \sum_{k=1}^d w_k^T (\alpha S_b' - (1-\alpha) S_w') w_k \\ \text{subject to } w_k^T w_k = 1 \quad k = 1 \dots d \end{cases} \tag{12}$$

where α is a adjust factor.

To solve the optimization problem (Eq. (12)), we can use a Lagrangian L

$$L(w_k, \lambda_k) = \sum_{k=1}^d w_k^T (\alpha S_b' - (1-\alpha) S_w') w_k - \lambda_k (w_k^T w_k - 1) \tag{13}$$

with multiplier λ_k . L has to be maximized with respect to λ_k and w_k , and then the derivatives of L with respect to w_k must vanish

$$\frac{\partial L(w_k, \lambda_k)}{\partial w_k} = ((\alpha S_b' - (1-\alpha) S_w') - \lambda_k I) w_k = 0 \quad k = 1, 2, \dots, d \tag{14}$$

Then this minimization problem can be converted to a generalized eigenvalue problem:

$$(\alpha S_b' - (1-\alpha) S_w') w_k = \lambda_k w_k \quad k = 1, 2, \dots, d \tag{15}$$

where λ_k is the eigenvalue of $\alpha S_b' - (1-\alpha) S_w'$, w_k is the corresponding eigenvectors.

Lastly, the embedding is as follows:

$$x_i \rightarrow y_i = W^T x_i, W = [w_1, w_2, \dots, w_d] \tag{16}$$

LCIP integrate the local between-class scatter matrix and within-class scatter matrix with the local structure information of each samples, and consider the global and local structure information. But MMC only consider the global structure information of samples and ignored the local structure information. Obviously, LCIP can extract more useful and discriminating feature from the original feature than MMC.

4 Experimental Results

In order to verify the effectiveness of the proposed method, we extract video feature (LCIP feature) using LCIP from original feature video feature, then segment video

shot of music, sport, documentary, movie and commercial TV. Meanwhile, we make an experiment with the same segment method using MMC feature. We select Recall and Precision as the appropriate evaluation criteria. The Recall and Precision are defined as follows [7]:

$$Precision = \frac{N - M}{N - M + F} \tag{17}$$

$$Recall = \frac{N - M}{N} \tag{18}$$

where N is the ground truth number of shot, M is the missed cuts and F is the number of false alarms.

In the experiment, original feature video feature is firstly build based on color feature and texture feature (316 dimensions). Then LCIP feature is extracted using the proposed LCIP with $k=25, \alpha = 0.5, d=55$, meanwhile MMC feature is extracted using MMC method with $d=55$. For simplicity, we use the method of literature [8] to segment shot. The experimental results are summarized in Fig.1.

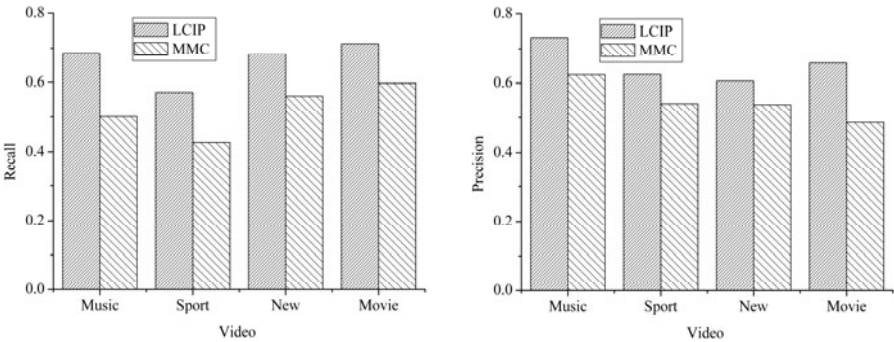


Fig. 1. Experimental results (Recall and Precision)

Fig.1 indicates that the shot segment method based on LCIP feature have a good results in different type videos, with the recall and precision over 57%, and the average recall and precision are 1.4%, 1.1% higher respectively than the results based on MMC feature. The reason is that we extract more useful and discriminating video feature for shot boundary detection. In other words, the proposed feature extraction method (LCIP) considers the global and local structure information integrating the local between-class scatter matrix and within-class scatter matrix with the local structure information of each sample, but MMC only consider the global structure information of samples and ignored the local structure information. So, we can conclude that LCIP can extract more useful and discriminating feature from the original feature than MMC.

5 Conclusion

This paper has presented an effective shot feature extraction method. It focuses on extracting more useful and discriminating video feature for segment video shot.

The main contributions of the paper are to present LCIP to extract more useful and discriminating video feature, which integrate the local between-class scatter matrix and within-class scatter matrix with the local structure information of each sample. The experimental results show that the proposed method is effective.

Acknowledgments. This project is supported by the Research Foundation of Science & Technology Department of Hunan Province (No.2011FJ3120, No.2011FJ3022), supported by Scientific Research Fund of Hunan Provincial Education Department (No.11C0221).

References

1. Li, Y.N., Lu, Z.M., Niu, X.M.: Fast Video Shot Boundary Detection Framework Employing Pre-Processing Techniques. *IET Image Proc.* 3(3), 121–134 (2009)
2. Camara-Chavez, G., Precioso, F., Cord, M.: Shot Boundary Detection by a Hierarchical Supervised Approach. In: 14th International Conference on Systems, Signals and Image Processing, pp. 197–200. IEEE Press, New York (2007)
3. Hansung, L., Jaehak, Y., Younghee, I., Joon-Min, G., Daihee, P.: A Unified Scheme of Shot Boundary Detection and Anchor Shot Detection in News Video Story Parsing. *Multimedia Tools Appl.* 51(3), 1127–1145 (2011)
4. Shekar, B.H., Sharmila Kumari, M., Holla, R.: Shot Boundary Detection Algorithm Based on Color Texture Moments. *Commun. Comput. Info. Sci.* 142(8), 591–594 (2011)
5. Fisher, R.A.: The Use of Multiple Measurements in Taxonomic Problems. *Annual of Eugenics* 7, 179–188 (1936)
6. Li, H.F., Jiang, T., Zhang, K.S.: Efficient and Robust Feature Extraction by Maximum Margin Criterion. *IEEE Trans. Neural Networks* 17(1), 157–165 (2006)
7. Yuan, J.H., Wang, H.Y., Xiao, L., Zheng, W.J., Li, J.M., Lin, F.Z., Zhang, B.: A Formal Study of Shot Boundary Detection. *IEEE Trans. Circuits Syst. Video Technol.* 17(2), 168–186 (2007)
8. Zhang, H.J., Kankanhalli, A.S.: Automatic Partitioning of Video. *Multimedia Syst.* 1(1), 10–28 (1993)

Quadrature Kalman Probability Hypothesis Density Filter for Multi-Target Tracking

Pu Zhang¹, Hongwei Li², and Yuan Huang¹

¹ Image Center, Beihang University, 100191, Beijing, China

zhangpu19870625@163.com

² Aviation Security, Civil Aviation Management Institute of China, 100102, Beijing, China

ahlhw@camic.cn

Abstract. A new Quadrature Kalman-Probability Hypothesis Density filter is proposed for nonlinear system model multi-target tracking. The algorithm estimates first-order statistical moment of posterior multi-target states with Probability Hypothesis Density (PHD) Filter, and updating targets' states from the recursion of Quadrature Kalman. Quadrature Kalman filter uses statistical linear regression method through a set of Gaussian-Hermite quadrature points to linearize nonlinear functions, Jacobian matrix solving is unnecessary and the linearized error is reduced. Simulation results prove that influence on the algorithm by non-linear system model is effectively decreased, the estimating accuracy of targets' number and states is advanced, and the tracking exactness is improved.

Keywords: Multi-target tracking, Random Finite Set, Probability Hypothesis Density, Quadrature Kalman Filter, Nonlinear System.

1 Introduction

Multi-target tracking (MTT) has been widely used in Intelligence Surveillance, Traffic Monitoring, Astronomy forecasts, Battlefield surveillance, Missile Defense and so forth[1]. Recently, in linearize system MTT, there are several mature theories, technique and algorithms, such as Nearest Neighbor (NN), Joint Probability Data Association (JPDA), Multiple Hypothesis Tracking (MHT) and Probability Multiple Hypothesis Tracking (PMHT) [2]. However, traditional methods based on state space cannot process targets whose states and number is time-varying, in addition, with the increasing of number and measurements of targets, the number of data association and computational complexity also increase exponentially, which will further increase the difficulty of multi-target tracking.

Mahler[3] proposed Probability Hypothesis Density (PHD) as the first-order estimate of the target's posterior probability, which can simplify the calculation process, yet in the reason of multiple integrations in PHD recursion there is no closed solution. Aim at this problem, Vo[4] etc. proposes Gaussian Mixture PHD (GMPHD) in linear system, as a large muti-target tracking systems are nonlinear, this render to nonlinear filtering problems[6]. Vo[5] etc. applied Extend Kalman Filter (EKF) and Unscented Kalman

Filter (UKF) to PHD recursion, proposed EKPHD and UKPHD, which achieves number-varying multi-target tracking in nonlinear system. In the process of linearizing nonlinear system, EKF needs to calculate Jacobian matrix of the nonlinear systems, and its only first-order accuracy usually render a large of linearization error, tracking results are not satisfactory. While UKF is based on Unscented Transformation (UT) and Kalman filter, which overcome a big error and pathological of EKF, especially selected a number of sampling points, lead to a more accuracy nonlinear approximation after changing mean and variance, but also inevitably bring linearization error, reducing the tracking performance. In order to resolve mentioned problems, Ienkan Arasaratnam etc[7]. proposed Quadrature Kalman Filter (QKF), this algorithm uses statistical linear regression method through a set of Gaussian-Hermite quadrature points to linearize nonlinear functions, Jacobian matrix solving is unnecessary and the linearized error is reduced, a higher filtering accuracy result is obtained than EKF and UKF.

This paper applies QKF to PHD recursion in order to achieve number-varying multi-target tracking in nonlinear system. Through updating of the targets' mean variance and weight, PHD filter obtains a more accurate target states prediction.

2 Quadrature Kalman Probability Hypothesis Density Filter

The heart of the QKF is the Gaussian-Hermite quadrature rule that computes the first two order moments of all conditional densities. The Gauss-Hermite rule does not approximate the nonlinear function explicitly; rather, it approximates the integral of the form (polynomial*Gaussian) numerically using a weighted quadrature point set. A n -point Gauss-Hermite rule is exact for all polynomials of degree $2n-1$ or less. Moreover, the QKF is derivative free, thereby broadening its practical applicability, and compared to EKF and UKF, QKF has a higher accuracy[7].

In linear Gaussian model system, if the prior probability distribution is Gaussian mixture, then all the subsequent posterior intensities are Gaussian distribution in PHD recursive process, in this way, we can use Gaussian mixture components to describe the targets' states in PHD filter, which is also called Gaussian Mixture Probability Hypothesis filter (GMPHD) [5]. So, (1) and (2) can be expressed as:

$$f(x_{k-1}, k) = N(x; F_{k-1}x_{k-1}, Q_{k-1}) \quad (1)$$

$$h(x_k, k) = N(z; H_k x_k, R_k) \quad (2)$$

Where $N(\cdot, m, P)$ denotes a Gaussian density with mean m and covariance P , F_{k-1} is the state transition matrix, H_k is the observation matrix.

In nonlinear system multi-target tracking, since the spontaneous birth targets and split targets are less affected by the system, we suppose that equation (3) and (8) are still applicable in GMPHD recursion. This paper proposes algorithm QK-PHD, the main idea of which is using a set of weighted Gaussian function to estimate nonlinear system model, then through statistic characteristics (target posterior intensity) and Kalman filter to obtain the parameters of the Gaussian components in $v_{S,k|k-1}(x)$ and $v_k(x)$, thus getting the recursive form of the nonlinear PHD, in this sense to estimate multi-targets' states.

From PHD predict step , in nonlinear system model, target intensity function still remain, including existence targets, disappearance targets and split targets, which is given by

$$v_{k|k-1}(x) = v_{s,k|k-1}(x) + v_{\beta,k|k-1}(x) + \gamma_k(x) \tag{3}$$

Suppose that at time $k-1$, the weight, mean and covariance matrix of Gaussian components in $v_{k-1}(x)$ are $\omega_{k-1}^{(i)}$, $m_{k-1}^{(i)}$ and $P_{k-1}^{(i)}$, $i = 1, 2, \dots, J_{k-1}$, and $P_{k-1}^{(i)}$ can be written as $P_{k-1}^{(i)} = S_{k-1}^{(i)}(S_{k-1}^{(i)})^T$, therefore, the intensity of existence target is given by

$$v_{s,k|k-1}(x) = p_{s,k} \sum_{j=1}^{J_{k-1}} w_{k-1}^{(j)} N(x; m_{s,k|k-1}^{(j)}, P_{s,k|k-1}^{(j)}) \tag{4}$$

where

$$w_{k|k-1}^{(i)} = P_{s,k} w_{k-1}^{(i)} \tag{5}$$

$$m_{s,k|k-1}^{(i)} = \sum_{l=1}^m \omega_l f(S_{k-1|k-1} \xi_l + m_{k-1}^{(i)}, k-1) \tag{6}$$

$$P_{k|k-1}^{(j)} = \sum_{l=1}^m \omega_l f(S_{k-1|k-1} \xi_l + m_{k-1}^{(i)}, k-1) f^T (S_{k-1|k-1} \xi_l + m_{k-1}^{(i)}, k-1) - m_{s,k|k-1}^{(i)} (m_{s,k|k-1}^{(i)})^T + Q_k \tag{7}$$

Here, $J_{k-1}, w_{k-1}^{(i)}, m_{k-1}^{(i)}, P_{k-1}^{(i)}$, $i = 1, 2, \dots, J_{k-1}$ is given model parameters of existence targets at time k ; $J_{\gamma,k}, w_{\gamma,k}^{(i)}, m_{\gamma,k}^{(i)}, P_{\gamma,k}^{(i)}$, $i = 1, 2, \dots, J_{\gamma,k}$ determine the shape of spontaneous targets; and $J_{\beta,k}, \omega_{\beta,k}^{(j)}, m_{\beta,k-1}^{(j)}, P_{\beta,k-1}^{(j)}, d_{\beta,k-1}^{(j)}$, $j = 1, 2, \dots, J_{\beta,k}$ determines the spawning intensity of a target at time k .

From PHD update step, the posterior intensity at time k is given by

$$v_k(x) = (1 - p_{D,k}) v_{k|k-1}(x) + \sum_{z \in Z_k} v_{D,k}(x; z) \tag{8}$$

where

$$v_{D,k}(x; z) = \sum_{j=1}^{J_{k|k-1}} w_k^{(j)}(z) N(x; m_{k|k}^{(j)}(z), P_{k|k}^{(j)}) \tag{9}$$

$$w_k^{(j)}(z) = \frac{P_{D,k} w_{k|k-1}^{(j)} q_k^{(j)}(z)}{\kappa_k(z) + P_{D,k} \sum_{\tau=1}^{J_{k|k-1}} w_{k|k-1}^{(\tau)} q_k^{(\tau)}(z)} \tag{10}$$

$$q_k^{(j)}(z) = N(z; z_{k|k-1}^{(j)}, P_{k|k}^{(j)}) \tag{11}$$

$$P_{k|k}^{(j)} = P_{k|k-1}^{(j)} - K_k^{(j)} P_{zz,k|k-1}^{(j)} (K_k^{(j)})^T \tag{12}$$

$$\mathbf{m}_{s,klk}^{(j)} = \mathbf{m}_{s,klk-1}^{(j)} + \mathbf{K}_k^{(j)} (\mathbf{z}_{klk}^{(j)} - \mathbf{z}_{klk-1}^{(j)}) \quad (13)$$

$$\mathbf{z}_{klk-1}^{(j)} = \sum_{l=1}^m \omega_l \mathbf{h}(\mathbf{S}_{klk-1} \boldsymbol{\xi}_l + \mathbf{m}_{s,klk-1}^{(j)}) \quad (14)$$

$$\mathbf{K}_k^{(j)} = \mathbf{P}_{xz,klk-1}^{(j)} (\mathbf{P}_{zz,klk-1}^{(j)})^{-1} \quad (15)$$

$$\mathbf{P}_{xz,klk-1}^{(j)} = \sum_{l=1}^m \omega_l \mathbf{X}_{l,klk-1}^{(j)} (\mathbf{Z}_{l,klk-1}^{(j)})^T - \hat{\mathbf{x}}_{klk-1}^{(j)} (\hat{\mathbf{z}}_{klk-1}^{(j)})^T \quad (16)$$

$$\mathbf{P}_{zz,klk-1}^{(j)} = \mathbf{R}_k + \sum_{l=1}^m \omega_l \mathbf{Z}_{l,klk-1}^{(j)} (\mathbf{Z}_{l,klk-1}^{(j)})^T - \hat{\mathbf{z}}_{klk-1}^{(j)} (\hat{\mathbf{z}}_{klk-1}^{(j)})^T \quad (17)$$

Equations (14)-(17) and (18)-(27) are predict and update steps of QK-PHD filter, and in nonlinear system, the proposed algorithm updates weight, mean and covariance matrix of Gaussian component through the recursion of QKF.

3 Simulations

In this section, we present simulated results to prove effective of our proposed algorithm comparing with EK-PHD and UK-PHD[5]. In the example, each target has a survival probability $P_{s,k} = 0.99$ and follow a nonlinear nearly-constant turn model[8]. The target state vector is $\mathbf{x}_k = [p_{x,k}, p_{y,k}, v_{x,k}, v_{y,k}, w_k]^T$, where w_k is the turn rate, and the state equation is given by $\mathbf{x}_k = \mathbf{A}(w_{k-1})\mathbf{x}_{k-1} + \mathbf{B}\zeta_k$ and measurement equation is

$$\mathbf{z}_k = \begin{bmatrix} \arctan(p_{x,k} / p_{y,k}) \\ \sqrt{p_{x,k}^2 + p_{y,k}^2} \end{bmatrix} + \boldsymbol{\varepsilon}_k$$

Where $\boldsymbol{\varepsilon}_k \sim \mathcal{N}(0, \mathbf{R}_k)$, $\mathbf{R}_k = \text{diag}([\sigma_\theta^2, \sigma_r^2])$, $\sigma_\theta^2 = 2 * \pi / 180$ (rad / s), $\sigma_r^2 = 20\text{m}$, $\Delta = 1\text{s}$, $\zeta_k \sim \mathcal{N}(0, \sigma_\zeta^2)$ and $\sigma_\zeta = 15\text{m} / \text{s}^2$, the clutter RFS follows the uniform Poisson over the surveillance region is $[-\pi, \pi]\text{rad} \times [-60, 60]\text{km}$, and the velocity of the target is $1.2\text{km} / \text{s}$.

The true target trajectories are plotted in Fig.1. There are 5 targets in the surveillance region, target 1, 2 and 3 start at time 1s, 3s and 12s, respectively, at the end of 90s, target 1 disappeared, and target 2 and 3 disappeared at time 100s. Target 4 and 5 are spawned from target 3 and 2 at time 32s and 56s, respectively. The pruning parameters for three algorithms are $T = 10^{-5}$, $U = 4$ and $J_{\max} = 200$.

In the simulation experiment we choose Wasserstein Distance (WD) [9], Circular Error Probability (CEP) [5] and the expected absolute error[5] on the number of targets as the rule to compare the three algorithms.

Through 100 times Monte Carlo simulations, we compare the performance when tracking time-varying targets of EK-PHD, UK-PHD and QK-PHD, we add 20 times

noise in the measurement of the targets. Fig.2. shows the comparability of WD, while we can see, in times $k = 1s \sim 31s$, the nonlinearity of the system is not distinct, three algorithms obtain even the same WD. However, in times $k > 31s$, the nonlinearity of the system is serious, compared with EK-PHD and UK-PHD, QK-PHD gets a lower WD. In the whole 100s range, the average WD of EK-PHD is 8.9358×10^6 , UK-PHD is 1.3309×10^4 and QK-PHD is 5.5920×10^3 , respectively. In this sense, QK-PHD can effectively track the number-varying multi-target in nonlinear system.

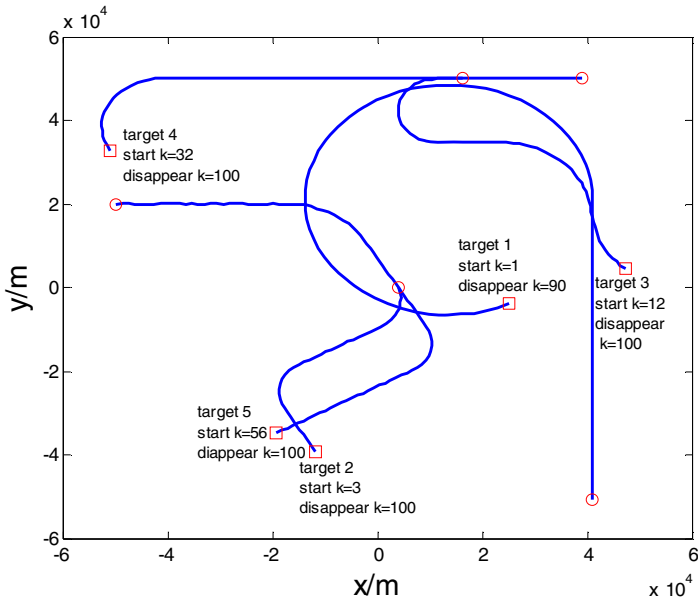


Fig. 1. Target trajectories

While Fig.3. is the CEP of the three algorithms, at times $k < 31s$, three algorithms even get nearly the same performance. And with the serious nonlinearity of the system, especially at the time when the target spawns, EK-PHD and UK-PHD have absolutely higher CEP than QK-PHD. This is because EKF uses first-order Taylor series truncation when linearizing the nonlinear system, which proposes a higher linearization error and renders it lose the target in the filtering process. While UKF is based on Unscented Transformation (UT) and Kalman filter, which bring linearization error, reducing the tracking performance. QKF uses statistical linear regression method through a set of Gaussian-Hermite quadrature points to linearize nonlinear functions, reducing the linearization error and obtaining a higher filtering accuracy result than EKF and UKF. From figure 2(b) we can see that at times $k = 32s, 56s$ and $k = 90s$ when the targets spawn and disappear, QK-PHD can accurately track the targets, proving a better filtering performance than EK-PHD and UK-PHD.

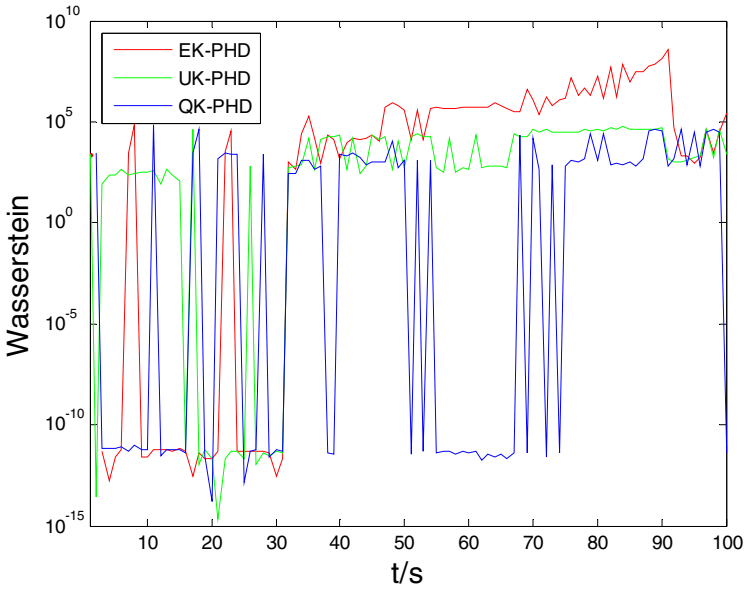


Fig. 2. WD comparable

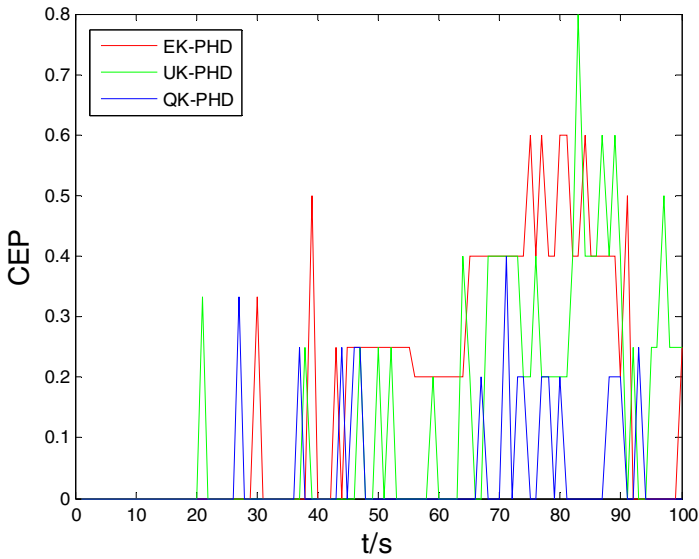


Fig. 3. CEP comparable

Fig.4. shows the expected absolute error comparable on the number of targets for the three algorithms. At time $k > 31s$, the nonlinearity of the system is very serious, which render the three algorithms a big error in estimating error of the number, but QK-PHD is better than the other two algorithms, EK-PHD and UK-PHD.

4 Conclusion

This paper combines GMPHD and QKF for nonlinear system multi-target tracking, the method can accurately track number-varying multi-target in cluster, undetected environment. Compared with EK-PHD and UK-PHD, in proposed algorithm, Jacobian matrix solving is unnecessary and the linearized error is reduced. Simulation results prove that influence on the algorithm by non-linear system model is effectively decreased, the estimating accuracy of targets' number and states is advanced, and the tracking exactness is improved.

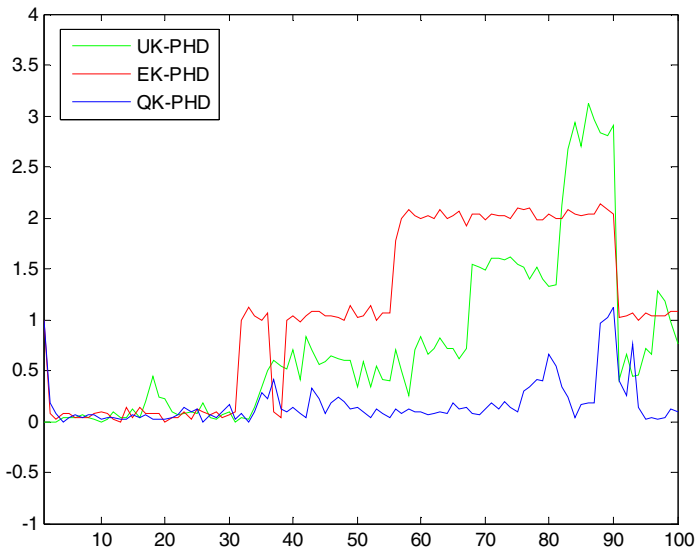


Fig. 4. Expected Number Error

References

1. Boston, M.A.: Design and analysis of modern tracking systems. Artech house (1999)
2. Yilmaz, A., Javed, O., Shah, M.: Object tracking: a survey. ACM Computing Surveys 38(4), 1–45 (2006)
3. Mahler, R.: Multitarget bayes filtering via first-order multitarget moments. IEEE Trans. on Aerospace and Electronic systems 39(4), 1152–1177 (2003)
4. Mahler, R.P.S.: Statistical Multisource Multitarget Information fusion. Artech House (2007)

5. Vo, B.N., Ma, W.K.: The Gaussian mixture probability hypothesis density filter. *IEEE Trans. Signal Processing* 55(7), 4091–4104 (2006)
6. Crassidis, J.L., Markley, F.L., Cheng, Y.: Survey of Nonlinear Attitude Estimation Methods. *Journal of Guidance, Control and Dynamics* 30(1), 12–28 (2007)
7. Arasaratnam, I., Haykin, S., Elliott, R.J.: Discrete-time nonlinear filtering algorithms using Gauss-Hermite quadrature. *Proc. IEEE* 95(5), 953–977 (2007)
8. Li, X.R., Jilkov, V.: Survey of maneuvering target tracking. *IEEE Trans. AES* 39(4), 1333–1364 (2003)
9. Hoffman, J., Mahler, R.: Multi-target miss distance via optimal assignment. *IEEE Transactions on Systems, Man and Cybernetics-Part A* 34(3), 327–366 (2004)

Kaiser Window Function Non-Local Means for Image Denoising

Hongwei Li¹, Pu Zhang², and Yuan Huang²

¹ Aviation Security, Civil Aviation Management Institute of China, 100102, Beijing, China
ahlhw@camic.cn

² Image Center, Beihang University, 100191, Beijing, China
zhangpu19870625@163.com

Abstract. Kernel function has a great influence on the results denoised by Non-Local Means (NLM), the original NLM method uses the gaussian kernel function to product the patch pixels, and the central pixel's 4-neighborhood and its 8-neighborhood are given the same kernel value. While in the fact that different neighborhood should be given different kernel values, and in this case, we proposed an improved NLM algorithm based on Kaiser Window function, in which the central pixel's different scale neighborhood has been assigned different values from the Kaiser Window function. Through a myriad of experiments, both visual quality and PSNR proved that our method is better than the original algorithm.

Keywords: Non-local Means, Kernel function, Gaussian kernel, Kaiser Window, Image denoising.

1 Introduction

Image denoising is a challenging problem that is still open in spite of the considerable amount of research devoted to them. Since the Non Local Means algorithm was first proposed by A. Buades[1] in 2005, a myriad of improved methods based on the Non-local Means have been introduced subsequently. The method of non-local means uses the redundancy information of the original image as gray value in the pixel domain to reduce the additive gauss white noise. When Alexei A. Efros etc. use the non-parametric method for texture synthesis[2] , they obtain a better quality for image synthesis, and then A. Buades etc. cites this non local algorithm for image denoising, which lead to an fabulous denoising quality. In order to preserve the structure of the texture as much as possible, in the patch, the error for nearby should be greater than for pixels far away. To achieve this effect, they set the two dimensional Gaussian kernel to product with the local patch, which preserves most structures of the denoised image. In the method, each pixel value is estimated as a weighted average of all others, and the pixels whose neighborhoods are the most similar to the neighborhood of the one to be denoised are given the largest weights. Vincent Duval[3] etc. deals with the parameter choice for the NLM algorithm, they rely on Stein's Unbiased Risk Estimate to locally set the former parameters, while the kernel function have not noticed in their paper. However, the researching work above only pay attention to the searching window and

patch width, or the edge of the whole image, they care less about the kernel function’s influence on the algorithm.

Alexander Wong[4] focuses on utilizing different weighting schemes, and they use Mexican hat wavelet function as the kernel function to product the patch, which leader to an improvement. However, the Mexican hat function is not a best choice for the image denoising, because of its equality value for the center pixel’s 4-neighborhood and 8-neighborhood. Joseph Salmon[5] study the influence of two important parameters: the size of the searching window and the weight given to the central patch, while they have not discussed the kernel function either. We discussed the influence of the kernel function for NLM method, and as we proposed the Kaiser Window function as the kernel function, both visual quality and PSNR prove that when the central pixel’s 4-neighborhood and 4-neighborhood give different value, the NLM denoised image will be better derived. In this paper, we also present other function as kernel functions, such as the average of the whole patch, the median of the difference between the two patches, the Mexican hat wavelet function, and so forth.

2 Non-Local Means Method

Suppose the original true image $x(i)$, $i \in I$ is corrupted by an additive noise process $n(i)$, where $i \in I$, and the observed image can be written as follow:

$$v(i) = x(i) + n(i) \tag{1}$$

The NLM algorithm restores the pixel of interest with a weighted average of non-local pixels in the image which are in a similar environment. The weight is computed based on the similarity between the neighborhood patches of the pixel of interest and contributing pixels.

Mathematically, the solution to obtain the original true image $x(i)$ by standard NLM method can be described as

$$\hat{x}(i) = \sum_{j \in I} \omega_{ij} v(j) \tag{2}$$

$$\omega_{ij} = \frac{1}{Z(i)} \exp\left(-\frac{G_a \left\|v(N_i) - v(N_j)\right\|_2^2}{h^2}\right) \tag{3}$$

Where $Z(i)$ is the normalizing factor

$$Z(i) = \sum_j \exp\left(-\frac{G_a \left\|v(N_i) - v(N_j)\right\|_2^2}{h^2}\right) \tag{4}$$

And ω_{ij} is a weight denoting the contribution from $v(j)$ to $\hat{x}(i)$, N_i and N_j is a squared neighborhood patch of pixel i . Parameter h controls the decay of the exponential function. G_a is the Gaussian kernel function, and it is defined in 2-D as

$$G_a(i, j; \sigma) = \frac{1}{2\pi\sigma^2} e^{-\frac{i^2+j^2}{2\sigma^2}} \quad (5)$$

The σ is standard deviation which determines the width of the Gaussian kernel.

The significance of the parameters h had already been underlined by [6] and [7] has proposed the influence of the central patch (the choice of the width are often between 5 and 9) and the size of the searching window R (the choice of which is often between 11 and 29), so we do not focus on them in this paper. The analysis of the parameters of NLM even forget another important parameter, the kernel function, which is of great importance in image denoising, and in this paper we will compare the Gaussian kernel with other kernel functions and change the kernel function value to show its influence to the denoised images.

3 Kernel Function

The original NLM method uses the normalized Gaussian kernel to produce the local patch to calculate the weight, while 8-neighborhood and 4-neighborhood of the center pixel have been given the same kernel value, in our experiments we find that although Gaussian kernel is a good choice, yet when we use different kernel values for one center pixel's 4-neighborhood and 8-neighborhood, the denoised image will get a better visual quality and a higher PSNR. In this section, we will give some window functions as the kernel function of the NLM method.

3.1 Kaiser Window Function

The Kaiser window is a one-parameter family of window functions used for digital signal processing, and is defined by the formula[12]:

$$\omega_n = \begin{cases} \frac{I_0(\pi\alpha\sqrt{1-(\frac{2n}{M}-1)^2})}{I_0(\pi\alpha)}, & 0 \leq n \leq M \\ 0 & \text{otherwise} \end{cases} \quad (6)$$

Where, in the equality, I_0 is the zero order Modified Bessel function of the first kind,

$$I_0(\beta) = 1 + \sum_{n=1}^{\infty} \left[\frac{(\beta/2)^n}{n!} \right]^2, \quad \beta = \pi\alpha. \quad (7)$$

And α is an arbitrary real number that determines the shape of the window. In the frequency domain, it determines the trade-off between main-lobe width and side lobe level, which is a central decision in window design. M is an integer, and the length of the sequence is $N = M + 1$. In order to be used as a kernel function for NLM, we extent it to 2-D, and its value are given in figure 1.

3.2 Other Window Function

In this section, we cite some other function as the NLM’s kernel function in order to compare their influence on the denoised images. These kernel or window functions are as follows in table 1 and based on these kernel function, we choose lena as the experiments figure, the visual can be seen in figure 2, and then , in section 4, we will display the influence in term of PSNR in figure 3.

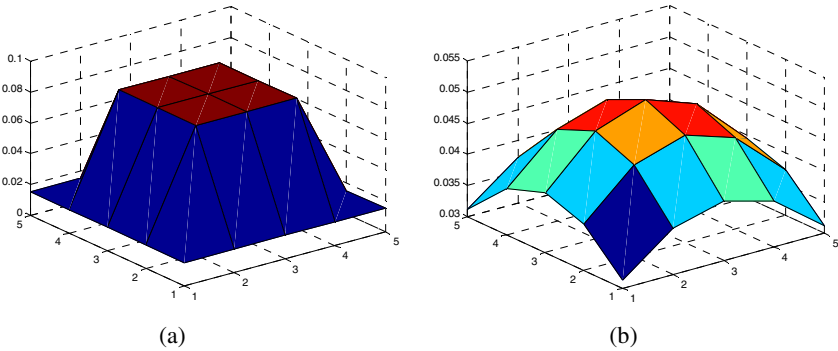


Fig. 1. Gaussian kernel (a) and Kaiser Window function (b)

We compare the kernel function above as the kernel function of NLM, they all be used in 2-demination images, and in the next section we will compare their influences to the denoised results.

Table 1. The kernel functions for NLM method

Type	$k(x,y)$
Laplacian Kernel[11]	$k(x, y) = \exp(-\frac{\ x - y\ }{\sigma})$
Average of the patch difference	$k(x, y) = \frac{1}{w * h} \sum_{x_i \in w, y_i \in h} \text{dist}(N(x_1, y_1), N(x_2, y_2))$
Median of the patch difference	$k(x, y) = \text{median}_{x_1, y_1 \in I} (\text{dist}(N(x_1, y_1), N(x_2, y_2)))$
Mexican hat wavelet function[8]	$\psi(t) = \frac{2}{\sqrt{3}\pi^{\frac{1}{4}}} (1 - \frac{t^2}{\sigma^2}) e^{-\frac{t^2}{2\sigma^2}}$

4 Influence of Kernel Function

In this section, we use the original NLM Gaussian kernel function compares with other window function, including the average value of the whole patch, the median value of the patch, the Kaiser window function and so forth. As we know, in each

small patch, the center pixel's value is derived from the difference between its own patch and other pixel's patch in the whole searching area. While the bigger difference, the lower similarity, and the smaller weight for the denoised pixel value. We proposed a new concept that in the same patch the center pixel's 4-neighborhood and its 8-neighborhood should contribute different values for the denoised pixel value, so we choose Kaiser window function as the kernel function instead. Within a myriad of experiment, we can notice that the kernel will greatly influence the image denoised by NLM method.



Fig. 2. Kernel functions performance with different images based on NLM method. From left to right, up to bottom are original image, noise image (20.14 dB), denoised by original NLM (25.50 dB), Kaiser Window function NLM (29.31dB), average patch difference (29.11 dB), median patch difference (25.62 dB), Laplacian kernel function (28.53 dB) and Mexican hat wavelet kernel function (25.67 dB), respectively.

As is suggested in Buades' paper[1], the neighborhood is set to be 7×7 and a 21×21 search window is used for computational purposes. We add different standard deviation of additive Gaussian white noise to the test images, and compare the results in terms of both visual quality and Peak Signal to Noise Ratio (PSNR) values.

In the experiments, we set the searching window is 11×11 , and the patch width 5×5 in order to reduce the computation time spending. From Fig.2., the kernel function will draw great influence on the image denoising with NLM, while from the results we can find that the proposed method based on Kaiser Window function indicates a better PSNR than the original NLM, and another interesting aspect is that when we use that average patch difference as the kernel function of NLM, the results are better when the image is corrupted by a higher white gaussian noise, but in the lower standard deviation, our proposed algorithm is a best one.

We add white gaussian noise by standard deviation 25 to the image peppers, while both PSNR and visual quality indicate that our proposed algorithm is better than the original NLM and NLM based on average patch difference. The image denoised by our proposed algorithm saves more textures and edges as well as more visual image details than the image denoised by any other kernel based methods. In the summary, our proposed method is an improved NLM method for image denoising. Fig.2. display the results denoised by all the present NLM methods, image lena proves that our proposed method is better than any other algorithms. The kernel function is of great importance for the NLM denoising, a better choose, a better result.

5 Conclusions

In this paper, we proposed an improved Non local means method for image denoising, through experiments we can see that the Kaiser Window we used in this paper is better than the original Non local means method which use the Gaussian kernel function as its kernel function. Compared with the original NLM, the proposed algorithm performs better and obtains smoothed images. Our proposed method also achieves a better result in preserving edges and thin structures.

References

1. Buades, A., Boll, B., Morel, J.M.: A non-local algorithm for image denoising. In: Proc. of the IEEE Int. Conf. on Computer Vision and Pattern Recognition (2005)
2. Efros, A.A., Leung, T.K.: Texture synthesis by non-parametric sampling. In: International Conference on Computer Vision, Corfu, Greece, pp. 1033–1038 (September 1999)
3. Duval, V., Aujol, J.F., Gousseau, Y.: On the parameter choice of the Non-Local Means, CMLA Preprint (July 2010)
4. Wong, A., Fieguth, P., Clausi, D.: A perceptually adaptive approach to image denoising using anisotropic non-local means. In: IEEE International Conference on Image Processing, pp. 537–540 (2008)
5. Salmon, J.: On two parameters for image denoising with non-local means. IEEE Signal Processing Letters 17(3), 269–272 (2010)
6. Buades, A., Coll, B., Morel, J.M.: a review of image denoising algorithms, with a new one. Multiscale Model. Simul. 4(2), 490–530 (2005)
7. Kervrann, C., Boulanger, J.: Optimal spatial adaptation for patch-based image denoising. IEEE Trans. Image Process. 15(10), 2866–2878 (2006)

A Method Based on FFT and Invariable Moment Features for UTAN

Zunyi Xu¹, Yi Liu¹, and Dongwu Huang²

¹School of Computer Science & Technology, Shandong Jianzhu University, Jinan, China

²Hydrographic Surveys Brigade of Tianjin Maritime Safety Administration, Tianjin, China
Zunyi Xu@sdjzu.edu.cn

Abstract. Traditionally, as the echo sounder is deployed in underwater terrain aided navigation system (UTAN), navigation and positioning accuracy is very low, even a large number of mismatches appear. In this paper, the multi-beam sounding has been introduced into UTAN, the input gray-scale image is transformed based on FFT from spatial domain to frequency domain. The Fourier phase correlation technique is used to estimate the candidate translations in order to decrease searching space. Hu invariable moments are then applied to obtain the best matching from candidate translations obtained from phase correlation. Based on different experiments to obtain the measured seabed topography, navigation data and multi-beam sounding data measured, the experimental result shows the proposed method can acquire higher accuracy of the navigation and positioning for the underwater vehicle, the INS error is reduced to about 10% of the original error, especially in the case of large original errors (less than 3km) for INS the accuracy is improved obviously.

Keywords: underwater terrain aided navigation, multi-beam sounding, phase correlation, Hu invariable moment features.

1 Introduction

Underwater terrain aided navigation (UTAN) is an important area of navigation and positioning for the underwater robots, submarine and other underwater vehicle [1-8]. As the echo sounder is deployed in UTAN and the speed of the underwater vehicle is a bit low, less data is collected in unit time, matching sequence is generated for a long time, a large change in error is engendered in INS, navigation and positioning accuracy is very low and even a large number of mismatches appear.

Since the multi-beam technology was developed in 1970s, it quickly became an important method to explore the sea floor topography due to its high efficiency, high resolution, high accuracy and full coverage technical characteristics [9-12]. Phase correlation and image invariant moment features have been successfully used in image registration, and the problems of image registration caused by image translation, rotation and scaling have been effectively solved [13-15].

In this paper, the multi-beam sounding is introduced into UTAN and image registration technique is used to improve the accuracy of the underwater terrain navigation and reduce the mismatch probability of that. First, the real-time grayscale

image from the multi-beam sonar has been re-sampled according to the resolution of the seabed terrain map. Then, the phase correlation technique based on Fast Fourier Transform (FFT) is used to estimate the candidate translations in order to improve the matching performance of UTAN. Finally, Hu invariable moment features are applied to obtain the best matching from candidate translations obtained from phase correlation, whose purpose is to eliminate the image rotation and distorted transformation due to INS error while the input image is collected.

2 Fundamental Theory

2.1 Phase Correlation Technique

The phase correlation technique is based on the Fourier Shift Theorem. This method can only deal with translation between two images in x-y axis [13].

Let $f_1(x, y)$ and $f_2(x, y)$ be two images that differ only by a displacement $(\Delta x, \Delta y)$ i.e.

$$f_2(x, y) = f_1(x - \Delta x, y - \Delta y) \quad (1)$$

Their corresponding Fourier transform $F_1(u, v)$ and $F_2(u, v)$ will be related by

$$F_2(u, v) = F_1(u, v)e^{-j2\pi(u\Delta x + v\Delta y)} \quad (2)$$

From the above equation, when the translation of $f(x, y)$ is generated in spatial domain, the phase-shift will occur but the amplitude of the Fourier transform is null in frequency domain. This will be used to match between two images $f_1(x, y)$ and $f_2(x, y)$.

The image displacement $(\Delta x, \Delta y)$ between $f_1(x, y)$ and $f_2(x, y)$ can be obtained as follows. Define the mutual energy spectrum of two images as follows:

$$G(u, v) = \frac{F_1(u, v)F_2^*(u, v)}{|F_1(u, v)||F_2^*(u, v)|} = e^{-j2\pi(u\Delta x + v\Delta y)} \quad (3)$$

where $F^*(u, v)$ is complex conjugate of $F(u, v)$.

Thus, the translation parameters $(\Delta x, \Delta y)$ can be estimated translation in x-y axis, by computing the Inverse FFT of (4)

$$F^{-1}(e^{-j2\pi(u\Delta x + v\Delta y)}) = \delta(x - \Delta x, y - \Delta y) \quad (4)$$

This function value is nonzero at the shifting place and zero at other place. The peak value of the function δ should be 1 in the ideal case, but it is often less than 1 because of noise and other reasons. The peak value describes the matching degree between two images.

2.2 Matching Feature of Moment Invariants

Moment invariant is a kind of image feature which is created by extracting translation, rotation and scaling invariants from the image. Hu moments are a classic moment invariants, which have been widely used in image registration successfully [16-17].

For a discrete image $f(x, y)$ with size of $M \times N$, $f(x, y)$ is the gray value for pixel (x, y) , $(p + q)$ order moment m_{pq} is defined as follows:

$$m_{pq} = \sum_{x=1}^M \sum_{y=1}^N x^p y^q f(x, y) \quad p, q = 0, 1, 2, \dots \tag{5}$$

The corresponding central moments is defined as

$$\mu_{pq} = \sum_{x=1}^M \sum_{y=1}^N (x - \bar{x})^p (y - \bar{y})^q f(x, y) \quad p, q = 0, 1, 2, \dots \tag{6}$$

where $\bar{x} = m_{10}/m_{00}$, $\bar{y} = m_{01}/m_{00}$, i.e they are the barycentric coordinates.

Normalized center moment η_{pq} of $(p + q)$ order moments for $f(x, y)$ is defined as:

$$\eta_{pq} = \frac{\mu_{pq}^r}{\mu_{00}^r} \quad p, q = 0, 1, 2, \dots \tag{7}$$

where $r = (p + q)/2$ $p, q = 0, 1, 2, \dots$

Hu 2-Dimension moment invariants are linear combination of the second order normalized central moments and the third order normalized central moments. Hu defined the set of seven invariant moments can be invariants to translation, rotation, and scale change, their specific expression see reference 16.

As the variation of the set of seven invariant moments may be relatively large and even be negative value, the actual moment invariants can be used as follows:

$$M'_k = \ln |M_k| \quad k = 1, 2, \dots, 7 \tag{8}$$

2.3 Correlation Function

Let $M = [(L_1, B_1, F_1), (L_2, B_2, F_2), \dots, (L_N, B_N, F_N)]^T$ is the reference image and $M' = [(L'_1, B'_1, F'_1), (L'_2, B'_2, F'_2), \dots, (L'_N, B'_N, F'_N)]^T$ is the real-time image, N is the length of matching sequence, (L_i, B_i, F_i) is the geographical coordinate and the value of terrain characteristics in the reference image, (L'_i, B'_i, F'_i) is the position of INS indicated and the value of terrain characteristics in the real-time image, where $i = 1, 2, \dots, N$.

The similarity measurement function is still using Mean Square Difference (MSD) in TERCOM algorithm, it is defined as [2]

$$MSD(F, F') = \frac{1}{N} \sum_{i=1}^N (F_i - F'_i)^2 \tag{9}$$

The best matching value is given by the minimum of $MSD(F, F')$. Euclidean distance is used as the minimum distance in this algorithm.

3 New Method Based on Multi-beam Sounding for UTAN

The framework based on multi-beam sounding for UTAN is given in Fig.1. The center of the search space, the search radius and the shape of the reference image are created by the navigation data from INS in the underwater topography map. As INS has a large random error when the underwater vehicle runs into the matching area, there are not only the larger translation and rotation but also the distorted transformations between the real-time image and the reference image as shown in Fig.2.

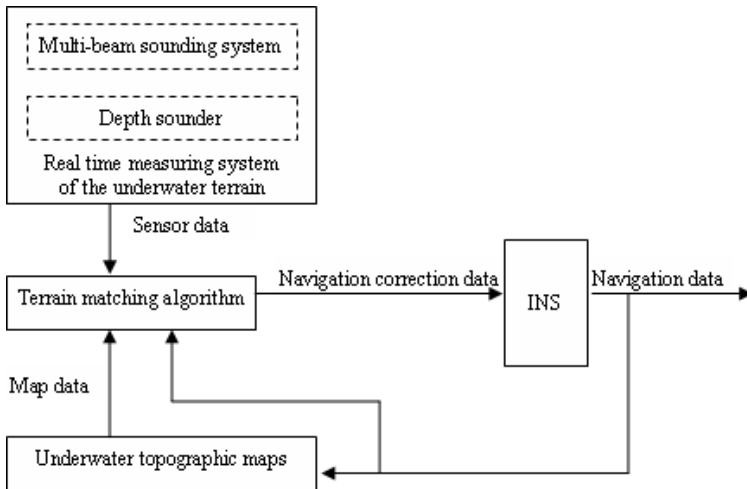


Fig. 1. The block diagram of UTAN based on multi-beam sounding

The proposed method based on multi-beam sounding for UTAN is presented in Fig.3. In order to eliminate the scaling between the real-time image and the reference image, the first step of the process is to re-sampling the input water depth data (very large density of measurement data) from multi-beam sounding system according to the submarine topographic map resolution which is stored in the computer. Then, HPF (High-pass filter) Module is used to filter noise and map the water depth to gray image, which the real-time image and reference image must be consistent depth and gray-level benchmarks. The real-time image and reference image are transformed from spatial domain to frequency domain by FFT so that phase correlation can be applied to detect the translation in order to reduce the computing time while using Hu invariant moments. Finally, the Hu invariable moments are then applied to obtain the best matching from candidate translations (10%) obtained from phase correlation.

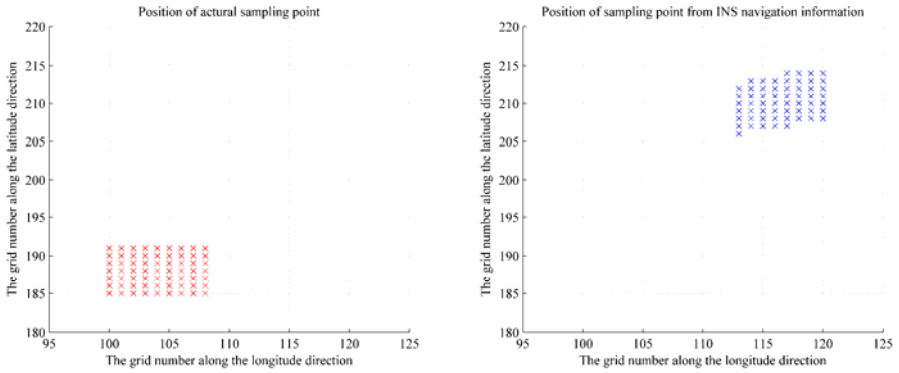


Fig. 2. The image distorted transformation between reference images and real-time images

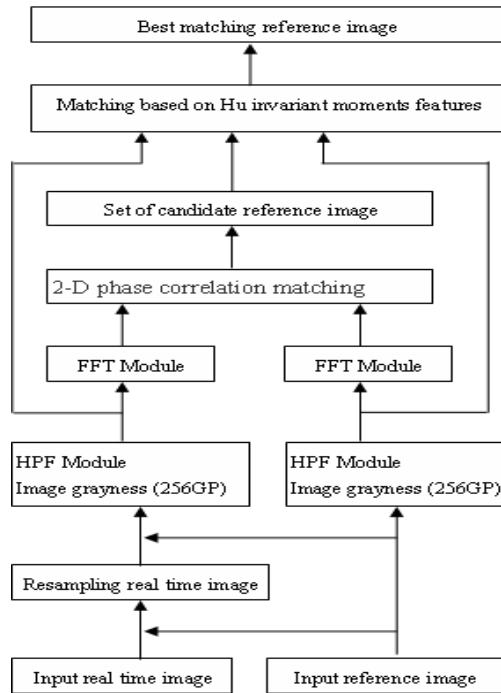


Fig. 3. Block diagram presents the proposed matching algorithm

4 Simulation Experimental Results

The experiment data are generated by simulation based on different experiments to obtain the measured seabed topography, INS navigation data, DGPS navigation data and multi-beam sounding data measured. They include INS navigation data, DGPS navigation data and multi-beam sounding swath data of the survey line in the same seabed terrain map.

The grid spacing is 100 meters and there are 274 x 274 grids in the submarine topographic map. The multi-beam sounding swath is 7 grids in width, the real-time image size is 7x9, which is sampled at point 75, 150 and 200 along the longitude direction (Fig.4). At the same time, the length of 64 grids of the real-time measurement sequence is created for the traditional TERCOM algorithm. The simulation experiments have been done for the proposed algorithm and the traditional TERCOM algorithm in the same environment based on Matlab 2010a respectively and the simulation results shown in Table 1.

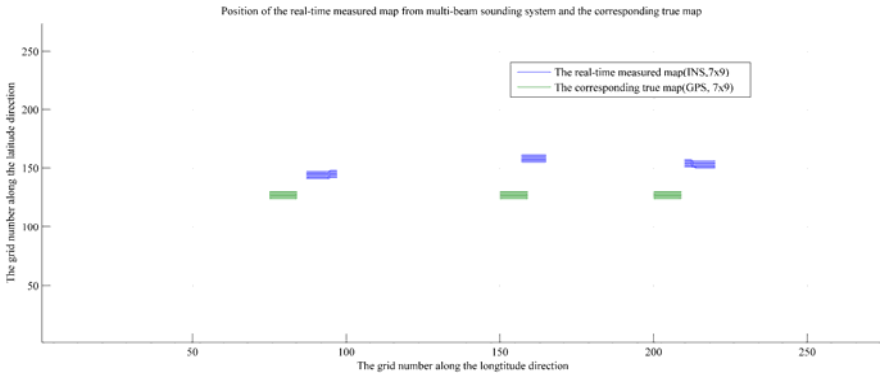


Fig. 4. Simulation measured real-time terrain map from the multi-beam swath

Table 1. A comparison of the new algorithm efficiency with TERCOM algorithm (Error unit: grid number, Running Time: s)

Real-time image	INS original error			Traditional TERCOM algorithm					Proposed algorithm				
	X	Y	R	X	Y	R	R%	Times	X	Y	R	R%	Times
Map75	12	18	21.6	6	7	9.2	42.6	3	1	2	2.2	10.2	7
Map150	7	31	31.7	11	9	14.2	44.8	3	1	4	4.1	12.9	6
Map200	10	27	28.8	13	13	18.4	63.9	3	1	3	3.2	11.1	7

The comparative result of the accuracy and running time between the proposed algorithm and the traditional TERCOM matching algorithm [2] is given in Table 1. As can be seen from Table 1, the proposed algorithm can acquire higher accuracy of the navigation and positioning for the underwater vehicle than that of the traditional method, the INS error is reduced to about 10% of the original error, especially in the case of large original error for INS (less than 3km) the accuracy is improved obviously. Meanwhile, the running time of the new algorithm is more than doubled, basically this can be ignored for the low speed underwater vehicle.

5 Conclusions

As the new method based on multi-beam sounding in UTAN take the phase correlation technique and Hu invariable moment feature of the image processing, it can acquire higher accuracy of the navigation and positioning for the underwater vehicle, the INS error has been reduced to about 10% of the original error, especially in the case of large original error (less than 3km) for INS the accuracy is improved obviously. Meanwhile, the running time of the new algorithm is more than doubled. The new method currently is based on the underwater topographic map grid to match, its matching accuracy also could be further improved using the sub-pixel image matching method, while its running time could be further reduced using the particle swarm optimization algorithm.

Acknowledgment. This work was financially supported by Natural Science Foundation of Shandong Province (Y2008G02), China National Natural Science Foundation (60972052), Scientific Research Foundation of Shandong Jianzhu University.

References

1. Li, L.: Recent status and development of Seabed terrain aided navigation technology. *Ship Electronic Engineering* 28(2), 17–21 (2008)
2. Nuqren, I., Jansson, M.: Terrain navigation for underwater vehicles using the correlated methods. *IEEE Journal Ocean Engineering* 29(3), 906–915 (2004)
3. Feng, Q.-T.: The research on new terrain elevation matching approaches and their applicability. A Doctoral Dissertation of National University of Defense Technology (2004)
4. Wang, K.-D., Chen, X.: Iterative closest contour point for underwater terrain aided navigation. *Journal of Astronautics* 27(5), 995–999 (2006)
5. Xu, Z.-Y., Yan, L., Liu, G.-J.: Study on comprehensive simulation technology for seabed terrain aided navigation. *Ship Science and Technology* 29(1), 123–128 (2007)
6. Xu, Z.-Y., Yan, L., Ning, S.-N.: Research on seabed terrain matching algorithm simulation based on Hausdorff distance. *Computer Engineering* 33(9), 7–9 (2007)
7. Zheng, T., Bian, S.-F., Wang, Z.-G.: The Terrain Matching Assistant Navigation Based on ICCP Algorithm. *Hydrographic Surveying and Charting* 28(2), 21–23 (2008)
8. Yuan, G.-N., Tan, J.-L., Yin, W.-W.: Seabed Terrain Aided Navigation Algorithm Based on Hybrid Particle Swarm Optimization. *Computer Simulation* 27(8), 122–126 (2010)
9. Yu, J.-H., Song, C.-L., Yan, L.: Digital Bathymetry and Correction Model for Multi-Beam Bathymetric Sonar System. *Acta Scientiarum Naturalium Universitatis Pekinensis* 44(3), 429–433 (2008)
10. Tang, C.-R.: Research on Multi-resolution Analysis and Recognition of Underwater Targets Acoustic Image. A Doctoral Dissertation of Harbin Engineering University (2009)
11. Zou, Y.-G., Zhai, J.-S., Liu, Y.-C., et al.: A Bottom Coverage Estimation Model Based on Trapezium for Multi-beam System. *Hydrographic Survey and Charting* 30(2), 15–18 (2010)
12. Zou, Y.-G., Zhai, J.-S., Liu, Y.-C., et al.: Analysis and Application of Echo Intensity Data in Simrad EM Multi-beam Sonar System. *Ocean Technology* 30(1), 48–51 (2011)

13. Samritjarapon, O., Chritsobhuk, O.: An FFT-Based technique and best-first search for image registration. In: 2008 International Symposium on Communications and Information Technologies, pp. 364–367 (2007)
14. Na, L.: Research on image matching and tracking. A doctoral dissertation of Xi'an Jiaotong University (2008)
15. Wu, G., Wu, C.-F., Hou, Q.-Y., et al.: Target location method based on invariable moment feature matching. *Optics and Precision Engineering* 17(2), 460–468 (2009)
16. Hu, M.K.: Visual pattern recognition by moment invariants. *IRET Transaction Information Theory, IT* 28, 179–187 (1962)
17. Chunhavittayatera, S., Chitsobhuk, O.: Image Registration using Hough Transform, Phase Correlation and Best-first search algorithm. In: The 2007 IAENG International Conference on Imaging Engineering, vol. 2, pp. 1898–1902 (2007)

Analysis of Singular Value under Kalman Filtering for Strapdown Inertial System Online Calibration

Guangtao Zhou¹, Jian Wang², and Kai Li¹

¹ College of Automation, Harbin Engineering University, No.145, Nantong Street 150001
Harbin, China

² Tianjin Navigation Instruments Research Institute, No. 268, Dingzigu Yihao Lu, 300131
Tianjin, China
waterlikai@163.com

Abstract. The observability of the system states are the key indexes to check the convergence accuracy and convergence speed of designed Kalman filter. First of all, the error dynamic system equation and observation equation of strapdown inertial navigation system (SINS) online calibration are described in this paper, and then the system can be demonstrated to meet the law of piece-wise constant system (PWCS). Finally, the singular value of the system states based on the singular value decomposition, which provides the necessary foundation of online calibration, are described.

Keywords: SINS, online calibration, observability, singular value.

1 Introduction

In order to improve the accuracy of inertial navigation systems, inertial system errors which mainly come from inertial sensors, need to be precisely calibrated. For the navigation error caused by marine SINS inertial sensors, using GPS to get the speed and position measurement information to calibrate the SINS navigation system error with the mobility of ship itself. Thus, it can provide the accurate error factor and attitude of inertial navigation device for the follow-up navigation. Therefore, it is increasingly important for the method of online calibration in practical application.

In this paper, taking the ship SINS for example, the dynamic model and observation equation were experienced, and the "speed + location" method of measuring information were used to analyze considerable measure of system. These studies will provide the improvement of online calibration.

2 Establishment of the Equation of State and Measurement

2.1 Selection of System State Variables and Error Equation

According to the error characteristics of SINS long-time work to choose the speed error, position error, misalignment angle, gyro drift, accelerometer zero bias as the state variable:

$$X(t) = \left[\phi_x \quad \phi_y \quad \phi_z \quad \delta V_x \quad \delta V_y \quad \delta L \quad \delta \lambda \quad \varepsilon_x \quad \varepsilon_y \quad \varepsilon_z \quad \nabla_x \quad \nabla_y \right]$$

Where, ϕ_x, ϕ_y, ϕ_z are east, north, heading angle; $\delta V_x, \delta V_y$ are east, north speed error; $\delta L, \delta \lambda$ are the latitude, longitude error; $\varepsilon_x, \varepsilon_y, \varepsilon_z$ are the gyroscope zero drift; ∇_x, ∇_y are the accelerometer bias.

Aftertaking into account the impact on the system comes from the error, the system error equations are listed as follows.

Platform misalignment angle error equation is:

$$\begin{aligned} \dot{\phi}_E &= -\frac{\delta V_N}{R} + (w_{ie} \sin L + \frac{V_E}{R} \tan L) \phi_N - (w_{ie} \cos L + \frac{V_E}{R}) \phi_U + C(1,1)\varepsilon_x + C(1,2)\varepsilon_y + C(1,3)\varepsilon_z \\ \dot{\phi}_N &= \frac{\delta V_E}{R} - w_{ie} \sin L \delta L - (w_{ie} \sin L + \frac{V_E}{R} \tan L) \phi_E - \frac{V_N}{R} \phi_U + C(2,1)\varepsilon_x + C(2,2)\varepsilon_y + C(2,3)\varepsilon_z \\ \dot{\phi}_U &= \frac{\delta V_E}{R} \tan L + (w_{ie} \cos L + \frac{V_E}{R} \sec^2 L) \delta L + (w_{ie} \cos L + \frac{V_E}{R}) \phi_E + \frac{V_N}{R} \phi_N + C(3,1)\varepsilon_x + C(3,2)\varepsilon_y + C(3,3)\varepsilon_z \end{aligned} \quad (1)$$

Speed error equation is:

$$\begin{aligned} \delta \dot{V}_E &= f_N \phi_U - f_U \phi_N + (V_N \tan L / R) \delta V_E + (2w_{ie} \sin L + V_E \tan L / R) \delta V_N \\ &\quad + (2w_{ie} \cos L V_N + V_N V_E \sec^2 L / R) \delta L + C(1,1)\nabla_x + C(1,2)\nabla_y \\ \delta \dot{V}_N &= f_U \phi_E - f_E \phi_U - 2(w_{ie} \sin L + V_E \tan L / R) \delta V_E - (2w_{ie} \cos L + \\ &\quad V_E \sec^2 L / R) V_E \delta L + C(1,1)\nabla_x + C(1,2)\nabla_y \end{aligned} \quad (2)$$

Position error equation is:

$$\begin{aligned} \delta \dot{L} &= \frac{\delta V_N}{R} \\ \delta \dot{\lambda} &= \frac{\delta V_E}{R} \sec L + \frac{V_E}{R} \sec L \tan L \delta L \end{aligned} \quad (3)$$

Among them, $C(i, j)(i, j = 1, 2, 3)$ are attitude matrixes for the corresponding elements, $w_i (i = x, y, z)$ are angular velocity of movement of ship, $f_i (i = x, y)$ are the accelerometer output.

2.2 Selection of Kalman Filter Equations

Suppose the system state equation is:

$$\begin{aligned} \dot{X}(t) &= A(t)X(t) + W(t) \\ Z(t) &= H(t)X(t) + V(t) \end{aligned} \quad (4)$$

Where, $A(t) = \begin{bmatrix} A_{3 \times 3} & B_{3 \times 2} & C_{3 \times 2} & D_{3 \times 3} & 0_{3 \times 2} \\ E_{2 \times 3} & F_{2 \times 2} & G_{2 \times 2} & 0_{2 \times 3} & J_{2 \times 2} \\ 0_{2 \times 3} & K_{2 \times 2} & M_{2 \times 2} & 0_{2 \times 3} & 0_{2 \times 2} \\ 0_{3 \times 3} & 0_{3 \times 2} & 0_{3 \times 2} & 0_{3 \times 3} & 0_{3 \times 2} \\ 0_{2 \times 3} & 0_{2 \times 2} & 0_{2 \times 2} & 0_{2 \times 3} & 0_{2 \times 2} \end{bmatrix}$ is the system vector matrix, $W(t)$ is the system noise matrix, $V(t)$ is the GPS velocity and position measurement noise vector, select $Z(t) = [dV_E^T \ dV_N^T \ dL^T \ d\lambda^T]^T$ as the measurement vector, so $H(t) = \begin{bmatrix} 0_{3 \times 3} & I_{2 \times 2} & 0_{2 \times 2} & 0_{2 \times 3} & 0_{2 \times 2} \\ 0_{2 \times 3} & 0_{2 \times 2} & I_{2 \times 2} & 0_{2 \times 3} & 0_{2 \times 2} \end{bmatrix}$ is the measurement matrix.

3 Certification of the SINS Online Calibration Principle to Meet the PWCS

We can see from the chapter 2, state equation and measurement equation of SINS online calibration are time varying. The PWCS used to analyze systematic observations, so that the considerable measure of the state of the system will be ensured in further. The corresponding homogeneous segmented system state equation and measurement equation of online calibration are:

$$\begin{aligned} \dot{X}(t) &= A(t)X(t) \\ Z(t) &= H(t)X(t) \end{aligned} \tag{5}$$

While the system state variables $\delta V = [\delta V_E \ \delta V_N]^T$ expanded to $\delta V = [\delta V_E \ \delta V_N \ 0]^T$, $\delta p = [\delta L \ \delta \lambda]^T$ expanded to $\delta p = [\delta L \ \delta \lambda \ 0]^T$, $\nabla = [\nabla_x \ \nabla_y]^T$ expanded to $\nabla = [\nabla_x \ \nabla_y \ 0]^T$, then $X(t)$ and $H(t)$ be column transformed as:

$$X(t) = [\delta v^T \ \delta p^T \ \phi^T \ \epsilon^T \ \nabla^T]^T, \quad H(t) = \begin{bmatrix} I_{3 \times 3} & 0_{3 \times 3} & 0_{3 \times 3} & 0_{3 \times 3} & 0_{3 \times 3} \\ 0_{3 \times 3} & I_{3 \times 3} & 0_{3 \times 3} & 0_{3 \times 3} & 0_{3 \times 3} \end{bmatrix}, \quad Z(t) = [dv^T \ dp^T]^T$$

The corresponding change in the vector-matrix system:

$$A(t) = \begin{bmatrix} B & C & A & D & 0 \\ F & G & E & 0 & J \\ K & M & 0 & 0 & 0 \\ 0 & 0 & 0 & 0 & 0 \\ 0 & 0 & 0 & 0 & 0 \end{bmatrix} \text{ This can be defined as: } \tilde{Q}_j = \begin{bmatrix} H \\ HA \\ HA^2 \\ \vdots \end{bmatrix} = \begin{bmatrix} I & 0 & 0 & 0 & 0 \\ 0 & I & 0 & 0 & 0 \\ B & C & A & D & 0 \\ F & G & E & 0 & J \\ \vdots & \vdots & \vdots & \vdots & \vdots \end{bmatrix}$$

Change \tilde{Q}_j in the implementation of elementary column is to be

$$\tilde{Q}_j = \begin{bmatrix} I & 0 & 0 & 0 & 0 \\ 0 & I & 0 & 0 & 0 \\ 0 & 0 & A & D & 0 \\ 0 & 0 & E & 0 & J \\ \vdots & \vdots & \vdots & \vdots & \vdots \end{bmatrix} \tag{6}$$

As the primary change will not change the matrix of the zero space, so $null(\tilde{Q}'_j) = null(\tilde{Q}_j)$. According to the definition of the zero space matrix can know that for any nonzero vector Y , if $Y \in null(\tilde{Q}'_j)$, Then there

$$\tilde{Q}'_j Y = 0 \tag{7}$$

Where there are $Y = [y_1^T \ y_2^T \ y_3^T \ y_4^T \ y_5^T]^T$. The joint (6) and (7) can infer

$$\begin{cases} y_1 = 0 \\ y_2 = 0 \\ A \cdot y_3 + D \cdot y_4 = 0 \\ E \cdot y_3 + J \cdot y_5 = 0 \end{cases} \tag{8}$$

If Y is a Iso part of $A(t)$ of zero space vector, the same

$$AY = \begin{bmatrix} B \cdot y_1 + C \cdot y_2 + A \cdot y_3 + D \cdot y_4 \\ F \cdot y_1 + G \cdot y_2 + E \cdot y_3 + J \cdot y_5 \\ K \cdot y_1 + M \cdot y_2 \\ 0 \\ 0 \end{bmatrix} \tag{9}$$

Alliance (8) and (9), taking into $y_4 \ y_5$ as small error, you can draw $AY = 0$. Thus $Y \in null(A)$, therefore, $null(\tilde{Q}_j) = null(A)$ established, thus proving the strap-line calibration system meet the theorem PWCS[1].

4 Singular Value Analysis of the "Speed + Position" SINS Online Calibration

Set the swing amplitude of pitch axis, roll axis and heading axis in the movement are respectively 2° , 2° , 4° , and the latitude $L = 45.78^\circ$, longitude $\lambda = 126.67^\circ$. To decompose the system, there be twelve singular values. 12 singular values were calculated corresponding to the initial value of state variables and draw the table, you can get the observability of the state variables.

Path one: North along the hull at the speed of 15m/s

Path two: East along the hull with a constant acceleration of 0.2g

Path three: North along the hull with a constant acceleration of 0.2g
 Path four: Along the hull with $4^\circ/s$ angular velocity and along the keel with 10m/s speed to the circular motion.

Table 1. The comparison of singular value in different path

Singular value	Path one	Path two	Path three	Path four
ϕ_x	17.78	17.85	17.86	16.98
ϕ_y	17.78	17.86	17.85	16.98
ϕ_z	5.26e-6	1.38e-4	1.38e-4	2.50e-5
δV_x	1	1	1	1
δV_y	1	1	1	1
δL	1	1	1	1
$\delta \lambda$	1	1	1	1
ϵ_x	2.06	2.68	2.67	2.75
ϵ_y	2.06	2.67	2.68	2.75
ϵ_z	2.30e-3	2.30e-3	2.30e-3	4.73e-3
∇_x	4.29e-8	4.27e-3	4.27e-3	0.068
∇_y	4.29e-8	4.27e-3	4.27e-3	0.068

We can know from the table above that: the singular value of δV_x δV_y δL $\delta \lambda$ are 1. Look at path one, the singular value of ϵ_z 、 ϕ_z are relatively low, but ∇_x 、 ∇_y are not observed. In the path two and three, it may improve the singular value of observations of the system. Because there are changes in both the change of force and in the attitude matrix. In the path four, singular value of state variables is higher than the motion conditions of simple change and simple lines. In conclusion, velocity with the external components and position information is fully observed, which can be a considerable higher measure, estimation accuracy of the Kalman filter of these state will be higher; It should also be noted that, the mobility of the hull has a greater impact on the considerable measure of system states, even the singular value information of system status with direct external measurement may be different at different times.

5 Conclusion

In SINS online calibration, the observability is important indicator of online calibration. In order to be able to achieve better calibration accuracy in a valid path, singular value of dynamic decomposition should be used to provide the plenty basis of improving the accuracy of estimates of Kalman filtering. An effective method to determine considerable measure of the state would be like this: based on observation of the dynamic system matrix singular value decomposition, fitting for the fully observed and un-fully observed systems. This paper provides a necessary foundation of the observability decomposition and error estimates of the online calibration.

References

1. Shuai, P., Chen, D., Jiang, Y.: A Method of the Observable Degree Analysis of Integrated GPS/SINS Navigation System. Chinese Space Science and Technology (1) (February 2004)
2. Lu, Z.-D., Wang, L.: In-flight calibration method for SINS. Journal of Chinese Inertial Technology 15(2) (April 2007)

Design of Automatic Block Section Signalling Layout of Applying Chaos Embedded Particle Swarm Optimization Algorithm Based on Skew Tent Map

Hua Rong

School of Railway Transportation, Shanghai Institute of Technology,
Shanghai 200235, China
huarong326@sina.com

Abstract. This paper analyzes the objectives and related factors in detail and presents an optimization model with two different objectives. In order to work out an efficient signalling layout scheme in combination with the practices of present railway line design, the paper discusses the steps of computer-based signalling layout optimization and the method to solve the model with the chaos embedded particle swarm optimization algorithm combined with STM (STMCP SO). Case study of signaling layout design of an existing railway line is conducted. The results demonstrate that using the STMCP SO to solve the optimization problem of signalling layout design is practicable, and this system is able to work out a satisfactory signalling layout scheme to promote the efficiency and quality of signaling layout design without any manual interference.

Keywords: Railway communication and signaling, Signalling layout, Block section, Chaos embedded particle swarm optimization, Train movement simulation.

1 Introduction

The design of automatic block sections is to determine the numbers and specific location of the pass signalling layout in each automatic block section, and seek safe, efficient and economical layout of the scheme in order to effectively organize train. At present the study to different signal display formats and to train impact in the domestic and foreign is more, while the study to solve the railway block section optimization problem is relatively less. Gill and Goodman etc. [1] proposed a heuristic ramp searching algorithm, and used it to solve the block section optimization problem of the subway system. C. S. Chang and others [2,3] applied the genetic algorithm and DE (Differential Evolution) algorithm based on Gill's study to optimize the subway system signalling layout design. The literature [4] introduced the method of manual block signalling layout in train movement hour curve. At present this problem on the research and application at domestic and foreign exist mainly following insufficient. (1) Foreign scholars once have studied the block section optimization of the urban rail transit system, but have not involved the trunk railway, because the constraint conditions of the trunk railway to be considered are even more and more complex

than the constraint conditions of the urban rail transit system to the block section optimization. (2) These current studies are mainly based on experience qualitative analysis, most solutions have simulated the experience of manual block layout design and have not analyzed systematically the goals and constraint conditions to the block section optimization.

In this paper, the optimization model of block signalling layout problem with two different strategies target has been established on the basis of analysis of various influencing factors, and the chaos embedded particle swarm optimization combined with STM (STMCP SO) algorithm to solve this model is discussed. Comparing with C. S. Chang and others' DE algorithm, the results indicate that the method of railway block section optimization design based on STMCP SO algorithm has a bigger superiority, and can obtain a good block section optimization plan with no human intervention, and is suitable to develop the block section optimization software system.

2 Objectives and Impact Factors of Block Section Optimization

2.1 Objectives of Block Section Optimization

The railway block section optimization is a much more complex and multi-objective constrained optimization problem which requires as much as possible to achieve better results on the basis of meeting necessary constraint conditions. These multi-objectives include:

- (1) Security. Ensuring the train movement security is the most important objective of railway signal system.
- (2) Efficiency. This is another important factor to be considered for the design work and train operating organization.
- (3) Economy. This is an important criterion for the design work, because the investment in equipment is required, but the block signalling layout scheme should take into account the number of equipment.

The above objectives are mutually influenced and mutually restricted. To ensure trains having the higher movement efficiency in automatic block section system will have to reduce unnecessary safety margins and have to increase equipment investment.

2.2 Impact Factors of Block Section Optimization

There are many impact factors of the railway block section layout. These impact factors mainly include:

- (1) Train emergency braking distance. To ensure the security of train movement, the train must be able to parking in front of the ban signaling, that is, the train can not advance recklessly the signal in any case.
- (2) Signal display formats. Signal display formats will affect the least number of block section and the track train interval between trains, as well as the block section number required to meet the train braking distance.
- (3) Track circuit length. Limit length of the track circuit is an important factor to affect the length of block section, etc.

3 Optimization Model

3.1 Variables Definition

What the block section optimization problem must solve is to obtain the signalling layout numbers in automatic block section N_{signal} and the specific location of each signalling $X_i (i=1, 2, \dots, N_{signal})$. Setting up two stations A and B, the outbound signalling location of A station is X_0 , and the stop signalling location of B station is $X_{N_{signal}+1}$, the number of block section is $N_{section}$, Then the block section length is $L_i = |X_i - X_{i-1}| (i=1, \dots, N_{section}; N_{section} = N_{signal} + 1; X_{i-1} < X_i)$. Figure 1 describes the above variables definition.

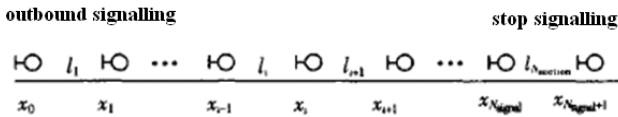


Fig. 1. The variables definition description

3.2 Objective Function

To meet the different application objectives, this paper proposes two kinds of objective strategies:

(1) Efficiency strategy. That is, as far as possible, it seeks the smallest track train interval time, so as to get the maximum through capacity. Its objective function is

$$f = \min \max(I_1, I_2, \dots, I_k) \tag{1}$$

Where, I_k is the track train interval time. To the four shows automatic block, the track train interval time usually in the situation needs to be separated by at least 4 block sections. In this case:

$$I_k = 0.06 \frac{l_k + l_{k+1} + l_{k+2} + l_{k+3} + l_{train}}{v} \tag{2}$$

Where, l_{train} is the train length, v is the train movement speed. To the four shows automatic block, $\max(I_1, I_2, \dots, I_k)$ is expressed as the maximum of I_k calculated which the train moves from outbound signalling until to $k+3$ that coincides with the stop signaling. Coefficient of 0.06 is produced in conversion from the km / h to the m / min.

(2) Economy strategy. That is, under meeting certain efficiency (satisfying the track train interval time H that is given) premise, it is as far as possible to pursue the plan having the least signalling numbers, its objective function is:

$$\min N_{signal} \tag{3}$$

3.3 Constraint Condition

Defining the constraint conditions of above two objective functions as follows:

$$l_{\min} \leq l_i \leq l_{circuit} \tag{4}$$

$$l_i \geq \max S_b(v_i, v_{i+1}, i_j) + S_0(v_0) \tag{5}$$

$$\sum_{i=1}^{N_{section}} l_i = |X_{n+1} - X_0| \tag{6}$$

$$\left[\frac{|X_{n+1} - X_0|}{l_{circuit}} \right] \leq N_{signal} \leq \left[\frac{|X_{n+1} - X_0|}{l_{\min}} \right] - 1 \tag{7}$$

‘Economy strategy’ needs also to meet:

$$l_k \leq H \tag{8}$$

In above constrain conditions, l_{\min} is the smallest length of block sections provided in ‘Railway technology management procedures’ or determined by the engineering design personnel according to the scene actual situation, $l_{circuit}$ is the track circuit limit length, $\max S_b(v_i, v_{i+1}, i_j)$ represents a maximum braking distance that is required at the brake start of X_{i-1} place from any higher speed grade to a adjacent lower speed grade. There are $N-1$ speed grades for automatic block system of $N(N \geq 4)$ shows. $S_0(v_0)$ is a outlook signal distance required by drivers (Generally takes 50 m). $|X_{n+1} - X_0|$ is a section length from the outbound signalling of A station to the stop signalling of B station between A station and B station. The formula (7) specifies a value range of signaling frame numbers N_{signal} . In addition to above constraint conditions, it is necessary to consider the factors that are difficult to quantify, such as the description in 1.2.

The above mathematical model is very difficult to find the effective optimization method to its solution, this paper uses adaptive chaos embedded particle swarm optimization algorithm to solve this problem.

4 Chaos Embedded Particle Swarm Optimization Algorithm of Model Solution

4.1 Chaos Embedded Particle Swarm Optimization Combined with STM (STMCP SO) Algorithm

In this paper, an chaos embedded particle swarm optimization combined with STM (STMCP SO) algorithm is used. In addition to initialize particle’s position and velocity

using chaotic variables in order to improve population’s diversity and ergodicity, the STMCP SO algorithm embeds chaotic variables with chaotic ergodic mechanism into the parameters of PSO algorithm, namely, it uses different random sequences to substitute separately random parameters r1 and r2 of PSO algorithm, so that chaotic variables generate random numbers which the PSO algorithm needs in each algorithm iteration. The particle velocity iterative formula of the STMCP SO algorithm can be expressed as:

$$v_{i,j}(t+1) = CF_1 v_{i,j}(t) + c_1 CF_{2,j}(t) [pbest_{i,j}(t) - x_{i,j}(t)] + c_2 CF_{3,j}(t) [gbest_{i,j}(t) - x_{i,j}(t)] \tag{9}$$

where, CF1 and CF2 are functions of chaotic variable map value, which have substituted the random numbers r1 and r2 of PSO algorithm. The chaotic search mechanism and the early-maturing judgment mechanism of STMCP SO algorithm is mainly reflected in the following: In addition to chaotic variables being used to initialize particle’s position and velocity, the three chaotic variables (CF1、CF2 and CF3) are applied to randomly generate chaos random values in each iteration optimization process in order to improve the population diversity and ergodicity, and avoid falling into local minima. According to the maximum inertia weight wmax and minimum inertia weight wmin, this paper designs the following formula:

$$CF_1 = \frac{w_{max} - w_{min}}{2} X_n + \frac{w_{max} + w_{min}}{2}, \quad n = 0 \downarrow 2 \dots \tag{10}$$

The chaotic random sequence values produced by CF1 are scaled to the values range of inertia weight.

4.2 Basic Operational Design

(1) Determining signalling numbers.

According to equation (7), listing optional signalling number range on line, and choosing a reasonable signalling number, this is also a necessary condition to determine the particle dimension of each signaling.

(2) Generating initial population.

To make the search space favor in feasible solution, the each dimension search range is restricted. The *i* is defined as *i*-th signaling on line, $X_{Low}(I,i)$ and $X_{up}(I,i)$ are constraint conditions in the range can be searched to each signalling position, where, *p* is the dimension, and *fLag* is the best location mark of population. The lower limit and upper limit values of the position range of signalling particles are initialized to 300, the particle velocity *veLoeity*(1, *i*) is initialized, the best historical position *Xbest*(1, *i*) of signalling particles is initialized, the best global position of signalling particles *PartieLes*(*fLag*, 1) is initialized.

(3) Defining the fitness function.

The definition of fitness function is directly related whether the STMCP SO is able to eventually converge to the optimal solution.

This paper defines three fitness functions, are as follows: Signalling numbers is situated generally between maximum number and minimum number, its fitness function is $fiiness=1/prod(I)$.

The efficiency strategy is to pursuit the train track time interval as far as possible in order to get the maximum through capacity, and its fitness function is $fitness = l / (1 + s * f(l, i))$.

In formula, $s = \sum fit A$, where, fit A is a processing function for the section length which is divided out.

The economy strategy is to pursuit methods of the least signalling number as far as possible under meeting the certain efficiency premise that is to meet a given train track interval time H, its fitness function is $fitness = l / (1 + s * f(l, i) * fit B)$.

5 Example Simulation

The station A and the station B is selected as a section to arrange through signalling, the outbound signalling location of the station A is set to 0km, and the stop signaling location of the station B is set to 15 km, so the section length is 15km. according to automatic block arrangement of the four display, and train length is 800 m, the train average movement speed in the section is set to 100km / h, the minimum length of block section is set to 1000m, the maximum length of block section is set to 1400m. In order to analyze results easily, the interval is assumed to have only an average slope (this example is 3 ‰). According to a large number of test calculations and result analysis, In this example, initial population is set to 20 and the optimization time is set to 10 and the maximum iteration number of each time is set to 250 time for getting the best optimization output result. Figure 2 and figure 3 show respectively the average fitness of the algorithm and the optimal fitness trends in two kinds of strategy situations. In the figure, the solid line is the average fitness and the dotted line is the best fitness.

5.1 Economy Strategy

Table 1. The continuous layout position of economy strategy

serial number	1	2	3	4	5
line position/km	1000	2200	3600	4925	6211
type	outbound	passing	passing	passing	passing
6	7	8	9	10	11
7600	8866	10155	11550	12800	14000
passing	passing	passing	passing	passing	stop

n=11, the final determine tracking interval time: Iz=4.1000

5.2 Efficiency Strategy

From Fig. 2 and Fig.3, with the iteration number increasing, the population average fitness and the best fitness decrease in continuous.

Table 2. The continuous layout position of efficiency strategy

serial number	1	2	3	4
line position/km	1000	2480	4100	5710
type	outbound	passing	passing	passing
5	6	7	8	9
7310	9010	10620	12385	14000
passing	passing	passing	passing	stop

n=9, the final determine racking interval time: Iz=4.85

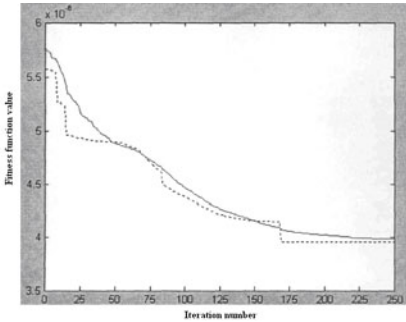


Fig. 2. Economy strategy

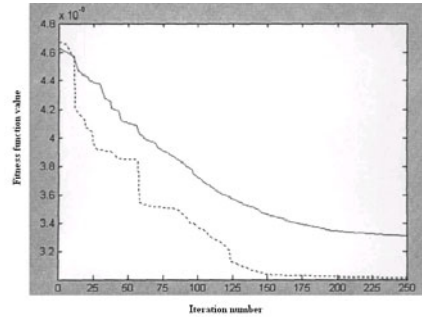


Fig. 3. Efficiency strategy

5.3 Comparison of the STMCP SO Algorithm and the DE (Differential Evolution) Algorithm

To further compare the performance of STMCP SO algorithm and the DE algorithm in railway block section optimization design, Fig. 4 draws the optimizing curve which compares the STMCP SO algorithm with DE algorithm when dimensions is 20 and particles is 40.

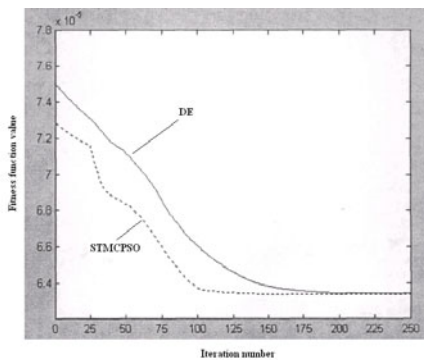


Fig. 4. The optimizing curve which compares the STMCP SO with DE

In Fig. 4, the horizontal axis shows the optimization iteration number, and the vertical axis shows the logarithm of fitness value (that is the logarithm of global minimum value given from each search). As can be seen from Fig.4, the convergence rate of STMCP SO algorithm is generally higher than that of DE algorithm, which is because the STMCP SO algorithm has increased chaotic multiple search mechanisms that can avoid premature, so the global optimization capabilities have been enhanced.

6 Conclusion

In this paper, the STMCP SO algorithm is applied to solve the signalling layout problem. (1) According to the practice of automatic block section design, this paper has proposed two different signalling layout optimization strategies. (2) Applying the STMCP SO algorithm to solve the signalling layout problem, this paper illustrates that the STMCP SO algorithm may be easier to achieve the optimal goal and meet different constraint conditions, and illustrates it is effective to solve this problem through case studies. (3) Comparing the performance of STMCP SO algorithm and DE algorithm in railway block section optimization design, the results show that the convergence speed of STMCP SO algorithm is superior to DE algorithm.

Acknowledgments. This work is supported by Shanghai Education Committee Science and Technology Foundation (11YZ228) and key project of Shanghai Education Committee Science and Technology Foundation (12ZZ191), China.

References

1. Milroy, I.P.: Aspects of Automatic train control. Loughbrough University, Australia (1990)
2. Chang, C.S., Sim, S.S.: Optimising train movements through coast control using genetic algorithms. IEE Proceedings Online no.19970797, IEE Proc. Electr. Power Appl. 144(1), 65–73 (1999)
3. Chang, C.S., Xu, D.Y.: Differential Evaluation based tuning of fuzzy automatic train operation for mass rapid transit system. IEE Proc. Electr. Power Appl. 143(3), 206–212 (2005)
4. Han, S.-H., Byen, H.-S., Baek, J.-H., An, T.-K., Lee, S.-G., Park, H.-J.: An optimal automatic train operation (ATO) Control using genetic algorithms (GA). In: 2003 IEEE TENCON, pp. 360–362 (2003)
5. Gill, D.C., Goodman, C.J.: Computer-Based Optimisation Tecluilque for Mass Transit Rail way Signaling Design. IEE Proc.-B 139(3), 261–275 (1998)
6. Chang, C.S., Du, D.: Improved Optimisation Methad Using Algorithms for Mass Transit Signal Ling Block-Lay-out Design. Proc. Electr. Power Appl. 45(3), 266–272 (2006)

Tourism Demand Forecast and Analysis to Shanxi Based on SVM

Jinling Guo

Department of Information and Engineering, Business College of Shanxi University,
Taiyuan 030031, China

Abstract. This paper intends to present a new support vector machine (SVM) model based on statistical learning theory at the small samples and complicated effect factors in Shanxi tourism demand data, at last, countermeasures are analyzed. Experimental results showed that SVM model used time series data outperforms traditional models.

Keywords: Support vector machine, tourism demand, forecast.

In the past 10 years, the tourism in Shanxi is rapidly developed. The revenue of the tourism is 58.16 billion Yuan in the year of 2007. It is equivalent to 10.2% of GDP. In the year of 2008, the gross income in tourism is 73.93 billion Yuan. It is equivalent to 10.7% of GDP. The tourism industry in the national economy becomes more and more important, it has become a pillar industry of Shanxi economy. Therefore, it is of great significance to establish tourism development strategy according to the reasonable forecast for Shanxi tourist demand.

At present, the forecast methods for tourism demand are mainly statistical methods and the neural network method. The statistical data of tourism in Shanxi Province exist small sample, relevant factors of complex situation. It brings more difficult to scientific and accurate prediction.

In this paper, the tourism demand forecasting model is set up by using Support Vector Machine (SVM). The model is applied in Shanxi tourism demand forecasting and for small sample of time series data processing. The influence factor to consider the complex problem is avoided.

1 SVM Theory

SVM is a kind of method based on statistical learning theory by Vapnik[1], through the structural risk minimization principle to improve the generalization ability. It can well solve the small sample, nonlinear, high dimension practical problems. It has set up a wide range of applications[2-4] such as the function approximation, a file in the financial time series analysis and prediction on the field.

SVM is based on the thought: first choose a nonlinear mapping $\phi(x)$, put n dimension sample vector $(x_1, y_1), \dots, (x_l, y_l) \in \mathbb{R}_n * \mathbb{R}$ from the original space mapping to character space, and structure the optimal linear decision-making function $y=f(x) = wT\phi(x)+b$, using the structural risk minimization principle. The high point of the

product in the feature space is replaced by using the original space kernel function of $K(x, y) = \langle \varphi(x), \varphi(y) \rangle$, to avoid the complex operation calculation.

For standard SVM, optimization problem is

$$\min \frac{1}{2} \|w\|^2$$

Subject to (for any $i=1,2,\dots,n$)

$$y_i [w \cdot x - b] \geq 1 \tag{1}$$

The optimization problem is worked out by solving Lagrange function of saddle points.

$$L(w, b, a) = \frac{1}{2} (w \cdot w) - \sum_{i=1}^l \alpha_i \{ [(x_i \cdot w) - b] y_i - 1 \} \tag{2}$$

A and b values are worked out By the least square method. So fitting function is:

$$f(x) = \sum_{i=1}^l \alpha_i K(x_i, x) + b \tag{3}$$

2 The Design of Tourism Demand Forecast Model in Shanxi Province Based on SVM

In this paper, the statistical data comes from the Shanxi statistics yearbook [5], including the domestic and international tourist visitors in the years of 2000-2002, 2004-2009.

In the paper, SVM is used to tourism forecast. Future value is estimated according to the past and current observations. It actually is to assume that there is a certain determined function between the future value and the past. In that moment, the $y(t-2)$, $y(t-1)$ and $y(t)$ are known, the requirement data $y(t+1)=f(y(t), y(t-1), y(t-2))$ is counted. In the experiment, data sequences $y(t-2)$, $y(t-1)$ and $y(t)$ are input, the predicted data $y(t+1)$ is output after SVM processing.

3 Prediction Experiment

In the experiment to predict domestic and foreign tourists, six training data and three test data are selected, using SVM method and neural network method respectively. To compare the result of prediction, the introduction of error index is as follows:

$$\text{Mean Absolute Percentage Error(MAPE)} = \frac{\sum_{i=1}^N \frac{|X_i - Y_i|}{Y_i}}{N} \times 100 \%$$

$$\text{Mean relative error square roots(MRESR)} = \sqrt{\frac{1}{N} \sum_{i=1}^N \left\{ \frac{X_i - Y_i}{Y_i} \right\}^2}$$

$$\text{Equal coefficient(EC)} = 1 - \frac{\sqrt{\sum_{i=1}^N (X_i - Y_i)^2}}{\sqrt{\sum_{i=1}^N X_i^2 + \sum_{i=1}^N Y_i^2}}$$

Among them, X_i represents the simulation output, Y_i is the actual visits.

The experimental effect using SVM method to forecast is shown in figure 1 and figure 2. The x axis is corresponding to the corresponding years (years of 2000 to 2002, 2004 to 2009) according to order, and the y axis is the corresponding tourism number (unit: ten thousand people). The circles are the result of the test data.

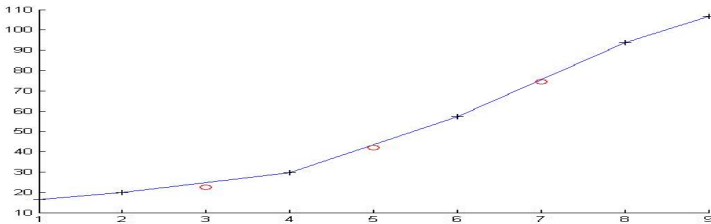


Fig. 1. Using SVM for domestic tourism demand forecasting

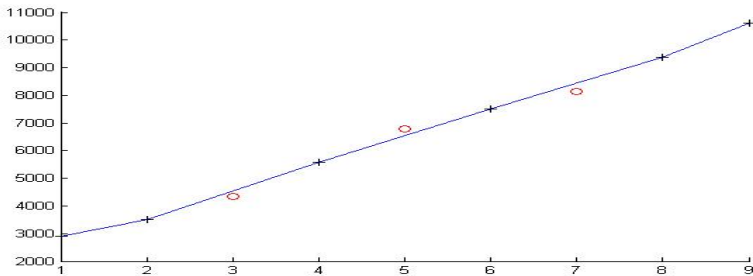


Fig. 2. Using SVM for foreign tourism demand forecasting

The experimental effect using neural network method to forecast is shows as table 1 and table 2.

Table 1. Using neural network method for domestic tourism demand forecasting Training data set as follows (unit: ten thousand people)

2000	2001	2004	2006	2008	2009
2904.8	3510	5538	7517	9383	10600

Result as follows(unit: ten thousand people) :

Year	2002	2005	2007
Practical value	4539	6545	8529
Predicted value	4468	6478	8620

Table 2. Using neural network method for international tourism demand forecasting Training data set as follows (unit: ten thousand people)

2000	2001	2004	2006	2008	2009
16.5	19.8	29.6	57.4	93.9	106.8

Result as follows(unit: ten thousand people) :

Year	2002	2005	2007
Practical value	24.8	42.1	73.8
Predicted value	22.5	40.7	76.1

Experimental results comparisons of the two methods are such as table 3 and table 4.

Table 3. The precision comparison of the domestic tourism demand forecasting

Prediction model	MAPE (%)	MRESR	EC
Neural network	10.60	0.83	0.926
Standard SVM	7.85	0.76	0.947

Table 4. The precision comparison of the international tourism demand forecasting

Prediction model	MAPE (%)	MRESR	EC
Neural network	10.89	0.156	0.920
Standard SVM	8.14	0.098	0.963

4 Conclusion

In the domestic tourism demand forecast, the use of SVM method is still made of high precision (MAPE = 7.85%), and the use of neural network model get MAPE = 10.60%. In the international tourism demand forecast, using SVM is made of high precision, and it is better than the neural network model, although the international tourism market is affected by many complex factors.

The simulation results show that SVM has the very good generalization performance. Therefore, SVM method has a lot of potential application in tourism demand analysis and prediction.

References

1. Vapnik, V.: *The Nature of Statistical Learning Theory*. Springer Verlag Press, New York (1995)
2. Gavin, C., Nicola, T.: Efficient leave-one-out cross-validation of kernel fisher discriminant classifiers. *Pattern Recognition* 11, 2585–2592 (2003)
3. Smola, A., Schölkopf: Linear programs for automatic accuracy control in regression. In: *Proceeding of the 9th International Conference on Artificial Neural Networks*, pp. 575–580. Springer, Berlin (1999)
4. Wang, W.J., Xu, Z.B., Lu, W.Z., Zhang, X.Y.: Determination of the spread parameter in the Gaussian kernel for classification and regression. *Neurocomputing* 55(3-4), 643–663 (2003)
5. *Statistics in Shanxi Province*. Shanxi Statistics Yearbook. China statistical publishing house, Beijing (2000-2009)

A Divide and Conquer Approach for Obstacles Surpassing of a Legged Robot

Antonio Bento Filho¹, Paulo Faria S. Amaral², and Benedito G. Miglio Pinto²

¹ Mechanical Eng. Department, Federal University of Espírito Santo, Vitória, Brazil
abento@ele.ufes.br

² Automatica Tecnologia S/A, Serra, ES, Brazil
pfsamaral@automatica.com.br, bmiglio@automatica.com.br

Abstract. Small obstacles are difficult to be detected and having their position precisely established from vision or other stereo obstacle detecting systems thus needing to be treated locally by the robot legs and foot. This work deals with the obstacle overcoming and curved walking capabilities of a four legged walking robot. Obstacle overcoming and avoidance is done using only information from contact sensors installed on the robot's feet. A divide and conquer approach was used to get over known obstacles. Obstacles considered are going a step up and down, going ramp up and down and overcoming a channel. Results include integrated movement sequence to go one step up in the floor.

Keywords: Obstacle, legged robot, mobile robot, robot, anthropomorphic.

1 Introduction

There has been great effort in studying mobile robots that use legs as their locomotion system. However, at the same time, legs pose a number of problems of their own. Indeed, legged-robot research focuses on everything related to leg motion and coordination during robot navigation [1].

The difficulty in developing legged vehicles is mainly to coordinate the large number of degrees of freedom that should be triggered on a simple motion of the robot from a point *A* to point *B*. The precise coordination of walking movements, so that the resulting dynamic forces during navigation keep the robot in balance, is a big challenge. These restrictions can be overcome by modeling statically, the dynamic balance of forces resulting from the movement of the robot.

Collisions with obstacles or irregularities in the floor can destroy the robot balance and it can fall due to lack of additional points of support or by collision of one leg with some elevation. Robot navigation requires obstacles detection and avoidance, while guiding the robot to its goal. It must consider known and unknown, moving or fixed obstacles in the robot's path and the needing for detection and avoidance strategies.

To operate safely in public environments, many successful systems use sensor based modules for the collisions prevention, to control the mobile robot. The main control structure is feeling - react: the reading of the sensor is analyzed continuously to determine a free collision movement.

2 Problem Definition

A. *Legged Robots*

The effort to develop legged mobile robots have been conducted on several fronts including: the studies of locomotion and biomechanics of animals and insects with legs; the construction of models to represent the movement of animals and insects with legs; the construction of mathematical models of equilibrium for legged robots in order to simulate the models built for the animals and insects with legs; the design and build of robots, legs and devices for special applications, research in animal locomotion and validation of locomotion models; and the design and construction of energy efficient actuators and mobile robot legs, capable of displaying both reactivity and adaptability to their operating environment.

This work concerns with a strategy for overcome or avoid obstacles using only information from sensors installed on the feet to perceive the obstacle and manage an autonomous sequence of complex integrated movements to move across the obstacle or deviate from it, preserving the robot's balance and stability [2], [3]. The complex movements and tracking sequences in operational space are proposed to be built from the combination of a small group of simple movements sequenced according to the contact keys switching sequence

The obstacle overcoming problems addressed are transposition or bypass in regular and firm ground, using only information obtained from sensors installed on the robot's feet. The obstacles considered are the step up, step down, step close, and channel slope. The approach used can be expanded to other complex autonomous movements like stair climbing with a legged robot.

B. *The Guar Robot*

The four legged walking robot Guar [4], which is capable walking straight and curved paths and detecting and overcoming known obstacles and its four degree of freedom (DOF) leg kinematics are shown in Fig. 1.

The mapping of the foot coordinates from the operational space, during walking and obstacle overcoming, into joint space is done by inverted kinematics and the matrix of the gait being executed synchronizes each foot trajectory and body lateral movements in the leg's operational space and leg's inverse kinematics maps them in joint space. The control performs a model for determination of the position, with respect to a fixed reference system stated in the start of movement. The actual position is achieved by computing the movement of the robot from the commands of movement of the legs [5].

The foot stroke trajectory is a straight line, as it's desired that the robot body would be maintained in a horizontal plane. Other configurations can be constructed to walk inclined paths, maintaining the robot body horizontal, and walk a horizontal path, maintaining the robot body inclined.

A polygonal trajectory was implemented, as shown in Fig. 2, where leg's thrust is from right to left, the vertical distances are measured from leg's coordinate system origin and the dimensions are in millimeters. At taking off point, associated with the left inclined segment in the generated path (in blue), the foot is moved upward with

horizontal speed equal to the robot speed, and a more high vertical speed, until it leaves completely the ground. Then it's accelerated to achieve a higher horizontal speed and describes the superior three segments trajectory and at the end of the third superior segments, it begins the landing movement in the right inclined segment in the generated path. During landing, the horizontal speed is set to the robot's ongoing speed and the vertical speed is lowered, until the feet touch the ground.

C. Curved Paths

The curved path stroke is showed in Fig. 3. The curved path algorithm is a drivability strategy that allows the robot turning while walking, without losing equilibrium and stability. Curved paths are accomplished by the four legs which incremental differential strokes tangent to the robot curve and inclined to its longitudinal axis.

The stroke path is done by small straight line segments in the foot operational space, as shown in Eq. (1), where: θ is the curve angle; R_o and R_i are the foot outside and inside curve radius; λ_o e and λ_i are the stroke pitch for the legs outside and inside the curve; and L and W are length and width between legs reference systems.

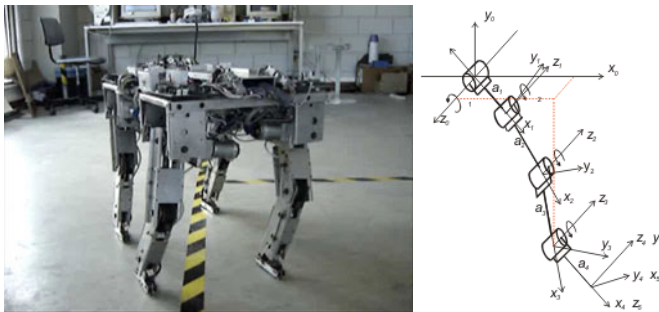


Fig. 1. Legged robot Guar4 turning left while walking (left); joints reference system (right)

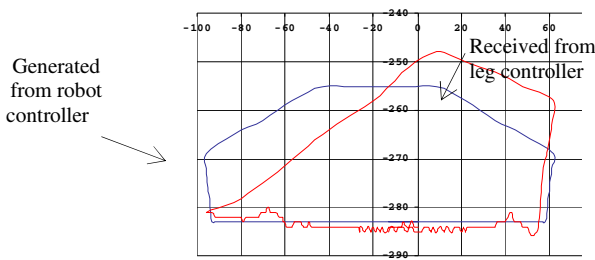


Fig. 2. Leg 3 joint 3: generated and received paths in saggital plane and operational space

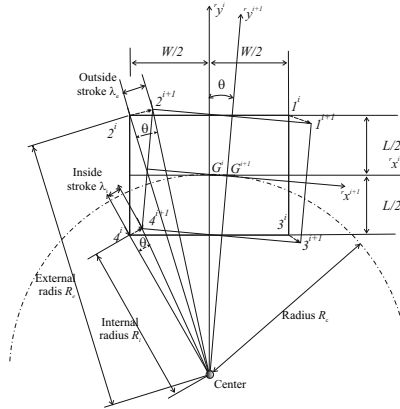


Fig. 3. Curved path stroke

$$\lambda_o = \theta * R_o = \theta \left[\left(R_o + \frac{W}{2} \right)^2 + \left(\frac{L}{2} \right)^2 \right]^{1/2}$$

$$\lambda_i = \theta * R_i = \theta \left[\left(R_o - \frac{W}{2} \right)^2 + \left(\frac{L}{2} \right)^2 \right]^{1/2}$$
(1)

As the straight path is also implemented through small straight line increments, to turn the robot in a curved path the only additional computational effort is to sum four 3×1 matrix with the small rectilinear segments that form the foot curved trajectory in foot's operational space to find the next foot position. The inverse kinematics then maps foot cartesian coordinates to leg joint coordinates.

D. Main Control Structure and Obstacles Detection and Overcoming

The main control cycle is showed in Fig. 4. The internal processes are: the *Collision Processing Unit* which manages the obstacle overcoming tasks; the *Gait Processing Unit* which manages the walking tasks; and a *Communication Unit* which manages the control system and robot's hardware communication.

The *Main* unit runs a fixed polling sequence process in the first processing level, checking all process branches and ends each control cycle running the *Communication Unit* processes.

The *Gait Processing Unit* process walking tasks for the incremental construction of the robot straight and curved paths, according to previous gait parameters set up.

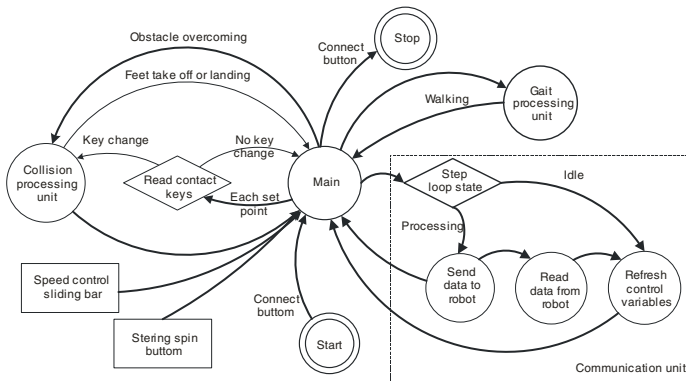


Fig. 4. Robot's main control cycle

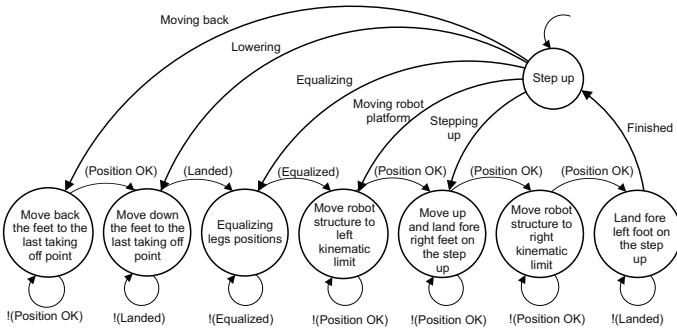


Fig. 5. Step up obstacle overcoming control cycle

The *Gait Processing Unit* process walking tasks for the incremental construction of the robot straight and curved paths, according to previous gait parameters set up.

The *Collision Process Unit* concerns with the overcome obstacles movement sequences and is fired by the main unit if the switching pattern switches to a known obstacle previously programmed. When a collision occurs, the main unit control cycle starts the collision unit and then all processes until the robot returns to its walking state is done within the collision unit. The actuator level performs direct joint control and contact keys data acquisition [6].

Small obstacle is difficult to be detected and having his position precisely established from vision or other stereo obstacle detecting systems thus needing to be treated locally by the robots legs and foot. This work presents a strategy for detecting and overcoming obstacles placed in the robot's foot trajectory using contact keys type collision sensors installed in the robot's feet. A scheme to detect obstacles in the robot legs path using proximity sensors, to improve the locomotion skill in complex environments, is also presented in [7]. In Fig. 6 it is shown the contact keys collision sensors installed on a Guara's feet. The contact keys lay out is to feel contact of the foot with horizontal and vertical surfaces. There are two double keys parallel connected horizontally installed on the front and on the back foot and two single keys

vertically installed on the front and on the back foot. In a collision, the system identifies the obstacle from the switch pattern and starts an integrated movement sequence to move the robot to transpose, or to turn aside the obstacle.

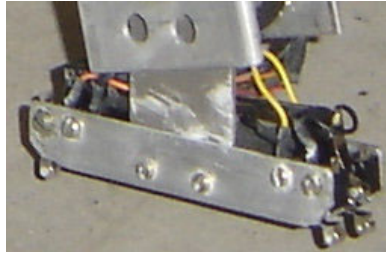


Fig. 6. Contact keys on the feet

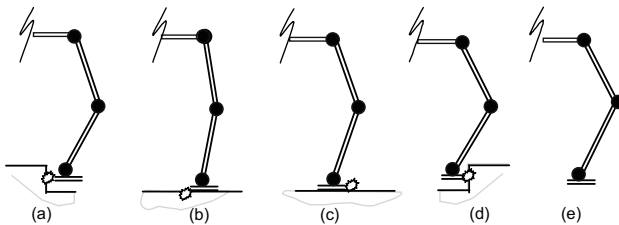


Fig. 7. Contact key switching patterns

In Fig. 7 it is shown the feet contact keys switching patterns. The keys can detect contact with: horizontal surfaces, Fig. 7 (b) pattern $[1011]$, and (c) pattern $[1101]$; vertical surfaces, Fig. 7 (a) pattern $[0111]$ and (d) pattern $[1110]$; and no contact pattern $[1111]$, Fig. 7 (e).

Contact switching occurs also in foot's taking off and landing events before and after its flight to a new stroke position, or when it's being moved during obstacle overcoming. The movement sequences studied were for the step up, step down, channel, step close, ramp and divert obstacles.

In Fig. 8 it is shown the main obstacle overcoming control cycle. Each obstacle has its own unique recognition key pattern and other obstacles patterns can be implemented.

In Fig. 5 it is shown the step up obstacle overcoming control cycle, which results are presented.

3 Results

In Fig. 9 the robot is showed turning right in a 90^0 corner with a radius of approximately 1.4 [m]. In Fig. 9 (a) the front right foot 2 is flying to a new stroke position. In Fig. 9 (b) the foot is landed, and the right rear foot 3 is flying, and it can be seen that the foot excursions a little to the center of the curve. In Fig. 9 (c) the robot is moving forward and

is being turned right as the front feet are being stroking from the center and the rear feet are being stroking out from the center of the curve. In Fig. 9 (c), (d) and (e) the outside legs 0 and 1 are then moved to a new stroke position.

Fig. 10 and Fig. 11 the robot is going up a step up in front of its walking path. The step is indefinitely placed and will only be perceived by the robot at the touch of one front feet key, which causes a state change in the feet key pattern. In Fig. 10 (a), the robot is walking, with right rear foot 3 flying to a new stroke position, and in Fig. 10 (b), the front right foot collides with the step up. In Fig. 10 (c), it's started a movement sequence that moves back and raises the right front feet 2 to its flight start position and moves the robot body left and back to its kinematic limits, before moving the foot 2 to the step up position.

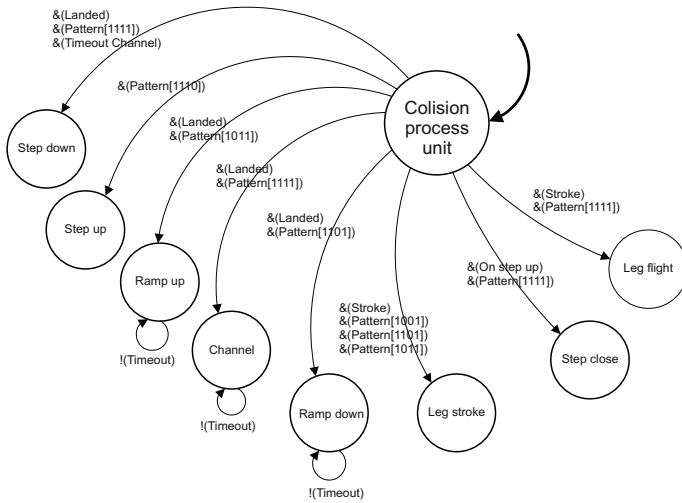


Fig. 8. Obstacle overcoming control cycle

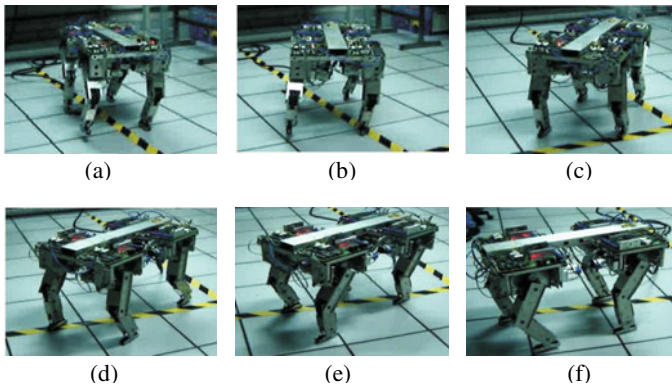


Fig. 9. Robot turning right in a 90° corner

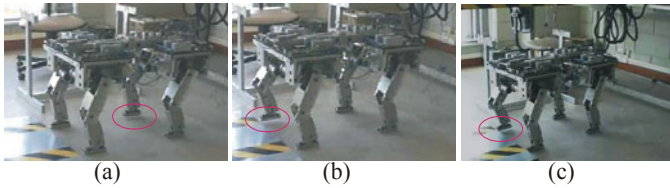


Fig. 10. Gait showing the on flight collision of the foot 2 on the first run

To overcome obstacles the proposed approach uses only the feet contact keys information and perform a sequence of movements to move the robot to overcome the obstacle, or deviate from it, preserving its balance and stability. To start overcoming any obstacle, before any leg aerial movement is done, the robot is moved to a know position that ensures the highest stability margin with the other legs that will remain in support.

In Fig. 11 (a) the front right foot 2 is being moved to the step up position. In Fig. 11 (b) the front right foot 2 is already in the step up position and starts moving the robot body to the right kinematic limit before moving the front left foot 0 to the step up position. In Fig. 11 (c) the front left foot 0 is being moved up to the step up surface and in Fig. 11 (d) the front left foot 0 is landed in the step up surface and the robot starts walking with the front feet 0 and 2 on the step upper surface and the back feet 1 and 3 in the step lower surface.

In Fig. 12(a) the robot is walking and leg 3 collides with the step and the same sequence done for the front 0 and 2 feet is repeated for the rear 1 and 3 feet. In Fig. 12(b) the right rear foot 3 is moved back and raised to its flight start position. the robot is being moved forward and to the left kinematic limit before the lifting of the rear right foot 3 to the step up. In Fig. 12 (c) the rear right foot 3 is landed in the step up, and the robot is being moved forward and to the right kinematic limit.

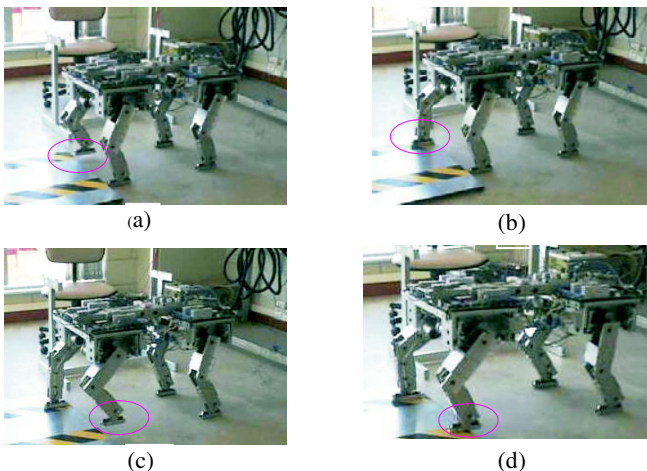


Fig. 11. Front feet going up a step

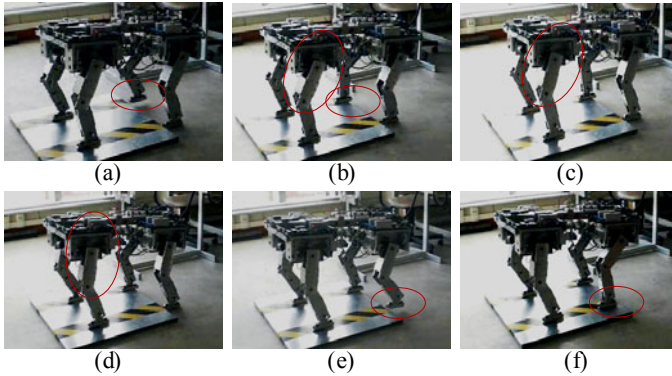


Fig. 12. Positioning the rear legs on the step up to restart walking

In Fig. 12 (d) the robot is still being moved forward and laterally to the right kinematic limit, before the lifting of the rear left foot l to the step up position. In Fig. 12 (e) the robot is lifting up the rear left foot l , which is landed in step up position in Fig. 12 (d). The task of lifting the entire robot to the step up surface is completed with the rear left foot 3 supporting in the upper step.

4 Conclusions and Future Work

The method used to address the problem of obstacle overcoming was to divide a complex movement task in a group of simple movements implemented in a known sequence that ensures robot stability, rather than develop a complex model to search a generic solution for the problem.

The main characteristic of this approach is that it allows the solution space dimension reduction and that it has no limits, being able to implement complex tasks such as going up in a stairs. The limits are the robot's leg's kinematic limits, which are very closed in the Guar robot.

Robots with stronger actuators and wider kinematic limits could support the implementation of libraries of obstacles, associated with the work environment of low speed robots. It could be seen that that, according to obstacle shape and dimensions acquired from contact keys and to the robot kinematic limits, sets of simple movements are combined to overcome the obstacle giving navigation skill and autonomy to the legged robot in an environment with known obstacles.

References

1. Garcia, E., Jimenez, M.A., De Santos, P.G., Armada, M.: The evolution of robotics research. *IEEE Robotics & Automation Magazine* 14(1), 90–103 (2007)
2. Amaral, P., Pinto, B.: A four legged walking robot with obstacle overcoming capabilities. In: *2010 3rd Conference on Human System Interactions (HSI)*, pp. 374–379 (2010)

3. Lima, L.E.M., Amaral, P.F.S., Antônio Filho, B.: Controle Da Estabilidade De Equilíbrio Para Um Robô Quadrúpede Com Uso De Lógica Nebulosa
4. Bento Filho, A.: Modelagem, Controle de Andadura e transposição de obstáculos de um robô quadrúpede com quatro graus de liberdade em cada perna
5. Filho, A.B., Amaral, P.F.S., Pinto, B.G.M., Lima, L.E.M.: Uma Metodologia Para a Localização Aproximada De Um Robô Quadrúpede
6. Lima, L.E.: Uma arquitetura de controle distribuído para um robô móvel quadrúpede com uso do barramento CAN
7. Hiroshi, I., Masayoshi, K.: Local obstacle recognition for a quadruped robot by distance sensors. In: Proceedings of 2003 IEEE International Conference on Robotics, Intelligent Systems and Signal Processing, vol. 1, pp. 501–506 (2003)

Hallucinating Face by Sparse Representation

Xue Cuihong, Yu Ming, Jia Chao, and Yan Gang

Hebei University of Technology, Tianjin, 300401
xuecuihong@scse.hebut.edu.cn

Abstract. A novel face hallucination method is proposed in this paper for the reconstruction of a high-resolution face image from Sparse Representation. By joint training two dictionaries for the low-and high-resolution image patches, the method efficiently builds sparse association between high-frequency components of HR image patches and LR image feature patches, and defines the association as a prior knowledge. Using MAP criteria to guide super-resolution reconstruction with respect to their own dictionaries. The learned Dictionary pair is a more compact representation of the patch pairs, reducing the computational cost substantially. Experiments show that the proposed method generates higher-quality images and costs less computational time than some recent face image super-resolution (hallucination) techniques, and achieves much better results than many state-of-the-art algorithms in terms of both PSNR and visual perception.

Keywords: Face hallucination, Super-resolution, Sparse Representation, MAP.

1 Introduction

Super-resolution predicts an image's high-resolution part from its low-resolution one, which is an inverse problem. In this paper we are concerned with learning-based [1–7] techniques' application in faces, which can be called face hallucination [1].

There are some learning-based super-resolution algorithms. Freeman et al. [3,4] propose an example-based approach to generic images where the LR to HR prediction is learned via a Markov networks. Image analogies [5] are based on a multi-scale auto-regression. Sun et al. [7] construct primal sketch priors to enhance the HR image. The above algorithms are only applied to generic images, rather than face images. Baker and Kanade [1,2] propose a face hallucination algorithm to learn a prior on the spatial distribution of the image gradient for frontal face images, and use Bayesian MAP theory to hallucinate the high-resolution face image from the low-resolution one. The results are better than the above three algorithms, but appear noisy at places. Liu et al. [6] develop a two-step statistical modeling approach that integrates both a global parametric model by PCA and a local nonparametric patch model by Markov networks. The resulting face images are smoother than Baker's and can retain global features well; Although the algorithm leads to good results, however the PCA model tends to lead to the results appear like the mean face and the local patch model is complicated and computationally demanding.

This paper focus on the above problem, in order to recover the SR face image from the given LR face image computational time saving and efficiently, this paper

presents a novel face hallucination method via sparse representation. The method can effectively build sparse association between high- and low-resolution image patches, which improves not only flexibility, but also demonstrates both effectiveness and robustness in regularizing the inverse problem.

2 Sparse Representation and Sparse Dictionary Learning

2.1 Sparse Representation

In order to search for the sparse representation, using an over-complete dictionary matrix $D \in R^{N \times L}$ that contains L prototype signal-atoms for columns, $D = \{d_j\}_{j=1}^L$, a signal $X \in R^N$ can be represented as a sparse linear combination of these atoms. The representation of X can be expressed as:

$$\min_{\alpha} \|\alpha\|_0, \text{ s.t. } x = D\alpha . \quad (1)$$

The vector $\alpha \in R^L$ contains the representation coefficients of the signal x . The function $\|\bullet\|_0$ represents the l_0 -norm, counts the non-zero entries. The Sparse Approximation is as follow:

$$\min_{\alpha} \|\alpha\|_0, \text{ s.t. } \|x - D\alpha\| \leq \varepsilon . \quad (2)$$

For super-resolution, the sparse vector α can be found by

$$\bar{\alpha} = \arg \min \{ \|x - D\alpha\|_2^2 + \lambda \|\alpha\|_0 \} . \quad (3)$$

Once $\bar{\alpha}$ is obtained, x can be estimated as $\bar{x} = D\bar{\alpha}$, l_0 -minimization is an NP-hard combinatorial search problem, is usually solved by greedy algorithms. The l_1 -minimization, as the closest convex function to l_0 -minimization, is used to solving the sparse coding problem:

$$\bar{\alpha} = \arg \min \{ \|x - D\alpha\|_2^2 + \lambda \|\alpha\|_1 \} . \quad (4)$$

The l_1 -norm sparsity regularization term can lead to better SR results. Recently sparse representation has been successfully applied to many other related inverse problem in image processing, such as denoising [8] and super-resolution, often improving on the state-of-the-art.

2.2 Dictionary Training

This paper uses the method which joint training the D_h and D_l dictionary for the HR and LR patches. Given the sampled training image patch pairs $P = \{X^h, Y^l\}$, where $X^h = \{x_1, x_2, \dots, x_n\}$ are the set of sampled high-resolution image patches and are the corresponding low-resolution image patches (or features), our goal is to learn dictionaries

for high-resolution and low-resolution image patches, so that the sparse representation of the high-resolution patch is the same as the sparse representation of the corresponding low-resolution patch. We force the high-resolution and low-resolution representations to share the same codes.

$$\min_{\{D_h, D_l, Z\}} \frac{1}{N} \|X^h - D_h Z\|_2^2 + \frac{1}{M} \|Y^l - D_l Z\|_2^2 + \lambda \left(\frac{1}{N} + \frac{1}{M}\right) \|Z\|_1 . \tag{5}$$

Where N and M are the dimensions of the high-resolution and low-resolution image patches in vector form. Here, (5) can be rewritten as

$$\min_{\{D_h, D_l, Z\}} \|X_c - D_c Z\|_2^2 + \bar{\lambda} \|Z\|_1 . \tag{6}$$

Where $X_c = \left[\frac{1}{\sqrt{N}} X^h, \frac{1}{\sqrt{M}} Y^l \right]^T$, $D_c = \left[\frac{1}{\sqrt{N}} D_h, \frac{1}{\sqrt{M}} D_l \right]^T$, $\bar{\lambda} = \lambda \left(\frac{1}{N} + \frac{1}{M}\right)$, We apply sparse K-SVD algorithm[9] to jointly train the D_h and D_l dictionary.

3 Hallucination Face via Sparse Representation

Super-resolution (SR) aims to reconstruct a high quality image x from its degraded measurement y . SR is a typical ill-posed inverse problem [1] and it can be generally modeled as:

$$Y = DHX . \tag{7}$$

Where D is a down sampling operator, H represents a blurring filter. X and Y denote the high-resolution and low-resolution faces. By using the sparse prior (2)(4), one can find the sparse representation by combine the high- and low-resolution patch, respecting spatial compatibility between neighbors using a high-pass algorithm[10] . The resulting optimization problem is:

$$\min_{\alpha} \|\bar{D}\alpha - \bar{y}\|_2^2 + \lambda \|\alpha\|_1 . \tag{8}$$

Where $\bar{D} = \begin{bmatrix} FD_l \\ \beta PD_h \end{bmatrix}$ and $\bar{y} = \begin{bmatrix} Fy \\ \beta w \end{bmatrix}$, β controls the tradeoff between matching the

LR input and finding a HR patch that is compatible with its neighbors. F can be an identity matrix or a (linear) feature extraction operator by using a high-pass filter [11,12], the method is first- and second-order gradients of the patch as representation, the four 1-D filters used to extract the derivatives are $f_1 = [-1, 0, 1]$, $f_2 = f_1^T$, $f_3 = [1, 0, -2, 0, 1]$, $f_4 = f_3^T$. matrix P extracts the region of overlap between current target patch and previously reconstructed HR image, and w contains the values of the previously reconstructed HR image on the overlap. For (7)(8), this optimization problem can be solved as maximum a posteriori (MAP) criteria:

$$X^* = \arg \max_x p(Y | X)p(X) . \tag{9}$$

$p(Y | X)$ is the image observation process, with the additive Gaussian white noise of standard deviation σ , $p(X)$ is a prior on the X

$$p(Y | X) = \frac{1}{\sigma\sqrt{2\pi}} \exp\left(-\frac{\|DHX - Y\|_2^2}{2\sigma^2}\right) . \tag{10}$$

$$p(X) = \exp(-c\rho(X)) . \tag{11}$$

The SR problem in (8) can be formulated using the reconstruction constraints as follow through (9)(10)(11):

$$X^* = \arg \min \|DHX - Y\|_2^2 + \lambda\rho(X) . \tag{12}$$

λ is a parameter used to balance the reconstruction fidelity and penalty of the prior term, $\rho(X)$ is a prior term regularizing the high-resolution solution. In this paper let F represents a matrix performing high-pass filtering. The (12) is changed to follows:

$$X^* = \arg \min_x \|DHX - Y\|_2^2 + \lambda\rho(FX) . \tag{13}$$

Details of Hallucination Face algorithm by sparse representation are shown:

- 1) Task: estimate HR image X^*
- 2) Input: training dictionaries D_h and D_l , a LR aligned face image Y .
- 3) Find a smooth HR face \tilde{X} through solving the optimization problem in (13)

$$\tilde{X} = \arg \min_x \|DHX - Y\|_2^2 + \lambda\rho(FX)$$
- 4) For each 3×3 patch y of \tilde{X} , from the left to right, and top to bottom, keeping one pixel overlap in each direction,
 - ① Compute and record the mean pixel value of y as m .
 - ② Solve the optimization problem with \bar{D} and \bar{y} defined in (8)

$$\min_{\alpha} \|\bar{D}\alpha - \bar{y}\|_2^2 + \lambda\|\alpha\|_1$$
 - ③ Generate the HR patch $x = D_h\alpha^* + m$. Put the patch x into a HR image X^* .
- 5) Output: SR face X^* .

4 Experimental Results

We use frontal face images in the FERET [13] face database as sources of our test face images, We select 100 face images(14 females and 30 males) as the training set, one person may have different facial features images. So we need to align the face images

and adjust each image into 96×128 pixel image. The low-resolution face images (24×32) are obtained from high-resolution face images through a smoothing and down-sampling procedure. 3×3 LR image patches are adopted, with one pixel overlap region with adjacent patches, and corresponding 9×9 HR image patches have 3 pixels overlap. We take 50000 patch pairs from training image and learn the sparse dictionary which is fixed as 1024.

This paper can achieves much better results than many state-of-the-art algorithms in terms of both PSNR and visual perception.

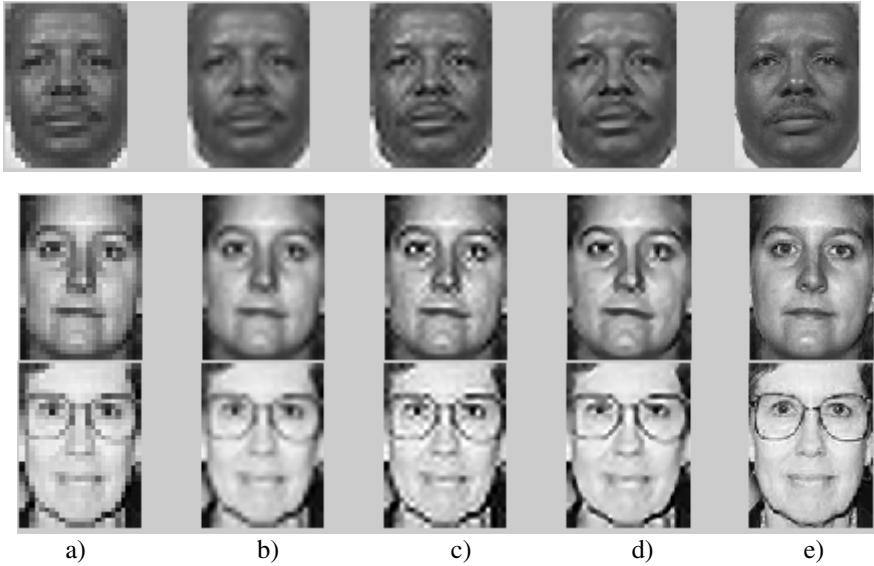


Fig. 1. Visual comparison results (a)low-resolution b) Bicubic Interpolation c)example-based method d)paper's method e)original image)

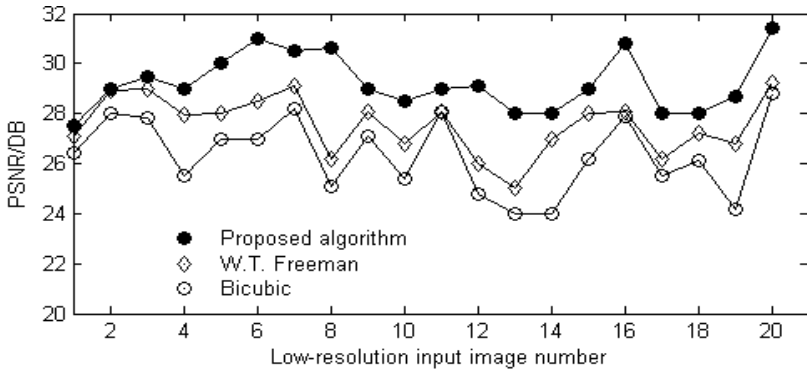


Fig. 2. PSNR comparison results

5 Conclusion

In this paper we present a novel Hallucinating face based on learning the sparse association between image patches. The proposed method searches for suitable representative example patches using a sparse association search algorithm by jointly trained the coupled dictionaries from high- and low-resolution image patch pairs. Comparing to existing approaches, this method perform better visual effect, and less time consuming.

References

1. Baker, S., Kanade, T.: Hallucinating faces. In: Proceedings of the IEEE International Conference on Automatic Face and Gesture Recognition, Grenoble, France, pp. 83–88 (2000)
2. Baker, S., Kanade, T.: Limits on super-resolution and how to break them. *IEEE Trans. Pattern Anal. Mach. Intell.* 24(9), 1167–1183 (2002)
3. Freeman, W.T., Pasztor, E.C.: Learning low-level vision. In: Proc. ICCV 1999, Kerkyra, Greece, pp. 1182–1189 (1999)
4. Freeman, W.T., Jones, T.R., Pasztor, E.C.: Example-based super resolution. *IEEE Computer Graphics and Applications* 22(2), 56–65 (2002)
5. Hertzmann, A., Jacobs, C.E., Oliver, N., Curless, B., Sales, D.H.: Image analogies. In: Proceedings of SIGGRAPH 2001, Los Angeles, California, pp. 327–340 (2001)
6. Liu, C., Shum, H.Y., Zhang, C.S.: A two-step approach to hallucinating faces: global parametric model and local nonparametric model. In: Proceedings of CVPR 2001, Kauai Marriott, Hawaii, pp. 192–198 (2001)
7. Sun, J., Zheng, N.N., Tao, H., Shum, H.Y.: Image hallucination with primal sketch priors. In: Proceedings of CVPR 2003, Madison, Wisconsin, pp. 729–736 (2003)
8. Lee, C., Eden, M., Unser, M.: High-quality image resizing using oblique projection operators. *IEEE Trans. Image Process.* 7(5), 679–692 (1998)
9. Li, M., Cheng, J., Le, X., Luo, H.-M.: Super-resolution Reconstruction Based on Improved Sparse Codin. *J. Opto-Electronic Engineering* 38(1), 127–133 (2011)
10. Mairal, J., Sapiro, G., Elad, M.: Learning multiscale sparse representations for image and video restoration. *J. SIAM Multiscale Modeling and Simulation* 7(1), 214–241 (2008)
11. Li, X., Orchard, M.T.: New edge-directed interpolation. *IEEE Trans. Image Process.* 10(10), 1521–1527 (2001)
12. Yang, J.C., Wright, J., Huang, T., et al.: Image Super-Resolution via Sparse Representation. *IEEE Trans. Image Processing* 19(11), 2861–2873 (2010)
13. Phillips, P.J., Moon, H., Rizvi, S., Rauss, P.J.: The FERET evaluation methodology for facere cognition algorithms. *IEEE Trans. Pattern Anal.* 22(10), 1090–1104 (2000)

Author Index

- Ahn, Jung-Hwan 369
Al-attar, Fatma Abdalnabi 81
Al-Khalidy, Mohammed Majid Mohammed 81
Amaral, Paulo Faria S. 799
- Bao, Yue 139, 155, 163, 171, 179
Biswas, Pradipta Vaskar 369
- Cai, Jianping 261
Cao, Jianzhong 117
Cao, Yingyu 51
Chao, Jia 809
Chen, Bo 31
Chen, Jianyong 473
Chen, Lei 633
Chen, Lin 213
Chen, Yadong 537, 699
Chen, Zhe 655, 663
Chen, Zhi 43
Chen, Zhijia 719
Chen, Zhiliang 147
Ciobotaru, Ticușor 73
- Deng, Shuangcheng 51
Deng, Zhongting 313
Ding, Lixun 397
Ding, Zuohua 713
Dong, Xue-ren 579
- Feng, Jianguo 431
Filaretov, Vladimir 347
Filho, Antonio Bento 799
- Gang, Yan 809
Gao, Chang-yuan 43
- Gao, Xiaohui 411
Gong, Wei 93
Grigore, Lucian 73
Gu, Fei 139, 155, 163, 171, 179
Gubankov, Anton 347
Guo, Hai-chun 25
Guo, Jing 529, 549, 557, 573
Guo, Jinling 793
Guo, Qiuping 193
Guo, Wei 389, 465
Guo, Xiao Feng 691
Guo, Yiwei 515, 523, 529
- Haga, Tashuya 163
Han, Jia 515
Han, Junwei 241, 283
Hao, Ying-ji 329
Hashimoto, Masaya 171
He, Bingwei 321
He, Ming-ye 329
Hou, Honglu 743
Hou, Yunhai 727
Huang, Dingjin 743
Huang, Dongwu 771
Huang, Guorong 491
Huang, Xiaogang 205
Huang, Yuan 757, 765
Huo, Juan 301
Huo, Meimei 261
Hwang, Kyung-Hwan 369
- Ileri, Recep 73
- Jiang, Fengling 227
Jiang, Lipei 51

- Jiang, Mingyue 713
 Jiang, Shanshan 257
 Jiang, Yuanbin 565
 Jiménez-Ramírez, Omar 707
 Jin, Guo-feng 361
 Jun, Chen 293

 Kan, Yong-Zhi 187
 Kang, Dong-Bae 369
 Khan, M. Waqas 31
 Kim, Hyung-Sun 615, 625
 Kong, Deqing 507
 Kong, Heon-Taek 625
 Kwon, Sookyoung 641

 Le, Trung 67
 Lee, Se-Yun 369
 Lei, Yu Long 423, 427
 Li, Boyang 397
 Li, Chengying 235
 Li, Diyang 397
 Li, Ershuai 727
 Li, GuiHua 431
 Li, Hongwei 757, 765
 Li, Hu 537, 699
 Li, Jing-zhao 251
 Li, Jun 719
 Li, Kai 779
 Li, Meng 147
 Li, Ran 557, 573
 Li, Xiangbao 751
 Li, Xiaoping 9
 Li, Xin 419, 663
 Li, Xing-hua 671
 Li, Xingzhong 427
 Li, Yunhua 51
 Li, Zhenyu 473
 Liang, Yuan-ning 655, 663
 Lim, Jae-Hyun 615, 625, 641
 Lin, Dongyi 321
 Liu, Binghan 677
 Liu, Feng-nan 579
 Liu, Haiwei 351
 Liu, Jianbao 453
 Liu, Jian Xun 227
 Liu, Shuai 213
 Liu, Wenbin 751
 Liu, Wenting 515
 Liu, Xianqun 227
 Liu, Yang 131

 Liu, Yi 771
 Liu, Yue 147
 Liu, Zhenjie 423, 427
 Lu, Jiangang 1
 Lu, Qiushi 31
 Lu, Shengli 147
 Lu, Tien 67
 Luo, Weizhong 751

 Ma, Guo-hong 649
 Ma, Yu-zhen 579
 Mao, Xuming 543
 Miglio Pinto, Benedito G. 799
 Ming, Yu 809
 Murray, Alan 301

 Neculăescu, Cristian 73
 Nguyen, Khang 67

 Pan, Lei 93

 Qi, Bin 139
 Qi, Zengkun 483
 Qin, Xingjun 537
 Qin, Xinxin 453
 Qing, Jia 649
 Quiroz-Juárez, Mario A. 707

 Ren, Gong-chang 25
 Ren, Hong-e 381
 Rong, Hua 785

 Sha, Yi 403
 Shao, Jie 473
 Shao, Keyong 607
 Shen, Gang 241, 283
 Shen, Haitao 403
 Shen, Lincheng 337
 Shen, Wei 199
 Shen, Zhan 221
 Shi, Fulian 523, 549, 557, 565, 573
 Shi, Wenyu 313
 Shi, Xuhua 305
 Shi, Yan 9
 Shimoyama, Akinobu 179
 Shing, Chen-Chi 111
 Shing, Marn-Ling 111
 Shuang, Feng 351
 Soloi, Anton 73
 Song, Yuan-jia 361
 Song, Yugui 587

- Sun, Da-jun 125
 Sun, Shihua 727
 Sun, Shuying 719
 Sun, Xia 251
 Sun, Youxian 1
 Sun, Yu 733

 Tan, Wen 227
 Tang, Linao 117
 Tang, Yao 117
 Tian, Cunzhi 193
 Tian, Hao 39
 Tian, Liguo 147
 Tian, Miaomiao 607
 Tian, Peng 275
 Tian, Shi-hai 43
 Tran, Nuong 67

 Umeda, Yusuke 155

 Vázquez-Medina, Rubén 707
 Vînturiş, Valentin 73

 Wang, Beibei 93
 Wang, Cong 649
 Wang, Gang 337
 Wang, Guohui 587
 Wang, Guo-wei 361
 Wang, Haijun 193
 Wang, Hang 537
 Wang, Hua 117
 Wang, Huanbao 59
 Wang, Hui 579
 Wang, Jian 779
 Wang, Juan 411
 Wang, Junzheng 199
 Wang, Qian 313
 Wang, Qinruo 267
 Wang, Ruhua 543
 Wang, ShuangShuang 275
 Wang, Wanshan 537, 699
 Wang, Wei 685
 Wang, Weizhi 677
 Wang, Wenbo 587
 Wang, Wenjiang 543
 Wang, Yaoxiong 351
 Wang, Ying 221, 685, 691
 Wang, Zhen 447
 Wang, Zhong 213
 Wen, Jian-Ping 465

 Wen, Jie Tao 423, 427
 Wu, Daiwen 593
 Wu, Feng 227
 Wu, Haifeng 313
 Wu, Haoyi 267
 Wu, Jianzhong 261
 Wu, Minghui 261
 Wu, Nan 633
 Wu, Qingyu 607
 Wu, Siliang 599
 Wu, Wenzheng 537
 Wu, Zhizong 473

 Xia, Heng 213
 Xia, Huan 205
 Xiang, Zhongzheng 549
 Xiao, Ying 9
 Xiao, Yongliang 751
 Xie, Li-jun 655
 Xie, Zhengyi 103
 Xiong, Jianbin 267
 Xu, Guangju 213
 Xu, Hui 251
 Xu, Qian 31
 Xu, Yayi 491
 Xu, Zunyi 771
 Xue, Cuihong 809
 Xue, Hongjun 543
 Xue, JinLin 495
 Xue, Qiong 257

 Yan, Wei 381
 Yang, Cai-xia 43
 Yang, Gelan 751
 Yang, Qinmin 1
 Yang, Xiao-wei 579
 Yang, Yong 25
 Yang, Zheng-wei 361
 Yang, Zhi-wei 25
 Yang, Zhonglin 453
 Yao, Hong 663
 Yasin, Awais 31
 Ye, Baoyu 267
 Ye, Zhengmao 241, 283
 Yin, Jianchuan 17
 Yin, Liyi 241
 Yin, Zhi-xiang 251
 Yong, Han 423
 Yu, Tianbiao 699
 Yu, Yang 329
 Yuan, Min-ying 125

- Zeng, Hua Bing 423, 427
Zhang, Daibing 337
Zhang, Dan 235
Zhang, Fugang 257
Zhang, Guojun 599
Zhang, Hong 103
Zhang, Jinghong 267
Zhang, Junwen 51
Zhang, Liping 431
Zhang, Pingdan 529
Zhang, Pu 757, 765
Zhang, Qin 205
Zhang, Tao 743
Zhang, Wei 361
Zhang, Wenfang 743
Zhang, Xu 523, 565
Zhang, Yan 549, 557
Zhang, Yifeng 213
Zhang, YuNan 275
Zhang, Yunqiu 397
Zhang, Zhenwei 543
Zhang, Zhiguang 699
Zhao, Jinsong 283
Zhao, Junwei 543
Zhao, Shuanfeng 389
Zhao, Xiangyu 411
Zhao, YuHui 275
Zhao, Zhan 491
Zheng, Binhui 1
Zheng, Xijian 103
Zhou, Guangtao 779
Zhu, Jingfu 419
Zhu, Lichun 403
Zhu, Ming 447
Zhu, Ning 389
Zhu, Shaoping 751
Zhu, Xinying 507
Zhu, Yunfeng 439
Zhu, Zhi-qiang 655
Zou, Zaojian 17